



Conference Proceedings of the 4th European sCO2 Conference 2021

Online Conference

Date: 23rd + 24th March, 2021

Conference Committee

Dieter Brillert, Universität Duisburg-Essen, Chair of Turbomachinery (conference chair)
Giuseppe Bianchi, Institute of Energy Futures, Brunel University London
Albannie Cagnac, EDF R&D, Fluid Dynamics, Power Generation and Environment Department
Václav Dostál, Czech Technical University in Prague
Uwe Gampe, Technische Universität Dresden, Chair of Thermal Power Machinery and Plants
Otakar Frýbort, Research Centre Řež, Energy Technology Department
Markus Haider, Technical University of Vienna, Institute for Energy Systems and Thermodynamics
Martin Rohde, Technical University of Delft, Department of Radiation Science & Technology
Jörg Starflinger, University of Stuttgart, Institute of Nuclear Technology and Energy Systems (IKE)
Teemu Turunen-Saaresti, LUT University, School of Energy Systems
Andreas Werner, Technical University of Vienna, Institute for Energy Systems and Thermodynamics

Imprint

Conference Proceedings of the 4th European sCO₂ Conference

ISSN 2510-7852

DOI 10.17185/dupublico/73942

URN: urn:nbn:de:hbz:464-20210330-130134-5

DuEPublico, Duisburg-Essen Publications Online
Universität Duisburg-Essen
<https://duepublico2.uni-due.de>

2021



This work may be used under a [Creative Commons Attribution 4.0 International license](https://creativecommons.org/licenses/by/4.0/).

Agenda - March 23

09:00 – 09:15

Introduction

Dieter Brillert (Speaker) University of Duisburg-Essen / UDE

09:15 – 09:45

Keynote Speech

Angelos Kokkinos (Speaker) Director of the Office of Advanced Fossil Technology Systems, U.S. Department of Energy

09:45 – 10:15

Coffee break 1

10:15 – 12:15

Turbomachines and Cycles - Session 1

Giuseppe Bianchi (Speaker) Brunel University London - Institute of Energy Futures

Subsessions

- **Numerical Analysis of a Centrifugal Compressor Operating With Supercritical CO₂**
Renan Emre Karaefe; Pascal Post; Marwick Sembritzky; Andreas Schramm; Matthias Kunick; Uwe Gampe; Francesca di Mare
- **Operational Analysis of a Self-Propelling Heat Removal System Using Supercritical CO₂ with ATHLET**
Markus Andreas Hofer; Michael Buck; Jörg Starflinger
- **Design considerations of sCO₂ turbines developed within the CARBOSOLA project**
Stefan Glos; Patrik Rene Lippe; Simon Kobler; Michael Wechsung
- **Simulation and Analysis of a Self-Propelling Heat Removal System Using Supercritical CO₂ at Different Ambient Temperatures**
Markus Hofer; Haikun Ren; Frieder Hecker; Michael Buck; Dieter Brillert; Jörg Starflinger

10:15 – 12:15

sCO₂ Applications and Energy Systems - Session 1

Andreas Werner (Speaker) Researcher, TU Wien, Institute for Energy Systems and Thermodynamics

Subsessions

- **Transient Analysis of the Super-critical Carbon Dioxide Cycle Coupled to Pressurized Water Reactor for Nuclear Powered Ships**
Jeong Yeol Baek; Jae Jun Lee; Jeong Ik Lee
- **The Development of a New Chemical Kinetic Mechanism for Combustion in Supercritical Carbon Dioxide**
James Michael Harman-Thomas; Kevin Hughes; Mohamed Pourkashanian
- **sCO₂ power cycle design without heat source limitations: Solar thermal particle technology in the CARBOSOLA project**
Lukas Heller; Stefan Glos; Reiner Buck
- **Analysis of sCO₂ Cycles for District Heating Applications**
Mathias Penkuhn; George Tsatsaronis

12:15 – 13:15

Lunch 1

13:15 – 15:15

sCO₂ Experiments and Loops - Session 1

Václav Dostál (Speaker) Czech Technical University in Prague - Energy Engineering

Subsessions

- **Closed-Loop Supercritical Carbon Dioxide Wind Tunnel: Design and Components**
Giuseppe Petruccelli; Antti Uusitalo; Aki Grönman; Teemu Turunen-Saaresti; Marta Zocca
- **Experimental investigations on the heat transfer characteristics of supercritical CO₂ in heated horizontal pipes**
Konstantinos Theologou; Rainer Mertz; Eckart Laurien; Jörg Starflinger
- **Sofia – sCO₂ facility for Supercritical Brayton Cycle Research**
Otakar Frybort; Karel Dockal; Petr Hajek; Tomas Melichar; Petr Vlcek; Vilem Hanzal; Petr Hajek; Antonin Zivny; Marek Paty; Ales Macalka; Miroslav Kapic
- **Design and Specification of a 10MW-Class sCO₂ Compressor Test Facility**
Jeongseek Kang; Alexander Vorobiev; Joshua Cameron; Scott Morris; Ryan Wackerly; Kyle Sedlacko; Jason Miller; Timothy Held

13:15 – 15:15

sCO₂ Applications and Energy Systems - Session 2

Andreas Werner (Speaker) Researcher, TU Wien, Institute for Energy Systems and Thermodynamics

Subsessions

- **Environmental assessment of a 25 MWe fossil fired supercritical CO₂ cycle**
Victor Maquart; Benoit Valentin; Albannie Cagnac
- **Greening a Cement Plant Using sCO₂ Power Cycle**
Ladislav Vesely; Prabu Thangavel; S. Gopinathan; Frybort Otakar; Ganesan Subbaraman; Jayanta Kapat
- **sCO₂ Power Cycle Development and STEP Demo Pilot Project**
Brian Lariviere; Scott Macadam; Michael McDowell; Markus Lesemann; John Marion
- **Adiabatic Compressed CO₂ Energy Storage**
Matteo Manzoni; Alberto Patti; Simone Maccarini; Alberto Traverso

15:15 – 15:30

Keynote Speech Q&A

Dieter Brillert (Speaker)

15:30 – 16:00

Coffee Break 2

16:00 – 17:30

Heat Exchanger and Transfer - Session 1

Martin Rohde (Speaker) Associate Professor,
Technische Universiteit Delft

Subsessions

- **Characterizing and modelling turbulence in supercritical fluids**
Rene Pecnik; Jie Ren; Gustavo Otero Rodriguez
- **Numerical dimensioning of a pre-cooler for sCO₂ power cycles to utilize industrial waste heat**
Sebastian Unger; Jonas Müller; Malini Bangalore Mohankumar; Sebastian Rath; Uwe Hampel
- **Conceptual Design, Optimisation and Qualification of Highly Efficient Brazed Plates and Fins Heat Exchangers for Heat Removal sCO₂ Brayton Cycle to Increase the Safety of Nuclear Power Plants**
Sarah Tioual-Demange; Vivien Voirin; Markus Hofer; Frieder Hecker; Michael Buck; Jörg Starflinger

16:00 – 17:30

Fluid and Material Aspects - Session 1

Uwe Gampe (Speaker) Technische Universität Dresden

Subsessions

- **Study of the Influence of Additives to CO₂ on Performance Parameters of a sCO₂-Cycle**
Sebastian Rath; Erik Mickoleit; Cornelia Breilkopf; Uwe Gampe; Andreas Jäger
- **Thermal efficiency gains enabled by using supercritical CO₂ mixtures in Concentrated Solar Power applications**
Francesco Crespi; Pablo Rodríguez-de Arriba; David Sánchez; Abubakr Ayub; Gioele Di Marcoberardino; Costante Invernizzi; Gonzalo S. Martínez; Paolo Iora; Daniele Di Bona; Marco Binotti; Giampaolo Manzolini
- **Investigation of material degradation and coolant chemistry for sCO₂ power cycles**
Jan Berka; Tomas Hlincik; Eliska Purkarova; Alice Vagenknechtova; Lucia Rozumova

Agenda - March 24

09:00 – 10:30

Turbomachines and Cycles - Session 2

Teemu Turunen-Saaresti (Speaker) Lappeenranta University of Technology

Subsessions

- **An Attempt for Establishing Pressure Ratio Performance Maps for Supercritical Carbon Dioxide Compressors in Power Applications**
Ihab Abd El Hussein; Sebastian Schuster; Dieter Brillert
- **Numerical Investigation Of A Simple Regenerative Heat To Power System With Coupled Or Independent Turbomachinery Drives**
Matteo Marchionni; Giuseppe Bianchi; Muhammad Usman; Apostolos Pesyridis; Savvas Tassou
- **Effect of the ambient temperature on the performance of small size sCO₂ based pulverized coal power plants**
Dario Alfani; Marco Astolfi; Marco Binotti; Paolo Silva

09:00 – 10:30

Turbomachines and Cycles & Fluid and Material Aspects - Session 2

Uwe Gampe (Speaker) Technische Universität Dresden

Subsessions

- **Preliminary Aerodynamic Design of a Supercritical Carbon Dioxide Compressor Impeller for Waste Heat Recovery Applications**
Shantanu Thada; A M Pradeep; Arunkumar Sridharan
- **Microstructural Evaluation of Preselected Steels for Turbine after Supercritical CO₂ Exposure**
Lucia Rozumova; Tomáš Melichar; Ladislav Velebil
- **Advanced Thermodynamic Power Cycles Utilizing Carbon Dioxide Based Mixtures as Working Fluids for High Temperature Waste Heat Recovery**
Abubakr Ayub; Gioele di Marcoberardino; Costante Mario Invernizzi; Paolo Iora

10:30 – 11:00

Coffee break 3

11:00 – 12:00

sCO₂ Applications and Energy Systems - Session 3

Albannie Cagnac (Speaker) EDF - R&D

Subsessions

- **Thermal design of latent heat thermal energy storage facility with supercritical CO₂**
Tomas Melichar; Karel Dockal; Otakar Frybort; Petr Hajek
- **Utilizing Industrial Waste Heat for Power Generation Using sCO₂ Cycles**
Hady Ramez Soliman; Björn Thorsson; Silvia Trevisan; Rafael Eduardo Guédez

11:00 – 12:00

Heat Exchanger and Transfer - Session 2

Joerg Starflinger (Speaker) Professor, University of Stuttgart

Subsessions

- **Modeling and Study of a Printed Circuit Heat Exchanger for Brayton Power Cycles Using Supercritical CO₂ Mixtures as Working Fluid**
Robert Valencia-Chapi; Olmo Fierros-Peraza; Luis Coco-Enríquez; Javier Muñoz-Antón
- **Evaluation of deterioration in vertical sCO₂ cooling heat transfer in 3 mm tube**
Andreas Wahl; Rainer Mertz; Eckard Laurien; Starflinger Joerg

12:00 – 13:00

Lunch 2

13:00 – 15:00

Turbomachines and Cycles - Session 3

Stefan Glos (Speaker) Siemens Energy AG, Germany

Subsessions

- **Binary interaction parameter uncertainty in the optimisation of a transcritical cycle: consequences on turbine design**
Omar Aqel; Martin White; Abdunaser Sayma
- **Mean-Line Analysis of Supercritical CO₂ Centrifugal Compressors by Using Enthalpy Loss Coefficients**
Haikun Ren; Alexander Johannes Hacks; Sebastian Schuster; Dieter Brillert
- **Exergoeconomic Analysis of Hybrid sCO₂ Brayton Power Cycle**
Abdurrahman Alenezi; Ladislav Vesely; Jayanta Kapat
- **Design and off-design analysis of a highly loaded centrifugal compressor for sCO₂ applications operating in near-critical conditions**
Alessandro Romei; Paolo Gaetani; Giacomo Persico

13:00 – 15:00

sCO₂ Applications and Energy Systems - Session 4

Otakar Frýbort (Speaker) Centrum Vyzkumu Rez, Czech Republic

Subsessions

- **Optimal design of supercritical CO₂ (S-CO₂) cycle systems for internal combustion engine (ICE) waste-heat recovery considering heat source fluctuations**
Jian Song; Yaxiong Wang; Jiangfeng Wang; Christos Markides
- **Techno-economic optimization method and its application to a sCO₂ gas turbine bottoming cycle**
Thiago Correa Veloso Gotelip; Uwe Gampe; Stefan Glos
- **Estimated Cost and Performance of a Novel sCO₂ Natural Convection Cycle for Low-grade Waste Heat Recovery**
Kelsi Katcher; Michael Marshall; Natalie Smith; Cole Replogle
- **Experiences of supercritical CO₂ applications in refrigeration and air conditioning systems**
Christian Doerffel; Christiane Thomas; Ullrich Hesse

15:00 – 15:15

Closing Session

Dieter Brillert (Speaker)

Papers

- Hofer, Markus; Ren, Haikun; Hecker, Frieder; Buck, Michael;
Brillert, Dieter; Starflinger, Jörg Page 14
Simulation and analysis of a self-propelling heat removal system using
supercritical CO₂ at different ambient temperatures
<https://doi.org/10.17185/dupublico/73943>
- Harman-Thomas, James M.; Pourkashanian, Mohamed; Hughes, Kevin Page 28
The Chemical kinetic mechanism for combustion in supercritical carbon dioxide
<https://doi.org/10.17185/dupublico/73944>
- Theologou, Konstantinos; Mertz, Rainer; Laurien, Eckart; Starflinger, Jörg Page 38
Experimental investigations on the heat transfer characteristics of supercritical CO₂
in heated horizontal pipes
<https://doi.org/10.17185/dupublico/73945>
- Valencia-Chapi, Robert; Fierros-Peraza, Olmo; Coco-Enríquez, Luis; Muñoz-Antón, Javier Page 48
Modeling and study of a printed circuit heat exchanger for Brayton power cycles
using supercritical CO₂ mixtures as working fluid
<https://doi.org/10.17185/dupublico/73946>
- Ayub, Abubakr; Di Marcoberardino, Gioele; Invernizzi, Costante M.; Iora, Paolo Page 58
Advanced thermodynamic power cycles utilizing carbon dioxide based
mixtures as working fluids for high temperature waste heat recovery
<https://doi.org/10.17185/dupublico/73947>
- Ren, Haikun; Hacks, Alexander; Schuster, Sebastian; Brillert, Dieter Page 68
Mean-line analysis for supercritical CO₂ centrifugal compressors by using
enthalpy loss coefficients
<https://doi.org/10.17185/dupublico/73948>
- Marchionni, Matteo; Bianchi, Giuseppe; Usman, Muhammad; Pesyridis, Apostolos;
Tassou, Savvas A. Page 78
Numerical investigation of a simple regenerative heat to power system
with coupled or independent turbomachinery drives
<https://doi.org/10.17185/dupublico/73949>
- Melichar, Tomáš; Dočkal, Karel; Frýbort, Otakar; Hájek, Petr; Filip, Radomír Page 88
Thermal design of latent heat thermal energy storage facility with supercritical CO₂
<https://doi.org/10.17185/dupublico/73950>
- Rozumová, Lucia; Melichar, Tomáš; Velebil, Ladislav Page 98
Microstructural evaluation of preselected steels for turbine after supercritical CO₂ exposure
<https://doi.org/10.17185/dupublico/73951>

- Glos, Stefan; Lippe, Patrik Rene; Schlehuber, Dominic; Kobler, Simon; Wechsung, Michael Page 106
Design considerations of sCO₂ turbines developed within the CARBOSOLA project
<https://doi.org/10.17185/dupublico/73952>
- Gotelip, Thiago; Gampe, Uwe; Glos, Stefan Page 113
Techno-economic optimization method and its application to a sCO₂ gas turbine
bottoming cycle
<https://doi.org/10.17185/dupublico/73953>
- Abd El Hussein, Ihab; Schuster, Sebastian; Brillert, Dieter Page 124
An attempt for establishing pressure ratio performance maps for supercritical
carbon dioxide compressors in power applications
<https://doi.org/10.17185/dupublico/73954>
- Doerffel, Christian; Thomas, Christiane; Hesse, Ullrich Page 131
Experiences of supercritical CO₂ applications in refrigeration and air conditioning systems
<https://doi.org/10.17185/dupublico/73955>
- Manzoni, Matteo; Patti, Alberto; Maccarini, Simone; Traverso, Alberto Page 137
Adiabatic compressed CO₂ energy storage
<https://doi.org/10.17185/dupublico/73956>
- Wahl, Andreas; Mertz, Rainer; Laurien, Eckart; Starflinger, Jörg Page 146
Evaluation of deterioration in vertical sCO₂ cooling heat transfer in 3 mm tube
<https://doi.org/10.17185/dupublico/73957>
- Thada, Shantanu; Pradeep, A. M.; Sridharan, Arunkumar Page 154
Preliminary aerodynamic design of a supercritical carbon dioxide compressor
impeller for waste heat recovery applications
<https://doi.org/10.17185/dupublico/73958>
- Aqel, Omar; White, Martin; Sayma, Abdulnaser Page 164
Binary interaction uncertainty in the optimisation of a transcritical cycle :
consequences on cycle and turbine design
<https://doi.org/10.17185/dupublico/73959>
- Heller, Lukas; Glos, Stefan; Buck, Reiner Page 177
sCO₂ power cycle design without heat source limitations : Solar thermal particle
technology in the CARBOSOLA project
<https://doi.org/10.17185/dupublico/73961>
- Frýbort, Otakar; Dočkal, Karel; Vlček, Petr; Hájek, Petr; Melichar, Tomáš; Kopic, Miroslav;
Živný, Antonín; Pátý, Marek; Macálka, Aleš; Hanzal, Vilém; Hájek, Petr Page 185
Sofia – sCO₂ facility for supercritical Brayton cycle research
<https://doi.org/10.17185/dupublico/73962>

- Maquart, Victor; Valentin, Benoît; Cagnac, Albannie Page 194
 Environmental assessment of a 25 MWe fossil-fired supercritical CO₂ cycle
<https://doi.org/10.17185/dupublico/73963>
- Song, Jian; Wang, Yaxiong; Wang, Jiangfeng; Markides, Christos N. Page 205
 Optimal design of supercritical CO₂ (S-CO₂) cycle systems for internal combustion
 engine (ICE) waste-heat recovery considering heat source fluctuations
<https://doi.org/10.17185/dupublico/73964>
- Rath, Sebastian; Mickoleit, Erik; Gampe, Uwe; Breitkopf, Cornelia; Jäger, Andreas Page 212
 Study of the influence of additives to CO₂ on the performance parameters of a sCO₂-cycle
<https://doi.org/10.17185/dupublico/73965>
- Karaefe, Renan Emre; Post, Pascal; Sembritzky, Marwick; Schramm, Andreas;
 Di Mare, Francesca; Kunick, Matthias; Gampe, Uwe Page 230
 Numerical analysis of a centrifugal compressor operating with supercritical CO₂
<https://doi.org/10.17185/dupublico/73966>
- Baek, Jeong Yeol; Lee, Jae Jun; Lee, Jeong Ik Page 241
 Transient analysis of the super-critical carbon dioxide cycle coupled to pressurized
 water reactor for nuclear powered ships
<https://doi.org/10.17185/dupublico/73967>
- Unger, Sebastian; Müller, Jonas; Bangalore Mohankumar, Malini; Rath, Sebastian;
 Hampel, Uwe Page 249
 Numerical dimensioning of a pre-cooler for sCO₂ power cycles to utilize industrial
 waste heat
<https://doi.org/10.17185/dupublico/73968>
- Romei, Alessandro; Gaetani, Paolo; Persico, Giacomo Page 257
 Design and off-design analysis of a highly loaded centrifugal compressor for sCO₂
 applications operating in near-critical conditions
<https://doi.org/10.17185/dupublico/73969>
- Berka, Jan; Hlinčík, Tomas; Purkarová, Eliška; Vagenknechtová, Alice; Rozumová, Lucia Page 267
 Investigation of material degradation and coolant chemistry for sCO₂ power cycles
<https://doi.org/10.17185/dupublico/73970>
- Tioual-Demange, Sarah; Voirin, Vivien; Hofer, Markus; Hecker, Frieder;
 Buck, Michael; Starflinger, Jörg Page 274
 Conceptual design and qualification of highly effective heat exchangers for heat
 removal sCO₂ Brayton cycle to increase the safety of nuclear power plants
<https://doi.org/10.17185/dupublico/73971>

- Crespi, Francesco; Rodríguez-de Arriba, Pablo; Sánchez, David; Ayub, Abubakr;
Di Marcoberardino, Gioele; Invernizzi, Costante Mario; Martínez, Gonzalo S.;
Iora, Paolo; Di Bona, Daniele; Binotti, Marco; Manzolini, Giampaolo Page 291
Thermal efficiency gains enabled by using supercritical CO₂ mixtures in Concentrated Solar
Power applications temperature industrial heat to power conversion at off-design conditions
<https://doi.org/10.17185/dupublico/73972>
- Pecnik, Rene; Ren, Jie; Otero-Rodriguez, Gustavo J. Page 301
Characterizing and modelling turbulence in supercritical fluids
<https://doi.org/10.17185/dupublico/73973>
- Penkuhn, Mathias; Tsatsaronis, George Page 307
Analysis of sCO₂ Cycles for District Heating Applications
<https://doi.org/10.17185/dupublico/73974>
- Kang, Jeongseek; Vorobiev, Alex; Cameron, Joshua D.; Morris, Scott C.; Wackerly, Ryan;
Sedlacko, Kyle; Miller, Jason D.; Held, Timothy J. Page 316
10MW-Class sCO₂ Compressor Test Facility at University of Notre Dame
<https://doi.org/10.17185/dupublico/73975>
- Soliman, Hady R.; Þórsson, Björn J.; Trevisan, Silvia; Guédez, Rafael Page 322
Utilizing Industrial Waste Heat for Power Generation Using sCO₂ Cycles
<https://doi.org/10.17185/dupublico/73976>
- Petrucelli, Giuseppe; Uusitalo, Antti; Grönman, Aki; Turunen-Saaresti, Teemu;
Zocca, Marta Page 333
Closed-loop supercritical carbon dioxide wind tunnel : design and components
<https://doi.org/10.17185/dupublico/73977>
- Vesely, Ladislav; Thangavel, Prabu; Gopinathan, S.; Otakar, Frybort;
Subbaraman, Ganesan; Kapat, Jayanta Page 343
Greening a cement plant using sCO₂ power cycle
<https://doi.org/10.17185/dupublico/73978>
- Lariviere, Brian; Marion, John; Macadam, Scott; McDowell, Michael; Lesemann, Markus;
McClung, Aaron; Mortzheim, Jason Page 352
sCO₂ power cycle development and STEP Demo pilot project
<https://doi.org/10.17185/dupublico/73979>
- Alenezi, Abdurrahman; Vesely, Ladislav; Kapat, Jayanta Page 363
Exergoeconomic analysis of a hybrid sCO₂ Brayton power cycle
<https://doi.org/10.17185/dupublico/73980>
- Alfani, Dario; Astolfi, Marco; Binotti, Marco; Silva, Paolo Page 379
Effect of the ambient temperature on the performance of small size sCO₂ based
pulverized coal power plants
<https://doi.org/10.17185/dupublico/73981>

Katcher, Kelsi M.; Marshall, Michael; Smith, Natalie R.; Replogle, Cole Page 389
Estimated cost and performance of a novel sCO₂ natural convection cycle
for low-grade waste heat recovery
<https://doi.org/10.17185/dupublico/73982>

Hofer, Markus; Buck, Michael; Starflinger, Jörg Page 400
Operational analysis of a self-propelling heat removal system using supercritical CO₂ with ATHLET
<https://doi.org/10.17185/dupublico/73983>

SIMULATION AND ANALYSIS OF A SELF-PROPELLING HEAT REMOVAL SYSTEM USING SUPERCRITICAL CO₂ AT DIFFERENT AMBIENT TEMPERATURES

Markus Hofer*
University of Stuttgart
Stuttgart, Germany
Email: hofer@ike.uni-stuttgart.de

Haikun Ren
University Duisburg-Essen
Duisburg, Germany

Frieder Hecker
Simulator Centre of KSG | GfS
Essen, Germany

Michael Buck
University of Stuttgart
Stuttgart, Germany

Dieter Brillert
University Duisburg-Essen
Duisburg, Germany

Jörg Starflinger
University of Stuttgart
Stuttgart, Germany

ABSTRACT

Innovative heat removal systems are currently investigated for use in existing and future nuclear power plants. One of them is the supercritical carbon dioxide (sCO₂¹) heat removal system, which is based on a closed Brayton cycle with sCO₂ as a working fluid.

This paper provides the design and layout of the sCO₂ cycle based on assumptions developed in the project sCO₂-4-NPP. The system is analysed over a wide range of ambient and steam-side conditions in ATHLET, using performance maps for the turbomachinery, which were designed recently. Bypasses are considered in the layout of the cycle to cope with special operation conditions, e.g. start-up. Different operational readiness states for the system are shown, which enable a fast start-up of the system. Air mass flow rate control is implemented to keep the compressor inlet temperature constant with controller parameters depending on the ambient temperature.

The performance analysis of the system suggests that it is a good option to operate the system at the design compressor inlet temperature of 55 °C at any ambient or steam-side boundary condition. With decreasing thermal power input, the rotational speed of the turbomachinery must be decreased to keep the system self-propelling. Turbomachinery design with a higher surge margin is preferred and different operation strategies are feasible and need to be tested in interaction with the nuclear power plant.

INTRODUCTION

In case of a station blackout and loss of ultimate heat sink accident in a boiling water reactor or pressurized water reactor, the plant accident management strongly depends on the recovery of electricity, e.g. by emergency diesel generators, or from external sources. If not available, core integrity will be violated, like in Fukushima Daiichi accident. Such scenarios inspire the development of advanced decay heat removal systems. Since space is a limitation in existing power plants, the supercritical carbon dioxide (sCO₂) heat removal system “sCO₂-HeRo” was proposed because of its compactness and self-propelling features [1–3]. Such a system could be incorporated in newly-built nuclear power plants as well as retrofitted to existing nuclear power plants. The system consists of a compact heat exchanger (CHX), a gas cooler, serving as the ultimate heat sink (UHS), and the turbomachinery, one compressor and one turbine mounted on a common shaft together with a generator. Since the momentum from the turbine is sufficient to simultaneously drive the compressor and generate more electricity than used by the fans of the UHS, the system is self-propelling. The excess electricity can even be used to support other accident measures, e.g. recharging batteries. CO₂ is selected as a working fluid because of its favourable fluid properties, enabling the design of a very compact system. Moreover, CO₂ is not combustible, non-toxic and commercially available. Figure 1 shows the scheme of the sCO₂-HeRo attached to the reactor pressure vessel of a boiling water reactor or to the steam generator of a pressurized water reactor. In the case of an accident in a boiling water reactor, the

¹ sCO₂ is defined as carbon dioxide at supercritical conditions with $p > 73.8$ bar and $T > 31$ °C

valve, which connects the CHX to the main steam line, opens automatically. Driven by natural circulation, the steam condenses and heats the $s\text{CO}_2$ in the CHX. The pressurized and heated $s\text{CO}_2$ is expanded in the turbine, which drives the compressor and generates power for the fans of UHS. After the turbine, the remaining heat of the $s\text{CO}_2$ is removed in the UHS. Finally, the $s\text{CO}_2$ is compressed and flows to the CHX. Similarly, the $s\text{CO}_2$ -HeRo can be attached to the secondary side of a pressurized water reactor. In the primary loop, natural circulation will develop due to the decay heat input from the reactor core and heat removal via the steam generator. Consequently, the $s\text{CO}_2$ -HeRo principle could be used for boiling water reactors as well as pressurized water reactors. Generally, it is important to analyse the interaction of the $s\text{CO}_2$ -HeRo system with the nuclear plant for both reactors separately due to their different thermal-hydraulic behaviour and restrictions. However, the $s\text{CO}_2$ loop should also be analysed separately to gain knowledge on the operation of the loop which can be used for both reactor types.

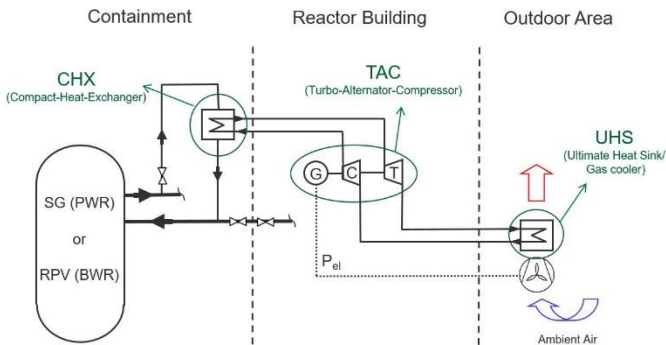


Figure 1: The $s\text{CO}_2$ heat removal system attached to the reactor pressure vessel (RPV) of a boiling water reactor (BWR) [1] or to the steam generator (SG) of a pressurized water reactor (PWR)

For the simulation of the thermo-hydraulic behaviour of nuclear power plants, different system codes are used, e.g. CATHARE, RELAP, TRACE, ATHLET and SCTRAN [4,5]. Because $s\text{CO}_2$ is considered as a working fluid for 4th generation reactor concepts as well as for the proposed heat removal system, work is in progress to extend these system codes for the simulation of $s\text{CO}_2$ power cycles [1,4,6–10]. Venker [1] investigated the feasibility of the $s\text{CO}_2$ -HeRo approach in detail and implemented first extensions in the ATHLET code for the simulation of the heat removal system. Hajek et al. [11] and Vojacek et al. [12] described the basic principles for the integration of the $s\text{CO}_2$ -HeRo into the European pressurized water reactor fleet including safety, reliability and thermodynamic design considerations. Hofer et al. [9] presented improved models for ATHLET, including heat exchanger and turbomachinery models. The turbomachinery models are performance map based and use a real gas similarity approach to account for changes in the inlet conditions. They also provided a design approach and analysed the $s\text{CO}_2$ cycle with varying decay heat at the maximum ambient temperature [13]. By adapting the

rotational speed of the turbomachinery, the cycle is successfully operated in part load. However, in some analysed cases, compressor surge was observed. As part of the project $s\text{CO}_2$ -4-NPP, the validation status for modelling $s\text{CO}_2$ cycles was provided for the codes CATHARE, Modelica and ATHLET including a blind benchmark [10]. Successful simulations were performed but it was also found that component models need further improvement and some numerical issues need to be solved in the future. Hexemer et al. [8,14] presented a detailed TRACE model of a recuperated $s\text{CO}_2$ cycle with two turbines. Component modelling, system control, steady state as well as transient results were discussed in detail. They highlighted the importance of performing detailed transient analysis before the system design is finalized. Moreover, attention is drawn to the problem of compressor surge and turbine flow reversal. Nathan [15] investigated control strategies for and the transient behavior of an indirect $s\text{CO}_2$ recompression cycle. The major control strategies are high and low temperature control, turbine bypass, and inventory control. These strategies enable successful cycle operation for different transients, like start-up and shutdown, part-load operation, loss-of-load, loss of heat sink and over-power. Vojacek et al. [16] investigated the control system of the $s\text{CO}_2$ loop at Research Centre Rez experimentally and numerically with Modelica. The parameters of a temperature controller were derived using the Cohen-Coon method. However, it was found that the controller parameters follow the behavior of the specific heat capacity of CO_2 and further manual tuning was inevitable to avoid oscillations.

In this study, the $s\text{CO}_2$ cycle is analysed using ATHLET. First, the preliminary cycle design and layout is presented. Secondly, component modelling and design are discussed briefly, divided into a turbomachinery and heat exchanger section. Thirdly, the control of the compressor inlet parameters via the UHS fan speed is investigated. Fourthly, the start-up of the cycle and different operational readiness states are discussed. Finally, the overall performance of the cycle is analysed highlighting the operational limits.

CYCLE DESIGN AND LAYOUT

In case of an accident, the task of the $s\text{CO}_2$ -HeRo system is to remove the decay heat reliably over several days. Assuming that other safety systems, as well as electricity supply, is unavailable, the system has to be self-propelling. This means that the power of the turbine must be sufficient to drive the compressor and the fans of the UHS. Moreover, the cycle must be able to remove the residual heat at any expected ambient condition while it decreases exponentially, reducing the power input into the cycle. Therefore, the system must be able to operate over a wide range of conditions. To follow the decay heat curve, the system consists of several units, which are shut down step by step. At the beginning of the accident, the maximum thermal capacity of all systems together can be lower than the initial decay heat, because an inventory loss in the reactor for a limited time span can be tolerated as long as the cooling of the core can be guaranteed [1,13].

This paper deals with the design of one unit of the heat removal system. As a first step, the unit is designed for the highest power input and the highest ambient temperature because this is the design point of the heat exchangers and the highest ambient temperature is the worst-case condition from a thermodynamic point of view. Some conditions in the CO₂ loop can be determined directly from the assumptions summarized in Table 2 in Annex A. These assumptions have been developed in the project sCO₂-4-NPP and will be improved continuously. Since the project aims to integrate the sCO₂-HeRo system into a pressurized water reactor, the steam side boundary conditions are chosen in accordance with this type of reactor. In a boiling water reactor, the steam pressures and temperatures will be slightly lower due to the lower blow-off pressure. However, in terms of the sCO₂ loop, this has only a minor effect. Therefore, the conclusions from the following analysis are valid for both reactor types. The assumptions in Table 2 are chosen conservatively, e.g. low isentropic turbomachinery efficiencies of 70 % at the design point and moderate temperature differences between the fluids in the heat exchangers are selected.

The remaining conditions in the CO₂ loop are determined through optimization, aiming for the highest excess power ΔP , which is defined as the turbine power reduced by the power consumption of the compressor and the fan. The excess power is maximized because it will decrease with decreasing thermal power input and the system should be able to operate self-propelling as long as possible. The only free parameter to be determined in the optimization procedure is the compressor inlet pressure. All other variables are calculated by basic thermodynamic relations. The optimization process is slightly improved compared to [13] because it also includes the size of the system by specifying its heat removal capacity and the piping pressure losses.

The results of the design process regarding power and mass flow rates are given in Table 3 and the thermodynamic cycle parameters in Table 4, both in Appendix A. The optimization yields an excess power of 283 kW at a relatively high compressor inlet pressure of 126.3 bar. The high operating pressure is a consequence of the need of a high fluid density at the compressor inlet despite the high compressor inlet temperature of 55 °C, which results from the high ambient design temperature of 45 °C.

From Figure 1 it can be observed that the components of the heat removal system are located at different places in the nuclear power plant. Therefore, the length of the connection pipes is assumed to be 22.5 m between each component. The pipe diameters are chosen with regard to density and flow speed to satisfy the specified pressure drop keeping in mind that some additional valves are necessary for the operation and control of the cycle. An inner diameter of 0.1 m was selected for the pipes connected to the compressor and 0.15 m was chosen for the pipes connected to the turbine, considering a pipe roughness of 50 μm. In the current layout, ball valves are included before and after the turbine to be able to disconnect it from the cycle and to avoid reverse flow at unfavourable conditions which might occur during start-up. The bypasses, which are introduced in the

following, include a control valve and a check valve with a form loss coefficient of 30 and 6, respectively. They are required for special operating conditions, e.g. for the start-up. In Figure 2, the detailed cycle layout is shown. It includes the bypasses and the controllers discussed in this paper. As mentioned before, the electrical power P_{el} of the turbomachinery (TAC) must be sufficient to power the fans of the UHS. To control the compressor and the turbine inlet condition, the fan speed n_{fan} of the UHS and the shaft speed n_{TAC} can be adapted, respectively. The control of the UHS is discussed and analysed in detail in the following but the control of the turbomachinery is only discussed qualitatively based on the results and will be analysed in more detail in the future. The following bypasses are considered in Figure 2:

- a turbine bypass, connecting turbine inlet and outlet
- a compressor recirculation, connecting compressor outlet and turbine outlet
- and a UHS bypass, connecting turbine outlet and compressor inlet

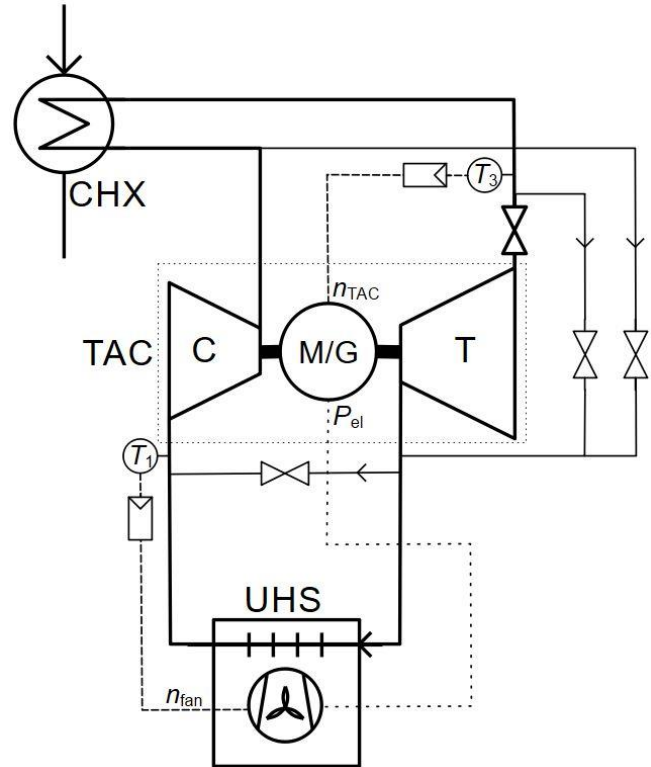


Figure 2: Detailed cycle layout including bypasses and controllers

The turbine bypass and the compressor recirculation are required for start-up and at very low turbomachinery rotational speeds to avoid compressor surge. Possibly only one of these bypasses might be necessary for a future design. The advantage of having the turbine bypass is that it enables fast heat-up of the cycle because the complete mass flow rate flows through the CHX. Furthermore, the turbine bypass can be used to increase the heat removal capacity of the system at full load. A disadvantage is a

higher pressure drop compared to the compressor recirculation. A lower pressure drop is favourable if the current operation point is close to the surge line. The UHS bypass might be required to keep the compressor inlet condition close to its design point at very low ambient temperatures. It enables mixing of hot and cold CO₂, e.g. when the fans of the UHS are switched off or running at minimum speed but the remaining cooling capacity delivers a compressor inlet condition which differs from the desired condition. A modular UHS design, which allows bypassing some UHS modules, is not considered a good alternative because the pressure and temperature in the disconnected modules will decrease considerably compared to the operating conditions of the cycle if the ambient temperature is low. This hampers reconnection of the units to the cycle when the disconnected modules are required again. This might be the case when a running module has to take over the heat removal function from a deliberately or inadvertently stopped module or when the ambient temperature increases again.

TURBOMACHINERY

The performance maps of the sCO₂ turbomachine employed in this study were generated by mean-line analysis codes for compressor and turbine [17]. By specifying the main geometry and inlet conditions of the compressor and turbine, the codes calculate the fluid properties at the inlet and outlet of each component, e.g. the impeller. This is achieved by employing the first law of thermodynamics and the so-called enthalpy loss coefficients. Subsequently, the outlet conditions such as enthalpy and pressure at the outlet of the compressor and turbine are given as the outputs of the codes. Finally, the ratio of total pressures or the specific total isentropic enthalpy difference and the total isentropic efficiencies are calculated.

The mean-line analysis code for the centrifugal compressor was validated with the experimental and numerical results of the project sCO₂-HeRo [17]. The code for the radial turbine was validated with the numerical results of the project sCO₂-HeRo.

In this study, two preliminary designs, labelled type 1 and type 2, of a sCO₂ centrifugal compressor and radial turbine, which are considered as components of the turbo-alternator-compressor (TAC), are applied to generate performance maps. The design of the compressor was carried out by an in-house code from the chair of turbomachinery (TM) at the University of Duisburg-Essen (UDE), while the experience in the project sCO₂-HeRo was taken into account for the design of the turbine. In Figure 3 and Figure 4, two performance maps are shown as an example. All other performance maps and the design parameters are included in Annex B. The presented maps are provided as the input of a recently developed turbomachinery model in ATHLET, which considers real gas effects. Varying inlet conditions are considered by transposing the presented maps to dimensionless maps. The model is based on a real gas similarity approach, which was presented by Pham et al. [18]. The implementation in ATHLET was described in [9].

Figure 3 and Figure 4 display the compressor performance maps of type 1 and type 2 concerning specific total isentropic enthalpy rise over mass flow rate at various rotational speeds.

The design point of Type 1 shown in Figure 3 is equal to the design point of the cycle. This design has a small surge margin. As shown in Figure 4, type 2 represents a design with a higher surge margin. The compressor design point of type 2 is still near the surge line but in terms of the cycle design point and during the operation of the cycle a higher margin to the surge line is achieved. Additionally, this provides a good part-load performance. For numerical reasons, the map also includes the instable area left of the surge line.

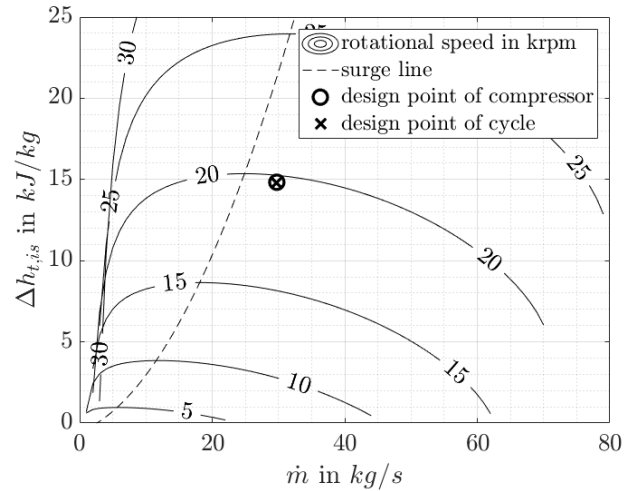


Figure 3: Compressor performance map of type 1 regarding total isentropic enthalpy rise over the mass flow rate

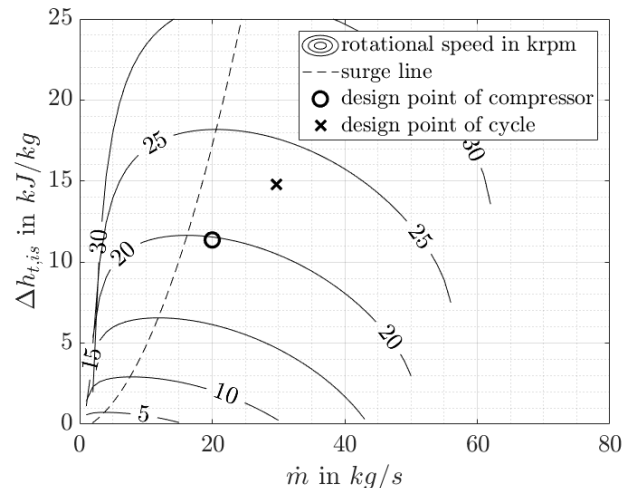


Figure 4: Compressor performance map of type 2 regarding total isentropic enthalpy rise over the mass flow rate

For the cycle design, the isentropic efficiencies of the turbine and compressor were conservatively set to 70 %, as shown in table 1. However, the calculated performance maps yield higher efficiencies around 80 % at the design point of the cycle, although without considering leakage and disk friction. Therefore, to stay in line with the efficiencies specified for the design point of the system and to conservatively account for

further losses, the efficiency of all applied performance maps was multiplied by a factor of 7/8.

HEAT EXCHANGERS

As shown in Figure 1, two heat exchangers are installed in the cycle, the compact heat exchanger (CHX) and the gas cooler, which is also called ultimate heat sink (UHS) in the following. For both heat exchangers, the standard approach of modelling just one representative channel or pipe was applied in ATHLET. The detailed model of the CHX was provided in [19] and the model of the UHS was introduced and validated in [10] and will be extended in this paper. The mentioned reference also includes a detailed description of the experimental UHS, which is scaled up in this paper. The design of both components was derived by scaling of the experimental heat exchanger geometry, which is also given in the mentioned references. Scaling means that the number of channels or pipes and the length is adapted but other geometric relations like the ratio of the heat transfer area on the air-side to the heat transfer area on the CO₂ side are kept constant. The design geometry of the upscaled components is given in Table 5 and Table 6 in Annex A, including the geometry of the heat conduction elements (HCOs), which model the heat conduction in ATHLET.

The upscaled CHX consists of 9000 channels per fluid, which could be arranged into 60 plates per fluid, yielding an approximate heat exchanger size of 1.1 m x 0.5 m x 0.3 m. In accordance with the experimental CHX, form loss coefficients were applied at the CHX inlet and outlet to account for the plenum pressure drop. These coefficients are chosen to match the specified design pressure drop of 2 bar, considering the channel pressure drop which is calculated by ATHLET. This yields 5 for the inlet and 0.5 for the outlet plenum in relation to the pipe flow area. The size of the plate-shaped HCO was adapted to match the thermal resistance of the real configuration and its density was chosen to match the mass of the CHX material.

The UHS consists of 732 pipes on the CO₂-side with an inner diameter of 10 mm and a length of 22 m. The bends of the CO₂ pipes are located outside of the airflow. To consider their fluid volume in the simulation, they were included in the pipe length. In the simulation, the UHS was modelled as a pure counter-current flow heat exchanger where the heat transfer occurs along the whole pipe length. To take the bends into account, the heat transfer area on the CO₂-side, which is the area inside the airflow, was matched by adapting the geometry of a plate-shaped HCO. The air-side is finned, yielding a total heat transfer area of 33000 m² on the air-side. The air-side temperature increase of 25 K was kept constant in the design compared to the experimental heat exchanger, yielding a total air mass flow rate of 382.3 kg/s. The UHS is by far the largest component in the cycle with a total structural mass of 1.81 t. In design conditions, 56.8 % of the total fluid mass of 817 kg is contained in the UHS. Therefore, the UHS represents the largest thermal inertia in the cycle.

The fans of the UHS are installed at the inlet/bottom because high outlet temperatures may occur at low fan speeds or especially when the fans are switched off. Switching the fans off

does not reduce the airflow to zero because a natural flow will develop induced by the density difference between the UHS inlet and outlet. To be able to control the UHS also with the fans switched off, it was assumed that this flow can be reduced further, e.g. by flaps at the UHS outlet. At the design point, the power of the fans was calculated by assuming a specific fan power requirement of 8.5 kW_{el}/MW_{th} [20]. In general, the power of the fans can be calculated from the hydraulic power and fan efficiency. The hydraulic power is defined as

$$\Delta P = \Delta p \dot{V} \sim \frac{\dot{m}^2}{0.5(\rho_{in} + \rho_{out}) \rho_{in}} \quad (1)$$

The pressure drop over the fan Δp is approximately proportional to the mass flow rate squared divided by an average density and the volume flow rate of the fan at the inlet is equal to the mass flow rate divided by the inlet density. Therefore, the power requirement of the fans in off-design conditions can be determined using this proportional relationship together with the design power. This simple approach represents the well-known cubic power dependence of the rotational speed of a pump at a fixed density and enables to calculate the fan power without detailed modelling of the air-side pressure drop.

The heat transfer coefficient on the air-side is determined by a Nusselt correlation, which was also extended and validated for low Reynolds numbers [10]. The relationship between the Reynolds number and the heat transfer coefficient on the air-side for this heat exchanger is exemplarily shown in Figure 5 for an ambient temperature of 45 °C and a wall temperature of 55 °C. At the design point, the heat transfer coefficient on the air-side varies around 28 W/m²K over the length of the UHS. Despite the increased heat transfer area due to the fins, the air-side limits the overall heat transfer.

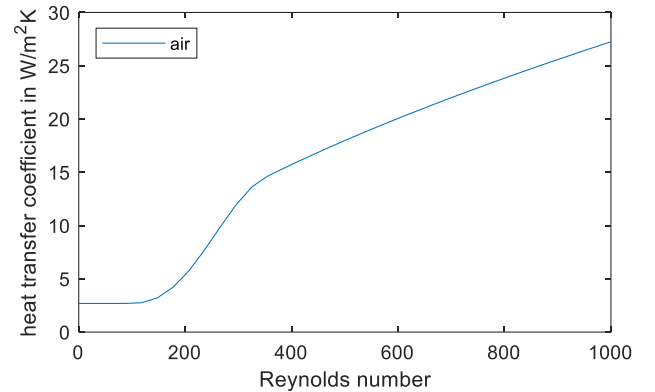


Figure 5: Heat transfer coefficient on the air-side as a function of air Reynolds number

CONTROL OF ULTIMATE HEAT SINK

The outlet condition at the CO₂ side of the UHS must be controlled to keep the compressor inlet in the desired operating range. One option would be to aim for a constant compressor inlet density. Another option is to keep the compressor inlet temperature constant. The advantages of temperature control are technical robustness and simple implementation. Furthermore, a certain temperature difference to the ambient air can be

maintained. This enables a fan operation with a reasonable power requirement. A possible disadvantage of temperature control is that the inlet density changes with pressure. Since no inventory control is considered in the current cycle, the cycle pressures are a function of the current operating condition. Moreover, care must be taken when temperature control is used for sCO₂ because near the pseudocritical point the temperature is almost constant while enthalpy and density are changing rapidly. This effect becomes more pronounced the closer the operational pressure is to the critical pressure of 73.8 bar. For this system, the design operational compressor inlet pressure with 126 bar is considerably above the critical pressure. At the design pressure of 126 bar and the design temperature of 55 °C, the gradient of the density is 14 kg/m³ per Kelvin. Compared to the intended density of about 550 kg/m³ this is assumed to be a moderate gradient. Therefore, temperature control was applied in this analysis. The effect of changing cycle pressure should be analysed later because in the interval from 110 bar to 140 bar, the density at 55°C changes from 415 kg/m³ to 619 kg/m³.

Technically, the speed of the fans should be the variable to be controlled. Due to the lack of a detailed model for the fans, for the simulations, the air mass flow rate was chosen instead as the controlled variable, based on the rationale that the volume flow rate is nearly proportional to the fan speed. Further, controlling the mass flow rate eliminates the influence of the density. The outlet temperature of the UHS is affected by the mass flow rate, inlet pressure and temperature on the CO₂-side. On the air-side, the mass flow rate and the inlet temperature are the relevant parameters. Additionally, wind, humidity and dirt may affect the performance of the UHS but this was not considered. For the determination of the controller parameters, the response of the system to a step function of the CO₂ mass flow rate was considered because this parameter might experience the fastest changes and affects the outlet temperature considerably. In this analysis, a PI-controller was used to control the mass flow rate of the air

$$\dot{m}_{air}(t) = \dot{m}_{air}(t_0) + K_p^* \Delta T(t) + K_i^* \int_{t_0}^t \Delta T(\tau) d\tau. \quad (2)$$

This can be readily implemented in ATHLET which provides a general model of a PIDT1 controller [21]. Before the controller is started, the air mass flow rate is specified as a function of time. Starting at the time t_0 , when the controller is switched on, it varies the air mass flow rate relative to $\dot{m}_{air}(t_0)$. The proportional gain K_p^* and the integral gain K_i^* directly provide the relation between the air mass flow rate in kg/s and the difference of the measured temperature and the set temperature ΔT in K. Therefore, these controller parameters need to be specified with their units.

The controller parameters were determined according to the simple approach of Nathan [15]. First, the proportional gain was selected as high as possible before oscillation occurs. Afterwards, the integral gain was tuned using the selected proportional gain.

The first tuning was conducted at the thermodynamic design conditions of the UHS with the CO₂ mass flow rate decreased to 50 % of its design value. This value was selected because the

system must be able to operate in part-load and at lower CO₂ mass flow rates where a changing air mass flow rate has a larger impact. The air mass flow rate required at these conditions is 35 % of its design value. A step increase of 20 % in the CO₂ mass flow rate was applied, resulting in an uncontrolled temperature increase of 5.5 K. Due to the large thermal inertia of the UHS, a new steady outlet temperature is reached after approximately 600 s. The selected proportional gain of 200 kg s⁻¹ K⁻¹ can reduce the increase to 0.4 K. The tuning of the integral gain is shown in Figure 6. In favour of stability, an integral gain of 5 kg s⁻² K⁻¹ was selected because it is already considerably faster than 2 kg s⁻² K⁻¹ and shows no oscillation at all. This enables stable operation even at lower mass flow rates.

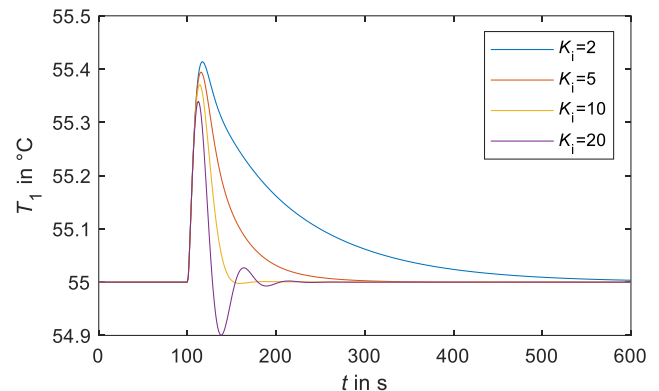


Figure 6: Tuning of the integral gain at the design ambient air temperature of 45 °C

After the tuning at an air temperature of 45 °C, a tuning at – 45 °C was conducted because the system should also be able to operate at extreme conditions. The resulting parameters are 20 kg s⁻¹ K⁻¹ for the proportional gain and 0.2 kg s⁻² K⁻¹ for the integral time constant, respectively. Compared to the previous controller parameters, these parameters differ by a factor of 10, which is reasonable because, at very low ambient temperatures, slight changes in the air mass flow rate have a large impact on the compressor inlet temperature. This is due to the large temperature difference from the CO₂ side to the airside which drives the heat flow. At intermediate ambient temperatures, the controller parameters can be interpolated linearly. In the following chapters, the determined controller parameters are used for the control of the cycle simulations.

STARTUP OF CYCLE

In this chapter, the start of the simulation and different operational readiness states of the system are discussed. It does not cover the start-up from cold shutdown conditions because this is expected to be very challenging at low ambient temperatures. At these temperatures, the CO₂ is in two-phase and liquid conditions and a large part of the fluid accumulates in the UHS and a (fast) start-up of the system might not be possible, e.g. due to material or turbomachinery limitations. Therefore, a new idea is to keep the system in an operational readiness state.

In this paper, an operational readiness state is defined as a state which should enable fast start-up of the system in case of an accident. Moreover, the thermal and electrical energy power consumption of the system must be reasonably low compared to the nuclear power plant. Thus, such a state should fulfil most of the following criteria. First, the compressor inlet condition should already be close to its design point but the rotational speed of the turbomachinery should be low to achieve a reasonable thermal and electrical power consumption. Secondly, a sufficiently high CHX outlet temperature is required to reduce the material stress in the CHX and to be able to start the turbine. Besides, the pressure ratio over the turbine must be high enough to attain forward flow through the turbine when the turbine is connected to the cycle. Thirdly, the throttled steam side limits the thermal power input to the CO₂ cycle. In case of an accident, the valve to the main steam line is opened completely leading to an increased thermal power input to the cycle which in turn allows to increase the speed of the turbomachinery.

The analysis aims to show the general challenges of the start-up and different operational readiness states. To reach this state, the simulation was initialized with a design compressor inlet temperature of 55 °C and a pressure of 101.2 bar resulting from an average density of 335 kg/m³. The air inlet temperature was set to the design temperature of 45°C and the air mass flow rate was set to 3 % of the design flow rate. This should approximately match the conditions with the fans switched off when the UHS is cooled by natural convection [10]. The valves at the turbine inlet and outlet were closed and the turbine bypass was completely open. The compressor recirculation and the UHS bypass were closed in this preliminary analysis.

The procedure shows the start-up and the different operational readiness states step by step. The exact schedule of the different steps needs to be analysed in more detail in interaction with the nuclear power plant. First, the turbomachinery rotational speed is increased to 20 % of the speed occurring at the cycle design point. Secondly, the cycle is heated up with a small amount of steam. Thirdly, the controller of the compressor inlet temperature is switched on with a set point of 55 °C. Fourthly, the opening of the turbine bypass is decreased to decrease the compressor mass flow rate and increase the pressure ratio and the CHX outlet temperature. This state is considered as the first operational readiness state (ORS1). The only difference to the next one (ORS2) is that the turbine bypass valve is throttled further, which yields a further increase of the pressure ratio and the CHX outlet temperature. To reach the last operational readiness state (ORS3), discussed here, the valves at the turbine are opened and the turbine bypass valve is closed completely. From this point, the thermal power of the CHX and the speed of the turbomachinery can be increased rapidly to design operation conditions. This represents the initial point of the cycle performance analysis in the next chapter. In Table 1 the conditions of the three operational readiness states are summarized for type 2 turbomachinery. This type is preferred due to the higher surge margin. The results in Table 1 are preliminary because the operating points are located far from the design point, where the accuracy of the models and the input

needs to be analysed further. Moreover, the guess for the turbomachinery speed and the steam mass flow rate, which determines the thermal power of the CHX, might be adapted, e.g. to further reduce the thermal power consumption. Taking this into account, it can be observed from the total power of the system that it might be possible to achieve a self-propelling operational readiness state (ORS3) at only 12 % of the design thermal power input. Additionally, the other two operational readiness states show a low required power at similar operating conditions. For all three states, the compressor inlet pressure is already close to its design point. Furthermore, a CHX outlet temperature of approximately 150 °C seems to be sufficient to start the turbine at these conditions. ORS 1 yields the highest surge margin due to the larger opening of the turbine bypass but shows the highest power consumption and the lowest CHX outlet temperature. ORS 2 and ORS 3 are very similar except for the turbine operating in ORS 3. Therefore, ORS 3 will be preferred if the self-propelling operation is confirmed in the future.

Table 1: Conditions for the operational readiness states (ORS) of the system with type 2 turbomachinery

	Unit	ORS1	ORS2	ORS3
Turbomachinery speed relative to the cycle design point	%	20	20	20
Turbine bypass valve	%	58	24	0
Turbine valves	%	0	0	100
Compressor inlet p	bar	117.3	122.1	122.6
Compressor outlet p	bar	119.4	125.2	125.7
CHX outlet T	°C	111	150	155
CHX thermal power	MW	1.2	1.2	1.2
Mass flow rate (CO ₂)	kg/s	8.5	5.9	5.7
Compressor efficiency	%	50.7	68.2	68.9
Turbine efficiency	%	0	0	71.4
Compressor power	kW	7.1	5.0	4.9
Turbine power	kW	0	0	6.5
Fan power	kW	0.6	0.4	0.4
Total power	kW	-7.7	-5.4	1.2

In the following, the challenges of the start-up are discussed. If the cycle is heated too fast, the rapidly expanding fluid in the CHX might build up pressure quickly, forcing the compressor to surge due to decreasing mass flow. Additionally, the control of the compressor inlet temperature needs to be switched on soon enough to avoid a density drop at the compressor inlet. Depending on the characteristic of the turbine bypass valve, the valve opening must be reduced considerably. In this analysis, the non-linear characteristic observed in [10] is assumed. At small openings, a further throttling must be done carefully to avoid compressor surge. Before the valves at the turbine are opened, it must be ensured that the current conditions will result in a forward flow over the turbine, e.g. pressure ratio must be high enough. Otherwise, no flow or even reverse flow may occur.

With the current model, this could be observed by a decreased time step and an infinite iteration in the search of an adequate mass flow balance between the bypass and the turbine.

CYCLE PERFORMANCE ANALYSIS

In this chapter, the cycle is analysed over a wide range of conditions to show the operational limits of the cycle. All analysed operation points were approached via transient ramps in the turbomachinery rotational speed and the steam mass flow rate, while the compressor inlet temperature T_1 was held constant by the controller and the steam inlet temperature was equal to its design value in Table 2. Then all boundary conditions were kept constant until a steady-state was reached. A change of less than 0.5 % in terms of the excess power output ΔP can be reached for all investigated cases. Most cases are considerably closer to a real steady-state with deviations of less than 0.1 %. The highest deviations occur at an ambient temperature of $-45\text{ }^\circ\text{C}$ and are discussed below. Additionally, it should be mentioned that the following figures are based on the conservative assumptions made in the design chapter. Less conservative assumptions, like higher turbomachinery efficiencies especially in part-load, will improve the performance of the system.

Figure 7 shows the excess power output ΔP of the cycle using type 2 performance maps at the design conditions, namely at a compressor inlet temperature of $55\text{ }^\circ\text{C}$ and an air inlet temperature of $45\text{ }^\circ\text{C}$. In terms of the power of the CHX \dot{Q}_{CHX} and turbomachinery rotational speed n , the cycle design point is located at 10 MW and 23 krpm, respectively. The turbomachinery rotational speed and the steam mass flow rate are varied from 20 % to 120 % compared to their value at the design point of the cycle. The colourmap indicates that the excess power is decreasing both with decreasing \dot{Q}_{CHX} and decreasing n . Moreover, Figure 7 shows regions in white where the cycle cannot be operated. First, in the lower right, the operation range is limited by the heat transfer in the CHX and the maximum steam temperature. Thermodynamically, the turbine inlet temperature T_3 is always lower than the maximum steam temperature. The maximum steam temperature results from the maximum operating pressure of the reactor in case of a BWR; for PWR it is determined by secondary pressure or the average primary coolant temperature in case of exposed steam generator tubes. The overheating, resulting from the latter case is assumed in Table 2 in Annex A. Secondly, in the upper left, the operation range is limited because the excess power output drops below zero, which means that the cycle is not self-propelling any more.

In Figure 7, it can be observed that ΔP decreases with decreasing \dot{Q}_{CHX} and n and an operation line in terms of maximum ΔP exists between the two borders. From a Carnot point of view, operation at the highest turbine inlet temperature should yield the highest efficiency. This operation line, which is equal to the right border of the operation range, is feasible because ΔP is higher than zero. Moreover, the compressor inlet pressure increases to about 135 bar with decreasing n along this line. This is a result of the decreasing density on the high-

pressure side. However, the highest ΔP does not occur at the highest turbine inlet temperature. This is mainly due to the turbine and compressor efficiencies departing from their optimal value. Over the whole speed range, the highest turbine efficiencies are reached for conditions where the turbine inlet density is close to its design inlet density. Therefore, another operation strategy would be to keep the inlet density of the turbine constant instead of the inlet temperature. Indirectly this also ensures relatively constant compressor inlet densities because both densities in the cycle are linked to each other as long as no CO_2 mass is removed or added. To keep the turbine inlet density constant, the turbine inlet temperature must be decreased with decreasing turbomachinery rotational speed because the pressure ratio and the turbine inlet pressure are also decreasing. However, it should be mentioned that the goal of the system is to reliably remove the decay heat and not to maximize its power output. Therefore, it needs to be analysed in the reactor simulations which strategy enables a more reliable operation in interaction with the nuclear power plant.

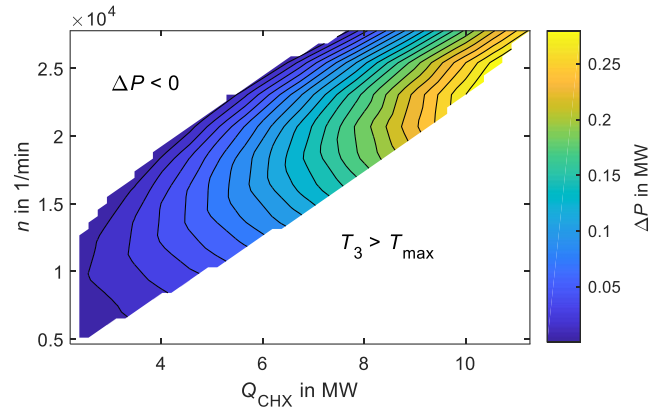


Figure 7: Excess power output of the cycle at $T_1 = 55\text{ }^\circ\text{C}$ and $T_{air,in} = 45\text{ }^\circ\text{C}$ with type 2 turbomachinery

Compared to the type 2 turbomachinery, operation with type 1 turbomachinery yielded slightly higher ΔP mainly because the compressor efficiency of type 1 is slightly higher. Regarding compressor efficiency, the highest difference is 2.9 % and occurs at the design point of the cycle because type 2 turbomachinery is designed for part-load operation with a higher compressor surge margin, as mentioned in the turbomachinery chapter. From the design point of the cycle, the resulting ΔP difference of 35 kW continuously decreases with decreasing speed. At the lowest speeds, the type 1 turbomachinery almost reaches the surge line. Therefore, care must be taken when this type of turbomachinery is applied, e.g. the compressor recirculation valve must be opened slightly to increase the surge margin. However, this might decrease the excess power to zero, resulting in a stop of the system. Furthermore, the higher surge margin of type 2 is an advantage during start-up. Due to these reasons, type 2 turbomachinery is preferred.

Figure 8 shows the excess power output ΔP of the cycle using type 2 performance maps at the off-design conditions, namely at a compressor inlet temperature of $35\text{ }^\circ\text{C}$ and an air

inlet temperature of 25 °C. For \dot{Q}_{CHX} and n the same range is shown as in Figure 7. At these conditions, different behaviour of ΔP can be observed. First, the area where ΔP is smaller than zero increases except for low \dot{Q}_{CHX} . Secondly, the maximum of ΔP is located at a lower \dot{Q}_{CHX} and n . Thirdly, the lower limit of the cycle performance map is slightly shifted to lower n , especially for higher \dot{Q}_{CHX} . The first two observations are mainly due to an increasing fan power. The required fan power increases significantly, especially at high \dot{Q}_{CHX} and n , because the required air mass flow rate considerably increases compared to the design airflow rate of the UHS and the required power increases cubically with air mass flow rate. The reason for the considerably higher demand of air mass flow rate is that the major part of the heat has to be removed at the pseudocritical temperature of CO₂ at a lower system pressure and in this case, this significantly decreases the available temperature difference between the CO₂ and the air. Additionally, the increased heat transfer coefficient on the CO₂-side hardly influences the overall heat transfer coefficient because the air-side limits the heat transfer. The third observation, the shift of the lower limit, results from the higher available enthalpy difference in the cycle. To reach the same \dot{Q}_{CHX} , a lower cycle mass flow rate is required and, therefore, a lower n compared to the previous case.

For these operation conditions, many operation points with the type 1 turbomachinery would be close to or beyond the surge line. This is because decreasing the compressor inlet temperature generally shifts the cycle operation closer to the surge line. Furthermore, controlling the compressor inlet temperature at pressures and temperatures closer to the critical point is probably inappropriate, as mentioned in the control chapter.

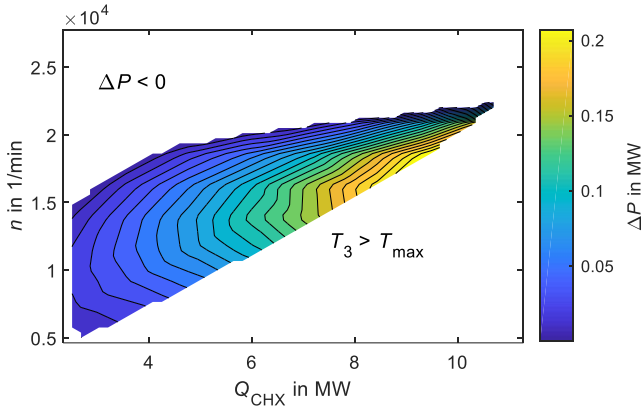


Figure 8: Excess power output of the cycle at $T_1 = 35$ °C and $T_{air,in} = 25$ °C with type 2 turbomachinery

After discussing these issues, the question arises how the cycle can be operated reliably over the whole range of ambient temperatures, e.g. from -45 °C to 45 °C. Since no inventory control is considered, a decreasing compressor inlet temperature also results in decreasing cycle pressure. Therefore, not only the performance changes significantly at lower compressor inlet temperatures but also the operation conditions might drop into the two-phase region. An easy approach to avoid all these issues would be to keep the compressor inlet temperature constant over

the whole range of ambient temperatures. As an example, the cycle performance at an ambient temperature of -45 °C with the compressor inlet kept constant at 55 °C is shown in Figure 9. At low ambient temperatures the cycle performance map qualitatively still equals the performance shown in Figure 7. The main difference is a generally higher ΔP resulting from a lower fan power because the fan speed of the UHS must be decreased to keep the compressor inlet temperature constant. For the operation of the cycle the same approaches, which were described for an ambient temperature of 45 °C, are valid. However, for very low ambient temperatures it might not be sufficient to only decrease the fan speed because the expected heat removal by natural convection would be too high. Thus, either the natural convection airflow must be throttled further, e.g. by flaps at the UHS outlet, or a part of the CO₂ flow must bypass the UHS to reach a constant compressor inlet temperature by mixing cold and hot CO₂. Moreover, it can be observed that the controller parameters need further tuning at very low air mass flow rates due to the non-linear behaviour of the heat transfer coefficient shown in Figure 5.

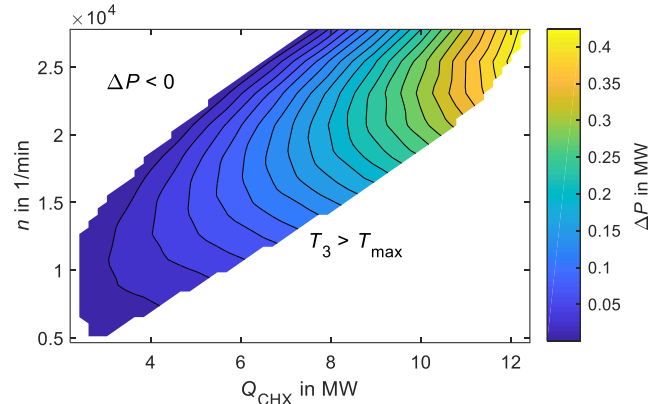


Figure 9: Excess power output of the cycle at $T_1 = 55$ °C and $T_{air,in} = -45$ °C with type 2 turbomachinery

As shown in Figure 7 and Table 3, the excess power at the design point is 283 kW. Since only a self-propelling system is required, the turbine power can be decreased. Therefore, it is an option to open the turbine bypass slightly to decrease the mass flow rate over the turbine and increase the mass flow rate in the cycle, resulting in higher heat removal from the nuclear power plant. However, the valve has to be operated at a very small opening. With the current valve design, the opening must be lower than 3.9 % to keep the system self-propelling. This opening increases the cycle mass flow rate by 6.3 kg/s and the thermal power of the CHX by 2.2 MW. For better control in this operation mode, a second turbine bypass with a smaller pipe diameter would be advantageous.

CONCLUSIONS

In this study, the sCO₂ heat removal system was designed and simulated under varying ambient and steam side boundary conditions, using the assumptions developed in the project sCO₂-4-NPP. Bypasses were considered in the layout of the

cycle to cope with special operation conditions, e.g. start-up. Since cold start-up at very low ambient temperatures is challenging, it was proposed to start the system from an operational readiness state. In this state, the turbomachinery and the fans are already under operation at low speeds and the compressor inlet condition is close to its design point. This enables fast start-up of the system in case of an accident in the nuclear power plant. At 20 % turbomachinery rotational speed compared to the design point of the cycle, a self-propelling system could be achieved at 12 % of the design thermal power.

To operate the system under changing ambient conditions, the compressor inlet condition needs to be controlled. Compressor inlet temperature control was selected because the cycle operation pressure was sufficiently higher than the critical pressure of CO₂. A PI-controller was used to change the mass flow rate of the fans. For low ambient temperatures, adapted controller parameters are required due to the higher sensitivity of the compressor inlet temperature to the air mass flow rate. Therefore, variable controller parameters which depend on ambient temperature are suggested. In the simulation, the controller was operated successfully over a wide range of conditions. However, the performance and the control of the UHS and the system at very low ambient temperatures with fans switched off should be analysed in more detail. If the UHS outlet condition cannot be controlled reliably, a UHS bypass could be used to mix hot and cold CO₂ to keep the compressor inlet at the desired condition.

The performance analysis of the system suggests that it is a good option to operate the system at the design compressor inlet temperature of 55 °C at any ambient or steam-side boundary condition. It is not preferred to operate the system closer to the critical point of CO₂ because this introduces further operational challenges. Due to higher isentropic efficiency, type 1 turbomachinery provides a higher excess power. However, type 2 turbomachinery is preferred due to the higher surge margin because only a self-propelling and reliable system operation is required. With decreasing thermal power of the CHX, the turbomachinery rotational speed must be decreased to keep the system self-propelling. Different operation strategies are feasible and need to be tested in interaction with the nuclear power plant. Keeping the turbine inlet density constant results in a higher excess power than constant turbine inlet temperature. A good start for the reactor simulations might be to keep the turbine inlet temperature constant at its design point because this should also balance the heat removal from the reactor when the decay power is lower than the heat removal capacity of the systems. At a higher decay power, the system should be operated at the maximum allowable speed to maximize the heat removal and keep the inventory loss of the reactor to a minimum. At these conditions, it might be possible to increase the heat removal further by opening the turbine bypass slightly.

The conclusions drawn in this work are valid for the sCO₂-HeRo system in general and are independent of the type of reactor. However, the next step is to simulate the heat removal system in interaction with the nuclear power plant because the thermal-hydraulic behaviour and the limitations depend on the

reactor type. An integrated analysis enables testing and further improvement of the operational strategies provided in this paper.

NOMENCLATURE

$\Delta h_{is,t}$	specific total isentropic enthalpy difference (J/kg)
\dot{m}	mass flow rate (kg/s)
n	rotational speed (1/min)
p	pressure (bar)
T	temperature (°C)
ΔP	excess power (MW)
\dot{Q}	thermal power (MW)

Subscripts

1	compressor inlet
3	turbine inlet
el	electrical

Acronyms

CHX	compact heat exchanger
HeRo	heat removal system
ORS	operational readiness state
sCO ₂	supercritical carbon dioxide
TAC	turbomachinery (turbo-alternator-compressor)
UHS	ultimate heat sink

ACKNOWLEDGEMENTS

The research presented in this paper has received funding from the Euratom research and training programme 2014-2018 under grant agreement No. 847606 “Innovative sCO₂-based Heat removal Technology for an Increased Level of Safety of Nuclear Power plants” (sCO₂-4-NPP).

The work of University of Stuttgart was also funded by the German Ministry for Economic Affairs and Energy (BMWi. Project No. 1501557) on basis of a decision by the German Bundestag.

REFERENCES

- [1] Venker, J. (2015) Development and Validation of Models for Simulation of Supercritical Carbon Dioxide Brayton Cycles and Application to Self-Propelling Heat Removal Systems in Boiling Water Reactors. Stuttgart. <https://doi.org/10.18419/opus-2364>
- [2] sCO₂-HeRo. <http://www.sco2-hero.eu/>
- [3] Benra, F.K., Brillert, D., Frybort, O., Hajer, P., Rohde, M., Schuster, S. et al. (2016) A supercritical CO₂ low temperature Brayton-cycle for residual heat removal. *The 5th International Symposium-Supercritical CO₂ Power Cycles*, 1–5. <https://doi.org/10.1007/s13398-014-0173-7.2>
- [4] Wu, P., Gao, C. and Shan, J. (2018) Development and Verification of a Transient Analysis Tool for Reactor System Using Supercritical CO₂ Brayton Cycle as Power Conversion System. *Science and Technology of Nuclear Installations*, Hindawi. 2018, 1–14.

- <https://doi.org/10.1155/2018/6801736>
- [5] Bestion, D. (2008) System code models and capabilities. *THICKET*, Grenoble. p. 81–106.
- [6] Mauger, G., Tauveron, N., Bentivoglio, F. and Ruby, A. (2019) On the dynamic modeling of Brayton cycle power conversion systems with the CATHARE-3 code. *Energy*, Elsevier Ltd. 168, 1002–16. <https://doi.org/10.1016/j.energy.2018.11.063>
- [7] Batet, L., Alvarez-Fernandez, J.M., Mas de les Valls, E., Martinez-Quiroga, V., Perez, M., Reventos, F. et al. (2014) Modelling of a supercritical CO₂ power cycle for nuclear fusion reactors using RELAP5–3D. *Fusion Engineering and Design*, North-Holland. 89, 354–9. <https://doi.org/10.1016/J.FUSENGDES.2014.03.018>
- [8] Hexemer, M. (2011) Supercritical CO₂ Brayton Cycle Integrated System Test (IST) TRACE Model and Control System Design. *Supercritical CO₂ Power Cycle Symposium*, 1–58.
- [9] Hofer, M., Buck, M. and Starflinger, J. (2019) ATHLET extensions for the simulation of supercritical carbon dioxide driven power cycles. *Kerntechnik*, 84, 390–6. <https://doi.org/10.3139/124.190075>
- [10] Hofer, M., Buck, M., Cagnac, A., Prusek, T., Sobceki, N., Vlcek, P. et al. (2020) Deliverable 1.2: Report on the validation status of codes and models for simulation of sCO₂-HeRo loop. sCO₂-4-NPP.
- [11] Hajek, P., Vojacek, A. and Hakl, V. (2018) Supercritical CO₂ Heat Removal System - Integration into the European PWR fleet. *2nd European SCO₂ Conference*, Essen. p. 0–7. <https://doi.org/10.17185/dupublico/460>
- [12] Vojacek, A., Hakl, V., Hajek, P., Havlin, J. and Zdenek, H. (2016) Deliverable 1.3: Documentation system integration into European PWR fleet. sCO₂-HeRo.
- [13] Hofer, M., Buck, M. and Starflinger, J. (2021) Operational analysis of a self-propelling heat removal system using supercritical CO₂ with ATHLET. *4th European Supercritical CO₂ Conference*, Prague.
- [14] Hexemer, M.J., Hoang, H.T., Rahner, K.D., Siebert, B.W. and Wahl, G.D. (2009) Integrated Systems Test (IST) Brayton Loop Transient Model Description and Initial Results. *S-CO₂ Power Cycle Symposium*, Troy. p. 1–172.
- [15] Carstens and Nathan. (2007) Control strategies for supercritical carbon dioxide power conversion systems. *Massachusetts Institute of Technology*.
- [16] Vojacek, A., Melichar, T., Hajek, P., Doubek, F. and Hoppe, T. (2019) Experimental investigations and simulations of the control system in supercritical CO₂ loop. *3rd European Conference on Supercritical CO₂ (SCO₂) Power Systems*. <https://doi.org/10.17185/dupublico/48916>
- [17] Ren, H., Hacks, A., Schuster, S. and Brillert, D. (2021) Mean-line analysis for supercritical CO₂ centrifugal compressors by using enthalpy loss coefficients. *4th European Supercritical CO₂ Conference*, Prague.
- [18] Pham, H.S., Alpy, N., Ferrasse, J.H., Boutin, O., Tothill, M., Quenaut, J. et al. (2016) An approach for establishing the performance maps of the sc-CO₂ compressor: Development and qualification by means of CFD simulations. *International Journal of Heat and Fluid Flow*, 61, 379–94. <https://doi.org/10.1016/j.ijheatfluidflow.2016.05.017>
- [19] Hofer, M., Buck, M., Strätz, M. and Starflinger, J. (2019) Investigation of a correlation based model for sCO₂ compact heat exchangers. *3rd European Supercritical CO₂ Conference*, Paris. p. 1–9. <https://doi.org/10.17185/dupublico/48874>
- [20] Alfani, D., Astolfi, M., Binotti, M., Silva, P. and Macchi, E. Off-design Performance of CSP Plant Based on Supercritical CO₂ Cycles. *SOLARPACES 2019: International Conference on Concentrating Solar Power and Chemical Energy Systems*.
- [21] Austregesilo, H., Bals, C., Hora, A., Lerchl, G., Romstedt, P., Schöffel, P. et al. (2016) ATHLET Models and Methods. Garching.

ANNEX A: CYCLE AND HEAT EXCHANGER DESIGN

In Table 2 the assumptions for the cycle design are given and in Table 4 and Table 3 the results of the cycle design are provided. Table 5 and Table 6 show the CHX and UHS design, respectively.

Table 2: Assumptions for the cycle design

Name	Value	Unit
Thermal power of one unit	10	MW
Steam pressure	82	bar
Steam inlet temperature	308	°C
Turbine inlet temperature	286.6	°C
Compressor inlet temperature	55	°C
Ambient temperature	45	°C
Pressure drop of CHX (CO ₂)	2	bar
Pressure drop of UHS (CO ₂)	0.25	bar
Piping pressure drop (CO ₂)	2	bar
Pressure ratio of the compressor	1.7	
Isentropic efficiency of the compressor	0.7	
Isentropic efficiency of the turbine	0.7	
Specific power of fans [20]	8.5	kW _{el} / MW _{th}

Table 3: Results of the cycle design

Name	Value	Unit
Thermal power of CHX	10.0	MW
Thermal power of UHS	9.6	MW
Compressor power	630	kW
Turbine power	994	kW
Fan power	82	kW
Excess Power	283	kW
CO ₂ mass flow rate	29.7	kg/s
steam mass flow rate (with $T_{H_2O,out} = 150$ °C)	4.6	kg/s
Air mass flow rate (with $T_{air,out} = 70$ °C)	382.3	kg/s

Table 4: Thermodynamic results of the cycle design

	p [bar]	T [°C]
Compressor inlet	126.3	55.0
Compressor outlet	214.7	80.8
CHX inlet	214.2	80.8
CHX outlet	212.2	286.6
Turbine inlet	211.7	286.6
Turbine outlet	127.5	243.2
UHS inlet	127.0	243.2
UHS outlet	126.8	55.0

Table 5: CHX design

Name	Value	Unit
Number of channels per side	9000	
Channel geometry	2x1	mm ²
Channel length	1.1	m
HCO total length (equal to channel length)	1.1	m
HCO width (equal to channel perimeter)	6	mm
HCO effective thickness	1.53	mm
Steel mass	972	kg

Table 6: UHS design

Name	Value	Unit
Number of pipes (CO ₂)	732	
Pipe diameter	10	mm
Pipe length	22	m
Total airflow area in UHS	240	m ²
Total heat transfer area (air)	33000	m ²
HCO total length (equal to pipe length)	22	m
HCO width (artificial to account for pipe section outside of the airflow)	27.5	mm
HCO effective thickness	1	mm
Total steel/aluminium mass	1.81	t

ANNEX B: PERFORMANCE OF TURBOMACHINE

The design parameters of type 1 and type 2 applied in this paper are displayed below.

Table 7: Design parameters of turbomachinery

	Parameter	Type 1	Type 2	Unit
Compressor	Inlet total pressure	126.3	126.3	bar
	Inlet total temperature	328.15	328.15	K
	Total pressure ratio	1.7	1.53	–
	Mass flow rate	29.7	20	kg/s
	Rotational speed	19728	19847	rpm
Turbine	Inlet total pressure	211.7	211.7	bar
	Inlet total temperature	559.72	559.72	K
	Total pressure ratio	1.66	1.66	–
	Mass flow rate	29.7	29.7	kg/s
	Rotational speed	19728	23139	rpm

The other performance maps of the applied turbomachines are displayed below:

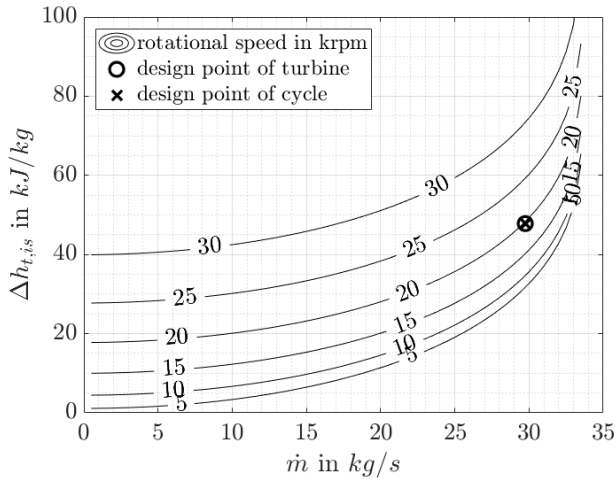


Figure 10: Turbine performance map of type 1 regarding total isentropic enthalpy drop over the mass flow rate

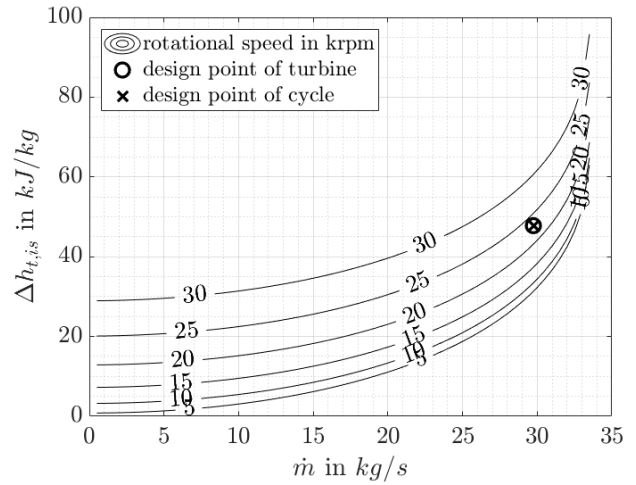


Figure 11: Turbine performance map of type 2 regarding total isentropic enthalpy drop over the mass flow rate

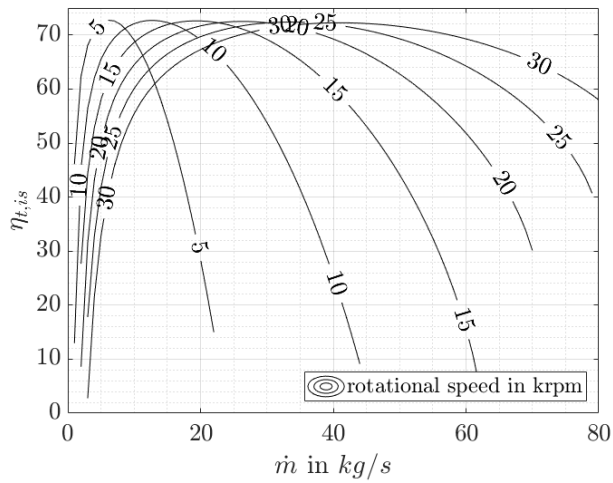


Figure 12: Compressor performance map of type 1 regarding total isentropic efficiency over the mass flow rate

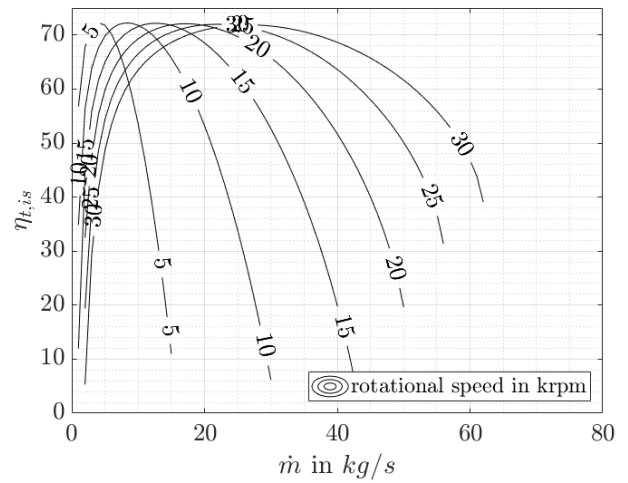


Figure 13: Compressor performance map of type 2 regarding total isentropic efficiency over the mass flow rate

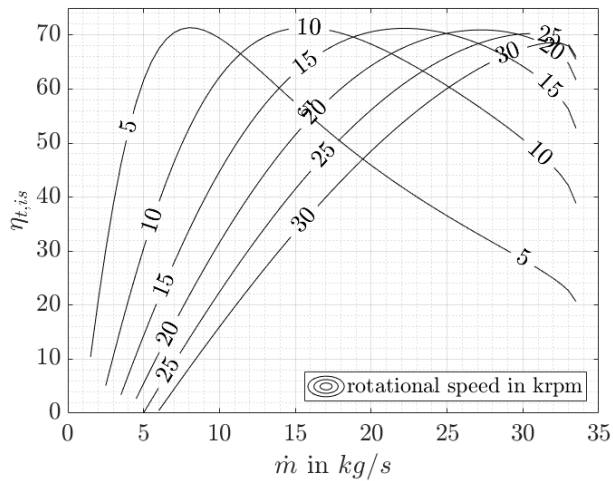


Figure 14: Turbine performance map of type 1 regarding total isentropic efficiency over the mass flow rate

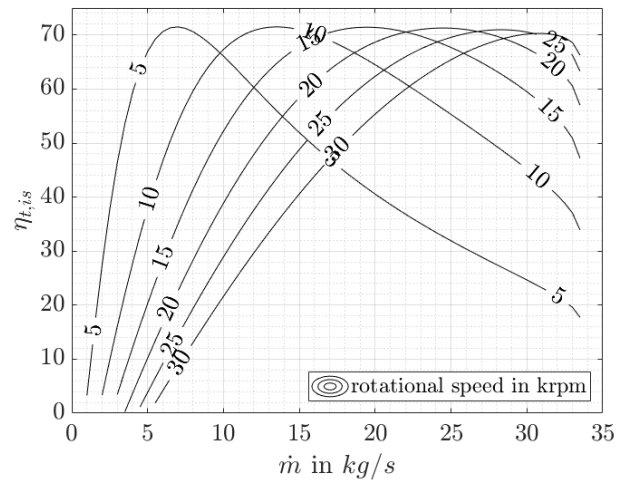


Figure 15: Turbine performance map of type 2 regarding total isentropic efficiency over the mass flow rate

CHEMICAL KINETIC MECHANISM FOR COMBUSTION IN SUPERCRITICAL CARBON DIOXIDE

James M. Harman-Thomas*

Department of Mechanical
Engineering
Energy 2050, Ella Armitage
Building
University of Sheffield
Sheffield, S3 7RD, UK
jmharman-
thomas1@sheffield.ac.uk

Mohamed Pourkashanian

Department of Mechanical
Engineering
Energy 2050, Ella Armitage
Building
University of Sheffield
Sheffield, S3 7RD, UK

Kevin J. Hughes

Department of Mechanical
Engineering
Energy 2050, Ella Armitage
Building
University of Sheffield
Sheffield, S3 7RD, UK

ABSTRACT

The Allam cycle is a thermodynamic cycle for the combustion of gaseous fuels under oxyfuel conditions with inherent carbon capture. As the CO₂ is captured intrinsically, the efficiency penalty of capture on the overall plant is small, meaning that Allam cycle power plants achieve a similar efficiency to traditional fossil fuel power plants without carbon capture and storage. At high-pressures and a high-CO₂ dilution, combustion mechanisms are poorly understood. Sensitivity and quantitative analysis of four established chemical kinetic mechanisms were used to determine important reactions and the best performing mechanisms at different conditions. CH₃O₂ chemistry was identified as a pivotal mechanism component for modelling methane combustion above 200 atm. The University of Sheffield (UoS) supercritical CO₂ (sCO₂) mechanism created in the present work better models the ignition delay time (IDT) of high-pressure combustion in a large dilution of CO₂. Quantitative analysis showed that the UoS sCO₂ mechanism was the best fit to the greatest number of IDT datasets and had the lowest average absolute error value, indicating the superior performance compared to four existing chemical kinetic mechanisms, well-validated for lower pressure conditions.

INTRODUCTION

The global atmospheric carbon dioxide (CO₂) concentration has rapidly increased since the industrial revolution due to anthropogenic emissions. The atmospheric CO₂ concentration now exceeds 400 parts per million (ppm) [1]. The power industry is a significant contributor to CO₂ emissions, due to a continued reliance on fossil fuels. Despite renewable energy becoming increasingly competitive, humanity's consumption of fossil fuels is not declining quickly enough, and thus new technologies to produce clean, emissions-free energy from fossil fuels are required [2].

One emerging technology is the Allam cycle which uses natural gas, or synthesis gas (syngas) from coal gasification, to produce electricity which inherently captures 100% of its emissions [3]. In a comparative review of emerging carbon capture and storage technologies, the Allam cycle was the only coal combustion technology that has the potential to reduce the production cost of electricity [4]. The Allam cycle is a basic thermodynamic cycle that burns the gaseous fuel and high-purity oxygen in a CO₂ dilution of up to 96% [3]. Following combustion, the water (H₂O) produced during combustion is removed to leave high-purity, pipeline-ready CO₂, most of which is recycled into the combustion chamber with the small amount produced from combustion being removed. The high-pressures of the Allam cycle at the turbine inlet, coupled with the greater power density of the supercritical CO₂ (sCO₂) working fluid compared to traditional steam or gas working fluids leads to Allam cycle power plants having a smaller footprint [3]. The Allam cycle achieves a high-efficiency by alleviating the energy penalty of the air separation unit (ASU) by utilising the waste heat from compression in the ASU in the main power cycle [5].

A major challenge that the Allam cycle faces is a lack of experimental data at high-pressure and a high dilution of sCO₂ [6]. Although current chemical kinetic mechanisms are well-validated at low pressures and low-CO₂ dilutions, at Allam cycle conditions, existing mechanisms are in poor agreement with the limited experimental data available. Mechanisms are required to be able to accurately model combustion and maximise the efficiency of the plant design. The present study evaluates how existing chemical kinetic mechanisms predict experimental data at high-CO₂ dilutions for different gaseous fuels and identifies which reactions have the greatest influence on the ignition delay time (IDT). A series of sensitivity analyses were then used to assist in creating a new mechanism which that accurately models high-pressure oxyfuel combustion.

* corresponding author(s)

OXY-FUEL COMBUSTION

The present study focused on methane, hydrogen, and syngas as these are the most important fuels to the Allam cycle. Methane is the primary component of natural gas and syngas is produced from coal gasification. The datasets used in the present study were selected due to their high-pressure and large dilution of CO₂. All of these IDTs were recorded using the shock tube experimental technique which creates an almost instantaneous, high-pressure, adiabatic conditions, and then reaction progress is monitored using various diagnostic techniques. Shock tubes do have some non-instantaneous pressure rise post-shock [7], which influences the IDT, which was omitted from the present study due to the data not being available. Having a large dilution of CO₂ has both physical and chemical effects on combustion. As well as having a different third body efficiency to other bath gases, CO₂ may have a catalytic effect on the reactions [8].

MODELLING PROCEDURE

The modelling work undertaken throughout this study was performed using ANSYS Chemkin-Pro 2019 R3 [9] and existing chemical mechanisms Aramco 2.0 [10-16], USC II [17], GRI 3.0 [18], and DTU [19, 20]. The IDT data was modelled for different test gases using the aforementioned chemical mechanisms. A closed homogeneous batch reactor with ‘constrain volume and solve energy equation’ problem type which resembles the adiabatic conditions of the test-gas region of the shock tube was used to model the IDT for all of the datasets. To determine the IDT, the mole fraction of OH was plotted against the reaction time at a given temperature. The IDT was defined as the difference between time-zero and the onset of ignition, the onset of ignition being defined as the time of the maximum gradient of the increasing OH concentration.

A series of sensitivity analyses were performed using OH species sensitivity at the IDT for a given temperature within a dataset. The temperatures were selected at points of large discrepancy between either the mechanism and the experimental data point or the different mechanisms being studied. The top ten most sensitive reactions were determined and plotted as a bar chart where increasing the reaction rate would reduce the IDT of a reaction with a positive sensitivity coefficient and increase the IDT for a reaction with a negative sensitivity coefficient.

The University of Sheffield (UoS) sCO₂ mechanism was created by interpreting the sensitivity analysis where the mechanism performed well and comparing the rate coefficients of the four mechanisms studied. This allowed the selection of the best rate coefficient to better model every dataset, without affecting the conditions where the mechanism performed well.

METHANE COMBUSTION

The highest-pressure data studied under a high-CO₂ dilution was selected preferentially for analysis. The datasets studied are from Pryor et al. [21], Shao et al. [7], Karimi et al. [22] and Barak et al. [23]. Table 1 shows the eleven datasets and the conditions that each dataset was recorded at. The error values used in IDT were taken from their respective publications.

Table 1. Methane datasets analysed in the present study.

Dataset	Reference	Average Pressure /atm	Equivalence Ratio (Φ)	CO ₂ Dilution (%)
M1	[21]	29.6	1.00	85.00
M2	[23]	79.9	1.00	36.50
M3	[22]	99.0	1.00	85.00
M4	[22]	97.0	0.50	80.00
M5	[22]	201.8	1.00	85.00
M6	[7]	32.2	1.00	77.50
M7	[7]	106.3	1.00	77.50
M8	[7]	260.0	1.00	77.50
M9	[7]	31.4	1.27	86.17
M10	[7]	74.7	1.27	86.17
M11	[7]	266.3	1.27	86.17

HYDROGEN COMBUSTION

The only published IDT data for hydrogen combustion in a high-CO₂ dilution is by Shao et al. [7]. The authors report an IDT value for hydrogen combustion diluted in 85% CO₂ at two different equivalence ratios shown in Table 2.

Table 2. Hydrogen datasets analysed in the present study.

Dataset	Reference	Average Pressure /atm	Equivalence Ratio (Φ)	CO ₂ Dilution (%)
H1	[7]	109.6	1.00	85.00
H2	[7]	270.6	1.00	85.00
H3	[7]	38.4	0.25	85.00

SYNTHESIS GAS COMBUSTION

Oxy-syngas combustion data has been published by Barak et al. [23, 24] was investigated during the present study.

Table 3. Syngas datasets analysed in the present study.

Dataset	Reference	Average Pressure /atm	Equivalence Ratio (Φ)	CO ₂ Dilution (%)
S1	[23]	78.9	1.02	91.80
S2	[23]	91.7	0.41	64.50
S3	[23]	89.6	0.41	92.20
S4	[23]	89.7	1.09	63.90
S5	[24]	41.5	1.00	85.00
S6	[24]	38.6	1.00	85.00
S7	[24]	38.5	1.00	85.00
S8	[24]	38.4	1.00	85.00

MECHANISM SELECTION

The four mechanisms used in this study were selected based on their suitability for modelling the combustion of lower hydrocarbons. GRI 3.0 contains 53 species and 325 reactions and is validated against IDTs for methane and ethane below 100 atm. USC II was released in 2007 and contains 111 species and 784 reactions and is applicable to the combustion of H₂/CO/C₁-C₄ compounds. Aramco 2.0 contains the greatest amount of chemistry of the selected mechanisms with 493 species and 2716 reactions and was developed for the combustion of C₁-C₄ hydrocarbons and hydrogen. The DTU mechanism contains 102 species and 894 reactions and was developed by the Technical

University of Denmark for the high-pressure combustion of H₂ and C₁/C₂ hydrocarbons.

The mechanisms are quantitatively evaluated using an average absolute error (E ,%) value using the following expression [25].

$$E = \frac{1}{N} \sum_{i=1}^N \left| \frac{X_{sim,i} - X_{exp,i}}{X_{exp,i}} \right| \times 100 \quad (1)$$

Where N represents the number of data points in the experimental set, $X_{sim,i}$ and $X_{exp,i}$ are the modelled and experimental results for the i th IDT datapoint respectively. A mechanism's E value gives a quantitative indication of performance. The smaller the E value, the smaller the difference between the experimental and measured data point and the better the mechanism is performing.

It must be noted that due to the error in the data points, the quantitative analysis cannot be considered a definite way to determine which mechanism is best performing when multiple mechanisms lie within error. However, due to the large number of datasets being studied, it is a good indicator of the mechanism's performance.

ANALYSIS OF METHANE DATASETS

Table 4 compares the four mechanisms for each experimental dataset. The mechanisms were ranked by i) the average absolute average error (E) and ii) the number of times the mechanism was the best fit to the data. Table 4 shows the Aramco 2.0 mechanism has the lowest average E value calculated from equation 1 followed closely by the DTU mechanism. Interestingly, the USC II mechanism was the best fit to the greatest number of datasets but has the largest average E value due to its poor performance in three conditions where Aramco 2.0 and DTU perform well: M5, M8, and M11. These three were the highest-pressure conditions measured (>200 atm), indicating a deficiency in the chemistry of methane combustion above 200 atm in the USC II mechanism. The sensitivity analysis of USC II and Aramco 2.0 across the methane datasets were used to identify which reactions led to the poor performance of USC II at high-pressure conditions.

Table 4. Quantitative analysis of the methane datasets.

	Aramco 2.0	DTU	GRI 3.0	USC II
M1	41.47	37.98	76.11	17.04
M2	17.10	12.60	54.37	9.55
M3	24.85	27.18	54.76	20.49
M4	14.26	13.44	56.66	8.24
M5	9.53	7.35	32.49	45.53
M6	60.09	47.06	23.63	38.39
M7	15.02	16.64	43.26	20.65
M8	26.87	37.65	204.32	323.56
M9	94.06	99.87	31.97	56.38
M10	18.91	25.79	57.11	13.79
M11	3.99	24.03	32.53	125.37
Average	29.65	31.78	60.66	61.73
No. Best Fit	3	1	2	5

Figure 1 shows the sensitivity analysis of the M11 condition at 1100 K for Aramco 2.0 and USC II which has a significant discrepancy between the modelled IDTs. One of the initial observations was the presence of the CH₃O₂ and CH₃O₂H species within the Aramco 2.0 sensitivity analysis which were absent in USC II. This is because USC II, as well as GRI 3.0, which also performs poorly under these conditions, does not contain CH₃O₂ and CH₃O₂H species, or any of their respective chemistry. In the paper in which the data was published, Shao et al. [7], modelled the data with Aramco 2.0 and FFCM-1 [26] and found a similar agreement between modelled IDTs at the lower pressure conditions and a large discrepancy above 200 atm. This is consistent with the current findings as the FFCM-1 mechanism does not contain CH₃O₂ and CH₃O₂H.

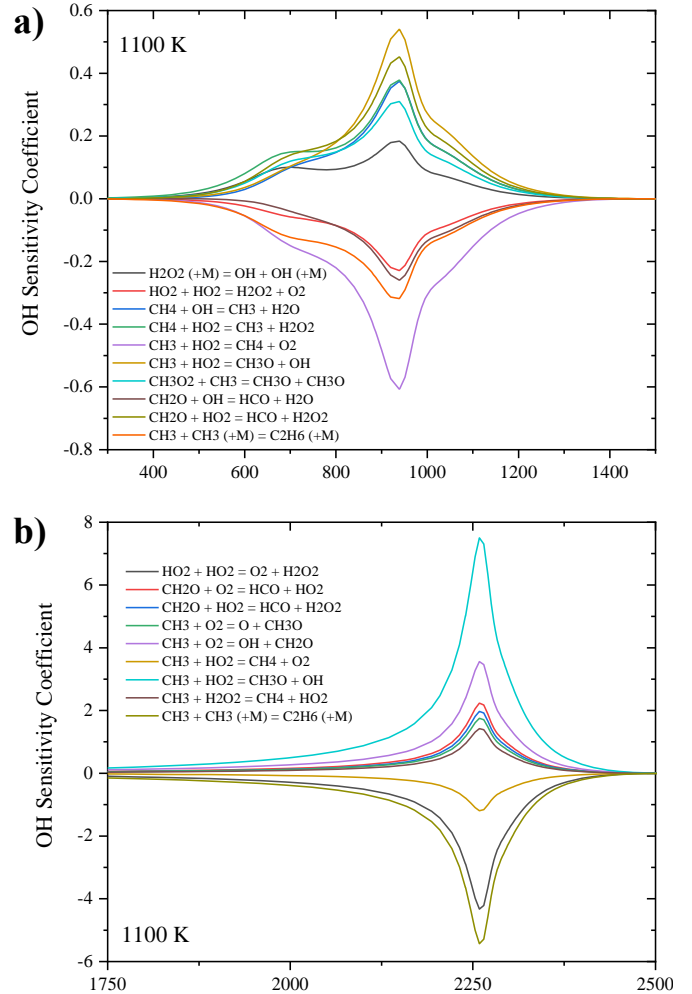
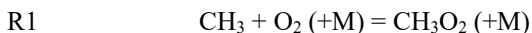


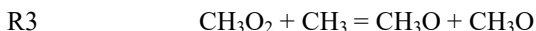
Figure 1: Temperature sensitivity coefficient against time for condition M11; a) Aramco 2.0 and b) USC II.

This observation is key to creating a mechanism that can model combustion in sCO₂. The formation of CH₃O₂ via the recombination of CH₃ and O₂ as shown in R1 has most recently been studied by Fernandes et al. [27] using a high-temperature, high-pressure flow cell in an argon and nitrogen bath gas.

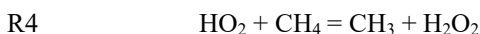
Although the authors do not report an error, they are in good agreement with existing experimental work. Therefore, the rate coefficient can be considered well known at temperatures below 700 K. However, none of this research was performed with a CO₂ bath gas, so despite the good agreement between the different bath gases studied, the rate coefficient may be different in a large dilution of CO and at higher temperatures.



There are two reactions of CH₃O₂ which appear in the sensitivity analysis for M5, M8, and M11: R2 and R3.



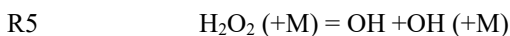
The rate coefficient of R2 used in Aramco 2.0 is from an unknown and unpublished source so is difficult to evaluate. The only published value of the rate coefficient of R2 comes from a review of chemical kinetic data of methane and related compounds by Tsang and Hampson [28]. The authors note there is no direct measurement and thus base their value on R4, a reaction which they argue should be similar. Due to it being an estimated rate coefficient, there is a large amount of uncertainty in the rate coefficient used for R2.



The rate coefficient used for R3 in Aramco 2.0 was theoretically calculated by Keiffer et al. [29] at 0.169 bar from 298-530 K in an oxygen bath gas. The reaction has been measured twice experimentally by Pilling and Smith [30] and Parkes [31] in argon and nitrogen and bath gases respectively, both at 298 K. Due to the importance of R3 during high-pressure combustion of methane, it is important to revisit this reaction at conditions more relevant to Allam cycle combustion.

Other reactions relevant to CH₃O₂ chemistry used in Aramco 2.0 use rate coefficients from Lightfoot et al. [32] between 600K and 719 K at atmospheric pressure. Previous research into CH₃O₂ kinetics has been in relation to atmospheric and low-temperature combustion chemistry [33].

In addition to the importance of CH₃O₂ chemistry, two other discrepancies between the sensitivity analysis of Aramco 2.0 and USC II for the M8 and M11 conditions were identified. Firstly, R5 appeared only for Aramco 2.0. The USC II mechanism uses an older rate coefficient from Baulch et al. [34] whereas Aramco 2.0 uses a more recent theoretical rate coefficient from Troe et al. [35] which was calculated with a CO₂ bath gas.



The second discrepancy noted was the Aramco 2.0 mechanism was considerably more sensitive to R6 than USC II. For this reaction, the USC II rate coefficient is taken from Reid et al. [36]

which is reported to be private communication. The theoretically calculated Aramco 2.0 rate coefficient from Jasper et al. [37] is in agreement with Srinivasan et al. [38] which incorporated experimental data.



The effect of altering the rate coefficients for R5 and R6, and adding CH₃O₂ chemistry into the USC II mechanism was investigated. These changes were made to the USC II mechanism sequentially as shown in figure 2 for conditions M8 and M11.

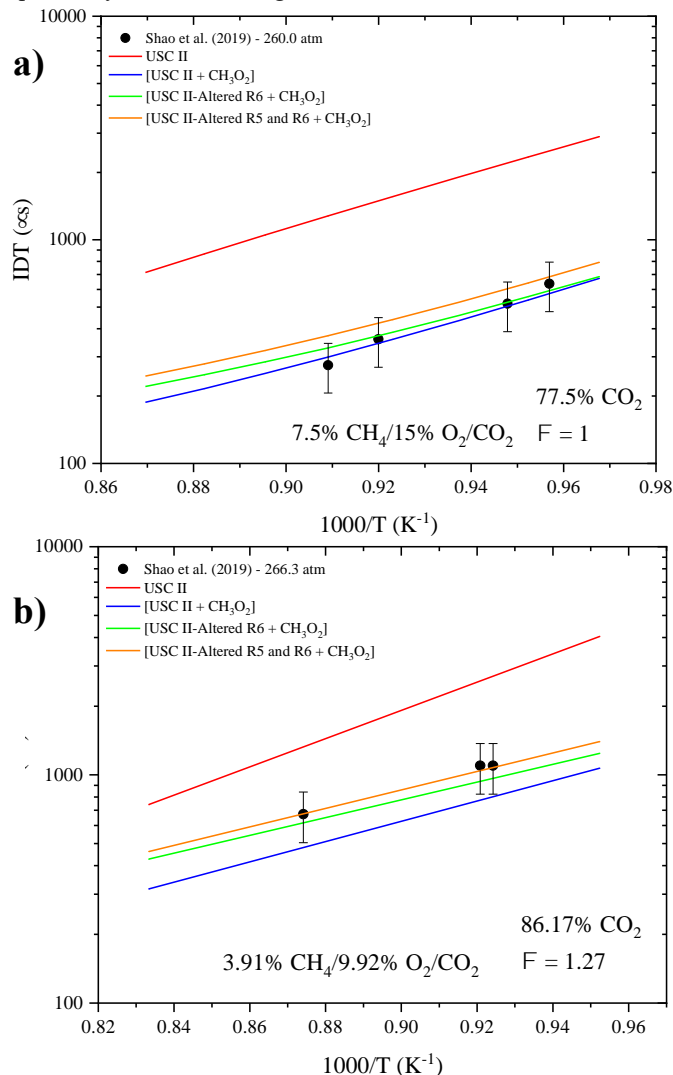


Figure 2: Sequential changes to USC II; a) M8 and b) M11; [USC II + CH₃O₂]: addition of CH₃O₂ chemistry from Aramco 2.0, [USC II-Altered R6 + CH₃O₂]: change R6 to Aramco 2.0 rate coefficient, [USC II-Altered R5 and R6 + CH₃O₂]: change R5 to the Aramco 2.0 rate coefficient.

Figure 2 highlights the importance of the chemistry of CH₃O₂ in high pressure combustion as the addition of the following reactions shown in Table 5 to the USC II mechanism

immediately led to a significant improvement in the mechanism's ability to model the experimental data. This observation is significant in the pursuit of the understanding the chemical kinetic mechanism of the Allam cycle. However, despite the importance of the reactions shown in Table 5, these rate coefficients are often from sources concerned with atmospheric and low-temperature combustion and therefore are difficult to extrapolate to the combustion conditions of the Allam cycle. Furthermore, some the rate coefficients A factors shown in table 5, have large uncertainty factors which can have a huge impact on the modelled IDTs. For example Tsang and Hampson [28] report an uncertainty factor of 10 in the A factor of the rate coefficient of R4 due to it being an estimate based on another reaction with no experimental data. Therefore, in order to create an accurate comprehensive kinetic mechanism of high-pressure combustion, the rate coefficients of the key reactions in the chemistry of CH_3O_2 must be determined at pressures and temperatures more relevant to conditions of the Allam cycle.

Table 5. Reactions of CH_3O_2 added to USC II.

Reaction	A	n	Ea	Reference
$\text{CH}_3\text{O}_2 + \text{CH}_3 = 2\text{CH}_3\text{O}$	5.08×10^{12}	0.00	-1411	[29]
$\text{CH}_4 + \text{CH}_3\text{O}_2 = \text{CH}_3 + \text{CH}_3\text{O}_2\text{H}$	9.60×10^{-01}	3.77	17810	Source Unknown
$\text{CH}_2\text{O} + \text{CH}_3\text{O}_2 = \text{HCO} + \text{CH}_3\text{O}_2\text{H}$	1.99×10^{12}	0.00	11660	[28]
$\text{CH}_3 + \text{O}_2 (+\text{M}) = \text{CH}_3\text{O}_2 (+\text{M})$	7.81×10^9	0.90	0	[27]
$\text{CH}_3\text{O}_2 + \text{O} = \text{CH}_3\text{O} + \text{O}_2$	3.60×10^{13}	0.00	0	[32]
$\text{CH}_3\text{O}_2 + \text{H} = \text{CH}_3\text{O} + \text{OH}$	9.60×10^{13}	0.00	0	[32]
$\text{CH}_3\text{O}_2 + \text{OH} = \text{CH}_3\text{OH} + \text{O}_2$	6.00×10^{13}	0.00	0	[32]
$\text{CH}_3\text{O}_2 + \text{HO}_2 = \text{CH}_3\text{O}_2\text{H} + \text{O}_2$	2.47×10^{11}	0.00	-1570	[32]
$\text{CH}_3\text{O}_2 + \text{H}_2\text{O}_2 = \text{CH}_3\text{O}_2\text{H} + \text{HO}_2$	2.41×10^{12}	0.00	9936	[28]
$2\text{CH}_3\text{O}_2 = \text{CH}_2\text{O} + \text{CH}_2\text{OH} + \text{O}_2$	3.11×10^{14}	-1.61	-1051	[32]
$\text{CH}_3\text{O}_2 + \text{CH}_3\text{O}_2 = \text{O}_2 + \text{CH}_3\text{O} + \text{CH}_3\text{O}$	1.40×10^{16}	-1.61	1860	[32]
$\text{H}_2 + \text{CH}_3\text{O}_2 = \text{CH}_2\text{OH} + \text{CH}_3\text{O}_2\text{H}$	1.50×10^{14}	0.00	26030	[28]
$\text{CH}_3\text{OH} + \text{CH}_3\text{O}_2 = \text{CH}_2\text{OH} + \text{CH}_3\text{O}_2\text{H}$	1.81×10^{12}	0.00	13710	[39]
$\text{CH}_3\text{O}_2\text{H} + \text{CH}_3\text{O} + \text{OH}$	6.31×10^{14}	0.00	42300	[32]
$\text{CH}_2\text{O}_2\text{H} = \text{CH}_2\text{O} + \text{OH}$	9.00×10^{14}	0.00	1500	Curran estimate.

ANALYSIS OF HYDROGEN DATASETS

There are only three published datasets for the IDT of hydrogen in sCO_2 from Shao et al. [7]. As seen in Table 6, Aramco 2.0 has the best average E value for the three hydrogen datasets but performs poorly at the H3 condition. This decline in performance for the H3 dataset is possibly due to the lower pressure or the 0.25 equivalence ratio as opposed to 1.00 for the H1 and H2 datasets.

Table 6. Quantitative analysis of hydrogen datasets.

	Aramco 2.0	DTU	GRI 3.0	USC II
H1	11.43	25.12	63.45	50.70
H2	12.20	20.58	79.90	74.33
H3	89.13	116.67	112.95	70.82
Average	37.59	54.12	85.43	65.28
No. Best Fit	2	0	0	1

The sensitivity analysis in Figure 3 shows the large temperature sensitivity of Aramco 2.0 to R5 and R7. R5 was discussed previously due to its importance in methane combustion, however, R7 did not appear in any sensitivity analysis for methane combustion. The rate coefficient used in Aramco 2.0 for R7 [40] is significantly faster at the temperatures concerned compared to the value used in USC II [28].

H3 - Aramco 2.0 vs. USC II

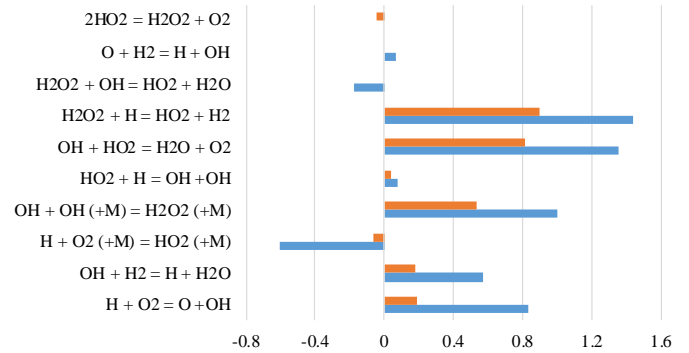
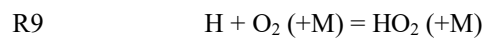
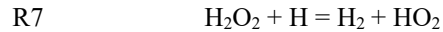


Figure 3: Comparison of the sensitivity analysis of H3 for Aramco 2.0 and USC II at 1274 K.

As the experimental data can already be well modelled for H1 and H2, the challenge with the mechanism improvement is to greatly improve H3, without adversely affecting the aforementioned conditions. Figure 3 shows the sensitivity analysis of H3 for Aramco 2.0 and USC II at 1274 K. One of the most obvious discrepancies between the two mechanisms is the relative importance of the competing pathways of R8 and R9 in USC II. The older rate coefficient for R8 used by USC II from Masten et al. [41] is approximately 50 times larger than the rate coefficient reported by Hong et al. [42] used in Aramco 2.0. Conversely, the difference in the rate coefficient used in Aramco 2.0 [43] and USC II [44] only differ by 10%. The ratio between R8 and R9 is therefore important and influential on the combustion chemistry.



The sensitivity analysis for the H1 and H2 conditions in figure 3 shows a similar discrepancy between R9 and R10.

The mixed performance between Aramco 2.0 and USC II appears to be caused by the large difference in the rate coefficients used for the R7 and R8. The effect of altering the rate coefficient of R7 in the USC II mechanism to the faster, and more recent rate coefficient from Ellingson et al. [40] to create [USC II-Altered R7] is shown in Figure 4 for the H1 and H2 conditions. Furthermore, for the H3 condition, the E value falls from 89 and 71 for Aramco 2.0 and USC II respectively to 30 for [USC II-Altered R7].

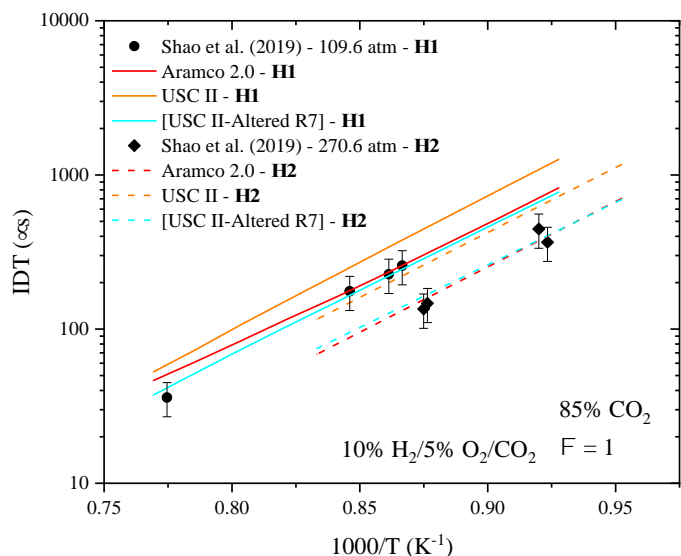


Figure 4: H3 dataset modelled by Aramco 2.0, USC II, and [USC II-Altered R7]: USC II with the updated R7 rate coefficient [40].

ANALYSIS OF SYNGAS DATASETS

Table 7 shows the average E values for the eight syngas datasets modelled from Barak et al. [23, 24].

Table 7. Quantitative analysis of syngas data.

	Aramco 2.0	DTU	GRI 3.0	USC II
S1	53.20	70.06	21.84	49.96
S2	66.05	94.50	31.40	109.03
S3	117.50	181.42	32.33	123.44
S4	126.76	158.27	84.69	196.60
S5	240.64	303.37	170.24	242.84
S6	259.59	341.14	169.83	277.12
S7	191.64	277.53	241.41	132.09
S8	174.54	287.50	139.00	89.63
Average E	153.74	214.22	111.34	152.59
No. Best Fit	0	0	6	2

GRI 3.0 performs best in six out of the eight datasets being studied and has the lowest average E value. Figure 5 displays the sensitivity analysis for the S3 condition of Aramco 2.0 and GRI 3.0 at 1280 K. The discrepancy between the two mechanisms can be explained by the significant difference in the rate coefficient for R7 and R10.



The rate coefficient of R10 used in GRI 3.0 [45] is significantly faster than that in Aramco 2.0 [46] leading to six orders of magnitude difference in the rate at 1200 K. Thus, explaining the much greater temperature sensitivity of R10 in GRI 3.0 compared to Aramco 2.0, DTU, and USC II which use the same rate coefficient.

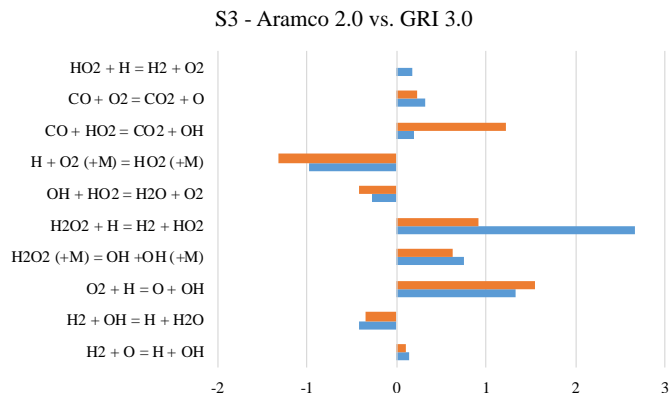


Figure 5: S3 dataset sensitivity analysis of GRI 3.0 and Aramco 2.0 at 1280 K.

Changing the rate coefficient for R10 for Aramco 2.0, DTU, and USC II to the faster rate coefficient led to a significant improvement for all three mechanisms across all of the conditions as shown in figure 6 for the S3 condition.

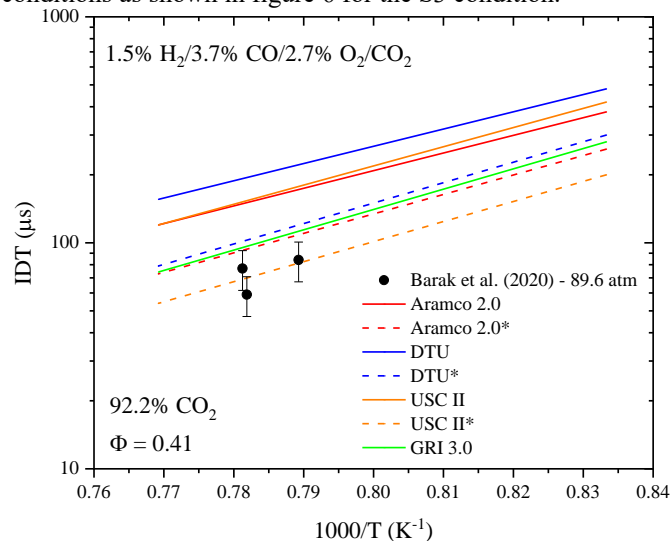


Figure 6: Mechanism comparison for the S3 condition with the R10 rate coefficient from Baulch et al. [45] denoted by *.

CREATION OF UOS sCO₂ MECHANISM

The analysis of the three different fuels was used for the development of a new mechanism that better modelled all the datasets studied. USC II was chosen as the base mechanism due to its significant initial improvement for the high-pressure methane data through the addition of CH_3O_2 chemistry shown in figure 2, whilst maintaining its superior performance at lower pressure. Table 5 shows the CH_3O_2 reactions and rate coefficients taken from the Aramco 2.0 mechanism which were added to

USC II. All other changes to the rate coefficients are recorded in Table 8.

Table 8. UoS sCO₂ mechanism alterations.

Reaction		A	N	E _a	Reference
H ₂ O ₂ + H =	USC II	6.1 x 10 ⁶	2.00	5200	[28]*0.5
HO ₂ + H ₂	New	2.2 x 10 ¹⁰	1.00	6000	[40]
CO + O ₂ =	USC II	1.1 x 10 ¹²	0	47700	[28]
CO ₂ + O	New	4.6 x 10 ¹²	0	60500	[47]
CO + HO ₂ =	USC II	1.6 x 10 ⁵	2.18	17940	[46]
CO ₂ + OH	New	6.0 x 10 ¹³	0	23000	[48]
CH ₃ + O ₂ =	USC II	3.1 x 10 ¹³	0	28800	[49]
O + CH ₃ O	New	7.6 x 10 ¹²	0	28320	[50]
CH ₃ + O ₂ =	USC II	3.6 x 10 ¹⁰	0	8940	[49]
OH + CH ₂ O	New	1.9 x 10 ¹¹	0	9842	[50]
CH ₃ + HO ₂	USC II	1.0 x 10 ¹²	0	0	[36]
= CH ₄ + O ₂	New	1.2 x 10 ⁵	2.23	-3022	[37]
CH ₃ + HO ₂	USC II	1.3 x 10 ¹³	0	0	[28]
= CH ₃ O + OH	New	1.0 x 10 ¹⁰	0.27	-688	[37]
CH ₃ + H ₂ O ₂	USC II	2.5 x 10 ⁴	2.47	5180	[51]
= CH ₄ + HO ₂	New (Reverse)	4.7 x 10 ⁴	2.50	21000	[52]
CH ₄ + H =	USC II	6.6 x 10 ⁸	1.62	10840	[53]
CH ₃ + H ₂	New	6.1 x 10 ⁵	2.50	9587	[52]

Table 9 shows the performance of the newly developed UoS sCO₂ mechanism against the four existing mechanisms studied for hydrogen, methane, and syngas data.

Table 9. Comparison of the developed UoS sCO₂ mechanism to the existing four mechanisms studied.

Dataset		Aramco 2.0	DTU	GRI 3.0	USC II	UoS sCO ₂
Hydrogen	<i>E</i> (%)	37.6	54.1	85.4	65.3	17.5
	No. Best Fit	1	0	0	0	2
Methane	<i>E</i> (%)	29.7	31.8	60.7	61.7	25.1
	No. Best Fit	2	0	2	4	3
Syngas	<i>E</i> (%)	153.7	214.2	111.3	152.6	76.2
	No. Best Fit	0	0	3	0	5
Average <i>E</i>		73.7	100.0	85.8	93.2	39.6
Total No. Best Fit		3	0	5	4	10

It should be noted that the smallest *E* value does not necessarily indicate the best fit due to the large error of 18-25% in the IDT, meaning multiple mechanisms may be within the error. However, across a large number of datasets, the average *E* value is a good indication of the best performing mechanism. Table 9 shows the UoS sCO₂ mechanism produces the best average *E* for all of the fuels studied and the greatest number of best fits. It is important to note that the rate coefficients selected are not a reflection on the quality of the rate coefficient as they were not measured in a CO₂ bath gas, the selection was based on creating the best fit to the available experimental data available.

CONCLUSION

Through studying a large number of high-pressure, high-CO₂ dilution datasets, the UoS sCO₂ mechanism has been created to more accurately model combustion at the conditions of the Allam cycle. The key findings from this investigation are the identification of reactions that are important in the modelling of the sCO₂ combustion and cause a discrepancy between the mechanisms being investigated.

The importance of CH₃O₂ chemistry in high-pressure methane combustion was discussed for the first time with relevance to the Allam cycle. It was noted during the methane analysis that the GRI 3.0 and USC II mechanisms performed poorly at high pressure conditions due to the absence of CH₃O₂ chemistry. The addition of the CH₃O₂ chemistry from Aramco 2.0 to USC II saw a significant improvement in the three highest pressure conditions. However, most of these reactions have been studied concerning atmospheric and low-temperature combustion so may be unreliable when extrapolated to the conditions of the Allam cycle.

The rate coefficients used in the creation of the UoS sCO₂ mechanism were based on which best modelled the experimental data. More high-pressure combustion data for methane, hydrogen and syngas is required to confirm which rate coefficients should be selected and validate the mechanism. This study furthers the current understanding of sCO₂ combustion of methane, hydrogen and syngas by assessing the performance of four combustion mechanisms well-validated at lower pressures and smaller CO₂ concentrations. Quantitative analysis of the newly developed UoS sCO₂ mechanism adapted from USC II has proven its superior ability to model IDT against existing chemical mechanisms which are well-validated for low pressures and smaller CO₂ concentrations. Whilst the UoS sCO₂ mechanism has been proven to perform best for the IDTs studied, more experimental data such as laminar flame speed is required for further validation that the mechanism better models all aspects of combustion. Overall, the present study allows the IDT of three different fuels to be more accurately modelled at conditions of the Allam cycle than by four existing, well-established chemical kinetic mechanisms

NOMENCLATURE

ASU – Air Separation Unit
E – Average Absolute Error
 IDT – Ignition Delay Time
 ppm – Parts Per Million
 sCO₂ – Supercritical CO₂
 UoS – University of Sheffield

ACKNOWLEDGEMENTS

This work has been supported by The EPSRC Centre for Doctoral Training in Resilient Decarbonised Fuel Energy Systems (Grant number: EP/S022996/1) and the International Flame Research Federation (IFRF).

REFERENCES

- [1] W. Broecker, When climate change predictions are right for the wrong reasons, *Climatic Change* 142 (2017) 1-6.
- [2] N. Abas, A. Kalair, N. Khan, Review of fossil fuels and future energy technologies, *Futures* 69 (2015) 31-49.
- [3] R.J. Allam, M.R. Palmer, G.W. Brown, J. Fetvedt, D. Freed, H. Nomoto, M. Itoh, N. Okita, C. Jones, High efficiency and low cost of electricity generation from fossil fuels while eliminating atmospheric emissions, including carbon dioxide, *GHGT-11* 37 (2013) 1135-1149.
- [4] T. Lockwood, A comparative review of next-generation carbon capture technologies for coal-fired power plant, 13th International Conference on Greenhouse Gas Control Technologies, *GHGT-13* 114 (2017) 2658-2670.
- [5] R.J. Allam, J.E. Fetvedt, B.A. Forrest, D.A. Freed, The oxy-fuel, supercritical CO₂ Allam cycle: new cycle developments to produce even lower-cost electricity from fossil fuels without atmospheric emissions, *Proceedings of the ASME Turbo Expo: Turbine Technical Conference and Exposition* 3b (2014).
- [6] S. Coogan, X. Gao, A. McClung, W. Sun, Evaluation of kinetic mechanisms for direct fired supercritical oxy-combustion of natural gas, *Conference: ASME Turbo Expo 2016: Turbo-machinery Technical Conference and Exposition*, Seoul, South Korea, 2016.
- [7] J.K. Shao, R. Choudhary, D.E. Davidson, R.K. Hanson, S. Barak, S. Vasu, Ignition delay times of methane and hydrogen highly diluted in carbon dioxide at high pressures up to 300 atm, *Proceedings of the Combustion Institute* 37 (2019) 4555-4562.
- [8] E.E. Wait, A.E. Masunov, S.S. Vasu, Quantum chemical and master equation study of OH + CH₂O → H₂O + CHO reaction rates in supercritical CO₂ environment, *International Journal of Chemical Kinetics* 51 (2019) 42-48.
- [9] ANSYS, CHEMKIN-PRO, 2019, pp. Reaction Design: San Diego: CA.
- [10] W.K. Metcalfe, S.M. Burke, S.S. Ahmed, H.J. Curran, A hierarchical and comparative kinetic modeling study of C1 – C2 hydrocarbon and oxygenated fuels, *International Journal of Chemical Kinetics* 45 (2013) 638-675.
- [11] Y. Li, C.-W. Zhou, K.P. Somers, K. Zhang, H.J. Curran, The oxidation of 2-butene: A high pressure ignition delay, kinetic modeling study and reactivity comparison with isobutene and 1-butene, *Proceedings of the Combustion Institute* 36 (2017) 403-411.
- [12] C.-W. Zhou, Y. Li, E. O'Connor, K.P. Somers, S. Thion, C. Keese, O. Mathieu, E.L. Petersen, T.A. DeVerter, M.A. Oehlschlaeger, G. Kukkadapu, C.-J. Sung, M. Alrefae, F. Khaled, A. Farooq, P. Dirrenberger, P.-A. Glaude, F. Battin-Leclerc, J. Santner, Y. Ju, T. Held, F.M. Haas, F.L. Dryer, H.J. Curran, A comprehensive experimental and modeling study of isobutene oxidation, *Combustion and Flame* 167 (2016) 353-379.
- [13] U. Burke, W.K. Metcalfe, S.M. Burke, K.A. Heufer, P. Dagaut, H.J. Curran, A detailed chemical kinetic modeling, ignition delay time and jet-stirred reactor study of methanol oxidation, *Combustion and Flame* 165 (2016) 125-136.
- [14] S.M. Burke, U. Burke, R. Mc Donagh, O. Mathieu, I. Osorio, C. Keese, A. Morones, E.L. Petersen, W. Wang, T.A. DeVerter, M.A. Oehlschlaeger, B. Rhodes, R.K. Hanson, D.F. Davidson, B.W. Weber, C.-J. Sung, J. Santner, Y. Ju, F.M. Haas, F.L. Dryer, E.N. Volkov, E.J.K. Nilsson, A.A. Konnov, M. Alrefae, F. Khaled, A. Farooq, P. Dirrenberger, P.-A. Glaude, F. Battin-Leclerc, H.J. Curran, An experimental and modeling study of propene oxidation. Part 2: Ignition delay time and flame speed measurements, *Combustion and Flame* 162 (2015) 296-314.
- [15] S.M. Burke, W. Metcalfe, O. Herbinet, F. Battin-Leclerc, F.M. Haas, J. Santner, F.L. Dryer, H.J. Curran, An experimental and modeling study of propene oxidation. Part 1: Speciation measurements in jet-stirred and flow reactors, *Combustion and Flame* 161 (2014) 2765-2784.
- [16] A. Kéromnès, W.K. Metcalfe, K.A. Heufer, N. Donohoe, A.K. Das, C.-J. Sung, J. Herzler, C. Naumann, P. Griebel, O. Mathieu, M.C. Krejci, E.L. Petersen, W.J. Pitz, H.J. Curran, An experimental and detailed chemical kinetic modeling study of hydrogen and syngas mixture oxidation at elevated pressures, *Combustion and Flame* 160 (2013) 995-1011.
- [17] H. Wang, X. You, A.V. Joshi, S.G. Davis, A. Laskin, F. Egolfopoulos, C. Law, USC Mech Version II. High-Temperature Combustion Reaction Model of H₂/CO/C1-C4 Compounds, 2007.
- [18] G.P. Smith, D.M. Golden, M. Frenklach, N.W. Moriarty, B. Eiteneer, M. Goldenberg, C.T. Bowman, R.K. Hanson, S. Song, W.C. Gardiner Jr., V.V. Lissianski, Z. Qin, GRI Mechanism 3.0. <http://combustion.berkeley.edu/gri-mech/version30/text30.html> (accessed 16th December 2019).
- [19] H. Hashemi, J.M. Christensen, P. Glarborg, High-pressure pyrolysis and oxidation of DME and DME/CH₄, *Combustion and Flame* 205 (2019) 80-92.
- [20] H. Hashemi, J.M. Christensen, S. Gersen, H. Levinsky, S.J. Klippenstein, P. Glarborg, High-pressure oxidation of methane, *Combustion and Flame* 172 (2016) 349-364.
- [21] O. Pryor, B. Koroglu, S. Barak, J. Lopez, E. Ninnemann, L. Nash, S. Vasu, Ignition delay times of high pressure oxy-methane combustion with high levels of CO₂ dilution, *Proceedings of ASME Turbo Expo 2017: Turbo-machinery Technical Conference and Exposition*, Charlotte, NC, USA, 2017.
- [22] M. Karimi, B. Ochs, Z.F. Liu, D. Ranjan, W.T. Sun, Measurement of methane autoignition delays in carbon dioxide and argon diluents at high pressure conditions, *Combustion and Flame* 204 (2019) 304-319.
- [23] S. Barak, O. Pryor, E. Ninnemann, S. Neupane, S. Vasu, X. Lu, B. Forrest, Ignition delay times of oxy-syngas and oxy-methane in supercritical CO₂ mixtures for direct-fired cycles, *Journal of Engineering for Gas Turbines and Power* 142 (2020).
- [24] S. Barak, E. Ninnemann, S. Neupane, F. Barnes, J. Kapat, S. Vasu, High-pressure oxy-syngas ignition delay times with CO₂ dilution: Shock tube measurements and comparison of the performance of kinetic mechanisms, *Journal of Engineering for Gas Turbines and Power* 141 (2018).
- [25] Y. Liu, J. Cheng, C. Zou, L.X. Lu, H.X. Jing, Ignition delay times of ethane under O₂/CO₂ atmosphere at different pressures

by shock tube and simulation methods, *Combustion and Flame* 204 (2019) 380-390.

[26] G.P. Smith, Y. Tao, H. Wang, Foundational Fuel Chemistry Model Version 1.0 (FFCM-1). <http://web.stanford.edu/group/haiwanglab/FFCM1/pages/FFCM1.html> (accessed 7th November 2019).

[27] R.X. Fernandes, K. Luther, J. Troe, Falloff curves for the reaction $\text{CH}_3 + \text{O}_2 (+\text{M}) \rightarrow \text{CH}_3\text{O}_2 (+\text{M})$ in the pressure range 2–1000 bar and the temperature range 300–700 K, *The Journal of Physical Chemistry A* 110 (2006) 4442-4449.

[28] W. Tsang, R.F. Hampson, Chemical kinetic data base for combustion chemistry. Part I. Methane and related compounds, *Journal of Physical and Chemical Reference Data* 15 (1986) 1087-1279.

[29] M. Keiffer, A.J. Miscampbell, M.J. Pilling, A global technique for analysing multiple decay curves. Application to the $\text{CH}_3 + \text{O}_2$ system, *Journal of the Chemical Society, Faraday Transactions 2: Molecular and Chemical Physics* 84 (1988) 505-514.

[30] M.J. Pilling, M.J.C. Smith, A laser flash photolysis study of the reaction $\text{CH}_3 + \text{O}_2 \rightarrow \text{CH}_3\text{O}_2$ at 298 K, *The Journal of Physical Chemistry* 89 (1985) 4713-4720.

[31] D.A. Parkes, The oxidation of methyl radicals at room temperature, *International Journal of Chemical Kinetics* 9 (1977) 451-469.

[32] P.D. Lightfoot, P. Roussel, F. Caralp, R. Lesclaux, Flash-photolysis study of the $\text{CH}_3\text{O}_2 + \text{CH}_3\text{O}_2$ and $\text{CH}_3\text{O}_2 + \text{HO}_2$ reactions between 60 K and 719 K - Unimolecular decomposition of methylhydroperoxide, *Journal of the Chemical Society-Faraday Transactions* 87 (1991) 3213-3220.

[33] E. Assaf, L. Sheps, L. Whalley, D. Heard, A. Tomas, C. Schoemaeker, C. Fittschen, The reaction between CH_3O_2 and OH radicals: Product yields and atmospheric implications, *Environmental Science & Technology* 51 (2017) 2170-2177.

[34] D.L. Baulch, C.J. Cobos, R.A. Cox, C. Esser, P. Frank, T. Just, J.A. Kerr, M.J. Pilling, J. Troe, R.W. Walker, J. Warnatz, Evaluated kinetic data for combustion modelling, *Journal of Physical and Chemical Reference Data* 21 (1992) 411-734.

[35] J. Troe, The thermal dissociation/recombination reaction of hydrogen peroxide $\text{H}_2\text{O}_2 (+\text{M}) \rightleftharpoons 2\text{OH} (+\text{M})$ III.: Analysis and representation of the temperature and pressure dependence over wide ranges, *Combustion and Flame* 158 (2011) 594-601.

[36] I.A.B. Reid, C. Robinson, D.B. Smith, Spontaneous ignition of methane: Measurement and chemical model, *Symposium (International) on Combustion* 20 (1985) 1833-1843.

[37] A.W. Jasper, S.J. Klippenstein, L.B. Harding, Theoretical rate coefficients for the reaction of methyl radical with hydroperoxyl radical and for methylhydroperoxide decomposition, *Proceedings of the Combustion Institute* 32 (2009) 279-286.

[38] N.K. Srinivasan, J.V. Michael, L.B. Harding, S.J. Klippenstein, Experimental and theoretical rate constants for $\text{CH}_4 + \text{O}_2 \rightarrow \text{CH}_3 + \text{HO}_2$, *Combustion and Flame* 149 (2007) 104-111.

[39] W. Tsang, Chemical kinetic data base for combustion chemistry. Part 2. Methanol, *Journal of Physical and Chemical Reference Data* 16 (1987) 471-508.

[40] B.A. Ellingson, D.P. Theis, O. Tishchenko, J. Zheng, D.G. Truhlar, Reactions of hydrogen atom with hydrogen peroxide, *The Journal of Physical Chemistry A* 111 (2007) 13554-13566.

[41] D.A. Masten, R.K. Hanson, C.T. Bowman, Shock tube study of the reaction $\text{H} + \text{O}_2 \rightarrow \text{OH} + \text{O}$ using OH laser absorption, *The Journal of Physical Chemistry* 94 (1990) 7119-7128.

[42] Z. Hong, D.F. Davidson, E.A. Barbour, R.K. Hanson, A new shock tube study of the $\text{H} + \text{O}_2 \rightarrow \text{OH} + \text{O}$ reaction rate using tunable diode laser absorption of H_2O near 2.5 μm , *Proceedings of the Combustion Institute* 33 (2011) 309-316.

[43] R.X. Fernandes, K. Luther, J. Troe, V.G. Ushakov, Experimental and modelling study of the recombination reaction $\text{H} + \text{O}_2 (+\text{M}) \rightarrow \text{HO}_2 (+\text{M})$ between 300 and 900 K, 1.5 and 950 bar, and in the bath gases M = He, Ar, and N_2 , *Physical Chemistry Chemical Physics* 10 (2008) 4313-4321.

[44] J. Troe, Detailed modeling of the temperature and pressure dependence of the reaction $\text{H} + \text{O}_2 (+\text{M}) \rightarrow \text{HO}_2 (+\text{M})$, *Proceedings of the Combustion Institute* 28 (2000) 1463-1469.

[45] D.L. Baulch, D.D. Drysdale, J. Duxbury, S. Grant, Evaluated kinetic data for high temperature reactions, Vol. 3: Homogeneous gas phase reactions of the O_2 - O_3 systems, the CO - O_2 - H_2 system, and of sulphur-containing species, Butterworths, 1976.

[46] X. You, H. Wang, E. Goos, C.-J. Sung, S.J. Klippenstein, Reaction kinetics of $\text{CO} + \text{HO}_2 \rightarrow$ products: ab initio transition state theory study with master equation modeling, *The Journal of Physical Chemistry A* 111 (2007) 4031-4042.

[47] G.B. Bacskay, J.C. Mackie, Oxidation of CO by SO_2 : A theoretical study, *The Journal of Physical Chemistry A* 109 (2005) 2019-2025.

[48] G.M. Atri, R.R. Baldwin, D. Jackson, R.W. Walker, The reaction of OH radicals and HO_2 radicals with carbon monoxide, *Combustion and Flame* 30 (1977) 1-12.

[49] C.L. Yu, C. Wang, M. Frenklach, Chemical kinetics of methyl oxidation by molecular oxygen, *The Journal of Physical Chemistry* 99 (1995) 14377-14387.

[50] N.K. Srinivasan, M.C. Su, J.W. Sutherland, J.V. Michael, Reflected shock tube studies of high-temperature rate constants for $\text{CH}_3 + \text{O}_2$, $\text{H}_2\text{CO} + \text{O}_2$, and $\text{OH} + \text{O}_2$, *The Journal of Physical Chemistry A* 109 (2005) 7902-7914.

[51] R.R. Baldwin, P.N. Jones, R.W. Walker, Determination of the rate constant for $\text{HO}_2 + \text{CH}_4 \rightarrow \text{H}_2\text{O}_2 + \text{CH}_3$ at 443 $^\circ\text{C}$, *Journal of the Chemical Society, Faraday Transactions 2: Molecular and Chemical Physics* 84 (1988) 199-207.

[52] D.L. Baulch, C.T. Bowman, C.J. Cobos, R.A. Cox, T. Just, J.A. Kerr, M.J. Pilling, D. Stocker, J. Troe, W. Tsang, R.W. Walker, J. Warnatz, Evaluated kinetic data for combustion modeling: Supplement II, *Journal of Physical and Chemical Reference Data* 34 (2005) 757-1397.

[53] M.J. Rabinowitz, J.W. Sutherland, P.M. Patterson, R.B. Klemm, Direct rate constant measurements for $\text{H} + \text{CH}_4$ yields $\text{CH}_3 + \text{H}_2$, 897-1729 K, using the flash photolysis-shock tube technique, *Journal of Physical Chemistry;(USA)* 95 (1991).

ANNEX A

SCO2 IDT DATA

Table A. Quantitative analysis of methane datasets compared to UoS sCO₂.

	Aramco 2.0	DTU	GRI 3.0	USC II	UoS sCO₂
M1	41.47	37.98	76.11	17.04	31.46
M2	17.10	12.60	54.37	9.55	11.35
M3	24.85	27.18	54.76	20.49	21.97
M4	14.26	13.44	56.66	8.24	4.61
M5	9.53	7.35	32.49	45.53	3.71
M6	60.09	47.06	23.63	38.39	46.16
M7	15.02	16.64	43.26	20.65	21.43
M8	26.87	37.65	204.32	323.56	20.95
M9	94.06	99.87	31.97	56.38	91.19
M10	18.91	25.79	57.11	13.79	18.66
M11	3.99	24.03	32.53	125.37	4.33
Average	29.65	31.78	60.66	61.73	25.08
No. Best Fit	2	0	2	4	3

Table B. Quantitative analysis of hydrogen datasets compared to UoS sCO₂.

	Aramco 2.0	DTU	GRI 3.0	USC II	UoS sCO₂
H1	11.43	25.12	63.45	50.70	7.60
H2	12.20	20.58	79.90	74.33	14.66
H3	89.13	116.67	112.95	70.82	30.13
Average	37.59	54.12	85.43	65.28	17.47
No. Best Fit	1	0	0	0	2

Table C. Quantitative analysis of syngas datasets compared to UoS sCO₂.

	Aramco 2.0	DTU	GRI 3.0	USC II	UoS sCO₂
S1	53.20	70.06	21.84	49.96	25.79
S2	66.05	94.50	31.40	109.03	32.17
S3	117.50	181.42	32.33	123.44	26.46
S4	126.76	158.27	84.69	196.60	73.07
S5	240.64	303.37	170.24	242.84	151.62
S6	259.59	341.14	169.83	277.12	172.76
S7	191.64	277.53	241.41	132.09	72.60
S8	174.54	287.50	139.00	89.63	55.42
Average	153.74	214.22	111.34	152.59	76.24
No. Best Fit	0	0	3	0	5

EXPERIMENTAL INVESTIGATIONS ON THE HEAT TRANSFER CHARACTERISTICS OF SUPERCRITICAL CO₂ IN HEATED HORIZONTAL PIPES

Konstantinos Theologou*

M. Sc.

Institute of Nuclear Technology and Energy Systems
(IKE), University of Stuttgart
Stuttgart, Germany

Email: konstantinos.theologou@ike.uni-stuttgart.de

Eckart Laurien

Prof. Dr.-Ing.

Institute of Nuclear Technology and Energy Systems
(IKE), University of Stuttgart
Stuttgart, Germany

Rainer Mertz

Dr.-Ing.

Institute of Nuclear Technology and Energy Systems
(IKE), University of Stuttgart
Stuttgart, Germany

Jörg Starflinger

Prof. Dr.-Ing.

Institute of Nuclear Technology and Energy Systems
(IKE), University of Stuttgart
Stuttgart, Germany

ABSTRACT

In the frame of the sCO₂-QA (qualification of analysis tools for the evaluation of a residual heat-driven, self-sufficient system for decay heat removal) project, a residual heat-driven self-sufficient sCO₂-operated decay heat removal system based on a Brayton cycle is simulated with the German thermal-hydraulics system code ATHLET (analysis of thermal-hydraulics of leaks and transients). The heat removal system consists of a compact heat exchanger in the containment, a turbo-compressor system located in the reactor building and a gas cooler in the outdoor area. The validation of ATHLET and other numerical codes as well as understanding the heat transfer characteristics of sCO₂ near the critical point requires experimental data. At IKE (Institute of Nuclear Technology and Energy Systems), the SCARLETT (supercritical carbon dioxide loop at IKE Stuttgart) test facility is available for various experiments with sCO₂.

This publication includes an experimental investigation of the thermal stratification in heated horizontal sCO₂ pipe flows. For this investigation, eight test series with overall 48 experiments were carried out in two pipes with inner diameters of 4 mm and 8 mm. The experiments were carried out at a pressure of approximately 7.75 MPa. The target values of mass flux were set at 400 kg/m²s and 800 kg/m²s and those of heat flux at 50, 90 and 130 kW/m², resulting in a heat to mass flux ratio of 62.5-225 J/kg. The inlet Reynolds numbers are between 16000 and 120000. The measured parameters are the flow rate, the pressure, the inlet and outlet fluid temperature as well as the

outer surface temperature along the test pipe in three different radial angles.

The results show the influence of the pipe diameter, Reynolds number, mass and heat flux on the temperature stratification. Also, inflow lengths were determined for a fully developed temperature stratification. This data set can be used for the validation of computer codes.

INTRODUCTION

Since the accidents in the boiling water reactors in Fukushima Daiichi in 2011, the reliable decay heat removal came into the focus of reactor safety research of nuclear power plants. This gave reason to create a new concept of a heat removal system. The concept of a residual heat-driven self-sufficient sCO₂-operated decay heat removal system is based on a simple Brayton cycle which was simulated with the German thermal hydraulics system code ATHLET [1]. Figure 1 shows a conceptual sketch of a boiling water reactor (BWR) with one decay heat removal system. The three main components of the sCO₂-operated decay heat removal system are a compact heat exchanger (CHX) located in the reactor containment, a turbo-compressor system (TCS) in the reactor building and a gas cooler located in the outdoor area. The CHX has to be compact because of space limitations in the containment. Driven by natural convection of the steam-cycle in the containment the sCO₂ is heated up inside the CHX and flows through a turbine to the gas cooler where the decay heat is transferred to an ultimate heat sink, e.g. the ambient air. Downstream, the compressor of the

* corresponding author(s)

TCS compresses the $s\text{CO}_2$ again. The turbine generates more energy than needed by the compressor so excess electrical energy generated by the generator can be used for different purposes, e.g. for charging the batteries of the power plant.

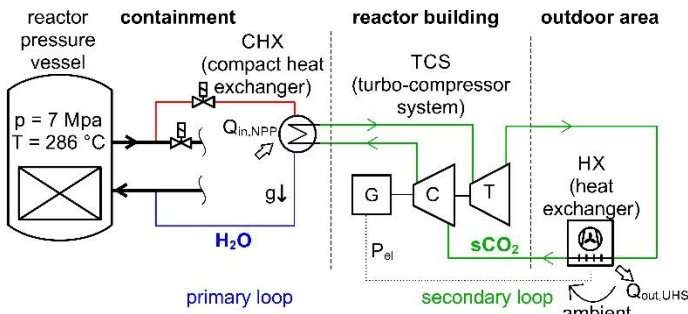


Figure 1: $s\text{CO}_2$ -operated decay heat removal system

The simulation of the cycle with ATHLET by Venker [1] showed the general feasibility of such a concept. However, the comparison of the calculated and the existing experimental data show large deviations in the area of the compressor inlet where the CO_2 is close to the critical point. The reason for this fact is that ATHLET uses correlations for heat transfer and pressure drop which are valid for constant fluid properties and not validated for the operation near the critical point. When using $s\text{CO}_2$ as working fluid these correlations have to be validated with experimental data due to non-constant fluid properties. While a lot of research is available for vertical pipes, there is a lack of experimental data for horizontal pipe flows. For this purpose, basic investigations on heated horizontal pipes are carried out first.

Direct Numerical Simulations (DNS) were carried out by Chu [2] for heated $s\text{CO}_2$ pipe flow with 1 mm and 2 mm inner diameter. The results show that buoyancy leads to a non-uniform distribution of wall temperature in the circumferential direction of the pipe. The results are limited to an inlet Reynolds number of 5400 due to the high computational effort of DNS. In the simulations, the variable fluid properties near the critical point lead to a temperature and density stratification in the horizontal flow direction. The fluid with the lower density is in the upper part of the cross-section and the fluid with the higher density is in the lower part. Experimental data for horizontal $s\text{CO}_2$ pipe flows can be found under cooling conditions by Dang and Hihara [3], Liao and Zhao [4] and Wahl et al. [5]. Other researchers investigate the heat transfer of $s\text{CO}_2$ in horizontal cooled pipes numerically [6–10].

Yu et al. [11] investigated the heat transfer of supercritical water in horizontal heated pipes with inner diameters of 26 mm and 43 mm experimentally and numerically and showed the effect of heat transfer deterioration on the top surface of the test pipe while an enhanced heat transfer occurs at the bottom surface. They considered the temperature difference between the top and the bottom of the test pipes as a measure for buoyancy effects in horizontal flows. This stratification effect disappeared with smaller pipe diameter. Bazargan and Fraser [12] presented

a new numerical model and a new experimental correlation for horizontal heated pipe flows of supercritical water and compared them with experimental data of a pipe with an internal diameter of 6.42 mm. The new correlation and the experiments are in good agreement but they found a lack of experimental data for horizontal supercritical fluid flows with buoyancy effects to evaluate models and empirical correlations.

EXPERIMENTAL SETUP AND METHODS

Experimental investigations of the heat transfer characteristics of $s\text{CO}_2$ are carried out in horizontal heated pipes with constant heat flux. Temperatures are measured on the top surface, on the bottom surface and on the side of the pipe to investigate effects of temperature stratification for parameters close to the critical point. The inner diameters of the pipes are 4 mm and 8 mm with inlet Reynolds numbers of 16000 to 120000.

The above-mentioned experiments are performed using the test facility SCARLETT. It was built at IKE and is in operation since 2016. SCARLETT is a supercritical CO_2 loop in which different test rigs can be implemented modularly. Figure 2 displays a simplified scheme of the test facility.

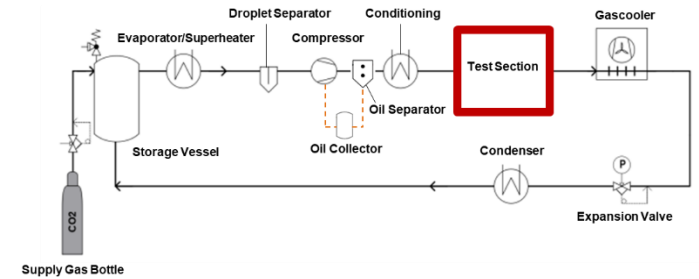


Figure 2: Simplified scheme of the test facility SCARLETT

Starting from the storage vessel the CO_2 flows into the evaporator where it will be overheated. A droplet separator guarantees that the piston compressor does not suck liquid CO_2 . Downstream of the compressor an oil recirculation system with an over-dimensioned coalescence separator extracts more than 99 % of the compressor lubricant and brings it back to the compressor. The oil-concentration of the $s\text{CO}_2$ in the test section was investigated experimentally and is less than 0.2 m%. During conditioning, the $s\text{CO}_2$ can be heated with a flow heater or cooled with cryostats depending on the purpose of the experiment. At the entrance of the modular test section, SCARLETT provides the CO_2 under defined conditions: Pressures between 7.5 MPa and 12 MPa, temperatures between 5 °C and 150 °C and mass flows between 0.013 kg/s and 0.111 kg/s. After leaving the test section, a gas cooler cools down the $s\text{CO}_2$. The expansion valve expands the $s\text{CO}_2$ into the two-phase region. A condenser liquefies the wet steam completely before it flows back to the storage vessel. For more detailed information about the SCARLETT see Flaig et al. [13].

diameter d_i , the unheated hydraulic inflow length L_{hyd} for a hydraulic fully developed flow has been calculated with the empirical formula of Munson [14] for a turbulent flow on the maximum expected Reynolds number.

$$\frac{L_{hyd}}{d_i} = 4.4Re^{\frac{1}{6}} \quad (1)$$

Alloy 625 was chosen for the pipe material because of its high specific electrical resistance. The inner roughness of the 4 mm pipe is $Ra = 0,549 \mu m$ and $Ra = 0,227 \mu m$ for the 8 mm pipe. The electrical power heating up the test pipes is measured directly at the DC power supply terminals to avoid voltage losses in the over-dimensioned copper terminals. The monitoring accuracy of the DC power supply is given with $\pm 0.2 \%$ of full scale.

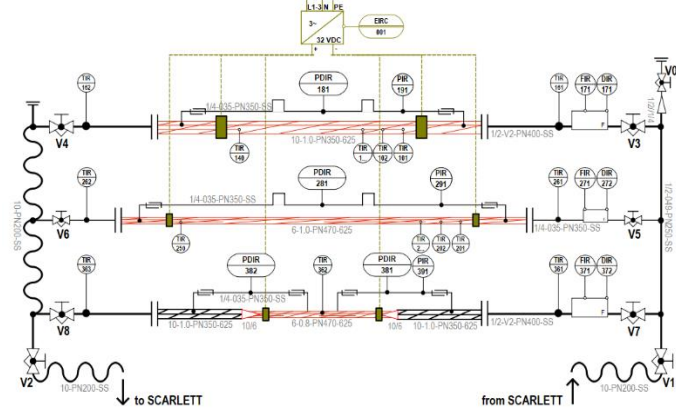


Figure 3: P&I Diagram of the test rig

For fundamental investigations of the heat transfer characteristics and pressure drop of sCO_2 near the critical point a new test rig was build up at IKE (Figure 3). The test rig consists of three tubular test sections with different pipe diameters. By bypassing the sCO_2 through the pipes, the mass flow can be adjusted. The test rig is variably mounted on a rack allowing experiments with horizontal, upward and downward mass flows. The first and the second test section have the same structure; the only difference is the inner diameter of the used test pipes (4 mm and 8 mm). The third pipe is used as a bypass of sCO_2 to adjust the mass flux through the other two test sections. The test pipes are heated up directly with a DC power supply. To insulate the test rig electrically from the test pipes special insulating flanges are used. The test sections were also thermally insulated with the synthetic high-temperature rubber “Armaflex”. At the entrance of the test pipes, the mass flows and the bulk temperatures of sCO_2 are measured using Coriolis mass flowmeters with an accuracy of $\pm 0.19 \%$ of full scale and PT100 resistance temperature sensors with a Class A accuracy $\pm(0,15+0,002 \cdot T \text{ RD})$. Figure 4 shows the dimensions of the test pipes with an inner diameter of 4 mm and 8 mm for the presented experiments.

The total length of the first test pipe is 2360 mm with a heated length of 1640 mm. The second test pipe is 2500 mm long with a heated length of 2040 mm. Forty temperature sensors are tied with a temperature resistant yarn straight in line in 40 mm distances on the outer surface of the first test pipe and fifty sensors on the second test pipe. By rotating the pipe axially in 90° increments three times and repeating the experiments with the same parameter configuration, three surface temperature profiles of the horizontal flow direction can be measured: The horizontal temperature profile for the pipe bottom (HB), the pipe top (HT) and the pipe side (HM). The sensors are surface thin-film resistance temperature sensors (PT100) with a Class A accuracy. The absolute pressure is measured in front of the heated area and the differential pressure is measured over the heated length. To measure the pressure inside the test pipe without influencing the flow a 1 mm hole has been drilled into the pipe wall. The accuracy of the differential and absolute pressure transmitters is $\pm 0.15 \%$ of full scale. With the inner pipe

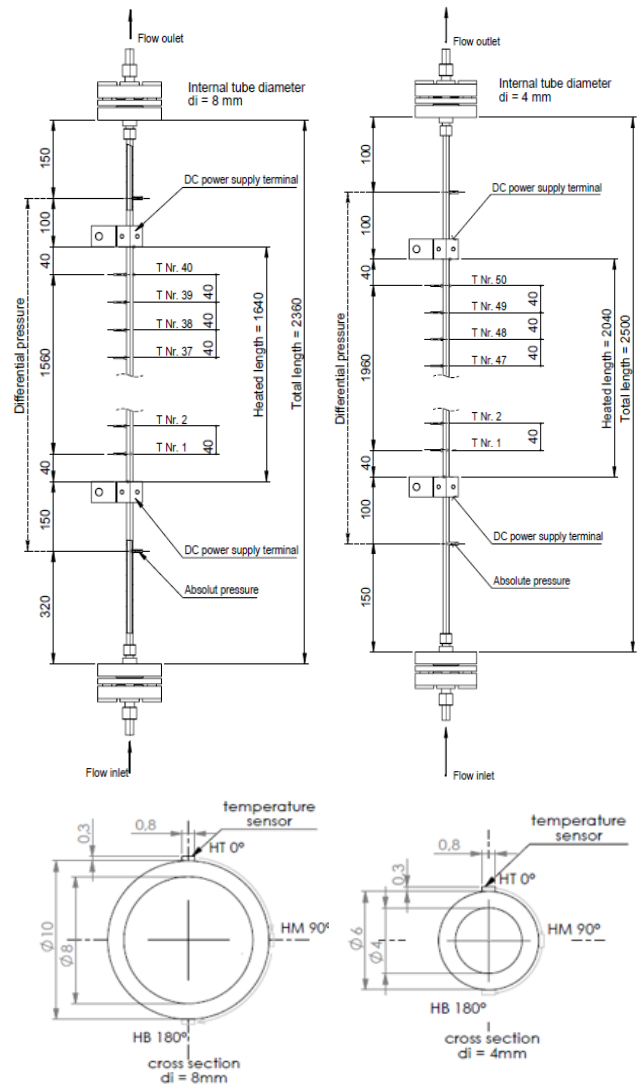


Figure 4: Dimensions of the 1st (left) and 2nd (right) test section

For the data acquisition, twenty-minute intervals with a 0.25 Hz recording frequency were selected. The arithmetic mean for each parameter was calculated using approximately 300 values. To ensure the reproducibility of the measurement some experiments were repeated two or three times. All experiments start after having reached steady-state conditions. To verify adiabatic conditions during the experiments the energy balance of the measured thermal and electrical heat flow was calculated with the transferred heat \dot{Q} , the mass flux \dot{m} , the specific enthalpy i , the electrical power P , the voltage U and the electrical current I :

$$|\dot{Q}_{el}| = |\dot{Q}_{th}| = \dot{Q} \quad (2)$$

$$\dot{Q}_{th} = \dot{m} * [i_{b,out}(T_{B,out}, p_{out}) - i_{b,in}(T_{B,in}, p_{in})] \quad (3)$$

$$\dot{Q}_{el} = P_{el} = U * I \quad (4)$$

For the detailed calculation of the heat transfer coefficient (htc) see Theologou et al. [15].

The following table gives an overview of the experimental parameters of the presented experiments.

Table 1: Experimental parameters

Parameter	Unit	Value
inner pipe diameter	mm	4, 8
flow orientation	-	horizontal
position of temperature sensors	-	HT (0 °), HM (90 °), HB (180 °)
inlet pressure	MPa	7.75
inlet temperature	°C	5, 20, 25, 30
mass flux	kg/m ² s	400, 800
heat flux	kW/m ²	50, 90, 130
inlet Reynolds numbers	-	16000-120000

RESULTS AND DISCUSSION

For the experimental investigation of the thermal stratification in heated horizontal sCO₂ pipe flows, eight test series (TS) were carried out with overall 48 experiments. Table 2 shows an overview of the actual values: the inner pipe diameter d_i , the inlet temperature of the bulk fluid $T_{b,in}$, the mass flux G , the heat flux \dot{q} , the absolute inlet pressure p_{in} , the pressure drop over the heated length Δp , the inlet Reynolds number Re_{in} , the heat loss (equation 2-4) and the arithmetic mean of the relative error for the heat transfer coefficient \bar{s}_h with the standard deviation σ_h . Within each TS, there are constant target values of the mass flux, the heat flux and the absolute inlet pressure. By axial rotation of the pipes, the outer surface temperatures can be measured at the three sensor positions (SP) HB, HM and HT. To be able to provide a temperature profile over a larger enthalpy range the inlet temperature of the fluid is varied.

The results are presented in eight Figures (Figure 5-Figure 12) which include two charts for each TS. In the left charts, the inner wall temperature profile is plotted over the bulk enthalpy and in the right charts, the local htc is plotted over the bulk enthalpy. Also, in the left-hand diagrams, the bulk fluid

temperature is plotted in grey for a constant pressure of 7.75 MPa. The dotted black lines in the figures represent the bulk fluid temperature and enthalpy at the pseudocritical point also for of pressure of 7.75 MPa. In the captions, the target value of the fluid inlet temperature and the position of the temperature sensors is described. The sensor positions on the top of the pipe surface is coloured red, green for the side and blue for the bottom surface. Experiments with higher inlet temperatures are coloured darker. The distance between two data points (DP) on the test pipe is 40 mm (Figure 4). This enables the determination of the inflow length which is necessary for the formation of the temperature stratification by counting the data points (1 DP = 40 mm = 10d).

Table 2 shows the heat losses $(1 - |\dot{Q}_{th}/\dot{Q}_{el}|)$. To calculate the heat losses, an enthalpy balance is presented in equation 2. If, however, the measured fluid outlet temperature is close to the pseudocritical temperature, this calculation is highly erroneous and may be unsuitable for determining the heat losses. This case occurs in some experiments in TS4, TS6 and TS7. Additionally, table 2 also shows the arithmetic mean of the relative error of the htc and the standard deviation. For the calculation of the local error of the inner wall temperature, the most relevant parameter is the accuracy of the PT100 $\pm(0,15+0,002 \cdot T \text{ RD})$. Further errors in this error calculation are the accuracy of the specification of the thermal conductivity of the pipe material and the accuracy of the diameter specification. Due to the fixed part of the PT100 accuracy, the maximum relative error always occurs at the first surface PT100 with the lowest temperature. The absolute error increases with increasing temperature and is in the measured range of the 4 mm pipe approximately ± 0.24 °C at 25 °C and ± 0.34 °C at 120 °C. For the 8 mm pipe, it is approximately ± 0.26 °C at 35 °C and ± 0.50 °C at 160 °C. The maximum relative (and the minimum absolute) error of the bulk fluid enthalpy is at the inlet of the test section with the fluid inlet temperature as the major influencing parameter. Further errors in this error calculation are the accuracies of the mass flow meter and the pressure sensor. For the experiments with a fluid inlet temperature of approximately 5 °C the maximum relative error is 0.8 % and for the experiments with a fluid inlet temperature of approximately 30 °C the maximum relative error is 1.6 %.

Table 2: Experimental overview

TS	d_i [mm]	SP	$T_{b,in}$ [°C]	G $\left[\frac{kg}{m^2s}\right]$	\dot{q} $\left[\frac{kW}{m^2}\right]$	p_{in} [MPa]	Δp [kPa]	Re_{in} [-]	$1 - \dot{Q}_{th}/\dot{Q}_{et} $ [%]	\bar{s}_h [%]	σ_h [%]
TS1	4	HB	7.1	420	51.0	7.73	5.11	17040	1.5	2.7	0.6
			20.2	417	51.1	7.77	4.31	21943	2.8	3.0	1.0
		HM	7.3	414	51.0	7.74	4.73	16868	1.4	2.4	0.6
			20.1	417	51.1	7.78	5.24	21895	1.5	2.7	1.0
		HT	5.4	424	51.0	7.74	5.16	16702	2.5	2.1	0.6
			20.0	415	51.1	7.76	4.32	21728	3.5	2.5	1.1
TS2	4	HB	6.6	819	51.0	7.74	6.74	32911	3.5	5.9	1.2
			25.1	810	51.0	7.76	8.05	48627	0.9	6.3	2.9
		HM	6.4	820	50.9	7.74	6.45	32873	2.6	5.5	1.1
			24.4	821	51.0	7.73	7.69	48372	1.9	5.7	2.2
		HT	4.9	834	50.9	7.74	6.59	32581	4.1	4.9	1.0
			24.8	833	51.0	7.74	8.17	49651	0.3	5.2	2.7
TS3	4	HB	6.5	813	91.7	7.76	10.62	32620	0.3	2.8	1.1
			20.2	810	91.8	7.78	11.64	42592	0.7	2.6	0.6
		HM	6.7	819	91.7	7.73	10.48	33024	0.1	2.7	1.1
			20.0	832	91.7	7.79	12.07	43594	0.4	2.5	0.6
		HT	5.0	817	91.7	7.75	10.30	31937	0.3	2.1	0.7
			19.9	856	91.7	7.77	12.05	44728	0.4	2.3	0.6
TS4	8	HB	6.5	411	50.4	7.71	2.44	33532	13.4	3.2	0.5
			25.1	405	50.4	7.71	1.29	49495	13.5	2.3	0.5
		HM	4.9	401	50.4	7.76	1.07	31811	11.1	2.2	0.5
			25.2	401	50.4	7.74	1.22	49022	13.1	1.7	0.5
		HT	6.4	400	50.4	7.71	2.46	32551	18.1	1.4	0.4
			25.0	403	50.4	7.69	1.16	49230	12.8	1.1	0.3
TS5	8	HB	6.5	405	89.8	7.71	3.00	33016	1.4	1.1	0.2
			20.1	405	89.8	7.74	2.43	43151	0.2	1.2	0.2
		HM	7.0	398	89.8	7.77	3.08	32754	1.3	0.9	0.1
			19.9	404	89.3	7.76	1.75	42897	0.1	0.9	0.2
		HT	6.5	401	89.8	7.72	2.78	32677	0.9	0.7	0.1
			19.9	406	89.8	7.71	2.40	43148	1.0	0.7	0.1
TS6	8	HB	20.0	802	50.2	7.73	2.66	85370	3.7	8.2	1.3
			29.7	793	50.3	7.70	2.96	116302	33.3	7.2	3.0
		HM	19.9	816	50.3	7.77	2.98	86568	3.6	7.1	0.9
			29.6	795	50.3	7.72	2.83	115525	33.2	6.0	3.1
		HT	19.9	798	50.3	7.73	2.58	84844	4.3	5.9	1.0
			30.0	796	50.3	7.79	2.93	117029	27.2	4.5	3.5
TS7	8	HB	6.5	801	90.3	7.72	3.30	65290	5.8	4.5	1.0
			20.0	793	90.2	7.77	3.12	84322	15.3	3.1	0.4
		HM	29.7	807	90.2	7.71	3.16	118406	6.2	2.5	0.3
			7.6	796	90.3	7.78	3.35	66165	6.7	3.9	0.5
		HT	19.9	800	90.2	7.78	2.76	84967	15.8	2.6	0.5
			29.8	810	90.2	7.72	3.18	118826	5.5	2.0	0.5
TS8	8	HM	6.2	800	90.3	7.74	3.57	64833	5.4	2.2	0.6
			19.9	798	90.2	7.73	2.62	84836	16.9	1.5	0.5
		HT	30.1	790	90.2	7.78	3.12	116490	4.4	1.4	0.6
			HB	6.5	799	130.4	7.73	3.42	65165	10.8	1.5
HM	7.2	801	130.4	7.80	3.60	65990	9.5	1.2	0.2		
	HT	6.2	810	130.4	7.74	3.71	65652	11.6	0.9	0.2	

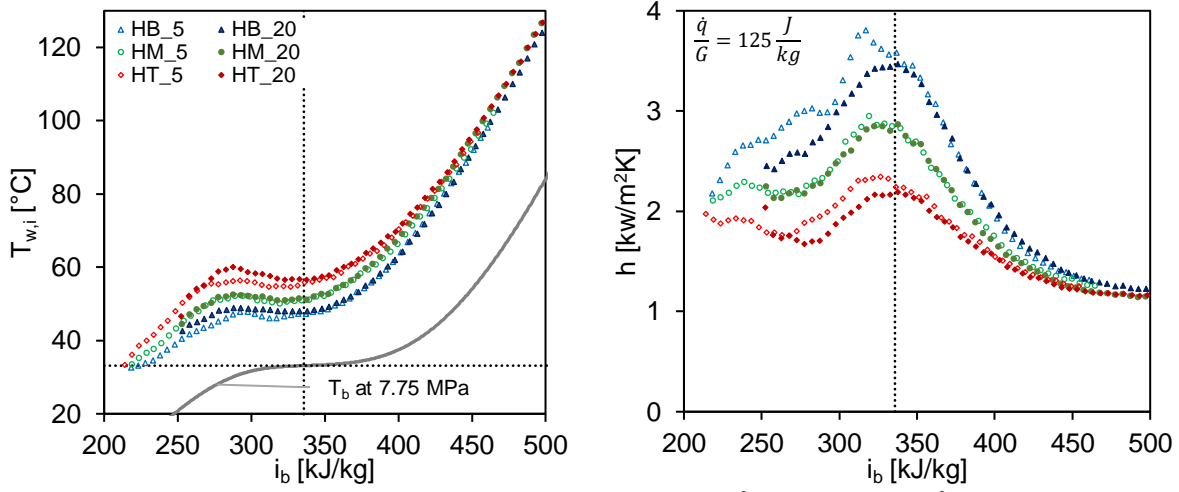


Figure 5: TS1 – $d_i = 4$ mm, $G = 400$ kg/m²s, $q^* = 50$ kW/m²

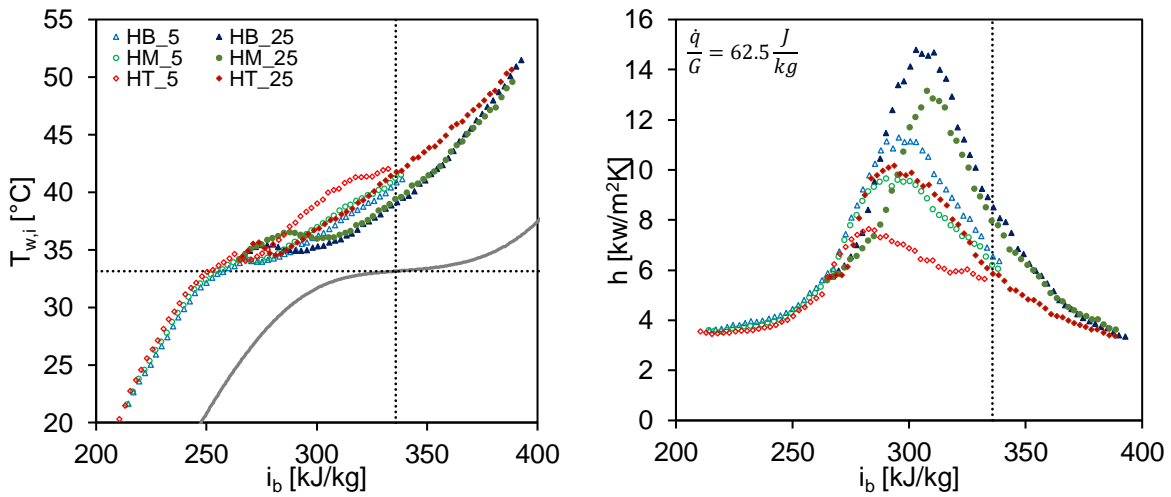


Figure 6: TS2 – $d_i = 4$ mm, $G = 800$ kg/m²s, $q^* = 50$ kW/m²

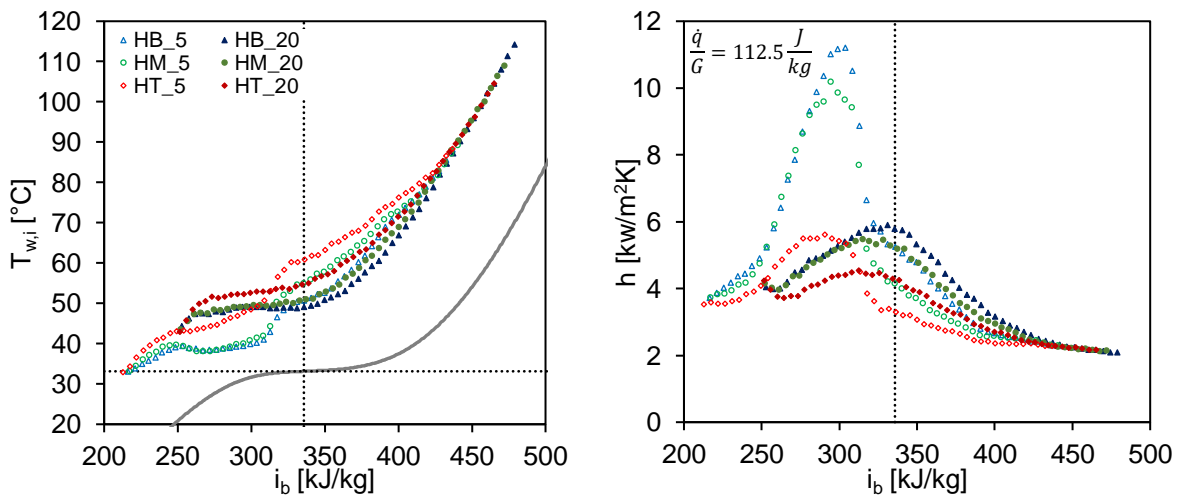


Figure 7: TS3 – $d_i = 4$ mm, $G = 800$ kg/m²s, $q^* = 90$ kW/m²

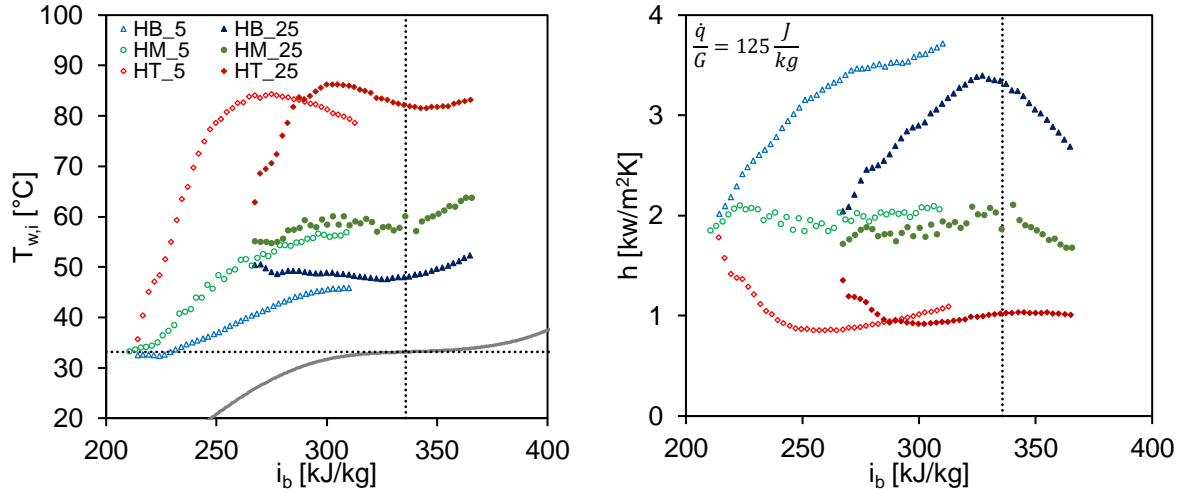


Figure 8: TS4 – $d_i=8\text{mm}$, $G=400\text{ kg/m}^2\text{s}$, $q^*=50\text{ kW/m}^2$

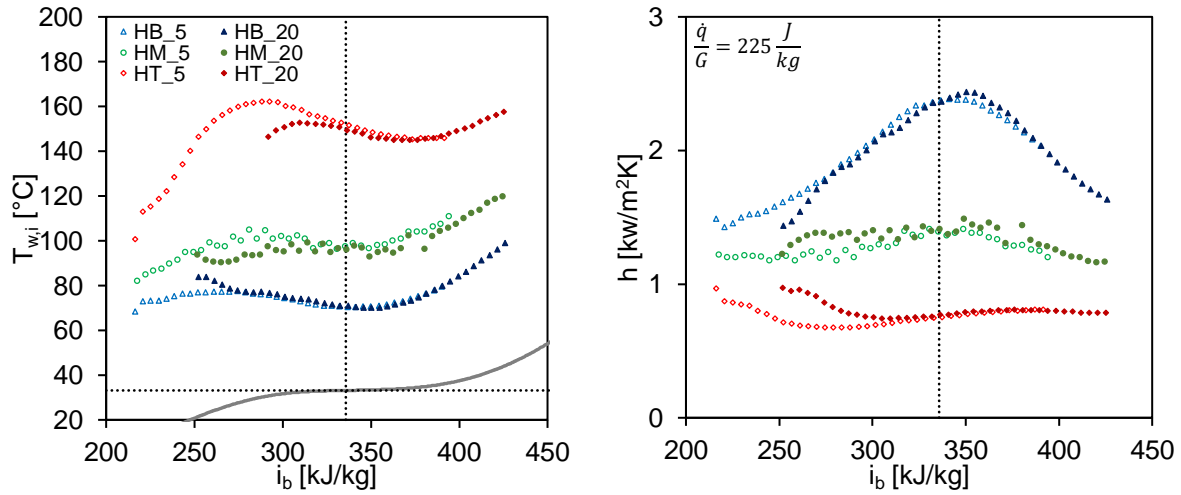


Figure 9: TS5 – $d_i=8\text{mm}$, $G=400\text{ kg/m}^2\text{s}$, $q^*=90\text{ kW/m}^2$

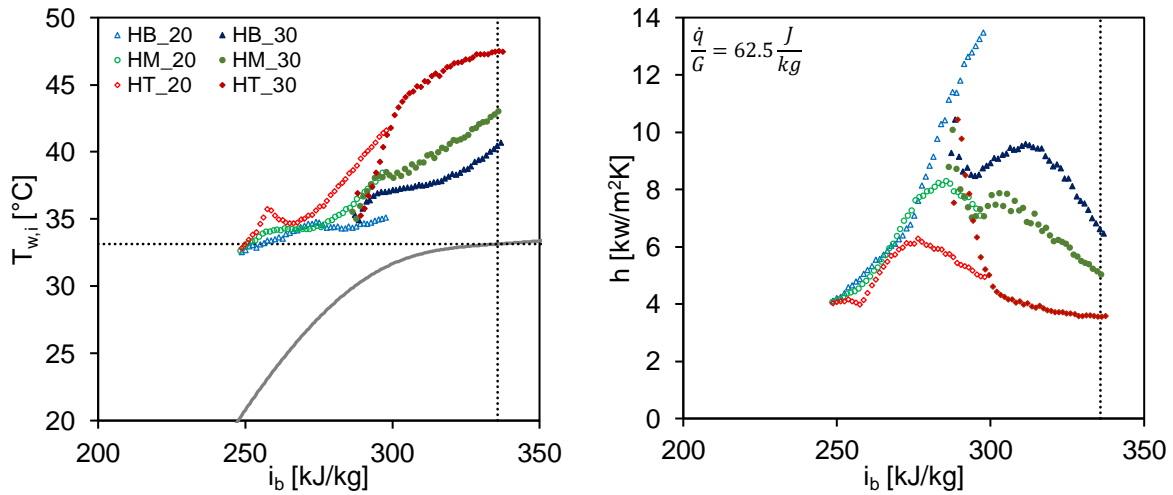


Figure 10: TS6 – $d_i=8\text{mm}$, $G=800\text{ kg/m}^2\text{s}$, $q^*=50\text{ kW/m}^2$

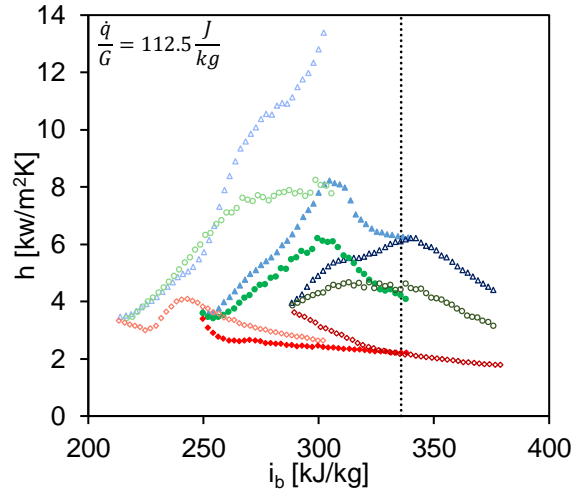
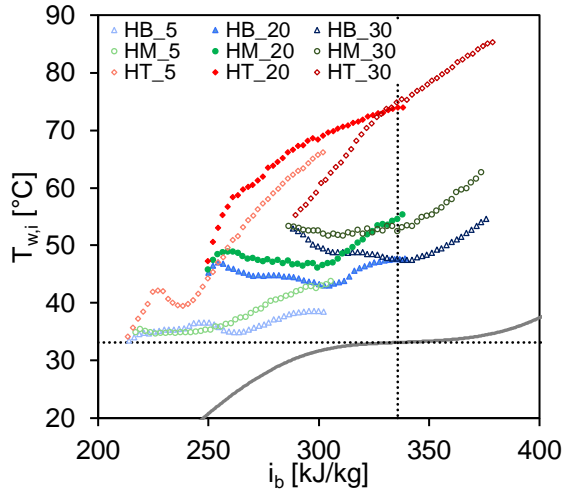


Figure 11: TS7 – $d_i= 8\text{mm}$, $G= 800 \text{ kg/m}^2\text{s}$, $q^*= 90 \text{ kW/m}^2$

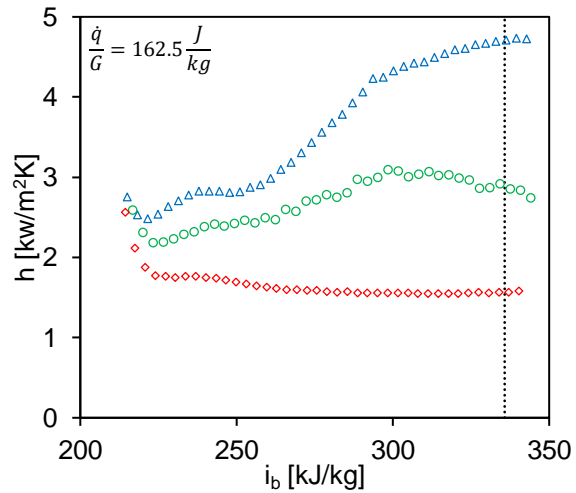
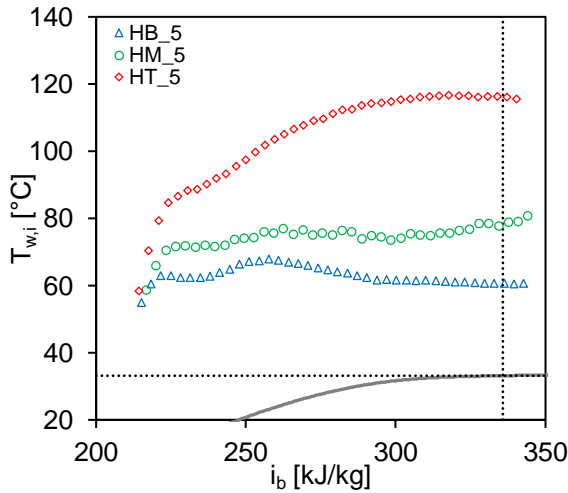


Figure 12: TS8 – $d_i= 8\text{mm}$, $G= 800 \text{ kg/m}^2\text{s}$, $q^*= 130 \text{ kW/m}^2$

In TS1 (Figure 5) six experiments of the 4 mm pipe were plotted for a heat flux of 50 kW/m^2 and mass flux of $400 \text{ kg/m}^2\text{s}$ leading to a ratio of 125 J/kg . For each sensor position, two experiments with different inlet temperatures of the bulk fluid ($5 \text{ }^\circ\text{C}$ and $20 \text{ }^\circ\text{C}$) were carried out. The overlapping of the wall temperature values indicates the end of the thermal inflow length (where the value of the inlet temperature has an influence). The results show a stable temperature stratification. Passing the pseudocritical temperature, the inner wall temperatures start to diverge until they reach the pseudocritical enthalpy. Then they begin to converge again what can be seen by the htc on the right chart. The values converge at an enthalpy of 450 kJ/kg . The maximum temperature difference between the surface at the top and the bottom is approximately 10 K .

For the second test series, (Figure 6) the mass flux has been increased to $800 \text{ kg/m}^2\text{s}$, so the heat flux to mass flux ratio decreases to 62.5 J/kg . Six experiments were carried out with fluid inlet temperatures of $5 \text{ }^\circ\text{C}$ and $25 \text{ }^\circ\text{C}$. In comparison to the TS1, no clear temperature stratification can be recognized. It is

visible that in the range of a mass fluid enthalpy between 300 and 400 kJ/kg in experiments at $5 \text{ }^\circ\text{C}$ and $25 \text{ }^\circ\text{C}$ fluid inlet temperature, the values for the temperature at HM and HB are very close together, while the values for HT are always higher. However, an overall scattering of the value profiles (HB, HM and HT) can be seen which converges after a bulk fluid enthalpy of 400 kJ/kg .

By increasing the heat flux up to 90 kW/m^2 in TS3 (Figure 7) the heat flux to mass flux ratio is similar to TS1. Nevertheless, in comparison to TS1, there is no clear temperature stratification. As in TS2, the temperature values of HB and HM are very close to each other, but the values of HT at the pseudocritical enthalpy are $5\text{-}10 \text{ K}$ higher. The value profiles converge at a bulk fluid enthalpy of 430 kJ/kg .

The following TSs (Figure 8-Figure 12) show the experimental results for the pipe with 8 mm inner diameter. Beginning with TS4 a mass flux of $400 \text{ kg/m}^2\text{s}$ and a heat flux of 50 kW/m^2 leads to a ratio of 125 J/kg , same as in TS1. The only

difference to TS1 is the inner pipe diameter that leads to higher Reynolds numbers (Table 2). By comparing TS1 and TS4, the temperature stratification in TS4 is more pronounced. The maximum temperature difference between the bottom and the top of the pipe is 45 K. The local temperature peak at the top of the pipe is associated with a deterioration of the htc. This effect cannot be seen at the bottom or the side of the pipe. TS4 can also be compared to TS3 because they have the same Reynolds number and approximately the same value of the heat to mass flux ratio. It shows that the larger inner pipe diameter of 8 mm in TS4 leads to more pronounced temperature stratification.

TS5 (Figure 9) presents the results of six experiments with a heat flux of 90 kW/m² and the highest heat to mass flux ratio of 225 J/kg. The results show a very clear temperature stratification with a maximum temperature difference of 90 K between the pipe bottom and the pipe top. The deterioration of heat transfer can be observed more distinctly at the top surface of the pipe.

Figure 10 shows the sixth TS with a mass flux of 800 kg/m²s and a heat flux of 50 kW/m², thus, the ratio is 62.5 J/kg, same as in TS2. Despite a higher Reynolds number in TS6 due to a larger diameter, the temperature stratification is more pronounced in the 8 mm pipe, so that the influence of the pipe diameter on the temperature stratification is higher than the influence of the Reynolds number.

With the increase of the heat flux to 90 kW/m² in TS7 (Figure 11) and 130 kW/m² in TS8 (Figure 12) the temperature stratification became much clearer. For TS7 the maximum temperature difference between the values of HB and HT is approximately 30 K and for TS8 approximately 60 K.

The fluid inlet temperatures of the experiments were chosen in such a way that an overlap of the inner wall temperatures occurs. This makes it possible to quantify the inlet length for a fully developed temperature stratification by a deviation of the inner wall temperatures at the pipe outlet of a previous experiment from the wall temperatures at the pipe inlet of the following experiment (at the next higher inlet fluid temperature of the bulk fluid). The maximum values of HT, HB and HT can be taken for this. For example, for TS5 the HT values of the 20 °C experiment converge to those of the 5 °C experiment after approximately 50*d_i* (10 data points with 40 mm distances correspond to 400 mm inflow length for the 8 mm pipe) and the HB values converge after approximately 30*d_i* (6 data points). Thus, the inlet length for a fully developed temperature stratification can be determined with 50*d_i*. For the 30 °C experiment in TS7, this results in an inlet length for a fully developed temperature stratification of 30*d_i* (22 data points of HB).

CONCLUSION

For the investigation of the heat transfer characteristics of sCO₂ in a case where buoyancy effects lead to a temperature stratification, 48 experiments were carried out for two horizontally oriented heated pipes with inner diameters of 4 mm

and 8 mm. The outer surface temperatures of the pipes were measured at three different radial pipe positions: The pipe top, the pipe bottom and the pipe side.

The experimental results show that an increased mass flux and Reynolds number with constant heat flux and constant inner diameter leads to reduced temperature differences between the top and the bottom of the pipe. If the ratio of heat to mass flux and the diameter are kept constant while increasing the mass flux and the Reynolds number, no clear temperature stratification appears. With a constant heat to mass flux ratio and Reynolds number, larger pipe diameters lead to more distinct temperature stratification. The results show that the influence of the pipe diameter on the temperature stratification is greater than the influence of the Reynolds number. This set of data can be used for validation of computer codes.

Experiments with higher pressures are planned to investigate the influence of the pressure on the thermal stratification. Furthermore, the results will be analyzed using criteria to determine the influence of buoyancy effects.

NOMENCLATURE

Variables

<i>d</i>	diameter [m] or [mm]
<i>G</i>	mass flux [kg/(m ² s)]
<i>h</i>	heat transfer coefficient [W/(m ² K)]
<i>i</i>	specific enthalpy [J/kg]
<i>I</i>	current [A]
<i>L</i>	length [m]
<i>P</i>	electrical power [W]
<i>p</i>	pressure [Pa] or [bar]
<i>Q̇</i>	heat transfer rate [W]
<i>q̇</i>	heat flux [W/m ²]
<i>R_a</i>	inner roughness [μm]
<i>Re</i>	Reynolds number [-]
<i>s</i>	error [%]
<i>T</i>	temperature [°C] or [K]
<i>U</i>	voltage [V]

Subscripts

b	bulk fluid
el	electric, calculated with el. power
h	heated length
hyd	hydraulic length
i	inner wall
in	inlet fluid conditions
x	local pipe position
o	outer wall
out	outlet fluid conditions
sur	surface of pipe
th	thermal, calculated with bulk fluid
w	pipe-wall

Abbreviations

ATHLET	analysis of thermal-hydraulics of leaks and transients
CHX	compact heat exchanger
DC	direct current
DNS	Direct Numerical Simulation
DP	data point
EUR	European Utility Requirements
HB	pipe bottom
HM	pipe side
HT	pipe top
htc	heat transfer coefficient
HX	heat exchanger
IKE	Institute of Nuclear Technology and Energy Systems
RD	reading accuracy
SCARLETT	Supercritical Carbon Dioxide Loop at IKE Stuttgart
sCO ₂	supercritical carbon dioxide
SP	sensor position
TCS	turbo-compressor system
TS	test series

ACKNOWLEDGEMENTS

The presented work was funded by the German Federal Ministry for Economic Affairs and Energy (BMWi. Project no. 1501557) on basis of a decision by the German Bundestag

REFERENCES

- [1] Venker, J. (2015). Development and validation of models for simulation of supercritical carbon dioxide Brayton cycles and application to self-propelling heat removal systems in boiling water reactors [Doctoral dissertation]. University of Stuttgart. (10.18419/OPUS-2364). Society (ANS).
- [2] Chu, X. (2016). Direct numerical simulation of heat transfer to supercritical carbon dioxide in pipe flows [Doctoral dissertation]. University of Stuttgart. (10.18419/OPUS-9056).
- [3] Dang, C. and Hihara, E. (2004). In-tube cooling heat transfer of supercritical carbon dioxide. Part 1. Experimental measurement. *International Journal of Refrigeration*, 7, pp. 736–747. (10.1016/j.ijrefrig.2004.04.018).
- [4] Liao, S. M. and Zhao, T. S. (2002). Measurements of Heat Transfer Coefficients From Supercritical Carbon Dioxide Flowing in Horizontal Mini/Micro Channels. *Journal of Heat Transfer*, 3, pp. 413. (10.1115/1.1423906).
- [5] Wahl, A.; Mertz, R.; Starflinger, J. (2019, 18-22. August). Experimental investigation of heat transfer in tubes to cool CO₂ near the critical point in horizontal flow orientation [Paper presentation]. *18th International Topical Meeting on Nuclear Reactor Thermal Hydraulics (NURETH-18)*. Portland, OR, USA. American Nuclear Society (ANS).
- [6] Xiang, M.; Guo, J.; Huai, X.; Cui, X. (2017). Thermal analysis of supercritical pressure CO₂ in horizontal tubes under cooling condition. *The Journal of Supercritical Fluids*, pp. 389–398. (10.1016/j.supflu.2017.04.009).
- [7] Yang, M. (2016). Numerical Study on the Heat Transfer of Carbon Dioxide in Horizontal Straight Tubes under Supercritical Pressure. *PloS one*, 7, pp. e0159602. (10.1371/journal.pone.0159602).
- [8] Yang, C.; Xu, J.; Wang, X.; Zhang, W. (2013). Mixed convective flow and heat transfer of supercritical CO₂ in circular tubes at various inclination angles. *International Journal of Heat and Mass Transfer*, pp. 212–223. (10.1016/j.ijheatmasstransfer.2013.04.033).
- [9] Cao, X. L.; Rao, Z. H.; Liao, S. M. (2011). Laminar convective heat transfer of supercritical CO₂ in horizontal miniature circular and triangular tubes. *Applied Thermal Engineering*, 14-15, pp. 2374–2384. (10.1016/j.applthermaleng.2011.03.038).
- [10] Du, Z.; Lin, W.; Gu, A. (2010). Numerical investigation of cooling heat transfer to supercritical CO₂ in a horizontal circular tube. *The Journal of Supercritical Fluids*, 1, pp. 116–121. (10.1016/j.supflu.2010.05.023).
- [11] Yu, S.; Li, H.; Lei, X.; Feng, Y.; Zhang, Y.; He, H.; Wang, T. (2013). Influence of buoyancy on heat transfer to water flowing in horizontal tubes under supercritical pressure. *Applied Thermal Engineering*, 1-2, pp. 380–388. (10.1016/j.applthermaleng.2013.05.034).
- [12] Bazargan, M. and Fraser, D. (2009). Heat Transfer to Supercritical Water in a Horizontal Pipe: Modeling, New Empirical Correlation, and Comparison Against Experimental Data. *Journal of Heat Transfer*, 6, pp. 61702. (10.1115/1.3082403).
- [13] W. Flaig; R. Mertz; J. Starflinger. (2018, 30-31. August). Design, control procedure and start-up of the sCO₂ test facility SCARLETT [Paper presentation]. *2nd European sCO₂ Conference 2018*. Essen, Germany. (10.17185/duublico/46081).
- [14] Munson, B. R.; Young, D. F.; Okiishi, T. H. (2006). *Fundamentals of fluid mechanics*, 5. ed. Wiley.
- [15] Theologou, K.; Mertz, R.; Laurien, E.; Starflinger, J. (2019, 19-20. September). An Assessment of the criteria for the onset of heat transfer deterioration with supercritical CO₂ in vertical heated single circular tubes [Paper presentation]. *3rd European supercritical CO₂ Conference*. Paris, France. (10.17185/duublico/48875).

**MODELING AND STUDY OF A PRINTED CIRCUIT HEAT EXCHANGER FOR
BRAYTON POWER CYCLES USING SUPERCRITICAL CO₂ MIXTURES AS
WORKING FLUID**

Robert Valencia-Chapi*

Universidad Politécnica de Madrid
Madrid, Spain
Email: robert.valencia.chapi@upm.es

Olmo Fierros-Peraza

Universidad Politécnica de Madrid
Madrid, Spain
Email: o.fierros@alumnos.upm.es

Luis Coco-Enríquez

Universidad Politécnica de Madrid
Madrid, Spain

Javier Muñoz-Antón

Universidad Politécnica de Madrid
Madrid, Spain

ABSTRACT

Brayton power cycle using supercritical carbon dioxide (s-CO₂) as a working fluid is a high-efficiency trend technology that has been under study for improvement. As most of the heat transfer in these cycles occurs in the regenerator, printed circuit heat exchangers (PCHE) have proved to be a useful device solution for this application because of their high surface-area-to-volume ratio. Moreover, recent studies have corroborated the improvement in the efficiency of a supercritical Brayton cycle by mixing components that raise the critical point of s-CO₂. This study focuses on the CFD modeling and analysis of a PCHE for fully turbulent conditions. The device's performance with straight channels regarding essential parameters such as heat recuperator conductance (UA), temperature, pressure drop, or turbulence is studied, as well as different configurations. A comparison between pure supercritical carbon dioxide and s-CO₂ mixtures (s-CO₂/CO₂, s-CO₂/H₂S, s-CO₂/NH₃, and s-CO₂/SO₂) is carried out.

INTRODUCTION

A supercritical fluid is a material that can behave as a gas and as a liquid at the same time. One of the most used supercritical fluids is carbon dioxide. It is a substance that can be obtained quickly and cheaply and is also a non-toxic or flammable material. s-CO₂ can be used in Brayton power cycles for a wide variety of generation plants, including fossil fuel plants [1], waste heat recovery [2], nuclear reactors [3] and concentrated solar energy (CSP) [4], which constitutes the focus of the present study. The fact that heat recovery is so important in the thermal efficiency of supercritical carbon dioxide Brayton cycles makes heat exchangers of relevance. These Brayton cycles favor the use of compact heat exchangers (CHE), such as

the printed circuit heat exchanger. This type of exchanger is used in Brayton cycles of CSP plants mainly as regenerators due to their high ratio between heat transfer area and volume and their suitability to work under very high temperature and pressure conditions.

Numerous studies can be found in the literature related to CFD analysis of compact heat exchangers. Ngo et al. [5] carried out pressure drop correlations in microchannel heat exchangers (MCHE) with zigzag configurations and S-shaped fins for supercritical CO₂ cycles nuclear reactors. Tsuzuki et al. [6] used a test bench to analyze the thermal and hydraulic performance of a PCHE for application with s-CO₂. Different CFD analyzes of PCHE emphasizing the optimization of design parameters have been elaborated by Kim et al. [7] and S.P. Kar [8]. Of particular interest is the study carried out by Jeong et al. [9] since different mixtures of s-CO₂ are proposed to move the critical point and thus improve supercritical compression. In this research line, Valencia et al. [10] study is essential since it will be used as a reference in this document to analyze the PCHE exchanger's performance. This study investigates the impact of s-CO₂ mixtures in a Brayton cycle with recompression for application in CSP. The mixtures used are divided into two groups, those that lower the critical point temperature and those that increase the critical point temperature. Analyzing the different mixtures with s-CO₂, Valencia concludes that the cycle's thermodynamic efficiency increases by 3-4% compared to the increase in the turbine inlet temperature.

The objectives of this study are various. On the one hand, the importance of validating the numerical analysis results of PCHE regenerators using supercritical carbon dioxide for the rest of the investigation. In this step, the validation of both the real gas models and the CFD tool's turbulence models is necessary. On the other hand, the simulation and modeling of a PCHE type heat exchanger for application in supercritical

Brayton cycles. These considerations lead to the main objective: analyze and compare different mixtures' performance that raises the critical point of s-CO₂ mixtures (s-CO₂/COS, s-CO₂/H₂S, s-CO₂/NH₃, and s-CO₂/SO₂). In this way, this study also seeks to validate the use of the different supercritical mixtures in Brayton cycles for application in CSP and to analyze their viability. The aim is to investigate the range of implications that regenerators may have in improving the cycle's efficiency already, using the mentioned supercritical mixtures. Besides, it seeks to analyze the impact on the heat exchange area and, therefore, on the cycle's economic efficiency, of the different supercritical mixtures studied.

SYSTEM DESCRIPTION

For the CFD simulation, the *Ansys Fluent 2019 R3* software has been used. Fig. 1 shows that two PCHE exchange channels are modeled, a cold channel and a hot channel, which are homogeneously placed at a 0.6 mm distance from each other. The channels have a diameter of 2 mm and a maximum length of 200 mm. Due to its good behavior under high-temperature conditions and pressure, the *Iconel 617 alloy* was chosen as the material of the exchanger's solid domain. It is an alloy in which nickel predominates and whose thermo-physical properties have been assumed to be constant, with the density (ρ) 8360 kg/m³, the isobaric specific heat (C_p) 0.417 kJ/kg·K, and the thermal conductivity (k) 21 W/m·K.

As previously mentioned, the supercritical CO₂ mixture with the different added components shifts the critical point. The new critical values of the various mixtures have been calculated using software developed by members of the Department of Energy Engineering of the Polytechnic University of Madrid [11]. The software is called SCSP (Supercritical Concentrated Solar Plant) and is based on the core of the software developed by Dyreby [12]. In Table 1, it can see the critical properties of the different mixtures. The properties of the flows were obtained from the REFPROP (Reference Fluid Properties) database, developed by NIST (National Institute of Standards and Technology) in the United States [13]. The cold fluid properties have been obtained for operating parameters of $T = 400$ K and $P = 22.5$ MPa, while for the hot fluid, they are $T = 630$ K and $P = 9$ MPa.

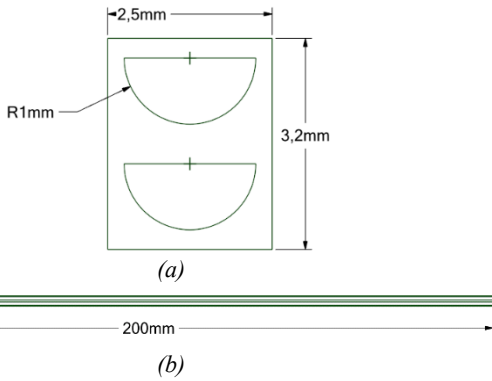


Figure 1: Geometry measurements; (a) front view, (b) side view.

In order to validate the numerical model used, this study tried to emulate the results of the investigation carried out by Meshram et al. [14] on CFD simulation of CO₂ supercritical in a PCHE. The reference study cited analyzes the behavior of pure supercritical carbon dioxide for different configurations of the printed circuit exchanger and different temperature ranges. The validation results can be seen in ANNEX A.

MATHEMATICAL MODELING

The equations (1)-(3) are the characteristic equations to calculate the fluid's behavior in the present study. The value of i in the momentum equation represents equations in x , y , and z directions, and j is a summation index ranging from 1 to 3 [14].

Continuity equation:

$$\frac{\partial(\rho u_j)}{\partial x_j} = 0 \quad (1)$$

Momentum equation:

$$\rho \frac{\partial(u_i u_j)}{\partial x_j} = -\frac{\partial p_i}{\partial x_j} + \mu \frac{\partial}{\partial x_j} \left(\frac{\partial u_i}{\partial x_j} + \frac{\partial u_j}{\partial x_i} - \frac{2}{3} \delta_{ij} \frac{\partial u_k}{\partial x_k} \right) \quad (2)$$

Energy equation:

$$\frac{\partial}{\partial x_j} [u_j(\rho E + p)] = \frac{\partial}{\partial x_j} \left((k_f + k_t) \frac{\partial T}{\partial x_j} \right) \quad (3)$$

The energy equation for the solid domain:

$$\frac{\partial}{\partial x_j} \left(k_s \frac{\partial T}{\partial x_j} \right) = 0 \quad (4)$$

This study's turbulence model is the Reynolds-averaged Navier – Stokes (RANS) standard $k - \epsilon$ model with wall function. This model is the most common due to its low computational cost. For this model, it is required to solve two additional equations: the equation for turbulent kinetic energy (k) and the equation for the dissipation rate of turbulent kinetic energy (ϵ). The transport equations [15] of this model are shown below:

$$\frac{\partial}{\partial t}(\rho k) + \frac{\partial}{\partial x_i}(\rho k u_i) = \frac{\partial}{\partial x_j} \left[\left(\mu + \frac{\mu_t}{\sigma_k} \right) \frac{\partial k}{\partial x_j} \right] + G_k + G_b - \rho \epsilon - Y_M + S_k \quad (5)$$

$$\frac{\partial}{\partial t}(\rho \epsilon) + \frac{\partial}{\partial x_i}(\rho \epsilon u_i) = \frac{\partial}{\partial x_j} \left[\left(\mu + \frac{\mu_t}{\sigma_\epsilon} \right) \frac{\partial \epsilon}{\partial x_j} \right] + C_{1\epsilon} \frac{\epsilon}{k} (G_k + C_{3\epsilon} G_b) - C_{2\epsilon} \rho \frac{\epsilon^2}{k} + S_\epsilon \quad (6)$$

Where μ_t is the turbulent viscosity, G_k represents the generation of turbulence of kinetic energy due to velocity gradients, G_b represents the generation of turbulence of kinetic

energy due to buoyancy, and Y_M is the contribution of fluctuating dilation to the total dissipation rate.

Table 1: Critical values of the different mixtures.

	Critical Temperature [K]	Critical Pressure [MPa]	Critical density [kg/m ³]
s-CO ₂ pure	304,13	7,3	467,6
s-CO ₂ /COS (70/30)	324,15	7,815	467,139
s-CO ₂ /H ₂ S (60/40)	322,34	8,234	431,384
s-CO ₂ /NH ₃ (81/19)	323,41	8,766	455,264
s-CO ₂ /SO ₂ (90/10)	322,53	8,525	488,593

Due to the fluids' supercritical conditions, it is impossible to use a typical real gas model. For this reason, the model used in the numerical simulation is the Aungier-Redlich-Kwong real gas model [16].

$$P = \frac{RT}{V - b + c} - \frac{a(T)}{V(V + b)} \quad (7)$$

Where the different parameters involved are obtained from the following expressions [17]:

$$a(T) = a_0 T_r^{-n} \quad (8)$$

$$c = \frac{RT_c}{P_c + \frac{a_0}{V_c + (V_c + b)}} + b - V_c \quad (9)$$

$$n = 0,4986 + 1,1735\omega + 0,4754\omega^2 \quad (10)$$

$$a_0 = 0,42747R^2T_c^2/P_c \quad (11)$$

$$b = 0,08664RT_c/P_c \quad (12)$$

Being P_c (Pa), the critical pressure, V_c (m³/kg), the critical specific volume, and ω the acentric factor.

A mesh dependence study was carried out to ensure the reliability of the results. Cell size was modified, emphasizing the y^+ value for this purpose. In the study by Salim et al. [18], it is confirmed that for $k-\epsilon$ turbulence models such as the one used in the present case, wall functions are the most appropriate since this turbulence model is valid for regions where turbulence is fully developed. The cells adjacent to the wall are therefore placed in the logarithmic region ($y^+ > 32.5$) to ensure the accuracy of the result. The expression that defines the wall function for the range of y^+ characteristic of this region is the following [19]:

$$y^+ = \frac{yu_\tau}{\nu} \quad (13)$$

$$u_\tau = \sqrt{\frac{\tau_w}{\rho}} \quad (14)$$

$$u^+ = \frac{1}{k} \ln(y^+) + B \quad (15)$$

Where y is the absolute distance from the wall, u_τ represents the so-called friction velocity, ν is the kinematic viscosity of the fluid and τ_w represents the shear stress in the wall. The Von Karman constant being $k = 0.41$ and the constant $B = 5.2$, where $u^+ = u/u_\tau$.

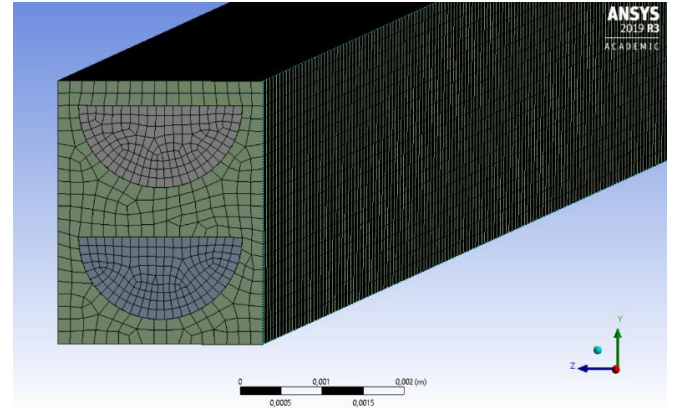


Figure 2: Final mesh.

RESULTS AND DISCUSSION

This section shows the results obtained in the different simulations and their comparison with the reference data of pure s-CO₂. The boundary conditions used in all the simulations are shown in Table 2. Since the simulation does not cover the entire exchanger and considers that the device has many more heat exchange channels, periodic conditions have been used on the upper and lower walls. The rest of the device has been assumed adiabatic in order to simplify the analysis.

Table 2: Boundary conditions.

Boundary	Boundary condition
Flow inlet	Inlet velocity
Flow outlet	Outlet pressure
Upper wall	Periodic
Bottom wall	Periodic
Sidewalls	Adiabatic
Front wall	Adiabatic
Back wall	Adiabatic

Table 3 shows the main boundary values of the $s\text{-CO}_2$ flows and mixtures used in the simulation. These conditions have been collected from the Meshram study [14] and have been reproduced in the present study:

Table 3: Boundary numerical values.

Property	Cold $s\text{-CO}_2$	Hot $s\text{-CO}_2$
Temperature [K]	400	630
Pressure [bar]	225	90
Velocity [m/s]	0,842	4,702

TEMPERATURE:

Fig. 3 shows the temperature profile, both the hot fluid and the cold fluid, of the different mixtures used. The figures indicate the values of the temperature obtained in the center of the channels. As can be seen, the $s\text{-CO}_2/\text{NH}_3$ mixture is the one that has the most significant slope in the temperature profile of the hot fluid, being, therefore, the one that cools the most. However, the opposite occurs in the cold fluid. It is found that the cold fluid with the most significant outflow temperature is pure $s\text{-CO}_2$. The rest of the mixtures have similar behaviors, having intermediate values between $s\text{-CO}_2$ and the mixture $s\text{-CO}_2/\text{NH}_3$.

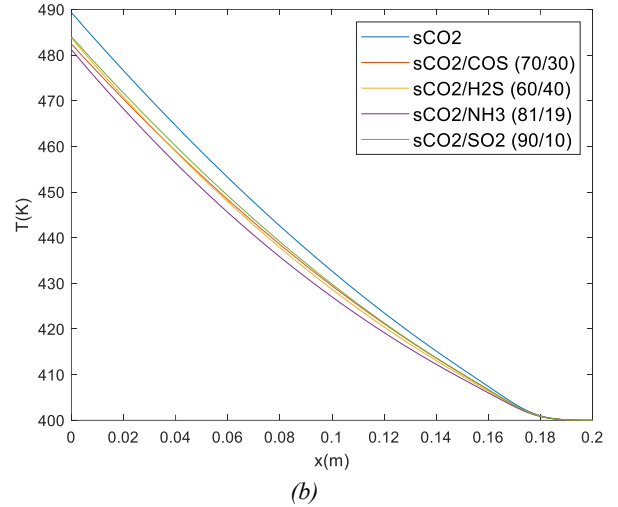
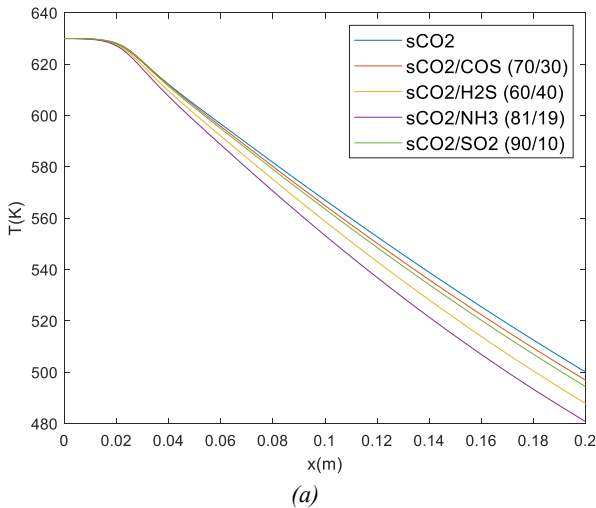


Figure 3: Temperature profile of the different mixtures; (a) hot fluid; (b) cold fluid.

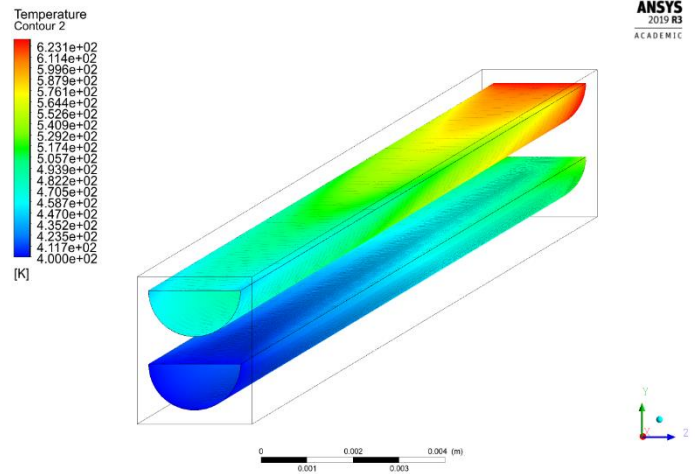


Figure 4: Temperature distribution in the fluid domain of the $s\text{-CO}_2/\text{NH}_3$ mixture.

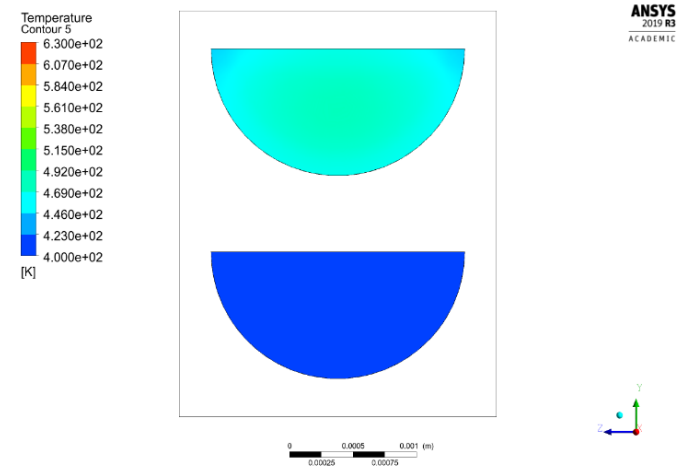


Figure 5: Temperature distribution of the $s\text{-CO}_2/\text{NH}_3$ mixture in the hot outlet section and the cold inlet section.

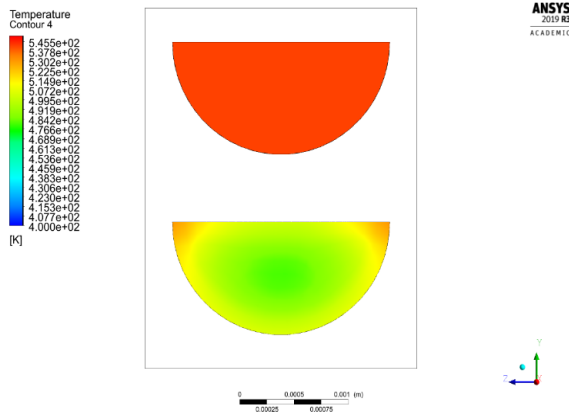


Figure 6: Temperature distribution of the s-CO₂/NH₃ mixture in the hot inlet section and the cold outlet section.

Previous figures (Fig. 4 - Fig. 6) show the temperature distribution in the fluid domains for the s-CO₂/NH₃ mixture, as well as the temperature distribution in the inlet and outlet sections of the ducts, where the difference of temperatures within the fluid volume in relation to the distance from the wall is appreciated.

PRESSURE LOSS:

Another parameter of great importance to study is the pressure drop in the exchanger channels. Fig. 7 shows the pressure loss profile for both hot and cold fluid for the different mixtures. It is observed that the hot fluid shows the most significant pressure loss, being even more than double the pressure drop of the cold fluid. Under the different operating conditions, the s-CO₂/COS mixture shows the greatest pressure loss, although without reaching very high values, the maximum is 3.0 kPa. The s-CO₂/SO₂ mixture, although with lower values than the previous one, also shows a greater pressure drop than pure s-CO₂. On the contrary, the mixtures s-CO₂/NH₃ and s-CO₂/H₂S show the least pressure loss, the maximum being 2.45 kPa in the hot fluid and barely 1.0 kPa to the cold fluid for the NH₃ case.

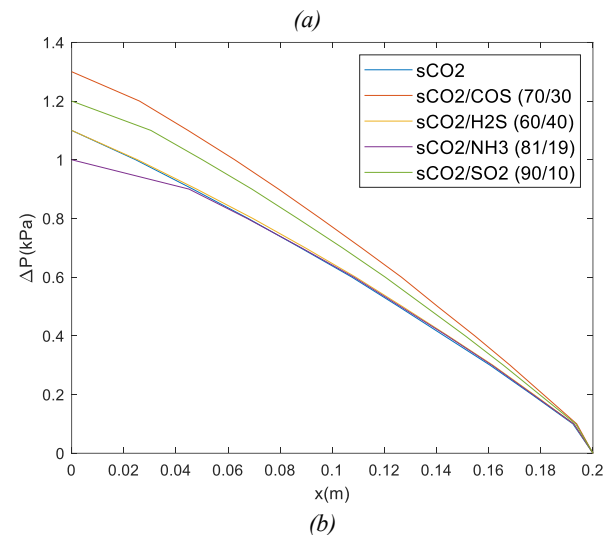
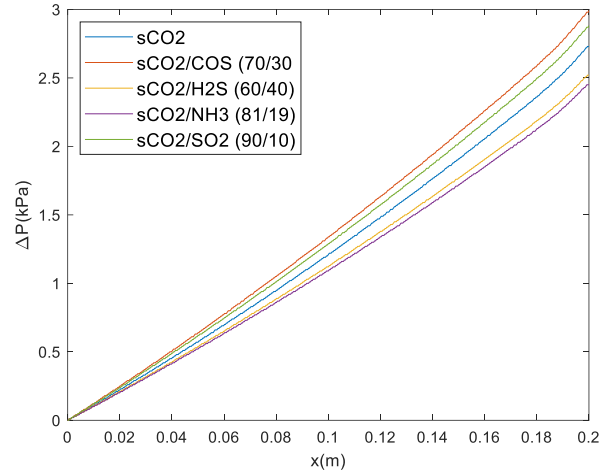


Figure 7: Pressure drop of the different mixes in the straight channels; (a) hot fluid; (b) cold fluid

TURBULENCE:

A relevant parameter in heat exchange applications is turbulence since high turbulence encourages greater heat exchange in a fluid. Comparing the different mixtures' turbulent kinetic energy in the center of the channels along the control volume is shown in Fig. 8. As can be seen, the turbulent kinetic energy (k) is very low in both the hot and cold conduits. However, the difference between the two flows is considerable; the hot flow's turbulence is much higher than that of the cold flow. In this case, the turbulence is unstable at the exchanged entrance, becoming stable and decreasing once it reaches the 0.05 m point. This comportment is because the velocity profile enters the undeveloped domain. The duct's initial section is where the velocity profile develops, being homogeneous in the rest of the exchanger. The mixtures s-CO₂/NH₃ and s-CO₂/H₂S show higher values than the rest, although this difference is not significant.

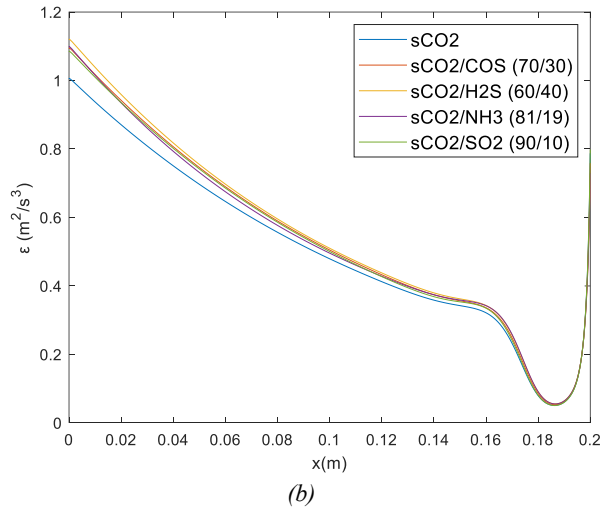
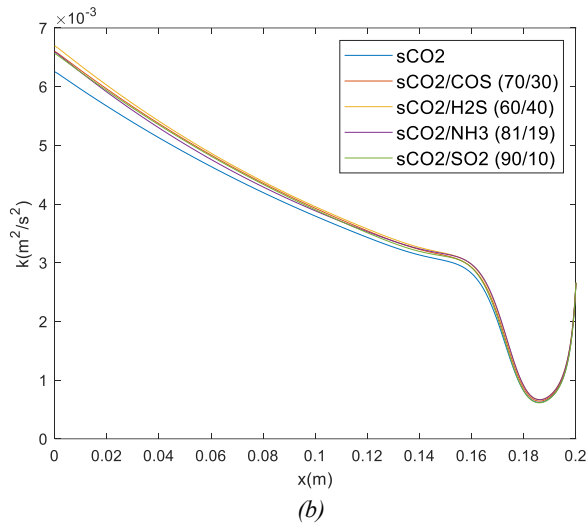
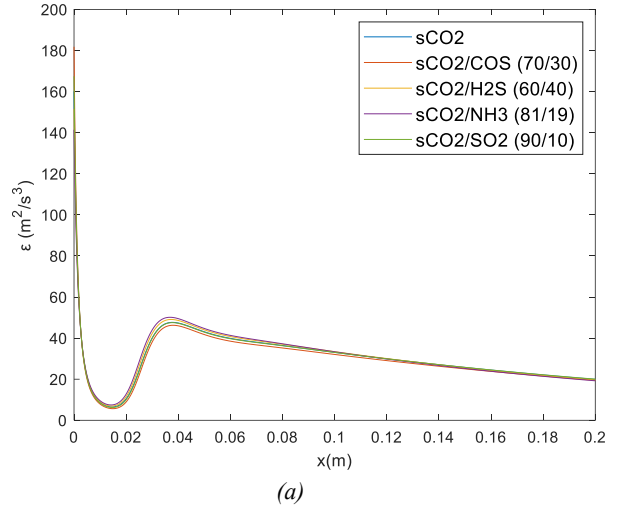
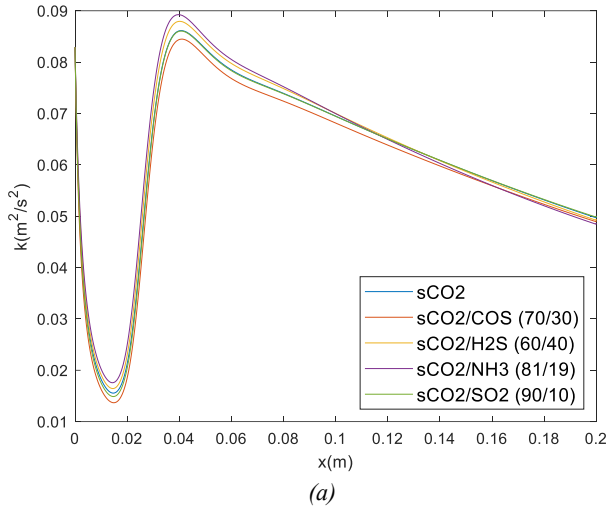


Figure 8: Turbulent kinetic energy of the different mixtures in the straight channels; (a) hot fluid; (b) cold fluid.

Figure 9: Dissipation rate of the different mixtures' turbulent kinetic energy in the straight channels; (a) hot fluid; (b) cold fluid.

Another important parameter related to turbulence in the $k-\epsilon$ model used is the dissipation of turbulent kinetic energy (ϵ). Fig. 9 shows this dissipation ratio along with the profile for the central value of both hot and cold ducts. It is found that this parameter behaves similarly to that studied previously so that the dissipation rate of turbulent kinetic energy in hot fluid is again much higher than in cold fluid. Furthermore, all the mixtures show very similar behavior, being the mixtures $s\text{-CO}_2/\text{NH}_3$ and $s\text{-CO}_2/\text{H}_2\text{S}$, which offer a slightly higher curve, as shown in Fig. 9. Fig. 10 shows the turbulent kinetic energy's visualization along the channels for the $s\text{-CO}_2/\text{NH}_3$ mixture.

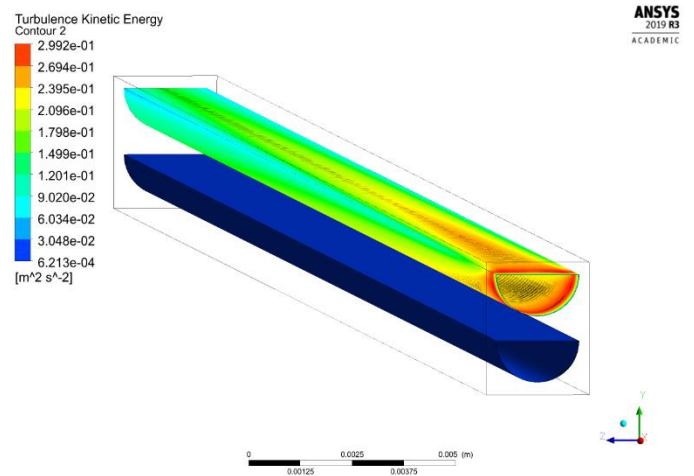


Figure 10: Turbulent kinetic energy of hot flow and cold flow for the $s\text{-CO}_2/\text{NH}_3$ mixture.

SURFACE HEAT FLUX AND EXCHANGE AREA:

Using the CFD software post-processor, the total surface heat exchanged flux was obtained as a fundamental parameter for this analysis, shown in table 4. This parameter describes the total heat exchanged through the channel surfaces.

Table 4: Surface heat flux of each mixture.

	Surface heat flux [kW/m ²]
s-CO ₂	90.037
s-CO ₂ /COS (70/30)	103.66
s-CO ₂ /H ₂ S (60/40)	91.25
s-CO ₂ /NH ₃ (81/19)	92.32
s-CO ₂ /SO ₂ (90/10)	98.64

All the mixtures analyzed have a higher surface heat flux than pure s-CO₂. The mix with the most increased heat flow is s-CO₂/COS, followed by the mixture s-CO₂/SO₂. The mixtures s-CO₂/H₂S and s-CO₂/NH₃ show lower values, despite having higher heat flux than pure s-CO₂. Fig. 11 shows the temperature variation along with the reliable domain for the carbonyl sulfide mixture.

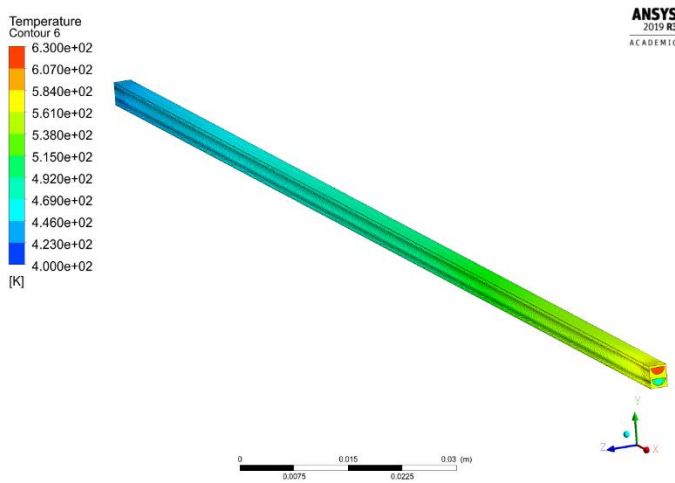


Figure 11: Temperature along the solid boundary of the mixture exchanger s-CO₂/COS.

The average heat transfer coefficients and the Nusselt numbers shown in Table 6 have been obtained using equations (16) and (17):

$$\underline{h} = \frac{q}{T_B - T_w} \quad (16)$$

$$Nu = \frac{hD_h}{k} \quad (17)$$

Where T_B (K) is the average apparent temperature of the fluid (bulk temperature), T_w (K), the average wall temperature, and D_h (m) refers to the hydraulic diameter.

As might be expected, the mixtures that previously showed higher heat fluxes are those with higher heat transfer coefficients, reaching the s-CO₂/COS mix a coefficient of 1857.85 W/m²K for the hot flux. However, in the cold flow, the s-CO₂/NH₃ mixture presents the highest heat transfer coefficient. Again, pure s-CO₂ shows a lower mean heat exchange coefficient in both hot and cold fluid.

In order to analyze the efficiency of the different mixtures, the necessary area of the heat exchanger must be taken into account to dissipate a fixed amount of heat of 8.9 MW, according to the reference study [14]. The area needed in the countercurrent supercritical recuperator to dissipate this amount of heat is obtained with the equation (18).

$$Q = UA\Delta T_{lm} \quad (18)$$

Where ΔT_{lm} (K) is the mean logarithmic temperature difference, and U (W/m²K) refers to the global heat transfer coefficient.

Table 5 presents the most relevant parameters of the analysis to compare the efficiency of the different mixtures. As can be seen, all the mixes offer better heat transfer performances than pure s-CO₂, being the s-CO₂/COS mixture, the one that presents a higher value of the global heat exchange coefficient. This behavior is reflected in the area of heat exchange necessary to dissipate the same amount of energy. In the s-CO₂/COS mixture, an area of 12.849 m² is required, representing a 12.62% reduction compared to the area needed to dissipate the same amount using pure s-CO₂. The mixture that shows the smallest difference with respect to pure s-CO₂ is the s-CO₂/H₂S mixture since it only reduces the necessary exchange area by 0.96%.

Table 5: Relevant parameters of each mixture.

	ΔT_{ml} [K]	\underline{U} [W/m ² · K]	Area [m ²]
s-CO ₂	119.443	854.067	14.704
s-CO ₂ /COS (70/30)	120.491	968.866	12.849
s-CO ₂ /H ₂ S (60/40)	114.586	898.874	14.563
s-CO ₂ /NH ₃ (81/19)	111.368	939.606	14.335
s-CO ₂ /SO ₂ (90/10)	118.315	940.831	13.475

Table 6: Average surface heat transfer coefficient, Reynolds number, and Nusselt number of the different mixtures.

	Reynolds (cold)	Reynolds (hot)	Nusselt (cold)	Nusselt (hot)	$\frac{h_{cold}}{[W/m^2 K]}$	$\frac{h_{hot}}{[W/m^2 K]}$
s-CO ₂	21080.52	23833.96	43.706	43.986	1851.094	1660.921
s-CO ₂ /COS (70/30)	20772.70	27341.45	47.386	51.536	2149.123	1857.850
s-CO ₂ /H ₂ S (60/40)	20279.52	22764.62	42.870	43.216	2038.296	1685.415
s-CO ₂ /NH ₃ (81/19)	20045.90	21230.44	40.957	40.276	2236.681	1698.906
s-CO ₂ /SO ₂ (90/10)	21555.17	25091.09	46.520	48.153	2107.748	1786.100

CONCLUSIONS

In this section, it is necessary to highlight that the objectives proposed for this research have been met. The model used for the simulation of s-CO₂ has been validated, and the comparative study of the different mixtures has been successfully carried out. It is concluded that the increase in performance in the Brayton cycle of certain mixtures that raise the temperature of the critical point is directly correlated with the increase in the performance of a PCHE recuperator. All the mixtures studied have shown better global heat transfer coefficients than pure supercritical carbon dioxide, which represents a reduction for the mixtures s-CO₂/COS (70/30), s-CO₂/H₂S (60/40), s-CO₂/NH₃ (81/19) and s-CO₂/SO₂ (90/10) of 12.62%, 0.96%, 2.51%, and 8.36%, respectively in the total heat exchange area. This inference can be extrapolated directly into considerable economic savings for high power ranges, which can be critical in driving research fields related to solar power generation supplemented with supercritical Brayton power cycles. These results yield highly relevant conclusions since they confirm the possibility of continuing Brayton cycles' improvement using PCHE exchangers as regenerators. It is, therefore, a step forward in the investigation of supercritical Brayton cycles, which in the future may represent important advances in the mitigation of greenhouse gas emissions.

Future research lines may be relevant to complete the present study. The need to study mixtures' behavior under different operating ranges (pressure and temperature) is essential to locate possible variability in the device's energy performance. It would also be of interest to analyze the results for variable Reynolds numbers, observing the different mixtures' behavior under these conditions.

On the other hand, an additional analysis for different PCHE geometries would yield parallel research lines of particular interest. Modifications in the diameter of the channels or comparisons between straight channels and zigzag channels, such as those made in the study by Meshram et al. [14] for pure s-CO₂, would provide additional information on the behavior of the different supercritical mixtures in relation to the temperature profile and the pressure drop under these geometries.

NOMENCLATURE

CFD:	Computational Fluid Dynamics
CHE:	Compact Heat Exchanger
COS:	Carbonyl Sulfide
CSP:	Concentrated Solar Power
H ₂ S:	Hydrogen Sulfide
NH ₃ :	Ammonia
NIST:	National Institute of Standards and Technology
PCHE:	Printed Circuit Heat Exchanger
RANS:	Reynolds-averaged Navier–Stokes
REFPROP:	Reference Fluid Properties
SO ₂ :	Sulfur Dioxide
s-CO ₂ :	Supercritical Carbon Dioxide
SCSP:	Supercritical Concentrated Solar Power Plant

ACKNOWLEDGEMENTS

This work has been supported by the Industrial Doctorates program of the Community of Madrid (IND2018/IND-9952).

REFERENCES

- [1] Mecheri, M., & Le Moullec, Y. (2016). Supercritical CO₂ Brayton cycles for coal-fired power plants. *Energy*, 103, 758-771. Pumps. Japan, Tokyo.
- [2] Manente, G., & Lazzaretto, A. (2014). Innovative biomass to power conversion systems based on cascaded supercritical CO₂ Brayton cycles. *Biomass and Bioenergy*, 69, 155-168.
- [3] Qi, H., Gui, N., Yang, X., Tu, J., & Jiang, S. (2018). The application of supercritical CO₂ in nuclear engineering: A review. *The Journal of Computational Multiphase Flows*, 10(4), 149-158.
- [4] Zhu, H. H., Wang, K., & He, Y. L. (2017). Thermodynamic analysis and comparison for different direct-heated supercritical CO₂ Brayton cycles integrated into a solar thermal power tower system. *Energy*, 140, 144-157.
- [5] Ngo, T. L., Kato, Y., Nikitin, K., & Ishizuka, T. (2007). Heat transfer and pressure drop correlations of microchannel heat exchangers with S-shaped and zigzag fins for carbon dioxide

cycles. *Experimental Thermal and Fluid Science*, 32(2), 560-570.

[6] Tsuzuki, N., Kato, Y., & Ishiduka, T. (2007). High performance printed circuit heat exchanger. *Applied Thermal Engineering*, 27(10), 1702-1707.

[7] Kim, S. G., Lee, Y., Ahn, Y., & Lee, J. I. (2016). CFD aided approach to design printed circuit heat exchangers for supercritical CO₂ Brayton cycle applications. *Annals of Nuclear Energy*, 92, 175-185.

[8] Kar, S. P. (2007). *CFD analysis of printed circuit heat exchanger* (Doctoral dissertation).

[9] Jeong, W. S., Lee, J. I., & Jeong, Y. H. (2011). Potential improvements of supercritical recompression CO₂ Brayton cycle by mixing other gases for the power conversion system of an SFR. *Nuclear Engineering and Design*, 241(6), 2128-2137.

[10] Valencia-Chapi, R., Coco-Enríquez, L., & Muñoz-Antón, J. (2020). Supercritical CO₂ Mixtures for Advanced Brayton Power Cycles in Line-Focusing Solar Power Plants. *Applied Sciences*, 10(1), 55.

[11] Enriquez, L. C. (2017). *Nueva generación de centrales termosolares con colectores solares lineales acoplados a ciclos supercríticos de potencia* (Doctoral dissertation, Universidad Politécnica de Madrid).

[12] Dyreby, J. J. (2014). *Modeling the supercritical carbon dioxide Brayton cycle with recompression* (Doctoral dissertation, The University of Wisconsin-Madison).

[13] Lemmon, E.W.; Bell, I.H.; Huber, M.L.; McLinden, M.O. NIST Standard Reference Database 23: Reference Fluid Thermodynamic and Transport Properties-REFPROP; version 10.0; Natl Inst Stand Technol Stand Ref Data Program: Gaithersbg, MD, USA, 2018.

[14] Meshram, A., Jaiswal, A. K., Khivsara, S. D., Ortega, J. D., Ho, C., Bapat, R., & Dutta, P. (2016). Modeling and analysis of a printed circuit heat exchanger for supercritical CO₂ power cycle applications. *Applied Thermal Engineering*, 109, 861-870.

[16] Augnier, R. H. (1995). A Fast, Accurate Real Gas Equation of State for Fluid Dynamics Analysis Applications. *Journal of Fluids Engineering*, 117, 277-281.

[17] ANSYS FLUENT 12.0/12.1 Documentation. 8.16.1 The Aungier-Redlich-Kwong Model.

[18] Salim, S. M., & Cheah, S. (2009). Wall Y strategy for dealing with wall-bounded turbulent flows. In *Proceedings of the international multiconference of engineers and computer scientists* (Vol. 2, pp. 2165-2170).

[19] Simscale (Mayo, 2018). What is y+ (yplus)?

ANNEX A

MODEL VALIDATION

The real gas model used in this phase of the study has been the NIST model, in which the REFPROP database is coupled to the Ansys Fluent finite volume analysis software. In Fig. 12, this study's results for the variables studied in this validation phase are shown. However, the validation will be limited to analyzing both the temperature profile and the pressure drop of the straight channel exchanger for the lowest temperature range (400K for cold s-CO₂ and 630K for hot s-CO₂).

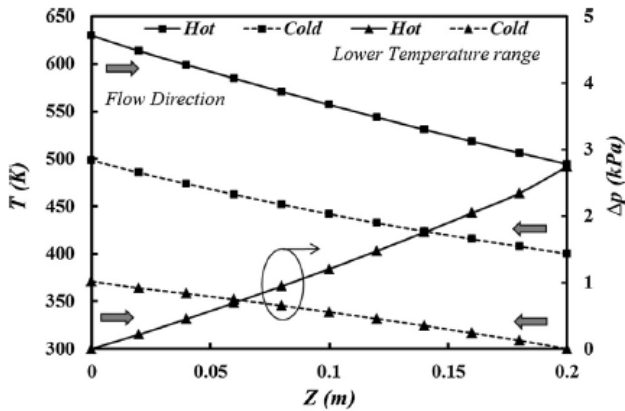


Figure 12: Temperature variation (left ordinate) and pressure drop (right ordinate) of the straight channel along the length for the lowest temperature range in the Meshram study [14].

In Fig. 13-14, comparing the temperature profile and the pressure drop obtained in the simulation with the reference study results are shown. As can be seen, the values obtained in the temperature profile simulation are very close to the reference values, the largest deviation being 2.35% in the case of hot fluid and 2% in the cold fluid. Also, in the case of pressure drop, the values obtained in the simulation are close to the reference values. Although the cold flow error seems high (maximum 16.3%), this is due to a low resolution of the simulation data. This behavior is expected to the tall order of magnitude of the pressure (22.5 MPa). However, for the hot flow, as the pressure is lower (9 MPa), more accurate results have been obtained, so the error, in this case, is closer to reality; the maximum error is 6.7%.

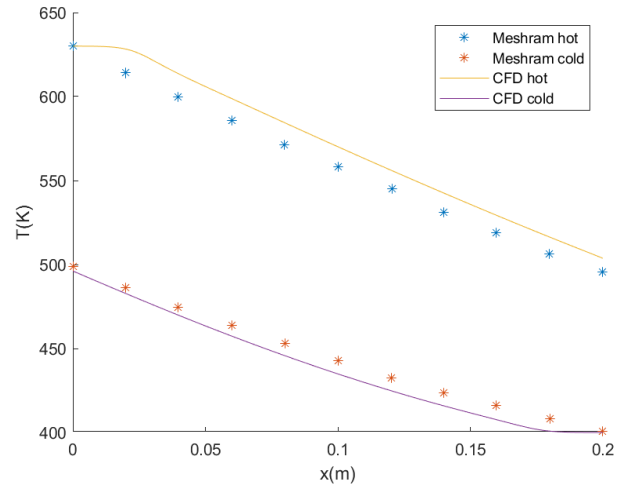


Figure 13: Comparison between reference temperature values and the values obtained in the simulation.

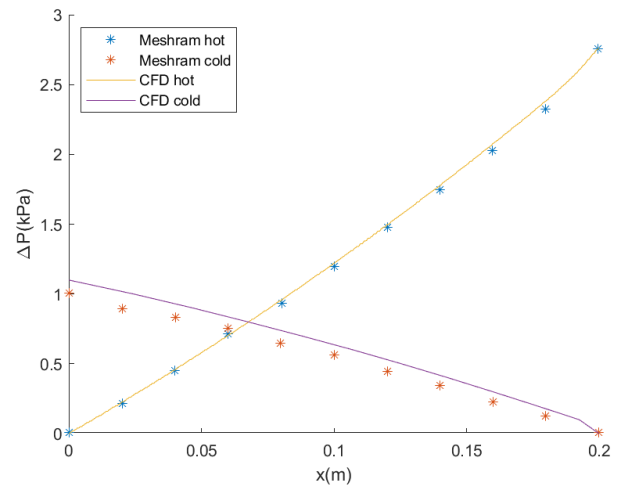


Figure 14: Comparison between reference pressure drop values and the values obtained in the simulation.

In this way, the model to be used is validated thanks to the comparative analysis carried out with the Meshram study [14].

ADVANCED THERMODYNAMIC POWER CYCLES UTILIZING CARBON DIOXIDE BASED MIXTURES AS WORKING FLUIDS FOR HIGH TEMPERATURE WASTE HEAT RECOVERY

Abubakr Ayub*
Universita Degli Studi Di
Brescia
Brescia, Italy
Email: a.ayub@unibs.it

**Gioele Di
Marcoberardino**
Universita Degli Studi Di
Brescia
Brescia, Italy

Costante M. Invernizzi
Universita Degli Studi Di
Brescia
Brescia, Italy

Paolo Iora
Universita Degli Studi Di
Brescia
Brescia, Italy

ABSTRACT

This paper proposed CO₂ mixtures as working fluids in closed Brayton power cycles using flue gases at relatively high temperature (400-450 °C) as waste heat source. Firstly, a comprehensive selection criterion is defined for choice of working fluids to be employed as additives in CO₂ mixtures. Secondly, the thermodynamic properties of the mixtures are calculated at different molar compositions using an appropriate equation of state. The binary interaction parameters involved in the equation of state are obtained with the help of available experimental VLE data or by estimation method in case of non-availability of the VLE data. As a benchmark, the study also investigates the thermodynamic performance of advanced sCO₂ cycle layouts to compare with the performance of cycles operating with CO₂ mixtures. Sensitivity analysis reveals that the power cycles operating with CO₂-Novec5110 mixture (with 0.2 mole fraction of Novec fluids) show 3 percentage points rise in cycle thermodynamic efficiency (0.219 versus 0.252) with lower cycle operating pressures as compared to recuperative with mass split sCO₂ cycle. In case of CO₂-R134a mixture working fluid (with 0.3 mole fraction of R134a), total efficiency of about 0.15 is obtained at cycle maximum pressure of 200 bars compared to simple recuperative sCO₂ cycle with total efficiency of 0.13 at rather higher maximum pressure of 400 bars.

INTRODUCTION

One of the possible ways of energy recovery from industrial waste heat is to use highly efficient thermal power thermodynamic engines. Organic Rankine Cycles (ORCs) and Steam Cycles are two prominent power cycles commercialized in last years for waste heat recovery[1]. In recent years, supercritical carbon dioxide (sCO₂) cycles are also investigated for vast range of waste heat sources from medium to high temperatures. sCO₂ cycles offer lower compression work due to higher density near critical point and compact turbomachinery.

Numerous studies analyzed thermodynamic performance of different sCO₂ cycle layouts namely partial heating cycle, dual recuperated cycle, precompression cycle, single-recuperated with dual expansion cycle and some novel cycle layouts [2], [3]. The main intend of these studies are: (i) to gain knowledge about contribution of different processes (intercooling, reheating, recompression and/or mass split) on total efficiency of the power cycle, and (ii) to select the best possible cycle layout in terms of power output, heat recovery and size footprint. In essence, the studies found that higher heat recovery effectiveness of sCO₂ power cycle comes with lower cycle thermodynamic efficiency. Moreover, sCO₂ cycle layouts which presented higher heat recovery effectiveness have higher maximum operating pressures and they are comprised of larger cycle components with complex operational scheme, for example Dual flow split with dual expansion cycle.

To mitigate this drawback, this study proposed novel carbon dioxide mixtures as working fluid in waste heat recovery power cycles. The use of CO₂ mixtures to alter the properties of CO₂ and to achieve higher cycle efficiency is recently explored by some research works [4], [5]. Here in this paper, we explored possibility of CO₂ based mixtures as working fluid in waste heat recovery power cycles to address following main challenges:

(i) to improve the heat recovery effectiveness of CO₂ power cycle, (ii) to reduce cycle maximum operating pressures in order to avoid mechanical stresses in cycle components and, (iii) to keep power cycle layout simpler.

SELECTION AND CHARACTERIZATION

The choice of appropriate additive (or dopant) for CO₂ mixtures is challenging since it depends on the heat source application, required thermodynamic properties, health and safety characteristics of working fluids. Particularly for heat recovery application, the required additive should possess following characteristics:

* corresponding author(s)

Table 1: Main physical properties of new refrigerants selected for CO₂ mixtures. Physical properties for Novec fluids are taken from [6].

Working fluid	T_{cr} (°C)	P_{cr} (bars)	Boiling point (°C)	Molecular weight	Molecular Complexity [7]	Acentric factor ω	Thermal stability
CO ₂	31.06	73.83	-78.45	44.0098	-9.340	0.223621	>700 °C
R134a	101.03	40.56	-25.92	102.031	-2.429	0.326878	350 to 370 °C
Novec 5110	146	21.44	26.5	266.04	17.145	0.429196	200-300°C
Novec 649	168.66	18.69	49.05	316.046	28.165	0.471	
HFO1234yf	94.7	33.82	-28.85	114.042	-1.017	0.282037	
HFO1234ze(E)	109.36	36.62	-18.17	114.042	0.046	0.32376	

Table 2: Safety and environmental impact characteristics of new refrigerants selected for CO₂ mixtures [8], [9].

Working fluid	ODP [10]	GWP in 100 years [10], [11]	Flammability [12]	Health [12]	Instability [12]
CO ₂	0	1	0	2	0
R134a	0	1370	0	1	1
Novec 5110	0	1	1	3	0
Novec 649	0	1	0	3	1
HFO1234yf	0	< 4.4	4	2	0
HFO1234ze(E)	0	6	n.a.	n.a.	n.a.

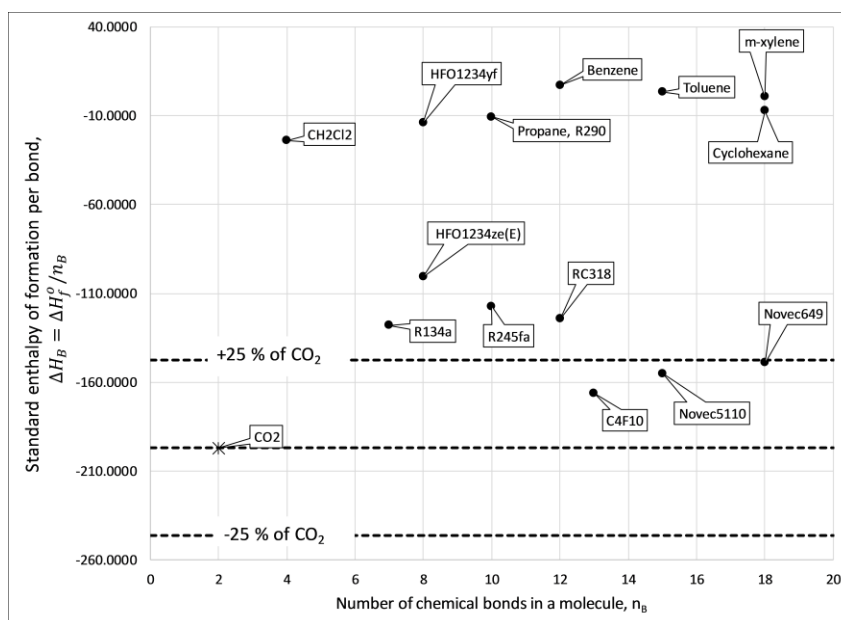


Figure 1: Standard enthalpy of formation per bond of some working fluids with respect to number of bonds in a molecule. Value of Novec5110 is taken from 3M™ producers. For Novec649, value is estimated using JOBACK group contribution method. Values of remaining fluids are taken from NIST and ASPEN databank. CO₂ is considered as reference fluid for comparison owing to its well established higher chemical stability.

1. Critical temperature (T_{cr}) higher than T_{cr} of CO₂ to enable condensation which possibly reduces the compression work in the power cycle
2. Moderate value of critical pressure (P_{cr}) to maintain operating pressures in the power cycle within allowable range suggested by mechanical design of cycle components.
3. Thermally stable at higher temperature i.e. thermal stability < 400°C is adequate for heat recovery from flue gases at 450°C.
4. Lower value of parameter of molecular complexity (value close to 0) is preferable to obtain larger expansion in turbine or to obtain more cooling of working fluid at turbine outlet while also avoiding the subcritical conditions.

5. Higher molecular weight which is beneficial in terms of lower turbine stages.
6. Lower ozone depletion potential (ODP) and global warming potential (GWP), nontoxic and non-flammable.

Practically, it is quite difficult to find a dopant which meet all the above mentioned criteria. However, criteria numbers 1 and 2 regarding P_{cr} and T_{cr} and criteria number 6 regarding environmental aspect of working fluid are considered foremost priority during screening of different chemical compounds available in literature. **Table 1** shows the main thermodynamic properties of potential candidate compounds which are selected as additive for CO₂ mixtures. The environmental and safety parameters of these compounds are shown in **Table 2**.

Novec 5110 (1,1,1,3,4,4,4-Heptafluoro-3-(trifluoromethyl)-2-butanone) and Novec 649 (1,1,1,2,2,4,5,5,5-nonafluoro-4-(trifluoromethyl)-3-pentanone) belongs to chemical family of fluorinated ketones. Empirical formulas of Novec 649 and Novec 5110 are C₆F₁₂O and C₅F₁₂O respectively. They are engineered fluid with environmentally friendly properties (ODP=0, GWP =1), especially produced by 3MTM to substitute high GWP working fluids like SF₆ and hydrofluorocarbons (HFCs). Novec fluids are stable till 300°C in the absence of water according to 3MTM producers [8]. However, further investigations on thermal stability at temperatures greater than 300 °C are necessary to enable their use in high temperature power cycle applications. In recent studies, Novec 649 is also used as working fluid in Organic Rankine Cycles.

HFO1234yf and HFO1234ze(E) are also environmentally friendly refrigerants belongs to chemical family of hydrofluoroethers. The maximum allowable operating temperature for these refrigerants suggested by thermal stability tests are 200 to 250 °C [13], [14]. R134a is also a good candidate fluid as an additive owing to its large use as working fluid in ORCs despite having larger GWP. The maximum allowable operating temperature of R134a is 350-370°C as per the experimental thermal stability tests [15].

For preliminary evaluation of thermochemical stability of some new additive fluids, the standard enthalpy of formation per bond (ΔH_B) is determined. The more negative value of standard enthalpy of formation (ΔH_f°) implies more stable compound. However, it is not wise to generalize all compounds with negative value of enthalpy of formation as stable compounds. For example, Benzene with positive value of enthalpy of formation (+48.7 KJ/mol) is well known as stable liquid. Therefore, a more in depth information about thermodynamic and chemical stability of a compound can be acquired using the knowledge of path of reaction followed and activation energy of a reaction. Anyways, ΔH_f° can be a useful parameter for first indication about thermochemical stability of any compound and can also be useful in classification of additives.

Figure 1 shows the parameter ($\Delta H_B = \Delta H_f^\circ/n_B$) with respect to number of chemical bonds in the molecule of additive fluid. CO₂ is considered as reference fluid for comparison owing to its well established higher chemical stability.

After selection of appropriate additive with desirable thermodynamic and environmental properties for CO₂ binary mixtures, the subsequent step is to analyze the fluid behavior of CO₂ mixture at different molar composition. This requires an accurate thermodynamic method: activity coefficient method or equation of state method depending on the range of temperatures and pressure in which the properties are needed. In this study, cubic Peng Robinson equation of state (PR-EoS) with van der Waals mixing rules is selected because of its applicability both at low pressures and higher pressures greater than critical point. Different modifications to PR-EoS and mixing rules are applied in recent research works to enhance the accuracy and applicability of EoS for polar and non-polar compounds.

Firstly, the calculation method requires pure fluid physical properties i.e. T_c , P_c , acentric factor (ω) and gas constant (R). These fluid properties for both CO₂ and the additive compound are available as reported in **Table 1**. Secondly, considering van der Waals mixing rule formulation for a binary mixture, one binary interaction parameter ($k_{i,j}$) is also needed to determine interaction coefficient $a_{i,j}$ as shown,

$$a_{i,j} = \sqrt{a_i a_j} (1 - k_{i,j}) \quad \text{Eq. 1}$$

Where, a_i and a_j are pure component parameters.

The accurate value of $k_{i,j}$ can be computed using regression analysis with available experimental or pseudo-experimental vapor-Liquid equilibrium (VLE) data. Once $k_{i,j}$ is determined, the PR-EoS is used to calculate pressure-temperature envelop at different mixture composition, densities, enthalpies and entropies at different isobars from subcritical to supercritical phases. All the thermodynamic properties calculations for pure fluids and CO₂ mixtures are carried out in Aspen Plus V10 simulation software [16].

It is also important to compute critical points CO₂ mixtures at different molar compositions and validate the results with available experimental critical point data (which mostly is not available for all CO₂ mixtures). In general, for a binary mixture, the critical temperature and pressure do not correspond to the maximum values on the saturation curve. Therefore, a numerical code is developed to calculate the actual critical point of binary mixtures. The algorithm of critical point code is based on the equations developed in ref [17], is programmed and executed in MATLAB version R2019a with the help of INTLAB toolbox [18]. The efficient root finding capability of INTLAB is exploited to solve the non-linear system of equations of critical point. The code requires pure component critical points, molar composition of each component, acentric factors and binary interaction parameter ($k_{i,j}$) corresponding to considered equation of state as input information to compute the critical points of a binary mixture. In addition, the initial interval which contains the minimum and maximum range in which the root can occur is also required. The code is capable to compute both stable and metastable critical points at given composition of any binary mixture without the need of initial guesses. More description on characterization of pure and mixture working fluids used in power plant application are given in ref [19].

For CO₂-Novec649 mixture, **Figure 2** shows the VLE at 40 °C and 50 °C calculated using PR-EoS with regressed $k_{1,2}$, the scatter points represents experimental VLE data. The pressure-temperature envelop and critical points locus at different mixture composition for CO₂-Novec649 mixture are shown in **Figure 3**. Same procedure is followed to compute VLE and P-T envelop for CO₂-134a, CO₂-R1234yf and CO₂-R1234ze(E) mixtures. The regressed values of $k_{1,2}$ for CO₂ mixtures considered in this study are reported in **Table 3**.

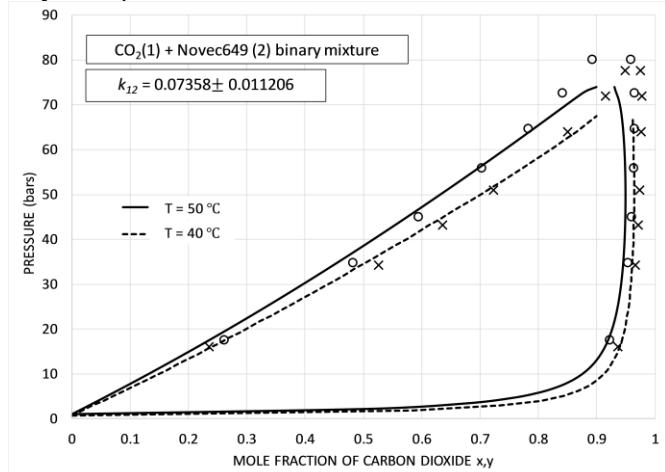


Figure 2: Vapor-Liquid equilibrium at two temperatures for CO₂-Novec649 mixture. Scatter points show experimental data [20]. Solid lines show computation using PR-EoS with regressed $k_{1,2}$.

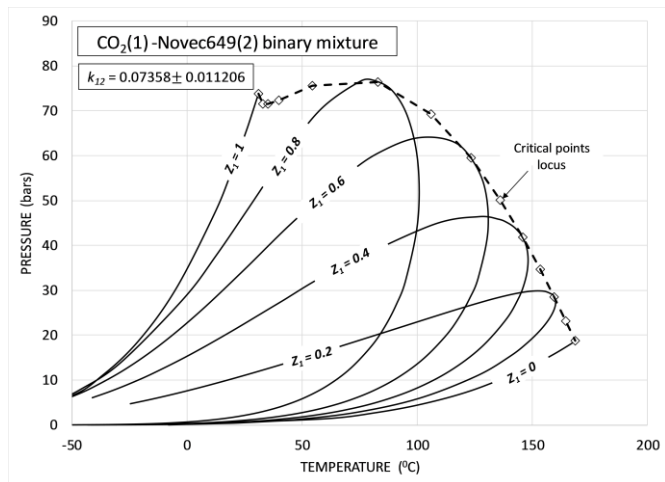


Figure 3: P-T envelop and vapor-liquid critical points of CO₂-Novec649 mixture at different molar composition.

In calculation of thermodynamic properties of CO₂ mixtures, there are instances when the experimental VLE data for a particular CO₂ binary mixture are not available for computation of interaction parameter $k_{1,2}$. For such cases, a correlation between $a_{1,2}$ and a_2 is developed by regressing the available data of 19 CO₂ mixtures (for example, CO₂-ethane, CO₂-H₂S, CO₂-propane etc.). Consequently, the correlation provide the

estimated value of $a_{1,2}$ to insert into Eq.1 and determine value of $k_{1,2}$. More details on this approach and regression model are given in ref [21]. Meanwhile, in this study, we used this developed correlation to compute $k_{1,2}$ of CO₂-Novec5110 mixture since the experimental VLE data is not present in literature for this mixture. The estimated value is,

$$k_{1,2} = 0.0699654 \pm 0.062841$$

Thus, with estimated $k_{1,2}$, PT envelop and critical points at different molar composition are calculated as shown in **Figure 4** for CO₂-Novec5110 mixture.

Table 3: Binary interaction parameters ($k_{1,2}$) required in van der Waals mixing rules for considered CO₂ mixtures.

CO ₂ mixture	$k_{1,2}$	Standard deviation	Source of experimental VLE data
CO ₂ -R134a	0.0166	0.00824	[22], [23]
CO ₂ -Novec649	0.07358	0.01120	[20]
CO ₂ -R1234yf	0.03943	0.00444	[24]
CO ₂ -R1234ze(E)	0.015631	0.00522	[25]

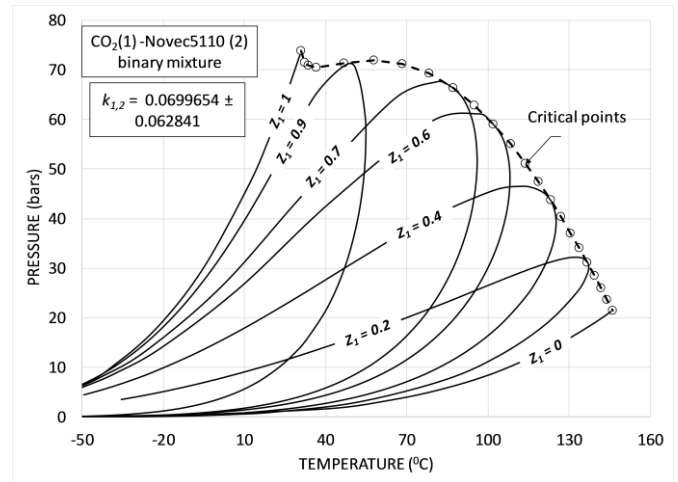


Figure 4: P-T envelop and vapor-liquid critical points of CO₂-Novec5110 mixture at different molar composition.

PURE CO₂ THERMODYNAMIC POWER CYCLES

This section discusses the thermodynamic analysis of supercritical carbon dioxide (sCO₂) power cycles exploiting flue gases at T=450°C as heat source. The characteristics of heat source and main operating parameters for cycle design point analysis are shown in **Table 4**. Different cycle layouts are studied in literature to enhance the heat recovery effectiveness of sCO₂ cycles [26]. However, in this paper, three cycle layouts are selected which are representative of both traditional and novel cycle layouts practiced in literature. Thermodynamic performance of the power cycles is evaluated using thermodynamic cycle efficiency ($\eta_{th} = \dot{W}_{net}/\dot{Q}_{in}$) and total efficiency ($\eta_{tt} = \dot{W}_{net}/\dot{Q}_{available}$) parameters.

Table 4: Operating parameters and common assumptions for thermodynamic simulation of power cycles.

Parameter	Value
P_{min} or P_1 (bars)	100
Pressure ratio (P_R)	1.5 to 6
T_{min} (°C)	35
$T_{exh, in}$ (°C)	450
\dot{m}_{exh} (kg/s)	100
Flue gases (percentage molar composition)[21]	28% CO ₂ , 58% N ₂ , 3% O ₂ , 11% H ₂ O
MITAPHE (°C)	50
MITA _{radiator} , MITA _{recup} (°C)	20
$\eta_{isent,comp}/\eta_{mech,comp}$	0.8 / 0.98
$\eta_{isent,turb}/\eta_{mech,turb}$	0.85/0.95

Simple recuperative power cycle (SRC)

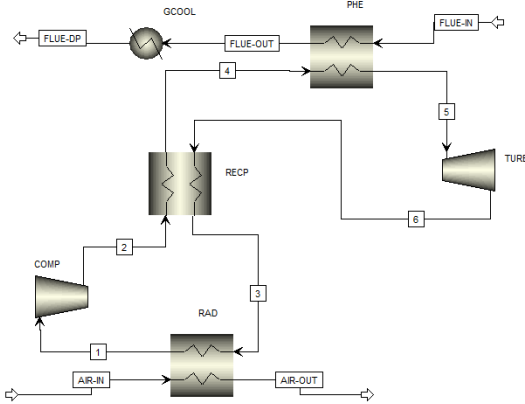


Figure 5: Schematic diagram of simple recuperative sCO₂ cycle layout for heat recovery (SRC).

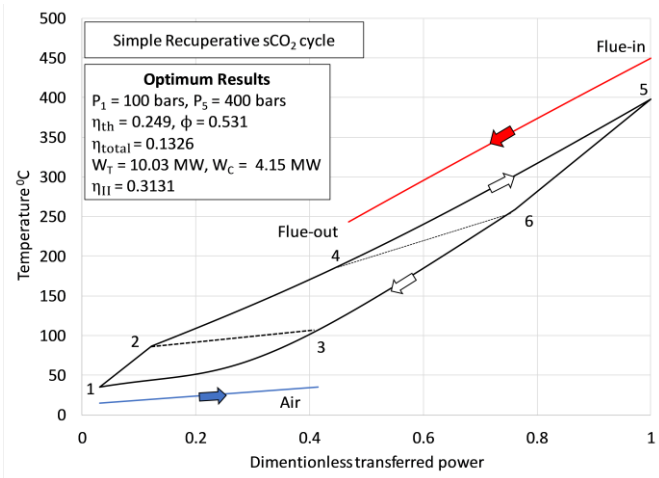


Figure 6: Thermodynamic process diagram and optimum results of simple recuperative sCO₂ cycle on temperature-dimensionless heat transferred plane.

The first reference CO₂ power cycle considered for heat recovery is simple recuperative sCO₂ power cycle as shown in **Figure 5**. The cycle thermodynamic performance is investigated at different minimum pressures (P_{min}), pressure ratio (P_R) and maximum temperature (T_{max}). Based on sensitivity analysis, optimum total efficiency is obtained at $P_{min} = 100$ bars, $T_{max} = 400$ °C and pressure ratio of 4. **Figure 6** demonstrates optimum cycle results in T-Q plane.

Recuperative cycle with mass split (RCS)

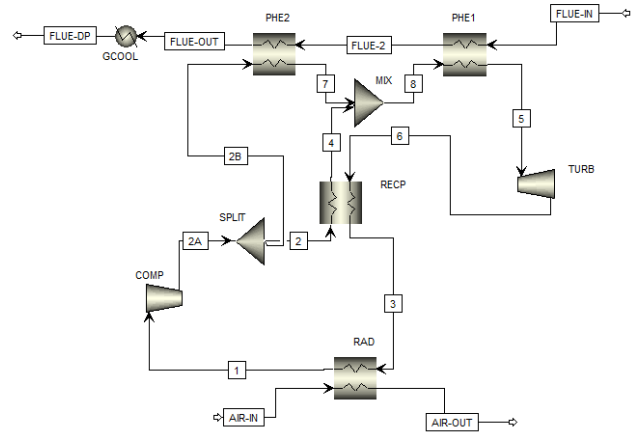


Figure 7: Schematic diagram of recuperative sCO₂ cycle with mass split (RCS).

This cycle scheme consists of mass split (x) and added heat recovery heat exchanger in addition to simple recuperative cycle layout as shown in **Figure 7**.

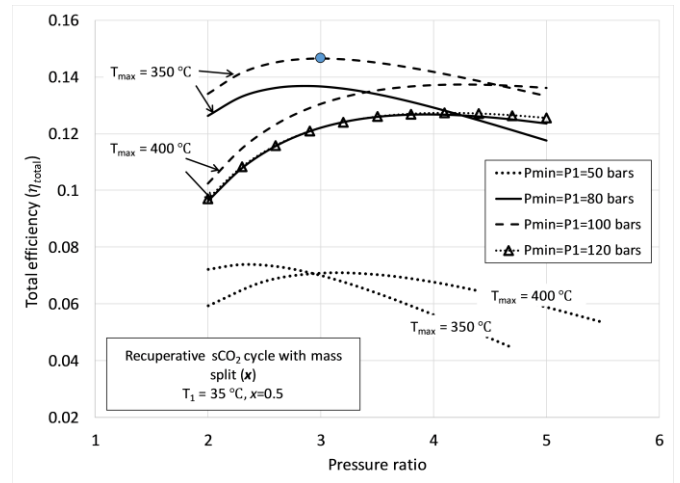


Figure 8: Total efficiency at different minimum cycle pressures and maximum cycle temperatures versus pressure ratio for recuperative cycle with mass split. Blue mark shows the optimum performance point.

Due to split of mass flow rate after compression process; certain CO₂ mass flow towards heat exchanger for heat recovery, remaining go towards recuperator depending on the specified

value of mass split. Two CO₂ streams after heating from heat exchanger and recuperator mix together and then heated in primary heat exchanger to achieve required turbine inlet temperature. The expansion in turbine occurs to minimum cycle pressure, followed by cooling of CO₂ stream in recuperator and through radiator to obtain minimum cycle temperature. The main aim of mass split (x) is to enhance heat recovery potential of the power cycle and to achieve more cooling of the flue gases as discussed previously in literature [26]. Sensitivity analysis is carried out to evaluate the effect of mass split on total efficiency and exergy efficiency of the cycle. The thermodynamic analysis at different cycle minimum pressures, pressure ratios and maximum temperatures is performed to study the effect of these variables and to obtain optimum performance conditions. The underlying idea is to assess the impact of mass split on cycle performance relative to simple recuperative cycle layout.

Keeping $x = 0.5$, **Figure 8** shows the influence of cycle minimum pressure and maximum temperature (or T_5) on total efficiency. The optimum performance is achieved at $P_R = 3$, $P_{min} = 100$ bars and $T_{max} = 350$ °C. At constant P_{min} , the total efficiency at $T_{max} = 350$ °C is better than at $T_{max} = 400$ °C. This is because, at lower value of T_{max} , the temperature at entry of primary heat exchanger reduces, which results in more utilization of heat from flue gases and more cooling of flue gases. Thus, larger cooling of flue gases improves the heat recovery effectiveness, hence total efficiency of the cycle.

At lower value of P_{min} i.e. $P_{min} = 50$ bars, the compression work increases significantly since the compression inlet conditions are far from critical point, this implies reduction in thermal efficiency, as a consequence reduction in the total efficiency of the cycle. At $P_{min} > 100$ bars for example 120 bars, the total efficiency is lower owing to reduction in thermal efficiency of the cycle.

$x=0.3$ is decided as optimum mass split since it results in both higher cycle thermal efficiency and total efficiency. Finally, the cycle optimum results are shown in **Figure 9** on T-Q plane.

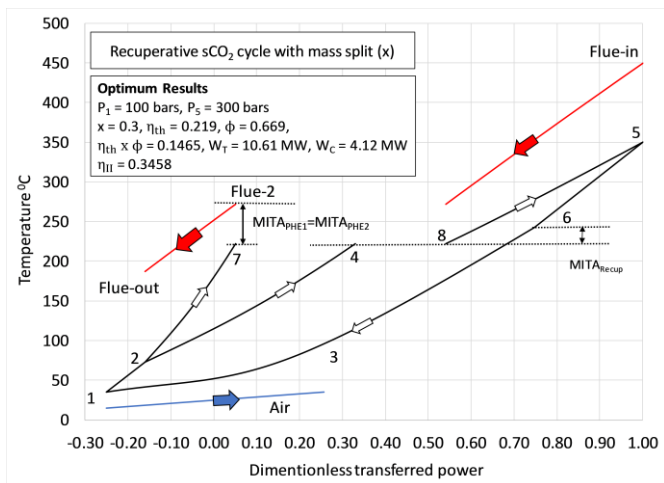


Figure 9: Thermodynamic process diagram and optimum results of recuperative with mass split sCO₂ cycle on temperature-dimensionless heat transferred plane.

Single Flow split dual expansion cycle (SFDE)

The schematic diagram of single flow split dual expansion cycle is shown in **Figure 10**. Cycle components in this configuration are greater due to addition of one low temperature (LT) turbine compared to RCS configuration. CO₂ is compressed in the main compressor and then flow is divided into two streams. One stream is heated in PHE and expanded in high temperature (HT) turbine. While, the other stream is heated in LTR and HTR followed by expansion in the LT turbine. The different mass flow in recuperators balances the heat capacities between hot and cold streams inside the recuperators in order to achieve better thermal match.

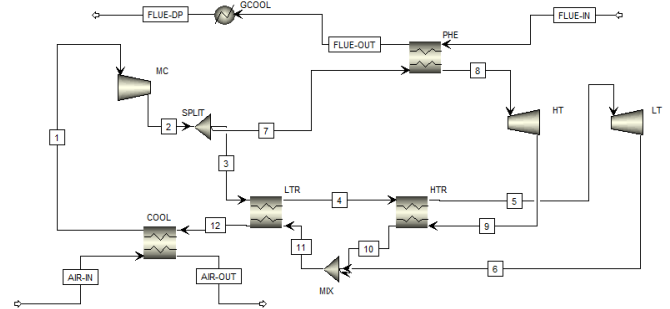


Figure 10: Schematic diagram of single flow split dual expansion cycle

As in the analysis of previous cycle configurations, the performance study of SFDE cycle also involves the sensitivity of cycle efficiency, heat recovery effectiveness and total efficiency at different T_{max} , P_R and P_{min} . However, the role of mass split in SFDE configuration is to enhance the turbine inlet temperature in LT turbine to improve the cycle efficiency. Besides, it is also essential to achieve same temperatures at mixer inlet (i.e. $T_6 \approx T_{10}$) to reduce mixing losses and in turn maintain higher cycle efficiency. On the other side, the temperature at the inlet of PHE (T_7) depends on the compressor outlet temperature, in other words, the pressure ratio (P_R).

In cycle thermodynamic calculations, optimum mass split x is calculated at which the cycle efficiency and total efficiency are higher. In addition, optimum point is also decided considering the sensitivity of total efficiency at different compressor inlet pressure (P_{min}). To ensure the accuracy of cycle thermodynamic model, cycle calculations are carried out at same conditions as given by Manente *et al* [27] and the results are compared. Validation of results shows that optimum mass split, cycle efficiency and total efficiency calculated using present approach are the same as computed by Manente *et al*.

The influence of different compressor inlet pressure (P_{min}) and T_{max} on total efficiency are presented in **Figure 11**. Maximum total efficiency is obtained at $T_{max} = 400$ °C, $P_{min} = 100$ bars and P_R of 2.9. Total efficiency is smaller at both P_{min} of 120 bars and 80 bars. At $P_{min} = 80$ bars, the temperature at entry of PHE (i.e. T_7) enhances which bring about reduction in heat recovery effectiveness. Whereas in case of $P_{min} = 120$ bars, there is very slight improvement in heat recovery effectiveness due to T_7 as

compared to $P_{\min} = 100$ bars, so the decrease in total efficiency in this situation is more attributed to lower cycle efficiency. **Figure 12** illustrates the optimum results on T-Q plane.

The efficiency losses in total efficiency ($\Delta\eta_{total}$) and resulting exergy efficiency at optimum conditions for SRC, RCS and SFDE cycles are recorded in **Table 5**. SRC shows higher η_{th} , however, it is not proven to be effective in heat extraction from flue gases. The total efficiency and exergy efficiency of RCS are higher with lower pressure ratio compared to SRC.

Thus, the introduction of mass split and addition of another heat exchanger (i.e. PHE2) results in higher thermodynamic quality of the RCS compared to SRC. Relative to SRC, there is 10.56 % and 16.29% improvement in total efficiency for RCS and SFDE cycles respectively. SFDE cycle tends to enhance heat recovery effectiveness and shows better exergy efficiency, however, the improvement is not justifiable in comparison to layout complexity of the power cycle.

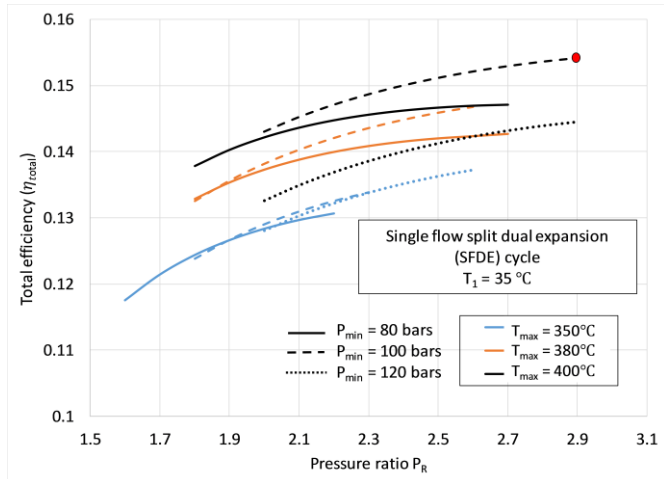


Figure 11: Simultaneous effect of cycle minimum pressure and maximum temperature on total efficiency of SFDE cycle. Red mark shows the optimum performance point.

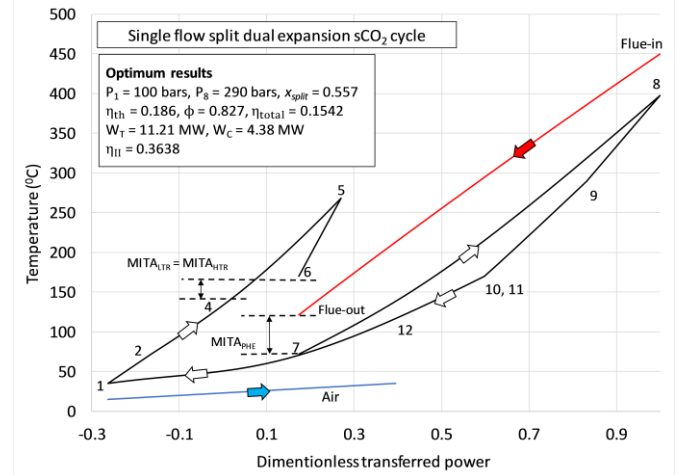


Figure 12: Thermodynamic process diagram and optimum results of single flow split dual expansion sCO₂ cycle on temperature-dimensionless heat transferred plane.

CO₂ MIXTURES WORKING FLUIDS IN THERMODYNAMIC POWER CYCLES

It clearly appears from thermodynamic analysis of pure CO₂ cycles that the gain in total efficiency can only be achieved by introducing mass split to obtain cascade heating and by dual expansion to enhance power output. Both cascading and dual expansion processes increase the components of power cycle and make operational scheme difficult in terms of size and cost of the power cycle. To cope with this problem, this study attempted to design CO₂-based binary mixtures as working fluids in simple recuperative cycle layout.

This section deals with thermodynamic performance of cycles operating with CO₂-Novec649 and CO₂-Novec5110 mixture as working fluids. The thermodynamic properties are calculated using PR-EoS as explained in the section 2. The cycles in case of CO₂ mixtures are transcritical cycles with pump inlet pressure (P_1) at bubble point corresponding to inlet temperature. As the molar composition of mixture changes, the pump inlet pressure also changes. Moreover, other design conditions and common assumptions are the same as given in **Table 4**.

Table 5: Summary of efficiency losses, total efficiency and exergy efficiency of three supercritical pure CO₂ heat recovery power cycles at optimum conditions.

Power cycles	T_{\max} (°C)	P_R	$\dot{Q}_{available}$ (kW)	\dot{W}_{max} (kW)	η_{ideal}	$\Delta\eta_{total}$	\dot{W}_{net} (kW)	η_{th}	ϕ	η_{total}	Exergy efficiency $\eta_{II} = \frac{\eta_{total}}{\eta_{ideal}}$
SRC	400	4	44279	18764	0.423	0.277	5873	0.249	0.532	0.132	0.313
RCS	350	3	44279	18764	0.423	0.262	6487	0.219	0.669	0.146	0.345
SFDE	400	2.9	44279	18764	0.423	0.254	6826	0.186	0.827	0.154	0.363

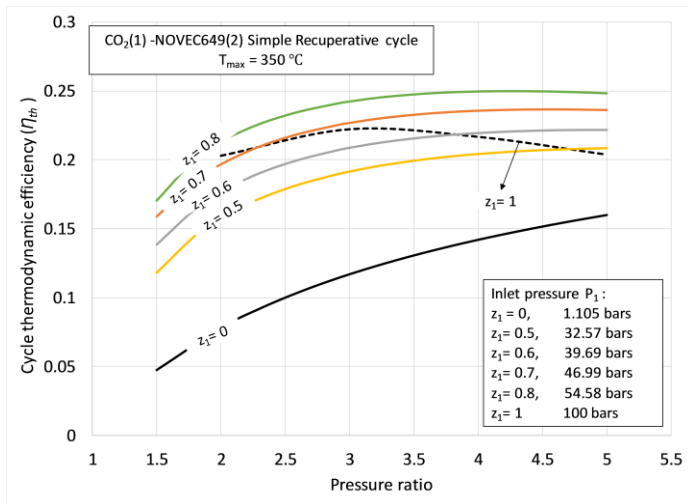


Figure 13: Influence of different mixture molar composition and cycle pressure ratio on cycle thermodynamic efficiency with CO₂-C₆F₁₂O (Novec 649) mixture working fluid.

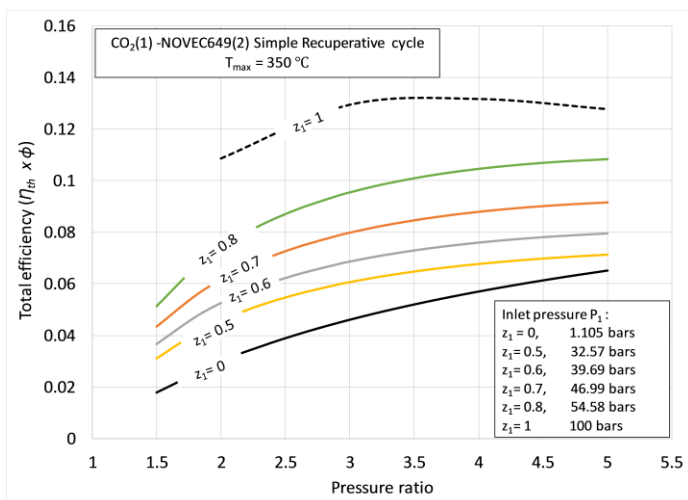


Figure 14: Influence of different mixture molar composition and cycle pressure ratio on total efficiency with CO₂-C₆F₁₂O (Novec 649) mixture working fluid.

Figure 13 and Figure 14 shows cycle efficiency and total efficiency respectively for CO₂-Novec649 mixture. Results shows that total efficiency of CO₂-Novec649 mixture remains lower than pure CO₂ cycle at all pressure ratios and mixture molar compositions. Increase in amount of CO₂ in the mixture brings about increase in total efficiency. On the other hand, thermodynamic cycle efficiency is greater than pure CO₂ at molar composition greater than 0.6 and pressure ratios higher than 3. Similar trend of cycle efficiency and total efficiency can be observed in case of CO₂-Novec5110 binary mixture as shown in Figure 15 and 16 respectively.

The main reason of lower total efficiency is higher molecular complexity of Novac fluids (see Table 1). The higher molecular complexity produces higher temperature at turbine outlet which

results in larger recuperator and higher temperature at inlet of PHE. Consequently, higher temperature at inlet of PHE reduces the heat recovery capability of power cycle, results in reduction of heat recovery effectiveness and total efficiency. Instead, the cycle thermodynamic efficiency in case of CO₂-Novac mixtures is higher since heat addition is occurring at higher temperature.

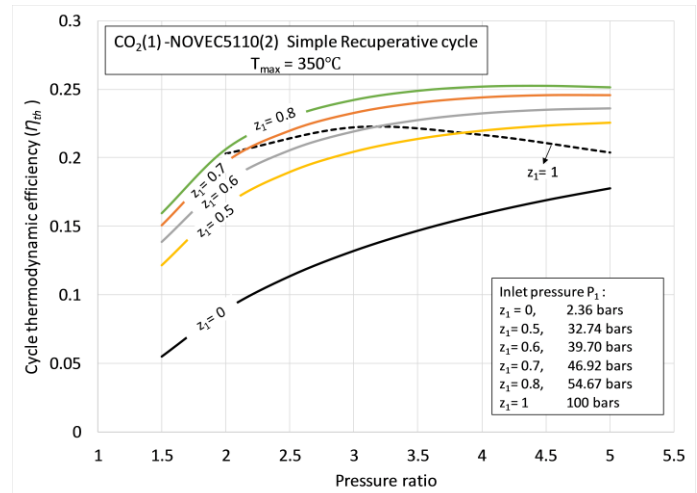


Figure 15: Influence of different mixture molar composition and cycle pressure ratio on cycle thermodynamic efficiency with CO₂-C₅F₁₀O (Novac5110) mixture working fluid.

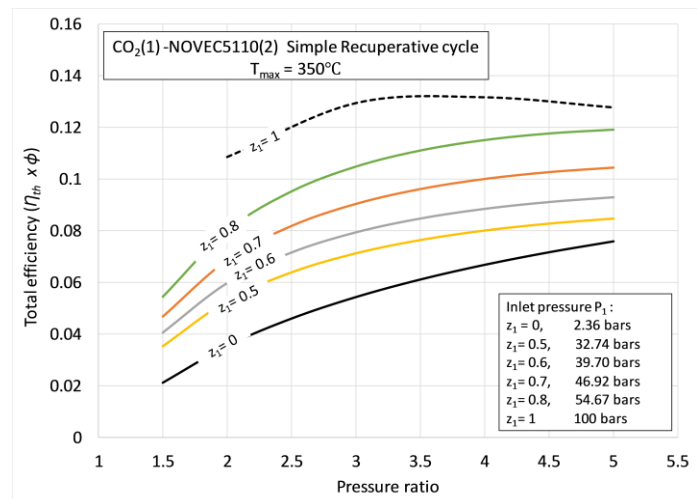


Figure 16: Influence of different mixture molar composition and cycle pressure ratio on total efficiency CO₂-C₅F₁₀O (Novac 5110) mixture working fluid.

Table 6 presents the thermodynamic results of some CO₂ mixtures power cycles in comparison with supercritical CO₂ power cycles. Comparison shows that CO₂-Novac mixtures working fluids with 20% amount (molar composition) of Novac fluid show comparable cycle thermodynamic efficiency compared to sCO₂ simple recuperative cycle (i.e. 0.249 versus 0.252) and 3 percentage points higher cycle thermodynamic efficiency compared to recuperative with mass split cycle (i.e.

0.219 versus 0.252). Whereas, around 2 percentage points lower total efficiency (i.e. 0.132 versus 0.117) is achieved which is the manifestation of higher molecular complexity of Novec fluids, as a consequence, lower power is produced.

The power cycle analysis for CO₂-R134a binary mixture at different mixture composition is also carried out and results are published in a recent research article [21]. For comparison of main outcome, Table 6 also shows the results of CO₂-R134a working fluid mixture with 30% molar composition of R134a operating in simple recuperative cycle. Results indicates that comparable total efficiency and cycle thermodynamic efficiency with lower maximum operating pressures are obtained compared to sCO₂ cycles.

Table 6: Comparison of promising thermodynamic cycle results for supercritical CO₂ and transcritical CO₂ mixtures power cycles.

Working fluid	η_{total}	η_{th}	\dot{W}_{net} (kW)	P_{max} (bars)	P_{min} (bars)
sCO ₂ (Simple recuperative cycle)	0.132	0.249	5873	400	100
sCO ₂ (Recuperative cycle with mass split)	0.146	0.219	6464	300	100
CO ₂ (0.8)- Novec649 (0.2)	0.108	0.248	4782	273	54.58
CO ₂ (0.8)- Novec5110 (0.2)	0.117	0.252	5180	246	54.67
CO ₂ (0.7)- R134a (0.3)	0.147	0.248	6509	200	24.54

CONCLUSION

This work proposed novel CO₂ based mixtures as working fluids for high temperature waste heat recovery closed Brayton sCO₂ power cycles. The goal is enhancing heat recovery effectiveness and total efficiency of sCO₂ power cycles keeping simple cycle layout and using novel CO₂ mixtures rather than pure CO₂ as working fluid. Firstly, selection criteria for choice of adequate additive in CO₂ mixtures is defined in which both thermodynamic and environmental characteristics are taken into account. Five refrigerants with lower ODP, lower GWP and favorable thermodynamic properties are selected as additives in CO₂ mixtures.

Peng-Robinson equation of state with van der Waals mixing rules is selected for computation of thermodynamic properties and critical points of CO₂ mixtures at different mixture molar composition. The binary interaction parameter ($k_{1,2}$) is estimated using regression with available experimental VLE data or by using already developed correlation in case of non-availability of experimental VLE data. Thermodynamic analysis of three promising sCO₂ cycle layouts are carried out in order to select best possible layout as benchmark to compare performance with CO₂ mixtures power cycles. An improvement of 10% and 16% in total efficiency is obtained for recuperative cycle with mass split (RCS) and single flow split dual expansion cycle (SFDE)

respectively compared to simple recuperative cycle (RCS). However, recuperative sCO₂ cycle with mass split is selected as compromise solution owing to its higher total efficiency, nominal plant complexity and comparatively lower cycle maximum pressure.

CO₂-Novec mixtures (with 20% molar composition of Novec fluid in the mixture) as working fluids in power cycles showed 3 percentage points higher cycle thermodynamic efficiency compared to recuperative with mass split sCO₂ power cycle.

For CO₂-Novec mixtures working fluids, heat addition is occurring at higher temperature which brings about higher cycle thermodynamic efficiency. On the other hand, the expansion in turbine is lower compared to pure CO₂ power cycles owing to higher molecular complexity of Novec fluids. In this point of view, CO₂-Novec fluids cannot be considered as promising mixtures for applications in which improvement in power output is the prime objective.

With CO₂-R134a mixture (with 30% molar composition of R134a in the mixture) as working fluid in simple cycle, comparable total efficiency and 3 percentage points rise in thermodynamic cycle efficiency is obtained compared to recuperative with mass split sCO₂ cycle.

The minimum and maximum operating pressures for power cycles operating with CO₂ mixtures are lower which is beneficial in component design point of view since lower pressures are proportional to lower mechanical stresses in cycle components. Results suggests that, employing CO₂ mixtures as working fluid is a much more convincing option for high temperature heat recovery owing to higher cycle efficiencies achievable with rather simple cycle layout and lower cycle maximum operating pressures compared to sCO₂ cycles. Nevertheless, the cycle analysis using novel working fluids helps in selection of promising fluids and optimum parameters for improvement in thermodynamic performance of sCO₂ power cycles. Besides cycle analysis, a great deal of research work is needed to calculate accurate thermodynamic and transport properties of novel CO₂ mixtures and decide thermal stability temperature experimentally.

NOMENCLATURE

GWP	Global warming potential
ODP	Ozone depletion potential
PHE	Primary or Heat recovery heat exchanger
PR-EoS	Peng Robinson equation of state
P_R	Pressure ratio
RCS	Recuperative cycle with mass split
SRC	Simple recuperative cycle
SFDE	Single flow split dual expansion cycle
ΔH_f°	Standard enthalpy of formation of a compound
ϕ	Heat recovery effectiveness
η_{total}	Total efficiency
η_{th}	Cycle thermodynamic efficiency
z_1	Molar composition of CO ₂

ACKNOWLEDGEMENTS

Authors would like to acknowledge 3M™ producers for providing pure fluid thermodynamic properties of Novec fluids.

REFERENCES

- [1] R. Scaccabarozzi, M. Tavano, C. M. Invernizzi, and E. Martelli, "Comparison of working fluids and cycle optimization for heat recovery ORCs from large internal combustion engines," *Energy*, vol. 158, pp. 396–416, 2018.
- [2] M. Marchionni, G. Bianchi, and S. A. Tassou, "Techno-economic assessment of Joule-Brayton cycle architectures for heat to power conversion from high-grade heat sources using CO₂ in the supercritical state," *Energy*, vol. 148, pp. 1140–1152, Apr. 2018.
- [3] A. Ayub, N. A. Sheikh, R. Tariq, M. M. Khan, and C. M. Invernizzi, "Exergetic optimization and comparison of combined gas turbine supercritical CO₂ power cycles," *J. Renew. Sustain. Energy*, vol. 10, no. 4, p. 044703, Jul. 2018.
- [4] M. Binotti, C. M. Invernizzi, P. Iora, and G. Manzolini, "Dinitrogen tetroxide and carbon dioxide mixtures as working fluids in solar tower plants," *Sol. Energy*, vol. 181, no. September 2018, pp. 203–213, 2019.
- [5] C. M. Invernizzi, "Prospects of mixtures as working fluids in real-gas Brayton cycles," *Energies*, vol. 10, no. 10, 2017.
- [6] X. Lin, Z. Cui, Z. Geng, J. Zhang, Z. Zhang, and J. Xu, "Calculation of Thermodynamic Physical Parameters of C₅F₁₀O/CO₂ and C₆F₁₂O/CO₂ Mixtures," in *Proceedings of the 2019 5th International Conference on Electric Power Equipment - Switching Technology: Frontiers of Switching Technology for a Future Sustainable Power System, ICEPE-ST 2019*, 2019, pp. 55–59.
- [7] C. M. Invernizzi, "Closed power cycles: Thermodynamic fundamentals and applications," *Lect. Notes Energy*, vol. 11, 2013.
- [8] 3M Canada Company, "3M safety data sheet, 3M Novec 649 Engineered Fluid," 2018.
- [9] 3M Canada Company, "3M safety datasheet, 3M Novec 5110 Engineered fluid," 2020.
- [10] J. M. Calm and G. C. Hourahan, "Physical, safety, and environmental data for current and alternative refrigerants," in *23rd International congress of refrigeration, ICR 2011, Prague, Czech Republic*, 2011, pp. 1–22.
- [11] J. Nouman, "Comparative studies and analyses of working fluids for Organic Rankine Cycles - ORC, Master of Science Thesis, EGI-2012-086MSC," KTH Industrial Engineering and Management, 2012.
- [12] National Fire Protection Association, *NFPA 704 - Standard System for the Identification of the Hazards of Materials for Emergency Response*. 2007.
- [13] M. Z. Irriyanto, H. S. Lim, B. S. Choi, A. A. Myint, and J. Kim, "Thermal stability and decomposition behavior of HFO-1234ze(E) as a working fluid in the supercritical organic Rankine cycle," *J. Supercrit. Fluids*, vol. 154, p. 104602, Dec. 2019.
- [14] C. M. Invernizzi, P. Iora, M. Preßinger, and G. Manzolini, "HFOs as substitute for R-134a as working fluids in ORC power plants: A thermodynamic assessment and thermal stability analysis," *Appl. Therm. Eng.*, vol. 103, no. January 2015, pp. 790–797, Jun. 2016.
- [15] C. M. Invernizzi and D. Bonalumi, *Thermal stability of organic fluids for Organic Rankine Cycle systems*. 2016.
- [16] Aspen Technology Inc., "Aspen Plus. The Chemical Industry's Leading Process Simulation Software." Bedford, Massachusetts 01730, USA.
- [17] M. L. Michelsen and R. A. Heidemann, "Calculation of critical points from cubic two-constant equations of state," *AIChE J.*, vol. 27, no. 3, pp. 521–523, 1981.
- [18] S. M. Rump, "INTLAB — INTerval LABoratory," in *Developments in Reliable Computing*, E. Tibor Csendes, Ed. Dordrecht: Springer Netherlands, 1999, pp. 77–104.
- [19] G. Di Marcoberardino *et al.*, "Experimental and analytical procedure for the characterization of innovative working fluids for power plants applications," *Appl. Therm. Eng.*, vol. 178, no. May, p. 115513, Sep. 2020.
- [20] K. Jeong, J. Im, S. Lee, and H. Kim, "(Vapour+liquid) equilibria of the {carbon dioxide+pentafluoroethane (HFC-125)} system and the {carbon dioxide+dodecafluoro-2-methylpentan-3-one (NOVEC™1230)} system," *J. Chem. Thermodyn.*, vol. 39, no. 4, pp. 531–535, Apr. 2007.
- [21] A. Ayub, C. M. Invernizzi, G. Di Marcoberardino, P. Iora, and G. Manzolini, "Carbon Dioxide Mixtures as Working Fluid for High-Temperature Heat Recovery: A Thermodynamic Comparison with Transcritical Organic Rankine Cycles," *Energies*, vol. 13, no. 15, p. 4014, Aug. 2020.
- [22] G. Silva-Oliver and L. A. Galicia-Luna, "Vapor-liquid equilibria for carbon dioxide + 1,1,1,2-tetrafluoroethane (R-134a) systems at temperatures from 329 to 354 K and pressures upto 7.37 MPa," in *Fluid Phase Equilibria*, 2002, vol. 199, no. 1–2, pp. 213–222.
- [23] J. S. Lim, J. M. Jin, and K.-P. Yoo, "VLE measurement for binary systems of CO₂+1,1,1,2-tetrafluoroethane (HFC-134a) at high pressures," *J. Supercrit. Fluids*, vol. 44, no. 3, pp. 279–283, Apr. 2008.
- [24] N. Juntarachat, A. Valtz, C. Coquelet, R. Privat, and J.-N. Jaubert, "Experimental measurements and correlation of vapor-liquid equilibrium and critical data for the CO₂ + R1234yf and CO₂ + R1234ze(E) binary mixtures," *Int. J. Refrig.*, vol. 47, pp. 141–152, Nov. 2014.
- [25] S. Wang *et al.*, "Vapor-liquid equilibrium and molecular simulation data for carbon dioxide (CO₂) + trans-1,3,3,3-tetrafluoroprop-1-ene (R-1234ze(E)) mixture at temperatures from 283.32 to 353.02 K and pressures up to 7.6 MPa," *Int. J. Refrig.*, vol. 98, pp. 362–371, Feb. 2019.
- [26] G. Manente and M. Costa, "On the Conceptual Design of Novel Supercritical CO₂ Power Cycles for Waste Heat Recovery," *Energies*, vol. 13, no. 2, p. 370, Jan. 2020.
- [27] G. Manente and F. M. Fortuna, "Supercritical CO₂ power cycles for waste heat recovery: A systematic comparison between traditional and novel layouts with dual expansion," *Energy Convers. Manag.*, vol. 197, no. April, p. 111777, 2019.

MEAN-LINE ANALYSIS FOR SUPERCRITICAL CO₂ CENTRIFUGAL COMPRESSORS BY USING ENTHALPY LOSS COEFFICIENTS

Haikun Ren*

University of Duisburg-Essen
Duisburg, Germany
Email: haikun.ren@uni-due.de

Alexander Hacks

University of Duisburg-Essen
Duisburg, Germany

Sebastian Schuster

University of Duisburg-Essen
Duisburg, Germany

Dieter Brillert

University of Duisburg-Essen
Duisburg, Germany

ABSTRACT

In order to develop the technology of carbon dioxide at so-called supercritical state (sCO₂)¹ further, quick and reliable design tools for the different system components, e.g. centrifugal compressors, are required. In this study, a computer program is developed to predict the performance of centrifugal compressors with sCO₂ as working fluid. This computer program is based on mean-line analysis, calculates the fluid parameters at selected sections of the meridional plane and plots the performance maps. So-called enthalpy loss coefficients are utilized to describe the difference between the isentropic and the polytropic process. In addition to previous studies, the presented model intends to predict the performance of sCO₂ centrifugal compressor with a shrouded impeller and a vaneless diffuser. For this purpose, corresponding loss coefficients are incorporated. Subsequently, the predicted results of this work are compared and validated with computational fluid dynamics (CFD) and experimental results from the EU-project sCO₂-HeRo. The prediction of the computer program fits within 5% deviation to the CFD results, and about 4% to the experimental results regarding to pressure ratio.

INTRODUCTION

In recent years, sCO₂ is considered to be applied in various industrial branches such as solvent and power cycles. In the field of sCO₂ power cycles, new designs of systems and their components are required to propel the technology up to a higher technology readiness level (TRL). For this purpose, quick and

reliable off-design tools for system components are needed to predict the performance characteristics of these components, especially for turbomachines of power cycle. Therefore, the so-called mean-line analysis is selected, which is widely used in the design process of turbomachines to quickly estimate and evaluate the performance of a design. By using such a method, various loss models must be taken into account, which describe the loss mechanisms of parts of the turbomachine and estimate the losses through the flow passage, in order to bring the calculation results close to reality. These loss models are already developed for example by Coppage et al. [1], Jansen [2], Johnston and Dean [3], Aungier [4]. Since many loss coefficients within these models are empirically obtained through experiments with conventional fluids like air or water, these models should be validated whether they can be utilized for CO₂.

In previous investigations, Lee et al. [5], Ameli et al. [6], and Romei et al. [7] have validated the application of conventional enthalpy loss coefficients for sCO₂ centrifugal compressors with the experimental results from Sandia National Laboratories (SNL) [8]. Similarly, Cho et al. [9] have investigated different sets of loss coefficients referred by Oh et al. [10], Galvas [11], and Lee et al. [12] and validated them with the experimental results from Korea Advanced Institute of Science and Technology (KAIST) and Korea Atomic Energy Research Institute (KAERI). The results from these investigations exhibit a good agreement with the experimental results in tendency. In addition to previous works, different configuration of centrifugal

¹ sCO₂ is defined as carbon dioxide at supercritical state, namely $p > p_{crit}$ and $T > T_{crit}$. The critical pressure p_{crit} and temperature T_{crit} of CO₂ are 73.75 bar and 304.13 K respectively.

compressor is considered in this work. The main contribution of this study is that the results of this work are validated quantitatively with the results from EU-project sCO₂-HeRo.

In this study, a computer program is established in MATLAB by utilizing the mean-line analysis and enthalpy loss coefficients in order to predict the performance of sCO₂ centrifugal compressor quickly within an acceptable deviation. This computer program is validated with the CFD and experimental results from sCO₂-HeRo, in which a shrouded 2D impeller and a vaneless diffuser are employed. Additionally, the computer program also considers parasitic works for validation with experiments, since they increase the input power of the compressor.

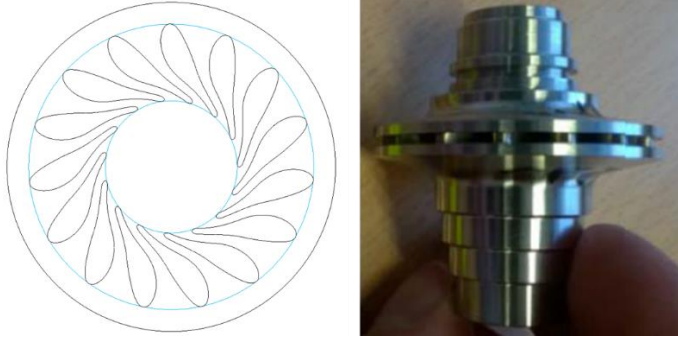


Figure 1: Compressor wheels of CO₂-HeRo [13]

MEAN-LINE ANALYSIS

In order to calculate the flow properties through a centrifugal compressor with mean-line analysis, sections are defined in Figure 2. According to this definition, 1-2 is the impeller, 3-4 is the diffuser, 4-5 is the volute, and 5-6 is the exit cone. Obviously, section 1 is the inlet and section 6 is the outlet of the compressor.

Especially for centrifugal compressors, parasitic works due to recirculation and disk friction must be considered, see Figure 2. The recirculation work is caused by swirl due to the backflow from diffuser to the impeller tip, normally found at low flow coefficient [4]. The disk friction, which is caused by the frictional force on the both side of the impeller exerted by the leakage flows in the clearance between impeller outer surface and the casing, builds torque against the direction of rotation and therefore causes an additional work [4]. These mechanisms lead to an additional power consumption to the shaft, which means an additional torque M_a on the shaft. Denoted the specific blade work by a , the total power consumption at the shaft is

$$P_t = \dot{m} \cdot a + \omega \cdot M_a, \quad (1)$$

with

$$a = u_2 c_{u2} - u_1 c_{u1}, \quad (2)$$

where \dot{m} is the mass flow rate through the impeller and ω the angular velocity of the impeller. u and c_u represent the

circumferential velocity and the circumferential component of the absolute velocity. 1 and 2 are the section number.

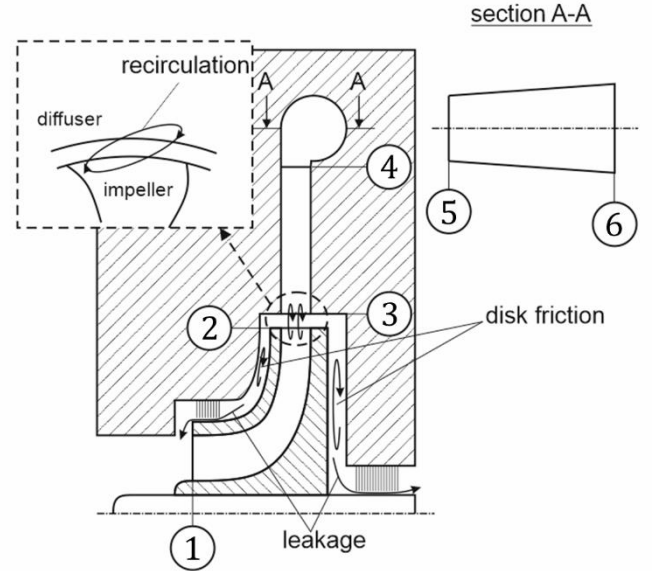


Figure 2: Meridional plane of a centrifugal compressor with defined sections and mechanisms of parasitic works

Since the recirculation is found inside the main flow passage and causes an energy dissipation, the recirculation work contributes a specific total enthalpy rise $L_{t,rc}$ to the main flow corresponding to this dissipation. Similarly, the disk friction at the impeller shroud side impacts the flow within the impeller due to the backflow from impeller tip to impeller inlet. Therefore, this part of disk friction work also leads to a specific total enthalpy rise $L_{t,df}$ which is corresponding to an energy dissipation. Although the disk friction on the both sides of the impeller contribute to the additional torque M_a in eq.(1), the disk friction on the impeller does not contribute to the energy dissipation of the main flow in an adiabatic system. Finally, a total specific enthalpy rise² $L_{t,p}$ due to the parasitic works beside the specific blade work a is given by

$$L_{t,p} = L_{t,rc} + L_{t,df}. \quad (3)$$

By estimating the circumferential component c_{u2} , the specific total enthalpy at the impeller outlet is calculated by the first law of thermodynamics for adiabatic flows:

$$h_{t2} = h_{t1} + a + L_{t,p}, \quad (4)$$

in which t represents parameters respect to total thermodynamic conditions. Thereafter, the losses are considered and the total pressure p_{t2} at impeller outlet is calculated. This is achieved by taking into account the difference between the specific total enthalpy at impeller outlet h_{t2} for the polytropic and $h_{t2,is}$ for the isentropic process, and by calculating $h_{t2,is}$ as

² The equations of $L_{t,rc}$ and $L_{t,df}$ are found in the annex.

$$h_{t2,is} = h_{t2} - L_{t,p} - L_{12}, \quad (5)$$

where L_{12} is the energy dissipation of the flow within the impeller, while $L_{t,p}$ is corresponding to the energy dissipation outside the impeller, as mentioned before. Finally, p_{t2} is calculated by $p_{t2} = p(h_{t2,is}, s_1)$ and other total fluid properties are calculated from the equation of state presented by Span and Wagner [14] and incorporated in NIST Refprop v8.0 [15] as $f(h_{t2}, p_{t2})$. Calculating the specific static enthalpy by $h_2 = h_{t2} - c_2^2/2$, all static fluid properties are known from the equation of state $f(h_2, s_2)$.

Afterward, the meridional component c_{m2} of the absolute flow velocity is calculated from the continuity equation, while the circumferential component is calculate by

$$c_{u2} = u_2 \cdot \left(1 + \frac{c_{m2}}{u_2} \cdot \cot\beta_2\right), \quad (6)$$

where β_2 is the prescribed relative flow angle³ at impeller outlet. Finally, the circumferential component c_{u2} is updated in an iterative process.

Similar steps apply to all other sections but with constant total specific enthalpy, which is equal to h_{t2} .

After calculating fluid parameters of all sections (1-6), the efficiency can be calculated using a desired definition. It does not impact the calculation of the thermodynamic parameters. This definition is provided in section "validation with CFD-simulations of sCO₂-HeRo".

ENTHALPY LOSS COEFFICIENTS

In this study, enthalpy loss coefficients ζ are used to quantify the aerodynamic losses within the impeller and are defined as:

$$\zeta_{i(i+1)} = \frac{L_{i(i+1)}}{\frac{1}{2}c_{i+1}^2} = \frac{h_{t(i+1)} - h_{t(i+1),is}}{\frac{1}{2}c_{i+1}^2}. \quad (7)$$

Only for the impeller, the relative velocity w is used instead of the absolute velocity c , and the specific total enthalpy rise $L_{t,p}$ caused by the parasitic works outside the impeller should be subtracted, as shown in eq.(5). Hence, there is

$$\zeta_{12} = \frac{L_{12}}{\frac{1}{2}w_2^2} = \frac{h_{t2} - L_{t,p} - h_{t2,is}}{\frac{1}{2}w_2^2}. \quad (8)$$

Finally, the loss coefficient for each part of the compressor can be calculated by

$$\zeta_{12} = \zeta_{inc} + \zeta_{bld} + \zeta_{sf} + \zeta_{mix}, \quad (9)$$

$$\zeta_{34} = \zeta_{vld}, \quad (10)$$

$$\zeta_{45} = \zeta_{vol}, \quad (11)$$

$$\zeta_{56} = \zeta_{exit}. \quad (12)$$

Details about the loss coefficients applied in the equations above are listed in the annex (Table 2).

VALIDATION WITH CFD-SIMULATIONS OF SCO₂-HERO

To validate the computer program, the compressor performance of sCO₂-HeRo is predicted and firstly compared with the CFD results according to [16], in which the CFD results are shifted by constant value of 0.1 kg/s to lower mass flow to account for the eye seal leakage. In this paper, the original CFD results are applied. Table 1 displays parameters used to calculate the compressor performance. Several parameters such as β_2 , B_1 and B_2 are derived from the CFD results, since the blade metal angle and blade contour do not reflect the actual flow parameters due to the thick blade profile shown in Figure 1. The diameter and the height of the vaneless diffuser inlet are regarded as same as those of the impeller outlet. In this case, parasitic works $L_{t,p}$ are not considered, since the CFD results do not include them.

Table 1: Parameters of the sCO₂-HeRo compressor [13]

Parameter	Symbol	Value	Unit
Total pressure	p_{t1}	78.3	bar
Total temperature	T_{t1}	306.15	K
Impeller tip diameter	d_2	38.2	mm
Impeller hub diameter	d_{1h}	17.8	mm
Impeller shroud diameter	d_{1s}	17.8	mm
Impeller blade number	z_{La}	15	—
Impeller outlet flow angle	β_2	147.2	°
Impeller inlet metal angle	$\beta_{1,bl}$	157.6	°
Impeller inlet blade height	b_1	2.1	mm
Impeller tip blade height	b_2	1.25	mm
Area blockage at impeller inlet	B_1	0.16	—
Area blockage at impeller outlet	B_2	0.32	—
Diffuser outlet diameter	d_4	84	mm
Volute outlet radius	r_{vol}	3.75	mm
Exit cone outlet radius	r_{exit}	7.9	mm

In Figure 3, predicted ratio of total pressures at selected rotational speeds (20 krpm, 30 krpm, 40 krpm, and 50 krpm) are compared with the CFD results. They are calculated by

$$\Pi_t = \frac{p_{t6}}{p_{t1}}. \quad (13)$$

For the calculation of the total parameters, the flow velocity at compressor outlet is neglected corresponding to the CFD results. The mean-line results are represented by lines, while the CFD results are displayed in symbols. At all selected rotational speeds, the mean-line results are in agreement with the CFD results. Quantitatively, a maximal deviation of 3.2% is found, which exhibits a very good quality of the prediction in this case. Similarly, regarding to the increase of the isentropic specific total

³ The flow angles are illustrated by Figure 10 in annex.

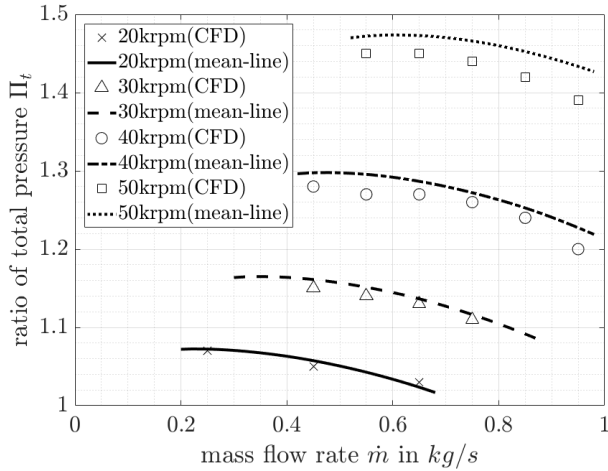


Figure 3: Comparison of ratio of total pressures between CFD and mean-line results for the compressor of sCO₂-HeRo

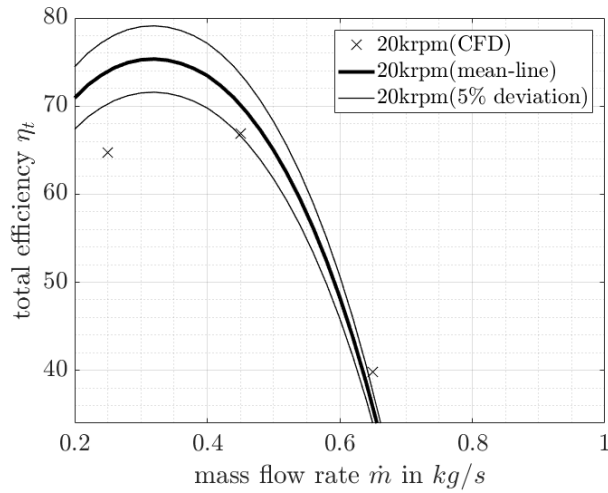


Figure 4: Comparison of efficiency between CFD and mean-line results for the compressor of sCO₂-HeRo at 20 krpm

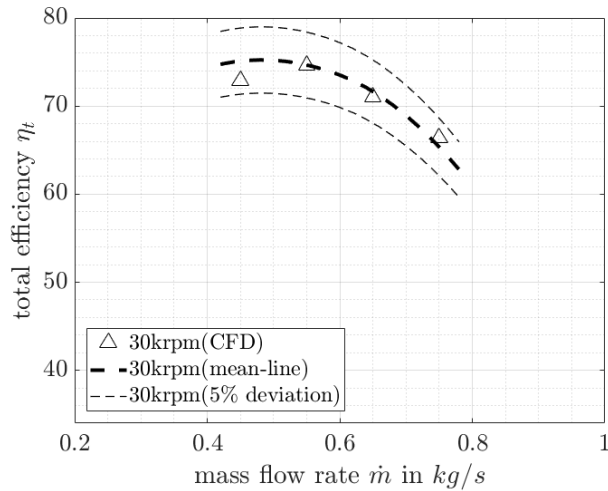


Figure 5: Comparison of efficiency between CFD and mean-line results for the compressor of sCO₂-HeRo at 30 krpm

enthalpy $\Delta h_{t,is}$, 77.8% of the cases are found within the 5% deviation region.

Furthermore, the efficiency of compressor are calculated by

$$\eta_t = \frac{\Delta h_{16,is} + (c_6^2 - c_1^2)/2}{a}, \quad (14)$$

where $\Delta h_{16,is}$ is the isentropic specific enthalpy change regarding to process 1 to 6. They are compared with the CFD results as well, see Figure 5 to Figure 7. In each diagram, the broad line represents the mean-line results, while the CFD results are marked by symbols. There are two narrower lines which present a 5% deviation to the mean-line results, to distinguish the difference between mean-line and CFD results quantitatively. The comparisons exhibit that the CFD results are found within the 5% deviation range in 83.3% of the cases, which indicates that the quality of the prediction is already good with regard to the efficiency.

Consequently, the computer program is considered as

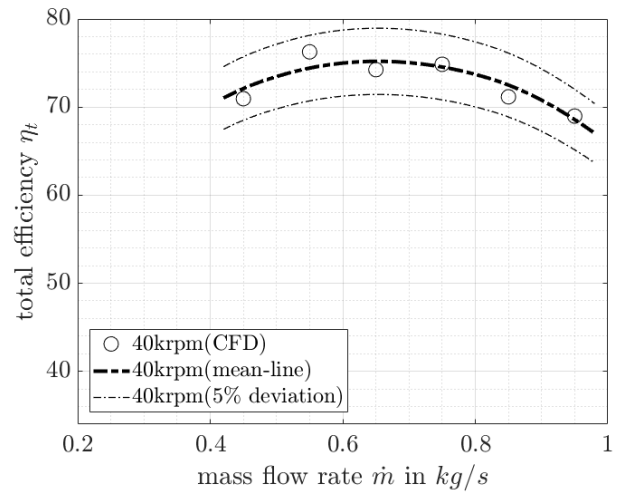


Figure 6: Comparison of efficiency between CFD and mean-line results for the compressor of sCO₂-HeRo at 40 krpm

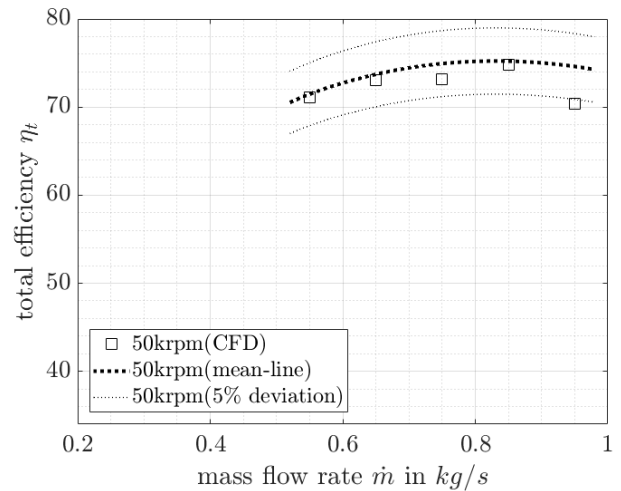


Figure 7: Comparison of efficiency between CFD and mean-line results for the compressor of sCO₂-HeRo at 50 krpm

verified with the CFD results of sCO₂-HeRo through the comparisons regarding to the ratio of total pressures and to the efficiency of compressor. It is specified that the prediction has an accuracy of 95% and indicates that the enthalpy loss coefficients employed in this computer program with corresponding configurations are appropriate.

VALIDATION WITH EXPERIMENTS OF SCO₂-HERO

In addition, the computer program is also validated with the experimental results of sCO₂-HeRo, which have been obtained in the SUSEN CO₂-loop at CVR Research Center Řež [17]. In this paper, only the pressure ratios from the experiments are presented, since the enthalpy rise and efficiency of the compressor are not determined precisely enough due to the measurement uncertainties in the experiments [16]. For the validation with experimental data, the parasitic works $L_{t,p}$, which lead to an additional specific total enthalpy rise beside the specific blade work a , are calculated by eq.(3). The leakage flows are considered as well and calculated by eq.(34) displayed in annex. For the calculation of the total parameters, the flow velocity at compressor outlet is neglected corresponding to the EXP results.

In Figure 8, the diagram illustrates the comparison between the mean-line results and the experimental results at rotational speeds of 20 krpm and 30 krpm. The experimental results are the same as in [16], displayed with symbols and error bars, and are denoted by EXP. The mean-line results are shown by lines. Graphically, the mean-line results correspond to the experimental results well in tendency. It is found that the experimental results have a maximal deviation of 3.9% to the mean-line results. This also indicates a high quality of the prediction. The computer program is hence regarded as validated with the experimental results of sCO₂-HeRo in terms of the pressure ratio.

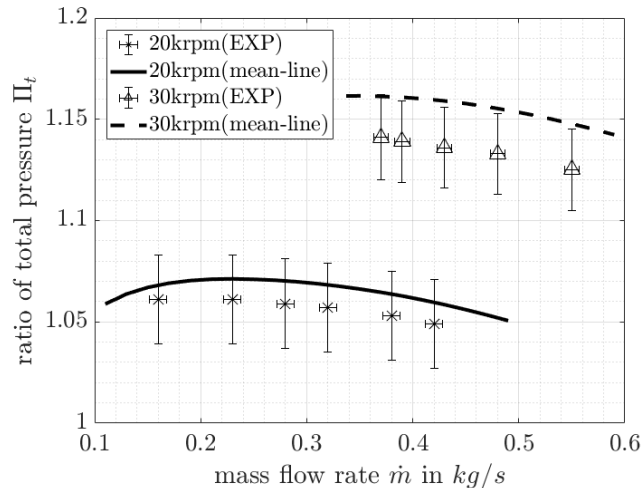


Figure 8: Comparison of the ratio of total pressures between EXP and mean-line results for the compressor of sCO₂-HeRo

CONCLUSIONS

In this study, a computer program based on mean-line analysis has been established for predicting the performance especially of sCO₂ centrifugal compressors. Corresponding loss coefficients are employed to fit compressor configurations like:

- Shrouded impeller,
- 2D blades,
- Vaneless diffuser.

The parasitic works and their effects are introduced in this paper as well. In this study, the parasitic works are only incorporated into the computer program by the validation with the experimental results.

In this paper, the impeller outlet flow angle from CFD data is used in the mean-line calculation, since no deviation model is available for this geometry. Similarly, the impeller inlet and outlet area blockage are also derived from CFD data. However, the program can easily be extended with deviations and blockage models, e.g., the models mentioned by Aungier [4]. The selection of suitable models impacts the accuracy of the program.

Consequently, the computer program is validated with the results of sCO₂-HeRo. The mean-line calculations fit the CFD results within a deviation of 3.2% and 5% regarding to pressure ratio and efficiency respectively. The comparison between the mean-line and experimental results of sCO₂-HeRo shows a fitting within 3.9% in terms of pressure ratio.

This computer program can be used later to support the design of sCO₂ centrifugal compressors with the configuration, which are validated in this study, by quickly predicting the performance.

NOMENCLATURE

Variables

a	Specific blade work (J/kg)
A	Area (m ²)
b	Blade height (m)
B	Area blockage (–)
c	Absolute velocity (m/s)
c_f	Skin friction coefficient (–)
C_M	Torque coefficient (–)
C_{Mr}	Torque coefficient for fully rough disk(–)
C_{Ms}	Torque coefficient for smooth disk(–)
D_f	Diffusion factor (–)
e	Peak-to-valley surface roughness (μm)
h	Static specific enthalpy (J/kg)
l_B	Flow passage length (m)
L	Specific loss / work (J/kg)
K	Clearance gap swirl parameter (–)
K_{sf}	Skin friction constant (–)
\dot{m}	Mass flow rate (kg/s)
M_a	Additional torque on the shaft (Nm)
p	Static pressure (Pa)
P_t	Power consumption at the shaft (W)

r	Radius (m)
Re	Reynolds number (–)
Re_r	Reynolds number, where disk becomes fully rough (–)
Re_s	Reynolds number, where roughness effects first appear (–)
s	Entropy (J/(kgK))
t	Disk/housing gap width (m)
T	Static temperature (K)
u	Circumferential velocity (m/s)
w	Relative velocity (m/s)
z	Blade number (–)

Greek symbols

α	Absolute flow angle respect to the circumferential velocity (°)
β	Relative flow angle respect to the circumferential velocity (°)
ε	Seal coefficient (–)
ϵ	Wake area fraction (–)
ζ	Enthalpy loss coefficient (–)
η	Efficiency (–)
μ	Dynamic viscosity (kg/(ms))
Π	Pressure ratio (–)
ρ	Density (kg/m ³)
$\bar{\rho}$	Mean density (kg/m ³)
ω	Angular velocity (rad/s)

Subscripts

AVE	Averaged
bl	Blade parameter
bld	Blade loading
df	Disc friction
$exit$	Exit of compressor
h	Hub parameter
i	Section number
in	Inlet parameter
inc	Incidence
is	Isentropic parameter
lk	Leakage
La	Impeller parameter
m	Meridional parameter
mix	Wake mixing
out	Outlet parameter
p	Parasitic works
rc	Recirculation
rms	Root mean square
s	Shroud parameter
sf	Skin friction
t	Total thermodynamic parameter
u	Circumferential component
vld	Vaneless diffuser
vol	Volute parameter
1 – 6	Section number

Abbreviations

CO ₂	Carbon Dioxide
KAERI	Korea Atomic Energy Research Institute
KAIST	Korea Advanced Institute of Science and Technology
sCO ₂ -HeRo	sCO ₂ -HeRo.eu project
SNL	Sandia National Laboratories
sCO ₂	Carbon Dioxide at so-called supercritical state
TRL	Technology Readiness Level
2D	Two dimensional
3D	Three dimensional

ACKNOWLEDGEMENTS

This project has received funding from the Euratom research and training programme 2014-2018 under grant agreement No 847606.

REFERENCES

- [1] Coppage, J. E.; Dallenbach, F.; Eichenberger, H. P.; Hlavaka, G. E.; Knoernschild, E. M.; Van Le, N. (1956). Study of supersonic radial compressors for refrigeration and pressurization systems. AiResearch Manufacturing Company, California.
- [2] Jansen, W. (1967). A method for calculating the flow in a centrifugal impeller when entropy gradients are present. Conference on Internal Aerodynamics, Cambridge.
- [3] Johnston, J. P.; Dean Jr., R. C. (1966). Losses in Vaneless Diffusers of Centrifugal Compressors and Pumps: Analysis, Experiment, and Design. Journal of Engineering for Power, 49-60, ASME.
- [4] Aungier, Ronald H. (1999). Centrifugal Compressors: A Strategy for Aerodynamic Design and Analysis. The ASME, New York.
- [5] Lee, J.; Lee, J. I.; Yoon, H. J.; Cha, J. E. (2014). Supercritical Carbon Dioxide turbomachinery design for water-cooled Small Modular Reactor application. Nuclear Engineering and Design, Vol. 270, 76-89.
- [6] Ameli, A.; Afzalifar, A.; Turunen-Saaresti, T.; Backman, J. (2019). Centrifugal Compressor Design for Near-Critical Point Applications. Journal of Engineering for Gas Turbines and Power, Vol. 141 / 031016, ASME.
- [7] Romei, A.; Gaetani, P.; Giostri, A.; Persico, G. (2020). The Role of Turbomachinery Performance in the Optimization of Supercritical Carbon Dioxide Power Systems. ASME, Journal of Turbomachinery, Vol. 142 / 071001.
- [8] Wright, S. A.; Radel, R. F.; Vernon, M. E.; Rochau, G. E.; Pickard, P. S. (2010). Operation and Analysis of a Supercritical CO₂ Brayton Cycle. Sandia Report SAND2010-0171, Sandia National Laboratories.
- [9] Cho, S. K.; Son, S.; Lee, J.; Lee, S.; Jeong, Y.; Oh, B. S.; Lee, J. I. (2020). Optimum loss models for performance prediction of supercritical CO₂ centrifugal compressor. Applied Thermal Engineering, 28 October 2020, 116255.

- [10] Oh, H. W.; Yoon, E. S.; Chung, M. K. (1997). An optimum set of loss models for performance prediction of centrifugal compressors. *Journal of Power and Energy*, Vol. 211, No. 4, 331-338, IMechE.
- [11] Galvas, M. R. (1973). FORTRAN program for predicting off-design performance of centrifugal compressors. NASA TN D-7487, Lewis Research Center and U.S. Army Air Mobility R&D Laboratory, Cleveland, Ohio.
- [12] Lee, J. (2016). Study of improved design methodology of S-CO₂ power cycle compressor for the next generation nuclear system application, Ph.D. dissertation, Korea Advanced Institute of Science and Technology.
- [13] Hacks, A.; Schuster, S.; Dohmen, H. J.; Benra, F.-K.; Brillert, D. (2018). Turbomachine design for supercritical carbon dioxide within the sCO₂-HeRo.eu. *ASME, Journal of Engineering for Gas Turbines and Power*, Vol. 140 / 121017.
- [14] Span, R.; Wagner, W. (1996). A New Equation of State for Carbon Dioxide Covering the Fluid Region from the Triple-Point Temperature to 1100K at Pressures up to 800 MPa. *Journal of Physical and Chemical Reference Data* 25, 1509.
- [15] Lemmon, E. W.; Huber, M. L.; McLinden, M. O. (2007). NIST Reference Fluid Thermodynamic and Transport Properties – REFPROP, Version 8.0, User’s Guide. Physical and Chemical Properties Division, National Institute of Standards and Technology.
- [16] Hacks, A.; Vojacek, A.; Dohmen, H. J.; Brillert, D. (2018). Experimental investigation of the sCO₂-HeRo Compressor. 2nd European supercritical CO₂ Conference, Essen, Germany.
- [17] Hacks, A.; Schuster, S.; Brillert, D. (2019). Stabilizing Effects of Supercritical CO₂ Fluid Properties on Compressor Operation. *Int. J. Turbomach. Propuls. Power* 2019, Vol. 4(3), 20.
- [18] Jiang, W.; Khan, J.; Dougal, R. A. (2006). Dynamic centrifugal compressor model for system simulation. *Journal of Power Sources* 158, 1333-1343, Elsevier.
- [19] Galerkin, Y. B.; Rekstin, A. F.; Solovyeva, O. A. (2019). Vaneless diffuser of the centrifugal compressor stage design method. *AIP Conference Proceedings* 2141, 030007.
- [20] Botha, B. W.; Moolman, A. (2005). Determining the Impact of the Different Losses on Centrifugal Compressor Design. *R & D Journal*, 21 (3), 23-31.
- [21] Daily, J. W. and Nece, R. E. (1960). Chamber Dimension Effects on Induced Flow and Friction Resistance of Enclosed Rotating Disks. *Transactions ASME, Journal of Basic Engineering*, Sep., 553-562.
- [22] Daily, J. W. and Nece, R. E. (1960). Roughness Effects on Fictional Resistance of Enclosed Rotating Disks. *Transactions ASME, Journal of Basic Engineering*, Mar., 217-232.
- [23] Lüdtke, K. H. (2004). *Process centrifugal compressors: basics, function, operation, design, application*. Springer Science & Business Media. K. H.

ANNEX

ENTHALPY LOSS COEFFICIENTS

All enthalpy loss coefficients used in this study are listed in Table 2.

The wake area fraction required to calculate the mixing losses is calculated according to Botha et al. [18]. It varies linearly with the mass flow rate and takes a value of 0.5 at the surge line as well as the choke line, and 0.366 at the design point ($\zeta_{inc} \approx 0$).

The calculation of the skin friction factor c_f is corresponding to the method described by Aungier [4]. Since the blade metal angle at the impeller outlet does not fit the actual flow parameters, the value of $\beta_{2,bl}$ in eq. (17) is substituted by β_2 shown in Table 1.

Equation (21) is derived from the total pressure loss coefficient introduced in [4], by neglecting the density change in the exit cone, since the density change is small in the exit cone.

Table 2: Enthalpy loss coefficients for various loss mechanisms

Incidence loss [18]:	$\zeta_{inc} = \left(\frac{u_1}{w_2} + \frac{c_{m1}}{w_2} \cdot \cot\beta_{1,bl} \right)^2$	(15)
Blade loading loss [1]:	$\zeta_{blld} = 0.1 \cdot D_f^2 \cdot \left(\frac{u_2}{w_2} \right)^2$	(16)
Skin friction loss [1,11]:	$\zeta_{sf} = 2 \cdot K_{sf} \cdot c_f \cdot \left(\frac{l_{B,La}}{d_2} \right) \cdot \left(\frac{w}{u_2} \right)_{AVE}^2 \cdot \left(\frac{u_2}{w_2} \right)^2$ $K_{sf} = \begin{cases} 5.6 & \text{impller without splitters} \\ 7 & \text{impller with splitters} \end{cases}$ $\left(\frac{l_{B,La}}{d_2} \right) = \frac{r_2 - r_{1,rms}}{d_2 \cdot \sin\beta_{2,bl}} \quad \text{acc. to [1]}$ $\left(\frac{d_{H,La}}{d_2} \right) = \frac{1}{\frac{z_{La}}{\pi \sin\beta_{2,bl}} + \frac{d_2}{b_2}} + \frac{\frac{d_{1s}}{d_2}}{\frac{2}{1 - \frac{d_{1h}}{d_{1s}}} + \frac{2z_{La}}{\pi \left(1 + \frac{d_{1h}}{d_{1s}} \right)} \sqrt{1 + \left[1 + \frac{\left(\frac{d_{1h}}{d_{1s}} \right)^2}{2} \right] \cdot \cot^2\beta_{1s,bl}}}}$ $\left(\frac{w}{u_2} \right)_{AVE}^2 = 0.5 \left\{ \left(\frac{c_{m1}}{u_2} \right)^2 + \left(\frac{d_{1,rms}}{d_2} \right)^2 + \left(\frac{w_2}{w_{1s}} \right)^2 \left[\left(\frac{c_{m1}}{u_2} \right)^2 + \left(\frac{d_{1s}}{d_2} \right)^2 \right] \right\}$	(17)
Mixing loss [3,10,20]:	$\zeta_{mix} = \left(\frac{c_{m2}}{w_2} \right)^2 \left(\frac{1 - \epsilon - \frac{b_3}{b_2}}{1 - \epsilon} \right)^2$ $\epsilon = 0.5 \sim 0.366$	(18)
Vaneless diffuser loss [19]:	$\zeta_{vld} = \frac{c_f}{4 \cdot \frac{b_3}{d_3} \cdot \sin\alpha_3} \cdot \left(1 - \frac{d_3}{d_4} \right) \cdot \left(\frac{c_3}{c_4} \right)^2$	(19)
Volute loss [4,7]:	$\zeta_{vol} = \left(\frac{c_{m4}}{c_5} \right)^2$	(20)
Exit cone loss [4]:	$\zeta_{exit} = \left(\frac{c_5 - c_6}{c_6} \right)^2$	(21)

PARASITIC WORKS:

The parasitic works summarize losses due to recirculation and disk friction, which are described below. After estimating all the parasitic works, the specific total enthalpy rise due to the specific parasitic works is calculated by eq.(3).

Recirculation work:

According to Oh et al. [10], the specific total enthalpy rise due to the recirculation work can be calculated as:

$$L_{t,rc} = 8 \cdot 10^{-5} \cdot \sinh \left[3.5 \left(\frac{\pi}{2} - \alpha_2 \right)^3 \right] \cdot D_f^2 \cdot u_2^2, \quad (22)$$

where α_2 is the absolute flow angle at impeller outlet given in radian. D_f is called diffusion factor and is given by

$$D_f = 1 - \frac{w_2}{w_{1s}} + \frac{0.75(a/u_2^2)}{\frac{w_{1s}}{w_2} \left[\frac{z_{La}}{\pi} \left(1 - \frac{d_{1s}}{d_2} \right) + 2 \frac{d_{1s}}{d_2} \right]}. \quad (23)$$

In eq. (23), w is the relative flow velocity, d the diameter, and z_{La} the blade number of the impeller. The index s represents hereon the parameter in terms of shroud side.

Disk friction work:

The specific total enthalpy rise due to the disk friction work is estimated with the torque coefficient C_M according to Daily and Nece [21, 22], which is expressed by

$$C_{M1} = \frac{2\pi}{(t/r)Re} \quad (24)$$

$$C_{M2} = \frac{3.7(t/r)^{0.1}}{\sqrt{Re}} \quad (25)$$

$$C_{M3} = \frac{0.08}{(t/r)^{1/6} Re^{1/4}} \quad (26)$$

$$C_{M4} = \frac{0.102(t/r)^{0.1}}{Re^{0.2}} \quad (27)$$

with

$$Re = \frac{\rho_2 \omega r_2^2}{\mu_2}, \quad (28)$$

where t is the clearance gap width between the disk and housing, r the radius, Re the Reynolds number of the disk, ρ the density, and μ the dynamic viscosity. The torque coefficient for smooth disk surface C_{Ms} is equal to the maximum of eq.(24) to eq.(27). The surface roughness first affects the torque coefficient at the Reynolds number Re equal to Re_s which is calculated by [22]

$$Re_s = 1100(e/r)^{-0.4} / \sqrt{C_{Ms}}, \quad (29)$$

where e is the peak-to-valley surface roughness height. The Reynolds number at a fully rough disk is calculated by [22]

$$Re_r = 1100(r/e) - 6 \cdot 10^6, \quad (30)$$

while the torque coefficient C_{Mr} for the fully rough disk is written as

$$C_{Mr} = \left(\frac{1}{3.8 \log_{10}(r/e) - 2.4(s/r)^{0.25}} \right)^2. \quad (31)$$

The final torque coefficient C_M is calculated by

$$C_M = \begin{cases} C_{Ms} & Re \leq Re_s \\ C_{Ms} + (C_{Mr} - C_{Ms}) \cdot \frac{\log_{10} \left(\frac{Re}{Re_s} \right)}{\log_{10} \left(\frac{Re_r}{Re_s} \right)} & Re_s < Re < Re_r \\ C_{Mr} & Re \geq Re_r \end{cases} \quad (32)$$

Since this torque coefficient considers both side of the disk, the specific enthalpy rise due to the disk friction at the impeller shroud side is finally calculated by

$$L_{t,df} = C_M \cdot \frac{\rho_2 \omega^3 r_2^5}{4\dot{m}}. \quad (33)$$

LEAKAGE FLOW THROUGH LABYRINTH SEAL:

Lüdtke [23] has given an expression to estimate the leakage flow through a labyrinth seal which is generally used within centrifugal compressor. The expression can be written as (replacing ideal gas assumption)

$$\dot{m}_{lk} = \zeta \cdot A \cdot \varepsilon \cdot \sqrt{p_{in}} \cdot \sqrt{\rho_{in}}. \quad (34)$$

where p_{in} and ρ_{in} represent the fluid pressure and density at the seal inlet respectively. The seal factor $\zeta \cdot A$ is not displayed in Hacks et al. [16]. However, it has been calculated by Hacks et al. through the experimental results of sCO₂-HeRo in Hacks et al. [16] and has a value of 0.0009 for the compressor. The seal coefficient is estimated by Figure 9. The pressure ratio of the seal is obtained by assuming that the outlet pressure p_{out} of the seals is as same as the inlet pressure of the compressor.

In order to calculate the pressure at the seal inlet, the pressure drop in the disk/housing gap is calculated by the equations according to Aungier [4]:

$$\frac{\partial p}{\partial r} = K^2 \omega^2 \rho r \quad (35)$$

with

$$K = \frac{0.46}{1 + \frac{t}{r}} + \frac{\dot{m}_{lk} \cdot \left(\rho \cdot r_2 \cdot \frac{u_2}{\mu}\right)^{0.2}}{2\pi \cdot \rho \cdot r_2 \cdot u_2 \cdot t} \cdot \left(1.75 \cdot \frac{c_{u2}}{u_2} - 0.316\right). \quad (36)$$

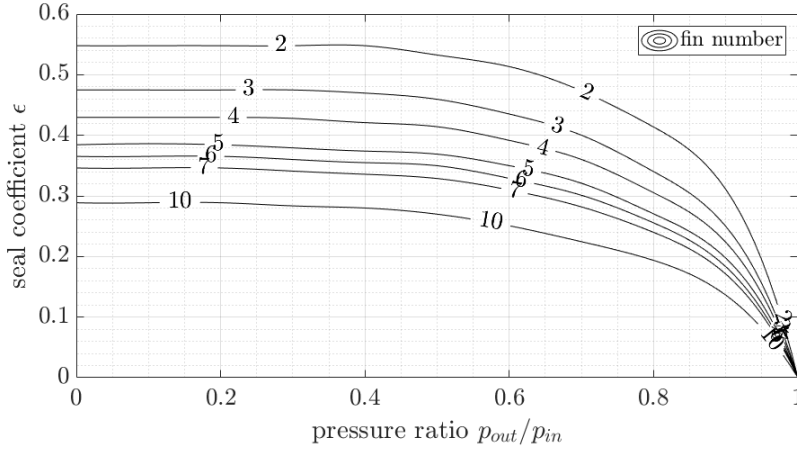


Figure 9: Seal coefficient according to Lüdtke [23]

FLOW ANGLES:

The flow angles defined in this paper are illustrated below:

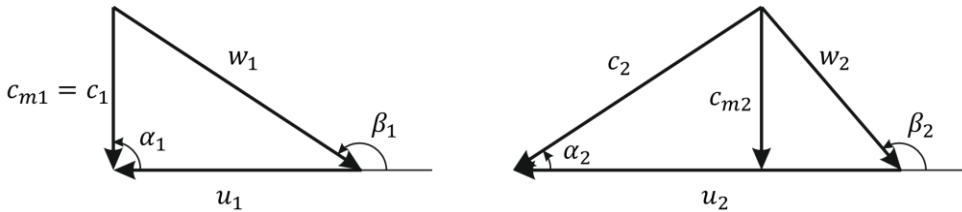


Figure 10: Velocity triangles at impeller inlet (left) and outlet (right)

NUMERICAL INVESTIGATION OF A SIMPLE REGENERATIVE HEAT TO POWER SYSTEM WITH COUPLED OR INDEPENDENT TURBOMACHINERY DRIVES

Matteo Marchionni*

Brunel University London
Uxbridge, United Kingdom

Email:matteo.marchionni@brunel.ac.uk

Giuseppe Bianchi

Brunel University London
Uxbridge, United Kingdom

Muhammad Usman

Brunel University London
Uxbridge, United Kingdom

Apostolos Pesyridis

Brunel University London
Uxbridge, United Kingdom

Savvas A. Tassou

Brunel University London
Uxbridge, United Kingdom

ABSTRACT

Supercritical CO₂ (sCO₂) power systems have the potential to revolutionise power generation. Among the possible layouts, the simple regenerative cycle is the most essential, yet potentially the most competitive for an industrial uptake of the sCO₂ technology at small-scales (<0.5MW_e) in high-grade waste heat to power applications (>400°C). To compensate for the efficiency downsides due to the basic architecture, this study investigates how turbomachinery could improve the design and part-load performance of sCO₂ power systems. With reference to the 50kW_e High Temperature Heat To power Conversion facility (HT2C) available at Brunel University London, this research numerically assesses pros and cons of a radial turbine and a compressor being simultaneously or independently driven. Two turbine designs with nominal total-static efficiency of 75% were developed using a mean-line methodology which further allowed to retrieve the operational and efficiency maps. These maps were later implemented in a one-dimensional simulation platform of the HT2C facility calibrated against equipment data. The differential performance of the coupled and independent turbomachinery drive solutions was assessed with reference to a broad range of industrial heat input conditions in terms of mass flow rate and temperature of the flue gas. The results show marginal benefits at design conditions due to the same turbine design specifics. The independent drive solution leads to worse performance for part load conditions below the nominal one. On the other hand, the dual optimisation of compressor and turbine speeds allows substantial benefits above the design point, particularly for deviations of the flue gas temperature. At 110% of the nominal heat source temperature, the independent drive solution increases the net thermal power output by 27%, namely from 75kW to 95kW. This is primarily due to a higher mass flow rate in the sCO₂ loop as well as a slightly higher pressure ratio.

INTRODUCTION

Supercritical CO₂ power has been receiving a large interest from the academic and industrial communities in the last decade [1]. The use of direct Joule-Brayton cycles in which the compression process takes place in the critical region indeed allows to increase the net power output with respect to a compression of CO₂ in the gas state [2]. Furthermore, the use of CO₂ as working fluid allows to overcome the temperature limitation of steam cycles, even the state-of-the-art ones [3]. Lastly yet importantly, the use of a high-pressure, non-toxic and non-flammable working fluid provides benefits in terms of footprint, safety as well as operational flexibility. This is a key requirement for thermal power generation during the next decades [4]. In fact, baseload power stations will be asked to adapt their load not only depending on the electricity demand but also based on the increasing penetration of renewable sources in the energy mix [5]. Despite these advantages, the Technology Readiness Level (TRL) of sCO₂ power equipment is still not sufficiently mature for a mass deployment, even though there are already commercial solutions up to 8 MW_e [6] and large pilot test facilities up to 10 MW_e (STEP) [7], 50MW_{th} (Net Zero) [8] or 300 MW_e (Allam Cycle Zero Emission Coal Power) [9] which are currently at a more advanced TRL.

A key shortcoming that sCO₂ power technology is currently experiencing is the large capital expenditure in comparison with Steam or Organic Rankine Cycles. Even though plenty of studies have been published on cycle analysis [10], optimal layouts seem to be the streamlined ones, such the simple regenerative [11] or recompressed cycles [12]. In the available experimental facilities based on the afore mentioned architectures, the turbomachines are of radial type due to the low pressure ratio and small mass flow rate [13]. More specifically, mature layouts consider the use

* corresponding author(s)

of a power turbine directly coupled with the electric generator and an ancillary pump [6, 14] or turboalternator [15] to provide flow to the CO₂ loop. Other test facilities instead employ a single shaft turbomachinery layout which constraints turbine and compressor to rotate at the same speed [16]. If on one hand independent drives of pump/compressor may lead to better performance, a single turbomachinery drive is definitely more cost effective. This is true especially for small-scale sCO₂ power units (<0.5MWe), such as the ones for high-grade waste to power conversion that find potential applications in the iron and steel, cement, and glass industries [17].

From a scientific viewpoint, there is a lack of complex cycle optimisation studies since this kind of investigations require detailed equipment models that eventually need to be linked together at system level. As concerns the turbomachinery modelling, this implies retrieving the maps from test data [18] or numerical mean line [19] or 3D CFD [4] simulations. An alternative approach to operating maps is the use of non-dimensional curves based on load and flow coefficients [20]. With regards to heat exchangers, off-design modelling approaches based on the global heat transfer coefficient have been developed [21]. However, such formulations are not optimal for dynamic and control studies given their less accurate predictions during transient operations and when the thermophysical properties show a high variability with the CO₂ temperature and pressure. Therefore, one dimensional models become a suitable trade-off between computational cost and accuracy.

In this paper, we investigated the performance impact of independent and coupled turbomachinery layouts for a small-scale heat to power system based on the High Temperature Heat To power Conversion facility (HT2C) available at Brunel University London [16]. This sCO₂ rig is based on a simple regenerative cycle and has 50 kW_e as nominal power output. Strengths and novel features of this study are the development of a numerical simulation platform calibrated on actual equipment data and the use of an innovative design methodology [22] to retrieve the turbomachinery operating maps. The comparison is made with reference to the same compressor and two turbine design configurations for each drive case.

SYSTEM DESCRIPTION

An overview of the HT2C facility is shown in Figure 1.a. The modelled sCO₂ system, displayed in Figure 1, employs three heat exchangers, two radial machines mounted on the same shaft, a receiver to prevent the fluid thermal expansion during transients and a series of valves, pipes and ancillaries. The standard 20ft container (Figure 1.b) gathers all the system components of the sCO₂ packaged unit except for the waste heat recovery unit, i.e. the primary heater of the sCO₂ loop, which is located along the exhaust line of the Process Air Heater (Figure 1.a). The primary heater and the sCO₂ loop are connected through two 10-meter pipes.

The direct heat recovery from the waste source is performed in the primary heater, where the adopted micro-tube technology allows to enhance the heat transfer between the flue gas (shell

side) and the CO₂ (tube side) without an excessive pressure drop on the gas side. A Printed Circuit Heat Exchanger (PCHE) and a Plate Heat Exchanger (PHE) are used as recuperator and gas cooler respectively.

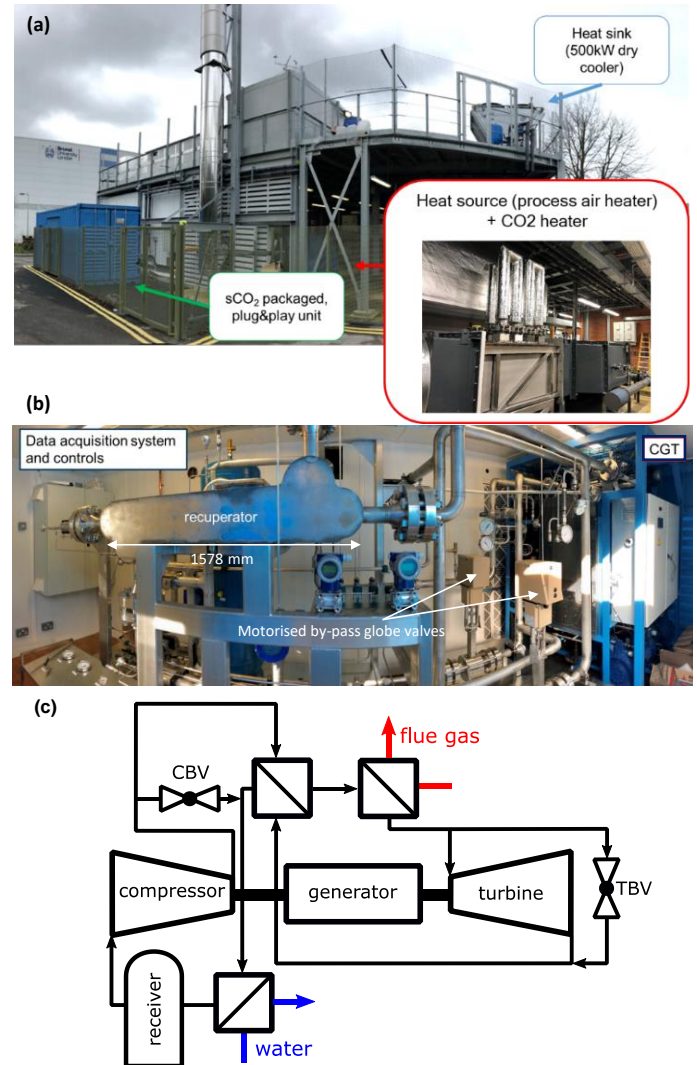


Figure 1: High Temperature Heat To power Conversion facility (HT2C) at Brunel University London: facility overview (a), sCO₂ loop inside the blue container shown in (b) and system layout (c).

In the Compressor-Generator-Turbine (CGT) assembly, which can be also seen on the right-hand side of Figure 1.b, the heat to power conversion occurs. A radial compressor and a turbine are mounted on the same shaft of a synchronous brushless generator. A complex ancillary system is used to ensure lubrication of the bearings and to reduce windage losses [23]. Two motorised compressor and turbine by-pass globe valves, shown in Figure 1.b, have been foreseen to control the system at nominal, startup, shutdown and emergency operations.

The waste heat source is simulated by a Process Air Heater, able to provide a flow of exhaust gases up to 1 kg/s at 1073.15K.

The heat sink is instead a 500 kW dry cooler system. The dry-cooler rejects the heat from a water/glycol mixture which, in turn, removes the residual heat from the CO₂ in the PHE gas cooler. Variable speed drives for the water pump and fans allow the variation of the heat removal and rejection rate.

A data acquisition system has been also installed in the container (left-hand side of Figure 1.b) to allow the remote control and monitoring of the unit. A thorough description of the HT2C facility is reported in [16].

MODELLING METHODOLOGY

The model of the sCO₂ heat to power conversion system has been developed in the commercial software GT-SUITE™, a CAE simulation platform based on a one-dimensional (1D) formulation of Navier-Stokes equations and on a staggered grid spatial discretization. This software tool allows to model each component independently through accurate input data, which relate to the geometrical features of the components as well as their performance data. This information can result either from an experimental campaign or, as in the current case, from more detailed or complex models. Each component can then be considered as a lumped or an equivalent 1D object. In the latter case, the object is discretized in a series of capacities, or volumes, connected by boundaries. The scalar variables (pressure, temperature, density, internal energy, enthalpy, etc.) are assumed to be uniform in each volume. On the other hand, vector variables (mass flux, velocity, mass fraction fluxes, etc.) are calculated for each boundary. The continuity, momentum and energy equations are used to calculate the mass flow rates, the pressure dynamics and the energy transfer through the volumes. The energy equation is expressed in terms of total enthalpy and its solution requires the computation of the local heat transfer coefficient through calibrated heat transfer correlations. A more detailed description of the modelling methodology is provided in [19, 24].

The model block diagram of the sCO₂ system investigated in this work is reported in Figure 2. Components are denoted with uppercase letters while the boundary conditions required for the simulations are indicated with lowercase ones. These boundary conditions are the revolution speed of the compressor-generator-turbine unit as well as the inlet temperatures, pressures and mass flow rates of the hot and cold sources. In the case of coupled turbomachinery drive, the speed boundary conditions are the same for both compressor and turbine. The thermodynamic properties of the working fluids are computed through an interface between the solver and the NIST Refprop database [25].

The heat exchangers and pipes are modelled as 1D equivalent objects. For the heat exchangers, the geometrical inputs are used to define the properties of the equivalent 1D channels. The performance data, related to several operating conditions of the devices, are provided by the manufacturers for the primary heater and the gas cooler, while for the PCHE recuperator, they have been retrieved through more complex models [26]. These data are then employed to calculate the best fitting coefficients of the Nusselt-Reynolds (Nu-Re) correlations

for the equivalent 1D networks that approximate the heat exchangers [4].

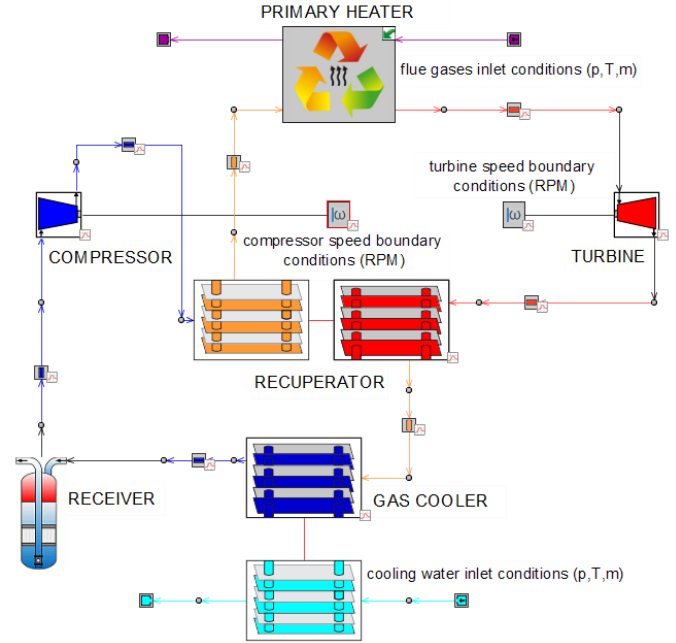


Figure 2: GT-SUITE model of the HT2C test facility.

Table 1: Flow parameters and geometrical features of the heat exchangers embedded in the sCO₂ heat to power conversion unit: primary heat exchanger or heater (PHX), Printed Circuit recuperator (PCHE) and gas cooler (PHE).

Flow parameters (heating/cooling fluid)		PHX	PCHE	PHE
Nominal heat duty	kW	388.3	630.0	237.5
Nominal UA value	kW/K	20.3	20.3	16.8
Pressure drop	kPa	64/11	120/128	8.7/89.1
Geometrical features (heating fluid/cooling fluid)				
Hydraulic diameter	mm	1.9/500	1.22	4.52
Wetted perimeter	mm	5.97	5.12	398.6
Cross sectional area	mm ²	3542/2.5e5	7121	451
Heat transfer area	m ²	14.8	12.0	6.2
Tubes/Channels/Plates	#	1250	2268	84
Material	-	IN-617	SS316L	SS316L
Dry weight	kg	97.6	305.0	52.4

Even though this modelling methodology is common to all the three heat exchangers considered, the gas cooler requires an additional correlation to account for possible condensation of CO₂. In this case, to predict the phase change, the formation of vapor bubbles or liquid droplets is addressed by evaluating the fluid density in each sub volume, while the two-phase area is computed using the vapour Rayleigh-Plesset formulation [27].

The pressure drops are computed using a modified version of the Colebrook relationship [28], which is valid for the turbulent regime ($Re_D > 2100$). Table 1 reports the flow

parameters and the geometrical features of the heat exchangers. A more extensive description of the modelling methodology is available in [4].

Pipes are considered as adiabatic and localized pressure drops are neglected. Only distributed ones are considered. The receiver has been modelled as a container (capacity) with fixed volume. It is situated downstream the gas cooler to absorb the thermal expansion of the fluid in the circuit, decoupling the high from the low-pressure side of the system (Figure 2). Its volume is 0.165 m^3 and accounts for almost 50% of the overall system capacity.

Mechanical and electrical losses of the electric motors and generators for turbomachines as well as the parasitic losses of the system ancillaries (water cooling pump and fans, oil pump for shaft lubrication, CO_2 drainage compressors) have been discarded. As such, all powers reported onwards are thermal.

TURBOMACHINERY INTEGRATION

As in the case of the CGT unit of the HT2C test facility, in the baseline case for this study, compressor and turbine rotate at the same speed. The performance maps of these machines result from 3D RANS CFD simulations whose modelling methodology has been discussed in [29]. The 3D modelling approach has been benchmarked against experimental data available from the Sandia National Laboratories [18]. The actual maps will be validated in the future against the experimental data once the facility will be commissioned. Inlet boundary conditions of the 3D model were the total pressure and temperature as well as the flow direction, which is considered normal to the boundary. Outlet average static pressure has been chosen as outlet boundary condition. The compressor operating and isentropic efficiency maps can be found in Figure 3.

Since the compressor operates close to the critical point, the real gas properties of the fluid must be considered and the use of reduced quantities via normalization can lead to errors in the compressor performance predictions [30]. To overcome this issue, the model considers multiple compressor maps at four reference states that span the whole CO_2 critical region (308.15K at 70, 75, 80 and 85 bar). At least five pressure ratios for each revolution speed are required to ensure an accurate interpolation of the operating curves. Beyond the speed range and the operating range available from the calibration data, a linear extrapolation method is used to predict the performance of the turbomachines. The extrapolated curves are mostly used to ensure a continuity during the starting phase of the numerical simulations. The small distortion located near the surge line at high revolution speeds is due to the supercritical CO_2 thermophysical properties, which affect the pressure changes inside the compressor at different speeds.

The compressor design resulted in the optimal operating region located close to the surge line, as shown in Figure 3.b, where the isentropic efficiency assumes a value of 0.8 in a range of revolution speeds and pressure ratios of 50000-90000 RPM and 1.3-2.0 respectively.

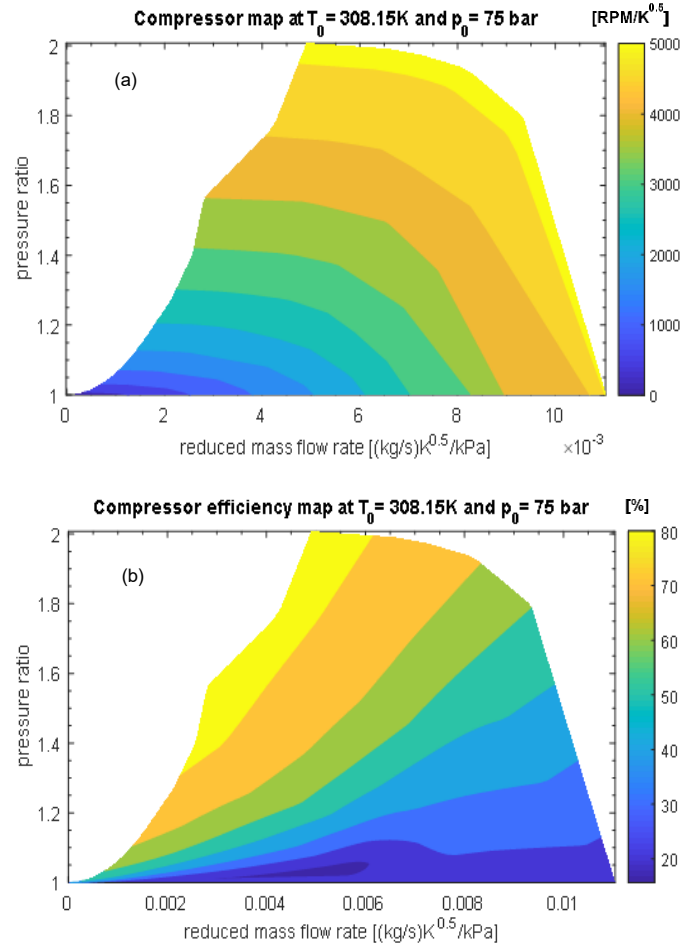


Figure 3: performance (a) and total to static isentropic efficiency maps (b) plotted respect the total to static pressure ratio and to the reduced mass flow rate. Reference state is 308.15K and 75bar. Revolution speed in (a) is expressed in reduced revolutions per minutes $[\text{RPM}/\text{K}^{0.5}]$, efficiency in (b) expressed in percentage points.

The turbine maps are reported in Figure 4 and are represented in a typical format adopted in turbomachinery [31]: the operating curves (Figure 4.a) and the total-to-static isentropic efficiency (Figure 4.b), expressed in percentage units, are reported as a function of the pressure ratio, the reduced mass flow rate $[(\text{kg/s})\text{K}^{0.5}/\text{kPa}]$ and the reduced revolution speed $[\text{RPM}/\text{K}^{0.5}]$. The reference state is 650K and 145 bar.

To assess the advantages of having independent turbomachinery drives, a new turbine has been designed following the methodology developed in [22]. The approach considers a three-step technique to design and optimise the turbine performance in part load/off-design conditions. A mean line procedure considers the design of the rotor, the stator and the volute of the turbine, assumed for simplicity as a circular cross section, in order to accurately estimate the fluid dynamic losses.

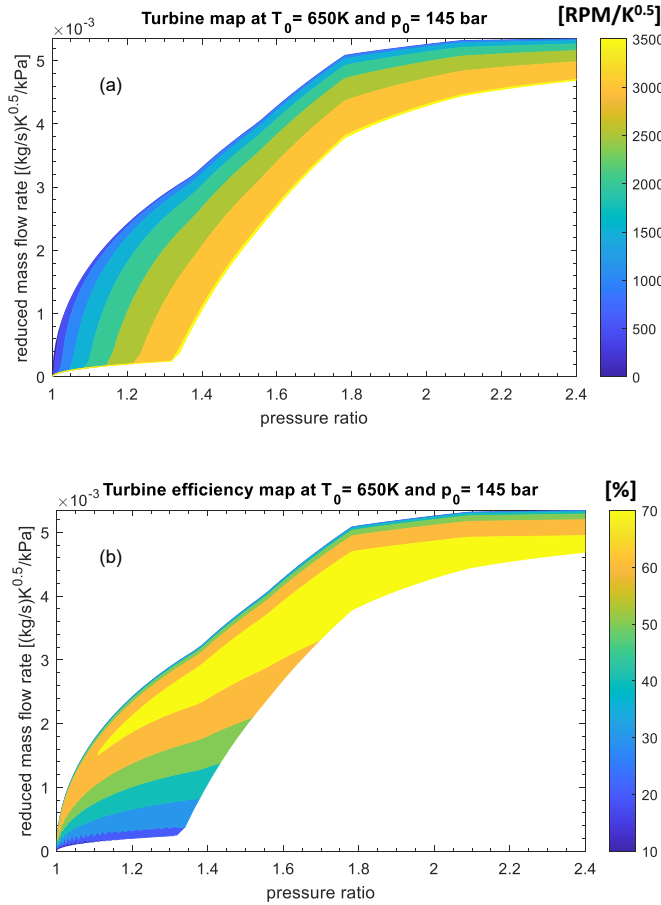


Figure 4: Turbine performance (a) and total to static isentropic efficiency maps (b) for Coupled Drive (CD) case plotted respect the reduced mass flow rate and the total to static pressure ratio. Reference state is 650.00K and 145bar. Revolution speed in (a) is expressed in reduced revolutions per minutes [RPM/K^{0.5}], efficiency in (b) expressed in percentage points.

To start the procedure, first, a set of geometrical and thermodynamics parameters are required [32, 33], chosen respectively by manufacturability considerations and according to the design operating point of the sCO₂ system object of this work.

Given these input data, an isentropic efficiency value at the design point of the turbine is estimated, which is used to compute the enthalpy drops in the rotor, stator and in the volute.

Consequently, a new isentropic efficiency value is calculated and compared with the previous estimated one. The procedure is repeated iteratively until a convergence is achieved. The MATLAB optimisation toolbox has been used to optimise the inlet parameters, using as objective function the isentropic efficiency of the machine. The resulting optimized numbers for key main dimensions including loading coefficient (ϕ), flow coefficient (ψ), rotor blade (Z) etc. were transferred to RITAL.

After this preliminary design stage, RITAL, a commercial 0D/1D software tool [34], has been used to calculate the turbine performance at off-design conditions, and thus obtain the operating and isentropic efficiency map of the machine. To do so, RITAL has been firstly calibrated to predict the turbine design conditions and then to calculate the off-design performance of the expander. The calibrated parameters of turbine design are presented in Table 2.

Table 2. Turbine design parameters for Coupled (CD) and Independent drive (ID) solutions

Design parameters		CD	ID
Inlet Pressure	[bar]	127.5	127.5
Inlet Temperature	[K]	653.15	753.15
Mass flow rate	[kg/s]	2.25	2.25
Pressure Ratio	[-]	1.7	1.7
Performance parameters			
Loading coefficient	[-]	0.854	0.918
Flow coefficient	[-]	0.090	0.215
Isentropic efficiency	[-]	0.75	0.75
Power output	[kW]	110	122.8
Geometrical features			
Wheel diameter	[mm]	57.1	50.9
Axial length	[mm]	15	15
Stator blades	#	6	17
Rotor blades	#	6	14

The maps resulted from this design and optimization process have been implemented in GT-SUITETM are displayed in Figure 5. The discontinuity in the turbine maps noticeable is due to the extrapolation of the turbine operating curves and isentropic efficiency lines made by the software for pressure ratios lower than 1.4.

Compared to the speed constrained turbine design, the independent one can provide a higher range of CO₂ mass flow rates even at lower pressure ratios. For instance, with reference to a pressure ratio of 1.2, the new turbine design can process for its entire revolution speed range a mass flow rate of working fluid going from 1.59 kg/s to 2.51 kg/s. For the same pressure ratio, the old turbine design could process a CO₂ mass flow rate varying in range only from 0.11 kg/s to 1.48 kg/s respectively. As concerns the isentropic efficiency, the old design presents an optimal operating value in a wider range of mass flow rates and pressure ratios compared to the new one.

RESULTS AND DISCUSSION

To investigate the benefits deriving from the adoption of independently driven turbomachinery, a series of simulations at different operating conditions of the sCO₂ heat to power conversion system have been carried out varying the thermal load supplied by the waste heat source. In particular, since the heat load of this stream is completely defined by its mass flow rate and inlet temperature, these conditions were changed during the simulations with respect to the design point at 1 kg/s and 923.15K. On the other hand, the cooling water mass flow rate

and inlet temperature have been kept equal to 1.6 kg/s and 298.15K respectively.

In each case, the net power output has been maximised acting on the compressor and turbine revolution speeds as independent variables. The optimisation algorithm employed is the Nelder Mead SIMPLEX one, which is suitable for finding a local minimum and at a low computational cost since no calculations of derivative terms are involved. For the independent drive configuration, two independent variables must be optimised, the compressor and turbine revolution speeds, and thus the method is a pattern search that compares function values at the three vertices of a triangle.

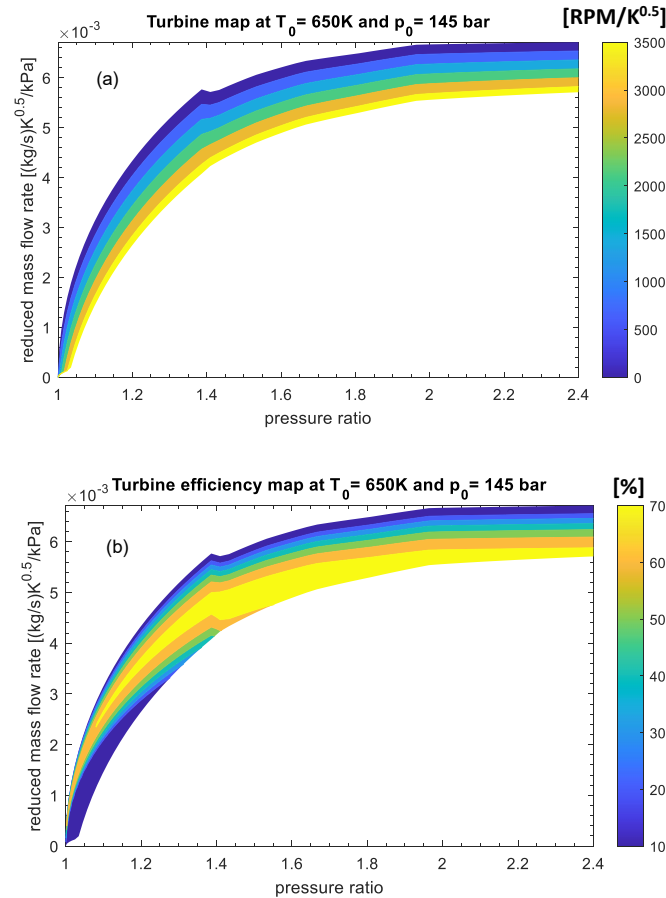


Figure 5: Turbine performance (a) and total to static isentropic efficiency maps (b) for Independent Drive (ID) case plotted respect the reduced mass flow rate and the total to static pressure ratio. Reference state is 650.00K and 145bar. Revolution speed in (a) is expressed in reduced revolutions per minutes $[\text{RPM}/\text{K}^{0.5}]$, efficiency in (b) expressed in percentage points.

The worst vertex, is rejected and replaced with a new vertex. A new triangle is formed and the search is continued. The process generates a sequence of triangles for which the values of the optimization function at the vertices get smaller and smaller. The size of the triangles is reduced and the coordinates of the

minimum point are found. When the sCO_2 system configuration with coupled turbomachines is considered, the optimisation method is similar but considers a segment line instead of a triangle, since only one independent variable must be optimised. Even if the algorithm adopted also allows to perform constrained optimisations by penalizing the regions which violate the constraints imposed [24, 35], in this study, no constraints have been imposed.

The results of the optimisation for the Coupled Drive (CD) case have been reported in Figure 6. For reduced thermal loads, i.e. waste heat mass flow rate and inlet temperature below 0.7 kg/s and 773K respectively, the system is not able to generate any power output since the power required by the compressor is equal or greater than the one generated by the fluid expansion in the turbine. This is mainly due to the low design pressure ratio of the cycle, which together with the low divergence of the CO_2 isobaric lines, requires the achievement of high turbine inlet temperatures to reach a positive power output. At higher thermal loads, i.e. for waste heat source mass flow rates and inlet temperatures above 1.3 kg/s and 1073K respectively, the sCO_2 unit is able to generate a maximum power output of 105kW, thanks to an increased turbine inlet temperature and cycle pressure ratio which consequently lead to a higher cycle thermal efficiency and enthalpy drop across the turbine.

Figure 7 shows the net power difference between independent and coupled turbomachinery drive simulations (ID-CD). At the same operating conditions, the adoption of independent drives for the turbine and compressor can lead to an improvement of the system performance. Indeed, for a heat source inlet temperature of 973 K and mass flow rates higher than 1.0 kg/s, 1.1 kg/s and 1.2 kg/s, decoupling the turbomachines leads to a net power output increase of 10 kW, 20 kW and 30 kW respectively. Close to the design point (1 kg/s, 923.15K), the independent speed regulation does not lead to any performance benefits. When the heat source mass flow rate and inlet temperature are below 1 kg/s and 900K, there is actually a slight decrease of the system net power output up to -10 kW. Hence, the independent drive solution is only beneficial for part-load operating conditions exceeding the design point. In particular, the additional power output is more affected by the heat source temperature than the mass flow rate.

A deeper insight on the power output trends is provided by the optimised performance of the compressor and the turbine in both the configurations investigated. In particular, Figure 8 displays the power required by the compressor (Figure 8.a) and the one generated by the turbine (Figure 8.b) when the machines are coupled. The compressor presents a low sensitivity to the thermal load supplied by the waste source, showing a power consumption increase of the 6.7% for a decrease of the thermal load of 30% (Figure 8.a). This worse performance mainly occurs since a reduction of the heat source inlet temperature or mass flow rate do not allow supercritical conditions of the working fluid at the compressor inlet. For the same thermal load variation,

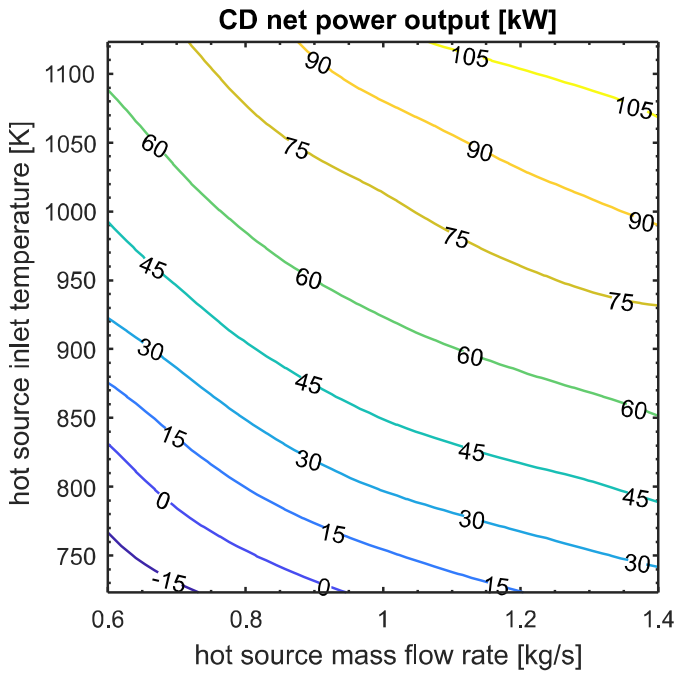
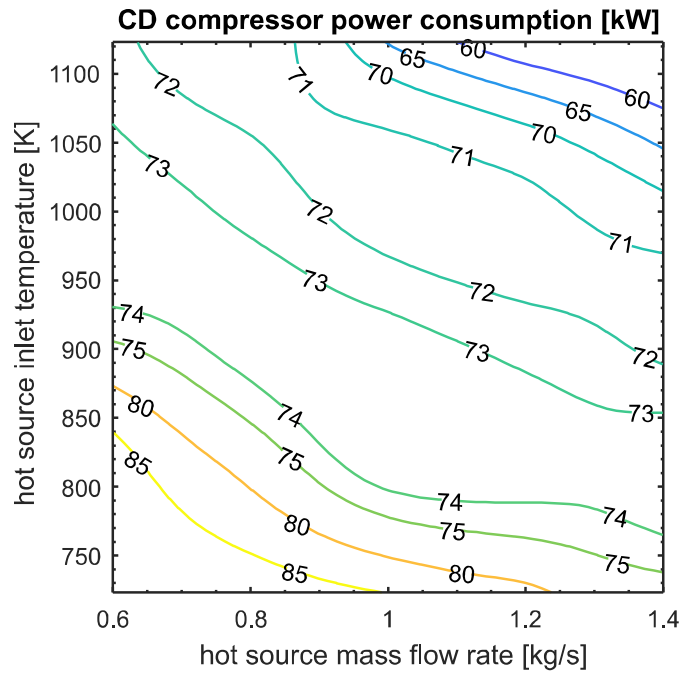


Figure 6: Net thermal power output at different heat inputs to the sCO₂ unit – Coupled turbomachinery Drive (CD)



(a)

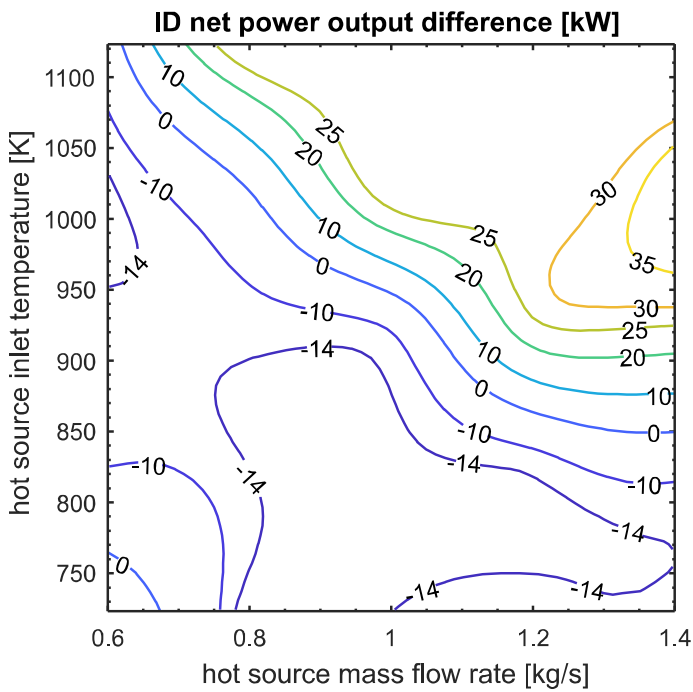
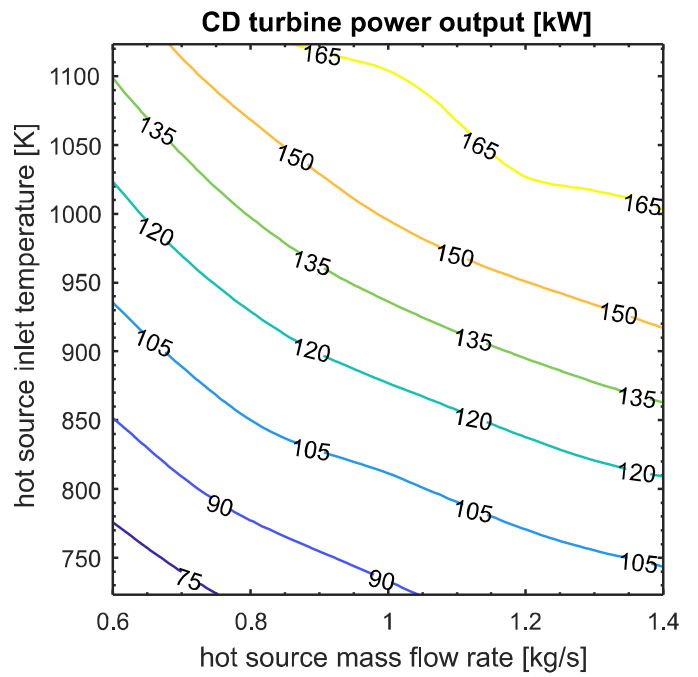


Figure 7: Differential net power output between Independent and Coupled turbomachinery Drive solutions (ID- CD)



(b)

Figure 8: Compressor (a) and turbine (b) thermal power for coupled drive (CD) configuration

the turbine shows a performance decrease of the 36.4% (Figure 7.b). Therefore, the optimisation of the turbine operating conditions based on the heat source availability is the most effective contribution to improve the system performance.

This is further evidenced in Figure 9, which shows the difference between the optimised compressor power consumption (Figure 9.a) and the power generated by the turbine (Figure 9.b) considering an ID configuration and the ones obtained in CD configuration. In fact, the improvement of sCO₂ system performance achieved in the ID case showed in Figure 7 is driven by an improvement of the turbine performance rather than the compressor ones. For instance, for a waste heat source mass flow rate and inlet temperature of 1 kg/s and 1000K respectively, the 20 kW increase in the system net power output (Figure 7) results from the optimisation of the turbine operating conditions (30 kW increase in the power generated, Figure 9.b). The performance increase is obtained thanks to a higher mass flow rate of CO₂ flowing across the machine which leads however to a small decrease in the compressor performance (10 kW increase in the power consumption, Figure 9.a) since the cycle pressure ratio remains almost constant.

Figure 10 shows the optimal speeds for the independent and coupled turbine designs. With reference to Figure 10.a, the turbine performance optimisation in the ID configuration is achieved by increasing the machine revolution speed accordingly to the thermal load provided by the heat source. In fact, assuming a unitary mass flow rate of the waste heat source, when the inlet temperature of the flue gas increase from 950K up to 1100K, the optimised turbine revolution speed is increased from 86000 RPM to almost 100000 RPM. For the CD configuration the revolution speed range of the turbine is constrained by the compressor design and cannot thus assume values higher than 90000 RPM, as showed in Figure 10.b, which displays the optimal revolution speed assumed by the compressor and the turbine for the different thermodynamic conditions of the waste heat source. Furthermore, it can be noticed in Figure 10 that when the thermal load supplied by the waste heat source decreases (mass flow rate and inlet temperature lower than 1 kg/s and 950K respectively) the maximisation of the system power output is achieved in both cases by lowering the revolution speed of the turbomachines, which are decreased down to the minimum value of 80000 RPM and 82000 RPM for the ID and CD configuration respectively. Indeed, the maximum and minimum value of the pressure in the cycle are fixed by the thermal loads in the primary heater and gas cooler respectively. For this given cycle pressure ratio, a decrease of the machine revolution speed leads to a slight increase of the CO₂ mass flow rate flowing in the sCO₂ loop, which consequently positively impacts the system net power output.

CONCLUSIONS

This paper assessed the performance implications of simple regenerative supercritical CO₂ (sCO₂) power cycles equipped with radial turbomachines being simultaneously or independently driven. The case study analysed was the 50kWe

sCO₂ test facility at Brunel University London, whose design conditions include a cycle pressure ratio of 1.7 and a turbine inlet temperature of 673K. The research methodology employed a 3D RANS CFD and a mean line approach for the design of the coupled and independent drive turbine configurations respectively. The turbine maps generated through the aforementioned methods have been used as inputs to a numerical one-dimensional modelling platform whose sub-models have been calibrated against equipment data of the test facility. The performance comparison was carried out at different heat inputs to the sCO₂ loop, which in the current waste heat recovery application came from a flue gas stream of 1kg/s at 923K. Despite being designed for the same nominal performance of 75% total-static isentropic efficiency, the need to match the compressor operating conditions led to very different turbine maps. For instance, at a pressure ratio of 1.2, the independently driven turbine allows a larger operational flow range (1.59-2.51 kg/s) than the speed constrained one (0.11 to 1.48 kg/s). The same design specifics led to similar nominal performance regardless of the turbine employed. For part load conditions below the design point, the independent drive solution leads to worse performance. On the other hand, when the heat source mass flow rate and temperature are above the design point, the dual optimisation of compressor and turbine speeds leads to a net power output increases up to 30%. This is primarily due to a higher mass flow rate in the sCO₂ loop that in the coupled drive configuration would significantly worsen the compressor efficiency. Hence, a coupled turbomachinery drive is advisable should the sCO₂ heat to power block operate close or below design conditions. Instead, an independent drive solution is preferred for frequent part load operation above the design specifics.

Future research will consider the cost and scale aspects for an optimal techno-economic design of simple regenerative sCO₂ power units. Additional focus will be devoted to the aerothermal compressor design optimisation to take into account the operational challenges in the critical region. Another driver of future research will be the scalability considerations for large sCO₂ power applications that will likely employ axial turbomachines rather than radial ones.

ACKNOWLEDGEMENTS

The research presented in this paper received funding from the European Union's Horizon 2020 research and innovation program under grant agreement No. 680599. Aspects of the work are also funded by the Engineering and Physical Sciences Research Council (EPSRC) of the UK under research grants (i) EP/V001752/1 'Industrial waste heat recovery using supercritical carbon dioxide cycles (SCOTWOHR)'; (ii) EP/P004636/1 'Optimising Energy Management in Industry (OPTEMIN)'; (iii) EP/K011820/1 related to the Centre for Sustainable Energy Use in Food Chains (CSEF), an End Use Energy Demand Centre funded by the Research Councils UK.

REFERENCES

- [1] M. White et al., Review of supercritical CO₂ technologies and systems for power generation, *Applied Thermal Engineering*, 2021, DOI: 10.1016/j.applthermaleng.2020.116447.
- [2] K. Brun, P. Friedman, R. Dennis, *Fundamentals and Applications of Supercritical Carbon Dioxide (sCO₂) Based Power Cycles*, 2017, ISBN 978-0-08-100804-1.
- [3] M. Mecheri, Y. L. Moullec, Supercritical CO₂ Brayton cycles for coal-fired power plants, *Energy*, 2016, DOI: 10.1016/j.energy.2016.02.111.
- [4] M. Marchionni, G. Bianchi, S. A. Tassou, Transient analysis and control of a heat to power conversion unit based on a simple regenerative supercritical CO₂ Joule-Brayton cycle, *Applied Thermal Engineering*, 2021 DOI: 10.1016/j.applthermaleng.2020.116214.
- [5] S. Bedogni, D1.2 – Report on Flexibility constraints, Load scenarios definition, 2018, URL: www.sCO2-flex.eu/documents/
- [6] Echogen power systems, URL: www.echogen.com/.
- [7] J. Marion et al., The STEP 10 MWe sCO₂ pilot plant demonstration, in: *Proceedings of the ASME Turbo Expo 2019*. DOI: 10.1115/GT2019-91917.
- [8] D. Freed et al., Progress update on the Allam cycle: Commercialization of Net Power and the Net Power demonstration facility, in: *14th Greenhouse Gas Control Technologies Conference Melbourne*, 2018.
- [9] 8 Rivers Capital, Allam cycle zero emission coal power plant, DOE Grant Proposal 89243319CFE000015, 2019.
- [10] F. Crespi et al., Supercritical carbon dioxide cycles for power generation: A review, *Applied Energy* (2017), DOI: 10.1016/j.apenergy.2017.02.048.
- [11] M. Marchionni et al., Techno-economic assessment of Joule-Brayton cycle architectures for heat to power conversion from high-grade heat sources using CO₂ in the supercritical state, *Energy*, 2018, DOI: 10.1016/j.energy.2018.02.005.
- [12] Y. Ahn et al., Review of supercritical CO₂ power cycle technology and current status of research and development, *Nuclear Engineering and Technology*, 2015, DOI: 10.1016/j.net.2015.06.009.
- [13] R. Fuller et al., Turbomachinery for supercritical CO₂ power cycles, *ASME Turbo Expo*, 2012, DOI: 10.1115/GT2012-68735.
- [14] A. J. Hacks et al., Operational experiences and design of the sCO₂-HERO loop, in: *3rd European Supercritical CO₂ Conference*, 2019, DOI:10.17185/dupublico/48906.
- [15] E. M. Clementoni et al., Startup and operation of a supercritical carbon dioxide Brayton cycle, *Journal of Engineering for Gas Turbines and Power*, 2014, DOI:10.1115/1.4026539
- [16] G. Bianchi et al., Design of a high-temperature heat to power conversion facility for testing supercritical CO₂ equipment and packaged power units, *Energy Procedia*, 2019, DOI: 10.1016/j.egypro.2019.02.109.
- [17] M. Marchionni et al., Review of supercritical carbon dioxide (sCO₂) technologies for high-grade waste heat to power conversion, *SN Applied Sciences*, 2020, DOI: 10.1007/s42452-020-2116-6.
- [18] S. A. Wright et al., Operation and analysis of a supercritical CO₂ Brayton cycle, 2010, DOI: 10.2172/984129.
- [19] M. Marchionni et al., An appraisal of proportional integral control strategies for small scale waste heat to power conversion units based on organic Rankine cycle, *Energy*, 2018, DOI: 10.1016/j.energy.2018.08.156.
- [20] J. J. Dyreby et al., Design and Part-Load Performance of Supercritical Carbon Dioxide Power Cycles, 2013, DOI: 10.1115/GT2013-95824.
- [21] D. Alfani et al., Part-load operation of coal fired sCO₂ power plants. in: *3rd European Conference on Supercritical CO₂ (sCO₂) Power Systems*, 2019. DOI: 10.17185/dupublico/48897.
- [22] F. Alshammari et al., Off-design performance prediction of radial turbines operating with ideal and real working fluids. *Energy Conversion and Management*, 2018, DOI: 10.1016/j.enconman.2018.06.093.
- [23] M. De Miol et al., Design of a single-shaft compressor, generator, turbine for small-scale supercritical CO₂ systems for waste heat to power conversion applications. *2nd European sCO₂ Conference 2018*. DOI:10.17185/dupublico/46086
- [24] Gamma Tech., *GT-SUITE Flow Theory Manual*, 2020.
- [25] E. Lemmon et al., NIST Standard Reference Database 23: Reference Fluid Thermodynamic and Transport Properties-REFPROP, National Institute of Standards and Technology, Standard Reference Data Program, Gaithersburg, 2018.
- [26] M. Marchionni et al., Numerical modelling and transient analysis of a printed circuit heat exchanger used as recuperator for supercritical CO₂ heat to power conversion systems, *App Ther Eng*, 2019, DOI:10.1016/j.applthermaleng.2019.114190.
- [27] A. Prosperetti, A generalization of the Rayleigh–Plesset equation of bubble dynamics. *Phys Fluids* 1982;25:409. DOI:10.1063/1.863775.
- [28] D. Brkić, Review of explicit approximations to the Colebrook relation for flow friction. *J Pet Sci Eng* 2011;77:34–48. DOI:10.1016/J.PETROL.2011.02.006.
- [29] S.S. Saravi, S.A. Tassou, An investigation into sCO₂ compressor performance prediction in the supercritical region for power systems, *Energy Procedia*, 2019, DOI:10.1016/J.EGYPRO.2019.02.098.
- [30] M. White, AI Sayma. A preliminary comparison of different turbine architectures for a 100 kW supercritical CO₂ Rankine cycle turbine 2018.
- [31] S. Son et al., Development of supercritical CO₂ turbomachinery off-design model using 1D mean-line method and Deep Neural Network. *Applied Energy*, 2020. DOI: 10.1016/j.apenergy.2020.114645.
- [32] H. Moustapha et al., Axial and radial turbines. *Conceptsnrec Com* 2003:10.
- [33] RH. Aungier, *Turbine Aerodynamics: Axial-Flow and Radial-Flow Turbine Design and Analysis*. ASME Press; 2006. doi:10.1115/1.802418.
- [34] NREC. RITAL | Preliminary Design n.d. <https://www.conceptsnrec.com/solutions/software/computer-aided-engineering/preliminary-design/rital>.
- [35] J. A. Nelder, R.Mead, A simplex method for function minimization. *The computer journal*, 1965, 7(4), 308-313.

THERMAL DESIGN OF LATENT HEAT THERMAL ENERGY STORAGE FACILITY WITH SUPERCRITICAL CO₂

Tomáš Melichar*

Research Centre Rez
Husinec-Rez, Czech Republic
Email: tomas.melichar@cvrez.cz

Karel Dočkal

Research Centre Rez
Husinec-Rez, Czech Republic

Otakar Frýbort

Research Centre Rez
Husinec-Rez, Czech Republic

Petr Hájek

Research Centre Rez
Husinec-Rez, Czech Republic

Radomír Filip

Research Centre Rez
Husinec-Rez, Czech Republic

ABSTRACT

Conversion of electric power to heat and from the stored heat back to power is the energy storage concept that allows high temperature and high-capacity accumulation (hundreds of MWh stored in the heat). Combination of the high temperature heat storage with use of the sCO₂ energy conversion cycle may provide highly efficient and very flexible energy storage system. An aluminum alloy was identified as a suitable accumulation material for the latent heat storage due to its high latent heat, appropriate melting point (577°C) and acceptable price. The energy storage system with Al-Si12 alloy as the heat storage material and the sCO₂ conversion cycle is being developed at CVR.

In this paper, design of a mock-up of the storage tank with the aluminum alloy, an electrical heating system and a sCO₂ heat exchanger will be presented. The storage tank with capacity of 300 kWh will be fabricated, connected to the sCO₂ experimental loop of CVR and operated at the relevant conditions to demonstrate capabilities of the energy storage concept. A thermal computational model that was developed to support design and optimization of the sCO₂/metal heat exchanger will be also presented. Based on the computational model results, feasibility of this concept for the high capacity energy storage will be discussed.

INTRODUCTION

Energy storage systems based on power-to-heat-to-power (P2H2P) concept have potential to accumulate high amount of energy (up to hundreds of MWh stored heat) for relatively long time periods comparing to other energy storage technologies. The P2H2P concept considers transformation of surplus electric

power to heat, storage of heat in the heat accumulation material and subsequent reversed heat to power conversion during increased electric energy demands using a thermal conversion cycle. Heat storage at high temperature level is essential to enhance thermal efficiency of the heat to power conversion cycle. Use of latent heat storage using phase change materials (PCM) as the heat accumulation material is an option to allow high-temperature and high-capacity energy storage. Comparing to sensible heat storage systems with lower specific heat capacity, the PCM-based storage tanks can have significantly lower dimensions. This is an important advantage, especially considering large systems with very high capacity, where costs of the heat storage vessel and the accumulation material itself forms significant part of total acquisition costs. A large number of available PCMs with various properties were identified [1]. Operational parameters and design of the heat storage system are influenced especially by melting point, latent heat and density of selected PCM but also other properties such as thermal (specific heat, thermal conductivity), physical (low vapor pressure at operational temperature, low volume variation during phase change), chemical (non-corrosiveness, chemical stability, compatibility with structural materials, non-poisonous) and economic (availability in abundant supply, cost per kWh of stored energy [2]) has to be considered.

An energy storage system with PCM and supercritical CO₂ (sCO₂) cycle for heat to power conversion is being investigated at Research Centre Rez (CVR), Czech Republic. In the current stage, a scale-down mock-up of an accumulation system is being developed. The system will be composed of a storage vessel equipped with electric heaters for charging and heat exchanger for discharging. The heat to power conversion cycle will be

* corresponding author(s)

simulated by existing large-scale experimental facility sCO₂ loop, built and operated by CVR. The sCO₂ loop facility provides wide range of operation parameters represented by sCO₂ temperature up to 550 °C, pressure up to 25 MPa and mass-flow rate up to 0.35 kg/s [3]. The binary eutectic alloy of aluminum and silicon (AlSi12) was selected as the accumulation material. This alloy was selected due to melting point compatible with the sCO₂ cycle (576 °C) [4], high heat of fusion (560 kJ/kg) [4] and acceptable price and availability. The compact storage tank with capacity of 300 kWh_t and both charge and discharge power of 50 kW was designed and will be fabricated and operated at CVR. The goal of the activity is to demonstrate the PCM-based energy storage system that coupled with the sCO₂ cycle in a small-scale and to demonstrate thermal performance during cyclic loading.

In this paper, thermal and mechanical design of the storage vessel equipped with the electric heaters and sCO₂ heat exchanger will be presented. Particular attention is paid on thermal analyses supporting design of the storage tank, that were carried out using a dedicated numerical model based on finite volume method (FVM) coupled with analytical approach. The model allows transient modeling of heat transfer and phase change of the accumulation materials and convective heat removal in the sCO₂ heat exchanger. The computational model, numerical results and final design of the storage tank will be reported. Moreover, feasibility of the full-scale storage system will be discussed based on obtained results.

SYSTEM DESCRIPTION

In this section, the experimental facility will be described. Although the main focus is placed on the storage part of the system, the existing sCO₂ loop that provides required operational parameters will be described as well. The sCO₂ loop is designed as a simple Brayton cycle with regeneration, where a turbine is replaced with a regulation valve.

The scheme of the investigated system is shown in Figure 1. The storage part of the system is formed by the storage vessel (SV). The SV is filled with approx. 2 000 kg of AlSi12 eutectic alloy. Charging of the accumulator is performed using electric resistive heaters (EH) that are transforming electric power to heat. The EH in the form of conventional resistive heating cartridges composed of a resistive wire, ceramic insulation and metal coating are immersed directly in the accumulation material. During discharging, the accumulated heat is removed using a thermal cycle with sCO₂. For this purpose, existing sCO₂ loop will be coupled with the storage vessel. The interface between the AlSi12 and sCO₂ is formed by heat exchanger (HX), which is also placed directly in the storage vessel. Design, layout and parameters of the storage vessel, heaters and heat exchanger will be presented in details in the following sections.

During the discharging operational regime, the sCO₂ inlets to the SV from the high pressure side of the sCO₂ loop. The sCO₂ parameters at the inlet to the SV are pressure of 25 MPa, mass-flow rate of 0.3 kg/s and temperature of approx. 420 °C. The inlet temperature is controlled by the existing electric heater

of the sCO₂ loop (H1 in Figure 1). The sCO₂ flows through the heat exchangers HX and is heated to 550 °C (that corresponds to 50 kW of removed heat considering mass-flow rate of 0.3 kg/s). This temperature is given by operational limits of the sCO₂ loop, but at the same time, is relevant the temperature level that is expected in real sCO₂ energy cycles. The hot sCO₂ goes to cooler C2. This cooler will be used to control maximum temperature of sCO₂ below 550 °C to protect the upstream components of the sCO₂ loop. The regulation valve RV simulates expansion in a turbine. The pressure is regulated to approx. 12.5 MPa. The sCO₂ then flows to existing oil cooler C3, where the fluid is cooled to 450°C (limit temperature of regenerative heat exchangers). After the cooler C3, high-temperature (HTR) and low-temperature (LTR) regenerative heat exchangers are located. After the LTR, the sCO₂ is cooled in water cooler C1 to approx. 25 °C. The forced circulation in the loop is ensured by pump P that ensures pressure in the high pressure part. The sCO₂ is preheated in the high-pressure side of both LTR and HTR.

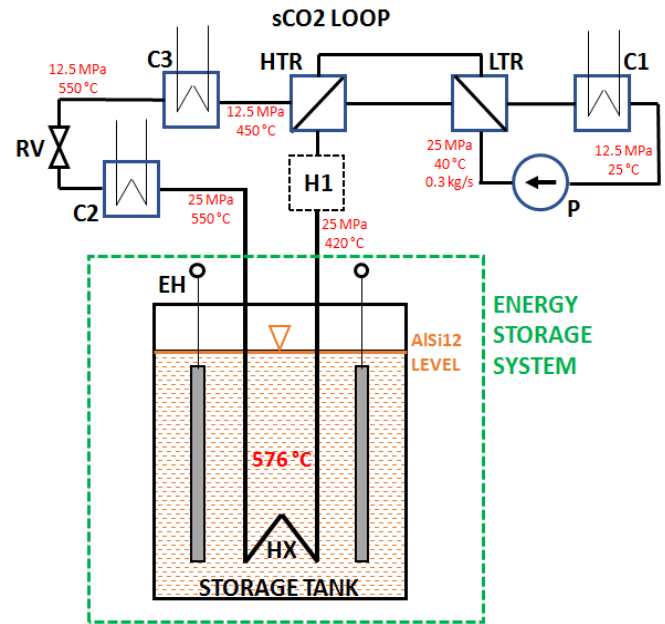


Figure 1: Scheme of the mock-up storage system

The main parameters of the mock-up storage system are summarized in Tab. 1.

Table 1: Main parameters of the mock-up storage system

Accumulation material	AlSi12
Volume of AlSi12	0.75 m ³
Operational temperature	550 – 600 °C
Nominal charging/discharging power	50 kW
Charging/discharging time	5 hours
Capacity of the storage vessel	300 kWh _t
sCO ₂ inlet temperature	420 °C
sCO ₂ nominal pressure	25 MPa
sCO ₂ nominal mass-flow rate	0.3 kg/s

As mentioned, the sCO₂ loop is designed as a simple Brayton cycle operated at the relevant sCO₂ thermal cycles parameters. It is also expected that the same technology will be used for charging of a real storage system (resistive electric heaters). Thus, the layout of the whole experimental system is practically identical to possible future real scale energy storage system. The experimental facility will therefore allow short term demonstration of the storage system in a small scale.

DESIGN OF THE STORAGE VESSEL

Dimensions of the storage vessel are based on volume of accumulation material that is needed to store required amount of heat. The SV volume *V* can be calculated using the following formula:

$$V = \frac{t \cdot P \cdot 3600}{h_f \cdot \rho}$$

Where *t* is time of charging / discharging (5 hours), *P* is charging / discharging power (50 000 W), *h_f* is heat of fusion of AlSi12 (560 000 W/kg) and *ρ* is density of AlSi12 (2700 kg/m³). Resulting minimum volume of AlSi12 is 0.6 m³. The volume is increased by 25% to 0.75 m³ compensate possible drop of heat of fusion that might be caused by impurities in the accumulation material. It is also expected that not all the accumulation material will be solidified during discharging. The volume corresponds to 2025 kg of AlSi12. The dimensions of the SV are internal diameter of 1.09 m and height of 1 m. The AlSi12 level corresponds to height of 0.8 m, the volume above the level will be filled with an inert gas (argon). The cover gas will ensure inert atmosphere in the SV that will reduce oxidation. Moreover, the cover gas will compensate volume expansion of the accumulation material during the phase change. Pressure slightly higher than the atmospheric will be kept in the SV to avoid penetration of the air inside the SV.

The CAD model of the SV with the main components is shown in Fig. 2. The HX is composed of U-tubes, the sCO₂ is distributed to the individual tubes in a manifold located above the AlSi12 level. The heaters are guided to the SV through an upper lid that is connected to the vessel by a flange. The lid is also equipped with holes for thermocouples and an inert gas pipeline. The SV is filled and drained from a dedicated filling vessel using a filling tube that ends slightly above the vessel bottom. Draining is performed by increasing of the inert gas pressure above the level and pushing AlSi12 to flow out through the filling tube. The external surface of the SV will be equipped with a thermal insulation.

One of the obstacles for long term operation of the systems is degradation of structural materials in the AlSi12 environment. The materials must be resistant to corrosion but at the same time, they must withstand mechanical loading. Several materials were identified as potentially applicable for the HX as well as for the other components that are facing the AlSi12. For example, Al based ceramics such as Al₂O₃, AlN or Si₃N₄ that could be used

as coatings showed good resistance [5], [6]. Boron Nitride coatings tested on crucibles with AlSi12 showed good results for 720 cycles while signs of corrosion (formation of intermetallic layers) were found on uncoated stainless-steel (SS) samples according to [7]. A refractory material TCON® (SiC, Al₂O₃ and AlSi12 composition) with good corrosion and wear resistance was developed specifically for Al containers [8]. A plasma-sprayed ceramic coating was used for a latent heat storage system prototype with AlSi12 and a Stirling engine. The coating showed good corrosion resistance but some cracks in the coating were observed after the experiments [9]. Metal materials are expected to be less resistant, although titanium or niobium showed relatively good behavior [10]. Even though a long-term operation of the experimental facility is not expected, an extensive materials research is needed before implementation of energy storage systems. A dedicated research of corrosion resistance of preselected materials for the HX was initiated at CVR in 2020.

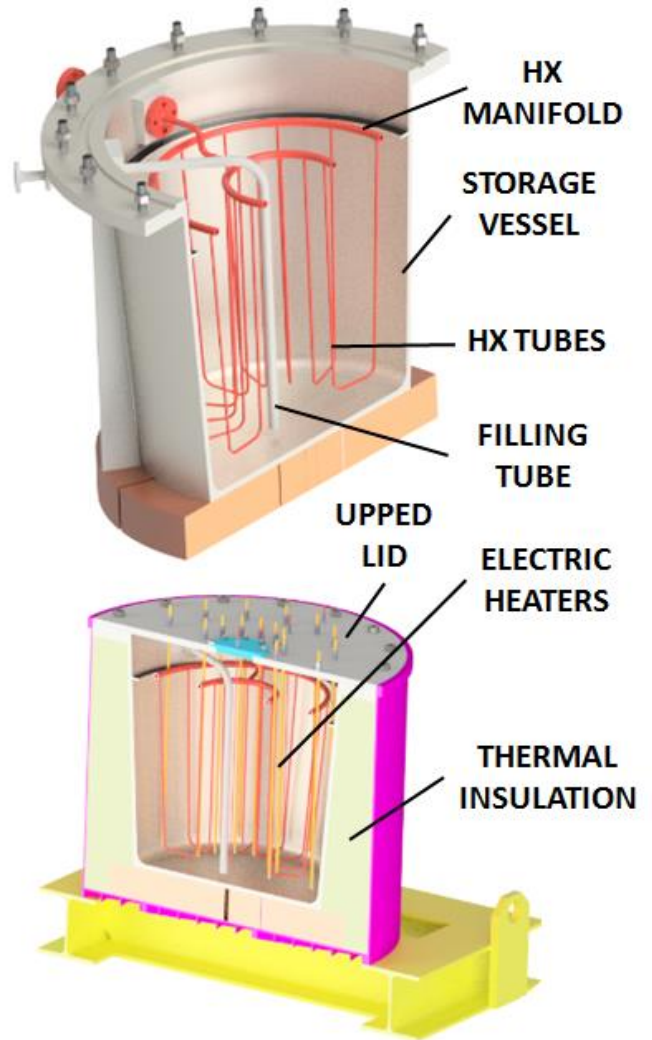


Figure 2: Model of the storage vessel

COMPUTATIONAL MODEL

In this section, the computational model that was prepared and utilized for detailed thermal analyses and optimization of the individual components will be described. The main motivation of the model development is to allow modelling of the whole vessel behavior at reasonable computational time and with acceptable accuracy. The model must consider transient heat transfer in the accumulation material including solidification and melting during both operational regimes (charging and discharging). Therefore, both the sCO₂ heat exchanger and the electric heaters must be modelled. Based on 3D nature of the computational domain and complexity of the physical behavior, Computational Fluid Dynamic (CFD) method seems to be suitable for this purpose. However, due to relatively large geometric size of the domain and long time periods to be simulated, full CFD modelling of both the AISi12 and sCO₂ domains was identified as inappropriate due to very high computational time. It was therefore proposed to simplify modelling of the sCO₂ heat transfer in the HX tubes. For this purpose, an approach represented by CFD modelling of the AISi12 domain coupled with simplified modelling of the convective heat transfer in the HX tubes was adopted. The simplified modeling of the convective heat transfer in sCO₂ based on analytical and empirical formulas is acceptable as number of correlations for heat transfer and pressure drop in tubes valid for relevant parameters is available. Moreover, there are significant benefits coming from use of the coupled model. A full CFD model would require relatively fine mesh (estimated up to dozens of millions mesh elements) and small time steps (below 1 s) to fulfill the CFL condition while relatively coarse mesh and time steps of up to dozens of seconds are sufficient for the coupled model. This will result in many times lower computational time and hardware requirements. The main characteristics of both methods are summarized in Tab. 2.

Table 2: Main characteristics of computational methods

	Full CFD	Coupled
Mesh size	High	Low
Time step	Low	High
Computational time	Very high	Low
Accuracy	High	Acceptable

The whole computational domain is shown in Fig. 3. Due to axisymmetric layout, just 12° sector of the vessel is considered with symmetry boundary condition (BC) applied on the lateral walls of the model. The heaters are simply modelled using heat flux boundary condition. As detailed modelling of temperature field in the heaters is not the fundamental issue of these analyses, thus the heaters structure is not included. The sCO₂ HX is represented by the convection BC applied on the channel surface. The zero heat flux BC representing the heat insulation is applied on the external surfaces. The CFD model therefore consists of just one fluid volume representing AISi12. The CFD model is prepared using CFD code ANSYS FLUENT 19.1.

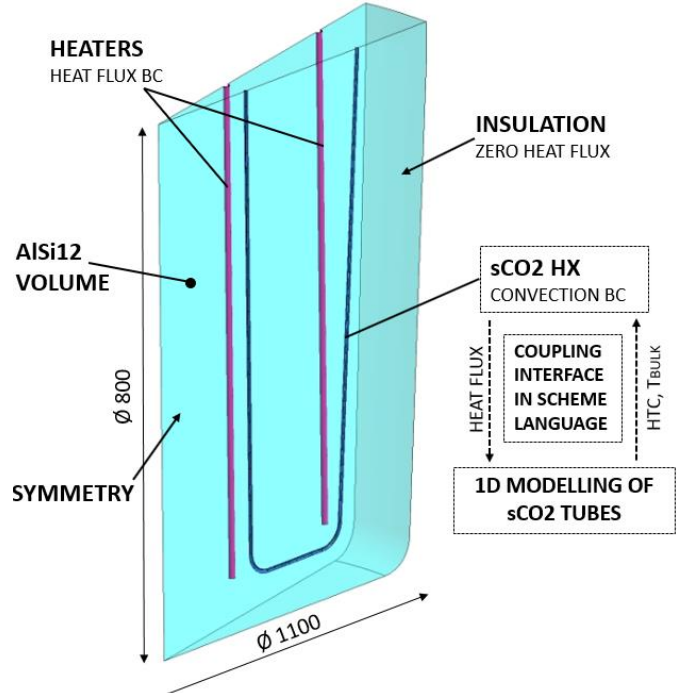


Figure 3: Computational domain

External 1D modeling of the sCO₂ HX channel is based on calculation of sCO₂ bulk temperature (T_{BULK}) and heat transfer coefficient (HTC) as an input for the convection BC in the CFD solver. The interface surface (the HX channel wall) is artificially split in smaller faces with respect to the flow direction. As thermal behavior of both fluids depends on one another, the parameters must be transferred in both ways. The coupling scheme is also indicated in Fig. 3. The 1D modeling as well as the communication between the CFD model and 1D model is ensured by Scheme programming language [11] that is fully compatible with the ANSYS Fluent environment. On the first face of the channel wall (corresponding to sCO₂ inlet), T_{BULK1} and HTC are set manually. On the consequent faces, T_{BULKi} is calculated from heat flux on the previous face given by the CFD solver according to the following formula:

$$T_{BULK\ i+1} = \frac{q_i \cdot A_i}{\dot{m} \cdot c_p} + T_{BULK\ i}$$

Where q_i is heat flux (W/m²), A_i is face area (m²), \dot{m} is mass flow rate in one HX channel (kg/s) and c_p is sCO₂ heat capacity. After every time step i , the set of q_i values is transferred from CFD model to Scheme model, where corresponding $T_{BULK\ i}$ values are being calculated. After that, $T_{BULK\ i}$ values then are transferred back to CFD model where they are used as the parameters of the convection BC. After this procedure, simulation of the next time step $i + 1$ can start.

It was found that HTC values are not significantly affected by change of corresponding sCO₂ bulk temperature and even less by pressure loss in the pipe. For this reason, constant value of

HTC was used for all HX channel surface. The HTC value was calculated from well-know Gnielinski correlation that is applicable for tubes geometries [3] and relevant ranges of Re and Pr numbers:

$$HTC = \frac{Nu \cdot \lambda}{D_h}$$

$$Nu = \frac{\left(\frac{f}{8}\right) \cdot (Re - 1000) \cdot Pr}{1 + 12.7 \cdot \left(\frac{f}{8}\right)^{0.5} \cdot \left(Pr^{\frac{2}{3}} - 1\right)}$$

$$f = (0.79 \cdot \ln Re - 1.64)^{-2}$$

for $Pr > 0.7$ and $Re > 2300$

Where λ is sCO₂ thermal conductivity and D_h is hydraulic diameter. Partial results and parameters can be seen in Tab. 3. The sCO₂ properties were considered for constant sCO₂ temperature of 500 °C and are summarized in Tab. 4.

Table 3: sCO₂ parameters

Total mass flow rate	0.3 kg/s
Mass flow rate per channel	0.02 kg/s
Hydraulic diameter	0.006 m
Flow velocity	4.3 m/s
Reynolds number	111 200
Prandtl number	0.75
Nusselt number	202
Heat transfer coefficient	2160 W/m·K

As mentioned, ANSYS Fluent was chosen as the numerical solver. As flow of AlSi12 is not modeled, less complex code based on FEM or FVM method could be used. However, the benefit of ANSYS Fluent code is the existing solidification / melting module [13] that has been already validated on solidification experiments in similar geometry [14]. The final computational grid is composed of 430 000 polyhedral elements. As only the energy equation is being resolved in the AlSi12 domain, the mesh requirements are not very strict. The 1D model is discretized to 67 face elements with an average length of 25 mm. The following settings and simplifications were adopted.

- Solidification / melting module is turned on.
- Flow equations are disabled. Therefore, natural convection of AlSi12 is not considered.
- Spatial discretization of second order was used.
- Time step of 30 s was considered.
- Constant materials properties were considered (Tab. 4). This is acceptable as the SV is operated in relatively small temperature range (approx. 550-600 °C).
- The HX tube structure is considered using “shell conduction” option [13].
- Constant HTC is assumed in the sCO₂ HX channels. However, relatively low effect of appropriate sCO₂ operational parameters on HTC was observed (less than 10%).

- 3D model has 430 000 finite volumes, 1D model has 67 elements.

Used material properties are summarized in Tab. 4.

Table 4: Used materials properties

AlSi12 Heat of Fusion	560 000 kJ/kg [4]
Melting point	576 °C [4]
AlSi12 Density	2 700 kg/m ³ [4]
AlSi12 Thermal Conductivity	180 (solid) 70 (liquid) [4]
AlSi12 Heat Capacity	1 038 J/kg·K (solid) 1 741 J/kg·K (liquid) [4]
sCO ₂ Density	164.9 kg/m ³ [12]
sCO ₂ Thermal Conductivity	0.061 W/m·K [12]
sCO ₂ Heat Capacity	1 249 J/kg·K [12]
sCO ₂ Dynamic viscosity	0.0000368 Pa·s [12]

HEAT EXCHANGER DESIGN

Proper design of the HX is essential to ensure required operational parameters and function of the facility. The HX is placed in the accumulation material and is in operation during discharging operational regime, when the accumulated heat in AlSi12 is removed by sCO₂. The fluid outgoing from the HX flows towards the thermal circuit for heat to power conversion.

At the beginning, a simple “0D” model of the HX was prepared for preliminary estimation of the basic dimensions of the HX. The number and diameter of tubes was designed in order to achieve reasonable flow velocities in the tubes (ensuring sufficiently high HTC and acceptably low pressure drop). Internal tube diameter of 6 mm and 15 tubes result in mass-flow rate of 0.02 kg/s and average velocity of 4.3 m/s in each tube. Regarding the tubes length, it was found that relatively short length of tubes is needed to remove required amount of heat power. This is given by relatively intense heat transfer at both sides of the HX. Moreover, the length of the tubes is also given by the nature of the SV behavior. As the accumulation material is operated at practically constant temperature during the phase change, higher heat flux occurs at the beginning of the tube, where temperature difference between the fluids is higher. At the outlet part of the HX tube, sCO₂ is heated to temperature close to the AlSi12 and the heat transfer is not too efficient. For this reason, the tubes are designed as a simple U-shape with length of 1.7 m.

In the next phase, the HX tubes layout was optimized using the complex computational model described in the previous section. The point of these analyses was to propose exact dimensions and to verify the component behavior. Moreover, as the tubes are considered as U-shaped, two positions of sCO₂ inlet and outlet are possible. If the sCO₂ enters the HX through the inner leg, the solidification will start from the center of the vessel. Conversely, if the cold sCO₂ enters the outer leg, the solidification will start

from the SV wall. Analyses of both options were carried out to evaluate temperature field and freezing process. The results are shown in Fig. 4 (for inlet in the outer leg) and in Fig. 5 (for inlet in the inner leg). The solidified fraction and temperature field was depicted for two times (the transient analyses started from constant temperature of AlSi12 of 600 °C).

In each picture, left side shows solidified fraction in the SV (blue color corresponds to solidified part while red color to liquid fraction). The right side of each picture shows temperature field.

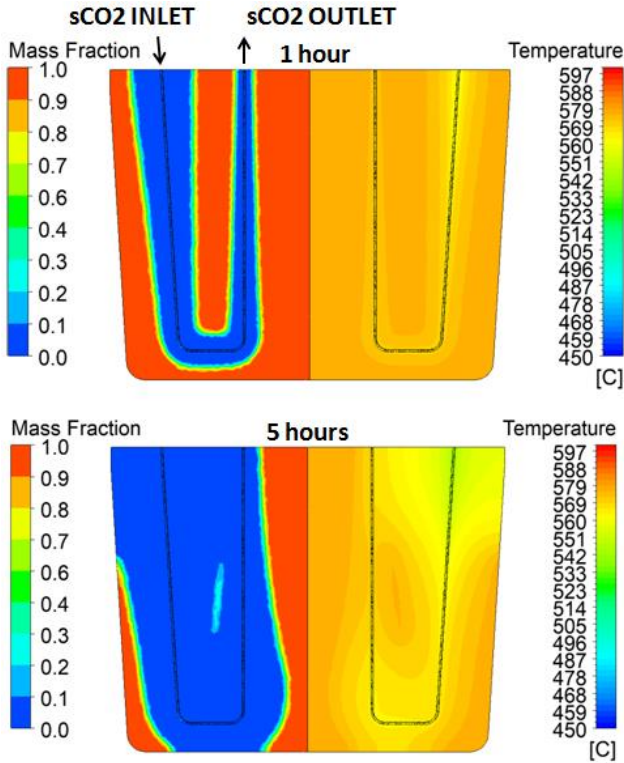


Figure 4: Solidification process and temperature field during discharging for sCO₂ inlet located in the outer leg of the HX

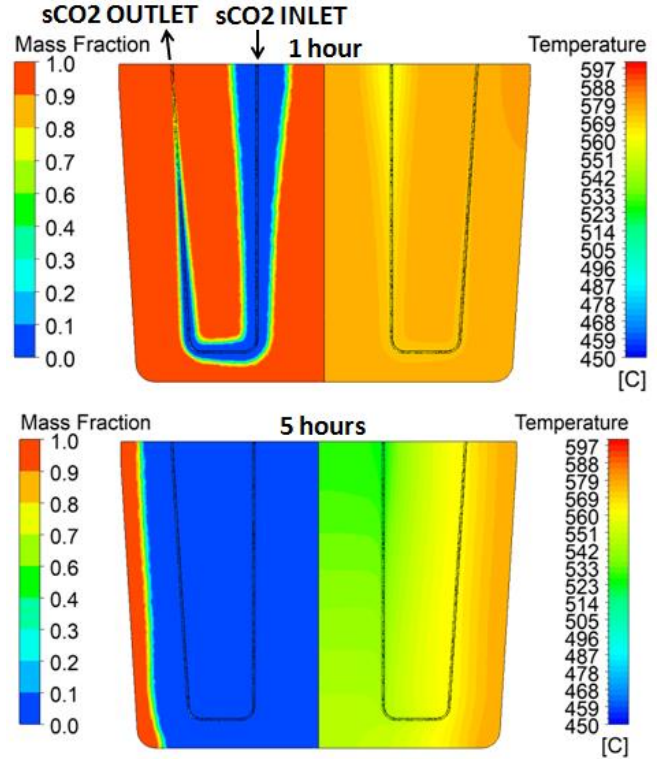


Figure 5: Solidification process and temperature field during discharging for sCO₂ inlet located in the inner leg of the HX

For the final layout, the option with inlet located in the inner leg was selected due to benefits that can be seen in Fig. 5 below. It can be observed that liquid fraction remain in the outer part of the SV. If the AlSi12 stays liquid in this location during both operational regimes, it can reduce additional stresses on the SV structure caused by volumetric change during the phase change. The disadvantage of this layout is the temperature distribution, which is less uniform comparing to the option with inlet located in the outer leg.

The final layout of the HX is shown in Fig. 6. The main parameters of the HX are then summarized in Tab. 5. Based on the analyses, it was found that inlet sCO₂ temperature of 420 °C will lead to discharging power of approx. 50 kWt.

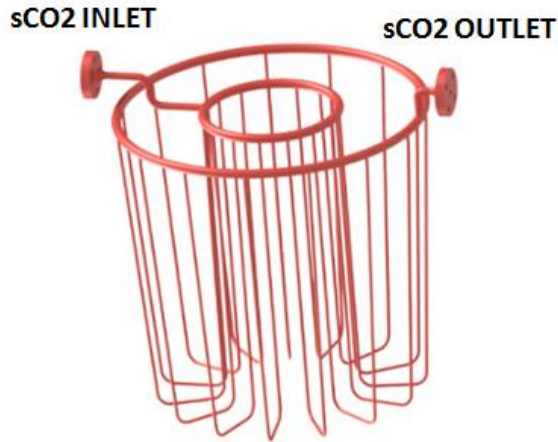


Figure 6: Layout of the HX

Table 5: Layout of the HX

Number of U-tubes	15
Inlet sCO ₂ temperature	420 °C
Tubes dimension	10 × 2 mm
Tube length	1.7 m
Total tubes length	25.5 m
Total heat transfer area	0.64 m ²
Heat power	50 kW

HEATERS DESIGN

The second important activity related to the SV thermal design is connected with layout of the heaters that are used for charging of the SV. The heaters are based on an available technology (electric resistive heating rods). The rods will be placed directly in the accumulation material. Proper layout of EH is essential to assure uniform temperature field and to avoid overheating of AlSi12. The first proposal of the EH is based on allowable maximum heat flux on the heaters surface, which should not exceed 16 W/cm². Taking into consideration this parameter, heating rods of outer diameter of 12 mm and active length of 0.78 m were selected. Based on this, it is clear that relatively low number of heaters would be needed to ensure required power input. However, the temperature field has to be examined to decide final number and positions of the heaters. For this purpose, the computational model was employed.

In Fig. 7, development of temperatures in the SV is depicted. Two layouts were considered (with 15 heaters and with 30 heaters). Fig. 7 shows minimum, maximum and average temperature and liquid fraction development. The continuous lines represent layout with 30 heaters, dashed lines represent layout with 15 heaters. It is obvious that temperature field for layout with 30 heaters is more uniform, where the maximum temperature difference does not exceed 25 °C. Moreover, the maximum temperature grows rapidly for layout with 15 heaters at the end of the charging cycle even before the all AlSi12 is melted. For this reason, the layout with 30 heaters was selected.

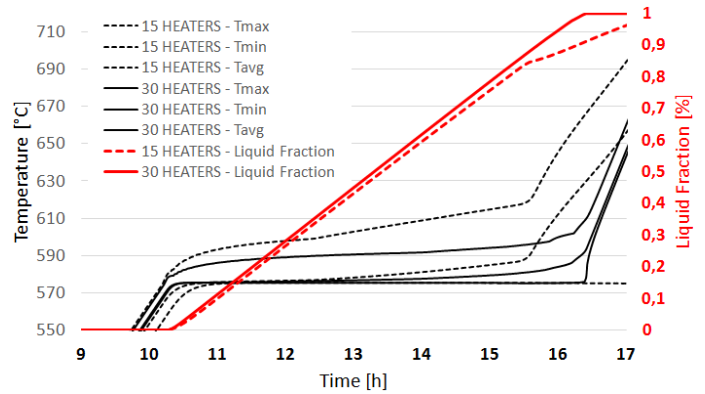


Figure 7: Layout of the HX

Using the computational model, exact positions of the heaters were optimized. The heating rods are split in two groups of 15 pieces that placed at two diameters. The inner heaters will be operated with lower power (1.09 kW per rod), while power of the outer heaters will be 2.26 kW. The main parameters of the EH are summarized in Tab. 6.

Table 6: Layout of the HX

Number of heating rods	30
Heating rods diameter	420 °C
Heating rods length	10 × 2 mm
Total power	50 kW
Heaters power	2.26 kW (outer) 1.09 kW (inner)
Power density	7.7 W/cm ² (outer) 3.7 W/cm ² (inner)

As mentioned, the sCO₂ loop is designed as a simple Brayton cycle operated at the relevant sCO₂ thermal cycles parameters. It is also expected that the same technology will be used for charging of a real storage system (resistive electric heaters). Thus, the layout of the whole experimental system is practically identical to possible future real scale energy storage system. The experimental facility will therefore allow short term demonstration of the storage system in a small scale.

CYCLE SIMULATION

Using the optimized geometry, the final model was used for simulation of complete cycle composed of charging and discharging of the SV. The simulation started from cold state (20 °C) at time 0 h (the simulation thus corresponds to the “first” charge as the other charges will start from preheated vessel). The SV was charged for 12.5 hours with constant heating power of 50 kW. After that, the heaters were turned off and the regime was switched to discharging. The SV was then discharged for 5 hour to time 17.5 h. Development of selected parameters is shown in Fig. 8. Liquid fraction development is depicted with red line. It can be seen than the maximum ration of liquid fraction was 95% at the end of charging. Black continuous line indicates average temperature of AlSi12 while black dashed line show outlet

temperature of sCO₂ (constant mass-flow rate was considered during the whole cycle). The blue lines represent heat power of the SV. It can be seen that discharging power is slightly higher than 50 kW. This can be compensated by decrease of sCO₂ flow rate or by increase of sCO₂ inlet temperature.

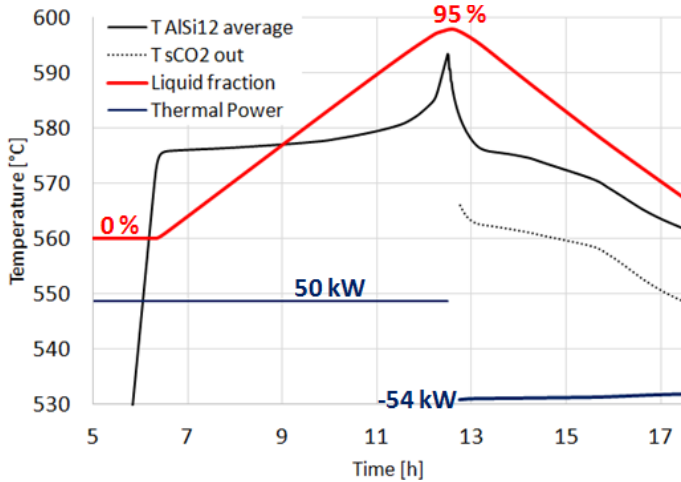


Figure 8: Time development of parameters in the storage vessel during the first cycle

Contours of liquid fraction and temperature field in the vessel during the cycle for four times of the cycle are shown in Fig. 9.

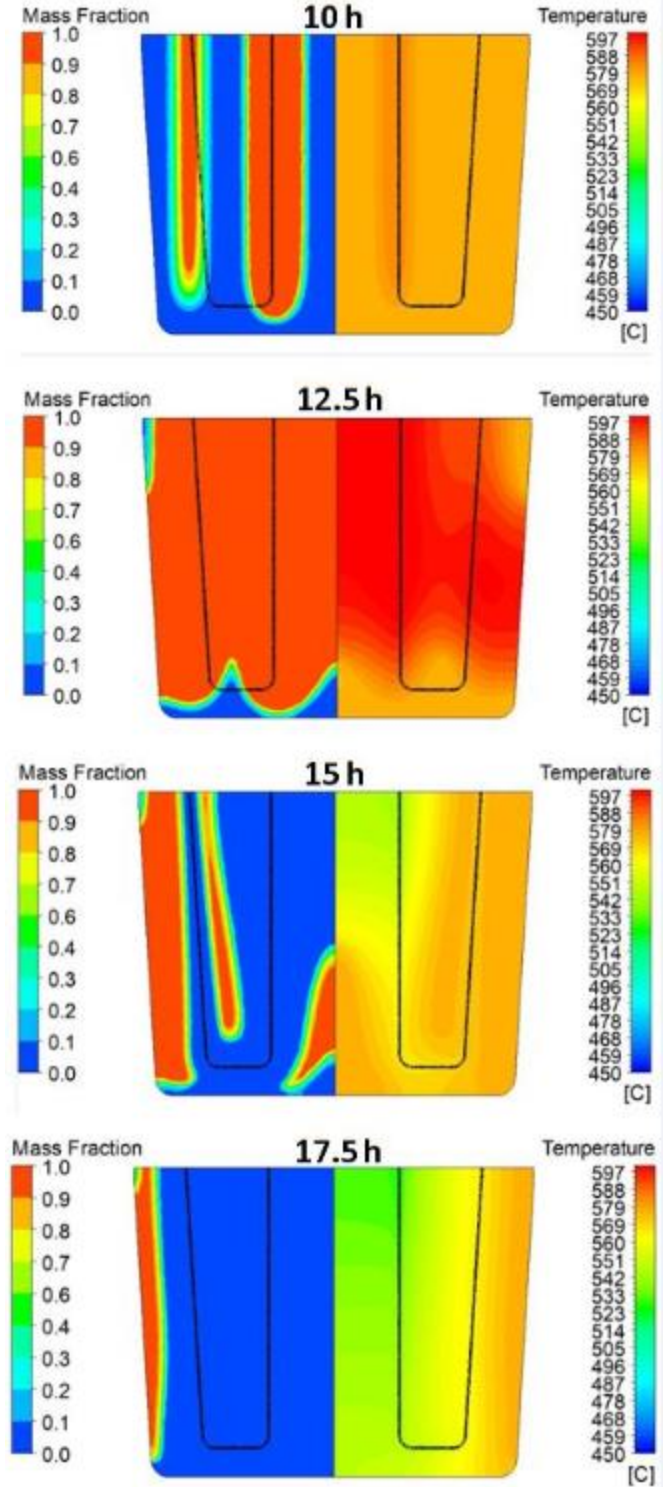


Figure 9: Solidification process and temperature field during the first cycle

CONCLUSIONS

The experimental facility allowing transformation of electric energy to heat, heat storage in latent heat of AlSi12 and subsequent heat removal using the sCO₂ thermal cycle was designed. The facility will allow demonstration of the storage system in the small scale. The dedicated numerical thermal model of the storage vessel was developed and applied to support the facility design. The following findings and outcomes were achieved.

- The numerical model that combines 3D modeling of the AlSi12 volume including phase change and 1D modeling of the sCO₂ heat exchanger was employed. The model allows simulation of behavior of the whole vessel for relatively long time periods at reasonable computational time.
- AlSi12 seems to be suitable accumulation material from the thermal point of view (high latent heat, high thermal conductivity, suitable melting point). However, structural materials or possible coatings degradation is significant obstacle for the long-term operation.
- The design supporting calculation showed significant benefits of the concepts regarding the components design. The heat exchanger requires small heat transfer area and thus low amount of material. This gives significant benefits comparing to other high capacity storage systems (such as rock-based or molted salt-based ones), where the heat exchangers forms significant cost of the facility.
- The computational model results showed suitable temperature and freezing front development during an operational cycle. Based on the results, operation of the facility seems to be feasible.
- Before implementation of larger systems, great focus should be placed on safety aspects. Even though the storage vessel will be operated at atmospheric pressure, high pressures are expected at the secondary fluid side (sCO₂). Possible rupture of the HX tube may lead in abrupt pressure increase in the storage vessel and subsequent accident. The HX tubes are exposed not only to internal pressure and secondary thermo mechanical stresses but also to additional stresses caused by AlSi12 expansion during phase change. Therefore, special attention must be paid on this issue.

As the next steps, the storage vessel will be fabricated and connected to the existing sCO₂ loop. Performance of the facility will be experimentally evaluated. Dedicated materials test will be carried out in the relevant AlSi12 environment to support materials selection. Moreover, the storage vessel components should be studied from the mechanical point of view.

NOMENCLATURE

CAD	Computer Aid Design
CFD	Computational Fluid Dynamic

CFL	Courant–Friedrichs–Lewy condition
CVR	Research Centre Rez
EH	Electric Heaters
FEM	Finite Elements Method
FVM	Finite Volumes Method
HX	Heat Exchanger
HTC	Heat Transfer Coefficient
HTR	High Temperature Recuperator
LTR	Low Temperature Recuperator
P2H2P	Power to Heat to Power
PCM	Phase Change Materials
sCO ₂	Supercritical Carbon Dioxide
SS	Stainless Steel
SV	Storage Vessel

ACKNOWLEDGEMENTS

This works was supported by TACR THETA2, project no. TK02030059 (Efekt).

REFERENCES

- [1] Kenisarin, M. M. (2010). High-temperature phase change materials for thermal energy storage. *Renewable and Sustainable Energy Reviews* 14 (2010) 955–970.
- [2] Zhou, C, Wu, S. Medium- and high-temperature latent heat thermal energy storage: Material database, system review, and corrosivity assessment. *Int J Energy Res.* 2019; 43: 621– 661. <https://doi.org/10.1002/er.4216>
- [3] Vojacek, A., Dostal, V., Goettelt, F., Rohde, M., and Melichar, T. (2019). Performance Test of the Air-Cooled Finned-Tube Supercritical CO₂ Sink Heat Exchanger. *ASME. J. Thermal Sci. Eng. Appl.* June 2019; 11(3): 031014. <https://doi.org/10.1115/1.4041686>
- [4] Wang X, Liu J, Zhang Y, Di H, Jiang Y. Experimental research on a kind of novel high-temperature phase change storage heater. *Energy Convers Manage* 2006;47(15–16):2211–22
- [5] Y. Zhao, H. Liu, C. Zhao, Experimental study on the cycling stability and corrosive property of Al-Si alloys as phase change materials in high-temperature heat storage, *Solar energy Materials and Solar Cells* 203 (2019) 110165.
- [6] R. Fukahori, T. Nomura, Ch. Zhu, N. Sheng, N. Okinaka, T. Akiyama: Thermal analysis of Al–Si alloys as high-temperature phase-change material and their corrosion properties with ceramic materials. *Applied Energy* 163 (2016) 1-8
- [7] A. Dindi, N.L. Ferber, D. Gloss, E. Rilby, N. Calvet: Compatibility of an Aluminium-Silicon metal alloy-based phase change material with coated stainless-steel containers. *Journal of Energy Storage* 32 (2020) 101961.
- [8] K.M. Peters, R. M. Cravens, J. G. Hemrick: Advanced ceramic composites for improved thermal management in molten aluminum applications. *Energy Technology Perspectives, TMS (The Minerals, Metals & Materials Society)*, 2009, pp. 241-247.

- [9] J. E. Rea et al.: Prototype latent heat storage system with aluminum-silicon as a phase change material and a Stirling engine for electricity generation. *Energy Conversion and Management* 199 (2019) 111992.
- [10] M. Yan, Z. Fan, Durability of materials in molten aluminum alloys, *Journal of Materials Science* 36 (2001) 258-295.
- [11] Dybvig, R. Kent, *The Scheme Programming Language*, Fourth Edition, 2009 (<https://www.scheme.com/tspl4/>)
- [12] NIST Standard Reference Database (REFPROP) v 9.0
- [13] Ansys Inc., 2013. *Ansys Fluent 15.0 - Theory Guide*. ANSYS Inc., USA.
- [14] Profir, M., Moreau, V., Melichar, T., 2020. Numerical and experimental campaigns for lead solidification modelling and testing. *Nuclear Engineering and Design* 359, 110482.

MICROSTRUCTURAL EVALUATION OF PRESELECTED STEELS FOR TURBINE AFTER SUPERCRITICAL CO₂ EXPOSURE

Lucia Rozumová*

Centrum vyzkumu Rez s.r.o.
Hlavní 130, Husinec-Rez, Czech Republic
Email: lucia.rozumova@cvrez.cz

Tomáš Melichar*

Centrum vyzkumu Rez s.r.o.
Hlavní 130, Husinec-Rez, Czech Republic
Email: tomas.melichar@cvrez.cz

Ladislav Velebil

Centrum vyzkumu Rez s.r.o.
Hlavní 130, Husinec-Rez, Czech
Republic

ABSTRACT

The energy conversion cycles with supercritical carbon dioxide (sCO₂) are being considered as an innovative technology with potential for replacement of conventional steam cycles within various applications such as nuclear, fossil or renewable energy resources. Due to extreme operational conditions including temperatures above 550°C and pressures up to 25 MPa, proper selection of materials is essential for a suitable design of the thermal circuit. Several materials that were identified as potentially suitable for the main components of the sCO₂ circuits were exposed in the sCO₂ relevant conditions in the sCO₂ experimental loop at Research Centre Rez (CVR). The experimental conditions were represented by the sCO₂ temperature of 550°C, pressure of 25 MPa, flow conditions and 1000 hours of exposure. Moreover, an additional test section where the sCO₂ flow velocity up to 100 m/s was achieved was designed and utilized to simulate turbine relevant conditions.

Suitability of the materials preselected for the sCO₂ turbomachinery will be evaluated and discussed in this paper. For the experiments, four types of materials (FB2, 17-4-PH, 625M, IN718) were selected. After the exposure, the corrosion behaviour and oxidation of the materials was investigated including surface analyses and cross sections examination. The paper presents the experimental parameters including the high velocity test section design. The materials degradation will be evaluated as well as the effect of the high velocity flow.

INTRODUCTION

The worldwide interest in the supercritical dioxide power cycle has increased steadily in the last decade. The use of CO₂ as a working fluid in a power cycle has been proposed by several researchers as a novel and promising cycle. The possibility of high efficiency is very encouraging. Benefits of smaller

turbomachinery and other parts compared to the parts of conventional steam cycles are obvious [1].

As a kind of efficient energy conversion system, the supercritical carbon dioxide (sCO₂) power generation system attracts increasing attention due to the advancement of its compact structure and the potential to improve the conversion efficiency. The use of carbon dioxide (CO₂) as a working fluid might produce higher efficiencies comparing to other gases due to unique thermodynamic properties (especially density changes near to the critical point) [2]. Supercritical carbon dioxide (sCO₂) is currently being considered as a working fluid for a Brayton cycle in next generation power systems for uses across nuclear, solar, and fossil power sources [3, 4, 5].

The safety is a critical for the design and operation of the sCO₂ cycle and material selection is one of the most important elements for long-term safe and stable operation of this power system. However, current research on the corrosion behaviour in high-temperature sCO₂ is still not fully understood [6, 7, 8]. The main topics for research and publication are turbomachinery, heat exchangers and new cycle proposals. The great interest expressed by the scientific community aims to theoretical analysis of the thermodynamic principles of the sCO₂ power cycle [9, 10]. Last but not least, the extensive research on the corrosion behaviour of commercial steels and alloys in high-temperature sCO₂ under different operating conditions is desirable and inevitable.

The corrosion study of 9Cr, 12Cr, and 18Cr steels in high-temperature sCO₂ for long-term compatibility tests for reactors with a design life of 60 years studied Furukawa et al. [11]. Holcomb et al. investigated the corrosion behaviour of austenitic heat-resistant steels and Ni-base alloys in sCO₂ environments [12]. The carburization behaviour of Fe-20Cr (wt.%) alloy in Ar-20CO₂ at 650 °C studied the research group of Young et al [13]. Rouillard et al. investigated the oxidation

* corresponding author(s)

and carburization behaviour of 9Cr steel in high-temperature CO₂ [14]. Corrosion and carburization behaviour of heat-resistant steels in a high-temperature supercritical carbon dioxide environment was evaluated in Goi's work [15]. Tan in his work evaluated Corrosion of austenitic and ferritic-martensitic steels exposed to supercritical carbon dioxide [16]. The mechanisms of carburization and of oxide failure are described Grabke in his work, and the measures and methods for control and prevention of carburization are evaluated, too [17, 18]. Carburisation of ferritic model Fe-Cr alloys by low carbon activity gases was examined in paper by Gheno [19].

It is very important to evaluate the corrosion performance and resistance including the oxidation and carburization of the key component materials in a high-temperature sCO₂ environment. Therefore, this paper aims to investigate the evaluation of pre-selected construction materials, corrosion resistance of four kinds of steels and alloys used in advanced thermal power generation systems in a high-temperature sCO₂ environment.

EXPERIMENTAL SYSTEM AND MATERIALS

To be able to carry out more in deep research in sCO₂ technologies the highly modular sCO₂ loop has been built in CVR as part of The Sustainable Energy Project (SUSustainable ENergy, SUSEN). SUSEN targeted to strengthen the research, development and innovative capabilities of the Czech Republic, which would enable raise of competitiveness and create highly qualified jobs to make the regions of the Czech Republic become important points of concentration of such activities in Europe.

Wide variety of research can be done at given loop. Such as heat transfer experiments, erosion, corrosion testing etc. The main operating parameters are:

- Max. operating temperature: 550°C
- Max pressure at high pressure site: 30 MPa
- Max. pressure at low pressure site: 15 MPa
- Max. flow rate: 0.35 kg.s⁻¹
- Total heating power: 110 kW

The main configuration is shown at simplified diagram Fig. 1.

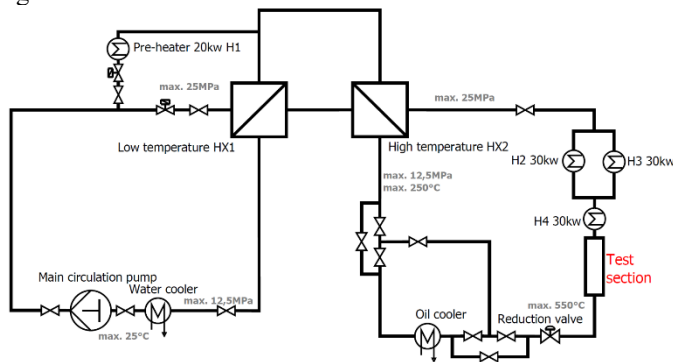


Figure 1: Simplified diagram of sCO₂ loop

The material samples for experiment had to be placed in predesigned test section, where the parameters of medium were regulated to the demanded values. The samples were held in place by tailored sample holder, which can be used again and again.

Design of test section

By nature, the sample holder has to be placed inside the test section (Fig. 2), which has following dimensions: 2 m in length and 58mm in inside diameter. The section is made from alloy Inconel 625. Both ends are flanged for easy assembly and disassembly. Holder itself consists from two main body parts. Corrosion (Fig. 2) and erosion part (Fig. 2), where the flow is accelerated by three narrow channels to 100 m.s⁻¹ at given parameters 20 MPa, 500 °C and mass flow 0.1 kg.m⁻¹ and possibly even to higher states.

Corrosion and erosion part

Main element of the corrosion part is its base, which has to insure anchoring the samples at predefined position and allows to use variety of samples of different dimensions. The dimensions are 10x2, 10x5, 20x2 and 40x4. For dimension 50x3 there is a base alone. Their length is not determined, and their thickness can be smaller. The given number is just its maximum value. Bases were cut out from sheet of metal and melted together. Through the centre goes shaft to detain pieces at their predesigned positions. On each part was used coating TiAlSiN (trading mark, MARVIN Si) from Czech company SHM s.r.o. This coating was intentionally selected so the nonconductive connection could be maintained and also disassembly was much easier after test run.

The erosion part was designed and optimized to reach high velocities in the narrow channels in order to simulate the flow conditions on the turbine blades. Results given by CFD calculations show that the current design reaches pressure drop of 1.1 MPa and average velocity through the narrow channel is 105.6 m.s⁻¹.

Many drafts were considered and processed till high level of design. As it's very common, several contradictory requirements had to be met. Main problem was linked with acceleration of the flow. From 0.1 kg.s⁻¹ at 550 °C and 20 MPa on diameter 58mm it had to be forced into very narrow channel to achieve at least 100m.s⁻¹. Such a doing was non-negotiable and caused that final product had to be very demanding on manufacturing and assembly precision. First half of the timespan of the design was therefore spent on finding solution, which could be manufactured, hopefully with ease, wouldn't be expensive and would perfectly meet the demands of the experiment on conditions, which has to be on material samples. To meet them, the section has to be perfectly sealed. Cause if it wouldn't, the flow which would go through leakage would cause velocity drop and requirement on velocity of the flow wouldn't be met. For these temperatures rubber, teflon or similar materials are out of the table, they wouldn't endure them. Mainly two possible options were evaluated. Some kind of graphite sealing or so called "metal to metal" sealing.

Graphite sealing with its less demands on surface finish was chosen over "metal to metal." How to divide the part to subparts and still be able to seal the thing, was the catch. Different overall symmetries, shapes of channels, division into components etc. was considered. As the final solution the design with 1/3 symmetry was chosen and it consist of main body part, graphite sealings, wedges and parts which acts as pressers to the sealings and holds samples at their place (Fig. 2) with only the need to seal the samples, so the flow wouldn't go behind them and to seal the sample holder outer diameter with inner diameter of the test section.

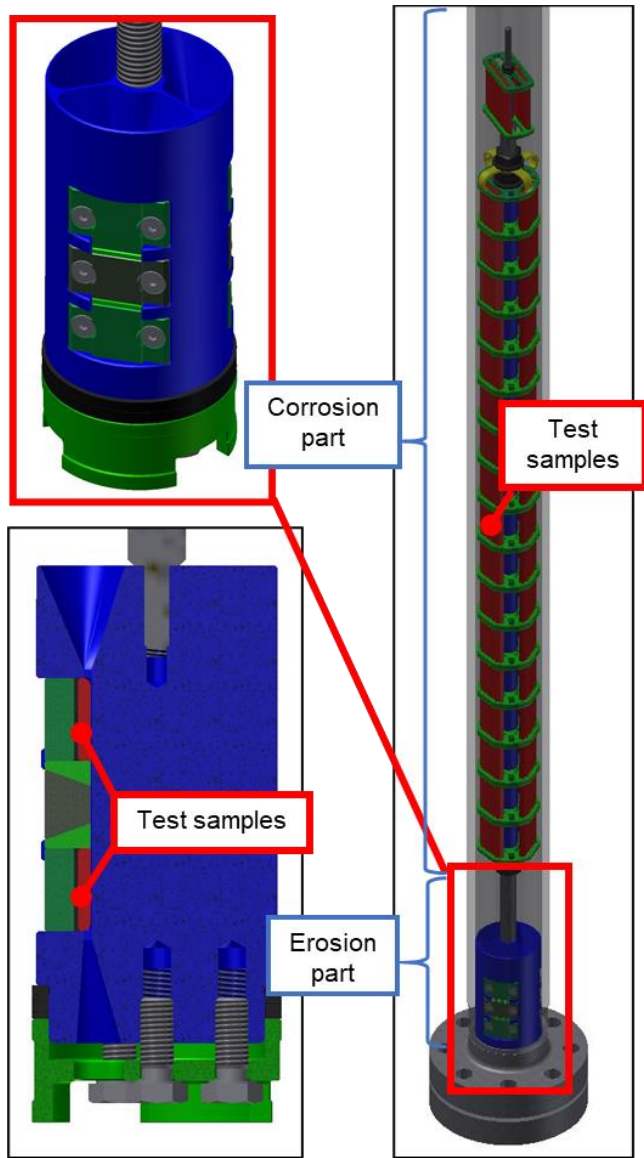


Figure 2: Sample holder, cross-section of the erosion part

This is done with graphite rope with dimensions 4x4mm. For the graphite to work properly as a sealing, it has to be more then mildly pressed. This is done by pressers at samples and for outer-inner diameter it's done by inner flange. Erosion part was

very demanding to be manufactured and on assemble precision. For main body part the method of 3D printing was consider. Unfortunately, the demand on surface roughness in the channel would not be possible to meet. Therefore, conventional machining had to do this job. Whole erosion part can take up to 6 pieces of samples of dimensions 20x10x3.

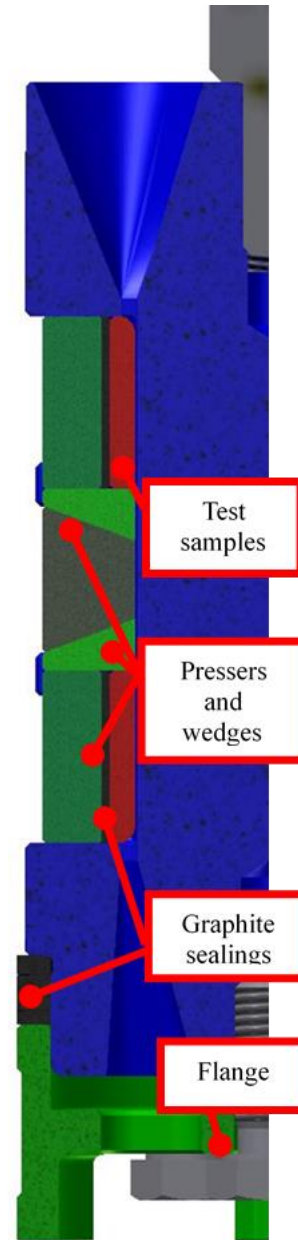


Figure 3: Cross-section of the erosion part

Assembling

At first all samples were imprinted with a mark, then cleaned with ethanol and acetylene by ultrasonic cleaner, weighed and those figures noted. Then all parts of sample holder where cleaned by same procedure. Assembling was carried out in clean

environment. Assembled sample holder is shown at Fig. 4. The test section is stationed vertically, therefore the sample holder has to be somehow anchored in the section. This is done when test section lays in horizontal position when disassemble. Sample holder is put inside at given place, where when it is in vertical position it can rest at inner edge of lower flange, which goes few millimetres inside. Before moving the section into its place in the loop, the graphite sealing at outside diameter of erosion part is pressed by inner section flange. This pressure can produce force big enough to counter gravity while sample holder is being transferred to its place.

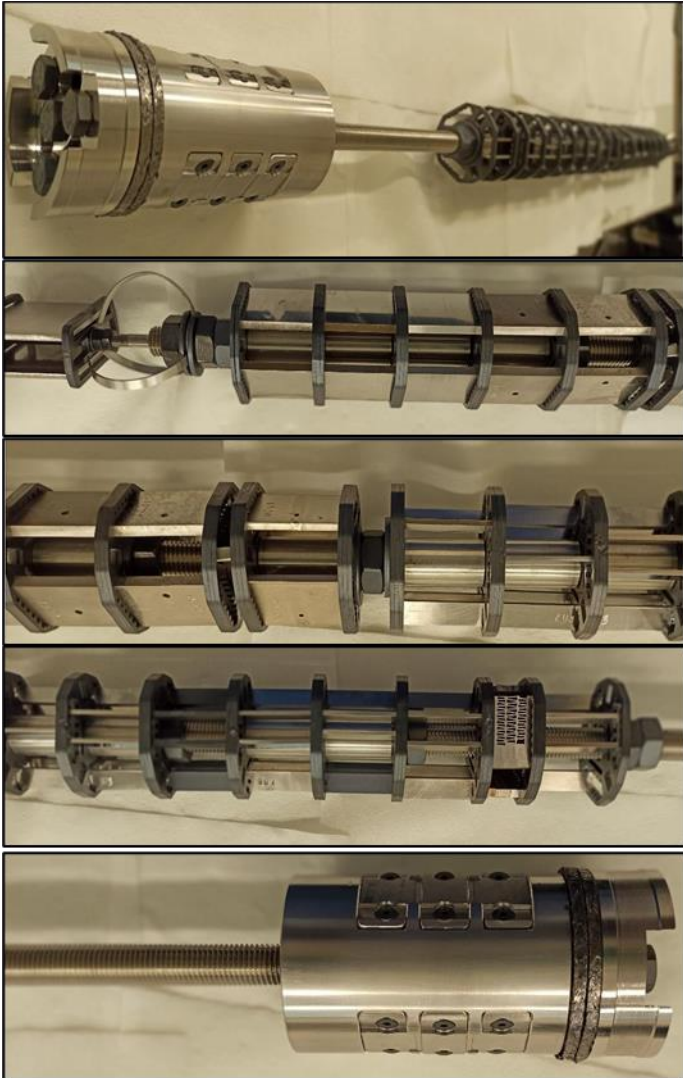


Figure 4: Assembled sample holder

Materials and test conditions

The experimental materials included four kinds of high-grade heat-resistant alloys, 9-12% Cr steel (FB2), martensitic precipitation-hardening stainless steel (17-4-PH), nickel-based superalloy (625M), corrosion-resistant nickel alloy (Inconel 718), which have been widely employed in various energy conversion, power plants, and nuclear industries because

of its exceptional properties of high-temperature strength and creep resistance. The chemical compositions of the studied materials are listed in Table 1.

Martensitic stainless steel, FB2 is the creep resistant steel, which was manufactured and developed for turbine rotor forging. It is 9-12% Cr boron-containing steel, primarily for steam temperatures $\geq 620^{\circ}\text{C}$. 17-4-PH is a chromium-nickel-copper precipitation-hardening martensitic stainless steel with an addition of niobium. 17-4-PH combines high strength and hardness with good corrosion resistance. Alloy 625M is a nickel-based superalloy that possesses high strength properties and resistance to elevated temperatures. It also demonstrates remarkable protection against corrosion and oxidation. It has the ability to withstand high stress and a wide range of temperatures, as well as being able to resist corrosion while being exposed to highly acidic environments. Alloy In718 is a high-strength, corrosion-resistant nickel chromium material. The age-hardenable alloy has resistance to post weld cracking, good tensile, fatigue, creep, and rupture strength.

Table 1: Chemical composition of studied materials (wt.%)

[%]	FB2	17-4-PH	625M	IN718
C	0.13	0.07	0.03	0.08
Mn	0.35	1.0	0.5	0.35
P	-	0.04	0.015	0.015
Cr	9.3	15-17.5	20-23	17-21
Mo	1.50	-	8-10	2.8-3.3
V	0.20	-	-	-
Al	-	-	0.4	0.20-0.80
S	-	0.03	0.015	0.015
Si	-	1	0.15	0.35
Nb	0.05	0.15-0.45	3.15-4.15(Nb+Ta)	4.75-5.5
N	0.020	-	0.2	-
Ni	0.1	3-5	58	50-55
B	0.01	-	-	0.0006
Ti	-	-	0.4	0.65-1.15
Fe	Bal.	Bal.	5	Bal.
Co	1.3	3-5	1	1
Cu	-	-	-	0.3
Ta	-	-	-	0.058

The test samples with the dimensions of 40 mm \times 10 mm \times 2 mm were made of tubes delivered by RINA

(project partner of the sCO₂ FLEX project). Prior to the test, the samples were ground up to 600 grit SiC paper, which is more representative of industrial surfaces, rather than fine polishing, then rinsed with deionized water, alcohol, and dried. The composition of the sCO₂ atmosphere was 99.995% in the corrosion experiment.

After the corrosion tests, the weight gains of the investigated materials were measured before and after the test using a Radwag AS 82/220.R2 Plus Analytical Balance. All the samples were weighed on an electronic balance with an accuracy of 0.00001 g. Micro-analysis of the surface corrosion products were characterized by Light Optical Microscope (LOM) and by Scanning Electron Microscopy (SEM) with Energy Dispersive Spectroscopy (EDS). An Olympus BX51P was used for characterization of the surface observation. A LYRA3 Tescan SEM integrated with EDS system was used for characterizing the morphology and compositions of the surface oxide corrosion product layer in both plan and cross-sectional views of the samples.

RESULTS AND DISCUSSION

Weight gain

Tab. 2 showed the weight gain of experimental materials in sCO₂ after exposition. The table shows the average value of the weight gain, that came from 3 parallel specimens. The measurement error is 0.015 mg. After 1000 h exposure, Tab. 2 showed that martensitic steel FB2 exhibited the largest weight gain, while others showed a much lower but similar weight gain. Relatively thin and continuous Cr₂O₃ layer would be formed on alloys containing at least 14 % Cr in high-temperature sCO₂ as reported in work Subramanian [20]. In718 with a higher Cr and Ni concentration showed the best corrosion resistance in a high-temperature sCO₂ environment.

Table 2: Weight gain of the investigated materials in sCO₂

Sample	Mass change [%]
FB2	1.17013
17-4-PH	0.00517
625M	0.00675
In718	0.00049

Characterization of the corrosion products

Fig. 5, 6, 7, 8 showed the surface morphology of the investigated materials in sCO₂ after exposure. Numerous lumpy structure and pronounced hillock oxides were observed on FB2, as shown in Fig. 5 b,c. As can be seen in Fig. 5a before exposure, the oxidation process is very significant in comparison with Fig. 5 b,c,d.

The continuous, thin oxide was observed on 17-4-PH in Fig. 6 b,c,d. The oxide formed on the surface doesn't copy the grooves after mechanical surface treatment. Structure of this oxide is very similar like FB2, but thinner.

Many irregular, and discontinuous oxides were found on 625M and In718 in Fig. 7, 8 b,c,d. Different shades on the surface indicate different thicknesses and probably is possible the change

in composition. Notably, numerous micrometer-sized nodular oxides were detected on In718 in Fig. 8 d.

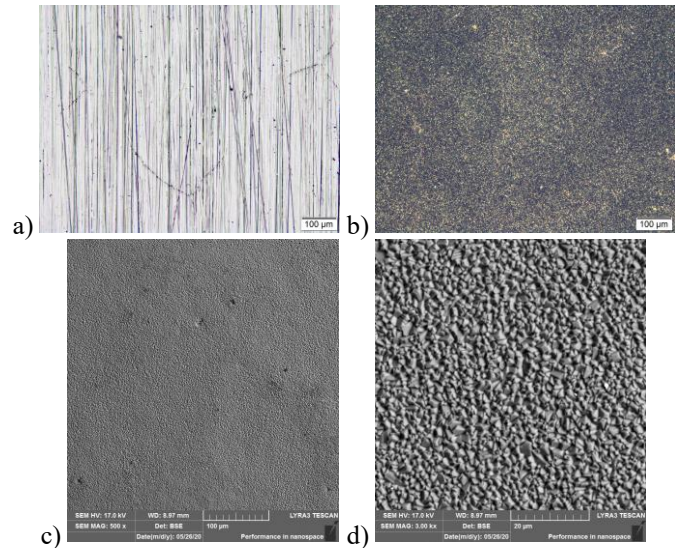


Figure 5: Surface morphologies of the FB2 before (a) and after sCO₂ exposure (b,c,d)

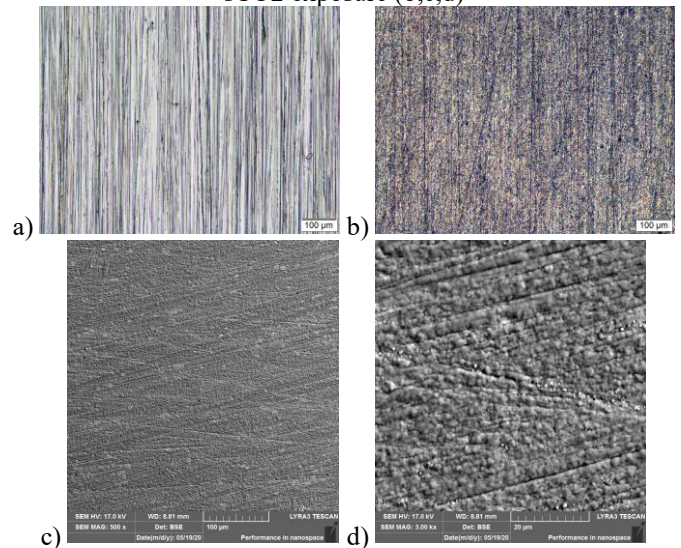
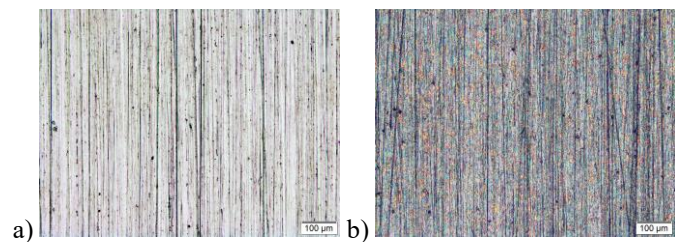


Figure 6: Surface morphologies of the 17-4-PH before (a) and after sCO₂ exposure (b,c,d)



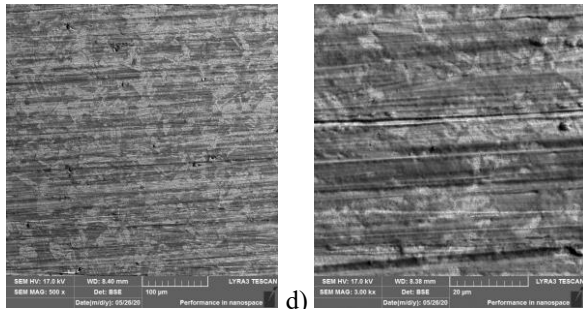


Figure 7: Surface morphologies of the 625M before (a) and after sCO₂ exposure (b,c,d)

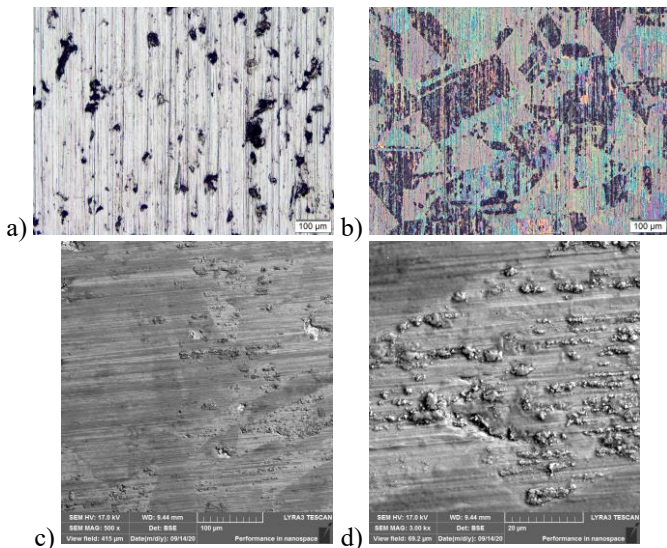


Figure 8: Surface morphologies of the In718 before (a) and after sCO₂ exposure (b,c,d)

Fig. 9-12 showed the cross-sectional morphologies of the investigated materials in exposure of sCO₂.

Surface observation showed the formation of oxide layer on the Fe-base. The oxide layer was thick and homogeneous all over the surface. Cross section of this material confirmed the thick homogeneous oxide layer without cracks and defects as can be seen on the Fig. 9. The oxide layer consists from the inner and outer layer, outer is on the Fe-base and inner is formed from the Fe-Cr-O spinel. Under the main layer is internal oxidation zone which is formed from mixed oxide on the Fe-Cr-O base. The thickness of these layers is around 22 μm for outer and around 18 μm for inner. The outer layer was formed by the diffusion of metal elements to the outside and the inner layer was formed by that of oxygen to the inside.

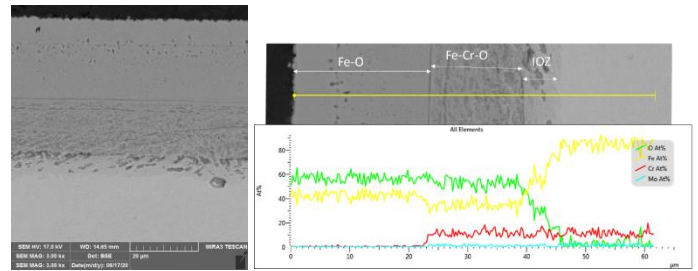


Figure 9: SEM cross section of the FB2 and EDX linescan of the oxide layer

On the martensitic steel 17-4-PH surface was formed the oxide layer. Optical surface analyses showed the different oxide thickness which means variability of colors. This claim confirms cross section observation on the Fig. 10. Cross-section observation showed the formation of either a single Cr-O layer and also localized duplex spinel oxide. Duplex spinel oxide is formed from outer Fe-O layer and inner Fe-Cr-O spinel. Fe-Cr-O spinel is formed inside to the steel.

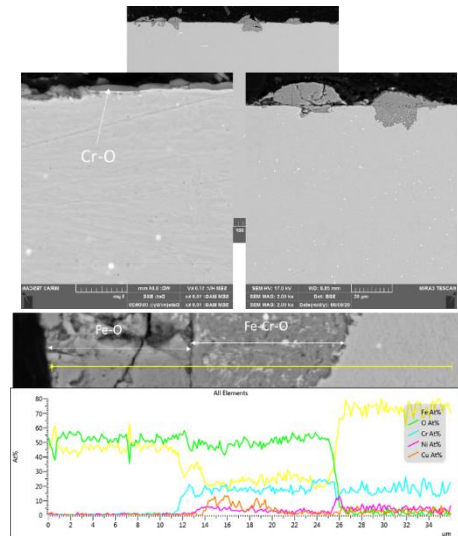


Figure 10: SEM cross section of the 17-4-PH and EDX linescan of the oxide layer

The surface of alloy 625M after exposure in sCO₂ is shown in Fig. 7, and the surface oxide was clearly observed and the different surface colours from LOM and SEM suggest the different thickness of the oxide on the surface, which is confirmed by the analysis in cross-section. Fig. 11 shows the EDS linescan of the oxide layer after exposure. According to the cross-sectional morphologies, the corrosion products on the 625M were composed of an outer layer of Cr-Ni-O, and an inner layer of Ni-Cr-O with depleted Cr part. The oxide layer was not homogeneous around all observed surface in cross-section observation.

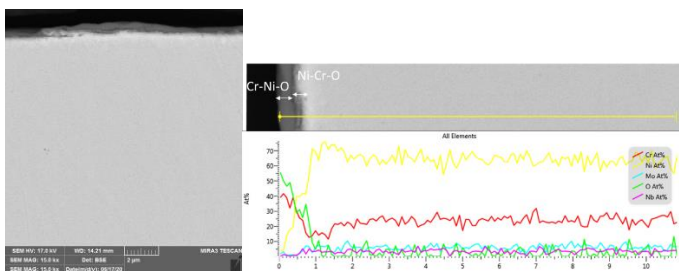


Figure 11: SEM cross section of the 625M and EDX linescan of the oxide layer

Fig. 8 showed the surface observation by LOM and SEM, these analyses showed the uneven oxidation. This claim confirms the cross-section observation as can we seen in Fig. 12. The Ni-base alloy In718 have a sufficient amount of Fe to develop an outer layer on the Fe-O, as shown in Fig. 12 linescan. Under the outer layer was observed the depleted part of Ni and Cr. The cross-section also suggests the creation of the cracks or defects, probably.

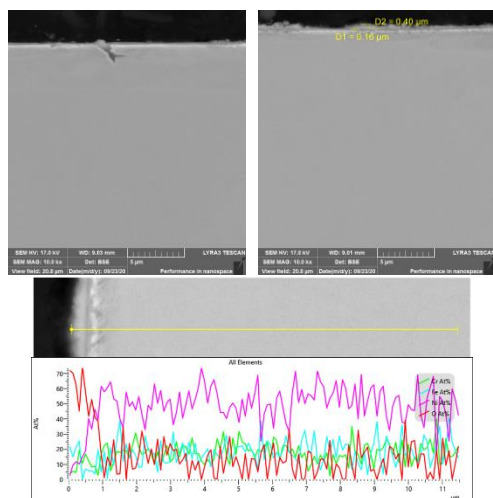


Figure 12: SEM cross section of the In718 and EDX linescan of the oxide layer

CONCLUSIONS

- I. The weight gain of the corrosion products corresponded with Cr content in base material, where is obvious that the less content of chromium and high content of iron they tend to create of oxide layer. These claims are also supported by the works of Gui, Furukawa, Tan [4, 11, 16, 17].
- II. FB2 has greater weight gain compared to other steels selected for sCO₂ power cycle components. This sample has thick and compact duplex layer on the surface, which could with time increase the thickness of outer layer with subsequent spalling. This can be reason of circuit pollution with the corrosion layers.
- III. 17-4-PH showed the very different behaviour in comparison to the other studied materials, because as the only one to form a significant nodules of the oxide

like in and out, which can cause the corrosion attack over the significant oxidation layer inside in material.

- IV. Chromia-forming alloys 625M and In718 showed better corrosion resistance than the FB2 and 17-4-PH due to the formation of the Fe-oxide or Cr-oxide rich scales on its surface. This result was mainly attributed to the higher Cr content in alloys 625M and In718. It was demonstrated that the corrosion performance of steels and alloys in supercritical carbon dioxide was mainly decided by the Cr content [4, 11, 16, 17].
- V. 625M formed a dense and continuous Cr-O oxide layer with Ni content and exhibited an excellent corrosion resistance in high-temperature sCO₂ environment. The sufficient Cr in the interior of the alloy supports the stability of the Cr oxide layer.

ACKNOWLEDGEMENTS

The presented work was financially supported by the H2020 sCO₂-FLEX project. This project has received funding from the European Union's Horizon 2020 research and innovation programme under grant agreement N° 764690.

Some of presented results were obtained with support of Technology Agency of Czech Republic, project "Purification and purity control of CO₂ gas in power cycles" No. TK02030023.

REFERENCES

- [1] F. Crespi, G. Gavagnin, D. Sánchez, G.S. Martínez. (2017). Supercritical carbon dioxide cycles for power generation: a review. *Appl. Energy*, 195, 152-183.
- [2] M.-J. Li, H.-H. Zhu, J.-Q. Guo, K. Wang, W.-Q. Tao. (2017). The development technology and applications of supercritical CO₂ power cycle in nuclear energy, solar energy and other energy industries. *Appl. Therm. Eng.*, 126, 255-275.
- [3] V. Dostál. (2005). *A Supercritical Carbon Dioxide Cycle for Next Generation Nuclear Reactors*, 154.
- [4] Y. Gui, Z. Liang, H. Shao, Q. Zhao. (2020). Corrosion behavior and lifetime prediction of VM12, Sanicro 25 and Inconel 617 in supercritical carbon dioxide at 600 °C. *Corrosion Science*, 175, 108870.
- [5] Y. Le Moullec. (2013). Conceptual study of a high efficiency coal-fired power plant with CO₂ capture using a supercritical CO₂ Brayton cycle. *Energy*, 49, 32-46.
- [6] B.A. Pint, J.R. Keiser. (2016). *Supercritical CO₂ Compatibility of Structural Alloys at 400-750 C*. Oak Ridge National Lab. (ORNL), Oak Ridge, TN (United States).
- [7] A. Meyer, B. Jacob, M. M. Anderson, K. Sridharan. Effect of supercritical CO₂ on the performance of 740H fusion welds. *Materials Science and Engineering: A*, 742, 2019, 414-422.
- [8] B. Pint, J. Keiser. (2015). Initial Assessment of Ni-Base Alloy Performance in 0.1 MPa and Supercritical CO₂.
- [9] G. Angelino. (1968). Carbon dioxide condensation cycles for power production. *J Eng Power*, 90, 287-295.
- [10] E. Feher. (1968). The supercritical thermodynamic power cycle. *Energy Convers Manage*, 8, 85-90.

- [11] T. Furukawa, Y. Inagaki, M. Aritomi. (2011). Compatibility of FBR structural materials with supercritical carbon dioxide. *Prog. Nucl. Energy*, 53, 1050-1055.
- [12] G.R. Holcomb, C. Carney, Ö.N. Doğan. (2016). Oxidation of alloys for energy applications in supercritical CO₂ and H₂O. *Corros. Sci.*, 109, 22-35.
- [13] D.J. Young, T.D. Nguyen, P. Felfer, J. Zhang, J.M. Cairney. (2014). Penetration of protective chromia scales by carbon. *Scr. Mater.*, 77, 29-32.
- [14] F. Rouillard. (2012). Corrosion of 9Cr steel in CO at intermediate temperature III: modelling and simulation of void-induced duplex oxide growth. *Oxid. Met.*, 77, 71-83.
- [15] Y. Gui, Z. Liang, Q. Zhao. (2019). Corrosion and carburization behavior of heat-resistant steels in a high-temperature supercritical carbon dioxide environment. *Oxid. Met.*, 92, 123-136.
- [16] L. Tan, M. Anderson, D. Taylor, T.R. Allen. (2011). Corrosion of austenitic and ferritic-martensitic steels exposed to supercritical carbon dioxide. *Corros. Sci.*, 53, 3273-3280.
- [17] H.J. Grabke. (1972). Oxygen transfer and carbon gasification in the reaction of different carbons with CO₂. *Carbon*, 10, 587-599.
- [18] H.J. Grabke, I. Wolf. (1987). Carburization and oxidation. *Mat. Sci. Eng.*, 87, 23-33.
- [19] T. Gheno, D. Monceau, J. Zhang, D.J. Young. (2011). Carburisation of ferritic Fe–Cr alloys by low carbon activity gases. *Corros. Sci.*, 53, 2767-2777.
- [20] G.O. Subramanian, H.J. Lee, S.H. Kim, C. Jang. (2018). Corrosion and carburization behaviour of Ni-xCr binary alloys in a high-temperature supercritical-carbon dioxide environment. *Oxid. Met.*, 89, 683-697.

DESIGN CONSIDERATIONS OF sCO₂ TURBINES DEVELOPED WITHIN THE CARBOSOLA PROJECT

Stefan Glos*

Siemens Energy AG
 Mülheim an der Ruhr, Germany
 Email:Stefan.glos@siemens.com

Patrik Rene Lippe

Siemens Energy AG
 Mülheim an der Ruhr, Germany

Dominic Schlehuber

Siemens Energy AG
 Mülheim an der Ruhr, Germany

Simon Kobler

Siemens Energy AG
 Erlangen, Germany

Michael Wechsung

Siemens Energy AG
 Mülheim an der Ruhr, Germany

ABSTRACT

Due to the great potential in terms of compactness and efficiency, supercritical CO₂ (sCO₂) power systems are being investigated in the field of scientific and industrial energy technology. The German research project CARBOSOLA has been initiated in order to drive the sCO₂ technology development in Europe by providing a test loop for research programs and basic component tests followed by an initial system and component design for a future demo plant. In a first project phase, the economic potential of the sCO₂ technology is evaluated and optimized for different use cases based on initial component designs and corresponding cost assumptions. For the CO₂ turbine, different design aspects have been investigated and assessed leading to first design concept.

INTRODUCTION

The CARBOSOLA project presented in this paper is intended to represent the entry into sCO₂ technology development in Germany. As shown in figure 1, the project structure is divided in two phases. In the first phase an analysis of the expected advantages is carried out. Therefore, the sCO₂ technology will be compared with conventional technologies in the fields of waste and exhaust heat recovery (WHR) and solar-thermal power plant technology (CSP) and subjected to a technical-economic evaluation and optimization. Waste heat recovery is expected to be the most promising market for sCO₂ applications in Europe. CSP has been the target application of the DOE-funded SunShot program driving the sCO₂-technology development in the United States. The envisaged technology comparison is intended to show what increase in efficiency can be expected when using sCO₂ compared to water/steam and what the electricity production costs are. However, the core of the project is the second phase including the component and system design of a technology demonstrator for the use of secondary heat as well as the theoretical and experimental methods required for further technology

development up to commercial maturity. Therefore, the development and commissioning of a modular sCO₂ test loop for generic experimental studies and component test at the Helmholtz Zentrum Dresden Rossendorf are completing the program.

The consortium of the BMWi funded project CARBOSOLA consists of TU Dresden and the Helmholtz Zentrum Dresden-Rossendorf covering the necessary scientific-technical investigations for technology and product development. Furthermore, DLR provides the expertise for the evaluation of solar thermal power plants and Siemens Energy has a high level of competence in the field of thermal energy conversion systems and covers the necessary know-how of all components involved such as turbines, compressors and heat exchangers.

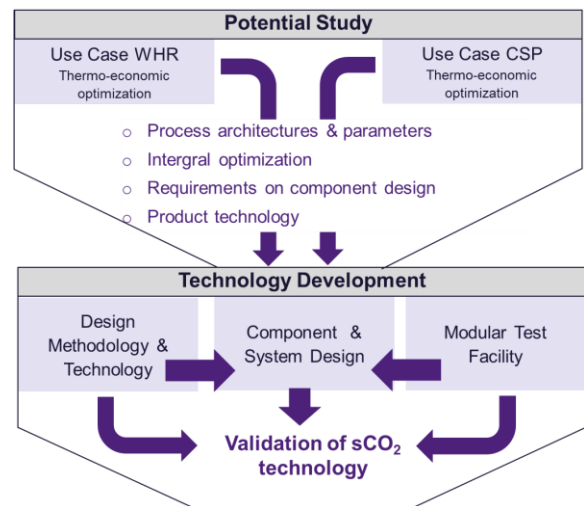


Figure 1: Structure of the CARBOSOLA project

* corresponding author(s)

The focus in this publication are the turbine design considerations derived within the first two work packages, i.e. the potential studies for a waste heat recovery application and a concentrated solar power plant. Design details considering design topology, technology and optimization approaches are discussed.

Beside small lab scale applications, only few sCO₂ turbomachinery designs have been realized so far. The only commercial system is the Echogen EPS-100 for waste heat recovery applications (up to 530°C turbine inlet temperature), which utilizes radial inflow turbines to generate approximately 8 MW [8]. However, a radial turbine topology is not likely to be optimal for large scale power generation plants. Within the Sunshot program a 10MW test loop is currently erected using an axial turbine concept [9]. Other conceptual designs studies for large scale sCO₂ turbomachinery have scaled up this concept for 50MW and 450 MW [10]. These concepts are addressing high temperature CSP applications (> 700°C turbine inlet temperature) which constrains the mechanical design to a certain extend.

50 MW sCO₂ TURBINE FOR WHR APPLICATION

For the waste heat recovery use case, the exhaust heat of two aeroderivative gas turbines was defined as heat source for the optimization of a sCO₂ cycle. Those gas turbines are often applied for mechanical drive of compressors in the oil and gas industry. Based on preliminary results of a techno-economic cycle optimization [1], whereas the cycle consists of one recuperator and a split primary heater, an initial turbine design has been carried out. The thermodynamic boundaries of the considered design case are listed in table 1.

Table 1: Thermal boundary conditions for a sCO₂ turbine in use case one (WHR)

Thermal boundary condition	Value
Inlet pressure [bar]	240
Inlet temperature [°C]	350
Mass flow [kg/s]	427
Inlet volume flow [m ³ /s]	2,1
Outlet pressure [bar]	64
Nominal shaft power [MW]	51

A first approach of the turbine geometry was derived by scaling a high-pressure barrel type steam turbine, whereby the scaling factor f_s is derived equation 1.

$$f_s = \sqrt{\frac{\dot{V}_{Steam}}{\dot{V}_{CO_2}}} \quad f_s(1)$$

With this methodology, i.e. dividing all lengths and diameters and multiplying the rotational speed of the original turbine with f_s , the axial and circumferential flow velocities inside the turbine are approximately equal to the initial, high efficient steam turbine leading to an appropriate geometry for

further optimizations. In figure 2 a general sketch of the obtained turbine design is shown. The turbine topology is a single-flow, double-shell design with inner and outer casing. The outer casing is of the barrel type with a circumferential split which allows rotational-symmetrical design without local material buildup even for high steam temperatures and pressures thus avoiding unsymmetrical deformation and thermal loading. Since the inlet temperature is quite low this design is assumed to be conservative and provides potential for further cost optimization in a next phase.

The drum blading comprises only 7 reaction stages whereby the exact degree of reaction is optimized individually for each individual stage (3DVTM: 3D blade with variable stage reaction). Figure 3 shows a sketch of the bladepath. Due to the scaling approach reasonable blade heights can be achieved leading to isentropic stage efficiencies up to 92,5 %.

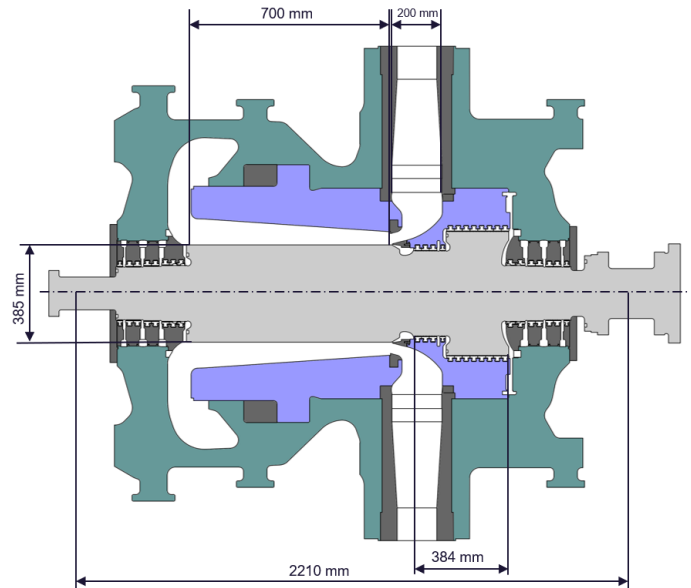


Figure 2: Sketch of the scaled high-pressure turbine

The use of 3DVTM blading represents the most advanced method of optimizing the high-pressure and intermediate-pressure blading. Siemens no longer works on the premise which has been applied for over a hundred years stipulating that the degree of reaction in a stage is an input variable for design calculations.

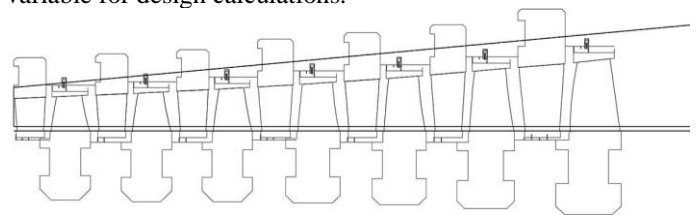


Figure 3: Sketch of the CO₂ turbine bladepath consisting of 7 stages 3DVTM blades

The use of numerical optimization methods has enabled Siemens to individually vary stage reaction and stage loading for every stage in order to obtain maximum efficiency. This allows efficiency to be increased by up to one percent as compared to blading with 50 % reaction. The 3DVTM blading is equipped with state-of-the-art 3D blade profiles such as 3DS blades (3DSTM: 3D blade design with reduced Secondary losses) for highest efficiencies.

In figure 4 an exergy loss analysis of the initial turbine design is shown. It can be deduced that in addition to the losses of the blading, the proportions of inflow, thrust balance piston and leakage cannot be neglected. It must be emphasized that the loss portion of the leakage does not include any additional power for potential recompression. A more detailed consideration of this aspect will follow in the further course of this paper.

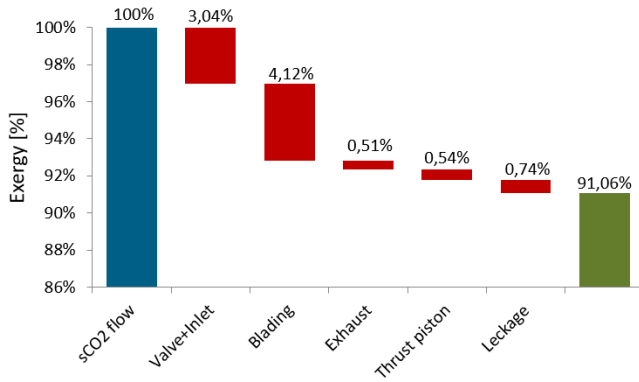


Figure 4: Exergy loss analysis of initial turbine design

Due to the high density of the working medium CO₂ associated with high losses at high velocities, special attention must be paid to the optimization of the inlet and exhaust geometry. Compared to a steam turbine for the same application (and thus same net output) and assuming same flow velocities and the same pressure loss coefficient of the inlet geometry the exergy loss of the CO₂ turbine would be approx. 16 times higher than the exergy loss of the steam turbine as documented in table 3.

Table 3: Exergy loss calculation for a generic pressure loss with $\zeta=1$ and 50 m/s for a CO₂ turbine and a steam turbine

	CO ₂ turbine	steam turbine
mass flow [kg(s)]	470	29,4
pressure [bar]	250	49
temperature [°C]	350	350
Density [kg/m ³]	213,6	18,8
ζ [-]	1	1
velocity [m/s]	50	50
pressure loss [bar]	2,7	0,2
Δs [kJ/kg K]	0,0020	0,0020
Exergy loss [KW]	272	17

Based on the above described scaling approach an initial inlet diameter of approximately 2 x 130 mm is obtained corresponding to a flow velocity of 78 m/s which is a common value for steam turbines. However, assuming the same flow velocity in the inlet valves this leads to an exergy loss of approximately 1,6 MW. In figure 5 the results of a calculus of variations is summarized. It is obvious that a reduction of the inlet flow velocity can reduce the exergy losses significantly. Balancing losses and design requirements, an inlet diameter of 200 mm was corresponding to a flow velocity of 33 m/s was chosen.

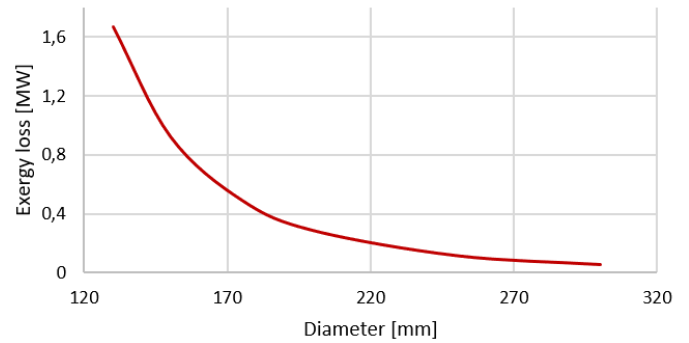


Figure 5: Exergy losses caused by pressure losses of the inlet and valve depending on the diameter

Beside the impact on the pressure losses, increased flow velocities may have an impact on the rotodynamic stability of the turbine. According to Hecker [2] asymmetrical inflow geometries may lead to local velocity differences which cause radial pressure differences. Due to the high fluid density these pressure differences are significant higher compared to steam turbines. The aerodynamic design of inlet and exhaust is therefore of particular importance. The influence of flow-induced lateral forces must be investigated in detail in further steps.

Another loss contributor according to figure 4 is the thrust equilibrium piston which compensates the axial forces of the moving blades due to the reaction blade technology. The entire pressure difference of the turbine is applied over the piston. The resulting leakage flow of the contactless seals, e.g. labyrinth seals, results in an exergy loss due to the throttling of the flow. According to Hecker et al. [3] no isenthalpic throttling over the sealing can be assumed and fluid friction effects need to be considered. The gas friction in labyrinth seals can be expressed by the wall shear stress by the following equations according to [3].

$$\tau = cf \times 0,5 \rho w^2 \quad (2)$$

$$cf(Re) = A \times [Re]^{(-0,2)} \quad (3)$$

This effect, which is well known from steam turbines, has been evaluated in a comparative calculation for a rotor geometry according to table 4 for both a steam leakage flow and a CO₂ leakage flow. The resulting windage losses and the related sealing mass flows are shown in figure 7 whereas the temperature increase over the isenthalpic temperature is provided in figure 6. The temperature rise of the CO₂ leakage flow is 13 K higher compared to the steam case. Since the CO₂ leakage flow across the sealing is 6 times higher compared to the steam leakage, the higher windage losses result only in this moderate temperature rise. Therefore, special attention must be paid, when optimizing the piston sealing, especially for higher turbine inlet temperatures. The resulting temperature rise must be considered in the mechanical design of rotor and casing. For the investigated WHR application this aspect is assessed to be uncritical due to the comparable low inlet temperature of the turbine.

Table 4: Parameters of a labyrinth sealing used for a comparison of the fluid friction effect for steam and CO₂

Parameter	
Mean labyrinth diameter [mm]	430
Length of labyrinth [mm]	384
Rotor frequency [1/s]	96

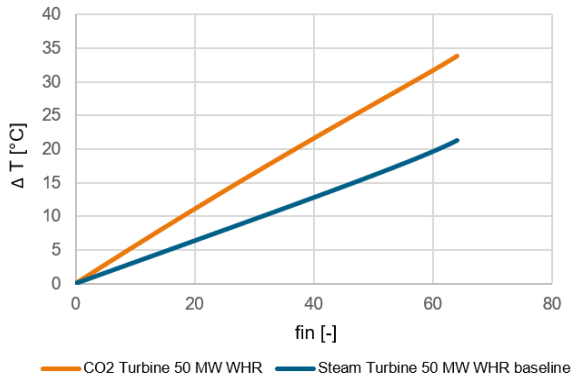


Figure 6: Temperature increase over the isenthalpic temperature for a labyrinth sealing for steam and CO₂

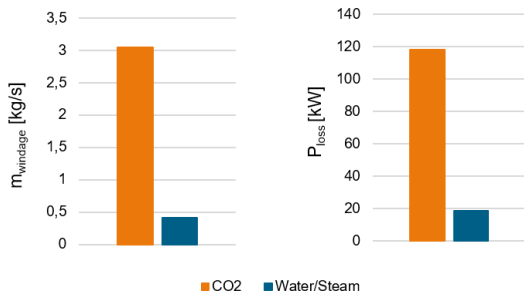


Figure 7: Comparison of leakage flow and fluid friction losses for a CO₂ turbine

For the optimization of the thrust piston geometry for the turbine design according figure 2 the length of piston equipped with labyrinth seals was stepwise increased leading to a reduction of the leakage flow. However, taking the overall exergy loss including the fluid friction into account an optimum piston length of approximately 330 mm, was chosen as shown in figure 8.

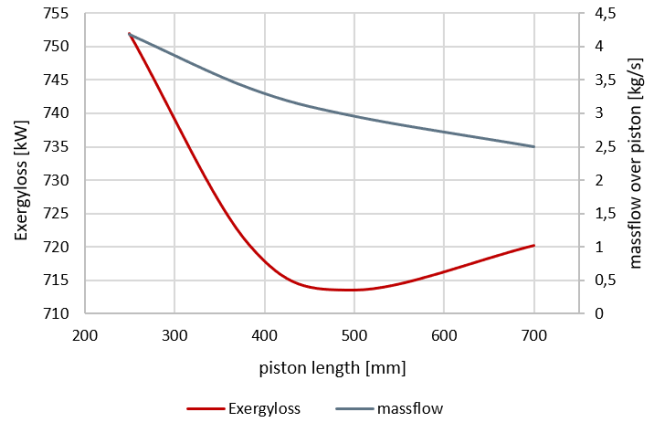


Figure 8: Impact of the piston length on the exergy loss taking fluid friction into account

Another important turbine component for realizing high efficiencies is the sealing technology. Dry gas seals are referenced in most sCO₂ applications due to their low leakage, and friction losses [5]. On the other hand, conventional turbine sealings such as labyrinth and brush sealings are beneficial with respect to costs and reliability. Assuming coated labyrinth sealings as baseline, a first approach of the sealing system was defined according to the sketch in figure 9.

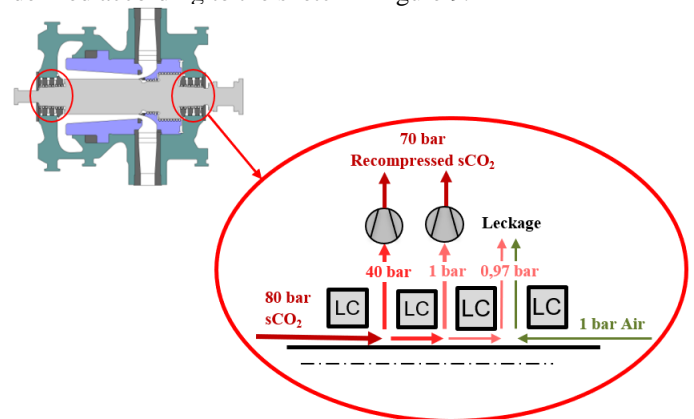


Figure 9: Initial calculation of sealing system based on coated labyrinth sealing technology (LC)

In this layout the CO₂ is throttled from the lower cycle pressure of approximately 80 bar via two sealings to defined pressure levels of 40 bar and 1,03 bar (slight overpressure) where the

sealing flow is partly recompressed and piped back into the power cycle. For the chosen geometry and pressures the required aux load amount to approx. 850 KW. At the end of the shaft, a slight vacuum is set between two further sealing elements in a suction hood from which the CO₂/Air mixture is discharged. In this case the CO₂ leakage amounts to 1,3 tons CO₂ per day outside the machine house. Both the high demand for auxiliary energy and the leakage rate show that conventional sealing technology is not sufficient to seal CO₂ turbines. In a next step brush seals have been considered for the first two sealing sections at each shaft end, but the results could only be improved slightly. In contrast to that the use of a dry gas seals results in a significant reduction of the leakage flows as summarized in table 5. Furthermore, no auxiliary compressors are required in this setup. On the other hand, dry gas seals require a clean gas supply [3] as shown in figure 9. It was assumed to extract this gas supply from the high-pressure line behind the recuperator and connect it via a pressure reduction and filter device with the sealing system. Overall, it can be stated that dry gas seals seem to be the best technology for sCO₂ turbines. However, the remaining leakage is not to be neglected from an operational point of view, as regular replenishment is necessary. Further system improvements must therefore be investigated and developed.

Table 5: Thermodynamic comparison of different sealing technologies for 50 MW sCO₂ turbine

Parameter	Labyrinth	Brushes	DGS
Leakage flow [t/d]	1,3	1,3	0,52
Aux. power [kW]	852	436	-
Exergy loss [kW]	1502	811	108

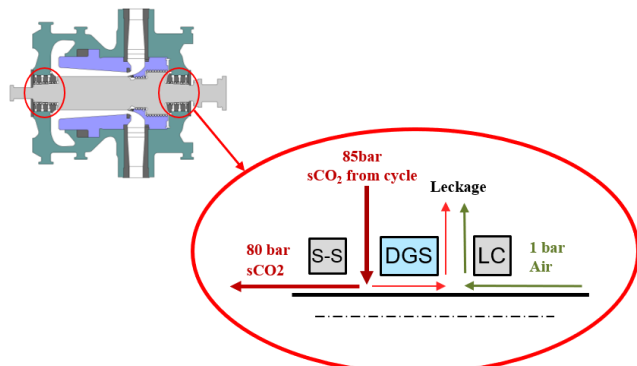


Figure 10: Dry-gas-sealing (DGS) system combined with tip to tip seal (S-S) and a coated labyrinth (L-C)

With the above described improvements, the power weighted isentropic efficiency (including leakages) could be improved from initial 87,5 % to 90,5 % as illustrated in figure 10. Compared to the reference cycle based on water/steam this is approximately 5 % pts better compared to a steam turbine for the same use case. Due to the short bearing span and the by

orders of magnitude lower volumetric flow at the exhaust, the estimated cost are about 50 % less than that of a steam turbine.

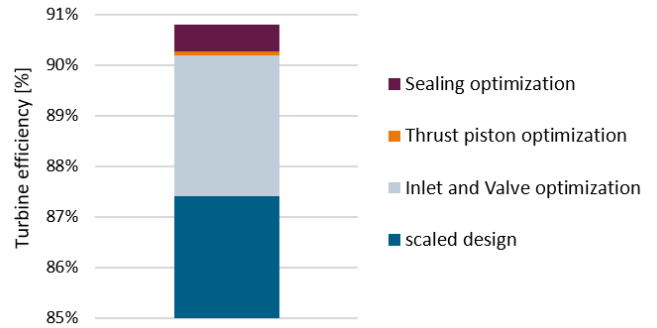


Figure 11: Isentropic turbine efficiency and breakdown of optimization measures

150 MW sCO₂ TURBINE FOR CSP APPLICATION

The second use case which is evaluated in the CARBOSOLA project is a concentrated solar power plant (CSP). With a similar methodology a preliminary techno-economic cycle optimization has been carried out for different upper process temperatures [5]. For a base case at 550 °C turbine inlet temperature and a molten salt based thermal storage system a simple recuperated cycle has been identified as the most economic cycle configuration. The thermodynamic boundaries of the turbine design case are listed in table 6. For comparison purposes the values of the steam turbine in the reference cycle are also listed.

Since the pressure levels and the volumetric flows at the inlet and the outlet fit very well to large high pressure steam applications the turbine topology can be derived from a Siemens H60 turbine, which is a single-flow, double-shell design with inner and outer casing operating at net frequency. With an optimized shaft diameter of approximately 650 mm only 13 reaction stages based on 3DS technology are necessary to provide 148 MW. Under consideration of all pressure losses, internal and external leakages, assuming DGS technology as described above, the power weighted isentropic efficiency amounts to 92 %.



Figure 11: High-pressure turbine from current Siemens Energy portfolio adapted for CSP application with 115 MW net-power.

The compatibility of materials is a major concern for the design and operation of sCO₂ power cycles and its components. The temperature depending corrosion behaviour of materials in CO₂ environment is subject of numerous research studies and Ni-base alloys are discussed as suitable materials. However, these studies are focussing essentially high temperature application of 700 °C or higher [6,7]. An assessment of the turbine material selection at moderate temperatures is currently part of an investigation within the CARBOSOLA project. For the above described base case with 550 °C turbine inlet temperature it is assumed that proven materials such as 1 % chromium steels for shaft and casings can be used.

Table 6: Thermal boundary conditions for a sCO₂ turbine and a steam turbine for use case 2 (CSP)

Thermal boundary condition	CO ₂ turbine	Steam turbine *)
Inlet pressure [bar]	260	170/34
Inlet temperature [°C]	550	550/550
Mass flow [kg/s]	946	85/79
Inlet volume flow [m ³ /s]	5,9	1,7/8,7
Outlet pressure [bar]	78	78/0,07
Outlet volume flow [m ³ /s]	15,6	5,7/797
Enthalpy difference [kJ/kg]	154,7	414/1154
Nominal shaft power [MW]	147	117

*) the second value corresponds to the reheat turbine

By comparing the parameters in table 6, some general statements can be made, which describe how sCO₂ turbines differ from steam turbines and what the special requirements are. Beside the well-known fact that the pressure levels of sCO₂ cycles are higher, especially at the low-pressure side, it is obvious that the expansion line, i.e. the enthalpy difference of the turbine is significant smaller compared to the steam turbine. Consequently, the mass flow in an sCO₂ cycle must be larger compared to a Rankine cycle assuming

the same power output.

In the considered use case, the reference cycle is operating also at a high-pressure level of 170 bar. Comparing the inlet volume flow of both turbines it can be seen that the value of the CO₂ turbine is approximately 3 times larger than the volume flow of the corresponding steam turbine. This leads to significant larger cross-sectional areas of the high-pressure piping and the inlet of the turbine. This difference becomes smaller when the reference steam process operates at a lower pressure as it is the case in the WHR example described in the first section of this paper.

On the other hand, the volume flow at the low-pressure side of the CO₂ turbine is several orders of magnitude smaller compared to the steam turbine. This results in a significantly lower space requirement within the nacelle, which significantly reduces secondary costs such as steel construction, foundations, etc.

Based of the derived turbine designs, a simplified efficiency model was derived in order to support further process optimizations within the two working packages of the CARBOSOLA project [1,2]. A simple mathematical relationship was fitted to data points, where the efficiency is a function of the volume flow and of the isentropic enthalpy difference. The dependency of the volumetric flow, which is well known from axial turbines, is mainly driven by leakage losses of the blades. Due to the comparatively small enthalpy difference across the turbine the impact of internal pressure losses, e.g. in inlet and outlet, and the impact of internal leakages is quite high as shown in the first sections of this paper. The smaller the enthalpy drop of a turbine, the greater the influence of these constant losses on the isentropic efficiency. In particular this consideration has led to a penalty of the turbine efficiencies in reheated cycle layouts of the CSP use case evaluation carried out by Heller et al. [5]. Figure 12 shows the efficiency curve for different inlet volume flows and isentropic enthalpy differences. The consideration of further influencing variables such as blading technology was not carried out for reasons of simplification.

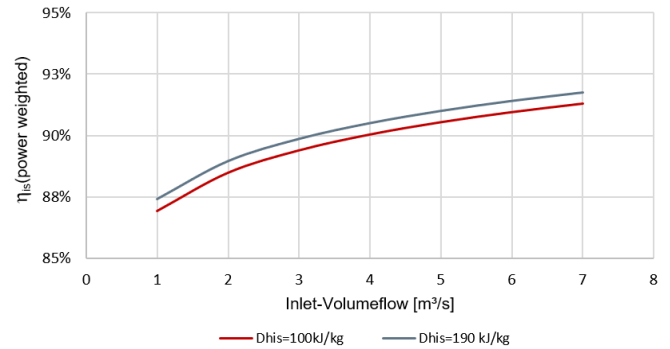


Figure 12: Isentropic efficiency of CO₂ turbine including all internal and external leakages (power weighted).

CONCLUSION AND OUTLOOK

In a first project phase of the Carbosola project, different aspects of the turbine design have been investigated leading to first design concepts for a waste heat recovery and a CSP use case. Due to the high density of the working medium CO₂ and the characteristic low enthalpy drop various aspects such as fluid friction, pressure losses, asymmetrical flow conditions and leakages are of greater importance than for steam or gas turbines and need to be further evaluated. All in all, very compact turbines can be achieved that are highly efficient and have a low footprint, especially due to the low volume flows at the cold end. Further investigations and design optimizations are envisaged in a next step of the project.

NOMENCLATURE

A	Constant
C	Windage coefficient
CSP	Concentrated Solar Power
DGS	Dry-Gas Seal
d	day
f	friction
is	isentropic
$L-C$	Coated labyrinth seal
P	Power [kW]
Re	Reynolds number
s	Entropy
sCO_2	Supercritical Carbon Dioxide
$S-S$	Fin-Fin seal
T	Temperature [°C or K]
t	tons
\dot{V}	Volume flow [m ³ /s]
w	Velocity
Δ	Difference
η	Efficiency
ρ	Density
τ	wall shear

ACKNOWLEDGEMENTS

These investigations were conducted as part of the research project CARBOSOLA. The authors would like to thank the Federal Ministry of Economics and Energy (BMWi) for the financial support as per resolution of the German Bundestag under grant numbers 03EE5001A. The authors alone are responsible for the content of this paper.



REFERENCES

- [1] Gothelip, T.G., Gampe, U., Glos, S. (2021). Techno-economic optimization method and its application to a sCO₂ gas turbine bottoming cycle. *4th European sCO₂ Conference 2021*
- [2] Hecker, S.: (2011). Strömungs- und strukturmechanische Untersuchung der Einströmung einer Dampfturbine, *Dissertation Ruhr Universität Bochum*
- [3] Hecker, S., Musch, Ch., Penkner, A., Glos, S. (2017). CFD based approach to predict the windage heating effect in steam turbine labyrinth seals. *1st Global Power and Propulsion Forum GPPF 2017*
- [4] Laxander, A., Fesel, A., Hellmig, B. (2019). Development and testing of dry gas seals for turbomachinery in multiphase CO₂ application, *3rd European sCO₂ Conference 2019*
- [5] Heller, L., Buck, R., Glos, S. (2021). sCO₂ power cycle design without heat source limitations: Solar thermal particle technology in the CARBOSOLA project, *4th European sCO₂ Conference 2021*
- [6] Subbaraman, G., Kung, S., Saari, H. (2018) Materials for Supercritical CO₂ Applications, *Tutorial at 6 th International sCO₂ Power Cycles Symposium 2018*
- [7] Pint, B.A., Unocic, K.A., Keiser, J.R. (2019) Effect of impurities on supercritical CO₂ compatibility, *3rd European sCO₂ Conference 2019*
- [8] A. Kacludis, S. Lyons, D. Nadav and E. Zdankiewicz (2012) Waste Heat to Power Applications using a Supercritical CO₂-based Power Cycle, *Power Gen International, Orlando, FL, 2012*
- [9] C. Kalra, D. Hofer, E. Sevincer, J. Moore and K. Brun (2014) Development of High Efficiency Hot Gas Turbo-expander for Optimized CSP sCO₂ Power Block Operation, *4th International sCO₂ Power Cycles Symposium, Pittsburgh, 2014*
- [10] R.A. Bidkar et al. (2016) Conceptual Designs of 50MWe and 450MWe Supercritical CO₂ Turbomachinery Trains for Power Generation from Coal. Part I: Cycle and Turbine, *5th International sCO₂ Power Cycles Symposium, San Antonio, 2016*

2021-sCO₂.eu-112

TECHNO-ECONOMIC OPTIMIZATION METHOD AND ITS APPLICATION TO AN sCO₂ GAS TURBINE BOTTOMING CYCLE

Thiago Gotelip*

Technische Universität Dresden
Dresden, Germany

Email: Thiago.Gotelip_Correa_Veloso@tu-dresden.de

Uwe Gampe

Technische Universität Dresden
Dresden, Germany

Stefan Glos

Siemens Energy AG
Mülheim, Germany

ABSTRACT

Cycle architecture, fluid parameter selection, and component design of an exhaust/waste heat recovery cycle require an integral approach. The exhaust/waste heat shall be utilized to a maximum but at minimum costs. The bottoming cycle needs to be aligned with the topping cycle regarding operational behavior, especially for a part load. To analyze potentials of exhaust heat recovery in a combined gas turbine sCO₂ cycle, the bottoming cycle's optimum cycle architecture and fluid parameters must be determined. A thermo-physical model of the sCO₂ bottoming cycle, including knowledge of component design, component behavior, and costs, is based on the multiobjective optimization procedure. As part of the CARBOSOLA project, techno-economic optimizations for a use case of exhaust heat recovery have been carried out. The paper aims to present the optimization methodology followed by the specific use case's boundary conditions, investigated sCO₂ cycle architectures, and results of optimum cycle architecture and fluid parameters for maximum heat recovery and minimum costs. Attention will also be paid to accurate modeling of heat exchangers operating near the critical point.

INTRODUCTION

Over the last decade, the application of supercritical CO₂ (sCO₂) for power generation has received substantial interest as the technology prospects shows high efficiency, compact equipment, low emission, higher operational flexibility and lower plant complexity.

The sCO₂ cycle operation near the CO₂ critical point gives the cycle essential characteristics such as very compact turbomachines, a compression in an almost incompressible region, allowing good efficiency characteristics to the compressor. Thus, this technology combines the advantages of the steam Rankine cycle and gas turbine cycle.

The thermodynamic properties suffer significant variations near the critical point, and the determination of these characteristics in this region as heat transfer and pressure drop of carbon dioxide (CO₂) are difficult to predict. These are crucial issues for the design of the cycle. Wahl [1] propose an investigation of the heat transfer and pressure drop of carbon dioxide near the critical point cooled in a 2 mm diameter. Significant effects on the mass flux, inlet pressure and cooling temperature on the heat transfer was analyzed. The investigations in [2–4] also present the characteristics of the sCO₂ cycle near the pseudo-critical point.

Accurate thermo-economic analysis of sCO₂ cycles is a driver for the development of the technology. Weiland et al., [5] reports on sCO₂ component cost scaling relationships that have been developed collaboratively from an aggregate set of vendor quotes, cost estimates, and published literature. Thermo-economic evaluation of sCO₂ power cycle design is also investigated in [6–8].

Several sCO₂ cycle architecture have been analyzed in previous studies. Milani et al., [9] identified in their study 14 representations of sCO₂ cycles from the literature. The authors categorized these representations into three common features sub-groups depending on the expected enhancement effect in the cycle thermal efficiency calculation: (1) heat recuperation enhancement, (2) turbine work boosting, and (3) compression work reduction. Crespi et al., [10] presented in their study a systematic thermodynamic analysis of 12 supercritical carbon dioxide cycles under similar working conditions. The analysis regarding different architectures is also analyzed in [11,12].

Recent studies on sCO₂ cycle optimization are summarized in [13]. The authors compile several analyses and optimization of the sCO₂ power cycle from the different aspects, including different types of heat sources, high-efficiency heat exchangers, cycle layouts and optimizations, and aerodynamic design of turbomachinery. Optimizations regarding cycle performance and

* corresponding author(s)

economic analysis are the objectives of other investigations like [14,15].

The multiobjective optimization proposed in this study evaluates different conflicting objective functions. A parametric analysis is insufficient for a comprehensive evaluation of the systems' performance investigated.

The multiobjective optimization process is very susceptible to objective functions, cost models, economic evaluation boundaries, equipment design, and equipment efficiency. This analysis is essential to provide the optimal operation conditions since only the precise combination of these variables allows the best technical and economic performance.

CARBOSOLA PROJECT

The CARBOSOLA project presented in this paper is intended to represent the entry into sCO₂ technology development in Germany. This requires an analysis of the expected advantages. Therefore, the sCO₂ technology will be compared with conventional technologies in the fields of waste and exhaust heat recovery (bottoming cycles of combined cycle gas turbine plants) and solar-thermal power plant technology (CSP) and subjected to a technical-economic evaluation. The technology comparison is intended to show what increase in efficiency can be expected when using sCO₂ compared to water/steam and what the electricity production costs are. However, the core of the project is the component and system design of a technology demonstrator to use secondary heat, construction and commissioning of a test loop, and the methods required for further technology development up to commercial maturity.

The consortium of public funded project CARBOSOLA under the lead of Siemens Energy comprises of four partners. TU Dresden and the Helmholtz Zentrum Dresden-Rossendorf covering the necessary scientific-technical investigations for technology and product development. Furthermore, DLR provides the expertise for the evaluation of solar thermal power plants and Siemens Energy has a high level of expertise in the field of power plant technology and covers the necessary know-how of all components involved such as turbines, compressors and heat exchangers.

THERMODYNAMIC PERFORMANCE

In this first work package of CARBOSOLA the exhaust heat of two aeroderivative gas turbines was defined as use case for the optimization of a sCO₂ cycle. Those gas turbines are often applied for mechanical drive of compressors in the oil and gas industry. Another application is combined heat and power generation. The thermodynamic boundaries of the considered use case are listed in Table 1.

The conceptual design process consists of two major activities – selecting the cycle architecture and sizing the equipment. The term “cycle architecture” refers to the general arrangement of turbines, pumps, recuperators and external heat exchangers. [14]

In this study, the optimization of five different architectures will be evaluated. This methodology considered the analysis of less complex configurations such as the Simple and Regenerative cycle and more elaborate architectures, referenced

as the number of their heat exchangers (heater and recuperator): 3H2R, 2H2R, 2H1R.

Table 1 Exhaust Gas Characteristics

Heat Source	2 x AGT on 1 sCO ₂
Pressure [bar]	1,04
Temperature [°C]	432
Cold Flue Gas Temperature [°C]	≥ 75
Mass Flow [kg/s]	337
Wet cooling tower parameters:	
Ambient Temperature [°C]	15
Wet Bulb Temperature [°C]	10,8
Approach Temperature [°C]	5
Warm Up Range [°C]	7

The 3H2R architecture, Figure 1, is based on the Dual Rail cycle configuration proposed in [16]. This configuration performs source heat recovery using three heaters and a high-temperature recuperator and low-temperature recuperator. This architecture is also discussed in [14,17,18] for the heat recovery of gas turbines. The schematic representation of the other architectures is presented in the annex.

The 2H2R architecture is a reference to the cascade cycle, originally proposed [19]. This configuration is composed of two heaters and two recuperators. This architecture is also investigated in [20] and [21], with modifications, such as one more compressor with intercooling.

The 2H1R architecture was proposed to combine the less complex cycles' characteristics with the more elaborate arrangements. This one is composed of two heaters and only one recuperator, of high temperature.

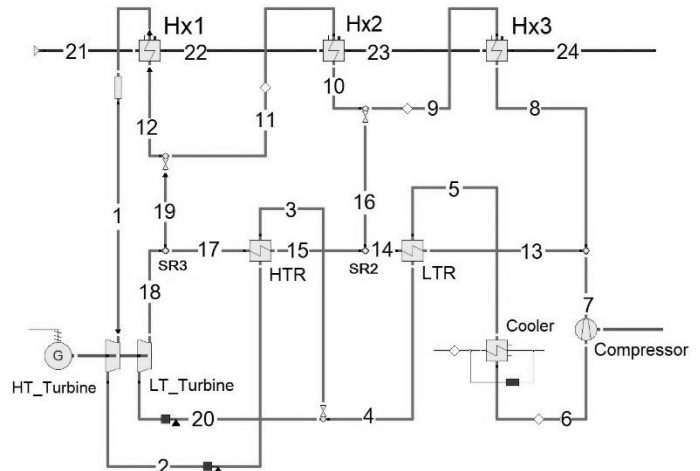


Figure 1: Layout scheme of sCO₂ architecture.

In Simple and Regenerative cycles, only one turbine performs the expansion, while the other configurations bases on processes divided into a high temperature and a low-temperature turbine. This study considers the split expansion as an optimization criterion in this study. In this way, the cycles' operation is also evaluated with the system's simplification using only one turbine. The consideration of this criterion modifies the

3H2R and 2H2R cycles of the same ones that were initially based.

Due to the variation of the CO₂ properties close to the critical point, the pinch point restriction is a fundamental constraint in sCO₂ operations. Figure 2 illustrates the behavior of the specific heat capacity for CO₂ using Refprop® data.

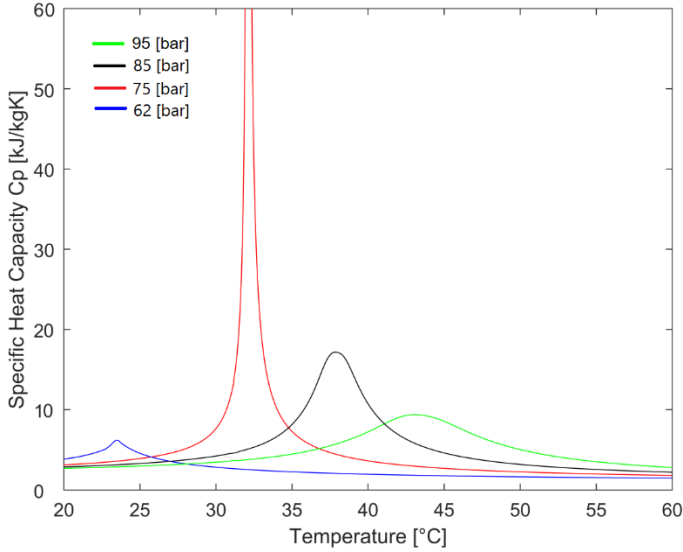


Figure 2: Specific heat capacity of CO₂ near the critical point. Elaborate by the author with Refprop® data.

As can be observed for each of the pressures in the supercritical region, above the critical CO₂ pressure, the specific heat capacity passes through a peak when it crosses the pseudocritical temperature. The pseudocritical temperature increases with the pressure, and moreover, the distinct peaks are flattened. [1]

The thermal conductivity to CO₂ in this region also shows a similar behavior, linked to the specific heat capacity behavior, Figure 3.

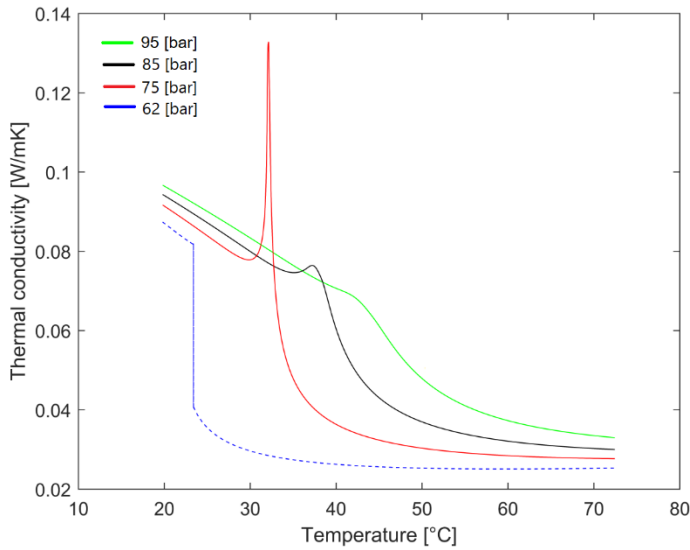


Figure 3: Thermal conductivity of CO₂ near the critical point. Elaborate by the author with Refprop® data.

In the gas region, the thermal conductivity increases when approaching the pseudocritical temperature. The higher pressures present higher thermal conductivity before the peak, although the value at the peak increases with the decreasing pressure. The pressure also shifts the pseudocritical temperature.

The properties of CO₂ close to the critical point is the object of study of [2–4]. The variation of these properties is a determining factor for the heat exchangers' design, significantly the cooler. The heat exchangers analysis in these cycles should be carefully investigated.

For calculating CO₂ properties in each heat exchanger, the variable property segmented calculation method (VPSC) is considered more suitable for non-constant thermal capacities process streams.

The VPSC method for property calculations consists of dividing the heat exchangers into several small blocks along the length. This methodology determines the working fluid's physical properties according to each block's inlet and outlet pressures, and the temperature is calculated by the LMTD method at each block. The overall conductance UA in each heat exchanger is defined by equations 1 and 2.

$$U \cdot A = \sum_{i=1}^n \left(\frac{\dot{Q}_i}{LMTD_i} \right) \quad 1$$

$$LMTD = \left[\frac{(\Delta T_{hot} - \Delta T_{cold})}{\ln(\Delta T_{hot} / \Delta T_{cold})} \right] \quad 2$$

i = number of segments for the heat exchanger.

In conventional LMTD, physical property is assumed to be constant during the solving process. According to Ke et al. [22], the LMTD is not appropriate for the thermal design of heat exchanger for sCO₂ applications, and the VPSC can be used to obtain more reliable results. The optimization tool model considers each heat exchanger's analysis divided into 100 sections to avoid these analysis errors. The method validation with Epsilon indicated relative errors lower than 0.1 The same methodology is adopted by Held [14] for a 25 sub-element discretized heat exchanger model.

ECONOMIC ANALYSIS

The equipment cost model follows the study of [5]. In this study, the authors used data from 93 vendor quotes to generate component cost models. The general equation for the cost of equipment is determined by [5]:

$$C = aSP^b \times f_T \quad 3$$

Where C is the component cost, a and b are fit coefficients, SP is the scaling parameter, and f_T is a temperature correction factor described by [5]:

$$f_T = \begin{cases} 1 & \text{if } T_{max} < T_{bp} \\ 1 + c(T_{max} - T_{bp}) + d(T_{max} - T_{bp})^2 & \text{if } T_{max} \geq T_{bp} \end{cases} \quad 4$$

where T_{bp} is the temperature breakpoint, typically 550 °C, and T_{max} is the maximum temperature rating of the component in units of °C.

Table 2 presents the equipment cost model that follows the model proposed by [5]. The heater's cost assumes the cost correlations of the recuperators. It is an approximation since the heat source is the exhaust gases from gas turbines. New correlations are being evaluated to represent the heaters more accurately in future analyses. The equation for cooling tower, piping, and auxiliary systems costs are omitted by confidentiality.

Table 2 Summary of the scaling parameters for cost correlation. Source: Adapted from [5]

Equipment	a	SP		b
Heater	49.45	UA_{Heater}	$[W_t/K]$	0.7544
Recuperator	49.45	UA_{Recu}	$[W_t/K]$	0.7544
Cooler	32.88	UA_{Cooler}	$[W_t/K]$	0.75
Axial Turbine	182600	P_{mec}	$[MW_t]$	0.5561
Generator	108900	P_e	$[MW_e]$	0.5463
Gearbox	177200	P_{mec}	$[MW_t]$	0.2434
Compressor (centrifugal)	1230000	P_{shaft}	$[MW_t]$	0.3992
Motor	399400	P_e	$[MW_e]$	0.6062

The study adopts the net present value methodology (NPV) and Levelized Cost of Energy (LCOE) as economic evaluation criteria.

NPV is defined as:

$$NPV = \sum_{n=1}^{n=25 \text{ years}} \frac{\text{Revenue} - (\text{Capex} - \text{Opex})}{(1 + \text{interestrate})^n} \quad 5$$

CAPEX: Capital expenditure of main components.

OPEX: Operational expenditure including operation and maintenance.

Table 3 presents a possible distribution of the costs. CAPEX is associated with fixed capital investment (FCI), although the construction costs that make up the indirect costs were not considered in this analysis and will be implemented in the following studies.

Table 3 Total investment decomposition. Source: Adapted from [23]

Fixed capital investment (FCI)	Direct costs (DC)	Onsite costs	Purchased Equipment Costs (PEC)	Calculated
			Others	
Indirect costs (IC)	Offsite costs	Civil work	%PEC	
		Service	%PEC	
		Engineering	%DC	
		Construction Costs	%DC	
		Contingency	%	

The Levelized Cost Of Electricity (LCOE) is an aggregated indicator of the overall process costs levelized during the power plant lifetime. It encompasses annualized cost of the investment (CAPEX) using a discount rate, the operational costs, and the obtained electric production [24].

$$LCOE = \frac{CAPEX \times f_a + OPEX}{P_e \times Hour_{year}} \quad 5$$

f_a : Discount factor that considers both the risk aversion of the investor and the investment distribution over the plant lifetime.

P_e : The electrical power output of the power plant.

$Hour_{year}$: The plant availability

OPTIMIZATION STRUCTURE

This research presents the optimization analysis of the sCO₂ bottoming cycle. The analysis tool OptDesign was developed to evaluate the performance of different sCO₂ cycle architectures for various applications.

The program compiled in MATLAB® determines the thermodynamic properties (based on the Refprop® data library) for each equipment. The thermo-physical model includes knowledge of component design, component behavior, and its costs. The model is used as part of the CARBOSOLA project for thermo-economic optimization based on the equipment and the system.

Figure 4 represents the logical flow process in the OptDesign tool. Initially, the heat source in each analysis case is characterized by chemical composition, mass flow, and thermodynamic condition. Table 4 shows the input parameters that define the thermodynamic balances of the cycle. These are the decision variables in multiobjective optimization.

Table 4 Variables included in multi-objective optimization.

	Discrete variable	Range	
Pressure Level [bar]	Pressure (HP)	200 – 300	
	Pressure (LP_{Sub})	57.2 - 65.8*	
	Pressure (LP_{Sup})	75 - 110	
Heater HX1	UTTD	> 10	$UTTD = T_{21} - T_{12}$
	Effectiveness	< 0.98	$\epsilon_{HX1} = \frac{T_{21} - T_{22}}{T_{21} - T_{12}}$
Recup. HTR	UTTD	> 5	$UTTD = T_2 - T_{17}$
	Effectiveness	< 0.98	$\epsilon_{HX1} = \frac{T_2 - T_3}{T_2 - T_{17}}$
Split ratio	SR2	0.1 - 1	$SR_2 = \frac{\dot{m}_{16}}{\dot{m}_{14}}$
			$SR_3 = \frac{\dot{m}_{19}}{\dot{m}_{17}}$
	SR3	0.1 - 1	

The model initially considers the isentropic efficiency of the pump/compressor and turbine as 80% and 90%, respectively.

The computational tool performs the mass and energy balance for each equipment of the cycle through its thermophysical models. With the determined parameters, it is

possible to evaluate the turbine's isentropic efficiency for the specified operating conditions. Industrial correlations determine the efficiency of the turbine from the volumetric flow of CO₂ at the equipment entrance. This similarity is not presented by confidentiality.

The calculation routines are updated with new turbine efficiency until the results reach convergence. The program counts with subroutines to investigate the heat exchangers' initial design for each evaluated condition to restrict unfeasible conditions. Once the cycle's operating conditions are determined, it performs an economic analysis to determine the equipment costs. The multi-objective optimization process means seeking a set of the best possible solutions based on a predetermined criterion. The tool allows the investigation of different objective functions, according to the analysis proposal.

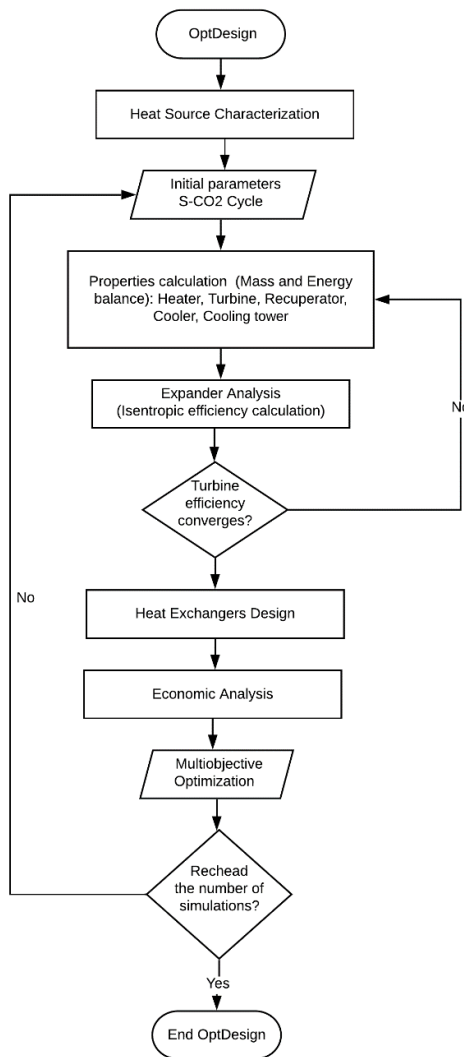


Figure 4: Flow chart of OptDesign optimization program.

The compressor inlet temperature is considered constant at 20°C. The minimum pressure of 57.29bar refers to the condensation pressure of CO₂ at 20°C, while the pressure 65.80bar determines the condensation temperature of 26°C, referring to the differential of 5K to the critical temperature of

CO₂. The comparison of the results of the main components is summarized in Table 5 for an operating condition of the 3H2R cycle architecture.

A multi-objective optimization problem requires the simultaneous satisfaction of several different and generally conflicting objectives, making it impossible to find a solution that satisfies all objectives simultaneously. Therefore, it is necessary to find a set of optimal solutions. [25]

The tool performs multi-objective computer-aided optimizations for different applications and configurations of sCO₂ cycles. In this way, it allows investigating the best-operating conditions and assists in the preliminary development of the cycle's equipment and architecture.

Table 5 Validation of OptDesign Thermodynamic Model.

		Ebsilon	OptDesign	Relative error
Heater 1	[MW]	81.71	81.70	0.014%
Heater 2	[MW]	43.97	43.96	0.014%
Heater 3	[MW]	0.57	0.57	0.012%
Recuparator HTR	[MW]	63.73	63.72	0.013%
Recuparator LTR	[MW]	3.28	3.28	0.013%
Cooler	[MW]	94.40	94.39	0.013%
Turbine Power	[MW]	44.06	44.05	0.014%
Compressor Power	[MW]	12.22	12.22	0.014%
Net Power	[MW]	31.84	31.84	0.014%
Mass Flow	[kg/s]	375.80	375.75	0.013%

Each combination of the optimization variables generates a candidate vector with its responses to all the cycle characteristics. For each architectural model of the CO₂ system, initially creates a starting population for the optimization algorithms using the Design of Experiment (DOE) techniques. The DOE performs a factorial distribution of the independent variables, generating suitable initial parameters. This procedure simultaneously minimizes the quantity of data while maximizing data quality.

In this study, three optimization scenarios were investigated, having as objective functions:

- Scenario 1: Maximization of net power and minimization of Fixed Capital Investments.
- Scenario 2: Maximization of the Net Present Value and minimization of Fixed Capital Investments.
- Scenario 3: Maximization of Net Present Value and minimization of the Levelized Cost of Energy (LCOE).

RESULTS

From the multi-objective optimization process, a set of optimal solutions called the Pareto front is obtained. It allows a decision-making process to select the final solution from the optimized set. Each of Pareto's front has, on average, 2000 results, which individually gather the combination of the operating parameters of the cycle. The NPV and LCOE values are presented in a normalized format due to confidentiality.

Initially is presented the optimization solutions of the 3H2R layout for the three optimization proposals: scenarios 1, 2, and 3. This analysis will be presented to 3H2R architecture due to its complexity, extending the analysis to the maximum amount of equipment. The results obtained and the operating conditions of each cycle are strongly dependent on the analysis criteria. The effect of the analysis criteria presented is similar in the remaining architectures.

Figure 5 presents the Pareto front of optimization for scenario 1. The solutions present the direct relationship between net power and costs as expected for these types of analysis.

In this analysis, the range of higher net power comes with a more expressive increase in costs. The NPV represented by the color scale reveals that the higher net power values do not favor NPV.

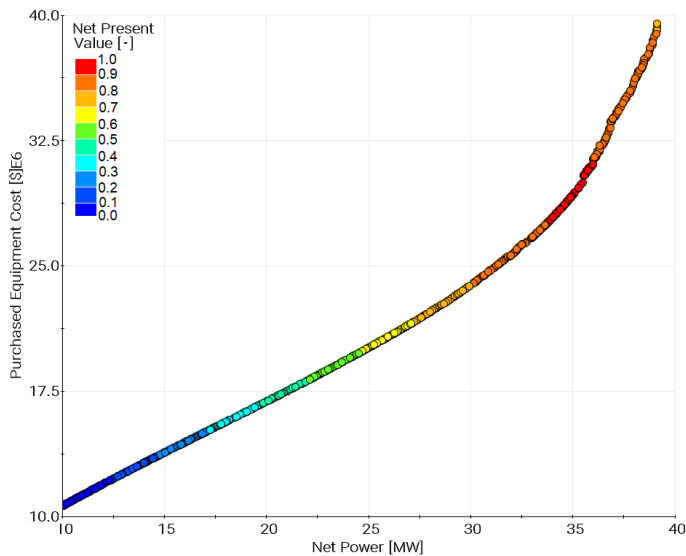


Figure 5: Results of scenario 1 of the 3H2R optimization.

Figure 6 presents the results of scenario 1 with the NPV perspective elucidating this remark.

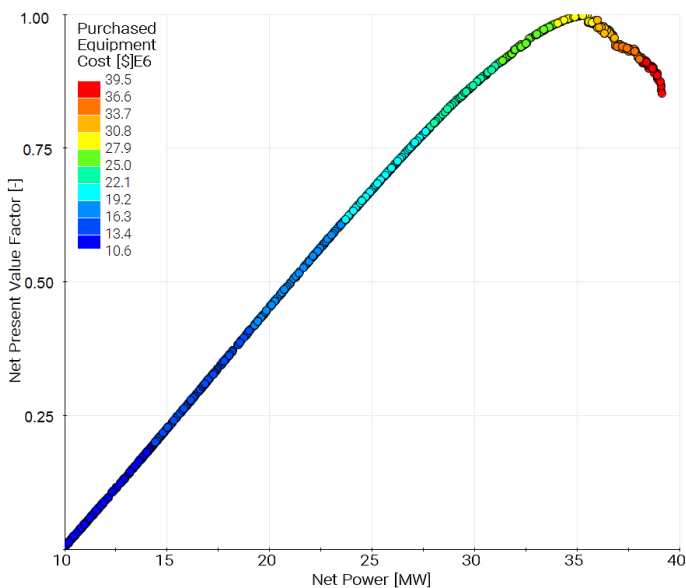


Figure 6: Scenario 1 results from an NPV perspective.

It is possible to perceive by the ascending part of the curve the limit in which the net power increase favors NPV. A sensitivity analysis on the Pareto front reveals that until reaching the NPV peak, the net power exerts a predominant factor on this parameter. While on the descending side of the curve, the costs revealed a more significant influence on it. One of the factors in this change is that higher powers are obtained with lower temperature difference in heat exchangers, significantly increasing the equipment costs.

Another relevant factor is that in the ascending range of NPV, their entirety leads to the cycle's configuration without the auxiliary expansion with the LT turbine.

The use of the LT turbine represents an additional cost of a second turbine with its auxiliary equipment. Thus, in the optimal results, the use of this equipment is justified when aiming to increase the net power, the increase of the mass flow is no longer supported by restrictions of temperature difference in heater 1.

Thus, the mass flow increase is allowed by dividing it in SR3, which is expanded in the LT turbine. These operating conditions reflect higher heat recovery in HTR and a significant increase in this equipment's costs.

The model for calculating the isentropic efficiency of the turbine is strongly dependent on the volumetric flow. The operating conditions of the CO₂ in the LT turbine penalize the equipment's efficiency, reducing to the range of 83% while the HT turbine operates close to 90%.

These factors indispose the LT turbine configuration from an NPV perspective. Although it can provide a net power increase, the LT turbine operating condition is associated with the evaluated curve's descending section.

Figure 7 presents the optimization solutions according to scenario 2. The Pareto front in this analysis is a range of the results presented in the previous analysis since the criteria that lead to NPV maximization are the same as those that lead to net power maximization. The gray representation in the graph refers to scenario 1, which here are not part of the optimal results because they provide lower NPV. This region refers to the descending part of the curve in the previous picture.

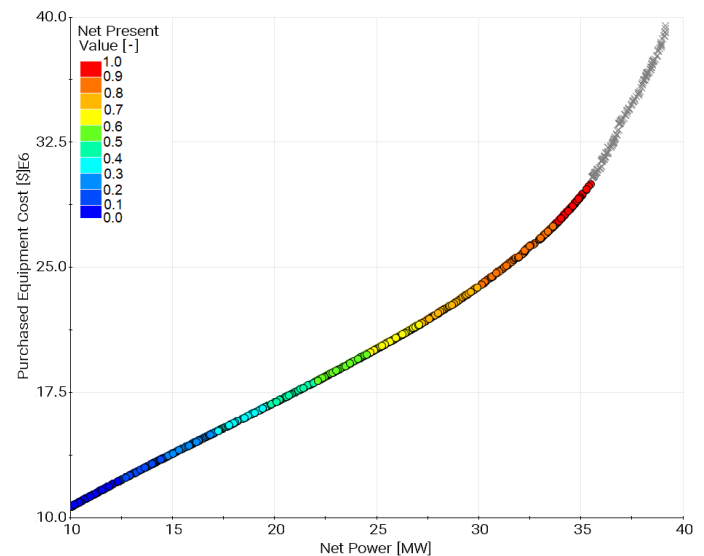


Figure 7: Results of scenario 2 of the 3H2R optimization.

The highest NPV condition, in this case, is 16.9% higher than the highest net power condition of scenario 2, even if the thermal efficiency of the cycle is 9.5% lower, and the net power is reduced in the same proportion.

Figures 8 and 9 present the cycle's exergetic analysis to maximize the net power and NPV maximization of the two optimization scenarios.

The condition that favors higher net power provides an exergetic efficiency of 67.16%, 13.7% superior to the condition in higher NPV. The net power maximization is achieved from the higher mass flow and increased heat recovery in the heat exchangers.

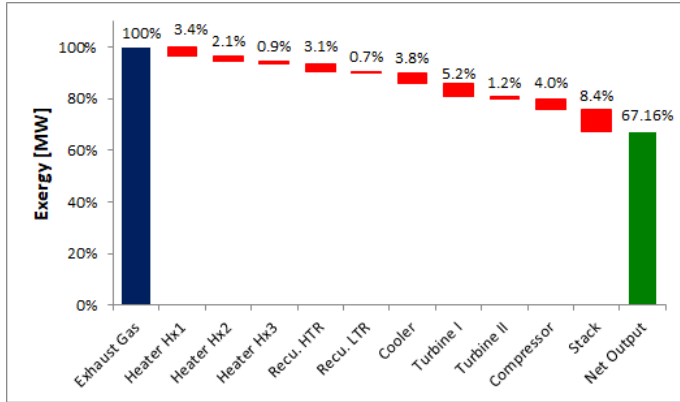


Figure 8: Exergetic analysis of higher net power condition. Optimization scenario 1.

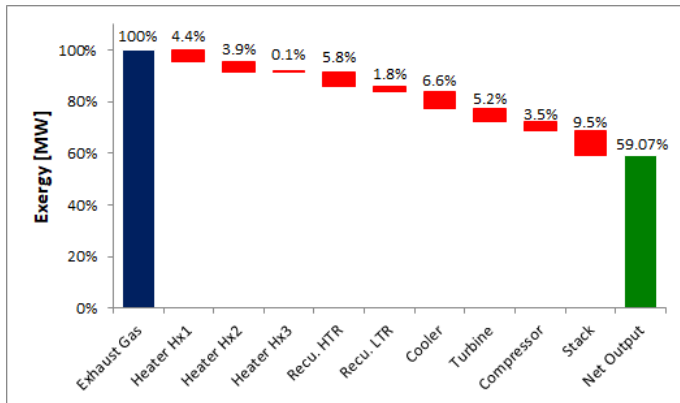


Figure 9: Exergetic analysis of higher NPV condition. Optimization scenario 2.

This analysis shows that the conditions for higher NPV operate comparatively with lower heat recovery, mainly in HTR, evidenced by the increase of exergy losses in this equipment and the cooler. There is also less heat recovery from the source, indicated by losses in heaters the stack. Although this condition leads to a less efficient cycle, it favors fewer costs by not operating with such reduced temperature differences.

Figure 10 presents the relationship between the three optimization scenarios results as reference LCOE, and net power Scenario 3 assumes LCOE minimization rather than FCI as an objective function of optimization. The color scale region represents the frontier of the optimal results of the third

optimization scenario. The green band of the graph represents the optimization values of scenario 2, which are not part of the optimal solutions of the new analysis. The gray region refers to the maximization of the net power, which provides a lower NPV.

The solutions reveal that the optimal ratio from the lowest LCOE to the highest NPV corresponds to the same operating conditions of scenario 2 regarding from 84% to the maximum value of NPV. This range is associated with net powers between 31.9 and 35.5 [MW].

According to each objective function, the optimal operating ranges portion depends on the equipment's cost functions. The boundaries of the system and the costs included in the NPV and LCOE analysis are also essential to determine the cycle operation conditions.

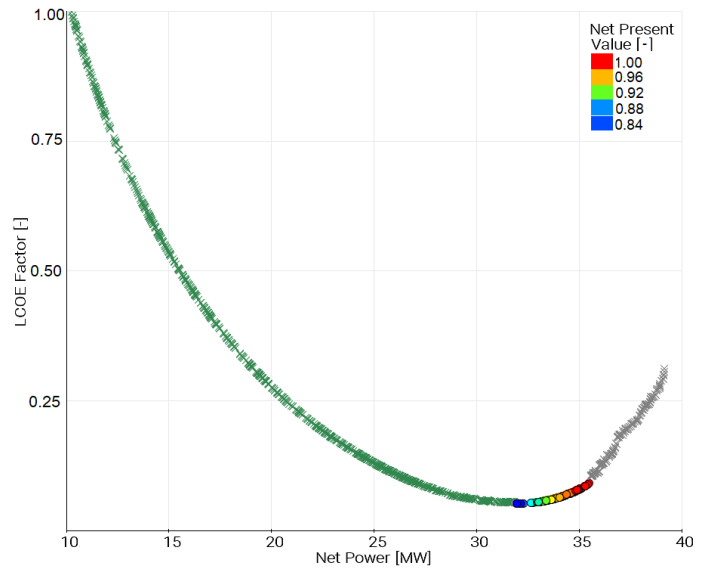


Figure 10: Scenario 3 results from a net power perspective.

ARCHITECTURE OPTIMIZATION

The three optimization approaches, scenarios 1, 2, and 3 were executed to evaluate the best operating conditions for the different sCO₂ cycle configurations: 3H2R, 2H2R, 2H1R, Regenerative, and Simple.

Optimization from the scenario 1 perspective reveals that when considering net power maximization, the more complex 3H2R and 2H2R systems allow for more efficient cycles providing higher power than the others.

Figure 11 presents each Pareto's front for scenario 2 optimization of Layouts 3H2R, 2H2R, 2H1R, Regenerative, and Simple.

The more complex 3H2R and 2H2R, although it may favor higher power ranges, which differentiate these configurations from the others, are economically penalized by the significant increase in equipment costs, not favoring NPV. In this perspective, these configurations are no longer an appreciable option.

The Regenerative and Simple layouts, less complex, are limited in their capacity to generate power. Since for the simple cycle operation, the CO₂ temperature at the turbine inlet is

significantly low (outlet temperature of the compressor), the amount of working fluid is restricted by the minimum temperature of the stack in the evaporator's mass balance. This way, the Simple cycle operates with the lower mass flow (66% of the 2H1R flow) and generates lower power.

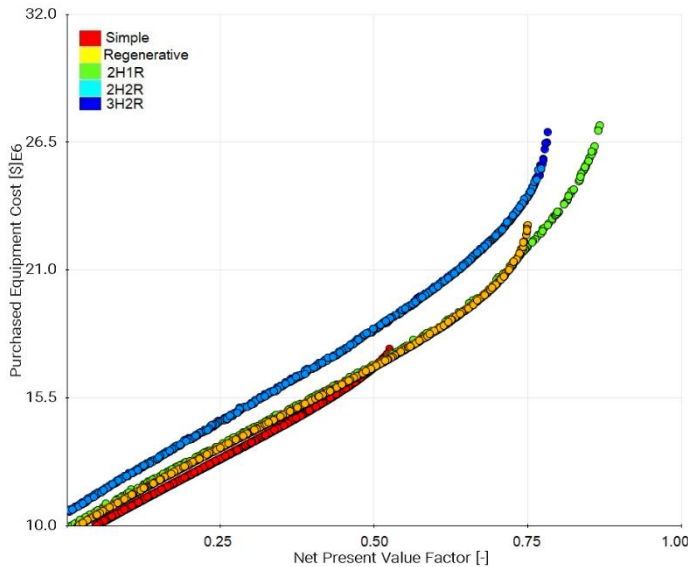


Figure 11: Optimization results of the different architectures for supercritical cycle.

The recuperator's use allows the Regenerative cycle an operation with a higher mass flow by providing a favorable condition to the working fluid at the evaporator entrance.

However, the maximum mass flow in this configuration occurs when it reaches the lower terminal temperature difference on heater 01. In this way, the heat recovered from the source in this configuration is the lowest, and the exhaust gas temperature after the heater is considerably higher.

This way, operation with the 2H1R configuration presents the best performance providing the highest NPV values associated with lower costs in subcritical and supercritical regions.

The optimization process presented in this paper also availed the subcritical operation condition. As in the supercritical operation, the 2H1R configuration had the best performance.

Figure 12 compares the optimization solutions for the 2H1R configuration to scenario 3 for supercritical and subcritical operating conditions. Comparing the optimal results in these two conditions highlights the potentialities and constraints of the supercritical cycle.

The NPV scale was normalized to the highest NPV condition, referring to the subcritical operation cycle. In this condition, the optimal solutions occur with NPV between 91.3% and its maximum value. The supercritical operation does not allow the same net power generation, and consequently, the range of optimal results corresponds to 81.5 to 88.6% of the reference value.

Analysis of the optimal solution range reveals that the net power is more significant than the costs to increase the NPV.

However, this relationship is reversed in the LCOE analysis, with costs being the prominent role.

Optimal solutions occur with a small range of LCOE. This parameter has been normalized to the superior condition of the supercritical cycle. The lowest supercritical LCOE condition occurs with a 2.1% reduction, while the subcritical cycle solutions range provides 2.3 to 4.8% lower LCOE.

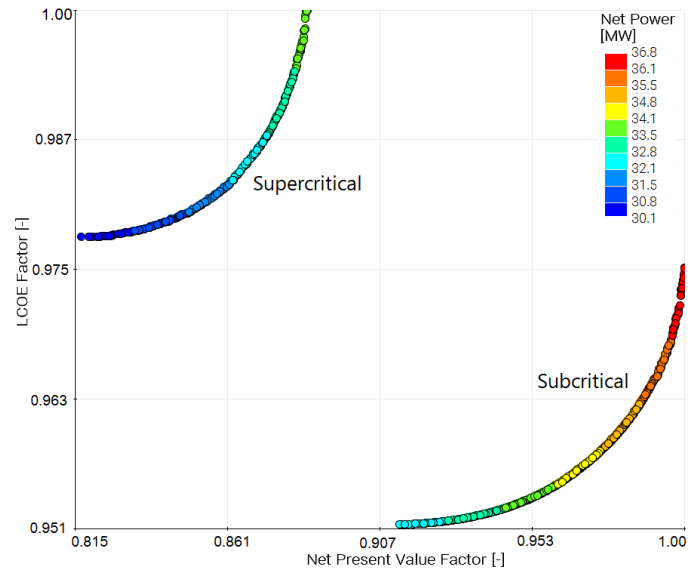


Figure 12: Comparison of 2H1R architecture optimization.

Figure 13 represents the Temperature-entropy (T-s) diagram to the maximum NPV operating parameters for both condition of 2H1R cycles.

The supercritical system is associated with lower costs, mainly related to the cooler. However, it provides less power generation in the optimum range. Since the pressure ratio in the turbine is invariably lower than in the subcritical configuration.

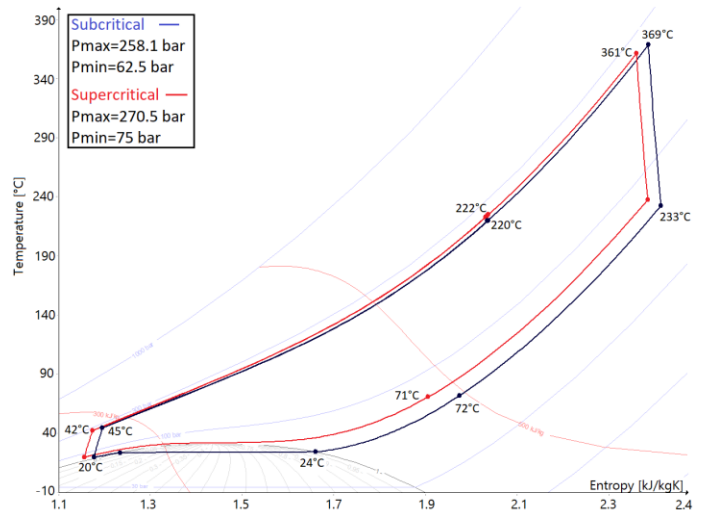


Figure 13: Operating conditions of 2H1R cycle at supercritical and subcritical conditions.

The supercritical system tends to slightly higher operating pressures and a significant increment in mass flow.

The operation with higher pressures (at turbine inlet) negatively affects the turbine's efficiency and equipment costs. Net power is a predominant aspect of this range of optimal results. Therefore, the turbine efficiency calculation is a very relevant and sensitive factor for determining the cycle's operation. As this parameter is strongly associated with CO₂ volume flow at the equipment inlet, the operating pressure range is directly related to this condition.

The turbine outlet temperature is higher in supercritical systems due to the higher pressure, limited to 75 bar. This way, it has as standard a more extensive heat recovery in the recuperator. It allows the cycle to operate with higher mass flows. These characteristics result in less heat recovery in the heater, penalizing the cycle's efficiency, to the detriment of lower equipment costs. Greater use of heat from the source would allow more significant power generation but lead to the supercritical cycle at higher costs, outside the optimal range.

Although the supercritical operation has lower costs than the subcritical, it is not enough to overcome its lower power generation power. It results in higher specific costs, higher LCOE, and a significant reduction of NPV.

Although the supercritical operation has less NPV than the subcritical cycle, it is less sensitive to variations in ambient conditions. An ambient temperature increase implies more complex restrictions in the subcritical cycle since it has lower temperature difference in the cooler.

Table 6 shows the range of each discrete variable of the optimization, referring to the range of optimal results and the analysis's immediate results. The operating conditions of heat exchangers have similar characteristics in both conditions.

Table 6 Discrete variables and main results of 2H1R optimization.

Discrete Variable		2H1R Sub.	2H1R Sup.
Pressure (<i>HP</i>)	[bar]	255 - 275	268 - 290
Pressure (<i>LP</i>)	[bar]	62.5 - 64.8	75
UTTD (<i>Hx₁</i>)	[-]	54 - 63	57 - 71
Effectiveness (<i>Hx₁</i>)	[-]	0.9 - 0.95	0.9 - 0.95
UTTD (<i>HTR</i>)	[-]	12 - 35	12 - 35
Effectiveness (<i>HTR</i>)	[-]	0.8 - 0.86	0.8 - 0.86
Results		2H1R Sub.	2H1R Sup.
Net Power	[MW]	32.2 - 36.8	30.1 - 33.9
Specific PEC	[\$/kW]	772 - 823	791 - 838

The 2H1R architecture analysis reveals that the equipment contributing to the highest costs are the heaters, followed by the cooler, cooling tower, recuperator, compressor, turbine, and remaining auxiliary equipment.

Sensitivity analyses of the optimal results point out the recuperator as the decisive equipment for the cycle's optimal operation. The recuperator's operating conditions are determinant for the system's mass flow, besides managing the heater and cooler operation. This equipment plays a decisive role in determining the correct equilibrium between power and costs for the optimal operation. In this case, the cost correlations of each component are determinant for this equilibrium setting.

Optimization reveals the most profitable operation. It enables the advancement of the component cost correlation according to the equipment's design development. Further

analyses with updated cost models will follow in the subsequent studies.

CONCLUSION

A thermo-economic model was performed, and three scenarios of multi-objective optimization were evaluated to determine the best conditions of five different sCO₂ cycle architecture of an exhaust/waste heat recovery cycle.

The optimization process is essential to provide the optimal operation conditions, which are very sensitive to objective functions, cost models, boundaries of the economic evaluation, equipment design, and equipment efficiency.

The 2H1R architecture configuration proposed in this study presents the most promising results. The optimal solutions for this architecture as a supercritical operation provide net power generation in the range of 30.1 - 33.9 MW and purchased equipment cost between \$23.8- \$28.5 million when aiming to maximize NPV and minimize LCOE.

Net power is the most relevant parameter for NPV maximization, while total costs are the main driver for LCOE analysis. Equipment cost models and economic analysis strongly influence this relation. It is decisive to the operating conditions of the cycle.

The results indicate a prominent potential for the proposed cycle configuration and operational conditions for exhaust heat recovery in a combined gas turbine sCO₂ cycle.

ACKNOWLEDGEMENTS

These investigations were conducted as part of the research project CARBOSOLA. The authors would like to thank the German Federal Ministry of Economics and Energy (BMWi) for the financial support as per resolution of the German Bundestag under grant numbers 03EE5001A (Siemens) and 03EE5001B (TU Dresden). The authors alone are responsible for the content of this paper.

NOMENCLATURE

<i>3H2R</i>	<i>3 Heaters and 2 Recuperators architecture</i>
<i>2H2R</i>	<i>2 Heaters and 2 Recuperators architecture</i>
<i>2H1R</i>	<i>2 Heaters and 1 Recuperator architecture</i>
<i>CAPEX</i>	<i>Capital expenditure of main C</i>
<i>DC</i>	<i>Direct cost</i>
<i>FCI</i>	<i>Fixed Capital Investment</i>
<i>HT</i>	<i>High temperature</i>
<i>HP</i>	<i>High pressure</i>
<i>HTR</i>	<i>High temperature recuperator</i>
<i>Hx</i>	<i>Heater</i>
<i>IC</i>	<i>Indirect cost</i>
<i>LCOE</i>	<i>Levelized Cost of Energy</i>
<i>LMTD</i>	<i>Log Mean Temperature Difference</i>
<i>LP</i>	<i>Low pressure</i>
<i>LT</i>	<i>Low temperature</i>
<i>LTR</i>	<i>Low temperature recuperators</i>
<i>NPV</i>	<i>Net Present Value</i>
<i>OPEX</i>	<i>Operational expenditure</i>
<i>PEC</i>	<i>Purchased Equipment Cost</i>
<i>SR</i>	<i>Split ratio</i>
<i>VPSC</i>	<i>Variable property segmented calculation</i>

REFERENCES

- [1] Wahl A, Mertz R, Starflinger J. Experimental investigation of heat transfer in tubes to cool CO₂ near the critical point in horizontal flow orientation. 18th Int. Top. Meet. Nucl. React. Therm. Hydraul. NURETH 2019, 2019, p. 2615–28.
- [2] Cabeza L, Gracia A de, Fernández I, Farid M. Supercritical CO₂ as heat transfer fluid: A review. *Appl Therm Eng* 2017;125:799–810.
- [3] Xu XY, Wang QW, Li L, Chen YT, Ma T. Study on thermal resistance distribution and local heat transfer enhancement method for SCO₂-water heat exchange process near pseudo-critical temperature. *Int J Heat Mass Transf* 2015;82:179–88.
- [4] Xiao G, Xing K, Zhang J, Yang T, Ni M, Cen K. Heat Transfer Characteristics of Sco₂ and Dynamic Simulation Model of Sco₂ Loop. 3 Rd Eur Supercrit CO₂ Conf 2019:1–11..
- [5] Weiland NT, Lance BW, Pidaparti S. SCO₂ POWER CYCLE COMPONENT COST CORRELATIONS FROM DOE DATA SPANNING MULTIPLE SCALES AND APPLICATIONS 2019:1–17.
- [6] Wright SA, Davidson CS, Scammell WO. Thermo-Economic Analysis of Four sCO₂ Waste Heat Recovery Power Systems. 5th Int Symp - Supercrit CO₂ Power Cycles 2016:1–16.
- [7] Carlson MD, Middleton BM, Ho CK. Cycles Using Component Cost Models Baselined With Vendor Data. *Proc ASME 2017 Power Energy Conf* 2017:1–7.
- [8] Penkuhn M, Tsatsaronis G. Thermo-economic modeling and analysis of sCO₂ Brayton cycles 2019.
- [9] Milani D, Luu MT, McNaughton R, Abbas A. Optimizing an advanced hybrid of solar-assisted supercritical CO₂ Brayton cycle: A vital transition for low-carbon power generation industry. *Energy Convers Manag* 2017;148:1317–31. <https://doi.org/10.1016/j.enconman.2017.06.017>.
- [10] Crespi F, Gavagnin G, Sánchez D, Martínez GS. Analysis of the Thermodynamic Potential of Supercritical Carbon Dioxide Cycles: A Systematic Approach. *J Eng Gas Turbines Power* 2018;140:1–10..
- [11] Wang K, He YL, Zhu HH. Integration between supercritical CO₂ Brayton cycles and molten salt solar power towers: A review and a comprehensive comparison of different cycle layouts. *Appl Energy* 2017;195:819–36.
- [12] Wang K, Li MJ, Guo JQ, Li P, Liu Z Bin. A systematic comparison of different S-CO₂ Brayton cycle layouts based on multi-objective optimization for applications in solar power tower plants. *Appl Energy* 2018;212:109–21.
- [13] Liao G, Liu L, E J, Zhang F, Chen J, Deng Y, et al. Effects of technical progress on performance and application of supercritical carbon dioxide power cycle: A review. *Energy Convers Manag* 2019;199:23.
- [14] Held TJ. Supercritical CO₂ cycles for gas turbine combined cycle power plants. *Power Gen Int* 2015.
- [15] Mecheri M, Zhao Q. Probabilistic technique for solving computational problem: application of ant colony optimization (aco) to find the best sco₂ brayton cycle configuration. 3rd Eur Supercrit CO₂ Conf Sept 19-20, 2019, Paris, Fr 2019:1–14.
- [16] Giegel J. Heat Engine System Having a Selectively Configurable Working Fluid Circuit. 20150076831, 2015.
- [17] Glos S, Wechsung M, Wagner R, Heidenhof A, Schlehuber D. Evaluation of sCO₂ power cycles for direct and waste heat applications. 2nd Eur Supercrit CO₂ Conf 2018:0–10.
- [18] Wagner R. Thermodynamische Analyse von Sperrvermerk Verbleib der Exemplare 2018.
- [19] Johnson G a, McDowell MW, Connor GMO, Sonwane CG. Supercritical CO₂ Cycle Development at Pratt and Whitney Rocketdyne. *ASME Turbo Expo* 2012 2012.
- [20] Kimzey G. Development of a Brayton Bottoming Cycle using Supercritical Carbon Dioxide as the Working Fluid. *EPRI Rep* 2012:1–31.
- [21] Cho SK, Kim M, Baik S, Ahn Y, Lee JI. Investigation of the bottoming cycle for high efficiency combined cycle gas turbine system with supercritical carbon dioxide power cycle. *Proc ASME Turbo Expo* 2015;9:1–12.
- [22] Ke H, Xiao Q, Cao Y, Ma T, Lin Y, Zeng M, et al. Simulation of the printed circuit heat exchanger for S-CO₂ by segmented methods. *Energy Procedia* 2017;142:4098–103..
- [23] Canepa R, Zunino P. Combined cycle power plant thermo-economic multi-objective optimization using evolutionary algorithm. 2014:1–10.
- [24] Zhao Q. Conception and optimization of supercritical CO₂ Brayton cycles for coal-fired power 2019.
- [25] Sotomonte C, Gotelip T, Coronado C., Nascimento M. Multi-objective optimization for a small biomass cooling and power cogeneration system using binary mixtures. *Appl Therm Eng* 2021;182.

ANNEX A

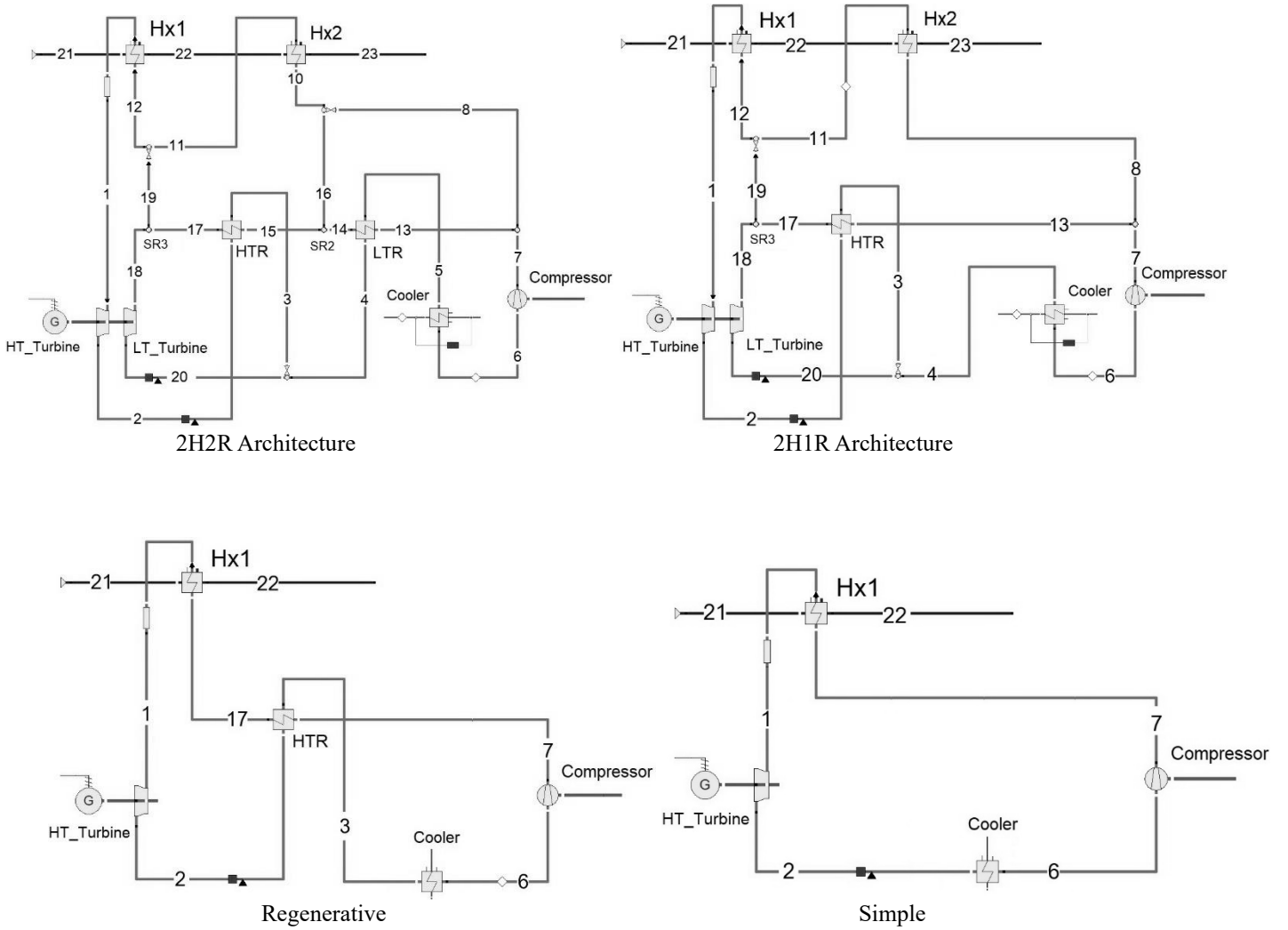


Figure 14: Classification of evaluated sCO₂ architectures.

AN ATTEMPT FOR ESTABLISHING PRESSURE RATIO PERFORMANCE MAPS FOR SUPERCRITICAL CARBON DIOXIDE COMPRESSORS IN POWER APPLICATIONS

Ihab Abd El Hussein *
University of Duisburg-Essen
Duisburg, Germany
ihab.abd-el-hussein@uni-due.de

Sebastian Schuster
University of Duisburg-Essen
Duisburg, Germany

Dieter Brillert
University of Duisburg-Essen
Duisburg, Germany

ABSTRACT

Carbon dioxide in the supercritical state (sCO₂) has drawn much interest lately. It is considered as a promising fluid for next-gen power plants with many researchers investigating this technology. Cycle simulation and control requires compressor performance maps valid for variable inlet conditions. In this paper, an attempt is made for establishing a pressure ratio based performance map for sCO₂ compressors in power applications. For that purpose the so-called Glassman approach is considered. This model has been originally established for fluids obeying the ideal gas law. Therefore, a modification is proposed to take into consideration the real gas equation of state and to allow wide variation of the isentropic volume exponent k_v . Computational fluid dynamics (CFD) is used to predict the performance of a single stage radial compressor. Results for different k_v values at the compressor inlet confirms the validity of the proposed model with both the polytropic efficiency and the reduced enthalpy deviations limited to 1 percent. On the other hand, predicted pressure ratio shows difference of around 3 percent from $k_v=7.1$ to $k_v=4.1$. A further decrease of k_v to 2.5 extends the difference up to 8 percent.

INTRODUCTION

With the increased environmental concerns and awareness regarding the global warming, renewable resources are gaining higher shares in the energy sector. These technologies have high intermittency in the power production and therefore, conventional fossil power plants are required to operate with high flexibility to balance these fluctuations.

Carbon dioxide in the supercritical state (sCO₂) has drawn much interest lately as an alternative fluid for next-gen power plants with many researcher investigating this technology. Especially in the so-called liquid-like region, sCO₂ is characterized by high density (0.5 to 0.7 of liquid water) and low viscosity (~ air). These properties among others promise small

components with reduced losses and consequently cycles with high flexibility and efficiency.

Cycle control and simulation requires reliable performance prediction of the compressor at variable inlet conditions. This can be done using for instance a mean-line model [2]. Though, such models requires validity and accuracy of the underlying loss estimation at variable inlet conditions. Alternatively, compressor performance map with reduced values are widely implemented for such purpose. For that, the compressor performance at a reference condition should be known, experimentally measured for example. This approach can ensure high prediction accuracy of the performance from a reference inlet condition to another given the validity of the applied formulation. In fact, most formulations are only valid for a constant isentropic exponent. However, this is not true for typical sCO₂ compressor inlet conditions (Fig. 1).

The isentropic volume exponent k_v is defined as [1]:

$$k_v = -\frac{v}{p} \cdot \frac{c_p}{c_v} \cdot \left(\frac{\partial p}{\partial v} \right)_T \quad (1)$$

For fluids obeying the ideal gas law, k_v reduces to the specific heat ratio which is also known as the isentropic exponent in such cases. Figure 1 illustrates k_v range for typical sCO₂ compressors inlet conditions.

To cope with its high variation for sCO₂, Barber Nichols Inc. adopted a formulation based on the work by Glassman [3]. Comparison of the results against experimental measurements showed good matching regarding the enthalpy change, yet efficiency predictions show up to 20 percent deviation from experimental data [4]. In a similar context, Jeong et al. [5] studied several formulations of the reduced maps and compared the results to experimental measurements and numerical results. In their study, where the specific heat ratio is used as the

* corresponding author(s)

isentropic exponent, none of the formulations was able to consistently predict the pressure ratio, efficiency or the enthalpy change. Moreover, Pham et al. [6] considered the conventional Mach number similarity, their study shows good prediction accuracy regarding the reduced enthalpy and efficiency of sCO₂ compressors with k_v ranging from 4.5 to 14 at its inlet. On the other hand, due to the wide range of k_v , the pressure ratio varied substantially and therefore a corrected pressure ratio instead of the actual one is proposed.

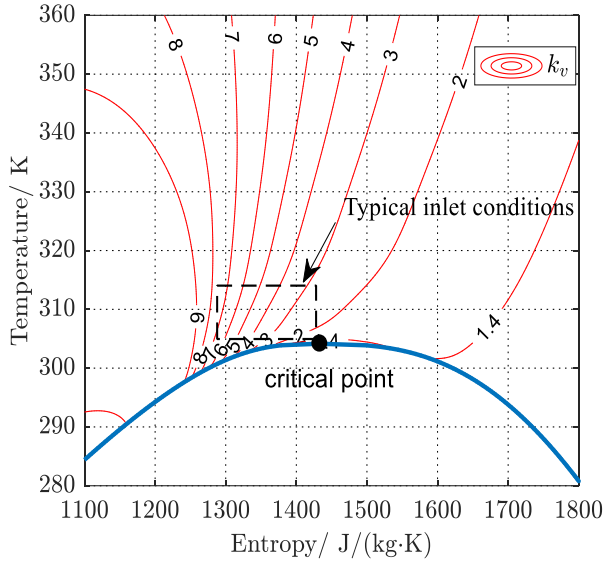


Figure 1: Variation of the isentropic volume exponent k_v with typical sCO₂ compressors inlet conditions

In this paper, an attempt is made to establish compressor map based on the pressure ratio for sCO₂ compressors. Such map would facilitate the cycle control and simulation by providing direct relation with a measured parameter (pressure).

UNDERLYING THEORY

The Buckingham Π-theorem [7] represents the foundation for the similarity analysis. For geometrically similar machines, the compressor performance can be related to four independent parameters:

$$(\eta, \pi, \Delta h) = f \left(\frac{\dot{m}}{\rho_{0t} \cdot a_{0t} \cdot D_2^2}, \frac{N \cdot D_2}{a_{0t}}, \frac{\rho_{0t} \cdot N \cdot D_2 \cdot b_2}{\mu_{0t}}, k_v \right) \quad (2)$$

Representing the reduced mass flow, reduced speed, Reynolds number and the isentropic exponent. By considering an isentropic compression process for a radially bladed impeller, the pressure ratio π can be related to the isentropic exponent k_v (Eq. 3).

$$\pi = [M_{u2}^2 \cdot (k_v - 1) + 1]^{\frac{k_v}{k_v - 1}} \quad (3)$$

With M_{u2} being the circumferential Mach number. For constant M_{u2} according to the Mach number similarity, π has a high dependence on the k_v value.

Alternatively, by considering a proportionality of the reduced speed with the critical velocity (Eq. 4), the dependence of π on k_v can be minimized.

$$N_{red} = \frac{N \cdot D_2}{a_{0t}} \propto \frac{N \cdot D_2}{v_{cr}} \quad (4)$$

The critical velocity is defined as the sonic speed once the flow is brought isentropically to Mach number equal 1 (Eq. 5) from the inlet total pressure p_{0t} and total temperature T_{0t} while assuming a constant k_v value obtained from the inlet conditions.

$$v_{cr} = \sqrt{\frac{2 \cdot k_v}{k_v + 1} \cdot Z_{0t} \cdot R \cdot T_{0t}} \quad (5)$$

With Z , being the compressibility factor and R , being the gas constant. Accordingly, the pressure ratio can be estimated for an isentropic compression following Eq. 6.

$$\pi = \left[2 \cdot C \cdot \frac{k_v - 1}{k_v + 1} + 1 \right]^{\frac{k_v}{k_v - 1}} \quad (6)$$

With $C = \Delta h / v_{cr}^2$. Figure 2 compares the pressure ratio using Eq.3 and Eq. 6.

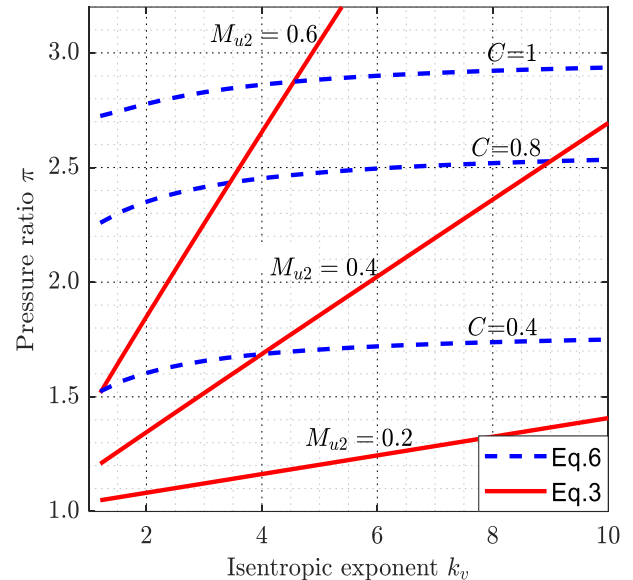


Figure 2: Dependence of the pressure ratio on k_v value for Mach number similarity and critical velocity proportionality

For the range of interest (k_v around 3 to 7), adoption of the rotational speed proportionality to the critical velocity results in

small variations of the pressure ratio. This is in contrast to the conventional Mach number similarity where the deviation is very high especially as M_{02} increases.

Similar proportionality can be considered from the reduced mass (Eq. 7)

$$\dot{m}_{red} = \frac{\dot{m}}{\rho_{0t} \cdot a_{0t} \cdot D_2^2} \propto \frac{c_m}{a_{0t}} \propto \frac{c_m}{v_{cr}} \quad (7)$$

In the original approach, Glassman assumes this proportionality to be equivalent to the ratio of the reduced mass flow to the reduced mass flow at choke condition. With the latter being only a function of the isentropic exponent [3]. Similar interpretation for considering the effect of k_v on the reduced mass flow is followed in the work of Roberts and Soljander [8]. Nevertheless, this assumption neglects the fact that the ratio of the density at the critical condition to the density at the total condition differs substantially with the k_v value (Fig. 3).

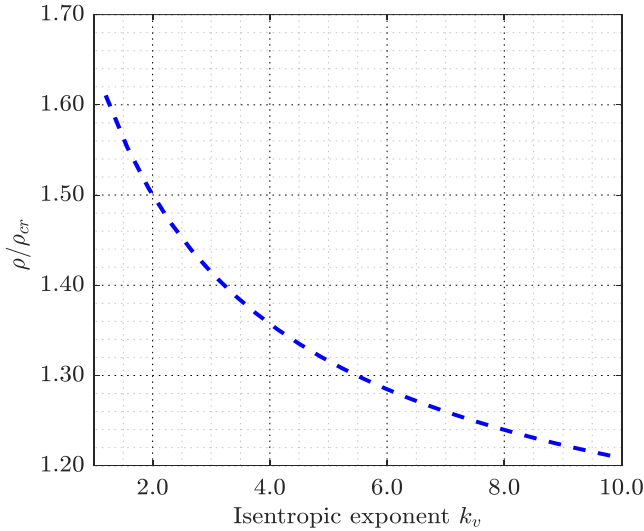


Figure 3: Ratio of the density to critical density with respect to k_v

In this work, the reduced mass flow rate is modified in comparison to the original Glassman approach, where the mass flow rate is reduced by the mass flow rate at critical velocity and total density. This produces, with the reduced speed (Eq. 4), the typical inlet flow coefficient (Eq.8).

$$\frac{\dot{m}}{\rho_{0t} \cdot v_{cr} \cdot D_2^2} \propto \frac{c_{m1}}{u_2} \quad (8)$$

Moreover, an additional term is added to match volume flow ratio across the compressor. Analogous to ideal gas process, the polytropic work of a real gas is approximated following Eq. 9

$$y = \frac{n}{n-1} \cdot Z_0 \cdot R \cdot T_0 \cdot (\pi^{\frac{n-1}{n}} - 1) \quad (9)$$

With n being the polytropic exponent ($pv^n = \text{constant}$) that might be estimated using the compressor inlet and outlet properties. This is used to estimate the volume flow ratio (Eq. 10)

$$\sigma = \frac{\dot{V}_4}{\dot{V}_0} = \pi^{\frac{-1}{n}} = \left(2 \cdot C \cdot \eta \cdot \frac{k_v}{k_v + 1} \cdot \frac{n-1}{n} + 1 \right)^{\frac{-1}{n-1}} \quad (10)$$

Consequently, the reduced mass considered in this work reads as follows:

$$\dot{m}_{red} = \frac{\dot{m} \cdot \sigma}{\rho_{0t} \cdot v_{cr} \cdot D_2^2} \quad (11)$$

METHODOLOGY

This work utilizes computational fluid dynamics (CFD) to study the accuracy of pressure ratio based performance maps. This is due to the limited available experimental data for sCO₂ compressors that are coupled with high uncertainty regarding the enthalpy change and the efficiency that limits the quantitative comparison.

A single stage radial compressor is considered for the study. The compressor design is generated using an in-house design tool for sCO₂ compressors [9]. Figure 4 illustrates a frontal view of the three dimensional impeller that features typical radial machine geometry with a specific speed and specific diameter of 0.23 and 4.5, respectively. The impeller has a slightly backward curved blade with $\beta_2 = 105^\circ$ from tangential direction. Downstream the impeller, a vaneless diffuser followed by a rectangular volute are implemented.

CFD simulations are conducted using the steady RANS solver of the commercial CFD code CFX 18 coupled with the SST turbulence model and the wall function in order to reduce the computational effort. Moreover, from a base mesh for a single passage, doubling the nodes number to around 500,000 resulted in approximately 0.5 efficiency point difference, another doubling of the nodes number resulted in a mere 0.05 efficiency point variation. Similarly, from a base mesh for the volute, increasing the mesh size to around 1 million nodes resulted in 1 efficiency point variation, while a further increase of the mesh size by around 1.6 factor produced only 0.02 efficiency point difference. Therefore, around 500,000 nodes and 1 million nodes for a single passage and for the volute, respectively, are considered to provide mesh independent results. Furthermore, fluid properties for sCO₂ are implemented through real gas tables calculated using the Span and Wagner equation of state [10] from the NIST Refprop database [11]. The real gas tables have a resolution of around 0.1 K for the temperature and around 0.22 bar for the pressure which is found to provide independent results. Simulations are considered converged when all the following criteria are met: RMS residuals fall below $1e^{-4}$, imbalance is less than 0.1 percent in all domains and constant or small variation of the enthalpy change within less than 0.2 percent. Assessment of the adopted numerical approach has been previously done using pressure ratio measurement of a sCO₂ compressor running near the critical point [12].

$$D_2/2 = 0.08 \text{ m}$$

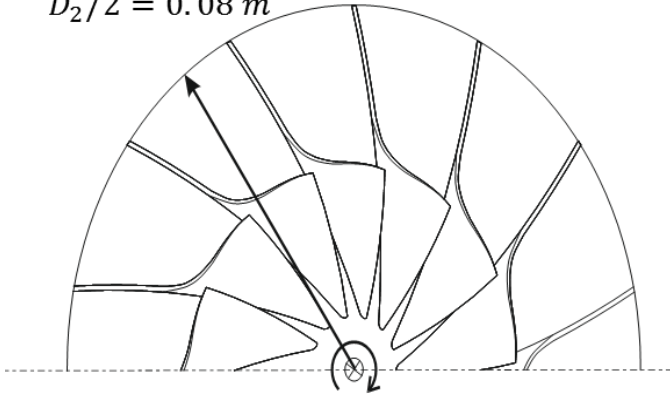


Figure 4: Frontal view of the impeller

Three inlet conditions at 318 K and 140 bar, 110 bar and 100 bar are selected for the simulations with k_v values of 2.5, 4.1 and 7.1, respectively. Additionally, selected inlet conditions have density values ranging from around 500 to 720 kg/m³ such that they are representative of the region of interest. Simulations are limited to one-phase flow and the location of the inlet conditions provided adequate distance from the two-phase region.

RESULTS

The simulations are conducted for a pressure ratio of around 2.2. From the properties at the different inlet conditions, the critical velocity is calculated and accordingly the rotational speed is found. This results in a circumferential Mach number M_{u2} variation from 0.5 to 0.76 with the value increasing for lower k_v value. In contrast, variation of the rotational speed is limited from around 22100 rpm to around 20300 rpm showing less than ten percent variation. In comparison, a Mach number similarity requires much larger rotational speed variation of around 60 percent for the considered inlet conditions. Moreover, given the small variation of rotational speed, Reynolds number variation is limited to a ratio less than 1.1. Therefore, correction for the effect of Re variation is considered unnecessary. Moreover, evaluation of σ term in the mass flow parameter (Eq.11) is done by considering constant values for $C=0.76$ and $\eta=0.9$ while n is a constant value for each inlet condition being a function of k_v and η . This is done in order to reduce the implicit nature of the mass flow parameter on the performance value and thus to promote the simplicity of the model implementation.

Figure 5 illustrates the predicted stage total polytropic efficiency (Eq. 12) in terms of the reduced mass flow rate for the different inlet conditions.

$$\eta_t = \frac{y_t}{\Delta h_t} \quad (12)$$

With y_t being the total polytropic work and Δh_t being the total enthalpy change. Considering $k_v=4.1$ as reference condition, an overall good matching of the stage polytropic efficiency is found in comparison with the other k_v values. Exception is observed for reduced mass flow rates lower than its Best efficiency point

(BEP), where high deviation between result for $k_v=2.5$ and the other two inlet conditions takes place. At this region, the efficiency experience high gradients with respect to the mass flow rate parameter. This is found to be a result of high recirculation and incidence losses at this region (Fig. 7). Therefore, the difference is thought to originate from the effect of the difference in the inlet flow coefficient which is around 6 percent higher for $k_v=2.5$ in comparison to $k_v=4.1$. Nevertheless, this is considered as a special case for the studied compressor that has a very small blade angle at the shroud. This leads to high recirculation losses at small inlet flow coefficient.

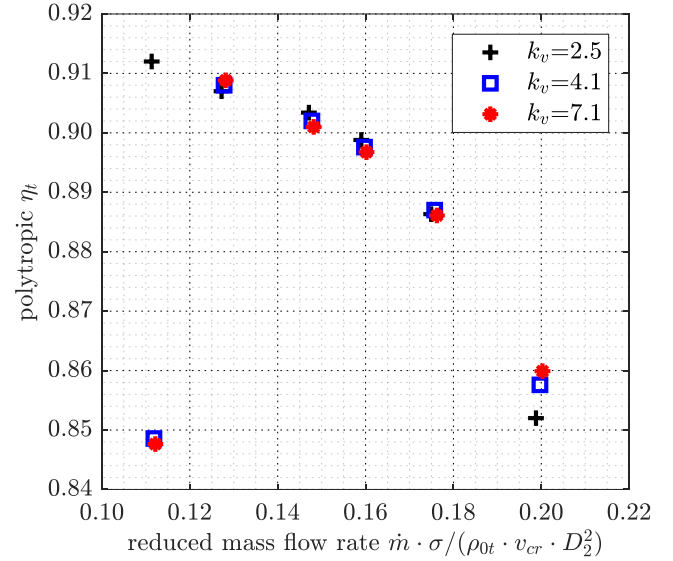


Figure 5: Variation of the stage total polytropic efficiency with respect to the reduced mass flow rate with k_v

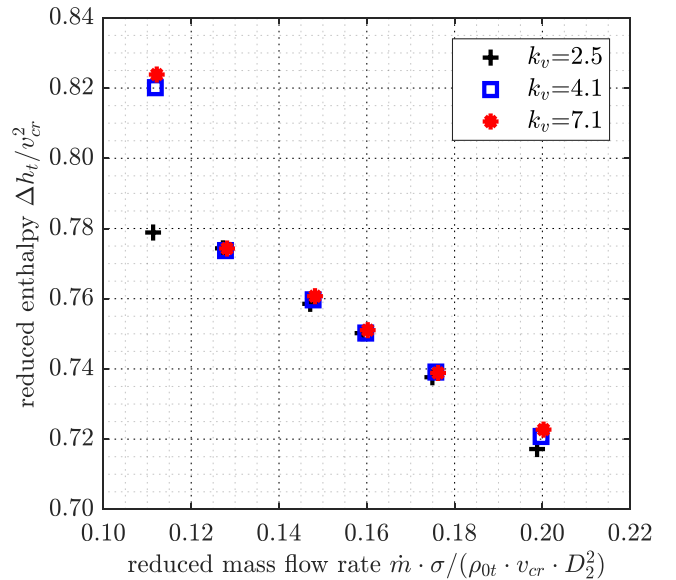


Figure 6: Variation of the reduced enthalpy change with respect to the reduced mass flow rate with k_v

A similar result is found regarding the reduced enthalpy change (Fig. 6) with a very good matching of the results for different k_v values. Left to the BEP of $k_v=4.1$, an exception to this matching is found which is related to the flow recirculation that causes distortion of the flow direction and consequently impacting the enthalpy change.

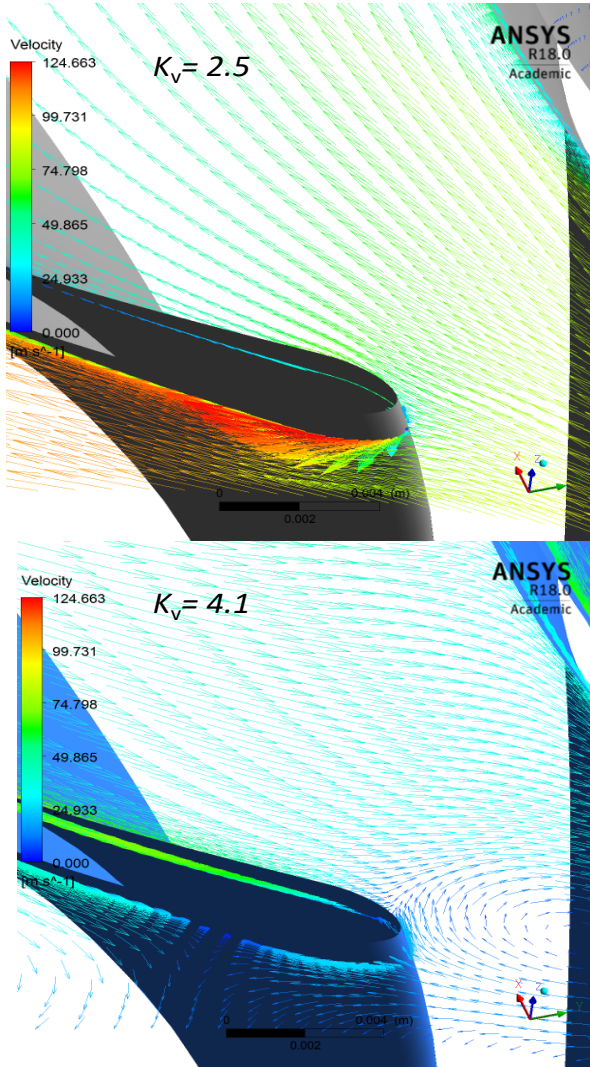


Figure 7: velocity vector at the rotor inlet at a constant span location of 0.95 for $k_v = 2.5$ and $k_v = 4.1$

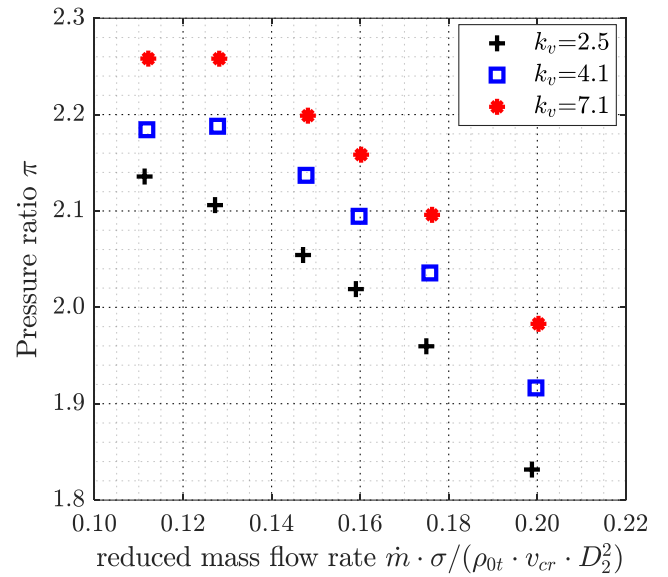


Figure 8: Predicted pressure ratio at constant reduced speed for different k_v values

The main attempt of this work is to establish pressure ratio based performance maps for sCO₂ compressors. Figure 8 depicts the predicted pressure ratio for the different k_v values. Due to the slight backward curvature of the blade outlet angle, predicted pressure ratio of each k_v line shows small reduction with respect to the reduced mass flow parameter. Results however, show a consistent deviation limited to around 3 percent between the cases with $k_v=7.1$ and $k_v=4.1$. A further decrease of the k_v to 2.5 increased the pressure ratio deviation to around 8 percent. Yet, with the good matching of reduced enthalpy and the polytropic efficiency, the deviation of pressure ratio is considered a result of an inherent characteristic of this formulation as can be seen in Fig. 2 where cases having equal reduced enthalpy change but different isentropic exponent would still have different pressure ratios.

CONCLUSION

In this paper, an attempt is made to establish pressure ratio based performance maps for sCO₂ compressors. For that purpose, the so-called Glassman approach is used in order to account for the effect of the isentropic exponent variation on the pressure ratio. A modification of the original mass flow parameter is introduced to account for the ratio of the inlet density to the critical density. Moreover, an additional term is also introduced that considers the effect of k_v of the volume flow ratio across the stage.

Validation of the model is conducted against CFD simulations of a single stage radial compressor with three k_v values of 2.5, 4.1 and 7.1 at the inlet. Results show good matching of the reduced enthalpy and the stage total polytropic efficiency with less than 1 percent deviation. Exception is found for small reduced mass flow rate, where recirculation and incidence losses that are dependent on the inlet velocity triangle

took place. The predicted pressure ratio shows a difference of around 3 percent between the case with $k_v=7.1$ and $k_v=4.1$. A further decrease of k_v to 2.5 widened the difference to around 8 percent.

Moreover, for the considered inlet condition and pressure ratio, the M_{u2} value varied from around 0.5 to around 0.75 in an inverse relation with k_v . At higher M_{u2} values shock losses might take place which can affect the validity of the model. Similarly, maximum variation of the inlet flow coefficient is around 10 percent between the studied cases. Depending on the considered compressor and its performance characteristic (efficiency variation with respect to mass flow rate), more conservative limit might be used especially in region where high variation of the efficiency take place as at low inlet flow coefficient in the studied compressor.

NOMENCLATURE

a	Sonic speed	m/s
b_2	Impeller exit width	m
c	Absolute velocity	m/s
C	Constant = $\Delta h/v_{cr}^2$	-
c_p	Specific heat capacity const. pressure	J/(kg · K)
c_v	Specific heat capacity const. volume	J/(kg · K)
D_2	Impeller diameter	m
h	Specific enthalpy	J/kg
s	Specific entropy	J/(kg · K)
k	Ideal gas isentropic exponent	-
k_v	Isentropic volume exponent	-
\dot{m}	Mass flow rate	kg/s
M_{u2}	Circumferential Mach number	-
N	Rotational speed	s^{-1}
n	Polytropic exponent	-
p	Pressure	Pa
R	Gas constant	J/(kg · K)
T	Temperature	K
u_2	Impeller tip speed	m/s
\dot{V}	Volumetric flow rate	m^3/s
v	Specific volume	m^3/kg
v_{cr}	Critical velocity	m/s
y	Polytropic work	J/kg
Z	Compressibility factor	-
Greek letter		
η	Polytropic efficiency	-
ρ	Density	kg/m^3
ρ_{cr}	Critical density	kg/m^3
π	Pressure ratio	-
μ	Dynamic viscosity	Pa·s
σ	Mass flow correction factor	-
Subscript		
m	Meridional component	
red	Reduced value	
t	Total condition	
0	Stage inlet	
2	Impeller tip	
4	Stage exit	

ACKNOWLEDGEMENTS

The work leading to these results has received funding from the European Union under grant agreement number 764690 for the sCO₂-Flex project under the HORIZON 2020 program.



REFERENCES

- [1] Kouremenos D. A., and Antonopoulos K. A. (1987). Isentropic exponents of real gases and application for the air at temperatures from 150 K to 450 K, *Acta Mechanica*, **65**(1-4), pp. 81–99.
- [2] Romei A., Gaetani P., Giostri A., and Persico G. (2020). The Role of Turbomachinery Performance in the Optimization of Supercritical Carbon Dioxide Power Systems, *Journal of Turbomachinery*, **142**(7), p. 1187.
- [3] Glassman A. J. (1972). Turbine Design and Application, *NASA SP_290_VOL1-3*, pp 57-60.
- [4] Wright s. A., Radel R. F., Venom M. E., Rochau G. E., and Pickard P. S. (2010). Operation and Analysis of a supercritical CO₂ Brayton Cycle: SANDIA REPORT SAND2010-0171.
- [5] Jeong Y., Son S., Cho S. k., Baik S., and Lee J. I. (2019). A Comparison Study for Off-Design Performance Prediction of a Supercritical CO₂ Compressor With Similitude Analysis, Volume 3A: Fluid Applications and Systems, American Society of Mechanical Engineers.
- [6] Pham H. S., Alpy N., Ferrasse J. H., Boutin O., Tothill M., Quenaut J., Gastaldi O., Cadiou T., and Saez M. (2016). An approach for establishing the performance maps of the sc-CO₂ compressor: Development and qualification by means of CFD simulations, *International Journal of Heat and Fluid Flow*, **61**, pp. 379–394.
- [7] Buckingham E. (1914). On Physically Similar Systems; Illustrations of the Use of Dimensional Equations, *Phys. Rev.*, **4**(4), pp. 345–376.
- [8] Roberts S. K., and Sjolander S. A. (2005). Effect of the Specific Heat Ratio on the Aerodynamic Performance of Turbomachinery, *Journal of Turbomachinery*, **127**(4), pp. 773–780.
- [9] Abd El Hussein I., Hacks A. J., Schuster S., and Brillert D. (2020). A Design Tool for Supercritical CO₂ Radial Compressors based on the Two-Zone Model. ASME, Turbomachinery Technical Conference & Exposition, September 21 – 25, 2020.
- [10] Span R., and Wagner W. (1996). A New Equation of State for Carbon Dioxide Covering the Fluid Region from the Triple-Point Temperature to 1100 K at Pressures up to 800 MPa, *Journal of Physical and Chemical Reference Data*, **25**(6), pp. 1509–1596.

- [11] Lemmon E. NIST Reference Fluid Thermodynamic and Transport Properties Database: Version 9.0, NIST Standard Reference Database 23.
- [12] Hacks A. J., Schuster S., and Brillert D. (2019). Stabilizing Effects of Supercritical CO₂ Fluid Properties on Compressor Operation†, *IJTPP*, **4**(3), p. 20.

EXPERIENCES FROM SUPERCRITICAL CO₂ APPLICATIONS IN REFRIGERATION AND AIR CONDITIONING SYSTEMS

Christian Doerffel*

Technische Universität Dresden
Dresden, Germany
Email: christian.doerffel@tu-dresden.de

Christiane Thomas

Technische Universität Dresden
Dresden, Germany

Ullrich Hesse

Technische Universität Dresden
Dresden, Germany

ABSTRACT

Carbon dioxide (CO₂) is a working fluid, which is suitable for various applications. Excellent heat transfer properties, especially in the supercritical area, make it attractive for thermal systems. As it is an environmentally friendly and non-flammable fluid, it is used in larger stationary systems e.g. in supermarket refrigeration systems as well as in small cycles, e.g. for mobile air conditioning (A/C) systems. There is no risk of pollution or major environmental damage due to leakage or accidental release of fluid. In addition to power cycles, CO₂ is suitable for cooling circuits for both subcritical (liquid-gas phase change) and transcritical applications. The latter includes supercritical heat rejection and subcritical heat absorption. Therefore, CO₂ refrigeration systems and their components, e.g. compressors, have special design requirements. They need to be specially adapted to the fluid properties such as pressures above 10 MPa and pressure differences up to 8 MPa. The efficiencies of refrigeration systems must be competitive to those of conventional refrigerants. This requires advanced system designs, which will be presented. Finally, possible synergies between CO₂ power systems and CO₂ refrigeration and heat pump systems will be discussed.

INTRODUCTION

Carbon dioxide was already one of the first working fluids used for refrigeration cycles. It appeared in patents in the 1850s and 1860s, and in 1869, Thaddeus Lowe constructed an ice making machine. In 1882 Carl von Linde designed a refrigeration machine using carbon dioxide in Germany. In the 1890s the manufacturing of CO₂ piston compressors started. This led to a widespread application of CO₂ in refrigeration and air conditioning, promoted by the fact that CO₂ is a safe, non-toxic and non-flammable refrigerant [1].

Especially ships were equipped with carbon dioxide cooling systems from the 1890s to the 1940s. Stationary CO₂ systems for brine cooling were manufactured, which were applied in cold storage rooms and refrigerators for food markets, restaurants, hotel kitchens, hospitals, etc.

The compressors used were slow-running (up to 325 rpm, usually around or below 100 rpm [1][2]) open type reciprocating piston compressors in either vertical or horizontal arrangements. The design followed the steam engines of that time, as the compressors were constructed with double-acting pistons and stuffing boxes for shaft sealing [1].

At this time, the cycles were operating mostly subcritically, which led to the necessity of using cooling towers for the heat rejection at high ambient temperatures [1][2].

In the 1940s and the following decades, CO₂ refrigeration machines disappeared and were replaced by systems using halogenated hydrocarbons (CFCs). In the late 1980s and early 1990s, the Norwegian scientist Gustav Lorentzen reintroduced CO₂ by proposing the use of CO₂ in transcritical cycles [3][4]. This led to a dynamic development, with these cycles being applied to heat pumps [5], mobile air conditioning systems [6][7][8] and stationary refrigeration systems [9].

Today, there is large and growing number of transcritically operating CO₂ refrigeration systems and a lot of research in this field. Furthermore, both the “warm” and the “cold” heat flow of these systems is used, whereas there currently is no coupling to electricity generation, which is contemplated by this contribution.

TRANSCRITICAL SYSTEMS

The essential points of the new interest in CO₂ as a working fluid were, on the one hand, its environmentally friendly properties (ODP = 0, GWP = 1) and, on the other hand, the possibilities offered by electronic control technologies, which

* corresponding author(s)

allowed controlling the high pressure in the supercritical area. This is crucial for efficient operation of the plant. The coefficient of performance (COP) as a metric of the energy efficiency of mechanically driven cooling cycles is defined as follows:

$$COP = \frac{\dot{Q}_{absorbed}}{P_{compressor}} = \frac{\dot{Q}_0}{P_{electric}}$$

Whereas for the corresponding heat pump cycles:

$$COP = \frac{\dot{Q}_{rejected}}{P_{compressor}} = \frac{\dot{Q}_{heating}}{P_{electric}}$$

In figure 1, transcritical CO₂ cycles with the same gas cooler outlet and evaporation temperatures are shown in a lg(p)-h-diagram. The heat rejection pressure or gas cooler outlet pressure p_{GC} of the displayed cycles varies from 8 MPa (80 bar) to 11 MPa (110 bar). The difference of the specific enthalpy 4-1 and 2-3 is the amount of absorbed (q_0) and dissipated (q_{GC}) heat. The difference of the specific enthalpy h between the points 1 and 2 indicates the specific compressor work $w_{compressor}$. By means of an electronic expansion valve, the heat rejection pressure can be adjusted. It is easy to see that the variation of the gas cooler pressure (p_{GC}) in the range 80 bar to 100 bar (8 MPa to 10 MPa) results in large differences in the absorbed and dissipated heat, while the power consumption changes only slightly.

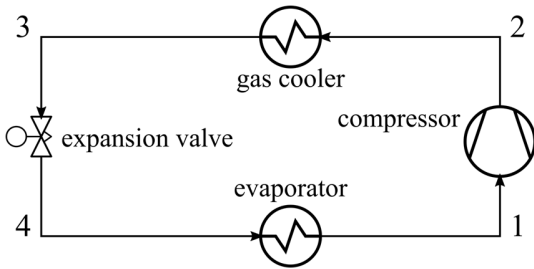


Figure 1: Basic cycle diagram with compressor, gas cooler, expansion valve and evaporator

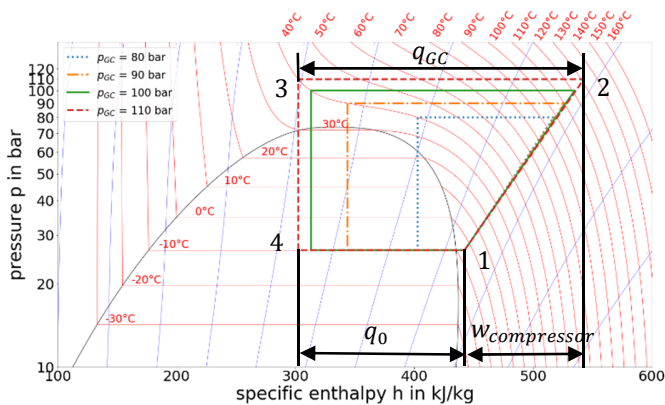


Figure 2: Lg(p)-h-diagram of CO₂ with transcritical cycles operating at different heat rejection pressure levels

For a given gas cooler outlet temperature t_3 , the dissipated heat changes less with increasing the pressure above a certain point, resulting in an optimum gas cooler pressure p_{GC} .

As an additional result of using a transcritical CO₂ cycle instead of subcritical cycles, a different concept is required for receivers or accumulators. In the supercritical region there is no phase separation and therefore it is not possible to have a high-pressure receiver with a varying liquid level after the condenser. Therefore, Lorentzen proposed different cycle arrangements, as shown in figures 2 to 4 [3].

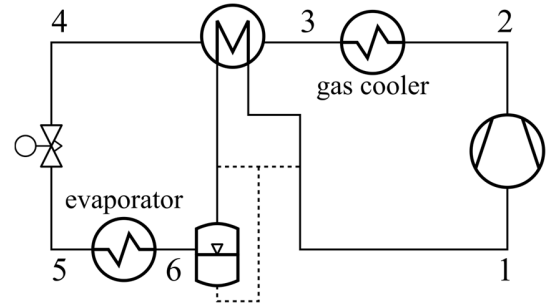


Figure 3: Cycle with accumulator after evaporator [3]

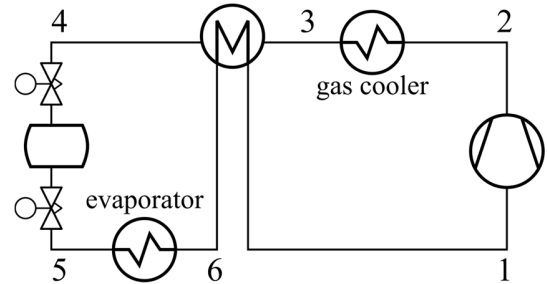


Figure 4: Cycle with intermediate pressure receiver in flow [3]

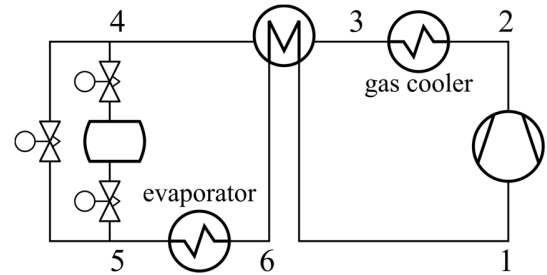


Figure 5: Cycle with receiver in branch flow [3]

In figure 3, a receiver/accumulator is used downstream of the evaporator and separates liquid from the gaseous phase. The gaseous phase enters an internal heat exchanger, ensuring that the fluid is superheated before entering the compressor. The liquid phase in the accumulator consists mainly of liquid CO₂ and oil for the lubrication of the compressor. In order to ensure the lubrication of the compressor, it is necessary that a small amount of this liquid phase is returned to the compressor, which can be added before or after the internal heat exchanger by an additional flow control device like an orifice. Figure 4 shows a

cycle using an intermediate pressure receiver after the internal heat exchanger, where the first valve between the internal heat exchanger and the receiver controls the high pressure. A second valve between the receiver and the evaporator controls the superheating after the evaporator. In figure 5, an additional valve is added to the cycle to ensure a minimum flow of refrigerant through the evaporator.

The cycle depicted in figure 3 is most commonly used for mobile applications due to its simple design and easy control. It is used for railway [8] and for automotive [6][7] air conditioning and heating. Especially when operating in heat pump mode, the efficiency of the system is better than in systems using other common refrigerants. Therefore, circuits for mobile application are often equipped with 3-way-valves or 4-way-valves for switching from cooling mode to heating mode. The compressors used for automotive A/C are usually either axial piston compressors driven by the car engine via a belt and clutch [6][7] or electrically driven scroll compressors using a frequency inverter.

Air conditioning and heat pump systems for trains have special requirements, as both the cooling and heating capacity can be on the magnitude of stationary systems, but the packaging requirements are strict due to the mobile application. Furthermore, the electrical power supply is of low quality due to high voltage peaks or voltage drops, which makes the use of frequency inverters uneconomical. Therefore, capacity control is performed by cylinder unloading, high-pressure variation and compressor cycling.

Typical compressors used for both railway and stationary systems are reciprocating piston compressors and rolling piston compressors, usually lubricated with POE oils or sometimes with PAG oils. Especially POE oils have excellent miscibility properties with CO₂, which makes them suitable for a wide variety of systems and applications, including widely distributed pipe networks. Additionally, POE oils are thermally stable, which is necessary for the high discharge temperatures of transcritical CO₂ cycles. PAG oils have a miscibility gap, which makes them suitable only for systems with short pipes, such as chiller units [10]. The miscibility gap could otherwise lead to oil entrapment in the cycle and missing oil in the compressor. This would harm the compressor in terms of wear, particularly in the bearings. The mentioned compressor types are suitable due to typical CO₂ mass flows in the range of 10⁻² kg/s to 10¹ kg/s, high pressure differences of up to 10 MPa, and the extremely low viscosities of CO₂ in the range of 10⁻⁵ Pa s to 10⁻⁴ Pa s. Due to their internal sealing concept, reciprocating and rolling piston compressors can handle the resulting high pressure differences and high forces very well. The area in which the point of state of the compressor suction gas is usually located is depicted in figure 6. Additionally, the typical operational field of the gas cooler or condenser is shown. These limits are derived from commercially available products of the refrigeration industry and show that there is lack of supercritically operating compressors and components that can withstand temperatures above 150 °C. This temperature limit results from the fact that the compressor oil decomposes at high

temperatures. Therefore, these are drawbacks for the development of high temperature heat pumps using CO₂ at a required temperature level above this limit. Due to problems mentioned above, the behavior of oils and oil-refrigerant mixtures is one subject of research at the TU Dresden.

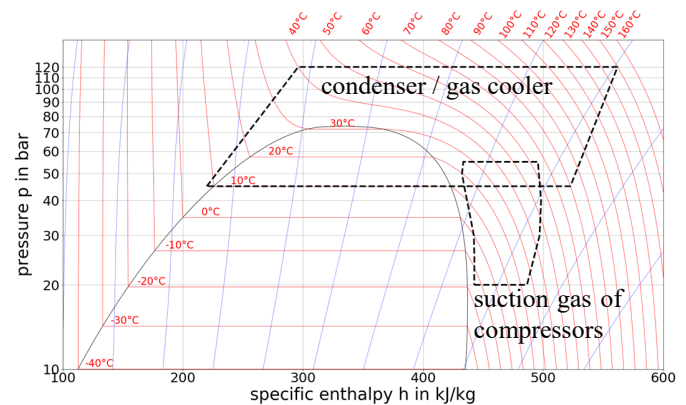


Figure 6: typical fields of application of compressors and heat exchangers for transcritical CO₂ cycles

The component arrangement of stationary systems differs slightly from that of the mobile systems. Usually they are set up with an intermediate pressure receiver, similar to the circuit shown in figure 4. In contrast, an additional valve is added to control the intermediate pressure in the receiver, as shown in figure 7. As a result, this receiver does not need to be designed for supercritical conditions and can therefore be less expensive. Furthermore, the amount of the so-called “flash gas” in the evaporator is reduced, which means that the vapor quality after the throttling valve is decreased. This results in better heat transfer properties in the evaporator. An internal heat exchanger can improve the cycle efficiency, but is not necessary. The design pressure of the evaporators is usually far below the critical pressure for cost reasons. During compressor stand-still, an unacceptable pressure rise would occur inside the receiver due to heat transfer into the receiver and evaporating carbon dioxide. To avoid this, a small chiller unit is installed, which keeps the pressure within an acceptable range by condensing the CO₂ inside the receiver at a temperature below ambient temperature.

As an enhancement, so called parallel compressors can be used for compressing the flash gas to high pressure instead of throttling it, as can be seen in figure 8. This leads to energy savings of about 10% to 20%, depending on chosen pressure levels [11][12].

Additionally, there are various approaches to recover the expansion work, as this could theoretically save up to 30% of energy consumption. Due to irreversibilities in compressors and expanders, only about 10% of the total energy consumption can be recovered in real systems. For this application there are approaches using axial flow turbines and asynchronous generators [13] as shown in figure 9.

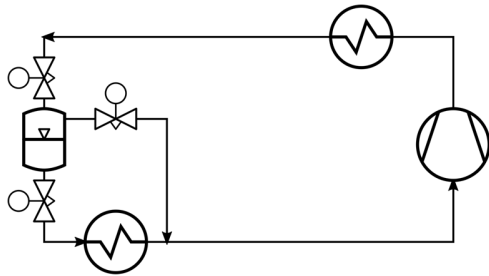


Figure 7: Cycle using an intermediate pressure receiver and a "flash gas bypass", typical circuit of stationary systems

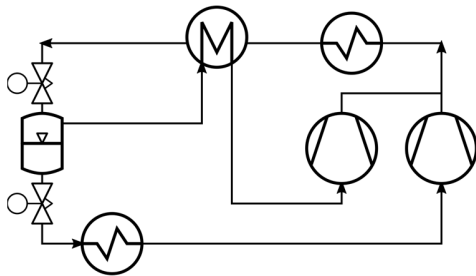


Figure 8: Cycle with intermediate pressure receiver and parallel compression

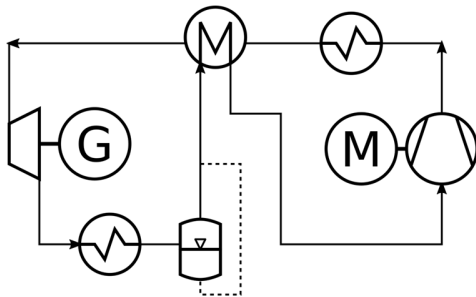


Figure 9: Cycle using an expansion turbine for expansion work recovery

Ejectors are another possibility to recover expansion work, as shown in figure 10 and figure 11. Ejectors, also known as jet pumps, compress a suction flow of low pressure by momentum transfer of an expanding motive flow from high pressure to a common intermediate pressure. Accordingly, the compressor suction port can be connected to the medium pressure receiver as depicted in figure 10. Neither a flash gas bypass valve nor parallel compressors are needed in this configuration. It is also possible to combine the parallel compression cycle with ejectors. This leads to a decreasing main compressor mass flow and increasing parallel compressor mass flow. As the specific work of the parallel compressor is lower than the specific work of the main compressor, the total energy consumption is reduced. Ejectors do not have any moving parts, except for needle-controlled ejectors in which the motive nozzle diameter and thus the motive flow is controlled by a needle. Therefore, ejectors provide a reliable and cost-effective solution for recovery of expansion work. Nevertheless, the control of systems with ejectors is still a challenge.

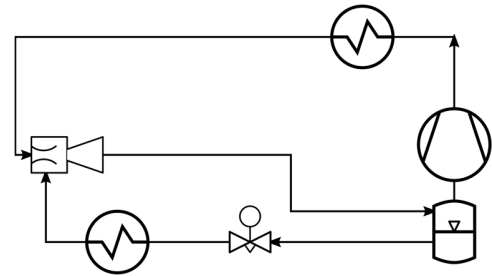


Figure 10: Cycle using an ejector for work expansion recovery

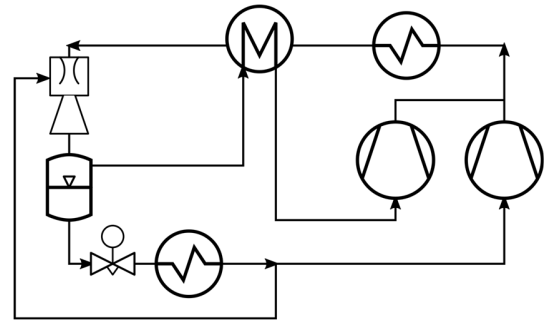


Figure 11: Cycle using ejector and parallel compression

A third possibility to recover expansion work is the use of displacement expansion machines, such as reciprocating type expanders. At the TU Dresden, the development of an expansion-compression-unit for heat pump applications was started in the 1990s. The work gained by the expander was used for a second compression stage after an intercooler as shown in figure 12. It was designed as a free piston machine with expander inlet valves actively controlled by electronics [5].

This machine and the associated circuit were developed for more than 20 years until the current design proved to be a promising solution, also in terms of controllability [14]. The setup is based on an economizer system, where the expansion work is used to drive the compressor of the subcooler (economizer) cycle, shown in figure 12. The expander-compressor-unit is a slow-running free piston machine and is designed for dry running operation. This cycle can increase the efficiency by about 25% compared to a basic cycle, according to figure 7. In combination with parallel compression, efficiency enhancement up to almost 50% can be achieved with an optimized control system [15][12].

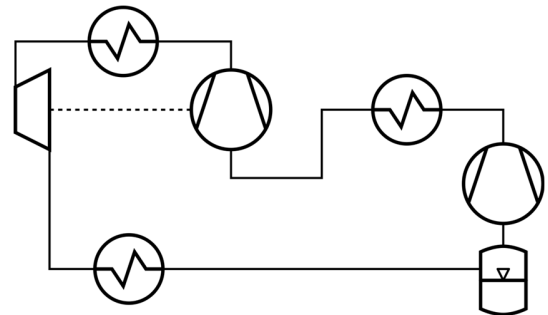


Figure 12: Cycle using an expansion-compression-unit

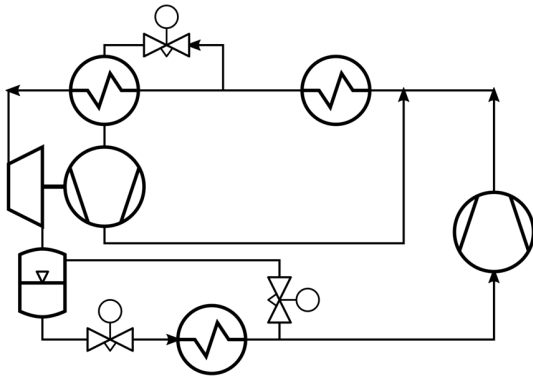


Figure 13: Cycle using an economizer cycle with an expansion-compression-unit

Furthermore, new stationary systems today are often designed for using both the hot and cold side, as the so-called heat recovery or hybrid systems. Some examples of their uses are for hot tap water production and for space heating. These systems use the maximum exergy available from the thermodynamic cycle. For power cycles the corresponding principle is known as combined heat and power (CHP) or cogeneration. The heat can even be used to drive a thermal refrigeration system such as absorption, adsorption or resorption systems, which leads to so-called tri-generation or combined cooling, heat and power generation (CCHP).

Tri-generation-systems, using only CO₂ as a working fluid, and supplying electricity, heating and cooling are subjects of future research. It seems possible to increase the efficiency or capacity of the power cycle as well as the cooling and heat pump cycles.

A simple design proposal can be found in figures 14 to 16. Especially if the heat source for the sCO₂ cycle provides latent heat at a high temperature level, a recuperator should be used as shown in figures 15 and 16. Changing the connection of the recuperator outlet between low pressure and medium pressure results in a different specific work [16], which could be interesting for the variation of the electric power and/or the recovered heat, if the low stage compressor offers sufficient capacity. The advantage of this system is a common cycle for waste heat recovery with power generation and cooling as well as the possibility to use the recovered heat for another thermally driven refrigeration system such as an adsorption chiller.

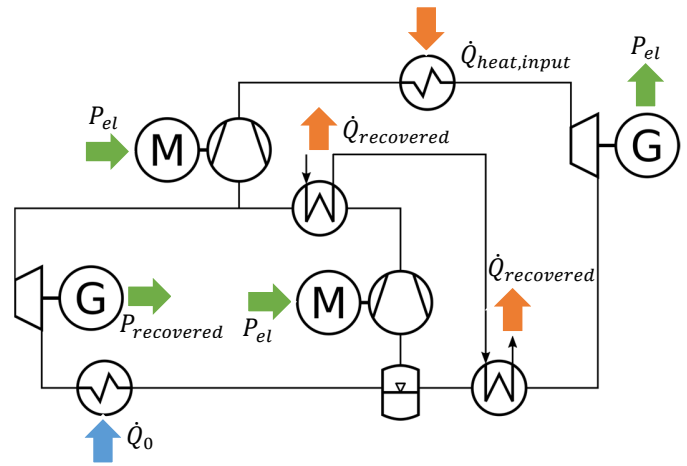


Figure 14: Proposed simple CO₂ tri-generation system using a sensible heat source and high temperature waste heat recovery

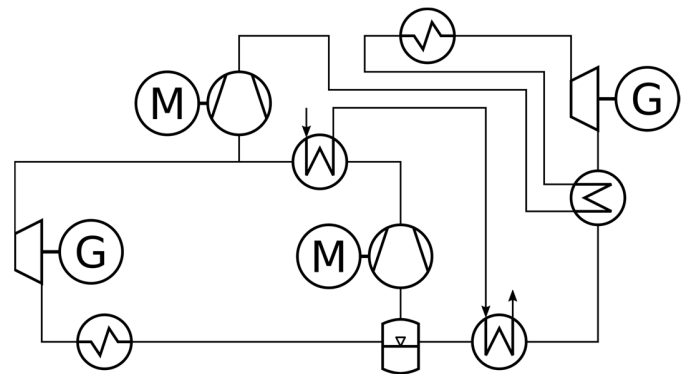


Figure 15: Proposed simple CO₂ tri-generation system using a latent heat source and low temperature waste heat recovery

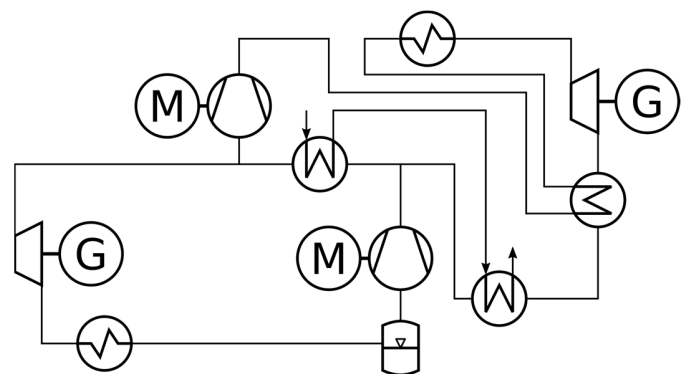


Figure 16: Proposed simple CO₂ tri-generation system using a latent heat source and low temperature waste heat recovery

SUMMARY AND CONCLUSIONS

In this contribution some aspects of technologies and common system designs of CO₂ cooling systems were presented. Both CO₂ power processes and transcritical CO₂ cooling cycles operate at least in parts in the supercritical region. Therefore, both fields face the similar advantages and challenges concerning thermophysical and chemical properties and component design. For example, both cycles need to dissipate their heat against a secondary fluid such as ambient air or water. Therefore, possible synergies are air-fluid and water-fluid heat exchangers for a design pressure between 12 MPa and 16 MPa. Currently, gas cooler heat exchangers are generally designed for 12 MPa at 150 °C, but there is a demand for heat exchangers that can withstand higher pressure levels, as the applications extend to higher heat dissipation temperatures. Other components such as ejectors, pumps and expansion turbines are used in both sCO₂ power cycles [16] and cooling cycles, so there can be advantageous synergies in component development and manufacturing. The development of high temperature heat pumps using CO₂ could be another promising field of cooperation. Going one step further, integrating a power system with a cooling and heating system to form a so called tri-generation system can lead to maximum system efficiencies and maximum utilization of limited resources.

NOMENCLATURE

<i>COP</i>	Coefficient of performance, efficiency (-)
<i>P</i>	Power (kW)
\dot{Q}	Heat flow (kW)
q_0	Specific cooling capacity
p_{GC}	Gas cooler pressure
p_0	evaporation pressure
PAG	polyalkylene glycol oils
POE	polyolester oils

ACKNOWLEDGEMENTS

The authors would like to thank the German Federal Ministry for Economic Affairs and Energy (Bundesministerium für Wirtschaft und Energie), which has financed this work within the project EFFCO2 (funding code: 03ET1541A).

REFERENCES

[1] Bodinus, W. S. (1999). The Rise and Fall of Carbon Dioxide Systems. ASHRAE Journal, Vol. 41, No. 4.
[2] Göttsche-Altona, G. (1907). Die Kältemaschinen. Verlag Johannes Kriebel, Hamburg, Germany.
[3] Lorentzen, G. (1989). Trans-Critical Vapour Compression Cycle Device. WO 90/07683. Norway, Trondheim.

[4] Lorentzen G. (1994). Revival of Carbon Dioxide as a Refrigerant. International Journal of Refrigeration, Vol. 17, No.5, p. 292-301.
[5] Heyl, P., (2000). Untersuchungen transkritischer CO₂-Prozesse mit arbeitsleistender Entspannung : Prozessberechnungen, Auslegung und Test einer Expansions-Kompressions-Maschine, Forschungsberichte des Deutschen Kälte- und Klimatechnischen Vereins e.V.; Vol. 62, Stuttgart, Germany.
[6] Hinrichs, J. (2005). Neue CO₂-Kompressoren für Kompaktfahrzeuge und Low Cost Systeme. Proceedings of the conference Deutsche Kälte-Klima Tagung 2005, Würzburg, Germany.
[7] Ayar, A., Heckt, R., (2005). R744 Kompressoren – geeignete Verdichter für jede Fahrzeugklasse. Proceedings of the conference Deutsche Kälte-Klima Tagung 2005, Würzburg, Germany.
[8] Schrank, P., Rauch, A., Presetschnik, A., Rieberer, R., (2019). Eco-friendly, energy- and cost-efficient A/C system with heat pump functionality using R744 for rail application. Proceedings of the IIR Conference on Ammonia and CO₂ refrigeration, Ohrid, North Macedonia.
[9] Elbel, S., Lawrence, N., (2016). Review of recent developments in advanced ejector technology. International Journal of Refrigeration, Vol. 62, p. 1-18.
[10] Bock, W., Puhl, C., 2010. Kältemaschinenöle. VDE Verlag, Berlin, Offenbach, Germany.
[11] Doerffel, C., Tannert, T., Hesse, U., (2019). Effect of the Operating Conditions on a Transcritical CO₂ Refrigeration Systems Efficiency. Proceedings of the International Conference on Ammonia and CO₂ Refrigeration Technologies, Ohrid, North Macedonia. Paper ID: 29.
[12] Doerffel, C., Thomas, C., Hesse, U., (2020). Experimental results of various efficiency enhancing measures for CO₂ refrigeration systems. Proceedings of the 14th IIR Gustav Lorentzen Conference on Natural Refrigerants, Kyoto, Japan.
[13] Steinjan, K., 2019. Expansionsmaschine für CO₂ Kälteanlagen. Proceedings of the conference Deutsche Kälte-Klima Tagung 2019, Ulm, Germany. Paper ID: II2-10.
[14] Nickl, J., Bartzsch, R., Hesse, U., (2016). CO₂-Anlage mit neuer Generation ECU. Proceedings of the conference Deutsche Kälte-Klima Tagung 2016, Kassel, Germany. Paper ID: III-05.
[15] Doerffel, C., Tannert, T., Hesse, U., 2019. Comparison of efficiency increasing methods in transcritical CO₂ refrigeration systems. Proceedings of The 25th IIR International Congress of Refrigeration, Montreal, Kanada.
[16] Crespi, F., Gavagnin, G., Sanchez, D., Martinez, G., 2017. Supercritical carbon dioxide cycles for power generation: A review. Applied Energy, Vol. 195, p. 152-183.

ADIABATIC COMPRESSED CO₂ ENERGY STORAGE

Matteo Manzoni*

TPG-DIME, University of Genoa
Genoa, Italy
matteo.manzoni2012@libero.it

Alberto Patti*

TPG-DIME, University of Genoa
Genoa, Italy
albe.patti@gmail.com

Simone Maccarini

TPG-DIME, University of Genoa
Genoa, Italy

Alberto Traverso

TPG-DIME, University of Genoa
Genoa, Italy
alberto.traverso@unige.it

ABSTRACT

As the energy market is moving worldwide towards low-emission solutions, there is a growing interest in plants capable of storing non-dispatchable renewable power, contributing to maintain the high quality level of current electrical infrastructure and ensuring spinning-reserve capability, complementing the lack of frequency control by most of solar and wind technologies. CO₂ cycles, including supercritical ones, could be a solution to achieve this goal. Most of current efforts on CO₂ cycles are devoted to study the most promising configurations for power production, including supercritical CO₂ plants for solar energy conversion. Basing on such extensive state of the art and growing knowledge, this paper aims to analyse innovative energy storage solutions involving closed cycles, employing different working fluids in sub-critical or supercritical conditions, including CO₂. Different plant configurations and operating conditions at 10 MWe design point are compared in terms of Round Trip Efficiency (RTE) and preliminary costs, benchmarked against traditional large scale storage solution such as CAES. Subcritical CO₂ cycles is shown to be a very promising solution with RTE>70% and attractive cost features, thus being a potential candidate for utility scale energy storage.

INTRODUCTION

The energy demand has grown exponentially in the last 150 years due to increase in population and industrial development. According to the International Energy Agency (IEA), prior to the present sanitary

crisis, energy demand was projected to increase by 12% between 2019 and 2030. Growth over this period is now 9% in one prediction, and only 4% in another one, both made by IEA [1]. Although the recession caused by the COVID-19 pandemic, this scenario of constant increase in energy demand points out the relevance of using renewable energy sources for a sustainable future. Furthermore, in the projected change in primary energy demand by fuel in 2020 relative to 2019 by IEA, only the renewables demand is expected to increase, by 0.8%; for example, oil demand could drop by 9% [2].

Nevertheless, the main feature of renewable sources is the unpredictability, which leads to problems of adaptation to the electrical grid.

Electricity customers usually have an uneven load profile during the day, resulting in load peaks; moreover, in the last decades an increase in the general demand and the introduction of non-dispatchable renewables resulted in greater peaks of the cumulative demand curve, increasing the need of systems able to shave peaks. In fact, the power system has to be sized for that peak load while during other parts of the day it is under-utilized. The extra costs in keeping up with the peak demand are passed to the customers in form of a power fee, i.e. paying for your maximum peak load [3]. The energy storage system is controlled to be charged during off peak hours and discharged during peak hours, reducing the net peak load and hence the power fee [4]. As a result of the problems presented, the need of an intense technological development aimed at improving energy storage appears clear. Therefore, a more accurate analysis of modern energy storage systems already

* corresponding author(s)

operating and a research of new process that could be introduced into the future market are imperative.

Energy storage solutions available at MW scale include Battery Energy Storage System (BESS), Pumped Hydro Storage (PHS) and Compressed Air Energy Storage (CAES). Regardless, even if PHS is highly developed, efficient and effective, its main issue is the dependence on the right morphological conditions.

However, at the moment solutions are needed to overcome operational problems related to the abovementioned systems, to improve performance, storage capacity and to reduce costs.

Overall, many applications of CO₂ as a working fluid are studied, especially in the fields of power cycles for renewable energy (such as CSP) and waste heat recovery (WHR) [5], due to their compactness and high efficiency. Instead in this paper the CO₂ is seen as a possible different solution to the energy storage problem, and so appropriate configurations of CO₂ and S-CO₂ closed cycles are discussed in detail.

ENERGY STORAGE PLANT

The plant design and the initial hypotheses regarding the thermodynamic parameters are extracted from the recent patent by Mr. Spadacini entitled “Energy Storage Plant and Process” [6], see Figure 1.

The cycle described include an energy accumulation phase (charge phase) followed by an energy release phase (discharge phase). Regarding the components, the system consists of a compressor (2), a turbine (3), a primary heat exchanger (5), a secondary heat exchanger (6), an ambient pressure tank (1), a high pressure tank (7), a motor/generator (4), a valve (8) and a non-return valve (9) as represented in Figure 1; other similar configurations are proposed in the patent but not accounted in this paper.

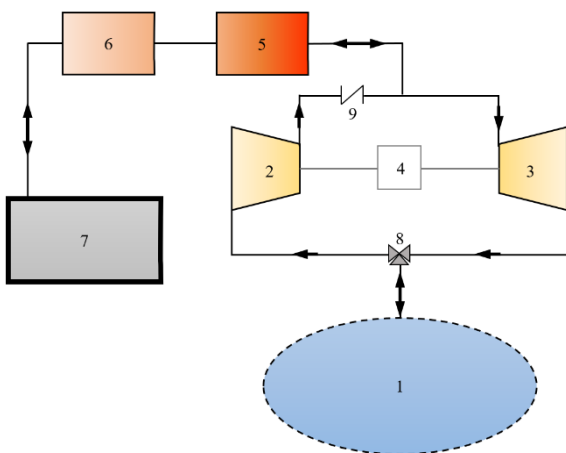


Figure 1: Simplified scheme of plant layout for energy storage

SUBCRITICAL CO₂ STORAGE SYSTEM

In this paragraph, a CO₂ closed loop in subcritical regime is examined. The system includes: a compressor (2), a turbine (3), a valve (8), a high-temperature heat exchanger-regenerator (SC-RIG) (5), a condenser/evaporator (6), an ambient pressure tank (1), a high pressure tank (7), a motor/generator (4) and a non-return valve (9).

Component	Assumptions
Heat exchanger-regenerator (SC-RIG) (5)	Pressure loss 1.5% of inlet pressure Exergetic loss
Condenser/Evaporator (6)	Pressure loss 1.5% of inlet pressure
Compressor (2)	Power set at 10000 kW Isentropic efficiency 0.85 Electrical efficiency 0.98 Mechanical efficiency 0.98
Turbine (3)	Isentropic efficiency 0.88 Electrical efficiency 0.98 Mechanical efficiency 0.98
High pressure tank (7)	No temperature and pressure loss
Ambient pressure tank (1)	In balance with atmospheric pressure
Charging time: 4 h	

Table 1: Assumptions for each plant component

During the energy storage phase, a compressor with a power set at 10000 kW is employed. See Table 1 for assumptions.

The calculations were made assuming a 4-hour charge duration. Knowing the power of the compressor and the charging time, it is quite easy to obtain the storage capacity.

As presented in the patent by Mr. Spadacini, the ambient pressure tank is a deformable balloon, made of flexible material, preferably plastic (e.g. PVC coated polyester fabric). Alternatively, it may have the structure of a gasometer [6].

Concerning the charging phase, carbon dioxide is in a reservoir in environmental conditions ($T_A = 293.15$ K; $P_A = 1.01325$ bar), subsequently the fluid is led through pipes to the compressor inlet (while the turbine outlet is blocked by a valve). The fluid is brought up to a pressure of 65 bar (state C) and to a temperature of 721 K, then it passes through the SC-RIG, storing heat that will be

supplied back during the discharge phase, and it arrives at the condenser inlet (state D).

Then, the fluid passes through the condenser, yielding the heat that will be re-used for the evaporation during the discharge phase. Afterwards, once reached the liquid saturation curve, CO₂ is stored in the tank at a pressure of 63 bar and at a temperature of 297 K (state E).

In Figure 2 the CO₂ charge phase is depicted on the T-s thermodynamic diagram.

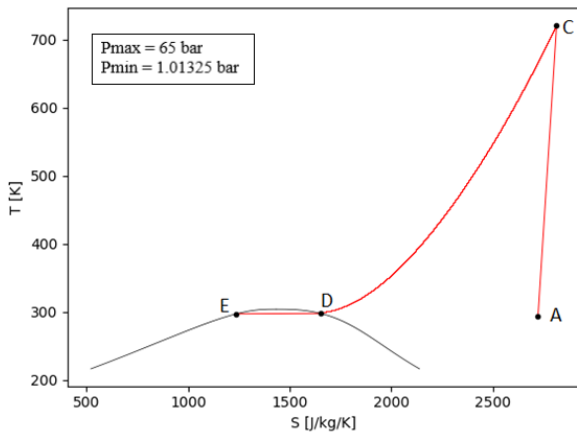


Figure 2: CO₂ charge phase on T-s diagram

The discharge phase begins from the high pressure tank. This reservoir has a temperature (297 K) close to the ambient one taken as a reference (293 K), therefore, assuming no pressure losses, the conditions inside the tank could be kept almost constant during the period of time in which the liquid remains there. Thus, the starting point of the discharge phase and the ending point of the charge phase have the same thermodynamic state.

Pressure losses are hypothesized in a similar way to the charge phase for the evaporator and for SC-RIG (see Table 1). Besides, an exergetic loss during the passage through the SC-RIG is considered in order to point out the temperature difference between charge phase (SC-RIG inlet, Fig. 2 state C) and discharge phase (SC-RIG outlet, Fig. 3 state H), due to the SC-RIG thermal effectiveness. The exergetic loss is calculated by reducing the specific enthalpy at the SC-RIG outlet during discharge phase (state H) by 2% compared to SC-RIG inlet during charge phase (state C). The specific enthalpy loss is used to emphasize both a non-perfect adiabaticity of the SC-RIG (minor effect) and its thermal effectiveness < 1 (major effect), i.e. heat is available at a lower temperature during the discharge phase.

During the release phase, the evaporator transfers the previously accumulated heat during condensation, warming the liquid carbon dioxide contained in the tank till it becomes saturated steam (state G). Afterwards, the fluid passes through the SC-RIG absorbing heat until it

reaches the turbine inlet at a temperature of 705 K and a pressure of 61.2 bar (state H). At last, CO₂ expands to generate electrical power and arrives at the ambient pressure tank (state J), which is connected to the turbine outlet by a valve.

In Figure 3 the CO₂ discharge phase is represented on the T-s thermodynamic diagram.

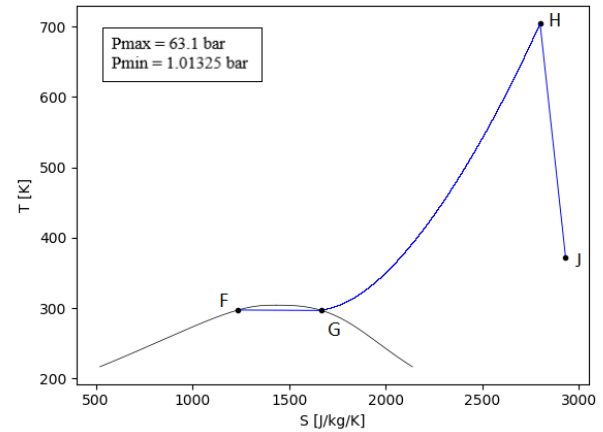


Figure 3: CO₂ discharge phase on T-s diagram

SUPERCRITICAL CO₂ STORAGE SYSTEM

In this paragraph, a CO₂ closed loop in supercritical regime is examined. The system includes: a compressor (2), a turbine (3), a high-temperature (5) and a low-temperature (6) exchanger-regenerator (SC-RIG), an ambient pressure tank (1) and a high pressure tank (7), a motor/generator (4), a valve (8) and a non-return valve (9).

The compressor delivery pressure is assumed 100 bar, as hypothesized in the Spadacini's patent [6].

The characteristics of the compressor (10000 kW), charging time (4 h) and the ambient pressure tank structure are the same as in the previous case. Regarding pressure losses, same prior assumptions are maintained. See Table 2 for assumptions. Two SC-RIGs are used instead of one, because in this way it is possible to compare the heat stored at constant temperature in the subcritical cycle (Fig. 2, line D-E) to the heat stored at low temperature in the supercritical case (Fig. 4, line D-E). The temperature of the CO₂ leaving the high-temperature SC-RIG (5) during the charge phase is set arbitrarily at 373 K (state D), according to the Spadacini's patent [6].

During the accumulation phase, carbon dioxide is in a reservoir in environmental conditions ($T_A = 293.15$ K; $P_A = 1.01325$ bar), then the fluid is led through pipes to the compressor inlet (while the turbine outlet is blocked by a valve). The fluid is brought up to a pressure of 100 bar (state C) and to a temperature of 780.6 K (about 60 K higher than subcritical CO₂), thus going beyond the

critical point. Then, it flows inside the first SC-RIG (C-D line) and next it passes through the second SC-RIG (D-E line). In the end, CO₂ is stored in the high pressure tank at 298.15 K and 97 bar (state E).

Component	Assumptions
High-temperature exchanger-regenerator (high-temperature SC-RIG) (5)	Pressure loss 1.5% of inlet pressure Exergetic loss
Low-temperature exchanger-regenerator (low-temperature SC-RIG) (6)	Pressure loss 1.5% of inlet pressure Exergetic loss
Compressor (2)	Power set at 10000 kW Isentropic efficiency 0.85 Electrical efficiency 0.98 Mechanical efficiency 0.98
Turbine (3)	Isentropic efficiency 0.88 Electrical efficiency 0.98 Mechanical efficiency 0.98
High pressure tank (7)	No temperature and pressure loss
Ambient pressure tank (1)	In balance with atmospheric pressure
Charging time: 4 h	

Table 2: Assumptions for each plant component

In Figure 4 the supercritical CO₂ charge phase is depicted on the T-s thermodynamic diagram.

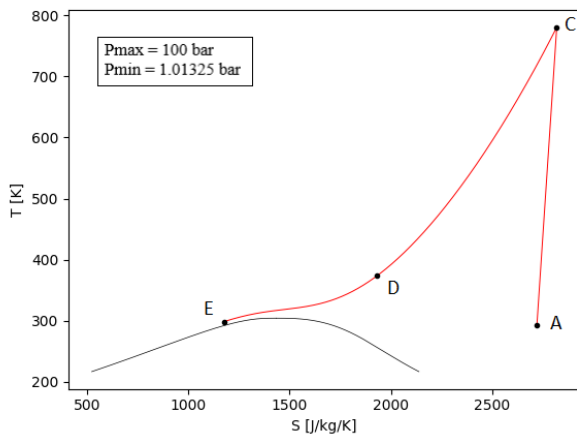


Figure 4: S-CO₂ charge phase on T-s diagram

State F, from which the discharge phase begins, is considered equal to state E as assumed in the subcritical case. Pressure losses are hypothesized in a similar way to the charge phase for the two SC-RIGs. In addition, two exergetic losses are considered during the passage through the SC-RIGs. During the release phase, the first SC-RIG heats up the carbon dioxide contained in the tank up to the temperature of 365 K (state G). Afterwards, the fluid passes through the second SC-RIG absorbing heat until it reaches the turbine inlet at a temperature of 763.6 K and a pressure of 94 bar (state H). Finally, CO₂ expands to generate electrical power and arrives at the reservoir at ambient pressure (state J), which is connected to the turbine outlet by a valve. In Figure 5 the supercritical CO₂ discharge phase is represented on the T-s thermodynamic diagram.

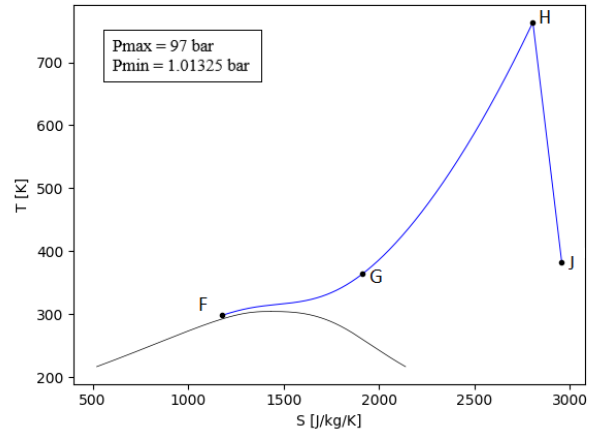


Figure 5: S-CO₂ discharge phase on T-s diagram

RESULTS FOR THE SUBCRITICAL CO₂ CYCLE

For the calculation of the thermodynamic characteristics of fluids, CoolProp 6.4.0 was used, it is an open source library of thermophysical properties, which can be implemented with programming languages such as Python and MATLAB [7].

The assumptions, made for each component, are summarised in Table 1.

Looking at Table 3, a critical aspect encountered is the considerable volume occupied by the reservoir at ambient pressure, which is supposed to be spherical in order to evaluate its diameter. The volume of the ambient pressure tank, before the beginning of the charge phase, contains the working fluid that guarantees a charging time of 4 h and a power of 10000 kW (the CO₂ mass within the tank is equal to 339747 kg). In atmospheric conditions, due to the low density of carbon dioxide (about 1.8 kg/m³), large volumes are required to be able to accumulate the entire mass of working fluid. However, despite the high volumes involved, liquified natural gas tanks of such size already exist in the world.

For example, the Adriatic LNG's offshore terminal has a Gravity Based Structure (GBS) which hosts two LNG tanks of 125000 m³ each [8].

The high pressure tank (supposed spherical as well) must be taken into account. Compared to reservoir at ambient pressure, looking at Table 3, the tank is about seven times smaller in diameter due to the higher accumulated CO₂ density (723 kg/m³). When designing the tank, it is of great importance to consider the wide pressure changes that can occur with small temperature variations. Indeed, during the isochoric transformation of liquid CO₂, reaching 35 °C would mean arriving at a tank pressure of 103 bar. In conclusion, it is necessary for the tank to be adiabatically insulated so that it is not affected by ambient temperature changes, and to be designed by considering stresses significantly higher than the nominal ones.

Since the cycle is subcritical, the CO₂ at high pressure is stored in a liquid phase. As a result, the process is isochoric, but referring to the compressor it is isobar, because as the fluid is gradually compressed, it liquefies in the condenser, in which a free surface of liquefied CO₂ is established (tank is not adiabatic).

Compressor work	423.8 kJ/kg
Heat stored at high temperature	530.3 kJ/kg
Heat stored at constant temperature	124.03 kJ/kg
CO ₂ mass flow	23.59 kg/s
Ambient pressure tank diameter	70.66 m
High pressure tank diameter	9.64 m
SC-RIG mass	861.8 t
SC-RIG volume	219.6 m ³
Turbine work	335.8 kJ/kg
Electrical power in 4 h discharge	7611 kW
RTE	76.1%

Table 3: Results for the subcritical CO₂ cycle

As regards the heat exchange, the heat stored at high temperature by SC-RIG (C-D line) is differentiated from that stored at constant temperature (D-E line). It is straightforward to understand that such heat is more relevant than the second both in energy (Tab. 3) and exergetic terms, since in the line D-E the fluid condenses at a temperature of about 297 K. The SC-RIG (component 5 in Fig. 1) has a longitudinal tapered shape in order to ensure a greater heat exchange surface between fluid and constituent material. The SC-RIG is a structured-type regenerator, such as a honeycomb structured, as in [9].

By hypothesis it is chosen a honeycomb constituted by steel, with a vacuum factor of 50%. In the aforementioned article [9] a regenerator made of mullite is analysed; however in this paper the SC-RIG is

assumed consisting of steel, since it is economical, it has good thermo-mechanical characteristics, temperature are intermediate and ceramic materials can be avoided, as they can cause dust release impacting on turbomachinery erosion. Then, a simple calculation was carried out for the preliminary sizing of the SC-RIG. The following steel values are used for the calculations: specific heat capacity $C_p = 500$ J/kgK and density $\rho = 7850$ kg/m³. Figure 6 shows the volumes occupied by the three components taken into account, i.e. the high pressure tank, the reservoir at ambient pressure and the SC-RIG.

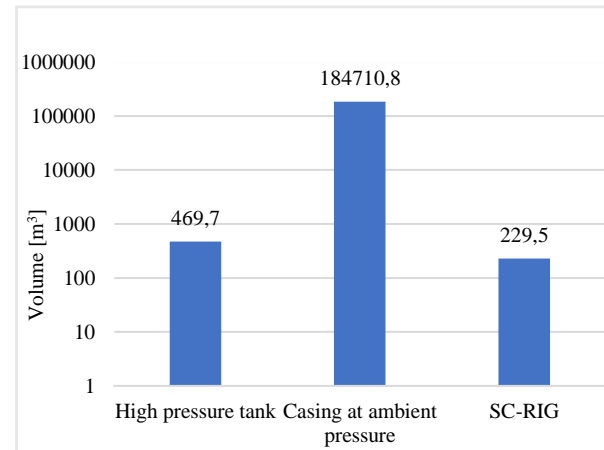


Figure 6: Comparison of storage volumes

As indicated in Table 3, the RTE is 76.1%, a value higher or anyway in line with modern advanced CAES solutions [10]. In addition, for a discharge phase that lasts three hours the electrical power generated (10147 kW) is similar to the power required by the compressor; indeed, the drain of the same mass of CO₂ in a shorter time increases the mass flow from 23.6 kg/s to 31.5 kg/s, validating the enhancement of turbine power despite the same specific work.

RESULTS FOR THE S-CO₂ CYCLE

As regards the results for the supercritical CO₂, Table 4 shows an increase in the work required by the compressor and in the heat stored at low temperature. The assumptions, made for each component, are summarised in Table 2.

The heat stored increase is due to the higher average temperature at which the heat exchange takes places compared to the subcritical condition; indeed, it is possible to make a comparison between the D-E section with an average temperature value of 297.5 K, for subcritical CO₂, and the same section for S-CO₂ with a temperature of 336 K.

This analysis, however, may not be entirely correct as the overall heat stored for the subcritical and supercritical charge phase is divided with different

criteria. For S-CO₂, the temperature of the working fluid coming out of the high-temperature SC-RIG is set at 373 K, while for subcritical CO₂ is equal to 297 K, thus allowing a greater storing of heat. For this reason, the heat stored at high temperature for S-CO₂ is lower than in the subcritical case despite the input temperature of this component is higher.

Compressor work	490.13 kJ/kg
Heat stored at high temperature	486.37 kJ/kg
Heat stored at low temperature	248.2 kJ/kg
CO ₂ mass flow	20.4 kg/s
Ambient pressure tank diameter	67.3 m
High pressure tank diameter	8.84 m
High-temperature SC-RIG mass	598.5 t
High-temperature SC-RIG volume	152.5 m ³
Turbine work	391.1 kJ/kg
Electrical power in 4 h discharge	7664 kW
RTE	76.6%

Table 4: Results for supercritical CO₂

A positive aspect found for S-CO₂ is the reduction of the occupied volumes, which involves a slight decrease in plant size and construction costs.

Since the specific work of the turbine and compressor increases compared to the subcritical case, while the power of the latter remains unchanged, the mass flow of working fluid decreases and consequently, for a charging time of 4 hours, a lower CO₂ mass will be required (294 ton versus 340 ton). In addition, the slight lowering of the diameter of the high pressure tank is also linked to an increase in CO₂ density inside it (812.7 kg/m³ versus 723 kg/m³).

Moreover, the high pressure tank is isochoric, which means that the overall process is transient by definition. To ensure a quasi isobaric pressure for the compressor/turbine during operation, it is possible to employ variable volume storage (e.g. with mobile internal membrane) or to exploit a thermal regulation (i.e. at the beginning of the charge phase it is possible to keep a higher storage temperature, and toward the end of the charge phase the temperature is lowered, increasing the density of CO₂). In addition, in supercritical regime, the density of the fluid varies greatly with temperature, therefore the storage temperature can be modulated in order to keep the pressure constant. So, referring to the high pressure tank, if the volume is constant, pressure may be kept also constant by a not adiabatic transformation.

In Table 4, SC-RIG volume is less than the subcritical case, because it has a lower heat exchanged and a higher temperature difference.

The low-temperature SC-RIG, on the other hand, is not analysed in detail, but problems related to a considerable heat storage, with a limited temperature difference of the component, can be supposed.

At last round trip efficiency (RTE) gains a slight percent increase going supercritical.

Figure 7 shows the volumes occupied by the three components taken into account, i.e. the high pressure tank, the reservoir at ambient pressure and the high-temperature SC-RIG.

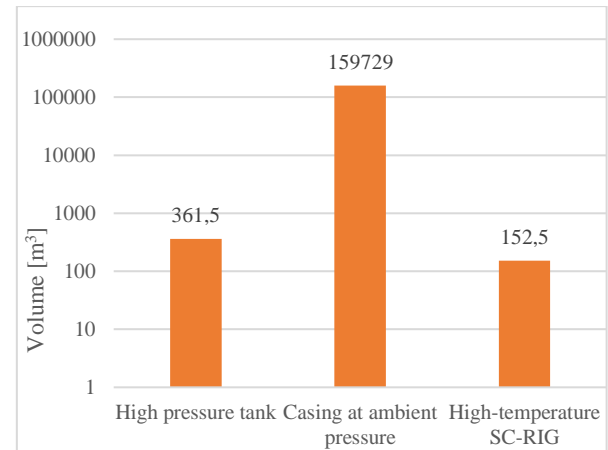


Figure 7 : Comparison of storage volumes for S-CO₂

However, it is possible to reduce the volume of the ambient pressure tank by acting on the charging times or power of the system in order to decrease the mass of CO₂ inside, but at the expense of the amount of energy that can be stored and the efficiency of the system. Figure 8 shows the trend of the ambient pressure tank volume as the charging time and power of the compressor change.

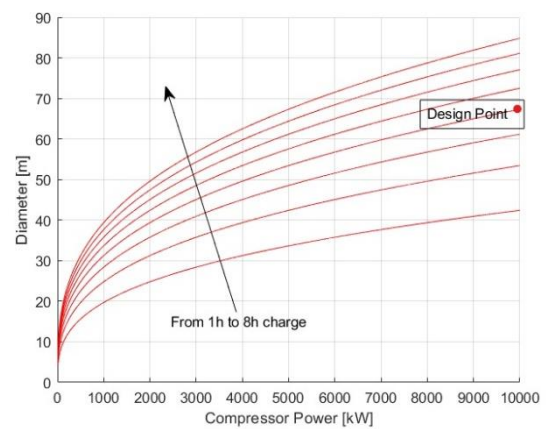


Figure 8: Ambient pressure tank diameter as a function of power and charging time

COMPARATIVE ANALYSIS

In the following paragraph a comparative analysis is carried out between some results obtained from different types of working fluid. Furthermore, Adiabatic Compressed Air Energy Storage (ACAES) is included as benchmark, since it works in a similar way to the cycles seen above.

In addition to carbon dioxide, other working fluids such as N_2O , SF_6 and H_2O are considered. The main assumptions used for CO_2 remain valid for other substances (see Tables 1 and 2). As regards the water, to maintain a similarity with the systems analysed previously, the minimum pressure is set to 0.05 bar and maximum pressure to the atmospheric one.

The first parameter considered is round trip efficiency (RTE), which is one of the main features of energy storage systems.

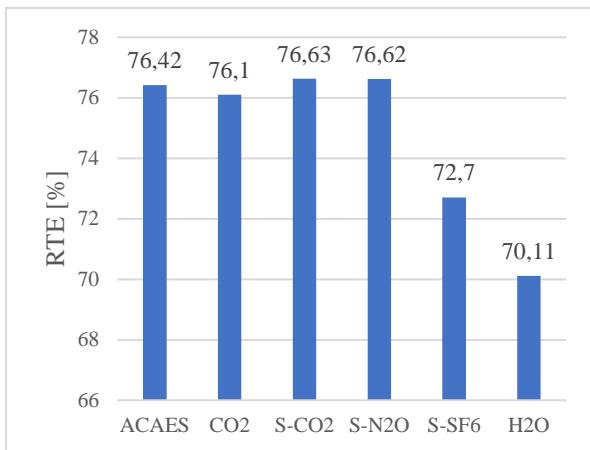


Figure 9: Comparison of RTE values

The second parameter taken into account is the volume of the reservoir (at a pressure of 0.05 bar for H_2O and at ambient pressure for other fluids). Then, this comparison allows to identify the fluid that, during the design phase, guarantees the smallest footprint of the accumulation volume.

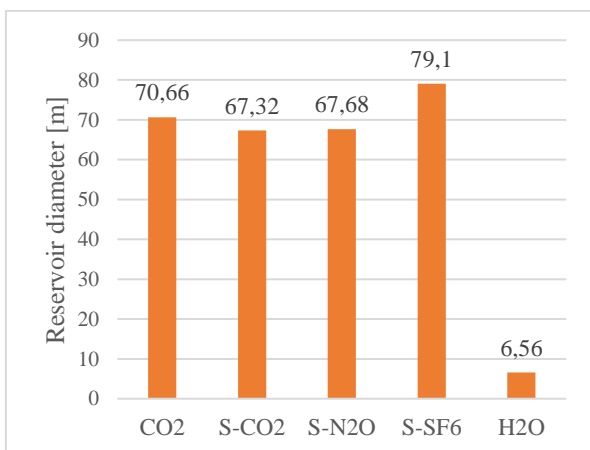


Figure 10: Comparison of reservoir diameters

Water is considered as a working fluid because the space required for accumulation will be reduced, thanks to the fact that at environmental conditions it can be easily stored in the liquid phase and therefore at a higher density than gases.

Comparison of masses of the various heat exchangers-regenerators (SC-RIG) is illustrated in Figure 11.

In addition, considering an average steel price of 0.90 €/kg, for configuration with CO_2 as a working fluid it would cost about € 800000, which clearly indicates its potential impact on system capital cost.

For S-SF₆ the value is high due to the increased mass flow rate in circulation and the lower ΔT of the SC-RIG.

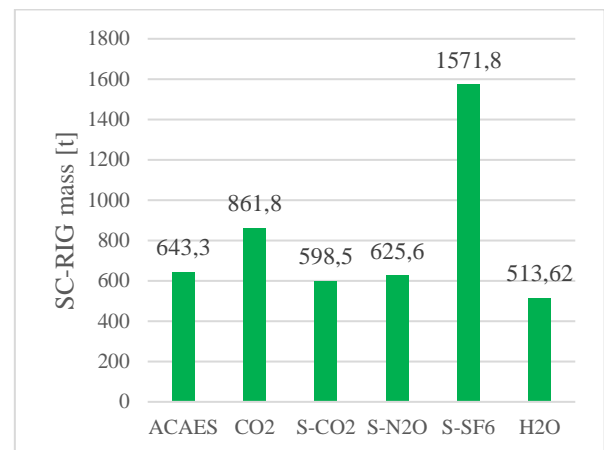


Figure 11: Comparison among SC-RIG weights

Finally, the ratio between the specific work of the compressor and the total stored heat is introduced as a comparison factor. For CO_2 and H_2O , the total heat is obtained from the sum between the one stored at high temperature (inside the SC-RIG) and the heat absorbed at a constant temperature during the phase change.

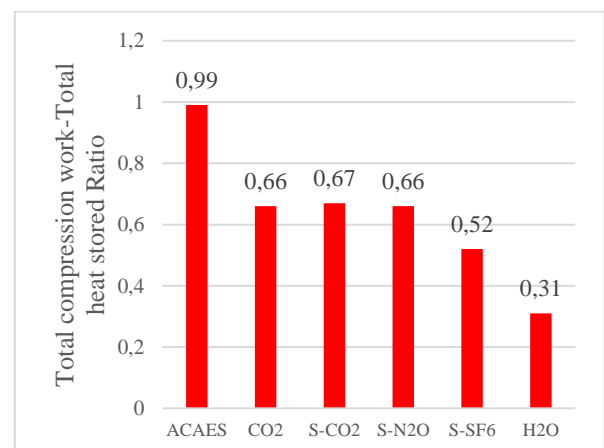


Figure 12: Comparison of compression work to stored heat ratios

For S-CO₂, S-N₂O and S-SF₆ the total heat is obtained from the sum between the heat stored at high

temperature (inside the high-T SC-RIG) and the heat absorbed at low temperature (inside the low-T SC-RIG). Water has a low value of this ratio (0.31) due to the high latent heat.

The analysis shows that the fluid able to guarantee the best performance, referring to RTE, is CO₂ in supercritical conditions. Furthermore, S-CO₂ is also competitive in the comparison among SC-RIG weights (Fig. 11) and in the comparison of reservoir diameters (Fig. 10), neglecting H₂O.

Anyway, since the performance of CO₂ and S-CO₂ is quite similar, it may not be worth complicating the plant using higher pressures. Therefore, it could be better opting for the subcritical cycle that would allow an easier management of high pressure tank despite a small decrease RTE.

Table 5 compares the parameters of greatest interest for the working fluids considered most suitable.

Working fluid	CO ₂	S-CO ₂	H ₂ O
RTE [%]	76.1	76.6	70.1
Electrical power [kW]	7611	7664	7012
Compression work [kJ/kg]	423.84	490.13	975.54
Heat stored at high-T [kJ/kg]	530.28	486.37	837.45
Reservoir diameter [m]	70.66	67.32	6.56
Tank diameter [m]	9.64	8.84	6.65

Table 5: Comparison between the most relevant parameters

CONCLUSIONS

The paper provides an overview of innovative energy storage systems via closed-loop cycles, assessed through a detailed but relatively straightforward thermodynamic analysis of the cycle.

Among the different working fluids considered (CO₂, N₂O, SF₆ and H₂O), the substance that guarantees the best performance, referring to RTE, is CO₂ in supercritical conditions (RTE = 76.6%).

Furthermore, an investigation was conducted for each fluid concerning the size of the tanks at atmospheric pressure, assumed spherical. It was found that for CO₂, N₂O and SF₆ the diameter of these components is a critical aspect to be carefully considered (for S-CO₂ the diameter is 67.32 m).

This system may seem similar to ACAES, with the advantage of constant pressure ratio, thanks to the CO₂ change of state (or cooling, in case of supercritical cycle).

In the future, it will be essential to carry out a comprehensive techno-economic analysis of the SC-RIG and the heat exchangers, since they are fundamental

components for the operation of the entire plant and they contribute to the overall efficiency and cost. Moreover, it will also be essential to study the dynamic behaviour of this storage system, using analogies and results from other application of CO₂ in power systems (e.g. [11]), in order to better understand the possible applications of this technology in the energy market.

NOMENCLATURE

CSP	Concentrated Solar Power
RTE	Round Trip Efficiency
SC-RIG	Heat Exchanger-Regenerator
S-CO ₂	CO ₂ in supercritical condition
S-N ₂ O	N ₂ O in supercritical condition
S-SF ₆	SF ₆ in supercritical condition
WHR	Waste Heat Recovery

REFERENCES

- [1] IEA (2020). World Energy Outlook 2020. France, Paris.
- [2] IEA (2020). Global Energy Review 2020. France, Paris.
- [3] Oudalov, A.; Chartouni, D.; Ohler, C.; Linhofer, G. (2006). Value Analysis of Battery Energy Storage Applications in Power Systems. Power Systems Conference and Exposition. PSCE '06. 2006 IEEE PES, pp.2206-2211.
- [4] Karmiris G.; Tengnér T. (2013). Peak Shaving Control Method for Energy Storage. Sweden, ABB AB, Corporate Research Center, Västerås.
- [5] Marchionni, M.; Bianchi, G.; Tassou, S. (2020). Review of Supercritical Carbon Dioxide (sCO₂) Technologies for High-grade Waste Heat to Power Conversion. SN Applied Sciences 2(4), DOI: 10.1007/s42452-020-2116-6.
- [6] Spadacini, C.; Inventor (2020). Energy Storage Plant and Process. Italy, Milan. Patent WO 2020/039416 A2.
- [7] Bell, I. H.; Wronski, J.; Quoilin, S.; Lemort, V. (2014). Pure and Pseudo-pure Fluid Thermophysical

- Property Evaluation and the Open-Source Thermophysical Property Library CoolProp. *Industrial & Engineering Chemistry Research* 2014 53 (6), 2498-2508. DOI: 10.1021/ie4033999
- [8] RINA Consulting S.p.A.; Adriatic LNG (2019). Documentazione Tecnica Allegata alla Domanda di Riesame dell'AIA, Sintesi non Tecnica. Italy, Genoa.
- [9] Mahmood, M.; Traverso, A.; Traverso, A. N.; Massardo, A. F.; Marsano, D.; Cravero, C. (2018). Thermal Energy Storage for CSP Hybrid Gas Turbine Systems: Dynamic Modelling and Experimental Validation. *Applied Energy* 212 (2018) 1240–1251. Italy, Genoa.
- [10] Wang, J.; Lu, K.; Ma, L.; Wang, J.; Dooner, M.; Miao, S.; Li, J.; Wang, D. (2017). Overview of Compressed Air Energy Storage and Technology Development. *Energies* 2017 10 (7), 991. Switzerland, Basel.
- [11] Lambruschini, F.; Liese, E.; Zitney, S.E.; Traverso, A. (2016). Dynamic Model of a 10 MW Supercritical CO₂ Recompression Brayton Cycle. ASME Paper GT2016-56459, BEST PAPER AWARD.

EVALUATION OF DETERIORATION IN VERTICAL sCO₂ COOLING HEAT TRANSFER IN 3 MM TUBE

Andreas Wahl*

Institute of Nuclear Technology and
Energy Systems (IKE), Stuttgart, Germany
andreas.wahl@ike.uni-stuttgart.de

Rainer Mertz

Institute of Nuclear Technology and
Energy Systems (IKE), Stuttgart, Germany

Eckard Laurien

Institute of Nuclear Technology and
Energy Systems (IKE), Stuttgart, Germany

Jörg Starflinger

Institute of Nuclear Technology and
Energy Systems (IKE), Stuttgart, Germany

ABSTRACT

In the frame of EU-project sCO₂-flex the design of a 25 MWe supercritical CO₂ (sCO₂) Brayton cycle will be designed. The system will be optimized to meet flexibility requirements, while reducing environmental impact and focusing on cost efficiency. In the context of a sCO₂ Brayton cycle, the gas cooler is a key component to achieve a high overall efficiency. Close to the critical point, due to varying properties, heat transfer and pressure drop of carbon dioxide (CO₂) are difficult to predict. In case of vertical flow, acceleration and buoyancy effects induced by strong density gradients can cause a significant deterioration of the heat transfer.

In this publication, the cooling heat transfer coefficient (*htc*) is investigated in a 3 mm diameter tube with vertical flow orientation. Commonly used calculation methods of the heat transfer coefficient are presented. Although developed for heating of sCO₂, the mixed convection criterion of Jackson and Hall [7] is used to evaluate the heat transfer deterioration. The effects of the CO₂ mass flux of 141 – 354 kg/m²s and bulk fluid temperatures of 20 – 50 °C with a constant pressure of 80 bar on the heat transfer were examined. The transition between forced and mixed convection can be explained by the *htc* -values. The upwards flow shows a steady decrease in the *htc* with the reduction of the mass flux. However, the downwards flow shows significant effects of buoyancy. At low mass flux the distinct peak in the *htc* at the pseudocritical temperature (T_{pc}) disappears.

INTRODUCTION

A sCO₂ Brayton cycle offers a number of benefits over competing power plant cycles. A high plant efficiency can be achieved due to the favourable fluid properties in the supercritical region. This is resulting in increased electricity production with the same fuel consumption [16]. The high density of sCO₂ allows to reduce the necessary compressor work and leads to a reduction in the overall size of the power plant [4]. The reduced size of turbomachinery, boiler and heat exchangers can be further translated into reduced capital costs. The moderate value of its critical pressure (7.38 MPa) makes CO₂ more economical than water where the critical point is much higher (22.1 MPa). A low heat rejection temperature leads to power cycles with high efficiencies. The critical temperature of CO₂ (31°C) contributes to that, however, it is not too low, to be cooled by the ambient temperature. CO₂ is a non-toxic and non-flammable natural working fluid with ODP = 1 (ozone depletion potential) and GWP = 1 (global warming potential). It is available in sufficient quantities at reasonable costs. In environmental, cost and safety terms, CO₂ is regarded as an ideal natural refrigerant [19].

The properties of sCO₂ (Figure 1) lead to significant differences in the heat transfer characteristics. This is caused by rapid changes of thermo physical properties close to the critical point. The thermophysical properties are derived by the NIST/REFPROP database [5]. Thus, specific equation of state [11] and transport equations [6, 23] were used.

The understanding of heat transfer enhancement and deterioration phenomena during cooling in a small diameter tube is crucial to develop new concept of compact heat exchanger for the Brayton cycle, able to work with high efficiency, speed and reliability under high CO₂ pressure and low pinch point. The thermo physical properties change strongly with temperature and pressure. As shown in Figure 1, the viscosity (η) and density (ρ) are strongly decreasing with increasing temperature. The

* corresponding author(s)

isobaric heat capacity (c_p) and thermal conductivity (λ) pass through a peak crossing the pseudocritical temperature.

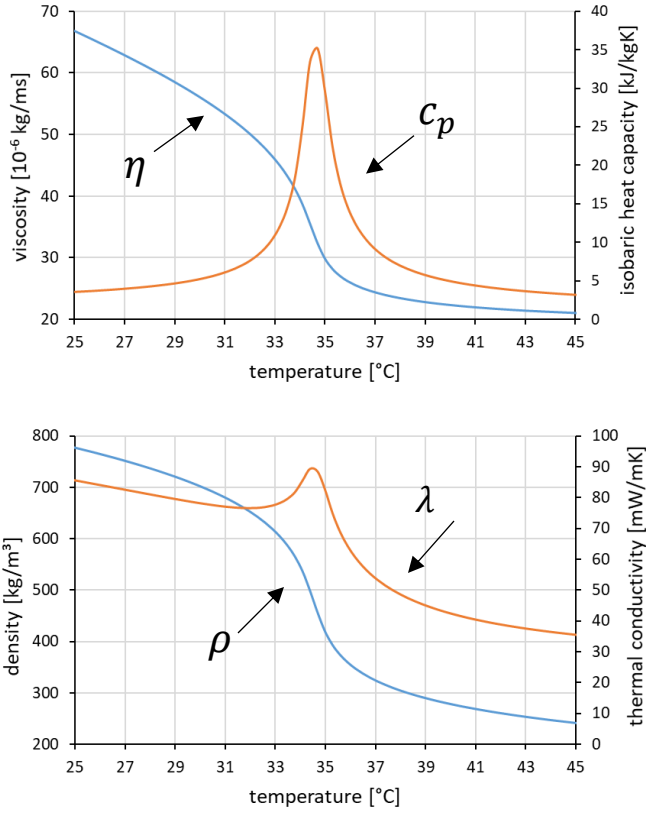


Figure 1: properties of CO₂ at 80bar

In this study, the heat transfer under cooling conditions was determined at different mass fluxes, temperatures and flow orientations. The effects of the parameters on the heat transfer were demonstrated.

STATE OF THE ART OF HEAT TRANSFER DURING COOLING

A number of researchers have experimentally investigated the cooling heat transfer and pressure drop performance of CO₂ in tubes of different sizes. The research has been concentrated on tubes ranging from 0.5 to 10.7 mm in horizontal flow [3, 10, 13, 14, 17, 18, 21, 25]. Limited research is available for cooling heat transfer in vertical flow orientation. Jiang et al. [8] investigated the heat transfer during cooling in a 2 mm diameter tube with a combination of experimental measurements and numerical simulations. The results show that the local heat transfer coefficients vary significantly along the tube for different flow orientations. Bruch [2] investigated experimentally the cooling heat transfer of sCO₂ in a copper tube with an inner diameter of 6 mm. The test section consists of two vertical tube-in-tube heat exchangers connected in series by means of a U-bend. In the experiment, the in- and outlet temperature of CO₂ and cooling media was measured and treated with an integral method to determine the heat transfer coefficient.

The method to approach the deteriorated heat transfer of supercritical fluids in general and supercritical CO₂ in specific was developed in the heating case. The research on sCO₂ heating in direct electrical heated tubes lead to the development of criterions for the deterioration of heat transfer in vertical flow. Different criterions can be found in literature which are either based on the effect of flow acceleration or on the effect of buoyancy [7, 15, 20]. The experiments conducted with circular tubes of different diameters work on validation and improvement of the criterions and equations [9, 12, 13]. Currently and ongoing experiments at IKE with a 4 mm and 8 mm tube will contribute to this field of research [22]. Bruch [2] is the only author who applied a deterioration criterion to the cooling heat transfer. The semi-empirical parameter ($Gr/Re^{2.7}$) by Jackson and Hall [7] was applied to characterize the influence of natural convection on turbulent vertical flow. Fundamentally, mixed convection can be described with the Richardson-number, which compares buoyancy forces and the inertial forces. The Richardson number Ri is defined as a ratio of the Grashof number Gr and the Reynolds number Re to the square:

$$Ri = \frac{Gr}{Re^2} \quad (1)$$

Using the parameter, mixed convection has a significant influence on the heat transfer when:

$$\frac{Gr}{Re^{2.7}} > 10^{-5} \quad (2)$$

The Grashof number Gr used by Jackson and Hall [7] is calculated with the difference between bulk density ρ_b and the average density $\bar{\rho}$:

$$Gr = \frac{(\rho_b - \bar{\rho}) \cdot \rho_b \cdot g \cdot d^3}{\eta_b^2} \quad (3)$$

The average density $\bar{\rho}$ is calculated with the approximation by Bae and Yoo [1]:

$$\bar{\rho} \approx \begin{cases} \frac{(\rho_w + \rho_b)}{2} & \text{for } T_w > T_{pc} \text{ or } T_b < T_{pc} \\ \left[\frac{\rho_b(T_b - T_{pc}) + \rho_w(T_{pc} - T_w)}{T_b - T_w} \right] & \text{for } T_w < T_{pc} < T_b \end{cases} \quad (4)$$

The selected pure forced convection correlation of Bruch [2] is the one by Jackson and Hall [7]:

$$Nu_{FC} = 0.0183 Re_b^{0.82} \overline{Pr}_b^{0.5} \left(\frac{\rho_b}{\rho_w} \right)^{-0.3} \quad (5)$$

The results of the experimental investigation were plotted in dimensionless form (Figure 2). The resulting functions of the downwards stream are the following:

$$\frac{Gr}{Re^{2.7}} < 4.2 \cdot 10^{-5}: \quad \frac{Nu_b}{Nu_{FC}} = 1 - 75 \left(\frac{Gr}{Re^{2.7}} \right)^{0.46} \quad (6)$$

$$\frac{Gr}{Re^{2.7}} > 4.2 \cdot 10^{-5}: \quad \frac{Nu_b}{Nu_{FC}} = 13.5 \left(\frac{Gr}{Re^{2.7}} \right)^{0.40} \quad (7)$$

The region of forced convection is present at $Gr/Re^{2.7} < 10^{-6}$ with only little difference to unity. With increasing mixed convection parameter, the heat transfer deteriorates strongly. The strongest deterioration is present in the mixed convection area. With further increase of the mixed convection factor, the flow regime converts to free convection. The heat transfer recovers in this area.

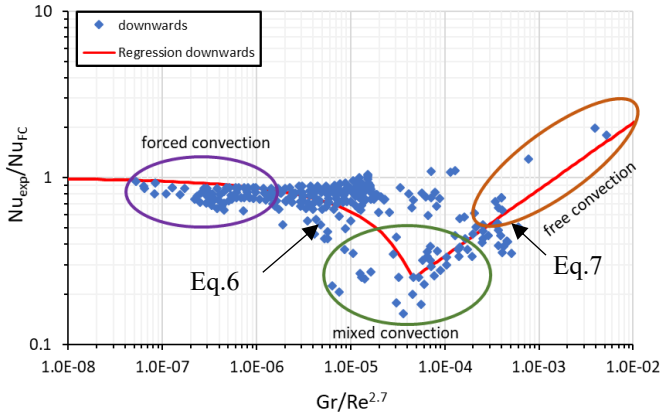


Figure 2: Evolution of Nusselt number with the mixed convection parameter by Bruch [15]

EXPERIMENTAL SET-UP

The SCARLETT test loop provides sCO₂ under defined boundary conditions. Figure 3 illustrates of the SCARLETT test loop, which is described as follows [24].

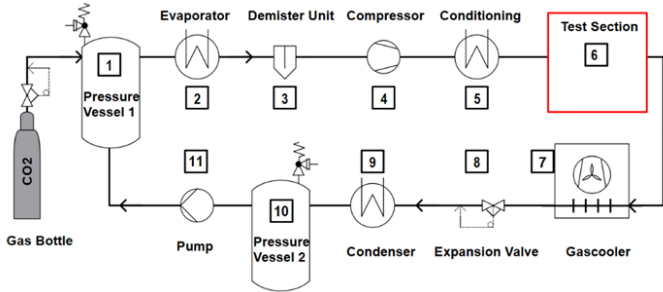


Figure 3: P&I diagram of the SCARLETT test loop

After evacuating the loop with a vacuum pump, the pressure vessels (1, 10) are filled with CO₂ by a gas bottle. During normal operation, liquid CO₂ flows from the pressure vessel 1 through an electrical heated evaporator (2) and is slightly superheated. After leaving a demister unit (3), where remaining liquid CO₂ is separated from the flow, it enters a compressor (4), where it is compressed to a certain pressure and simultaneously heated by the compression.

Before entering a test section, there is a conditioning (5) of the sCO₂, which means that a defined temperature can be adjusted via cooling or heating the sCO₂ mass flow rate. In the test-section (6) different kind of experiments can be performed. After leaving the test section, the sCO₂ is cooled down in a gas cooler (7) followed by the expansion in an expansion valve (8). Before it enters the pressure vessel 2 (10) the CO₂ can be cooled down

again in a condenser (9). Finally, it is pumped back from the pressure vessel 2 into the pressure vessel 1. The sCO₂ mass flow rate in the SCARLETT test loop can be adjusted from about 30 to 110 g/s. Lower mass flow rate in the test section can be achieved by bypassing with needle valves. It must be mentioned, that the achievable mass flow rate depends on the compressor performance map, which leads to less mass flow rate at higher pressures and vice versa. The sCO₂ temperature at the inlet of the test section can be varied from about 0 to 140 °C and the pressure up to 110 bar.

The test section applied in this report consists of a stainless steel tube with 1000 mm length. The inner diameter is 3 mm and the outer tube diameter is 5 mm. The experimentally cooled length of the tube is 500 mm. The annulus were designed to lead the thermocouples to the inner tube, deliver the cooling media in- and outflow, and close the annulus stream leak-tight. The flanges center the tube in the annulus. The differential pressure was measured by drilling holes into the tube wall. With 100 mm of adiabatic length at both sides of the tube, the differential pressure was measured at a length of 700 mm (Figure 4). The accuracy of the pressure transducer was 0.15 % of full range of 1/100 bar.

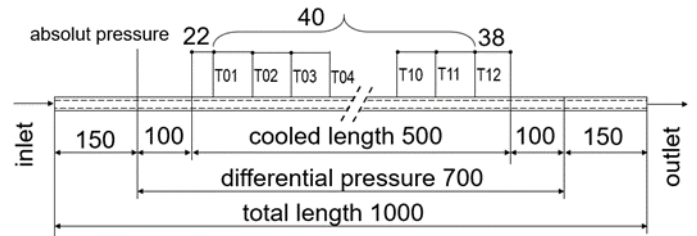


Figure 4: Detailed view of the test tube (All dim. in mm)

T-type thermocouples are soldered into milled channels on the surface of the tube (Figure 5). Before the installation, the thermocouples were calibrated within a range of 5–60 °C by the use of a high accurate reference resistance temperature detector (RTD, calibrated to 0.02 K). The resulting accuracy of the T-type thermocouples was ±0.1 K. The thermocouples are coated with stainless steel leading to high durability against corrosion.

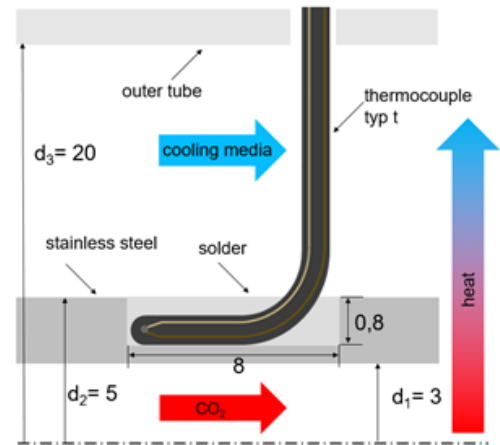


Figure 5: Detailed view of the thermocouple soldering in the tube surface (All dim. in mm)

The heat conductance in the thermocouple wire could lead to a measurement error, thus the thermocouples have to be embedded a certain length inside the tube to eliminate this influence. The T-type thermocouples have a diameter of 0.5 mm. They are bended and laid in the milled channels (0.8x0.8x8mm depth/width/length). Additional to the measurement errors, the error of the manual soldering process has to be considered. For example, the manufacturing inaccuracies of the milled channels, the placing in the channel to the assumed accuracy of the wall temperature of the stainless-steel tube of ± 0.2 K. The bending of the thermocouple leads to an asymmetry of the temperature measurement points in the cooled length. The first measurement position (T_{01}) is at 22 mm of the cooled length. The spacing is equal along the tube with 40 mm between the measurement positions. The thermocouples were mounted in-line. The solder alloy used to connect the tube with the thermocouples was a 96 % tin and 4 % silver mixture with implemented colophony. This material has a low temperature melting point (Solidus: 221 °C, Liquidus 238 °C), which does not exceed the temperature range of T-type thermocouples (-40 °C...+350 °C) and leads to a good thermal connection of the two components due to the high thermal conductivity. The accuracy of the RTD's to measure both flows at in- and outlet were ± 0.1 K. The accuracy of the Coriolis-type mass flow meter was assumed to be 0.3 %. All measurement quantities of the test section are displayed in Figure 6.

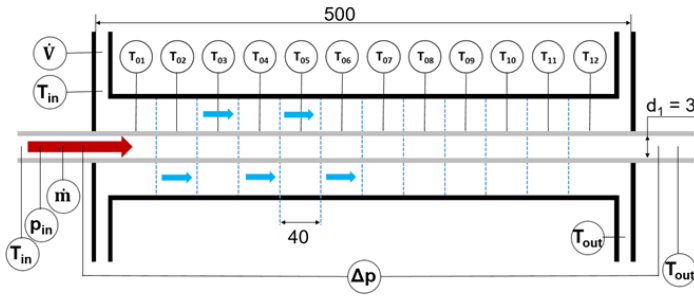


Figure 6: measured quantities in the experiment(All dim. in mm)

DATA REDUCTION

The removed heat can be calculated with the in- and outlet temperatures T_{in} T_{out} , inlet pressure p_{in} and differential pressure Δp of the CO_2 flow:

$$\dot{Q}_{CO_2} = \dot{m}_{CO_2} * [h_{in}(T_{in}, p_{in}) - h_{out}(T_{out}, p_{in} - \Delta p)] \quad (9)$$

The temperature difference in the cooling media flow between in and outlet is too small to apply a caloric determination. The heat flux is calculated as following:

$$\dot{q}_{CO_2} = \frac{\dot{Q}_{CO_2}}{\pi d L} \quad (10)$$

The CO_2 bulk temperature $T_{CO_2,b}$ for each experiment is the average of in- and outlet.

$$T_{CO_2,b} = \frac{T_{CO_2,in} + T_{CO_2,out}}{2} \quad (11)$$

The twelve tube temperature measurements are averaged:

$$T_t = \frac{\sum_{i=1}^{12} T_{t,i}}{12} \quad (12)$$

The heat conduction of the tube wall leads to a difference between the measured tube wall $T_{R,i}$ and the CO_2 wall temperature $T_{CO_2,w}$. For this reason, the tube wall measurement is assumed to be central between inner and outer surface:

$$T_{CO_2,w} = T_t + \dot{q}_{CO_2} \cdot \frac{\ln\left(\frac{4 \text{ mm}}{3 \text{ mm}}\right)}{2\pi L \lambda} \quad (13)$$

The heat transfer coefficient is defined as the ratio of heat flux and temperature difference between CO_2 bulk and wall:

$$htc_{CO_2} = \frac{\dot{q}_{CO_2}}{\Delta T} \quad (14)$$

Caused by the fact, that in the supercritical region c_p and htc can change strongly, it is important to evaluate different definitions of the temperature difference ΔT . One option, as considered by Yoon et al. [25], Son et al. [21] and Liu et al. [14], is to calculate the difference of both averaged values $T_{CO_2,b}$ (Eq.11) and $T_{CO_2,w}$ (Eq.13):

$$\Delta T_{average} = T_{CO_2,b} - T_{CO_2,w} \quad (15)$$

A second approach is to calculate the logarithmic mean temperature difference (LMTD):

$$\Delta T_{LMTD} = \frac{(T_{in} - T_{CO_2,w,1}) - (T_{out} - T_{CO_2,w,12})}{\ln\left(\frac{T_{in} - T_{CO_2,w,1}}{T_{out} - T_{CO_2,w,12}}\right)} \quad (16)$$

with the CO_2 -wall temperature at the first and the last measurement $T_{CO_2,w,1} / T_{CO_2,w,12}$ as applied by Liao [13] and Dang [3]. The study aims to determine the htc as a local set of values. However, the changing thermophysical properties along the tube influence the heat transfer calculation. The LMTD method is based on the assumption of a constant property fluid. To limit the changes of the properties between the in- and outlet of CO_2 , the temperature difference of the experiments was kept low if T_b is close to T_{pc} .

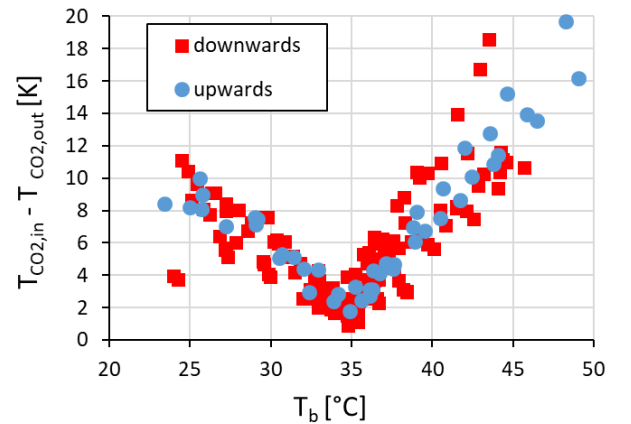


Figure 7: Temperature difference $T_{in} - T_{out}$ over T_b

Higher temperature differences were only measured far away from T_{pc} (Figure 7). It results in a difference of both approaches of between +10% and -20% (Figure 8). In the vicinity of the pseudocritical temperature T_{pc} , htc_{ave} is up to 10% higher. Towards lower and higher temperatures, this tendency is reversed. In the liquid like region, the htc_{LMTD} is up to 10% higher and in the gas like region up to 20% higher. However, to ensure the accuracy of \dot{q}_{CO_2} determination, it is important to measure above a certain temperature difference between in-and outlet. This is due to the high c_p close to T_{pc} . To meet both requirements the temperature difference close to T_{pc} was kept around 2 K. The inaccuracies based on the measurements was kept below 20%. This assessment shows the good agreement of both approaches. However, only has little influence on the final evaluation of heat transfer deterioration which is based on a direct comparison of both flow direction. As from now, htc_{LMTD} is presented in reference to htc .

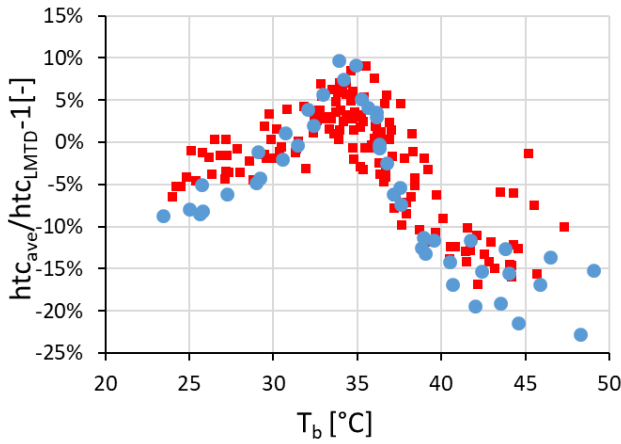


Figure 8: Difference of htc_{ave} / htc_{LMTD} over T_b

EXPERIMENTAL DATA

In this report, the experimental results of 204 experiments are presented. The parameter range is displayed in Table 1.

Table 1: Experimental parameter and number of experiments

CO ₂		
temperature[°C]	pressure [bar]	mass flux [kg/m ² s]
51-20	80	141-354

flow orientation ± 2°	
upwards	45
downwards	159

VERTICAL FLOW ORIENTATION

In the vertical upwards flow, free convection induces additional turbulence. The effective direction of forced convection is upwards while free convection is in downwards direction. The interaction of both effects leads to a parabolic velocity profile, which increases the velocity difference between the wall and the centreline and thus, increases the heat transfer.

From literature [2], it is known, that this influence is much smaller than in the downwards flow. In Figure 9, the htc -values for mass fluxes from 141 kg/m²s to 283 kg/m²s are shown. As expected, all three mass fluxes show a similar trend with a peak close to T_{pc} . It can be seen, that the enhancement of the mass flow leads to higher htc due to increases turbulent diffusion. Horizontal error bars represent temperature change from the inlet to the outlet of the test section, and vertical error bars represent the uncertainty in the measurement. Only two error bars are displayed with the aim to keep the diagram readable. The error bar shows what was mentioned previously, the temperature difference in the CO₂ flow is small to decrease the uncertainties in the heat transfer coefficient.

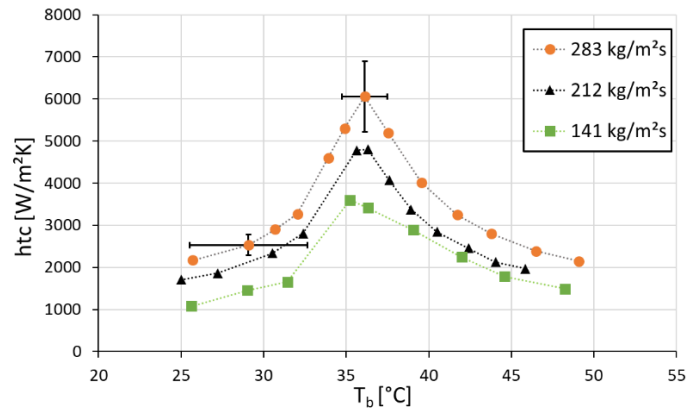


Figure 9: htc over T_b for different mass flux in vertical upwards flow

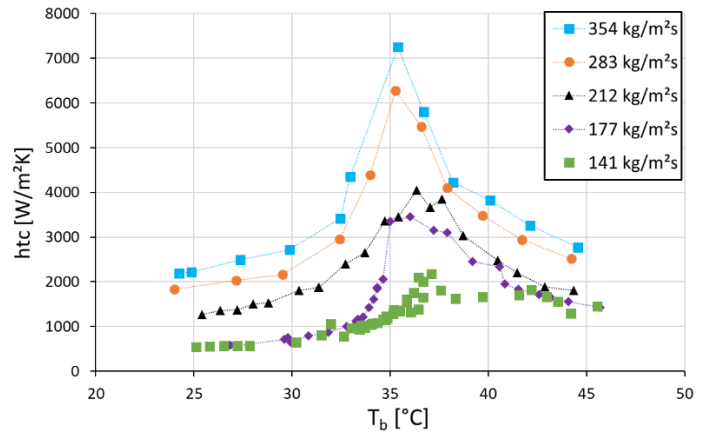


Figure 10: htc over T_b for different mass flux in vertical downwards flow

In the vertical downwards flow, the effective direction of both forced and free convection are in downwards direction. In this case, a m-shaped velocity profile develops. Due to this interaction, the velocity difference between wall and centreline is reduced, which can handicap the radial energy transfer. In the downwards flow, it is expected to see significant deterioration of the heat transfer, that means discrepancies to the forced convection regime. In Figure 10, the h_{tc} -values for mass fluxes from $141 \text{ kg/m}^2\text{s}$ to $354 \text{ kg/m}^2\text{s}$ in the vertical downwards flow are shown. With the reduction of the mass flux from $354 \text{ kg/m}^2\text{s}$ to $283 \text{ kg/m}^2\text{s}$, a constant decrease of the h_{tc} -values can be seen. With further reduction of the mass flux, clear evidence of mixed convection is present. In the liquid like region ($T_b < 34.6^\circ\text{C}$), the h_{tc} drops between $212 \text{ kg/m}^2\text{s}$ and $177 \text{ kg/m}^2\text{s}$ relatively strong. However, the h_{tc} remains constant with further reduction. At T_{pc} , a strong reduction of the h_{tc} can be seen at $G = 177 \text{ kg/m}^2\text{s}$. At this mass flux the abrupt change in the thermo physical properties seems to induce deterioration. The h_{tc} at $G = 141 \text{ kg/m}^2\text{s}$ shows a flat trend and thus, disagrees clearly from forced convection. In the temperature region $T_b < 33^\circ\text{C}$ and $T_b > 42^\circ\text{C}$, the h_{tc} is constant with further reduction from $G = 177 \text{ kg/m}^2\text{s}$ to $141 \text{ kg/m}^2\text{s}$.

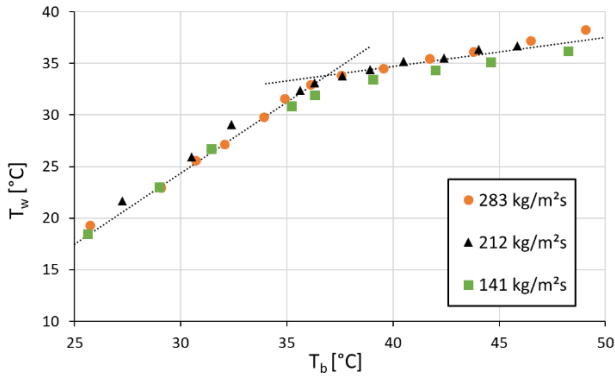


Figure 11: T_w over T_b for different mass flux in vertical upwards flow

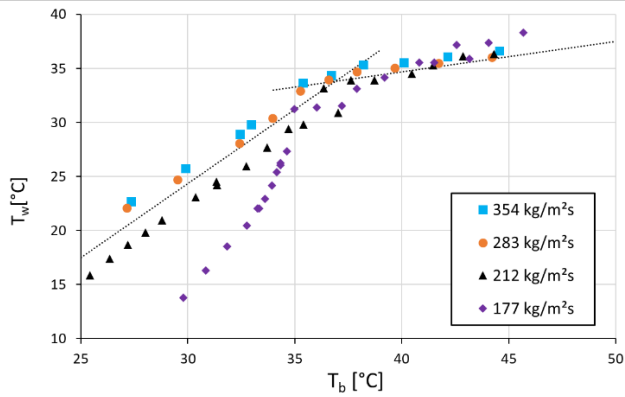


Figure 12: T_w over T_b for different mass flux in vertical downwards flow

In Figure 11 and Figure 12, the wall temperatures are presented as a function of the bulk temperature. In the upwards flow, the enhancement of the heat transfer with increasing mass flux leads to no difference in the wall temperature. The dotted lines visualize the tendencies. The differences between the gas and liquid-like region are significant. In the downwards flow, the heat transfer deterioration causes a strong decrease of the wall temperatures.

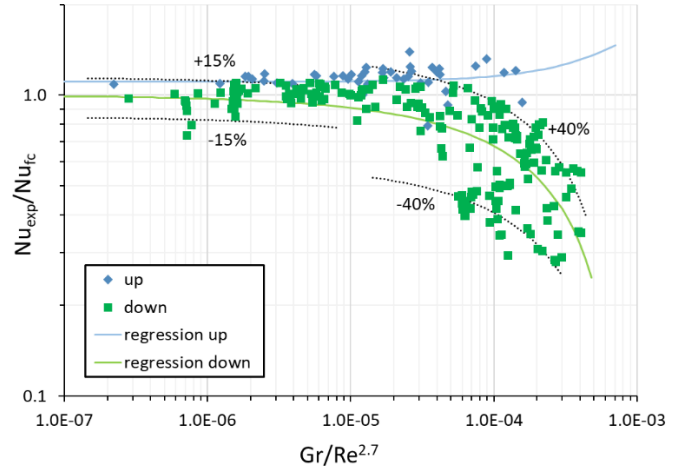


Figure 13: Evolution of ratio Nu_{exp}/Nu_{fc} with the mixed convection parameter $Gr/Re^{2.7}$ of the downwards and upwards flow

In Figure 13, results are presented in dimensionless form. For low values of the mixed convection parameter $Gr/Re^{2.7}$, forced convection is the predominant mechanism of heat transfer. The influence of free convection is negligible and the ratio Nu_{exp}/Nu_{fc} is close to unity for both flow directions. This also indicates a good agreement with the chosen forced convection equation by Dang [9]. As the parameter $Gr/Re^{2.7}$ increases, buoyancy forces are stronger and differences appear with flow direction. Heat transfer is enhanced in upwards flow and deteriorated in downwards flow. In the downwards flow a clear trend can be seen, however, the mean variation is relatively high. The transition to free convection, which is characterised with the recovery of the Nu_{exp}/Nu_{fc} ratio was not detected within the experimental boundary conditions. Equation 17 and 18 are the functions of the plotted regression of Figure 13.

$$\text{upwards: } \frac{Nu_b}{Nu_{fc}} = 1.107 + 510.2 * \frac{Gr}{Re^{2.7}} \quad (17)$$

$$\text{downwards: } \frac{Nu_b}{Nu_{fc}} = 1 - 46.4 * \left(\frac{Gr}{Re^{2.7}} \right)^{0.540} \quad (18)$$

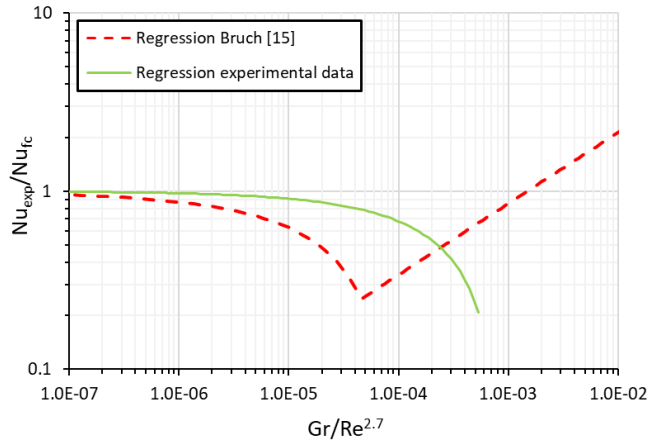


Figure 14: Comparison of proposed correlation of downwards flow with the correlation by Bruch [2]

Figure 14 compares the experimental regression (green) with the equation by Bruch [2]. The experiments show deterioration at higher $Gr/Re^{2.7}$ values. This might indicate, that the tube diameter is a relevant factor of the heat transfer deterioration in cooling heat transfer. It seems like that the phenomena of deterioration and recovery is shifted towards higher $Gr/Re^{2.7}$ values. The heat transfer recovery is expected to appear near the end of the plotted regression at $Gr/Re^{2.7} \approx 10^{-3}$. However, the experimental facility with its fixed cooling length would reduce the accuracy to an unacceptable level with further reduction of the mass flux.

CONCLUSION

At the IKE University Stuttgart, an experimental investigation was conducted to evaluate the heat transfer in a vertical cooled tube with 3 mm inner diameter. The results show an influence of mixed convection at a stepwise reduction of the mass flux. The transition from forced convection to mixed convection can be seen by means of the drop in the heat transfer coefficient. The analysis of the experimental data with the Jackson criterion resulted in a significant trend. However, the deterioration in downwards flow appeared at higher values of the criterion as detected by Bruch [15]. This comparison indicates that an influence on the diameter might be existing.

The findings of this report show, that in the design of the chiller for a supercritical CO_2 power cycle the flow direction could be an influencing factor. Usually, the CO_2 flows in horizontal tubes. The rotation speed of the fan controls the removed heat. If the vertical flow orientation is in consideration for such a heat exchanger, the designer should avoid the mixed convection flow area.

ACKNOWLEDGEMENT

This project has received funded by the European Union's Horizon 2020 research and innovation programme under grant agreement No 764690

NOMMENCLATUR

c_p	(J/kgK)	specific heat
d	(mm)	diameter
g	(m/s ²)	acceleration of gravity
G	(kg/m ² s)	mass flux
Gr	(-)	Grashof number
h	(kJ/kg)	specific Enthalpy
htc	(W/m ² K)	heat transfer coefficient
L	(m)	length of discretization
\dot{m}	(kg/s)	mass flow rate
Nu	(-)	Nusselt number
p	(bar)	pressure
Pr	(-)	Prandtl number
Q	(W)	heat
\dot{q}	(W/m ²)	heat flux
Re	(-)	Reynolds number
Ri	(-)	Richardson number
T	(°C)	temperature
V	(l/s)	volumetric flow

Greek symbols

Δp	(bar)	pressure drop
η	(kg/ms)	dynamic viscosity
λ	(W/mK)	heat conductivity
ρ	(kg/m ³)	density

subscripts

b	bulk
CO_2	carbon dioxide
exp	experiment
fc	forced convection
in	inlet
LMTD	logarithmic mean temperature difference
out	outlet
pc	pseudo critical
t	tube
w	wall

REFERENCES

- [1] Bae, J. H., Yoo, J. Y., and Choi, H. 2005. Direct numerical simulation of turbulent supercritical flows with heat transfer. *J. Heat Transfer* 17, 10, 105104.
- [2] Bruch, A., Bontemps, A., and Colasson, S. 2009. Experimental investigation of heat transfer of supercritical carbon dioxide flowing in a cooled vertical tube. *International Journal of Heat and Mass Transfer* 52, 11-12, 2589–2598.
- [3] Dang, C. and Hihara, E. 2004. In-tube cooling heat transfer of supercritical carbon dioxide. Part 1. Experimental measurement. *International Journal of Refrigeration* 27, 7, 736–747.
- [4] Dostal, V., Driscoll, M. J., and Hejzlar, P. 2004. A Supercritical Carbon Dioxide Cycle for Next Generation Nuclear Reactors. MIT-ANP-TR-100.
- [5] E. W. Lemmon, M. L. Huber, M. O. McLinden. 2010. REFPROP. Reference Fluid Thermodynamic and Transport Properties. NIST SRD 23, United States of America.
- [6] Fenghour, A., Wakeham, W.A., Vesovic, V. 1998. The Viscosity of Carbon Dioxide.
- [7] Jackson, J. D. and Hall, W. B. 1979. Forced Convection Heat Transfer to Fluids at Supercritical Pressure. Institution of Mechanical Engineers, Conference Publications 2.
- [8] Jiang, P.-X., Zhao, C.-R., Shi, R.-F., Chen, Y., and Ambrosini, W. 2009. Experimental and numerical study of convection heat transfer of CO₂ at super-critical pressures during cooling in small vertical tube. *International Journal of Heat and Mass Transfer* 52, 21-22, 4748–4756.
- [9] Kim, D. E. and Kim, M.-H. 2011. Experimental investigation of heat transfer in vertical upward and downward supercritical CO₂ flow in a circular tube. *International Journal of Heat and Fluid Flow* 32, 1, 176–191.
- [10] Kondou, C. and Hrnjak, P. 2011. Heat rejection from R744 flow under uniform temperature cooling in a horizontal smooth tube around the critical point. *International Journal of Refrigeration* 34, 3, 719–731.
- [11] Kunz, O., Klimeck, R., Wagner, W., and Jaeschke, M. 2007. The GERG-2004 Wide-Range Equation of State for Natural Gases and Other Mixtures. GERG TECHNICAL MONOGRAPH 15 (2007).
- [12] Lei, X., Zhang, Q., Zhang, J., and Li, H. 2017. Experimental and Numerical Investigation of Convective Heat Transfer of Supercritical Carbon Dioxide at Low Mass Fluxes. *Applied Sciences* 7, 12, 1260.
- [13] Liao, S. M. and Zhao, T. S. 2002. Measurements of Heat Transfer Coefficients From Supercritical Carbon Dioxide Flowing in Horizontal Mini/Micro Channels. *Journal of Heat Transfer* 124, 3, 413.
- [14] Liu, Z.-B., He, Y.-L., Yang, Y.-F., and Fei, J.-Y. 2014. Experimental study on heat transfer and pressure drop of supercritical CO₂ cooled in a large tube. *Applied Thermal Engineering* 70, 1, 307–315.
- [15] McEligot, D. M. and Jackson, J. D. 2004. “Deterioration” criteria for convective heat transfer in gas flow through non-circular ducts. *Nuclear Engineering and Design* 232, 3, 327–333.
- [16] Mendez, C. M. and Rochau, G. sCO₂ Brayton Cycle: Roadmap to sCO₂ Power Cycles NE Commercial Applications -SAND2018-6187. Sandia National Laboratories. SAND2018-6187. DOI=10.2172/1452896.
- [17] Oh, H.-K. and Son, C.-H. 2010. New correlation to predict the heat transfer coefficient in-tube cooling of supercritical CO₂ in horizontal macro-tubes. *Experimental Thermal and Fluid Science* 34, 8, 1230–1241.
- [18] Pitla, S. S., Groll, E. A., and Ramadhyani, S. 2002. New correlation to predict the heat transfer coefficient during in-tube cooling of turbulent supercritical CO₂. *International Journal of Refrigeration* 25, 7, 887–895.
- [19] Riffat, S. B., Afonso, C. F., Oliveira, A. C., and Reay, D. A. 1997. Natural refrigerants for refrigeration and air-conditioning systems. *Applied Thermal Engineering* 17, 1, 33–42.
- [20] S. Petukhov, B., A. Kurganov, V., and B. Ankudinov, V. 1983. Heat transfer and flow resistance in the turbulent pipe flow of a fluid with near-critical state parameters. *Teplofizika Vysokikh Temperatur* 21.
- [21] Son, C.-H. and Park, S.-J. 2006. An experimental study on heat transfer and pressure drop characteristics of carbon dioxide during gas cooling process in a horizontal tube. *International Journal of Refrigeration* 29, 4, 539–546.
- [22] Theologou, K., Mertz, R., Laurien, E., and Starflinger, J., Eds. 2019, 19-20. September. An Assessment of the criteria for the onset of heat transfer deterioration with supercritical CO₂ in vertical heated single circular tubes. DuEPublico: Duisburg-Essen Publications online, University of Duisburg-Essen, Germany.
- [23] Vesovic, V., Wakeham, W.A., Olchoway, G.A., Sengers, J.V., Watson, J.T.R., and Millat, J. 1990. The transport properties of carbon dioxide.
- [24] W. Flaig, R. Mertz, and J. Starflinger, Eds. 2018, 30-31. August. Design, control procedure and start-up of the sCO₂ test facility SCARLETT.
- [25] Yoon, S. H., Kim, J. H., Hwang, Y. W., Kim, M. S., Min, K., and Kim, Y. 2003. Heat transfer and pressure drop characteristics during the in-tube cooling process of carbon dioxide in the supercritical region. *International Journal of Refrigeration* 26, 8, 857–864.

**PRELIMINARY AERODYNAMIC DESIGN OF A SUPERCRITICAL CARBON
DIOXIDE COMPRESSOR IMPELLER FOR WASTE HEAT RECOVERY
APPLICATIONS**

Shantanu Thada*

Dept. of Mechanical Engineering,
Indian Institute of Technology Bombay
Mumbai, India

A M Pradeep

Dept. of Aerospace Engineering,
Indian Institute of Technology Bombay
Mumbai, India

Arunkumar Sridharan

Dept. of Mechanical Engineering,
Indian Institute of Technology Bombay
Mumbai, India

ABSTRACT

Supercritical Carbon dioxide (S-CO₂) Brayton cycles have garnered significant attention in the recent past as an alternative source for renewable energy. The present research provides a simplistic, yet robust methodology to appropriately size and design the impeller of a centrifugal compressor for a 12.5 MW_e waste heat recovery S-CO₂ power plant. Two prominent variants of the S-CO₂ cycle are studied and optimized with the aim of maximizing the power output using genetic algorithm. To calculate the geometry from the inlet and exit thermodynamic conditions of the optimized cycle, conservation equations are solved. The impeller is sized and a brief study on condensation in the impeller throat is performed. The effect of multi-staging on condensation is investigated. Further, the performance model is coupled with the design scheme to dynamically modify the impeller geometry. Using the developed model, the geometrical parameters of the S-CO₂ impeller are calculated. In addition to the geometry, certain impeller performance parameters are reported and are observed to lie within the permissible limits.

INTRODUCTION

Advancements in the technology of power generation have undergone significant growth in the past two centuries. Although the fundamental principle of electricity generation remains unchanged, technologies of heat-to-power conversion have evolved with a straightforward goal of improving the process efficiency as well as production capacity. In the year 2018, primary energy consumption has grown fastest since 2010 at a rate of 2.9%, doubling its 10-year average of 1.5% per annum [1]. The use of fossil fuels to generate power has brought large-scale industrialization. However, the problem of climate change has provided a push towards the innovation of renewable technologies for power generation.

Along with the use of renewables, re-using the waste heat produced by the various industrial sectors improves the overall thermodynamic efficiency of the process. The process of re-using waste heat from exhaust streams to produce power is referred to as waste heat recovery (WHR) in this study. Recovery of waste heat is known to have benefits such as reduction in fuel/energy consumption cost, reduction in pollution, increment in process efficiency, and a smaller power block [2]. Waste heat recovery has applications in energy intensive industries such as the metal industry (Iron, Aluminum, Steel), Glass, Paper, and Cement manufacturing industries. Waste heat source are classified based on the source temperature, primarily into three categories: High (>600°C), Medium (250°C - 600°C) and Low (<250°C) [3]. For medium-to-low heat source temperatures, the challenges involved with installing a WHR unit includes the presence of low-quality heat source, the capital cost for installation and the maintenance costs.

Among the different options for generating power from a waste-heat source, the supercritical Carbon dioxide Brayton cycle offers higher cycle efficiency at lower temperatures, reduced power block and wide range of operational temperatures. The concept of CO₂ being used as a working fluid for power generation was first introduced when Sulzer Ltd. filed a patent [4] for a partial condensation CO₂ Brayton reactor in 1948. Feher in 1968 [5], proposed the first simple recuperated Brayton cycle (RC) configuration. Feher reported that the designed configuration is advantageous as it provides higher thermal efficiency, no turbine blade erosion, no pump cavitation, low volume to power ratio, single stage turbine and pump. Another prominent S-CO₂ cycle configuration known as the recuperated recompression Brayton cycle (RRC) was proposed by Angelino in 1968 [6]. The RRC configuration has a smaller precooler size due to lower CO₂ mass flow rate as well as a lower pinch point in Low Temperature Recuperator (LTR), thereby increasing the cycle thermal efficiency. The

* corresponding author(s)
Email: s.thada@gmail.com

schematic of the RC and RRC configurations are presented in Figure 1 and 2 respectively.

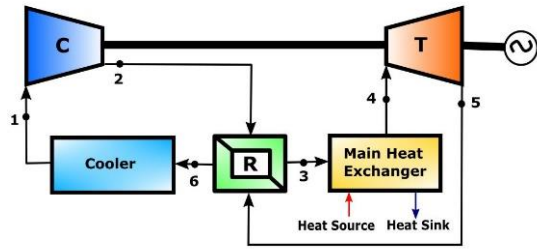


Figure 1: Schematic of the S-CO₂ RC configuration

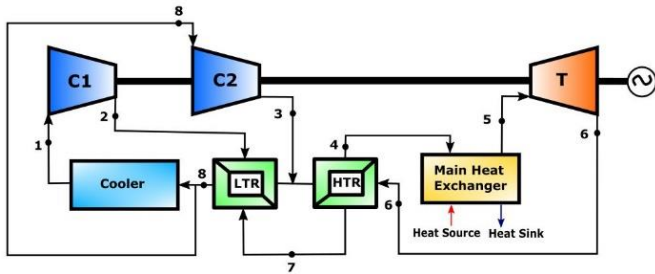


Figure 2: Schematic of the S-CO₂ RRC configuration

For a supercritical cycle, the compression process occurs close to the supercritical point which introduces certain challenges in its design. Turbomachinery for S-CO₂ has a variety of problems related to local condensation, corrosion and losses associated with them. Typically, three types of losses may occur due to condensation: kinematic relaxation loss, thermodynamic wetness loss and breaking loss, which needs to be properly assessed [7]. Strong variations in properties near the critical point restricts the use of empirical loss correlations developed for conventional air-based turbomachinery. Specifically, in the compressor, the impeller is the one of the few rotating parts that further complicates the design process. The design methodology for an S-CO₂ compressor needs to be appropriately modified to deal with these challenges.

Conventional air-based design methodology for generating the geometry of a centrifugal compressor requires certain modifications to account for the above stated challenges for unconventional fluids. The present study addresses the literature gap of turbomachinery design for non-ideal working fluids, specifically, CO₂ in supercritical state. The primary objective of the study is to develop a geometry of a centrifugal compressor impeller for a waste heat recovery (WHR) S-CO₂ power plant for industrial applications. A preliminary design methodology is developed to calculate the geometrical parameters of a centrifugal compressor based on the thermodynamic cycle parameters. To achieve this, first, two prominent configurations of the S-CO₂ cycle are thermodynamically optimized using genetic algorithm methodology for a defined waste-heat source.

CYCLE DESIGN AND OPTIMIZATION

As identified in Wright et al. [8], one of the first commercial applications for S-CO₂ power systems is likely to be 5-20 MWe Waste Heat Recovery (WHR) power systems for industrial applications (particularly steel mills, cement plants). The present study focuses on developing a S-CO₂ cycle for WHR with a power generation capacity of 12.5 MWe. The waste-heat source is designed based on studying the exhaust gas characteristics of various small to medium scale plants in the cement industry [9]. The characteristics of the flue gases generated from the heat source are provided in Table 1. The cooler air exhaust temperature in a cement plant typically lies in the range of 400°C - 450°C with a mass flow rate equal to 50kg/s for a 1 MTPA clinker production capacity. Based on the inputs provided, various configurations of the S-CO₂ cycles are explored. Since the idea is to use a waste-heat source, it is important to design a power conversion system that delivers the maximum net power output. Calculations are performed using codes written on MATLAB R2018a [10] with the CoolProp [11] add-on to calculate the properties of Carbon dioxide based on Span & Wagner equation of state. The governing equations for every component of the thermodynamic cycle are based on the solution of steady-state mass, momentum and energy balance.

Table 1: Exhaust Gas Characteristics of the Waste-Heat Source

Working Fluid	Air
Inlet Temperature of Exhaust Gas	450°C
Inlet Pressure of Exhaust Gas	1 atm
Mass Flow Rate of Exhaust Gas	50 kg/sec
Ambient Temperature	25°C

Thermodynamic Cycle Modelling

Primary components of an S-CO₂ Brayton cycle comprise of compressor(s), turbine, source heat exchanger, cooler and recuperator(s). Along with the schematics, the cycle states for RC and RRC configuration are numbered in the schematics presented in Figure 1 and 2, respectively. Thermodynamic model of these components is based on conservation equations of mass and energy. Energy balance across the main heat exchanger for RC configuration is depicted in Equation 1, while the enthalpy balance across the recuperator is depicted in Equation 2. In the model, input parameters such as the compressor efficiency, turbine efficiency and fractional pressure drop in heat exchangers are assumed to be constant. Primary inputs to the model are the design variables, which outputs the remaining states at the entry and exit of each component. For the RC configuration, the design variables include the compressor inlet pressure, compressor exit pressure, compressor inlet temperature, mass flow rate and terminal temperature difference. The RRC configuration includes an additional design variable other than the design variables of the RC configuration, i.e., the main compressor mass flow fraction. Using the thermodynamic states obtained from the model,

performance parameters such as the thermal efficiency and net power output are calculated. In the heat exchangers, it has been observed in multiple studies like Mohagheghi et. al [12], Khadse et. al [13], that the pinch point lies at the cold end of the recuperator. Terminal temperature difference at the cold end of the recuperator is an input parameter to the model, and is assumed equal to the pinch point.

$$\dot{m}_{air} \times (h_{entry} - h_{exit}) = \dot{m}_{CO_2} \times (h_4 - h_3) \quad (1)$$

$$h_3 - h_2 = h_5 - h_6 \quad (2)$$

Optimization Methodology

A thermodynamic cycle optimization consists of obtaining a set of input design variables that maximizes the performance parameter(s). Certain constraints are imposed during this optimization to ensure that the mass, momentum and energy conservation are not violated. In this study, Genetic Algorithm (GA) is used to perform the optimization. As stated by Mitchell [14], GA is an optimization algorithm based on a nature-based selection process which imitates the biological evolution, using the bio-inspired operators such as mutation, crossover and selection.

In a typical optimization process, derivative-based techniques are used to find the minimum of a defined function. However, for any function that has several local optimum points, it is likely that the technique results into capturing the local and not the global optimum. In contrast to the gradient based technique, GA does not require any analytical relations governing the system, it treats the system as a black box [12]. Here, a pre-defined waste heat source is available for waste-heat to power conversion, and the objective is to generate the maximum net power output from the available resource. Therefore, for this study, the objective function is the net power output of the S-CO₂ cycle. The iterative methodology followed by the Genetic Algorithm can be summarized in five steps:

1. Generate a random population of individuals. The individual's identity is determined using a set value of the decision variables.
2. Evaluate the fitness function for each individual. The fittest individuals, with greater values of fitness function are selected as parents to reproduce the next generation.
3. Create a new population using the fundamental rules of genetics inclusive of crossover, mutation and selection, with same number of individuals as in the previous generation.
4. Use the newly generated population to iterate the process of evaluation of fitness function, selection of fittest individuals and application of crossover, mutation and selection.
5. Repeat the iterative process until the best individual does not change its value for several generations i.e., until convergence is obtained.

Since the adopted methodology of GA for optimization is a stochastic technique, it is possible that at the end of the first run, the optimized minimum value differs slightly. Therefore, in some studies like Khadse et. al [13], a sensitivity analysis is performed where the bounds of decision variables are narrowed down and the optimization is further performed to capture the optimal value. In the present study for all practical purposes, the value obtained at the end of first run can be used for further analysis, as it sufficiently captures the minima with good accuracy.

Assumptions and Input Parameters

Certain inherent assumptions are made during the modelling of the different S-CO₂ cycle configurations. Firstly, it is assumed that there are negligible heat losses occurring in the recuperators and main heat exchanger. Secondly, the involved turbo-machineries have a constant adiabatic efficiency throughout the operation. Thirdly, the working fluid CO₂, operates in steady state. For the present study, the compressor efficiency is set to 70% while the turbine efficiency is set to 85%. To model the pressure-drop in the heat exchangers, a fractional pressure drop coefficient is used as suggested by Angelino [6], Mohagheghi and Kapat [12] and Khadse et. al [13]. For all heat exchangers involved in the cycles, the pressure drop is set to 2% of the inlet pressure.

For all practical purposes, the lower and upper bounds of the design variables are fixed, based on certain thermodynamic as well as material strength limitations. To avoid any occurrence of condensation, the lower limit of the compressor inlet temperature is set to 310 K, a value higher than the critical temperature of CO₂ (304.13 K). The lower limit of the compressor inlet pressure is fixed as 75 bar, which is higher than the critical pressure of CO₂. The higher limit of the compressor exit pressure is set to 330 bar due to the constraint of the structural capacity of the heat exchangers. State-of-the-art printed circuit heat exchangers are designed to operate at 250 to 350 bar [13] and hence the highest pressure of the cycle is limited by the structural performance of its components. The bounds of all the design variables for RC and RRC configuration are presented in Table 2 and Table 3 respectively.

Table 2: Input Bounds for the RC configuration

Design Variables for RC configuration	Lower Limit	Upper Limit
Compressor Inlet Pressure, P_1 (bar)	74	100
Compressor Exit Pressure, P_2 (bar)	120	330
Compressor Inlet Temperature, T_1 (K)	310	420
Mass Flow Rate of CO ₂ , \dot{m}_{CO_2} (kg/s)	20	100
Terminal Temperature Difference, ΔT_{ttd} (K)	10	40

Table 3: Input Bounds for the RRC configuration

Design Variables for RRC configuration	Lower Limit	Upper Limit
Compressor Inlet Pressure, P_1 (bar)	74	100
Compressor Exit Pressure, P_2 (bar)	120	330
Compressor Inlet Temperature, T_1 (K)	310	420
Mass Flow Rate of CO ₂ , \dot{m}_{CO_2} (kg/s)	20	100
Terminal Temperature Difference, ΔT_{ttd} (K)	10	40
Main Compressor (C1) Mass Flow to Total Mass Flow Fraction, f	0	1

Optimization Results

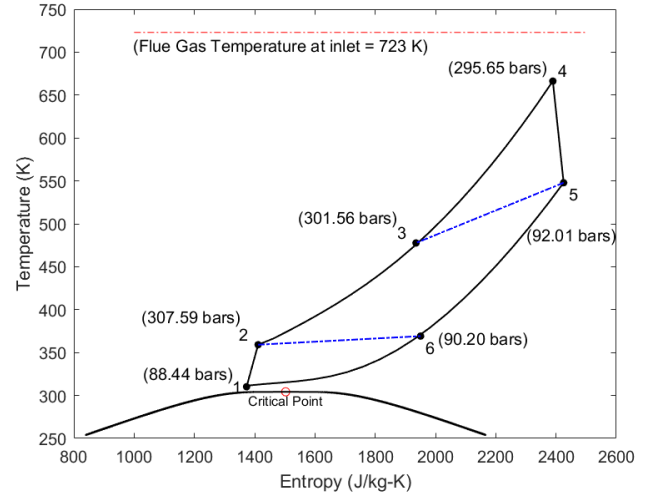
Providing the initial inputs listed above, the algorithm is run for 100 generations. For a successful run of the optimization process of the RC configuration, it is observed that the best performing individual is with a power-output value, $\dot{W}_{net} = 3.13$ MW. For the best performing individual, optimized values of the design variables and T-s Diagram of RC configuration are listed in Table 4 and Figure 3, respectively. For the optimized RC configuration, the turbine inlet temperature is 666.23 K. It is noted that approximately 56% of the total heat available in the waste-heat source is utilized. The thermal efficiency of the optimized cycle is 25.09%. As presented in Table 5, for the optimized RRC configuration, it is observed that the mass flow fraction through the main compressor approaches the value equal to 1. This is in agreement with Mohagheghi's study [12], which states that for lower CO₂ to exhaust gas stream mass flow rates, the RRC configuration approaches the RC configuration. Therefore, no significant advantage of splitting the mass flow rate is observed in the RRC configuration.

Table 4: Optimized Design Variables of RC Configuration

Optimized Design Variables for RC Configuration	Values
Compressor Inlet Pressure, P_1 (bar)	88.44
Compressor Exit Pressure, P_2 (bar)	307.59
Compressor Inlet Temperature, T_1 (K)	310.13
Mass Flow Rate of CO ₂ , \dot{m}_{CO_2} (kg/s)	48.76
Terminal Temperature Difference, ΔT_{ttd} (K)	10
Net Power Output of the Cycle, \dot{W}_{net} (MW)	3.13

Table 5: Optimized Design Variables of RRC Configuration

Optimized Design Variables for RC Configuration	Values
Compressor Inlet Pressure, P_1 (bar)	92.88
Compressor Exit Pressure, P_2 (bar)	303.00
Compressor Inlet Temperature, T_1 (K)	310
Mass Flow Rate of CO ₂ , \dot{m}_{CO_2} (kg/s)	48.17
Terminal Temperature Difference, ΔT_{ttd} (K)	10.4
Main Compressor Mass Flow Fraction, f	1
Net Power Output of the Cycle, \dot{W}_{net} (MW)	2.94

**Figure 3: T-s Diagram of the optimized RC configuration**

COMPRESSION SYSTEM DESIGN

Supercritical CO₂ Brayton cycles are characterized by relatively high operational pressures and moderate operational temperatures. Being in the proximity of critical point, the density of working fluid is high and hence the cycle components are compact. The volumetric flows in turbomachinery are low and hence even for high power outputs in the range of 5-10 MWe, centrifugal compressors can be employed. Using non-dimensional scaling, the size of turbomachinery is estimated from the desired power output [15]. In addition to the complexities involved non-ideal fluid modelling and simulation, the rotational motion of the impeller of a centrifugal compressor introduces additional complexity in the design process. The present study focuses on the preliminary aerodynamic design of a centrifugal compressor impeller for the optimized RC configuration. For the optimized cycle, the total-to-total pressure ratio of the compressor is 3.478. Typically, centrifugal compressors are expected to deliver a pressure ratio close to four in a single stage, hence, it is likely to achieve the pressure rise for the optimized cycle in a single stage. The isentropic efficiency assumed for the compressor is 0.7.

Initial Sizing

The methodology of conventional air-based turbomachinery sizing using Balje's Diagram [16] has been adopted in the past literature such as Fuller et al. [17] and Monje et al. [18]. Contours of compressor efficiencies are plotted against the specific speed (N_s) and specific diameter (D_s) for different types of turbomachinery, as defined in Equations 3 and 4, respectively.

$$N_s = \frac{\omega \times \dot{V}^{0.5}}{\Delta h_s^{0.75}} \quad (3)$$

$$D_s = \frac{d \times \Delta h_s^{0.25}}{\bar{v}^{0.5}} \quad (4)$$

First, it is assumed that the compression process occurs in a single stage. The inlet and exit (isentropic and actual) properties are calculated assuming the compressor efficiency to be 0.7. From the thermodynamic entry and exit states of the compressor, the isentropic enthalpy rise and volume flow rate are calculated. For the specific speed, optimum value is identified to lie in the range of 0.6-0.75 as established in Monje et al. [18]. Inserting the optimum value of N_s in Equation 3, the RPM is calculated. Further, the resulting value of specific diameter is calculated using Balje's diagram. Value of the obtained D_s is plugged into Equation 4 to obtain the impeller diameter. For a single stage, the resulting diameter for the impeller comes out to be 0.102 m while the resulting RPM has a value of 47460.

The calculations performed above establish that the S-CO₂ turbomachinery components are relatively small in size due to high density of the working fluid. Smaller turbomachinery components typically operated on high RPM (>10000) to accommodate the required mass flow rate. According to Fuller [17], there are several disadvantages of high RPM, including reduced life, higher maintenance costs and higher risk of condensation in the impeller throat. If the RPM is to be kept low, the compression might result into a multi-stage process. Additionally, the problem of condensation needs to be addressed for a single as well as a multi-stage S-CO₂ compressor. Therefore, to study the effects of multi-staging on condensation, the compression process is split into two stages. For the two-stage compression process, the specific enthalpy rise is divided into two equal parts and the impeller diameter and RPM are calculated using equations 3 and 4.

To quantify the phenomenon of condensation, a Mach number termed as "Acceleration Margin to Condensation" (AMC) is defined by Brenes [18] and shown in Equation 5. If the throat Mach number is greater than the AMC, it is assumed that the fluid at the impeller throat has accelerated into the two-phase dome and therefore condensation has occurred.

$$M_{AMC} = \frac{c_{sat}}{a_{sat}} = \frac{\sqrt{2 \times (h_{o1} - h(s_{sat}, T_{sat}))}}{a(s_{sat}, T_{sat})} \quad (5)$$

The choice of the hub and tip radius, to calculate the throat mach number, is not based on a fixed methodology, and is in fact based on diffusion constraints in the impeller as well as structural constraints of the shaft. Therefore, imposing a structural constraint on the shaft, the value of minimum shaft diameter is calculated using Equation 6, as stated by Loewenthal [19]. Typically, the material used for the shaft of a centrifugal compressor is Al S I 4330 [20]. Using the shear modulus of this material and previously assumed isentropic efficiency of the compressor as 70%, the minimum diameter

comes out to be 3.44 mm. Therefore, any value above the minimum diameter can be considered.

$$d_{axis,minimum} = \sqrt[3]{\frac{16 \times \dot{W}_m}{\omega \times \pi \times \tau_m}} \quad (6)$$

Now, an iterative method is adopted to calculate the throat Mach number for each stage. The value of impeller inlet hub radius is fixed based on the above structural constraint and a safety factor. The value of tip radius at the inlet is varied such that it remains higher than the hub radius and lower than the impeller exit radius. Using the inlet hub radius, inlet tip radius, inlet stagnation conditions and the RPM, the area at impeller inlet is calculated and the velocity diagram is solved by invoking the continuity equation. Assuming isentropic flow and equating the stagnation properties, static properties at the impeller throat are calculated and the velocity triangle is solved. The absolute and relative velocity at the throat along with the static thermodynamic properties are used to calculate the throat mach number. The throat area is calculated as depicted in Figure 4. The results are plotted graphically in Figure 5 and 6 for the single and two-stage compressors with hub radius set to a value of 7.525 mm for both cases. The value of hub radius is set assuming a sufficient factor of safety, in this particular scenario, equivalent to 4.5.

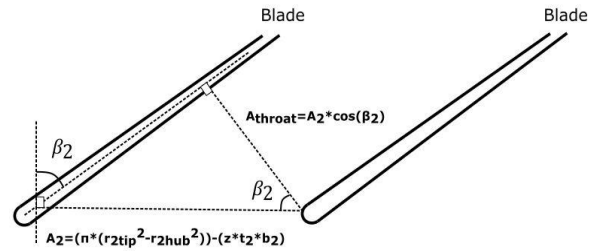


Figure 4: Area Calculation for Impeller Throat

It should be noted that in Figure 5 for the single-stage compressor, for tip radius more than 0.035 m, relative Mach number at throat is higher than the AMC and therefore, condensation might occur. Therefore, for a single stage compressor, tip radius less than 0.03 m should be selected. For the first stage of the two-stage (Figure 6), the value of relative and absolute Mach number remains less than AMC for all values of the tip radius. This is because the RPM, and therefore the Mach numbers of the multi-stage compressors are low. However, since multi-stage compression process leads to additional component costs and the single stage compressor does not show any condensation below a certain tip radius, the single stage compression process is selected.

Based on the condensation analysis, the inlet hub radius and inlet tip radius values are selected to be equal to 7.525 mm and 21.5 mm respectively. The resulting hub-to-tip ratio for the compressor is 0.35. Few other parameters, such as the number

of blades, thickness of each blade and clearance gap are chosen by the user based on prior design experience.

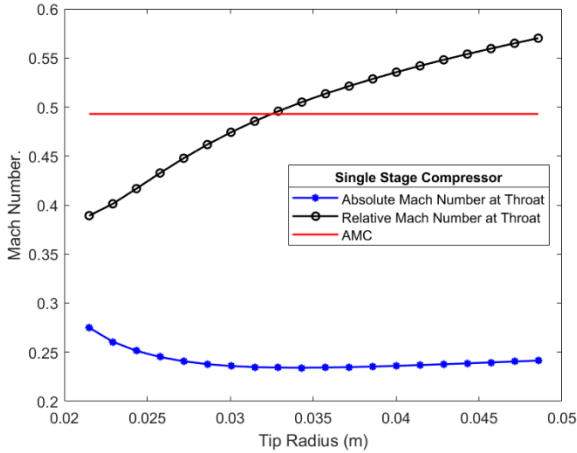


Figure 5: Absolute and Relative Mach Number at Throat for a Single Stage Compressor

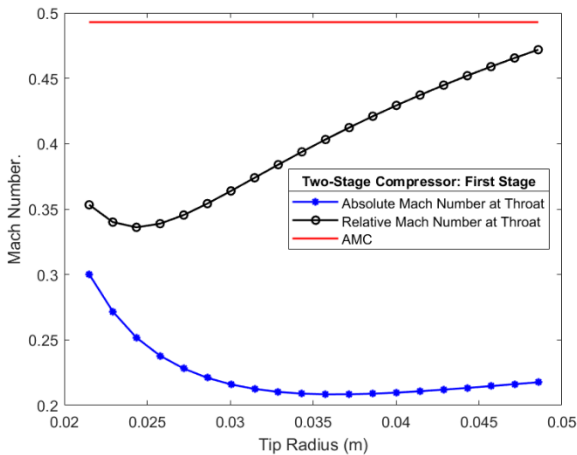


Figure 6: Absolute and Relative Mach Number at Throat for First Stage of Two-Stage Compressor

Methodology of Inverse Design

The methodology of inverse design consists of obtaining the geometry of the compressor from the inlet and exit stagnation properties, mass flow rate and RPM. A modified version of the inverse design methodology developed by Brenes [18] is adopted in the present work. To obtain the geometry of a S-CO₂ centrifugal compressor impeller, a computerized preliminary inverse design process is developed in this section. A set of operating conditions, listed below, is provided to the program and conservation equations of mass, momentum and energy are solved to calculate the geometrical parameters.

1. Total thermodynamic conditions at inlet and exit
2. Mass flow rate
3. RPM of the impeller

4. Hub and shroud diameters at impeller inlet
5. Tip diameter at impeller exit
6. Equation of State for working fluid

This preliminary design program is directly interfaced with the aerodynamic performance analysis tool adopted from Aungier’s work [21], to dynamically modify the geometry and enhance performance. The performance analysis tool takes in the inlet thermodynamic conditions, mass flow rate, RPM and compressor geometry as the input, and outputs the exit thermodynamic conditions. The program is developed in MATLAB [10] with CoolProp [11] add-on. This performance analysis tool is validated using experimental data published by the Sandia National Labs [22]. The geometrical parameters of the impeller are provided by Wright et. al. [22] and Vilim [23]. Static pressure at the impeller exit is compared to the experimental value, presented in Table 6. Given the complexity of the model, a mean deviation of 4.7% with a peak of 7% for the static pressure at the impeller exit seems satisfactory.

Table 6: Comparison of Experimental and Analytical Performance for the S-CO₂ Impeller

ω (RPM)	T_{o1} (K)	P_{o1} (bar)	\dot{m} (kg/sec)	P_3 (exp.) (bar)	P_3 (mod.) (bar)	Error (%)
10000	305.5	76.76	0.45	76.76	77.614	1.11
20000	305.5	76.76	0.77	78.54	81.98	4.38
49000	306.3	78.54	1.82	94.25	98.13	4.12
60000	306.9	79.97	2.22	102.11	109.21	6.95
64900	307.9	82.11	2.41	108.53	116.17	7.04

The flow is solved at the inlet and exit of different sections of inducer and impeller. At each station of the compressor, the thermodynamic properties and velocity triangles are deduced, which in turn outputs the geometrical parameters of the compressor. For the present study, the calculation is performed at the inducer inlet, inducer exit or impeller inlet, impeller throat and impeller exit. Figure 7 highlights the different stations of a centrifugal compressor.

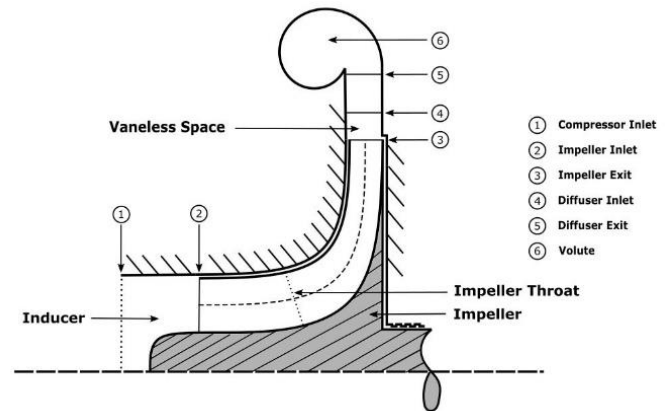


Figure 7: Highlighted Stations of a Centrifugal Compressor

Inducer Design

The primary target of the inducer design methodology is to evaluate the velocity triangle at the inlet to the inducer and set the blade metal angle equal to the relative velocity angle with the meridional direction, thereby assuming null incidence. The iterative algorithm is initialized assuming no losses. Using the inputs provided, the static properties and further, the velocity triangles are calculated at different stations. The relative flow angle at the inducer exit is set to the blade metal angle. At the throat, it is ensured that the absolute and relative mach numbers remain lower than AMC, to avoid any condensation. Using the obtained blade metal angle, the performance analysis tool for inducer calculates the total exit pressure at the inducer exit or impeller inlet. The algorithm for inducer design is highlighted in Figure 8.

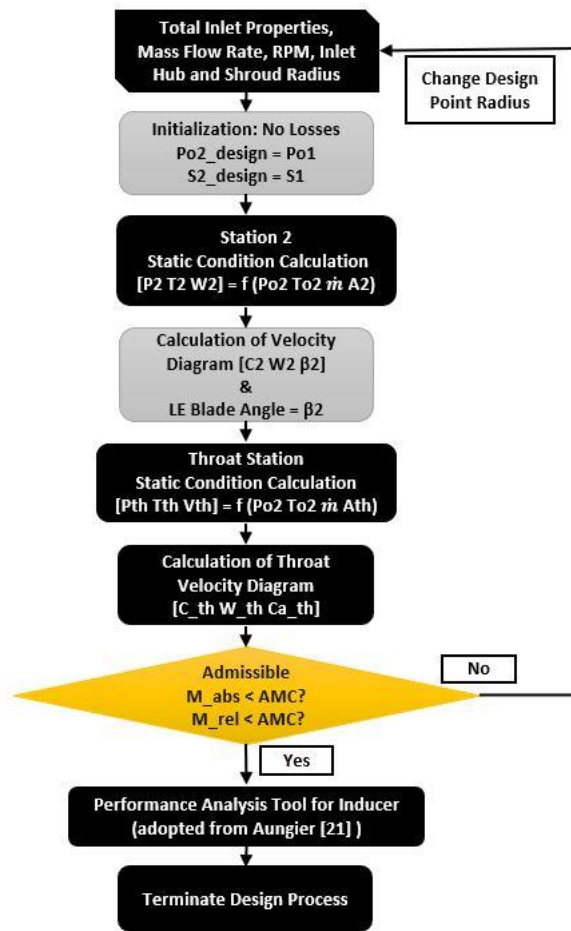


Figure 8: Algorithm for the Inducer Design

Impeller Design

The exit conditions of the inducer obtained from the inducer simulation are used to initiate the design process of the impeller. The focus of the design process for the impeller is to solve the velocity triangle at the impeller exit for which the

desired pressure ratio is achieved (P_{06}/P_{01}). Along with this, performance parameters such as the slip and distortion factor are also calculated. It is known that certain losses occur in the static components of a compressor i.e., diffuser and volute. Prior to obtaining the performance of the compressor, an estimate of these losses is to be made and incorporated in the design process. Similarly, the isentropic efficiency is guessed to initiate the design process.

Losses in the diffuser and volute, $\kappa_{diff-vol}$ are assumed to be of a constant value during the design process of impeller. Using this term, the total pressure at the exit of the impeller is calculated. For the present study, the value of $\kappa_{diff-vol}$ is assumed to be 1%. The exit pressure of the compressor, P_{06} , is calculated from the compressor inlet and exit pressure of the optimized S-CO₂ RC configuration.

$$\kappa_{diff-vol} = \frac{P_{03} - P_{06}}{P_{03}} \quad (7)$$

As a design choice, the ratio of the absolute meridional velocity at the outlet and the inlet of the impeller is kept equal to 1.375. This number is selected by varying the ratio for the impeller and observing the satisfactory values of exit total thermodynamic conditions using the design algorithm presented in the current section.

For the present study, performance parameters such as the slip factor is adopted from Weisner's correlation [24], as depicted in Equation 8. The distortion factor, λ is another performance parameter, calculated using the expression adopted from Aungier [21].

$$\sigma_{weisner} = 1 - \frac{\sqrt{\sin(\beta_3)}}{z^{0.7}} \quad (8)$$

To initialize the solution, performance parameters such as slip and distortion factors are assumed to be 1 while the losses are assumed to be zero. The Euler turbine equation is used to calculate C_{w3} at the exit of the impeller. Using the tangential velocity, the slip factor correlation is used to calculate the relative flow angle β_3 , and the velocity triangle at station 3 is subsequently solved. The blade exit angle β_3 is set equal to the relative flow angle at the impeller exit. The continuity equation is used to calculate the blade height at the impeller exit. Thus, the geometry of the impeller is completely defined. Subsequently, the performance analysis code of the impeller is executed, with the geometrical parameters calculated previously as input to the code. The performance analysis code calculates the exit static pressure and performance parameters such as slip and distortion factors which are updated in the design process and iterated to achieve convergence. Once, the solution is obtained, the isentropic efficiency of the impeller is calculated and further updated leading to an external iterative loop. Finally, the converged

value of isentropic efficiency is obtained. Algorithm of impeller design methodology is depicted in Figure 9.

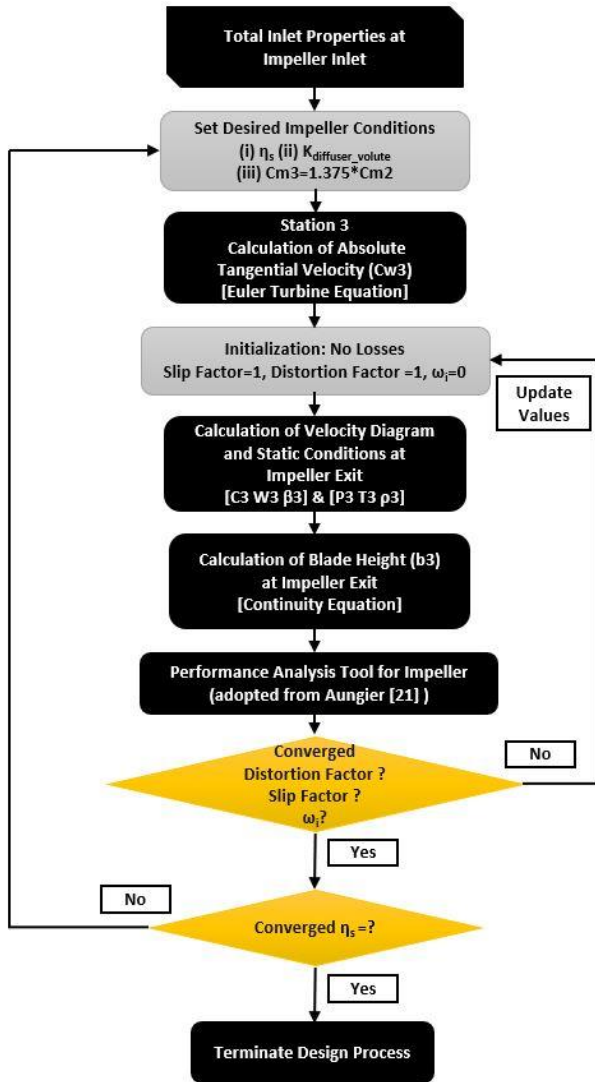


Figure 9: Algorithm for the Impeller Design

DESIGN RESULTS

The geometrical details of the S-CO₂ centrifugal compressor obtained through the inverse design methodology are presented in this section. Certain geometrical parameters are assumed based on prior design experience and are constant throughout the design process. These parameters, with their chosen values, are presented in Table 7.

The calculated geometry of the impeller is presented in Table 8. Note that some parameters are obtained by solving the inverse problem while others are calculated from empirical correlations. Using the values provided in Table 8, two Bezier curves are fitted at the hub and shroud of the impeller to define the flow path of the compressor. Figure 10 shows the schematic of the S-CO₂ impeller with the calculated geometry.

Table 7: Input Geometrical Parameters for Impeller Design

Number of Full Blades	12
Number of Splitter Blades	0
Blade Thickness at Impeller Leading Edge	1 mm
Blade Thickness at Impeller Trailing Edge	1 mm
Clearance Gap between the Shroud and Blade	0.25mm

Table 8: Calculated Geometry of the S-CO₂ Impeller

Impeller Geometry (calculated from design code)	Value
Impeller Inlet Radius at Hub	7.525 mm
Impeller Inlet Radius at Shroud	21.5 mm
Impeller Exit Tip Radius	50 mm
Blade Angle of the Impeller Leading Edge (at Mean Radius)	46.44°
Blade Angle of the Impeller Trailing Edge	-11.74° (backward)
Angle between Streamline and Shaft at Impeller Inlet	0°
Angle between Streamline and Shaft at Impeller Exit	90°
Axial Length of the Impeller	38.7 mm
Full Length of the Impeller Blade	68.0 mm
Blade Height at Impeller Inlet	13.725 mm
Blade Height at Impeller Exit	2.6 mm

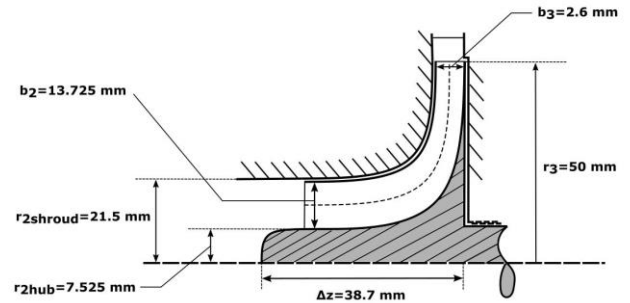


Figure 10: Calculated Geometrical Parameters of the Impeller

Solutions of the velocity triangles at different stations are depicted using velocity triangles presented in Figure 11 and 12. First, it should be noted that all the velocities are subsonic. Secondly, the negative relative angle at the impeller exit implies that the blade is backswept. The absolute velocity angle, α is also slightly on the higher side, which would result into a higher leading-edge blade angle of the diffuser.

A comparison of the desired performance of the centrifugal compressor to the resulting performance from the 1D mean-line analysis code is presented in Table 9. Error in the desired and actual value of exit total pressure is ~ 4%. Thermodynamic

parameters such as the total temperature, enthalpy and entropy have deviations less than 0.3% from the desired values. The density is quite sensitive to change in thermodynamic properties in the supercritical zone, resulting in an error of 1%. For all practical purposes, the performance of the impeller seems to be satisfactory.

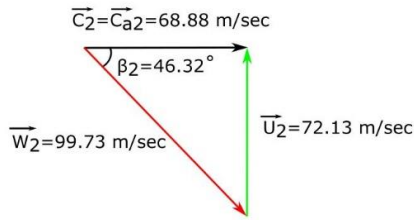


Figure 11: Velocity Triangle at Impeller Inlet

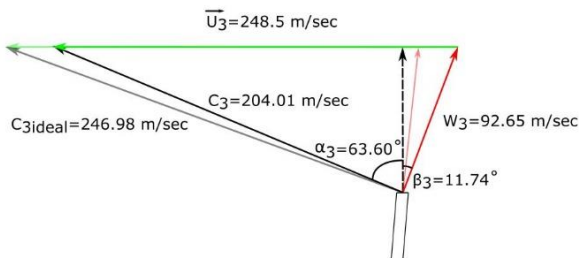


Figure 12: Velocity Triangle at Impeller Exit

Table 9: Performance Comparison of the S-CO₂ Impeller with the Optimized Cycle Parameters

Thermodynamic Properties at Impeller Exit (at mean radius)	Desired Value (From Cycle Optimization)	Calculated Value (From 1D Mean-line Analysis Code)	Deviation (%)
P _o (bar)	307.59	319.44	3.85
T _o (K)	359.16	359.93	0.22
h _o (kJ/kg)	361.86	361.81	0.01
ρ _o (kg/m ³)	736.67	728.06	1.10
S (kJ/kg-K)	1.412	1.410	0.14

For the designed S-CO₂ impeller, the converged isentropic efficiency is reported as 70.07%. This value is very close to the desired value of the compressor, which was fixed during the cycle optimization process as well as an initial guess for the compressor design. The slip factor the S-CO₂ impeller comes out to be 0.826 while the value distortion factor is reported to be 1.389.

CONCLUSIONS

This investigation focused on obtaining the geometrical parameters of a centrifugal compressor for a S-CO₂ cycle using a preliminary one-dimensional design technique. It is found that for the pre-defined heat source, S-CO₂ RC configuration

outperforms the RRC configuration. Further, using the method of genetic algorithms, the cycle is optimized and the inlet and exit thermodynamic states of the compressor are defined.

The RRC configuration tends to approach the RC configuration for low heat inputs, as observed in the present study. Along with the identification of range of pressures where the maximum power output is obtained, material constraints is an important aspect that needs to be looked at while selecting and designing components. In the current study, the higher side pressure is restricted by the current heat exchanger technology utilized for S-CO₂ cycles.

Operating close to the critical point is advantageous for the cycle as the net power input to the compressor is reduced. However, close to the critical point, it is likely that the flow accelerates into the two-phase zone. This is a major cause of instability in the code as two-phase is not handled by the currently developed code. A robust model should accommodate handling of two-phase flow during a simulation. A brief condensation analysis ensures that the throat section of the compressor which is more prone to formation of liquid remains free of any condensation.

In addition to modelling of the two-phase fluid, a complete design process includes more practices to fully develop a working compressor. First, the compressor design is completed once all sections, such as the diffuser and volute are defined. The current study focuses only on the inducer and impeller design, and therefore, design of the diffuser and volute models are to be included. Additionally, a CAD model of the compressor is to be generated and a CFD study is to be performed to analyze the performance of the compressor.

NOMENCLATURE

Roman Symbols

<i>A</i>	Annular Area
<i>a</i>	Speed of Sound
<i>b</i>	Blade Height
<i>C</i>	Absolute Velocity
<i>D_s</i>	Specific Diameter
<i>d</i>	Diameter
<i>h</i>	Specific Enthalpy
<i>K</i>	Total Loss in Diffuser and Volute
<i>M</i>	Mach Number
<i>ṁ</i>	Mass Flow Rate
<i>N_s</i>	Specific Speed
<i>P</i>	Pressure
<i>r</i>	Radius
<i>S</i>	Entropy
<i>s</i>	Fractional Pressure Drop
<i>T</i>	Temperature
<i>t</i>	Blade Thickness
<i>U</i>	Rotational Speed
<i>W</i>	Relative Velocity
<i>Ẇ</i>	Power
<i>z</i>	Number of Blades

Greek Symbol

α	Absolute Flow Angle
β	Relative Flow Angle
Δ	Change
η	Efficiency
π_c	Pressure Ratio
ρ	Density
σ	Slip Factor
τ	Shear Stress Limit
ω	Angular Velocity
$\bar{\omega}$	Total Pressure Loss Coefficient

Subscripts and Superscripts

o	Total or Stagnation State
a	Value at Actual State
m	Meridional Component
s	Value for Isentropic Process
sat	Saturated Condition
th	Throat
$turb$	Turbine
U	Tangential Component
\bar{x}	Mean Value of x
\vec{x}	Vector x

Abbreviations

LTR	Low Temperature Recuperator
HTR	High Temperature Recuperator
MTPA	Million Tons Per Annum
RC	Recuperated Cycle
RRC	Re-compressed Recuperated Cycle
S-CO₂	Supercritical Carbon dioxide
WHR	Waste Heat Recovery

REFERENCES

- [1] IEA (2019), World Energy Outlook 2019, IEA, Paris, <https://www.iea.org/reports/world-energy-outlook-2019>
- [2] Johnson, Ilona, Choate, William T., and Davidson, Amber. *Waste Heat Recovery Technology and Opportunities in U.S. Industry*. United States: N. p., 2008. Web. doi:10.2172/1218716.
- [3] Naik-Dhungel, Neeharika, 2012, "WASTE HEAT TO POWER SYSTEMS", Combined Heat and Power Partnership, U.S. Environmental Protection Agency.
- [4] Sulzer, 1948, "Verfahren zur Erzeugung von Arbeit aus Wärme," Swiss Patent: 269 599.
- [5] Feher, E. G., 1968, "The Supercritical Thermodynamic Power Cycle," *Energy Conversion*, 8(2), pp. 85–90
- [6] Angelino, G., 1968, "Carbon Dioxide Condensation Cycles," *J. Eng. Power*, Julio, pp. 287–295.
- [7] Lettieri, C., Yang, D., and Spakovszky, Z., 2015, "An Investigation of Condensation Effects in Supercritical Carbon Dioxide Compressors," *J. Eng. Gas Turbines Power*, 137(8), pp. 1–8.
- [8] Wright, S. A., Davidson, C. S., and Scammell, W. O., 2016, "Thermo-Economic Analysis of Four SCO₂ Waste Heat Recovery Power Systems," 5th Int. Symp. - Supercrit. CO₂ Power Cycles, pp. 1–16.
- [9] Khurana, S., Banerjee, R. and Gaitonde, U., 2002, "Energy balance and cogeneration for a cement plant," *Applied thermal engineering*, 22(5), pp.485-494.
- [10] MATLAB, 2010. version 9.4.0.813654 (R2018a), Natick, Massachusetts: The MathWorks Inc.
- [11] Bell, I.H., Wronski, J., Quoilin, S. and Lemort, V., 2014, "Pure and pseudo-pure fluid thermophysical property evaluation and the open-source thermophysical property library CoolProp," *Industrial & engineering chemistry research*, 53(6), pp.2498-2508.
- [12] Mohagheghi, M., and Kapat, J., 2013, "Thermodynamic Optimization of Recuperated S-CO₂ Brayton Cycles for Waste Heat Recovery Applications," 4th Int. Symp. - Supercrit. CO₂ Power Cycles, 53(9), pp. 1689–1699.
- [13] Khadse, A., Blanchette, L., Kapat, J., Vasu, S., Hossain, J., and Donazzolo, A., 2018, "Optimization of Supercritical CO₂ Brayton Cycle for Simple Cycle Gas Turbines Exhaust Heat Recovery Using Genetic Algorithm," *J. Sol. Energy Eng. Trans. ASME*, 140(7).
- [14] Mitchell, M., 1998, "An Introduction to Genetic Algorithms (Complex Adaptive Systems)," MIT Press.
- [15] Fleming, D., Holschuh, T., Conboy, T., Rochau, G., and Fuller, R., 2012, "Scaling Considerations for a Multi-Megawatt Class Supercritical CO₂ Brayton Cycle and Path Forward for Commercialization," pp. 953–960.
- [16] Balje, O. E., 1981, "Turbomachines. A Guide to Design, Selection and Theory."
- [17] Fuller, R., Preuss, J., and Noall, J., 2012, "Turbomachinery for Supercritical CO₂ Power Cycles," pp. 961–966.
- [18] Monje, B., Sánchez, D., Savill, M., Pilidis, P., and Sánchez, T., 2014, "A Design Strategy for Supercritical CO₂ Compressors," *Proc. ASME T.E.*, 3B, pp. 1–11.
- [19] Loewenthal, S. H., 1984, "Design of Power-Transmitting Shafts.," NASA Ref. Publ.
- [20] Dowson, P., Bauer, D., and Laney, S., 2008, "Selection of Materials and Material Related Processes for Centrifugal Compressors and Steam Turbines in the Oil and Petrochemical Industry," *Proc. thirty-seventh Turbomachinery Symposium*.
- [21] Aungier, R. H., 2000, "Centrifugal Compressors: A Strategy for Aerodynamic Design and Analysis," ASME Press.
- [22] Wright, S. a, Radel, R. F., Vernon, M. E., Rochau, G. E., and Pickard, P. S., 2010, "Operation and Analysis of a Supercritical CO₂ Brayton Cycle," SANDIA Rep. SAND2010-0171, (September), p. 101.
- [23] Vilim, R. B., 2010, "A One-Dimensional Compressor Model for Super-Critical Carbon Dioxide Applications," *International Congress on Advances in Nuclear Power Plants 2010, ICAPP 2010*.
- [24] Wiesner, F. J., 1967, "A Review of Slip Factors for Centrifugal Impellers," *J. Eng. Gas Turbines Power*, 89(4), pp. 558–566.

BINARY INTERACTION UNCERTAINTY IN THE OPTIMISATION OF A TRANSCRITICAL CYCLE: CONSEQUENCES ON CYCLE AND TURBINE DESIGN

Omar Aqel*

Department of Mechanical
Engineering and Aeronautics, City
University of London
London, UK

Email: Omar.Aqel@city.ac.uk

Martin White

Department of Mechanical
Engineering and Aeronautics, City
University of London
London, UK

Email: Martin.White@city.ac.uk

Abdulnaser Sayma

Department of Mechanical
Engineering and Aeronautics, City
University of London
London, UK

Email: A.Sayma@city.ac.uk

ABSTRACT

Doping CO₂ with an additional fluid to produce a CO₂-based mixture is predicted to enhance the performance of the supercritical CO₂ power cycle and lower its cost when adapted to Concentrated Solar Power plants. A consistent fluid mixture modelling process is necessary to reliably design and predict the performance of turbines operating with CO₂-based working fluids. This paper aims to quantify the significance of the choice of an Equation of State (EoS) and the uncertainty in the binary interaction parameter (k_{ij}) on the cycle and turbine design.

To evaluate the influence of the thermodynamic model, an optimisation study of a 100 MW_e simple recuperated transcritical CO₂ cycle is conducted for a combination of three mixtures, four equations of state, and three possible values of the binary interaction parameter. Corresponding multi-stage axial turbines are then designed and compared based on the optimal cycle conditions.

Results show that the choice of the dopant fraction which yields maximum cycle thermal efficiency is independent from the fluid model used. However, the predicted thermal efficiency of the mixtures is reliant on the fluid model. Absolute thermal efficiency may vary by a maximum of 1% due to the choice of the EoS, and by up to 2% due to k_{ij} uncertainty. The maximum difference in the turbine geometry due to EoS selection corresponded to a 6.3% (6.6 cm) difference in the mean diameter and a 18.8% (1.04 cm) difference in the blade height of the final stage. On the other hand, the maximum difference in turbine geometry because of k_{ij} uncertainty amounted to 6.7% (5.6 cm)

in mean diameter and 27.3% (2.73 cm) in blade height of the last stage.

INTRODUCTION

Several studies have identified the potential of supercritical carbon dioxide (sCO₂) cycles to outperform traditional steam cycles in concentrated solar power (CSP) plants [1]–[6]. However, the lack of cooling water hinders the performance of CSP plants and reduces its thermal efficiency. This is because the use of air-cooled condensers prevents condensing cycles, increases the cycle's compression work, and limits its efficiency.

Doping CO₂ with an additional fluid to produce a CO₂-based mixture could alleviate the limitations of dry cooling. It does so by increasing the critical temperature of the working fluid and expanding the operation of transcritical carbon dioxide (tCO₂) cycles, which compress the fluid in its liquid state and expand it in its supercritical state, into arid environments [7].

A variety of dopants have been considered in the past. Xia et al. [8] identified organic dopants that might improve cycle thermal efficiency. However, Invernizzi et al. [9] concluded that organic dopants, such as hydrocarbon mixtures, are not stable enough for temperatures above 400 °C, which is below the expected temperature range of CSP, and hence alternatives are needed.

Inorganic dopants with critical temperatures higher than that of CO₂, such as dinitrogen tetroxide (N₂O₄) or titanium tetrachloride (TiCl₄), were proposed by Bonalumi et al. [10] and further studied by Manzolini et al. [11]. Results showed that they may achieve cycle efficiencies of up to 50%, reduce the specific

* corresponding author(s)
Email address: Omar.Aqel@city.ac.uk

cost of the power block by 50%, and reduce the levelised cost of electricity (LCoE) by 11 to 13% with respect to a conventional steam cycle. Moreover, the power block cost may be reduced by 20% compared to pure sCO₂.

Regardless of the working fluid, the choice of the thermodynamic equation that describes the fluid's state properties (fluid model) affects cycle performance prediction and equipment sizing. Specifically, the thermodynamic properties determine the cycle thermal efficiency and equipment sizing, while the transport properties affect equipment sizing. However, transport properties are not considered in this study because they are not directly calculated by an equation of state (EoS). It is also worth noting that the choice of the fluid model does not alter the actual behavior of the fluid or the cycle, but only effects the ability to predict their behavior.

The influence of the fluid model on the estimated cycle performance and equipment sizing has been investigated in the past. Zhao et al. [12] conducted a selection procedure which compared six EoS to identify the best option for the modelling of a pure CO₂ working fluid in a recompression cycle. The six EoS compared were of three types: (1) Cubic-type, including the Peng-Robinson (PR), the Peng-Robinson combined with Boston-Mathias alpha function (PR-BM), and the Soave-Redlich-Kwong (SRK); (2) Virial-type, including the Lee-Kesler-Plöcker (LKP) and the Benedict-Webb-Rubin modified by Starling and Nishiumi (BWRS); and (3) Helmholtz-type in the form of the Span-Wagner (SW) EoS. It was concluded that the SW EoS provided the most accurate predictions of CO₂ properties in the near-critical and supercritical regions.

In the study by Zhao et al. [12], the Mean Absolute Percentage Error (MAPE) in the specific heat calculated by SW EoS was 0.5% compared to experimental data. Other EoS resulted in MAPE of about 2% in the calculated specific heat values. At most the variation in thermal efficiency was within 2% depending on the EoS. In terms of equipment sizing, they noted that a deviation of 10% in recuperator size (specified by the product of the overall heat transfer coefficient U and heat exchange area A) and compressor diameter is possible depending on the choice of EoS. The variation in the compressor size was attributed to its operation near the critical point where evaluation of the specific heat capacity becomes less precise. Conversely, the influence on turbine diameter was found to be more limited (from 0.2% to 3.0%), which is expected since equations of state converge to the ideal gas law at high temperatures above the critical dense-gas region.

The study of mixtures adds another uncertainty in thermodynamic property predictions because of the use of the Binary Interaction Parameter (k_{ij}), which is a correction factor applied to an EoS to account for intermolecular interactions between mixture components. A value for k_{ij} may be obtained by regressions based on experimental Vapor-Liquid Equilibrium

(VLE) data, where k_{ij} is calibrated to fit the EoS predictions with empirical results. It is also possible to predict the value of k_{ij} using models such as the predictive-Peng Robinson or the Enhanced-Predictive-Peng-Robinson-78 equation of state [13]. However, predictive models will not be used in this study since experimental data is available for all the mixtures involved.

Di Marcoberardino et al. [14] compared the cycle performance of a CO₂/C₆F₆ mixture using five different EoS. The choice of EoS resulted in an inconsistent cycle thermal efficiency which ranged from 40.5% to 42.5%. They also noted that the choice of the EoS slightly effects the identification of the optimal dopant molar fraction. In the same study, they varied k_{ij} by +/-50% and found that it had a limited effect on the cycle efficiency (+/-0.2%). However, they did not study the effect of k_{ij} on equipment sizing, nor did they investigate its influence in other mixtures.

Previous studies have indicated that thermodynamic property prediction is most consistent near the turbine operating conditions [12], [14]. Therefore, it follows that the turbine should be the component least affected by the fluid model. However, it has not yet been shown to what extent any small variation will impact the final turbine geometry or performance predictions. Answering this question will help with future design efforts by guiding the most suitable choice for the EoS to be used during the mean-line design and numerical computational-fluid dynamic simulation of the turbine, which is a critical component of the cycle.

The aim of the current work is to investigate the sensitivity of key cycle and turbine design parameters to the choice of EoS and k_{ij} uncertainty within a simple recuperated transcritical cycle layout using CO₂-based mixtures as working fluids. Ultimately, the aim is to quantify the effect of EoS and k_{ij} on turbine design. A large scale 100 MWe CSP power plant is considered as a test case because it is the target scale of the SCARABEUS project [15].

METHODOLOGY

Working fluid modelling

This work is part of a research effort that aims to explore the use of CO₂-based working fluids in CSP plants. Therefore, the choice of dopants is focused on those that increase the critical temperature of CO₂ to enable the operation of transcritical cycles in CSP plants. Although the list of chemical compounds is virtually endless, the choice of dopant can be focused by a set of desirable dopant properties: (1) critical temperature above 70 °C; (2) thermal stability above 700 °C; and (3) solubility in CO₂ in all cycle conditions. The minimum critical temperature is set to ensure compression occurs far enough from the critical point that the liquid's properties are not drastically affected by small changes in temperature. A critical temperature of 70 °C is a safe

distance away from the design pump inlet temperature of 52 °C that liquid compression is ensured.

Based on the above criteria, the chosen dopants are: H₂S, C₆F₆, and an unnamed Non-Organic Dopant (NOD). The latter dopant will not be named as it remains confidential within the project consortium. The former two of these dopants have been considered for CO₂ power cycles in previous publications [14], [17]. The main dopant thermophysical parameters of interest are shown in Table 1.

Table 1. Select properties of CO₂ and dopants

Compound	Molecular Weight (g/mol)	Critical Temperature (K)	Critical Pressure (MPa)
CO ₂	44.01	31.0	7.382
H ₂ S	34.08	100.4	8.963
C ₆ F ₆	186.1	242.8	3.273
NOD	>60	<125	<7.000

To calculate the thermophysical properties of the working fluids the thermodynamic models available within Simulis Thermodynamics were used [18]. Validation details were described in the authors' earlier work [19].

The four candidate EoS that were selected for the study are shown in Table 2. The EoS were chosen as to cover three different types: Cubic, Virial, and SAFT. Among these, the cubic types are the most popular owing to their accuracy in the estimation of VLE properties for most fluids. They also require little computational overhead because of their simplicity. However, the accuracy of cubic EoS are limited with highly polar compounds. Although they have the ability to describe mixtures accurately, the application of virial type EoS is limited to low and moderate density fluids. SAFT equations of state are known to produce accurate property estimations away from the critical point and are suitable for systems in which the strength of association varies from weak hydrogen bonds to strong covalent bonds. However, their accuracy comes at a high computational cost.

Table 2. Equations of State used to model the mixtures.

Equation of State	Type	Reference
Peng-Robinson (PR)	Cubic	[20]
Benedict-Webb-Rubbin modified Starling-Nishiumi (BWRS)	Virial	[21]
Soave-Redlich-Kwong (SRK)	Cubic	[22]
Perturbed Chain Statistical Associating Fluid Theory (PC-SAFT)	SAFT	[23]

The cubic EoS requires the definition of the following fluid-specific parameters: acentric factor, critical temperature, and critical pressure. In addition to the parameters required to solve a cubic EoS, the PC-SAFT model requires the following parameters for each pure component of the mixture: (i) the characteristic segment number m , (ii) the characteristic segment size parameter σ , and (iii) the characteristic segment energy parameter ε/k . These parameters are listed in Table 3.

Table 3. SAFT parameters for the pure components

Dopant	m	σ (Å)	ε/k (K)	Reference
CO ₂	1.8464	2.98388	140.00	Simulis preset
NOD	>2	>2	>200	Undisclosed
H ₂ S	1.6686	3.0349	229	[24]
C ₆ F ₆	3.779	3.396	221.65	[14]

Along with the EoS, a k_{ij} value must be specified for each mixture. In this study, k_{ij} was calculated against regressed Vapor-Liquid Equilibrium (VLE) experimental data and used to tune the mixing models for each mixture and EoS pair. Determining the value of k_{ij} required an optimisation problem. By tuning k_{ij} , the calculated VLE lines were manipulated and compared with experimental data to find the best-fit k_{ij} value. An unconstrained gradient-based optimisation approach was used. The weighted least mean square method was used as the objective function. Like the simple least square method, it minimises the residuals between experimental and calculated data, but it also weighs each residual with the experimental uncertainty of the experimental data. The objective function is reduced or expanded depending on the availability of experimental data. The objective function for the optimisation is defined as:

$$f(k_{ij}) = \frac{1}{n_e} \sum_{i=1}^{n_e} \left[\left(\frac{\hat{x}_{1,i} - \tilde{x}_{1,i}}{u_{x_{1,i}}^e} \right) + \left(\frac{\hat{y}_{1,i} - \tilde{y}_{1,i}}{u_{y_{1,i}}^e} \right) + \left(\frac{\hat{T}_i - \tilde{T}_i}{u_{T_i}^e} \right) + \left(\frac{\hat{P}_i - \tilde{P}_i}{u_{P_i}^e} \right) \right] \quad \text{Eq. 1}$$

Where T is the temperature, P is the pressure, and x and y are the liquid and vapour molar fractions of CO₂, respectively. The accents (^) and (~) indicate the measured and calculated values, respectively. Experimental uncertainty is represented by the term u^e . The number of experiments is denoted by n_e .

The Mean Absolute Percentage Error (MAPE) is a measure of the accuracy of the thermodynamic model. The lower it is, the more accurate is the model. The MAPE is calculated as follows:

$$MAPE = \frac{100\%}{n_e} \sum_{i=1}^{n_e} \left| \frac{\tilde{U}_i - \hat{U}_i}{\tilde{U}_i} \right| \quad \text{Eq. 2}$$

where U corresponds to either the temperature or pressure. The MAPE may be used to compare the accuracy of the models to determine their suitability. Based on the MAPE values presented in Table 4, the two cubic equations of state (PR and SRK) are more suitable than the virial equation of state (BWRS) for all mixtures.

Table 4. Binary interaction coefficient and its associated MAPE for each CO₂-based mixture and EoS combination

	Binary Interaction Parameter (k_{ij})			
	PR	BWRS	SRK	PC-SAFT
NOD	0.0214	0.0182	0.0249	-0.0939
C ₆ F ₆	0.0332	0.0626	0.0394	-0.0571
H ₂ S	0.0871	0.0453	0.0871	-0.0393
Mean Absolute Percentage Error (MAPE %)				
	PR	BWRS	SRK	PC-SAFT
NOD	2.089	1.938	2.068	4.722
C ₆ F ₆	2.619	5.028	2.374	2.227
H ₂ S	0.3862	0.4901	0.4025	0.275
No. of exp. pts		Source of data		
NOD	48	Undisclosed		
C ₆ F ₆	64	[25]		
H ₂ S	122	[26]		

The increase in k_{ij} fidelity with the availability of experimental data is noticeable from Table 4. Among the three mixtures, the experimental data for CO₂/H₂S is the most abundant, thus it has the lowest MAPE in property estimation.

Since the uncertainty in k_{ij} depends on the available VLE data, each mixture has a different range of uncertainty. However, to properly compare the influence of k_{ij} uncertainty in each mixture, a uniform uncertainty of $\pm 50\%$ is applied to all k_{ij} estimates. This negates the effect of VLE data availability when comparing mixtures, which can always be collected through experiments to narrow the uncertainty margins and improve model fidelity.

Thermodynamic cycle model

A simple recuperated tCO₂ cycle is suitable for the purposes of this study because it is a viable option for CSP applications with

CO₂-based mixtures. A schematic of the tCO₂ cycle and its Temperature–Entropy diagram are shown in Figure 1.

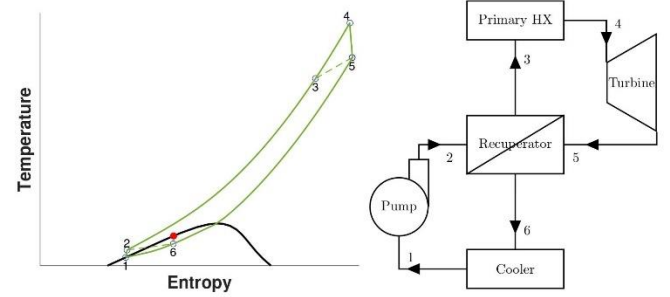


Figure 1. Temperature-Entropy diagram and cycle layout of a simple recuperated tCO₂ cycle operating with a CO₂/C₆F₆ mixture.

The cycle is modelled by applying the first law of thermodynamics to all equipment. Cycle thermal efficiency is expressed as the ratio of the net work produced to the heat consumed by the cycle in Eq.3:

$$\eta_o = \frac{W_n}{q_H} \quad \text{Eq. 3}$$

The losses within the pump and turbine are approximated by assuming isentropic efficiencies for each component, as expressed by Eq.4 and Eq.5:

$$\eta_p = \frac{h_2 - h_1}{h_2 - h_{1s}} \quad \text{Eq. 4}$$

$$\eta_t = \frac{h_4 - h_5}{h_4 - h_{5s}} \quad \text{Eq. 5}$$

where the subscript ‘s’ denotes the outlet conditions assuming isentropic compression and expansion.

The recuperator effectiveness determines the ratio of the actual heat load to the maximum attainable heat load from the stream with the lowest heat-capacity rate, as expressed in Eq.13:

$$\epsilon = \frac{h_5 - h_6}{\min[(h_{T5,P3} - h_{T2,P2}), (h_{T5,P5} - h_{T2,P6})]} \quad \text{Eq. 6}$$

The cycle state points are determined by setting the pump inlet temperature (T_1), the turbine inlet temperature (T_4), pressure ratio, component efficiencies, and pressure drops. Within this study, T_1 and T_4 will be set according to the values expected in state-of-the-art dry-cooled CSP plants.

Turbine model

For a large 100 MW turbine, a multi-stage axial architecture is recommended [27]. A 1-D mean line turbine design approach was used to model the turbine. The main parameters used to inform turbine design are shown in Eq. 7 to Eq. 9. The blade-loading coefficient (ψ), turbine flow coefficient (ϕ), and degree of reaction (Λ) control the blade speed, fluid axial velocity, and the expansion in the stator and rotor:

$$\psi = \frac{\Delta h_{oi}}{U_i^2} \quad \text{Eq. 7}$$

$$\phi = \frac{C_{ai}}{U_i} \quad \text{Eq. 8}$$

$$\Lambda = \frac{\Delta h_{ri}}{\Delta h_{oi}} \quad \text{Eq. 9}$$

where Δh_{oi} is the total enthalpy drop across the stage, U_i is the blade speed of the rotor at the mean radius, C_{ai} is the axial flow velocity at the rotor outlet of the stage, and Δh_{ri} is the enthalpy drop across the rotor. Further details on this design approach are reported in Salah et al. [28]. The number of stages is based on preliminary stress calculations of a previous publication [19].

The specific speed in Eq. 10 is a ratio used to indicate a turbine's size and shape [29].

$$N_s = \frac{N\dot{V}_5^{\frac{1}{2}}}{\Delta h_{oi}^{\frac{3}{4}}} \quad \text{Eq. 10}$$

where N_s and N are the specific speed and nominal speed, respectively. The volume flow rate out of the turbine is represented by \dot{V}_5 (in m^3/s).

Optimisation program

A MATLAB program was developed to study the effect of the EoS and k_{ij} on optimal cycle and turbine design. The flowchart in Fig A.1 illustrates the calculation processes for a single CO_2 mixture. The flowchart shows four layers, three of which are parametric studies which change the EoS, k_{ij} , and dopant molar fraction. The inner most layer identifies the optimal cycle condition for the given EoS, k_{ij} , and dopant molar fraction combination. Once optimum cycle conditions are found, the program then produces a turbine geometry using the turbine boundary conditions resulting from the optimal cycle.

Cycle conditions are chosen to simulate those of a CSP plant with dry cooling. Assuming an ambient dry-bulb temperature of 40°C and a minimum temperature difference of 10°C in the condenser, the pump inlet temperature (T_1) is fixed to 50°C . Liquid flow into the pump is assumed to be subcooled by 2°C below the saturation pressure. Therefore, the pump inlet pressure (P_1) is set equal to the saturation pressure at 52°C . The turbine inlet

temperature (T_4) is fixed to 700°C , which is the targeted temperature of advanced CSP receiver employing sodium salt as its Heat Transfer Medium (HTM). Finally, the turbine inlet pressure (P_4) is limited to 25 MPa as recommended by Dostal et al. [30]. The turbine design parameters were set based on authors experience. Both the cycle and turbine design inputs are shown in Table 5 and Table 6, respectively.

Table 5. Inputs required for cycle solution

Fixed Parameters			
Parameter		Range	Unit
Dopant Molar Fraction	X_f	Max(65)	%
Turbine inlet temperature	T_4	700	$^\circ\text{C}$
Pump inlet temperature	T_1	50	$^\circ\text{C}$
Pump efficiency	η_p	85	%
Turbine efficiency	η_t	90	%
Generator efficiency	η_G	99	%
Net electrical power	\dot{W}_n	100	MW
Pressure drop primary heat exchanger	$\Delta p/p$	0.015	-
Pressure drop in recuperator high and low-pressure sides	$\Delta p/p$	0.01 and 0.015	-
Pressure drop in condenser	$\Delta p/p$	0.02	-
Dependant Parameters			
Pump inlet pressure	P_1	$P_{sat@T_1+2}$	MPa
Turbine inlet pressure	P_4	Max (25)	MPa
Optimised Parameters			
Pressure Ratio (PR)	r	2 – 4	-
Recuperator Effectiveness	ϵ	70 – 98	%

Table 6. Inputs required for turbine design

Parameter		Value	Unit
Rotational speed		3000	RPM
Number of stages		4	-
Turbine efficiency	η_t	90	%
Loading coefficient	ψ	1.65	-
Flow coefficient	ϕ	0.23	-
Degree of reaction	Λ	0.5	-

RESULTS AND DISCUSSION

Attention is first given to the choice of the optimal dopant molar fraction. This is important because it defines all subsequent fluid properties. In essence, a variation in the dopant molar fraction of

a mixture produces different fluids. As seen in Figure 2, the thermal efficiency of the cycle is affected by the dopant molar fraction, the EoS, and the value of k_{ij} , but this effect differs depending on the mixture. Generally, thermal efficiency fluctuates around $\pm 0.1\%$ to $\pm 0.3\%$ of the baseline value for both variations in the EoS and k_{ij} . The largest variation due to k_{ij} is 0.7% and it is observed in BWRS when used with $\text{CO}_2/\text{C}_6\text{F}_6$. Among the four EoS, the two cubic EoS, PR and SRK, are the least sensitive to variations in k_{ij} . This is confirmed by the averaged MAPE values shown in the Figure 2 for each combination. The MAPE was calculated by comparing the results obtained with k_{ij} variations against the baseline of no variation in k_{ij} .

Moreover, the cycle thermal efficiency for all mixtures and EoS shows a positive correlation with k_{ij} , where higher values of k_{ij} produce cycles of higher thermal efficiencies. Also common among mixtures is that the thermal efficiency exhibits the same trend with dopant fraction regardless of the EoS or k_{ij} , which suggests that the dopant fraction that yields the highest thermal efficiency is independent of the fluid model used. This is further confirmed through Figure 3, which shows that neither EoS nor k_{ij} affect the choice of the optimal dopant fraction. Furthermore, during the optimisation it was found that all optimal cycles lead to the maximum permissible pressure at turbine inlet (i.e., 25 MPa).

Taking a closer look at the thermal efficiency for the same optimal dopant fractions reveals some differences in the prediction of cycle performance. Figure 4 shows the maximum percentage difference resulting from the choice of the EoS and the variation in k_{ij} . The maximum percentage difference

between the EoS was calculated based on the difference between the EoS that yields the lowest efficiency and the EoS that yields the highest. The maximum percentage difference resulting from k_{ij} variation was calculated by comparing the efficiency change due to k_{ij} variation with the baseline case of no variation in k_{ij} .

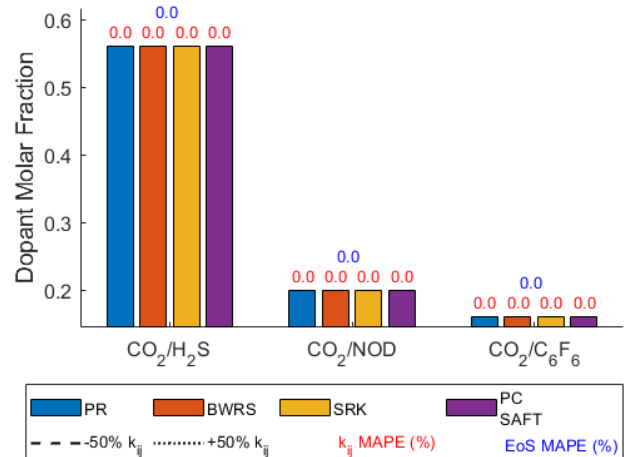


Figure 3. Effect of choice of EoS and variation in k_{ij} on the optimal dopant molar fraction.

As observed from Figure 4, different mixtures respond differently to the EoS. Cycles operating with $\text{CO}_2/\text{C}_6\text{F}_6$ are affected the most, with a maximum percentage change of 2.3%, which equates to a 1% nominal change in efficiency between SRK and PC-SAFT. The other two dopants are affected half as

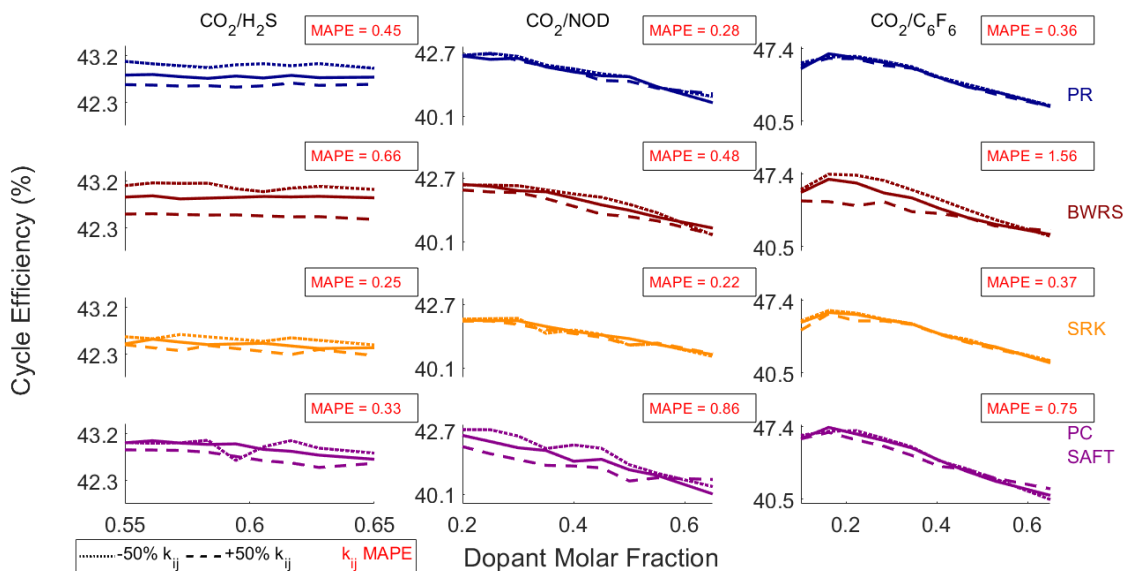


Figure 2. The effect of dopant molar fraction on cycle thermal efficiency depending on the choice of EoS and the variation in k_{ij} .

much. Overall, the effect of k_{ij} variation is less pronounced, except when modelling a $\text{CO}_2/\text{C}_6\text{F}_6$ mixture using the BWRS EoS where a decrease in the value of k_{ij} results in cycle efficiency estimates lower by more than 2% nominal efficiency (i.e. 44.77% compared to 46.90%).

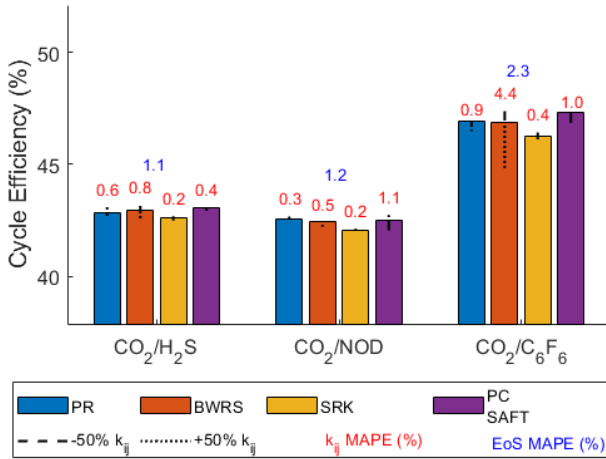


Figure 4. Effect of choice of EoS and variation in k_{ij} on cycle thermal efficiency.

Before investigating the effect on turbine design, the change in pump design will be addressed. Because of real-gas effects any deviation in the EoS leads to a larger variation in properties near the saturation region. This variation is apparent in the design point parameters of the pump, indicated by the differential head and volume flow rate. As observed in Figure 5, both head and flow rate change with EoS and k_{ij} . For all cases, the change in flow rate is greater than the change in head. In the most extreme

case, the SRK predicts almost twice the flow rate for $\text{CO}_2/\text{H}_2\text{S}$ and $\text{CO}_2/\text{C}_6\text{F}_6$ than the PC-SAFT does. Consequently, half as many pumps may be predicted to be required if the PC-SAFT EoS is used to model the cycle. The change in head and flow rate is also significant due to k_{ij} variation. The maximum change in flow rate and pump head is 34.2% and 14.7%, respectively, if the BWRS is used to model $\text{CO}_2/\text{C}_6\text{F}_6$. These findings agree with previous studies which identified the significant influence of the fluid model on the pump in particular.

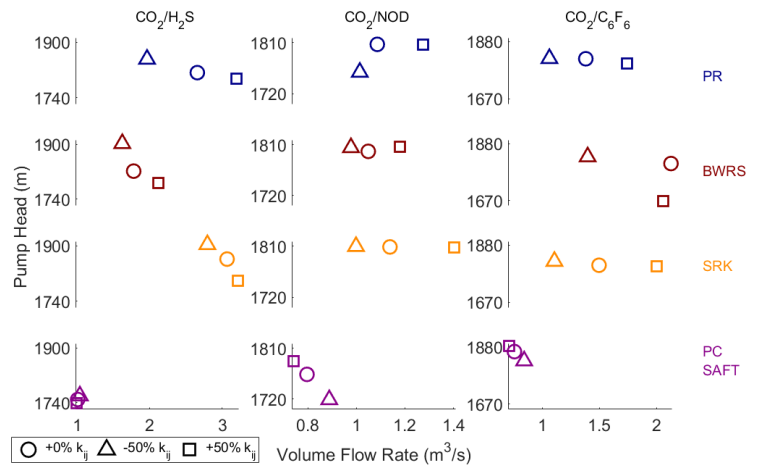


Figure 5. Effect of choice of EoS and variation in k_{ij} on the pump specific speed.

As seen in the following figures, the fluid properties at turbine inlet are less affected by the change in the fluid model than the properties at pump inlet. This is partly because of the aforementioned real gas effects at pump inlet, but also because

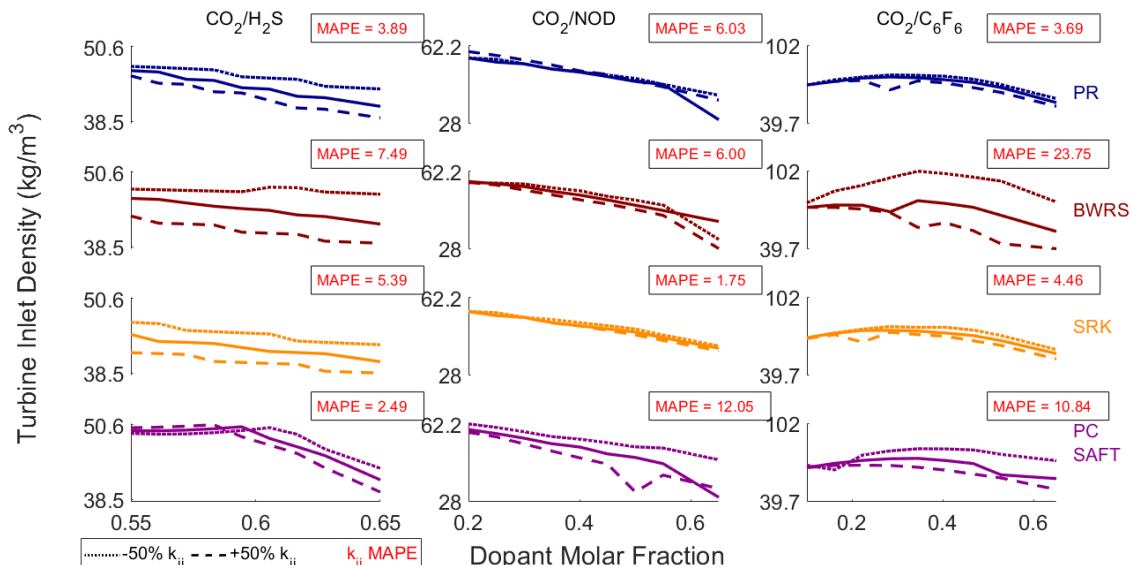


Figure 6 The effect of dopant molar fraction on the fluid's density at turbine inlet depending on the choice of EoS and the variation in k_{ij} .

the turbine inlet conditions are identical for all cases (700 °C and 25 MPa), while the pump inlet pressure varies depending on the EoS and k_{ij} . However, there is an observable variation in turbine inlet density, as shown in Figure 6. The maximum MAPE between the baseline models of the EoS are 8.3%, 2.4%, and 4.5% for H₂S, NOD, and C₆F₆ mixtures, respectively. Therefore, the turbine inlet density of cycles operating with CO₂/NOD is generally less sensitive than those operating with the other two. Moreover, The variation in density for the optimal blend fraction, described in Figure 7, is less severe than the general trend shown in Figure 6, yet the MAPE is still the highest for CO₂/C₆F₆.

Similar to the trend observed in pump design variation, the two cubic EoS exhibit the lowest sensitivity to k_{ij} variation even away from the critical point. This consistency suggests that cubic EoS are more robust and may be a good option in the absence of quality experimental data from which k_{ij} can be calibrated. Among the four EoS, the BWRS is the most sensitive to k_{ij} variation, therefore precise k_{ij} values are recommended when employing the BWRS EoS.

The density of the fluid directly affects the expansion work of the turbine. Therefore, its variation is reflected in the variation in the turbine specific work. As seen in Figure 8 and Figure 9, the trend in specific work variation is similar to that in density, but in the opposite direction. Turbine loading, mechanical stresses, and number of stages are partly determined by the specific work, since the specific work is related to blade speed through the loading coefficient and the blade speed is constrained based on mechanical design constraints. A difference of 13.7% in density like that observed between SRK and PC-SAFT for CO₂/H₂S could produce slightly different turbine designs, as seen later.

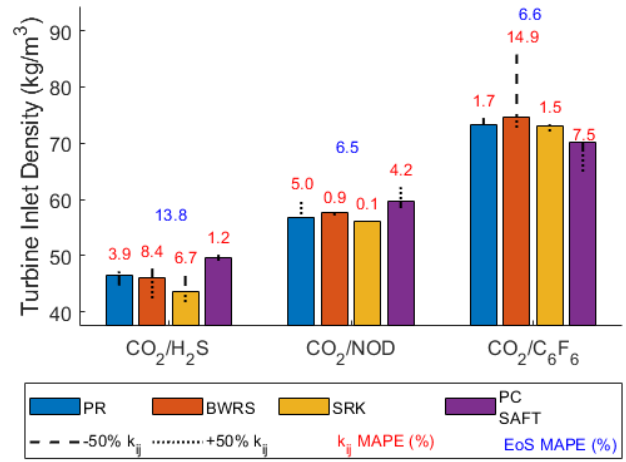


Figure 7 Effect of choice of EoS and variation in k_{ij} on the density of the fluid at turbine inlet.

The implications of density dissimilarity and the subsequent dissimilarity in turbine specific work are reflected in the specific speed of the turbine, shown in Figure 10. The specific speed was calculated for the entire turbine (across the four stages) by substituting the total enthalpy drop across the turbine in Eq.10. Although the percentage change is considerable for some cases, such as 21% for BWRS with CO₂/C₆F₆, the nominal change in specific speed is miniscule; no larger than 0.3 rad/s for the same case. This indicates that the resulting turbine designs will be comparable in shape and size for all EoS and k_{ij} values.

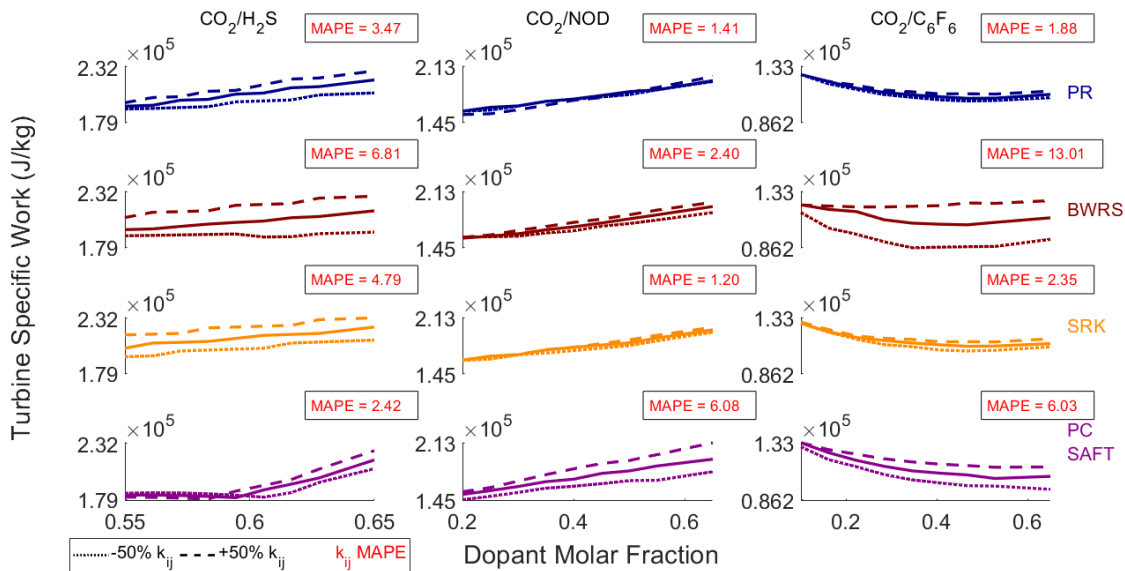


Figure 8 The effect of dopant molar fraction on the turbine specific work depending on the choice of EoS and the variation in k_{ij} .

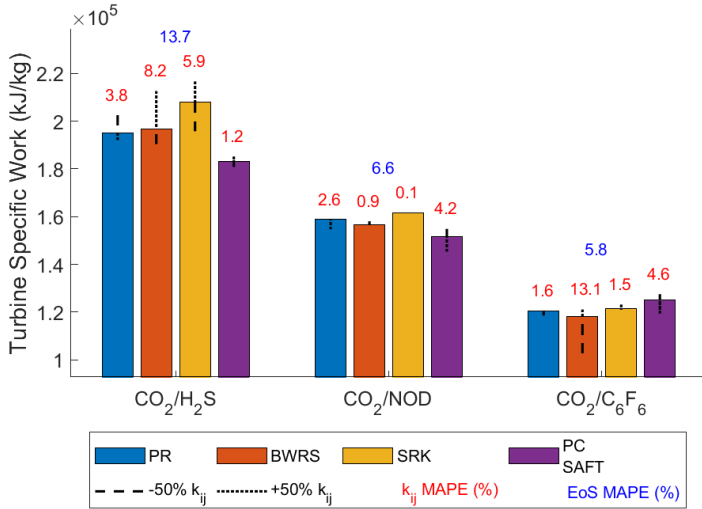


Figure 9 Effect of choice of EoS and variation in k_{ij} on the turbine specific work

The changes in turbine design parameters culminate in the resulting turbine geometry represented by its mean diameter and blade height. The turbine mean diameter is measured at the meridional profile midspan of the turbine blades and is assumed to be constant across all turbine stages. The meridional blade profile of the turbine geometry corresponding to the optimal dopant fraction for each mixture, EoS, and k_{ij} variation combinations are presented in Figure 11. Consistent with the trends observed in the previous figures, the effect of EoS is more pronounced in CO₂/H₂S mixtures. The largest difference is between SRK and PC-SAFT, which amounts to 6.3% (6.6 cm) difference in the mean diameter and a 18.8% (1.04 cm)

difference in the blade height at the final stage. The EoS effects the other two mixtures half as much.

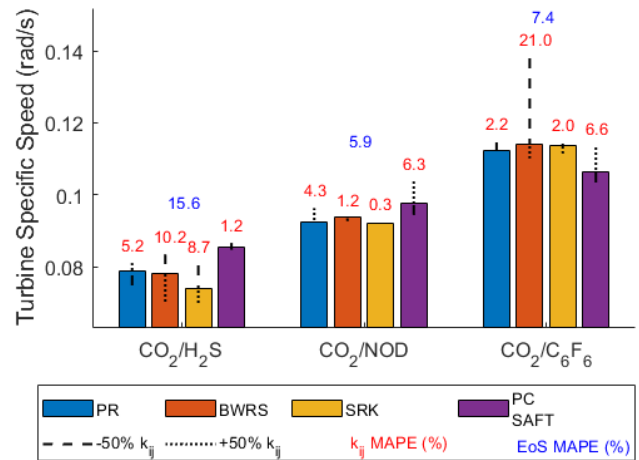


Figure 10 Effect of choice of EoS and variation in k_{ij} on the turbine specific speed

The effect of k_{ij} variation on turbine geometry is smaller than that of the EoS, except in the case of BWRS with CO₂/C₆F₆ which yields a difference of 6.7% (5.6 cm) in mean diameter and 27.3% (2.73 cm) in blade height of the last stage when k_{ij} is set to 0.5 of its baseline values. The mixture and EoS combinations that are practically insensitive to k_{ij} variations are: CO₂/H₂S with PC-SAFT, CO₂/NOD with BWRS or SRK, and CO₂/C₆F₆ with PR or SRK. Moreover, the PR EoS with CO₂/H₂S or CO₂/NOD mixtures or PC-SAFT with CO₂/C₆F₆ are also

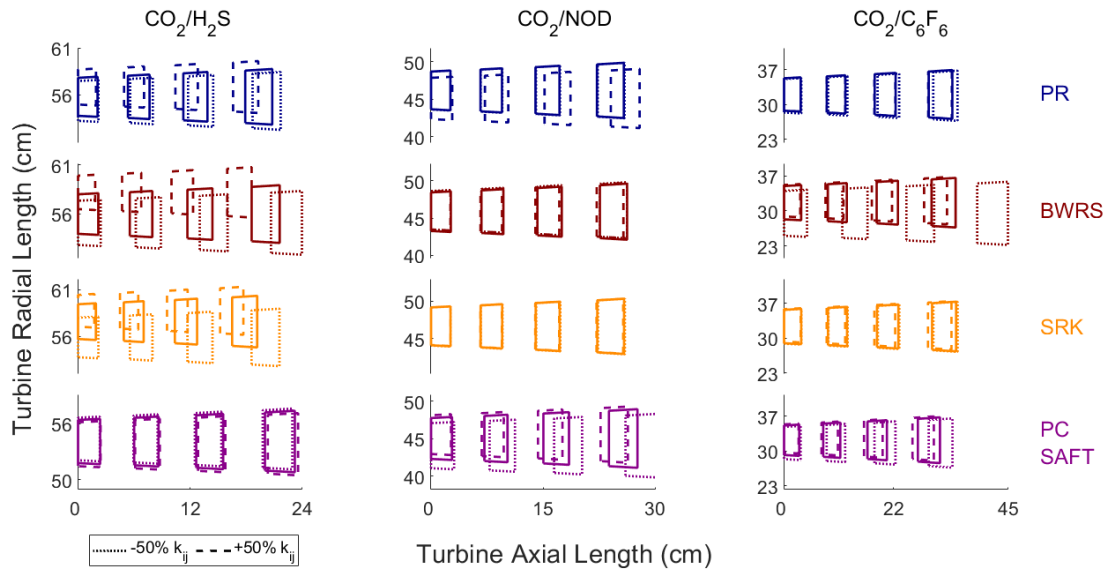


Figure 11 The meridional flow path for the four-stage turbine corresponding to the optimal dopant fractions.

relatively insensitive to k_{ij} variations as they exhibit only small variations. Even though the turbine geometry is affected by fluid model variations, that effect does not change the turbine design fundamentally as seen in Figure 11. The same was revealed through the small change in turbine specific speed.

The Mach number of a fluid is important to determine whether subsonic or supersonic flow is present. By assuming similar velocities for all cases, the Mach number may be compared by comparing the speed of sound at turbine inlet. As shown in Figure 12, the speed of sound remains fairly constant regardless of the fluid model. The MAPE due to k_{ij} variation for all EoS and mixture combinations were less than 0.2%. Moreover, the MAPE due to EoS selection is 2.0% at its highest for CO₂/C₆F₆. Overall, it seems that Mach number prediction will unlikely to be affected by the fluid model.

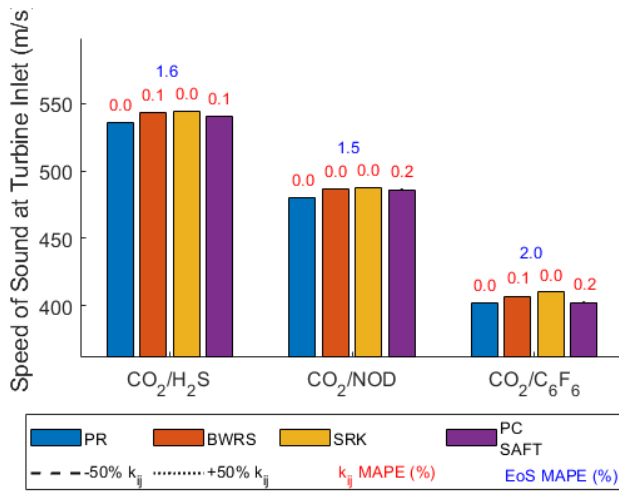


Figure 12 Effect of choice of EoS and variation in k_{ij} on the speed of sound at turbine inlet.

CONCLUSION

In this paper, the sensitivity of cycle and turbine design to the fluid property model was investigated. The study included three CO₂-based mixtures (CO₂/H₂S, CO₂/NOD, and CO₂/C₆F₆) in combination with four equations of state (PR, BWRS, SRK, and PC-SAFT), each modelled under scenarios of k_{ij} uncertainty ($\pm 50\%$).

It was found that the choice of the dopant fraction which yields maximum cycle thermal efficiency for each mixture is independent from the fluid model used. However, the predicted optimal thermal efficiency of the mixtures is reliant on the fluid model. Absolute thermal efficiency may vary by a maximum of 1% due to the choice of the EoS when modelling CO₂/C₆F₆, and by up to 2% due to k_{ij} uncertainty when the BWRS EoS is used to model CO₂/C₆F₆. Moreover, cycle thermal efficiency was

observed to have a positive correlation with the k_{ij} value for all mixture and EoS combinations.

In terms of turbine design, among the three mixtures, CO₂/NOD is the least sensitive to the fluid model, while the other two are nearly equally sensitive. Furthermore, the two cubic equations of state, PR and SRK, are generally less sensitive to k_{ij} variation the other two EoS, except for the case of CO₂/H₂S. This suggests that they offer more robust property prediction in the absence of quality experimental data. On the other hand, the BWRS EoS is especially sensitive to k_{ij} uncertainty, thus requires precise model calibration before it can be used reliably. Lastly, the maximum difference in the turbine geometry due to the choice of the EoS amounted to 6.3% (6.6 cm) difference in the mean diameter and a 18.8% (1.04 cm) difference in the blade height at the final stage. On the other hand, the maximum difference in turbine geometry as a result of k_{ij} uncertainty amounted to 6.7% (5.6 cm) in mean diameter and 27.3% (2.73 cm) in blade height of the last stage.

NOMENCLATURE

Acronyms	
BWRS	Benedict-Webb-Rubin-Starling
CSP	Concentrated Solar Power
EoS	Equation of State
HTM	Heat Transfer Medium
MAPE	Mean Absolute Percentage Error
MITA	Minimum Internal Temperature Approach
PC-SAFT	Perturbed Chain Statistical Associating Fluid Theory
PR	Peng-Robinson
sCO ₂	Supercritical Carbon Dioxide
SRK	Soave-Redlich-Kwong
tCO ₂	Transcritical Carbon Dioxide
VLE	Vapor-Liquid Equilibrium
Symbols	
η	Efficiency
ϵ	Effectiveness
k_{ij}	Binary interaction coefficient
ψ	Loading coefficient
ϕ	Flow coefficient
Λ	Degree of reaction
h	Specific enthalpy, J/kg
ρ	Density, kg/m^3
H	Head, m
N	Rotational speed, RPM
P	Pressure, MPa
r	Pressure ratio

T	Temperature, °C
-----	-----------------

ACKNOWLEDGEMENTS

This project has received funding from the European Union's Horizon 2020 research and innovation programme under grant agreement No. 814985.

REFERENCES

- [1] S. Polimeni, M. Binotti, L. Moretti, and G. Manzolini, "Comparison of sodium and KCl-MgCl₂ as heat transfer fluids in CSP solar tower with sCO₂ power cycles," *Sol. Energy*, vol. 162, pp. 510–524, Mar. 2018.
- [2] K. Wang, Y. L. He, and H. H. Zhu, "Integration between supercritical CO₂ Brayton cycles and molten salt solar power towers: A review and a comprehensive comparison of different cycle layouts," *Appl. Energy*, vol. 195, pp. 819–836, 2017.
- [3] T. Neises and C. Turchi, "A comparison of supercritical carbon dioxide power cycle configurations with an emphasis on CSP applications," in *Energy Procedia*, 2014, vol. 49, pp. 1187–1196.
- [4] M. Atif and F. A. Al-Sulaiman, "Energy and exergy analyses of solar tower power plant driven supercritical carbon dioxide recompression cycles for six different locations," *Renewable and Sustainable Energy Reviews*, vol. 68. Elsevier Ltd, pp. 153–167, 01-Feb-2017.
- [5] M. Cerio Vera, "S-CO₂ for efficient power generation with energy storage," 2015.
- [6] J. D. Osorio, R. Hovsopian, and J. C. Ordonez, "Effect of multi-tank thermal energy storage, recuperator effectiveness, and solar receiver conductance on the performance of a concentrated solar supercritical CO₂-based power plant operating under different seasonal conditions," *Energy*, vol. 115, pp. 353–368, Nov. 2016.
- [7] T. G. Lewis, T. M. Conboy, and S. A. Wright, "Supercritical CO₂ Mixture Behavior for Advanced Power Cycles and Applications," 2011.
- [8] J. Xia, J. Wang, G. Zhang, J. Lou, P. Zhao, and Y. Dai, "Thermo-economic analysis and comparative study of transcritical power cycles using CO₂-based mixtures as working fluids," *Appl. Therm. Eng.*, vol. 144, pp. 31–44, Nov. 2018.
- [9] C. M. Invernizzi and T. Van Der Stelt, "Supercritical and real gas Brayton cycles operating with mixtures of carbon dioxide and hydrocarbons," *Proc. Inst. Mech. Eng. Part A J. Power Energy*, vol. 226, no. 5, pp. 682–693, Aug. 2012.
- [10] D. Bonalumi, S. Lasala, and E. Macchi, "CO₂-TiCl₄ working fluid for high-temperature heat source power cycles and solar application," *Renew. Energy*, 2018.
- [11] G. Manzolini, M. Binotti, D. Bonalumi, C. Invernizzi, and P. Iora, "CO₂ mixtures as innovative working fluid in power cycles applied to solar plants. Techno-economic assessment," *Sol. Energy*, vol. 181, no. June 2018, pp. 530–544, 2019.
- [12] Q. Zhao, M. Mecheri, T. Neveux, R. Privat, and J. N. Jaubert, "Selection of a Proper Equation of State for the Modeling of a Supercritical CO₂ Brayton Cycle: Consequences on the Process Design," *Ind. Eng. Chem. Res.*, vol. 56, no. 23, pp. 6841–6853, 2017.
- [13] S. Lasala, A.-P. Martinez, and J.-N. Jaubert, "A Predictive Equation of State to Perform an Extending Screening of Working Fluids for Power and Refrigeration Cycles," in *Organic Rankine Cycles for Waste Heat Recovery - Analysis and Applications*, IntechOpen, 2020.
- [14] G. Di Marcoberardino, E. Morosini, and G. Manzolini, "Influence of the Equations of state on the performance of CO₂ + C₆F₆ as innovative working fluid in transcritical cycles," Unpublished, 2021.
- [15] M. Binotti, G. Di Marcoberardino, P. Iora, and C. Invernizzi, "SCARABEUS: Supercritical carbon dioxide / alternative fluid blends for efficiency upgrade of solar power plants SCARABEUS: Supercritical Carbon Dioxide / Alternative Fluid Blends for Efficiency Upgrade of Solar Power Plants," vol. 130002, no. December, 2020.
- [16] SCARABEUS, "SCARABEUS Project," 2019. [Online]. Available: <https://www.scarabeusproject.eu/>. [Accessed: 13-Nov-2019].
- [17] X. Liu, Z. Xu, Y. Xie, and H. Yang, "CO₂-based mixture working fluids used for the dry-cooling supercritical Brayton cycle: Thermodynamic evaluation," *Appl. Therm. Eng.*, vol. 162, no. 17923, p. 114226, 2019.
- [18] ProSim, "Simulis Thermodynamics," 2019. [Online]. Available: <http://www.prosim.net/en/software-simulis-thermodynamics-mixture-properties-and-fluid-phase-equilibria-calculations-3.php>. [Accessed: 13-Nov-2019].
- [19] O. Aqel, M. White, M. Khader, and A. Sayma, "Sensitivity of transcritical cycle and turbine design to dopant fraction in CO₂-based working fluids," *Appl. Therm. Eng.*, 2021.
- [20] D. Y. Peng and D. B. Robinson, "A New Two-Constant Equation of State," *Ind. Eng. Chem. Fundam.*, vol. 15, no. 1, pp. 59–64, 1976.
- [21] H. Nishiumi and S. Saito, "An improved generalized BWR equation of state applicable to low reduced temperatures," *J. Chem. Eng. Japan*, vol. 8, no. 5, pp. 356–360, 1975.
- [22] G. Soave, "Equilibrium constants from a modified Redlich-Kwong equation of state," *Chem. Eng. Sci.*, vol. 27, no. 6, pp. 1197–1203, 1972.
- [23] J. Gross and G. Sadowski, "Perturbed-chain SAFT: An equation of state based on a perturbation theory for chain molecules," *Ind. Eng. Chem. Res.*, vol. 40, no. 4, pp. 1244–1260, 2001.
- [24] A. Yazdi, A. Najafloo, and H. Sakhaeinia, "A method for thermodynamic modeling of H₂S solubility using PC-

- SAFT equation of state based on a ternary solution of water, methyldiethanolamine and hydrogen sulfide,” *J. Mol. Liq.*, vol. 299, 2020.
- [25] A. M. A. Dias *et al.*, “Vapor - Liquid equilibrium of carbon dioxide - Perfluoroalkane mixtures: Experimental data and SAFT modeling,” *Ind. Eng. Chem. Res.*, vol. 45, no. 7, pp. 2341–2350, 2006.
- [26] J. A. Bierlein and W. B. Kay, “Phase-Equilibrium Properties of System Carbon Dioxide-Hydrogen Sulfide,” *Ind. Eng. Chem.*, vol. 45, no. 3, pp. 618–624, 1953.
- [27] J. J. Sienicki, A. Moiseyev, R. L. Fuller, S. A. Wright, and P. S. Pickard, “Scale Dependencies of Supercritical Carbon Dioxide Brayton Cycle Technologies and the Optimal Size for a Next-Step Supercritical CO₂ Cycle Demonstration,” 2011.
- [28] S. I. Salah, M. A. Khader, M. T. White, and A. I. Sayma, “Mean-Line Design of a Supercritical CO₂ Micro Axial Turbine,” *Appl. Sci.*, pp. 1–20, 2020.
- [29] O. E. Baljé, “A study on design criteria and matching of turbomachines: Part A-similarity relations and design criteria of turbines,” *J. Eng. Gas Turbines Power*, vol. 84, no. 1, pp. 83–102, 1962.
- [30] V. Dostal, M. J. Driscoll, and P. Hejzlar, “A Supercritical Carbon Dioxide Cycle for Next Generation Nuclear Reactors,” 2004.

Appendix A

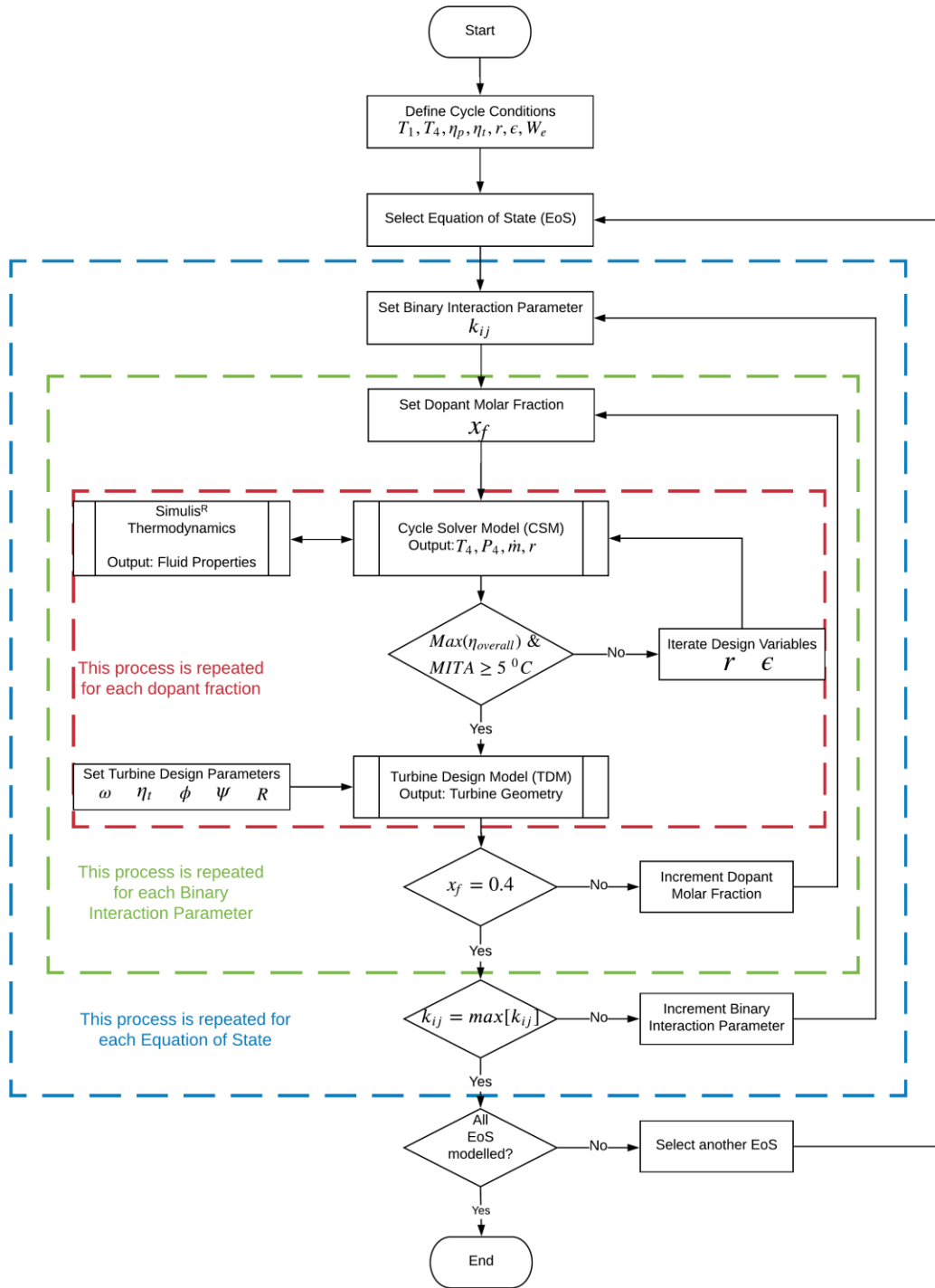


Fig A1. Flowchart of the sensitivity study for a single CO₂ mixture.

SCO₂ POWER CYCLE DESIGN WITHOUT HEAT SOURCE LIMITATIONS: SOLAR THERMAL PARTICLE TECHNOLOGY IN THE CARBOSOLA PROJECT

Lukas Heller*

German Aerospace Center (DLR)
Stuttgart, Germany
Email: Lukas_Heller@gmx.de

Stefan Glos

Siemens Energy AG
Mülheim an der Ruhr, Germany

Reiner Buck

German Aerospace Center (DLR)
Stuttgart, Germany

ABSTRACT

Supercritical CO₂ power cycles have been proposed to lower the levelized cost of electricity generated by Concentrating Solar Power (CSP) plants due to their high thermal efficiency and low equipment cost. In this study, a simplified techno-economic model was developed to compare the performance of molten salt and solid particle CSP technologies with various sCO₂ cycle layouts and parameters. It was found that systems employing particle technology consistently have a lower levelized cost than molten salt systems, mainly due to the latter's high storage system cost, caused by a low temperature spread. Furthermore, less complex process layouts without reheat or intercooling and even without recompression render lower levelized cost, which is caused by increasing costs for compressors, motors and recuperators in high-performance layouts. Compared with the reference system based on a steam power block, the best sCO₂ processes achieve similar LCOE values but not the often-proposed significant improvements. These findings are highly dependent on some of the cost models, mainly for the primary heat exchanger and for indirect power block costs, which will be refined in a next step.

INTRODUCTION

Supercritical CO₂ (sCO₂) power cycles have the potential to reach considerably higher thermal efficiencies than state of the art steam cycles while minimizing the size and number of components. To reach high thermal efficiencies, the average temperature at which heat is supplied to the cycle has to be very high. Concentrating solar power (CSP) technology allows for this as the heat transfer medium downstream the sCO₂-primary heat exchanger is reintroduced into the solar receiver, making CSP-sCO₂ processes appear like a perfect match.

Unfortunately, heat transfer media used in commercial CSP plants have limiting upper and lower temperature constraints. Currently, the maximum temperature reached in these plants is approximately 565 °C for molten salt, which does not allow for using the most efficient high-temperature sCO₂ cycles.

Contrary to these state-of-the-art heat transfer media, certain ceramic particles have no temperature limitations within the

relevant technological range (0 °C... 1000 °C). This leads to the following potential advantages when combined with sCO₂ cycles:

- Very high temperature sCO₂ processes can be employed, leading to high thermal efficiencies.
- High approach temperatures to the primary heat exchanger (PHX) can be realized, leading to smaller heat transfer area requirements and, therefore, costs.
- Even when a small sCO₂ temperature rise is desired in the PHX in order to improve cycle efficiency, the temperature spread between hot and cold particles can still be kept comparatively large due to the high approach temperature. This temperature spread has a direct and significant effect on the cost of the thermal energy storage (TES) system cost [1].

Particle technology therefore allows for employing high temperature, highly recuperated sCO₂ power blocks (PBs) reaching thermal efficiencies in excess of 50 %. Although it is tempting to define a system for maximum efficiency, the choice should be based on the techno-economic optimum of the whole plant. The recompression cycle is commonly seen as the most efficient layout for an sCO₂ PB and has been proposed numerous times for integration with CSP [1-4]. Although this layout achieves high thermodynamic performance, it requires large and costly internal recuperators for this as well as a small temperature rise in the PHX. This leads to increased costs of the cycle equipment but also of the solar components, mainly the TES system. Due to their much lower cost, simple recuperated cycles, for example, have been found to be competitive on a techno-economic level [3, 5]. Other studies have found that, particularly for molten salt systems, partial cooling layouts can be beneficial as they increase the PHX temperature rise [6].

Besides the choice of the process layout, their main parameters (e.g. turbine inlet temperature, upper and lower cycle pressure, terminal temperature differences in all heat exchangers, ...) also have a strong impact on the cycle components' costs as well as on the solar components (via the PHX). This adds up to a large number of variables with non-obvious system-wide optima.

* corresponding author(s)

Table 1. Location and solar field assumptions

(*Adjusted for same annual energy yield as MS system)

(** Includes TES thermal losses and receiver limitations for min. load and startup)

dp: design point; a: annual

Parameter	Value	
	MS	Pa
Location	Postmasburg, RSA	
Design PB capacity (semi-net)	115 MW _e	
Design point ambient temperature	19 °C	
Solar multiple	2.4	~ 2.5*
TES capacity	12 h	
Collector field efficiency, dp	70 %	73.5 %
Collector field efficiency, a	58 %	52.7 %
Receiver efficiency, dp	Depending on cold tank temperature (~91.7 % @ 290 °C)	90 %
Receiver efficiency, a	Receiver efficiency, dp x 94.4 %	86.7 %
Dumping efficiency, a**	93 %	98 %
Plant gross-to-net	95 %	97.5 %
PB efficiency, a	PB efficiency,dp x 99 %	

Within Work Package 2 of the CARBOSOLA project, funded by the German Ministry for Economic Affairs and Energy, Siemens Energy and DLR are assessing the economic potential of sCO₂ cycles for CSP power plants. The present study concerns the initial step of this undertaking: the pre-selection of a small number of CSP technologies and sCO₂ processes, which are expected to have the highest techno-economic potential. The main areas described are the definition of investigated systems and boundary conditions, their thermodynamic modeling, economic models and, finally, results. The used models employ numerous simplifying assumptions due to the lack of maturity of, and therefore data for, the technologies. This is particularly true for the cost models of some major sCO₂ and particle components. In further works, the identified processes will be designed in more detail leading to improved cost and performance models.

BOUNDARY CONDITIONS AND DESCRIPTION OF INVESTIGATED SYSTEMS

The main boundary conditions for the modeled power plants are presented in Table 1. The location has been chosen because the Redstone Solar Power Plant is planned to be erected there and reference data exists from previous projects [7]. The location is noteworthy for a high annual direct normal irradiation (DNI) and rather moderate mean ambient temperatures.

Two different CSP technologies are investigated and modeled: State of the art molten salt (MS) and next-generation solid Particles (Pa). The maximum operating temperature of MS has been set to 565 °C. In a further variant, salt temperatures of up to 615 °C are assumed to be reachable although this has not yet been proven. This variant is meant to show the potential of sCO₂ cycles in combination with evolutions to the MS technology [7]. It was assumed that the MS receiver system operates at the same efficiency for all receiver outlet temperatures, which is obviously optimistic for the 615 °C case. The maximum particle temperature has been set to 900 °C in all variants.

All assumptions presented in Table 1 regarding the MS system (except for the receiver efficiency dependency on receiver inlet temperature, which is based on internal studies), were derived from a previous project [7]. The data for the Pa system is mainly based on internal studies at DLR for systems employing the CentRec© particle receiver. More information on the technology can be found in recent publications [1, 8]. The solar multiple, which is a measure for the oversizing of the solar field with respect to the steam generator, of the Pa systems was adjusted to render the identical annual electricity output as the MS systems.

TECHNO-ECONOMIC MODEL

The simplified annual yield model for the pre-selection process does not include hourly time steps for the performance calculation of the solar field but instead uses average annual values (shown in Table 1) for the subsystems. This allows for the comparison of the performance of tens of thousands of variants of the sCO₂ PB.

The subsystem costs for each variation of the PB or solar technology is calculated by setting the design point electricity yield (according to Table 1) and calculating the necessary rating of all subsystems via their design point efficiencies. This would result, e.g., in a larger solar field for a less efficient power block (all other efficiencies unchanged).

The focus of this study is the sCO₂ PB, its predicted performance and cost as well as the influence it has on the overall plant performance and cost. As mentioned above, the simplified model used here only requires a design-point simulation of the PB, meaning that part-load behavior is not modeled. The performance of the cycles and the rating of their components is calculated in the power plant simulation software Epsilon Professional V. 14.03 by STEAG Energy Services GmbH. Thermodynamic results were validated with data from the literature and very good agreement was found. Some of the major assumptions and ranges of optimization parameters are provided in Table 2.

Table 2: Assumptions and variables of sCO₂ cycles

Parameter	Value
$\Delta p_{\text{Recuperators (low pressure side)}}$	2 %
$\Delta p_{\text{Recuperators (high pressure side)}}$	3 %
Δp_{PHX}	2 %
$\Delta p_{\text{Cooler/IC}}$	0.6 %
$\eta_{\text{PHX,thermal}}$	99 %
$\eta_{\text{Turbines,isentropic}}$	91 %
$\eta_{\text{Compressors,isentropic}}$	87 %
$\eta_{\text{Motors,electric}}$	97 %
$\eta_{\text{Generator}}$	98.7 %
$\Delta p_{\text{air,Cooler/IC}}$	5 mbar
Turbine inlet pressure	260 bar
Turbine inlet temperature	500 °C ... 650 °C
$(U*A)_{\text{Cooler/IC}}$... 18 MW/K
Compressor inlet pressure	45 bar ... 100 bar
$TTD_{\text{Recuperator}}$	5 K ... 80 K
Recompression fraction	0.25 ... 0.45
$TTD_{\text{PHX,high-pressure}}$	5 K ... 195 K
$TTD_{\text{PHX, low-pressure}}$	5 K ... 195 K

Table 3: Overview of modeled process layouts

Name	Cycle type				RH	IC
	Simple Recuperated	Recompression	Partial cooling			
01_simple	x					
02_simple_RH	x				x	
03_simple_IC	x					x
04_simple_RH_IC	x				x	x
05_recomp		x				
06_recomp_RH		x			x	
07_recomp_IC		x				x
08_recomp_RH_IC		x			x	x
10_partialC			x			
09_partialC_RH			x	x		

A total of ten process layouts were modeled (see Table 3). They were simple recuperated cycles and recompression cycles with and without reheat (RH) or intercooling (IC) and partial cooling cycles with and without RH. Figure 1 depicts Layout 08 with those components marked that would fall away for layouts without RH (red), without IC (blue) and without recompression/partial cooling (green). The results in terms of efficiency and component rating were postprocessed to derive the overall system costs and levelized cost of electricity (LCOE) as the main optimization target.

The economic model contains specific costs for the main PB equipment, indirect costs as a percentage of the PB equipment

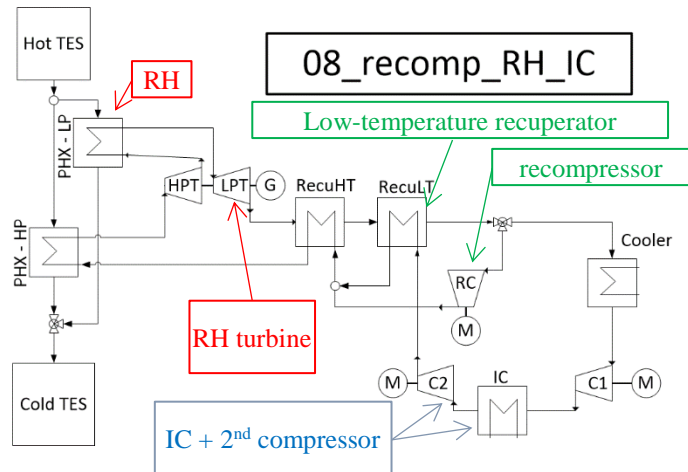


Figure 1: Schematic of an example process ("08")

costs and specific costs for all solar subsystems (see Annex A). Furthermore, EPC indirect costs and owner's costs are added to render the total owner's costs ($C_{\text{owner,total}}$). These are then used to calculate the LCOE via the following simplified correlation

$$LCOE = (FCR * C_{\text{owner,total}} + O\&M_a) / \sum P_{\text{out}}$$

Therein, FCR represents the fixed charge rate, $O\&M_a$ the annual operation and maintenance costs and $\sum P_{\text{out}}$ the cumulative annual electricity output of the plant.

Arguably the biggest challenge in assessing the techno-economic performance of a technology that has never been constructed (especially not at the considered scale) is to estimate the cost of its components, indirect costs and those for operation and maintenance. In very few sources in open literature are cost models for sCO₂ components over a range of operating parameters published. Recently, however, Weiland et al. [9] developed cost correlations for most major components of CSP-driven sCO₂ power blocks based on quotes from potential industrial suppliers. The equipment cost of all sCO₂ components, except for the primary heat exchanger, were calculated using these correlations. The cost of the Pa-PHX was calculated using a correlation proposed for particle-sCO₂ heat exchangers [1], which assumes high-grade materials that allow for high TITs. The MS-PHX cost correlation was derived from a study for molten salt systems operating at temperatures of up to 650 °C [6]. Once preliminary designs of the main components have been developed by Siemens Energy, these cost assumptions will be updated in a future study.

In order to compare the found results to the state of the art, the method described above was also used to calculate the performance of MS and Pa plants employing one of two different steam cycle PBs (with a turbine inlet temperature, TIT, of either 550 °C or 600 °C). As the variants with a TIT of 600 °C

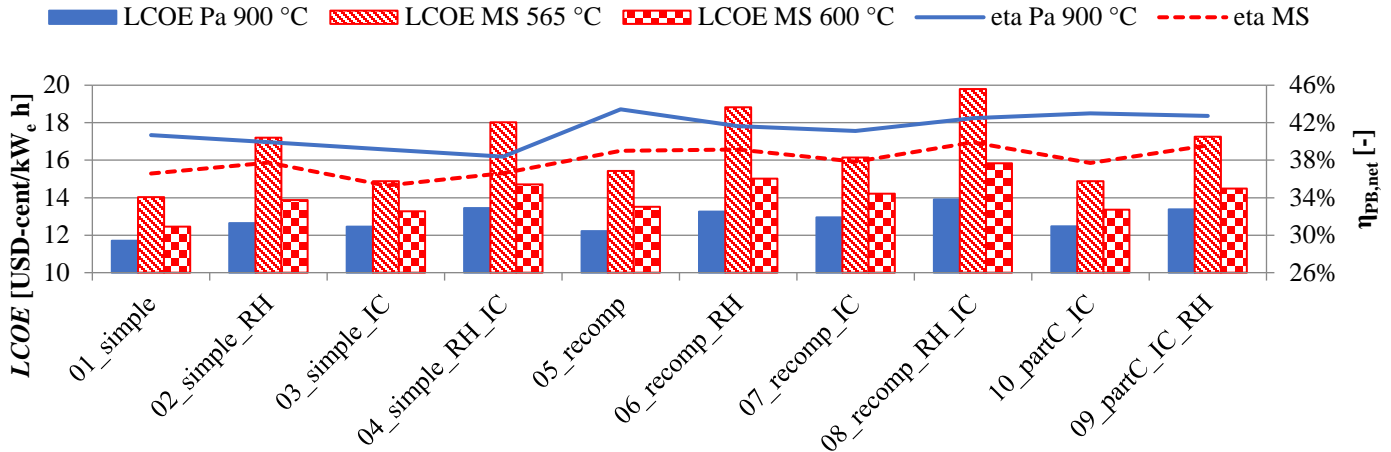


Figure 2: LCOE and PB efficiencies for cost optimized variants of all cycles and heat transfer media

produced similar LCOE values and Pa systems performed slightly better than MS systems, the Pa system with a TIT of 550 °C was chosen as the reference. It has a net PB efficiency of 42.7 % at an LCOE of 11.1 USD-cent/kW_e h.

RESULTS

Before discussing the quantitative results of the techno-economic analysis, it should once more be stressed that they should be seen as a qualitative indication only. The actual values for levelized cost of electricity are highly dependent on many assumptions, especially economic ones, which have a high uncertainty in this early development stage of the investigated technologies. That being said, the comparison of the processes with each other and with the reference steam system should give an indication for general trends and for which ones to pursue further.

At first, the simulated processes with the lowest LCOE were identified for each layout and each heat transfer medium. For these 30 variants, the LCOE and PB net efficiency are depicted in Figure 2. There are several observations to be made from this figure.

1. Electricity generated by Pa systems has the lowest cost for every layout. Even if the MS temperature can be increased to 615 °C without cost or performance penalties on the solar equipment, TES and PHX, the LCOE of MS systems is still higher than of Pa systems. The main cost drivers for this difference are the TES and the receiver system, as can be seen in Figure 3. Increasing the sCO₂ process temperature in MS systems, which would be possible for the 615 °C case, increases the cost of the TES system and the PHX even further (not shown in figure).
2. Due to the large influence of the TES cost on the MS systems, sCO₂ processes with a larger temperature rise in the PHX are preferred compared with Pa systems. Although they produce a lower PB efficiency for the MS systems (red dashed line) compared with the Pa configurations (blue solid line).

3. Less complex PB layouts produce a lower LCOE. This is especially true for the simple recuperated cycle without IC or RH (“01”).
4. The calculated LCOE of all systems is higher than that of the reference plant. Given the fidelity of the models, the difference lies within the range of uncertainty, though.
5. When optimized for LCOE, most configurations have a lower PB efficiency than the reference steam cycle (42.7 %). However, efficiency was not an objective in the optimization.

In Figure 4, the total cost of each Pa layout’s PB is further divided up into the main equipment and indirect costs. The top bar (“Rest + indirect”) includes mostly indirect costs of the power block (for civil works, instrumentation and control, electrotechnics, etc.) as well as contingencies & profit of the PB technology provider. These latter costs are calculated via cost adders on top of the total PB equipment costs and add up to 79 % (see also ANNEX A).

Another observation that can be made from Figure 4 is that the cost of the PHX is, with current cost models, of a comparable magnitude to that of all other PB equipment (excluding indirect costs). This is further discussed in the Conclusions and Outlook Section. Furthermore, the cost of the PB incl. PHX of all optimized systems is rather high, ranging from approximately 1300 USD/kW_e for Layout 01 to 2000 USD/kW_e for Layout 08. Commonly stated cost targets for sCO₂ cycles are much lower (~ 900 USD/kW_e) and the expected efficiencies considerably higher (> 45 %) [4, 10].

Besides indirect costs and the PHX, the dominating cost contributions stem from the recuperators, the compressors plus motors, the cooling system and piping, meaning that the turbine(s) only make up a small share of the total costs. One noteworthy trend is that the compressor plus motor costs increase significantly for more complex layouts. This is caused by the increased quantity of compressors from one unit (“01” & “02”) to two units (“03” through “06”) and three units (“07” through “10”). As the scaling exponent for compressor costs is very low, the quantity of units has a large influence on the equipment costs.

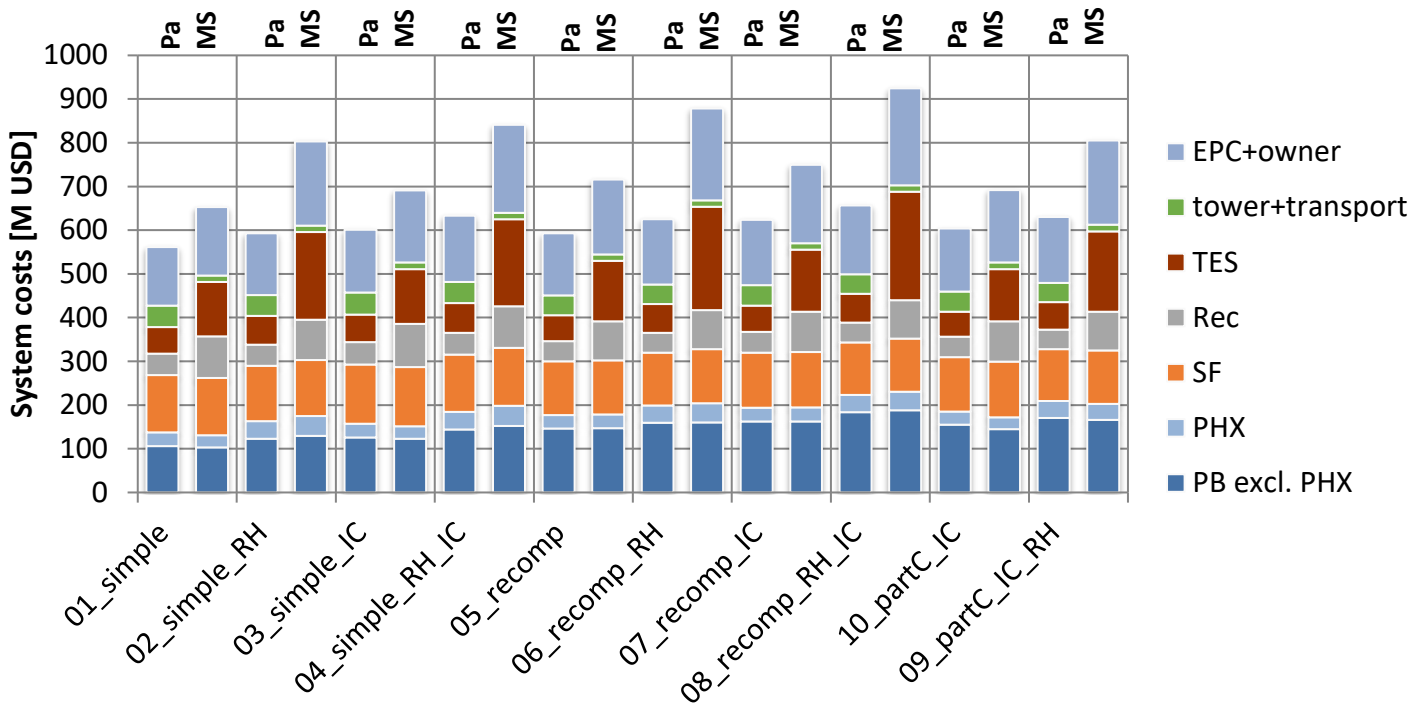


Figure 3: Subsystem costs of all layouts for Pa technology (left bars for every layout) and MS 565 °C systems (right bars)

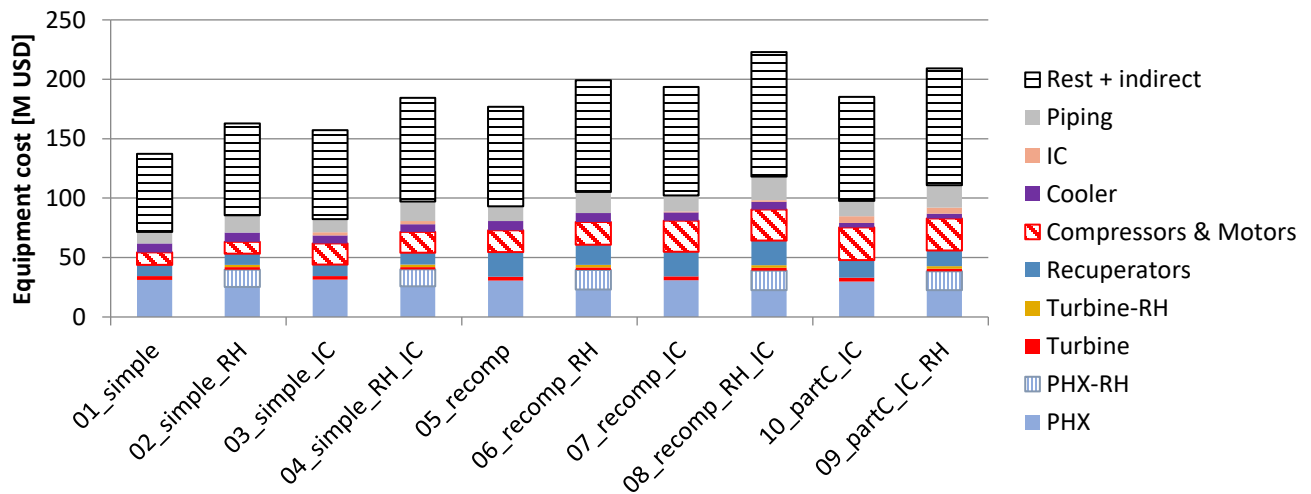


Figure 4: PB equipment costs of all variants employing particle technology and with a TIT of 550 °C

CONCLUSIONS AND OUTLOOK

There are three major conclusions to be drawn from the techno-economic optimization conducted in this study: Firstly, particle technology appears to be considerably more suitable for CSP-sCO₂ power plants compared with state-of-the-art molten salt or even an optimistic assumption for a system with evolutionary improvements. Therefore, molten salt systems are not pursued any more within the CARBOSOLA project, focusing entirely on particle technology.

Secondly, the comparison of different LCOE-optimized variants of sCO₂ processes showed that simpler layouts with fewer components are more economical than more efficient but more expensive ones. The simple recuperated cycle without reheat or intercooling showed consistently the best economic performance. Some of the subsystems and equipment contributing majorly to this trend are the TES, compressors, recuperators and piping. It can be concluded that the cost savings due to a larger temperature spread in the TES system outweigh the additional cost of an increased heliostat field.

Thirdly, all investigated sCO₂ processes render higher LCOE values than the steam reference plant, however, the best-performing cycles come close. This is in contrast to expectations that this new technology can provide very high thermal efficiencies at significantly lower PB investment cost than the state of the art. While some other studies have found comparable LCOE or specific costs for CSP plants with steam and sCO₂ power blocks [5, 11], others predict very low LCOE values for sCO₂-based plants [1, 4, 12, 13].

For this large discrepancy, several possible explanations come to mind. Many studies appear to assume much lower (or no) indirect costs associated with the power block equipment. As there is a cost adder of 79 % for these used in the current study, the PB cost would be almost doubled compared with those models. Lowering this factor would obviously improve the comparison with steam cycles.

An explanation for the rather high LCOE values found for all sCO₂ variants but also for the reference system are conservative assumptions in the financial model. The used values for the fixed charge rate of 9.37 % might be conservative but does not seem unrealistic.

Finally, the implemented Pa-PHX cost model was derived for very high temperature processes and might, therefore, also be conservative for the modeled process parameters. An appropriate cost reduction term for lower sCO₂ process temperature, e.g. a TIT of 550 °C, could have a significant impact on the equipment costs but also the overall plant performance. Much more optimistic cost correlation for Pa-sCO₂ heat exchangers can be found in the literature [3].

The next step within the Carbosola Project is the preliminary design of core components of sCO₂ power blocks. Findings from that work will help improve the presented models and validate the findings.

NOMENCLATURE

CSP	Concentrating solar power
IC	Intercooling
MS	Molten salt technology system
Pa	Particle technology system
PB	Power block
PHX	Primary heat exchanger
RH	Reheat
sCO ₂	Supercritical CO ₂
TES	Thermal energy storage
TIT	Turbine inlet temperature
<i>LCOE</i>	Levelized cost of electricity (USD/kW h)
<i>P</i>	Electric Power (W _e)
<i>TTD</i>	Terminal temperature difference (K)
<i>U*A</i>	Heat exchanger conductance-area product (W/K)
Δp	Relative pressure drop (%)
η	Efficiency (%)

ACKNOWLEDGEMENTS

The authors would like to thank the German Federal Minister for Economic Affairs and Energy for the financial

support of the project Carbosola (reference number: 03EE5001C).

REFERENCES

1. Buck, R. and S. Giuliano, *Impact of solar tower design parameters on sCO₂-based solar tower plants*. 2nd European sCO₂ Conference 2018: 30-31 August 2018, Essen, Germany, 2018: p. 160-167.
2. Dyreby, J., et al., *Design Considerations for Supercritical Carbon Dioxide Brayton Cycles With Recompression*. Journal of Engineering for Gas Turbines and Power, 2014. **136**(10).
3. Ho, C.K., et al., *Technoeconomic Analysis of Alternative Solarized s-CO₂ Brayton Cycle Configurations*. Journal of Solar Energy Engineering, 2016. **138**(5).
4. Albrecht, K.J., M.L. Bauer, and C.K. Ho. *Parametric Analysis of Particle CSP System Performance and Cost to Intrinsic Particle Properties and Operating Conditions*. in *ASME 2019 13th International Conference on Energy Sustainability collocated with the ASME 2019 Heat Transfer Summer Conference*. 2019.
5. Crespi, F.M., *Thermo-economic assessment of supercritical CO₂ power cycles for concentrated solar power plants*, in *Department of Energy Engineering School of Engineering - ETSI*. 2019, University of Seville: Seville.
6. Neises, T. and C. Turchi, *Supercritical carbon dioxide power cycle design and configuration optimization to minimize levelized cost of energy of molten salt power towers operating at 650 °C*. Solar Energy, 2019. **181**: p. 27-36.
7. Giuliano, S., et al., *HPMS - High Performance Molten Salt Tower Receiver System*. 2017.
8. Ebert, M., et al., *Operational experience of a centrifugal particle receiver prototype*. 2019. **2126**(1): p. 030018.
9. Weiland, N.T., B.W. Lance, and S.R. Pidaparti. *sCO₂ Power Cycle Component Cost Correlations From DOE Data Spanning Multiple Scales and Applications*. in *ASME Turbo Expo 2019: Turbomachinery Technical Conference and Exposition*. 2019.
10. Vijaykumar, R.B., Matthew L.; Lausten, Mark; Shultz, Abraham M., *Optimizing the Supercritical CO₂ Brayton Cycle for Concentrating Solar Power Application*, in *The 6th International Supercritical CO₂ Power Cycles Symposium*. 2018: Pittsburgh, Pennsylvania.
11. Cheang, V.T., R.A. Hedderwick, and C. McGregor, *Benchmarking supercritical carbon dioxide cycles against steam Rankine cycles for Concentrated Solar Power*. Solar Energy, 2015. **113**: p. 199-211.
12. Mecheri, M., Z. Qiao Dr, and P.F. nd European supercritical Co₂ Conference September, *Probabilistic technique for solving computational problem:*

application of Ant Colony Optimization (ACO) to find the best sCO₂ Brayton cycle configuration. 3rd European Conference on Supercritical CO₂ (sCO₂) Power Systems 2019: 19th-20th September 2019, 2019: p. 319-331.

13. Trevisan, S., R. Guédez, and B. Laumert, *Thermo-economic optimization of an air driven supercritical CO₂ Brayton power cycle for concentrating solar power plant with packed bed thermal energy storage.* Solar Energy, 2020. **211**: p. 1373-1391.

ANNEX A

COST MODELS AND ECONOMIC ASSUMPTIONS

$$C_{\text{Component}} = f_T(a + b * x^c)$$

Component	f_T (for $t_{\text{fluid,max}} > 550 \text{ }^\circ\text{C}$)	a	b	c	x	Source
PHXs			3266.8 USD	0.66	$UA_{\text{PHX}}/(\frac{W_t}{K})$	based on [1]
Turbines	$1 + 1.106\text{E-}04 * (t_{\text{fluid,max}} - 550 \text{ }^\circ\text{C})^2$		182 600 USD	0.5561	$P_{\text{shaft}}/\text{MW}_t$	[9]
Generator			108 900 USD	0.5463	$P_{\text{electric}}/\text{MW}_e$	
Compressors			6 220 000 USD	0.1114	$\dot{V}_{\text{inlet}}/(\frac{\text{m}^3}{\text{s}})$	
Motors			399 400 USD	0.6062	$P_{\text{electric}}/\text{MW}_e$	
Recuperators	$1 + 0.02414 * (t_{\text{fluid,max}} - 550 \text{ }^\circ\text{C})$		49.45 USD	0.7544	$UA_{\text{PHX}}/(\frac{W_t}{K})$	
ACC			32.88 USD	0.75	$UA_{\text{PHX}}/(\frac{W_t}{K})$	

\dot{V} : Volume flow (m^3/s)

Item	Value	Reference quantity
sCO ₂ storage	2 000 000 USD	-
Piping + valves (excl. RH piping)	15 %	PB equipment cost
RH piping	5 %	PB equipment cost
PB indirect costs* + technology provider services, profit and contingencies	79 %	PB direct cost
EPC services and contingencies + owner's cost	29 %	Total power plant direct cost

*Includes: Electronics; Instrumentation & Control; Construction, Commissioning, Project Management; Civil works; Engineering; Auxiliary systems

Parameter	Value	Reference	Comment
FCR	9.37 %	Total power plant investment cost	Fixed charge rate, derived for an interest rate of 8 % and a plant lifetime of 25 years.
$O\&M_a$	2 %	Total power plant direct cost	Annual operating and maintenance cost

SOFIA – SCO₂ FACILITY FOR SUPERCRITICAL BRAYTON CYCLE RESEARCH

Otakar Frýbort*
Research Centre Rez
Husinec-Rez, Czech Republic
Email: otakar.frybort@cvrez.cz

Karel Dočkal
Research Centre Rez
Husinec-Rez, Czech Republic

Petr Vlček
Research Centre Rez
Husinec-Rez, Czech Republic

Petr Hájek
Research Centre Rez
Husinec-Rez, Czech Republic

Tomáš Melichar
Research Centre Rez
Husinec-Rez, Czech Republic

Miroslav Kapic
Doosan Škoda Power
Pilsen, Czech Republic

Antonín Živný
NUMsolution
Prague, Czech Republic

Marek Pátý
NUMsolution
Prague, Czech Republic

Aleš Macálka
NUMsolution
Prague, Czech Republic

Vilém Hanzal
ÚJV Řež
Husinec-Rez, Czech Republic

Petr Hájek
ÚJV Řež
Husinec-Rez, Czech Republic

ABSTRACT

In the frame of national project sCO₂-Efekt supported by Czech technological agency TAČR, Research Centre Rez (CVR) is developing an innovative, effective and flexible energy storage system. This system is based on the P2H2P (Power to Heat to Power) technology also called Carnot battery, with the utilization of a sCO₂ Brayton cycle for heat to power conversion. In frame of the project, the key components of the storage system will be developed and experimentally verified. The key components are mainly the compressors and turbines and the storage tank. To be able to test the compressor and turbine, an experimental test facility called Sofia is also being developed. The main parameters of the Sofia facility are temperature up to 550°C, maximal test pressure of 25MPa, and flow rate of about 25kg/s. The highest possible power of the turbine to be tested is up to 1.5MW electrical. In this paper, the conceptual design of the large-scale experimental facility is described including its main components.

INTRODUCTION

The influence of the human population on the Earth climate is undeniable and many studies are currently focused on this

topic. European Union, as well as the other countries, are spending huge amounts of money for the research leading to the reduction of CO₂ emissions. To deal with the energy needs of the population, great efforts have been made to develop various methods of capturing the carbon dioxide produced from fossil power plants. Anyway, all these methods are connected with a significant decrease in global power plant efficiency. Clean power production from a coal power plant seems to be possible, but due to low global efficiency, it can be considered as a waste of primary resources and is not sustainable. A great source of low carbon electrical power is nuclear energy. On the other hand, many countries are withdrawing from nuclear energy due to safety reasons and generally, in Europe the electricity production from nuclear plants is expected to gradually fade.

A fast-growing industry in the past decade is linked to renewable resources. Water power plants are constantly getting better, but there is not any great potential for the capacity increase at least in Europe. There is a wide application of wind and solar plants and there can be possibly at least in certain areas to assure all necessary power production from these resources. The main issue is the time stability of the electricity production of the solar (photovoltaics) and wind plants. The application of energy storage systems with sufficiently high capacity seems to be the only way to zero carbon emission energy.

* corresponding author(s)

Research Centre Rez (CVR) develops high capacity mid-term energy storage system based on Power to Heat to Power (P2H2P) principle also known as Carnot Battery [1]. One of the concepts that are currently being developed is based on direct power transformation to heat using of direct electrical resistant heating elements. The heating elements are located directly in a storage tank. The tank is filled with the storage media which is aluminum based alloy AlSi12. In an effort to minimize the amount of the alloy and simultaneously reduce volume of the storage tank, latent heat for the heat storage is utilized. For reverse power production, a sCO₂ cycle is considered. The whole concept is very innovative and promises the efficiency of this system higher than 40% with theoretical further improvement up to 50%.

In the frame of the currently solved project sCO₂-Efekt, the key scaled-down components are being developed and will be tested. As the key components, the sCO₂ compressors, turbines, and the storage tank are considered. To be able to test the sCO₂ turbomachinery, the experimental circuit is also being developed. The main components (except of the storage tank as it will be tested separately and is described in detail in [2]) and the whole layout of the experimental circuit is further described in this article. Moreover, detailed computational analyses supporting the design of a compander are presented.

The realization of the Sofia facility follows previous extensive R&D activities in the field of sCO₂ at CVR, represented mainly by the realization and operation of the sCO₂ Loop intended for thermal-hydraulic and materials research. The CVR's sCO₂ loop is designed as a simple Brayton cycle with regeneration with a heating power of 110 kW and operational sCO₂ parameters up to 30 MPa and 550 °C [3]. The loop was utilized within H2020 sCO₂-HeRo project [4] for testing of cycles components or within H2020 sCO₂-FLEX project [5] for materials research. Other experimental loops are operated worldwide. SCARLETT facility is operated by the University of Stuttgart, Germany [6]. The facility is primarily intended for sCO₂ fluid and cycle properties near the critical point with operational conditions up to 150 °C and 12 MPa. A small-scale test loop was commissioned at the Technical University of Vienna within H2020 SCARABEUS project [7]. The sCO₂-HeRo loop was built and coupled with the PWR glass model at the Simulation Centre of KSG/GfS, Essen, Germany [8]. The facility is intended for simulation of decay heat removal from a PWR reactor. Obviously, the Sofia facility will significantly increase experimental possibilities in terms of the facility size and operational parameters comparing to the other European loops. Several larger-scale loops simulating Brayton cycles in various modification equipped with power turbines in the power range of hundreds of kW are operated in the USA such as Sandia National Laboratories recompression loop [9], Naval Nuclear Laboratory Integrated Test System [10], Echogen EPS100 [11] and SwRI SunShot test loop [12]. Other small-scale loops are operated in Japan (bench-scale experimental facility of Tokyo Institute of Technology, [13]) and Korea (SCIEL facility, sCO₂ Pressurizing Experiment at KAIST [14]).

MAIN FEATURES AND CO₂ SOFIA FACILITY LAYOUT

For the designed energy storage system, the recompression Brayton cycle is being considered. The expected power of the system is between 10 and 50 MWe for several hours. Mainly, for this reason, the axial power turbine was selected as the most suitable turbine solution. Further application of the cycle with a higher power was also taken into account in these considerations. 10 MW is stated in the literature as the minimum power for application of the axial turbine with acceptable efficiency. The implementation cost of a 10 MW sCO₂ power cycle far exceeds the possibility of the project. For this reason, 1MW of output power was selected as a reasonable power level for the experimental facility. In this scale, the axial turbine is feasible and the experimental results will be still relevant for validation and verification of the numerical tools used for designing the turbine.

In an effort to demonstrate the benefits of the sCO₂ cycle in comparison with the common Rankine steam cycle, different studies consider the highest working temperature over 600 °C or even 700 °C. It is probably possible to design the power circuit for such working temperatures, but it leads to the need to use very expensive high-temperature alloys. Selection of such high working temperatures would also increase the risks related to the unsuccessful demonstration of the key components. Considering all these aspects, 565°C was chosen as the design temperature. The design pressure level was set to 26,5MPa according to the cycle calculations that were preliminarily performed.

For further industrial application, the one shaft layout of the cycle can be expected. It reduces the number of turbines or electrical motors and eventually a number of dry gas seals which are always connected with certain CO₂ losses. Taking into account the necessary flexibility of the experimental facility, each turbo component will be located on a separate shaft in our case. Unfortunately, it is out of the scope of this project to build a full recompression cycle, therefore the simple Brayton cycle with regeneration will be built. The PID of the Sofia experimental stand is depicted in Figure 1.

STARTING COMPRESSOR

The first component which is the point of interest is called the starting compressor. The name itself indicates the purpose of the use. As the main circulating compressor is driven by its own turbine and it is not equipped with a motor, the starting compressor is needed to put the circuit into operation. At the beginning of the project work, the starting compressor was expected to be able to suck the liquid CO₂ and further get over to slightly supercritical conditions at the outlet. It was finally decided to reach the supercritical parameters all over the circuit before the compressor start-up. Anyway, the start-up from the subcritical (liquid at the inlet) conditions will be experimentally verified. To reach the supercritical parameters, the pressurizer and gas boiler will be used.

According to performed cycle calculations, design parameters for the starting compressor were established. The design parameters are summarized in Tab. 1.

Table 1: Design parameters of the starting compressor

Design pressure	10 MPa
Nominal pressure inlet	8.4MPa
Inlet pressure range	5 – 9 MPa
Nominal pressure outlet	9.4MPa
Nominal mass flow rate	11 kg/s
Nominal inlet temperature	35°C
Inlet temperature range	20-40°C
Nominal power of the motor	55 kW
Speed control	Frequency converter
Nominal speed	40 000 rpm

The starting compressor is designed as a hermetic machine with an encapsulated motor. The compressor wheel will be of the radial type with an inducer. The shaft will be supported by gas bearings directly lubricated by sCO₂.

The starting compressor is being developed within the sCO₂-Efekt project by the company Sobriety [15].

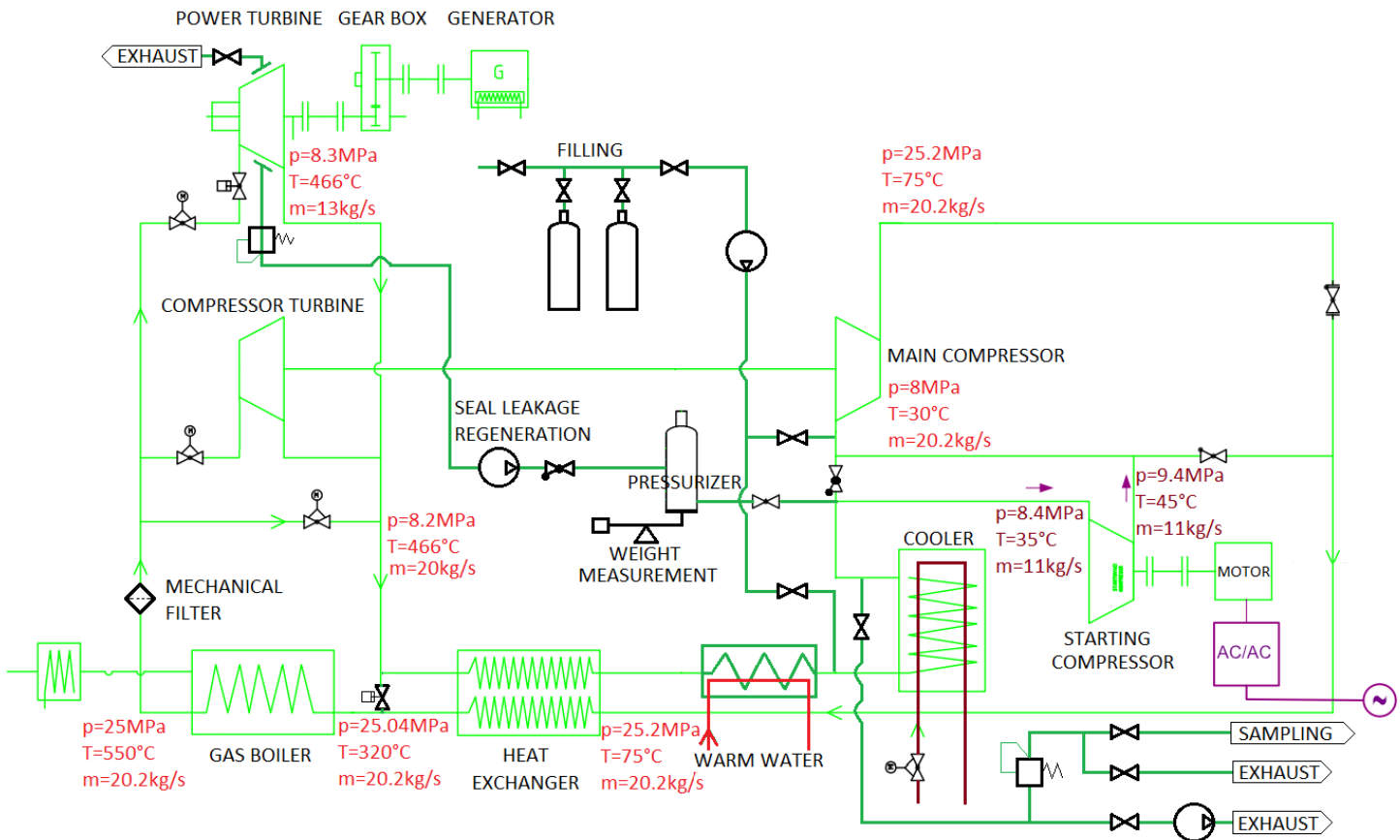


Figure 1: PID of Sofia experimental facility

COMPANDER

The main circulating compressor is driven by its radial turbine (expander), therefore the whole machine is called compander. It is not equipped with any motor therefore it needs to be started with the support of the starting compressor. As can be seen in Figure 1, both compressors work in series. Once the compander becomes self-sustainable, the starting compressor is bypassed and doesn't increase the pressure loss of the circuit anymore. The compander is designed as a hermetic one, where the shaft is supported by the gas bearings. The nominal parameters of the compander are listed in Table 2.

Table 2: Nominal parameters of the compander

	Compressor	Turbine
Inlet temperature	30°C	550°C
Outlet temperature	75°C	460°C
Inlet pressure	8MPa	25MPa
Outlet pressure	25.5MPa	8.5MPa
Mass flow	20.3kg/s	7kg/s

The design procedure of the compander was an iterative process that requires the consideration of multiple different aspects. The ultimate goal is to achieve a highly aerodynamically efficient design that at the same time fulfills structural and thermal constraints and has low manufacturing costs. The presented design process comprised the integration of several commercial and in-house tools into a complex multiphysics environment (Figure 2).

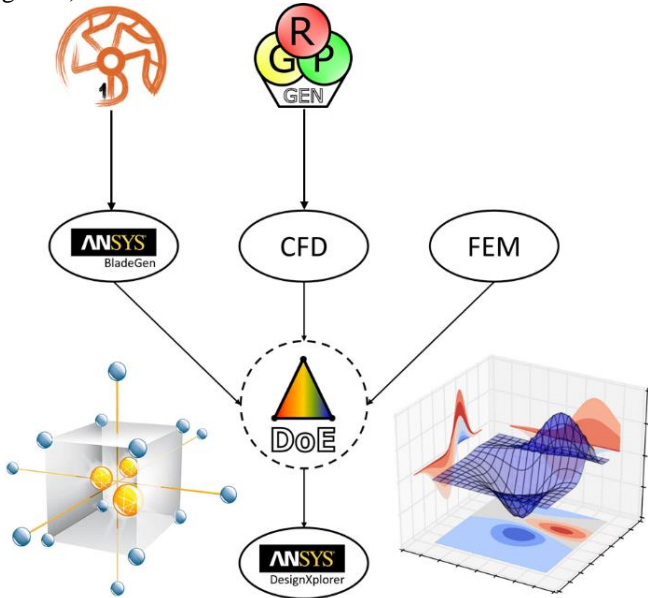


Figure 2: Design procedure

The first iteration was obtained with the in-house software DesignCC which enhances the classical 1D approach with machine learning techniques. The initial design then served as an input for a multi-objective optimization procedure, targeting the following parameters:

- Maximized aerodynamic efficiencies of the compressor and turbine
- Structural stresses on the compressor and turbine wheels within the material limits
- The lowest structural eigenfrequency sufficiently higher than the rotational speed
- Minimized net axial force on the bearings

The in-house tool DoEpar, paired with ANSYS DesignXplorer, was employed to generate design tests spanning over the delimited design space. Three-dimensional CFD simulations were performed in ANSYS CFX for the evaluation of the aerodynamic performance of each design. In order to represent the working fluid accurately, the working medium was represented by a real gas model whose thermodynamic properties were specified with the in-house tool RGPgen. The aerodynamic evaluations were complemented by stress analysis in ANSYS Mechanical.

Computational geometry and mesh

The computational geometry comprises a radial compressor stage, a radial turbine stage and an interconnecting leakage flow channel with radial and one axial labyrinth seal. The compressor stage consists of an impeller with 9 main blades and 9 splitter blades, a bladeless diffusor and a volute. The turbine stage features a volute, a confusor with 31 blades and a rotor with 36 blades. The shroud-tip clearance is included for both wheels and the turbine blades incorporate a single-cavity squealer tip design. The computational domain is shown in Figure 3.

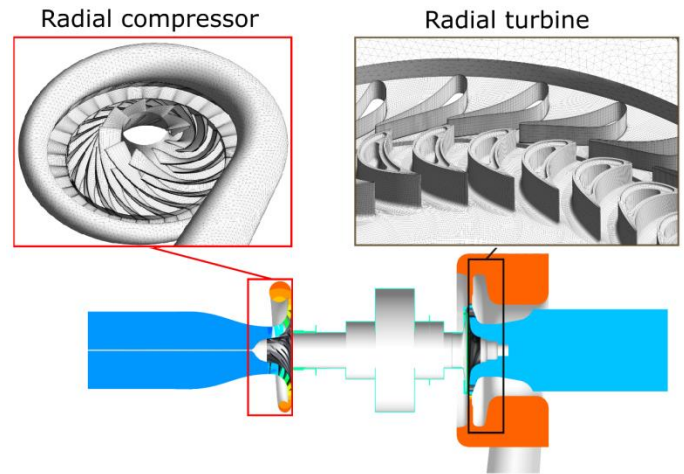


Figure 3: Compander geometry and mesh (static pressure contours)

The simulation of the complete compander featuring both stages and the leakage flow channel imposes high requirements on computational resources. In order to facilitate running a large number of evaluations within a reasonable amount of time, the computational costs needed to be reduced as much as possible while maintaining the high fidelity of the model. The computational domain was therefore reduced to a single passage

per blade row and the mixing-plane approach was employed for the interfaces. Once the optimization procedure was finished, the final design was verified with a whole annulus model. The computational efficiency was also aided by the use of multiblock structured meshes where possible, generated in ANSYS TurboGrid. Only the two volutes were discretized with unstructured tetrahedral meshes created in ANSYS ICEM, as the complexity of structured mesh generation would in their case outweigh the computational benefits. The complete mesh for the whole annulus simulations comprised 30.1 million cells. The number of elements and nodes per each part of the computational domain is listed in Table 3.

Table 3: Mesh overview

Component	Mesh type	Nodes ($\times 10^6$)	Elements ($\times 10^6$)
Compressor inlet	Hexa	0.16	0.14
Compressor wheel and diffuser	Hexa	1.83	1.62
Compressor volute	Tetra	0.093	0.33
Leakage flow passage	Hexa	20.16	18.02
Turbine volute	Tetra	0.16	0.53
Turbine wheel and confusor	Hexa	9.94	9.25
Turbine outlet	Hexa	0.24	0.22
Total		32.58	30.12

Flow solver and boundary conditions

The results presented in this study were obtained with whole-annulus computations performed in ANSYS CFX. A steady-state approach with a frozen-rotor treatment of interfaces between stationary and rotating components was employed, allowing resolving circumferential nonuniformities at reasonable computational costs. The working fluid was modelled as a continuous mixture of real gases, representing CO₂ in liquid and supercritical states. The fluid properties were defined by tables generated with RGPgen. The computational model was based on RANS equations with the SST turbulence model and wall functions. The turbine operating conditions were defined by imposing total quantities at the inlet and static pressure at the outlet, while the total inlet quantities and the outlet mass-flow were specified for the compressor. Both the compressor and the turbine operate with the same shaft speed of 68000 RPM. An overview of the boundary conditions is given in Table 4.

Table 4: Boundary conditions

	Compressor	Turbine
Rotational speed	68 000rpm	68000rpm
Pressure inlet	8MPa	24MPa
Pressure outlet	-	8.5MPa
Temperature inlet	30 °C	550 °C
Mass flow	20.9kg/s	-

Results and Discussion

The flow simulation of the compander including the compressor stage, the turbine stage and the interconnecting leakage flow channel was successfully completed. The global parameters characterizing the performance of both stages are shown in Table 5.

Table 5: Calculated performance parameters

	Compressor	Turbine
Mass flow rate	20.9 kg/s	6.19 kg/s
Total to Total efficiency	78.33%	78.79%
Pressure ratio	3.19	2.81
Axial force	-2.26 kN	2.37 kN

The compressor operated with a total-to-total efficiency of 78.33%, while the value of $\eta_{T2T}=78.79\%$ was achieved for the turbine. Notable is the good balance between turbine and compressor axial forces with the net sum of 110 N. The imposed axial load on bearings is thus minimized, allowing to reduce their size.

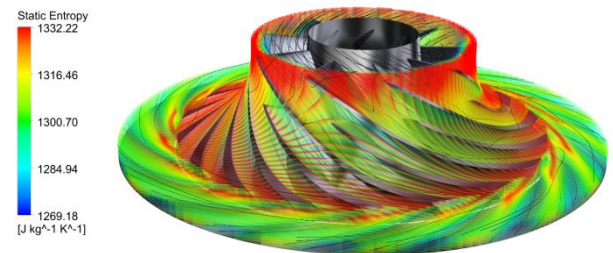


Figure 4: Compressor entropy and streamlines visualization

A visualization of the impeller and bladeless diffuser flow is provided in Figure 4, using three-dimensional entropy contours and streamlines. The high entropy regions cover the entire shroud of the impeller and extend partially also along the diffuser shroud. Here the circumferentially varying signature of blade wakes is captured thanks to the whole-annulus frozen rotor approach adopted in the simulation. Several streamlines mark the tip leakage flow, crossing across the blade tips through the tip clearance, in some cases over multiple blade passages.

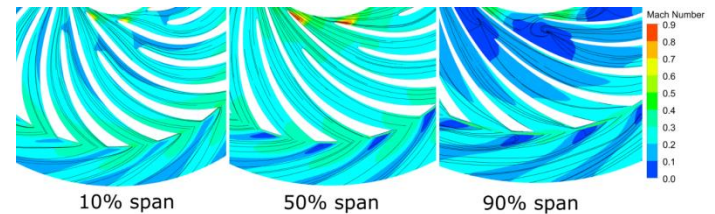


Figure 5: Compressor Mach number contours and streamlines in B2B planes

A more detailed insight can be obtained with the use of relative Mach number plots in blade-to-blade planes, as visualized in Figure 5 for the 10%, 50%, and 90% span. The flow enters the impeller with an average Mach number 0.38 and remains

subsonic in the whole stage, although nearly sonic pockets appear along the leading edges (LE) of the main blades. The maximum Mach number 0.93 is reached near the LE in the midspan cut. In the 10% and 50% cuts, the flow remains well attached to both the main and splitter blades with no signs of separation. The 90% cut reveals vortex regions forming between every two main blades upstream of the splitter LE. The diffuser flow is in all of the depicted cuts characterized by distinct wakes extending downstream of the impeller blades.

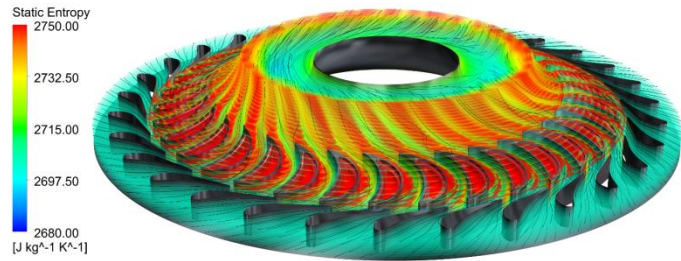


Figure 6: Turbine entropy and streamlines visualization

The visualization of three-dimensional entropy contours and streamlines is provided also for the turbine confuser and rotor in Figure 6. The stator flow is characterized by a relatively homogeneous entropy distribution. Strong entropy generation occurs due to the tip leakage flows in the rotor blade cavities and during the consequent mixing of the tip leakage vortex with the passage flow. The high entropy regions remain attached to the shroud even downstream of the rotor blades, whereas the lower span flow retains less elevated entropy levels.

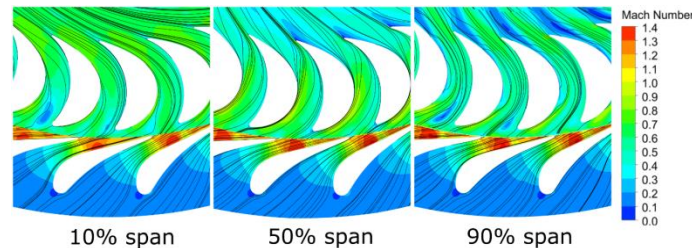


Figure 7: Turbine Mach number contours and streamlines in B2B planes

As shown in Figure 7 by means of the blade-to-blade relative Mach number contours, the stator flow is transonic with the highest Mach value of 1.43. The stage is characterized by a low degree of reaction, hence the flow entering the rotor blade row with a relative Mach number 0.58 is not subjected to further acceleration. The 10% span cut shows a well attached flow, but mild separation appears in the rotor trailing edge region at midspan. A distinct low Mach number region is detected at 90% span near the aft part of rotor blade suction side, marking the presence of the tip leakage vortex.

GAS BOILER

The required maximum heat supply to the cycle was set to 6 MW. As the required power is relatively high, it is not possible to feed the facility with electricity. Therefore, a gas boiler was identified as the only possible solution. The boiler as the only source of heat has to assure the heating of sCO₂ up to 550°C. It has to be able to operate with a wide range of thermal power. The boiler is expected to be one of the components enabling to reach the supercritical conditions during the start-up procedure.

The design parameters and specific behavior of sCO₂ don't allow using a membrane boiler with simultaneous usage of standard materials. The main reason is relatively low heat transfer coefficient on the sCO₂ side in comparison with water. The selected design considers the lining boiler with a tube heat exchanger. Even in this composition, usage of the most common materials like T91 or T92 for the heat exchanger is not allowed and thus the chosen material is 304H Stainless Steel.

The temperature of sCO₂ at the inlet of the boiler reaches in nominal operation 320 °C. It significantly increases chimney heat loss. For that reason, the boiler is equipped with an economizer and the waste heat is used to heat up the technical water used for heating of adjacent buildings.

The overall dimensions and other parameters are listed in table 5.

Table 5: Design parameters of the boiler

Design pressure	26.5 MPa
Nominal Pressure	25 MPa
Design temperature	565 °C
Nominal inlet temperature	320 °C
Nominal outlet temperature	550 °C
Nominal CO ₂ mass flow rate	22 kg/s
Heat power of ignition burner	100 kW
Maximum heating power supplied to sCO ₂	6000 kW
Total heating power	6850 kW

POWER TURBINE

As already mentioned in the previous chapters, the power turbine is designed as the axial one. The main reason was the further focus on the units with higher electrical power. The required similarity with the final application also helped to decide on the overall concept of the machine.

The turbine workspace is created by 5 axial stages with the blade length starting at four millimeters. The rotor of the turbine is equipped with two dry gas seals and is supported by common oil-lubricated slide bearings. The whole turbine is placed directly on the gearbox. The nominal speed of the turbine was set to 20 000 rpm. The main design parameters are summarized in Table 6. The 3D layout is visualized in Figure 8.

Table 6: Design parameters of the power turbine

Design pressure	26.5 MPa
Nominal pressure inlet	25 MPa
Nominal pressure outlet	8.5 MPa
Nominal mass flow rate	13 kg/s
Nominal inlet temperature	550 °C
Inlet temperature range	20-40 °C
Nominal power of the turbine	1050 kW
Nominal speed	20 000 rpm
Number of blade stages	5

The power turbine including the gearbox and electrical generator is being designed and will be supplied by Doosan Škoda Power [16].

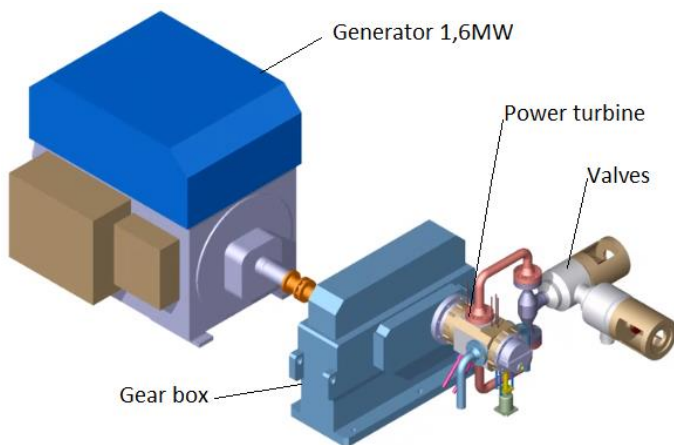


Figure 8: Assembly of power turbine, gear box and electrical generator

As the power turbine is equipped with dry gas seals, its operation is connected with the sCO₂ leakage. The leaks escape at two different pressure levels. The first leakage is created by pure CO₂ and on the pressure less than 5 bar. As the mass flow is relatively high, it is boosted by a specially modified piston compressor back to the cycle. The second leakage escapes at almost atmospheric pressure level and it is mixed with air. For this reason, it is led by the exhaust system out of the experimental hall.

PRESSURIZER

The pressurizer has in this case two main functions. It of course supports the possibility of the setup of required pressure on the low-pressure side of the cycle. At the same time, it avoids the need of releasing the CO₂ content out of the cycle in case of initial overfill and the need for fast boosting of CO₂ into the cycle. The second function is the storage of the CO₂ during the shutdown period. The overall internal volume of the cycle is a preliminary estimate to 1.5 cubic meters whilst the content of sCO₂ will be about 400 kg. According to Figure 1, the pressurizer will be connected to the circuit between the main cooler and compressor inlet. The design pressure of the vessel

was set to 10 MPa with a total volume of 600 l. Under the ambient temperature of about 20 °C, the pressurizer is able to accumulate whole CO₂ content in the liquid phase during the outage period.

The design temperature of this component is 100 °C. Thus most of the CO₂ content can be released to the circuit during the cycle operation.

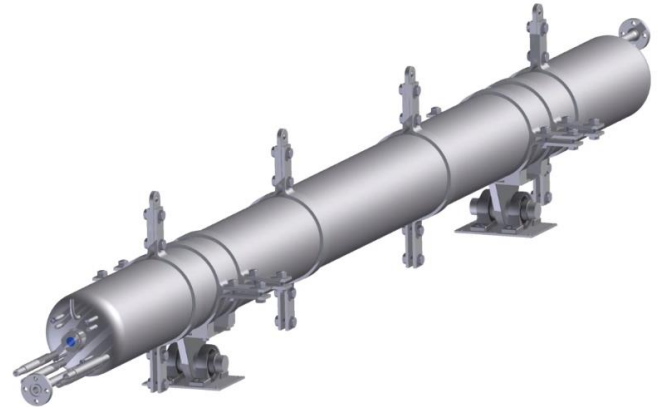


Figure 9: 3d model of the pressurizer

According to the described functions, there is a need for temperature control inside the vessel. It is equipped with a set of heating rods with a total thermal power of 12 kW to be able to increase the internal temperature sufficiently fast. The pressurizer is further equipped with two independent cooling systems. The first one uses cooling water from the main cooling system and it is used during normal operation of the system. The second cooling system acts for conditioning the pressure during the shutdown period. The cooling power of this system is about 2 kW and solves mainly to cover the heat loss. Its main purpose is to prevent overpressure and opening of the safety valve, which is of course present.

Last but not least sense of the pressurizer is enabling testing of the cycle power control using sliding pressure regulation. The pressurizer is shown in Figure 9.

RECUPERATIVE HEAT EXCHANGERS

Heat exchangers for the sCO₂ cycles have been already widely investigated [17]. To achieve good efficiency the cycle needs to be highly regenerative. Due to relatively high thermal power and low convective heat transfer, the heat transfer area needs to be large while pressure loss should be as low as possible. Taking into account high pressure and temperature, the use of compact heat exchangers seems to be the most suitable option. The best example is the utilization of printed circuit heat exchangers (PCHE) it the most famous experimental unites developed by Sandia National Laboratories and Echogen [18]. Despite the expanding implementation of compact heat exchangers and the growth of competition in this industry, the prices of PCHX are still very high.

Another possibility could be a fin and plate heat exchanger. This HX technology is widely used for low-temperature applications, but during the last years, a lot of effort is paid to the development of high temperature and high-pressure heat exchangers of this type as well [5]. Once the fin and plate HX is able to deal with challenging parameters commonly used in the sCO₂ cycles, it will be a very good compromise between the price and performance.

COOLING SYSTEM

There are two coolers in the circuit. The first stage cooling is ensured by heating water and it cools down the CO₂ to a temperature of about 70°C. The water is heated up to 105°C and the heat is further used for heating of the adjacent buildings. The second stage of cooling is ensured by raw water from the river Vltava. It is important to mention that the system is expected to be operated during the heating period only. During this period, the river water temperature fluctuates between 5 and 15 °C. There is a temperature limit of 26 °C for the released cooling water, which is pumped back to the river. The temperature is sufficiently low so there is no fear about the cooling ability. On the other hand, it can cause undesirable undercooling. The system is currently being designed and this risk is taken into account.

The coolers will be in the form of partly brazed plate type heat exchangers with the optional number of plates. The filtered cooling water will be pumped from the underground storage vessel by two pumps, each of the power of about 30kW.

CONCLUSIONS AND FURTHER ACTIVITIES

The large scale experimental facility SOFIA intended for demonstration of the sCO₂ cycle and its components are being realized in the frame of the sCO₂-Efekt project at CVR. The feasibility, conceptual study, and basic design were finished at the end of the year 2020. The layout of the circuit as well as design parameters is presented. Moreover, the individual components of the circuit are described in detail including basic design analyses and features.

In the next phase, the detailed design will be finished (the year 2021) and fabrication of the Sofia experimental facility will start. The power turbine, compander, and gas boiler will be manufactured and assembled separately. According to the project planning the whole SOFIA facility will be assembled at the end of 2022. The following phase will be dedicated to the testing of the developed component and overall cycle performance verification. These activities will be carried out within the sCO₂-Efekt project, which ends in October 2023. The preliminary 3D model of the Sofia facility except the cooling system is shown in Figure 10. It is expected that further extension of the experimental facility to the recompression cycle will be carried out within follow-up projects. At the same time, a large -scale heat storage tank of relevant thermal storage capacity should be finished and connected to the sCO₂ facility. These follow-up activities are preliminarily scheduled for 2025.

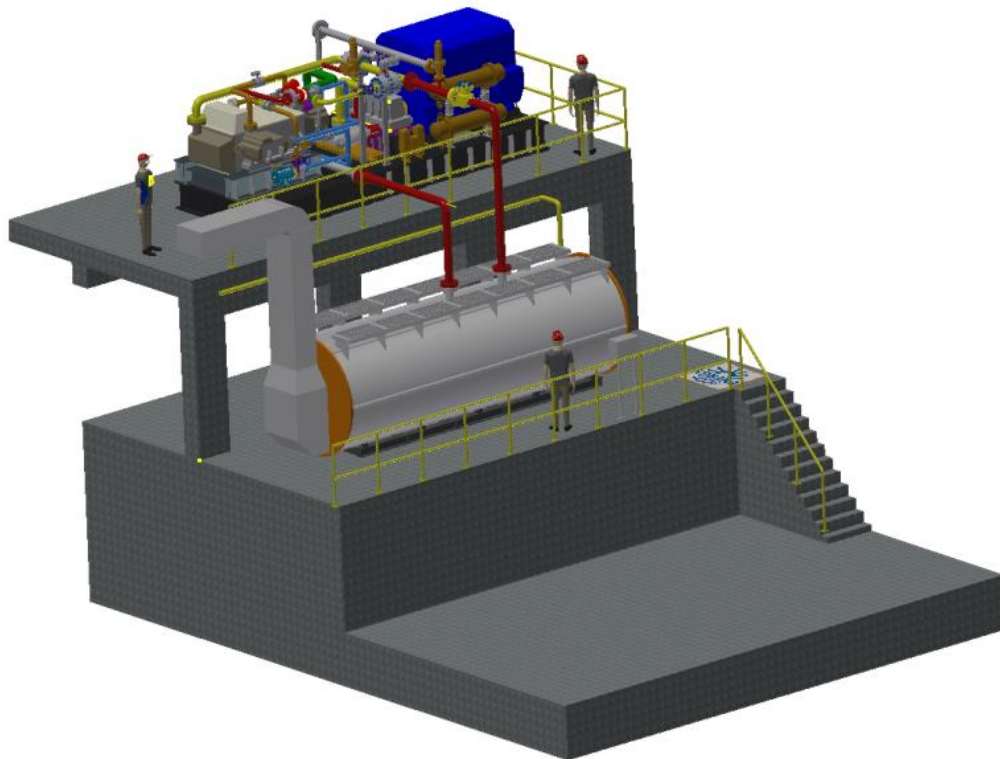


Figure 10: preliminary 3d model of Sofia facility

NOMENCLATURE

B2B	Blade to Blade
CFD	Computational Fluid Dynamics
CVR	Research Centre Rez
FEM	Finite Elements Method
LE	Leading Edge
P2H2P	Power to Heat to Power
PID	Process Instrumentation Diagram
RANS	Reynolds-Averaged Navier-Stokes
RPM	Revolutions per Minute
sCO ₂	Supercritical Carbon Dioxide
SST	Shear Stress Transport
PCHE	Printed Circuit Heat Exchanger
HX	Heat Exchanger

ACKNOWLEDGEMENTS

This work was supported by TACR THETA2, project no. TK02030059 (Efekt).

REFERENCES

- [1] Dumont, O., et al.: Carnot battery technology: A state-of-the-art review, *Journal of Energy Storage*, Volume 32, December 2020, 101756
- [2] Melichar, T., et al.: Thermal design of latent heat thermal energy storage facility with supercritical CO₂, The 4th European sCO₂ Conference for Energy Systems (this conference)
- [3] Vojacek, A., Dostal, V., Goettelt, F., Rohde, M., and Melichar, T. (2019). Performance Test of the Air-Cooled Finned-Tube Supercritical CO₂ Sink Heat Exchanger. *ASME. J. Thermal Sci. Eng. Appl.* June 2019; 11(3): 031014. <https://doi.org/10.1115/1.4041686>
- [4] H2020 sCO₂-HeRo project, <http://www.sco2-hero.eu/>
- [5] H2020 sCO₂-FLEX project, <https://www.sco2-flex.eu/>
- [6] Flaig W., Mertz R., Starflinger J.: Setup of the Supercritical CO₂ Test Facility 'SCARLETT' for Basic Experimental Investigations of a Compact Heat Exchanger for an Innovative Decay Heat Removal System, *Journal of Nuclear Engineering and Radiation Science* 4 (3), 2018
- [7] H2020 SCARABEUS project, <https://www.scarabeusproject.eu/>
- [8] A. Hacks et al., operational experiences and design of the sco2-hero loop, 3rd European supercritical CO₂ Conference, 2019, Paris, France.
- [9] J. Pasch, T. Conboy, D. Fleming, G. Rochau: Supercritical CO₂ Recompression Brayton Cycle: Completed Assembly Description. Sandia report SAND2012-9546, 2012.
- [10] J. Lewis, E. Clementoni, T. Cox: Effect of Compressor Inlet Temperature on Cycle Performance for a Supercritical Carbon Dioxide Brayton Cycle. The 6th International Supercritical CO₂ Power Cycles Symposium, 2018.
- [11] 10 MW Supercritical CO₂ Turbine Test project Final Report, 2013 (<https://www.osti.gov/servlets/purl/1117025/>)
- [12] J. Moore, S. Cich, M. Day, T. Allison, J. Wade: Commissioning of a 1 MWe Supercritical CO₂ Test Loop. The

6th International Supercritical CO₂ Power Cycles Symposium, 2018.

- [13] Utamura, M, Hasuike, H, Ogawa, K, Yamamoto, T, Fukushima, T, Watanabe, T, & Himeno, T. "Demonstration of Supercritical CO₂ Closed Regenerative Brayton Cycle in a Bench Scale Experiment." *Proceedings of the ASME Turbo Expo 2012: Turbine Technical Conference and Exposition. Volume 3: Cycle Innovations; Education; Electric Power; Fans and Blowers; Industrial and Cogeneration.* Copenhagen, Denmark. June 11–15, 2012. pp. 155-164. ASME
- [14] Fundamentals and Applications of Supercritical Carbon Dioxide (sCO₂) Based Power Cycles 1st Edition, Woodhead Publishing Series in Energy, 2017. Edited by K. Brun, P. Friedman, R. Dennis.
- [15] Sobriety s.r.o., <https://www.sobriety.cz/en/>
- [16] Doosan Škoda Power s.r.o., <http://www.doosanskodapower.com/en/>.
- [17] V. Dostal, M.J. Driscoll, P. Hejzlar, (2004): A Supercritical Carbon Dioxide Cycle for Next Generation Nuclear Reactors, (MSc. Thesis, MIT)
- [18] Brun, K., Friedman, P., Dennis, R., (2017): Fundamentals and Application of Supercritical Carbon Dioxide (sCO₂) Based Power Cycles, Woodhead Publishing Series in Energy, (book)

ENVIRONMENTAL ASSESSMENT OF A 25 MWE FOSSIL-FIRED SUPERCRITICAL CO₂ CYCLE

Victor MAQUART
Armines
Sophia Antipolis, France

Benoît VALENTIN*
EDF R&D
Chatou, France
Email: benoit.valentin@edf.fr

Albannie CAGNAC
EDF R&D
Chatou, France

ABSTRACT

In a global effort to decrease human-sourced Greenhouse-Gas (GHG) emissions, the operation of GHG-emitting plants is only justified if they offer a sufficient flexibility to satisfy a highly variable net electric demand in electric grids with a significant share of intermittent renewable power plants. The EU-funded project sCO₂-Flex aims at designing a highly flexible 25-MWe supercritical CO₂ cycle suitable for such a complementarity with renewable energies, and testing its main components. However the performance of such a cycle should not be reached at the expense of its environmental impact. Therefore the present paper focuses on the analysis of the environmental impact of such a plant, following most of the guidelines of the Life Cycle Assessment (LCA) method, as described in the ISO 14040-14044 standards.

The assessment described in this paper was conducted on the open source software OpenLCA using the database Ecoinvent, both acknowledged by the LCA community. It encompasses four major steps: goal and scope definition of the project, inventory analysis of the data, impact analysis and interpretation. Data was picked directly from the Ecoinvent database, gathered from the project's contributors, or extrapolated from hypotheses if data was to be missing in the inventory analysis. To compensate the uncertainties due to lack of data on equipment scaling and operation practices, an extensive sensitivity analysis has been carried out to bring additional robustness to the study.

Considering the two impact categories selected in this paper (global warming potential at 100 years scope and abiotic resource depletion), the sCO₂-Flex plant outperforms the

reference water/steam plant for global warming potential thanks to its higher efficiency. This is however at the expense of a considerably higher abiotic resource depletion. Regarding the latter impact category, the most significant uncertainties arise from the amount of nickel-based-alloys used in the boiler.

INTRODUCTION

Supercritical CO₂ Brayton cycles attract wide interest due to their increased compactness as compared to steam Rankine cycles. This compactness is expected to translate into gains in flexibility (start-up time and consumption, part-load efficiency, transient speed...) and costs, and is likely to come together with an increased nominal cycle efficiency. Those two major advantages are to be checked in the project sCO₂-Flex [1,2], by achieving the detailed design of a 25 MWe coal-fired supercritical CO₂ cycle.

While flexibility is key to a good complementarity with variable renewable energies, improvements in efficiency and compactness should make a plant more environmentally benign than the current state of the art, that is, steam Rankine cycles. However, the overall environmental impact of a plant depends on a variety of parameters (fuel consumption, quantity and quality of materials used, dispatch strategy...) at different stages of the plant's life (construction, operation, decommissioning). That is why the present study follows, whenever possible, the guidelines of Life Cycle Assessment as described in standards ISO 14040 and 14044 [3,4]. It should be mentioned that this study cannot, strictly speaking, be considered a valid Life Cycle Assessment, as no critical review has been carried on to date.

* corresponding author(s)

The literature is quite abundant regarding the Life Cycle Assessment of coal power plants, however a vast majority of studies focus on greenhouse gas emissions only and are difficult to compare due to very different assumptions. The World Energy Council [5] and Turconi et al. [6] compiled data about the emissions to air of all power production technologies. Whitaker et al. [7] screened publications about greenhouse gas emissions of coal-fired power plants and harmonized their results for a better comparison in spite of different assumptions. Weisser [8] provided guidelines for the Life Cycle Analysis of power production technologies. In particular, this publication identified the main parameters affecting the results: contrary to other types of power plants, the lifetime emissions of coal plants are significantly dependent on the type of fuel burnt and the extraction practices. Finally, Mills [9] investigated the suitability of life cycle assessment methods for the comparison of different coal power plant technologies and focused on the emissions during both combustion and non-combustion stages of the plant's life.

METHOD

Scope of the study

As usual in Life Cycle Assessment, all inputs and outputs are normalized by a reference unit, which is usually the main product delivered by the process analyzed. In the case of the sCO₂-Flex plant, it is the average kWh delivered to the Czech grid, as the boiler was designed for a Czech coal. Due to that choice, the results for the sCO₂-Flex plant are compared to an average coal-based Czech kWh. The analysis is restricted to the construction of equipment, landscaping, fuel treatment and supply as well as maintenance and power plant operation.

Because of the multiple uncertainties about the project development and its end of life policy, it was assumed that neither the ashes nor the buildings were recycled. This is a conservative assumption, and its consequences are discussed further at the end of this paper.

Reference plant's description

In coherence with the reference unit chosen, the reference to which the environmental impact of the sCO₂-Flex plant is to be compared is an average existing Czech coal power plant, taken from the database Ecoinvent v3.6 [10]. That plant involves a steam cycle, and its performances result from the average of Czech Republic's installed coal power plants. Its main features are presented in Table 1.

The reference plant does not physically exist: it is a model built by Ecoinvent, using data from several Czech plants, in order to reflect the average environmental impact of the Czech coal power plants.

Table 1: Reference plant's main features [11]

Assumption	Value	Unit
Dispatch strategy	5800	h/year
Plant life time	26	years
Plant average yearly efficiency	33.3	%
Plant gross output at full load	> 250	MWe

It should be highlighted that the benchmark plant is significantly bigger (> 250 MW vs. 25 MW) and older (26 years old in 2007 vs. state-of-the-art) than the sCO₂-Flex plant. While being bigger is a considerable advantage in terms of efficiency, being older involves a penalty in performance. The meaning of these differences is discussed in the interpretation section.

sCO₂-Flex plant performance assumptions

In order to determine the number of kWh produced over all the plant's lifetime (with a direct impact on the construction phase's importance) and the amount of coal needed (which is of importance for the exploitation phase), it is necessary to make major assumptions on the way the plant will be used. They are summarized in Table 2. Both plants do not have the exact same dispatch strategy: the lifetime of the sCO₂-Flex plant was set to 30 years and its annual number of hours equivalent full-load was adjusted so as to match the total number of running hours over the reference plant's lifetime. As a result, both plants are assumed to produce power for 150000 hours equivalent full-load, which allows a fair comparison.

Table 2: Main assumptions on the plant's dispatch and performance.

Assumption	Value	Unit
Dispatch strategy	5000	h/year
Plant life time	30	years
Plant yearly efficiency	36.4	%
Plant gross output at full load	25	MWe
Plant net output at full load	23.3	MWe

The first annual simulations of the plant, which correspond to a work still in progress, indicate that on the Czech market, a higher capacity factor can be reached. That aspect is treated in a dedicated sensitivity study at the end of this paper. The yearly efficiency was estimated using the assumptions of Table 3.

Table 3: Main assumptions for the calculation of sCO₂-Flex plant's yearly efficiency

Assumption	Value	Unit
Cycle gross efficiency	42.3	%
Boiler LHV efficiency	92.5	%
Yearly number of start-ups	30	-
Energy penalty for a start-up	20	MWhth
Overall auxiliary consumption & losses	1.720	MWe

The plant burns Bilina-HP1 coal [2], whose ash-free chemical composition on a molar basis is C: 37.85%, H: 34.81%, O: 9.16%, N: 0.40%, S: 0.25%, H₂O: 17.53% with a LHV equal to 16.9 MJ/kg.

Selection of the impact categories and impact assessment methods

In the life cycle assessment method, the role of the impact categories is to identify the different damages on environment and human health that result from the product's use during its whole life cycle. The impact assessment methods that convert inventory results (that is, flows of mass or energy in or out of the process) into environmental impacts are regularly updated. Though not the most recent one, ILCD 2016 [12] is still the most widely used in the Life Cycle Assessment community. All the selected impact categories used in the study were estimated using that method.

As the present study aims at having results that are as general as possible, the effects on human health and ecosystem quality are not in the scope of this assessment. They are considered too sensitive either to the type of coal burnt in the plant or to the precise location of the plant. That leaves two indicators on which sCO₂-Flex power plant is compared to average Czech power plants:

- GHG emissions are widely considered the main issue concerning coal plants. Their impact is assessed using the Global Warming Potential (GWP) on 100 years of each greenhouse gas documented in the IPCC climate change synthesis report [13]. GWP is expressed in kg CO₂ equivalent (kg CO₂-eq).
- To be sustainable, one must avoid using too much rare materials for the construction of the plant. The depletion of resources is evaluated by the Abiotic Resource Depletion (ARD) [14]. In this indicator, the contribution of each material corresponds to the ratio between its mass consumption by the process and the square of its global reserve, normalized by the same ratio for antimony (Sb),

which is taken as the reference material. This results in an indicator measured in kg Sb equivalent (kg Sb-eq).

Description of the model

This study was carried out using OpenLCA v1.10 [15] with the database Ecoinvent v3.6 [10].

As mentioned above, the major steps considered in the environmental assessment are the following:

1. The sCO₂-Flex power plant construction, divided in the present study into two sub steps:

- The elements of the thermodynamic cycle: the boiler, the turbine, the two compressors, the high temperature recuperator, the low temperature recuperator, the pipework, the cooling equipment;
- The generic elements of the mechanical structure, of the coal supply chain at the plant, the instrumentation, the inventory management and the flue gas treatment;

For each element of the thermodynamic cycle, a dedicated process was created to model its production taking as inputs the resources (most of the time, specific alloys not available in the Ecoinvent database, whose production was modelled by creating a specific sub process), and energy use. The transport of the assembled equipment to the plant was then modelled using generic goods transport process data.

Concerning the generic elements of the plant's structure, due to a lack of data at this stage of the project the choice was set on extrapolating them linearly with regards to installed capacity from a batch of hard coal-fueled power plants available in the Ecoinvent database (100MW and 500MW).

Because of the limited data on different installed capacities for hard coal power plants available in Ecoinvent to carry out the linear regression, this aspect is subject to a sensitivity analysis at the end of this article.

2. The fuel supply chain, which encompasses the extraction of hard coal, its transport and preparation. The coal is supposed to come from the European market (well-documented in Ecoinvent) and is either extracted from underground or surface mines then prepared to be used as a fuel for the plant. It is finally transported by truck, boat or train. Once delivered to the plant, the coal is stored.

3. The operation of the plant for electricity production. This phase encompasses several sub-steps:

- Coal combustion in the boiler
- Electricity production by expansion of the CO₂ in the turbine
- Flue gas treatment
- Collection and treatment of ashes from the combustion.

The diagrams summing up the different processes and their arrangement in the OpenLCA process tree are shown in

Annexes A to D. All the processes whose name begins with “Market”, concerning hard coal supply or electricity supply are directly taken from the Ecoinvent database; the others concerning the manufacturing of sCO₂-flex’s specific equipment were created manually.

Origin of the input data

The generic data concerning the coal supply network was taken from the database Ecoinvent v3.6, in particular the fluxes that involve:

- The processes of the coal supply chain (extraction, preparation and road haul);
- The transport of equipment from their factory to the location of the plant. For this item, typical values of road haul in Europe were taken, as well as the latest criteria of environmental regulation concerning heavy goods vehicles;
- The construction of structural works and generic equipment relative to fossil-fueled plants (chimney, dedusting filters and desulfuration tower). Because of the lack of data concerning these generic equipments at this stage of the project, the data was estimated by linear extrapolation on nameplate power (ranging from 100 to 500 MWe), from power plants documented in Ecoinvent.

RESULTS

The inventory results are summarized in Table 4 to Table 7 (emissions to air, emissions to water, consumption of fossil fuels, consumption of metals). From those impacts, the two selected impact categories (GWP and ARD) are defined by gathering and pondering the input and output fluxes depending on their potential effect on environment. The overall impact results are shown in Table 8. They are systematically normalized to the reference unit, that is 1 kWh delivered to the Czech grid.

Table 4 - Summary of the emissions to air

	sCO ₂ -Flex	Average Czech coal plant	Unit
CO ₂	1,03	1,09	kg/kWh
N ₂ O	1,62E-05	1,45E-05	kg/kWh
SF ₆	4,25E-09	3,40E-09	kg/kWh
SO _x	1,47E-03	1,21E-03	kg/kWh
NO _x	2,77E-03	2,68E-03	kg/kWh
Particles	2,78E-03	2,32E-03	kg/kWh
VOC	1,58E-04	1,27E-04	kg/kWh
Arsenic	3,07E-08	2,14E-08	kg/kWh
Cadmium	8,80E-09	6,05E-09	kg/kWh
Chromium	3,20E-07	1,79E-07	kg/kWh
Copper	1,78E-07	9,89E-08	kg/kWh
Lead	1,47E-07	1,18E-07	kg/kWh
Mercury	2,07E-08	2,11E-08	kg/kWh
Nickel	3,26E-07	2,22E-07	kg/kWh
Zinc	1,75E-07	1,35E-07	kg/kWh

Table 5 - Summary of the emissions to water

	sCO ₂ -Flex	Average Czech coal plant	Unit
Arsenic	8,03	7,03	mg/kWh
Cadmium	0,67	0,48	mg/kWh
Chrome	9,10	6,93	mg/kWh
Copper	40,9	18,6	mg/kWh
Lead	6,27	2,40	mg/kWh
Mercury	0,203	0,163	mg/kWh
Nickel	74,3	55,4	mg/kWh
Zinc	89,4	70,3	mg/kWh

Table 6 - Summary of the fossil fuel consumption

	sCO ₂ -Flex	Average Czech coal plant	Unit
Oil	10,8	15,2	g/kWh
Lignite	4,78	6,80	g/kWh
Coal	457	672	g/kWh
Gas	3,94E-03	1,18E-02	Nm ³ /kWh
Uranium	1,70E-04	2,43E-04	g/kWh

Table 7 - Summary of the metal consumption

	sCO ₂ -Flex	Average Czech coal plant	Unit
Aluminium	69,6	86,3	mg/kWh
Chromium	44,0	35,2	mg/kWh
Copper	117	30,7	mg/kWh
Iron	2930	3300	mg/kWh
Nickel	130	26,4	mg/kWh
Water	0,266	0,370	m ³ /kWh

Table 8: Impact results for the two selected categories

Impact category - indicator	Value sCO ₂ -Flex (unit)	Value average Czech plant (unit)
Climate change – GWP 100a	1.123 (kg CO ₂ -Eq per kWh)	1,168 (kg CO ₂ -Eq per kWh)
Resources - mineral, fossils and renewables	2.202E-06 (kg Sb-Eq per kWh)	9,71E-07 (kg Sb-Eq per kWh)

A more detailed comparison, over all three phases of the plants’ life cycles, is shown on Figure 1 for GWP. On that criterion, the sCO₂-Flex plant has a lesser impact. The construction phase can be considered negligible in GWP, while the operation phase produces the major part of the GHG emissions.

The total impacts results for the ARD impact category are displayed in Figure 2. On this criterion, the phase of plant operation has a very marginal impact. This impact category is dominated by the fuel supply phase, and in the case of the sCO₂-Flex plant, the construction phase. Here the sCO₂-Flex

plant appears to have a significantly higher impact than the average Czech plant used as a reference.

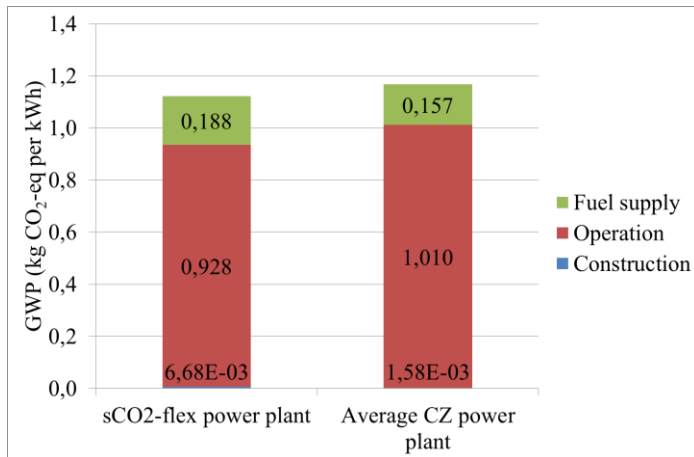


Figure 1: Detailed impact results for the GWP category

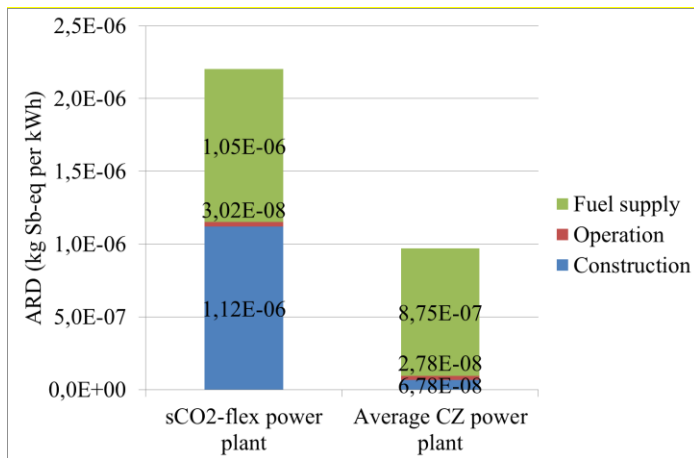


Figure 2: Detailed impact results for the ARD category

INTERPRETATION AND SENSITIVITY ANALYSIS

The main results presented above show that the sCO₂-Flex plant can be expected to outperform most Czech plants in GHG emissions abatement but will need more mineral resources for its construction. While the result on GWP could be challenged by a sensitivity study, there is no such debate on ARD.

It must however be noticed that ARD is usually a bigger issue for renewable energies than for fossil-fueled plants, as renewable energies, in spite of their very low GWP, exhibit a considerable consumption of non-renewable materials. A comparison of the sCO₂-Flex plant with world average PV and wind plants is provided on Figure 3. While the plant designed in sCO₂-Flex has a higher ARD than average wind power, it still performs significantly better than PV on that account.

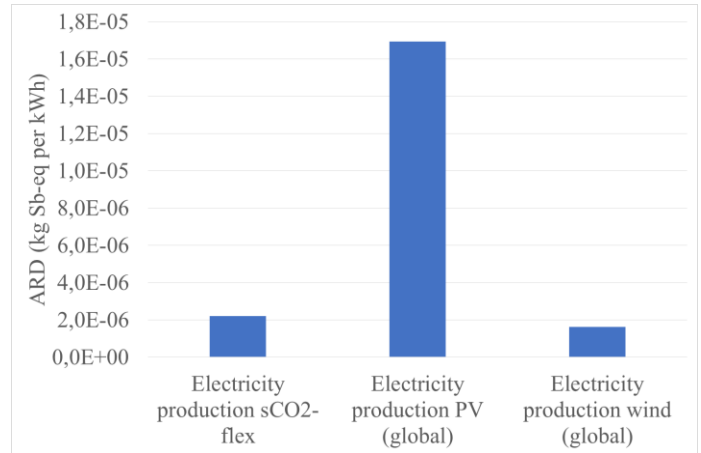


Figure 3: Comparison of sCO₂-Flex plant's ARD with common renewable energies

The fraction of nickel-based alloys in the boiler (which is the major element of the plant responsible for the ARD, see Figure 4) is a major stake both for environmental impact and for costs, and may still decrease, thus improving the plant's environmental impact. Conversely, the share of nickel-based alloys may still increase further if higher temperatures and efficiencies are sought. A sensitivity study is therefore dedicated to the share of nickel-based alloys in the boiler.

As can be seen on Figure 4, the share of nickel-based alloys in the boiler has a major influence on the overall ARD impact of the plant. When changing from 51% (which corresponds to the current knowledge of sCO₂-Flex plant's design) to 100%, the impact on ARD due to nickel-based alloys nearly doubles, while the impact due to iron-based alloys decreases by a similar factor. The overall impact increases significantly.

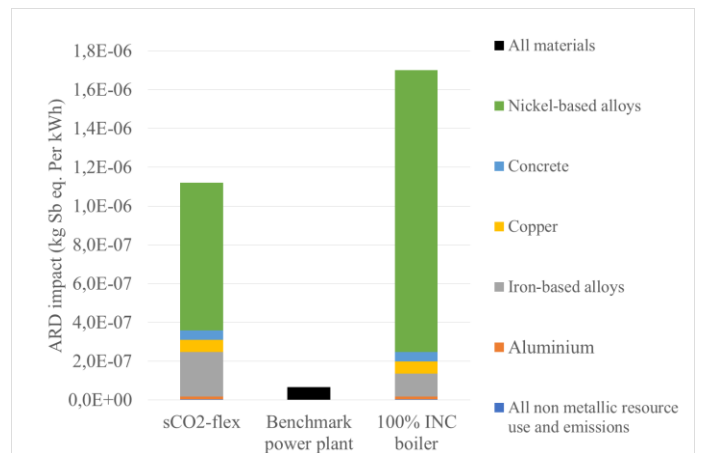


Figure 4: ARD impact on the construction phase split by material, with a sensitivity study on the share of Nickel-based alloys in the boiler

It must also be observed that even without including the effect of nickel-based alloys, the sCO₂-Flex plant has a

significantly higher ARD than the benchmark plant. That may be due to the fact that apart from the major equipments of the supercritical plant, the construction materials were extrapolated linearly from data available for much bigger plants (100 and 500 MWe outputs) and the need for construction materials is likely to have been widely overestimated in the process. Another plausible cause is that the iron-based alloys used in the sCO₂-Flex boiler are still high-alloyed steels, with a strong impact on ARD (though not so strong as nickel-based alloys).

Depending on the future size of the plant, its efficiency may increase, with a double effect on the plant's environmental footprint: its specific GHG emissions would decrease during operation, and the capacity factor, i.e. the number of hours of full-load equivalent production over one year, would increase, thus diminishing the relative importance of the construction phase. The results of the dedicated sensitivity studies are displayed on Figure 5 and Figure 6.

When changing the plant's efficiency, the choice was made not to affect the plant's net output. Only the amount of coal provided and burnt changed, which only had an impact on the fuel supply and operation phases. This lowers the ARD of the plant in those two phases; however, the most significantly lowered impact is GWP, as shown on Figure 5. Construction is not impacted by a change in efficiency, if one assumes that the plant's design is not affected.

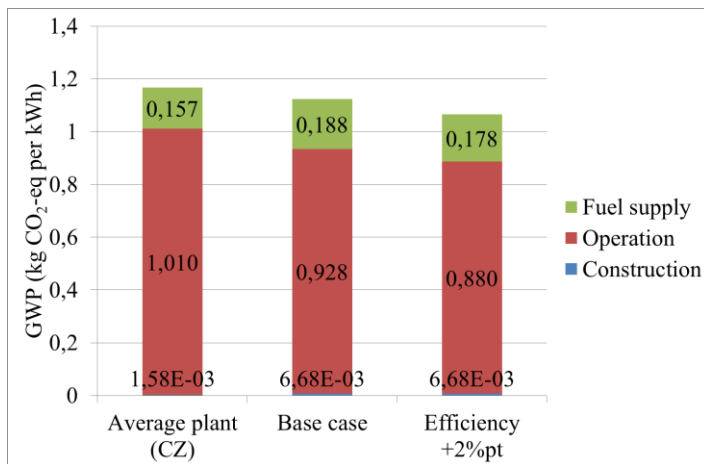


Figure 5: Impact of a +2%pt increment in plant efficiency (LHV-based) on GWP

As regards dispatch strategy, if one considers that the plant's yearly efficiency is unchanged there is no impact on fuel supply and plant operation phases. Such a change only affects the impact of the construction phase, as the same design allows the production of more kWh. As mentioned above, the dispatch strategy is directly dependent on the plant's efficiency. Nevertheless the extent of that effect is market-dependent, and could not be modeled in the present study.

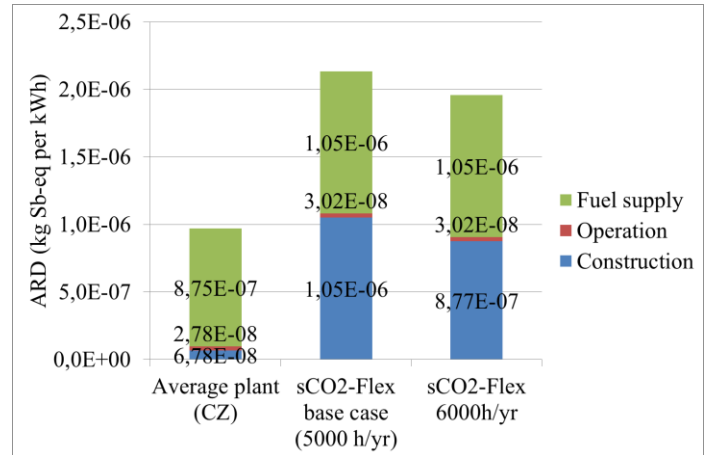


Figure 6: Impact on ARD of a +1000 h/yr full-load equivalent dispatch

Finally, one of the unexpected results is that the sCO₂-Flex plant has a higher impact during its fuel supply phase (see Figure 1 and Figure 2). As the same module for coal mining and supply was used for the sCO₂-Flex plant and for the average Czech plant used as benchmark, the impact of coal supply depends linearly on the amount of coal used during the plant's life. Thus using a coal with lower moisture contents, resulting in a higher LHV (and assuming, in a first approach, that it does not affect significantly the plant's design and emissions), should result in a lower coal consumption for the same power output, thus in a lower environmental impact during the phase of fuel supply.

Figure 7 and Figure 8 show that, for both GWP and ARD, an increase of coal LHV by 20% nearly equalizes the impact of sCO₂-Flex plant and the benchmark plant on their fuel supply phase. This confirms the significant sensitivity of this phase's impact to the type of coal that is used, and its low relevance when trying to perform a general comparison between supercritical CO₂ and steam cycles.

Additionally, a number of other parameters were subject to a sensitivity study:

- the amount of construction materials can be shown to have a limited impact on the overall ARD (-2.7% for a -20% decrease in structural materials consumption).
- the transport distance of equipment and the energy consumption during materials production have little to no impact on the plant's overall ARD and GWP, as ARD is dominated by coal supply and use of materials for construction, and GWP is dominated by the combustion and supply of coal during operation.
- oil and gas consumption during operation also have no impact on the overall result, as a double consumption has no visible effect on the plant's GWP during operation. This is not surprising, as oil and gas are typically used during cold start-ups only, that is only a few hours per year.

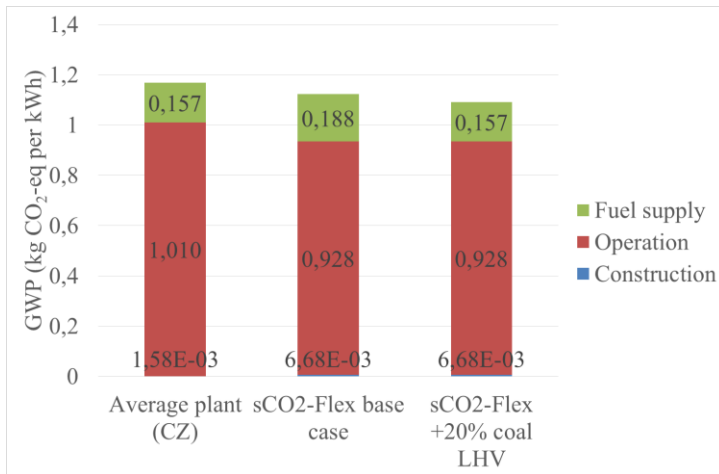


Figure 7: Impact on GWP of using a coal with +20% LHV

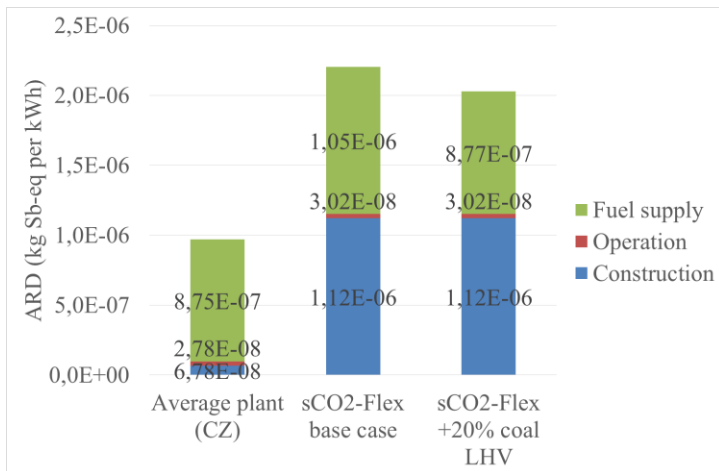


Figure 8: Impact on ARD of using a coal with +20% LHV

CONCLUSION

The partial environmental assessment of the supercritical CO₂ cycle developed in the project sCO₂-Flex shows that this technology can be expected to bring a significant improvement on GWP, to the expense of a considerably higher ARD. The use of nickel-based alloys is the major penalty on such a plant (construction materials probably overestimated, but no significant impact on that conclusion). That is where efforts should be made, from both economic and environmental points of view. Nevertheless, as the present study assumes a total absence of reuse of recycling, the actual impact of such a plant can be expected to be lower.

The comparison between the plant developed in sCO₂-Flex and the average Czech plant taken as benchmark is asymmetric in several ways. For instance, GWP reduction should be taken with care as it results from the higher efficiency of a small, state-of-the-art plant as compared to a big, old average plant. The net effect of age and size on efficiency is not clear at this point. Similarly, the fuel used in both plants is not the same: while the fuel used in the reference plant reflects the average

fuel consumption of Czech coal power plants, a specific fuel had to be selected for the detailed design of the sCO₂-Flex boiler. This has an artificial influence on the environmental impact of the fuel supply phase. Finally, the impact of an increased efficiency on the dispatch strategy of the plant could not be taken into account in the present study.

Further works on the subject could include the environmental impact assessment of a small state-of-the-art water/steam plant, designed with the same constraints as in sCO₂-Flex. Furthermore, the supercritical CO₂ cycle developed in sCO₂-Flex should also provide additional flexibility and substantial changes in maintenance and operation (much smaller turbine making maintenance easier and availability potentially higher). An estimate of the impact of these improvements on the annual dispatch of the plant would be a precious addition to the present study.

NOMENCLATURE

ARD = Abiotic Resource Depletion (kg Sb-eq)

GHG = GreenHouse Gas(es)

GWP = Global Warming Potential (kg CO₂-eq), here considered on 100 years

kg CO₂-eq = kilogram CO₂ equivalent

kg Sb-eq = kilogram antimony equivalent

LHV = Lower Heating Value

PV = PhotoVoltaic power

ACKNOWLEDGEMENTS

The sCO₂-Flex project has received funding from the European Union's Horizon 2020 research and innovation programme under grant agreement N° 764690.

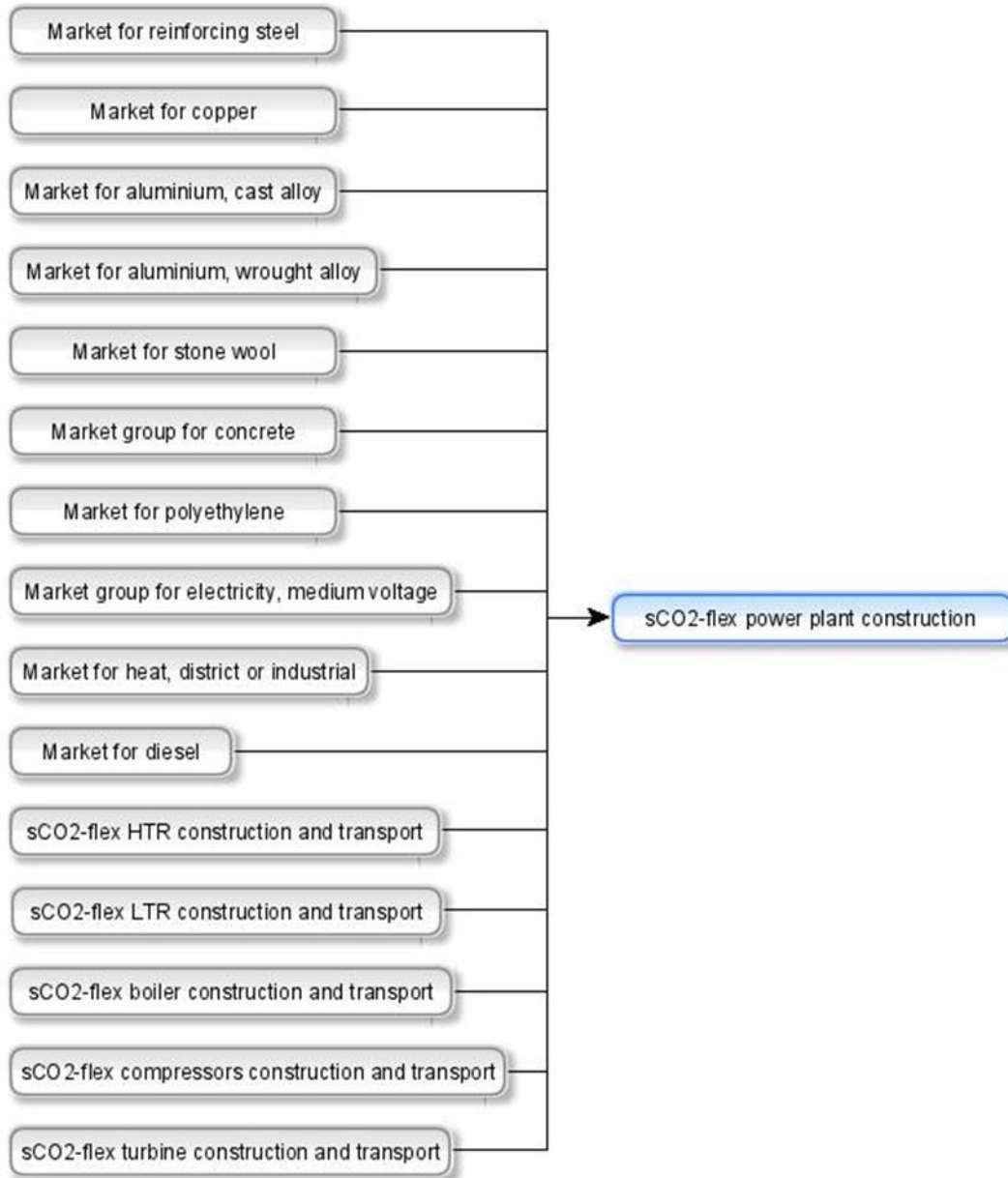
REFERENCES

- [1] Mecheri, M., and Bedogni, S., 2018, *Report on the Selected Cycle Architecture*, D1.3.
- [2] Alfani, D., Astolfi, M., Binotti, M., Macchi, E., and Silva, P., 2019, "Part-Load Operation of Coal Fired sCO₂ Power Plants," *Proceeding of the 3rd European Supercritical CO₂ Conference*, Paris, France.
- [3] 2006, "ISO 14040: Environmental Management - Life Cycle Assessment - Principles and Framework."
- [4] 2006, "ISO 14044: Environmental Management - Life Cycle Assessment - Requirements and Guidelines."
- [5] World Energy Council, 2004, *Comparison of Energy Systems Using Life Cycle Assessment*, World Energy Council.
- [6] Turconi, R., Boldrin, A., and Astrup, T., 2013, "Life Cycle Assessment (LCA) of Electricity Generation Technologies: Overview, Comparability and Limitations," *Renewable and Sustainable Energy Reviews*, **28**, pp. 555–565.
- [7] Whitaker, M., Heath, G. A., O'Donoghue, P., and Vorum, M., 2012, "Life Cycle Greenhouse Gas Emissions of Coal-

- Fired Electricity Generation: Systematic Review and Harmonization,” *Journal of Industrial Ecology*, **16**, pp. S53–S72.
- [8] Weisser, D., 2007, “A Guide to Life-Cycle Greenhouse Gas (GHG) Emissions from Electric Supply Technologies,” *Energy*, **32**(9), pp. 1543–1559.
- [9] Mills, S. J., IEA Coal Research, and Clean Coal Centre, 2005, *Coal Full Life Cycle Analysis*, IEA Coal Research, Clean Coal Centre, London.
- [10] Wernet, G., Bauer, C., Steubing, B., Reinhard, J., Moreno-Ruiz, E., and Weidema, B., 2016, “The Ecoinvent Database Version 3 (Part I): Overview and Methodology,” *Int J Life Cycle Assess*, **21**(9), pp. 1218–1230.
- [11] Dones, R., Bauer, C., and Röder, A., 2007, “Kohle,” *Sachbilanzen von Energiesysteme-Men: Grundlagen Für Den Ökologischen Vergleich von Energiesystemen Und Den Einbezug von Energiesys-Temen in Ökobilanzen Für Die Schweiz*, Paul Scherrer Institut Villigen, Swiss Centre for Life Cycle Inventories, Dübendorf, CH.
- [12] Wolf, M.-A., Pant, R., Chomkamsri, K., Sala, S., Pennington, D., European Commission, and Joint Research F06776Centre, 2012, *The International Reference Life Cycle Data System (ILCD) Handbook: Towards More Sustainable Production and Consumption for a Resource-Efficient Europe.*, Publications Office, Luxembourg.
- [13] Intergovernmental Panel on Climate Change, ed., 2014, “Anthropogenic and Natural Radiative Forcing,” *Climate Change 2013 - The Physical Science Basis*, Cambridge University Press, Cambridge, pp. 659–740.
- [14] van Oers, L., Guinée, J. B., and Heijungs, R., 2020, “Abiotic Resource Depletion Potentials (ADPs) for Elements Revisited—Updating Ultimate Reserve Estimates and Introducing Time Series for Production Data,” *Int J Life Cycle Assess*, **25**(2), pp. 294–308.
- [15] Ciroth, A., 2007, “ICT for Environment in Life Cycle Applications OpenLCA — A New Open Source Software for Life Cycle Assessment,” *Int J Life Cycle Assess*, **12**(4), pp. 209–210.

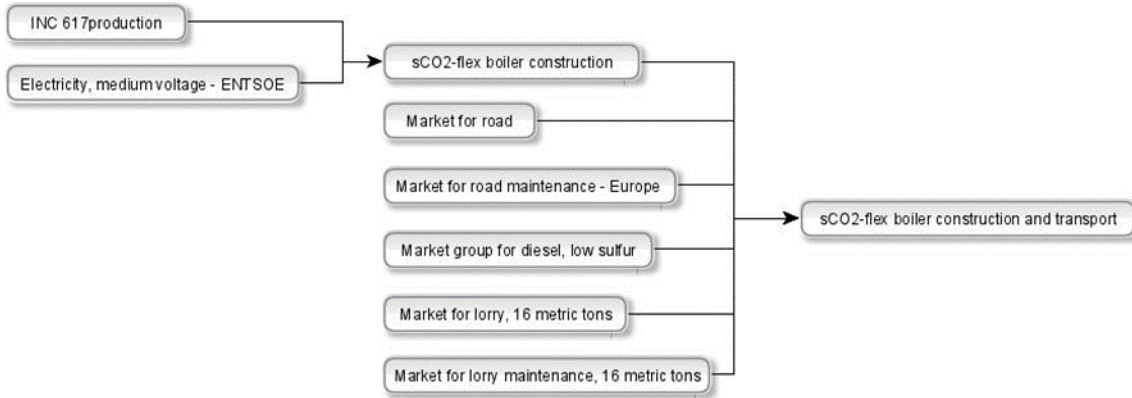
ANNEX A

PROCESS DIAGRAM FOR THE SCO₂-FLEX POWER PLANT CONSTRUCTION



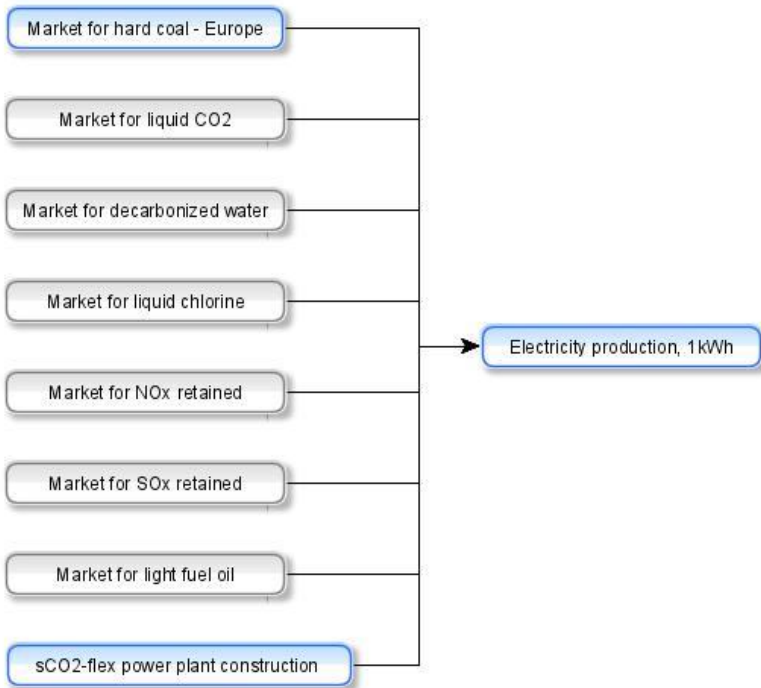
ANNEX B

DETAIL OF THE PROCESS DIAGRAM FOR THE sCO₂-FLEX BOILER CONSTRUCTION AND TRANSPORT



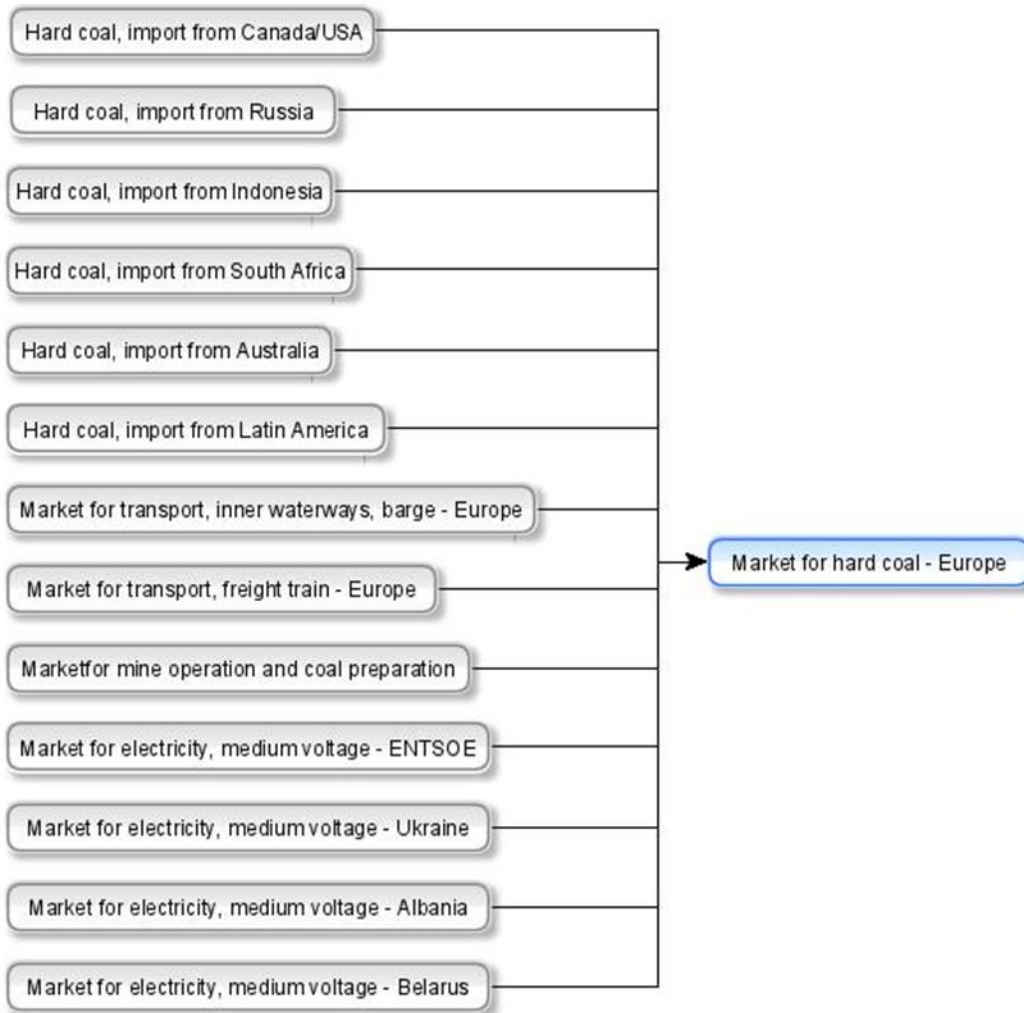
ANNEX C

PROCESS DIAGRAM FOR THE OPERATION PHASE OF THE sCO₂-FLEX PLANT



ANNEX D

PROCESS DIAGRAM FOR THE FUEL SUPPLY PHASE OF THE SCO₂-FLEX PLANT



OPTIMAL DESIGN OF SUPERCRITICAL CO₂ (S-CO₂) CYCLE SYSTEMS FOR INTERNAL COMBUSTION ENGINE (ICE) WASTE-HEAT RECOVERY CONSIDERING HEAT SOURCE FLUCTUATIONS

Jian Song

Imperial College London
London, UK

Jiangfeng Wang

Xi'an Jiaotong University
Xi'an, China

Yaxiong Wang

Xi'an Jiaotong University
Xi'an, China

Christos N. Markides*

Imperial College London
London, UK

c.markides@imperial.ac.uk

ABSTRACT

Supercritical CO₂ (S-CO₂) cycle systems have emerged as an attractive alternative for internal combustion engine (ICE) waste-heat recovery thanks to the advantages offered by CO₂ as a working fluid, including robust performance and system compactness. The engine exhaust gases are the main available heat source from ICEs with promising thermodynamic potential for further utilisation, and whose conditions, i.e., temperature and mass flow rate, vary based on the ICE operating strategy/load. These heat source variations have a critical influence on the performance of a bottoming S-CO₂ cycle system, which needs to be carefully considered in the design stage. This paper explores the optimal design of S-CO₂ cycle systems for ICE waste-heat recovery considering heat source fluctuations as well as the probability of their occurrence as arising from actual ICE operation. A variety of heat source conditions are selected for separate designs of an S-CO₂ cycle system and performance prediction under all possible scenarios is evaluated via detailed design and off-design models, so as to select the optimal design that is able to match the heat source fluctuations and exhibit the best performance from thermodynamic and economic perspectives. The advantage of this approach relative the conventional ones that only consider one specific design condition is that it avoids either over- or under-sizing of the S-CO₂ cycle system, which also achieves comprehensive insight of the interplay between the bottoming heat recovery system and the ICE, and provides valuable guidance for further system optimisation.

INTRODUCTION

More than half of the energy through fuel combustion in internal combustion engines (ICEs) is dissipated in the form of waste heat mainly via exhaust gases and jacket water [1]. Therefore, waste-heat recovery is considered as an important pathway for ICE performance improvement, of which organic Rankine cycle (ORC) appears as an attractive solution [2-5]. More recently, supercritical CO₂ (S-CO₂)

cycles have also emerged as a promising option for ICE waste-heat recovery thanks to the advantages offered by CO₂ as a working fluid, including better thermal match with the heat source, compact system structure and avoidance of working fluid decomposition under high-temperature conditions in particular for the recovery of engine exhaust gases [6,7]. S-CO₂ cycle systems also offer potential to be applied in a wide range of applications such as solar [8,9], nuclear [9,10] and geothermal energy utilisation [11,12].

Extensive research on S-CO₂ cycle systems for ICE waste-heat recovery is available, showing the growing interest in adopting this promising heat-to-power generation technology in the specific area to further enhance ICE performance. Chen et al. [13] compared the performance of supercritical CO₂ Brayton cycle and transcritical CO₂ cycle for heat recovery from automobiles via a theoretical study and the results revealed that S-CO₂ cycle had a higher efficiency thanks to the higher operating pressure. Song et al. [14] updated a single preheating S-CO₂ cycle system by adding a regeneration branch and an increase of 7% in net power output was achieved. Further to that work, a combined S-CO₂ cycle and ORC system was presented for a wide range of ICEs, with results indicating that a power output improvement of up to 40-70% could be obtained by the addition of the bottoming cycle system [15]. Hou et al. [16] analysed a combined-cycle system that coupled S-CO₂ recompression and regenerative cycles for marine engine waste-heat recovery and the system was able to offer various advantages including sufficient heat utilisation, high system compactness and low cost. Sharma et al. [17] presented a regenerative S-CO₂ recompression cycle also for shipboard applications and an increase up to 25% in engine power output at rated condition was achieved.

Most of the previous research focuses on the design and optimisation of S-CO₂ cycle systems with a specific heat source condition, i.e., fixed temperature and mass flow rate, normally at

* corresponding author(s)

the rated operating condition of the ICE. It is common that ICEs will be operated under frequent part-load conditions, which results in different heat source conditions for the bottoming heat recovery system. In other words, the S-CO₂ cycle system will be forced to operate under off-design conditions associated with the ICE load and its performance as well as the improvement in the ICE power output will be significantly influenced. Therefore, the off-design performance of the S-CO₂ cycle system needs to be considered in the design stage to avoid performance deterioration due to the mismatch between the determined system configurations (e.g., sizes and geometry of the components) and the heat source conditions, which has been rarely taken into consideration in the previous studies. This paper seeks to explore the optimal design of an S-CO₂ cycle system for ICE waste-heat recovery considering the heat source fluctuations and the probability of occurrence of such part-load conditions. All the possible heat source conditions corresponding to actual ICE operating load are selected for separate designs of the S-CO₂ cycle system and performance evaluation under all possible scenarios via detailed design and off-design models are performed, so as to select the optimal design scheme from thermodynamic and economic perspectives.

METHODOLOGY

System description

Recuperated S-CO₂ cycle system is considered in this study for waste-heat recovery from engine exhaust gases, of which the schematic diagram and the corresponding T - s diagram are shown in Figures 1 and 2. The CO₂ working fluid is firstly compressed by the compressor and heated in the recuperator by the hot CO₂ stream that flows from the turbine. CO₂ continuously absorbs heat from the engine exhaust gases and then expands in the turbine to produce power. Afterwards, CO₂ goes into the pre-cooler to be cooled down to start the next cycle.

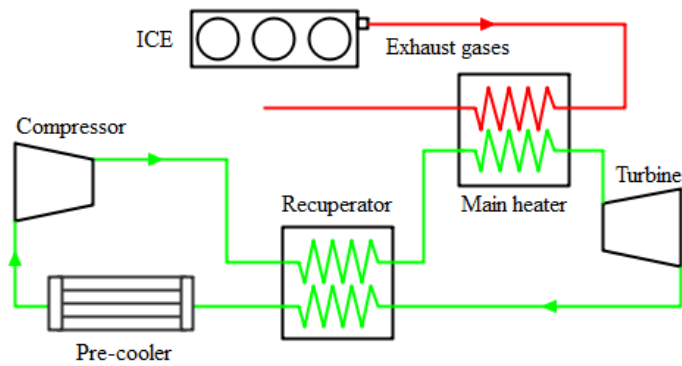


Figure 1: Schematic diagram of recuperated S-CO₂ cycle system for ICE waste-heat recovery.

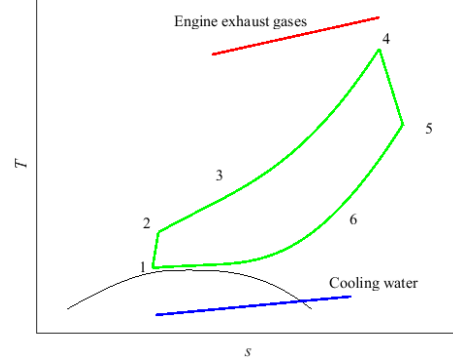


Figure 2: T - s diagram of recuperated S-CO₂ cycle system for ICE waste-heat recovery.

Thermodynamic models of the S-CO₂ cycle system can be found in the authors' previous work [14,15] and they are omitted here.

Turbine model

A one-dimensional (1-D) design and off-design model of radial-inflow turbines [18,19] based on the mean-line method is used to predict the turbine efficiency, which has been employed in ORC [20] and CO₂-based systems [6,21]. In the design model, all relevant parameters, including the nozzle and rotor velocity coefficients, velocity ratio, reaction degree, wheel diameter ratio, absolute flow angle at the rotor inlet and relative flow angle at the rotor outlet, are optimised simultaneously in order to achieve the highest turbine efficiency. While in the off-design model, the geometry of the turbine determined by the design stage is provided as input and the flow characteristics as well as the working fluid parameters are predicted.

The peripheral efficiency of the radial-inflow turbine can be expressed as:

$$\eta_u = 2\bar{u}_1 \cdot \left(\frac{\varphi \cdot \sqrt{1-\Omega} \cdot \cos \alpha_1 - \bar{D}_2^2 \cdot \bar{u}_1 + \bar{D}_2 \cdot \psi \cdot \cos \beta_2}{\left[\Omega + \varphi^2 \cdot (1-\Omega) - 2\varphi \cdot \sqrt{1-\Omega} \cdot \bar{u}_1 \cos \alpha_1 + \bar{D}_2^2 \cdot \bar{u}_1^2 \right]^{1/2}} \right). \quad (1)$$

Taking incidence loss, friction loss and leakage losses into consideration, the radial-inflow turbine efficiency is given by:

$$\zeta_1 = \frac{\left[w_1 \cdot \sin(\beta_1 - \beta_{1,opt}) \right]^2}{2 \cdot \Delta h_s}, \quad (2)$$

$$\zeta_f = \frac{K_f \cdot \frac{(\rho_1 + \rho_2)}{2} \cdot u_1^3 \cdot \left(\frac{D_1}{2} \right)^2}{2 \cdot m \cdot w_2^2 \cdot \Delta h_s}, \quad (3)$$

$$\zeta_1 = \frac{w_1^3 \cdot N_{rotor}}{8\pi \cdot \Delta h_s} \cdot \sqrt{\left[0.4 \cdot 0.004 \cdot K_{c1} + 0.75 \cdot 0.00023 \cdot K_{c2} \right] \cdot \left[-0.3 \cdot (0.0004 \cdot 0.00023 \cdot K_{c1} \cdot K_{c2}) \right]}, \quad (4)$$

$$\eta_T = \eta_u - \zeta_1 - \zeta_f - \zeta_1. \quad (5)$$

Heat exchanger models

Shell-and-tube heat exchangers are selected for the S-CO₂ cycle system, and the Bell-Delaware method [22] is used to

calculate heat transfer coefficients (HTCs) and pressure drops. The shell-side (heat source) HTC and pressure drop are given by:

$$\alpha_s = \alpha_i \frac{c_{p,s} G_s}{Pr_s^{2/3}} \left(\frac{\mu_s}{\mu_w} \right)^{0.14} j_c j_l j_b j_s j_r, \quad (6)$$

where j_c , j_l , j_b , j_s and j_r are correction factors accounting for combined effects of baffle cut and spacing, for baffle leakage effects, for bundle bypass flow, for variable baffle spacing in the inlet and outlet sections, and for adverse temperature gradient build-up in laminar flow:

$$\Delta P_s = \left[(N_b - 1) R_b R_1 + 2 \left(1 + \frac{N_{tcw}}{N_{tcc}} \right) R_b R_s \right] \cdot \quad (7)$$

$$\frac{2 f_s N_{tcc} G_s^2}{\rho_s} \left(\frac{\mu_s}{\mu_w} \right)^{-0.14} + \frac{(2 + 0.6 N_{tcw}) G_w^2}{2 \rho_s} N_b R_1$$

The HTC of tube side with supercritical CO₂ working fluid is given by (Ptukhov-Krasnoshchekov-Protopopov correlation):

$$\alpha_i = \frac{\lambda}{d_i} \frac{(f/8) Re Pr}{\left[12.7 (f/8)^{0.5} (Pr^{2/3} - 1) + 1.07 \right]}. \quad (8)$$

$$\left(\frac{\bar{c}_p}{c_{p,bulk}} \right)^{0.35} \cdot \left(\frac{\lambda_{bulk}}{\lambda_{wall}} \right)^{-0.33} \cdot \left(\frac{\mu_{bulk}}{\mu_{wall}} \right)^{0.11}$$

The total HTC of heat exchanger is given by:

$$\frac{1}{U} = \frac{1}{\alpha_i} \cdot \frac{d_o}{d_i} + r_{ft} \cdot \frac{d_o}{d_i} + \frac{\delta_w}{\lambda_w} \cdot \frac{d_o}{d_m} + r_{fs} + \frac{1}{\alpha_s}. \quad (9)$$

The heat exchanger area is given by:

$$A = \frac{Q}{U \cdot \Delta T}. \quad (10)$$

where ΔT is the log mean temperature difference (LMTD) between the hot side and the cold side.

Cost models

The module costing technique is used to calculate the bare module cost of each component, with the chemical engineering plant cost index (*CEPCI*) to obtain the capital cost of the systems [23]. Therefore, the specific investment cost (*SIC*) is calculated by Eqs. (10)-(14) with the coefficients for each component summarised in Ref. [15].

$$C_{BM} = C_p^0 F_{BM} = C_p^0 (B_1 + B_2 F_M F_p), \quad (11)$$

$$\log(C_p^0) = K_1 + K_2 \log(X_i) + K_3 [\log(X_i)]^2, \quad (12)$$

$$\log(F_p^0) = C_1 + C_2 \log(p_i) + C_3 [\log(p_i)]^2, \quad (13)$$

$$C = \sum_i C_{BM} \frac{CEPCI_{2017}}{CEPCI_{2001}}, \quad (14)$$

$$SIC = \frac{C}{W_{net}}, \quad (15)$$

where i denotes different components, $CEPCI_{2001} = 397.0$ and $CEPCI_{2017} = 567.5$ [24], which are dimensionless numbers employed to updating capital cost required to erect a power-cycle system from a past date to a later time.

The levelised cost of electricity (*LCOE*), which represents the present value of electricity production price considering the

economic lifetime of a system and the costs incurred in the construction, operation and maintenance, is given by:

$$LCOE = \frac{C + \sum_{n=1}^N \frac{C_{O\&M}}{(1+i)^n}}{\sum_{n=1}^N \frac{P}{(1+i)^n}}, \quad (16)$$

where C is the initial investment cost of the system, $C_{O\&M}$ is the annual operating and maintenance cost (set as 1.65% of the initial investment cost [25]), i is the discount rate (considered as 5% [25]), P is the annual power generated by the system, with an annual operation hours (set as 8000 h) and N is the expected lifetime (totally 15 years in this study).

Conditions and assumptions

An ICE with a rated power of 1000 kW [26] is selected in this paper and the heat source conditions corresponding to engine load are shown in Table 1. The temperature of engine exhaust gases changes from 540 °C to 470 °C while the mass flow rate decreases from 1.56 kg/s to 0.72 kg/s when the engine condition changes from the rated one (100%) to a part-load of 40%, which indicates significant difference among the heat source conditions.

Table 1. Exhaust gases conditions corresponding ICE load.

Load	100%	90%	80%	70%	60%	50%	40%
Temperature (°C)	540	532	530	527	525	515	470
Mass flow rate (kg/s)	1.56	1.41	1.23	1.10	0.99	0.86	0.72

The model of the S-CO₂ for ICE waste-heat recovery used in this study was developed using in-house MATLAB codes, with working fluid properties acquired from NIST REFPROP [27]. The interior-point algorithm in MATLAB's *fmincon* function has been chosen as the solver to maximise the net power output under each heat source condition.

The main conditions and assumptions are given below:

(1) The minimum operating temperature and pressure of the S-CO₂ cycle system are 31.5 °C and 7.5 MPa, respectively, to ensure that the working fluid is in the supercritical state; the maximum operating pressure is 20 MPa.

(2) The pinch point temperature differences in all heat exchangers in the design stage are set to 10 °C.

(3) The compressor efficiency is assumed to be 0.8 at both design and off-design conditions, which will be explored in future work by implementing detailed design and off-design models.

(4) The heat sink (cooling water) temperature is set to 15 °C and the maximum mass flow rate of the heat sink is 10 kg/s.

(5) The temperature of engine exhaust gases after heat recovery is set to be >120 °C in order to avoid acid corrosion in the corresponding pipes and heat exchangers [28].

(6) Heat losses throughout the system are neglected.

(7) All processes take place at steady state conditions.

RESULTS AND DISCUSSION

Cycle parameters as well as turbine design parameters are optimised simultaneously in the design stage to achieve the maximum net power output under each heat source condition corresponding to different ICE operating load. In other words, separate design schemes in terms of cycle parameters and components are obtained for all possible heat source conditions shown in Table 1. The maximum net power output and the corresponding *SIC* are shown in Figure 3, indicating that performance of the optimal designs (from a thermodynamic perspective) is closely related to the given heat source conditions. More precisely, the maximum net power output obtained from the separate designs decreases from 166 kW to 59 kW when the ICE load changes from the rated value (100%) to a part-load of 40%, while the *SIC* increases from 4630 \$/kW to 8190 \$/kW.

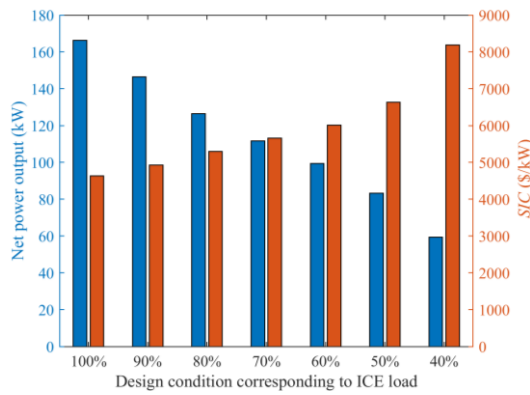


Figure 3: Net power output and corresponding *SIC* of the separate designs of S-CO₂ cycle system for ICE waste-heat recovery. Cycle parameters and turbine design parameters are optimised simultaneously to achieve the maximum net power output under each heat source condition corresponding to different ICE load shown in Table 1.

Detailed information of the separate designs for each heat source condition including turbine inlet and outlet conditions, CO₂ mass flow rate, areas of heat exchangers (recuperator, main heater and pre-cooler) and turbine efficiency are shown in Figs. 4-7, respectively. It can be seen from Figure 4 that the optimal turbine inlet and outlet pressures of the separate designs are nearly the same under different design conditions for the S-CO₂ cycle system to deliver the maximum net power output, while the optimised turbine inlet temperature decreases with the heat source temperature. Figure 5 shows that CO₂ mass flow rate corresponding to the separate designs decreases with the thermal load of the heat sources. It can be seen from Figure 6 that the main heater dominates in all designs as the density as well as the heat transfer coefficient of exhaust gases is much lower than the CO₂ working fluid, which also confirms that system compactness can be achieved as an advantage of CO₂-based systems thanks to the working fluid properties. Moreover, although the total heat exchanger area is larger with higher ICE load as well as more heat available from the engine exhaust

gases, the corresponding *SIC* is still lower due to the high power output (see Figure 3). Figure 7 shows that the turbine efficiency is within the range of 84% to 86%, indicating the optimisation enables high-efficiency design under various heat source and operating conditions.

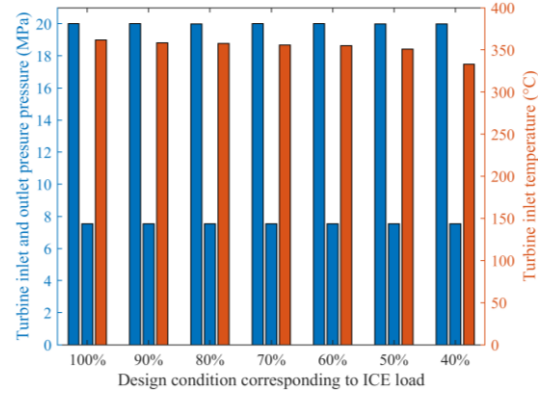


Figure 4: Turbine inlet and outlet conditions of the separate designs for each heat source condition corresponding to different ICE load.

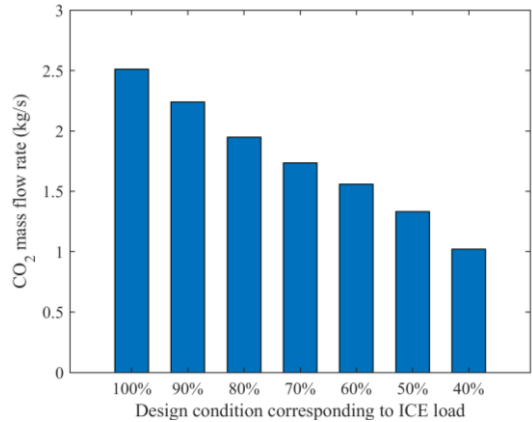


Figure 5: CO₂ mass flow rate of the separate designs for each heat source condition corresponding to different ICE load.

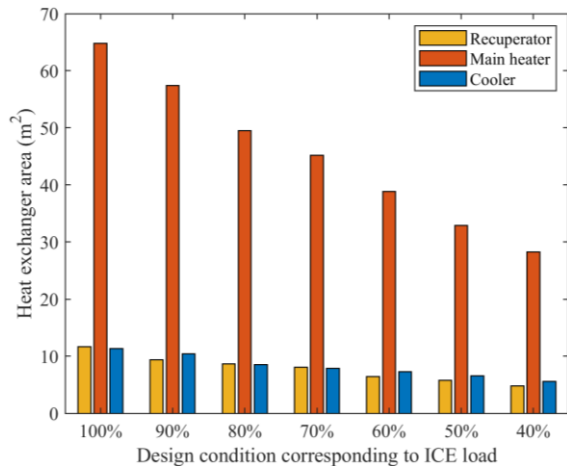


Figure 6: Heat exchanger areas of the separate designs for each heat source condition corresponding to different ICE load.

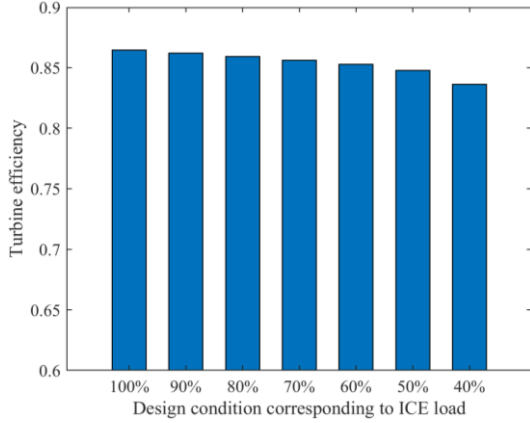


Figure 7: Turbine efficiency of the separate designs for each heat source condition corresponding to different ICE load.

In order to select the optimal design among the schemes shown above, off-design performance of each separate design under all possible heat source conditions are evaluated via detailed off-design models. System operating parameters in the off-design stage are also optimised to achieve the maximum power output, which corresponds to the optimal control strategy in practical applications. Figure 8 shows that all separate designs experience a decrease in power output when the ICE load changes to be lower as the heat input to the S-CO₂ cycle system decreases. The design scheme for the rated condition (100% ICE load) provides a higher net power output under most heat source conditions, while the difference becomes smaller with lower ICE load.

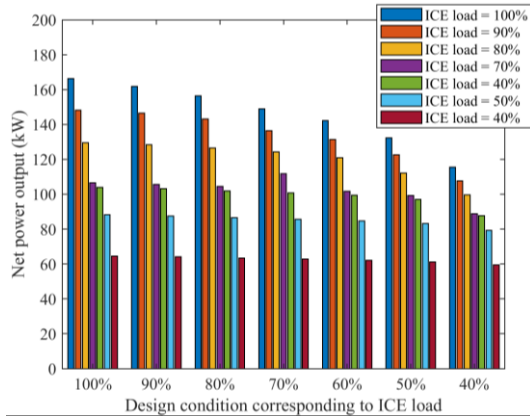


Figure 8: Off-design performance of the separate designs under all possible heat source conditions.

The seven ICE operating conditions listed in Table 1 are considered as actual variations and the probability of occurrence of the ICE operating conditions will vary with different end-users as well as demand profile. Two cases are assumed to indicate the variations, i.e., one considers the same probability of occurrence for all possible conditions (equal-weighted scenario) and the other accounts for different weights for all the conditions as reported in

Ref. [29], with 20.6%, 18.3%, 16.2%, 14.1%, 12.5%, 10.6% and 7.7% (different-weighted scenario), respectively.

It can be seen that the design corresponding to ICE rated load (100%) yields the maximum annual power output under both scenarios (922 MWh and 1330 MWh, respectively), and outperforms other designs significantly under the different-weighted scenario. The corresponding *LCOE* of the design at the rated heat source condition is the highest under the equal-weighted scenario (94 \$/MWh), while it is the lowest under the different-weighted scenario (65 \$/MWh). Therefore, the design at rated heat source condition is the optimal under the different-weighted scenario in terms of both thermodynamic and economic perspectives, while under the equal-weighted scenario, the design at the rated heat source condition is the optimal from the thermodynamic perspective, and the design corresponding to ICE load of 40% has the lowest *LCOE* of 75/MWh.

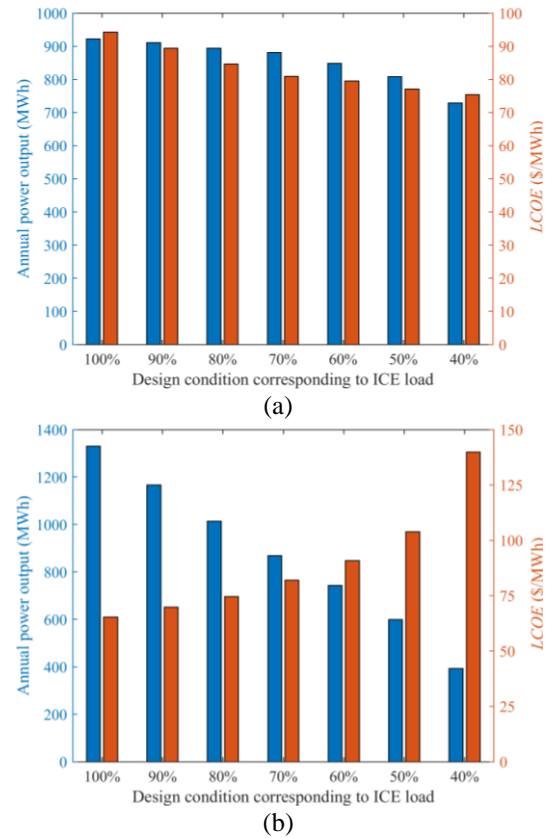


Figure 9: Annual power output and *LCOE* of separate design for each heat source condition corresponding different ICE load: (a) under equal-weighted scenario, and (b) under different-weighted scenario.

CONCLUSIONS

In this paper we explore the optimal design of S-CO₂ cycle systems for ICE waste-heat recovery considering heat source fluctuations arising from the ICE operating load. Separate designs are presented for each heat source condition to achieve the maximum net power output. The design corresponding to the ICE rated load (100%) provides the maximum net power output of

166 kW with a corresponding *SIC* of 4630 \$/kW, which is also the lowest among all design schemes. The off-design performance of all separate designs is evaluated at all possible heat source conditions and the design scheme for the ICE rated load is found to provide a higher net power output under most conditions. Two scenarios, i.e., equal-weighted and different-weighted, are considered in order to estimate the annual performance of the S-CO₂ cycle system. For the equal-weighted scenario, the design for the rated load ICE condition is the optimal from the thermodynamic perspective and the maximum annual power output reaches 922 MWh. The design for the 40% ICE load condition yields the lowest *LCOE* of 75 \$/MWh. The design for the rated load condition is the optimal for the different-weighted scenario with a maximum annual power output of 1330 MWh and the lowest *LCOE* of 65 \$/MWh. The advantage of the methodology presented herein relative to conventional approaches that only consider one specific design condition is that it enables us to avoid either over- or under-sizing of the S-CO₂ cycle system, which also allows us to gain a more complete understanding of the interplay between the bottoming heat recovery system and the ICE, while providing valuable guidance for further system optimisation and operation.

NOMENCLATURE

Symbols

B_i, C_i, K, F_M, F_P	constants for cost models
C	cost (\$)
c_p	specific heat capacity (J/kg·K)
d, D	diameter (m)
f	friction factor
j, R	correction factors
K_{c1}, K_{c2}	leakage loss factor
K_f	friction loss factor
G	mass flux (kg/m ² ·s)
h	enthalpy (J/kg)
i	discount rate
m	mass flow rate (kg/s)
N	number, lifetime (year)
p	pressure (Pa)
P	power (kW·h)
Pr	Prandtl number
Q	thermal load (W)
q	heat flux (W·m ²)
Re	Reynolds number
r_f	fouling resistance
R_p	surface roughness (m)
s	entropy (J/kg)
T	temperature (K)
u	peripheral velocity (m/s)
U	heat transfer coefficient (W/m ² ·K)
w	relative velocity (m/s)
W	power output (W)
X	component capacity

Greek symbols

α	heat transfer coefficient (W/m ² ·K)
α_1	absolute flow angle in rotor inlet (°)
β_1	relative flow angle in rotor inlet (°)
β_2	relative flow angle in rotor outlet (°)
η	efficiency
λ	thermal conductivity (W/m·K)
μ	viscosity (Pa·s)
ρ	density (kg/m ³)
ζ	loss factor
φ	nozzle velocity coefficient
ψ	rotor velocity coefficient
Ω	reaction degree

Subscripts

b	bundle bypass flow; baffle
BM	bare module
bulk	bulk temperature of fluid
f	friction loss
i	component
I	incidence loss
l	leakage loss
n	net power output
opt	optimal
O&M	operating and maintenance
s	shell side, isentropic
t	tube side
T	turbine
tcc	tube rows in crossflow
tcw	tube rows in baffle window
u	peripheral
w	wall

Abbreviations

<i>CEPCI</i>	chemical engineering plant cost index
<i>HTC</i>	heat transfer coefficient
<i>ICE</i>	internal combustion engine
<i>LCOE</i>	levelised cost of electricity
<i>LMTD</i>	log mean temperature difference
<i>ORC</i>	organic Rankine cycle
<i>S-CO₂</i>	supercritical CO ₂
<i>SIC</i>	specific investment cost

ACKNOWLEDGEMENTS

This work was supported by the UK Engineering and Physical Sciences Research Council (EPSRC) [grant numbers EP/P004709/1, and EP/R045518/1]. Data supporting this publication can be obtained on request from cep-lab@imperial.ac.uk.

REFERENCES

- [1] Shu G, Zhao M, Tian H, Huo Y, Zhu W. Experimental comparison of R123 and R245fa as working fluids for waste heat recovery from heavy-duty diesel engine. *Energy* 2016;115:756–69.
- [2] Song J, Song Y, Gu C. Thermodynamic analysis and performance optimization of an organic Rankine cycle

- (ORC) waste heat recovery system for marine diesel engines. *Energy* 2015;82:976-85.
- [3] Li X, Song J, Yu G, Liang Y, Tian H, Shu G, Markides CN. Organic Rankine cycle systems for engine waste-heat recovery: Heat exchanger design in space-constrained applications. *Energy Convers Manag* 2019;199:111968.
- [4] Le Brun N, Simpson M, Acha S, Shah N, Markides CN. Techno-economic potential of low-temperature, jacket-water heat recovery from stationary internal combustion engines with organic Rankine cycles: A cross-sector food-retail study. *Appl Energy* 2020;274:115260.
- [5] Chatzopoulou MA, Markides CN. Thermodynamic optimisation of a high-electrical efficiency integrated internal combustion engine–Organic Rankine cycle combined heat and power system. *Appl Energy* 2018;226:1229-51.
- [6] Song J, Li X, Ren X, Tian H, Shu G, Gu C, Markides CN. Thermodynamic and economic investigations of transcritical CO₂-cycle systems with integrated radial-inflow turbine performance predictions. *Appl Therm Eng* 2020;165:114604.
- [7] Li X, Tian H, Shu G, Zhao M, Markides CN, Hu C. Potential of carbon dioxide transcritical power cycle waste-heat recovery systems for heavy-duty truck engines. *Appl Energy* 2019;250:1581-99.
- [8] Iverson BD, Conboy TM, Pasch JJ, Kruijenga AM. Supercritical CO₂ Brayton cycles for solar-thermal energy. *Appl Energy* 2013;111:957-70.
- [9] Li M, Zhu H, Guo J, Wang K, Tao W. The development technology and applications of supercritical CO₂ power cycle in nuclear energy, solar energy and other energy industries. *Appl Therm Eng* 2017;126:255-75.
- [10] Ahn Y, Bae SJ, Kim M, Cho SK, Baik S, Lee JI, Cha JE. Review of supercritical CO₂ power cycle technology and current status of research and development. *Nuc Eng Technol* 2015;47:647-61.
- [11] Ahmadi MH, Mehrpooya M, Pourfayaz F. Exergoeconomic analysis and multi objective optimisation of performance of a Carbon dioxide power cycle driven by geothermal energy with liquefied natural gas as its heat sink. *Energy Convers Manag* 2016;119:422-34.
- [12] Sarkar J. Review and future trends of supercritical CO₂ Rankine cycle for low-grade heat conversion. *Renew Sust Energy Rev* 2015;48:434-51.
- [13] Chen Y, Lundqvist P, Platell P. Theoretical research of carbon dioxide power cycle application in automobile industry to reduce vehicle's fuel consumption. *Appl Therm Eng* 2005;25:2041-53.
- [14] Song J, Li X, Ren X, Gu C. Performance improvement of a preheating supercritical CO₂ (S-CO₂) cycle based system for engine waste heat recovery. *Energy Convers Manag* 2018;161:225-33.
- [15] Song J, Li X, Wang K, Markides CN. Parametric optimisation of a combined supercritical CO₂ (S-CO₂) cycle and organic Rankine cycle (ORC) system for internal combustion engine (ICE) waste-heat recovery. *Energy Convers Manag* 2020;218:112999.
- [16] Hou S, Wu Y, Zhou Y, Yu L. Performance analysis of the combined supercritical CO₂ recompression and regenerative cycle used in waste heat recovery of marine gas turbine. *Energy Convers Manag* 2017;151:73-85.
- [17] Sharma OP, Kaushik SC, Manjunath K. Thermodynamic analysis and optimisation of a supercritical CO₂ regenerative recompression Brayton cycle coupled with a marine gas turbine for shipboard waste heat recovery. *Therm Sci Eng Prog* 2017;3:62-74.
- [18] Wasserbauer CA, Glassman AJ. Fortran program for predicting off-design performance of radial-inflow turbines. NASA Technical Note 1975.
- [19] Glassman AJ. Computer program for design analysis of radial-inflow turbines. NASA Technical Note 1976.
- [20] Da Lio L, Manente G, Lazzaretto A. A mean-line model to predict the design efficiency of radial inflow turbines in organic Rankine cycle (ORC) systems. *Appl Energy* 2017;205:187-209.
- [21] Zhou A, Song J, Li X, Ren X, Gu C. Aerodynamic design and numerical analysis of a radial inflow turbine for the supercritical carbon dioxide Brayton cycle. *Appl Therm Eng* 2018;132:245-55.
- [22] K. Thulukkanam. Heat exchanger design handbook. Second Edition. CRC Press, 2013.
- [23] Turton R, Bailie RC, Whiting WB, Shaeiwitz JA. Analysis, synthesis and design of chemical processes. Third Edition. Pearson Education, 2008.
- [24] www.chemengonline.com/cepci-updates-january-2018-prelim-and-december-2017-final
- [25] Shu G, Shi L, Tian H, Deng S, Li X, Chang L. Configurations selection maps of CO₂-based transcritical Rankine cycle (CTRC) for thermal energy management of engine waste heat. *Appl Energy* 2017;186:423-35.
- [26] Wang X, Shu G, Tian H, Feng W, Liu P, Li X. Effect factors of part-load performance for various organic Rankine cycles using in engine waste heat recovery. *Energy Convers Manag* 2018;174:504-15.
- [27] NIST. Reference Fluid Thermodynamic and Transport Properties Database (REFPROP), 2016.
- [28] Bahadori A. Estimation of combustion flue gas acid dew point during heat recovery and efficiency gain. *Appl Therm Eng* 2011;31:1457-62.
- [29] Li X, Shu G, Tian H. Integrating off-design performance in designing CO₂ power cycle systems for engine waste heat recovery. *Energy Convers Manag* 2019;201:112146.

STUDY OF THE INFLUENCE OF ADDITIVES TO CO₂ ON THE PERFORMANCE PARAMETERS OF A SCO₂-CYCLE

Sebastian Rath*

TU Dresden

Dresden, Germany

Email: sebastian.rath@tu-dresden.de

Erik Mickoleit

TU Dresden

Dresden, Germany

Uwe Gampe

TU Dresden

Dresden, Germany

Cornelia Breilkopf

TU Dresden

Dresden, Germany

Andreas Jäger

TU Dresden

Dresden, Germany

ABSTRACT

Compared to existing technologies, thermodynamic cycles based on supercritical carbon dioxide (sCO₂) are leading to higher efficiencies and a more compact design of the components. However, it is possible to improve the performance of sCO₂-based power cycles by using mixtures of CO₂ with suitable additives, as also discussed in the literature for some applications such as concentrated solar power plants or the usage of geothermal heat.

The large variety of possible fluid combinations makes an experimental investigation of all conceivable additives considerably difficult. Therefore, a more viable alternative is to set up a model for the power cycle and conduct a screening in order to identify promising candidates for working fluid mixtures. In a next step these could subsequently be experimentally verified. In order to carry out a screening, a preferably accurate and likewise predictive mixture model is needed.

This work investigates the potential to optimize the characteristics of sCO₂ power cycles by selectively adding different substances in varying amounts to CO₂. For the theoretical screening, the reference equation of state for CO₂ was applied in combination with a multi-fluid mixture model. In the literature studies were mainly limited to mixtures for which adjusted mixture models are available. In contrast, in this work the use of a predictive mixture model allows a screening of additional fluids for which multi-parameter equations of state are available (e.g. alkanes, alkenes, alcohols, and hydrofluorocarbons). The predictive model, which was recently developed at our institute, allows the use of the excess Gibbs energy model COSMO-SAC in combination with the multi-fluid mixture model. Applied to an exemplary thermodynamic cycle, changes in efficiency compared to the use of pure CO₂ have been evaluated. Several promising mixture candidates have been

identified. Additionally, shifts of the critical point have been investigated and are discussed.

INTRODUCTION

The usage of supercritical CO₂ (sCO₂) as a working fluid in power cycles, such as concentrated solar power plants, waste-heat recovery, or nuclear plants, is a current topic in science and industry [1–4]. SCO₂ offers some distinct advantages when compared to other working fluids. For example, due its liquid-like density in the supercritical state, components of the power cycle become significantly smaller than components of a comparable steam cycle. Furthermore, due to the relatively low critical temperature of CO₂ ($\vartheta_c \approx 31$ °C), sCO₂ can also be utilized as a working fluid when the heat source has a relatively low temperature, as for example in geothermal applications [1]. However due to the strong variation of fluid properties near the critical point, even small changes in the conditions at the inlet can cause large deviations in efficiency. Consequently, appropriate solutions must be found to ensure stable process parameters even under changing environmental conditions without cutting back the efficiency too much. In this context one option could be the use of mixtures that have a less dynamic variation of the fluid properties in the considered range.

While the advantages of pure CO₂-cycles have already been studied quite extensively in the literature [5–7], the application of mixtures with CO₂ has not been studied to the same extend yet. Baik and Lee [8] investigated a simple Brayton cycle and investigated the influence of six additives (SF₆, R-123, R-134a, R-22, R-32, and toluene) to CO₂ on several performance parameters of the cycle. They used equations of state implemented in the thermophysical property software NIST REFPROP (2010) as well as an in-house software in order to calculate the properties of the mixtures. Baik and Lee found R-

* corresponding author(s)

32 to be the most promising additive for the simple Brayton cycle and conducted experiments for the binary mixture of CO₂+R-32 in order to confirm their results. They conclude that R-32 and toluene are promising candidates that could reduce the decrease of efficiency in summer due to higher cooling temperatures. Binotti et al. [9,10] used the Peng-Robinson equation of state implemented in AspenPlus v9.0 in order to investigate the application of the mixtures CO₂ + TiCl₄ and CO₂ + N₂O₄ as working fluids in solar power plants. For some of the investigated mixture compositions and boundary conditions of the process, Binotti et al. [9,10] found that the efficiency of the process can be increased when using mixtures compared to the efficiency when using pure CO₂ as working fluid. Manzolini et al. [11] investigated the effect of using mixtures of CO₂ + TiCl₄ and CO₂ + N₂O₄ instead of pure CO₂ on the levelized cost of electricity for solar power plants. They also used the Peng-Robinson equation of state in order to calculate the properties of the mixtures and found that, according to their calculations, the mixture of CO₂ with either N₂O₄ or TiCl₄ are promising candidates to reach lower levelized costs of electricity as compared to solar power plants with pure CO₂ as working fluid. However, they also note that relatively simple equations of state (i.e. the Peng-Robinson equation of state) have been used in their model in order to calculate the results and therefore, the results need further validation.

Recently, our group has developed a predictive combination of the multi-fluid mixture model with excess Gibbs energy models (g^E -models) [12,13]. In this model, the best equations of state available for the pure substances, for example the reference equation of state for CO₂ by Span and Wagner [14], can be used together with best available predictive models, such as the g^E -models UNIFAC [15] or COSMO-SAC [16–18]. It has already been demonstrated that this model yields good results when used for a screening in refrigeration cycles [19,20]. In this work, the predictive mixture model is applied to a power cycle for the first time. Two different configurations of the power cycle were studied and all substances for which accurate multi-parameter equations of state are available have been considered as additives to CO₂.

MIXTURE MODELS

In this work, multi-fluid mixture models have been used to calculate the thermophysical properties of the various CO₂ mixtures, which have been considered as alternative working fluids for two different power cycle configurations as discussed in the subsequent section. The multi-fluid mixture model, as proposed by Lemmon and Tillner-Roth [21] and developed further by Kunz et al. [22,23], Gernert and Span [24], and Herrig [25] reads

$$\alpha(\tau, \delta, \vec{x}) = \sum_{i=1}^N x_i [\alpha_{oi}^0(\rho, T) + \ln(x_i) + \alpha_{oi}^r(\delta, \tau)] + \sum_{i=1}^{N-1} \sum_{j=i+1}^N x_i x_j F_{ij} \alpha_{ij}^r(\tau, \delta). \quad (1)$$

where α denotes the dimensionless Helmholtz energy, \vec{x} is the vector of mole fractions in the mixture with x_i denoting the mole fraction of component i , N is the number of components in the mixture, T is the temperature and ρ is the density. α_{oi}^0 denotes the ideal part and α_{oi}^r the residual part of the dimensionless Helmholtz energy of component i in the mixture. α_{ij}^r is the binary specific departure function for components i and j in the mixture and F_{ij} are parameters of the binary specific departure functions. The inverse reduced temperature τ is defined as

$$\tau = T_r/T \quad (2)$$

and the reduced density can be calculated according to the relation

$$\delta = \rho/\rho_r \quad (3)$$

The reducing temperature T_r and the reducing density ρ_r are calculated with the functional forms proposed by Klimeck [26] and Kunz et al. [22,23], which read

$$T_r = \sum_{i=1}^N \sum_{j=1}^N x_i x_j \beta_{T,ij} \gamma_{T,ij} \frac{x_i + x_j}{\beta_{T,ij}^2 x_i + x_j} (T_{c,i} \cdot T_{c,j})^{0.5} \quad (4)$$

and

$$\frac{1}{\rho_r} = \sum_{i=1}^N \sum_{j=1}^N x_i x_j \beta_{v,ij} \gamma_{v,ij} \frac{x_i + x_j}{\beta_{v,ij}^2 x_i + x_j} \frac{1}{8} \left(\rho_{c,i}^{-\frac{1}{3}} + \rho_{c,j}^{-\frac{1}{3}} \right)^3. \quad (5)$$

$\beta_{T,ij}$, $\gamma_{T,ij}$, $\beta_{v,ij}$, and $\gamma_{v,ij}$ are adjustable parameters for each binary pair of components i and j in the mixture, T_c are the critical temperatures and ρ_c the critical densities of the components in the mixture. One of the main advantages of this mixture model is its flexibility. The residual part of the dimensionless Helmholtz energy α_{oi}^r required in Equation (1) can be calculated from highly accurate multiparameter equations of state, such as the reference equation of state for CO₂ by Span and Wagner [14]. However, if no multiparameter equation of state is available for a component i in the mixture, any other equation of state could be translated to the dimensionless Helmholtz energy. As an example, Bell and Jäger [27] provide Helmholtz energy translations of common cubic equations of state, i.e., the Soave-Redlich Kwong equation of state (SRK) [28,29] and the Peng-Robinson equation of state (PR) [30].

In this work, only substances for which multiparameter equations of state are available, have been considered as additives to CO₂ in order to increase the efficiency of the power cycles discussed in the following section. The considered substances and the multiparameter equations of state used [31–81] to calculate thermophysical properties for these substances are listed in Table A in Annex A: Note that for some of the considered substances unpublished equations of state are available in NIST REFPROP 10.0 [31], which have been used in this work.

For some mixtures of CO₂ with other substances multi-fluid mixture models with adjusted parameters are available, see, e.g., Gernert and Span [24], Kunz et al. [23], or Herrig [25]. However, for many mixtures considered in this screening no multi-fluid mixture model with adjusted parameters are available in the literature. Therefore, these mixtures need to be modeled

predictively with the multi-fluid mixture model. The simplest possibility of using the multi-fluid mixture model predictively is omitting the departure function in Equation (1), i.e., $\alpha_{ij}^r = 0$. For the reducing temperature T_r and the reducing density ρ_r either linear mixing rules or Lorentz-Berthelot combining rules can be used, see [22]. Linear mixing rules yield

$$T_r = \sum_{i=1}^N x_i T_{c,i} \quad (6)$$

and

$$\frac{1}{\rho_r} = v_r = \sum_{i=1}^N x_i v_{c,i} = \sum_{i=1}^N x_i \frac{1}{\rho_{c,i}} \quad (7)$$

and Lorentz-Berthelot combining rules are used by setting

$$\beta_{T,ij} = 1, \gamma_{T,ij} = 1, \beta_{v,ij} = 1, \text{ and } \gamma_{v,ij} = 1. \quad (8)$$

However, linear mixing rules and Lorentz-Berthelot combining rules often do not yield good predictive results, as for example demonstrated by Jäger et al. [12,13,82]. Therefore, a recently developed combination of multi-fluid mixture models with g^E -models by Jäger et al. [12,13] has been applied to predictively calculate mixture properties. The multi-fluid mixture model in combination with a theoretically-based departure function that depends on a g^E -model reads

$$\alpha(\tau, \delta, \vec{x}) = \sum_{i=1}^N x_i [\alpha_{oi}^0(\rho, T) + \ln(x_i) + \alpha_{oi}^r(\delta, \tau)] + \frac{\ln(1 + b\rho)}{\ln(1 + b\rho_{\text{ref}})} \left[\frac{g_{\text{GE}}^{\text{E,r}}}{RT} - \sum_{i=1}^N x_i [\alpha_{oi}^r(\delta_{\text{ref}}, \tau) - \alpha_{oi}^r(\delta_{i,\text{ref}}, \tau_i)] \right]. \quad (9)$$

In Equation (8), b denotes the co-volume of the mixture, see [13], according to

$$b = \sum_{i=1}^N x_i b_i \quad (10)$$

with b_i being modified co-volumes of the components i in the mixture (see [13])

$$b_i = \frac{v_{s,i}^L}{u} \quad (11)$$

with $u = 1.17$ denoting the inverse packing fraction and $v_{s,i}^L$ is the molar volume of the saturated liquid of component i at the reference pressure $p_0 = 101325$ Pa. The density ρ_{ref} at p_0 is given by the linear mixing rule

$$\frac{1}{\rho_{\text{ref}}} = \sum_{i=1}^N x_i v_{s,i}^L. \quad (12)$$

In Equation (8), $g_{\text{GE}}^{\text{E,r}}$ denotes the residual part of the excess Gibbs energy, which in this work has been calculated with the COSMO-SAC model by Hsieh et al. [18].

The model COSMO-SAC was published by Lin and Sandler [16,17] and is a modification of the conductor-like screening

model for real solvents (COSMO-RS) developed by Klamt et al. [83–85]. The COSMO-SAC model used in this work is the model proposed by Hsieh et al. [18], which is an improvement of the original COSMO-SAC model by Lin and Sandler [16]. The residual excess Gibbs energy $g_{\text{GE}}^{\text{E,r}}$ can be obtained by the relation

$$g_{\text{GE}}^{\text{E,r}} = RT \sum_{i=1}^N x_i \ln(\gamma_{i,S}^r), \quad (13)$$

where $\gamma_{i,S}^r$ is the residual activity coefficient of component i in a liquid system S . According to the COSMO-SAC model suggested by Hsieh et al. [18], $\gamma_{i,S}^r$ can be calculated by the relation

$$\ln(\gamma_{i,S}^r) = n_i \sum_t^{\text{nhb,OT,OH}} \sum_{\sigma_m} p_i^t(\sigma_m^t) [\ln(\Gamma_S^t(\sigma_m^t)) - \ln(\Gamma_i^t(\sigma_m^t))]. \quad (14)$$

The input required to evaluate Equation (14) are COSMO-calculations for each component in the mixture of interest, see Klamt and Schüürmann [86]. The model assumes that the molecule is placed in a perfect conductor and subsequently screening charges σ are calculated on a molecule-shaped cavity. The obtained screening charges are averaged on a standard surface in order to obtain the screening charges σ_m of the standard segments m , see [18,87]. In Equation (14), n_i denotes the number of standard surface segments of molecule i . $p_i(\sigma_m)$ is the σ -profile of molecule i , which describes the probability of finding a segment with screening charge density σ_m on the surface of molecule i . It is defined by

$$p_i(\sigma_m) = \frac{A_i(\sigma_m)}{A_i}, \quad (15)$$

with A_i being the surface area of molecule i according to the COSMO-calculation and $A_i(\sigma_m)$ denoting the surface area of molecule i with a surface charge density σ_m . In the COSMO-SAC model of Hsieh et al. [18], the σ -profile is split into three contributions, a non-hydrogen-bonding part $p_i^{\text{nhb}}(\sigma_m^{\text{nhb}})$ and two hydrogen-bonding profiles considering hydrogen-bonding of hydroxyl groups $p_i^{\text{OH}}(\sigma_m^{\text{OH}})$ and hydrogen-bonding of other atoms $p_i^{\text{OT}}(\sigma_m^{\text{OT}})$. It is

$$p_i(\sigma) = p_i^{\text{nhb}}(\sigma) + p_i^{\text{OH}}(\sigma) + p_i^{\text{OT}}(\sigma). \quad (16)$$

More detailed information on how the sigma-profiles are generated from the COSMO-calculations can be taken from [18,87]. For illustration, the σ -profile and the screening charge densities for CO_2 are displayed in Figure 1.

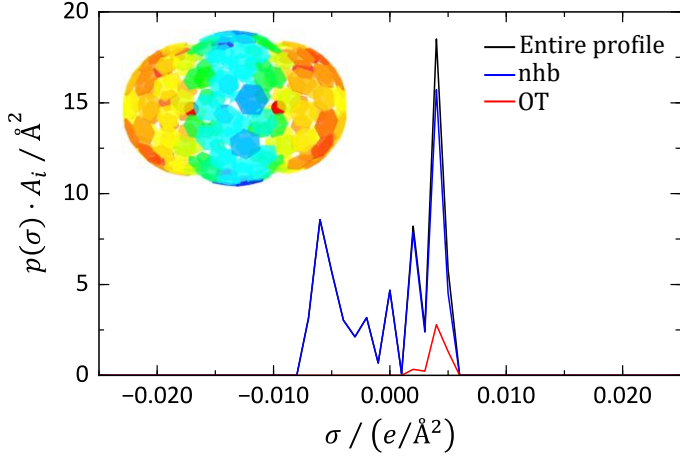


Figure 1: Screening charge densities for CO₂ (colored hexagons) from COSMO-calculations taken from the database by Bell et al. [87] and σ -profile multiplied by the surface area A_i (“Entire profile”, solid black line) split into the non-hydrogen-bonding (“nhb”, solid blue line) and hydrogen-bonding (“OT”, solid red line) part.

The segment activity coefficients of the segments m belonging to profile t in the mixture $\Gamma_S^t(\sigma_m^t)$ can be calculated from the system of equations

$$\ln(\Gamma_S^t(\sigma_m^t)) = -\ln \left\{ \sum_s^{\text{nhb,OH,OT}} \sum_{\sigma_n^s} p_S^s(\sigma_n^s) \Gamma_S^s(\sigma_n^s) \cdot \exp \left[-\frac{\Delta W(\sigma_m^t, \sigma_n^s)}{RT} \right] \right\}. \quad (17)$$

The σ -profiles $p_S^s(\sigma_n^s)$ of the mixture can be calculated according to

$$p_S^s(\sigma_n^s) = \frac{\sum_{i=1}^N x_i A_i p_i(\sigma_n^s)}{\sum_{i=1}^N x_i A_i}. \quad (18)$$

The exchange energy $\Delta W(\sigma_m^t, \sigma_n^s)$ of two surface segments m and n can be obtained from the electrostatic and hydrogen-bonding contribution

$$\Delta W(\sigma_m^t, \sigma_n^s) = \left(A_{ES} + \frac{B_{ES}}{T^2} \right) (\sigma_m^t + \sigma_n^s)^2 - c_{hb} (\sigma_m^t - \sigma_n^s)^2. \quad (19)$$

A_{ES} , B_{ES} , and c_{hb} are constants of the model, which are given by Hsieh et al. [18]. Finally, the segment activity coefficients of the segments m belonging to a profile t if only pure component i is present can be calculated by solving the system of equations

$$\ln(\Gamma_i^t(\sigma_m^t)) = -\ln \left\{ \sum_s^{\text{nhb,OH,OT}} \sum_{\sigma_n^s} p_i^s(\sigma_n^s) \Gamma_i^s(\sigma_n^s) \cdot \exp \left[-\frac{\Delta W(\sigma_m^t, \sigma_n^s)}{RT} \right] \right\}. \quad (20)$$

All equations of state used in this work are available in the thermophysical property software TREND 4.0 [88]. The

COSMO-files for all components studied in this work have been taken from the database provided by Bell et al. [87], which is an extension of the database of Mullins et al. [89]. The algorithms for phase equilibrium calculations with TREND are described in the works of Gernert et al. [90] and Jäger [91].

CYCLE MODELING

For comparison of the mixtures, two different sCO₂ cycle architectures have been chosen. As shown in Figure 2, the first layout consists of a simple cycle including only the essential main components. Starting at the compressor inlet in point 1, the fluid is compressed to the upper pressure level at point 2. Subsequently, heat is added in an isobaric heater until the upper temperature level is reached in point 3 corresponding to the turbine inlet. After expansion to point 4, excess heat is rejected in a cooler going back to the starting conditions. Figure 2 shows the second layout, in which a recuperator extends the simple cycle. In this way, a part of the heat at the turbine outlet (point 5) is transferred back to the compressed fluid (point 2) reducing the amount of heat to be added in the heater.

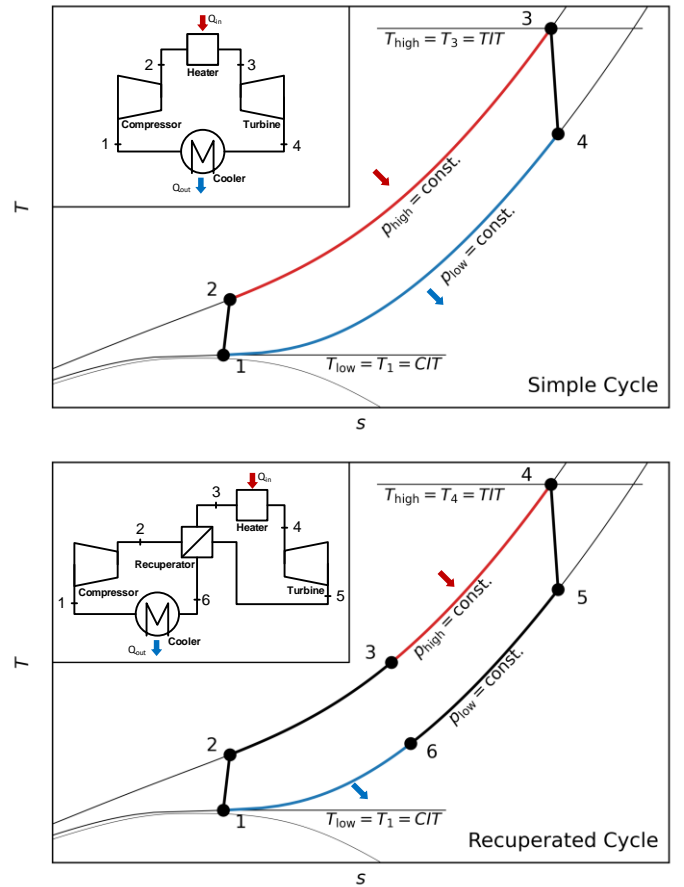


Figure 2: Block diagrams and T - s diagrams of the considered cycle architectures.

The recuperation in the second cycle was modeled by setting a minimum pinch point difference at the cold end of the recuperator, i.e., $T_6 = T_2 + \Delta T_R$, where ΔT_R denotes the temperature difference at the pinch point. In addition to that, a simplified check if the pinch point is violated anywhere along the recuperator has been done by a stepwise calculation of the heat transfer. Using the mixture models described before, calculations were done for both layouts based on preset values for pressure and temperature at the inlets of the compressor and the turbine. Beside all relevant fluid properties, such as enthalpy or density, the number and type of simultaneously present thermodynamic phases at each state point as well as the mixtures boiling temperature at both pressure levels were calculated. For comparison of the working fluids, the thermal efficiency was used which can be calculated by the relation

$$\eta_{\text{th,SC}} = 1 - \frac{h_4 - h_1}{h_3 - h_2} \quad (21)$$

for the simple cycle and

$$\eta_{\text{th,RC}} = 1 - \frac{h_6 - h_1}{h_4 - h_3} \quad (22)$$

for the recuperated cycle. The boundary conditions applied to the thermodynamic cycles are listed in Table 1.

Table 1: Boundary conditions applied to the process calculations.

Boundary condition	Symbol	Value
Minimum temperature	$\vartheta_{\text{low}} \equiv \text{CIT}$	31 ... 40 °C
Maximum temperature	$\vartheta_{\text{high}} \equiv \text{TIT}$	500 °C
Lower pressure level	p_{low}	7.4 MPa
Upper pressure level	p_{high}	20 MPa
Compressor efficiency	η_c	0.8
Turbine efficiency	η_T	0.9
Min. pinch point difference recuperator	ΔT_R	10 K

Temperatures were oriented to an exemplary waste heat recovery application with possible air-recooling to ambient conditions. The lower temperature level has been varied within a range of 31 °C to 40 °C while the upper temperature has been fixed at 500 °C. The lower temperature corresponds to the temperature at the compressor inlet and the upper temperature is the temperature at the turbine inlet. Pressure levels were set to a near critical value of 7.4 MPa for the lower pressure level and 20 MPa for the upper pressure level. Losses were treated in terms of isentropic efficiencies for the compressor and the turbine. For the recuperator, a minimum pinch point difference of 10 K was applied. Pressure losses were completely neglected. In all cases, the operation of both process architectures of the cycle with pure CO₂ was used as a basis for comparison. With reference to the considered temperature range of $\vartheta_{\text{low}} = 31 \dots 40$ C at the compressor inlet, Figure 3 shows the changes (differences) in thermal efficiency compared to $\vartheta_{\text{low}} = 31$ °C representing the temperature closest to the critical point regarding the set boundary conditions. As can be seen in the graph, with the exception of a small peak just above 31 °C, the efficiency drops

significantly with increasing inlet temperature. At 40 °C, a decrease of about 6% for the simple cycle and about 4% for the recuperated cycle can be noted. The aforementioned small increases are due to the pseudo-critical point at the chosen pressure of $p_{\text{low}} = 7.4$ MPa, which is slightly higher than the critical pressure $p_c = 7.3773$ MPa [92].

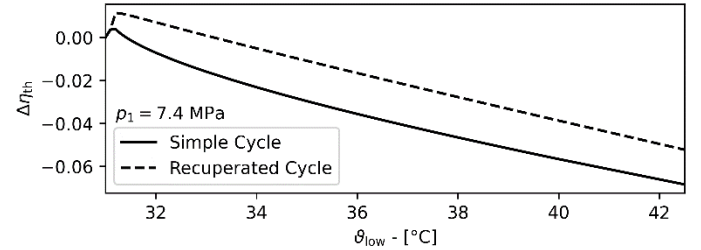


Figure 3: Difference of the thermal efficiencies calculated with varying ϑ_{low} and the thermal efficiency for $\vartheta_{\text{low}} = 31$ °C for the simple cycle and the recuperated cycle with pure CO₂. All other boundary conditions have been set according to the values listed in Table 1.

RESULTS AND DISCUSSION

To identify promising mixing partners for a more detailed examination, calculations were done for a total of 135 fluids and for a compressor inlet temperature of 40 °C, which corresponds to the most inefficient inlet conditions regarding the boundary conditions specified in this work, see Table 1, and the usage of pure CO₂, see Figure 3. Since multiphase flows might lead to problems, for example in the compressor or turbine, this study has been restricted to mixtures that do not decompose into several phases at the state points of the cycle. This means that all mixtures existing in more than one phase in any of the state points of the process have been excluded from this study. In addition to that, concerning the recuperated case, all combinations leading to pinch-point violations in the recuperator were also discarded. Figure 4 shows the results for the remaining 111 fluids in terms of the change in efficiency as a function of the mole fraction of the mixture. Starting with the groups of alkenes, alkynes, and alkanes it can be seen that for the simple cycle configuration almost all substances cause a reduction in efficiency with increasing mole fraction. However, a small improvement in the efficiency is obtained when adding up to 5% of propyne, see Figure 4a. A slightly positive trend can also be assumed for propadiene, although to a lesser extent. For both of these fluids, the mixtures decompose in two phases for the studied mole fractions higher than 5%. In contrast, an opposite pattern regarding the efficiencies can be observed for the recuperated case. With the exception of methane, all fluids lead to an improvement in efficiency, which tends to increase with higher mole fractions. Particularly noticeable is propane with an increase of about 4% at a mole fraction of 40%, see Figure 4d. In the group of aromatics, alcohols, ethers, and naphthenics, only small changes can be noted for both cycles. The reversal of efficiency trends when comparing the simple with the recuperated cycle also occurs for these substances. Similar to the

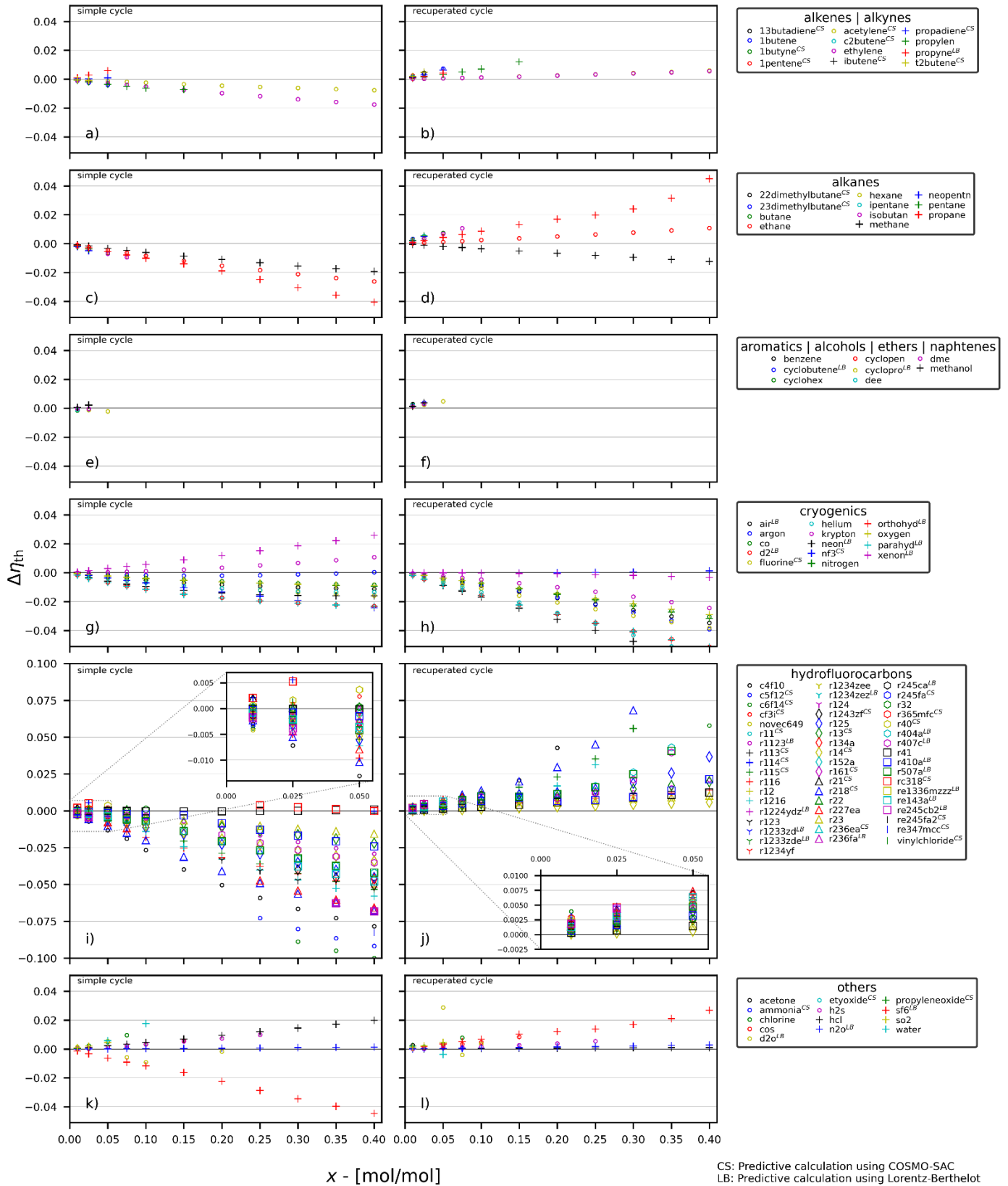


Figure 4: Efficiency change of the considered mixtures compared to cycles with pure CO₂ as working fluid for the minimum process temperature $\vartheta_{low} = 40$ °C and all other boundary conditions as given in Table 1.

previously discussed substances, most of the substances in this group that have led to a negative effect in the simple cycle cause positive changes in the recuperated case. However, methanol is exceptional, as it slightly increases the efficiency in both cases for low concentrations. As indicated by the absence of plot points for higher mole fractions in Figure 4e and f, another significant aspect of this group of fluids is a strongly decreasing solubility of the mixing partners with increasing mole fraction. When the solubility limit is reached, more than one fluid phase is present at some of the state points. Consequently, the corresponding results were discarded during the pre-selection process. Contrary to the groups mentioned before, a distinct improvement of the efficiency for the simple cycle can be found in the group of cryogenic fluids for several species. As shown in Figure 4g, the addition of krypton causes an improvement in efficiency of approx. 1% at a molar fraction of 40%, while the same amount of xenon leads to a calculated increase in efficiency of over 2.5%. An increasing efficiency with increasing mole fractions can also be assumed for argon at mole fractions of argon higher than 40%, which, however, have not been investigated in this study. At a closer look, it is remarkable that all three mentioned fluids are from the group of noble gases. Furthermore, for xenon, krypton, and argon, the increase in efficiency correlates with the respective ordinal number. Figure 5 shows a separate comparison of the results for the noble gases. For the binary mixture of xenon + CO₂, Lorentz-Berthelot combining rules (LB) have been applied as neither an adjusted mixture model is available nor a σ -profile for xenon in order to apply COSMO-SAC are available. In order to estimate the validity of the results for xenon regarding the efficiency calculations, results for krypton calculated with the multi-fluid mixture model with adjusted parameters have been compared to results for krypton using the LB-model. Figure 5 shows that for the binary mixture of CO₂ + krypton the deviations of these models in calculated thermal efficiencies for the simple cycle are rather small. It can therefore be assumed that the LB-model also provides reasonable results for CO₂ + xenon. Looking at the recuperated case in Figure 4h,

it can be seen that the efficiency of xenon shows only a slight downward trend, instead of decreasing rapidly as many of the other fluids in the cryogenics group. For krypton, however, the reversal of the trend is more apparent, i.e., for the simple cycle the efficiency increases with increasing mole fractions of krypton and for the recuperated cycle the efficiency decreases. Almost all other fluids in this group lead to a loss of efficiency for both cycle architectures further decreasing with higher mixing ratios. Contrarily, in the group of hydrofluorocarbons, see Figure 4i and j, the reversal of the trends is again evident for most fluids. Especially at higher mole fractions of the additives, see for example the addition of R-115, R-125 or R-218, a distinct reduction in efficiency for the simple cycle and on the contrary a noticeable increase of the efficiency for the recuperated cycle is apparent. Apart from this, several mixtures with low mole fractions of the additive can be found, which slightly improve the efficiency for both cycle architectures. As can be seen in the detailed views of Figure 4i and Figure 4j, this applies, for example, to R-114 and RC-318 for mole fractions of 2.5% and to R-40 and CF₃I for mole fractions up to 5%. For R-32, our model could not confirm the potential improvements in simple cycle efficiencies previously reported by Baik and Lee [8]. When comparing the two cycles in this group, it is also noticeable that the recuperated case contains a significantly lower number of fluids than the simple cycle, which is a result of pinch point violations in the recuperator and discarding of all of the mixtures for which this violations occurred. By taking a closer look at the results for the simple cycle, RC-318 yields phases splits at the state points of the cycle between 2.5% and 25%, see Figure 4i. Regarding the results of the last group (“others”) in Figure 4k and Figure 4l, most substances show positive changes in efficiency for both cycle layouts. Especially by adding hydrochloric acid (HCl) or water an increase up to 2% has been calculated for the simple cycle. While the addition of water has no positive effect in the recuperated case, mainly the addition of hydrogen sulfide (H₂S) or carbonyl sulfide (COS) leads to better efficiencies in both cases. Sulfur hexafluoride (SF₆) behaves differently than the other fluids in this group as it shows a distinct improvement in the recuperated case and a decrease in the simple cycle. Compared to propane (see and Figure 4c and d), there is a remarkable similarity in the behavior. With increasing mole fraction, both fluids lead to a strong reduction of efficiency in the simple cycle, whereas under the aforementioned keyword “trend reversal”, an even strong improvement can be observed in the recuperated case. However, note that CO₂ + SF₆ has been modeled with the simple LB-model as neither a model with adjusted parameters nor a σ -profile for SF₆ in order to use COSMO-SAC are available. Regarding the results for heavy water (D₂O), a sudden change in efficiency occurs in the recuperated case when comparing the molar fractions of 5% and 7.5%. For CO₂ + water an adjusted mixture model exists [24] whereas for CO₂ + heavy water the LB-model had to be used. As there is a lack of similarity between the results for normal water and heavy water, it is assumed that the sudden changes stem from erroneous behavior of the simple predictive mixture model. In order to carry out a representative investigation of several

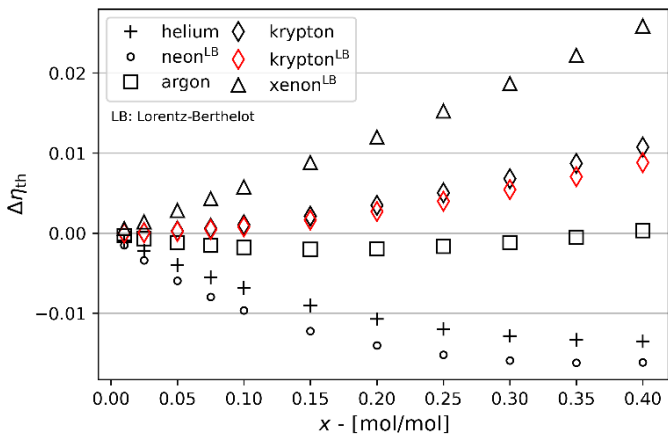


Figure 5: Comparison of the difference in efficiencies of the simple cycle model for mixtures with various noble gases from the efficiency for pure CO₂.

influences on the efficiency, five promising mixing partners were selected for a more detailed investigation. The selected fluids are listed in Table 2 including their largest influence on the efficiencies of both types of cycles.

Table 2: Selection of promising mixing partners for a more detailed analysis.

Name	Chemical symbol	Mixing Model	$\Delta\eta_{th,max}$ Simple cycle	$\Delta\eta_{th,max}$ Recuperated cycle
Carbonyl sulfide	COS	Adjusted	$\approx +1.0\%$	$\approx +0.5\%$
Krypton	Kr	Adjusted	$\approx +1.2\%$	$\approx -2.2\%$
Propane	C ₃ H ₈	Adjusted	$\approx -4.2\%$	$\approx +4.2\%$
Sulfur hexafluoride	SF ₆	LB	$\approx -4.2\%$	$\approx +2.3\%$
Xenon	Xe	LB	$\approx +2.2\%$	$\approx -0.25\%$

Based on the previously mentioned performance in the recuperated case, propane and SF₆ were selected. Due to the significant increase in efficiency in the simple cycle, the noble gases xenon and krypton have also been selected. From the last group, COS was selected for a more detailed examination as it shows increasing efficiencies with increasing mole fractions for both cycle process architectures. In the same group, similar efficiency changes but with a smaller impact in the recuperated case can be seen when adding H₂S. Furthermore, significant efficiency increases were also observed for several hydrofluorocarbons for the recuperated cycle. However, since the majority of the species with significant impact on efficiency have high global warming potentials (GWP) and/or ozone depletion potentials (ODP) (e.g. R-218, R-115, RC-318, R-404A) [93,94], these species were not considered further. Additionally, also water and HCl were not further investigated, despite significant positive effects on efficiency, because HCl is rather harmful and many mixture compositions of CO₂ + water lead to phase splits. For the evaluation of the influencing factors causing the efficiency variations, Figure 6 shows the process cycles in the h - s diagram for several concentrations of the selected mixing partners. Additionally, a representation of the changes in the enthalpy differences (compared to the cycle with pure CO₂) is given by bar charts. In these charts, Δh_C stands for the compression work, Δh_R for the recuperated heat (recuperated case, points 2-3), Δh_H denotes the heat added in the heater (recuperated case, points 3-4), Δh_T denotes the enthalpy difference in the turbine and $\Delta h_{Q,tot}$ stands for the total heat added between the compressor exit and the turbine inlet. Beginning from the top with xenon it can be seen that with increasing mole fractions the position of the isobars remains almost unaffected. However, it is more apparent that the upper end of the cycle, even though the turbine inlet temperature TIT remains constant, moves towards lower enthalpy values with increasing molar fractions of xenon. In this way, the amount of total heat $\Delta h_{Q,tot}$ reduces. Thus, the efficiency of the simple cycle increases by compensating the slight deteriorations regarding the enthalpy differences of the compressor Δh_C and the turbine Δh_T with a distinct decrease of the added heat. At the same time, the heat transferred in the recuperator Δh_R is reduced,

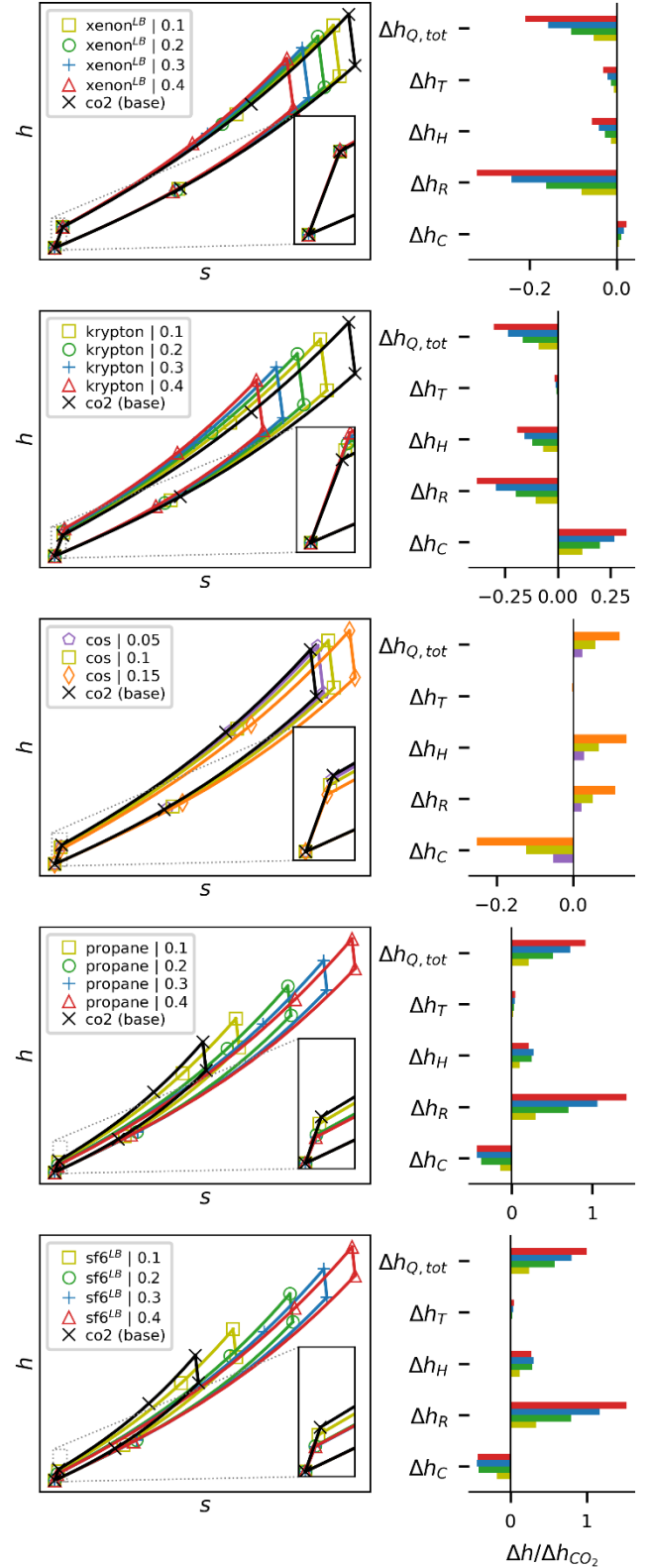


Figure 6: Effects of selected mixtures on the shape and location of the process in the h - s diagram and the differences in enthalpies in the components compared to the cycle with pure CO₂.

which in the recuperated case cancels out the positive increase in efficiency. Similar results are obtained for krypton. The resulting relative reduction of $\Delta h_{Q,tot}$ and Δh_H is even greater than for xenon but gets compensated by a significant increase of Δh_C , clearly reducing the increase in efficiency of the simple cycle compared to xenon. Again, the same effects as for xenon lead to a more significant drop in the performance of the recuperated case. Contrary to the two noble gases, the plots for COS show a slight decrease of the slopes of the isobars in the h - s diagram with increasing mole fractions. Additionally, higher amounts of COS lead to higher enthalpy values for the upper temperature level resulting in an increase of heat to be added, as can be seen for $\Delta h_{Q,tot}$ and Δh_H in the bar chart. While the turbine output Δh_T remains almost the same, the compression work Δh_C reduces significantly, which results in the positive change in efficiency for both cycle architectures as shown in Figure 4. Furthermore, the enthalpy differences change unevenly with increasing mole fractions, see Figure 6. Using the example of the enthalpy difference in the compressor Δh_C , the change from a mole fraction of 0.10 to 0.15 is significantly greater than from 0.05 to 0.10. By comparing the plots for propane and SF₆ it can be seen that both the shape of the cycles as well as the bar charts representing the relative enthalpy differences are almost identical for both fluids. The slopes of the isobars decrease noticeably with increasing concentrations for both fluids. The compressor work Δh_C is reduced by up to approximately 40% while the enthalpy difference in the turbine remains nearly unaffected. The bar charts show that the total heat input $\Delta h_{Q,tot}$ needs to be more than doubled for higher mole fractions. As the increase in added heat significantly exceeds the aforementioned savings of compressor work, this mainly causes the previously discussed deterioration of the simple cycle efficiency for both fluids. Regarding the recuperated cases, it is noticeable that the amount of heat available for recuperation increases even more than the amount of total heat needed. For the highest mole fractions, the recuperated heat increases to approximately 140% of the recuperated heat when using pure CO₂. Furthermore, it is apparent that the recuperated heat increases significantly more with the mole fraction of propane or SF₆ than the heat Δh_H that needs to be added in the heater.

Figure 7 shows critical curves as well as phase envelopes for some of the studied binary mixtures. The algorithms for calculating phase equilibria and critical points, which are implemented in TRENDS 4.0, are described in refs. [90,95]. As can be seen in the uppermost subplot, adding xenon hardly influences the form and shape of the phase boundaries compared to pure CO₂. The critical point itself shifts with higher mole fractions to lower temperatures and lower pressures approaching the critical point of xenon. Compared to the other substances studied, the critical point of xenon is relatively close to the critical point of CO₂. This explains the previously discussed similarity regarding the cold end of the cycle and the isobars. By contrast, adding krypton to CO₂ clearly shifts the position of the dew and bubble line. Regarding the temperature, the critical point moves to lower values with higher concentrations of

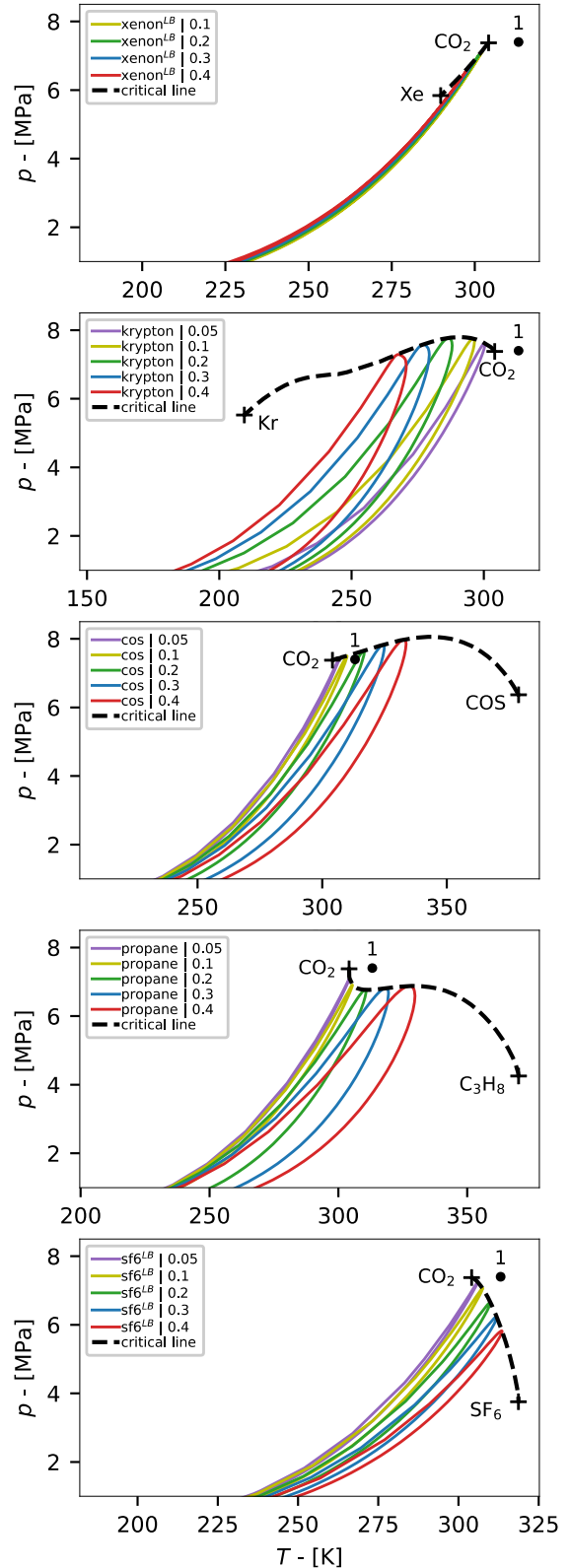


Figure 7: Critical curves and phase envelopes for the studied mixtures. Point 1 marks the CIT used in the screening.

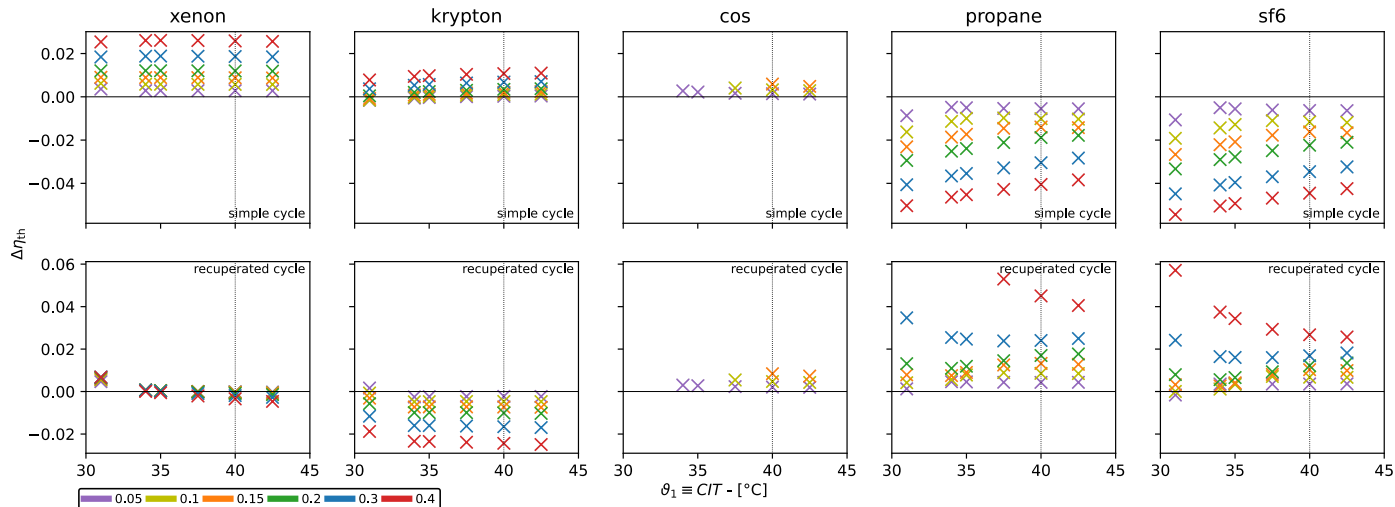


Figure 8: Temperature dependence of the change in efficiency for the selected mixtures.

krypton in CO₂. The critical pressure on the other hand increases up to a molar fraction of approximately 0.2 and then reduces with higher concentrations. In contrast to the other fluids in Figure 7, the addition of COS initially changes the critical point towards higher pressures and higher temperatures, so that it gets gradually closer to the inlet conditions of the compressor. This results in a reduction of the compressor work shown in Figure 6. From a molar fraction of approx. 0.17, both the critical pressure and critical temperature are higher than the pressure and temperature at the compressor inlet, respectively. Thus, these points were rejected because of the presence of two fluid phases in the pre-selection. For both propane and SF₆, higher concentrations result in a change of the critical point to lower pressures and higher temperatures. Nevertheless, in contrast to the *h-s* diagrams in Figure 6, Figure 7 shows considerable differences for both fluids. Note that the critical curves of SF₆ and Xenon have been calculated with the simple LB-model and therefore larger deviations from the real fluid behavior may occur, see, e.g., ref. [12,13,96,97]. For propane, the calculated critical pressure drops steeply up to a molar fraction of about 0.2. Subsequently, the pressure slightly increases up to a molar fraction of 0.4 and then drops sharply with higher concentrations. On the other hand, for SF₆ the calculated critical pressure shows an immediate and persistent decrease. Thus, the critical temperature of propane + CO₂ mixtures increases to higher values than the critical temperature of SF₆ + CO₂ mixtures investigated in this study.

Applying the boundary conditions defined in Table 1, Figure 8 shows the change in thermal efficiency for different concentrations of the selected mixtures (see Table 2) over the entire range of compressor inlet temperatures (CIT). For the two noble gases xenon and krypton, the change in efficiency calculated for the simple cycle remains almost constant for all concentrations over the entire temperature range. Only krypton shows a slight drop at lower temperatures. It is remarkable that xenon shows hardly any deterioration of the efficiency against

pure CO₂ at any time. In the recuperated case, both fluids show a small increase in efficiency towards lower temperatures. For COS, the efficiencies compared to pure CO₂ increase slightly with decreasing temperatures for both cycles. However, due to the absence of the corresponding points in the plot, it is noticeable that the mixture decomposes into more than one phase both at lower temperatures and at high concentrations of COS in CO₂. Even with a comparatively low molar fraction of 0.05, the entire temperature range cannot be covered without several fluid phases being present in one or more cycle points. This is consistent with the previously discussed shift of the critical point to higher pressures and temperatures at higher concentrations. Equivalently to Figure 6, propane and SF₆ also show almost the same behavior in Figure 8. In contrast to SF₆, however, propane shows a pinch-point violation in the recuperated case at high concentrations. Apart from this, both fluids show a significant decrease in efficiency (compared to pure CO₂) of the simple cycle at lower temperatures across all concentrations. Despite different boundary conditions, the trend for SF₆ is consistent with the results previously reported by Baik and Lee [8]. In contrast to the simple cycle, for both fluids this effect is mostly reversed in the recuperated case. For lower temperatures, higher efficiency increases are achieved with a steeper decline for higher concentrations. Only at low concentrations, a reduction of the increase in efficiency to low temperatures can be seen.

CONCLUSIONS

In this work, the potential for increasing the thermal efficiency by adding additives to pure CO₂ was evaluated based on an exemplary application of a sCO₂ cycle. Using predictive mixing models as well as accurate multi-fluid mixture models with adjusted parameters, a comprehensive screening for 135 fluids was performed for two different cycle layouts. From these results, five potential mixture candidates were chosen and investigated in detail. Within this selection, efficiency increases of more than 4% compared to a cycle with pure CO₂ and the same

boundary conditions are predicted. For simple cycle applications, the use of the noble gases xenon and krypton has been found to be particularly interesting. Especially xenon offers a noticeable efficiency increase over a wide temperature range with similar cycle properties compared to pure CO₂. In the recuperated case, the largest increases in thermal efficiency have been calculated for SF₆ and propane, when omitting the hydrofluorocarbons having a large GWP and/or ODP. However, upon closer investigation it was found that a large amount of heat would need to be recuperated when using the binary mixtures of CO₂ with propane or SF₆ in a recuperated cycle. This would lead to a large size of the heat exchanger and therefore is most likely not economically feasible.

Since this study was mainly concerned with a theoretical screening of potential additives to CO₂ in order to increase the thermal efficiency, in a further step additional investigations concerning the selected mixtures would be necessary. For example the thermal stability of additives and chemical reactions should be investigated, as studies show that SF₆ and COS possibly decompose into other substances at temperatures close to or below the maximum temperature of the cycles investigated in this study [98–100].

In general, it has been shown in this work that the increases in efficiency can be attributed to different effects depending on the fluid, the molar composition of the mixture, and the boundary conditions. All of these parameters have an influence on the compression enthalpy, amount of heat to be added to the cycle and heat available for recuperation, which directly influence the thermal efficiency. It has been demonstrated that the critical point can be shifted within certain limits to lower as well as to higher pressures and temperatures when adding a suitable mixing partner. However, special care needs to be taken in order to avoid multi-phase flows in sensitive components, as adding a substance might lead to phase splits as discussed for example for COS. This all requires the mixture to be adapted to the respective application.

This work was restricted to predicting the efficiency of two cycle configurations using binary mixtures of CO₂ with other substances for which multi-parameter equations of state are available. Future work will focus on the application of this method to more complex cycle architectures and variable boundary conditions. Furthermore, the amount of mixtures investigated could be significantly increased by considering multi-component mixtures and by extending the database of the pure fluids by on the one hand using simpler equations of state for the pure fluids (e.g. cubic equations of state) and on the other hand perform COSMO-calculations for missing substances.

NOMENCLATURE

Symbols

A	molecular surface area (\AA^2)
A_{ES}	constant of COSMO-SAC ($\text{kcal \AA}^4 \text{ mol}^{-1} \text{ e}^{-2}$)
b	co-volume ($\text{m}^3 \text{ mol}^{-1}$)
B_{ES}	constant of COSMO-SAC ($\text{kcal \AA}^4 \text{ K}^2 \text{ mol}^{-1} \text{ e}^{-2}$)
c_{hb}	constant of COSMO-SAC ($\text{kcal \AA}^4 \text{ mol}^{-1} \text{ e}^{-2}$)

∂	partial derivative
F	parameter of the departure function
g	molar Gibbs energy (J mol^{-1})
i	index of summation
j	index of summation
n	number of standard surface segments of a molecule
N	number of components in the mixture
p	pressure (Pa)
$p(\sigma)$	sigma-profile
R	universal gas constant ($\text{J mol}^{-1} \text{ K}^{-1}$)
T	temperature (K)
x	mole fraction
\vec{x}	vector of mole fractions

Greek symbols

α	dimensionless Helmholtz energy
β	model parameter
δ	reduced density
γ	model parameter
Γ	Segment activity coefficient
η	Efficiency
ϑ	temperature ($^{\circ}\text{C}$)
ρ	molar density (mol m^{-3})
σ	screening charge density (e \AA^{-2})
τ	reduced temperature (-)

Subscripts

c	property at the critical point
ES	electrostatic
GE	property calculated from an excess Gibbs energy model
hb	hydrogen-bonding
i	property of component i
j	property of component j
o	property of a pure fluid
r	reducing property
s	property at saturation (at vapor-liquid equilibrium)
T	related to the turbine
C	related to the compressor
R	related to the recuperator
tot	total (amount)
ref	property at reference pressure

Superscripts

0	ideal gas property
E	excess property
L	property of a liquid phase
r	residual property

Chemical Formulas

CO ₂	carbon dioxide
N ₂ O ₄	dinitrogen tetroxide
SF ₆	sulfur hexafluoride
TiCl ₄	titanium(IV) chloride

Abbreviations

CIT	Compressor inlet temperature
COSMO	Conductor-like screening model
COSMO-RS	Conductor-like screening model for real solvents
COSMO-SAC	Conductor-like screening model segment activity coefficients
CS	The binary mixture was modeled predictively with the combination of the multi-fluid mixture model with COSMO-SAC
GWP	Global warming potential
LB	The binary mixture was modeled predictively using Lorentz-Berthelot combining rules
ODP	Ozone depletion potential
PR	Peng-Robinson equation of state
SAFT	Statistical associating fluid theory
SRK	Soave-Redlich-Kwong equation of state
TIT	Turbine inlet temperature

ACKNOWLEDGEMENTS

This work was carried out within the Supercritical Carbon Dioxide-Lab (suCOO-Lab) of the School of Engineering Sciences of TU Dresden. The authors want to thank the School of Engineering Sciences of TU Dresden for partial funding of the presented results.

REFERENCES

- [1] Y. Ahn, S.J. Bae, M. Kim, S.K. Cho, S. Baik, J.I. Lee, J.E. Cha, Review of supercritical CO₂ power cycle technology and current status of research and development, *Nucl. Eng. Technol.* 47 (2015) 647–661. <https://doi.org/10.1016/j.net.2015.06.009>.
- [2] C. Geng, Y. Shao, W. Zhong, X. Liu, Thermodynamic Analysis of Supercritical CO₂ Power Cycle with Fluidized Bed Coal Combustion, *Journal of Combustion*. 2018 (2018) 1–9. <https://doi.org/10.1155/2018/6963292>.
- [3] U. Gampe, J. Henoch, G. Gerbeth, F. Hannemann, S. Rath, U. Hampel, S. Glos, Concept and preliminary design of a 600 °C+ sCO₂ test facility, in: Proceedings of the 2nd European SCO₂ Conference 2018, Essen, Germany, 2018. <https://doi.org/10.17185/dupublico/46084>.
- [4] J. Yin, Q. Zheng, Z. Peng, X. Zhang, Review of supercritical CO₂ power cycles integrated with CSP, *Int J Energy Res.* 44 (2020) 1337–1369. <https://doi.org/10.1002/er.4909>.
- [5] V. Dostal, P. Hejzlar, M.J. Driscoll, The Supercritical Carbon Dioxide Power Cycle: Comparison to Other Advanced Power Cycles, *Nuclear Technology*. 154 (2006) 283–301. <https://doi.org/10.13182/NT06-A3734>.
- [6] O. Kizilkan, Performance assessment of steam Rankine cycle and sCO₂ Brayton cycle for waste heat recovery in a cement plant: A comparative study for supercritical fluids, *Int J Energy Res.* (2020) er.5138. <https://doi.org/10.1002/er.5138>.
- [7] S. Glos, M. Wechsung, R. Wagner, A. Heidenhof, D. Schlehner, Evaluation of sCO₂ power cycles for direct and waste heat applications, (2018). <https://doi.org/10.17185/DUEPUBLICO/46082>.
- [8] S. Baik, J.I. Lee, Preliminary Study of Supercritical CO₂ Mixed With Gases for Power Cycle in Warm Environments, in: Volume 9: Oil and Gas Applications; Supercritical CO₂ Power Cycles; Wind Energy, American Society of Mechanical Engineers, Oslo, Norway, 2018: p. V009T38A017. <https://doi.org/10.1115/GT2018-76386>.
- [9] M. Binotti, C.M. Invernizzi, P. Iora, G. Manzolini, Dinitrogen tetroxide and carbon dioxide mixtures as working fluids in solar tower plants, *Solar Energy*. 181 (2019) 203–213. <https://doi.org/10.1016/j.solener.2019.01.079>.
- [10] M. Binotti, G. Di Marcoberardino, P. Iora, C.M. Invernizzi, G. Manzolini, Supercritical carbon dioxide/alternative fluid blends for efficiency upgrade of solar power plant, Proceedings of the 3rd European Supercritical CO₂ Conference. (2019). <https://doi.org/10.17185/DUEPUBLICO/48892>.
- [11] G. Manzolini, M. Binotti, D. Bonalumi, C. Invernizzi, P. Iora, CO₂ mixtures as innovative working fluid in power cycles applied to solar plants. Techno-economic assessment, *Solar Energy*. 181 (2019) 530–544. <https://doi.org/10.1016/j.solener.2019.01.015>.
- [12] A. Jäger, I.H. Bell, C. Breitung, A theoretically based departure function for multi-fluid mixture models, *Fluid Phase Equilib.* 469 (2018) 56–69. <https://doi.org/10.1016/j.fluid.2018.04.015>.
- [13] A. Jäger, E. Mickoleit, C. Breitung, A Combination of Multi-Fluid Mixture Models with COSMO-SAC, *Fluid Phase Equilib.* 476 (2018) 147–156. <https://doi.org/10.1016/j.fluid.2018.08.004>.
- [14] R. Span, W. Wagner, A New Equation of State for Carbon Dioxide Covering the Fluid Region from the Triple-Point Temperature to 1100 K at Pressures up to 800 MPa, *J. Phys. Chem. Ref. Data*. 25 (1996) 1509–1596. <https://doi.org/10.1063/1.555991>.
- [15] A. Fredenslund, R.L. Jones, J.M. Prausnitz, Group-Contribution Estimation of Activity Coefficients in Nonideal Liquid Mixtures, *AIChE J.* 21 (1975) 1086–1099.
- [16] S.-T. Lin, S.I. Sandler, A Priori Phase Equilibrium Prediction from a Segment Contribution Solvation Model, *Ind. Eng. Chem. Res.* 41 (2002) 899–913. <https://doi.org/10.1021/ie001047w>.
- [17] S.-T. Lin, S.I. Sandler, A Priori Phase Equilibrium Prediction from a Segment Contribution Solvation Model. - Additions and Corrections, *Ind. Eng. Chem. Res.* 43 (2004) 1322–1322. <https://doi.org/10.1021/ie0308689>.
- [18] C.-M. Hsieh, S.I. Sandler, S.-T. Lin, Improvements of COSMO-SAC for vapor–liquid and liquid–liquid equilibrium predictions, *Fluid Phase Equilibria*. 297 (2010) 90–97. <https://doi.org/10.1016/j.fluid.2010.06.011>.
- [19] E. Mickoleit, A. Jäger, C. Breitung, Carrier-Fluid Screening for a Three-Phase Sublimation Refrigeration Cycle with CO₂ Using Reference Equations of State and

- COSMO-SAC, *J. Chem. Eng. Data.* (2019) 1124–1134. <https://doi.org/10.1021/acs.jced.9b00514>.
- [20] E. Mickoleit, C. Breikopf, A. Jäger, Influence of Equations of State and Mixture Models on the Design of a Refrigeration Process, *Int. J. Refrig.* 121 (2021) 193–205. <https://doi.org/10.1016/j.ijrefrig.2020.10.017>.
- [21] E.W. Lemmon, R. Tillner-Roth, A Helmholtz Energy Equation of State for Calculating the Thermodynamic Properties of Fluid Mixtures, *Fluid Phase Equilib.* 165 (1999) 1–21.
- [22] O. Kunz, R. Klimeck, W. Wagner, M. Jaeschke, The Gerg-2004 Wide Range Equation of State for Natural Gases and Other Mixtures GERG TM15 2007, VDI-Verl., Düsseldorf, Germany, 2007.
- [23] O. Kunz, W. Wagner, The GERG-2008 Wide-Range Equation of State for Natural Gases and Other Mixtures: An Expansion of GERG-2004, *J. Chem. Eng. Data.* 57 (2012) 3032–3091. <https://doi.org/10.1021/je300655b>.
- [24] J. Gernert, R. Span, EOS-CG: A Helmholtz energy mixture model for humid gases and CCS mixtures, *J. Chem. Thermodyn.* 93 (2016) 274–293. <https://doi.org/10.1016/j.jct.2015.05.015>.
- [25] S. Herrig, New Helmholtz-energy equations of state for pure fluids and CCS-relevant mixtures, Dissertation, Ruhr-Universität Bochum, 2018.
- [26] R. Klimeck, Entwicklung einer Fundamentalgleichung für Erdgase für das Gas- und Flüssigkeitsgebiet sowie das Phasengleichgewicht, Dissertation, Ruhr-Universität Bochum, 2000.
- [27] I.H. Bell, A. Jäger, Helmholtz Energy Transformations of Common Cubic Equations of State for Use with Pure Fluids and Mixtures, *J Res Natl Inst Stan.* 121 (2016) 238–263. <https://doi.org/10.6028/jres.121.011>.
- [28] O. Redlich, J.N.S. Kwong, On the Thermodynamics of Solutions. V. An Equation of State. Fugacities of Gaseous Solutions., *Chem. Rev.* 44 (1949) 233–244.
- [29] G. Soave, Equilibrium Constants from a Modified Redlich-Kwong Equation of State, *Chem. Eng. Sci.* 27 (1972) 1197–1203. [https://doi.org/10.1016/0009-2509\(72\)80096-4](https://doi.org/10.1016/0009-2509(72)80096-4).
- [30] D.-Y. Peng, D.B. Robinson, A New Two-Constant Equation of State, *Ind. Eng. Chem. Fund.* 15 (1976) 59–64. <https://doi.org/10.1021/i160057a011>.
- [31] E.W. Lemmon, I.H. Bell, M.L. Huber, M.O. McLinden, REFPROP, NIST Standard Reference Database 23 Version 10.0, Boulder, USA, 2018.
- [32] E.W. Lemmon, E.C. Ihmels, Thermodynamic properties of the butenes: Part II. Short fundamental equations of state, *Fluid Phase Equilib.* 228–229 (2005) 173–187. <https://doi.org/10.1016/j.fluid.2004.09.004>.
- [33] A. Polt, B. Platzer, G. Maurer, Parameter der Thermischen Zustandsgleichung von Bender für 14 Mehratomige Reine Stoffe, *Chem. Tech. (Leipzig)*. 44 (1992) 216–224.
- [34] E.W. Lemmon, R. Span, Short Fundamental Equations of State for 20 Industrial Fluids, *J. Chem. Eng. Data.* 51 (2006) 785–850. <https://doi.org/10.1021/je050186n>.
- [35] M. Thol, E.W. Lemmon, R. Span, Equation of State for Benzene for Temperatures from the Melting Line up to 725 K with Pressures up to 500 MPa, *High Temp. - High Pressures.* 41 (2012) 81–97.
- [36] D. Bücker, W. Wagner, Reference Equations of State for the Thermodynamic Properties of Fluid Phase n-Butane and Isobutane, *J. Phys. Chem. Ref. Data.* 35 (2006) 929–1019. <https://doi.org/10.1063/1.1901687>.
- [37] U. Setzmann, W. Wagner, A New Equation of State and Tables of Thermodynamic Properties for Methane Covering the Range from the Melting Line to 625 K at Pressures up to 100 MPa, *J. Phys. Chem. Ref. Data.* 20 (1991) 1061–1155. <https://doi.org/10.1063/1.555898>.
- [38] E.W. Lemmon, R. Span, Thermodynamic Properties of R-227ea, R-365mfc, R-115, and R-131I, *J. Chem. Eng. Data.* 60 (2015) 3745–3758. <https://doi.org/10.1021/acs.jced.5b00684>.
- [39] Y. Zhou, J. Liu, S.G. Penoncello, E.W. Lemmon, An Equation of State for the Thermodynamic Properties of Cyclohexane, *J. Phys. Chem. Ref. Data.* 43 (2014) 043105. <https://doi.org/10.1063/1.4900538>.
- [40] H. Gedanitz, M.J. Davila, E.W. Lemmon, Speed of Sound Measurements and a Fundamental Equation of State for Cyclopentane, *J. Chem. Eng. Data.* 60 (2015) 1331–1337. <https://doi.org/10.1021/je5010164>.
- [41] K.M. de Reuck, R.J.B. Craven, Methanol, *International Thermodynamic Tables of the Fluid State - 12*, IUPAC, Blackwell Scientific Publications, London, 1993.
- [42] E.W. Lemmon, R.T. Jacobsen, S.G. Penoncello, D.G. Friend, Thermodynamic Properties of Air and Mixtures of Nitrogen, Argon, and Oxygen From 60 to 2000 K at Pressures to 2000 MPa, *J. Phys. Chem. Ref. Data.* 29 (2000) 331–385. <https://doi.org/10.1063/1.1285884>.
- [43] C. Tegeler, R. Span, W. Wagner, A New Equation of State for Argon Covering the Fluid Region for Temperatures from the Melting Line to 700 K at Pressures up to 1000 MPa, *J. Phys. Chem. Ref. Data.* 28 (1999) 779–850.
- [44] I.A. Richardson, J.W. Leachman, E.W. Lemmon, Fundamental Equation of State for Deuterium, *J. Phys. Chem. Ref. Data.* 43 (2014) 013103. <https://doi.org/10.1063/1.4864752>.
- [45] R. Span, E.W. Lemmon, R.T. Jacobsen, W. Wagner, A. Yokozeki, A Reference Equation of State for the Thermodynamic Properties of Nitrogen for Temperatures from 63.151 to 1000 K and Pressures to 2200 MPa, *Journal of Physical and Chemical Reference Data.* 29 (2000) 1361–1433.
- [46] J.W. Leachman, R.T. Jacobsen, S.G. Penoncello, E.W. Lemmon, Fundamental Equations of State for Parahydrogen, Normal Hydrogen, and Orthohydrogen, *J. Phys. Chem. Ref. Data.* 38 (2009) 721–748. <https://doi.org/10.1063/1.3160306>.
- [47] R. Schmidt, W. Wagner, A New Form of the Equation of State for Pure Substances and Its Application to Oxygen, *Fluid Phase Equilibria.* 19 (1985) 175–200.

- [48] M.O. McLinden, R.A. Perkins, E.W. Lemmon, T.J. Fortin, Thermodynamic Properties of 1,1,1,2,2,4,5,5,5-Nonafluoro-4-(trifluoromethyl)-3-pentanone: Vapor Pressure, (p , ρ , T) Behavior, and Speed of Sound Measurements, and an Equation of State, *J. Chem. Eng. Data.* 60 (2015) 3646–3659. <https://doi.org/10.1021/acs.jced.5b00623>.
- [49] J. Wu, Y. Zhou, E.W. Lemmon, An Equation of State for the Thermodynamic Properties of Dimethyl Ether, *Journal of Physical and Chemical Reference Data.* 40 (2011) 023104. <https://doi.org/10.1063/1.3582533>.
- [50] D. Bücker, W. Wagner, A Reference Equation of State for the Thermodynamic Properties of Ethane for Temperatures from the Melting Line to 675 K and Pressures up to 900 MPa, *J. Phys. Chem. Ref. Data.* 35 (2006) 205–266. <https://doi.org/10.1063/1.1859286>.
- [51] J. Smukala, R. Span, W. Wagner, New Equation of State for Ethylene Covering the Fluid Region for Temperatures From the Melting Line to 450 K at Pressures up to 300 MPa, *J. Phys. Chem. Ref. Data.* 29 (2000) 1053–1121. <https://doi.org/10.1063/1.1329318>.
- [52] M. Thol, G. Rutkai, A. Köster, M. Kortmann, R. Span, J. Vrabec, Fundamental equation of state for ethylene oxide based on a hybrid dataset, *Chem. Eng. Sci.* 121 (2015) 87–99. <https://doi.org/10.1016/j.ces.2014.07.051>.
- [53] M. Thol, G. Rutkai, A. Köster, M. Kortmann, R. Span, J. Vrabec, Corrigendum to ‘Fundamental equation of state for ethylene oxide based on a hybrid dataset’ [*Journal of Chemical Engineering Science* 121 (2015) 87–99], *Chem. Eng. Sci.* 134 (2015) 887–890. <https://doi.org/10.1016/j.ces.2015.06.020>.
- [54] K.M. de Reuck, *International Thermodynamic Tables of the Fluid State-11 Fluorine*, Pergamon Press, Oxford, 1990.
- [55] B.A. Younglove, Thermophysical Properties of Fluids. I. Argon, Ethylene, Parahydrogen, Nitrogen, Nitrogen Trifluoride, and Oxygen, *J. Phys. Chem. Ref. Data.* 11 (1982) 1–11.
- [56] E.W. Lemmon, M.O. McLinden, W. Wagner, Thermodynamic Properties of Propane. III. A Reference Equation of State for Temperatures from the Melting Line to 650 K and Pressures up to 1000 MPa, *J. Chem. Eng. Data.* 54 (2009) 3141–3180. <https://doi.org/10.1021/jc900217v>.
- [57] R.T. Jacobsen, S.G. Penoncello, E.W. Lemmon, A fundamental equation for trichlorofluoromethane (R-11), *Fluid Phase Equilib.* 80 (1992) 45–56. [https://doi.org/10.1016/0378-3812\(92\)87054-Q](https://doi.org/10.1016/0378-3812(92)87054-Q).
- [58] V. Marx, A. Pruß, W. Wagner, Neue Zustandsgleichungen fuer R 12, R 22, R 11 und R 113. Beschreibung des thermodynamischen Zustandsverhaltens bei Temperaturen bis 525 K und Druecken bis 200 MPa, VDI Verlag, Düsseldorf, 1992.
- [59] J.W. Magee, S.L. Outcalt, J.F. Ely, Molar Heat Capacity C_v , Vapor Pressure, and (p , ρ , T) Measurements from 92 to 350 K at Pressures to 35 MPa and a New Equation of State for Chlorotrifluoromethane (R13), *Int. J. Thermophys.* 21 (2000) 1097–1121. <https://doi.org/10.1023/A:1026446004383>.
- [60] B. Platzer, A. Polt, G. Maurer, Thermophysical properties of refrigerants, Springer-Verlag, Berlin; New York, 1990.
- [61] S.G. Penoncello, E.W. Lemmon, R.T. Jacobsen, Z. Shan, A Fundamental Equation for Trifluoromethane (R-23), *J. Phys. Chem. Ref. Data.* 32 (2003) 1473–1499. <https://doi.org/10.1063/1.1559671>.
- [62] R. Tillner-Roth, A. Yokozeki, An International Standard Equation of State for Difluoromethane (R-32) for Temperatures from the Triple Point at 136.34 K to 435 K and Pressures up to 70 MPa, *J. Phys. Chem. Ref. Data.* 26 (1997) 1273–1328. <https://doi.org/10.1063/1.556002>.
- [63] M. Thol, L. Piazza, R. Span, A New Functional Form for Equations of State for Some Weakly Associating Fluids, *Int. J. Thermophys.* 35 (2014) 783–811. <https://doi.org/10.1007/s10765-014-1633-1>.
- [64] K. Gao, J. Wu, P. Zhang, E.W. Lemmon, A Helmholtz Energy Equation of State for Sulfur Dioxide, *J. Chem. Eng. Data.* 61 (2016) 2859–2872. <https://doi.org/10.1021/acs.jced.6b00195>.
- [65] B.A. Younglove, M.O. McLinden, An International Standard Equation of State for the Thermodynamic Properties of Refrigerant 123 (2,2-Dichloro-1,1,1-Trifluoroethane), *J. Phys. Chem. Ref. Data.* 23 (1994) 731–779. <https://doi.org/10.1063/1.555950>.
- [66] M.E. Mondéjar, M.O. McLinden, E.W. Lemmon, Thermodynamic Properties of *trans*-1-Chloro-3,3,3-trifluoropropene (R1233zd(E)): Vapor Pressure, (p , ρ , T) Behavior, and Speed of Sound Measurements, and Equation of State, *J. Chem. Eng. Data.* 60 (2015) 2477–2489. <https://doi.org/10.1021/acs.jced.5b00348>.
- [67] M. Richter, M.O. McLinden, E.W. Lemmon, Thermodynamic Properties of 2,3,3,3-Tetrafluoroprop-1-ene (R1234yf): Vapor Pressure and p - ρ - T Measurements and an Equation of State, *J. Chem. Eng. Data.* 56 (2011) 3254–3264.
- [68] M. Thol, E.W. Lemmon, Equation of State for the Thermodynamic Properties of *trans*-1,3,3,3-Tetrafluoropropene [R-1234ze(E)], *Int J Thermophys.* 37:28 (2016) 1–16.
- [69] E.W. Lemmon, R.T. Jacobsen, A New Functional Form and New Fitting Techniques for Equations of State with Application to Pentafluoroethane (HFC-125), *J. Phys. Chem. Ref. Data.* 34 (2005) 69–108. <https://doi.org/10.1063/1.1797813>.
- [70] R. Tillner-Roth, H.D. Baehr, An International Standard Formulation for the Thermodynamic Properties of 1,1,1,2-Tetrafluoroethane (HFC-134a) for Temperatures from 170 K to 455 K and Pressures up to 70 MPa, *J. Phys. Chem. Ref. Data.* 23 (1994) 657–729. <https://doi.org/10.1063/1.555958>.
- [71] S.L. Outcalt, M.O. McLinden, A Modified Benedict–Webb–Rubin Equation of State for the Thermodynamic Properties of R152a (1,1-difluoroethane), *J. Phys. Chem.*

- Ref. Data. 25 (1996) 605–636. <https://doi.org/10.1063/1.555979>.
- [72] H. Qi, D. Fang, K. Gao, X. Meng, J. Wu, Compressed Liquid Densities and Helmholtz Energy Equation of State for Fluoroethane (R161), *Int. J. Thermophys.* 37 (2016). <https://doi.org/10.1007/s10765-016-2061-1>.
- [73] X. Rui, J. Pan, Y. Wang, An equation of state for the thermodynamic properties of 1,1,1,2,3,3-hexafluoropropane (R236ea), *Fluid Phase Equilib.* 341 (2013) 78–85. <https://doi.org/10.1016/j.fluid.2012.12.026>.
- [74] J. Pan, X. Rui, X. Zhao, L. Qiu, An equation of state for the thermodynamic properties of 1,1,1,3,3,3-hexafluoropropane (HFC-236fa), *Fluid Phase Equilib.* 321 (2012) 10–16. <https://doi.org/10.1016/j.fluid.2012.02.012>.
- [75] Y. Zhou, E.W. Lemmon, Equation of State for the Thermodynamic Properties of 1,1,2,2,3-Pentafluoropropane (R-245ca), *Int. J. Thermophys.* 37:27 (2016) 1–11. <https://doi.org/10.1007/s10765-016-2039-z>.
- [76] R. Akasaka, Y. Zhou, E.W. Lemmon, A Fundamental Equation of State for 1,1,1,3,3-Pentafluoropropane (R-245fa), *J. Phys. Chem. Ref. Data.* 44 (2015) 013104.
- [77] E.W. Lemmon, Pseudo-Pure Fluid Equations of State for the Refrigerant Blends R-410A, R-404A, R-507A, and R-407C, *Int. J. Thermophys.* 24 (2003) 991–1006.
- [78] S. Herrig, M. Thol, A.H. Harvey, E.W. Lemmon, A Reference Equation of State for Heavy Water, *J. Phys. Chem. Ref. Data.* 47 (2018) 043102. <https://doi.org/10.1063/1.5053993>.
- [79] M. Thol, F.H. Dubberke, E. Baumhögger, R. Span, J. Vrabec, Speed of Sound Measurements and a Fundamental Equation of State for Hydrogen Chloride, *J. Chem. Eng. Data.* 63 (2018) 2533–2547. <https://doi.org/10.1021/acs.jced.7b01031>.
- [80] C. Guder, W. Wagner, A Reference Equation of State for the Thermodynamic Properties of Sulfur Hexafluoride (SF₆) for Temperatures from the Melting Line to 625 K and Pressures up to 150 MPa, *J. Phys. Chem. Ref. Data.* 38 (2009) 33–94.
- [81] W. Wagner, A. Pruß, The IAPWS Formulation 1995 for the Thermodynamic Properties of Ordinary Water Substance for General and Scientific Use, *J. Phys. Chem. Ref. Data.* 31 (2002) 387–535. <https://doi.org/10.1063/1.1461829>.
- [82] A. Jäger, E. Mickoleit, C. Breitkopf, Accurate and predictive mixture models applied to mixtures with CO₂, Proceedings of the 3rd European Supercritical CO₂ Conference. (2019). <https://doi.org/10.17185/DUEPUBLICO/48891>.
- [83] A. Klamt, Conductor-like screening model for real solvents: a new approach to the quantitative calculation of solvation phenomena, *J. Phys. Chem.* 99 (1995) 2224–2235.
- [84] A. Klamt, V. Jonas, T. Bürger, J.C. Lohrenz, Refinement and parametrization of COSMO-RS, *J. Phys. Chem. A.* 102 (1998) 5074–5085.
- [85] A. Klamt, F. Eckert, COSMO-RS: a novel and efficient method for the a priori prediction of thermophysical data of liquids, *Fluid Phase Equilib.* 172 (2000) 43–72.
- [86] A. Klamt, G. Schüürmann, COSMO: a new approach to dielectric screening in solvents with explicit expressions for the screening energy and its gradient, *J. Chem. Soc., Perkin Trans.* 2 (1993) 799–805. <https://doi.org/10.1039/P29930000799>.
- [87] I.H. Bell, E. Mickoleit, C.-M. Hsieh, S.-T. Lin, J. Vrabec, C. Breitkopf, A. Jäger, A Benchmark Open-Source Implementation of COSMO-SAC, *J. Chem. Theory Comput.* 16 (2020) 2635–2646. <https://doi.org/10.1021/acs.jctc.9b01016>.
- [88] R. Span, R. Beckmüller, T. Eckermann, S. Herrig, S. Hielscher, A. Jäger, E. Mickoleit, T. Neumann, S.M. Pohl, B. Semrau, M. Thol, TREND. Thermodynamic Reference and Engineering Data 4.0, Lehrstuhl fuer Thermodynamik, Ruhr-Universitaet Bochum, Bochum, Germany, 2019.
- [89] E. Mullins, R. Oldland, Y.A. Liu, S. Wang, S.I. Sandler, C.-C. Chen, M. Zwolak, K.C. Seavey, Sigma-Profile Database for Using COSMO-Based Thermodynamic Methods, *Ind. Eng. Chem. Res.* 45 (2006) 4389–4415. <https://doi.org/10.1021/ie060370h>.
- [90] J. Gernert, A. Jäger, R. Span, Calculation of Phase Equilibria for Multi-Component Mixtures Using Highly Accurate Helmholtz Energy Equations of State, *Fluid Phase Equilib.* 375 (2014) 209–218. <https://doi.org/10.1016/j.fluid.2014.05.012>.
- [91] A. Jäger, Complex Phase Equilibria of Gas Hydrates and Other Solid and Fluid Phases Modeled with Highly Accurate Equations of State, Dissertation, Ruhr-Universität Bochum, 2016. <https://hss-opus.ub.ruhr-uni-bochum.de/opus4/frontdoor/index/index/docId/4546> (accessed April 12, 2019).
- [92] K. Brun, P. Friedman, R. Dennis, Fundamentals and applications of supercritical carbon dioxide (sCO₂) based power cycles, 1st edition, Elsevier, Waltham, MA, 2017.
- [93] EU, Regulation (EU) No 517/2014 of the European Parliament and of the Council of 16 April 2014 on fluorinated greenhouse gases and repealing Regulation (EC) No 842/2006, 2014. <https://eur-lex.europa.eu/eli/reg/2014/517/oj/eng> (accessed October 19, 2020).
- [94] J.S. Daniel, G.J.M. Velders, A.R. Douglass, P.M.D. Forster, D.A. Hauglustaine, I.S.A. Isaksen, L.J.M. Kujipers, A. McCulloch, T.J. Wallington, Halocarbon Scenarios, Ozone Depletion Potentials, and Global Warming Potentials, Scientific Assessment of Ozone Depletion. (2016).
- [95] I.H. Bell, A. Jäger, Calculation of Critical Points from Helmholtz-Energy-Explicit Mixture Models, *Fluid Phase Equilib.* 433 (2017) 159–173. <https://doi.org/10.1016/j.fluid.2016.10.030>.
- [96] N. Polikhronidi, R. Batyrova, A. Aliev, I. Abdulgatov, Supercritical CO₂: Properties and Technological Applications - A Review, *J. Therm. Sci.* 28 (2019) 394–430.
- [97] N. Ribeiro, T. Casimiro, C. Duarte, M. Nunes da Ponte, A. Aguiar-Ricardo, M. Poliakoff, Vapor-Liquid Equilibrium and Critical Line of the CO₂ + Xe System. *Critical Behavior*

- of CO₂ + Xe versus CO₂ + n-Alkanes, *J. Phys. Chem. B.* 104 (2000) 791–795.
- [98] L. Calderazzi, P.C. di Paliano, Thermal stability of R-134a, R-141b, R-1311, R-7146, R-125 associated with stainless steel as a containing material, (1997) 9.
- [99] F. Zeng, J. Tang, Q. Fan, J. Pan, X. Zhang, Q. Yao, J. He, Decomposition Characteristics of SF₆ under Thermal Fault for Temperatures below 400 J, 21 (2014) 10.
- [100] R.J. Ferm, The Chemistry Of Carbonyl Sulfide, *Chem. Rev.* 57 (1957) 621–640.
<https://doi.org/10.1021/cr50016a002>.

ANNEX A

EQUATIONS OF STATE USED FOR THE SCREENING

The multi-parameter equations of state used in the multi-fluid mixture model are listed in Table A1.

Table A1: Substances considered in the screening and references (Ref.) for multi-parameter equations of state used for these substances.

Substance (IUPAC name)	Ref.	Substance name used in this work
buta-1,3-diene	[31]	13butadiene
but-1-ene	[32]	1butene
but-1-yne	[31]	1butyne
pent-1-ene	[31]	1pentene
acetylene	[31]	acetylene
(2Z)-but-2-ene (cis-2-butene)	[32]	c2butene
ethene	[51]	ethylene
2-methylprop-1-ene (isobutene)	[32]	ibutene
propa-1,2-diene	[31]	propadiene
propene	[31]	propylene
propyne	[33]	propyne
(2E)-but-2-ene (trans-2-butene)	[32]	t2butene
2,2-dimethylbutane	[31]	22dimethylbutane
2,3-dimethylbutane	[31]	23dimethylbutane
<i>n</i> -butane	[36]	butane
ethane	[50]	ethane
<i>n</i> -hexane	[31]	hexane
2-methyl-butane (isopentane)	[34]	ipentane
2-methylpropane (isobutane)	[36]	isobutan
methane	[37]	methane
2,2-dimethylpropane (neopentane)	[34]	neopentn
<i>n</i> -pentane	[31]	pentane
propane	[56]	propane
benzene	[31,35]	benzene
cyclobutene	[31]	cyclobutene
cyclohexane	[39]	cyclohex
cyclopentane	[40]	cyclopen
cyclopropane	[33]	cyclopro
ethoxyethane	[63]	dee
methoxymethane (dimethyl ether)	[49]	dme
methanol	[41]	methanol
dry air (0.7812 N ₂ , 0.2096 O ₂ , 0.0092 Ar)	[42]	air ¹
argon	[43]	argon

Table A1 (continued)

Substance (IUPAC name)	Ref.	Substance name used in this work
carbon monoxide	[34]	co
deuterium	[44]	d2
fluorine	[54]	fluorine
helium	[31]	helium
krypton	[34]	krypton
neon	[31]	neon
nitrogen trifluoride	[55]	nf3
nitrogen	[45]	nitrogen
orthohydrogen	[46]	orthohyd
oxygen	[47]	oxygen
parahydrogen	[46]	parahyd
xenon	[34]	xenon
decafluorobutane	[31]	c4f10
dodecafluoropentane	[31]	c5f12
tetradecafluorohexane	[31]	c6f14
trifluoro(iodo)methane	[38]	cf3i
dodecafluoro-2- methylpentan-3-one	[48]	novec649
trichloro(fluoro)methane (R-11)	[57]	r11
1,1,2-trifluoroethene (R-1123)	[31]	r1123
1,1,2-trichloro-1,2,2- trifluoroethane (R-113)	[58]	r113
1,2-dichlorotetrafluoro- ethane (R-114)	[60]	r114
1-chloro-1,1,2,2,2- pentafluoroethane (R-115)	[38]	r115
hexafluoroethane	[34]	r116
dichloro(difluoro) methane (R-12)	[58]	r12
hexafluoropropene (R-1216)	[31]	r1216
(Z)-1-chloro-2,3,3,3- tetrafluoropropene (R-1224yd(Z))	[31]	r1224ydz
2,2-dichloro-1,1,1- trifluoroethane (R-123)	[65]	r123
trans-1-chloro-3,3,3- trifluoroprop-1-ene (R-1233zd(E))	[66]	r1233zde
2,3,3,3-Tetrafluoroprop- 1-ene (R-1234yf)	[67]	r1234yf
(1E)-1,3,3,3-Tetrafluoro- 1-propene (R-1234ze(E))	[68]	r1234zee

Table A1 (continued)

Substance (IUPAC name)	Ref.	Substance name used in this work
(Z)-1,3,3,3-tetrafluoroprop-1-ene (R-1234ze(Z))	[31]	r1234zez
2-chloro-1,1,1,2-tetrafluoroethane (R-124)	[31]	r124
3,3,3-trifluoroprop-1-ene	[31]	r1243zf
1,1,1,2,2-Pentafluoroethane (R-125)	[69]	r125
chloro(trifluoro) methane (R-13)	[59]	r13
1,1,1,2-Tetrafluoroethane (R-134a)	[70]	r134a
tetrafluoromethane (R-14)	[60]	r14
1,1-difluoroethane (R-152a)	[71]	r152a
Fluoroethane (R-161)	[72]	r161
dichloro(fluoro) methane (R-21)	[60]	r21
Octafluoropropane (R-218)	[34]	r218
chloro(difluoro) methane (R-22)	[58]	r22
1,1,1,2,3,3,3-Heptafluoropropane (R-227ea)	[38]	r227ea
trifluoromethane (R-23)	[61]	r23
1,1,1,2,3,3-hexafluoropropane (R-236ea)	[73]	r236ea
1,1,1,3,3,3-hexafluoropropane (R-236fa)	[74]	r236fa
1,1,2,2,3-pentafluoropropane (R-245ca)	[75]	r245ca
1,1,1,3,3-pentafluoropropane (R-245fa)	[76]	r245fa
difluoromethane (R-32)	[62]	r32
1,1,1,3,3-pentafluorobutane (R-365mfc)	[38]	r365mfc
chloromethane (R-40)	[63]	r40
44 wt% R-125, 4 wt% R-134a, 52 wt% R143a (R-404a)	[77]	r404a ¹
23 wt% R-32, 25 wt% R-125, 52 wt% R-134a (R-407c)	[77]	r407c ¹
fluoromethane (R-41)	[34]	r41
50 wt% R-32, 50 wt% R-125 (R-410a)	[77]	r410a ¹
50 wt% R-125, 50 wt% R-143a (R-507a)	[77]	r507a ¹
octafluorocyclobutane (R-C-318)	[60]	rc318
(Z)-1,1,1,4,4,4-hexafluorobut-2-ene (R-1336mzz(Z))	[31]	re1336mzz

Table A1 (continued)

Substance (IUPAC name)	Ref.	Substance name used in this work
1,1,1,2,2-pentafluoro-2-methoxyethane (R-245cb2)	[31]	re245cb2
1,1,1,3,3-pentafluoro-2-(1,1,1,3,3-pentafluoropropan-2-yloxy)propane (R-245fa2)	[31]	re245fa2
1,1,1,2,2,3,3-heptafluoro-3-methoxypropane (R-347mcc)	[31]	re347mcc
chloroethene (vinyl chloride)	[31]	vinylchloride
propan-2-one (acetone)	[34]	acetone
ammonia	[31]	ammonia
chlorine	[25]	chlorine
carbonyl sulfide (² H ₂)water (deuterium oxide)	[34]	cos
oxyrane (ethylene oxide)	[78]	d2o
hydrogen sulfide	[52,53]	etyoxide
hydrogen chloride	[34]	h2s
nitrous oxide	[79]	hcl
2-methyloxirane	[34]	n2o
sulfur hexafluoride	[31]	propyleneoxide
sulfur dioxide	[80]	sf6
water	[64]	so2
	[81]	water

¹ These mixtures have been treated as pseudo pure-fluids applying the noted pseudo pure-fluid equations of state.

NUMERICAL ANALYSIS OF A CENTRIFUGAL COMPRESSOR OPERATING WITH SUPERCRITICAL CO₂

Renan Emre Karaefe*,
Pascal Post, Marwick Sembritzky, Andreas Schramm,
Francesca di Mare
Ruhr University Bochum
Faculty of Mechanical Engineering
Chair of Thermal Turbomachines and Aeroengines
44801 Bochum, Germany
Email: emre.karaefe@rub.de

Matthias Kunick
Zittau/Goerlitz University of Applied Sciences
Faculty of Mechanical Engineering
02763 Zittau, Germany

Uwe Gampe
Technische Universität Dresden
Faculty of Mechanical Science and Engineering
Chair of Thermal Power Machinery and Plants
01062 Dresden, Germany

ABSTRACT

This study investigates the performance of a centrifugal compressor stage operating with supercritical CO₂. The candidate geometry comprises a channel diffuser and is based on main dimensions of a test-loop compressor operated by Sandia National Laboratories. A non-dimensional performance curve is derived through three-dimensional RANS calculations performed with an in-house compressible CFD solver and is compared to experimental data as well as a meanline analysis that is conducted applying a single-zone modelling approach, including internal and external loss models. Within the CFD simulations, real gas thermophysical properties of carbon dioxide are assessed through an accurate and efficient tabulation procedure, the Spline-Based Table Look-Up Method (SBTL), which is optimised for the density-based solver architecture. The conducted RANS calculations show an ideal head rise of up to 41 % through the channel diffuser compared to an ideal head assessment considering the impeller. The applied meanline methodology pro-

vides good agreement with the impeller performance characteristics derived from RANS calculations over the entire investigated flow range. Except for flow coefficients exceeding values of $\phi \approx 0.043$, where an abrupt decrease of the ideal head recovery is identified in the CFD assessments, which is not resembled by the meanline diffuser model, also satisfactory agreement of the meanline stage performance characteristics with the CFD results is obtained. Hence, applicability of the corresponding meanline loss models for sCO₂ compressor analysis is indicated.

INTRODUCTION

Closed power cycles utilising supercritical carbon dioxide as the working fluid exhibit several advantages compared to conventional power cycles. These power systems are predominantly designed as Brayton cycles where the compression is conducted at thermodynamic states that are lying close to the vapour-liquid critical point of CO₂ and are therefore characterised by a high fluid density. Hence, compression work is reduced significantly. Furthermore, high fluid density enables compact component de-

*Address all correspondence to this author.

sign and ultimately paves the way for a small physical footprint of the overall plant. Supercritical power systems can also be coupled to a variety of heat sources, allowing for a broad range of applications.

Despite increased research efforts, there are still enduring challenges which need to be overcome until sCO₂ cycles can be commercialised. Key issues concern reliable process control, the design of compact and effective heat exchangers as well as the realisation of satisfactory turbomachinery performance characteristics. Predominantly, centrifugal compressors are applied in sCO₂ Brayton cycles and, in particular, the main compressor of a recompression layout is expected to be a radial configuration for a broad range of system scales due to its lower volume flow and wider range to facilitate variations in gas properties [8].

Design and analysis methods are sophisticated for centrifugal compressors operating with fluids obeying the ideal gas law. However, because of the scarcity of reference data, the validity of respective methods is still uncertain when these are applied to compressors operating with real fluids. In particular, fluid states near the critical point are characterised by highly non-linear and rapidly changing property behaviour. Addressing these issues, predictive CFD simulations, accounting for thermophysical real gas properties with a high degree of accuracy, allow for an insight into the dynamic development of flow field and are therefore an important tool to improve the aerothermal design and analysis of sCO₂ turbomachinery.

The majority of numerical studies of sCO₂ compressors in the literature refer to a main compressor geometry operated in a compression test-loop by Sandia National Laboratories (SNL). The compressor has undergone extensive testing and until today provides one of the very few cases for which experimental reference data as well as the respective compressor geometry is at least partially documented in the form of main dimensions. In one of the first studies related to the SNL compressor, Pecnik et al. [26] performed 3D RANS calculations of a main compressor impeller resembling the SNL main compressor design. A computed speed line indicated higher head generation compared to the experimental data used for validation purposes. Deviations were attributed to the simplified geometry not considering the vaned diffuser and the impeller clearance. Analysis of the flow field showed thermodynamic states of the flow domain lying within the vapour-liquid region. These were identified at the impeller blade tip suction side and the trailing edge, as a result of flow acceleration and the decrease of static conditions. In following studies of the research group, the complete stage geometry, comprising the vaned diffuser and tip clearance, was modeled. A significant reduction in head generation was observed for a single operating point compared to the previous study, giving better agreement with the referenced experimental data [31]. Performance map calculations conducted for three rotational speeds in [32] showed that the shares of fluid zones located close to the impeller leading edges with state conditions

in the two-phase region increase for higher rotational speeds, whereas a reversed dependency was observed regarding the regions close to the trailing edges.

Baltadjiev et al. [6] introduced a time scale ratio relating liquid droplet formation time to the residence time of flow under subcritical conditions in order to quantify the possibility of condensation within a low-flow-coefficient sCO₂ compressor stage. For all investigated operating conditions away from the critical point, the time scale ratio was much smaller than one, suggesting improbability of condensation. Nevertheless, the authors pointed out that a time scale ratio of 1 could be reached for operating points that are more closely located to the critical point, due to an increased subcritical expansion and asymptotically vanishing surface tension.

3D RANS simulations of the SNL compressor were also conducted by Ameli et al. [1; 3], who focused on the effects of lookup table resolution of the applied bilinear interpolation routine on performance and flow field predictions. It was shown that higher table resolutions resulted in a better agreement with experimental data regarding efficiency, whereas the assessment of pressure ratio proved to be rather insensitive. Especially, the resolution of near-critical properties was stressed, as the authors stated that 0.5 % error in the lookup table can have a significant impact on the performance prediction at close-critical operating conditions. The authors also showed that higher table resolutions resulted in an increased assessment of flow regions within the two-phase region because of lower values of speed of sound.

In a preliminary study prior to this work [19], the performance as well as the flow field of an impeller geometry resembling the main dimensions of the SNL main compressor were investigated. Reasonable performance metrics were derived for two compressor inlet states lying in the supercritical and gas phase region, respectively. A high degree of machine similitude was observed for compressor operation at these inlet states through a non-dimensional performance curve representation. Similar to the observations from the authors referenced before, the flow field highlighted fluid zones inside the vapour-liquid region near the blade leading edge suction sides due to flow acceleration. These were quantified by their volumetric share for different flow coefficients. Contrary to previously cited authors, who all used bilinear interpolation techniques to account for the thermophysical properties of CO₂, property table interpolation was conducted through the Spline-Based-Table-Lookup Method (SBTL) [20; 21]. The method indicated low computational overhead compared to an ideal gas reference calculation while providing accuracies within the deviation of the underlying state equation, being the Span-Wagner equation of state [35].

Building on the previous work [19], this study extends the compressor performance testing to also account for the channel type diffuser that was not modeled before. This is believed to improve the comparability with the experimental results as a vaned

diffuser can generally reduce the operating range and also exhibit upstream effects. In order to provide a further reference for the previous and current performance assessments, a meanline analysis based on internal and external loss models, originally qualified for the application with conventional compressors, will be conducted. In this way, also the applicability of respective models for the application with regard to CO₂ compressors can be evaluated.

The paper is structured as follows. First, the numerical framework comprising the in-house CFD solver and the real gas tabulation approach as well as the meanline analysis procedure will be presented. Afterwards, a test case description will be provided followed by an description of the deduced compressor stage geometry and numerical setup. Results of the numerical analysis methods will be compared with each other and to data from the previous study [19] as well as experimental results reported by Wright et al. [38; 39] and Fuller & Eisemann [14].

3D CFD PROCEDURE

A density based compressible in-house CPU/GPU hybrid CFD solver [29] is applied for simulations in this work. The Navier-Stokes equations

$$\partial_t \underline{w} + \text{div} \left(\underline{F}^a - \underline{F}^d \right) = \underline{s}, \quad (1)$$

complemented by constitutive equations as well as expressions for thermodynamic state are solved in their Reynolds-averaged form. Conservative variables, flux terms and source terms are specified as follows (given for the absolute frame of reference for brevity):

$$\underline{w} := (\rho, \rho \underline{u}, \rho E) \quad (2)$$

$$\underline{F}^a := (\rho \underline{u}, \rho \underline{u} \otimes \underline{u} + p \underline{I}, \rho \underline{u} H) \quad (3)$$

$$\underline{F}^d := \left(\underline{0}, \underline{\tau}, \underline{u} \cdot \underline{\tau} - \underline{q} \right) \quad (4)$$

$$\underline{s} := \underline{0}. \quad (5)$$

The applied formulation of the NS-equations for the rotating frame of reference is given in [27]. The viscous shear stress tensor and the heat flux vector are defined through Stokes' and Fourier's law for a Newtonian fluid, respectively:

$$\underline{\tau} := \mu(\rho, e) \left(\text{grad} \underline{u} + (\text{grad} \underline{u})^T - 2/3 \text{div} \underline{u} \underline{I} \right) \quad (6)$$

$$\underline{q} := -\lambda(\rho, e) \text{grad} T(\rho, e). \quad (7)$$

Spatial discretisation is performed on structured grids applying a finite-volume approach. Advective fluxes are discretised based on a second order AUSM+ scheme [28] utilising a piecewise

linear MUSCL reconstruction [36] and central scheme discretisation is applied for diffusive fluxes. The resulting ordinary differential equations are integrated in time through an implicit LUSGS scheme and the Spalart-Allmaras turbulence model [34] is employed for closure of the RANS equations. Recent solver applications comprise the thematic fields of non-equilibrium wet steam [29], including the first LES of a condensing wet steam cascade [30], humid air [16], and sCO₂ [19].

REAL GAS PROPERTY TABULATION

Thermophysical properties of CO₂ are derived from the Span-Wagner multiparameter reference equation of state (SW-EOS) as well correlations for molecular viscosity and thermal conductivity given by Laesecke et al. [22] and Huber et al. [15], respectively. As the SW-EOS is too computationally expensive in the context of a 3D CFD simulation, all thermophysical properties are pre-computed and accessible in the solver via a software library applying the Spline-Based Table Look-Up Method (SBTL) [20; 21]. The SBTL was developed for the fast calculation of thermophysical properties in complex process simulations. Based on spline interpolation techniques applying lower order polynomials, such as biquadratic or bicubic spline functions, the SBTL overcomes fundamental problems adherent to local interpolation routines, e.g. the most commonly applied bilinear interpolation method. Unlike local bilinear interpolation, biquadratic spline functions yield continuous first derivatives. Moreover, biquadratic spline polynomials can be solved quickly with regard to their independent variables. Hence, numerically consistent backwards functions can be calculated, which are faster than those obtained from the inversion of bicubic polynomials. Furthermore, simple search algorithms can be applied due to the construction of splines on piecewise equidistant nodes of transformed variables, allowing for linearisation.

Tabulation is performed based on density and internal energy as the independent thermodynamic variables of choice because these can be directly deduced from the conservative variables:

$$\rho(\underline{w}) = \rho, \quad e(\underline{w}) = \rho^{-1} \left(\rho E - (2\rho)^{-1} \rho \underline{u} \right). \quad (8)$$

The range of validity of the SBTL property library is specified as follows: 216.59 K ≤ T ≤ 1300 K; 0.5 kPa ≤ p ≤ 100 MPa. Permissible deviations of SBTL spline functions are listed in table 1. These are within the uncertainties of the underlying EOS and transport property correlations, except at the critical point, where isobaric heat capacity and thermal conductivity become infinite.

In all simulations, thermodynamically stable states are considered only, i.e. fluid properties in the vapour-liquid region are calculated as a homogenous equilibrium mixture.

TABLE 1: Permissible deviations for the development of SBTL functions from the reference equation of state by Span and Wagner [35] as well as the correlations for viscosity and thermal conductivity [15; 22]

SBTL function	liquid region	gas region
$p(v, e)$	$p \leq 2.5 \text{ MPa}$ $ \Delta p/p < 10^{-5}$	$p > 2.5 \text{ MPa}$ $ \Delta p < 0.5 \text{ kPa}$
$T(v, e)$	$ \Delta T < 1 \text{ mK}$	$ \Delta T < 1 \text{ mK}$
$s(v, e)$	$ \Delta s < 10^{-6} \frac{\text{kJ}}{\text{kgK}}$	$ \Delta s < 10^{-6} \frac{\text{kJ}}{\text{kgK}}$
$a(v, e)$	$ \Delta a/a < 10^{-5}$	$ \Delta a/a < 10^{-5}$
$\lambda(v, e)^1$	$ \Delta \lambda/\lambda < 10^{-5}$	$ \Delta \lambda/\lambda < 10^{-5}$
$\mu(v, e)$	$ \Delta \mu/\mu < 10^{-5}$	$ \Delta \mu/\mu < 10^{-5}$

¹ The correlation of the thermal conductivity [15] shows some discontinuities along the $T = 1.5 \cdot T_c = 456.1923 \text{ K}$ isotherm. Along this isotherm, the deviations in thermal conductivity are larger than the permissible values but within the uncertainty of the underlying correlation itself.

MEANLINE ANALYSIS PROCEDURE

The meanline analysis is performed sequentially as well as iteratively for the stage components and applies a single-zone modelling approach. A loss model set proposed and validated by Oh et al. [25] for the application with centrifugal compressors operating with conventional working fluids obeying the ideal gas law is incorporated in the impeller analysis. Recently, the loss model set was also utilised for performance calculations of sCO₂ compressors by different researchers and stated to be applicable [2; 23; 33]. The set was suggested on basis of various possible combinations of most of the internal and external loss models in the literature. It accounts for six mechanisms of internal and three sources of external (parasitic) losses, the latter giving rise to the impeller stagnation enthalpy without contributing to pressure rise:

$$\Delta h_t = W_{Euler} + \sum W_{external} \quad (\text{assuming adiabatic flow}). \quad (9)$$

An overview of the applied loss correlations, which are formulated as enthalpy losses, is presented in table A1 for the reader's convenience. Also, a schematic h,s-diagram is presented in figure 1 illustrating the impeller process path and the contribution of internal and external losses. Complementary to the loss models, the common slip correlation

$$\sigma = 1 - \frac{\sqrt{\cos \beta_{2,bl}}}{Z_{bl}^{0.7}} \quad (\text{meridional angle system}), \quad (10)$$

based on the formulation by Wiesner [37] is applied in order to assess the actual work input and deviation angle compared to the idealised case where the fluid would be perfectly guided by the impeller blades:

$$W_{Euler} = u_2 c_{2\theta} - u_1 c_{1\theta} = u_2 (\sigma u_2 + c_{2m} \tan \beta_{2,bl}). \quad (11)$$

The applied vaned diffuser analysis is based on a modelling approach presented by Aungier [5]. Three sources of aerodynamic losses are adopted which are given in a total pressure loss coefficient formulation

$$p_{t4} = p_{t3} - (p_{t3} - p_3) \sum_i \bar{\omega}_i, \quad (12)$$

and are listed in table A1. The vaned diffuser discharge flow angle is computed by applying axial-flow compressor correlations transformed to the radial plane. Details are given in [5].

Within the meanline analysis, real gas thermophysical properties of CO₂ are considered through direct calls to the CoolProp property library [7].

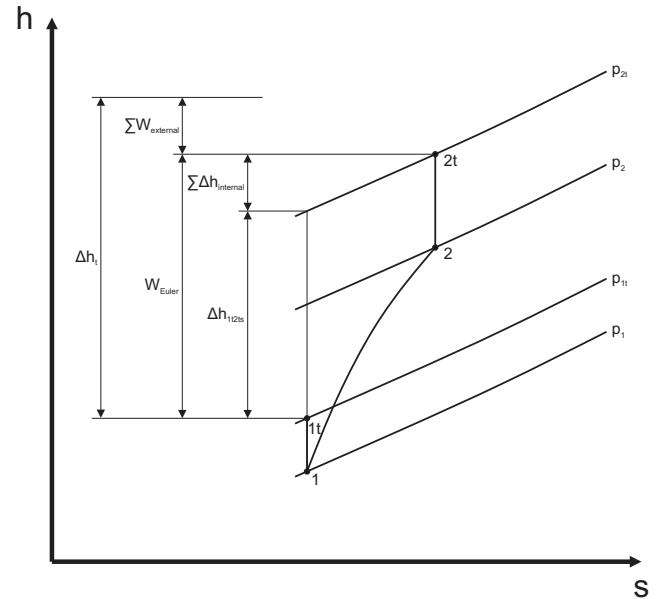


FIGURE 1: Schematic h,s-diagram illustrating the impeller process path as well as internal impeller loss and external loss contributions

sCO₂ COMPRESSOR TEST CASE

The main compressor installed in a sCO₂ compression test-loop which is operated by Sandia National Laboratories [39] is taken as a reference case. As only main dimensions of the

compressor are reported, this work investigates a newly generated compressor geometry resembling the same main dimensions. The SNL main compressor stage comprises a backward swept impeller with splitter blades and a channel type (wedge) diffuser. It is designed for operation at a total inlet state that thermodynamically lies close to the critical point of carbon dioxide ($T_i/T_c \approx 1.004$, $p_i/p_c \approx 1.042$). The design rotational speed is specified with 75 krpm and the design mass flow rate is given as 3.5 kg/s. Expressed through non-dimensional parameters, the given specifications correspond with a flow coefficient of $\phi = 0.037$ and a peripheral Mach number of $Ma_u = 0.73$. The SNL compressor was designed by Barber Nichols Inc. on basis of a surrogate fluid that results in comparable key parameters based on turbomachinery similarity principles and which can be more closely approximated by an ideal gas model. It is stated that this approach provides a way to use existing loss models and design tools [39].

The SNL main compressor has undergone extensive experimental investigations [14; 38; 39], most notably performance tests. Because a comparison of numerical results with experimental performance data is subject to this work, knowledge of the experimental instrumentation and data assessment is important to ensure comparability with regard to an appropriate numerical setup and postprocessing of data. Resistance temperature detectors and total pressure transducers were installed at the stage inlet and outlet. In addition, a static pressure tap was located at the impeller exit [38; 39]. Hence, reported experimental total-to-static performance data is interpreted to refer to the impeller. Accordingly, it is stated that isentropic impeller efficiencies were assessed through meanline analysis codes and compared to experimental data [38]. Although it is principally possible to deduce enthalpy and ultimately efficiency from tem-

perature and pressure measurements in the supercritical state, it is important to note that enthalpy is extremely sensitive to small changes of these state variables. As a matter of fact, experimental efficiencies were derived from electrical power measurements with corrections for electric and mechanical losses rather than enthalpy calculations from measured pressures and temperatures [38]. Note, that the exact positions of the measuring devices were not reported.

GEOMETRY GENERATION AND COMPUTATIONAL SETUP

In a preliminary study [19], only the impeller wheel of SNL main compressor was considered. In this work, the investigated geometry is extended to account for the full compressor stage comprising a channel type diffuser. No detailed blade coordinates are publicly reported for the reference case and only partial information on main dimensions is given in [39]. Thus, a compressor geometry with similar main dimensions is designed and investigated in this work. All publicly reported main dimensions are listed in table 2 for the reader's convenience. Additional geometric data was deduced from part drawings depicted in [14; 39] and the final compressor design (see figure 3) was generated through a preliminary compressor design/analysis tool and its interface to a 3D blade generation module [9; 10].

The computational domain was created with an automated multi-block structured mesh generator [24] and is reduced to the consideration of a single impeller and diffuser passage due to rotational periodicity and the applied mixing-plane rotor-stator interface approach. Within each blade row, full one-to-one grid connections avoid the need for interpolation between adjacent blocks. The mesh size counts approximately 1.5 million cells for the impeller and 630.000 cells for the diffuser passage. While free-stream and inter-blade regions are meshed through H-grid topologies, O-grid topologies are applied at near-blade areas. The computational grid is shown in figure 2.

Total pressure and total temperature as well as a uniform normal direction of flow along with a turbulent viscosity ratio are specified as boundary conditions at the domain inlet. A constant static pressure is defined at the outlet of the vaneless space prolongation. All walls are treated as adiabatic and the no-slip condition is applied.

TABLE 2: Compressor stage main dimensions taken from [39]

Number of impeller main / splitter blades	6 / 6	
Inducer shroud radius	9.37	[mm]
Inducer hub radius	2.54	[mm]
Inducer blade angle at tip	50	[deg]
Impeller exit radius	18.68	[mm]
Impeller exit width	1.71	[mm]
Impeller exit blade angle (backswept)	-50	[deg]
Impeller blade thickness	0.76	[mm]
Number of diffuser blades	17	
Diffuser exit vane angle	71.5	[deg]

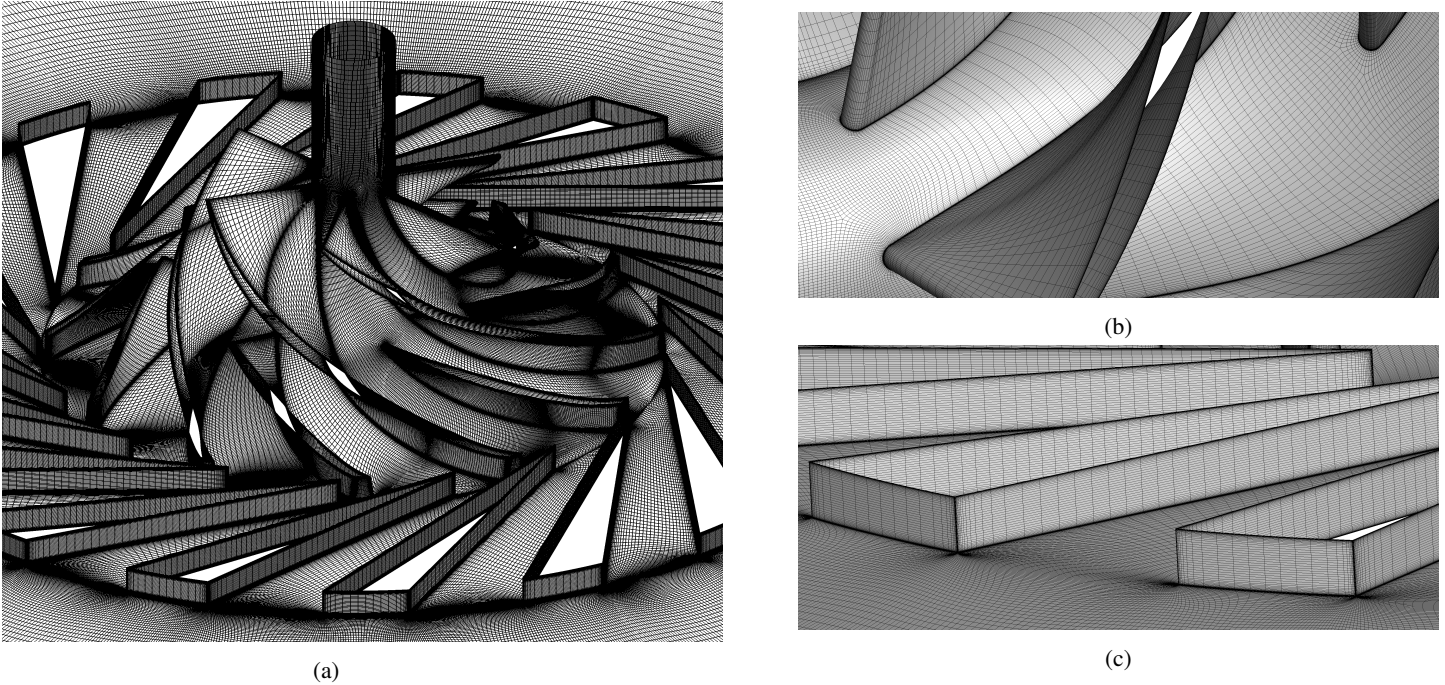


FIGURE 2: Computational grid (repeated surface representation): (a) Stage view, (b) Impeller main and splitter blade leading edge region, (c) Channel diffuser trailing edge region

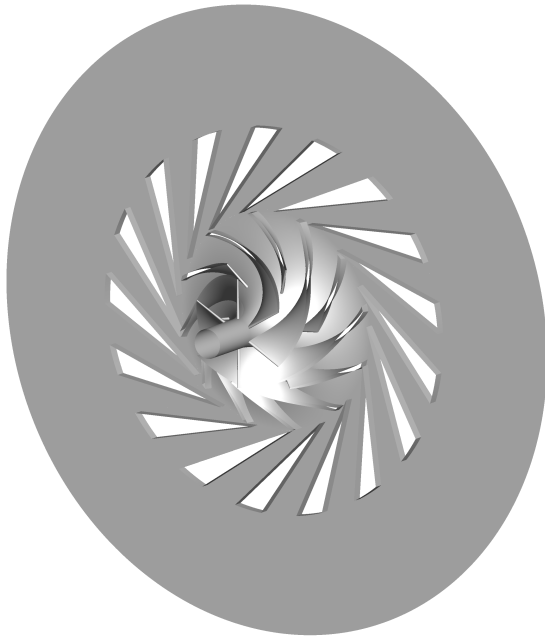


FIGURE 3: 3D model of the compressor stage based on main dimensions of the SNL main compressor

PERFORMANCE ANALYSIS

In a previous study [19], the performance characteristics of the impeller wheel were numerically assessed for two distinct inlet states - a close-critical operating state near the design condition and a subcritical compressor inlet state in the gas phase, the latter being potentially relevant during cycle startups [14]. For both investigated states, almost identical non-dimensional performance curves were derived, indicating a high degree of machine similarity and thus, high relaxation of the dependency on the inlet state by applying a non-dimensional representation. In this work, the performance testing is extended to account for a configuration including a channel type diffuser and is conducted at a supercritical compressor total inlet condition at $T_i/T_c \approx 1.03$ and $p_i/p_c \approx 1.05$. The candidate state point is depicted in the T,s-diagram in figure 4, together with an underlaid contour line plot of the compressibility factor

$$Z = p/(\rho RT), \quad (13)$$

indicating the highly non-ideal thermodynamics of the operating regime.

The performance assessment is conducted at 50 krpm rotational speed as most of the experimental data provided by Wright et al. [38; 39] and exclusively all of the data given by Fuller & Eisemann [14] for the SNL reference case were obtained at this rotational speed. Note, that no experimental data is reported for the design rotational speed at 75 krpm and no ef-

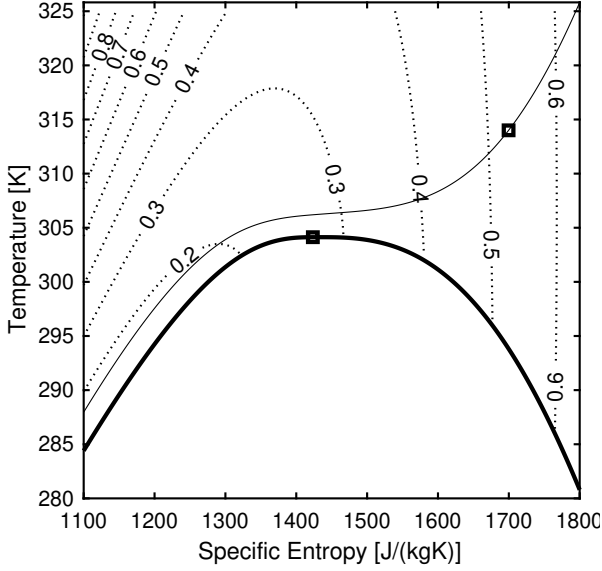


FIGURE 4: T,s-diagram showing the investigated compressor total inlet state at $T_t = 314$ K, $p_t = 77.5$ bar. Contour lines illustrate the compressibility factor.

efficiency data is provided by Fuller & Eisemann [14]. Because of extreme deviations in the experimental inlet states, e.g. accounting for variations of total density in the range $(344...686) \text{ kg/m}^3$ for the data set specified by Wright et al. [39], all reference data is provided in either corrected or non-dimensional form. The same set of non-dimensional performance parameters, as applied in the preceding study [19], is adopted here for the sake of comparison: The ideal head coefficient

$$\psi = (h_{i,s} - h_{1,t}) / u_2^2 \quad (14)$$

and the total-to-static isentropic efficiency

$$\eta_s = (h_{i,s} - h_{1,t}) / (h_{2,t} - h_{1,t}), \quad (15)$$

are both illustrated as a function of the flow coefficient

$$\phi = 4 \cdot \dot{V}_1 / (\pi \cdot d_2^2 \cdot u_2). \quad (16)$$

Note, that the index i in equation 14 and equation 15 refers either to the intrastage (between the impeller trailing edge and the channel diffuser leading edge) or the stage exit position evaluated at $r/r_2 = 1.008$ and $r/r_2 = 2.055$, respectively.

Figure 5 shows the non-dimensional performance curve representation of the conducted RANS and meanline calculations, which are both evaluated at the intrastage and stage exit position. Additionally, the experimental data reported by Wright et al. [38; 39] and Fuller & Eisemann [14] as well as results of the previous RANS study [19] analysing the sole impeller geometry (followed by some vaneless space) are presented. As the meanline analysis is applied sequentially, an evaluation at the intrastage position is analogous to the sole consideration of the

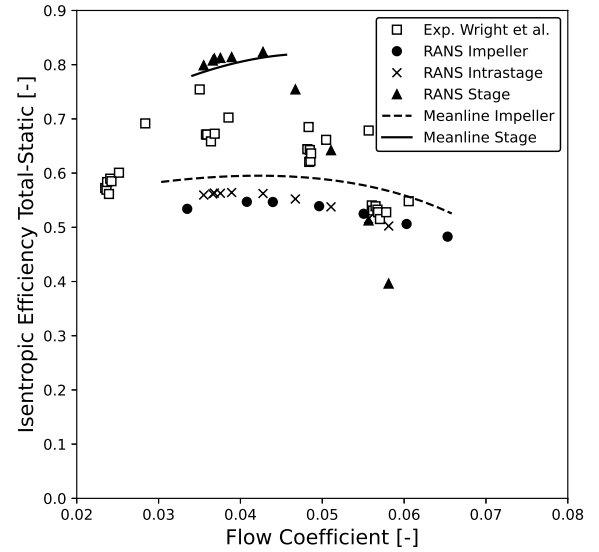
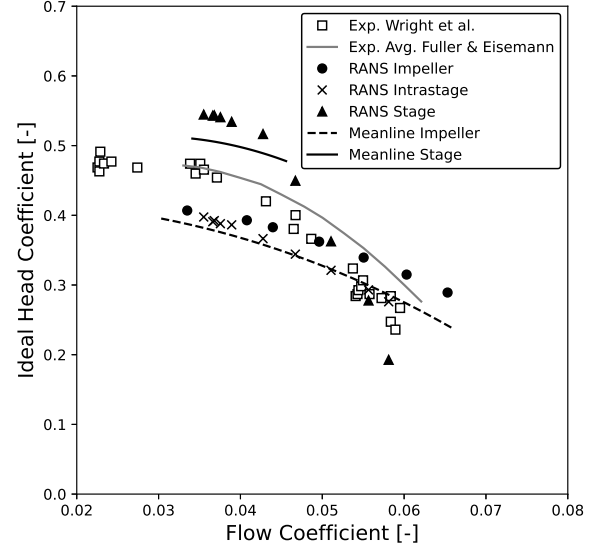


FIGURE 5: Non-dimensional compressor performance. Experimental data refer to Wright et al. [38; 39]¹ and Fuller & Eisemann [14]. The latter did not report efficiency data. RANS simulations of the standalone impeller geometry were conducted in [19].

impeller.

Comparing both RANS calculations evaluated behind the impeller exit, a steeper ideal head characteristic is obtained through a performance assessment of the channel diffuser stage

configuration. This difference might be attributed to the short radial distance between the impeller trailing and diffuser leading edges (measuring merely 0.3 mm) and associated increase of static pressure due to close locations of stagnation points near the evaluation plane. Both ideal head curves are noticeably flatter compared to those of the experimental data sets, which might be owed to geometric disparities between the real compressor geometry and the investigated design based on similar main dimensions. In particular, deviations in blade angle distributions might affect head generation. Also, differences in the uncertain data assessment positions could lead to discrepancies, especially regarding static flow quantities. However, the impeller meanline analysis, also conducted on basis of main dimensions, is in much better agreement with the CFD data regarding the slope of the impeller ideal head characteristic. This observation is important to note because it shows that both numerical methodologies, which share the same input of data, also show consistent trends in their output. In particular, good agreement between the impeller meanline analysis and the intrastage RANS evaluation can be observed, indicating the applicability of the associated impeller aerodynamic loss models for compressors operating with sCO₂.

With regard to calculated impeller isentropic efficiencies, no significant quantitative discrepancies can be observed between the two RANS assessments, which show about ten percentage points reduced maximum efficiencies compared to the experimental data exhibiting a high degree of scatter by outliers. Note, that experimental efficiencies were derived from motor power measurements and corrections for mechanical and electric losses through correlations, which also entail uncertainties. Because of the exclusion of external losses in the experiments, external losses are also excluded within this meanline study. This also ensures better comparability with the conducted RANS simulations, where these are not assessed. A good agreement with the experimental flow coefficient value at which the maximum impeller efficiency is obtained is noticed for the RANS calculation evaluated at the intrastage plane. Respective values are in accordance with the design flow coefficient of the machine stated earlier. The meanline isentropic impeller efficiency characteristic agrees well with CFD data with regard to its shape, but shows slightly higher values over the entire flow range and a maximum efficiency of about 60 %. This can be expected, as only a limited number of loss contributing mechanisms is assessed through the meanline approach.

An ideal head rise of 13-41 % is observed in the flow range of $\phi \approx 0.036 \dots 0.051$ by considering the channel type diffuser in the RANS simulations conducted in this study. For higher flow coefficients, the diffuser increasingly fails to provide recovery of ideal head. The meanline analysis comprising the diffuser shows about 6-7 % reduced ideal head compared to the RANS calculations for flow coefficients up to $\phi \approx 0.043$ and demonstrates a good agreement regarding efficiency for this flow range. How-

ever, for higher flow coefficients, the applied diffuser model formulation is not able to resemble the abrupt decline in ideal stage head as well as isentropic efficiency, as indicated by the CFD analysis. The fact that a rapid decrease of the ideal head or isentropic efficiency characteristic can not be observed in the provided experimental data indicates that the interpretation of these data sets being associated with the impeller wheel holds plausible and likely.

CONCLUSION AND OUTLOOK

In this work, the performance characteristics of a centrifugal compressor stage operating with supercritical CO₂ are investigated by means of 3D RANS simulations as well as a single-zone meanline analysis procedure applying loss correlations. In order to account for thermophysical real gas properties, the applied in-house density based compressible CFD solver is coupled to a software library implementation of the Spline-based Table Look-Up Method (SBTL) [20; 21] adopted for CO₂ applications. The investigated compressor stage is based on main dimensions of a test-loop compressor operated by Sandia National Laboratories. The compressor performance is assessed for a supercritical inlet operation state through a non-dimensional speed curve representation, which is compared to experimental data as well as numerical data obtained from a preceding study [19], in which only the impeller geometry was considered.

With regard to the previous study, a steeper impeller head curve is derived through the CFD analysis considering the complete stage geometry. This indicates a noticeable upstream effect of the channel diffuser located closely to the impeller trailing edge. However, impeller efficiencies previously derived on basis of the simplified geometry considering a standalone impeller are comparable in quality as well as quantity. The overall trends regarding the impeller performance are satisfyingly resembled by the meanline analysis, which suggests the applicability of the applied internal loss model set and slip correlation for performance predictions of sCO₂ impellers.

A potential ideal head rise of up to 41 % through the channel type diffuser is identified by the RANS calculations. However, this potential diminishes abruptly for flow coefficients exceeding values of $\phi \approx 0.043$. This behaviour can not be resembled by the applied diffuser model in the meanline approach. Nevertheless, the meanline analysis provides a good agreement with CFD data in the flow coefficient range where practical recovery of ideal head is predicted, thus, also suggesting applicability of respective conventional diffuser loss and deviation models for CO₂ compressors, provided that real gas properties are accounted for in the general meanline procedure.

Transient simulations of the compressor will be subject to future research in order to increase the fidelity of the performance assessment considering dynamic rotor-stator-interaction.

NOMENCLATURE

Abbreviations

Avg.	average
CFD	computational fluid dynamics
EOS	equation of state
Exp.	experiment
RANS	Reynolds-Averaged Navier Stokes
SBTL	Spline-Based Table Look-Up Method
sCO ₂	supercritical carbon dioxide
SNL	Sandia National Laboratories
SW	Span-Wagner

Subscripts

1	impeller inlet
2	impeller exit
3	channel diffuser inlet
4	channel diffuser exit
bl	blading
c	critical
i	station index
s	isentropic
t	total

Symbols

$\bar{\omega}$	total pressure loss coefficient
β	relative flow angle
\dot{V}	volume flow
η_s	total-to-static isentropic efficiency
λ	thermal conductivity coefficient
μ	dynamic viscosity
ϕ	flow coefficient
ψ	ideal head coefficient
ρ	density
σ	slip factor
$\underline{\tau}$	stress tensor
\underline{F}^a	advective flux tensor
\underline{F}^d	diffusive flux tensor
\underline{I}	identity tensor
\underline{q}	heat flux vector
\underline{s}	source term vector
\underline{u}	velocity vector
\underline{w}	conservative variables vector
a	speed of sound
d_2	impeller tip diameter
E	specific total internal energy
e	specific internal energy
H	specific total enthalpy
h	specific enthalpy
Ma_u	peripheral Mach number
p	pressure
R	specific gas constant
T	temperature
t	time variable

u_2	impeller tip speed
W	specific work
Z	compressibility factor
Z_{bl}	number of blades

References

- [1] Ameli, A., Turunen-Saaresti, T., and Backman, J. (2016). Numerical Investigation of the Flow Behavior Inside a Supercritical CO₂ Centrifugal Compressor. *Proceedings of the ASME Turbo Expo 2016*. ASME Paper No. GT2016-57481.
- [2] Ameli, A. et al. (2018a). Compressor Design Method in the Supercritical CO₂ Applications. *Supercritical CO₂ Power Cycles Symposium 2018*. Pittsburgh, Pennsylvania, USA.
- [3] Ameli, A. et al. (2018b). Effects of Real Gas Model Accuracy and Operating Conditions on Supercritical CO₂ Compressor and Flow Field. *Journal of Engineering for Gas Turbines and Power*, 140(6).
- [4] Aungier, R. H. (1995). Mean Streamline Aerodynamic Performance Analysis of Centrifugal Compressors. *Journal of Turbomachinery*, 117(3):360–366.
- [5] Aungier, R. H. (2000). *Centrifugal Compressors. A Strategy for Aerodynamic Design and Performance Analysis*. ASME Press.
- [6] Baltadjiev, N. D., Lettieri, C., and Spakovszky, Z. S. (2015). An Investigation of Real Gas Effects in Supercritical CO₂ Compressors. *Journal of Turbomachinery*, 137(9).
- [7] Bell, I. et al. (2014). Pure and Pseudo-pure Fluid Thermophysical Property Evaluation and the Open-Source Thermophysical Property Library CoolProp. *Industrial & Engineering Chemistry Research*, 53(6):2498–2508.
- [8] Brun, K., Friedman, P., and Dennis, R. (2017). *Fundamentals and Applications of Supercritical Carbon Dioxide (sCO₂) Based Power Cycles*. Woodhead Publishing.
- [9] Concepts NREC LLC (2018a). AxCent64 (8.7.13.0).
- [10] Concepts NREC LLC (2018b). Compal (8.7.13.0).
- [11] Conrad, O., Raif, K., and Wessels, M. (1979). The Calculation of Performance Maps for Centrifugal Compressors With Vane-Island Diffusers. *Proceedings of the Twenty-fifth Annual International Gas Turbine Conference and Exhibit and Twenty-second Annual Fluids Engineering Conference*. New Orleans, Louisiana, USA.
- [12] Coppage, J. E. et al. (1956). Study of Supersonic Radial Compressors for Refrigeration and Pressurization Systems. WADC TECHNICAL REPORT 55-257, Airesearch Manufacturing Company.
- [13] Daily, J. W. and Nece, R. E. (1960). Chamber Dimension Effects on Induced Flow and Frictional Resistance of Enclosed Rotating Disks. *Journal of Basic Engineering*, 82(1):217–230.
- [14] Fuller, R. L. and Eisemann, K. (2011). Centrifugal Compressor Off-Design Performance for Super-Critical CO₂. *Super-*

critical CO₂ Power Cycles Symposium 2011. Boulder, Colorado, USA.

[15] Huber, L. and Sykioti, E. A. (2016). Reference Correlation of the Thermal Conductivity of Carbon Dioxide from the Triple Point to 1100 K and up to 200 MPa. *Journal of Physical and Chemical Reference Data*, 45(1).

[16] Iseni, S., Post, P., and di Mare, F. (2019). Numerical Analysis of the Influence of Air Humidity on a Transonic Compressor Stage. *International Gas Turbine Congress 2019*. Paper No. ThAM16.1, Tokyo.

[17] Jansen, W. (1967). A Method for Calculating the Flow in a Centrifugal Impeller When Entropy Gradients Are Present. *Royal Society Conference on Internal Aerodynamics (Turbomachinery)*. Cambridge, UK.

[18] Johnston, J. P. and Dean, R. C., Jr. (1966). Losses in Vaneless Diffusers of Centrifugal Compressors and Pumps: Analysis, Experiment, and Design. *Journal of Engineering for Power*, 88(1):49–60.

[19] Karaefe, R. E. et al. (2020). Numerical Investigation of a Centrifugal Compressor for Supercritical CO₂ Cycles. *Proceedings of the ASME Turbo Expo 2020*. ASME Paper No. GT2020-15194, 2020.

[20] Kunick, M. (2018). Fast Calculation of Thermophysical Properties in Extensive Process Simulations with the Spline-Based Table Look-Up Method (SBTL). *Fortschrittberichte VDI*. Nr. 618, Reihe 6, Energietechnik.

[21] Kunick, M. et al. (2015). CFD Analysis of Steam Turbines With the IAPWS Standard on the Spline-Based Table Look-Up Method (SBTL) for The Fast Calculation of Real Fluid Properties. *Proceedings of the ASME Turbo Expo 2015*. ASME Paper No. GT2015-43984.

[22] Laesecke, A. and Muzny, C. D. (2017). Reference Correlation for the Viscosity of Carbon Dioxide. *Journal of Physical and Chemical Reference Data*, 46(1).

[23] Lee, J. et al. (2012). Design Methodology of Supercritical CO₂ Brayton Cycle Turbomachineries. *Proceedings of the ASME Turbo Expo 2012*. ASME Paper No. GT2012-68933.

[24] NUMECA International (2018). AutoGrid5 (13.1).

[25] Oh, H. W., Yoon, E. S., and Chung, M. K. (1997). An Optimum Set of Loss Models for Performance Prediction of Centrifugal Compressors. *Proceedings of the Institution of Mechanical Engineers, Part A: Journal of Power and Energy*, 211(4):331–338.

[26] Pecnik, R., Rinaldi, E., and Colonna, P. (2012). Computational Fluid Dynamics of a Radial Compressor Operating with Supercritical CO₂. *Journal of Engineering for Gas Turbines and Power*, 134(12).

[27] Post, P. (2020). *Development of Efficient Numerical Methods for Non-Ideal Compressible Fluid Flows in Propulsion and Power*. PhD thesis, Ruhr-Universität Bochum.

[28] Post, P. and di Mare, F. (2018). Highly Efficient Euler-Euler Approach for Condensing Steam Flows in Turbomachines.

GPPS 2018. Montreal, Canada.

[29] Post, P., Sembritzky, M., and di Mare, F. (2019). Towards Scale Resolving Computations of Condensing Wet Steam Flows. *Proceedings of the ASME Turbo Expo 2019*. ASME Paper No. GT2019-91269.

[30] Post, P., Winhart, B., and di Mare, F. (2020). Large Eddy Simulation of a Condensing Wet Steam Turbine Cascade. *Proceedings of the ASME Turbo Expo 2020*. ASME Paper No. GT2020-16064, 2020.

[31] Rinaldi, E., Pecnik, R., and Colonna, P. (2013). Steady State CFD Investigation of a Radial Compressor Operating with Supercritical CO₂. *Proceedings of the ASME Turbo Expo 2013*. ASME Paper No. GT2013-94580.

[32] Rinaldi, E., Pecnik, R., and Colonna, P. (2015). Computational Fluid Dynamic Simulation of a Supercritical CO₂ Compressor Performance Map. *Journal of Engineering for Gas Turbines and Power*, 137(7).

[33] Romei, A. et al. (2020). The Role of Turbomachinery Performance in the Optimization of Supercritical Carbon Dioxide Power Systems. *Journal of Turbomachinery*, 142(7).

[34] Spalart, P. R. and Allmaras, S. R. (1992). A One-Equation Turbulence Model for Aerodynamic Flows. *30th Aerospace Sciences Meeting and Exhibit*.

[35] Span, R. and Wagner, W. (1996). A New Equation of State for Carbon Dioxide Covering the Fluid Region from the Triple-Point Temperature to 1100 K at Pressures up to 800 MPa. *Journal of Physical and Chemical Reference Data*, 25(6):1509–1596.

[36] van Leer, B. (1979). Towards the Ultimate Conservative Difference Scheme. V. A Second-Order Sequel to Godunov's Method. *Journal of Computational Physics*, 32(1).

[37] Wiesner, F. J. (1967). A Review of Slip Factors for Centrifugal Impellers. *Journal of Engineering for Gas Turbines and Power*, 89(4):558–566.

[38] Wright, S. A. et al. (2009). Supercritical CO₂ Compression Loop Operation and Test Results. *Supercritical CO₂ Power Cycles Symposium*. Troy, NY, USA.

[39] Wright, S. A. et al. (2010). Operation and Analysis of a Supercritical CO₂ Brayton Cycle. SANDIA REPORT SAND2010-0171, Sandia National Laboratories.

Annex A

TABLE A1: Set of internal and external (parasitic) loss models

Loss mechanism	Loss model		Reference
Impeller:			
Incidence	$\Delta h_{inc} = \sigma \cdot \frac{(w_{1\theta} - w_{1\theta,bl})^2}{2}$	$\sigma = 0.5 \dots 0.7$	Conrad et al. [11]
Blade loading	$\Delta h_{bl} = 0.05 \cdot D_f^2 \cdot u_2^2$	$D_f = 1 - \frac{w_2}{w_{1r}} + \frac{0.75 \cdot W_{Euler} / u_2^2}{w_{1r} / \mu_2 \left[\frac{Z_{bl}}{\pi} \left(1 - \frac{d_{1L}}{d_2} \right) + 2 \frac{d_{1L}}{d_2} \right]}$	Coppage et al. [12]
Skin friction	$\Delta h_{sf} = 2c_f \frac{L_{fl}}{d_{hb}} \bar{w}^2$	$\bar{w} = \frac{(2w_2 + w_{1r} - w_{1h})}{4}$	Jansen [17]
		$L_{fl} \approx \frac{\pi}{8} \left(d_2 - \frac{d_{1r} + d_{1n}}{2} - b_2 + 2L_{ax} \right) \left(\frac{2}{\cos \beta_{1r} + \cos \beta_{1h} + \cos \beta_2} \right)$	
		$d_{hb} = \frac{d_2 \cos \beta_2}{\frac{Z_{bl}}{\pi} + \frac{d_2 \cos \beta_2}{b_2}} + \frac{d_2 \left(\frac{d_{1r}}{d_2} + \frac{d_{1h}}{d_2} \right) \left(\frac{\cos \beta_{1r} + \cos \beta_{1h}}{2} \right)}{\frac{Z_{bl}}{\pi} + \left(\frac{d_{1r} + d_{1n}}{d_{1r} - d_{1n}} \right) \left(\frac{\cos \beta_{1r} + \cos \beta_{1h}}{2} \right)}$	
		$c_f = 0.0412 Re^{-0.1925}; Re = \frac{d_{hb} \bar{w}}{\nu}$	
Clearance	$\Delta h_{cl} = u_2^2 0.6 \frac{\delta_{cl}}{b_2} \frac{c_{2\theta}}{u_2} \times \sqrt{\frac{4\pi}{b_2 Z_{bl}} \left[\frac{r_{1r}^2 - r_{1h}^2}{(r_2 - r_{1r})(1 + \rho_2 / \rho_1)} \right]} \frac{c_{2\theta}}{u_2} \frac{c_{1m}}{u_2}$		Jansen [17]
Mixing	$\Delta h_{mix} = \frac{c_2^2}{2[1 + (c_{2\theta} / c_{2m})^2]} \cdot \left[\frac{1 - \varepsilon - B}{1 - \varepsilon} \right]^2$		Johnston & Dean [18]
External:			
Disk friction	$W_{df} = f_{df} \frac{\bar{\rho} r_2^3 u_2^3}{4m}$	$\bar{\rho} = \frac{\rho_1 + \rho_2}{2}; f_{df} = \begin{cases} \frac{2.67}{Re_{df}^{0.5}}, & Re_{df} < 3 \cdot 10^5 \\ \frac{0.0622}{Re_{df}^{0.2}}, & Re_{df} \geq 3 \cdot 10^5 \end{cases}$	Daily & Nece [13], as quoted by Oh et al. [25]
Recirculation	$W_{rc} = 8 \cdot 10^{-5} \sinh(3.5\alpha_3^2) D_f^2 u_2^2$		Oh et al. [25]
Leakage	$W_{lk} = \frac{\dot{m}_{cl} u_{cl} u_2}{2m}$	$u_{cl} = 0.816 \sqrt{2\Delta p_{cl} / \rho_2}; \dot{m}_{cl} = \rho_2 Z_{bl} \delta_{cl} L_{fl} u_{cl}$	Aungier [4]
		$\Delta p_{cl} = \frac{\dot{m}(c_2 c_{2\theta} - r_1 c_{1\theta})}{Z_{bl} r_{bl} L_{fl}}; \bar{r} = \frac{r_1 + r_2}{2}; \bar{b} = \frac{b_1 + b_2}{2}$	
Channel Diffuser:			
Incidence	$\bar{\omega}_{inc} = \begin{cases} 0.8 \left[(c_3 - c_3^*) / c_3 \right]^2, & c_3 \leq c_{3S} \\ 0.8 \left[\left((c_3 / c_{3S})^2 - 1 \right) c_{ih}^2 / c_3^2 + (c_{3S} - c_3^*)^2 / c_{3S}^2 \right], & c_3 > c_{3S} \end{cases}$		Aungier [5]
Skin friction	$\bar{\omega}_{sf} = 4c_{f,diff} (\bar{c} / c_3)^2 L_B / d_{h,diff} / (2\delta / d_{h,diff})^{0.25}$		Aungier [5]
Mixing	$\bar{\omega}_{mix} = \left[(c_{m,wake} - c_{m,mix}) / c_3 \right]^2$		Aungier [5]

Note: Equations are presented for the meridional angle convention. The table nomenclature is given in SI-Units. B : ratio of diffuser inlet depth to impeller tip flow passage depth, b : width, c : absolute velocity, $c_{f,diff}$: diffuser skin friction coefficient, d : diameter, $d_{h,diff}$: average diffuser hydraulic diameter, h : specific enthalpy, L_{ax} : axial length of impeller, L_B : length of blade mean camberline, \dot{m} : mass flow, r : radius, u : peripheral velocity, W : specific work, w : relative velocity, Z_{bl} : number of blades, α : absolute flow angle, β : relative flow angle, δ_{cl} : clearance gap width, ε : fraction of blade-to-blade space occupied by the wake, μ : dynamic viscosity, ν : kinematic viscosity, ρ : density, $(\circ)_1$: impeller inlet, $(\circ)_2$: impeller exit, $(\circ)_3$: channel diffuser inlet, $(\circ)_{bl}$: blading, $(\circ)_h$: hub, $(\circ)_m$: meridional, $(\circ)_S$: value at onset of blade stall, $(\circ)_r$: tip, $(\circ)_{th}$: throat parameter, $(\circ)_\theta$: tangential, $(\circ)^*$: condition at minimum loss incidence angle

TRANSIENT ANALYSIS OF THE SUPER-CRITICAL CARBON DIOXIDE CYCLE COUPLED TO PRESSURIZED WATER REACTOR FOR NUCLEAR POWERED SHIPS

Jeong Yeol Baek
KAIST
Daejeon, Republic of Korea

Jae Jun Lee
KAIST
Daejeon, Republic of Korea

Jeong Ik Lee*
KAIST
Daejeon, Republic of Korea
Email: jeongiklee@kaist.ac.kr

ABSTRACT

Recently, nuclear-powered ships have attracted attention due to international regulations on greenhouse gas emissions and the trend of rapid and large-scale ships. In order for a nuclear system to be used in marine propulsion, it is important to achieve small in size and should be able to respond to rapid load demand changes. In this study, a super-critical carbon dioxide (S-CO₂) cycle is proposed as a power conversion system for pressurized water reactors (PWR) for marine propulsion. The S-CO₂ cycle has been attracting attention as the next-generation power conversion system that can be an alternative to the steam Rankine cycle due to its small system size and higher efficiency. The conceptual design of the S-CO₂ power conversion system is first performed under the reference reactor conditions, including cycle design and component design. To conduct system analysis, MARS-KS code, one of the nuclear thermal-hydraulic safety analysis codes developed by Korea Atomic Energy Research Institute (KAERI) and actively used for the safety review calculation of a nuclear power plant by Korea Institute of Nuclear Safety, is improved to accurately simulate the S-CO₂ power conversion system combined with PWR. The PID controller based automatic control strategy of the entire system is designed to respond to rapid load changes. Transient analyses are performed with the newly developed system analysis code under various scenarios.

INTRODUCTION

Worldwide trade has been growing due to economic globalization and it is estimated that shipping is responsible for the transport of 95% of global commerce. Due to the trend of constructing large-scale and fast ships while international regulations on greenhouse gas emissions are becoming more stringent, the attention to nuclear-powered merchant ships is increasing. However, many studies suggest that nuclear propulsion systems need to be improved for better economy for the nuclear-powered merchant ship.

Most of the nuclear propulsion systems currently in operation such as naval reactors or icebreakers are using a combination of the pressurized water reactor (PWR) and steam

Rankine cycle. Among various types of reactor core, the PWR has been found to be most suitable to nuclear-powered ships in terms of safety and performance although there have been many studies over the past few decades to apply various types of nuclear reactors to ship propulsion. However, there are still some economic drawbacks in using the steam Rankine cycle as the power conversion system for nuclear merchant ships. Due to the very large volume of components such as steam turbine and condenser, cargo carrying capacity is reduced which is critical to economic success of the merchant ship. In addition, system layout becomes complicated due to many auxiliary systems related to steam cycle such as steam quality control, water chemistry control, and large-sized pure water inventory tank. It means that the manning cost is also very high since it requires a lot of crews. Therefore, more compact and simple power conversion system is required for nuclear merchant ships to be economically competitive.

The super-critical carbon dioxide (S-CO₂) Brayton cycle which can be an alternative to conventional Rankine cycle has received substantial attention as the most promising power conversion system due to its simple layout and compactness [1]. System configuration can be much simpler due to lower purification system requirements compared to the steam Rankine cycle. These characteristics offer the potential for significant operational and capital cost benefits. Additionally, an S-CO₂ Brayton cycle keeps single phase all the time during operation, which makes the system to quickly respond to the load change or system disturbance and has less risk of flow instability. Therefore, the S-CO₂ cycle is expected to have many advantages when adopted as a power conversion system of nuclear-powered ships.

In order to apply nuclear systems for the marine propulsion, it should exhibit superior load following capability under severe load changes as shown in Table 1. Therefore, in this paper, a new nuclear propulsion system which couples the S-CO₂ power conversion system to a pressurized water reactor is designed in conceptual level and transient analyses under severe load changes are conducted to demonstrate the feasibility of the proposed system concept for the marine application.

* corresponding author(s)

Table 1: General information of nuclear merchant ships

Parameter	NS Savannah	NS Otto Hahn	NS Mutsu	
Displacement (tons)	21,800	25,790	25,790	
Reactor thermal power	74 MW	38 MW	38 MW	
Cruising speed	21 knots (39 km/h)	17 knots (31 km/h)	17 knots (31 km/h)	
Cargo capacity [tons]	10,000	14,000	8,242	
Crew	124	63	80	
Load change requirement	Increase	20% - 80% in 10s (6%/s)	10% - 100% in 90s (1%/s)	18% - 90% in 30s (2.4%/s)
	Decrease	100% - 20% in 3s (26.7%/s)	100% - 10% in 1s (90%/s)	100% - 18% in 1s (82%/s)

REFERENCE REACTOR

Since the design of primary coolant system and reactor core is beyond the scope of this paper, it is referred to the existing reactor system. To select a reference reactor core, the engine power required for ship propulsion has to be determined. The total engine power of the recently built diesel-powered large container ships is approximately 100 MW. Based on the current trend of container ship power, thermal characteristics of reactor core are referred to SMART reactor developed by KAERI (Korea Atomic Energy Research Institute), which is an integral-type PWR with the thermal power of 330 MW [2]. For nuclear propulsion systems which experience frequent power maneuvering, not only the thermal characteristics but also the reactor feedback characteristics are important. Reactor feedback coefficients are referred from the Autonomous Transportable On-demand Reactor Module (ATOM), which is a water-cooled autonomously operating integral type small modular reactor (SMR) under development by a university consortium led by KAIST with the thermal power of 450 MW [3]. A notable feature that ATOM differs from the SMART is that ATOM is designed as a soluble-boron-free (SBF) reactor. Therefore, the primary system could be much simpler and it targets the passively autonomous load-follow operation with strongly negative moderator temperature coefficient (MTC). To summarize the reference reactor, the primary reactor system is referred to thermal characteristics of SMART reactor while the reactor feedback characteristics of ATOM reactor are adopted. The

major parameters of the primary system are summarized in Table 2.

Table 2: Major parameters of the primary system

Reactor type	Integral PWR
Core thermal power [MW _{th}]	330
System Pressure [MPa]	15
Core inlet temperature [°C]	296
Core outlet temperature [°C]	323
$\dot{m}_{coolant}$ in core [kg/sec]	2090

DESIGN SUMMARY OF S-CO₂ SYSTEM

The S-CO₂ system was conceptually designed under the conditions of the reference reactor. Figure 1 shows the design procedure. First, a power cycle optimization is performed assuming machinery properties such as the pressure drop and effectiveness of heat exchangers, and isentropic efficiency of each turbomachinery. From the results of the cycle optimization, main components are designed in conceptual design level. This procedure is repeated until both pre-assumed machinery properties, such as the turbomachinery efficiency, and physically allowable geometry of components are consistent. Since the system design is not the main topic of this paper, the design is covered briefly.

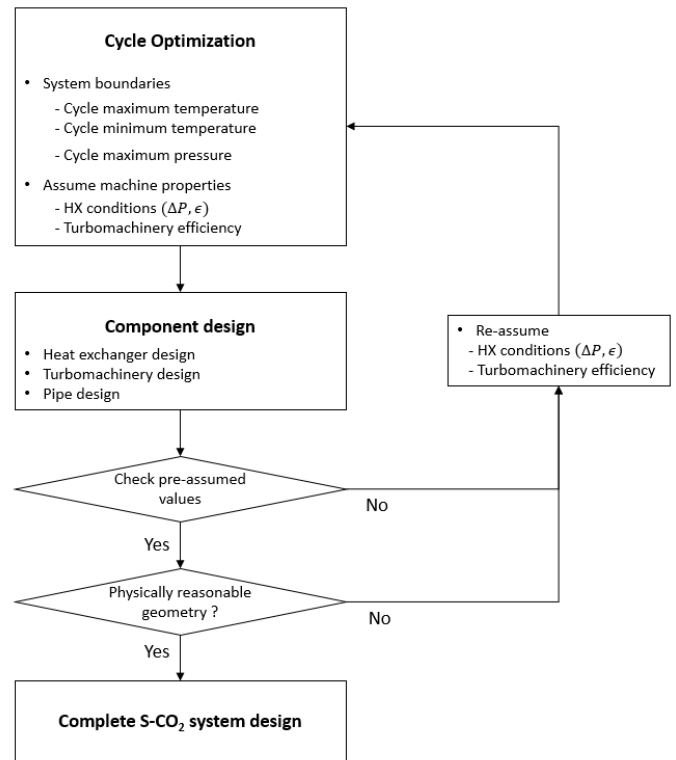


Figure 1: S-CO₂ system design procedure.

Before conducting the design of a thermodynamic cycle, cycle layout has to be selected. Due to the relatively low turbine

inlet temperature (TIT) under the PWR temperature conditions, recompression cycle was chosen which is generally known as the most efficient cycle among the basic cycle layouts. The cycle optimization was performed with an in-house S-CO₂ cycle analysis code, named in KAIST-ESCA (Evaluator for Super-critical CO₂ cycle based on Adjoint method) [4]. Table 3 summarizes the optimized results of S-CO₂ cycle design.

Table 3: Cycle design results

Maximum pressure [MPa]	15
Maximum temperature [°C]	315
Minimum temperature [°C]	32
IHX pressure drop [kPa]	100
$\Delta P_{HTR,hot}$ [kPa]	100
$\Delta P_{HTR,cold}$ [kPa]	50
$\Delta P_{LTR,hot}$ [kPa]	100
$\Delta P_{LTR,cold}$ [kPa]	50
HTR effectiveness [%]	95
LTR effectiveness [%]	90
Turbine efficiency [%]	92
Main compressor efficiency [%]	85
Recompressing compressor efficiency [%]	88
Turbine expansion ratio	1.799
Flow split ratio [%]	55.857
Turbine work [MW _e]	153.58
Main compressor work [MW _e]	18.79
Recompressing compressor work [MW _e]	37.2
Cycle net work [MW _e]	97.6
Cycle thermal efficiency [%]	29.58

S-CO₂ recompression cycle has three turbomachinery: turbine, main compressor, and recompressing compressor. To design each turbomachinery, the type of turbomachinery was firstly determined. Sandia National Laboratories (SNL) studied the scale dependency of S-CO₂ turbomachinery and element technology [5]. Since the proposed system produces about 100 MW of electric power, turbomachinery is designed in axial type. In case of propulsion configuration, electric propulsion system is considered due to its high flexibility in propulsion arrangement, and all the turbomachinery are directly connected to single shaft. For load transient calculation, the moment of inertia of each component is also important. Since each component attached to the shaft has not been fully designed and optimized in this study, it is assumed that the moment of inertia of the proposed system is scaled from the GFR data which is 2400MW_{th} direct S-CO₂ cooled fast reactor [6]. Each turbomachinery design was obtained from an in-house code, namely KAIST-TMD (TurboMachinery Design) code which is based on 1-D mean stream line analysis adopting a real gas approach to overcome limitations for utilizing the conventional design methods near the critical point [7]. From the KAIST-TMD code, geometry and off-design performance map of each turbomachinery were obtained.

The proposed system has four heat exchangers: intermediate heat exchanger (IHX), high temperature recuperator (HTR), low temperature recuperator (LTR), and precooler (PC). Since the volume of the S-CO₂ turbomachinery is typically much smaller than that of the heat exchanger, the size of the S-CO₂ power conversion system is closely related to the size of the heat exchanger. In this respect, except PC, the type of heat exchangers was selected as printed PCHE (Printed Circuit Heat Exchanger) which is a robust heat exchanger combining compactness, low pressure drop, high effectiveness and the ability to operate with a very large pressure difference between hot side and cold side. PC was designed as the shell and tube heat exchanger since PCHE is not recommended when sea water is used as cooling medium due to impurity related issues such as fouling and scaling. Each heat exchanger was designed with an in-house code, KAIST-HXD (Heat eXchanger Design) which is based on the 1-D finite difference method (FDM) and the overall heat transfer coefficient (U) with counter-current flow configuration [8]. In case of PCHE correlations, Kim suggested a CFD-aided correlation covering wide range of Reynolds number to facilitate PCHE designs for the S-CO₂ Brayton cycle application [9]. For the design of shell and tube type precooler, Gnielinski correlation is used.

Pipe design is also important since it is directly related to the capital cost, the total amount of fluid mass, and the size of total system. However, most of procedures in pipe design are based on the water or steam system and there is very limited research on the pipe design of the S-CO₂ system. Therefore, in this study, pipes are preliminarily designed with a simple method using the optimal flow velocity and ASME standard.

After the S-CO₂ power conversion system is designed, the size of main machinery room is estimated as presented in Figure 2. Table 4 compares the machinery room size of NS Savannah and the proposed system. From the results of conceptual design, it is demonstrated that the total volume of power conversion system can be significantly reduced when the S-CO₂ cycle is adopted.

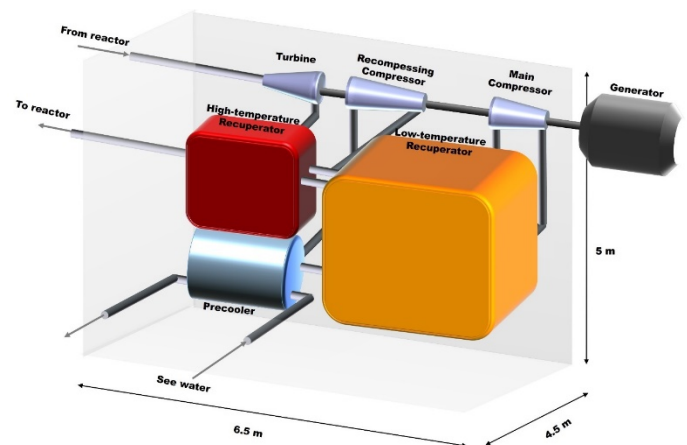


Figure 2: Configuration of S-CO₂ power conversion system.

Table 4: Main machinery room size of NS Savannah and the proposed system

	NS Savannah	Proposed system
Thermal power	74 MW _{th}	330 MW _{th}
Power conversion system	Steam cycle (9-stage HPT, 7-stage LPT)	S-CO ₂ recompression cycle
Length	17 m	6.5 m
Width	24 m	4.5 m
Height	9.8 m	5 m
Volume	3998.4 m ³	146.25 m ³

DEVELOPMENT OF SYSTEM ANALYSIS CODE

Multi-dimensional Analysis of Reactor Safety (MARS) code was developed by Korea Atomic Energy Research Institute (KAERI). The code was developed for realistic multi-dimensional thermal hydraulic system transient analysis of water-cooled reactor and has been actively used for the safety review calculation of a nuclear power plant by Korea Institute of Nuclear Safety (KINS). The code was developed on the basis of the RELAP5/MOD3.2.1.2 and the COBRA-TF code of USNRC. The MARS code basic field equations consist of two phasic continuity equations, two phasic momentum equations, and the phasic energy equations for the two field non-equilibrium model [10].

In order for nuclear power to be applied to ship propulsion, the system has to be capable of operating over a wide range of power levels, especially during the ingress and egress to ports. It also should exhibit much faster response power changes than land-based nuclear reactors. To analyze rapid power transients of the proposed system, the system code has to conduct realistic performance analysis of power conversion system, as well as the safety analysis of the reactor core. However, since MARS code focuses on analyzing water-cooled reactor core transients, it needs to be improved to accurately simulate the S-CO₂ power conversion system. Figure 3 shows the conceptual diagram of MARS code improvements. To summarize improvements, three options are added to the original MARS code. Firstly, in order to accurately predict physical properties of S-CO₂, NIST database is directly imported into MARS code. Secondly, to simulate realistic transient behavior of heat exchangers, PCHE heat transfer correlation is added to heat structure sets in MARS code. Finally, a new turbomachinery model based on the off-design performance map and CEA similitude method are added to accurately simulate S-CO₂ turbomachinery.

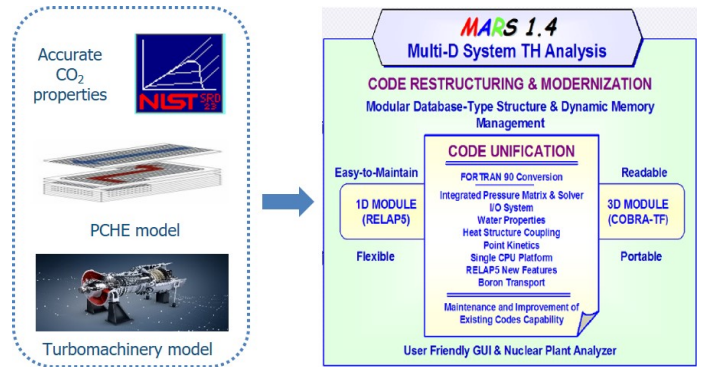


Figure 3: Conceptual diagram of MARS code improvements.

To demonstrate the reliability of the newly developed code, code validation has been performed with experimental data. The selected experimental loop is SCIEL (Supercritical CO₂ Integral Experiment Loop) facility installed in KAERI. Experimental data is generated during compressor performance test of SCIEL and data when compressors are maintaining their rotational speed at 35,000 RPM is used for validation. Figure 4 shows description of the test section of SCIEL facility and MARS model. Compressor performance test was conducted by adjusting control valve area to reduce the pressure of compressed fluid. Since the geometrical information of the precooler is unknown, it was processed as a boundary. Therefore, the purpose of this validation is to ensure that the developed code can accurately simulate the flow near the critical point and newly added compressor model. Figure 5 shows results of code validation which compare pressure and temperature at each point between experimental data and MARS code simulation result. The results of validation suggest that the improved MARS code can well simulate the flow near the critical point and S-CO₂ turbomachinery.

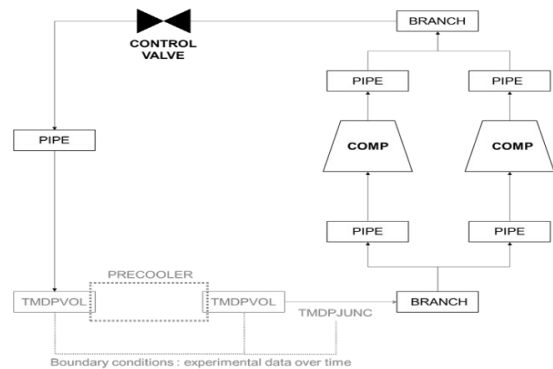
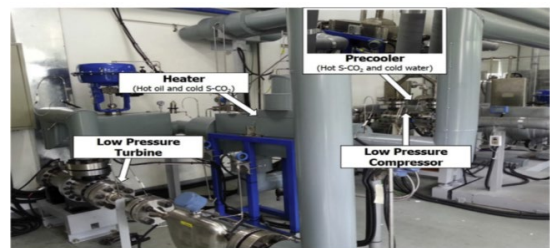


Figure 4: MARS modeling and SCIEL facility.

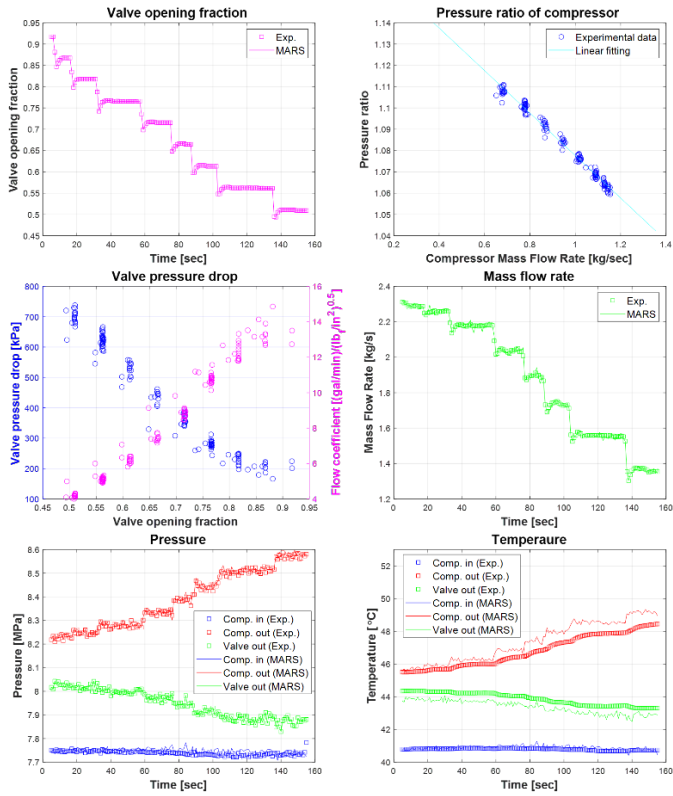


Figure 5: Code validation results.

SIMULATION RESULTS

To conduct system analysis, the total system which consists of reactor core and the designed S-CO₂ power conversion system is modeled with the improved MARS code. Figure 6 shows the nodalization diagram of steady state input deck of the whole system. The primary side is modeled similar to the modeling of a conventional PWR. The reactor core is modeled with hot channel and average channel. The reactor system consists of a reactor core, four main coolant pumps, and a pressurizer. Although the number of designed IHX is twelve, it is modeled in four trains to reduce the complexity of input deck. S-CO₂ power conversion system is modeled with design values of each component including heat exchangers, turbomachinery, and pipe. Turbine, main compressor, and recompressing compressor are connected to single shaft, and the generator component is also connected to shaft component at only steady state simulation. Flow split is modeled by two motor valves keeping the flow split ratio constant at design value. Heat sink side of pre-cooler is modeled boundary volumes which represents the sea water. Table 5 compares the design values with the converged steady state values from the MARS code simulation. The error at every point is less than 1 %, indicating that the entire system is very accurately modeled with the developed code.

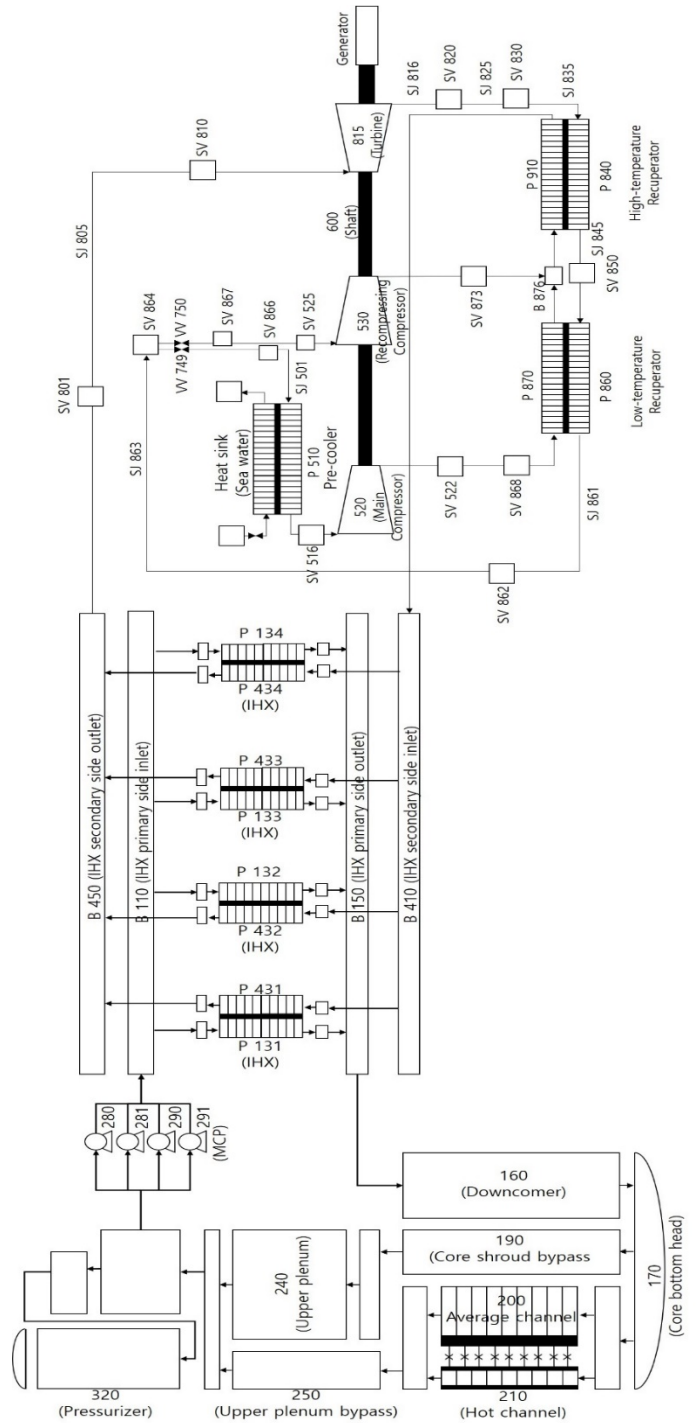
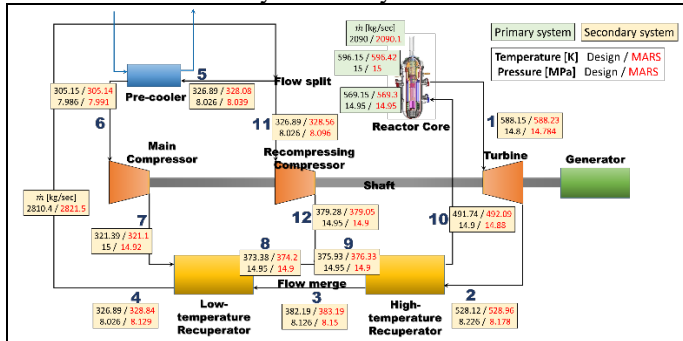


Figure 6: Nodalization diagram of total system modeling with the improved MARS code.

Table 5: Errors of steady state analysis



Primary system	Location	Property	Error [%]
	Hot leg	Temperature	Temperature
Pressure			0.0
Cold leg		Temperature	0.097
		Pressure	0.0
Total	Mass flow rate	0.01	
Secondary system	1	Temperature	0.073
		Pressure	0.04
	2	Temperature	0.3
		Pressure	0.87
	3	Temperature	0.69
		Pressure	0.012
	4	Temperature	0.4
		Pressure	0.17
	5	Temperature	0.4
		Pressure	0.17
	6	Temperature	0.003
		Pressure	0.05
	7	Temperature	0.056
		Pressure	0.4
	8	Temperature	0.05
		Pressure	0.13
	9	Temperature	0.18
		Pressure	0.13
	10	Temperature	0.016
		Pressure	0.0
11	Temperature	0.4	
	Pressure	0.17	
12	Temperature	0.36	
	Pressure	0.13	
Core	Mass flow rate	0.29	
-	Flow split ratio	0.0	

To analyze the transient response of the proposed system, development of control logic should be preceded. Figure 6 shows the control scheme of the proposed power conversion system. There are five parameters to be controlled in the S-CO₂ cycle: low pressure, high pressure, flow split ratio (FSR), main compressor inlet temperature (MCIT), and shaft frequency. the main control mechanism responding to power change is turbine

bypass which is generally known to show the most rapid response to load transients.

Low pressure is controlled to keep the cycle minimum pressure above the critical pressure during part load operation. The pressure controls are accomplished through the limited inventory control. Although the system inventory is not continuously controlled to match varying loads, when the LTR outlet pressure drops below 7.5MPa, the fluid is charged from the low pressure tank and discharged from the high pressure tank when the HTR inlet pressure exceeds the primary side pressure as shown in Figure 7.

In the S-CO₂ recompression cycle, flow split ratio has to be controlled to be operated stably and prevent compressor surge. It is basically maintained as the designed value during system transients by adjusting opening fractions of two motor valves. The reason for keeping the flow split ratio at the design value is to allow two compressors to operate as close to the design point as possible. In addition, compressor surge should be prevented by controlling the flow split ratio. Under all the possible transients, system has to be operated maintaining sufficient compressor surge margin. It is conducted by measuring the mass flow rate at the LTR outlet and the mass flow rate at the PC inlet. The compressor surge limit is determined as 10 % in this study.

The main compressor inlet temperature is controlled to not deviate significantly from the critical temperature. If MCIT falls below the critical temperature, the liquidation of CO₂ may occur, resulting in problems of the system integrity, and if it rises above the critical temperature, the cycle efficiency rapidly decreases. MCIT control is conducted by regulating the mass flow rate of heat sink depending on the deviation from the designed MCIT.

As the load changes, the rotational speed of the shaft is changed by the shaft dynamic. Since the electric propulsion system with single shaft configuration is considered, the rotational speed of shaft should be maintained during load transients. To control the shaft speed, turbine bypass valve is designed to be autonomously operated based on the proportional-integral-differential (PID) controller. Ziegler-Nichols rule is applied for tuning PID parameters [11]. PID gains for turbine bypass valve is optimized under the 10% step reduction from 100% load.

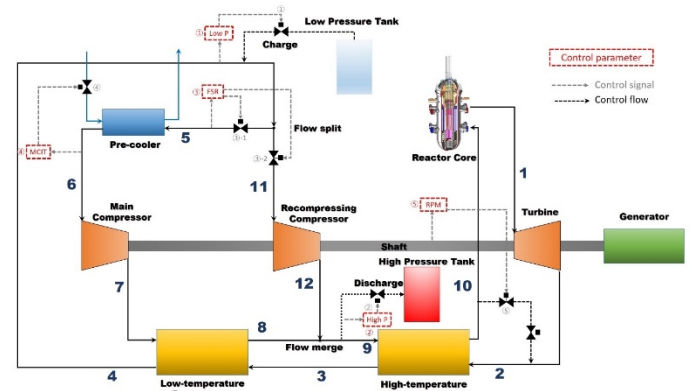


Figure 7: Control scheme of S-CO₂ power conversion system.

To demonstrate feasibility of the proposed system to ship propulsion, transient behavior under fast load changes has been analyzed with the developed system analysis code. In this paper, transient response is investigated under the actual load change requirement for nuclear merchant ships operated in the past as shown in Table 1: NS Savannah, NS Otto Hahn, and NS Mutsu. The applicability to nuclear merchant ships is examined by considering two criteria. First, total system should be stably operated under these fast load transients without significant fluctuations of operational parameters. Second, all the safety related variables should be kept with sufficient margin including fuel centerline temperature (FCT), peak cladding temperature (PCT), the minimum departure from nucleate boiling ratio (MDNBR), shaft speed, and compressor surge margin. The criteria for shaft rotational speed is set to 0.2Hz which is the frequency acceptance limit of typical nuclear power plants. The limit for compressor surge margin is 10 % as mentioned previously in the control scheme development section. In all cases, load transient is given after 100 seconds of 100 % full power operation. The maximum time step is set to 0.005 seconds considering the severe load changes.

Since the three load change requirements are similar, the simulation results showed almost the same trend. Therefore, only the results from the NS Savannah case are shown in this paper. Figures 8 and 9 show the responses of the reactor core and the S-CO₂ power conversion system, respectively, under the NS Savannah requirement. As shown in Figure 8, reactor power follows the load changes using only reactor feedback coefficients without significant fluctuations. Since the reactor system has the strong moderator temperature coefficients, the small change in the primary coolant temperature effectively adjusts core thermal power even under the severe load changes. Although the primary side pressure rapidly increases, it is recovered to the stable operating range within few seconds. In case of safety parameters, even if there is an increase of about 5°C for PCT and about 70°C for FCT, it does not seriously affect the reactor safety since these are in the range of normal operations. MDNBR also does not show significant reduction since reactor power exhibits the fast response, which indicates there are no safety issues in the primary system.

The S-CO₂ power conversion system also shows stable responses under the NS Savannah load change requirement as shown in Figure 9. Since the turbine bypass is the main mechanism responding to the load changes, turbine plays the major role with the load changes while the total compressor work remains nearly constant. Due to the automatic operation of the turbine bypass valve, the turbine torque is rapidly adjusted with the changed load and the rotational speed of the shaft is well controlled within the range of 0.2 Hz. Although there is a deviation of about 1°C from the design point of the MCIT, it is quickly controlled to the design point by regulating the mass flow rate of heat sink sea water. Similar results were found in other two requirements. Therefore, it is confirmed that the proposed system can be stably operated under load change requirement for ship propulsion.

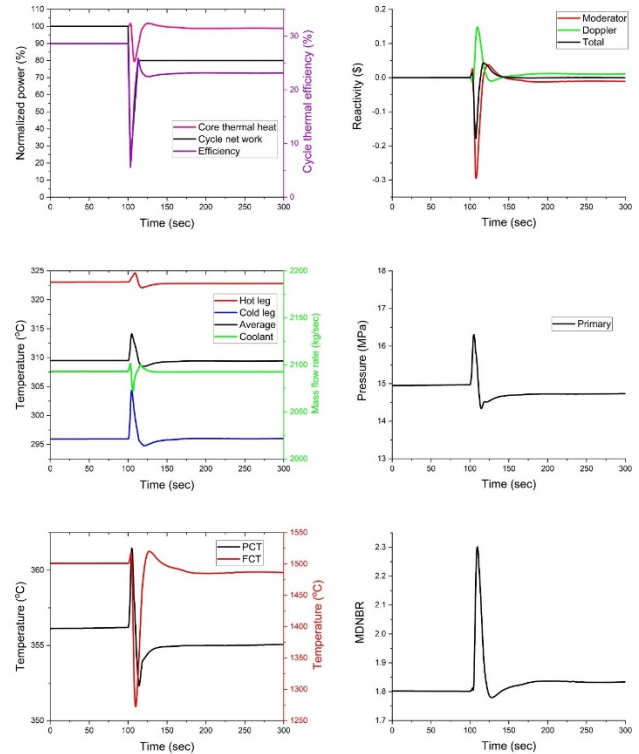


Figure 8: Reactor core response under NS Savannah load change requirement.

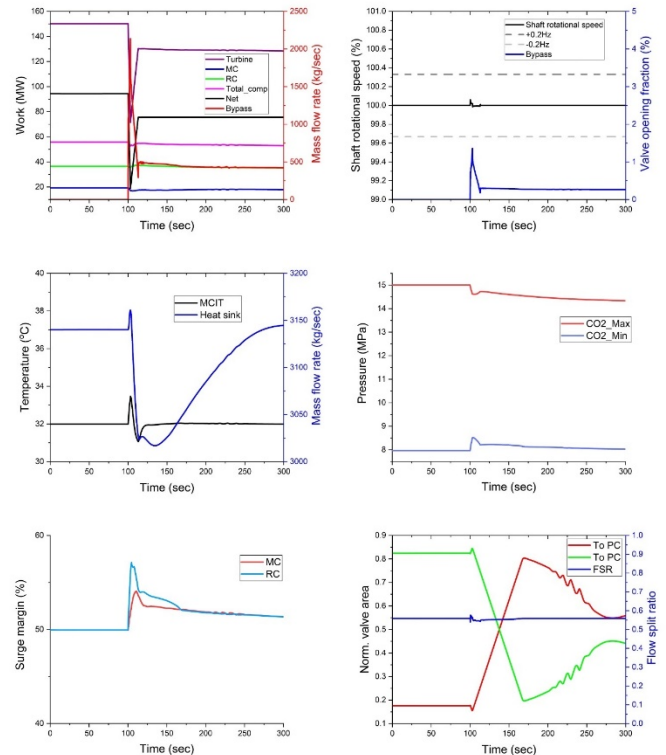


Figure 9: S-CO₂ cycle response under NS Savannah load change requirement.

SUMMARY AND CONCLUSIONS

In this paper, transient responses under severe load changes of the S-CO₂ cycle coupled to PWR were analyzed to investigate its applicability to nuclear propulsion system. Reactor primary system is referred to thermal characteristics of SMART reactor and reactor kinetics of ATOM reactor. The S-CO₂ power conversion system is designed under the primary reactor conditions including cycle design, component design, and pipe design. It is confirmed that the size of power conversion system is significantly reduced compared to conventional shipboard steam power system. MARS-KS code is improved to accurately simulate the S-CO₂ power conversion system combined with PWR. To demonstrate the reliability of the newly developed code, code validation is performed with experimental data of SCIEL facility. The control logic of the S-CO₂ power conversion system is developed based on the turbine bypass control considering the severe load changes. To investigate applicability of total system to nuclear propulsion system, transient simulations have been performed under actual load change requirements of the nuclear merchant ships. The proposed system exhibits stable response under the load change requirements without significant fluctuations of operational parameters and reduction in safety margins. This proves the potential of the proposed system. In the near future, more transients will be analyzed to further prove the applicability of the proposed system.

NOMENCLATURE

\dot{m} mass flow rate
 ΔP pressure drop

ACKNOWLEDGEMENTS

This research was supported by Basic Science Research Program through the National Research Foundation of Korea (NRF) funded by the Ministry of Science, ICT & Future Planning (NRF-2016R1A5A1013919).

REFERENCES

- [1] V. Dostal, P. Hejzlar, and M. J. Driscoll, "High-performance supercritical carbon dioxide cycle for next-generation nuclear reactors," *Nucl. Technol.*, vol. 154, no. 3, pp. 265–282, 2006.
- [2] IAEA, "System-Integrated Modular Advanced Reactor (SMART)," 2011.
- [3] A. A. E. Abdelhameed, X. H. Nguyen, J. Lee, and Y. Kim, "Feasibility of passive autonomous frequency control operation in a Soluble-Boron-Free small PWR," *Ann. Nucl. Energy*, vol. 116, pp. 319–333, 2018.
- [4] S. Son, J. Y. Heo, and J. I. Lee, "Evaluation of the Optimal Point Variation of the S-CO₂ Cycle While Considering Internal Pinch in Recuperator," in *Proceedings of the ASME Turbo Expo (Vol. 9). American Society of Mechanical Engineers (ASME)*, 2018.
- [5] D. D. Fleming *et al.*, "Scaling Considerations for a Multi-Megawatt Class Supercritical CO₂ Brayton Cycle and Commercialization," *Sandia Rep.*, vol. SAND2013-9, no. November, 2013.
- [6] M. A. Pope, "Thermal hydraulic design of a 2400 MW_{th} direct supercritical CO₂-cooled fast reactor," *Massachusetts Inst. Technol.*, 2006.
- [7] S. K. Cho, J. Lee, J. I. Lee, and J. E. Cha, "S-CO₂ Turbine Design for Decay Heat Removal System of Sodium Cooled Fast Reactor," in *Proceedings of the ASME Turbo Expo 2016: Turbomachinery Technical Conference and Exposition. Volume 9: Oil and Gas Applications*, 2016.
- [8] S. Baik, S. G. Kim, J. Lee, and J. I. Lee, "Study on CO₂ – water printed circuit heat exchanger performance operating under various CO₂ phases for S-CO₂ power cycle application," *Appl. Therm. Eng.*, vol. 113, pp. 1536–1546, 2017.
- [9] S. G. Kim, Y. Lee, Y. Ahn, and J. I. Lee, "CFD aided approach to design printed circuit heat exchangers for supercritical CO₂ Brayton cycle application," *Ann. Nucl. Energy*, vol. 92, pp. 175–185, 2016.
- [10] "MARS CODE MANUAL VOLUME I: Code Structure, System Models, and Solution Methods," vol. I, no. December, 2009.
- [11] J. G. Ziegler and N. B. Nichols, "Optimum settings for automatic controllers," *trans. ASME*, vol. 64, no. 11, 1942.

NUMERICAL DIMENSIONING OF A PRE-COOLER FOR sCO₂ POWER CYCLES TO UTILIZE INDUSTRIAL WASTE HEAT

Sebastian Unger*

HZDR, Institute of Fluid Dynamics
Dresden, Germany
Email: s.unger@hzdr.de

Jonas Müller

HZDR, Institute of Fluid Dynamics
Dresden, Germany

Malini Bangalore Mohankumar

HZDR, Institute of Fluid Dynamics
Dresden, Germany

Sebastian Rath

Technical University Dresden,
Institute of Power Engineering,
Dresden, Germany

Uwe Hampel

HZDR, Institute of Fluid Dynamics
Dresden, Germany

ABSTRACT

The annual waste heat available from industry in the European Union is more than 2,700 PJ. Consequently, the utilization of the unexploited thermal energy will decisively contribute to a reduced overall power consumption and lower greenhouse gas emissions. Supercritical carbon dioxide (sCO₂) power cycles offer a variety of advantages for that purpose compared to established power cycles. Such are a high conversion efficiency and a turbomachinery with high power density. The pre-cooler is one of the essential components in an sCO₂ power cycle and the prediction of the flow and heat transfer characteristics is a challenging task. In the present investigation, cycle layouts were developed for one waste heat source: a gas compressor station. The pre-cooler design as well as the boundary conditions of the numerical simulation were assessed by an analytical model. The most promising design was the printed circuit heat exchanger with inlet temperatures between 209 °C and 352 °C. Subsequently, these heat exchangers were examined in more detail by the numerical code ANSYS CFX for sCO₂ mass fluxes between 100 kg/(m² s) and 900 kg/(m² s). The pressure drop along the sCO₂ channel was found insensitive to the channel diameter, but increased with the channel length and mass flux. However, the pressure drop of the coolant stream significantly depends on the channel diameter and thus a larger coolant channel diameter is recommended to maintain a reasonably low pressure drop. The overall heat transfer coefficient is limited by the heat transfer on the coolant side. Ultimately, pre-cooler designs were proposed for a waste heat system of a gas compressor station, consisting of compact modular stainless steel plates with an sCO₂ channel diameter of 0.5 mm, a coolant channel diameter of 0.8 mm, an sCO₂ mass flux of 700 kg/(m² s) and a coolant mass flux of 1029 kg/(m² s). Based on these results more complex channels designs, including internal fins were

studied. The fin height was optimized, in order to improve the heat transfer performance.

INTRODUCTION

An enhanced energy utilization is an upcoming requirement in many industrial processes, in order to reduce energy consumption while maintaining economic prosperity [1]. One of the highest energy demands occur in the industrial sector. A considerable amount of the energy consumption is rejected and lost to the environment by waste heat. Thus, the recovery of the waste heat is essential to improve the overall energy utilization, to enhance the efficiency and to reduce the carbon foot print of industrial applications. Therefore, existing technologies for waste heat recovery aim to reconvert the waste heat into mechanical - and furthermore into electrical power. The supercritical CO₂ power cycle represents an attractive alternative to the established power cycles. An essential component in an sCO₂ power cycle is the pre-cooler, which cools the CO₂ close to the critical point in order to achieve optimal compressor inlet conditions required to minimize the compression work. The design of the pre-cooler may be a challenging task due to the complex heat transfer behavior [2].

Thus, Liao and Zhao [3] experimentally investigated the heat transfer of carbon dioxide under cooling conditions in horizontal tubes of 0.5 mm to 2.16 mm diameter. The influences of mass flux, inlet temperature, and pressure were investigated. The results showed a significant influence of buoyancy on the HTC up to Reynolds number of 105. The influence became weaker with decreasing tube diameter and increasing Reynolds number. Dang and Hihara [4] investigated the heat transfer and pressure drop of CO₂ in horizontal tubes with diameter between 1 mm and 6 mm. In the study, the heat transfer coefficient increases with mass flux and reducing tube diameter. Ngo et al.

* corresponding author(s)

[5] performed experiments with zigzag and s-shaped fins on micro-channel heat exchangers. The s-shaped fins showed slightly smaller heat transfer, but significantly less pressured drop compared to the zigzag channel. Li et al. [6] performed experimental investigations on the heat transfer of CO₂ in printed circuit heat exchangers for heating and cooling conditions. The heat transfer coefficient reaches a maximum when the temperature approaches the pseudo-critical point (the pseudo-critical point is defined as the temperature, for a given pressure, at which the specific heat exhibits a maximum). The numerical work of Pitla et al. [7] studied the turbulent heat transfer of sCO₂ under cooling conditions. A validation of the numerical model by experimental data was done. Van Abel et al. [8] applied numerical methods to investigate a PCHE with zigzag channels regarding heat transfer and pressure drop. The zigzag channels achieved great heat transfer compared to the straight channel. Serrano et al. [9] developed mathematical models based on empirical correlations for the heat transfer of printed circuit heat exchangers. Based on these model optimized sizing and performance of heat exchangers for fusion power plants were proposed. Xu et al. [10] studied airfoil-shaped fins in a printed circuit heat exchanger. It was found, that the staggered fin arrangement is more suitable than a parallel fin arrangement. Baik et al. [11] investigated the performance of wavy-channel printed circuit heat exchangers and found a significant enhancement compared to the straight channels. Furthermore, an increase of wave amplitude or decrease of wave period improves the heat exchanger performance. In the numerical model of Wang et al. [12] the turbulent heat transfer of cooled sCO₂ in horizontal tubes was studied. A wide range of different operation condition was analyzed a heat transfer correlations proposed. The heat transfer increases with mass flux, tube diameter and close to the pseudo-critical point. From the literature survey it can be seen, that several studies analyze the heat transfer behavior of sCO₂ under cooling conditions by experimental and numerical methods. Some authors investigate novel channel geometries and flow paths such as airfoil-shape and zigzag channels. The present study aims to propose a pre-cooler for a sCO₂ power cycle, which recovers industrial waste heat. Based on the boundary conditions, determined by the power cycle, the channel diameters for both fluid will be numerical optimized. For the optimum design an internal fin geometry will introduced and studied.

ANALYSIS OF INDUSTRIAL WAST HEAT SOURCES

Industrial waste heat is heat, which arises in industrial processes as an undesired byproduct due to inefficiencies and thermodynamic limitations in the equipment and processes. This chapter aims to give an overview on the recovery of industrial waste heat in the European Union. In the present study the sources will analyzed based on heat quantity and heat quality. In the end of the chapter, two possible industrial waste heat sources will be selected for the subsequent investigation.

The project “Heat Roadmap Europe” aims to analyses the heating and cooling sector in Europe in order to identify potentials for sustainable heating and decarbonization [13]. In the

study of Connolly et al. [14] this values for the industrial waste heat amounts for 27 individual countries in the European Union were presented. In another study, Persson et al. used the European Pollutant Release and Transfer Register in combination with sector-specific standard efficiencies to determine the waste heat potential [15]. Based on both studies, Figure 1 compares the distribution of the potential waste heat amount of the individual countries.

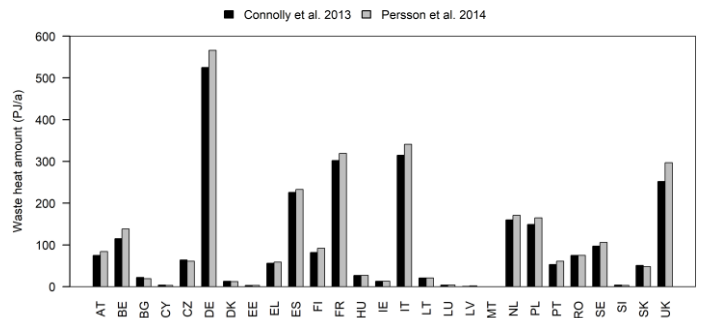


Figure 1: Industrial waste heat amount of individual countries in the European Union according to [14] and [15].

Brückner [16] estimated the lower limitation of waste heat from exhaust gas for Germany from the emission law database. A lower reference temperature of 35 °C was assumed as standardized value to evaluate the waste heat potential. The cumulative industrial waste heat amount of Germany is shown in Figure 2 for different temperature T_{src} , Carnot efficiency η_C and amounts of waste heat \dot{Q}_{wh} . The most relevant industry sectors for utilizing waste heat are the cement industry, ceramic industry, iron and steel industry, aluminum and copper industry, glass industry, chemical industry, gas transmission and storage, paper and pulp industry as well as the food industry.

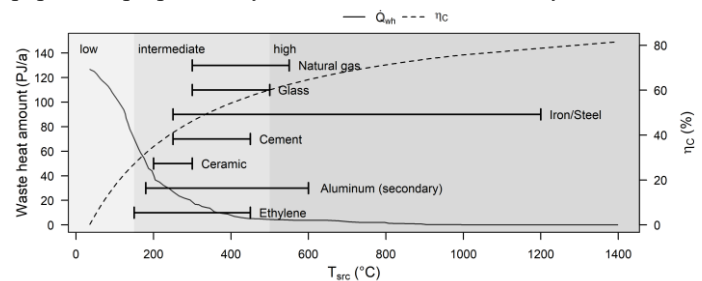


Figure 2: Cumulative industrial waste heat amount \dot{Q}_{wh} of Germany with respect to temperature T_{src} and Carnot efficiency η_C [16].

It is evident that the extraction and transport of natural gas has a considerable waste heat potential. For the present study, a specific industry is selected as an example for waste heat recovery. In this context, the exemplary waste heat utilization of a gas compressor station was selected as a reference for this study. In this case, the main component delivering the mechanical energy for the compression is usually a gas turbine fueled by the natural gas branched from the pipelines with an air-fuel equivalence of $\lambda=5$. The waste heat of this turbine remains

unused in many cases and were therefore considered as a heat source for the present investigation. The parameters were oriented at the MAN 1304-12N [17]. Both the turbine and the Parameters are shown in Figure 3. A steady-state operation of the waste heat source was assumed for the subsequent calculations.

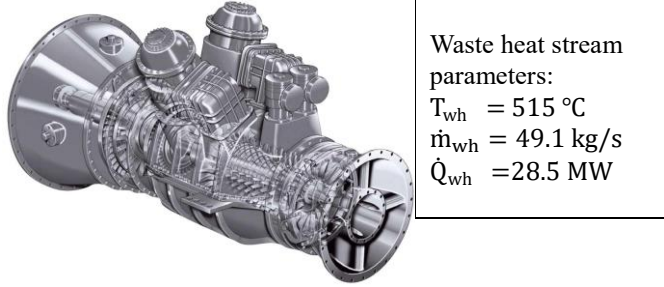


Figure 3: Selected waste heat source - MAN 1304-12 gas turbine and the corresponding waste heat stream parameters [17].

POWER CYCLE AND PRE-COOLER SELECTION

There are several sCO₂ power cycle layouts to convert thermal power into mechanical power. A mathematical model of the power cycle was developed in MATLAB and two scenarios were analyzed. As depicted in Figure 4 these are a simple layout including compressor, primary heat exchanger, turbine and pre-cooler, as well as the same layout including a recuperator.

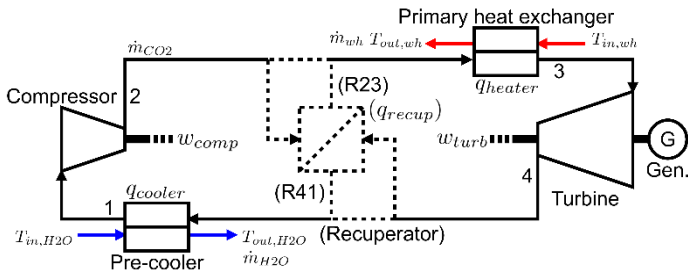


Figure 4: sCO₂ power cycle for waste heat recovery.

Both designs were calculated for a minimum pressure of 75 bar, a minimum temperature of 35 °C, a terminal temperature difference of 5 K and the efficiencies shown in Table 1.

Table 1: Efficiencies of the components in the power cycle.

Component	Turbine	Compressor	Recuperator
Efficiency	90 %	85 %	90 %

As one can see from Figure 5 the net power output of the recuperated cycle is only 5% higher compared to the power cycle without recuperator. Since the heat exchanger inlet temperature is higher in case of a recuperated cycle, the heat flow of the waste heat stream can only be utilized to this lower temperature. As a consequence, waste heat stream temperature leaves the primary heat exchanger at higher temperature and a considerable amount of thermal energy will not be used. In future studies the utilization of the remaining heat will be investigated. Based on this result, a pre-cooler was selected operating at an inlet pressure of 7.5 MPa, a mass flow rate of 85.6 kg/s and temperature up to 352 °C.

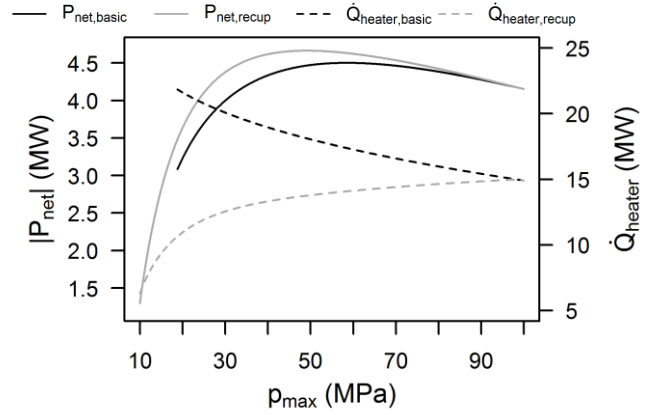


Figure 5: Net power and heat duties of the sCO₂ power cycle.

NUMERICAL MODEL

The commercial fluid dynamic code ANSYS CFX was applied to simulate the pre-cooler. The geometry consists of a sCO₂ channel, a coolant channel and a heat exchanger body. Both channels are divided into an entrance section, a heat exchanger section and an exit section as one can see in Figure 6. The inlet temperature and pressure of the coolant channel was 35 °C and 1 bar. The entrance sections were considered to achieve a fully developed flow in the heat transfer area, in order to have comparable flow conditions. However, in a real application the fluid flows into the individual channels from a header (distributor) and may not be fully developed. The top and bottom part of the solid body uses periodic boundaries, the side of the domains were defined as symmetry and between the channels and the solid body, heat transfer conjugation was used. The solid material was assumed to be 316 L with an thermal conductivity of 16.2 W/mK.

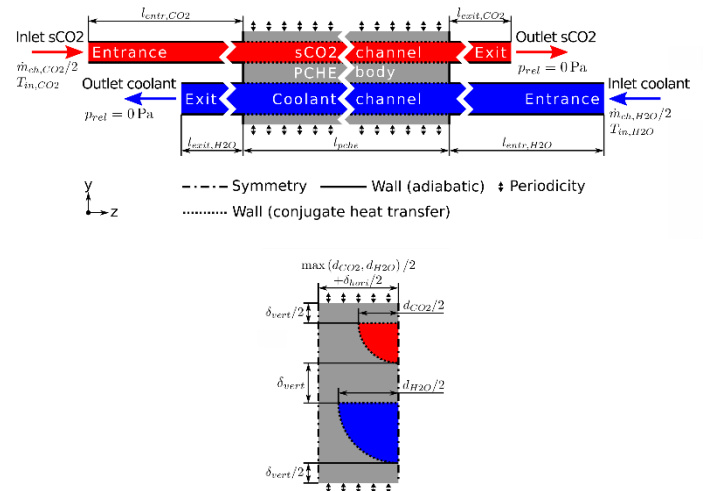


Figure 6: Domains, boundary conditions and geometry of the pre-cooler model.

In this investigation the fluid properties of sCO₂ is taken from the CoolProp library. The used conservation equations for mass, momentum and energy, also known as Navier-Stokes equations are

$$\frac{\rho \delta u_i}{\delta x_i} = 0 \quad (1)$$

$$\rho \left(u_j \frac{\delta u_i}{\delta x_j} \right) = - \frac{\delta p}{\delta x_i} + \frac{\delta}{\delta x_j} \left((\mu + \mu_T) \left(\frac{\delta u_i}{\delta x_j} + \frac{\delta u_j}{\delta x_i} \right) \right) \quad (2)$$

$$\rho c_p \left(u_j \frac{\delta T}{\delta x_j} \right) = \frac{\delta}{\delta x_j} \left(\left(\lambda + \frac{\mu_T c_p}{Pr_T} \right) \frac{\delta T}{\delta x_j} \right) \quad (3)$$

These partial differential equations are discretized and the velocity vector field and scalar temperature field were solved numerically. The turbulent Prandtl number has been set to $Pr_T=0.9$ as suggested by Yuan [18] and the turbulent viscosity μ_T was calculated by

$$\mu_T = \rho \frac{k}{\omega} \quad (4)$$

The Reynolds number of the coolant channel is approximately at 450 and thus the flow was modeled as laminar. Since the Reynolds number varies between 7,000 and 14,000 for the sCO₂ channel in the present study, the Shear Stress Transport (SST) model was applied for the transient and turbulent region, to calculate the turbulence kinetic energy and the turbulence frequency. Furthermore, the experimental results of Kruijenga et al. [19] as well as the pressure drop correlation of Blasius and Colebrook were used to validate the numerical model for two different operating conditions, which is a mass flux of 326 kg/(m²s) and 762 kg/(m²s) for a channel diameter of 1.9 mm. This comparison is shown in Figure 7 for the heat transfer and in Figure 8 for the pressure drop. The heat transfer can be predicted with sufficient accuracy and the pressure drop is very well represented.

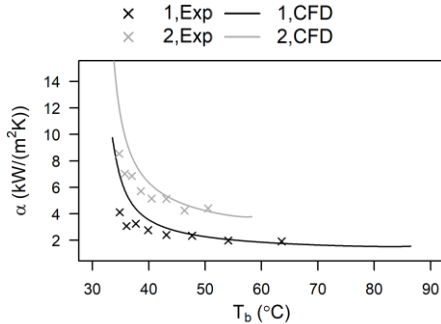


Figure 7: Validation of the heat transfer of the CFD model by experiments from literature.

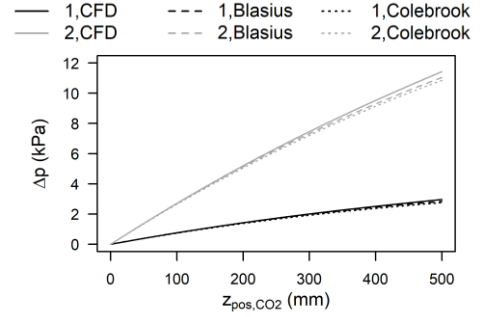


Figure 8: Validation of the pressure drop of the CFD model by empirical correlations from literature.

In order to validate the independency of the numerical results from the applied mesh, eight different meshes of different grid density were studied. A hexaeder dominant grid was applied, using inflation layer on the boundary between fluid and solid and the element size was controlled along the flow channels and at the cross section. In the Figure 9 the heat transfer coefficient and in the Figure 10 the pressure drop are shown along both channels from the finest mesh 1 to the coarsest mesh 8. The mesh 2 having 2.5 million nodes was used for further analysis, since there is no improvement to the mesh 1. Additionally, the boundary layer can be well resolved for a dimensionless wall distance of $y^+ < 1$.

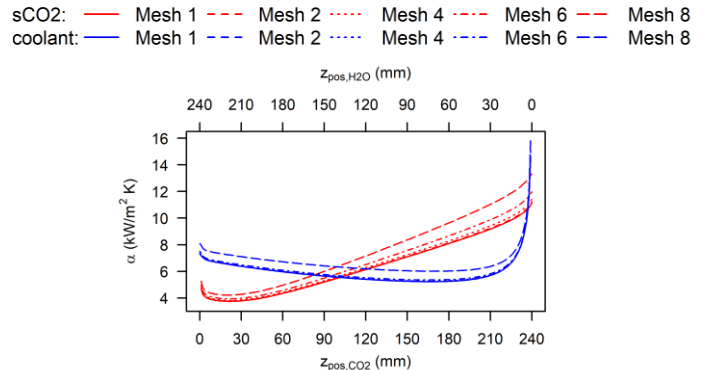


Figure 9: Heat transfer results of the mesh independency study.

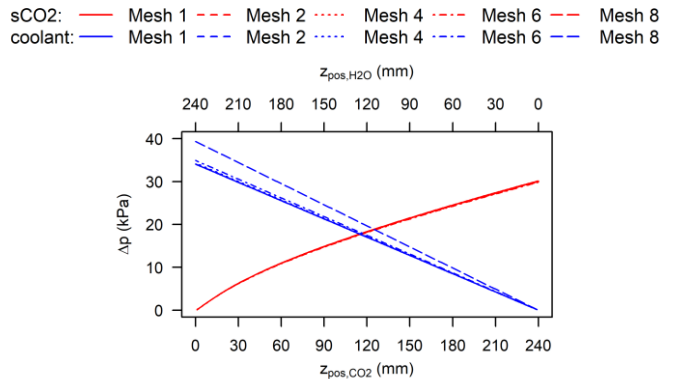


Figure 10: Pressure drop results of the mesh independency study.

The numerical simulation was used to study the effect of channel diameter for both fluids between 0.5 mm and 1.1 mm. For assessment of the pre-cooler, the volumetric heat flux and the pressure drop were used. Here, the volumetric heat flux represents the heat flow per volume of the heat exchanger.

RESULTS OF THE SIMULATION

In the Figure 11 the numerical results are visualized for different axial positions along the sCO₂ channel for a 0.5 mm sCO₂ channel, a 0.8 mm coolant channel and a sCO₂ mass flux density of 700 kg/(m²s). It can be seen, that at the 40 mm position the temperature and velocity distribution are still inhomogeneous, from 80 mm on both distributions become more homogeneous and nearly equalize.

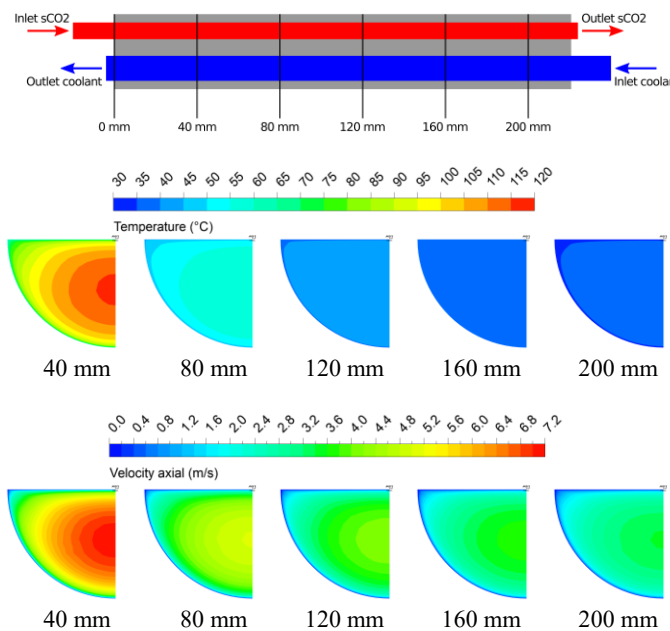


Figure 11: Temperature and velocity distribution of the sCO₂ channel at different axial positions.

The numerical results were compared with empirical results calculated from the Jackson correlation [20] for the heat transfer and the Colebrook correlation for pressure drop. The diameter of the coolant channel was changed from 0.5 mm to 0.8 mm and 1.1 mm, and the diameter of the sCO₂ channel was changed between 0.5 mm and 0.8 mm. The heat transfer results of different combinations of the channel dimensions are shown in Figure 12 and Figure 13 for different mass flux. In this and the following plots, the combination of sCO₂ channel to coolant channel diameter are expressed as sCO₂-coolant, e.g. 5-11 represents a 0.5 mm sCO₂ channel and a 1.1 mm coolant channel diameter. As expected the heat transfer increases with the mass flux, due to higher convection. Furthermore, the smallest channel diameter achieve the greatest heat transfer performance. In case of the 8-5 configuration there is a sharp increase in the analytical, correlation based, calculation. This is due to the change in flow regime from laminar to turbulent within the calculation scheme.

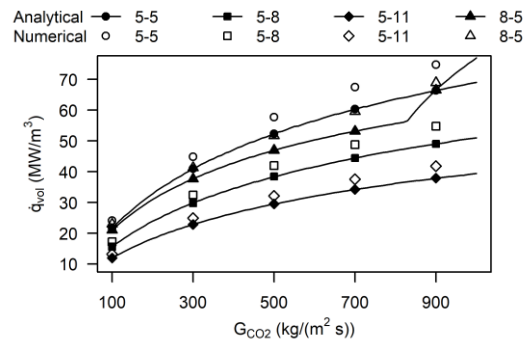


Figure 12: Numerical and analytical heat flux density results for different channel diameter.

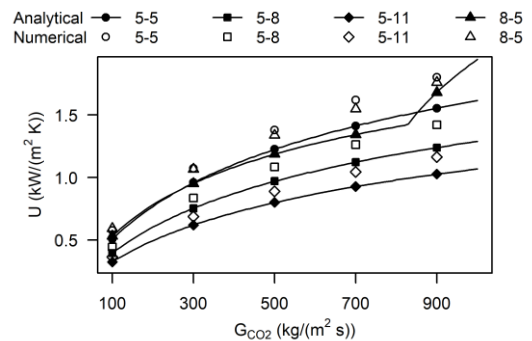


Figure 13: Numerical and analytical overall heat transfer coefficient results for different channel diameter.

The pressure drop characteristics of both channels is shown in Figure 14 for the CO₂ side and in Figure 15 for the coolant side for varying mass fluxes. Similar to the heat transfer increases the pressure drop for both channels as the mass flux rises. The pressure drop of the sCO₂ channel changes only little with geometry. In fact, only the 8-5 configuration increases the pressure loss, due to a decrease of heat transfer surface area and consequently longer channel length. The pressure drop in the coolant channel increases as the channel diameter reduces. In fact, the highest pressure drop occur for the 0.5 mm channel diameter. One reason may be the reduced friction surface area at lower channel diameter. The pressure drop of the 8-5 configuration is very high, since the required mass flux to transfer the heat is higher.



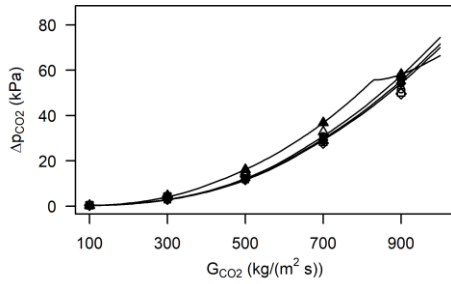


Figure 14: Numerical and analytical pressure drop results of the CO₂ for different channel diameter.

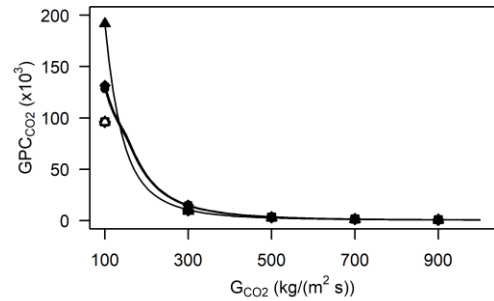


Figure 16: Global performance criterion results of the CO₂ for different channel diameter.

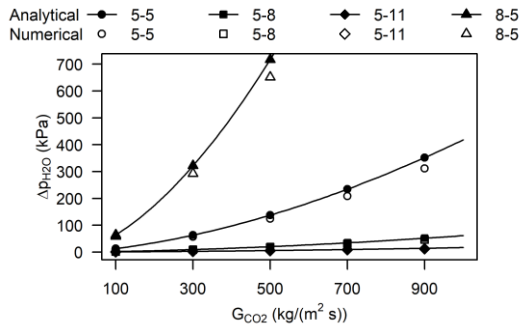


Figure 15: Numerical and analytical pressure drop results of the coolant for different channel diameter.

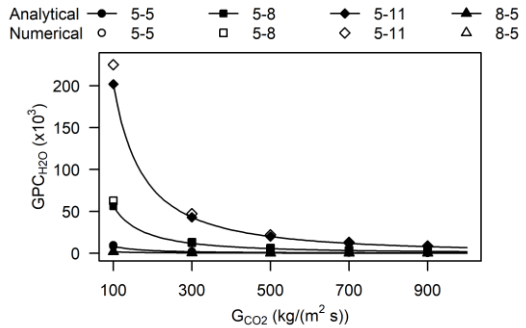


Figure 17: Global performance criterion results of the coolant for different channel diameter.

As one can see, the heat transfer as well as the pressure drop both increase as the channel diameter reduce. In order to determine a beneficial configuration, the global performance of the pre-cooler for the sCO₂ flow path will be calculated. The global performance criterion represents the ratio of heat flow to the required pumping power due to pressure drop and is shown in Figure 16 for the CO₂ side and in Figure 17 for the coolant side. The global performance reduces as the mass flux density increases, due to the strong increase in pressure drop. As the mass flux exceeds 300 kg/(m²s) the global performance criterion is almost independent of the channel diameter for the sCO₂ channel. However, the global performance related to the coolant channel is strongly influenced by the channel diameter. It can be seen, that a higher diameter results in a superior performance. Hence, a high coolant channel diameter and a small sCO₂ channel diameter was chosen and used for further analysis. In fact, the configuration 5-8 achieves the greatest performance at a mass flux of approximately 700 kg/(m²s). At this parameters a compactness of 627 m²/m³ can be achieved. In general analytical and numerical results show same trends and good agreement for the heat transfer and nearly identical values for pressure drop.



Based on this optimization an internal fin structure of the channels was investigated. Here different internal fin heights were modeled and numerical simulated by the CFD code. The fin height was varied between 0.04 mm and 0.12 mm and the heat transfer and pressure drop was calculated as before. The fin design and the temperature distribution of both channels is shown in Figure 18 for the different fins.

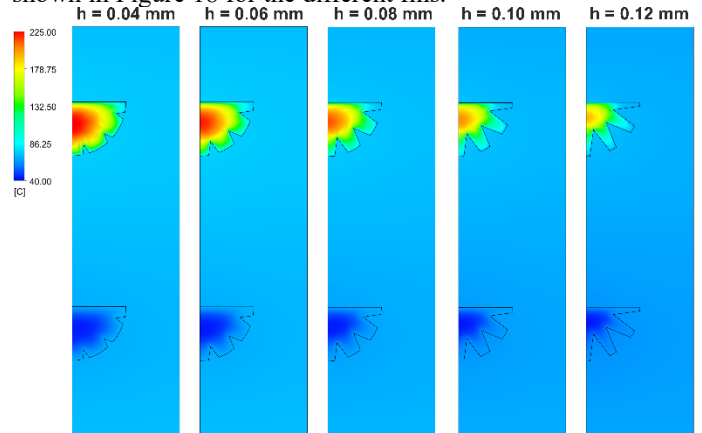


Figure 18: Temperature distribution of both channels for different fin heights.

In Figure 19 the volumetric heat flux and in Figure 20 the pressure drop are shown as a function of the mass flux density for different internal fin heights. As one can see, the heat transfer increases as the fin height increases, since the turbulence increases and the heat conduction of the fins allow higher

temperatures in the bulk flow of the sCO₂ channel. Nevertheless, the pressure drop along the flow channel rises as the fin height increases. Reason for that is the additional friction surface due to the fins. Similar to the channel diameter a tradeoff between heat transfer and pressure drop needs to be found.

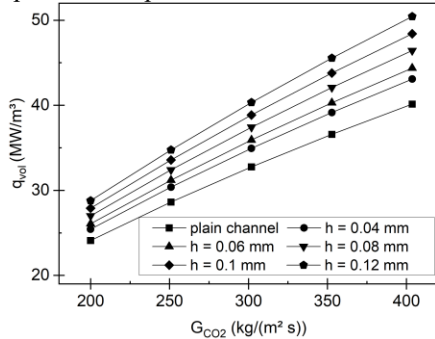


Figure 19: Numerical results of heat transfer and pressure drop for different internal fins in the channel.

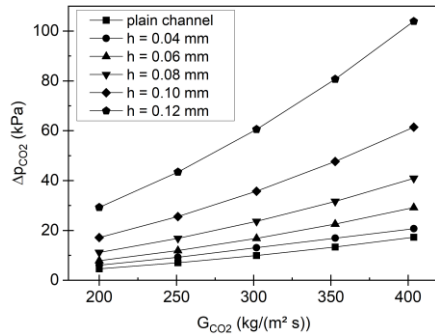


Figure 20: Numerical results of heat transfer and pressure drop for different internal fins in the channel.

In order to determine the optimum fin configuration the ratio of heat transfer to pressure drop will be evaluated by the global performance criterion. In Figure 21 the global performance is shown for different mass fluxes and fin heights. It can be seen, that the fin height of 0.4 mm achieves the greatest global performance followed by the 0.6 mm fins. For fin heights greater than 0.6 mm the higher pressure drop is dominating over the heat transfer enhancement. Hence, the global performance is lower compared to the plain channel. Therefore, a finned channel applying 0.4 mm is recommended for the pre-cooler.

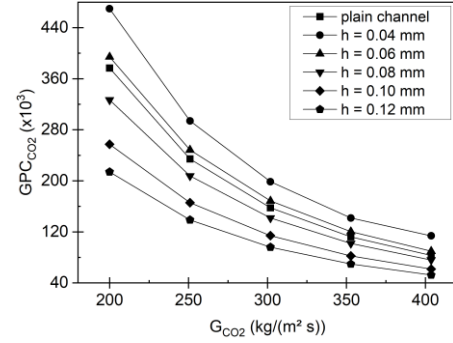


Figure 21: Global performance criterion calculated from the numerical results for different internal fins in the channel.

CONCLUSION

In the present investigation, the design of a pre-cooler for a waste heat driven sCO₂ power cycle was analyzed. Thus, the potential of waste heat recovery were studied and categorized depending on the quantity and the quality of available heat sources. As a reference case, the exhaust gas stream of a turbine of a gas compressor station was used. For this waste heat source, a simple power cycle layout was calculated and the boundary conditions, such as temperature, pressure and mass flow rate, of the liquid cooler were determined. On this base the pre-cooler was calculated analytical by applying heat transfer and pressure drop correlations, and numerical by using the commercial fluid dynamic code ANSYS CFX. Different channel diameters were investigated to determine the optimum heat exchanger design. It was found, that the heat transfer and pressure drop increases for smaller channel diameter, for constant inlet velocity, temperature and pressure. However, the influence of the sCO₂ channel diameter on the pressure drop was small. The global performance criterion was used to determine the optimum design for both channel diameter considering both heat transfer and pressure drop. For the optimum configuration of 0.5 mm sCO₂ channel diameter and 0.8 mm coolant channel diameter an internal fin structure was introduced and the fin height was analyzed. The heat transfer and the pressure drop increase with fin height. In order to determine the best tradeoff between heat transfer and pressure drop, the global performance was used. Thus, the greatest performance was found for a fin height of 0.4 mm, which can be recommended for the design of a pre-cooler.

NOMENCLATURE

G_{CO_2}	mass flux of the CO ₂ channel, kg/(m ² s)
G_{H_2O}	mass flux of the CO ₂ channel, kg/(m ² s)
GPC_{CO_2}	global performance criteria of the CO ₂ channel, -
GPC_{H_2O}	global performance criteria of the coolant channel, -
h	internal fin height, m
\dot{m}_{CO_2}	mass flow rate of the CO ₂ stream, kg/s
\dot{m}_{H_2O}	mass flow rate of the coolant stream, kg/s
\dot{m}_{wh}	mass flow rate of the waste heat stream, kg/s
p	pressure, Pa

P_{net}	net power output, W
Δp	pressure difference, Pa
\dot{Q}_{Heater}	heat flow rate to the primary heat exchanger, W
\dot{Q}_{wh}	heat flow rate of the waste heat stream, W
\dot{q}_{vol}	volumetric heat flux density, W/m ³
T_b	temperature of the bulk fluid, °C
T_{wh}	temperature of the waste heat stream, °C
U	overall heat transfer coefficient, W/m ² K
Z_{pos}	longitudinal positions along the channel, m
α	heat transfer coefficient, W/mK

ACKNOWLEDGEMENTS

This work is part of the research project CARBOSOLA funded by the German Federal Ministry of Economic Affairs and Energy (BMWi) under the grant number 03EE5001D. Responsibility if the content of this publication lies with the authors.

REFERENCES

- [1] Federal Ministry for Environment, Nature Conservation and Nuclear Safety, (2016). Klimaschutzplan 2050, pp. 1-96.
- [2] Brun K., Friedman P., Dennis R. (2017). Fundamentals and Applications of Supercritical Carbon Dioxide (sCO₂) Based Power Cycles. ISBN: 978-0081008041.
- [3] Liao S. M., Zhao T. S. (2002). Measurements of Heat Transfer Coefficients from Supercritical Carbon Dioxide Flowing in Horizontal Mini/Micro Channels. *Journal of Heat Transfer* 124, pp. 413-420.
- [4] Dang C., Hihara E. (2004). In-tube cooling heat transfer of supercritical carbon dioxide. Part 1. Experimental measurement. *International Journal of Refrigeration* 27, pp. 736-747.
- [5] Ngo T. L., Kato Y., Nikitin K., Ishizuka T. (2007). Heat transfer and pressure drop correlations of microchannel heat exchangers with S-shaped and zigzag. *Experimental Thermal and Fluid Science* 32, pp. 560-570.
- [6] Li H., Krüizenga A., Anderson M., Corradini M., Luo Y., Wang H., Li H. (2011). Development of a new forced convection heat transfer correlation for CO₂ in both heating and cooling modes at supercritical pressures. *International Journal of Thermal Sciences* 50, pp. 2430-2442.
- [7] Pitla P. P., Groll E. A., Ramadhyani S. (2002). New correlation to predict the heat transfer coefficient during in-tube cooling of turbulent supercritical CO₂. *International Journal of Refrigeration* 25, pp. 887-895.
- [8] Van Abel E. N., Anderson M. H., Corradini M. L. (2011). Numerical investigation of pressure drop and local heat transfer of supercritical CO₂ in printed circuit heat exchangers. *Supercritical CO₂ Power Cycle Symposium*. Boulder, USA.
- [9] Serrano I. P., Cantizano A., Linares J. I., Moratilla B. Y. (2014). Modeling and sizing of the heat exchangers of a new supercritical CO₂ Brayton power cycle for energy conversion for fusion reactors. *Fusion Engineering and Design* 89, pp. 1905-1908.
- [10] Xu X., Ma T., Li L., Zeng M., Chen Y., Huang Y., Wang Q. (2014). Optimization of fin arrangement and channel configuration in an airfoil fin PCHE for supercritical CO₂ cycle. *Applied Thermal Engineering* 70, pp. 867-875.
- [11] Baik J.-Y., Jeon S., Kim B., Jeon D., Byon C. (2017). Heat transfer performance of wavy-channeled PCHEs and the effects of waviness factors. *International Journal of Heat and Mass Transfer* 114, pp. 809-815.
- [12] Wang J., Guan Z., Gurgenci H., Veeraragavan A., Kang X., Hooman K. (2019). A computationally derived heat transfer correlation for in-tube cooling turbulent supercritical CO₂. *International Journal of Thermal Sciences* 138, pp. 190-205.
- [13] Heat Roadmap Europe. URL: <https://heatroadmap.eu/>.
- [14] Connolly D. (2013). Heat Roadmap Europe 2050. Second pre-study for the EU27. Tech. rep.. Aalborg University, Halmstad University, Ecofys Germany GmbH, PlanEnergi.
- [15] Persson U., Möller B., Werner S. (2014). Heat Roadmap Europe: Identifying strategic heat synergy regions. *Energy Policy* 74, pp. 663-681.
- [16] Brückner S. (2016), Industrielle Abwärme in Deutschland - Bestimmung von gesichertem Aufkommen und technischer bzw. wirtschaftlicher Nutzbarkeit. PhD Thesis, TU Munich.
- [17] MAN Diesel & Turbo. THM Gas Turbines. URL: https://turbomachinery.mandieselturbo.com/docs/librariesprovider4/Turbomachinery_doc/thm-gas-turbines.pdf?sfvrsn=14.
- [18] Yuan, Z. (2000). Numerical study of periodically turbulent flow and heat transfer in a channel with transverse fin arrays. *International Journal of Numerical Methods for Heat and Fluid Flow* 10, pp. 842-861.
- [19] Krüizenga A., Anderson M., Fatima R., Corradini M., Towne A., Ranjan D. (2011). Heat Transfer of Supercritical Carbon Dioxide in Printed Circuit Heat Exchanger Geometries. *Journal of Thermal Science and Engineering Applications* 3.
- [20] Jackson J.D. (2002). Consideration of the heat transfer properties of supercritical pressure water in connection with the cooling of advanced nuclear reactors. The 13th Pacific basin nuclear conference. Shenzhen, China.

Design and off-design analysis of a highly loaded centrifugal compressor for sCO₂ applications operating in near-critical conditions

Alessandro Romei, Paolo Gaetani, Giacomo Persico

Laboratory of Fluid Machines
Energy Department, Politecnico di Milano
Via Lambruschini 4, Milano 20156

ABSTRACT

The closed gas cycle based on supercritical carbon dioxide (sCO₂) is a promising solution to realize highly efficient power systems arranged in compact devices. However, the technical feasibility of these so-called sCO₂ power systems relies on the development of non-conventional components, whose features are dictated by the peculiar character of the working fluid.

The compressor is a key component of the system and its design demands the set-up of novel guidelines, due to the near-critical thermodynamic condition of the fluid, which (i) makes the machine operate with a very low flow function, (ii) experiences steep changes in properties across the machine, and (iii) is prone to phase-change in the intake part of the machine.

In this study we revise the entire design workflow of a prototype sCO₂ centrifugal compressor, from the preliminary definition of the machine, to the mean-line design, and finally to the detailed definition of the meridional channel and of the blade shape, highlighting the aspects making the machine alternative to conventional ones. The compressor aerodynamics is then analyzed by resorting to a high-fidelity Computational Fluid Dynamics (CFD) model in both design and off-design conditions, considering three speed-lines and low/high flow rate margins. Results show the capabilities and limitations of conventional low-fidelity design procedures for designing sCO₂ compressors, especially at off-design conditions, and shed light on the technical implications of the thermodynamic character of the fluid, especially in connection to the onset of phase change in the intake region of the impeller and in the tip clearance.

INTRODUCTION

The use of carbon dioxide operating in thermodynamic supercritical conditions (sCO₂) as working fluid in closed gas cycles offers the opportunity to exploit multiple classes of hot sources alternative to fossil fuels, ranging from nuclear energy [1], [2] to concentrated solar power [3] and waste heat [4], owing to the expected higher efficiency and smaller plant footprint with respect to conventional configurations such as steam or organic Rankine cycles [5], [6]. With respect to competitive technologies, sCO₂ power systems also benefit of compactness, thanks of the high density of the working fluid, which ultimately

offers the opportunity of an effective control of the dynamics of the plant [7].

A key component of sCO₂ power systems is the main compressor, which is usually of centrifugal architecture and operates close to the thermodynamic critical point. The corresponding compression process allows for a significant reduction of the work required thanks to the liquid-like properties of CO₂ in these thermodynamic conditions. However, the large departure from the ideal-gas thermodynamics [8], [9], [10], as well as the potential occurrence of two-phase flows [11], [12] poses challenges in the aerodynamic design of impeller blade and meridional channel. The set-up of reliable design tools that comply with the above non-ideal effects is crucial to accelerate the development and the success of the entire technology.

Most of the studies available in Literature on sCO₂ compressors, and cited above, analyze the aerodynamics and thermodynamics of the flow within the machine or discuss the validation of computational tools for compressor flow analysis [13]. However, few works (see for example [14], [15]) focus on the design process of such non-conventional machines. In the present study, we discuss the entire design workflow of a prototype centrifugal compressor for sCO₂ applications, from the thermodynamic optimization of the cycle to the detailed definition of the meridional channel and of the blades. The study is complemented by an aerodynamic analysis of the machine in design and off-design conditions, performed by resorting to a high-fidelity CFD model which introduces the thermodynamic issues of the fluid and their aerodynamic implications.

The paper is structured as follows. At first, the energy application is defined, the thermodynamic cycle is optimized and the mean-line design of the compressor is presented. Then, the specific design guidelines for the meridional channel and the blades are introduced and applied to define the impeller. The CFD model is finally applied to assess the design and verify the compressor operation in off-design condition, also in comparison to corresponding mean-line predictions. The analysis of the two-phase flow at the impeller intake and within the tip clearance concludes the paper.

REFERENCE CYCLE AND COMPRESSOR TARGETS

To produce a meaningful compressor design for sCO₂ applications, preliminary cycle considerations are needed to set compressor boundary conditions and targets. Among the multitude of available cycle arrangements, the recompressed layout [5] is selected. The basic idea is to split the recuperative process downstream of the turbine in two units with different flow rates to cope with the sharp increase of the specific heat capacity at constant pressure when approaching the thermodynamic critical point. The main cycle routines and assumptions for pressure drops and pinch-point temperatures are reported in Romei *et al.* [16], in which tailored correlations that link the turbomachinery efficiencies in design conditions with cycle pressure ratio and size parameter are also provided.

For this specific task, the hot-source temperature is fixed at $T_{hs} = 550\text{ °C}$, while the minimum cycle temperature is $T_1 = 32\text{ °C}$. The target electrical power is $P = 50\text{ MW}_{el}$. According to Crespi *et al.* [6], these temperature range and power can fit both nuclear and concentrating solar power applications. To derive the remaining conditions, an optimisation procedure is used to maximise the cycle electrical efficiency η_{el} by varying the minimum pressure P_1 and split factor SF , i.e. the relative amount of mass flow diverted to the second recuperator. The optimization is carried out with the `patternsearch` algorithm available in the MATLAB® Optimization toolbox. The optimization is run in a parametric way, varying the cycle pressure ratio β_{cycle} between 2 and 4 with a step of 0.25. Each optimization is run five times with a different initialization to get the global optimum at each pressure ratio. The outcome of these optimization routines are collected in the trend of the optimized efficiency against the cycle pressure ratio reported in Figure 2. The envelop of the maxima shows an optimum of the cycle efficiency for $\beta = 3.25$, which is then selected as a reference for the following compressor design.

A single-stage compressor is considered to have reduced costs and footprint. Alongside the pressure ratio, the entire cycle is determined, hence compressor requirements are wholly delineated and reported in Figure 1. In the same figure, the initial path of the corresponding isentropic compression is displayed in the T-s thermodynamic plane, highlighting the severe non-ideal effects that occur in the near-critical region in terms of the compressibility factor $Z = Pv/RT$. Moreover, the proximity of the intake conditions to the saturation curve may provoke phase

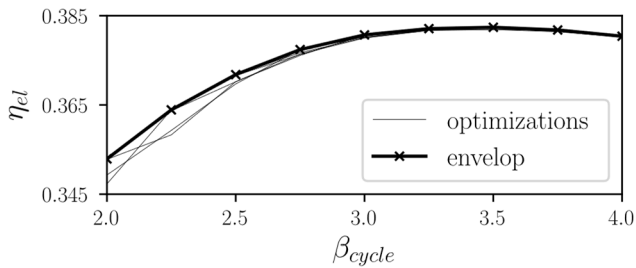


Figure 2: Trend of the optimized cycle efficiency with cycle pressure ratio.

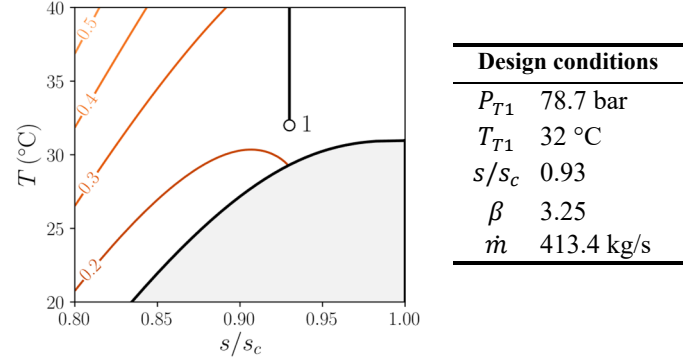


Figure 1: Intake thermodynamic conditions (point 1) reported in a T-s thermodynamic plane with superposed the compressibility factor map. The two-phase domain is highlighted in gray. On the right table, compressor requirements and overall boundary conditions.

transition as a consequence of local flow accelerations, the latter proportional to the local blade loading. The saturation pressure along an isentropic expansion from the upstream thermodynamic state is $P_{sat} = 71.0\text{ bar}$, leading to a safety margin between the intake state and saturation condition lower than ten bars. All these aspects, i.e. non-ideal effect, occurrence of two-phase flows, high blade loading, potential transonic/supersonic flow regimes, lead to an extremely complex aerodynamic design, which will be the core of the following discussions.

MEAN-LINE PRELIMINARY DESIGN

The mean-line formulation was proven to be effective for the analysis of centrifugal compressors for sCO₂ applications, as widely documented in literature [2, 13, 16]. In the present study, the mean-line code was run parametrically for several design variables to seek for the highest compressor efficiency while complying with the requirements described in the previous section. A parametric study was preferred over a blind optimization technique to have track of different compressor designs with comparable performance, then making a final decision based on the minimization of phase-change triggers (e.g., blade blockage and inlet velocities).

Within a mean-line framework, pitchwise average of aerodynamic and thermodynamic quantities are computed across all component by resolving balance equations (continuity, energy and Euler equations for velocity triangles) complemented with a generalised thermodynamic treatment based on the Span-Wagner multi-parameter equation of state [17]. Relative velocities consider the radial blade evolution at the impeller inlet. As all mean-line formulations, the detailed blade shape is inherently ignored and will be discussed separately in the next section.

The performance estimates are computed by resorting to correlations that model the internal flow physics and the main sources of loss mechanism. The following loss correlations are used in this work: (i) impeller incidence [18], (ii) impeller skin-friction [19], accounting for roughness [20] and blade curvature [21] in the determination of the friction coefficient, (iii) blade

diffusion [22], (iv) tip clearance [19] corrected according to Refs. [21, 23], (v) the flow recirculation at the impeller outlet [24] (vi) mixing downstream of the impeller [25], and (vii) friction losses at the endwalls of the vaneless diffuser. The work provided by the impeller is increased to account for the recompression of a fraction of the leakage flow [26]. In this preliminary phase, the vaned diffuser and the volute are also modelled. Specifically, the vaned diffuser performance are estimated on the basis of available diffuser databooks, corrected for incidence variations in off-design performance [27]. Furthermore, the skin-friction losses are estimated in the volute, besides the dissipation of the residual radial component of the velocity at the diffuser outlet. In the following CFD analyses, these latter two components are omitted and will be discussed in future works. Finally, the impeller slip factor is estimated with the Wiesner correlation [28] corrected for the splitter blade length [20]. For sake of brevity, the detailed description of the code is not reported, however it follows standard mean-line implementations discussed in textbooks [20, 27].

As for the inlet section, the shaft diameter was determined by means of simplified mechanical calculations accounting for the transmitted power. Then, the hub diameter D_{1h} is selected assuming a safety factor of 1.08 on the shaft diameter, thus ensuring a torque transmission without mechanical issues. Given the hub diameter, the blade height b_1 was chosen to minimize the tip Mach number in the rotating frame of reference $M_{w,1t}$. During this phase, the inlet blade angle β_{1g} was constrained in the range $-80 \div -10$ deg (measured from the meridional direction, the negative sign indicates a direction opposed to the peripheral speed) to prevent an excessive flow distortion. The number of blades is varied as well, also considering splitter blades. Notwithstanding comparable performance, the splitter configuration is ultimately selected, with splitters starting at the normalized full-blade streamwise location $s_{norm} = 0.175$. This choice represents a convenient trade off between a reduction in the blade blockage at inlet and a reduction of the blade loading due to the increased blade pitch at the splitter location. The rotational speed was also part of the parametric investigation, and it was varied in the range $8000 \div 13000$ rpm.

As for the outlet section, the absolute flow angle was constrained in the range $60 \div 75$ deg; the upper limit was imposed to prevent an excessive tangential flow direction in off-design conditions, which may be responsible of earlier instabilities in the diffuser component. To this end, backward blades ($\beta_{2g} < 0$ deg) are chosen and varied in the range $-35 \div -55$ deg. Finally, an open impeller design is considered.

From this analysis, a candidate compressor was selected and depicted in Figure 3 alongside the main geometrical dimensions. At nominal conditions, the flow coefficient is $\phi = 0.021$, the peripheral Mach number $M_{u2} = 0.86$ and the peripheral Reynolds number $Re_{u2} \approx 10^9$. The shroud and hub contours are generated with ANSYS-BladeGen[®], employing spline curves that pass through the geometrical quantities provided by the mean-line code. The vaned diffuser and the

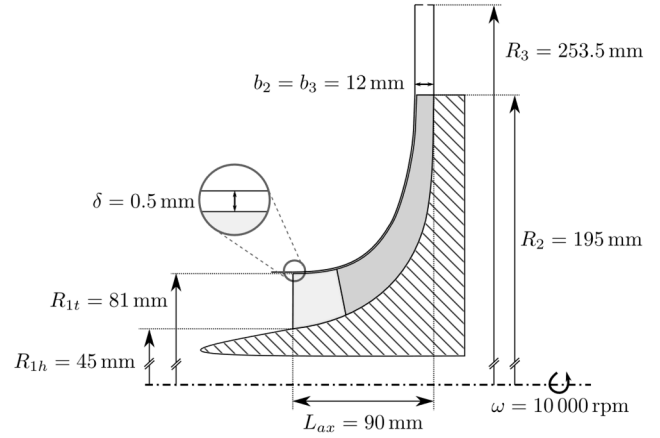


Figure 3: Meridional channel of the impeller and vaneless diffuser along with main geometrical dimensions.

volute are not reported in the figure because they will be not simulated in the next section.

The vaneless diffuser has a radial extension of 30% of the impeller radius: this value, close to the upper value of common design practices, is chosen to reduce the absolute Mach number at the vaned diffuser entrance so to ensure a good rangeability of the entire machine. For the present investigation, the vaneless pinch is neglected, but it may be included in the future to adjust the absolute flow angle when the vaned diffuser will be simulated as well.

CRITERIA FOR BLADE DESIGN

The step from a mean-line design in terms of main geometrical quantities to a complete compressor prototype requires the definition of the blade profiles and the three-dimensional stacking.

As for the blade profiles, the mean-line code provides information about the geometrical angles at the inlet and outlet section. In particular, the inlet section is split in three relevant sections, namely the hub (0% span), midspan (50% span) and tip (100% span) section. As a result of the mean-line analysis, the geometric angles at these three sections are $\beta_{1g} = -43.1, -53.7, -60.5$ deg, respectively (angles are measured from the meridional direction), assuming optimal incidence [18]. The outlet geometrical angle results $\beta_{2g} = -45$ deg. Given these boundaries, several blade angle distributions are available to pass from inlet to outlet blade angle. In the context of sCO₂ centrifugal compressor, the choice of the blade angle distribution is particularly crucial, because it directly sets the aerodynamic loading of the blade front part. The more the front blade is loaded, the more the flow locally accelerates on the suction side, the more the local thermodynamic state penetrates inside the saturation dome.

One key parameter that controls the blade loading is the wrap angle φ , i.e. the angle between the meridional plane passing through the leading edge and the one passing through the trailing edge. A low wrap-angle profile, sketched in Figure 4(a), is

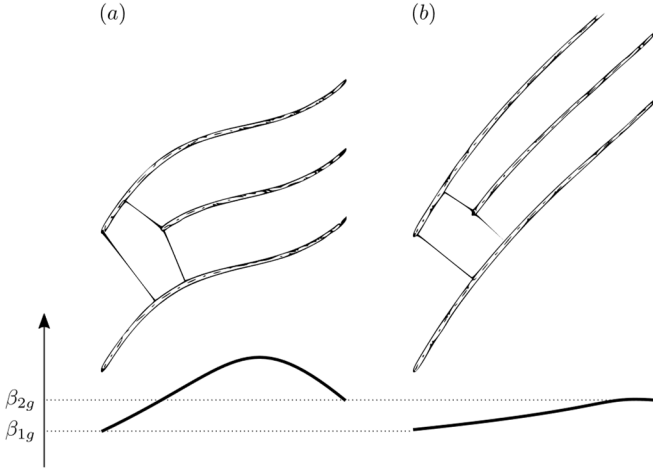


Figure 4: Influence of the wrap angle on the blade angle distribution: (a) low wrap-angle profile, and (b) high wrap-angle profile.

characterized by a limited wetted surface, thus limiting the skin-friction loss. For the same reason, the aerodynamic loading is generally high because it is concentrated on a smaller blade length. As a consequence, the fluid accelerating on the front part of the blade is more prone to phase transition. By increasing the wrap angle, the blade extends for a larger part of the circumference, hence the loading is distributed on a higher blade surface. The loading rise is generally smoother, as evidenced in Figure 4(b) for an exemplary high wrap-angle profile. Although local accelerations prompted by the aerodynamic loading are reduced in this latter configuration, the available area for the flow passage is reduced as well, see the clear reduction in the impeller throat between the two examples in Figure 4. A smaller impeller throat also promotes phase-change phenomena because the flow has to accelerate to compensate the reduction in the flow passage. At the same time, a high wrap angle contributes to a long and narrow (i.e. of small hydraulic diameter) blade channel. From this analysis, it is clear that a trade-off in the wrap angle has to be found to reduce the skin friction and diffusion losses and, at the same time, the occurrence and the extension of phase transition in sCO₂ centrifugal compressor operating in near-critical conditions. For the present design, after preliminary CFD runs, a relatively high-wrap angle is selected, i.e. $\varphi = 85$ deg.

To ease the blade manufacturability, the three-dimensional profile stacking is performed with the Flank-Milling technique. The blade thickness distribution varies linearly from 2 mm at the leading edge to 3 mm at the trailing edge regardless of the radial coordinate. The leading edge is generated with an ellipse arc with ratio among semi-axis of 2.5. The trailing edge is cut-off at R_2 . Such thickness distribution results from an internal expertise, but rigorous mechanical stress analyses are planned for the near future. The final three-dimensional impeller shape is displayed in Figure 5.

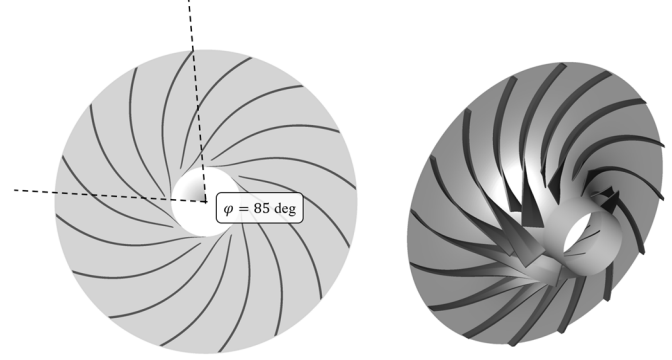


Figure 5: Three-dimensional impeller geometry.

COMPUTATIONAL FRAMEWORK

When dealing with multi-phase flows, there are several modeling strategies that can be adopted, depending on the computational cost and flow regime. The simulation of a highly loaded centrifugal compressor operating with CO₂ in near critical conditions represents an extremely challenging case from the computational perspective (complex thermodynamics coupled with high-speed flows in a rotating reference frame), hence the simulation tool needs to balance the solution accuracy with computational efficiency and robustness.

To this end, a two-fluid flow representation (with reference to the Brennen's classification [29]) is employed in the present work, named *barotropic model*, which also assumes that (i) the phases are in thermal and mechanical equilibrium, and (ii) any thermodynamic/transport property of the mixture Ψ only depends on the pressure, e.g. $\Psi = \Psi(P)$. Owing to the barotropic assumption, the equation of state is simply $\rho = \rho(P)$. In this work, such relationship is interpolated from the REFPROP[®] estimate at the upstream isentrope, referring to the thermodynamic equilibrium mixture density when the isentrope crosses the saturation curve. As the intake conditions are close to the critical point, meta-stability effects are neglected in the determination of the barotropic equation of state. The resulting functional trend for this specific thermodynamic condition is represented by the black curve in Figure 6. As the equation of state does not depend on thermal quantities, the equations of motion are decoupled from the energy equation, which does not

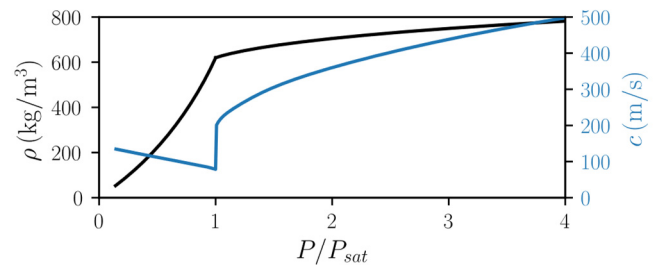


Figure 6: Barotropic equation of state $\rho = \rho(P)$ and corresponding speed of sound.

need to be explicitly resolved. The speed of sound in both single- and two-phase domain is computed as derivative of the barotropic equation of state, i.e. $c = \sqrt{(\partial P / \partial \rho)_s}$. The kink in the density curve at the saturation pressure translates in a jump of the speed of sound (blue curve in Figure 6), which is more than halved when phase change initiates. This result is aligned with the homogeneous equilibrium theory [30]. An average molecular viscosity between the inlet and outlet state is also provided. Finally, the two-equation turbulence model $k - \omega$ SST [31] closes the Reynolds-averaged Navier-Stokes (RANS) equations.

The barotropic model is implemented in ANSYS-CFX® following the procedure outlined in Persico *et al.* [12], which uses a logistic function to interpolate separately the two branches (in the single-phase and in the two-phase regions) of the barotropic function reported in Figure 6. The barotropic model was validated against the experiments of Nakagawa *et al.* [32], which were carried out for supercritical intake thermodynamic conditions close to the ones considered in the present study. The overall agreement was found to be remarkable from both the qualitative and quantitative point of views, revealing pressure differences between experiment and simulations of the order of 2% [12]. This assessment qualifies the model as adequate for simulating compressible two-phase flows within sCO₂ turbo-compressors, in which the heat transfer can be neglected.

Simulations were performed assigning at the inlet the total pressure, purely meridional flow, turbulence intensity equal to 5% and eddy viscosity ratio equal to 1; at the outlet, the mass flow rate was assigned at the design flow coefficient, while an average static pressure, accepting 5% of tolerance across the outlet surface, is assigned and varied each time to generate the off-design performance maps. No-slip boundary conditions are imposed to the solid walls, also assuming a grain-sand roughness of $6.2 \mu m$. Counter-rotating boundary conditions are also assigned both at the shroud to simulate an open impeller with a normal tip clearance $\delta = 0.5 mm$ and at the vaneless diffuser (stationary component). Finally, periodic boundary conditions are exploited to simulate a single flow passage containing both the main and the splitter blade. High-resolution numerical schemes are used in the discretization of the flow advection term, while second-order central difference scheme for the diffusion term. The advection term in turbulence equations is discretized with a first-order upwind scheme.

Meshes are generated with ANSYS-Turbogrid®. Three hexahedral meshes are considered with an increasing number of

	Coarse	Medium	Fine
Hub BL	9	13	18
Shroud BL	9	13	18
Tip Clearance	9	18	28
Overall span	40	70	100
Bl2Bl Impeller	25,000	75,000	150,000
Overall	1.9×10^6	8.8×10^6	2.4×10^7

Table 1: Cell distribution for the grid assessment.

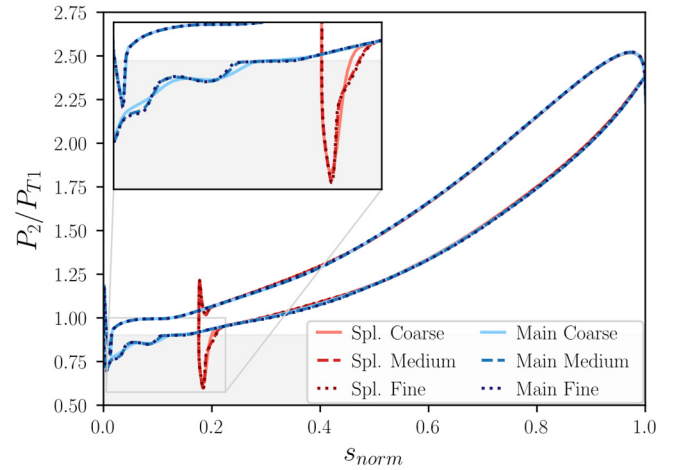


Figure 7: Blade loading distributions of the main and splitter blade at midspan for different grid refinements. The gray area identifies the region $P < P_{sat}$, where P_{sat} is the saturation pressure obtained through an isentropic transformation.

elements, allocated as in Table 1. A cell clustering is imposed close to the walls, with a first layer distance approximately equal to the sand-grain roughness, thus resorting to modified wall function to properly account for the roughness effects. In terms of integral quantities, only small differences are found among the three meshes, with a maximum discrepancy in terms of total-to-total efficiency of 0.1 percentage point between the coarse and the fine mesh. Some visible differences are found in the resolution of the flow field, especially in the front part of the blade where two-phase supersonic flows are established. The results are summarized in Figure 7, where the blade loading of the main and splitter blade is reported for the three meshes. The medium mesh closely follows the trends of the finer mesh, while the coarse mesh considerably smooths the loading distribution in the front part of the blades, although recovering a good agreement afterwards. The medium mesh is ultimately selected for the following analyses as it provides a complete flow description at the minimum computational cost.

COMPRESSOR PERFORMANCE

The compressor performances are analyzed for three representative speedlines, namely 60%, 80% and 100% of the nominal one. For these speeds, the peripheral Mach number is $M_{u2,des} = 0.52, 0.69, 0.86$, respectively. The wide range of rotational speed is chosen to ensure an adequate flexibility of the power cycle in off-design conditions. The performance map in terms of total-to-total pressure ratio and efficiency are reported in Figure 8, in which CFD predictions are compared with the original mean-line estimates. The pressure ratio agreement is remarkable, with no relevant differences among the two methodologies. It has to be noted that the design pressure ratio is slightly higher the one required by the cycle (3.46 against the

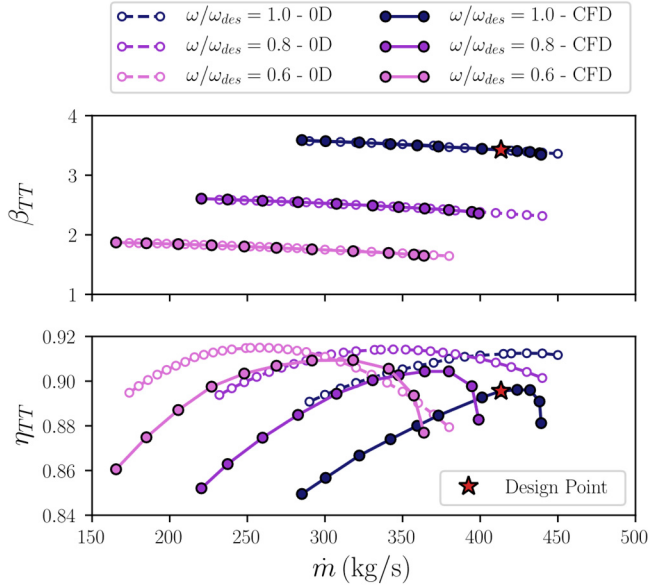


Figure 8: Performance maps of the centrifugal compressor obtained with CFD simulations and mean-line analyses.

required 3.25) because the vaned diffuser and the volute are not included in the present analysis. Larger discrepancies are found in the efficiency predictions, with errors of the order of 2 percentage point, aligned and even better than other mean-line results [33, 34]. The mean trend of the efficiency curve is generally captured except at high flow rate for the speedline at 80% and 100%. From a similitude perspective, one might expect similar behavior across the operational range owing to the high Reynolds number ($Re_{u2} > 5 \times 10^8$ for the lowest rotational speed) and small contribution of the compressibility (in these thermodynamic conditions, the CO_2 behaves in a liquid-like manner, with only marginal variation of the ratio ρ_2/ρ_1 across the three speedlines at given flow coefficient).

The underlying reason for the abrupt drop in the efficiency trend at high flow rates when the rotational speed increases is the role of multi-phase effects. The distribution of vapor mass fraction on the blade-to-blade plane at midspan is reported in Figure 9 for the design conditions. Three regions in which cavitation occurs (transition from liquid to vapor phase driven by pressure) can be recognized: (i) a wider region on the front

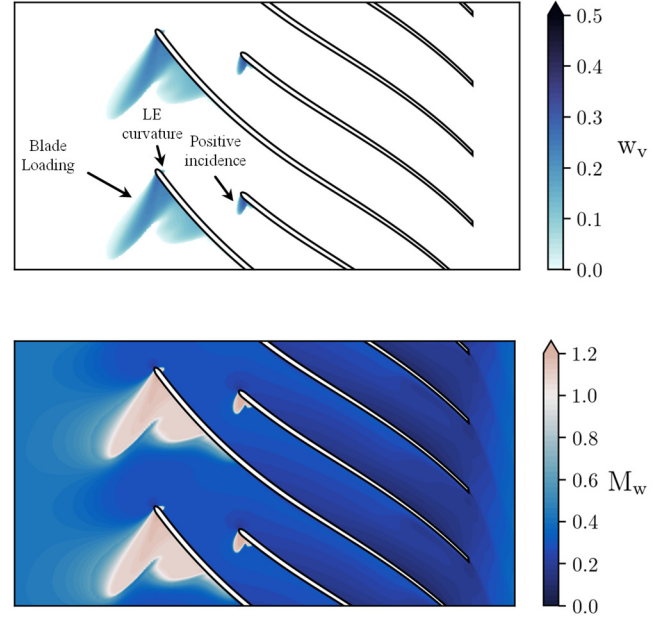


Figure 9: Vapor mass-fraction (top) and relative Mach number (bottom) flow field in the blade-to-blade plane at midspan (50%) for design flow coefficient and rotational speed.

suction side of the main blade induced by the local aerodynamic loading, (ii) a tiny region on the front pressure side given by the flow acceleration around the elliptic leading edge, and (iii) a small region on the splitter suction side, mainly provided by a positive incidence on the splitter blade. All these features can also be recognized in the blade loading in Figure 7. The vapor mass fraction in these regions can reach values of the order of 30%. Notice that, given the combination of high pressure ratio and operation in the near-critical region, the occurrence of cavitation is in practice unavoidable. However, from a mechanical perspective, the cavitation is expected to be less harmful than what usually occurs in conventional turbopumps, because the density ratio between the two phases in these conditions is at least one order of magnitude smaller. In correspondence of the multi-phase zones, the relative Mach number, reported in the same figure, shows a sudden increase; the flow regime passes from highly subsonic ($M_w < 1$ in the blue

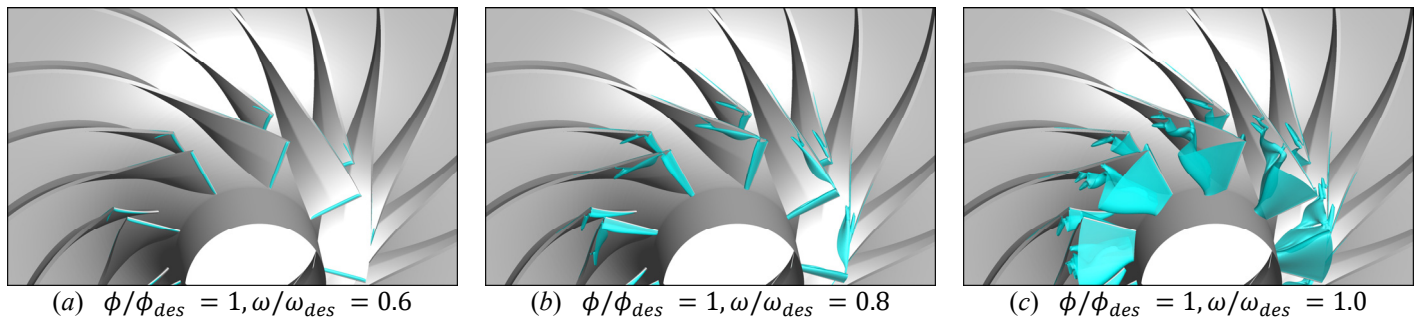


Figure 10: Extension of the two-phase region for the design flow coefficient at different rotational speed.

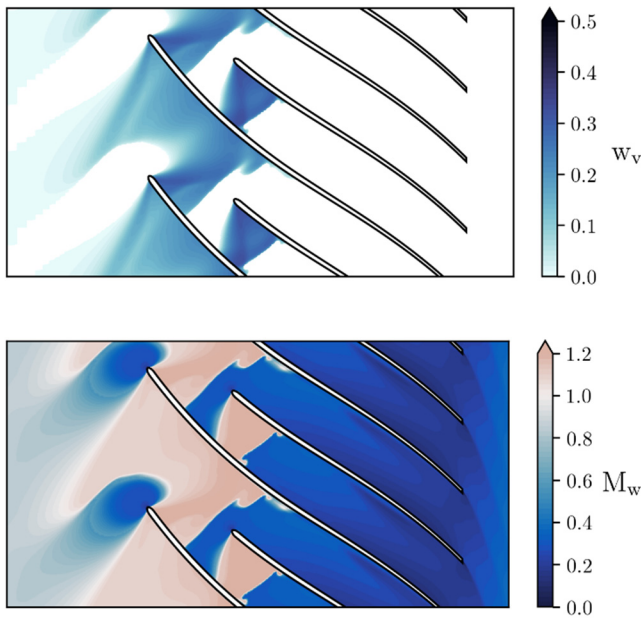


Figure 11: Vapor mass-fraction (top) and relative Mach number (bottom) flow field in the blade-to-blade plane at midspan (50%) for $\phi/\phi_{des} = 1.06$ and $\omega/\omega_{des} = 1.0$.

region) to supersonic ($M_w > 1$ in the red region) when the flow transits. This phenomenon is strictly related to the behavior of the sound speed under the assumption of thermodynamic equilibrium, as already explained in Figure 6.

The occurrence and the amount of phase change is strictly related to the flow aerodynamics. The higher the target pressure ratio, the larger the blade loading and the accelerations involved. Therefore, when reducing the rotational speed, the velocities are generally lower, as well as the resulting blade loading and pressure ratio. The influence of the rotational speed on the two-phase region extent is reported in Figure 10. At the nominal rotational speed, the two-phase region interests the whole span, mainly developing on the main blade suction side. When the rotational speed is 80% of the design one, the region dramatically reduces in its extent, although it still develops on the whole span. The larger region is located at the tip region, where the relative velocities are higher. Finally, moving to the lowest rotational speed, i.e. 60% of the design one, the two-phase region is almost completely suppressed, and the only contribution to its generation is provided by the leading-edge curvature. Indeed, at this rotational speed the acceleration of the flow on the suction side is not prompting the phase transition.

Up to now the discussion focused on the design flow rate. Analogous considerations apply when moving along the same speedline. In particular, when the flow rate increases, the velocities are generally higher to cope with the large amount of flow to be delivered. In this context, the phase-change phenomena are more prominent. As a consequence, at nominal

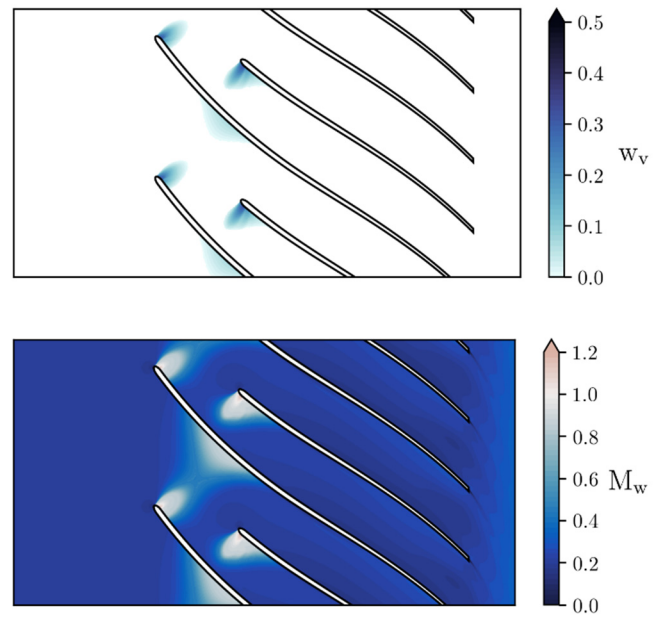


Figure 12: Vapor mass-fraction (top) and relative Mach number (bottom) flow field in the blade-to-blade plane at midspan (50%) for $\phi/\phi_{des} = 1.38$ and $\omega/\omega_{des} = 0.6$.

speed the right limit (choking limit) on the compressor map is found at 106% of the design flow rate. For this case, the flow field at midspan is reported in Figure 11. It can be readily recognized that the phase change affects the whole blade channel, there inducing a supersonic Mach number. Specifically, a region vapor-free is observed at the leading edge where the flow impinges on the blade. In this zone, the velocity goes to zero and the static pressure approaches the design total pressure, which is above the saturation limit. However, both the suction and the pressure side are severely affected by two-phase flow. At flow rates larger than the nominal one, the flow approaches the blade with a negative incidence, that causes a consistent acceleration right after the leading edge to recover the blade angle direction. In this location, the flow meets the flow coming from the adjacent blade suction side, which also undergoes to phase transition due to local acceleration on the blade surface. Such flow accelerations are sufficient to affect the whole blade channel, hence inducing a choked compressor operation. An analogous flow field is also found at the hub profile, confirming that the whole machine is choked.

At the lowest rotational speed, the operating range extends up to 145% of the nominal flow. To show the impact of two-phase flow at this rotational speed, the flow field at midspan is reported in Figure 12 for a mass flow rate increased by 38% with respect to the design one. As a result of a lower rotational speed and, by velocity triangles composition, of overall lower relative velocities, the two-phase regions are significantly reduced compared to those in Figure 11. In these conditions, the two-

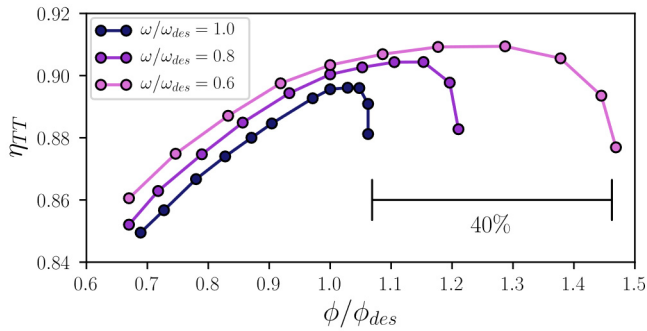


Figure 13: Dimensionless performance maps in terms of flow coefficient and total-to-total efficiency.

phase flow is mainly triggered by incidence effect, which prompts a localized acceleration on the pressure side. The flow on suction side also undergoes to phase change, but the two zones are not connected, hence the free-stream remains in single phase with a Mach number considerably lower than the unity.

At low flow rates, the phase transition is hampered by the low relative velocities, although localized two-phase regions can also be established because of a positive incidence angle [12]. However, their contribution seems to be marginal to the determination of the left operational limit (surge line), which is still determined by an excessive flow diffusion that causes flow instabilities in the impeller channel.

Finally, the aerodynamic analyses described in this section demonstrated that two-phase effects influence the compressor operational range by limiting the right limit, as further clarified by Figure 13. Specifically, the onset of phase transition sets an early choking of the compressor, reducing the operational range of about 40% with respect to phase-change-free operation. Moreover, as phase transition is mainly prompted by local effects (blade loading, incidence) rather than global effects that affect the free stream (e.g., blade blockage), conventional mean-line codes are not able to predict this early reduction in operational range, as visible by the comparison between mean-line and CFD predictions at the nominal speed in Figure 8.

Tip clearance

In the previous section it was pointed out that the onset of phase change in these specific thermodynamic conditions promotes supersonic flow regime and choking operation. Notwithstanding the detrimental effect on the compressor range, the trigger of choking may be used to some extent to limit the leakage flow rate in the design of open impellers. Moreover, as the leakage flow is localized in the tip section, the relative velocities are higher and, consequently, two-phase effects are also more prominent, as also evidenced in Figure 10.

The streamlines are reported for the design case in Figure 14. The sonic iso-surface shows that the tip leakage features a supersonic flow regime in the initial part of the main and splitter blade. Analogous streamlines are extracted for the other speedlines at the design flow coefficient; the sonic region is reduced when the rotational speed is 80% of the nominal one,

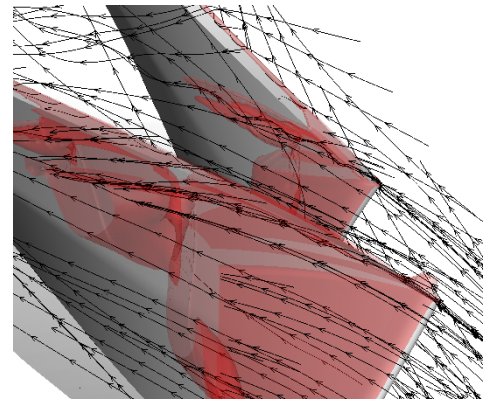


Figure 14: Streamlines at the design flow coefficient and rotational speed. In red, the iso-surface $M_w = 1$ is reported.

while it is practically absent for the lowest rotational speed, in which the two-phase region is prompted only by the flow curvature around the leading edge. The relative amount of the total flow rate passing through the gap of the main and splitter blade is 17.6%, approximately equal for the three cases under examination. The same relative amount of leakage seemingly suggest that the occurrence of sonic conditions prompted by the onset of two-phase flows has not a relevant effect on the leakage and on the corresponding losses. As a conclusive remarks, it is worth to underline that the present computational methodology only considers the different compressibility between the single- and two-phase fluid under mechanical and thermodynamic equilibrium assumption, without accounting for heterogeneous and phase-change effects on the frictional coefficient [29] that may instead play a role in the interstitial gap.

CONCLUSION

The paper discusses the design process and the computational assessment of a prototype centrifugal compressor for sCO₂ applications. Starting from the optimization of the thermodynamic cycle to derive realistic boundary conditions and requirements, a single-stage highly loaded compressor (pressure ratio greater than 3) was introduced, discussing the peculiar design of sCO₂ compressors operating in the near-critical region. In particular, the discussion focused on the blade-design strategies to minimize the front loading, with the aim of minimizing the onset of phase change at the compressor intake.

The resulting three-dimensional compressor configuration was analyzed in design and off-design conditions using both a low-fidelity mean-line tool and a high-fidelity CFD model. Results confirmed the expected compressor performance in design conditions, with the two simulations tools showing excellent agreement in terms of pressure ratio and reasonable agreement in terms of efficiency (differences within 1.5–2%). However, the CFD simulations showed wide regions potentially exposed to cavitation, prompting there supersonic flow regime because of the drop in the speed of sound when the

thermodynamic state falls in the two-phase domain. Starting from such a severe configuration at nominal flow rate, choking quickly occurs as soon as the compressor is operated at higher flow rate (106% of the nominal value) due to the enlargement of the two-phase region to the whole intake of the machine. This effect, originated by the front loading and by the incidence on the main and splitter blades, cannot be captured by the low-fidelity tool, which overestimates the choked-flow condition with respect to the CFD prediction.

As the angular speed is reduced, the compressor loading reduces as well, and the above effects progressively weakens. Consequently, the agreement between the mean-line and CFD predictions greatly improves at high flow rate too. For the lowest angular speed, the onset of phase change is limited in local areas close to the leading edge due to blade curvature and it has not a relevant effect on the compressor performance. As a result, the free-stream does not undergo to phase change even at high flow rate, hence the compressor range is increased of about 40% with respect to the nominal rotational speed, in which phase-change effects are prominent. Finally, although the tip clearance is also affected by phase-change phenomena at the nominal speed, the relative fraction of flow rate passing through the clearance remains practically unaltered compared to cases at a lower rotational speed in which only single-phase flows are detected in the interstitial gap.

This study has shown that the compressor loading drives the phase change, which cannot be eliminated even by resorting to tailored design strategies. The onset of phase change has a relatively weak impact on the compressor efficiency (at least in according to the present computational methodology, that neglects the entropy produced during the phase transition), but it strongly reduces the right operation limit of the compressor. High-fidelity CFD tools are required to properly master this effect. Future works will also include the vaned diffuser and the volute in the design chain, besides analyzing off-design operation of the compressor when the intake thermodynamic conditions are varied.

NOMENCLATURE

Acronym

BL	boundary layer
Bl2Bl	blade-to-blade plane
sCO ₂	supercritical carbon dioxide
CFD	computational fluid dynamics
RANS	Reynolds-averaged Navier-Stokes

Roman Symbol

c	speed of sound
h	specific enthalpy
\dot{m}	mass flow rate
M	Mach number
M _{u2}	peripheral Mach number u_2/c_{T1}
M _w	relative Mach number
P	pressure
Re _{u2}	peripheral Reynolds number $\rho_{T1}u_2D_2/\mu_{T1}$
s	specific entropy
S _{norm}	normalized streamwise direction

T	temperature
v	absolute velocity
w	relative velocity
w _v	vapor mass fraction
Z	compressibility factor

Greek Symbol

β	pressure ratio
β_g	impeller blade angle
δ	tip clearance
ϕ	flow coefficient $\dot{V}/(u_2D_2^2)$
φ	wrap angle
η	isentropic efficiency
η_{el}	net cycle efficiency
μ	molecular viscosity
ω	rotational speed
ρ	density

Subscripts

(·) _c	critical condition
(·) _{des}	design condition
(·) _{sat}	saturation (at fixed entropy)
(·) _T	total condition
(·) _{TT}	total-to-total
(·) ₁	impeller inlet/midspan
(·) _{1h}	impeller hub
(·) _{1t}	impeller tip
(·) ₂	impeller outlet
(·) ₃	vaneless diffuser outlet

REFERENCES

- [1] V. Dostal, A Supercritical Carbon Dioxide Cycle for Next Generation, Ph.D. thesis, Massachusetts Institute of Technology, 2004.
- [2] J. Lee, J. I. Lee, H. J. Yoon and J. E. Cha, "Supercritical Carbon Dioxide Turbomachinery Design for Water-Cooled Small Modular Reactor Application," *Nucl. Eng. Des.*, vol. 270, pp. 76-89, 2014.
- [3] T. Neises and C. and Turchi, "A Comparison of Supercritical Carbon Dioxide Power Cycle Configurations With an Emphasis on CSP Applications," *Energy Procedia*, vol. 49, p. 1187–1196, 2014.
- [4] M. Marchionni, G. Bianchi and S. Tassou, "Review of supercritical carbon dioxide (sCO₂) technologies for high-grade waste heat to power conversion," *SN Applied Sciences*, vol. 2, no. 611, 2020.
- [5] G. Angelino, "Carbon dioxide condensation cycles for power production," *ASME Paper No. 68-GT-23, J. Eng. Power* 90, 1968.
- [6] F. Crespi, G. Gavagnin, D. Sanchez and G. S. Martinez, "Supercritical carbon dioxide cycles for power generation: A review," *Applied Energy*, pp. 152-183, 2017.
- [7] M. Marchionni, L. Chai, G. Bianchi and S. Tassou, "Numerical modelling and transient analysis of a printed circuit heat exchanger used as recuperator for supercritical CO₂ heat to power conversion systems," *Applied Thermal Engineering*, vol. 161, no. 114190, 2019.
- [8] S. A. Wright, R. F. Radcl, M. E. Vernon, G. E. Rochau and P. S. Pickard, *Operation and Analysis of a Supercritical CO₂ Brayton Cycle*, Sandia Report SAND2010-0171, 2010.
- [9] J. S. Noall and J. J. Pasch, "Achievable Efficiency and Stability of Supercritical CO₂ Compression Systems Main Compressor

- Design Discussion," in *The 4th International Symposium—Supercritical CO₂ Power Cycles*, Pittsburgh, PA, USA, 2014.
- [10] N. D. Baltadjiev, C. Lettieri and Z. S. Spakovszky, "An investigation of real gas effects in supercritical CO₂ centrifugal compressors," *Journal of Turbomachinery*, vol. 137, 2015.
- [11] A. Hosangadi, Z. W. T. Liu, V. Ahuja and J. Busby, "Modeling Multiphase Effects in CO₂ Compressors at Subcritical Inlet Conditions," *Journal of Engineering for Gas Turbines and Power*, vol. 141, 2019.
- [12] G. Persico, P. Gaetani, A. Romei, L. Toni, E. F. Bellobuono and R. Valente, "Implications Of Phase Change On The Aerodynamics Of Centrifugal Compressors For Supercritical Carbon Dioxide Applications," in press in the *Journal of Engineering for Gas Turbines and Power*, 2021.
- [13] A. Ameli, T. Turunen-Saaresti and J. Backman, "Numerical investigation of the flow behavior inside a supercritical CO₂ centrifugal compressor," *Journal of Engineering for Gas Turbines and Power*, vol. 140, no. 6, p. 122604, 2018.
- [14] A. Hacks, S. Schuster, H. J. Dohmen, F. K. Benra and D. Brillert, "Turbomachine Design for Supercritical Carbon Dioxide Within the sCO₂-HeRo.eu Project," *Journal of Engineering for Gas Turbines and Power*, vol. 140, 2018.
- [15] R. Pelton, T. Allison, S. Jung and N. Smith, "Design of a Wide-Range Centrifugal Compressor Stage for Supercritical CO₂ Power Cycles," in *ASME Turbo xpo 2017*, Charlotte, NC, USA, 2017.
- [16] A. Romei, P. Gaetani, A. Giostri and G. Persico, "The role of turbomachinery performance in the optimization of supercritical carbon dioxide power systems," *Journal of Turbomachinery*, vol. 142, no. 7, p. 071001, 2020.
- [17] R. Span and W. Wagner, "A New Equation of State for Carbon Dioxide Covering the Fluid Region from the Triple-Point Temperature to 1100 K at Pressures up to 800 MPa," *Journal of Physical and Chemical Reference Data*, vol. 25, no. 6, pp. 1509-1596, 1996.
- [18] M. R. Galvas, "FORTRAN program for predicting off-design performance of centrifugal compressors," NASA TN D-7487, 1973.
- [19] W. Jansen, "A method for calculating the flow in a centrifugal compressor impeller when entropy gradients are present," in *Royal Society conference on internal aerodynamics (turbomachinery)*, 1967.
- [20] R. H. Aungier, *Centrifugal Compressors: a strategy for aerodynamic analysis and design*, New York: ASME Press, 2000.
- [21] D. S. Musgrave, "The prediction of design and off-design efficiency for centrifugal compressor impellers," *ASME 22nd fluids engineering conference*, 1980.
- [22] C. Rodgers, "A Diffusion Factor Correlation for Centrifugal Impeller Stalling," *J. Eng. Power*, vol. 100, no. 4, pp. 592-601, 1978.
- [23] J. J. Brasz, "Investigation Into the Effect of Tip Clearance on Centrifugal Compressor Performance," in *ASME 1988 International Gas Turbine and Aeroengine Congress and Exposition*, Amsterdam, The Netherlands, 1988.
- [24] J. E. Coppage, F. Dallenbach, H. Eichenberger, G. E. Hlavaka, E. M. Knoernschild and N. Van Lee, "Study of supersonic radial compressors for refrigeration and pressurization systems," WADC report 55-257, 1956.
- [25] J. P. Johnston and R. C. Dean, "Losses in vaneless diffusers of centrifugal compressors and pumps," *Trans. ASME Journal of Engineering for Power*, pp. 49--62, 1966.
- [26] R. H. Aungier, "Mean Streamline Aerodynamic Performance Analysis of Centrifugal Compressors," *Journal of Turbomachinery*, vol. 117, no. 3, pp. 360-366, 1995.
- [27] A. Whitfield and N. Baines, *Design of radial turbomachines*, Logman Singapore Publishers Ltd., 1990.
- [28] F. J. Wiesner, "A Review of Slip Factors for Centrifugal Impellers," *Trans. ASME: J. Eng. Gas Turbines Power*, pp. 558--572, 1967.
- [29] C. E. Brennen, *Fundamentals of Multiphase Flows*, Cambridge University Press, 2005.
- [30] M. De Lorenzo, P. Lafon, J. M. Seynhaeve and Y. Bartosiewicz, "Benchmark of Delayed Equilibrium Model (DEM) and classic two-phase critical flow models against experimental data," *International Journal of Multiphase Flow*, vol. 92, pp. 112-130, 2017.
- [31] F. R. Menter, "Two-Equation Eddy-Viscosity Turbulence Models for Engineering Applications," *AIAA Journal*, vol. 32, no. 8, pp. 1598-1605, 1994.
- [32] M. Nakagawaa, M. Serrano Beranaa and A. Kishinec, "Supersonic two-phase flow of CO₂ through converging-diverging nozzles for the ejector refrigeration cycle," *International Journal of Refrigeration*, vol. 32, pp. 1195-1202, 2009.
- [33] A. Meroni, B. Zühlsdorf, B. Elmegaard and F. Haglind, "Design of Centrifugal Compressors for Heat Pump Systems," *Applied Energy*, vol. 232, pp. 139-156, 2018.
- [34] J. Schiffmann and D. Favrat, "Design, experimental investigation and multi-objective optimization of a small-scale radial compressor for heat pump applications," *Energy*, vol. 35, no. 1, pp. 436-450, 2009.

INVESTIGATION OF MATERIAL DEGRADATION AND COOLANT CHEMISTRY FOR sCO₂ POWER CYCLES

Jan Berka*

Centrum vyzkumu Rez s.r.o. and University of
chemistry and technology Prague
Rez, Czech Republic
Email: jan.berka@cvrez.cz

Tomas Hlinčík

University of chemistry and technology Prague
Prague, Czech Republic

Eliška Purkarová

University of chemistry and
technology Prague
Prague, Czech Republic

Alice Vagenknechtová

University of chemistry and
technology Prague
Prague, Czech Republic

Lucia Rozumová

Centrum vyzkumu Rez s.r.o.
Rez, Czech Republic

ABSTRACT

sCO₂ power cycles are characterized by the enhanced efficiency of thermal to electric power conversion and more compact turbine size compared with the steam power cycle. The organizations from Czech Republic take part the extensive research activities in this field. The research infrastructure including sCO₂ experimental loop was constructed. The sCO₂ coolant chemistry and material degradation are among the solved topics. The objectives are to identify impurities in sCO₂ medium and propose the purification and purity control system. Another objective is to gain data of structural material degradation in sCO₂ medium. First results concerning impurities and materials were obtained during laboratory tests and the 1000 h operation of the sCO₂ loop. The most important of them are presented in the paper and also conference presentation.

INTRODUCTION

The increasing electric power consumption and the CO₂ emissions reduction requirements demands new, effective energy sources. One way of increasing the conversion of mechanical power to electric power is by using carbon dioxide as a working medium in the power cycle. Currently, the power cycles that are based on supercritical CO₂ (sCO₂) have been investigated [1, 2]. Carbon dioxide becomes supercritical above a critical temperature of 30.98 °C (304.13 K) and above a pressure of 7.32 MPa [2]. The sCO₂ power cycle efficiency of the conversion of mechanical power to electric power may exceed 50% compared to the conventional steam power cycle, which has a maximum efficiency of approximately 40% [3, 4]. The efficiency of sCO₂ increases within the temperature range of 500–950 °C. Therefore, this technology is suitable for power

conversions in both high temperature non-nuclear and nuclear technologies, including the generation IV nuclear reactors [5]. Another advantage of the sCO₂ cycles is that they use more compact turbines compared to the turbines for the steam power cycle [6].

The sCO₂ cycles are subject of worldwide research and development program, in which organizations from Czech Republic are also involved. One of the topics of the extensive research program is the sCO₂ coolant chemistry (i.e. purity, purification and purity control of CO₂ medium) and resistivity of structural materials in sCO₂ medium.

SUPERCritical CARBON DIOXIDE LOOP IN REZ

The research activities are related (also) to the Supercritical carbon dioxide loop (sCO₂ loop; see the scheme on Figure 1). The purpose of the loop is to measure the thermohydraulic performance and physical parameters of the sCO₂ circuits, the loop also enables the exposure of material samples in sCO₂ environment.

For the main parameters of the loop, see Table 1. The function of the loop could be described as follows: after the passage through the heat exchanger in the high-pressure section (7), CO₂ flows to two parallel (8) and one serial (9) heater branches. After heating, the medium flows to the test section (10). Behind the test section, the reduction valve (11) is placed, which reduces the medium pressure to 12.5 MPa. Due to the accurate temperature reduction, part of the flow is passed through the oil cooler (12), and the second part flows through the bypass. Following that, the medium reaches the low-pressure part of the high temperature heat exchanger (7), which

has a maximum allowed temperature of 450 °C. It then flows to the low temperature heat exchanger (1). Next, it flows through

the cooler (4), which is situated before the entrance to the main circulator (3).

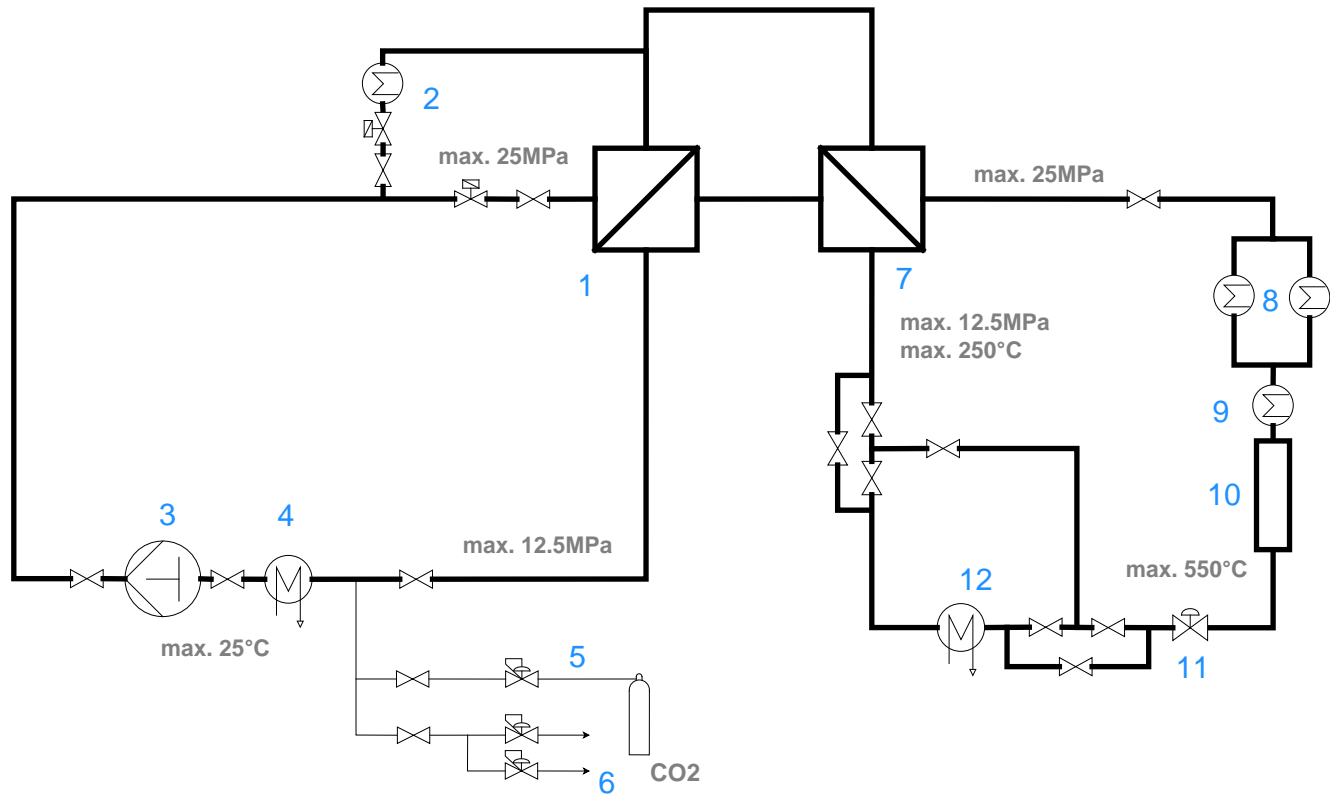


Figure 1: Scheme of the Supercritical carbon dioxide experimental loop. 1: low temperature heat exchanger, 2: preheater, 3: main circulation pump, 4: cooler, 5: CO₂ dosing system, 6: sampling system, 7: high temperature heat exchanger, 8: parallel heaters, 9: heater, 10: test section, 11: reduction valve, 12: cooler

Table 1: The main parameters of the Supercritical carbon dioxide experimental loop

Maximum medium temperature	550 °C
Maximum pressure in the high-pressure section	25 MPa
Maximum pressure in the low-pressure section	12.5 MPa
Maximum flow rate	0.4 kg.s ⁻¹
The loop volume	0.08 m ³

SCO₂ POWER CYCLES CHEMISTRY

Contrary of the water or helium cooled power systems there is not much information about sCO₂ power cycle medium chemical composition, typical impurities content, purification and purity control systems. Some knowledge can be transferred from the operation's experience with the nuclear reactors, which use carbon dioxide (not in a supercritical state)

as a primary coolant. These reactors have been operated in Great Britain (MAGNOX and Advanced Gas Cooled Reactors) [7], and the first nuclear power plant in former Czechoslovakia, which is A1, also used carbon dioxide as a primary coolant [8].

Impurities can get into the CO₂ (or sCO₂) medium by several ways. Some impurities can be contained in the source CO₂ gas stored in pressure vessels. Within the research program composition of several different CO₂ gases available on the market was verified and compared. The results are summarized in Table 2. As a source gas for sCO₂ power stations the CO₂ with purity 3.0 or 4.5 will be used for economical reason.

Table 2: CO₂ purity available on the market in Czech Republic

CO ₂ type	Purity	Impurities (vppm)					
	% vol.	H ₂ O	O ₂	CO	C _n H _m	N ₂	Oil
SFC/SFE	99.9993	1	2	0,5	1	3	-
CO ₂ for food industry (E290)	99.5	52	-	10	-	-	5
4.8	99.998	5	2	1	2	10	-
4.5	99.995	5	15	1	2	30	-
R-744	99.9	10	15	1	2	30	-
3.0	99.9	120	500	-	50	500	-
5.3	99.9993	1	2	0,5	1	3	-

Another sources of impurities in CO₂ in power cycles can be also the leakage of air or moisture from surrounding environment, lubricants from devices connected to the circuits, residual organics on internal surfaces from production and (not least) as products of chemical reactions in the circuit. In case of sCO₂ cycle with direct combustion the sCO₂ may contain also combustion products [5]. Typical admixtures in the CO₂ medium are as follows: O₂, H₂O, H₂, CO, CH₄, N₂ [5, 9]. In the direct combustion cycles that use synthesis gas as a fuel, SO₂, SO₃, NO, NO₂, and halogen compounds may be present in the medium. . Examples of the medium composition in the direct combustion power cycles are listed in Table 3.

Table 3: Examples of the medium composition in the turbine inlet for the direct combustion cycle, according to the used fuel [10, 11]

Component	Natural gas (vol. %)	Synthesis gas (vol. %)
CO ₂	91.80	95.61
H ₂ O	6.36	2.68
O ₂	0.20	0.57
N ₂	1.11	0.66
Ar	0.53	0.47

The higher content of impurities (units of % by vol. or more) can influence the thermodynamic properties of the medium. For example, the power consumption of the compressor when working with a medium that is near the critical point increases by six percent, whereas the medium purity decreases by 4.4%. With a medium of 90.9% purity, the compressor power consumption increases by 34% compared to 100% with pure CO₂. This increase in power consumption is caused by a decrease in the medium density, which is due to the impurities [9].

In cycles with indirect heating the content of impurities is expected to be lower – probably below 1 % by vol. The medium composition may be similar to primary CO₂ coolant in nuclear power plants, e.g. the most significant admixtures in A1 power plant primary coolant were H₂O (about 1000 mg.kg⁻¹) and oil (1 – 5 mg.kg⁻¹) [8].

The admixtures in the CO₂ medium even in lower contents may enhance corrosion and degradation of components. Higher content of oil (1 % by weigh and more) in the medium may negatively affect the heat transfer properties caused by deposition of oil an internal surfaces [3, 12].

SCO₂ PURIFIACATION METHODS

Data concerning CO₂ purification in power engineering are relatively rare. In some experimental devices, oil separators are used. For example, in the SCARLETT loop, the oil separator is located behind the compressor. The separator separates 99% of the oil that is contained in the medium in the loop [13]. To limit the damage to the turbines and other parts of the devices, the particle separators are inserted into the circuit. For lower flow rates, the “Y filters” (Figure 2) can be used, through which the medium passes.

Some gaseous impurities are expected to be effectively separated by adsorption methods. The experimental verification of these methods for CO₂ purification is in the experimental program for next years.

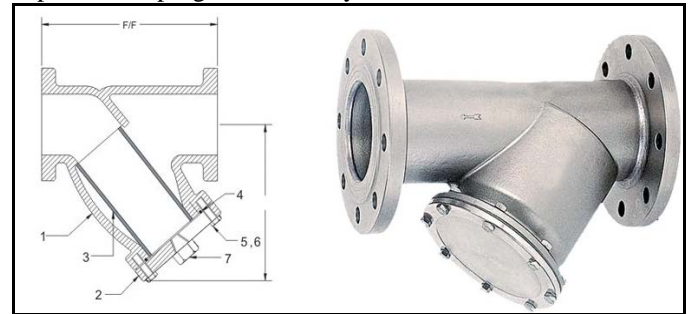


Figure 2: The Y-filter [14]

METHODS OF ANALYTICAL PURITY CONTROL

For CO₂ purity control several analytical methods can be assumed, e.g. gas chromatography with thermal conductivity detector (GC-TCD), mass spectroscopy detector (GC-MS) or helium ionization detector (GC-HID), analyzers based on infra red spectroscopy, etc. Every method is suitable for specific compounds detection. The method selection and verification for CO₂ purity control in sCO₂ loop is also in experimental program for next years.

Currently, the combination of the gas chromatography with the helium ionization detector (GC-HID) directly connected with sampling site of the loop and the moisture analyzer is based on changes to the infrared light wavelength. Experience with these technologies was gained in connection with another technology: the high temperature helium experimental loop. The details were published in cit. [15]. The GC-HID method is sensitive when determining the content of H₂, CO, CH₄, O₂, and N₂. Detection limit for some of these compounds is below 0.1 vppm. Gas chromatography methods are not suitable H₂O content determination. The disadvantage of methods based on gas chromatography is that this method is relatively slow. The analysis of one sample lasts approximately 20 minutes.

The moisture (H₂O) analyzer with probe placed directly to the CO₂ circuit enables continuous moisture content monitoring. The detection limit is about 1 vppm of H₂O, pressure and temperature limits for the probe are 20 MPa and 70 °C respectively. During operation approx. 40 kg per day of CO₂ was continuously replaced by “new” one (by dosing and blowing off).

SCO₂ PURITY CONTROL DURING SCO₂ OPERATION CAMPAIGN

During the last 1 000 hours operation campaign (in 2019/2020) the monitoring of CO₂ medium purity was performed. The monitoring was aimed to the organic impurities. The source organics in the circulating medium could be the residual oil, degreasers and dissolvents from production and also the leakage of oil e.g. from circulator. During operation of the loop the organics take the chemical reaction by which another compounds may be formed. The topic with more details is commented in citation [16], which deals with reactions of residual organic compounds during High Temperature Helium Loop operation.

Before operation the loop was filled with high-purity CO₂ (4.8), therefore the minimum impurity level from source gas was expected. The sCO₂ loop was operated at a temperature of 550 °C in the test section and a pressure of 20 MPa in the high-pressure section of the loop.

The purity was monitored by sampling of medium during operation. The first sample was taken after 170 operation

hours, the sampling was repeated after 360 and 820 operation hours. The samples were taken by passing the gas through the sampling tubes with the active carbon. The volume of the samples was 10 – 170 l , with a pressure of 100 kPa and temperature of 25 °C. In the next step, the compounds that were adsorbed by the active carbon were desorbed by carbon disulfide, which was subsequently determined by the GC-MS technique.

The amount of the organic compounds in the loop’s medium that were determined in the samples has been recorded in the chart in Figure 3. The contents of the organic impurities in the medium decreased from ca. 1800 to 5 ng.l⁻¹ (at 25°C and 1 bar). In the sample after 170 operation hours several organic compounds contained a large amount of benzene. The relative distribution of the organic compounds in this sample is shown in Figure 4. In the samples after 360 and 820 operation hours, only benzene was detected. The source of the organic compounds in the loop medium could be the residual organics from the loop production, and subsequent conversion by chemical reactions. The amount of organic impurities significantly decreased during the loop operation, which is likely to be due to the continuous new CO₂ dosing in the loop. The amount of undesired organic compounds was significantly lower compared to that during operation of another experimental device (see cit. [16]). Though the compounds were able to be detected by sensitive analytic method based on GC-MS.

Table 4: Chemical composition of alloys exposed in sCO₂ loop (% by weigh)

	C	Mn	Cr	Mo	V	Al	Si	Nb	W	Ni	Ti	Cu	Fe
T92	0.07-0.13	0.3-0.6	8.5-9.5	0.3-0.6	0.15-0.25	0.04 max	0.5max	0.04-0.09	1.5-2.0	0.4 max			Bal.
HR6W	0.1	1.5	21.5-24.5				1.0	0.1-0.35	6.0-8.0	Bal.	0.05-0.20		20-30
HR235	0.06 max	0.65 max	31	5.6		0.4 max	0.6 max	1.0 max		Bal.	0.5 max	3.8	1.5 max
SS 316L	0.21	0.36	16.5	2	<0.001	<0.001	0.34	<0.001	<0.001	10	<0.001	<0.001	Bal.
800 H	0.06	0.7	20.5	<0.001	<0.001	0.28	0.5	0.01	<0.001	30.5	0.34	0.1	46.7
Inconel 738	0.11	-	16	2	-	3.4	-	0.9	2.6	Bal.	-	-	-
Inconel 617	0.05-0.15	1	20-24	8-10	-	0.8-1.5	Max. 1	-	-	Bal.	Max. 0.6	Max. 0.5	Max. 3

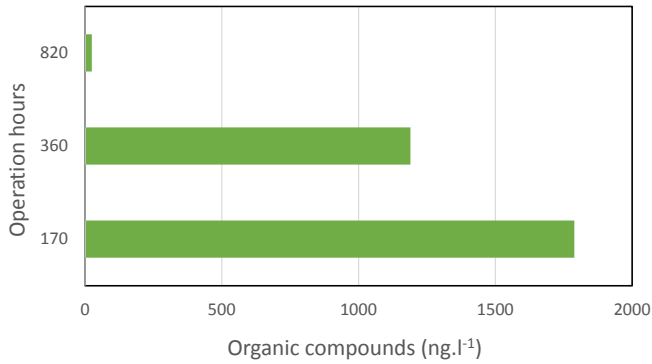


Figure 3: The sum of the organic compounds in the CO₂ medium during sCO₂ loop operation

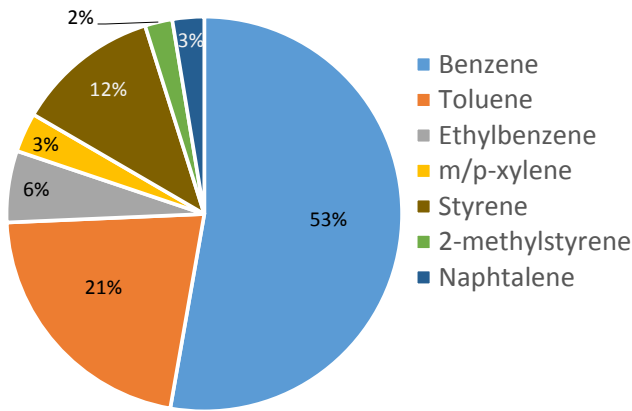


Figure 4: The relative distribution of organic compounds in sCO₂ medium after 170 operation hours

TEST OF MATERIAL DEGRADATION IN SCO₂ LOOP

During 1000 h. sCO₂ loop operation (550 °C@20 MPa) the samples of metallic alloys were exposed in the test section of the loop. In sum about 20 types of alloys were exposed. Some samples were provided with special coating for resistivity enhance. The ferritic (e.g. T92) and austenitic steels (e.g. 316L) and also nickel based alloys (e.g. Inconel 738 and 617) were among tested alloys. The chemical composition of selected alloys is listed in Table 4. The high resistance of some of these alloys was already verified in other environments, mentioned nickel based proved high corrosion resistance and mechanical stability even at temperatures near 900 °C.

After exposure the differences in weigh of samples were recorded and the corrosion and changes of the samples were investigated by using the optical and electron microscopy (Scanning Electron Microscopy with Energy-dispersive X-ray spectroscopy – SEM-EDX). The investigation has been in progress and not all data have not been evaluated in the time of finishing this paper.

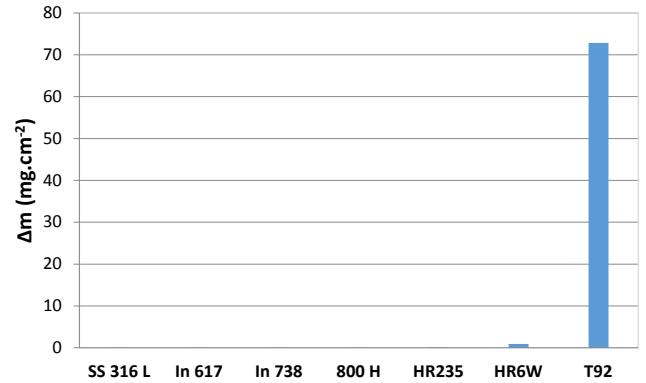


Figure 5: Mass gains of metallic alloys samples after 1000 h exposure in sCO₂ loop (550 °C@20 MPa)

On the chart in Figure 5 the mass gains of (selected) alloys samples are compared. The significant differences among particular alloys are evident. The highest mass gain (almost 100 mg per cm² of sample surface) was stated in case of ferritic steel T92. On the other hand the mass gains of austenitic steels and nickel based alloys were much lower, generally below 1 mg.cm⁻².

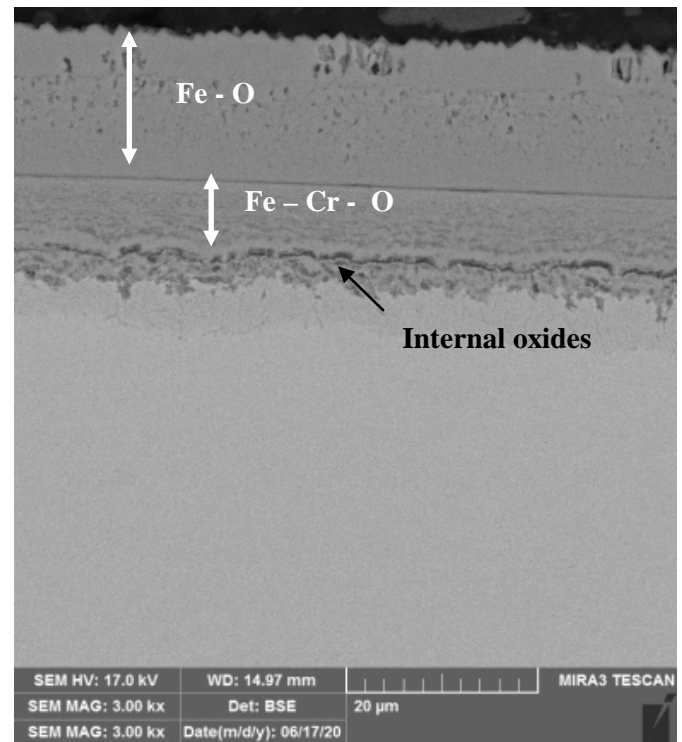


Figure 6: SEM image of sample cross section of ferritic steel T92



Figure 7: SEM image of sample cross section of nickel based alloy HR6W

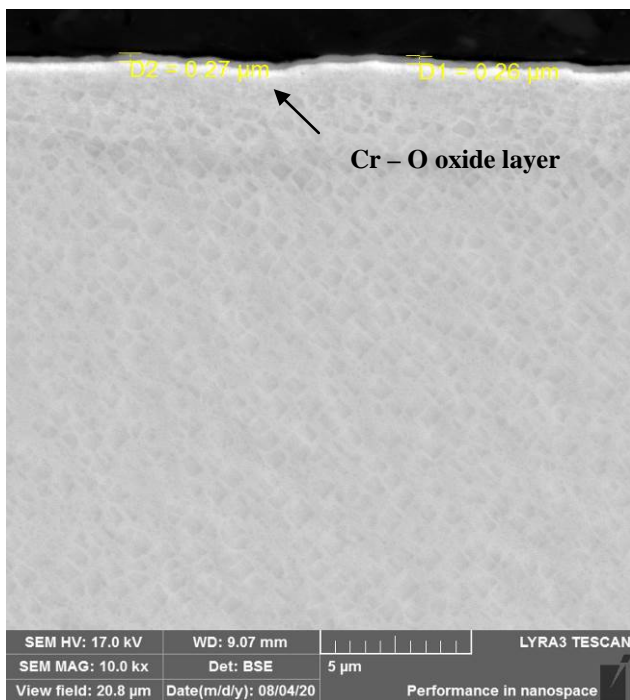


Figure 8: SEM image of sample cross section of nickel based alloy Inconel 738

The differences in mass gains correspond with microscopic observation of sample cross sections. On the surface of ferritic steel P91 the more than 20 μm thick double oxide layer was observed. The outer layer was formed of iron oxides, the inner

layer was formed of iron and chromium oxides (see Figure 6). Under the oxide layer internal oxides were observed. On the surfaces of nickel based alloys only thin chromium layers (thickness about 0.2 – 0.3 μm) were observed. As examples the SEM images of the sample cross section of alloy HR6W (Figure 7) and Inconel 738 (Figure 8) are shown. More results will be available after finalization of samples investigation and evaluation.

CONCLUSION

The organizations from Czech Republic take part of extensive research program of power system using supercritical carbon dioxide. The sCO₂ power cycle chemistry and resistance of materials in sCO₂ are among the research topics. As typical impurities in sCO₂ cycles with indirect heating O₂, H₂O, H₂, CO, CH₄, N₂ and in some case also organic compounds (oil, etc.) were identified. As analytical methods suitable for CO₂ purity control Gas Chromatography with Helium Ionization Detector (GC-HID) connected directly with sampling point of the circuit and optical hygrometer with probe placed directly to the sCO₂ circuit were proposed. The methods will be tested. For trace concentrations of organic compounds determination the Gas Chromatography with Mass Spectrometry detector (GC-MS) can be used. This method was verified by analysis of real samples from sCO₂ loop operation. For separation of impurities from CO₂ the processes based on adsorption will be tested within the continuation of research program.

During the 1000 hours operation of sCO₂ experimental loop (with 550 °C and 20 MPa in test section) the test of material resistance was performed. Samples of about 20 kinds of alloys (ferritic and austenitic steels and nickel based alloys) were exposed in the test section of the loop. The investigation and evaluation of samples corrosion and degradation is not finished yet. However according to the preliminary results the significant corrosion was observed on ferritic steels. The thickness of corrosion layer on T92 was about 20 μm and the internal oxidation under surface layer was also observed. The austenitic steels and nickel base alloys proved high corrosion resistance in sCO₂ at 550 °C. On the samples of these materials only very thin oxide layers after exposure were observed.

The activities will continue in the next years of experimental program.

ACKNOWLEDGEMENTS

The presented work was financially supported by Technology Agency of Czech Republic (TACR) project No. TK02030023.

REFERENCES

- [1] sCO₂ Power Cycles for Fossil Fuels. (2020) Department of Energy. [online]. [vid. 2020-04-03]. Available on: <https://www.energy.gov/sco2-power-cycles/sco2-power-cycles-fossil-fuels>

- [2] E. G. Feher, (1967). "The Supercritical Thermodynamic Power Cycle".
- [3] K. Brun, P. Friedman, R. Dennis, (2017) "Fundamentals and Applications of Supercritical Carbon Dioxide (sCO₂) Based Power Cycles, Woodhead Publishing, Duxford.
- [4] M. Li, H. Zhu, J. Guo, K. Wang, W. Tao, (2017) Applied Thermal Engineering 126, pp. 255–261.
- [5] K. Brun, P. Friedman a R. Dennis, (2017) "Fundamentals and Applications of Supercritical Carbon Dioxide (sCO₂) Based Power Cycles".
- [6] M. Perschilli, A. Kacludis, E. Zdankiewitz, T. Held. (2012) "Supercritical CO₂ Power Cycle Developments and Commercialization: Why sCO₂ can Displace Steam." Power-Gen India & Central Asia, pp. 1–15. Available on: <http://www.echogen.com/documents/why-sco2-can-displace-steam.pdf>
- [7] PRIS - Power Reactor Information System. Operational & Long-Term Shutdown Reactors [online]. Available on: <https://pris.iaea.org/PRIS/WorldStatistics/OperationalReactors/ByType.aspx>
- [8] K. Feik, J. Kmošena. (2010) "Jadrová elektrárň A1 v kocke". Bratislava, Slovakia.
- [9] T Hudský. (2015) "Special purification and purity control methods for advanced nuclear reactors", Diploma thesis, UCT Prague.
- [10] EPA, Environmental Protection Agency. (2015) "Standards of performance for greenhouse gas emissions from new, modified, and reconstructed stationary sources: electric utility generating units"
- [11] EPRI, Electric Power Research Institute. (2014) "Performance and Economic Evaluation of Supercritical CO₂ Power Cycle Coal Gasification Plant"
- [12] C. Dang., K. Hoshika, a E. Hihara (2012) "Effect of Lubricating Oil on the Flow and Heat-Transfer Characteristics of Supercritical Carbon Dioxide". International Journal of Refrigeration 35, pp.1410–1417.
- [13] W. Flaig., R. Mertz, J. Starflinger (2018) "Setup of the supercritical CO₂ test facility "SCARLETT" for basic experimental investigations of a compact heat exchanger for an innovative decay heat removal system". Journal of Nuclear Engineering and Radiation Science 4(3), pp. 1–11
- [14] Cast steel y type strainer. pmtengineers.com [online]. Available on: http://www.pmtengineers.com/images/product/cast_steel_y_ty_pe_strainer.jpg
- [15] J. Berka, J. Matěcha, M. Černý, I. Víden, F. Sus, P. Hájek (2012) "New experimental device for VHTR structural material testing and helium coolant chemistry investigation – High Temperature Helium Loop in NRI Řež" Nuclear Engineering and Design 251 pp. 203–207.
- [16] J. Berka, I. Víden, V. Kozmík (2012), "Organic Compounds Detectable in He Loop of Experimental Research Device for Simulation of Nuclear Reactor Cooling at Opening Operation", Chem. Listy 106, 980 - 987

**CONCEPTUAL DESIGN AND QUALIFICATION OF HIGHLY EFFECTIVE HEAT EXCHANGERS FOR HEAT
REMOVAL sCO₂ BRAYTON CYCLE TO INCREASE THE SAFETY OF NUCLEAR POWER PLANTS**

Sarah Tioual-Demange*

Fives Cryo
Golbey, France
Sarah.tioual-demange@fivesgroup.com

Vivien Voirin

Fives Cryo
Golbey, France

Markus Hofer

IKE – University of Stuttgart
Stuttgart, Germany

Frieder Hecker

KSG | GfS
Essen, Germany

Michael Buck

IKE – University of Stuttgart
Stuttgart, Germany

Jörg Starflinger

IKE – University of Stuttgart
Stuttgart, Germany

ABSTRACT

The sCO₂-4-NPP European project aims to develop an innovative technology based on supercritical CO₂ (sCO₂) for heat removal to improve the safety of current and future nuclear power plants.

The heat removal from the reactor core will be achieved with multiple highly compact self-propellant, self-launching, and self-sustaining cooling system modules, powered by a sCO₂ Brayton cycle.

Heat exchangers are one of the key components required for advanced Brayton cycles using supercritical CO₂. To this end, two compact and highly effective brazed plates and fins heat exchangers are designed:

- a main heat recovery heat exchanger (CHX), which allows the heat transfer directly from the steam generator to the sCO₂-4-NPP cycle,
- a heat sink exchanger (DUHS), which evacuate the remaining heat to the atmosphere.

An important work has been achieved in the frame of this project to conceive the preliminary design of these components, in close collaboration between Fives Cryo, a French brazed plates and fins heat exchangers manufacturer, the Institut für Kernenergetik und Energiesysteme (IKE) of University of Stuttgart and KSG/GfS Institute, a simulator center, both in Germany.

In fact, several constraints needed to be taken into account. For instance, for the DUHS, the low fans power available for the cycle and the necessary air flow for effective heat exchange

implies considering almost inexistent pressure drops on the air side.

To this end, very specific design ideas has been adressed to meet the desired thermal duty.

Also, this project benefits from the recent results achieved among the european project sCO₂-flex, related to the mechanical resistance of heat exchanger components, the assembly process and their thermal and hydraulic performances, along with Fives Cryo expertise and background.

A second challenge of the sCO₂-4-NPP project is to qualify the designed plates and fins heat exchangers, at cycle operating conditions, in order to meet with pressure vessels codes and regulations according to nuclear requirements.

This paper presents the work achieved on the design of DUHS heat exchanger components and a preliminary part of the qualification of this equipment according to nuclear power plants regulations.

INTRODUCTION

Chernobyl and Fukushima Dai-ichi nuclear accidents are one of the worst catastrophes that the world have seen. In fact, both accidents were classified at the 7th level of the International Nuclear and radiological Event Scale (INES) due to the important amount of radioactive rejections.

Fukushima Dai-chi accident, for instance, combined both impacts of nuclear accident and high magnitude earthquake. This earthquake caused degradation of the nuclear installation and a loss of confinement. The earthquake also generated an important Tsunami – with higher waves over 15 meters height -

* corresponding author(s)

which led to a break-down of the primary cooling systems due to deterioration of seawater intakes, leading to reactor cores melting and spent fuel pool overheating. Important environmental, sanitary and psychological impacts were caused by this disaster ([1],[2]).

Avoiding such dramatic accident is the leitmotiv of the European project sCO₂-4-NPP, which started on autumn 2019 for 3 years, by bringing in nuclear power plants an innovative technology to remove excess heat in case of nuclear accidents, based on supercritical CO₂ (sCO₂).

This new technology will constitute a backup cooling system, linked to the secondary cooling loop which is attached to the steam generator of a Pressurized Water Reactor (PWR) (figure 1) or a Boiling Water Reactor (BWR) [3] (figure 2).

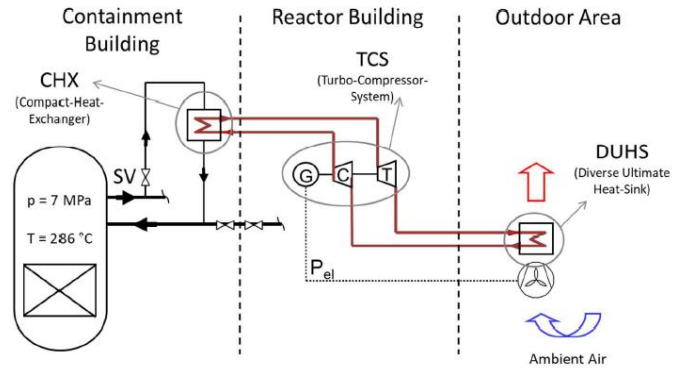


Figure 2: Excess heat removal technology constituting a backup cooling system, linked to the secondary cooling loop which is attached to the steam generator of a Boiling Water Reactor (BWR) [3].

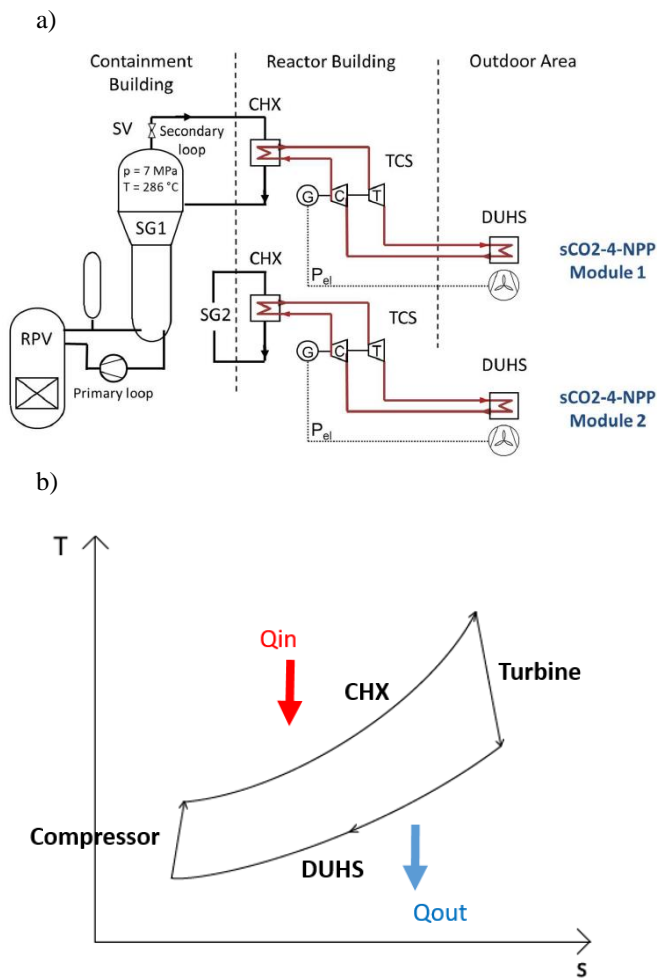


Figure 1: a) Excess heat removal technology constituting a backup cooling system, linked to the secondary cooling loop which is attached to the steam generator of a Pressurized Water Reactor (PWR), and b) the corresponding T-s diagram.

The backup system is based on a closed Brayton thermodynamic cycle ([4],[5]). In case of an accident, a safety valve opens to enable the release of the steam produced by the steam generator into the Compact Heat Exchanger (CHX). The supercritical CO₂ is heated up in the CHX and flows then through the turbine which is linked to the compressor and the generator on the same shaft. The supercritical CO₂ flows through the Diverse Ultimate Heat Sink (DUHS) to be cooled by exchange with ambient air, and then goes through the compressor to restore its initial pressure to flow again in the CHX.

Multiple advantages are given by this back-up cooling system modules. They are highly compact so they will not require any major modifications in existing nuclear power plants, self-propellant, self-sustaining and self-launching. They are completely independent of nuclear power plants which makes them easily able to be retrofitted to existing European reactors.

The work presented in this paper focuses mainly on one of the two heat exchangers components, the DUHS. Several constraints need to be taken into account during the design process. In fact, the heat exchangers need to be as compact as possible in size to fit into the available space outside the reactor building. Also, the design should be achieved according to tough operating conditions. Last but not the least, the heat exchangers must be compliant with the rules given by nuclear power plants codes and regulations for materials, manufacturing processes, quality control and testing aspects.

STATE OF THE ART

Systems implemented for heat removal from european PWRs and BWRs are essentially “active” safety systems. “Active” means that these systems rely on pumps which are

activated by motors, themselves powered by electrical source, to allow the transport of water to cool reactors cores. The majority of back-up systems are electricity-powered. The disadvantages of such active systems are that they require external power supply, and to move important quantities of water, so the reservoirs need to be refilled regularly.

Fukushima Dai-ichi disaster proved the disadvantages of the dependence of these safety systems on energy and water supply. Another major disadvantage is the need for operators interventions while an accident occurs.

The recent developments of light water reactors, “passive” safety systems have emerged. These “passive” systems are powered by natural driving forces such as pressure differences, gravity of density differences; no electrical power supply is then required. The disadvantages are that they are not able to be retrofitted to existing nuclear power plants, but only can accompany newly designed reactors. In fact, they require important space or height for installation because the driving forces are low.

For all the reasons mentioned above, sCO₂-4-NPP heat removal system is an interesting and innovative candidate, since it will be:

- easily retrofitted to existing power plants,
- independent of any external source (water or energy...),
- compact system presenting low fingerprint,
- free of operators intervention need.

Supercritical CO₂ based thermodynamic cycles are the subject of several projects on multiple applications, amongst them, sCO₂-flex project, Echogen, STEP-initiative, NetPower ... ([6], [7], [8], [9]).

For the nuclear applications, different applications are enabled by sCO₂ ([10]). For instance, used in Brayton cycle, it was proven that this fluid is highly effective for energy conversion from nuclear heat to electrical power, suitable for generation IV reactors (lead cooled, sodium cooled and molten salt cooled reactors).

Only one project, sCO₂-Hero, addressed specific nuclear power plant boundary conditions with a suggestion of modular heat removal systems to be attached to existing installation without any external power required. This objective was achieved through the construction of a 200 kW sCO₂ loop in a unique PWR glass model at KSG/GfS ([11], [12], [13], [14]).

The project allowed to reach TRL3 (Technology Readiness Level). Some limitations are still to be investigated further, which will be addressed by sCO₂-4-NPP project.

For heat exchangers, the components need to be designed according to severe transient operating conditions, and since they need to be compact, no use of such technology is available yet in nuclear power plants.

BRAZED PLATES AND FINS HEAT EXCHANGERS TECHNOLOGY DEVELOPPED BY FIVES CRYO

Plates and fins heat exchangers (PFHE) technology was selected for this application since it benefits from important compactness and economic cost. A real asset for this technology is the interesting mechanical properties and integrity which could be enhanced to reach Printed Circuit Heat Exchangers (PCHE) level ([15], [16]), well known for withstanding very high pressure levels and temperature constraints, and mostly used for Brayton cycles applications using supercritical CO₂ ([17], [18]). The low material density in PFHE makes it also very attractive solution in comparison to PCHE.

Figure 3 shows an overview of PFHE concept, where the flows are represented by red, green and blue colors, in order to illustrate the adaptability of such technology. However, sCO₂ Brayton cycles only require 2 fluids.

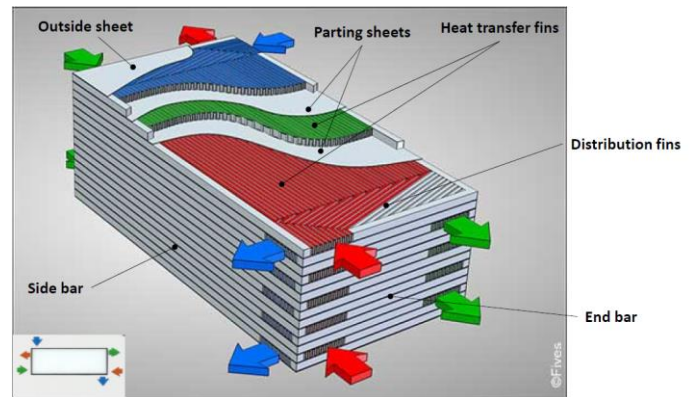


Figure 3: Example of a standard design of a Plates and Fins Heat Exchanger (PFHE) manufactured at Fives Cryo.

A Plates and Fins Heat Exchanger consists of multiple stacked layers, constituted of fins, which are corrugated metal sheets aiming the maximization of heat exchange area. Each fin geometry is characterized by its sheet thickness, fins height, and number of fins per meter. The layers are separated one from the other via parting sheets with a certain thickness, depending on the desired heat exchange; and each layer is closed with lateral bars. The constituted “sandwich” is assembled by diffusion-brazing technique, thanks to filler metal plating on the parting sheets. This filler metal has a liquidus below the solidus of the base metal, which means that the melting point of the filler metal is slightly lower than the base metal. The heat treatment will then allow filler metal melting; after cooling, the filler metal solidifies to ensure all parts cohesion.

After brazing procedure, headers and nozzles are welded on all inlet/outlet sections of the layers (also called “passages”) to allow fluids circulation without mixing, as shown on the **figure 4**.

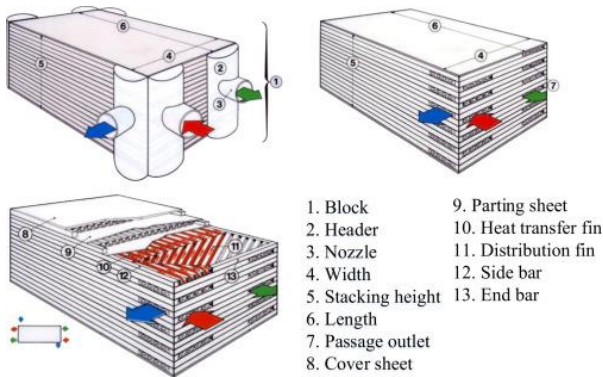


Figure 4: Detailed description of all parts of a brazed Plates and Fins Heat Exchanger (PFHE).

DIVERSE ULTIMATE HEAT SINK (DUHS) DESIGN

Diverse Ultimate Heat Sink (DUHS) design should focus on its size and characteristics, since they are both important elements for nuclear power plants sCO₂ based heat removal system implementation and operation.

In fact, the construction of this system need to be adapted to avoid any breach of nuclear safety and plant security, and resist to heavy weather, earthquake, flooding, pressure waves from detonations and fire, all extreme situations that could lead to reactor malfunction where heat removal system will be needed the most.

Also, penetration of the reactor safety vessel has to be minimized, and the heat removal system has to fit into the existing infrastructure. All piping ways should be as short as possible, in order to be placed as close as possible to the reactor building. To mitigate earthquake relative movement between the components and the reactor building, load from components masses needs to be directed to the basement of the reactor building.

The DUHS heat exchangers components are the most space-consuming, as long with their mass load. A first rough estimation of the area available for DUHS installation is about 540 m² (15 m x 36 m). Since it is not possible to consider an installation as a massive block due to air circulation, a block of 6 cells with a size of 6 m x 15 m each needs to be adopted [19]. 12 Ventilators with about 16' diameter would have been needed, with a shaft power of 46 kW (each), and a pressure of 188 Pa (1.88 mbar) ([3], [19]). The area for heat transfer was given with about 80 000 m², about 76 000 m² for the fins and 4000 m² for the pipe surfaces. From these data, with an effectiveness of 75% for the ventilators, a volume flow of 7.9 x 10⁶ m³/h (some 2200 m³/s) can be estimated.

A way to increase the flexibility to react on decay heat decrease in the long run after shutdown, is to split up the heat removal system into several blocks [3]. Furthermore, equipping each steam generator of a pressurized water reactor with at least one strain would give more flexibility to operate the system not only for heat removal but for steam generator tube leaks (SGTL) too. By definition of a standardized size for such a loop, a modular approach for PWR with different rated power can be taken.

The heat removal capability of one strain should be around 10 MW, where approximately 9.5 MW have to be removed by the DUHS. The maximum air temperature to be considered is 45 °C.

The **table 1** shows the input data used for sCO₂-4-NPP DUHS components design for each unit cell.

FLUID		CO ₂	AIR
TOTAL FLOWRATE	kg/s	30.49	132.49
OPERATING PRESSURE	MPa a	11.92	0.1
ALLOWABLE PRESSURE DROP	kPa	25	0
TEMPERATURE IN	°C	238.66	45
TEMPERATURE OUT	°C	55	115.22
SPECIFIED HEAT TRANSFERRED	MW	9.419	9.419
CORRECTED MTD (GLOBAL)	°C	23.693	

Table 1: Thermodynamic input data used for sCO₂-4-NPP DUHS design.

The calculated output data are shown in **table 2**.

FLUID		CO ₂	AIR
CALCULATED PRESSURE DROP	kPa	8	0
DESIGN TEMPERATURE	°C	-30 °C / 300 °C	
DESIGN PRESSURE	MPa g	23	1
HYDRAULIC TEST PRESSURE	MPa g	29.9	1.3

Table 2: Output design data used for sCO₂-4-NPP DUHS. Calculated pressure drops are considered at nominal flow rate x1

The design leads to 20 heat exchangers cores for each unit, each core has the following dimensions:

- Width : 2000 mm
- Height : 987 mm
- Length : 570 mm

For a total number of 120 cores for all 6 units.

Each core is a counter-flow heat exchanger with a total number of layers of 196 per core.

The layer are distributed as follows:

- 64 layers for CO2
- 128 layers for air
- 4 “dummy” layers, which are inactive layers, 2 on bottom stacking and 2 on top, to guarantee the mechanical integrity of the heat exchangers cores.

The material for DUHS cores construction is 316 Ti stainless steel (UNS number S31635 / W. number 1.4571). This alloy is suitable for brazing-diffusion bonding and it can withstand high temperature and high temperature differences between fluids. It also benefits from a high mechanical strength and corrosion/erosion resistance.

Each layer with a height of 4 mm. Both CO2 and air layers contain “plain” fins but with different geometries, as shown on table 3.

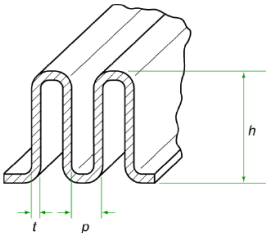
	CO2 side fins	Air side fins
Thickness t (mm)	0.3	0.15
Height h (mm)	4	4
FPM p (Fin Per meter)	787.4	393.7
Geometry of “plain fins”		

Table 3: Output design data used for sCO2-4-NPP DUHS.

The parting sheets between DUHS cores layers are 1 mm thick, external sheets are 4 mm thick.

The thermal performances of our DUHS design are achieved thanks to a smart design: in fact, the stacking pattern used is called “double-banking” [24], leading to an arrangement of 2 air layers against 1 CO2 layer alternatively. Also, for CO2 side, each layer is constituted of 6 passes as shown on figure 3, which allows to connect the headers and nipples on only one side of each heat exchanger core (see figure 5), which is quite practical in order to gain space on the unit.

Therefore, there are no headers intended for air side (table 4), since we consider a circulation through the whole width perpendicularly, with subtracting obviously the lateral bars width, as shown on figure 6; which corresponds to an effective passage width of 1928 mm.

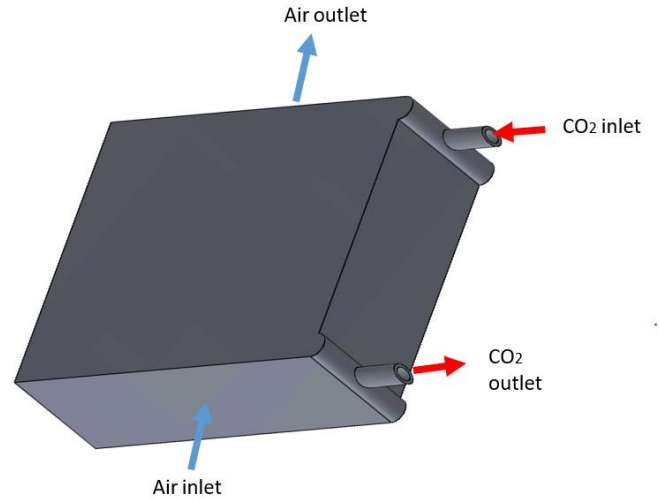


Figure 5: Overall DUHS sketch.

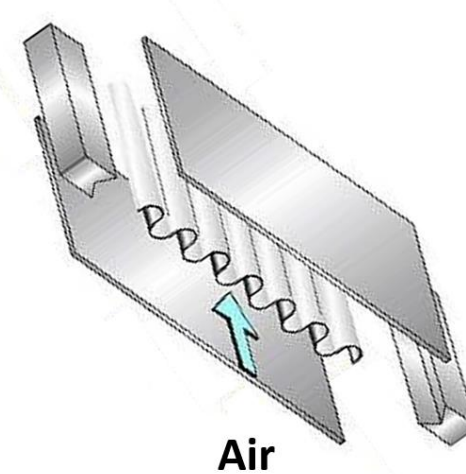
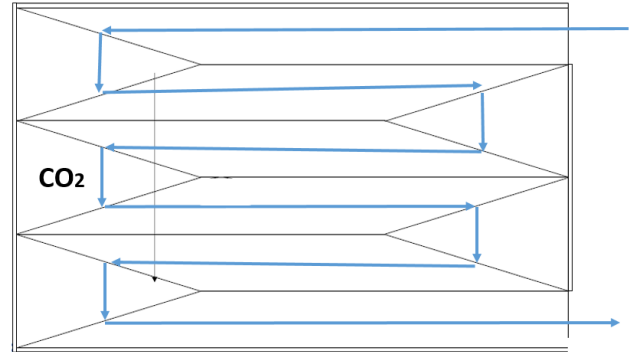


Figure 6: Geometry of CO2 and Air passages. Fluids circulation is indicated with the blue arrows.

FLUID		CO2	AIR
EFFECTIVE PASSAGE WIDTH	mm	83	1928
EFFECTIVE PASSAGE LENGTH	mm	12000	560
TOTAL HEAT TRANSFER AREA	m ²	9376	13581
TOTAL FREE FLOW AREA	cm ²	3002	178802
NOZZLE SIZE (NOMINAL) IN/OUT	mm	2x40	2x40
CONNECTIONS (NOM.) IN/OUT	inch	40 x 1.5	40 x 1.5

Table 4: Output design data used for sCO₂-4-NPP DUHS.

This DUHS design allows to develop a total heat transfer area of 9376 m² for CO₂ and of 13581 m² for air for 1 unit of 10 MW (see **table 4**).

HEAT EXCHANGERS QUALIFICATION ACCORDING TO NUCLEAR POWER PLANTS REGULATION

In addition to sCO₂ cycle heat exchangers design, the project sCO₂-4-NPP aims also to clearly define the qualification strategy for these equipments, including the validation of some key points to assess that the heat exchanger technology is suited for nuclear power plants.

In compliance with the construction code RCC-M [20] and the European Regulation of Nuclear Pressure Vessel [21], Fives Cryo is constituting a note which aim is to present the approach to be followed and the main important and specific documents to be carried out so that the equipment manufactured meets the criteria of the nuclear PED regulation and the selected nuclear construction code. At this stage of the project, not all technical design choices have been yet fixed for the equipments, thus, the qualification methodology needs to be finalized afterwards, and will be presented in full in a future paper.

The documents identified and listed below are considered important for an appropriate design and manufacturing review in accordance with the nuclear PED regulation:

- Risk and hazards analysis (for pressure and radiation aspects) according to the nuclear PED regulation,
- Instruction for use according to the nuclear PED regulation,
- The list of Important Activities for the Protection of Interests (IAPI) according to modified decree BNI 07/02/2012 [22],
- Definition of the Necessary Dimensions to meet the Essential Safety Requirements (NDESR) and control methods,
- The nuclear particular material appraisals according to the nuclear PED regulation,
- The list of material,
- Supply specifications for base metal and filler metal,
- Capacity of inspection in service according to the nuclear PED regulation,

- The program of fabrication,
- The procedures of controls,
- The visual inspection procedure at the end of fabrication,
- The marking procedure,
- The procedure of materials tracing.

For this paper, we will focus on a brief overall description of the content of 4 documents from the previous list:

- Risk and hazards analysis,
- The list of Important Activities for the Protection of Interests (IAPI),
- Definition of the Necessary Dimensions to meet the Essential Safety Requirements (NDESR) and control methods,
- Capacity of inspection in service according to the nuclear PED regulation.

Considering a level 3 defined by the nuclear power plant owner (or nuclear power plant operator) according to ESPN classification, a radiological classification of the system of RP C class and a class 3 according to RCC-M.

1- Risk and hazards analysis

The objectives of the risk and hazards analysis are:

- To identify failure modes (and causes of these failures) which could create operational risks on the pressure aspect and on the radioactivity aspect (hazardous phenomena, such as loss of integrity like fluid leaks or energy release, or noncompliance with the radiological rules),
- To find solutions to remove or reduce (as reasonably possible) the causes of failure. These causes are to be investigated in all phases of life of the equipment (design/manufacture/operation) and for all design situations,
- To identify the applicable essential safety requirements for the equipment.

To this end, it is mandatory to define the physical (as on **figure 7**) and functional description of the heat exchangers required for the heat removal system (as of **figures 1 and 2**).

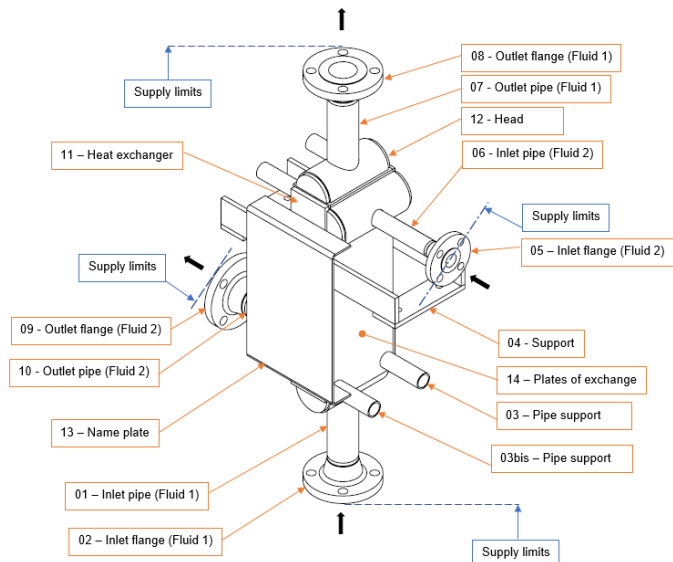


Figure 7: Physical description of a heat exchanger equipment required for risk and hazards analysis.

A functional analysis limited to the circuits defined for the fluids circulating in the heat exchanger is then established (an example is shown on **Annex A**), defining the circuits as blocks, the aim is to specify which parts of the heat exchanger, with its specific designation and function, are in contact with the fluids, and its classification, following :

- PCRFP: Parts contributing to pressure resistance
- PP: Part under pressure
- PDA: Directly Attached Party (and are not PCRFP)

A list of permanent connections and bolted connections on pressure parts also needs to be established, and a list of selected materials limited to the parts contributing to the resistance to pressure, and to the parts and components acting as parades (directly attached parts, part of the supply) as specified on the examples on **Annex A**.

The risk analysis lists also the codes and standards used for design and manufacture (here the RCC-M and European standards), and the regulatory classification of the equipment and allowable limits (minimum and maximum allowable pressures and temperatures). The calculation of the category and level is achieved in accordance with the European Directive [21] and the ESPN order, taking into account the fluid group, the volume per circuit, and the pressures. The classification about radiation protection is also given.

Supply and equipment limitations are an important elements to specify for risk analysis. In fact, we consider that the equipment (in the regulatory sense) consists exclusively of:

- PCRFP (Parts contributing to pressure resistance),
- Parts directly attached to the parts contributing to the pressure resistance.

The supply consists of:

- The regulatory equipment as described above,
- Other elements that are delivered with the equipment, according to a given list.

A specific mention of what the supply does not include is also part of the analysis.

Last but not the least, input data required for risk analysis are to be specified, including:

- Situations and loads; such as charges communicated by the operator in normal operating conditions and Highly Improbable Situations (HIS) and any other charges that could be identified by the manufacturer.
- Aggressions
- Environmental conditions; such as environmental chemistry, ambient conditions and radiological data
- Interface conditions

2- List of Important Activities for the Protection of Interest (IAPI) for ESPN level 3 : equipment manufactured according to RCC-M

This part aims to explain the measures taken by the manufacturer of the heat exchangers, to meet the requirements contract reflecting the requirements of the BNI order [22] for supplies important to safety (IPS) in nuclear power plants. It lists the Important Activities for the Protection of Interests (IAPI) and associated Technical Controls (TC) for the design, the procurement/subcontracting and for the manufacturing (see tables in **Annex B**).

3- Definition of the Necessary Dimensions to meet the Essential Safety Requirements (NDES) and control methods

The purpose of this document is to define the NDES, such as shapes, uncertainty measurements, resolution, maximum allowable error, specification limits and tolerances; the control of these NDES and the traceability of the controls in compliance with the regulation [21] and [23] for the heat exchangers components.

The NDES are the regulatory dimensions in connection with:

- The pressure risks: these NDES are the dimensions for which non-compliance with the specifications call into question the results of design related to applicable Essential Safety Requirements (ESR). These are the dimensions (input data and/or output data), considered important by the manufacturer for the pressure risks at the design stage, in the implementation of equations for design by formula or in calculation models for a design by analysis.

- The radiological risks: these are the dimensions that make it possible to satisfy radiation protection requirements. For example, this can be the slope of a flow, the roughness of a part...
- The overpressure protection: these are the dimensions related to compliance with the protection against overpressure. For example, the flow diameter (for an injection nozzle) or the stroke of a safety accessory...
- An identified dimension during the risks / hazards analysis.

The equipment technical drawing is the mean to identify these NDESR. This identification is based on a dialogue between design teams and manufacturing teams to ensure that the identified NDESR are measurable during manufacturing stage, either directly or indirectly.

The identified NDESR are given in Annex C of this document.

This table gives:

- The reference and the designation of the NDESR,
- The reference of the drawing,
- The design value of the NDESR,
- The specification limit for this value,
- The stage of control/measurement,
- The measuring devices,
- The resolution of the measuring device.

The NDESR are generally:

- Thicknesses of parts for the pressure resistance (thickness of flanges, of heads, of cones, of pipes...),
- Inside or outside diameters of parts for the pressure resistance,
- Geometry of threads,
- Radii of connections ...

For these NDESR control and measurement, a control procedure is established: a document defining the procedures allowing to assess the conformity of an equipment with the technical drawings.

This procedure must contain the following parts:

- Scope (equipment...),
- Applicable documents,
- Reference documents,
- Required qualifications for the operators in charge of the control / measurement,
- Preparation of surfaces and ambient conditions (degreasing, cleaning, temperature ...),
- Measurement method:

- o Geometry of the part, type and range of dimension,
- o Measuring device with its measuring range and its resolution,
- o Units,
- o Accessibility, configuration of the part,
- Extent of control,
- Stage of control,
- Verification of measurement tools,
- Rules for the sampling,
- Measurement uncertainty of measuring devices,
- Compliance criteria,
- Recording methods of control / measurement,
- Report content.

4- Capacity of inspection in service according to the nuclear PED regulation

The purpose of this last document is to report and justify of the inspectability of the heat exchangers in compliance with the PED and the nuclear regulation [21], to ensure a permanent safety of the equipment (after the first commissioning by the owner) and to ensure the radiation protection of the stakeholders performing the inspection of the equipment.

The manufacturer must ensure the feasibility of inspections (visual, dimensional, NDT, etc.) to meet the needs identified in the risks analysis and reported in the instruction for use manual. This feasibility includes an analysis of the adequacy between the suggested means of examination and:

- The geometry,
- The accessibility,
- The grade,
- The type of degradations,
- The conditions of radiation protection.

The assumptions considered for this analysis are as follows:

- o Insulation is removable,
- o Equipment is decontaminated before inspection,
- o Surfaces are clean,

The necessary inspection for the in-service safety (internal / external) shall be realized equipment without fluid, without pressure and at room temperature.

If the fluid is radioactive, surfaces that may be touched during the inspection should be cleaned beforehand to limit contamination.

The in-service safety inspection are carried out under the responsibility of the power plant operator by qualified and

competent personnel who shall be able to identify the potential defects and degradations and to assess their severity.

These actions are carried out under the responsibility of the power plant operator who is in charge of shutting down the installations.

The accessibility to the equipment and environment where it is installed shall be clearly defined and indicated by the power plant operator. A specific attention is given to the definition of the area classification in terms of radiation, and the dose rate is calculated. It is recommended to make a dosimetric survey of the area in order to establish the most accurate dose rate.

However, the classification of the area may change, it is imperative to check the nuclear power plant operator's radiation protection map at the time of inspection.

Also, it is the responsibility of the operator to make available the necessary means (scaffolding...) for the inspection of the equipment in accordance with the regulations.

Equipment inspection occurs in 2 major steps: internally and externally.

Internal inspection applies to all internal surfaces accessible without compromising the pressure vessel integrity, as follows:

- Internal surfaces of the elements subjecting to pressure,
- Internal surfaces of the inlet and outlet nozzles and flanges,
- Internal surfaces of welds,
- Surfaces of accessible internal elements in the equipment (some parts of distribution fins...)

Internal inspection can be carried out with an endoscope, which could be accessorized with a pole to limit the exposure of hands.

External inspection of the equipment is applied on its external surface, which includes:

- External surfaces of the elements subject to pressure and attached parts on equipment,
- External surfaces of the inlet and outlet nozzles and flanges,
- External surfaces of welds.

Insulation of the equipment shall be removed. External surfaces of the equipment (external sheets, headers, pipes, welds...) shall be inspected by installing specific means of access. The welds are all marked on technical drawings of the equipment.

Generally, only a direct visual control is required. In case of doubt, a dye penetrant test can be carried out.

An example of an inspection table specifying areas to be controlled, defects to be detected, means of inspection and estimated duration for inspection is presented in **Annex D**.

CONCLUSION

The sCO₂-4-NPP project aims to develop an innovative technology based on a Brayton cycle using supercritical CO₂ for heat removal to improve the safety of current and future nuclear power plants.

The cycle's components are subject to severe operating conditions due to the nature of this working fluid. In particular, heat exchangers are equipments confronted to high levels of pressure and temperature.

The prior usual choice for this application is PCHE technology, thanks to its thermal and hydraulic performances but especially for its mechanical integrity. PFHE developed at Fives Cryo, thanks to its higher compactness at a moderate cost, could be a better choice for sCO₂ Brayton cycle applications if its mechanical and corrosion resistance are improved.

To that end, a new development is performed: in the frame of sCO₂-4-NPP project and its precursor sCO₂ flex project [9], Fives Cryo develops the design and manufacturing of stainless steel heat exchangers.

An additional important step is also to qualify the designed heat exchangers according to regulatory and licensing requirements dedicated to nuclear power plants environment. Some overall regulatory aspects are addressed in this paper.

Interesting progress was achieved on these topics. This gives a fair confidence to succeed in PFHE technology qualification to be part of future sCO₂ Brayton cycles for heat removal in nuclear power plants, by the end of the sCO₂-4-NPP project.

NOTATIONS TABLE

sCO₂: Supercritical CO₂

CHX: Compact Heat eXchanger

DUHS: Diverse Ultimate Heat Sink

PWR: Pressurized Water Reactor

BWR: Boiling Water Reactor

PFHE: Plates and Fins Heat Exchanger

PCHE: Print Circuit Heat Exchanger

HIS: Highly Improbable Situation

TC: Technical Controls

NDESR: Necessary Dimensions to meet the Essential Safety Requirements

ESR: Essential Safety Requirements

DESIGN CALCULATIONS TABLE

Effective passage width:

For CO₂, width of the passes

For AIR, heat exchanger width – lateral bars (2000-2x36)

Effective passage length:

For CO₂, number of passes x heat exchanger width (6 x 2)

For AIR, heat exchanger length – 5mm indent at each side

Total heat transfer area:

Number of cores x number of layers / core x effective width x effective length x fins area / m²

Total free flow area:

Number of cores x number of layers / core x effective width x fin free flow area / m

Air flow rate:

It has been calculated to balance the exchanger in terms of heat. The Brazed plate fin heat exchanger are usually insulated, and consequently, we do not consider any heat leak to the outside.

ACKNOWLEDGEMENTS

This project has received funding from the Euratom research and training programme 2014- 2018 under grant agreements No 662116 (sCO₂-Hero), No 764690 (sCO₂-Flex) and No 847606 (sCO₂-4-NPP).



DISCLAIMER

“This text reflects only the author’s view and the Commission is not liable for any use that may be made of the information contained therein.”

REFERENCES

- [1] Yotaro Hatamura (2015). The 2011 Fukushima Nuclear Power Plant Accident, How and Why it Happened. Elsevier Ltd.
- [2] Tomoyuki Kobayashi (2019). Social Identity Threats Following the Fukushima Nuclear Accident and its Influence on Psychological Distress. Japan

- [3] Jeanne Venker (2015). Development and Validation of Models for Simulation of Supercritical Carbon Dioxide Brayton Cycle and Application to Self-Propelling Heat Removal Systems in Boiling Water Reactors. Germany
- [4] M. E. Siddiqui (2018). Energy Analysis of the S-CO₂ Brayton Cycle with Improved Heat Regeneration. Saudi Arabia.
- [5] K. R. Zada (2018). Analysis of Supercritical CO₂ Brayton Cycle Recuperative Heat Exchanger Size and Capital Cost with Variation of Layout Design. USA.
- [6] <https://www.sco2-flex.eu/>
- [7] <https://www.echogen.com/>
- [8] <https://www.step-initiative.org/>
- [9] <https://netpower.com/>
- [10] Houbo Qi (2018). The Application of Supercritical CO₂ in Nuclear Engineering : A Review. USA.
- [11] <http://www.sco2-hero.eu/>
- [12] Marcel Straët (2017). Cycle Calculations of a Small-Scale Heat Removal System with Supercritical CO₂ as Working Fluid. Germany.
- [13] Alexander Hacks (2018). Turbomachine Design for Supercritical Carbon Dioxide within the sCO₂-Hero.eu Project. Germany.
- [14] Ales Vojacek (2018). Performance Test of the Air-Cooled Finned-Tube sCO₂ Sink Heat Exchanger. Czech Republic.
- [15] Sarah Tioual-Demange (2019). Highly Efficient Plate-Fin Heat Exchanger (PFHE) Technical Development for s-CO₂ Power Cycles. France.
- [16] Sarah Tioual-Demange (2020). Industrial Technical Development and Qualification of Highly Efficient Stainless Steel Plates and Fins Heat Exchanger For Heat Removal Supercritical CO₂ Brayton Cycle Applied to Nuclear Power Plants. France.
- [17] D. Shiferaw (2016). Economic Analysis of sCO₂ Cycles with PCHE Recuperator Design Optimisation. USA.
- [18] I. Jentz (2015). Modeling the Mechanical Integrity of Airfoil Printed Circuit Heat Exchangers. USA.
- [19] GEA (2013). Luftkühler – Datenblatt. Luftgekühlter Wärmetauscher für CO₂. Germany.
- [20] AFCEN RCC-M (Rules of Conception and Construction of Mechanical Equipments for Nuclear Sites 2018 edition).
- [21] PED Directive 2014/68/EU on the harmonization of the laws of EU member states concerning pressure vessels construction.
- [22] Order of 07/02/2012 on General Rules on Basic Nuclear Installations (BNI).
- [23] Order of 30/12/15 on nuclear pressure vessels and safety accessories for pressure vessels protection.
- [24] K. Nikitin (2006). Printed Circuit Heat Exchanger Thermal-Hydraulic Performance in Supercritical CO₂ Experimental Loop. Japan.

ANNEX A

EXAMPLES FOR PHYSICAL AND FUNCTIONAL ANALYSIS

1- Functional analysis table (limited to the blocks “circuit 1” and “circuit 2”)

Block	Part number	Designation	Function	Component classification (Part)	Part in contact with the fluid
Circuit 1	01	Inlet pipe	Inlet nozzle for fluid 1	PP	Yes
Circuit 1	02	Inlet flange	Inlet nozzle for fluid 1	PP	Yes
	03 / 03bis	Pipe support	To maintain exchanger in service	PDA	No
	04	Support	To maintain exchanger in service	PCRP	No
Circuit 2	05	Inlet flange	Inlet nozzle for fluid 2	PP	Yes
Circuit 2	06	Inlet pipe	Inlet nozzle for fluid 2	PP	Yes
Circuit 1	07	Outlet pipe	Outlet nozzle for fluid 1	PP	Yes
Circuit 1	08	Outlet flange	Outlet nozzle for fluid 1	PP	Yes
Circuit 2	09	Outlet flange	Outlet nozzle for fluid 2	PP	Yes
Circuit 2	10	Outlet pipe	Outlet nozzle for fluid 2	PP	Yes
Circuit 1 and 2	11	Heat exchanger	To ensure heat transfer between two fluids	PP	Yes
Circuit 1 and 2	12	Head		PP	Yes
	13	Name plate	To identify the unit	PDA	No
Circuit 1 and 2	14	Plates of exchange	participates in heat transfer between two fluids	PP	Yes

- PCRP: Parts contributing to pressure resistance
- PP: Part under pressure
- PDA: Directly Attached Party (and are not PCRP)

2- List of permanent connections and bolted connections on pressure parts

*The numbers corresponds to **figure 7** above*

Designation	Type	Classification		
		Assembly on the parts contributing to the resistance to pressure (and which are not parts under pressure)		
		Resuming the pressure forces	Tightness	Other
Assembly between pipe nozzle (01,06,07,10) and head (12)	<u>Welded</u>	X		
Assembly between Support (04) and heat exchanger (11)	<u>Welded</u>	X		
Assembly between plate of exchange (14)	<u>Brazing</u>	X	X	
Assembly between pipe nozzle (01,06,07,10) and flange nozzle (02,05,08,09)	<u>Welded</u>	X		
Assembly between heat exchanger (11) and head (12)	<u>Welded</u>	X		

3- Selected materials (table limited to parts contributing to the resistance to pressure, to the parts and components acting as parades (directly attached parts, part of the supply), to the parts and components acting as parades, for the blocks "circuit 1" and "circuit 2")

Component	Part number	Materials	Reference
Inlet pipe	01	Austenitic Stainless steel	Z2 CND 17-12 according to STR M3304
Inlet flange	02	Austenitic Stainless steel	Z2 CND 17-12 according to STR M3301
Pipe	03	Austenitic Stainless steel	Z2 CND 17-12 according to STR M3304
Support	04	Austenitic Stainless steel	Z2 CND 17-12 according to STR M3307
Inlet flange	05	Austenitic Stainless steel	Z2 CND 17-12 according to STR M3301
Inlet pipe	06	Austenitic Stainless steel	Z2 CND 17-12 according to STR M3304
Outlet pipe	07	Austenitic Stainless steel	Z2 CND 17-12 according to STR M3304
Outlet flange	08	Austenitic Stainless steel	Z2 CND 17-12 according to STR M3301
Outlet flange	09	Austenitic Stainless steel	Z2 CND 17-12 according to STR M3301
Outlet pipe	10	Austenitic Stainless steel	Z2 CND 17-12 according to STR M3304
Heat exchanger	11	Austenitic Stainless steel	
Head	12	Austenitic Stainless steel	
Name plate	13	Austenitic Stainless steel	Z2 CND 17-12 according to STR M3307
Plates of exchange	14	Austenitic Stainless steel	Z2 CND 17-12 according to STR M3307

ANNEX B

LIST OF IAPI AND ASSOCIATED TECHNICAL CONTROLS

1- For design

	AIP	Defined requirements			Associated Technical Controls		
		Main characteristics and/or parameters of the RCC-M	Information necessary for carrying out operations	Recording	Type	Recording	
Design	1	Studies / design	Allowable stresses Grades Thicknesses (dimensions) Corrosion allowance Drawings	Input Data : => Design temperatures (mini/maxi) / design pressures (mini/maxi) => Fluids => Seismic studies => Regulatory and radiation data from the Operator => Specification of equipment => Load cases to be taken into account for each situation	- Calculation note of pressure vessel - Calculation note of Supports - Drawings - Risks and Hazards Pressure and Radiation analysis	Carrying out the technical control of the studies : - Calculation notes - Drawings - Procurement specifications - Manufacturing and test procedures. Verification of study documents by individuals different from those that made them	Visa of the first page of each document Visa of checking sheets
	2	Studies / preparation	Provisional chronological list of procurement operations, of manufacturing operations, of control operations and of testing operations	Input data : => Procurement specification from Operator => Regulatory and radiation data from the Operator => Drawings BPE => Manufacturing and test procedures	- List of applicable documents - Follow up document - Welding book - Welding tracking forms - Brazing book	Verification by Quality Department Verification by Welding Department Verification of documents (welding book, brazing book, welding tracking forms...) by individuals different from those that made them	Visa of the first page of each document

	AIP	Defined requirements			Associated Technical Controls	
		Main characteristics and/or parameters of the RCC-M	Information necessary for carrying out operations	Recording	Type	Recording
Procurement / Subcontracting	10	<ul style="list-style-type: none"> - Dimensions - Marking - Chemical analysis - Mechanical properties - Corrosion test - Defects in the material after transformation (forging, casting...) 	<ul style="list-style-type: none"> - Draw ings - Procurement material specifications - Subcontracting order 	<ul style="list-style-type: none"> - Report / certificate of material from provider - Folow up document 	<ul style="list-style-type: none"> - Verification at reception of material by warehouse site of the material / parts - Verification at reception by quality personnel of the report / certificate of material - Quantitative and qualitative verification 	<ul style="list-style-type: none"> - Visa of follow up document
	20	<ul style="list-style-type: none"> - Mechanical properties - Metallurgical structure 	<ul style="list-style-type: none"> - Used furnace - Thermocouple (nb, mark, location) - Identification of the part - Position of the part in the furnace - Description of the thermal cycle - Sample of mechanical test 	<ul style="list-style-type: none"> - Records of heat treatment - Records of mechanical tests - Temperatures diagrammes for furnace and material / parts (during heat treatment) 	<ul style="list-style-type: none"> - Validation of the different steps of heat treatment - Verification of the recorded curves - Verification of the mechanical characteristics 	<ul style="list-style-type: none"> - Visa of follow up documents of provider - Eventual visa of other documents associated to verification
	30	<ul style="list-style-type: none"> - Defects in the fabrication of the part - Weld / brazing defects 	<ul style="list-style-type: none"> - Interpretation - Devices used - Mark of blocks control - Personnel - Adjustments - Parameters of radio examination - Radio element used - X ray cassette composition - Exposure time - Elements / chemicals for radiogram developing - Recording of control results 	<ul style="list-style-type: none"> - Procedures - Reports of examinations - Radiogramms - Data acquisition 	<ul style="list-style-type: none"> - Verification of information necessary for carrying out operations - Film sample replay (at least 3% of radiograms) - Verification of application of procedures (UT/RT) - Verification of used parameters (RT/UT) - Verification of examinations reports - Verification of the qualification of testing personnel - Verification of testing procedures RT/UT by certified Expert level 3 and by EDF - Validation NDT procedure by the manufacturer - Verification of the calibration of used devices 	<ul style="list-style-type: none"> - Visa of follow up documents of provider - Eventual visa of other documents associated to verification
	40	<ul style="list-style-type: none"> - Application of RCC-M Part F - Qualification of procedure if necessary - Thickness, coat of paint - Paint system used 	<ul style="list-style-type: none"> - Specification of Client / Operator 	<ul style="list-style-type: none"> - Report of thickness - Report of adhesion 	<ul style="list-style-type: none"> - Verification of personnel qualifications for painting - Calibration of used devices - Verification of temperature and humidity - Verification of conditioning / packaging with products for use in nuclear power plant - Verification of painting according to procedures - Verification of reports (thickness and adhesion) 	<ul style="list-style-type: none"> - Visa of follow up documents of provider - Eventual visa of other documents associated to verification
	50	<ul style="list-style-type: none"> - Surfaces, denseness - Technological defects - Dimensional visual - Chemical analysis - Mechanical properties - Appropriate metallurgical structure 	<ul style="list-style-type: none"> - Welding / brazing procedure forms (w elding energy...) - Chemical analysis for filler metal and base metal - Skills of welders / brazers / personnel - Non destructive tests to be realized 	<ul style="list-style-type: none"> - Qualification of procedure welding / brazing reports (QMOS) - Records of welders / personnel qualification - Acceptance form of filler metal - Tracking forms for welding and brazing - Reports of examinations 	<ul style="list-style-type: none"> - Verification of approval of welding book and brazing - Verification of welders qualifications - Verification of results for dimensionnal and visual inspection - Verification of filler metal lots - Verification of appropriate welding / brazing procedures forms - Verification of results for non destructive tests (surfacic and volumetric) - Realization of specimens coupons - Verification of eventual repairs 	<ul style="list-style-type: none"> - Visa of follow up documents of provider - Eventual visa of other documents associated to verification

	AIP	Defined requirements			Associated Technical Controls		
		Main characteristics and/or parameters of the RCC-M	Information necessary for carrying out operations	Recording	Type	Recording	
Fabrication	100	Receipt/Identification of supplier and/or prefabricated material	Compliance with contractuel requirements	<ul style="list-style-type: none"> - Procurement specification - Drawings - Inspection certificate / Fabrication report 	Visa on the follow up document	Quantitative and qualitative verification	Visa on the follow up document
	200	Non destructive volumetric testing of welds	Weld defects	<ul style="list-style-type: none"> - Interpretation - Devices used - Mark of blocks control - Personnel - Adjustments - Parameters of radio examination - Radio element used - X ray cassette composition - Exposure time - Elements / chemicals for radiogram developing - Recording of control results 	<ul style="list-style-type: none"> - Procedures - Reports of examinations - Radiograms - Data acquisition 	<ul style="list-style-type: none"> - Verification of information necessary for carrying out operations - Films sample replay (at least 3% of radiograms) - Verification of application of procedures (UT/RT) - Verification of used parameters (RT/UT) - Verification of examinations reports - Verification of the qualification of testing personnel - Verification of testing procedures RT/UT by certified Expert level 3 and by EDF 	<ul style="list-style-type: none"> - Visa of follow up documents - Eventual visa of other documents associated to verification
	300	Machining (bevel, drilling...)	Dimensions	Procedure of welding / brazin	<ul style="list-style-type: none"> - Report of dimensionnal / visual inspection - Report of dye penetrant test 	<ul style="list-style-type: none"> - Verification of necessary informations - Verification of application of applicable procedures - Verification of records of dye penetrant test - Verification of the qualification of personnel in charge of examination 	<ul style="list-style-type: none"> - Visa of follow up documents - Eventual visa of other documents associated to verification
	400	Forming (hot bending, cold bending, rolling...)	<ul style="list-style-type: none"> - Affected materials (dimensions, denseness, physical properties...) - Technological defects - Mechanical properties - Residual stresses 	<ul style="list-style-type: none"> - Qualification of forming - Heat treatment - Skills of the personnel 	<ul style="list-style-type: none"> - Report of the parameters - Trackings heets 	<ul style="list-style-type: none"> - Reports of forming procedures qualifications - Verification of forming parameters in workshop - Realization of specimens coupons 	<ul style="list-style-type: none"> - Visa of follow up documents - Eventual visa of other documents associated to verification
	500	Implementation of permanent ass embles (marking, welding, brazing, buttering, weld adding...)	<ul style="list-style-type: none"> - Surfaces, denseness - Technological defects - Dimensional visual - Chemical analysis - Mechanical properties - Appropriate metallurgical structure 	<ul style="list-style-type: none"> - Welding / brazing procedure forms (welding energy...) - Chemical analysis for filer metal and base metal - Skills of welders / brazers personnel - Non destructive tests to be realized 	<ul style="list-style-type: none"> - Qualification of procedure welding / brazing reports (QMOS) - Records of welders / brazer / personnel qualification - Acceptance form of filer metal - Tracking forms for welding and brazing - Reports of examinations 	<ul style="list-style-type: none"> - Verification of approval of welding book and brazing book - Verification of welders / brazers qualifications - Verification of results for dimensionnal and visual inspection - Verification of filer metal lots - Verification of appropriate welding / brazing procedures forms - Verification of results for non destructive tests (surfacic and volumetric) - Realization of specimens coupons - Verification of eventual repairs - Verification of welding / brazing parameters (first application by procedure and by personnel and by site) 	<ul style="list-style-type: none"> - Visa of follow up documents - Eventual visa of other documents associated to verification
	600	Geat treatment (partial simulated, final)	<ul style="list-style-type: none"> - Mechanical properties - Metallurgical structure 	<ul style="list-style-type: none"> - Used furnace - Thermocouple (nb, mark, location) - Identification of the part - Position of the part in the furnace - Description of the thermal cycle - Sample of mechanical test 	<ul style="list-style-type: none"> - Records of the heat treatment - Records of mechanical tests - Temperatures diagrammes furnace and parts (during heat treatment) 	<ul style="list-style-type: none"> - Presence during the differents steps of heat treatments - Verification of the recorded curves - Verification of the mechanical characteristics 	<ul style="list-style-type: none"> - Visa of follow up documents - Eventual visa of other documents associated to verification
	700	Cleaning	<ul style="list-style-type: none"> - Management of temporary elements - Risk management for Foreign Material Exclusion FME - Elimination of foreign material 	<ul style="list-style-type: none"> - Installation - Removal 	Follow up document	<ul style="list-style-type: none"> - Verification of the installation and removal procedures - Verification of the removal of temporary elements and FME (by internal and external visual inspection) 	<ul style="list-style-type: none"> - Visa of follow up documents - Eventual visa of other documents associated to verification
	800	Assembly of static equipment (flanges, piping, nozzles...)	<ul style="list-style-type: none"> - Completion of pressure equipment - Presence of all compliant assemblies - Documents for hydraulic test / burst test - Tightening of flanges - Identification / marking of equipment 	<ul style="list-style-type: none"> - Follow up fabrication - Follow up assemblies - Form for hydraulic test and burst test - Drawings 	<ul style="list-style-type: none"> - Follow up document - Procedure for hydraulic test and burst test - Records / reports 	<ul style="list-style-type: none"> - Verification of tightening flanges - Verification of approval of hydraulic test procedures and burst test procedure - Realization of hydraulic test and burst test of equipment - Verification of non conformity forms 	<ul style="list-style-type: none"> - Visa of follow up documents - Report for hydraulic test - Report of burst test - Eventual visa of other documents associated to verification

ANNEX C

LIST OF NDESR (OR DNRE)

References DNRE	Designation of part	DNRE of the part	Value to be measured	Specification limits from design	Specification limits reduced by EMT	Procurement standard	Drawing reference	Control stage	Measuring device	Measuring range (Resolution) of measuring device
A1	Head outlet fluid 1	External diameter of pipe nozzle	60.3 mm	± 1 mm	± 1 mm	NFEN10216-5	xxx	Procurement	Calliper	0-300 (0,01)
A2		Thickness of pipe nozzle	2.6 mm	± 0,1 mm	± 0,07 mm	NFEN10216-5	xxx	Procurement	Measuring arm	0-60 (0,03)
A3		Position of nozzle on head	200.0 mm	± 2,0 mm	± 1 mm	-	xxx	After permanent assembly	Tape measure	0-300 (1)
A4		Closure end diameter	88.9 mm	± 1 mm	± 1 mm	NFEN10216-5	xxx	Procurement	Calliper	0-300 (0,01)
A5		Closure end thickness	3.2 mm	± 0,1 mm	± 0,07 mm	NFEN10216-5	xxx	Procurement	Measuring arm	0-60 (0,03)
A6		Outside diameter flange	19.0 mm	± 0,1 mm	± 0,07 mm	NFEN1092-1	xxx	Procurement	Measuring arm	0-60 (0,03)
A7		Diameter drilling flange	100.0 mm	± 2,0 mm	± 2,0 mm	NFEN1092-1	xxx	Procurement	Calliper	0-150 à 0-300 (0,01)
B1	Support	Weld throat pipe support / plate	4.0 mm	min	4.1 mm mini	-	xxx	After assembly	Throat measuring	0-20 (0,1)
B2		Position of support	200.0 mm	± 2,0 mm	± 1 mm	-	xxx	After permanent assembly	Tape measure	0-300 (1)
R1	All	Internal roughness	3,2 ou 6,3 microm	mini	mini	-	xxx	After permanent assembly	Visual touch pad	-
U1	All	Out of roundness	2,0 mm	maxi	2,0 mm maxi	-	xxx	Procurement	Calliper	0-300 (0,01)
T11	Sampling	Thickness of fin	1,0 mm	± 0,1 mm	± 0,07 mm	NFEN10028-7	xxx	After forming and brazing	Measuring arm	0-60 (0,03)
H11		Heigh of fin	50,0 mm	± 1 mm	± 1 mm	NFEN10028-7	xxx	After forming and brazing	Calliper	0-300 (0,01)
F11		Fins Per Inch (FPI)	20,0 mm	± 1 mm	± 1 mm	NFEN10028-7	xxx	After forming and brazing	Calliper	0-300 (0,01)
yyy	yyy	yyy	yyy	yyy	yyy	yyy	yyy	yyy	yyy	yyy

ANNEX D

EXAMPLE OF EXTERNAL INSPECTION TABLE

<i>Area to be inspected / controlled</i>	<i>Defects to be detected (residual risks of hazards analysis)</i>	<i>Means of inspection</i>	<i>Estimated duration</i>
Entire equipment except welds	Control as complete as possible to identify: <ul style="list-style-type: none"> - Possible traces of corrosion (pitting, presence of corrosion products cracking, heat-insulating corrosion...) - Mechanical failure (deformations, shocks, cracks, fatigue...) 	Direct visual control Eye + lighting	25 min
Circular weld C1	Identical	Direct visual control Eye + lighting	10 min
Circular weld C2	Identical	Direct visual control Eye + lighting	10 min
Weld L1	Identical	This weld is accessible and can be seen directly on half of its perimeter. Since the weld is subjected to the same operating conditions throughout its circumference, it is considered that the visible half is representative of the non-visible half.	5 min
Flange nozzle outlet fluid 1	Check absence of sagging and the condition of the flange facing when removing the flanges	Direct visual control Eye + lighting	5 min
Flange nozzle inlet fluid 1	Check absence of sagging and the condition of the flange facing when removing the flanges	Direct visual control Eye + lighting	5 min
Flange nozzle outlet fluid 2	Check absence of sagging and the condition of the flange facing when removing the flanges	Direct visual control Eye + lighting	5 min
Flange nozzle inlet fluid 2	Check absence of sagging and the condition of the flange facing when removing the flanges	Direct visual control Eye + lighting	5 min
Critical part detected	Loss of thickness if necessary	Measurement of residual thickness by US (by external side)	

Total estimated duration for the external inspection of equipment: xx min.

THERMAL EFFICIENCY GAINS ENABLED BY USING SUPERCRITICAL CO₂ MIXTURES IN CONCENTRATED SOLAR POWER APPLICATIONS

F. Crespi¹, P. Rodríguez-de Arriba¹, D. Sánchez^{1*}, A. Ayub², G. Di Marcoberardino², C. Invernizzi², G.S. Martínez¹, P. Iora², D. Di Bona³, M. Binotti⁴, G. Manzolini⁴

¹ Department of Energy Engineering, University of Seville, Seville, Spain

² Dipartimento di Ingegneria Meccanica e Industriale, Università degli Studi di Brescia, Brescia, Italy

³ LEAP S.c.a.r.l., Laboratorio Energia e Ambiente Piacenza, Italy

⁴ Dipartimento di energia, Politecnico di Milano, Milano, Italy

ABSTRACT

Supercritical Carbon Dioxide (sCO₂) power cycles have been proposed for Concentrated Solar Power (CSP) applications as a means to increase the performance and reduce the cost of state-of-the-art CSP systems. Nevertheless, the sensitivity of sCO₂ systems to the usually hot ambient temperatures found in solar sites compromises the actual thermodynamic and economic gains that were originally anticipated by researchers of this innovative power cycle.

In order to exploit the actual potential of sCO₂ cycles, the utilization of dopants to shift the (pseudo)critical temperature of the working fluid to higher values is proposed here as a solution towards enabling exactly the same features of supercritical CO₂ cycles even when ambient temperatures compromise the feasibility of the latter technology. To this end, this work explores the impact of adopting a CO₂-based working mixture on the performance of a CSP power block, considering hexafluorobenzene (C₆F₆) and titanium tetrachloride (TiCl₄) as possible dopants. Different cycle options and operating conditions are studied (250-300 bar and 550-700°C) as well as molar fractions ranging between 10 and 25%.

The results in this work confirm that CO₂ blends with 15-25%(v) of the cited dopants enable efficiencies that are well in excess of 50% for minimum cycle temperatures as high as 50 or even 55°C. It is also confirmed that, for these cycles, turbine inlet temperature and pressure hardly have any effect on the characteristics of the cycle that yields the best performance possible. In this regard, the last part of this work also shows that cycle layout should be an additional degree of freedom in the optimisation process inasmuch as the best performing layout changes depending on boundary conditions.

INTRODUCTION

FROM THE FIRST STEPS TO SUCCESSFUL DEMONSTRATION

The sCO₂ power cycle technology has triggered a growing interest in the scientific community in the last ten years. It currently stands out as the strongest alternative to steam turbines in the next generation of Concentrated Solar Power plants. Such interest is brought about by the higher thermal efficiency of the cycle and arguably smaller footprint of the equipment, features that were already recognised in the pioneering works by Angelino and Feher in the late sixties. The former author identified 650°C as the breakeven turbine inlet temperature (TIT) beyond which sCO₂ power cycles attain better thermodynamic performance than both air Brayton and water/steam Rankine cycles [1]. At the same time, Feher discussed the benefits of compressing sCO₂ in the vicinity of the critical point, taking advantage of the low compressibility factor in that region [2].

After a long period without interest in the technology, a large amount of research works have been published in the last fifteen years. In 2004, Vaclav Dostal's Ph.D thesis put sCO₂ in the spotlight again, identifying the *Recompression* and *Partial Cooling* sCO₂ cycles as the best candidates for IV Generation Nuclear reactors, capable of taking thermal efficiency close to 50% for a turbine inlet temperature of 650°C [3]. A little later, the work carried out by the National Renewable Energy Laboratory explored advanced configurations of the same *Recompression* layout for CSP applications, adding intercooling and reheat and indeed confirming the potential of the cited cycle in this application [4,5]. This theoretical work received a crucial experimental support by SANDIA National Lab, whose first-of-a-kind experimental loop proved the benefits enabled by sCO₂ condensation in terms of turbomachinery design and operational flexibility [6]. This has later been confirmed by experimental activities carried out by other institutions at the small scale [7,8].

* corresponding author(s)

Email: ds@us.es

From a commercial, larger-scale standpoint, the technology achieved a milestone when the Waste Heat Recovery Unit developed by Echogen was deployed to the market [9], becoming the first sCO₂ system to be ever commercialised. This was followed by the much larger system developed by NetPOWER and based on the Allam cycle. A 50 MWt oxy-combustion sCO₂ cycle running on natural gas started up in May 2019, demonstrating the unmatched capability of this technology to produce carbon-free electricity from fossil fuels [10].

FIRST DOUBTS AND INTRODUCTION TO sCO₂ BLENDS

Riding the wave of theoretical works developed in the first decade of the 21st century, the potential of the sCO₂ power cycle to enable thermal efficiencies higher than 50% in a variety of applications was widely acknowledged by the scientific community. Nevertheless, more detailed analyses published in recent years, and including not only thermal but also economic considerations, reveal that there are important challenges ahead of the technology.

For instance, as a common denominator, a large number of research works consider a fairly low temperature at compressor inlet, around 35 °C, in order to perform the compression process near the critical point. This is because the low compressibility factor of sCO₂ at such conditions enables a significant reduction of compression work, hence increasing thermal efficiency. Nevertheless, this assumption is utterly unrealistic for CSP applications, since sites with the very high solar resource needed (Direct Normal Irradiation) are usually located in desertic areas with ambient temperatures much higher than 35°C. If higher minimum cycle temperatures (~50°C) are taken into account, thermal efficiency drops significantly and the potential gains with respect to conventional steam cycles become unclear. This is further discussed in a later section.

In the light of these considerations, the interest in the sCO₂ power cycle technology for CSP applications decreases largely as the performance gain with respect to state-of-the-art steam turbines and the technology readiness level (TRL) is reduced substantially.

Nevertheless, the addition of certain dopants to the raw carbon dioxide used in conventional sCO₂ cycles, yielding the so-called sCO₂ blends, has been identified by the SCARABEUS project as a groundbreaking route towards reverting this situation. Several authors have investigated this concept in the very last years: Invernizzi et al. (partners of SCARABEUS) studied the performance of Brayton cycles running on sCO₂ blended with various hydrocarbons [11], while Jeong et al. presented a similar study employing different gases (such as N₂, O₂ or He) as chemical dopants [12]. Bonalumi et al. (also partners of SCARABEUS) claimed that employing a binary mixture of CO₂ and TiCl₄ in lieu of pure CO₂ could lead to efficiency gains as high as 5% and 3% in Brayton and *Recompression* cycle respectively [13]. Along the same lines, Baik et al. investigated the performance of Brayton cycles employing CO₂/R32 and CO₂/Toluene mixtures and confirmed that these working fluids enable better performance than pure sCO₂ at high heat sink temperatures [14]. Finally, Manzolini et

al. (partners of SCARABEUS) investigated the use of N₂O₄ and TiCl₄ as chemical dopants in order to improve the efficiency of solar tower plants and, accordingly, reduce the cost of electricity [15].

It is in this context that the SCARABEUS project started in 2019, with the aim to demonstrate that the application of supercritical CO₂ blends to CSP plants has the potential to increase thermal efficiency above 50% when the minimum cycle temperature is as high as 50°C. This enhancement of thermal performance comes along with a reduction of CAPEX by 30%, OPEX by 35% and LCOE to 96€/MWh, which is 30% below the current state-of-the-art steam-based CSP plants in a similar location [16].

Bearing all this in mind, the present paper aims to provide an assessment of the performance gain that could be expected from the utilisation of sCO₂ blends in CSP plants under realistic boundary conditions. To this end, the main concept of the SCARABEUS project is thermodynamically reviewed first. Then, the blends considered in this study are introduced, along with a brief description of the simulation tools used and of the two reference cycle layouts: *Recuperated Rankine* and *Precompression*. Finally, a comparison between the results obtained with the different mixtures is developed, with the aim to estimate the performance gains enabled by the adoption of the sCO₂-based blends as against a similar plant using steam turbines.

SCARABEUS PROJECT - CONCEPT

The enthalpy rise across a compression stage can be calculated through integration of Eq. (1). Assuming the process to be isentropic, Eq. (1) can be simplified and so compression work can be expressed as in Eq. (2), where the specific volume of the non-ideal working fluid depends on the compressibility factor Z . This relates the actual specific volume of the non-ideal gas to the specific volume of the gas at the same temperature and pressure, should it behave ideally.

$$dh = Tds + vdp \quad (1)$$

$$Wc = \int_1^2 vdp = \int_1^2 \frac{ZRsT}{p} dp \quad (2)$$

Equation (2) suggests that compression work can be reduced if compressibility decreases, and this could potentially have a beneficial impact on cycle efficiency (all things being equal). This idea led Feher to propose a supercritical cycle [2] where compression takes place in the vicinity of the critical point with a liquid-like specific volume (i.e. a significantly lower specific volume and compressibility factor than in the gas phase). Unfortunately, a side-effect of working near this point is the large increase of the isobaric specific heat, which leads to a larger irreversibility in the recuperative heat exchanger. This was also identified by Angelino who, nevertheless, proposed different cycle layouts to overcome these problems related to heat transfer whilst still exploiting the compression work reduction [1].

Table 1 presents the impact of minimum temperature (bounded by ambient temperature) on cycle performance for a

large number of sCO₂ cycle layouts. These layouts are taken from previous work by some of the authors, which provided a systematic approach to selecting pure sCO₂ cycles for CSP applications [17]. The cycles are modelled with Thermoflex software, with the same boundary conditions as in previous works [17] and setting isentropic efficiencies to 93%, 89% and 83% for turbines, compressors and pumps respectively. The *Transcritical CO₂* configuration, a recuperated Rankine-like cycle with a pump inlet temperature of 15°C, is added to the comparison for the sake of completeness and in spite of not being feasible at intermediate-high ambient temperature. The high thermal efficiency at lower temperatures, for which the cycle is feasible, will be further discussed in the following sections.

Cycle layout	$\eta_{th@32^{\circ}C}[\%]$	$\eta_{th@50^{\circ}C}[\%]$	$\Delta\eta[pp]$
Simple Recuperated	46.2	43.5	2.7
Precompression	50.0	46.9	3.1
Recompression	51.4	43.1	8.3
Recompr.+IC+RH	53.0	49.1	3.9
Partial Cooling	51.6	46.6	4.0
Partial Cooling+RH	53.9	48.9	5.0
Double Reheated	54	44.3	9.7
Schroder - Turner	49.0	45.3	3.7
Modified Allam	45.6	43.5	2.1
Transcritical CO ₂	48.3 (15°C)	-	-

Table 1: Thermal efficiency of selected sCO₂ power cycles for compressor inlet temperatures of 32°C and 50°C. Turbine inlet pressure and temperature are set to 300 bar and 750°C.

The trends observed in Table 1 come about because of the impact of compressor/pump inlet temperature on fluid compressibility, which rises rapidly when departing from the critical temperature, hence increasing compression work. For instance, for a compressor inlet pressure of 1.1 times the critical pressure, the compressibility factor increases from 0.28 to 0.65 when temperature changes from 34 to 61°C [18]. Additionally, compressor outlet temperature increases more than proportionally due not only to the higher inlet temperature but, also, higher compressibility. This means a lower potential for heat recovery in the cycle given that both turbine inlet temperature and pressure ratio remain the same for 32 and 50°C.

A significant efficiency drop is observed when raising this temperature from 32°C (very close to the critical temperature) to 50°C (more realistic for usual CSP locations), regardless of cycle layout: between 2 and almost 10 percentage points. Moreover, for some layouts, like the *Transcritical CO₂* cycle, the cycle cannot be implemented at 50°C anymore.

In addition to the evident detrimental effect of ambient temperature on cycle performance, with efficiency drops between 2 and 10 percentages depending on cycle configurations, a twofold observation can be made. On the one

hand, most of the cycles in the comparison exhibit thermal efficiencies that are just slightly higher than steam Rankine cycles under similar boundary conditions (42%). On the other hand, those layouts achieving substantially higher efficiencies in the order of 49% imply very complex layouts which, in addition to compromising operability, also lead to significantly higher capital costs. This is the case of the *Recompression+IC+RH* and *Partial Cooling +RH* cycles which have been proved not cost effective in spite of their high thermal efficiency [19].

In order to counteract the effects discussed in the previous section, the SCARABEUS project explores the opposite strategy. Rather than trying to reduce compressor inlet temperature to operate near the critical point, which is irremediably constrained by ambient conditions, the critical temperature of the working fluid is increased by adding dopants to the raw CO₂. This enables not only lower compressibility and compression work but also, and more interestingly, condensation of the working fluid at high ambient temperatures. This has already been explored preliminarily by Di Marcoberardino et al. in the context of the SCARABEUS project [20]. These authors considered a mixture of CO₂ and C₆F₁₄ in a cycle with condensation at 50°C and a turbine inlet temperature of 400°C, proving that thermal efficiency could be increased by 3-4 percentage points with respect to pure sCO₂ if the appropriate dopant composition were used.

SIMULATION TOOLS

In order to study the impact of adopting sCO₂-based blends on the thermal performance of the power cycle, a series of simulations are run with the commercial software Thermoflex [21]. Two different cycles are considered, *Recuperated Rankine* and *Precompression*, whose layouts are provided in Figure 1. The former is a well-known configuration, adapted here to operate with sCO₂-blends whilst the *Precompression* layout originally proposed by Angelino [1] presents a somewhat unique and extremely interesting feature among the other sCO₂ power cycles. In contrast with other more popular configurations, such as *Recompression* or *Partial Cooling* (which present a flow-split before the low temperature recuperator in order to enhance thermal performance and avoid pinch-point problems), the potential of the *Precompression* layout lies on the addition of a compressor in the low-pressure side of the cycle, between the low and high-temperature recuperators. This particular feature overcomes the restriction imposed by the compression process on turbine exhaust pressure, thus enabling to control the compression and expansion ratios of the cycles separately. The additional degree of freedom can then be used to enhance thermal efficiency.

One of the critical tasks in SCARABEUS is to identify the optimal working fluid (dopant composition and molar fraction) that yields the largest thermal efficiency gain. To this aim, different dopants have already been studied by some of the authors [20] and some others are currently under investigation by the project partners. In this study, two of such dopants are considered: C₆F₆ (dopant D1) and TiCl₄ (dopant D2). The former

is an organic, aromatic compound, characterised by low toxicity but high flammability and unconfirmed thermal stability at high temperatures. The latter is a low cost fluid whose thermal stability has been proven at 550 °C, although it presents a very aggressive water reactivity, which may affect its actual feasibility at commercial scale. Further investigations regarding this particular aspect are currently undertaken by SCARABEUS consortium. A short evaluation of these two dopants in the context of NFPA 704 code is provided in Table 2.

	Health Hazard	Flammability	Chemical Reactivity	Special Hazard
sCO ₂	2	0	0	SA
C ₆ F ₆	1	3	0	-
TiCl ₄	3	0	2	W

Table 2: Dopant hazard according to NFPA 704 [22].

With varying molar fractions of these two dopants, the blends in Table 3 are obtained, where X and YY in the blend code DXCY stand for dopant D1/D2 and molar fraction (%) respectively. Table 3 also provides the saturation pressure of each blend corresponding to a bubble temperature of 50°C; this latter temperature is set as the minimum cycle temperature of choice for cycle analysis. These two, 50°C and P_{cond} are therefore the temperature and pressure at pump inlet (station 1 in both layouts in Figure 1).

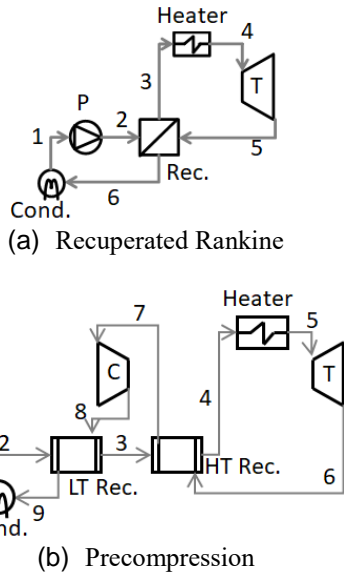


Figure 1: Recuperated Rankine and Precompression layouts.

For each blend, the thermophysical properties of the mixture have been obtained with Aspen [23], employing the Peng-Robinson equation of state calibrated on experimental data of the corresponding Vapour-Liquid-Equilibrium (VLE) conditions [24, 25].

It is worth noting that the critical conditions reported in Table 3 change significantly with blend composition, what gives room to tailoring the optimum working fluid to a given minimum

cycle temperature (i.e., ambient temperature). The criterion to determine the feasible range of compositions that can be used in the cycles considered is thus based on the margin between critical temperature (T_{cr}) and temperature at pump inlet (T_I), which is set to 30°C in this work. Accordingly, for the T_I of choice, 50°C, only those blends whose compositions yield critical temperatures higher than 80°C are eligible; for instance, according to the information in Table 3, blends based on dopant D1 with a molar fraction lower than 10% do not meet this criterion and are, therefore, discarded. This possibility to adapt the composition of the blend to the desired pump inlet temperature turns out to be a very powerful feature of SCARABEUS, since different mixtures can be tailored to specific CSP locations (ambient conditions). This is highlighted in the concluding section.

Blend	Composition [% molar]	MW [g/mol]	T_{cr} [°C]	P_{cr} [bar]	P_{cond} [bar]
D1C10	CO ₂ -C ₆ F ₆ [90-10]	58.21	80.28	112.4	83.51
D1C15	CO ₂ -C ₆ F ₆ [85-15]	65.32	102.1	121.3	77.52
D1C20	CO ₂ -C ₆ F ₆ [80-20]	72.42	121.9	123.6	71.83
D1C25	CO ₂ -C ₆ F ₆ [75-25]	79.52	139.8	121.1	66.36
D2C15	CO ₂ -TiCl ₄ [85-15]	65.86	93.76	190.9	99.53
D2C20	CO ₂ -TiCl ₄ [80-20]	73.15	149.6	243.7	97.63
D2C25	CO ₂ -TiCl ₄ [75-25]	80.43	192.0	247.1	94.52

Table 3: Specifications of CO₂ blends. P_{cond} is the condensation pressure corresponding to a bubble temperature of 50°C.

The Recuperated Rankine and Precompression cycles have been modelled for all the sCO₂ blends in Table 3, for a Turbine Inlet Temperature of 550/700°C and a maximum cycle pressure of 250/300 bar. For the resulting twenty-eight cases, the gross output of the cycle is 100 MW and the specifications of turbomachinery (isentropic efficiency) and heat exchangers (minimum pinch-point, pressure drops) are those summarised in Table 4.

PIT [°C]	TIT [°C]	P_{max} [bar]	η_{is} [%] Pump/Turb/Compr
50	550/700	250/300	88 / 93 / 89
ΔT_{min} [°C]	ΔP_{HEATER} [%]	ΔP_{COND} [%]	ΔP_{REC} [%] Low P / High P
5	1.5	0	1 / 1.5

Table 4: Boundary conditions and specifications of turbomachinery and heat exchangers.

ANALYSIS OF THE RESULTS

A thorough discussion on the actual potential of CO₂-blends to improve the thermal performance of sCO₂ power cycles is presented in this section. First of all, the combinations of blend and cycle layout enabling thermal efficiencies higher than 50% are identified. Then, the performance of cycles using these selected blends is analysed in detail in order to identify the root causes of the superior thermodynamic performance; this second step of the analysis is done for the case at 700°C and 250 bar, herein considered as the most representative of SCARABEUS. Later, the dependence of the best combination of layout and blend on the operating and boundary conditions of the cycles is discussed. Finally, the influence of working fluid composition on the characteristics of certain equipment is investigated, with a particular focus on turbine and cooler/condenser.

BEST COMBINATION OF FLUID BLEND AND CYCLE LAYOUT

The thermal efficiencies of the *Recuperated Rankine* and *Precompression* cycles for the entire set of boundary conditions presented in Table 4 are reported in Figures 2 and 3 respectively. These are compared with the thermal efficiency of a state-of-the-art steam-based CSP plant (live steam temperature is set to 550°C) and, for the sake of completeness, with an ultra-supercritical Rankine cycle (live steam pressure and temperature set to 300 bar and 625°C/650°C). These two reference values are reported in Figures 2 and 3 with solid (labelled *St.R*) and dashed (labelled *Usc.R*) lines respectively.

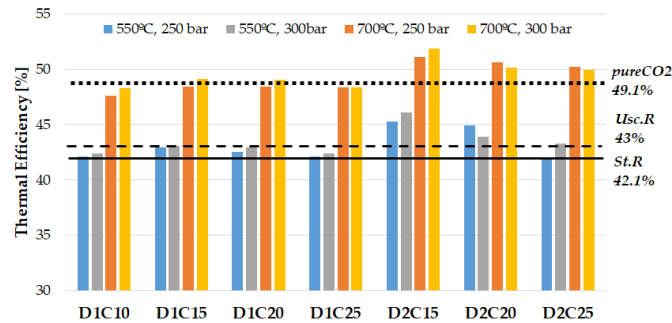


Figure 2: Thermal efficiency obtained by *Recuperated Rankine* cycle for different operating conditions and blends.

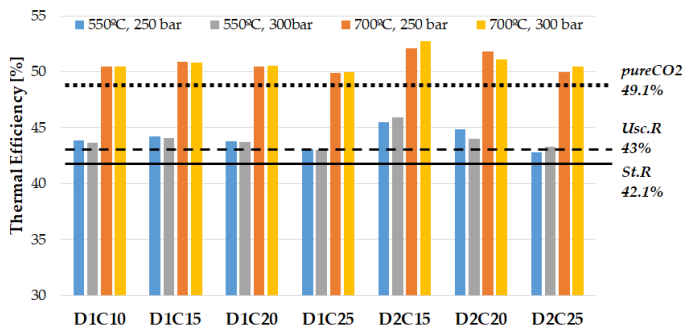


Figure 3: Thermal efficiency obtained by *Precompression* cycle for different boundary conditions and employing different blends.

The thermal efficiency of the *Recompression+IC+RH* cycle running on pure sCO₂ and a minimum cycle temperature of 50°C is also reported in Figures 2 and 3 with a dotted line (labelled *pureCO2*). The value is taken from Table 1 and aims to represent the best case scenario of a pure-sCO₂ power cycle bounded by the same extreme temperatures.

The information in Figures 2 and 3 confirms that using sCO₂-blends enables better thermal efficiency than when pure sCO₂ or steam Rankine cycles are used. This becomes even more important in the light of the more complex (thus expensive) layout of conventional CSP plants with respect to the proposed solutions. As expected, it is also confirmed that the impact of increasing turbine inlet temperature on thermal efficiency is stronger than that of increasing maximum cycle pressure.

For the *Recuperated Rankine* cycle operating with CO₂-C₆F₆ mixtures (D1), the corresponding efficiency when TIT=550°C is visibly higher than for the standard steam Rankine cycle, and the difference increases dramatically when this temperature increases to 700°C, even if compared against an ultra-supercritical steam cycle working at 625°C/650°C. For the best case in Figure 2, given by D1C15 at 300 bar & 700°C, the *Recuperated Rankine* cycle presents slightly better performance than the *Recompression+IC+RH* layout working with pure sCO₂, even though the latter presents a significantly more complex layout and operates with 50°C higher TIT.

It is also interesting that CO₂-TiCl₄ mixtures (D2) present, for the most part, thermal efficiency higher than CO₂-C₆F₆ and, depending on operating conditions, the other technologies in Figure 2 (sCO₂ and steam). Furthermore, amongst the D2CYY cases, it is the D2C15 blend which yields the best performance, outperforming all the other candidates at 700°C by a large margin, attaining a thermal efficiency well above 50% ($\eta_{th}=52\%$). This result is extremely interesting, bearing in mind that even if the complexity of the *Recuperated Rankine* cycle is similar to that of a *Simple Recuperated* (recuperated Brayton) cycle working on sCO₂, the former achieves much better performance: the efficiency of a *Recuperated Rankine* cycle working on D2C15 at 700°C turbine inlet temperature (51.9%) is 8 percentages higher than that of a *Simple Recuperated* (Brayton) cycle running on sCO₂ at 750°C (43.5%).

Some comments about the better performance enabled by the specific features of the *Precompression* cycle, as reported in Figure 3, are worth noting. As already highlighted for this cycle, turbine exhaust pressure is not constrained by condenser pressure, thanks to the incorporation of a compressor between the two recuperators (see Figure 1). This increases the complexity but enables a much more flexible optimisation of compressor pressure ratio, regardless of turbine expansion ratio, after which thermal efficiency can be increased substantially. Indeed, utilising D1 blends in this cycle enables a thermal efficiency gain in the order of 2 percentage points with respect to the base sCO₂, depending on the molar fraction of dopant and operating conditions. DIC10 and DIC15 yield the largest gains, 2.8pp and 2.4pp, at 250 bar & 700°C, with the latter achieving 50.9% thermal efficiency and being the optimum mixture overall amongst the CO₂-C₆F₆ cases. Interestingly, for this combination

of layout and blend, increasing the maximum pressure of the cycle has hardly any effect on η_{th} in spite of the significantly higher specific work (see Figure 4).

Using blends based on D2 in the *Precompression* cycle enables higher thermal efficiencies than the same fluid in the *Recuperated Rankine* but, in this case, the rise in η_{th} is in the order of 1 percentage point only. This happens when a D2C15 blend is used in cycles working at 250 bar and 700°C, for which thermal efficiency increases from 51.1 to 52.1%. This depicts a situation where the *Precompression* cycle steps forward as a better performing option overall, for which all the candidate mixtures achieve thermal efficiencies in the 50-52% range when running the cycle at 700°C. For this cycle, adding a 15-20% molar fraction of C₆F₆ yields the best performance whereas 15% is best for mixtures based on TiCl₄.

The heat and mass balance sheets of a *Precompression* cycle operating with pure CO₂ and D2C15 are reported in Tables 5 and 6, showing also the compressibility factors at each cycle station.

Cycle Station	T [°C]	P [bar]	h [kJ/kg]	s [kJ/kgK]	ρ [kg/m ³]	Z [-]
1	50.0	102	-128.3	-1.179	408.4	0.409
2	103	250	-95.41	-1.169	576.0	0.611
3	214	246	98.36	-0.7111	304.6	0.877
4	498.5	243	462.1	-0.1179	160.6	1.04
5	700	239	716.1	0.1774	123.3	1.05
6	546	76.5	534.1	0.1952	48.96	1.01
7	231	75.7	170.5	-0.3615	83.52	0.951
8	268	104	204.0	-0.3547	106.4	0.956
9	110	103	10.27	-0.7791	184.3	0.772

Table 5: Heat and mass balance of the *Precompression* cycle with pure CO₂. Compressor and turbine inlet temperatures are 50°C and 700°C. Maximum cycle pressure is 250 bar. Station numbers as per Figure 1.

Cycle Station	T [°C]	P [bar]	h [kJ/kg]	s [kJ/kgK]	ρ [kg/m ³]	Z [-]
1	50.0	99.5	-7016	-1.231	1184	0.206
2	63.9	250	-7002	-1.225	1132	0.519
3	283	246	-6689	-0.501	399.4	0.879
4	537	243	-6420	-0.099	229.1	1.04
5	700	239	-6257	0.087	183.8	1.06
6	573	84.6	-6370	0.097	78.64	1.01
7	288	83.8	-6639	-0.290	128.5	0.921
8	307	101	-6625	-0.287	148.3	0.925
9	71.6	99.5	-6938	-0.991	466.6	0.490

Table 6: Heat and mass balance of the *Precompression* cycle with D2C15. Compressor and turbine inlet temperatures are

50°C and 700°C. Maximum cycle pressure is 250 bar. Station numbers as per Figure 1.

The beneficial influence of working fluid composition on thermal performance is now seen to be brought about by the effect of a lower compressibility across the compression stage (stations 1-2 and, to a lesser extent, 7-8 in Figure 1).

With regard to specific work (W_s), the *Precompression* cycle presents, as expected, a significantly higher W_s than the *Recuperated Rankine* cycle, owing to the higher expansion ratio enabled by the utilisation of a compressor between turbine outlet and pump inlet. This is shown in Figure 4 and 5 where the impact of turbine inlet temperature and peak cycle pressure can also be assessed. The figure also shows that both cycles and dopants exhibit similar W_s patterns for different blends: the blends with the smallest fraction of dopant (D1C10 and D2C15) always enable the highest specific work (for a given set of boundary conditions), and this decreases progressively as higher fractions are considered. For a given dopant, this is due to the increasing molar weight of the mixture, corresponding to an increasing circulating mass flow rate in the power cycle.

Generally speaking, TiCl₄-based (D2) blends present lower specific work than D1 mixtures, contrary to the pattern observed earlier for thermal efficiency. For this reason, a compromise between η_{th} and W_s is mandatory when selecting the best blend for a given cycle layout, even if the weight of thermal efficiency on this decision is expectedly much heavier than that of specific work.

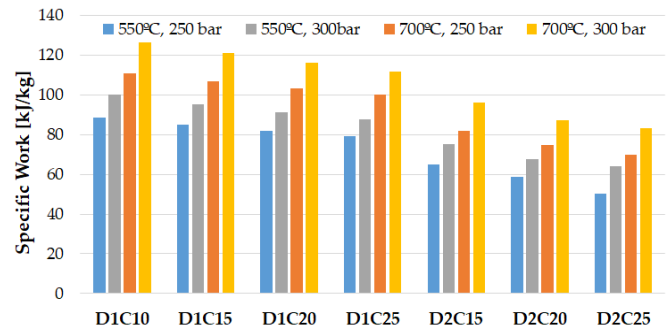


Figure 4: Specific work of the *Recuperated Rankine* cycle for different operating conditions and blends.

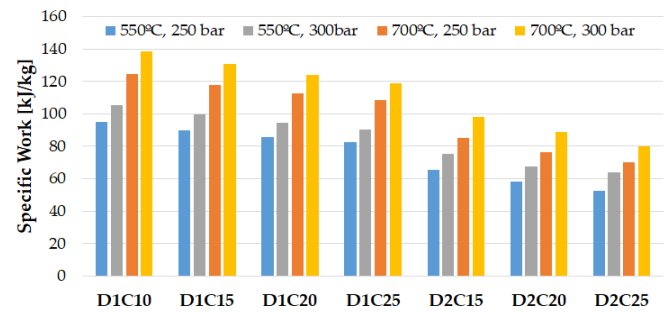


Figure 5: Specific work of the *Precompression* cycle for different operating conditions and blends.

BEST COMBINATION OF CYCLE LAYOUT AND BLEND COMPOSITION - INFLUENCE OF OPERATING CONDITIONS

Earlier sections of this work have revealed that D1C15 and D2C15 yield highest thermal efficiency for all the operating conditions taken into account and considering a minimum cycle temperature of 50°C. This means that variations of either turbine inlet temperature or maximum cycle pressure do not have any influence on this selection; i.e., the optimum blend remains the same regardless of further changes in these parameters. This conclusion is nevertheless not applicable to the minimum temperature of the cycle (pump inlet) whose variations impact which the optimum blend choice is. Given the dependence of this temperature on ambient temperature, this sets up a tight link between the location of the plant and the composition of the optimum blend.

In order to explore this further, a parametric analysis of the impact of ambient temperature on blend selection is performed for the *Recuperated Rankine* cycle. The results are provided in Table 7, where the performance of a *Simple Recuperated* Brayton working on pure sCO₂ at 250 bar and 700°C is added for the sake of comparison.

There are several interesting aspects in Table 7. Remarkably, CO₂-blends prove to enable higher thermal efficiency than pure CO₂, employing a cycle with similar complexity. Nevertheless, an absolute best-performing blend regardless of minimum cycle temperature cannot be identified. Indeed, for the C₆F₆-based mixtures, D1C15 is found to yield the best performance for pump inlet temperatures equal or lower than 50°C (best cases highlighted in bold). At higher temperatures, D1C20 becomes the best mixture of choice. The pattern is similar for the mixtures based on TiCl₄: D2C15 yields the best performance for minimum cycle temperatures equal or higher than 50°C whilst D2C20 becomes the best blend at lower temperature.

PIT →	30°C	35°C	40°C	45°C	50°C	55°C	60°C
CO ₂	-	43.69	43.15	42.60	42.06	41.51	40.96
D1C10	50.96	50.21	49.36	48.61	47.64	47.03	45.94
D1C15	51.39	50.4	50.10	49.19	48.43	47.99	47.02
D1C20	50.50	50.25	49.97	48.76	48.41	48.19	47.05
D1C25	50.46	49.29	48.82	48.59	48.34	47.13	46.97
D2C15	53.47	52.98	52.45	51.89	51.14	50.30	49.42
D2C20	54.48	53.23	52.62	52.42	50.65	50.24	48.84
D2C25	52.54	51.35	50.73	49.64	48.34	47.13	46.97

Table 7: Thermal efficiency ([%]) of the *Recuperated Rankine* cycle for different blends and pump inlet temperatures.

According to these results, the possibility to tailor the composition of the working fluid to the ambient conditions of the plant site in order to maximise performance becomes evident. This is an extremely powerful feature of this study, which goes beyond the application of the concept to Concentrated Solar Power plants and paves the way for the further optimisation of

supercritical power cycles using CO₂ blends in other applications (for instance nuclear or waste heat recovery applications).

IMPACT ON COMPONENT PERFORMANCE AND DESIGN

In this section, interesting aspects of component design and performance are discussed. For the turbine, two parameters are usually employed to preliminarily assess design and manufacturability: Volumetric Expansion Ratio (*VER*) and Size Parameter (*SP*) [26]. The former is defined as the ratio from specific volume at turbine outlet to specific volume at turbine inlet, assuming isentropic expansion, Eq. (3)a.

$$\text{a) } VER = \frac{v_{4s}}{v_3}; \quad \text{b) } SP = \frac{\sqrt{v_{4s}}}{\Delta h_{is}^{1/4}} \quad (3)$$

Large values of this parameter imply large area variations across the turbine which, inevitably, lead to larger aerodynamic losses and a larger number of stages to accommodate the large density variations. Therefore, the volumetric expansion ratio provides a qualitative indication of the expected isentropic efficiency and stage count of the turbine.

The size parameter is defined as the ratio from the square root of the volumetric flow at turbine outlet to the enthalpy change across the turbine (Δh_{is}) to the power of 0.25, in both cases assuming an isentropic expansion. This parameter is linked to turbine size, thus being a suitable indicator to compare size (and cost, for a given set of boundary conditions) of turbines operating with different blends and it is also linked to turbine efficiency. Turbines with smaller size parameters are more likely to suffer from tip leakage losses and low Reynolds number effects. Therefore, all things being equal, one would be interested in cycles and blends yielding low volumetric expansion ratios and high size parameters, in order to achieve the highest turbine efficiency.

These two parameters are reported in Table 8 for the reference *Recuperated Rankine* cycle working at 250 bar and 700°C. The *VER* values reported are low regardless of the mixture, which confirms that the aerodynamic design of the turbine is not challenging in terms of a largely three-dimensional flow. Nevertheless, in spite of this favourable *VER* overall, it is interesting to verify that the addition of larger fractions of dopant has the effect of increasing the volumetric expansion ratio due to the higher molecular weight of the resulting mixture.

The size parameter is higher values for CO₂-TiCl₄ than for the CO₂-C₆F₆ blends, contrary to *VER*, and it also exhibits a proportional increase with the molar fraction of dopant. In any case, the values of both *VER* and *SP* in Table 8 suggest that the aerodynamic design of turbines for the cases analysed does not pose large challenges (as far as the annulus is concerned).

Cooler design and operation stems as one of the most critical tasks to undertake in CSP plants, usually located in desertic areas with extremely high ambient temperatures. This becomes even more challenging if condensing cycles are considered and if the use of air-cooled condensers turns out mandatory due to water scarcity.

Blend	VER [-]	SP [m]
D1C10	2.410	0.1882
D1C15	2.598	0.1903
D1C20	2.800	0.1930
D1C25	3.024	0.1961
D2C15	2.026	0.2031
D2C20	2.062	0.2077
D2C25	2.121	0.2109

Table 8. Volumetric expansion ratio and size parameter for a *Recuperated Rankine* cycle operating at 250 bar and 700°C with CO₂-TiCl₄ than for the CO₂-C₆F₆ blends.

In state-of-the-art CSP plants using steam turbines, the flow entering the condenser is partly condensate already. Typically, 10% of the turbine exhaust mass flow has already condensed inside the turbine. This is somewhat similar to what happens when CO₂-based blends are used, given that the fluid entering the condenser is partly in liquid state. Nevertheless, in this case, this previous condensation does not take place inside the turbine but across the low-pressure side of the low-temperature recuperator. The beneficial aspect of this condensation upstream of the condenser, which can be observed in the heat and mass balance provided in Table 6, is a reduction of the duty of this component, what lowers not only its cost but also the auxiliary power needed to reject heat to the environment.

Interestingly, the particular composition of the CO₂ blend used in the cycle has an impact on steam quality at condenser inlet and, accordingly, on condenser duty. This is shown in Figure 6 where the blue and yellow bars stand for specific and overall duty of the condenser (left axis) whereas inlet quality is reported by the black markers (right axis). The values apply to a *Recuperated Rankine* cycle operating at 250 bar and 700°C, with 50°C pump inlet temperature and a power output of 100 MW.

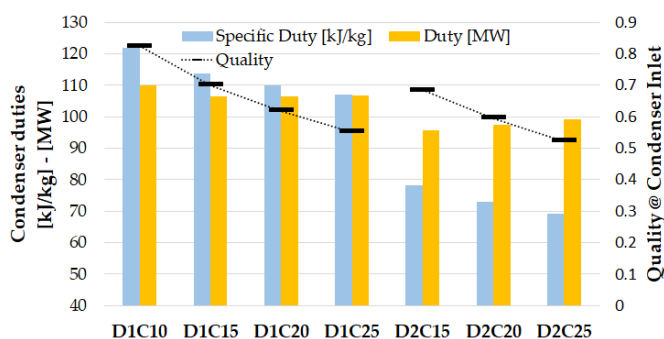


Figure 6: Specific and absolute condenser duty Duty (left axis) and fluid quality at condenser inlet (right axis) of a 100 MW *Recuperated Rankine* cycle operating at 250 bar and 700°C.

In the chart, quality at condenser inlet and specific duty show a decreasing trend for increasing molar fraction. This pattern suggests that the use of mixtures of a higher dopant fraction could reduce the specific duty of the condenser, hence reducing the associated auxiliary power and cost. Nevertheless,

a look at the absolute duty reveals that this metric is almost constant for all D1 blends whereas it increases slightly at higher molar fractions of dopant for D2 mixtures. This is, of course, due to the counteracting effect of a visibly higher mass flow rate for increasing dopant concentration, as shown in Figure 7; this could have also been deduced from the specific work patterns in Figure 4, in a context where cycle output (MW) remains constant. In summary, the reduction in condenser specific duty cannot counterbalance the effect of the increased circulating mass flow and, therefore, does not necessarily correspond to smaller equipment.

Overall, it is confirmed that peak thermal efficiency is provided by the blends for which the absolute duty of the condensers, for given gross cycle output, is minimum (as it was to be expected).

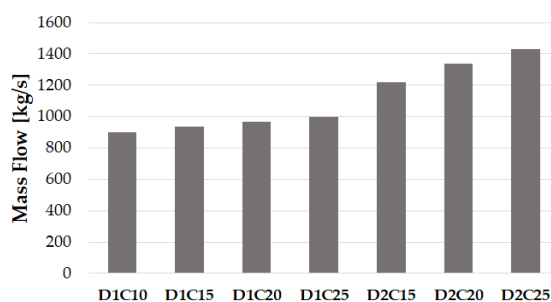


Figure 7: Circulating mass flow of a 100MW *Recuperated Rankine* cycle operating at 250 bar and 700°C.

SCARABEUS: A PARADIGM SHIFT

It has already been stated in earlier sections that thermal efficiency of the cycle is generally enhanced when shifting from a *Recuperated Rankine* cycle to a *Precompression* cycle. However, the thermal efficiency variation experienced in this move is not homogenous; rather, it happens to depend strongly on the working fluid considered. This is clearly observed in Table 9 which has a seemingly irregular pattern. The reason for this pattern is actually found in the fundamental thermodynamic behaviour of the cycles, which depends itself on the different thermophysical properties of the various candidate mixtures.

At a macro-scale, the thermal efficiency enabled by TiCl₄ mixtures in a *Recuperated Rankine* cycle, Table 7, proved to be higher than when using C₆F₆. Now, Table 9 reveals that the performance gain brought about by the adoption of the *Precompression* layout is larger for C₆F₆ blends than for cases based on TiCl₄. From a different angle, this indicates that, despite starting from a lower efficiency, CO₂-C₆F₆ mixtures seem to have a larger margin for performance improvement out of modifications of cycle layout than CO₂-TiCl₄.

As a consequence of this, the more relevant conclusion of this work, second to the very high efficiencies enabled by CO₂ blends, is the new approach to the design of supercritical cycles using these mixtures. Indeed, the optimisation of working fluid composition for a given dopant and set of boundary and operating conditions does not make sense anymore or, to say it better, is incomplete. In order to really accomplish full

optimisation for a given dopant and boundary conditions, leading to the attainment of the highest efficiency possible, it is mandatory to perform a simultaneous optimisation of cycle layout and fluid composition. This approach to cycle optimisation is currently under development at University of Seville for the SCARABEUS project although, at this stage, more research is still needed to fully understand the behaviour of CO₂-based blends in different cycle configurations. If confirmed, this paradigm shift would certainly pave the way for a more flexible and comprehensive understanding of sCO₂ power cycles technology development.

Blend	550°C & 250bar	550°C & 300bar	700°C & 250bar	700°C & 300bar
D1C10	+1.76	+1.28	+2.84	+2.14
D1C15	+1.25	+1.04	+2.44	+1.68
D1C20	+1.27	+0.81	+2.07	+1.53
D1C25	+0.99	+0.63	+1.53	+1.59
D2C15	+0.25	-0.18	+0.97	+0.84
D2C20	-0.05	+0.12	+1.15	+0.96
D2C25	+0.86	+0.01	-0.22	+0.54

Table 9: Thermal efficiency gains (pp) when shifting from a *Precompression* cycle to a *Recuperated Rankine* cycle for the given operating conditions. Figures are in percentage points.

CONCLUSIONS

This work has investigated the actual potential of CO₂-based blends to enhance the performance of sCO₂ power cycles when applied to boundary and operating conditions characteristic of Concentrating Solar Power applications. The objective of the assessment, set forth at the beginning of the paper, was to verify the performance gains that could be attained thanks to the utilisation of working fluids incorporating carbon dioxide and different dopants with the overall effect to shift the pseudocritical temperature of the resulting mixture to a value higher than the critical temperature of CO₂.

With this in mind, two different dopants have been studied, C₆F₆ and TiCl₄, with molar fractions ranging from 10 to 25%, and their performances have been assessed in two cycle layouts, *Recuperated Rankine* and *Precompression*. In both cases, minimum cycle temperature (temperature at pump inlet) has been set to 50°C, corresponding to an intermediate-high ambient temperature representative of typical CSP locations. For the sake of completeness, the maximum pressure and temperature of the working fluid have been changed in a range of interest as well.

The assessment described in the afore-described framework yields the following conclusions:

- For a given minimum cycle temperature, there is a minimum molar fraction of dopant below which condensation is not feasible. This sets a lower limit of dopant concentration which is specific to each dopant composition. For the dopants considered in this analysis and a PIT of 50°C, this lower limit is found between 10 and 15%.

- Using CO₂-based mixtures in supercritical cycle layouts proves to enable η_{th} well in excess of 50%, even for ambient temperatures as high as 50°C. This is well above what state-of-the-art Rankine cycles running on steam are currently achieving in CSP plants, thus meaning an unprecedented upsurge in performance for this type of application.
- This performance of supercritical cycle layouts using CO₂-based mixtures is also much better than what conventional supercritical CO₂ can attain for the same boundary conditions. This is due to the deleterious effect of high ambient temperatures on the compression process in the latter cycles. The gain enabled CO₂-based mixtures is in the order of 5-6 percentage points (more than 10% relative performance improvement with respect to an equivalent embodiment with pure CO₂).
- The performance of supercritical cycle layouts using CO₂-based mixtures shows a weak dependence on turbine inlet pressure whereas the influence of minimum and maximum cycle temperatures is very strong. Nevertheless, regarding temperature, whilst both temperatures determine thermal efficiency, turbine inlet temperature does not have any influence on the composition of the blend yielding the best performance. This seems to be dependent on minimum cycle temperature only.
- Component design, in particular turbine design, seems to be not compromised by the utilisation of the new WFs.
- When CO₂-based mixtures are used, cycle optimisation must include WF composition and cycle layout as independent variables. This is because the layout yielding the best η_{th} changes as mixture composition changes.

In addition to the specific conclusions listed above, there are two main, general conclusions drawn from this work. First and foremost, the discussion in this work confirms that achieving thermal efficiencies well in excess of 50% at attainable turbine inlet temperatures is now possible. This is because the CO₂-blend concept overcomes the main Achilles' heel of conventional supercritical CO₂ power cycles. Second, CO₂ mixtures pave the way for new CSP plants which can actually be tailored to the boundary conditions that are specific to each CSP plant. In other words, fluid composition and cycle layout could be tuned specifically to these boundary conditions in order to squeeze the thermodynamic potential of the concept as much as possible.

Further research by the authors will search new dopants and cycle layouts that could bring even larger gains whilst also developing new optimisation strategies that can automate this decision making process.

NOMENCLATURE

CIT	Compressor Inlet Temperature	[°C]
CSP	Concentrated Solar Power	
ΔT_{min}	Minimum temperature difference in HX	[°C]
ΔP_{HX}	HX Pressure drop	[%]
ΔH_{is}	Turbine isentropic enthalpy variation	[J/kg]
η_{is}	Isentropic Efficiency	[%]
η_{th}	Cycle Thermal Efficiency	[%]
h	Enthalpy	[J/kg]

MW	Molar Weight	[g/mol]
pp	Percentage point	[%]
s	Entropy	[J/kgK]
Pcr	Critical Pressure	[bar]
Pmax	Maximum Cycle Pressure	[bar]
PIT	Pump Inlet Temperature	[°C]
Rs	Specific Gas Constant	[J/kgK]
SA	Simple Asphyxiant Gas	[-]
sCO ₂	Supercritical Carbon Dioxide	
SP	Turbine Size Parameter	[m]
Tcr	Critical Temperature	[°C]
TIT	Turbine Inlet Temperature	[°C]
TIP	Turbine Inlet Pressure	[bar]
v	Specific Volume	[m ³ /kg]
V	Volumetric flow	[m ³ /s]
VER	Volumetric Expansion Ratio	[-]
W	React with water	[-]
Wc	Compression Work	[J/kg]
WF	Working Fluid	[-]
Z	Compressibility Factor	[-]

ACKNOWLEDGEMENTS

The SCARABEUS project has received funding from the European Union's Horizon 2020 research and innovation programme under grant agreement N ° 814985.

REFERENCES

- [1] G. Angelino, 1969. *Real gas effects in carbon dioxide cycles*. In ASME Gas Turbine Conference and Products Show, Cleveland, OH.
- [2] E.G. Fehér, 1968. *The supercritical thermodynamic power cycle*. Energy Convers Manag 8, pp. 85–90.
- [3] V. Dostal, 2004. *A supercritical carbon dioxide cycle for next generation nuclear reactors*. PhD thesis, Massachusetts Institute of Technology.
- [4] C.S. Turchi, Z. Ma, J. Dyreby, 2012. *Supercritical Carbon Dioxide Power Cycle Configurations for use in Concentrating Solar Power Systems*. ASME Turbo Expo, Copenhagen.
- [5] T.W. Neises, C.S. Turchi, 2014. *Supercritical CO₂ Power Cycles: Design Considerations for Concentrating Solar Power*. 4th Supercritical CO₂ Power Cycles Symposium, Pittsburgh, PA.
- [6] S.A. Wright et al., 2011. *Modeling and Experimental Results for Condensing Supercritical CO₂ Power Cycles*, SAND2010-8840 report, Sandia National Laboratories, Albuquerque, NM.
- [7] K.J. Kimball and E.M. Clementoni, 2012. *Supercritical Carbon Dioxide Brayton Power Cycle Development Overview*. ASME Turbo Expo 2012, Copenhagen.
- [8] J. Cho et al., 2016. *Development of the Supercritical Carbon Dioxide Power Cycle Experimental Loop in KIER*. ASME Turbo Expo, Seoul.
- [9] M. Persichilli et al. 2011. *Transforming Waste Heat to Power Through Development of a CO₂-Based Power Cycle*. Electric Power Expo, Rosemount, IL.
- [10] NET Power's clean energy demonstration plant, La Porte, Texas. <https://www.power-technology.com/projects/net-powers-clean-energy-demonstration-plant-la-porte-texas/>. Retrieved October 30th 2020.
- [11] C.M. Invernizzi, T. Van Der Stelt, 2012. *Supercritical and real gas Brayton cycles operating with mixtures of carbon dioxide and hydrocarbons*. Proc Inst Mech Eng Part A J Power Energy 226, pp. 682– 693.
- [12] W.S. Jeong, J.I. Lee, Y.H. Jeong, 2011. *Potential improvements of supercritical recompression CO₂ Brayton cycle by mixing other gases for power conversion system of a SFR*, Nucl Eng Des 241, pp. 2128–2137.
- [13] D. Bonalumi, S. Lasala, E. Macchi, 2020. *CO₂-TiCl₄ working fluid for high-temperature heat source power cycles and solar application*, Renew Energy 147, pp. 1–13.
- [14] S. Baik, J.I. Lee, 2018, *Preliminary study of supercritical CO₂ mixed with gases for power cycle in warm environments*, Proceedings of ASME Turbo Expo, Lillestrom.
- [15] G. Manzolini et al., 2019. *CO₂ mixtures as innovative working fluid in power cycle applied to solar plants: techno-economic assessment*. Solar Energy 181, pp. 530-544.
- [16] Supercritical CARbon dioxide Alternative fluids Blends for Efficiency Upgrade of Solar power plants. <https://www.scarabeusproject.eu/>. Retrieved October 30th 2020.
- [17] F. Crespi et al., 2017. *Analysis of the Thermodynamic Potential of Supercritical Carbon Dioxide Cycles: A Systematic Approach*. J Eng Gas Turb Power 140, pp. 051701.
- [18] C.M. Invernizzi, 2017. *Prospect of Mixtures as Working Fluids in real-Gas Brayton Cycles*. Energies 10, pp. 1649.
- [19] F. Crespi et al., 2019. *Capital Cost Assessment of Concentrated Solar Power Plants Based on Supercritical Carbon Dioxide Power Cycles*, J Eng Gas Turb Power 141, pp. 071011.
- [20] G. Di Marcoberardino et al., 2020. *Experimental and analytical procedure for the characterization of innovative working fluid for power plants applications*. Appl Therm Eng 178, pp. 115513.
- [21] ThermoFlow Inc, ThermoFlow suite - ThermoFlex software. https://www.thermoflow.com/products_generalpurpose.html. Retrieved October 30th 2020.
- [22] National Fire Protection Association <https://www.nfpa.org/codes-and-standards/all-codes-and-standards/list-of-codes-and-standards/detail?code=704> Retrieved December 14th 2020.
- [23] Aspen Plus - Leading process simulator software <https://www.aspentech.com/en/products/engineering/aspen-properties>. Retrieved October 30th 2020.
- [24] A.M.A. Dias, J.L. Daridon, J.C. Pa, 2006. *Vapor - Liquid Equilibrium of Carbon Dioxide - Perfluoroalkane Mixtures: Experimental Data and SAFT Modeling*, Ind Eng Chem Res 45, pp. 2341–2350.
- [25] W.K. Tolley, R.M. Izatt, J.L. Oscarson, 1992. *Titanium tetrachloride-supercritical carbon dioxide interaction: A solvent extraction and thermodynamic study*, Metall. Trans. B. 23, pp. 65–72.
- [26] A. Perdichizzi, G. Lozza, 1987, *Design Criteria and Efficiency Prediction for Radial Inflow Turbines*, ASME Gas Turbine Conference and Exhibition, Anaheim, CA.

CHARACTERIZING AND MODELLING TURBULENCE IN SUPERCRITICAL FLUIDS

R. Pecnik¹, J. Ren² and G.J. Otero-R.¹
(r.pecnik@tudelft.nl)

¹*Delft University of Technology, Leeghwaterstraat 39, 2613 CB Delft, The Netherlands*

²*University of Nottingham, University Park, Nottingham, NG7 2RD UK*

ABSTRACT

From concentrated solar power plants to rocket engines, energy conversion systems are continually reengineered to perform ever better. Often this involves fluids being pushed into the supercritical region, where highly non-ideal thermodynamic effects are at play. Yet, our fundamental understanding of flow physics at such conditions lags behind to successfully realize these exciting engineering applications. Especially, the sharp variations in all thermophysical properties close to the critical point and the high optical density at supercritical pressures lead to significantly richer flow physics and even more intricate phenomena in turbulence. In this talk we will present our recent fundamental on turbulence in supercritical fluids, which are relevant in all component of a supercritical power cycle. We will elucidate how and when flows with supercritical fluids transition to turbulence and how compressible effects can be characterized and modelled for turbulent heat transfer.

INTRODUCTION

The continuous demand to increase the efficiency of energy conversion systems and the productivity of process plants forces engineers and scientists to use fluids at increasingly higher pressures and temperatures. For instance, to increase the thermal efficiency of power plants, engineers are currently developing a thermodynamic power cycle that operates with carbon dioxide in the supercritical region, at pressures and temperatures high enough to exceed the critical point where fluids behave in a highly non-ideal way. Such a power cycle has the potential to enable a break-through of cost-competitive, utility-scale solar thermal power plants. Another example where pressures and temperatures of fluids continuously increase is in the development of more powerful rocket engines. The idea of engineers is to use rocket fuels at supercritical conditions not only to increase fuel mixing with the oxidizer but also to cool the rocket engine using the fuel before it is injected into the combustion chamber. While cooling the rocket nozzle, the fuel is heated from initially cryogenic conditions into the supercritical region. The net result is a rocket engine that provides higher specific thrust, enabling space access with increasingly higher payloads.

One of the major obstacles in successfully realizing these technologies is the limited knowledge of turbulence in the supercritical fluid region, especially when flows are

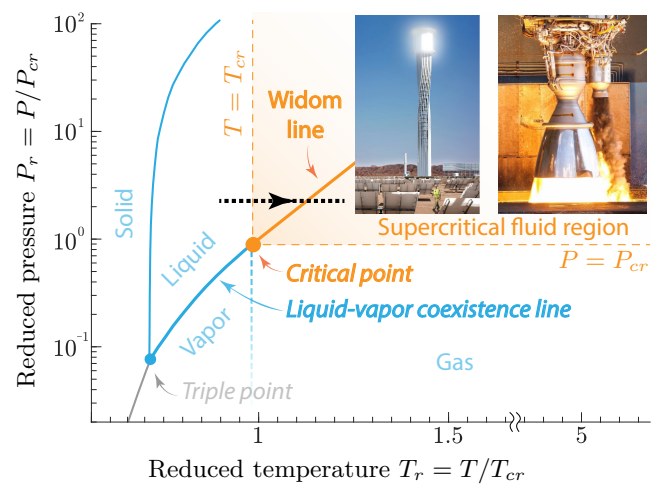


Figure 1: Pressure – temperature phase diagram of an arbitrary substance indicating the thermodynamic critical point and the supercritical fluid region. P_{cr} and T_{cr} are critical pressure and temperature, respectively. Two applications are shown which will operate in the supercritical regime.

heated or cooled across the Widom line (see black dotted line in figure Figure (1)) in the supercritical region. The sharp variations in all thermophysical properties in the vicinity of the Widom line lead to significantly richer flow physics and even more intricate phenomena in turbulence.

In this paper we will discuss three topics related to flows in the supercritical fluid region. In the first topic we will discuss **boundary layer instability** with fluids in the vicinity of the critical point, where we will identify the range of disturbances to which a given laminar base flow is unstable and how these instabilities can trigger the development of turbulence. In the second topic we will discuss how **fully developed turbulent flows** with highly non-ideal fluids can distinctively be characterized by the semi-local Reynolds number and a scaling approach we proposed recently in Ref. [1]. In the third topic we will show how this scaling approach can be used to properly sensitize common **turbulence models** to account for the “leading-order effect” of variable properties on wall bounded turbulence.

TRANSITION TO TURBULENCE

Most of the present knowledge on stability and laminar-turbulent transition is limited to ideal gases [3] or incompressible flows, where thermodynamic properties are constant. On the other hand, numerical simulations of real gas effects (high-temperature chemical effects) in hypersonic flows has just gone through an initial stage [6, 7, 8]. These effects, often referred to as real-gas effects, include vibrational excitation, dissociation and recombination of gas species, ionization, radiation and surface ablation. Apart from the high-temperature chemical effects, stratifications in thermodynamic or/and transport properties can substantially influence the stability (see review by Govindarajan & Sahu [9], and references therein). These stratifications exist both naturally (e.g. in the Earth's outer core) and artificially (e.g. exert wall heating/cooling), revealing some of the non-ideal-gas effects.

We recently investigated the stability of boundary layer flows with fluids close to the critical point [10], through linear stability theory [11], direct numerical simulation and inviscid analysis. To account for the full non-ideal gas effects, one must take the non-ideal equation-of-state into consideration as well as the complicated functions of thermodynamic/transport properties in terms of its thermodynamic state, which can be determined by two independent thermodynamic quantities (such as density and internal energy). We study boundary layer flows with carbon dioxide (CO₂) at a constant pressure of 80 bar, which is above the critical pressure (73.9 bar). The flow conditions are such chosen that different thermodynamic regimes of interests shall be well revealed.

If a fluid at constant supercritical pressure is heated, such that the Widom line is crossed (see black dotted line in figure Figure (1)), highly non-ideal effects are at play. In the vicinity of the Widom line, which is an extension of the liquid-vapor coexistence line into the supercritical fluid regime (see solid orange line in figure Figure (1)), a seemingly continuous phase transition from a compressible liquid to a dense vapor occurs with large changes in all thermophysical properties [12, 13, 14]. As the temperature at the wall increases towards the Widom line (due to viscous heating), the stability of the flow increases significantly (see neutral stability curves in the right column of figure Figure (2) (a,b) for two different Mach numbers). By crossing the Widom line, figure Figure (2)(c), a novel and peculiar second mode (Mode II) appears which overlaps with Mode I. Until now, such a phenomenon has not been observed and further research is required to unveil this intriguing mechanisms using advanced theory, comprehensive simulations and novel experiments.

To characterise the boundary layer flow we use the Reynolds number, Re_∞ , Prandtl number, Pr_∞ , Eckert number, Ec_∞ and the Mach number, Ma_∞ (all based on freestream parameters) which are given as:

$$Re_\infty = \frac{\rho_\infty^* u_\infty^* l_0^*}{\mu_\infty^*}, \quad Pr_\infty = \frac{\mu_\infty^* C_{p\infty}^*}{\kappa_\infty^*},$$

$$Ec_\infty = \frac{u_\infty^{*2}}{C_{p\infty}^* T_\infty^*}, \quad Ma_\infty = \frac{u_\infty^*}{a_\infty^*}. \quad (1)$$

The subscript ∞ denotes freestream values, superscript $*$ stands for dimensional variables, l_0^* is a chosen length scale, a_∞^* is the speed of sound in the freestream. Note that for an ideal gas $Ec_\infty = (\gamma - 1)Ma_\infty^2$, where γ is the heat capacity ratio. In linear stability theory, l_0^* is chosen to be the local boundary layer thickness scale δ^* ,

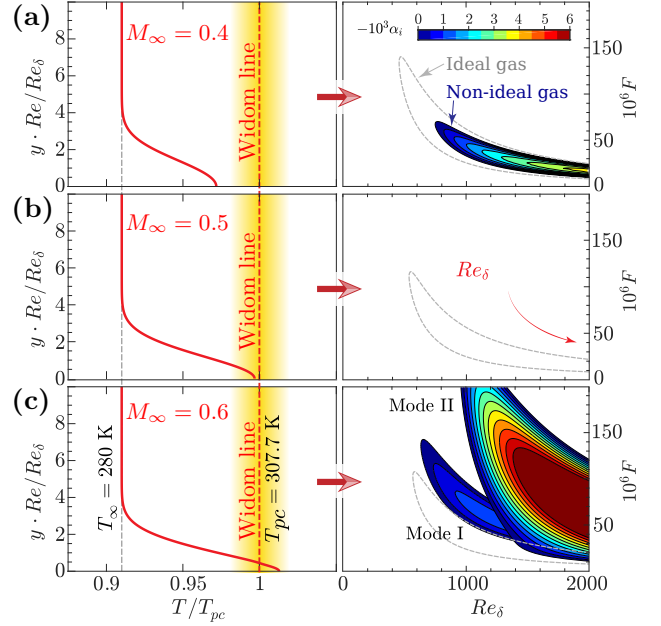


Figure 2: Boundary layer temperature profiles (left column) and corresponding neutral stability curves as function of Reynolds number, Re_δ , and perturbation frequency, F , (right column) for cases with increasing free stream Mach number ($M_\infty = [0.4, 0.5, 0.6]$). The equivalent ideal gas solution is shown in gray to highlight differences. The wall is adiabatic and the free stream temperature is at 280 K.

which results in the definition of Re_δ :

$$\delta^* = \left(\frac{\mu_\infty^* x^*}{\rho_\infty^* u_\infty^*} \right)^{1/2},$$

$$Re_\delta = \frac{\rho_\infty^* u_\infty^* \delta^*}{\mu_\infty^*} = \left(\frac{\rho_\infty^* u_\infty^* x^*}{\mu_\infty^*} \right)^{1/2}. \quad (2)$$

Besides the known stabilization of compressibility effects (increase Ec_∞), the boundary layer flow is further stabilized by non-ideal gas effects in the subcritical or supercritical regime. In either regime, the temperature profile remains below or above T_{pc} , the stabilization is more prominent when T_∞ is closer to T_{pc} and/or Ec_∞ is increased.

The most interesting results lie in the transcritical regime, where the temperature profile crosses the pseudo-critical point ($T_{pc} = 307.7$ K). We show in figure Figure (3) a detailed evolution of the growth rate with $T_\infty = 280$ K by gradually increasing the Eckert number from $Ec_\infty = 0.11$ to $Ec_\infty = 0.202$, such that the insulated wall temperature increases. Figure Figure (3)(a,b) shows the neutral curve of Mode I, while in figure Figure (3)(c) we show Mode II that becomes unstable at $Ec_\infty \geq 0.19$. It appears that the maximum critical Reynolds number Re_δ occurs at $Ec_\infty = 0.16$. The flow enters the transcritical regime (the temperature crosses the pseudo-critical point) at $Ec_\infty \geq 0.17$, and the growth rate and the extent of the neutral curve of Mode I again increases. Figure Figure (3)(b) shows the evolution of Mode I in the transcritical regime. With an increase in Ec_∞ , the range of unstable Re_δ decreases, while the range for unstable F increases. Most noteworthy is the growth rate of Mode II, which increases much faster with Ec_∞ and becomes much larger than Mode I. This indicates that the flow in the transcritical regime is

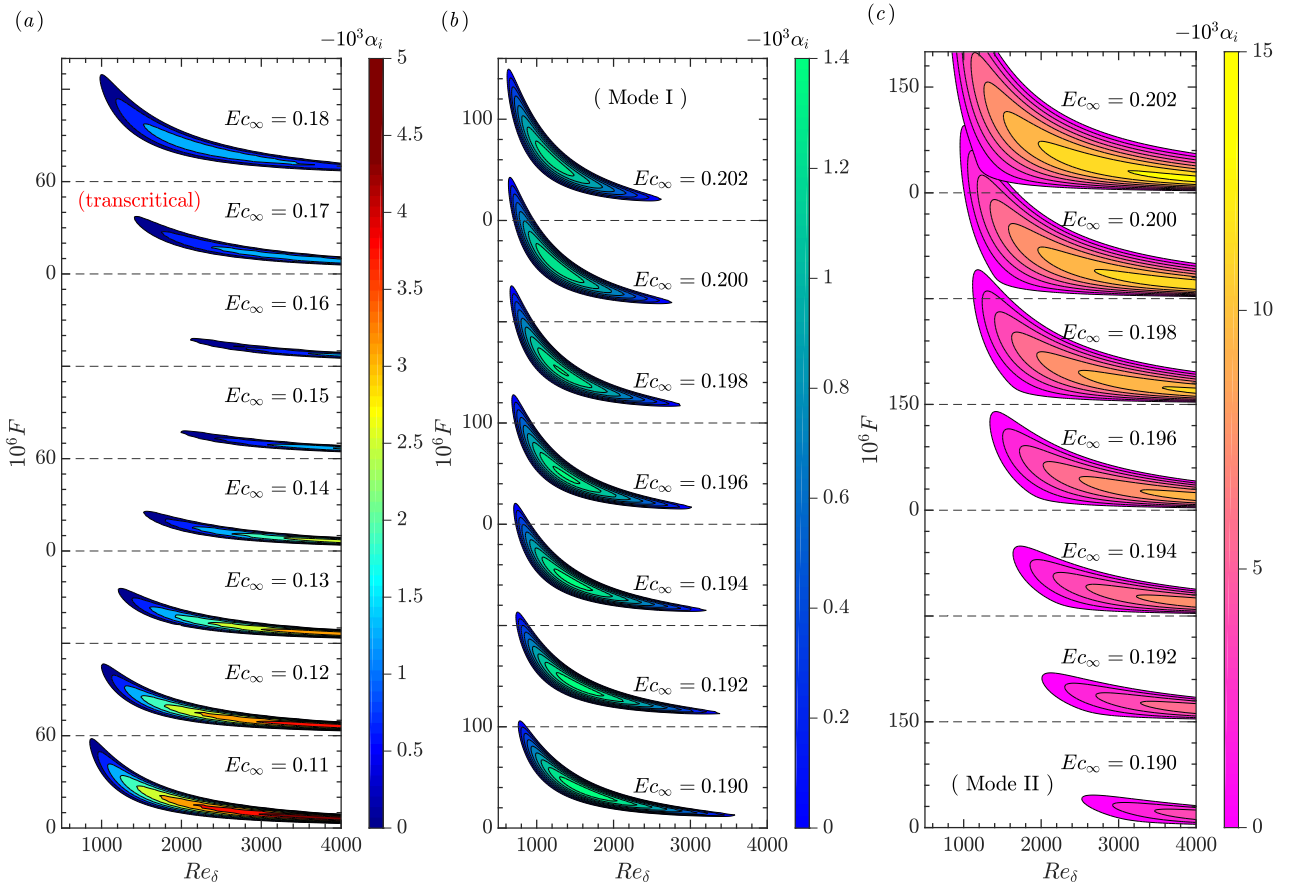


Figure 3: Growth rates of perturbations in the $F - Re_\delta$ stability diagram with $T_\infty^* = 280$ K. (a) $Ec_\infty = 0.11, 0.12, \dots, 0.19$, (b) $Ec_\infty = 0.194, 0.196, \dots, 0.202$.

significantly destabilized by non-ideal gas effects through Mode II.

The inviscid analysis shows that in the transcritical regime, Mode II is not caused by the trapped acoustic waves which is deemed to give rise to higher modes in hypersonic flows. We show that the generalized inflection point criterion expressed in density $D(\rho_0 DU_0)$ is valid for non-ideal gases. As result, an inviscid mechanism is present in the trans- and supercritical regimes in contrast to the subcritical regime which contains the viscous instability only.

FULLY TURBULENT FLOWS

Figure (4) shows three turbulent channel flow simulations using DNS. The fluid is volumetrically heated, while the temperature at the wall is kept at a constant value. Different constitutive relations for density, ρ , and viscosity, μ , as a function of temperature, T , were used. The case CRe_τ^* (figure (a)) corresponds to a flow for which density and viscosity are decreasing away from the wall, such that the semi-local Reynolds number Re_τ^* is constant across the whole channel height. The semi-local Reynolds number is defined as

$$Re_\tau^* \equiv \frac{\sqrt{\langle \rho \rangle / \rho_w}}{\langle \mu \rangle / \mu_w} Re_\tau, \quad (3)$$

where $\langle \cdot \rangle$ denotes Reynolds averaging, the subscript w indicates quantities at the isothermal wall (no averaging at the wall is required), $Re_\tau = \rho_w u_{\tau w} h / \mu_w$ is the friction Reynolds number based on friction velocity, $u_{\tau w}$, and a characteristic length, h . Although this case has arbitrary

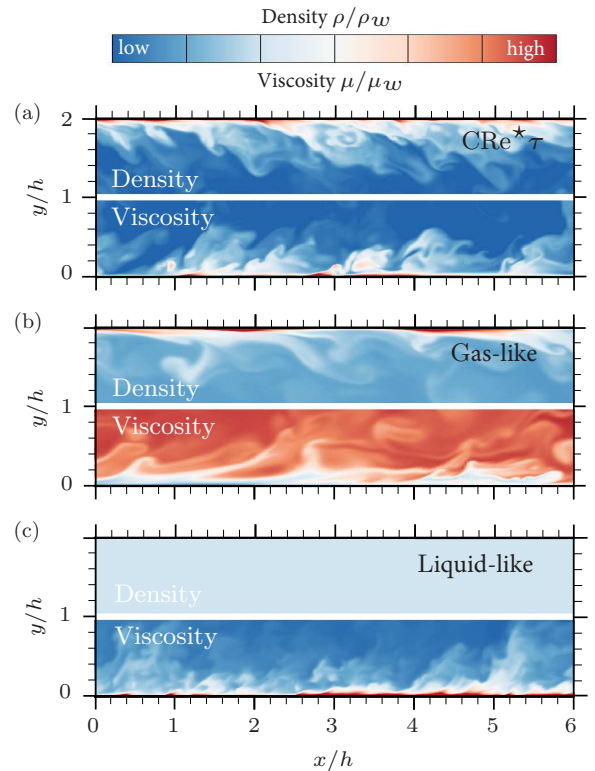


Figure 4: Contour plots of instantaneous density ρ (top half) and dynamic viscosity μ (lower half) for cases CRe_τ^* (a), Gas-like (b), and Liquid-like (c).

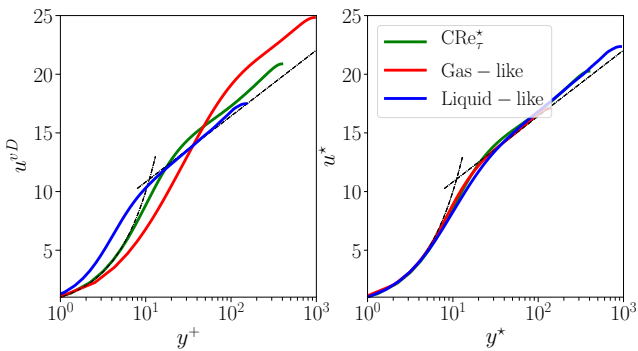


Figure 5: Contour plots of instantaneous density ρ (top half) and dynamic viscosity μ (lower half) for cases CRE_{τ}^* (a), Gas-like (b), and Liquid-like (c).

thermophysical properties, it is worthwhile to mention that it bears similarities to supercritical fluids, for which both density and viscosity decrease when heated across the pseudo-critical temperature [15, 16]. The cases GL and LL (figure (b) and (c)) are flows with gas-like and liquid-like property variations that both have large gradients in Re_{τ}^* . More details on the governing equations, the numerical scheme and the DNS cases can be found in [1].

The streamwise velocity profiles are shown in Figure (5). Note, the van Driest velocity transformation (left figure), which is defined as $u^{vD} = \int \sqrt{\langle \rho \rangle / \rho_w} d(\langle u \rangle / u_{\tau_w})$, is not capable to provide a collapse for the velocity profiles of these three DNS cases. On the other hand, the velocity scaling as proposed by [17], and later independently derived by [18], provides a good collapse for all cases (right figure). The u^* -velocity scaling based on the semi-local Reynolds number is expressed as,

$$u^* = \int_0^{\bar{u}^{vD}} \left(1 + \frac{y}{Re_{\tau}^*} \frac{dRe_{\tau}^*}{dy} \right) d\langle u^{vD} \rangle. \quad (4)$$

This transformation has been obtained by scaling the Navier-Stokes equation using semi-local scales, which is the key to account for the leading-order effect of variation in thermophysical properties on turbulence. This semi-local scaling approach provides a framework to collapse other turbulence properties as well and consequently provides insight to properly models turbulence as discussed in the next section.

TURBULENCE MODELING

Common turbulence models for solving the Reynolds-averaged Navier-Stokes (RANS) equations do not correctly account for variations in thermodynamic/transport properties, such as density and viscosity, which can cause substantial inaccuracies in predicting important quantities of interest, for example, heat transfer and drag. RANS equations with simple extensions of eddy viscosity models (EVM) are currently used to predict turbulence in supercritical fluids. For example, if the turbulent kinetic energy (TKE) equation is derived on the basis of the compressible Navier-Stokes equations, additional terms appear, i.e. pressure-work and -dilatation, dilatational dissipation, and additional terms related to fluctuations of density, velocity, pressure, etc. The modification of the TKE in flows with strong heat transfer has been attributed to these terms and according models have been proposed in the past [19, 20, 21]. A different approach

to sensitize turbulence models for compressible flows with large density variations, was proposed by Catris and Aupoix [22]. They used the formulation developed by Huang *et al.* [23] for the closure coefficients, to modify the diffusion term of the turbulent dissipation transport equation. Additionally, they argued that the diffusion of TKE acts upon the energy per unit volume $[(kg \ m^2/s^2)/m^3]$ of turbulent fluctuations, which can be expressed as ρk . The diffusion of TKE is therefore based on ρk , while the diffusion coefficient is divided by the density on the basis of dimensional consistency.

Based on the semi-locally scaled turbulent kinetic energy equation, introduced in [1], we analytically derive a modification of the diffusion term of turbulent scalar equations to improve the prediction of eddy viscosity models for wall-bounded turbulent flows with strong gradients in the thermo-physical properties. The modifications are based on the fact that the “leading-order effect” of variable properties on wall bounded turbulence can be characterized by the semi-local Reynolds number only [18]. For instance, the modified TKE equation reads (averaging operators omitted),

$$\frac{\partial \rho k}{\partial t} + \frac{\partial \rho k u_j}{\partial x_j} = P_k - \rho \varepsilon + \frac{1}{\sqrt{\rho}} \frac{\partial}{\partial x_j} \left[\frac{1}{\sqrt{\rho}} \left(\mu + \frac{\mu_t}{\sigma_k} \right) \frac{\partial \rho k}{\partial x_j} \right]. \quad (5)$$

If compared to the conventional model for the TKE, the newly derived equation shows only one major difference that lies in the diffusion term. The diffusion term that emerges from the semi-local scaling methodology is a function of ρk (instead of k), while the diffusion coefficient and the overall diffusion term are divided by $\sqrt{\rho}$. This is similar to the density corrections proposed by [22], except that in [22], only the diffusion coefficient is divided by ρ .

The developed methodology is generic and applicable to a wide range of eddy viscosity models. We have applied the same methodology to several turbulent scalars (ε , ω , among others) of common eddy viscosity models: the eddy viscosity correlation of Cess [24], the one-equation model of Spalart Allmaras (SA) [25], the low Reynolds number $k - \varepsilon$ model of Myong and Kasagi (MK) [26], Menter’s shear stress transport model (SST) [27], and the four-equations $v^2 - f$ model (V2F) [28]. An additional modification we have introduced is to replace y^+ and Re_{τ} , e.g. within the eddy viscosity correlation of Cess and for the damping function of the MK turbulence model, by their semi-local counterparts, namely y^* and Re_{τ}^* [1].

We have tested the EVM to available direct numerical simulations (DNS) of volumetrically heated fully developed turbulent channel flows with varying thermo-physical properties which have been introduced earlier. The density and the viscosity are a function of temperature and different constitutive relations are used, that resemble behaviours of liquids (LL), gases (GL), supersonic fluids (SS), and fluids close to the vapour-critical point (CRE_{τ}^*).

The results are reported in Figure (6) in terms of u^* (see equation (4)) and u^{vD} , which is the van Driest velocity transformation. The modifications clearly improve the EVM for flows with strong variations on the thermo-physical properties. A substantial improvement is seen in Cess and the MK model; the damping function of these modified models is able to correctly account for variations of transport properties. Interestingly, the original SA model, originally developed for external flow, gives

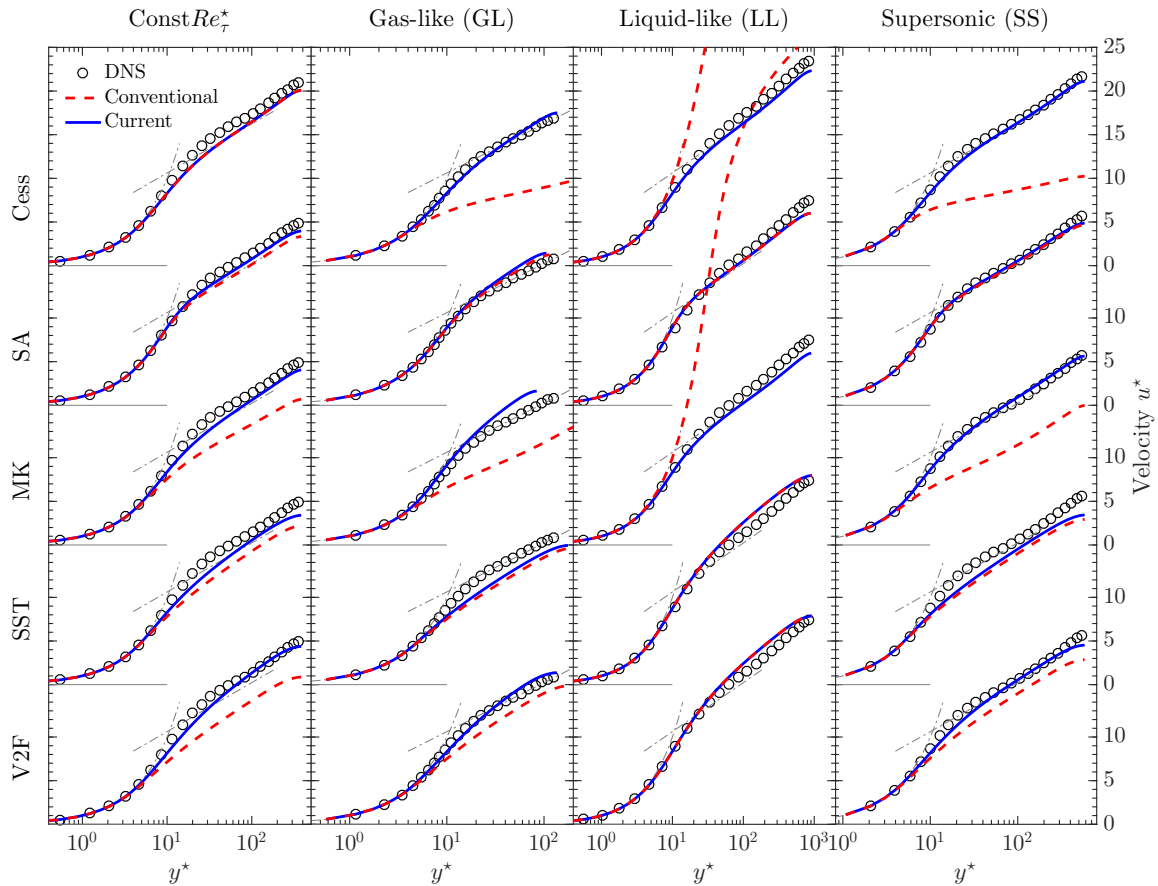


Figure 6: Universal velocity transformation u^* with respect to the semi-locally scaled wall normal distance y^* for a fully developed turbulent channel. The grey dashed lines represent $u^* = y^*$ and $u^* = 1/\kappa \ln(y^*) + C$, the viscous sublayer and log-law region, respectively, where $C = 5.5$.

the most reliable results, with respect to other conventional EVM, for the cases studied. For the modified SST model, the performance with respect to the universal law of the wall is not satisfactory. The modified V2F formulation improves the collapse with the DNS data if compared to the conventional form for all the cases. For the profile of u^* , a good collapse is seen with the DNS data for most of the modified EVM, outperforming the original models.

CONCLUSION

Several conclusions can be drawn on the topics discussed in this paper, which are separately discussed hereafter.

Boundary layer stability The compressibility effects close to the critical point strongly stabilise the boundary layer. Using modal stability analysis we showed that for conditions where the free-stream temperature is below the pseudo-critical point, the maximum boundary layer stabilisation is achieved when the temperature at the wall increase towards the Widom line. Once the temperature at the wall crosses the Widom line, due to an increase in Mach number, a novel instability mode appears. The growth rate of this mode increases much faster with Ec_∞ and becomes much larger than Mode I. This indicates that the flow in the transcritical regime is significantly destabilised by non-ideal gas effects.

Fully developed turbulent flows We have recently derived a simple scaling transformation of the Navier-Stokes equations using semi-local quantities, which allows to account for the “leading order effect” of variable properties on turbulence. One outcome of this approach

is a velocity transformation that allows to collapse velocity profiles for channel flows with arbitrary variations in density and viscosity.

Turbulence modelling Based on the semi-local scaling framework we have also derived a novel methodology to improve eddy viscosity models for predicting wall-bounded turbulent flows with strong variations in thermo-physical properties. The major difference of the new methodology is the formulation of the diffusion term in the turbulence scalar equations. The conclusion is that the diffusion of turbulent kinetic energy acts upon the energy per unit volume and not per unit mass. In general, the modified EVMs result in a much better agreement with the DNS data in terms of velocity profiles and heat transfer of fully developed turbulent channel flows with variable property fluids. The next step in modelling turbulence should focus on effects related to very large density fluctuations (larger than the ones considered herein) and to turbulence deterioration emerging from flow acceleration and buoyancy forces.

REFERENCES

- [1] R. Pecnik and A. Patel, “Scaling and modelling of turbulence in variable property channel flows,” *Journal of Fluid Mechanics*, vol. 823, no. R1, 2017.
- [2] A. Sameen and R. Govindarajan, “The effect of wall heating on instability of channel flow,” *Journal of Fluid Mechanics*, vol. 577, pp. 417–442, 2007.
- [3] A. Fedorov, “Transition and stability of high-speed boundary layers,” *Annual Review of Fluid Mechanics*, vol. 43, no. 1, pp. 79–95, 2011.

- [4] L. M. Mack, "Boundary-layer linear stability theory," in *AGARD Report No. 709 Special Course on Stability and Transition of Laminar Flow*, 1984.
- [5] S. Kawai, "Direct numerical simulation of transcritical turbulent boundary layers at supercritical pressures with strong real fluid effects," in *54th AIAA Aerospace Sciences Meeting*, p. 1934, 2016.
- [6] X. Zhong and X. Wang, "Direct numerical simulation on the receptivity, instability, and transition of hypersonic boundary layers," *Annual Review of Fluid Mechanics*, vol. 44, no. 1, pp. 527–561, 2012.
- [7] O. Marxen, T. E. Magin, E. S. Shaqfeh, and G. Iaccarino, "A method for the direct numerical simulation of hypersonic boundary-layer instability with finite-rate chemistry," *Journal of Computational Physics*, vol. 255, pp. 572–589, 2013.
- [8] O. Marxen, G. Iaccarino, and T. E. Magin, "Direct numerical simulations of hypersonic boundary-layer transition with finite-rate chemistry," *Journal of Fluid Mechanics*, vol. 755, pp. 35–49, 2014.
- [9] R. Govindarajan and K. C. Sahu, "Instabilities in viscosity-stratified flow," *Annual Review of Fluid Mechanics*, vol. 46, pp. 331–353, 2014.
- [10] J. Ren, O. Marxen, and R. Pecnik, "Boundary-layer stability of supercritical fluids in the vicinity of the widom line," *Journal of Fluid Mechanics*, vol. 871, pp. 831–864, 2019.
- [11] J. Ren, S. Fu, and R. Pecnik, "Linear instability of poiseuille flows with highly non-ideal fluids," *Journal of Fluid Mechanics*, vol. 859, pp. 89–125, 2019.
- [12] G. G. Simeoni, T. Bryk, F. A. Gorelli, M. Krisch, G. Ruocco, M. Santoro, and T. Scopigno, "The Widom line as the crossover between liquid-like and gas-like behaviour in supercritical fluids," *Nature Physics*, vol. 6, pp. 503–507, 2010.
- [13] D. Bolmatov, V. V. Brazhkin, and K. Trachenko, "Thermodynamic behaviour of supercritical matter," *Nature Communications*, vol. 4, pp. 1–7, 2013.
- [14] D. Banuti, "Crossing the widom-line – supercritical pseudo-boiling," *The Journal of Supercritical Fluids*, vol. 98, pp. 12 – 16, 2015.
- [15] J. W. Peeters, R. Pecnik, M. Rohde, T. van der Hagen, and B. Boersma, "Turbulence attenuation in simultaneously heated and cooled annular flows at supercritical pressure," *Journal of Fluid Mechanics*, vol. 799, pp. 505–540, 2016.
- [16] H. Nemati, A. Patel, B. J. Boersma, and R. Pecnik, "The effect of thermal boundary conditions on forced convection heat transfer to fluids at supercritical pressure," *Journal of Fluid Mechanics*, vol. 800, pp. 531–556, 2016.
- [17] A. Trettel and J. Larsson, "Mean velocity scaling for compressible wall turbulence with heat transfer," *Physics of Fluids*, vol. 28, no. 2, p. 026102, 2016.
- [18] A. Patel, B. Boersma, and R. Pecnik, "The influence of near-wall density and viscosity gradients on turbulence in channel flows," *Journal of Fluid Mechanics*, vol. 809, pp. 793–820, 2016.
- [19] P. G. Huang, P. Bradshaw, and T. J. Coakely, "Turbulence models for compressible boundary layers," *AIAA Journal*, vol. 32, no. 4, pp. 735–740, 1994.
- [20] S. Sarkar, G. Erlebacher, M. Hussaini, and H. Kreiss, "The analysis and modelling of dilatational terms in compressible turbulence," *Journal of Fluid Mechanics*, vol. 227, pp. 473–493, 1991.
- [21] O. Zeman, "A new model for super/hypersonic turbulent boundary layers," in *31st Aerospace Sciences Meeting*, p. 897, 1993.
- [22] S. Catris and B. Aupoix, "Density corrections for turbulence models," *Aerospace Science and Technology*, vol. 4, no. 1, pp. 1–11, 2000.
- [23] P. Huang, P. G., Coleman, G. N., Bradshaw, "Compressible Turbulent channel flows, DNS results and modelling," *JFM*, no. 1995, pp. 185–218, 1995.
- [24] R. Cess, "A survey of the literature on heat transfer in turbulent tube flow," *Res. Rep.*, pp. 8–0529, 1958.
- [25] P. R. Spalart, S. R. Allmaras, *et al.*, "A one equation turbulence model for aerodynamic flows," *RECHERCHE AEROSPATIALE-FRENCH EDITION-*, pp. 5–5, 1994.
- [26] N. Myong, H.K. and Kasagi, "A New Approach to the Improvement of k-e turbulence model for wall-bounded shear flows," *JSME*, vol. 33, no. 2, 1990.
- [27] F. R. Menter, "Zonal Two Equation k-w, Turbulence Models for Aerodynamic Flows," *AIAA paper*, p. 2906, 1993.
- [28] P. A. Durbin, "Separated Flow Computations with the k-e-v2 Model," *AIAA Journal*, vol. 33, no. 4, pp. 659–664, 1995.

ANALYSIS OF sCO₂ CYCLES FOR DISTRICT HEATING APPLICATIONS

Mathias Penkuhn*

Technische Universität Berlin
Chair of Energy Engineering and
Environmental Protection
Berlin, Germany
Email: mathias.penkuhn@tu-berlin.de

George Tsatsaronis*

Technische Universität Berlin
Chair of Energy Engineering and
Environmental Protection
Berlin, Germany
Email: georgios.tsatsaronis@tu-berlin.de

ABSTRACT

Supercritical CO₂ (sCO₂) power cycles provide the possibility to significantly improve power generation from fossil fuels and renewable sources considering thermodynamic efficiency, economic feasibility, and operational flexibility. In addition to standalone power generation, the application of sCO₂ cycles to cogeneration for combined heat and power processes can be a highly attractive option with respect to further development, and commercialization. In particular, the incorporation of a heat extraction option for district heating can be favorable regarding the overall cycle efficiency for temperate and cold climate regions because of the thermodynamic properties of sCO₂. The current study thus focuses on the modeling, simulation, and thermodynamic analysis of different, simple sCO₂ cycle designs for waste heat applications incorporating heat extraction for district heating. Different technological options, like backpressure turbines, split-flow recooling, as well as turbine extraction designs, and their effects on cycle design, operation, and efficiency are analyzed. The results show that sCO₂ based cycles enable engineers to achieve high-efficiency power generation also in combination with heat extraction for district heating, comparable to conventional water-steam-based cycles. Furthermore, the split-flow recooling design provides the possibility to extract a significant amount of heat without affecting the power generation.

INTRODUCTION

The application of supercritical CO₂ (sCO₂) in power generation cycles has received considerable attention during the last decade. Having been rediscovered as a natural, alternative working fluid for thermodynamic cycles, sCO₂ offers the potential to realize high-efficiency power cycle designs, combined with low-emissions and favorable economics [1]. Other, yet unproven, prospects suggest the potential for providing smaller equipment sizes and higher operational flexibility because of simpler power cycle designs compared to conventional water-steam-based power cycles [1]. All the above-mentioned benefits are driving extensive

worldwide research and development programs representing a significant effort for future implementation and commercialization of the technology.

The spectrum of potential applications [1, 2] of sCO₂ in direct and indirect power cycles encompasses different possible heat sources for thermal power cycles. These include fossil [3–5], nuclear [6–8], solar and geothermal sources [9–12], and waste heat recovery [13–15]. In contrast to state-of-the-art water-steam-based technologies [16, 17], sCO₂ power cycles are characterized by high temperatures and pressures, low-pressure ratios, and a high recuperation requirement. Because of the supercritical conditions, the thermodynamic efficiency of heat transfer is significantly improved while high-pressure and low-pressure ratio designs result in low specific compression work and therefore compact turbomachinery designs [1].

Most research has concentrated on the identification of thermodynamically efficient cycle designs for standalone power generation, where, e.g., the recompression cycle and the split-flow expansion cycle designs have been identified as particularly promising options for standalone and waste heat recovery applications [18–20]. With a large set of potential designs being available, it is necessary to identify the most promising design options that are simple and offer a substantial economical or operational advantage regarding potential fields of application [21–23].

In this context, the use of sCO₂ for cogeneration processes is a potentially promising technological option [24]. Possible applications have been found for multi-effect desalination processes and industrial heat extraction [25–27]. In particular, the high-temperature thermal energy above 70 °C, that is available as waste heat in sCO₂ applications makes it ideal for integration in cogeneration systems where this heat can be effectively utilized instead of being rejected unused. In general, the same considerations apply to district heating in temperate and cold climates, thereby making it a potential application for future cogeneration processes using sCO₂ power cycles [28, 29]. Cogeneration in the form of combined heat and power (CHP) is generally considered advan-

* corresponding author(s)

Table 1: Gas turbine specifications

(a) Gas turbine data	
Model	GE 9E.04
Net power output	143.17 MW
Gas turbine efficiency	36.60 %
Exhaust mass flow	416.00 kg/s
Exhaust temperature	545.30 °C
Exhaust pressure	1.04325 bar
(b) Gas turbine flue gas composition	
Nitrogen (N ₂)	74.731 % (mol)
Oxygen (O ₂)	13.364 % (mol)
Argon (Ar)	0.895 % (mol)
Carbon Dioxide (CO ₂)	3.433 % (mol)
Water (H ₂ O)	7.577 % (mol)

tageous compared to the separate generation of heat and power [30]. CHP processes and their thermodynamic characteristics are well-understood [17]. However, today, the design of CHP plants is almost exclusively based on conventional water-steam-based cycle designs.

The following study investigates the possibility of using cogeneration for power generation and heat extraction for district heating in sCO₂ power cycles. In the present study CO₂ is used for the bottoming cycle in a gas turbine combined cycle application. The focus is put on simple, recuperated cycles that are further developed to incorporate potentially more effective design options for CHP applications. Such options comprise the use of backpressure turbine, split-flow, and turbine extraction cycle designs [17]. The suggested cycle designs options are then analyzed, compared, and discussed based on different thermodynamic metrics.

SYSTEM DESCRIPTION

In the present study, sCO₂ based power cycles for waste heat recovery in gas turbine combined cycles are investigated, in particular, regarding their possible use for cogeneration regarding district heating applications.

Cycle Design

In order to evaluate and analyze the different sCO₂ cycle design options for gas turbine combined cycle cogeneration, a suitable gas turbine design is used as the basis. In the present study, a GE 9E.04 gas turbine [31] is employed as the reference topping cycle incorporating the given ISO operating specifications. Available data is used for adjusting the specifications regarding changes in gas turbine exhaust backpressure due to the pressure drop in the waste heat recovery heat exchanger assuming that similar values for high-efficiency waste heat recovery applications can be expected and used as the design basis [32]. The results of the gas turbine modeling and simulation are given in Table 1.

In the literature, various sCO₂ power cycle designs for standalone power generation are available, of which only a limited design subset is considered suitable for waste heat applications [18]. However, the most important design decisions are guided by the main features of an sCO₂ power cycle. Particularly, the specific properties of CO₂ induce power cycle designs that show

high-temperature, high-pressure but low-pressure ratio characteristics that further have to be highly recuperative for achieving high cycle efficiencies. The simplest design that complies with these characteristics is the recuperated cycle design shown in Figure 1a which further acts as the reference for the derivation of all subsequent cycle designs.

The simple, recuperated cycle of Design (1) consists of a motor-driven, main compressor C1, and an expansion turbine M1 that drives the electric generator G1. Heat is recovered from the hot flue gas downstream of the gas turbine using the waste heat exchanger E1. The cooler E3 is used for heat rejection to the environment. As the CO₂ stream at the turbine outlet is still at a high temperature, the recuperator E2 is used to preheat a fraction of the high-pressure CO₂ stream for improving the cycle efficiency. Because of the large temperature difference between the working fluid on the hot and cold side of the recuperator, the recuperator itself is divided into two separate parts thus comprising a high-temperature (E2A) and a low-temperature (E2B) section.

Possible design options for incorporating cogeneration options in the present design can be derived from conventional water-steam-based cogeneration designs [17]. These options include conventional backpressure turbines, and turbine extraction designs, of which the design characteristics are well-understood as they are widely employed in CHP applications. However, in contrast to these conventional design options, the characteristics of an sCO₂ cycle also allow for a split-flow, recooling option downstream of the recuperator E2 where a portion of the CO₂ stream is used in the heat exchanger E4 for extracting thermal energy (heat) for district heating.

In case of the backpressure turbine cycle (Design 1), the cooler E3 is simply substituted by the heat exchanger E4 for district heating return and supply (DHRS) that extracts the available heat for district heating downstream of the recuperator E2 as shown in Figure 1a. The thermodynamic properties of the sCO₂ in the DHRS heat exchanger E4 are highly nonlinear because of the specific properties of CO₂ near the critical point. This influences the turbine outlet pressure, which is determined by the allowable temperature difference at the heat exchanger outlet, as well as the low-pressure recuperator outlet temperature regarding the possible occurrence of an internal pinch point in heat exchanger E4. The compressor inlet temperature is also limited by the available district heating return temperature. However, it is higher than the cooling water temperature, thereby shifting the compressor inlet conditions away from the critical point.

Another option is the use of the split-flow, recooling configuration in Design 2. The sequential use of the cooler E3 and the heat exchanger E4 for district heating provides an additional degree of freedom thereby enabling a lower turbine outlet pressure compared to the backpressure turbine configuration. The heat exchanger E4 for heat extraction for district heating is integrated downstream of the recuperator E2 in a split-flow arrangement. Because of the high temperature for waste heat rejection after the recuperator, a certain amount of the working fluid's thermal energy can be further utilized without negatively affecting the power generation.

The last design option for cogeneration applications considered in the present study is the turbine extraction design. This

configuration incorporates both options of Design 1 into a single-cycle design that allows for gradually adjusting the amount of heat that is extracted from the cycle for district heating. This cycle is depicted in Figure 1c and basically allows for any operation between standalone power generation and full backpressure operation. However, a more complex recuperator design is required as the high-temperature turbine extraction stream is also to be used in recuperator E2. Furthermore, an additional compressor is required because of the different pressure levels of the extraction and re-cooled streams. For reasons of simplicity, the current study neglects off-design effects in the compressor train, e.g. compressor surge, that limit the available operating characteristics.

It is still possible to incorporate even more of the above-mentioned features to achieve even higher cycle efficiencies. However, the focus of the present study remains at investigating the influence of incorporating a cogeneration option for district heating in waste heat sCO₂ power cycles. Therefore, more complex designs are not considered here.

Cycle Simulation and Design Parameters

The different sCO₂ power cycle designs for district heating applications are modeled and simulated using Epsilon Professional [33]. The parameterization of the simulation is based on best-practice guidelines that represent available knowledge concerning sCO₂ cycle design. This enables the benchmarking and evaluation of different designs based on steady-state simulations [19, 34]. The thermodynamic properties of CO₂ are calculated using REFPROP [35, 36].

Based on the available data [19, 34], the main design is characterized by a compressor inlet pressure of 80 bar and a turbine inlet pressure of 240 bar. The compressor inlet temperature for the designs that feature a re-cooler is assumed to be 32 °C using cooling water (CW) that is available onsite. In case of the backpressure turbine design, the compressor inlet temperature is determined by the minimum allowable temperature difference in heat exchanger E4. The turbine inlet temperature is set by assuming a minimum temperature difference of 10 K and a maximum effectiveness of 0.9 for the recuperator E2 thus maximizing the amount of heat recuperated in E2 and improving the overall cycle efficiency. A complete overview of the different simulation parameters is given in Table 2. As the current study is used for scoping purposes, no further parameter optimization has been conducted.

In order to determine the influence of the district heating supply and return temperature on the sCO₂ power cycle design and efficiency, three different sets are defined. In particular, the temperature split of 90/50 °C is used as a reference case as it can be considered as state-of-the-art in district heating network configurations [37, 38].

- Set A: 90/50 °C
- Set B: 70/40 °C
- Set C: 110/60 °C

Future district heating network designs are likely to be realized with even lower supply and return temperatures as chosen for Set B. In contrast, previous district heating network design generations are characterized by higher supply and return temperatures as represented by Set C.

METHODOLOGY

In the present study, a conventional thermodynamic approach for analyzing the different cycles is used. Therefore, energy-based metrics are employed to characterize the efficiency of the different cycle designs incorporating cogeneration for district heating.

Based on thermodynamic first-law principles, the efficiency of a standalone power cycle can be characterized by its thermodynamic efficiency η_w . It is defined as the ratio of generated net power, in the form of electric or mechanical power, and the thermal energy supplied by the fuel to the overall system [16].

$$\eta_w = \frac{\dot{W}_{net}}{\dot{m}_{fuel} \cdot LHV_{fuel}} \quad (1)$$

For cogeneration CHP plants, the overall thermodynamic efficiency η_{ov} is then calculated as the sum of the net power \dot{W}_{net} generated by the cycle and the additional heat \dot{Q} extracted for heating purposes [17, 39].

$$\eta_{ov} = \frac{\dot{W}_{net} + \dot{Q}}{\dot{m}_{fuel} \cdot LHV_{fuel}} = \eta_w + \eta_q = \eta_{GT} + \eta_{CO_2} + \eta_q \quad (2)$$

As a result, the overall thermodynamic efficiency is the sum of the power generation efficiency η_w , and heat generation efficiency η_q . The power generation efficiency itself consists of both cycle efficiencies, η_{GT} and η_{CO_2} , for the topping and bottoming cycles. As power and heat are not fully comparable by the first-law of thermodynamics because of differences in their thermodynamic quality, the overall thermodynamic efficiency η_{ov} is therefore also referred to as the energy utilization factor [39].

Another important parameter that characterizes a CHP plant is the power to heat ratio σ which determines the proportion of electric power to heat generated in a CHP process [17].

$$\sigma = \frac{\dot{W}_{net}}{\dot{Q}} = \frac{\eta_w}{\eta_q} \quad (3)$$

If the CHP process uses a split-flow or a turbine extraction configuration, the overall generated power is generally reduced because of the heat extraction at a constant fuel rate. Therefore, the power loss coefficient β , defined by

$$\beta = \frac{\Delta \dot{W}_{net}}{\dot{Q}} \Big|_{\dot{m}_{fuel} LHV_{fuel} = \text{constant}} \quad (4)$$

characterizes the reduction in available power at a constant fuel rate if heat is extracted.

All the defined parameters are only valid for a given operation point and change depending on the power and heat load, the return and supply temperature of the district heating network, and the site-specific environment conditions. However, if a suitable framework for benchmarking is employed, different designs can be evaluated and compared effectively, thereby characterizing the available technological potential [40].

RESULTS

Using the data that is obtained by the simulations, the previously discussed thermodynamic parameters are calculated for the different sCO₂ CHP cycle designs which provide the basis for detailed analyses and discussions.

Table 2: Simulation parameters used for the analysis of the sCO₂ power cycles designs based on benchmarking data given by Weiland and Thimsen [34], and Crespi et al. [19].

Unit ID	Parameter	Value
M1A	Turbine Inlet Pressure	240 bar
M1A/B	Turbine Isentropic Efficiency	90 %
M1A/B	Turbine Mechanical Efficiency	99 %
C1A/B	Compressor Inlet Pressure	80 bar
C1A/B	Compressor Isentropic Efficiency	85 %
C1A/B	Compressor Mechanical Efficiency	99 %
C1M	Motor Efficiency	95 %
G1	Electric Generator Efficiency	98.5 %
E1	Minimum Temperature Difference	10 K
E2A/B	Minimum Temperature Difference	10 K
E2A/B	Maximum Recuperator Effectiveness	0.9
E3	Cooler Outlet Temperature	32 °C
E4	Minimum Temperature Difference	5 K

Thermodynamic Analyses

The results of the simulations of the different sCO₂ power cycle designs for CHP are given in Table 3. In general, all the different cycle configurations can be regarded as high-efficiency designs. Detailed results of the sCO₂ bottoming cycles are depicted in Table 4.

In comparison, the standalone, non-optimized, power generation efficiency of the sCO₂ combined cycle is comparable to conventional water-steam-based combined cycles, which is given with 54.9 % for a two pressure non-reheat water-steam bottoming cycle for a GE 9E.04 gas turbine [31]. Furthermore, the energy utilization factor for CHP is also within the expected range of 80-90 % for combined cycle applications [41]. Therefore, it becomes clear that the application of sCO₂ cycles for CHP is a potential technological alternative to conventional water-steam-based cycles.

As expected, the simple recuperated, recooling Design (1) for standalone power generation exhibits the highest net power of 206.02 MW for combined cycle operation compared to 216 MW for the conventional water-steam-based combined cycle design. The overall thermodynamic efficiency is 52.65 % and the thermodynamic efficiency of the sCO₂ cycle is 16.06 %. In comparison, considering the backpressure turbine configuration for the reference district heating network temperature split of 90/50 °C, the net power is reduced to 186.62 MW. Thus, the power generation efficiency is reduced compared to the standalone power cycle, as exhibited by a power generation efficiency of 47.69 %. However, the overall efficiency, i.e., the energy utilization factor, accounts to 89.18 %. The power generation efficiency of the sCO₂ cycle amounts to 11.10 %. The power-to-heat ratio for the backpressure turbine configuration is 1.15 and the power-loss coefficient is 0.12. Both parameters illustrate the large amount of low temperature thermal energy that is available in sCO₂ cycles at the cost of a marginally reduced power generation.

This special characteristic of sCO₂ cycles becomes clearly visible when analyzing the results of the split-flow, recooling configuration of Design (2). In this case, the power generation is slightly reduced in standalone power generation mode because

of the higher hot stream outlet temperature at the recuperator E2 that is required for heat extraction at heat exchanger E4 for district heating. However, this feature enables the extraction of a certain amount of heat at constant power generation. Thus, the net power amounts to 200.52 MW with an overall thermodynamic efficiency of 51.24 % for standalone power generation and an overall thermodynamic efficiency at maximum heat extraction of 64.88 %. The power-to-heat ratio and the power loss coefficient are calculated to be 3.76 and 0, respectively. The total amount of heat that can be extracted by this design is about 1/3 of the heat available in the backpressure turbine design.

The last configuration considered in this study is the turbine extraction Design (3) that combines both configurations which are represented by Design (1). By integration of a turbine extraction, it is possible to continuously adjust the amount of heat extracted for district heating from the cycle. Therefore, the different thermodynamic parameters characterizing the cycle design at maximum power generation and heat extraction are the same as for Design (1).

However, in contrast to Design (1), the Designs (2) and (3) using the split-flow, recooling, and turbine extraction design features provide the possibility of adjusting the amount of heat that is available for district heating. This is depicted in Figure 2 where the net power of each design is shown as a function of the heat extracted of from cycle. Here, the standalone, recooling and backpressure turbine configurations of Design (1) define the reference points. The split-flow, recooling configuration of Design (2) is capable of extracting a certain amount of heat without any power loss as shown by its constant line and represented by its power-loss coefficient. In contrast, the turbine extraction configuration is, virtually, capable of switching completely between recooling operation for standalone power generation and maximum heat extraction by switching to full backpressure operation at the cost of a reduced power generation.

Sensitivity Analysis and Discussion

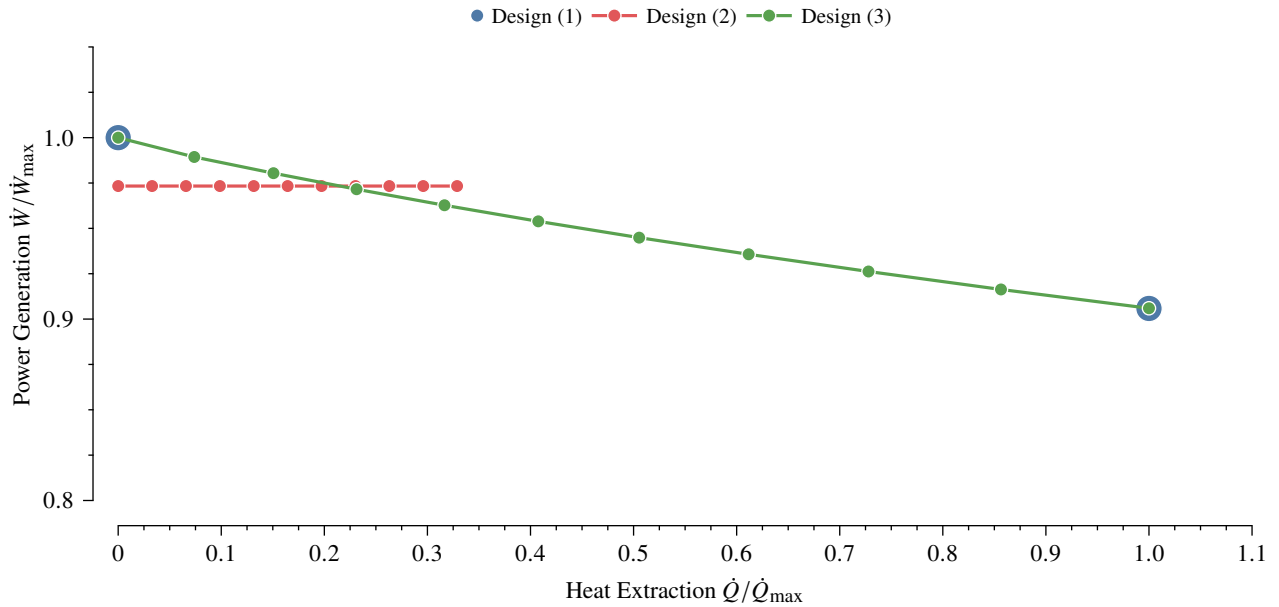
An important aspect for the potential application of sCO₂ power cycles for district heating is the dependency on the design

Table 3: Results of the combined cycle design analyses.

ID	Case	DH Supply/Return 90/50 °C				DH Supply/Return 70/40 °C				DH Supply/Return 110/60 °C			
		\dot{W}_{net} (MW)	\dot{Q}_{dh} (MW)	η_w (%)	η_{ov} (%)	\dot{W}_{net} (MW)	\dot{Q}_{dh} (MW)	η_w (%)	η_{ov} (%)	\dot{W}_{net} (MW)	\dot{Q}_{dh} (MW)	η_w (%)	η_{ov} (%)
Design (1)	max \dot{W}	206.02	–	52.65	52.65	206.02	–	52.65	52.65	206.02	–	52.65	52.65
	max \dot{Q}	186.62	162.35	47.69	89.18	196.46	151.79	50.21	88.99	172.99	176.93	44.21	89.42
Design (2)	max \dot{W}	200.52	–	51.24	51.24	203.36	–	51.97	51.97	197.96	–	50.59	50.59
	max \dot{Q}	200.52	53.38	51.24	64.88	203.36	58.14	51.97	66.83	197.96	52.40	50.59	63.98
Design (3)	max \dot{W}	206.02	–	52.65	52.65	206.02	–	52.65	52.65	206.02	–	52.65	52.65
	max \dot{Q}	186.62	162.35	47.69	89.18	196.46	151.79	50.2	88.99	172.99	176.93	44.21	89.42

Table 4: Detailed results of the sCO₂ bottoming cycles.

ID	Case	DH Supply/Return 90/50 °C			DH Supply/Return 70/40 °C			DH Supply/Return 110/60 °C		
		η_{CO_2} (%)	σ (–)	β (–)	η_{CO_2} (%)	σ (–)	β (–)	η_{CO_2} (%)	σ (–)	β (–)
Design (1)	max \dot{W}	16.06	–	–	16.06	–	–	16.06	–	–
	max \dot{Q}	11.10	1.15	0.12	13.62	1.29	0.06	7.62	0.98	0.19
Design (2)	max \dot{W}	14.66	–	–	15.38	–	–	14.00	–	–
	max \dot{Q}	14.66	3.76	0.00	15.38	3.50	0.00	14.00	3.78	0.00
Design (3)	max \dot{W}	16.06	–	–	16.06	–	–	16.06	–	–
	max \dot{Q}	11.10	1.15	0.12	13.62	1.29	0.06	7.62	0.98	0.19

**Figure 2:** Power and heat generation for the different cycle designs. The recooling and backpressure turbine configuration of Design (1) are used as the reference.

temperatures of the district heating network. The reference case that has been analyzed regarding the supply and return temperatures of 90/50 °C has already shown a considerable potential. This is now further investigated by a sensitivity study where three different sets of supply and return temperatures are analyzed.

The results are shown in Tables 3 and 4. Compared to the reference case, a reduction of the supply and return temperature to 70/40 °C generally allows for a higher power efficiency be-

cause of the increased potential to recover thermal energy in the recuperator E2. In case of the backpressure turbine and turbine extraction configurations, a lower return temperature also improves the electric efficiency as the compressor inlet temperature is significantly lower and which can also be used to decrease the turbine outlet pressure. Both features contribute to the reduction of the power-loss coefficient.

In contrast, in case of a higher supply and return temperature

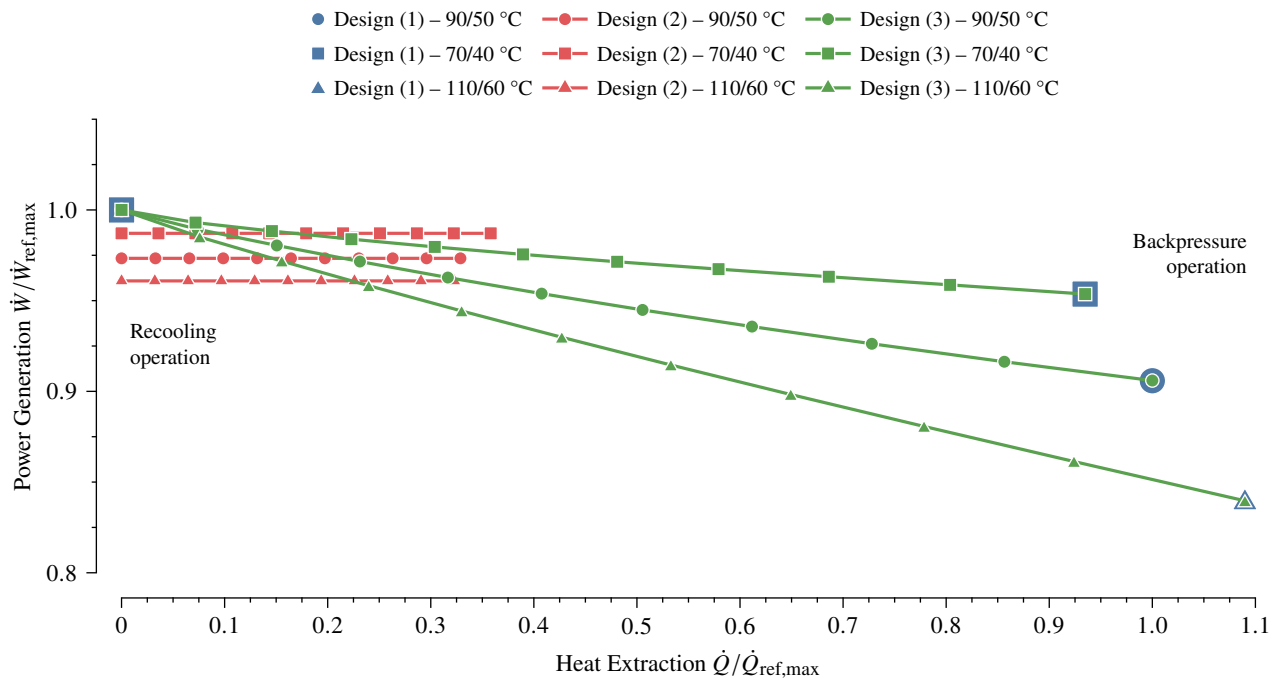


Figure 3: Sensitivity of the power and heat generation regarding changes in the supply and return temperature of the district heating system. The supply/return temperature configuration 90/50 °C is taken as the reference.

of 110/60 °C, the power efficiency is reduced compared to the reference case because of the reduced potential of recovering thermal energy in the recuperator E2. This becomes significant in case of the backpressure turbine and turbine extraction configurations. However, the impact on the split-flow, recooling configuration is in general smaller because the return temperature does not affect the compression efficiency as the cooler E3 is used for providing a constant compressor inlet temperature.

Another important information is provided by the dependency of the generated power when adjusting the amount of heat extracted from the cycle as depicted in Figure 3. Both configurations of Design (1) with a supply and return temperature of 90/50 °C are used as the reference configuration for reasons of comparability. As the standalone power generation configuration is not affected by the changes in the supply and return temperatures, the reference point does not change. In contrast, by increasing the supply and return temperatures, the power generation is significantly affected in the backpressure turbine and turbine extraction configurations. However, in case of the split-flow, recooling configuration, this effect is less significant. On the other hand, if the supply and return temperatures are reduced, the effect on the power generation is reduced for the backpressure turbine and turbine extraction configurations. In case of the split-flow, recooling configuration, the power generation almost approaches the standalone power generation configuration in terms of its power efficiency.

The analyses of the different sCO₂ cycle configurations in gas turbine combined cycle designs for cogeneration for district heating have shown that sCO₂ cycles can be effectively used in such a setting. High power efficiencies can be realized while providing the possibility to also efficiently extract a significant amount of heat.

Depending on the cycle design, a certain amount of heat can be extracted without negatively affecting the power generation, e.g., by the split-flow, recooling design. This is an interesting feature that cannot be found in conventional water-steam-based waste heat recovery systems that are used for cogeneration.

Another important feature is the additional degree of freedom that is introduced by the recuperator that thermally decouples the high temperature and low temperature parts in sCO₂ cycles. Thereby, the influence of increased heat extraction on the power generation is reduced because of the possibility to adjust the cycle design with respect to the low temperature thermal energy level that is required in district heating.

CONCLUSIONS

The present study investigates the potential of using sCO₂ power cycles as the bottoming cycle in gas turbine combined cycles for cogeneration. Based on the design information of an sCO₂ cycle for standalone power generation, different designs and configurations have been analyzed and discussed. It has been shown that even a simple, recuperated sCO₂ cycle design can be used for high-efficiency power generation comparable to conventional water-steam-based cycle designs. Because of the large amount of available low-temperature thermal energy, sCO₂ cycles can be effectively used in combined heat and power applications for district heating. In particular, if future district heating network designs are designed and operated at even lower supply and return temperatures, an sCO₂ bottoming cycle provides the possibility to extract a significant amount of heat without negatively affecting the power generation by effectively decoupling the high temperature and low temperature side of the sCO₂ cycle by the recuperator as shown for the split-flow design.

Based on the promising results of the present study, the different cycle designs options are to be analyzed in more detail. As the recuperated cycle analyzed in this study represents the simplest of all sCO₂ cycle configurations, other cycle designs incorporating split-flow expansion, and intercooling compression configurations should be investigated. Furthermore, the combination of the split-flow, recooling, and turbine extraction designs can result in further advantages by effectively combining the characteristics of both configurations reducing the impact of the heat extraction on the power generation. In general, the use of sCO₂ power cycles as a bottoming cycle in combined cycles for power generation and district heating can be considered a viable future application.

NOMENCLATURE

\dot{m}	Massflow (kg/s)
\dot{W}	Power (MW)
\dot{Q}	Heat rate (MW)
LHV	Lower heating value (kJ/kg)
β	Power loss coefficient (–)
η	Thermal efficiency (–)
σ	Power to heat ratio (–)

Superscripts and subscripts

fuel	Fuel
net	Net
ov	Overall
q	Heat
w	Power

Acronyms

C	Compressor
CHP	Combined heating and power
CW	Cooling water
DH	District heating
DHRS	District heating return and supply
E	Heat exchanger
G	Generator
M	Turbine, electric motor

REFERENCES

- [1] Brun, K., Friedman, P. and Dennis, R., (eds.) *Fundamentals and Applications of Supercritical Carbon Dioxide (sCO₂) Based Power Cycles*. Woodhead Publishing (2017).
- [2] Zhu, Q. “High-efficiency power generation – review of alternative systems.” Technical Report No. CCC/247, International Energy Agency (IEA). 2015.
- [3] Le Moullec, Y. “Conceptual study of a high efficiency coal-fired power plant with CO₂ capture using a supercritical CO₂ Brayton cycle.” *Energy* Vol. 49 (2013): pp. 32–46. DOI: 10.1016/j.energy.2012.10.022.
- [4] Mecheri, M. and Le Moullec, Y. “Supercritical CO₂ Brayton cycles for coal-fired power plants.” *Energy* Vol. 103 (2016): pp. 758–771. DOI: 10.1016/j.energy.2016.02.111.
- [5] Weiland, N. T. and White, C. W. “Techno-economic analysis of an integrated gasification direct-fired supercritical CO₂ power cycle.” *Fuel* Vol. 212 (2018): pp. 613–625. DOI: 10.1016/j.fuel.2017.10.022.
- [6] Ahn, Y., Bae, S. J., Kim, M., Cho, S. K., Baik, S., Lee, J. I. and Cha, J. E. “Review of supercritical CO₂ power cycle technology and current status of research and development.” *Nuclear Engineering and Technology* Vol. 47, No. 6 (2015): pp. 647–661. DOI: 10.1016/j.net.2015.06.009.
- [7] Dostal, V., Hejzlar, P. and Driscoll, M. J. “High-performance supercritical carbon dioxide cycle for next-generation nuclear reactors.” *Nuclear Technology* Vol. 154, No. 3 (2006): pp. 265–282. DOI: 10.13182/nt154-265.
- [8] Dostal, V., Hejzlar, P. and Driscoll, M. J. “The supercritical carbon dioxide power cycle: comparison to other advanced power cycles.” *Nuclear Technology* Vol. 154, No. 3 (2006): pp. 283–301. DOI: 10.13182/nt06-a3734.
- [9] Garg, P., Kumar, P. and Srinivasan, K. “Supercritical carbon dioxide Brayton cycle for concentrated solar power.” *The Journal of Supercritical Fluids* Vol. 76 (2013): pp. 54–60. DOI: 10.1016/j.supflu.2013.01.010.
- [10] Turchi, C. S., Ma, Z., Neises, T. W. and Wagner, M. J. “Thermodynamic study of advanced supercritical carbon dioxide power cycles for concentrating solar power systems.” *Journal of Solar Energy Engineering* Vol. 135, No. 4 (2013): p. 041007. DOI: 10.1115/1.4024030.
- [11] Iverson, B. D., Conboy, T. M., Pasch, J. J. and Kruijenga, A. M. “Supercritical CO₂ Brayton cycles for solar-thermal energy.” *Applied Energy* Vol. 111 (2013): pp. 957–970. DOI: 10.1016/j.apenergy.2013.06.020.
- [12] Binotti, M., Astolfi, M., Campanari, S., Manzolini, G. and Silva, P. “Preliminary assessment of sCO₂ cycles for power generation in CSP solar tower plants.” *Applied Energy* Vol. 204 (2017): pp. 1007–1017. DOI: 10.1016/j.apenergy.2017.05.121.
- [13] Chen, H., Goswami, D. Y. and Stefanakos, E. K. “A review of thermodynamic cycles and working fluids for the conversion of low-grade heat.” *Renewable and Sustainable Energy Reviews* Vol. 14, No. 9 (2010): pp. 3059–3067. DOI: 10.1016/j.rser.2010.07.006.
- [14] Huck, P., Freund, S., Lehar, M. and Peter, M. “Performance comparison of supercritical CO₂ versus steam bottoming cycles for gas turbine combined cycle applications.” *Proceedings of the 5th International Symposium – Supercritical CO₂ Power Cycles*. 2016. San Antonio, USA.
- [15] Wright, S. A., Davidson, C. S. and Scammell, W. O. “Thermoeconomic analysis of four sCO₂ waste heat recovery power systems.” *Proceedings of the 5th International Symposium – Supercritical CO₂ Power Cycles*. 2016. San Antonio, USA.
- [16] Haywood, R. W. *Analysis of Engineering Cycles – Power, Refrigerating and Gas Liquefaction Plant*, 4th ed. Pergamon Press (1991). DOI: 10.1016/B978-0-08-040738-8.50002-5.
- [17] Horlock, J. H. *Cogeneration – Combined Heat and Power (CHP)*. Krieger Publishing Company (1997).
- [18] Crespi, F., Gavagnin, G., Sánchez, D. and Martínez, G. S. “Supercritical carbon dioxide cycles for power generation: a review.” *Applied Energy* Vol. 195 (2017): pp. 152–183. DOI: 10.1016/j.apenergy.2017.02.048.
- [19] Crespi, F., Gavagnin, G., Sánchez, D. and Martínez, G. S. “Analysis of the thermodynamic potential of supercritical carbon dioxide cycles: a systematic approach.” *Journal of Engineering for Gas Turbines and Power* Vol. 140, No. 5 (2017): p. 051701. DOI: 10.1115/1.4038125.

- [20] Liu, Y., Wang, Y. and Huang, D. “Supercritical CO₂ Brayton cycle: a state-of-the-art review.” *Energy* Vol. 189 (2019): p. 115900. DOI: 10.1016/j.energy.2019.115900.
- [21] Penkuhn, Mathias and Tsatsaronis, George. “Exergoeconomic analyses of different sCO₂ cycle configurations.” *6th International sCO₂ Power Cycles Symposium*. 2018. Pittsburgh, USA.
- [22] Penkuhn, Mathias and Tsatsaronis, George. “Thermoeconomic modeling and analysis of sCO₂ Brayton cycles.” *3rd European Conference on Supercritical CO₂ (sCO₂) Power Systems 2019*. 139: pp. 310–318. 2019. Paris, France. DOI: 10.17185/dupublico/48909.
- [23] Penkuhn, M. and Tsatsaronis, G. “Systematic evaluation of efficiency improvement options for sCO₂ Brayton cycles.” *Energy* Vol. 210 (2020): p. 118476. DOI: 10.1016/j.energy.2020.118476.
- [24] Wu, D. W. and Wang, R. Z. “Combined cooling, heating and power: a review.” *Progress in Energy and Combustion Science* Vol. 32, No. 5 (2006): pp. 459–495. DOI: 10.1016/j.peccs.2006.02.001.
- [25] Lee, W. W., Bae, S. J., Jung, Y. H., Yoon, H. J., Jeong, Y. H. and Lee, J. I. “Improving power and desalination capabilities of a large nuclear power plant with supercritical CO₂ power technology.” *Desalination* Vol. 409 (2017): pp. 136–145. DOI: 10.1016/j.desal.2017.01.013.
- [26] Sharan, P., Neises, T., McTigue, J. D. and Turchi, C. “Cogeneration using multi-effect distillation and a solar-powered supercritical carbon dioxide Brayton cycle.” *Desalination* Vol. 459 (2019): pp. 20–33. DOI: 10.1016/j.desal.2019.02.007.
- [27] Moroz, L., Burlaka, M. and Rudenko, O. “Study of a supercritical CO₂ power cycle application in a cogeneration power plant.” *Proceedings of the 4th International Symposium – Supercritical CO₂ Power Cycles*. 2014. Pittsburgh, USA.
- [28] Wiltshire, R., (ed.) *Advanced District Heating and Cooling (DHC) Systems*. Woodhead Publishing (2016).
- [29] Mazhar, A. R., Liu, S. and Shukla, A. “A state of art review on the district heating systems.” *Renewable and Sustainable Energy Reviews* Vol. 96 (2018): pp. 420–439. DOI: 10.1016/j.rser.2018.08.005.
- [30] IEA. “Cogeneration and district energy.” Technical report no., International Energy Agency IEA. 2009.
- [31] General Electric. “2019 Gas Power Systems Catalogue.” (2019).
- [32] Brooks, F. J. “GE gas turbine performance characteristics.” Technical Report No. GER 3567H, General Electric (GE). 2000.
- [33] STEAG Energy Services GmbH. “Epsilon Professional.” (2019).
- [34] Weiland, N. and Thimsen, D. “A practical look at assumptions and constraints for steady state modeling of sCO₂ Brayton power cycles.” *Proceedings of the 5th International Symposium – Supercritical CO₂ Power Cycles*. 2016. San Antonio, USA.
- [35] Lemmon, E. W., Huber, M. L. and McLinden, M. O. “NIST reference fluid thermodynamic and transport properties – REFPROP.” Technical Report No. NIST Standard Reference Database 23, U.S. Department of Commerce. 2013.
- [36] White, C. W. and Weiland, N. T. “Evaluation of property methods for modeling direct-supercritical CO₂ power cycles.” *Journal of Engineering for Gas Turbines and Power* Vol. 140, No. 1 (2017): p. 011701. DOI: 10.1115/1.4037665.
- [37] Lund, H., Werner, S., Wiltshire, R., Svendsen, S., Thorsen, J. E., Hvelplund, F. and Mathiesen, B. V. “4th generation district heating (4GDH) – integrating smart thermal grids into future sustainable energy systems.” *Energy* Vol. 68 (2014): pp. 1–11. DOI: 10.1016/j.energy.2014.02.089.
- [38] Lund, H., Østergaard, P. A., Chang, M., Werner, S., Svendsen, S., Sorknæs, P., Thorsen, J. E., Hvelplund, F., Mortensen, B. O. G., Mathiesen, B. V., Bojesen, C., Duic, N., Zhang, X. and Möller, B. “The status of 4th generation district heating: research and results.” *Energy* Vol. 164 (2018): pp. 147–159. DOI: 10.1016/j.energy.2018.08.206.
- [39] Bejan, A., Tsatsaronis, G. and Moran, M. J. *Thermal Design and Optimization*. Wiley (1996).
- [40] Zoelle, A. “Quality guidelines for energy system studies: process modeling design parameters.” Technical Report No. NETL-PUB-22478, U.S. Department of Energy. 2019.
- [41] Gülen, S. C. *Gas Turbine Combined Cycle Power Plants*. CRC Press (2019). DOI: 10.1201/9780429244360.

**10MW-CLASS sCO₂ COMPRESSOR TEST FACILITY AT UNIVERSITY OF NOTRE
DAME**

Jeongseek Kang*

Notre Dame Turbomachinery Lab
University of Notre Dame
Notre Dame, IN, USA
Email:jkang6@nd.edu

Alex Vorobiev

Notre Dame Turbomachinery Lab
University of Notre Dame
Notre Dame, IN, USA

Joshua D. Cameron

Notre Dame Turbomachinery Lab
University of Notre Dame
Notre Dame, IN, USA

Scott C. Morris

Notre Dame Turbomachinery Lab
University of Notre Dame
Notre Dame, IN, USA

Ryan Wackerly

Echogen Power systems
Akron, Ohio, USA

Kyle Sedlacko

Echogen Power systems
Akron, Ohio, USA

Jason D. Miller

Echogen Power systems
Akron, Ohio, USA

Timothy J. Held

Echogen Power systems
Akron, Ohio, USA

ABSTRACT

The compressor is a key component in closed-loop Brayton Cycles and advanced electrothermal energy storage systems. The use of sCO₂ as the primary working fluid had many advantages for these systems. However, due to the unique operating conditions and fluid properties, there remains significant challenges for the development of high efficiency compression systems with sCO₂. Detailed experimental measurements from sCO₂ compressors are extremely difficult to obtain, given the small size and very high power requirements. This has limited the majority of current experimental results to very small scale, single stage, centrifugal compressors. Larger, multi-stage axial compressors are of significant interest for sCO₂ systems, but have not been subject to experimental investigations.

The present communication describes the design and salient characteristics of a new, 10MW-class closed-loop sCO₂ or CO₂ compressor test facility. The 10MW drive system allows for a physical scale that allows testing of both axial and centrifugal compressor types with flow passages large enough to enable detailed experimental measurements., including surveys through the flow passage, steady and unsteady performance measurements, and aeromechanical measurements on vanes or blades.

INTRODUCTION

The use of supercritical CO₂ as the working fluid in closed-loop Brayton Cycles and advanced electrothermal energy storage systems has shown great promise in delivering electricity with high efficiency, flexibility of heat source, and reduced power-plant size and cost [1, 2]. However, a number of new technology advancements must be realized in order to make sCO₂ cycles commercially viable. One of the major components is the compressor, which provides the pressure increase needed in the cycle. Some characteristics of sCO₂ in regard to its application in a compressor differ from those seen with air or gas which is widely used for turbo compressors. Higher density inside the compressor, overall higher operating pressure ranges, and drastic change of fluid properties near the critical point each present unique challenges for compressor design.

Recent experimental studies of sCO₂ compressor in compressor test loops [3-8] or in power cycle loops [9-15] have successfully demonstrated the operation of sCO₂ compressors in closed loops test environment. However, due to the small demonstration scale or due to limited available driving power, all of them were designed with a centrifugal type compressor with small scale where efficiency must be sacrificed resulting in low overall cycle efficiency. Also studies on detail flow

* corresponding author(s)

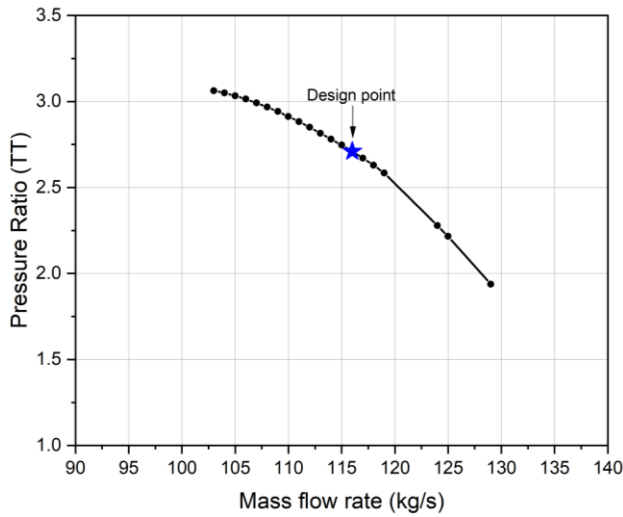


Figure 1: Predicted map of a 3-stage axial compressor @ design point

measurement were not suitable due to the very small flow passages through the compressor.

With this background, Notre Dame Turbomachinery Laboratory and Echogen Power Systems has designed a 10 MW-class sCO₂ compressor test facility to be built at the University of Notre Dame. The test compressor is driven by a 10 MW variable speed motor with a speed increasing gear box. A water/Glycol cooled heat exchanger absorbs added energy from the test compressor. The closed loop is designed to reach steady operation where the addition of energy through the drive motor and the absorption of energy through cooling flow are equal. A CO₂ inventory management system with CO₂ tank and supply system was designed to supply CO₂ from initial operation to test operation.

The choice of a 10 MW size sCO₂ compressor test facility has various merits in terms of scale. It allows use of commercial hardware for many of the components of the test compressor and facility [16]. Also it enables the facility to test the multi-stage axial compressor as well as centrifugal compressors with flow passages wide enough to allow a detailed flow field investigation through various flow measurement technologies. The experiments will include detailed measurements that will significantly advance our understanding of the design, performance, efficiency, and operability of sCO₂ compressors for advanced power systems.

At the time of this writing, the construction of the drive train with a variable speed motor, a gear box, a torquemeter and relevant control systems is complete and has been fully commissioned. Also, a unique data acquisition/control system was developed and tested. This includes the ability to conduct real-time post processing and control with 100s or 1000s of

steady and unsteady acquisition channels. The design of the closed CO₂ test loop is funded by the U.S. Department of Energy and will be complete in mid-2021. Initial sCO₂ axial compressor tests will begin in 2021.

TEST COMPRESSOR : 3-STAGE AXIAL COMPRESSOR

The first compressor to be tested at the facility is a three stage axial compressor. Its design condition is in Table 1 and its predicted map is shown in figure 1.

Table 1: Design point of 3-stage axial compressor

# of compressor stages	-	3
Inlet total pressure	MPa	2.77
Inlet total temperature	°C	97.94
Mass flow rate	kg/s	116
Pressure ratio	-	2.706
Design point aero power	MW	9.09
Design speed	rpm	19,800

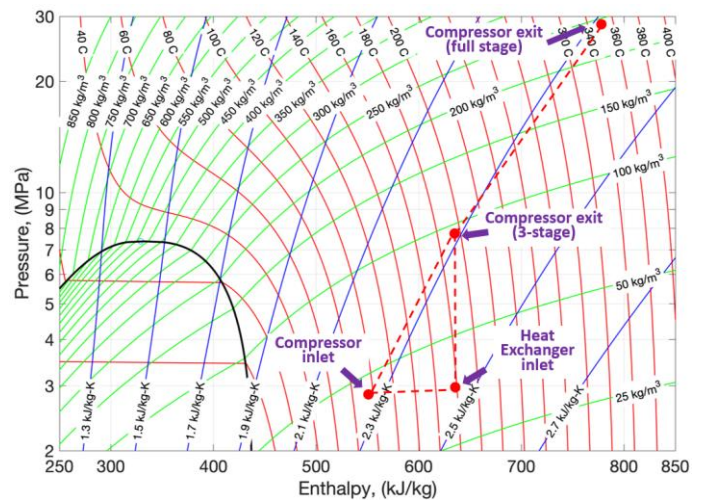


Figure 2: *p-h* diagram of the 3 stage test compressor in test loop vs full stage compressor operating point.

The 3-stage test compressor is a scaled version of first 3 stages of a 100 MW class multi-stage axial compressor designed for a sCO₂-based energy storage system. The objective of the program is to study and ultimately demonstrate a high efficiency, multi-stage, axial sCO₂ compressor. Pressure ratio of the full stage compressor is 10.27. The first three stages of the full machine will be tested in the designed test facility with a design-point pressure ratio and mass flow rate of approximately 2.6 and 116 kg/s, respectively.

CLOSED TEST LOOP

The specification of the CO₂ compressor test loop is shown in table 2 and a schematic diagram of the test facility is shown

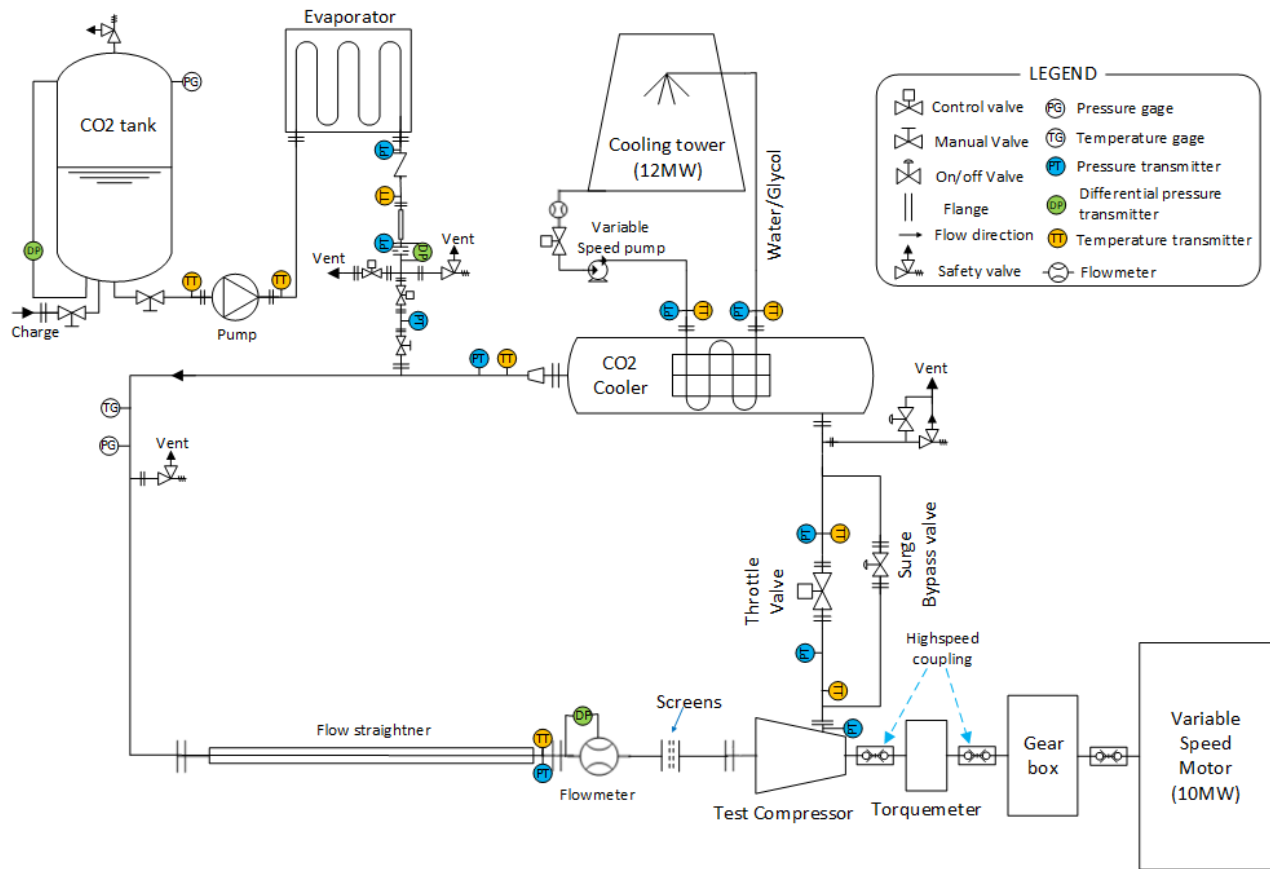


Figure 3: Schematic diagram of sCO₂ compressor test facility.

in figure 3. Images of the design implementation showing the overall scale and layout of the equipment is shown in figure 4. The CO₂ compressor test loop can be divided into the main closed loop and the CO₂ inventory system. The closed test loop is where CO₂ gas recirculates to feed the test compressor continuously with CO₂. The back-pressure to the compressor is provided and controlled by a throttle valve. Heat is then removed through a CO₂/Water heat exchanger. The return flow then moves through a long straight piping section prior to entering a mass flow meter. The inventory system stores CO₂ in a CO₂ tank and supplies CO₂ for testing. This system includes a CO₂ tank, an evaporator, a feed pump, a flowmeter, and associated valves.

Table 2: Design specifications of compressor test loop

Max inlet pressure	MPa	10
Max exit pressure	MPa	30
Max heat exchanger heat rejection rate	MW	12

The pressure resistance of the closed loop was calculated using an in-house code where all the components in the closed loop are divided into 20 nodes and each node is modeled with its performance characteristics. Figure 5 shows pressure resistance of each components in the main CO₂ test loop in

single stage and two stage compressor configurations. The main interest in the single stage configuration is the maximum combined pressure loss at the maximum compressor flow rate condition to confirm the operability of the test facility with a wide range of flowrates. Losses from the components were found to be small enough to allow mapping the test in full flowrate range in a single stage configuration. Most of the pressure resistance to balance the pressure increase by the compressor is to be generated through throttling at the compressor exit.

The CO₂ inventory system supplies CO₂ gas before and during the testing. Before testing, the inventory system fills the closed test loop with CO₂ at the desired compressor inlet pressure. The inventory system operates continuously during testing to make up for the small leakage flow through the compressor seal and to account for the changes of the total mass of CO₂ gas present in the closed loop with compressor operating conditions due to pressure and temperature changes in the loop.

An important aspect of the mechanical design of the facility is the thermal growth of the materials due to the coefficient of thermal expansion. The overall piping length of the facility as

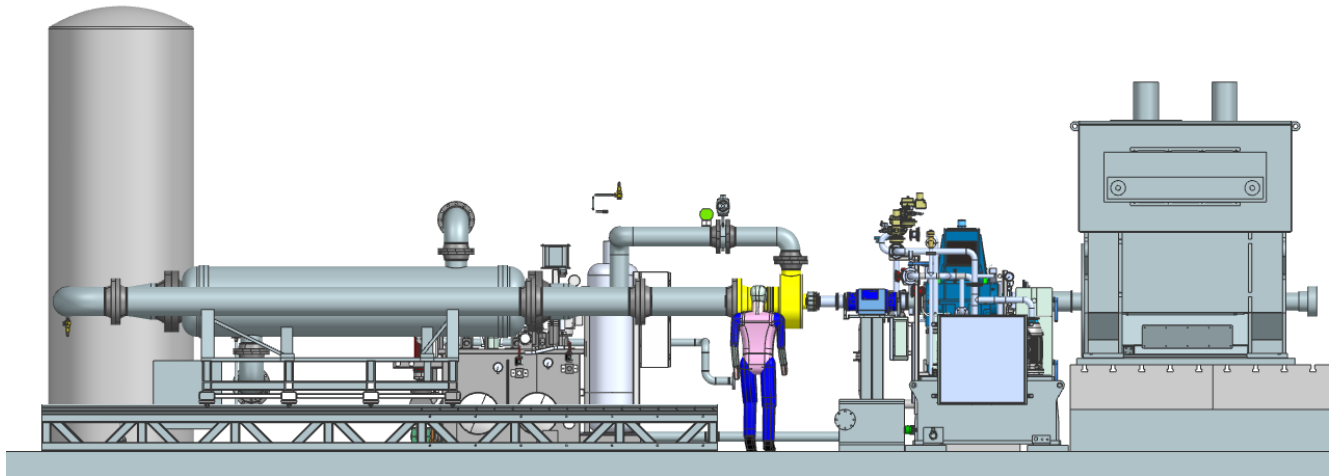


Figure 4a: Layout of CO₂ compressor test facility.

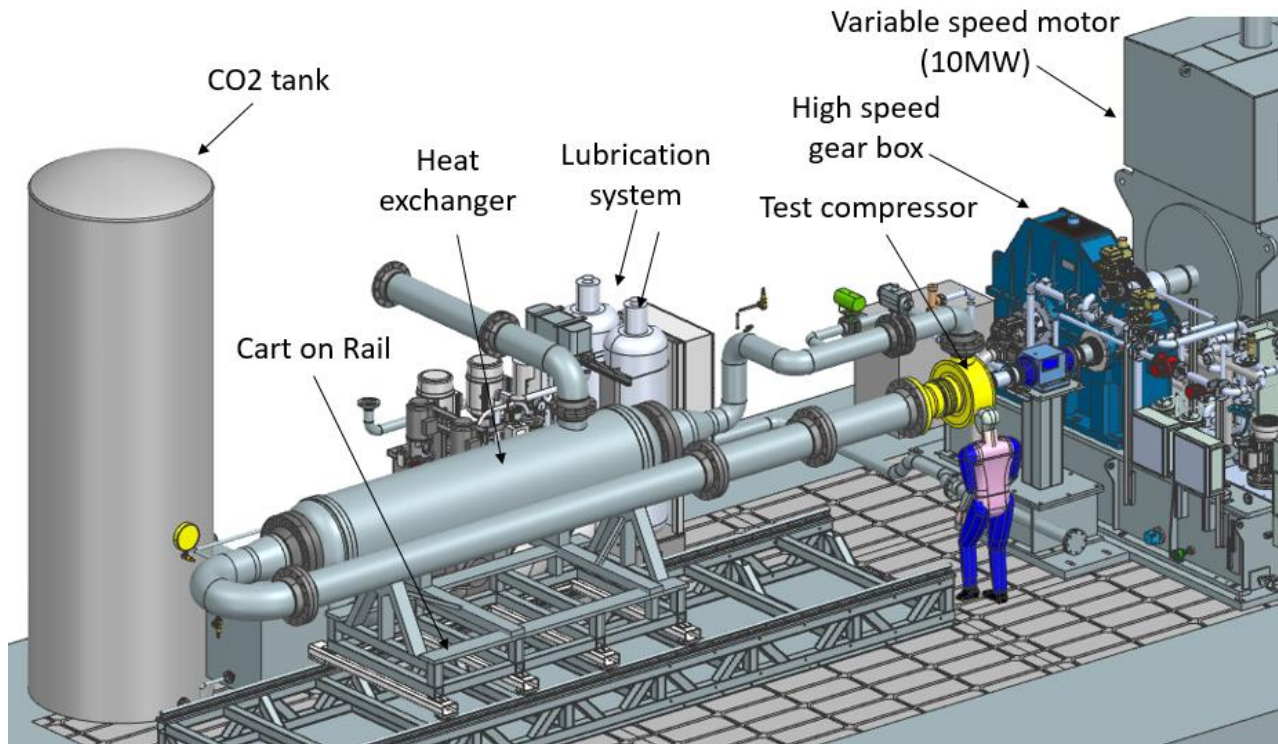


Figure 4b: CAD model of CO₂ compressor test facility. A main CO₂ closed loop, a CO₂ tank and inventory system, test rig lubrication system, and drive train (a motor, a gear box, and a torquemeter) is shown in the model.

shown in figure 4 can grow up to 25 mm at the design operating temperature. To maintain the alignment of the compressor inlet duct along the axis of shaft rotation and to allow large thermal growth in the axial direction, linear roller bearings and rails are designed between the test loop cart and the base structure to allow thermal growth in axial direction. And the center line of main pipe is fixed to align with the test rig while allowing the thermal growth of pipes in horizontal direction.

DRIVE TRAIN

The test facility is equipped with a 10 MW variable speed motor which drives the test compressor through a speed increasing gear box and a torquemeter. The specification of the motor, gear box and torquemeter is shown in table 3. All the components in the drive system are designed to be bi-directional

to accommodate test compressors with any rotational direction. The drive system is also designed to be capable of absorbing power up to 10 MW which means it can be converted to a turbine test facility if necessary. In that case the motor works as a generator and dynamometer. Generated electricity can be fed to electric grid to be used for any purpose.

Table 3: Specification of compressor drive system

Motor	Max. power	MW	10
	Full load speed	kg/s	116
Gear Box	Max. output speed	rpm	19,945
	Rated power	MW	10
Torquemeter	Nominal torque	Nm	7,000
	Nominal speed	rpm	21,000

DATA ACQUISITION SYSTEM

The data acquisition system was designed to meet the requirements of the expected test instrumentation and real-time data processing requirements. The low speed data acquisition system can measure 2,000 channels of pressure, thermocouples, RTDs, voltage signals, and current signals with an acquisition frequency up to 1 kHz. The high speed data acquisition system can measure hundreds of channels of dynamic pressure, proximity signals, vibration, blade tip clearance signals, and strain gages up to 200 kHz per channel. A telemetry system and 16 channels of light probe system for blade vibration was integrated with the main data acquisition system.

CONCLUSION

A 10 MW-class sCO₂ compressor test facility has been designed. The 10MW scale allows sCO₂ compressor testing of both axial and centrifugal compressor types with flow passages large enough to enable advanced experimental studies of CO₂ compressors, including detailed flow survey, steady and unsteady performance measurement, and aeromechanical research on vanes or blades including blade vibrations and flutter. The facility is to be built at the University of Notre Dame in 2021 with a schedule to test the first CO₂ axial compressor in 2021.

ACKNOWLEDGEMENTS AND DISCLAIMER

This material is based upon work supported by the U.S. Department of Energy’s Office of Energy Efficiency and Renewable Energy (EERE) under the Solar Energy Technologies Office Award Number DE-EE0008997. The views expressed herein do not necessarily represent the views of the U.S. Department of Energy or the United States Government.

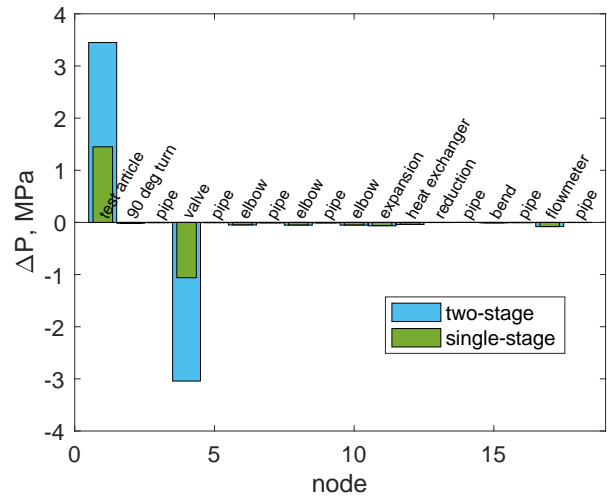


Figure 5: Pressure resistance of the main CO₂ test loop in single stage and two stage compressor configurations. Losses from the components are found to be small to allow mapping the test in single stage configuration. Most of the pressure resistance is generated through throttling at compressor exit.

REFERENCES

- [1] Dostal, V., Driscoll, M.J., and Hejzlar, P., 2014, “A Supercritical Carbon Dioxide Cycle for Next Generation Nuclear Reactors,” MIT-ANP-TR-100.
- [2] Timothy J. Held, 2014, “Initial Test Results of a Megawatt-Class Supercritical CO₂ Heat Engine,” The 4th International Symposium - Supercritical CO₂ Power Cycles, Sep 9-10, Pittsburgh, Pennsylvania, USA.
- [3] Steven A. Wright, Milton E. Vernon, Ross F. Radel, & Robert L. Fuller, 2009, “Supercritical CO₂ Main Compressor Performance Measurements,” SAND2009-0980C.
- [4] Steven A. Wright, Ross F. Radel, Milton E. Vernon, Gary E. Rochau, and Paul S. Pickard, 2010, “Operation and Analysis of a Supercritical CO₂ Brayton Cycle,” Sandia Report, SAND2010-0171.
- [5] Masanori Aritomi, Takao Ishizuka, Yasushi Muto, Nobuyoshi Tsuzuki, 2011, “Performance Test Results of a Supercritical CO₂ Compressor Used in a New Gas Turbine Generating System,” JSME Journal of Power and Energy Systems, Vol. 5, No. 1, pp.45-59.
- [6] Jekyoung Lee, Seong Gu Kim, Jae Eun cha, and Jeong Ik Lee, 2014, “Uncertainty on Performance Measurement of s-CO₂ Compressor Operating near the Critical Point,” The 4th International Symposium - Supercritical CO₂ Power Cycles, Sep 9-10, Pittsburgh, Pennsylvania, USA.

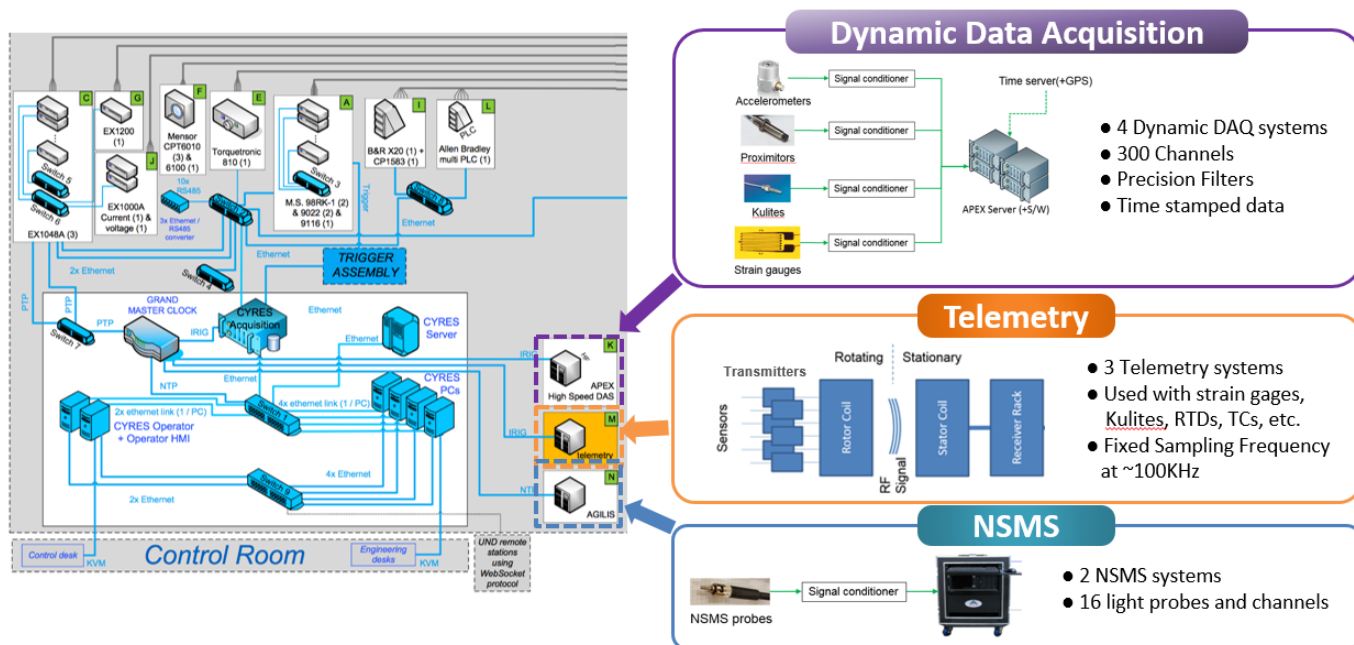


Figure 6: Schematic of the data acquisition system. Low speed data acquisition system for temperatures, pressures, flowrates, etc. and high speed data acquisition system for vibrations, dynamic pressures, strain gages, light probes, and the telemetry system are connected with the main facility control system.

[7] Eduardo Anselmi, Ian Bunce, Vassilios Pachidis, 2019, “An Overview of Initial Operating Experience With the Closed-Loop sCO₂ test Facility at Cranfield University,” ASME GT2019-91391.

[8] Schuster, S., Hacks, A., Brillert, D., 2020, “Lessons from testing the sCO₂-HeRo turbo-compressor-system,” The 7th International Supercritical CO₂ Power Cycles Symposium, Mar 31-Apr 2, San Antonio, Texas, USA.

[9] Jeff S. Noall, James J. Pasch, 2014, “Achievable Efficiency and Stability of Supercritical CO₂ Compression Systems,” Supercritical CO₂ Power Cycle Symposium, Sep 9-10, Pittsburgh, Pennsylvania, USA.

[10] Clementoni, E. M., & Cox, T. L., 2014, “Steady State Power Operation of a Supercritical Carbon Dioxide Brayton Cycle,” The 4th International Symposium - Supercritical CO₂ Power Cycles, Sep 9-10, Pittsburgh, Pennsylvania, USA.

[11] Jae Eun Cha, Seong Won Bae, Jekyoung Lee, Seong Kuk Cho, Jeong Ik Lee, Joo Hyun Park, 2016, “Operation Results of a Closed Supercritical CO₂ Simple Brayton Cycle,” The 5th International Supercritical CO₂ Power Cycles Symposium, Mar 28-31, San Antonio, Texas, USA.

[12] Junhyun Cho, Hyungki Shin, Ho-Sang Ra, Gibong Lee, Chulwoo Roh, Beomjoon Lee, Young-Jin Baik, 2016, “Research on the Development of a small scale supercritical CO₂ Power Cycle Experimental test loop,” The 5th

International Supercritical CO₂ Power Cycles Symposium, Mar 28-31, San Antonio, Texas, USA.

[13] Jacqueline Lewis, Eric Clementoni, and Timothy Cox, 2018, “Effect of Compressor Inlet Temperature on Cycle Performance for a Supercritical Carbon Dioxide Brayton Cycle,” ASME GT2018-75182.

[14] Bongsu Choi, Junhyun Cho, Hyungki Shin, Jongjae Cho, Chulwoo Roh, Beomjoon Lee, Gibong Lee, Ho-Sang Ra, Young-Jin Baik, 2019, “Development of a Hundreds of kW-Class Supercritical Carbon Dioxide Power Cycle Test Loop in KIER,” ASME GT2019-90681.

[15] Alexander Hacks, Ales Vojacek, Hans J. Dohmen, and Dieter Brillert, 2018, “Experimental Investigation of the sCO₂-HeRo Compressor,” 2nd European Supercritical CO₂ Conference, August 30-31, Essen, Germany.

[16] Steven A. Wright, Tom M. Conboy, and Gary E., Rochau, 2011, “Break-even Power Transients for two Simple Recuperated S-CO₂ Brayton Cycle Test Configurations,” SCO₂ Power Cycle Symposium, May 24-25, Boulder, Colorado, USA.

2021-sCO₂.eu-148

UTILIZING INDUSTRIAL WASTE HEAT FOR POWER GENERATION USING sCO₂ CYCLE

Soliman, Hady R.*

KTH Royal Institute of Technology
Energy Department
Stockholm, Sweden
hady@kth.se

Pórrsson, Björn J.*

KTH Royal Institute of Technology
Energy Department
Stockholm, Sweden
bjto@kth.se

Trevisan, Silvia

KTH Royal Institute of Technology
Energy Department
Stockholm, Sweden

Guédez, Rafael

KTH Royal Institute of Technology
Energy Department
Stockholm, Sweden

ABSTRACT

The industrial sector accounts for approximately 30% of the global total energy consumption and 50% of that is lost as waste heat. Recovering waste heat from industries and utilizing it as an energy source is a sustainable way of generating electricity. Supercritical CO₂ (sCO₂) cycles can be used with various heat sources including waste heat. Current literature primarily focuses on the cycle's thermodynamic performance without investigating the economics of the system. This is mainly due to the lack of reliable cost estimates for the cycle components. Recently developed cost scaling makes it possible to perform more accurate techno-economic studies on these systems. This work aims to model waste-heat-to-power systems and by performing sensitivity analysis on various system components, attempts to determine which factors require the most attention to bring this technology into commercialization. The industries with the largest unutilized waste heat are cement, iron and steel, aluminum and gas compressor stations. In this work, models of different sCO₂ cycle configurations were developed and simulated for these industries. The techno-economic model optimizes for the highest Net Present Value (NPV) using an Artificial Bee Colony algorithm. The optimization variables are the pressure levels, split ratios, recuperator effectiveness, condenser temperature and the turbine inlet temperature limited by the heat source. The results show industries can cut down costs by €8-34M using this system. Furthermore, the system can achieve an LCOE between 2.5-4.5 c€/kWh which is competitive with ORC (3.2-18 c€/kWh) and steam cycles (3-9 c€/kWh). Out of the modeled industries, waste heat recovery in the steel industry yields the highest NPV of €34.6M.

INTRODUCTION

The amount of CO₂ in the air has been increasing steadily with human activity. This has led to global warming, an increase of temperatures on the Earth. The power and industry sectors produce around 60% of global CO₂ emissions [1]. Several

solutions have been addressing this problem, by trying to reduce energy demand, reusing elements in a circular economy or using renewable energy. However, a solution that can allow industries to increase their energy efficiency which reduces electricity consumption from the power sector is utilizing their waste heat to produce electricity.

Hammond and Norman [2] calculated the waste heat coming out of industries in the UK, based on research and data gathered by McKenna and Norman [3]. Papapetrou et al. [4] continued that research by scaling it up for the EU, accounting for different energy intensities and energy efficiency improvements. They showed that for the EU alone, the potential of industrial waste heat is 314 TWh/year, with 33% at temperatures of 100-200°C (100 TWh/year), 25% between 200-500°C (78 TWh/year) and the rest above 500°C (124 TWh/year).

Campana et al. [5] analyzed 44 audits and feasibility studies of different factories. They found that the four industries with the highest potential for energy recovery within the EU were gas compression and storage facilities (10.5 TWh/year), the iron and steel industry (6.0 TWh/year), cement industry (4.6 TWh/year), and glass industry (0.6 TWh/year).

McKenna and Norman [3] concluded that even though the Aluminum industry has a lot of waste heat, most of it is low grade waste heat. Therefore, it is excluded from the analysis along with the glass industry.

The most common methods to generate power from waste heat are Kalina, Organic Rankine cycles (ORC), and conventional steam cycles. However, Kalina and ORCs are limited by their low efficiencies. The sCO₂ cycle is an emerging technology that can achieve high efficiencies over a broad range of temperatures and is able to utilize various heat sources. The system has compact components and is therefore significantly smaller than steam cycles, which can be very beneficial for waste heat recovery applications. Steam Rankine cycles require water conditioning and condensate control to avoid corrosion, fouling and scaling of components, whereas CO₂ is non-corrosive, non-

* corresponding author(s)

fouling and non-scaling. At medium temperatures, sCO₂ is preferred over ORC due to its compactness, cost and high thermal efficiency [6]. These systems can be used for waste heat recovery from fuel cells [7], nuclear reactors [8], different industries and Concentrated Solar plants [9].

For the development of the sCO₂ technology, modeling and simulation are essential to support decisions of investment and development. In this work a techno-economic model was developed to optimize the system performance in order to maximize the Net Present Value (NPV) of a waste heat recovery system. The optimization of thermal systems involves many decision variables and constraints. Conventional methods for this optimization apply an iterative procedure which may lead to solutions at local optimum. Advanced optimization algorithms, such as evolutionary and swarm intelligence-based algorithms, offer solutions to this problem. They are able to find a solution closer to the global optimum, with reasonable computational costs. Patel et al. [10] performed optimizations for various thermal systems using eleven of the most popular advanced optimization algorithms. They concluded that for the Brayton Power Cycle an algorithm called Artificial Bee Colony (ABC) was best suited for optimization of the system. The techno-economic model in this paper will therefore use that optimization algorithm for the sCO₂ Brayton Cycle.

Several companies including Echogen, GE and Netpower along with various research facilities (Sandia, Oak Ridge, KAIST (Korea Advanced Institute of Science and Technology) have all been working on developing the sCO₂ cycle. Within the EU, the EC has funded two projects (HeRo and Flex) [11]. They aim at developing a small-scale Brayton sCO₂ cycle and a modular flexible coal power plant based on sCO₂ cycle.

Recently General Electric, led by Vinnemier published a study on the usage of sCO₂ cycles as storage in thermal power plants. Their modeling shows that the cycle can have a round trip efficiency of 60% [12].

Echogen has been working on a MW scale sCO₂ cycle for waste heat recovery [13]. They have built a 2.4 MW plant to recover waste heat from a gas turbine using a simple recuperating cycle. Siemens Energy is also installing a sCO₂ plant to recover the waste heat for Canadian energy company, TC Energy. It is expected to supply electricity for 10,000 homes this year [14].

INDUSTRY DATA

Based on data from cement plants, the waste heat comes out at 300 °C with a flow rate of 74 kg/s from the preheaters and 40 kg/s from the clinker cooler as shown in Figure 1. The waste heat flow is relatively constant and has a specific heat capacity of 1.30 kJ/kg.K This was confirmed by an IFC report and Cembureau [15], [16]. In the iron and steel industry, a large source of waste heat is in the coke production process shown in Figure 2. By implementing a method called Coke Dry Quenching (CDQ) there are two high grade heat streams available for power production. First, is the inert gas used to cool down the coke which consists of 76.5% N₂, 12% CO₂, 8.5% CO and 3% H₂. Second, is the exhaust from the coke oven called Coke Oven Gas (COG) [17]. The EU produces 37 million tons of coke per year

in 62 facilities [18]. This is equivalent to coke production of 19 kg/s in an average facility resulting in 24 kg/s of waste gas flow, which varies little with time [17]. As for the COG, the average coke battery produces 365 m³/t_{coal} of COG [19]–[21]. For an average size facility this is equivalent to a mass flow of 3.65 kg/s at constant rate [21].

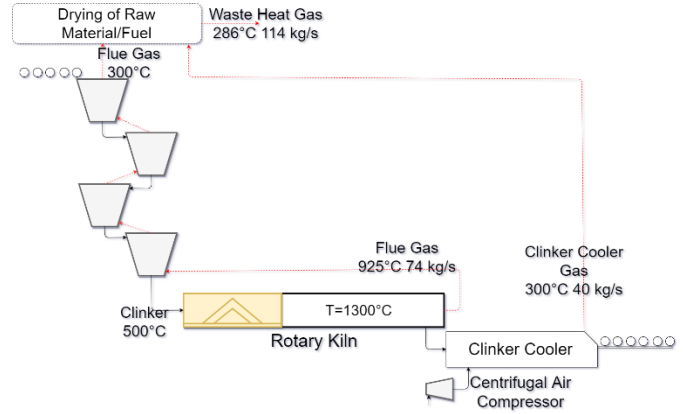


Figure 1: Material and energy streams in a cement plant.

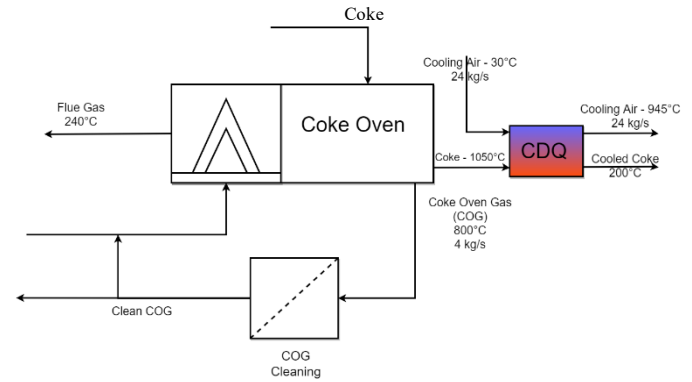


Figure 2: Material and energy streams in a coke plant.

Bianchi et al. [22] studied Gas Compression Stations (GCS) and investigated an average size compressor station and the amount of waste heat there. They concluded that the flue gas had a flow rate of 69 kg/s and temperature of 540°C. However, to account for backup units [5] and that gas compression do not run at constant load [23], a medium sized plant has a constant flow rate of 66 kg/s. The industrial waste heat fluid flow properties mentioned are summarized in Table 1 where:

\dot{m}_{HS} is Waste Heat Mass Flow Rate (kg/s)

T_{HS} is Waste Heat Temperature (°C)

$c_{p,HS}$ is Waste Heat Fluid Specific Heat Capacity (kJ/kg.K)

Table 1
Industrial waste heat flows.

Industry	T_{HS}	\dot{m}_{HS}	$c_{p,HS}$
Cement Upstream	925	74	1.3
Cement Downstream	300	114	1.3
CDQ	945	24	*a+bT+cT ² +dT ³
GCS	520	66	1.68

*coefficients (a,b,c,d) from [24].

PERFORMANCE MODEL

The cycles that were modeled were the Simple Recuperated Brayton Cycle (SRBC) and the Recompression cycle which has been shown to have very high thermal efficiency [25]. Additional cycle configurations were investigated to compare their effectiveness for waste heat recovery applications. Hou et al. investigated two combined cycle configurations for waste heat recovery in gas turbines and the performance improvements

that they can offer for that application[26]. The Preheating and Dual Recuperated cycles were studied by Wright et al. for waste heat recovery applications and showed how they are better suited compared to the SRBC and Recompression cycle [27]. In this work all six of these cycle configurations are compared to further the understanding of which configuration is optimal for waste heat recovery applications. The cycles were modeled in MATLAB and are illustrated in Figure 3.

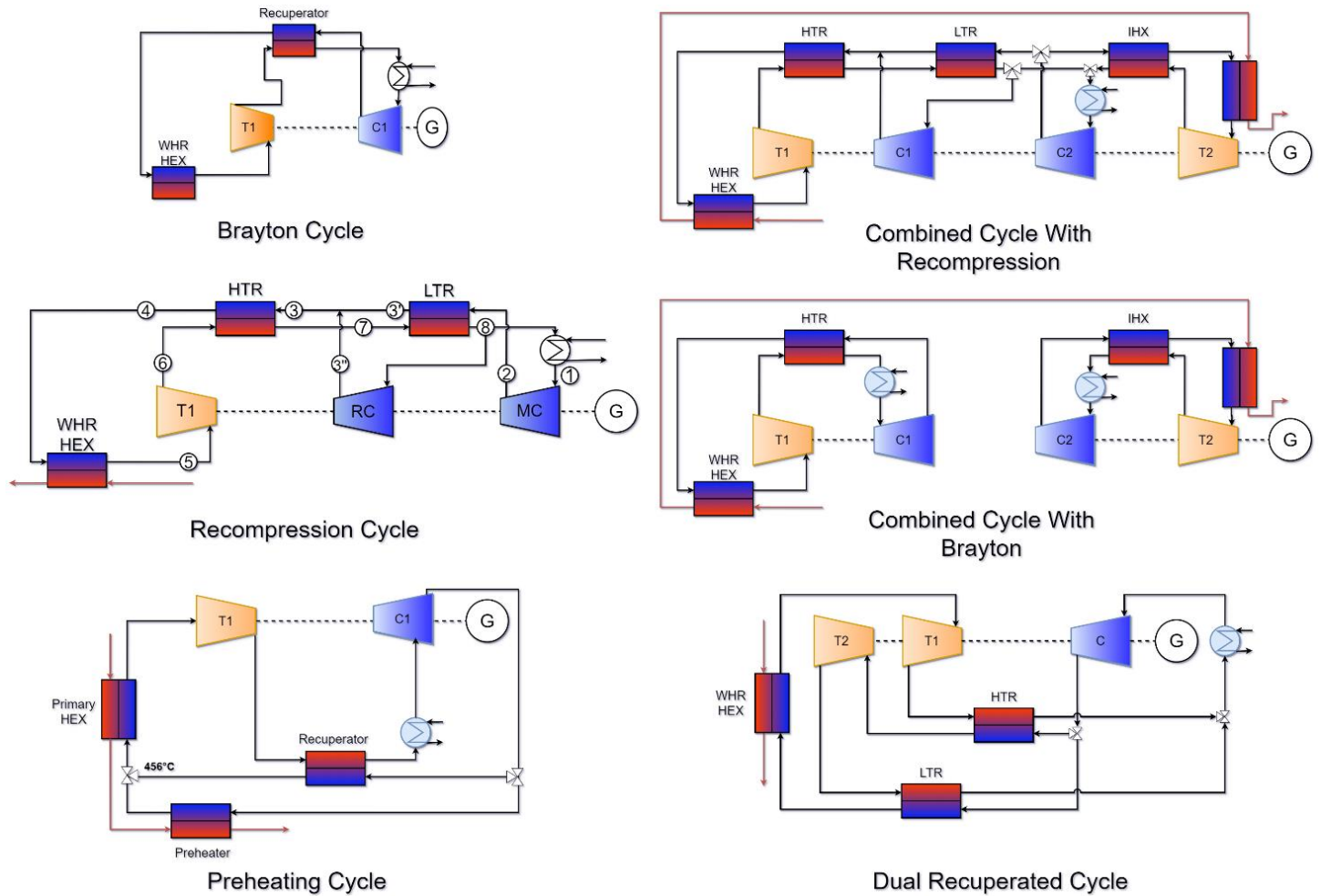


Figure 3: Supercritical CO₂ cycle configurations

The functionality of the model is demonstrated for the sCO₂ recompression cycle. Figure 4 demonstrates the logic flow of the techno-economic optimization model. It starts by reading inputs about the waste heat flow fluid properties mentioned in Table 1 along with the cooling medium temperature. Then, an initial population of employed bees is generated, i.e. a set of various design variables is generated. The design variables and their constraints are summarized in Table 2. The design variable for the temperature difference between the heat source T_{HS} and the Turbine Inlet Temperature (TIT) is dependent on which heat source is being utilized. Therefore, that design variable varies relative to the industry being investigated. A maximum value of 700°C for the turbine inlet temperature was used due to the

limitation of the turbine cost scaling model developed by Weiland et al. [28].

Table 2

Design variables for recompression cycle optimization.

Design Variable	Lower Bound	Upper Bound
High Pressure Level (P_h), MPa	18.0	25.0
Low Pressure Level (P_l), MPa	7.38	12.5
Split Ratio (SR)	0.5	1.0
Effectiveness of HTR (ϵ_{HTR})	0.550	0.999
Effectiveness of LTR (ϵ_{LTR})	0.550	0.999

Primary Heater Approach Temperature (ΔT_{HS}), °C	* $T_{HS} - 700$	$T_{HS} - 280$
Main Compressor inlet Temperature (T_1), °C	32.0	50.0
Temperature Difference between Heat Source outlet and primary heat CO ₂ inlet ($\Delta T_{MH,out}$), °C	4	200

*If $T_{HS} < 704^\circ\text{C}$ then lower bound $\Delta T_{HS} = 4$

Turbomachinery

The design point performance of the turbine and compressors are modeled assuming adiabatic operation with a constant isentropic efficiency η_{is} . The fluid enters the turbomachinery with the specific enthalpy and entropy h_{in} and s_{in} . The isentropic specific enthalpy at the outlet $h_{out,is}$ is then determined and the isentropic specific work w_{is} calculated using Equation 1

$$w_{is} = h_{in} - h_{out,is} \quad (1)$$

Using the definition of isentropic efficiency, the actual specific work (w) for a turbine and a compressor can then be calculated using Equations (2) and (3) respectively.

$$w_{turbine} = w_{is} \cdot \eta_{is} \quad (2)$$

$$w_{compressor} = \frac{w_{is}}{\eta_{is}} \quad (3)$$

Finally, the specific enthalpy at the outlet can be calculated using Equation (4).

$$h_{out} = h_{in} - w \quad (4)$$

Heat Exchangers (HEXs)

As can be seen in Figure 3, the recompression cycle consists of three different types of heat exchangers (two recuperators, primary heater and cooler). One of the challenges and interesting properties of sCO₂ is the change of its fluid properties around the critical point. Therefore, normal heat transfer correlations cannot be used for the modeling of an sCO₂ system [29].

Recuperator

The recuperators are modeled assuming a counter-flow configuration. Three main working principles are utilized to calculate all four thermodynamic states at both sides of the recuperators. Firstly, the law of energy conservation across the HEX is used to calculate the final state when three are fully defined. Secondly, the definition of heat exchanger effectiveness, and lastly, the Log Mean Temperature Difference (LMTD) approach to determine the conductance of the HEX.

The fluid enters the hot and cold side of the recuperator with specific enthalpy ($h_{h,in}, h_{c,in}$) and exits the hot side with

specific enthalpy ($h_{h,out}$), all of which are determined from known temperatures and pressures.

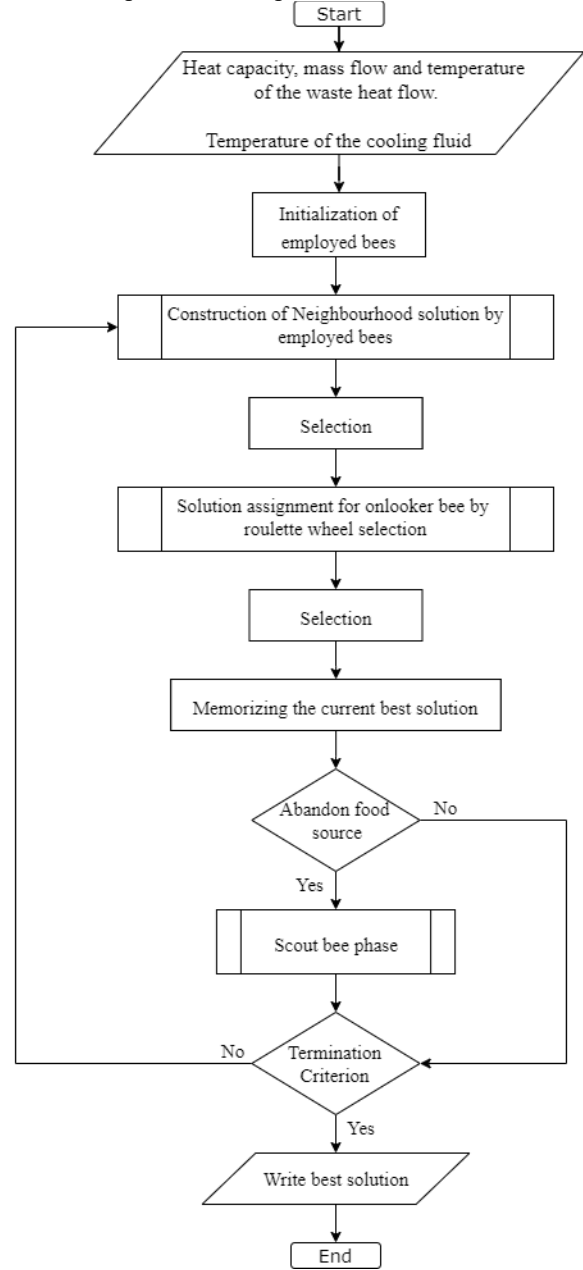


FIGURE 4: Optimization Model

Using the law of energy conservation, the cold side outlet specific enthalpy ($h_{c,out}$) can be determined as shown by Equation (5):

$$h_{c,out} = h_{c,in} + \frac{\dot{m}_h \cdot (h_{h,in} - h_{h,out})}{\dot{m}_c} \quad (5)$$

For a recuperator that has the same fluid on both hot and cold sides this equation can be simplified. For the HTR the mass flow rate is equal on both sides and therefore cancel out. Due to the split flow in the recompression cycle the mass flow rates are

not equal but their ratio is known and is the split ratio (SR). Therefore Equation (5) is simplified to:

$$h_{c,out} = h_{c,in} + \frac{(h_{h,in} - h_{h,out})}{SR} \quad (6)$$

From the determined specific enthalpy and known pressure losses across the HEX all thermodynamic states are fully defined.

Equation (7) shows the definition of heat exchanger effectiveness.

$$\epsilon = \frac{\text{Actual heat transfer}}{\text{Maximum possible heat transfer}} = \frac{q}{q_{max}} \quad (7)$$

The actual heat transfer may be determined from either the energy lost by the hot fluid or the energy gained by the cold fluid, as shown in Equation (8).

$$q = \dot{m}_h c_h \cdot (T_{h,in} - T_{h,out}) = -\dot{m}_c c_c \cdot (T_{c,in} - T_{c,out}) \quad (8)$$

To calculate the maximum possible heat transfer, the maximum temperature difference present in the HEX is used, which is the difference between the inlet temperatures for the hot and cold fluids. Furthermore, the fluid that might undergo the maximum temperature difference is the one with the minimum value of $\dot{m}c$. The maximum possible heat transfer can then be determined using Equation (9).

$$q = (\dot{m}c)_{min} \cdot (T_{h,in} - T_{c,in}) \quad (9)$$

By selecting the appropriate side to calculate the actual heat transfer, the effectiveness can be determined by knowing the temperatures across the HEX. Equation (10) shows a general way of expressing the effectiveness.

$$\epsilon = \frac{\Delta T(\text{Minimum Fluid})}{\text{Maximum Temperature Difference in heat Exchanger}} \quad (10)$$

The minimum fluid is always the one undergoing the larger temperature change in the heat exchanger. The maximum temperature difference in the heat exchanger is always the temperature difference of the hot and cold fluid inlets [30].

The heat transfer rate across a heat exchanger can be expressed using the LMTD method according to Equation (11).

$$\dot{Q} = (UA)\Delta T_{LMTD} \quad (11)$$

where ΔT_{LMTD} for a counter-flow configuration can be expressed as,

$$\Delta T_{LMTD} = \frac{(T_{h,out} - T_{c,in}) - (T_{h,in} - T_{c,out})}{\ln\left(\frac{T_{h,out} - T_{c,in}}{T_{h,in} - T_{c,out}}\right)} \quad (12)$$

This method involves two important assumptions. First one is that the specific heats of the fluids do not vary with temperature,

and the second that the convection heat transfer coefficients are constant throughout the heat exchanger. In the case of sCO₂ cycles, both these assumptions are likely to be broken due to the large variations in thermodynamic properties of CO₂ under supercritical conditions. Therefore, to accurately capture the effects of changing fluid properties, each heat exchanger is discretized into sub-section connected in series [31].

Using this approach, the total conductance of a recuperator is determined using the known inlet and outlet conditions. The total heat transfer rate (\dot{Q}) through the heat exchanger is calculated and evenly distributed amongst the discretized sub-sections. Assuming that the pressure losses across the HEX are linear, the inlet and outlet states for each sub-section can be fully defined. Using Equation (11) the conductance of each sub-section can be determined:

$$(UA)_i = \frac{\dot{Q}_i}{\Delta T_{LMTD,i}} \quad (12)$$

The total conductance for the recuperator is then the sum of all sub-section conductance values.

$$(UA) = \sum (UA)_i \quad (13)$$

B. Primary Heater

From the approach described above the thermodynamic properties at every point in the sCO₂ cycle can be determined. From the known fluid properties of the waste heat, the total heat transfer rate of the heat exchanger can be calculated. An energy balance across the heat exchanger can then be used to calculate the mass flow rate of CO₂. Following the same approach of the recuperators, the total conductance of the primary heat exchanger can be calculated.

C. Cooler:

An air-cooling system for Brayton cycles conventionally has cross-flow configuration. Since a cross-flow heat exchanger has two fluid flows in perpendicular directions, a fluid flowing in parallel channels will observe opposite side fluids at different temperatures. This means that numerical modeling of this system needs to be two-dimensional, resulting in huge increase in computation cost [32]. Therefore, to improve computation time, a simplification is made by assuming an approach temperature of 15°C and calculating the heat exchanger conductance using the known temperatures on the CO₂ side.

The subroutine of solution assignments for the various bee groups, mentioned in Figure 4, represents the evaluation of a food source that an individual bee has found. The subroutine uses generated design variables for a food source and calculates the solution, or fitness, at that particular location. A flow diagram of the model iteration logic for that subroutine can be seen in Figure 5. The approach follows a similar approach as Dyreby [33] aside from the different design variable inputs. These alterations were made for optimizing waste heat recovery applications specifically.

The operating assumptions for the sCO₂ waste heat recovery cycles are shown in Table 3 [34]. The open source C++ library named CoolProp was used to obtain fluid properties [35].

Table 3
Operating assumptions for the sCO₂ cycle.

sCO ₂ Assumption	Symbol	Value
Compressor isentropic efficiency	η_{comp}	89%
Turbine isentropic efficiency	$\eta_{turbine}$	93%
Generator efficiency	η_{gen}	98%
Cooling fluid inlet temperature	TCS	25 °C

During this iterative process it is possible for a temperature cross-over to occur, a condition where the hot side temperature drops below the cold side temperature in a particular region on a particular iteration. In this instance the method of calculating the UA value would give a complex number. This occurrence implies that the results for this iteration are non-physical due to a violation of the Second Law of Thermodynamics. This situation is handled by checking whether all conductance values are real numbers. If not, the fitness function returns a value of negative infinity so that the optimization algorithm ignores that solution. A limitation of the optimization algorithm is the fact that there will always be a possibility of not finding the global optimum. However, the success rate of the ABC algorithm for Brayton power cycle optimization has been found to be 96% [10]. Therefore, by running each calculation 10 times and using the best value, means that the approach should only fail to find the global optimum once every 100 Trillion times.

Like the model developed by Dyreby [33], a combination of the secant and bisection methods are used for both iteration loops to adjust T_7 and T_8 . Even though the secant method has a higher rate of convergence, it can potentially predict new values outside of valid bounds, leading to divergence of the method. By reverting back to the bisection method when the secant method fails this can be avoided [36].

ECONOMIC MODEL

The economic assumptions used to calculate the cycle's KPIs for the optimization algorithm are shown in Table 4.

Table 4
Economic Assumptions Used in Calculating KPIs

Economic Assumptions	Symbol	Value
Nominal Discount Rate	i	6%
Lifetime	n	25 years
Annual Operating Hours	N_h	7446 hours (15%)
Electricity Price	el_{price}	€0.065/kwh _e

The NPV was calculated using equation (14), where E_t is the electricity generated. The assumed electricity price was based on the prices that the surveyed European cement plants pay.

$$NPV = \sum_{t=0}^n \frac{el_{price} \times E_t - costs}{(1+i)^n} \quad (14)$$

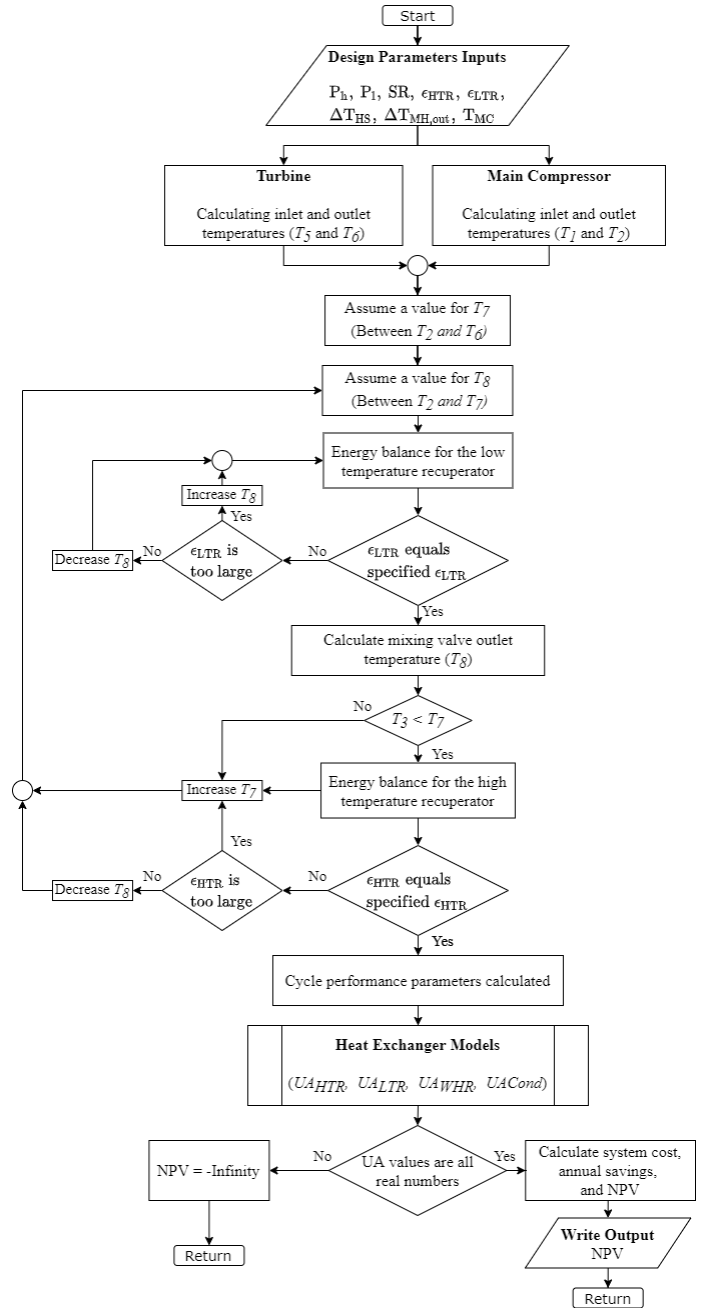


Figure 5: Iterative process logic flow for the cycle model

Thermal efficiency is defined as the ratio between electrical power produced by the cycle (\dot{P}_e) and thermal power extracted from the heat source (\dot{Q}_{th}).

$$n_{th} = \frac{\dot{P}_e}{\dot{Q}_{th}} \quad (15)$$

Exergy Efficiency is defined as the ratio between electrical power produced by the sCO₂ power cycle and available heat in the waste heat exhaust ($Q_{exhaust}$).

$$n_{ex} = \frac{\dot{P}_e}{\dot{Q}_{exhaust}} \quad (16)$$

Waste Heat utilization is defined as the ratio of waste heat transferred to the sCO₂ cycle (Q_{WHEX}) relative to the available heat in the waste heat exhaust.

$$WHU = \frac{Q_{WHEX}}{Q_{exhaust}} \quad (17)$$

Levelized Cost of electricity is defined as the net present cost of electricity generation for a generating plant over its lifetime [37].

$$LCOE = \frac{\text{sum of costs over time}}{\text{sum of power generated}} = \frac{\sum_{t=0}^n \frac{\text{Costs}}{(1+i)^t}}{\sum_{t=0}^n \frac{E_t}{(1+i)^t}} \quad (18)$$

Weiland et al. [28] recently developed a cost scaling model for the components in a sCO₂ cycle. The model is based on a total of 129 vendor quotes, and spans cycle size ranges of 5-750 MW_e. It uses an appropriate scaling parameter (SP) for different components and includes a temperature correction factor f_T for certain components to account for the increase in cost at higher temperatures. The cost scaling can be expressed in a general way using Equation (18).

$$C_E = a \cdot SP^b \cdot f_T \quad (18)$$

where,

$$f_T = \begin{cases} 1, & \text{if } T_{max} < T_{bp} \\ (1 + c \cdot (T_{max} - T_{bp}) + d \cdot (T_{max} - T_{bp})^2), & \text{if } T_{max} \geq T_{bp} \end{cases}$$

and C_E is the equipment cost for an individual cycle component, a is the reference cost, and b is the cost exponent in order to consider economy of scale. Reference costs and exponents are from Weiland et al. [28].

The direct equipment capital cost (C_{DE}) is calculated according to Bailie et al. [38], and can be expressed on a general form as Equation (19):

$$C_{DE} = C_E \cdot (1 + \alpha_M)(1 + \alpha_L) \quad (19)$$

where α_m and α_L are the multiplication factors for installation cost of materials and labor, respectively. These factors are also based on Weiland et al. [28]. System piping costs can vary anywhere between 5-20% of total power block capital costs, depending on the cycle operating conditions [39]. For the analysis performed in this research a value of 10% was used. Additionally, direct capital accounting for improvements to site, instrumentation and controls, and other miscellaneous Balance of Plant (BOP) systems are also added [40].

Indirect costs include Engineering, Procurement and Construction cost (EPC) along with contingencies. The EPC costs are assumed to be 9% of the total direct capital cost [41]. The contingencies depend on the status of the technology being considered and are assumed to be 30% of the combined direct capital expenditures and EPC cost [42].

Operation and Maintenance (O&M) costs include taxes, maintenance material costs, and labor costs that account for operating, maintenance, administrative and support labor [43]. A correction factor of 25% was included to exclude the costs associated with the coal gasification section of the power plant modeled by Weiland et al. [43].

RESULTS

Different industries were analyzed in this model. The inputs into the model are mentioned in Performance Model section. Table 5 shows the optimal cycle configuration and net power output for each industry. Figure 6 shows the NPV, LCOE and the Payback Period (PP) of the industries. Figure 7 shows the CO₂ mitigated and efficiencies per industry.

Table 5
Optimum cycle configuration and size for each industry.

Industry	Configuration	Net Power Output [MW]
Cement Upstream	SRBC	9.4
Cement Downstream	SRBC	5.5
CDQ	Preheating	10.9
GCS	Preheating	13

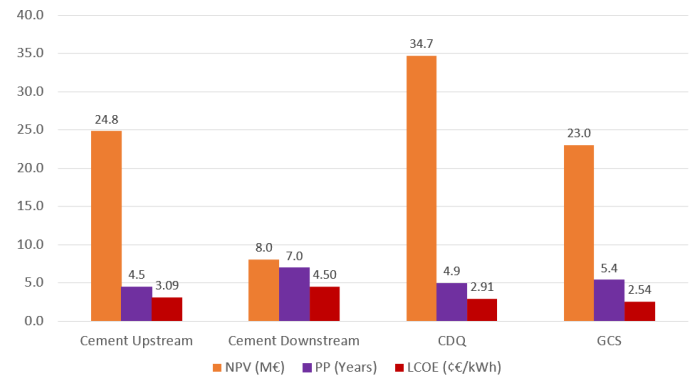


Figure 6: NPV and PP of the waste heat recovery systems.

The sCO₂ cycle for these industries yielded LCOEs between 2.5-4.5 c€/kWh. Waste heat recovery applications using ORC systems can achieve LCOE between 3.2-18 c€/kWh [44]–[47]. Previous studies on waste heat recovery using steam cycles have found them to achieve an LCOE between 3-9 c€/kWh [37,39]. While these ranges are relatively similar, sCO₂ cycles have the additional benefits of compactness and less water consumption.

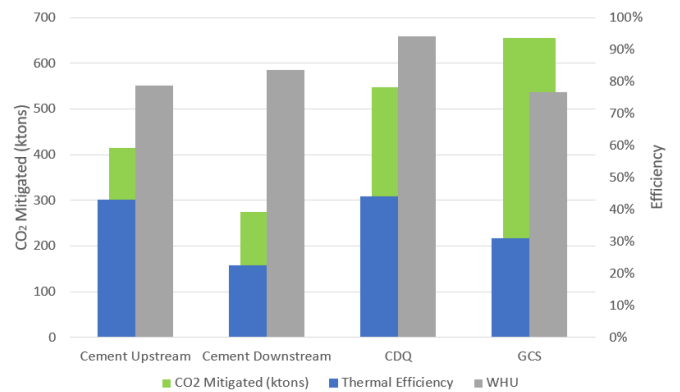


Figure 7: Mitigated emissions, thermal efficiency and waste heat utilization of the waste heat recovery systems.

A modern cement facility utilizes 60% of the available waste heat using 4-stage preheater. The addition of a downstream or

upstream sCO₂ cycle would result in 84% or 79% waste heat utilization, respectively. Therefore, as can be seen in Figure 7, the downstream and upstream sCO₂ cycles utilize additional 24% and 19% waste heat, respectively.

To compare between different cycle configurations, the CDQ process in the Iron and Steel industry is used. The different cycle efficiencies and NPVs are shown in Figure 8. The preheating cycle yields the highest exergy efficiency and NPV.

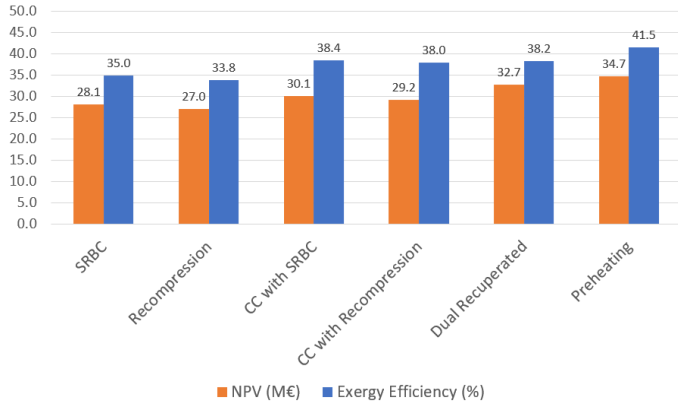


Figure 8: NPV and exergy efficiency of the different cycle configurations for Coke Dry Quenching.

Effect of Split Ratio on NPV

Recompression cycle has been gaining a lot of attention in the past years due to its high thermal efficiency. Figure 8 shows that the other cycle configurations all yield a higher NPV than the Recompression cycle. As can be seen in Figure 9, the thermal efficiency increases as the split ratio decreases until it reaches a maximum. On the other hand, the NPV decreases as the split ratio decreases. This means that it is more economic to use a SRBC than a recompression cycle. Even though recompression cycles can give higher thermal efficiencies, they are limited by their ability to utilize waste heat sources resulting in lower NPV and exergy efficiency. The NPV has a sharp increase around split ratio of 0.65 which is due to the system being able to use a smaller and less expensive motor to drive the recompressor.

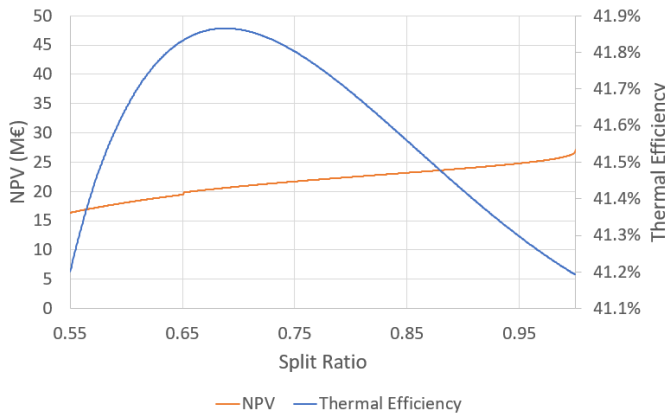


Figure 9: NPV and thermal efficiency at different split ratio for the Recompression Cycle.

System Costs

The power block has the highest contribution to the Capital Expenditures (CAPEX) as can be seen in Figure 10. The CDQ WHR (Waste Heat Recovery) section also has a large share of the total cost, or 31%. This is because it has an intermediate loop using inert gas as heat transfer fluid. Since this is a relatively new technology, the contingencies cost is also high at 16% of the CAPEX cost.

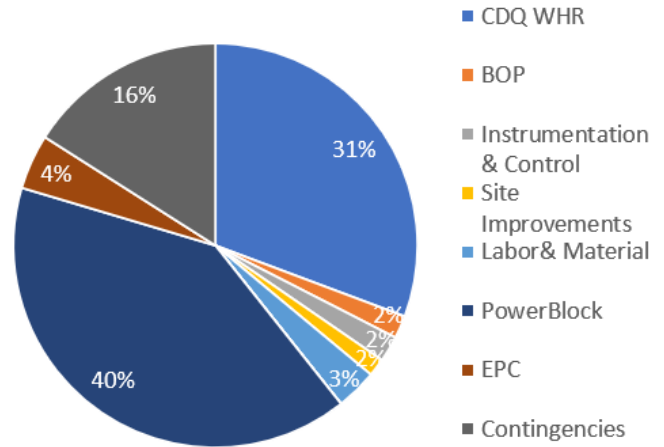


Figure 10: CAPEX share among main plant components

Sensitivity Analysis

A sensitivity analysis is carried out to determine which factors affect the NPV mostly. The error ranges of the cost model [28] are chosen as the sensitivity ranges. Results show that the components' price do not affect the NPV significantly. Were the power block to increase in cost by 35% the NPV increases by only 13%. This shows that the uncertainty in the cost estimation model will not greatly impact the NPV. Among the different components, the compressor's cost has the greatest impact. Figure 11 shows the impact of the change in price of all power block components.

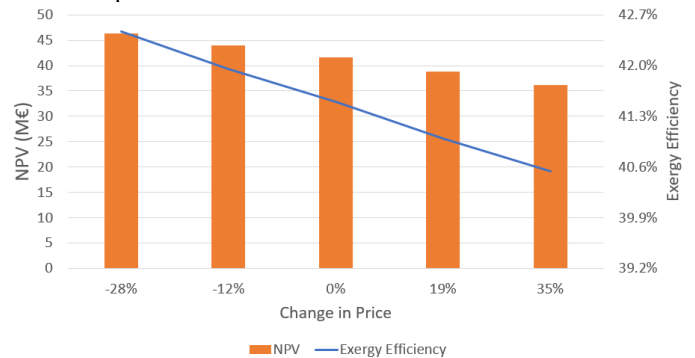


Figure 11: Sensitivity Analysis of Change in Power Block Price

For the other factors, the electricity price has the highest impact on NPV as can be seen in Figure 12. An increase in the electricity price of 29% would increase the NPV by 37%.

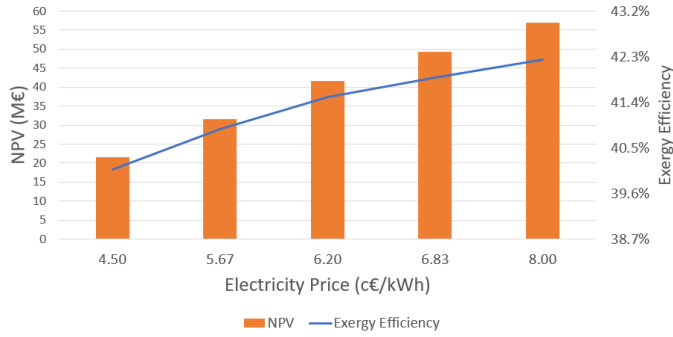


Figure 12: Sensitivity Analysis of Change in Electricity Price

CONCLUSION

In this work the relationship between thermal efficiency, exergy efficiency, and cost of the sCO₂ power cycles for waste heat recovery was investigated.

The optimal trade-off between the economics and thermodynamic performance of an sCO₂ cycle was estimated using a techno-economic optimization structure of the different cycle parameters. The approach compares six different cycle configurations and optimizes for the highest NPV cycle. The pressure levels of the cycle along with the recuperators' effectiveness were optimized for the different industries and configurations to yield the highest NPV.

The results show that sCO₂ cycles can be competitive on an LCOE basis with both ORC and steam cycles for waste heat recovery applications.

With the constraints assumed in this work, the highest NPV for a medium size coke dry quenching process in an iron and steel plant was €34.6M. This system had a thermal efficiency of 44%, a payback period of 4.9 years and LCOE of 2.91 c€/kWh. It was deduced that even with their higher thermal efficiencies, recompression cycles provide lower economic value for waste heat recovery. This is due to their limited temperature glide in the primary heater, resulting in lower waste heat utilization. It was discovered that the preheating cycle is best suited among the cycles analyzed.

The turbomachinery needed to operate this cycle is a concern. CO₂ has high density at supercritical conditions, which makes the machinery required compact. However, this also means higher stresses on the blades, this might prohibit the use of single shaft machines with few stages. Assessing these thermomechanical stresses may be an important factor to include while modeling these systems, which was excluded in the cost models that were used in this work.

More analysis is needed for (a) the cycle operation with variable waste heat (b) operation at off-design point, (c) the investigation of start-ups, shut-downs and load changes and (d) dual operation of compressors as turbines and vice versa. Future work will focus on supercritical cycle systems at large scale to properly evaluate their commercialization.

NOMENCLATURE

ABC Artificial Bee Colony
BOP Balance of Plant

CAPEX Capital Expenditures
CC Combined Cycle
CDQ coke dry quenching
COG Coke Oven Gas
 c_p Specific Heat Capacity
 $c_{p,HS}$ Waste Heat Fluid Specific Heat Capacity
 ϵ Effectiveness
 $E_{l,price}$ electricity price
EPC Engineering, Procurement and Construction
GCS Gas Compression Station
 h Enthalpy
HEX Heat Exchanger
HTR High Temperature Recuperator
 i Nominal Discount Rate
LCOE Levelized Cost Of Energy
LMTD Log Mean Temperature Difference
LTR Low Temperature Recuperator
 \dot{m}_{HS} Waste Heat Mass Flow Rate
 n Efficiency
 n Lifetime
 N_h Annual Operating Hours
NPV Net Present Value
O&M Operation and Maintenance
ORC Organic Rankine Cycle
PP Payback Period
SR Split Ratio
SRBC Simple Recuperated Brayton Cycle
sCO₂ Supercritical Carbon Dioxide
 T_{HS} is Waste Heat Temperature
TIT Turbine Inlet Temperature
UA Heat Exchanger Conductance
WHU Waste Heat Utilization
WHR Waste Heat Recovery
 w_{is} Isentropic Specific Work

ACKNOWLEDGEMENTS

We would like to thank Francesco Campana for the work he carried out in estimating the waste heat potential in EU. We would also like to thank him for explaining to us the methodology they used. Special thanks to the managers of the cement plants that answered our questions. We are grateful for Rafael Guédez and Silvia Trevisan who gave us a lot of resources and guided our way of thinking.

REFERENCES

- [1] Lead, "Sources of CO₂," CARBON DIOXIDE CAPTURE AND STORAGE, p. 75.
- [2] G. P. Hammond and J. B. Norman, (2014), "Heat recovery opportunities in UK industry," Appl. Energy, vol. 116, pp. 387–397.
- [3] R. C. McKenna and J. B. Norman, (2010), "Spatial modelling of industrial heat loads and recovery potentials in the UK," Energy Policy, vol. 38, no. 10, pp. 5878–5891.
- [4] M. Papapetrou, G. Kosmadakis, A. Cipollina, U. La Commare, and G. Micale, (2018), "Industrial waste heat: Estimation of the technically available resource in the EU per industrial sector, temperature level and country,"

- Appl. Therm. Eng., doi: 10.1016/j.applthermaleng.2018.04.043.
- [5] F. Campana *et al.*, (2013), “ORC waste heat recovery in European energy intensive industries: Energy and GHG savings,” *Energy Convers. Manag.*, vol. 76, pp. 244–252.
- [6] X. Wang and Y. Dai, (2016), “Exergoeconomic analysis of utilizing the transcritical CO₂ cycle and the ORC for a recompression supercritical CO₂ cycle waste heat recovery: A comparative study,” *Appl. Energy*, vol. 170, pp. 193–207.
- [7] D. Sanchez, J. M. M. de Escalona, R. Chacartegui, A. Munoz, and T. Sanchez, (2011), “A comparison between molten carbonate fuel cells based hybrid systems using air and supercritical carbon dioxide Brayton cycles with state of the art technology,” *J. Power Sources*, vol. 196, no. 9, pp. 4347–4354.
- [8] L. Dunhuang, Z. Yaoli, and G. U. O. Qixun, (2015), “Modeling and analysis of nuclear reactor system using supercritical-CO₂ brayton cycle,” *J. Xiamen Univ. (Natural Sci.)*, vol. 54, no. 5, pp. 608–613.
- [9] R. Singh, S. A. Miller, A. S. Rowlands, and P. A. Jacobs, (2013), “Dynamic characteristics of a direct-heated supercritical carbon-dioxide Brayton cycle in a solar thermal power plant,” *Energy*, vol. 50, pp. 194–204.
- [10] V. K. Patel, V. J. Savsani, and M. A. Tawhid, *Thermal System Optimization - A Population-Based Metaheuristic Approach* *{\vert\$}* Vivek K. Patel *{\vert\$}* Springer. Springer International Publishing, 2019.
- [11] “sCO₂-flex.” 2019.
- [12] P. Vinnemeier, M. Wirsum, D. Malpiece, and R. Bove, (2016), “Integration of heat pumps into thermal plants for creation of large-scale electricity storage capacities,” *Appl. Energy*, vol. 184, pp. 506–522.
- [13] T. J. Held, “Initial test results of a megawatt-class supercritical CO₂ heat engine,” in *The 4th International Symposium–Supercritical CO₂ Power Cycles*, 2014 2014, pp. 9–10.
- [14] F. Krull, “Power from waste heat: Maximum yield with supercritical carbon dioxide,” *Siemens Energy*. [Online]. Available: <https://www.siemens-energy.com/global/en/news/magazine/2020/waste-heat-to-power-with-sco2-turbines.html>.
- [15] A. Doğan *et al.*, “Waste heat recovery in Turkish cement industry: review of existing installations and assessment of remaining potential,” (2018).
- [16] Cembureau, “Key Facts & Figures.” 2019.
- [17] S. Qin and S. Chang, (2017), “Modeling, thermodynamic and techno-economic analysis of coke production process with waste heat recovery,” *Energy*, vol. 141, pp. 435–450.
- [18] Eurostat, “Eurostat - Data Explorer.” Aug. 2020.
- [19] S. Ndlovu, G. S. Simate, and E. Matinde, *Waste production and utilization in the metal extraction industry*. CRC Press, 2017.
- [20] K. C. Tran, G. Harp, O. Sigurbjörnsson, C. Bergins, and T. Buddenberg, (2016), “Carbon Recycling for Converting Coke Oven Gas to Methanol for the Reduction of Carbon Dioxide at Steel Mills,” *MefCO₂*: Auderghem, Belgium.
- [21] Satyendra, “Coke Oven Gas, its Characteristics and Safety Requirements – IspatGuru.” 2015.
- [22] M. Bianchi *et al.*, (2017), “Techno-economic analysis of ORC in gas compression stations taking into account actual operating conditions,” *Energy Procedia*, vol. 129, pp. 543–550.
- [23] S. L. Gómez-Alález, V. Brizzi, D. Alfani, P. Silva, A. Gostri, and M. Astolfi, (2017), “Off-design study of a waste heat recovery ORC module in gas pipelines recompression station,” *Energy Procedia*, vol. 129, pp. 567–574.
- [24] T. M. Miller, “CRC Handbook of Chemistry and Physics 88th edn, ed DR Lide.” Boca Raton, FL: CRC Press, 2008.
- [25] K. Wang, M.-J. Li, J.-Q. Guo, P. Li, and Z.-B. Liu, (2018), “A systematic comparison of different S-CO₂ Brayton cycle layouts based on multi-objective optimization for applications in solar power tower plants,” *Appl. Energy*, vol. 212, pp. 109–121.
- [26] S. Hou, Y. Wu, Y. Zhou, and L. Yu, (2017), “Performance analysis of the combined supercritical CO₂ recompression and regenerative cycle used in waste heat recovery of marine gas turbine,” *Energy Convers. Manag.*, vol. 151, pp. 73–85.
- [27] S. A. Wright, C. S. Davidson, and W. O. Scammell, “Thermo-economic analysis of four sCO₂ waste heat recovery power systems,” in *Fifth International SCO₂ Symposium, San Antonio, TX, Mar, 2016* 2016, pp. 28–31.
- [28] N. Weiland, B. Lance, and S. Pidaparti, “sCO₂ Power Cycle Component Cost Correlations from DOE Data Spanning Multiple Scales and Applications (Final),” (2019).
- [29] L. F. Cabeza, A. de Gracia, A. I. Fernández, and M. M. Farid, (2017), “Supercritical CO₂ as heat transfer fluid: A review,” *Appl. Therm. Eng.*, vol. 125, pp. 799–810.
- [30] J. Holman, *Heat Transfer (Int’l Ed)*. McGraw-Hill Education / Asia, 2018.
- [31] G. Nellis and S. Klein, *Heat Transfer*. Cambridge University Press, 2012.
- [32] A. Moisseytsev, J. J. Sienicki, and Q. Lv, “Dry Air Cooler Modeling for Supercritical Carbon Dioxide Brayton Cycle Analysis,” doi: 10.2172/1342159.
- [33] J. J. Dyreby, “Modeling the supercritical carbon dioxide Brayton cycle with recompression,” The University of Wisconsin-Madison, 2014.
- [34] S. Trevisan, R. Guédez, and B. Laumert, “Supercritical CO₂ Brayton Power Cycle for CSP With Packed Bed TES Integration and Cost Benchmark Evaluation,” in *ASME Power Conference*, 2019 2019, vol. 59100, p. V001T06A010.

- [35] I. H. Bell, J. Wronski, S. Quoilin, and V. Lemort, (2014), "Pure and Pseudo-pure Fluid Thermophysical Property Evaluation and the Open-Source Thermophysical Property Library CoolProp," *Ind. Eng. Chem. Res.*, vol. 53, no. 6, pp. 2498–2508, doi: 10.1021/ie4033999.
- [36] R. Canale and S. Chapra, *Numerical Methods for Engineers*. McGraw-Hill Science/Engineering/Math, 2009.
- [37] I. IRENA, (2019), "Renewable power generation costs in 2018. Report," Int. Renew. Energy Agency, Abu Dhabi.
- [38] R. C. Bailie, W. B. Whiting, J. A. Shaeiwitz, R. Turton, and D. Bhattacharyya, *Analysis, Synthesis, and Design of Chemical Processes*. Pearson, 2018.
- [39] C. White, D. Gray, J. Plunkett, W. Shelton, N. Weiland, and T. Shultz, "Techno-economic Evaluation of Utility-Scale Power Plants Based on the Indirect sCO₂ Brayton Cycle." Sep. 2017.
- [40] C. W. White, W. W. Shelton, N. T. Weiland, and T. R. Shultz, "sCO₂ Cycle as an Efficiency Improvement Opportunity for Air-fired Coal Combustion," in *The 6th International Supercritical CO₂ Power Cycles Symposium*, 2018 2018, pp. 27–29.
- [41] M. Turner and A. T. Samaei, "Quality Guidelines for Energy System Studies: Capital Cost Scaling Methodology: Revision 3 Reports and Prior," (2019).
- [42] K. Gerdes, W. M. Summers, and J. Wimer, "Quality Guidelines for Energy System Studies: Cost Estimation Methodology for NETL Assessments of Power Plant Performance," (2011).
- [43] N. Weiland, W. Shelton, T. Shultz, C. W. White, and D. Gray, "Performance and Cost Assessment of a Coal Gasification Power Plant Integrated with a Direct-Fired sCO₂ Brayton Cycle," (2017).
- [44] C. E. C. Rodríguez *et al.*, (2013), "Exergetic and economic comparison of ORC and Kalina cycle for low temperature enhanced geothermal system in Brazil," *Appl. Therm. Eng.*, vol. 52, no. 1, pp. 109–119.
- [45] R. Pili, A. Romagnoli, H. Spliethoff, and C. Wieland, (2017), "Techno-economic analysis of waste heat recovery with ORC from fluctuating industrial sources," *Energy procedia*, vol. 129, pp. 503–510.
- [46] C. Zhang, A. Romagnoli, J. Y. Kim, A. A. M. Azli, S. Rajoo, and A. Lindsay, (2017), "Implementation of industrial waste heat to power in Southeast Asia: an outlook from the perspective of market potentials, opportunities and success catalysts," *Energy Policy*, vol. 106, pp. 525–535.
- [47] A. Doğan *et al.*, "Waste heat recovery in Turkish cement industry: review of existing installations and assessment of remaining potential," The World Bank, (2018).
- [48] M. Persichilli, T. Held, S. Hostler, E. Zdankiewicz, and D. Klapp, (2011), "Transforming waste heat to power through development of a CO₂-based-power cycle," *Electr. Power Expo*, vol. 10.

CLOSED-LOOP SUPERCRITICAL CARBON DIOXIDE WIND TUNNEL: DESIGN AND COMPONENTS

Giuseppe Petruccioli*

Lappeenranta-Lahti University of Technology LUT
Lappeenranta 53850, Finland
Giuseppe.Petruccioli@lut.fi

Antti Uusitalo

Lappeenranta-Lahti University of Technology LUT
Lappeenranta 53850, Finland

Aki Grönman

Lappeenranta-Lahti University of
Technology LUT
Lappeenranta 53850, Finland

Teemu Turunen-Saaresti

Lappeenranta-Lahti University of
Technology LUT
Lappeenranta 53850, Finland

Marta Zocca

Lappeenranta-Lahti University of
Technology LUT
Lappeenranta 53850, Finland

ABSTRACT

Closed-loop supercritical CO₂ cycles (sCO₂) offer an innovative and efficient solution to achieve a reduction in primary energy consumption. CO₂ has a low Global Warming Potential (GWP) compared to conventional fluorocarbon-based refrigerants, which makes it suitable for refrigeration cycles. Successful deployment of this technology is dependent on further experimental research. A significant effort is required to study the behavior of CO₂ in the thermodynamic region close to the critical point, where sharp variations in thermophysical properties and real gas behavior are observed.

This paper presents the preliminary design of the LUTsCO₂ facility. The experimental setup is designed to allow detailed studies on expansion and heat transfer of CO₂ near the critical point. The transcritical refrigeration cycle is preferred as the experimental layout because of its operational flexibility and the commercial availability of components. Furthermore, a closed-loop cycle has the major advantage of running the loop continuously, which would not be possible with a blowdown test rig. The preliminary design of the main components is discussed with an emphasis on the heat exchangers. The latter are designed to operate by crossing the pseudo-boiling line, and they thus experience a considerable variation in CO₂ properties. This phenomenon has a direct consequence on the design of the heat exchangers and requires the application of advanced heat transfer correlations that consider whether the CO₂ is in a liquid-like or gas-like state. In addition, the supersonic test section is briefly described. This component comprises a converging-diverging nozzle, which performs a supersonic expansion from the supercritical region up to the two-phase region, followed by a normal shock wave, which allows the large kinetic head available to be recovered in the diverging section.

INTRODUCTION

Continuous growth in energy demand and increasingly stringent emission regulations are driving research and industry to develop and adopt new technologies with higher process efficiencies. The usage of sCO₂ power cycles is considered a promising solution capable of achieving this aim. The works of Angelino [1] and Feher [2] originally pointed out the main advantage of the sCO₂ power cycles, namely the ability to act as a highly efficient energy conversion technology. The unique properties of CO₂ in the supercritical region lead to higher cycle efficiencies [3-4], thus resulting in a decrease of fuel consumption and emissions. Furthermore, the high operating densities enable the turbomachinery and heat exchangers employed in these cycles to be reduced in size, leading to very compact systems, with a consequent reduction in costs and footprint. sCO₂ power cycles are able to operate with heat sources across a wide temperature range and they are therefore suitable for many different power generation applications [3-7].

Allam et al. [8] proposed an innovative fossil fuel-based oxy-combustion transcritical power cycle (the Allam cycle), which is a high-pressure, low-pressure ratio, highly recuperated Brayton cycle. The combustion products are used to drive the turbine and the water resulting from the combustion is separated from the recirculating CO₂ flow after being cooled down to near ambient temperature. The excess CO₂ (5% of the total recycle flow) is exported for sequestration or utilization, thus ensuring a near complete capture of the greenhouse gases.

In view of the potential shown by sCO₂ power cycles, the United States Department of Energy (DOE) has funded a number of projects focusing on the application of sCO₂ power cycles in concentrated solar power (CSP) systems. As part of the SunShot project [9], Southwest Research Institute (SwRI) and GE developed a novel high-temperature MW-scale turboexpander

* corresponding author(s)

optimized for CSP applications ($TIT > 700\text{ }^{\circ}\text{C}$) that is installed in a simple recuperated Brayton cycle. $s\text{CO}_2$ can also be used as a working fluid for bottoming cycles, for example, in waste heat recovery (WHR) applications, filling an important gap for heat source temperatures higher than $700\text{ }^{\circ}\text{C}$ [10]. Steam cycles suffer from corrosion issues at such temperatures [10-11], and $s\text{CO}_2$ would therefore be a possible optimal solution. Echogen developed the first commercial 8-MWe closed $s\text{CO}_2$ Brayton cycle heat engine for WHR with heat source temperatures in the range of $300\text{-}600\text{ }^{\circ}\text{C}$ [12].

As a rather new technology, the approach faces several challenges, mainly caused by the unique fluid properties of the CO_2 in the supercritical region, which complicate the operation and control of these cycles as well as the design of the turbomachinery and the heat exchangers. Consequently, many institutions have built their own $s\text{CO}_2$ experimental facility in recent years to assist in research, development and deployment of $s\text{CO}_2$ systems.

The first integral $s\text{CO}_2$ power cycles were developed by the Sandia National Laboratories (SNL) [13] and the Knolls Atomic Power Laboratories (KAPL) [14]. The SNL designed a 250 kWe recompression Brayton cycle for nuclear power applications, that operates with two TAC (turbine-alternator-compressor) units. KAPL (Knolls Atomic Power Laboratory) and BAPL (Bettis Atomic Power Laboratory) demonstrated the applicability of the simple recuperated cycle for water-cooled reactor applications operating at relatively low temperatures ($TIT \sim 300\text{ }^{\circ}\text{C}$). The Tokyo Institute of Technology and the Institute of Applied Energy (IAE) built and tested a 10 kWe recuperated Brayton cycle to conduct studies on $s\text{CO}_2$ power generation [15]. KAERI (Korean Atomic Energy Research Institute), in collaboration with KAIST (Korea Advanced Institute of Science and Technology) and POSTECH (Pohang University of Science and Technology), constructed the $s\text{CO}_2$ Integral Experimental Loop (SCIEL) [16], which is a 300 kWe recuperated Brayton cycle with two stages of compression and expansion. The distinctive feature of the SCIEL is its high-pressure ratio (target of 2.67). In KIER (Korean Institute of Energy Research), a 12.6 kWe simple un-recuperated Brayton power cycle experimental loop was built to test its feasibility and a 60 kWe-class recuperated Brayton cycle is being developed to operate as a bottoming cycle using hot flue-gases as a heat source [17]. Cranfield University is working with Rolls-Royce to develop an experimental facility to explore the possibility of employing $s\text{CO}_2$ for bottoming power cycle applications [18]. The transcritical refrigeration cycle configuration was chosen in the initial phase to demonstrate the robustness and controllability of the system. Brunel University London is focusing the attention on $s\text{CO}_2$ power cycles employed in WHR from high temperature sources (up to $780\text{ }^{\circ}\text{C}$) and has constructed the High Temperature Heat To power Conversion (HT2C) facility [19]. The designed 50 kWe simple recuperated Brayton cycle uses an 830 kWth gas-fired process air heater as heat source. The Zhejiang university built an $s\text{CO}_2$ test loop to investigate the heat transfer characteristics of $s\text{CO}_2$ from ambient temperature to $600\text{ }^{\circ}\text{C}$ at supercritical pressures (up to 15 MPa) [20]. The same

research group is designing a 150 kWe $s\text{CO}_2$ Brayton cycle coupled with a solar solid particle receiver. In the EU-funded $s\text{CO}_2$ -HeRo (supercritical CO_2 Heat Removal system) project, three different experimental facilities have been built to study heat transfer in the supercritical region [21-23]. A multipurpose test facility – the supercritical carbon dioxide loop at IKE Stuttgart (SCARLETT) – was built at the Institut für Kernenergetik und Energiesysteme (IKE) in Stuttgart [21]. The test section is installed in a transcritical refrigeration cycle and allows studies of turbulent heat transfer under different operating conditions in the supercritical region. The second experimental loop of the $s\text{CO}_2$ -HeRo project was built at CVR (Research Centre Rez) in the Czech Republic as part of the Sustainable Energy project (SUSEN) [22]. The SUSEN facility is an electrically heated recuperated Brayton cycle, designed to perform material research for temperatures up to $550\text{ }^{\circ}\text{C}$ and pressures up to 30 MPa. The experience gained from operation of the two loops was used in design of the $s\text{CO}_2$ -HeRo loop constructed at the PWR glass model at the Simulator Centre of KSG/GfS in Essen [23]. The $s\text{CO}_2$ -HeRo loop is a small-size un-recuperated Brayton cycle that aims to demonstrate the applicability of $s\text{CO}_2$ power cycles to safe and efficient removal of residual decay heat from nuclear fuel in the event of an accident.

Even though intensive research and development is currently underway, some key aspects of $s\text{CO}_2$ behavior require further investigation. One of these is heat transfer in proximity of the pseudo-boiling line, where the significant variation in the properties of the CO_2 greatly reduces the accuracy of well-established heat transfer correlations. Moreover, the dynamics of fluids in supercritical conditions is significantly affected by the real gas effects and additional experimental research is thus required to provide the data needed for validation of the numerical codes. This background led to the decision to build a closed-loop $s\text{CO}_2$ test rig at Lappeenranta-Lahti University of Technology LUT. The designed facility can fill the gap between very small-size experimental facilities (a few kWe) and large power cycle facilities (a few hundred kWe). Fundamental studies of supersonic CO_2 in the supercritical and two-phase region can be conducted in the nozzle installed in the facility, and heat transfer across the pseudo-boiling line can be investigated by measurement of temperature and heat transfer coefficient in the heated section. This paper aims to describe the design of the experimental cycle and its components, i.e. the heat exchangers and the supersonic test section. The structure of the paper is the following: 1) The thermophysical properties are described and an equation for the pseudo-boiling line is determined; 2) an overall description of the test loop that will be installed in the Laboratory of Fluid Dynamics at the Lappeenranta-Lahti University of Technology is given; and 3) the preliminary design of the components is reported and discussed.

THERMOPHYSICAL PROPERTIES AND WIDOM LINE

In the supercritical region, the thermophysical properties of fluids undergo significant nonlinear variation as the thermodynamic conditions approach the critical point. The

variations in properties such as the isobaric specific heat, density, dynamic viscosity and thermal conductivity greatly influence the design, operability and control of components operating in this region, e.g., the compressor and the heat exchangers. Figures 1 and 2 show the isobaric specific heat, density and thermal conductivity of CO₂ as a function of temperature along one subcritical isobar and three supercritical isobars close to the critical pressure, which has a value of 73.8 bar. In subcritical conditions, the specific heat and other thermodynamic response functions diverge along the liquid-vapor coexistence line. In the supercritical region, no divergence is observed, and this concept is replaced by that of a maximum, which can be identified for each response function [24]. The set of the maxima in the supercritical region is the so-called Widom line or pseudo-boiling line. The following analysis is based on the Widom line identified by the isobaric specific heat (Fig. 1), which can be defined as:

$$\left(\frac{\partial c_p}{\partial T}\right)_P = \left(\frac{\partial^2 h}{\partial T^2}\right)_P = 0 \quad (1)$$

Fluid crossing the Widom line at pressures close to the critical pressure ($P < 3P_{cr}$) experiences a liquid-like to gas-like transition that mimics the subcritical liquid-gas phase change, with the major difference being that the heat supplied in the supercritical region expands and heats the fluid. Banuti [25] derived an analytical expression for the c_p -based Widom line starting from the Clapeyron equation and assuming, based on empirical evidence, a linear relation between the natural logarithm of the pressure and the temperature along the Widom line:

$$\frac{P_{pb}}{P_{cr}} = \exp\left[\frac{T_{cr}}{P_{cr}}\left(\frac{dP}{dT}\right)_{cr}\left(\frac{P_{pb}}{P_{cr}} - 1\right)\right] \quad (2)$$

Equation 2 can be rewritten in terms of reduced quantities ($P_r = P/P_{cr}$ and $T_r = T/T_{cr}$) as:

$$P_r = \exp[A(T_r - 1)] \quad (3)$$

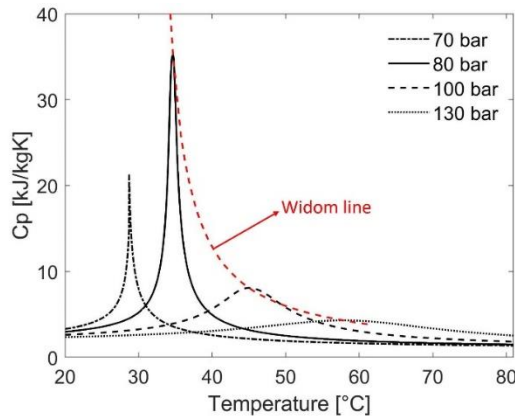


Figure 1: Isobaric specific heat of CO₂ as a function of temperature for four isobars close to the critical pressure.

where A is a fluid constant:

$$A = \frac{T_{cr}}{P_{cr}} \left(\frac{dp}{dT}\right)_{cr} \quad (4)$$

Banuti suggested a value of 5.5 for coefficient A for simple fluids such as oxygen, argon and nitrogen. On the other hand, more complex fluids such as water or carbon dioxide show large deviations when this value is used. In this regard, an exponential regression on the values of maximal c_p calculated from the NIST database [26] was carried out specifically for the CO₂. This calculation results in a coefficient A equal to 6.505, giving the following expression for the CO₂ Widom line:

$$P_r = \exp[6.505 \cdot (T_r - 1)] \quad (5)$$

Figure 3 shows the maximal c_p in the supercritical region and compares the results obtained using the NIST database and the exponential regression (Eq. 5).

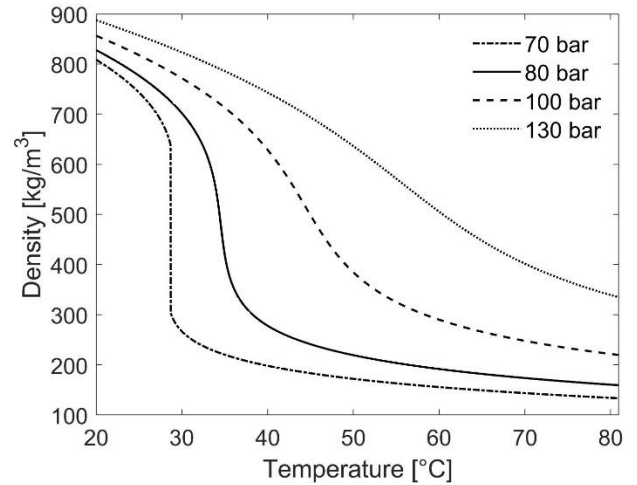


Figure 2: Density of CO₂ as a function of temperature for four isobars close to the critical pressure.

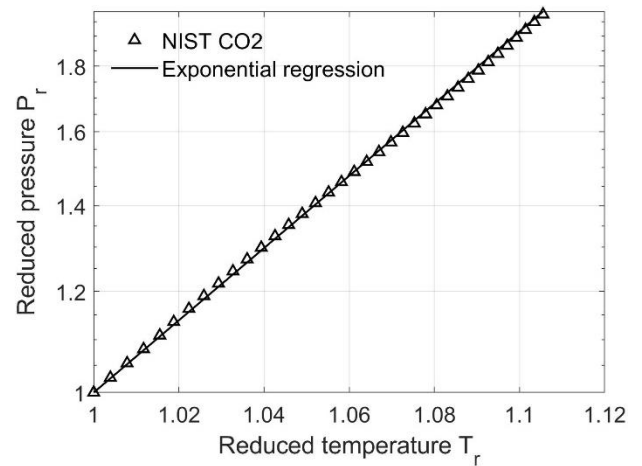


Figure 3: Comparison of maximal c_p in the supercritical region between NIST and exponential regression (Eq. 5)

point, an expansion valve expands the CO₂, setting the operating pressure of the downstream heater and supersonic test section. Hence, the temperature at the test section inlet is controlled by the electric heater, which is divided into multiple power modules to allow additional flexibility. The cycle can operate with or without the supersonic test section, depending on the purpose of the experimental activity, by means of a three-way plug valve. For an open test section, a total pressure loss, caused by the shock wave occurring in the test section, must be estimated and accounted for in the overall design of the loop. The magnitude of this loss is in the order of 7 bar at the design conditions and needs to be carefully controlled to avoid the pressure at the test section outlet being lower than the critical pressure, which would induce condensation inside the gas cooler. After leaving the test section, the fluid is cooled to room temperature by a water-cooled plate heat exchanger. Downstream of the gas cooler, the fluid is expanded a second time, through an expansion valve, into the two-phase region. At this point, the CO₂ is completely evaporated by the heat provided by the hot CO₂ and it is subsequently superheated by 10 °C to prevent the presence of liquid inside the compressor.

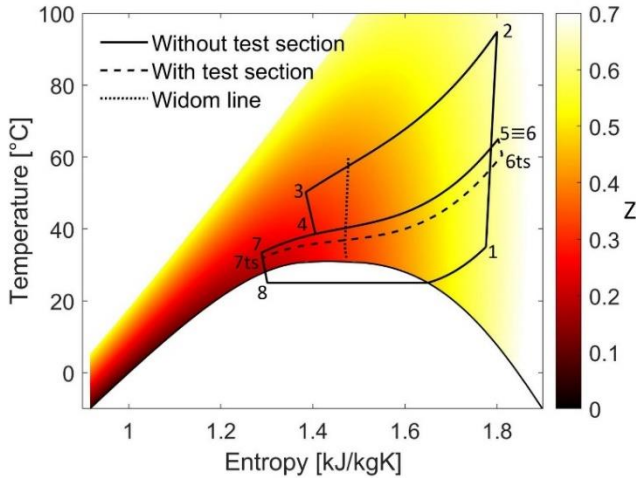


Figure 5: Temperature-specific enthalpy diagram superposed to the compressibility factor map

HEAT EXCHANGERS – PRELIMINARY DESIGN

The heat exchangers are one of the most critical components in sCO₂ cycles, because the unique fluid properties in the supercritical region mean that conventional design methods developed under an assumption of constant fluid properties, e.g. the LMTD (log-mean temperature difference) method, are not applicable. In the preliminary design phase, the heat transfer area was estimated with a finite difference method. The whole geometry of the heat exchanger was divided into several nodes and the heat transfer coefficient was evaluated for each subsection. A graphical representation of the iterative algorithm is given in Fig. 6. The CO₂ properties are calculated from the NIST database [26] and are based on the Span-Wagner equation of state [27]. The presented 1D model neglects potential buoyancy effects and it is thus applicable only for non-buoyant

flows. In the event that buoyancy is not negligible, more advanced correlations should be employed. Alternatively, 3D unsteady turbulence resolving CFD simulations would also provide an accurate solution. This subject will be discussed further in the description of the electric heater, where the flow is strongly buoyant.

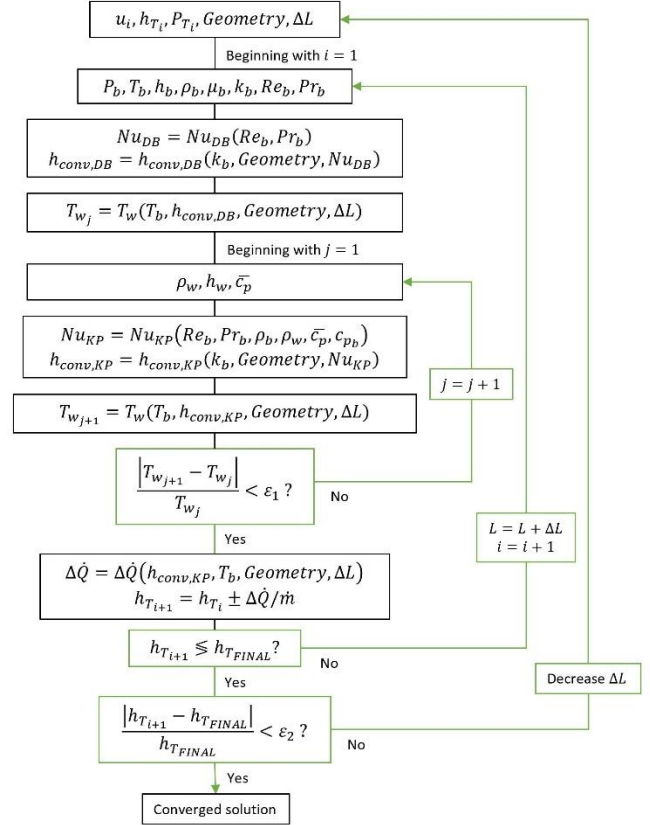


Figure 6: Algorithm to determine the heat transfer area

The initial guess solution for calculation of the convective heat transfer coefficient, h_{conv} , in the iterative computation was provided by the calculation of the Nusselt number through the Dittus-Boelter correlation [28]:

$$Nu_{DB} = 0.023 Re_b^{0.8} Pr_b^m \quad (6)$$

$$\begin{cases} m = 0.3 & \text{Cooling} \\ m = 0.4 & \text{Heating} \end{cases}$$

The solution provided by the Dittus-Boelter correlation was however considered insufficiently accurate in the supercritical region [29], and it is therefore only used to calculate an initial value for the wall temperature, which is subsequently used to evaluate the Nusselt number calculated with the modified Krasnoschekov and Protopopov correlation [30]:

$$Nu_{KP} = 0.0183 Re_b^{0.82} Pr_b^{0.4} \left(\frac{\rho_w}{\rho_b}\right)^{0.3} \left(\frac{\bar{c}_p}{c_{pb}}\right)^n \quad (7)$$

$$\bar{c}_p = \frac{1}{T_w - T_b} \int_{T_b}^{T_w} c_p dT = \frac{h_w - h_b}{T_w - T_b} \quad (8)$$

$$n = \begin{cases} 0.4 & \text{for } T_b < T_w \leq T_{pb} \text{ or } 1.2T_{pb} \leq T_b < T_w \\ 0.4 + 0.2 \left(\frac{T_w}{T_{pb}} - 1 \right) & \text{for } T_b \leq T_{pb} < T_w \\ 0.4 + 0.2 \left(\frac{T_w}{T_{pb}} - 1 \right) \left[1 - 5 \left(\frac{T_b}{T_{pb}} - 1 \right) \right] & \text{for } T_{pb} < T_b \leq 1.2T_{pb} \text{ and } T_b < T_w \end{cases} \quad (9)$$

ELECTRIC HEATER

The electric heater is a fundamental component of the experimental loop, because it allows direct measurements of the temperatures and heat transfer coefficients across the pseudo-boiling line, where sharp gradients in fluid properties drastically increase the difficulty of fully characterizing heat transfer phenomena. The flow is split in two parts upstream of the heating section: the main flow rate (98% of the total) is directed to a 200-kW circulation heater, which consists of heating elements inserted in a vessel, and the residual flow rate passes through a uniformly heated pipe equipped with multiple thermocouples to perform experimental measurement of wall temperature profiles, particularly at the top and bottom surfaces of the pipe. The operating parameters of the heated test section are listed in Table 2. Dense CO₂ is heated from the liquid-like region up to 90 °C. When the fluid properties cross the Widom line, very strong buoyancy forces are generated, which have a strong impact on the flow field and the heat transfer, pushing the dense gas towards the bottom wall. Various nondimensional parameters can be used to estimate the magnitude of the buoyancy effect on the flow. The Grashof number, Gr , well represents the strength of the secondary flows induced by the buoyancy force and is defined as:

$$Gr = \frac{g(\rho_b - \rho_w)\rho_b d^3}{\mu^2} \quad (10)$$

For horizontal flows, the buoyancy effect can be considered negligible when [31-32]:

$$\frac{Gr}{Re_b^2} < 10^{-3} \quad (11)$$

Figure 7 shows the variations of the internal diameter, the length of the pipe and the maximum value of Gr/Re_b^2 along the pipe as a function of the inlet velocity. Gr/Re_b^2 does not reach the threshold value expressed in Eq. 11 required to assume negligible buoyancy effects within the considered range of inlet velocities. A value of 0.2 m/s was chosen in the design phase to reduce the overall dimensions of the component. A numerical simulation of the heated test section was carried out and the results are briefly discussed in the next section.

Table 2: Design parameters of the heated test section.

Parameter	Value	Unit
Mass flow rate	0.032	kg/s
Operating pressure	90	bar
Bulk temperature (In – Out)	38.59 – 90	°C
Heat flux	25	kW/m ²
Inlet Reynolds number	$5.27 \cdot 10^4$	-

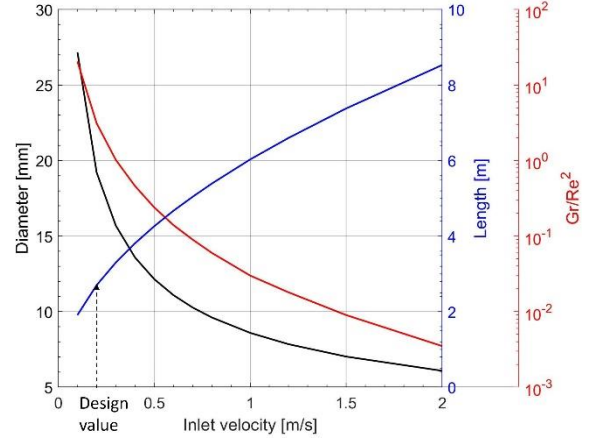


Figure 7: Geometry of the pipe and maximum Gr/Re_b^2 along the pipe as a function of the inlet velocity

Numerical simulation

The real-gas CFD simulation of the heated test section was performed with the commercial solver Fluent. The choice of turbulence model plays a fundamental role, since the turbulence caused by the buoyancy forces have a significant effect on the heat transfer. Recent research [33] has reported that accurate solutions for buoyant supercritical flows can be achieved with two-equation RANS models for limited ranges of heat fluxes (up to 26.9 kW/m²), mass flow rates (0.146÷0.151 kg/s) and values of Gr/Re_b^2 (up to 0.26). The experimental data published by Adebisi and Hall [34] are used to validate the numerical model employed in this study. The case with the most similar operating conditions (i.e., mass flux, heat flux, temperatures) is simulated applying the two-equation $k-\varepsilon$ RNG model and the Wall-Modeled LES (WMLES), which employs a hybrid RANS/LES formulation to overcome the high resolution requirements of the LES for wall boundary layers. The SIMPLEC algorithm is used for pressure-velocity coupling, the QUICK scheme is applied for discretization of the momentum and energy equations, and, when the RANS model is applied, the second order upwind is adopted for turbulent kinetic energy and turbulent dissipation rate equations. The grid requirements are very strict, particularly in the near-wall region, and at least 10 cells are placed within the boundary layer region. The turbulent Prandtl number is assumed to vary linearly from 0.85 to 0.9 moving towards the wall. A constant cross-section area of pipe with adiabatic walls is added upstream of the heated pipe in order to obtain a fully developed turbulent flow. The calculated temperature profiles at the top wall of the heated pipe are presented in Fig. 8 for both validation

case and designed test section. The area averaged temperature along the test section is also reported. Both the turbulence models show some discrepancies with the experimental data, mostly due to the complexity of the flow field within the pipe which has a large impact on the heat transfer. However, the results provided by both methodologies are considerate sufficient for the purposes of this analysis and the WMLES is used to simulate the designed test section. The computed wall temperatures are much higher than those of the validation case. This difference is due to the slightly higher heat fluxes involved and, more importantly, the stronger buoyancy forces generated and evaluated through Eq. 10. The velocity contours and tangential velocity vectors at the outlet section are depicted in Fig. 9, where two secondary flows are clearly visible in the upper and lower part of the pipe. The fluid properties in the upper part quickly cross the pseudo-boiling line in the heated section. The consequent liquid-like to gas-like transition produces sharp gradients of density, which in turn generate buoyancy forces and affect the flow field within the pipe.

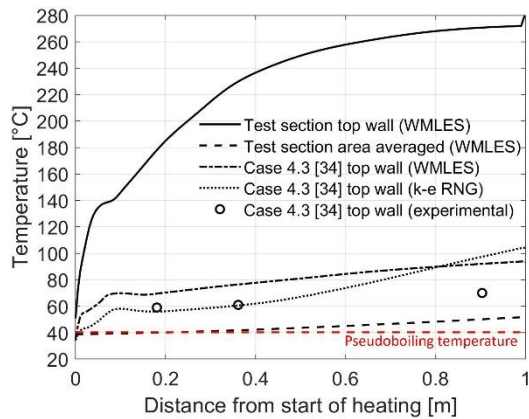


Figure 8: Calculated temperatures within the heated pipe.

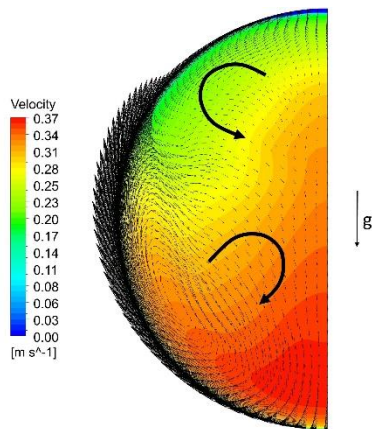


Figure 9: Velocity contours and tangential velocity vectors at the outlet of the heated test section.

GAS COOLER

The hot gas leaving the supersonic test section is cooled to near-ambient temperature (~ 32 °C) in the gas cooler. The

preliminary design of this component was done assuming a simple countercurrent shell-and-tube configuration with the hot CO₂ flowing in 100 tubes. The cooling medium in the shell-side is water that is heated from 10 °C to 35 °C. Figure 10 shows the calculated variation of the CO₂ properties along the heat exchanger. As previously described, the peak of the isobaric specific heat indicates the position where the pseudo-boiling line is crossed. Large variation of other properties is also evident as the fluid passes from a gas-like state to a liquid-like state. The temperature-heat diagram of the gas cooler is presented in Fig. 11, together with the calculated convective heat transfer coefficient of the CO₂. The maximum value of the latter is reached when the pseudo-boiling line is crossed. The maximum calculated value of Gr/Re_b^2 along the heat exchanger is $3 \cdot 10^{-4}$, therefore it can be inferred that the buoyancy effects are negligible (Eq. 11). Once the operating conditions of the gas cooler had been assessed, selection of the component was carried out. The selected gas cooler is a brazed plate heat exchanger, which is able to withstand extremely high operating pressure thanks to thin external frames in carbon steel. The design parameters of the gas cooler are reported in Table 3 and the technical drawing is presented in Fig. 12.

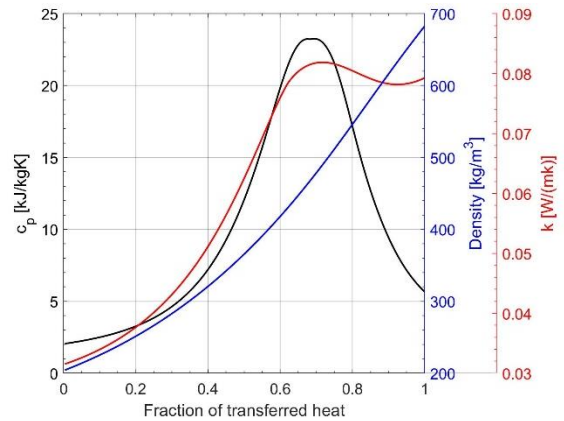


Figure 10: Variations of isobaric specific heat, density and thermal conductivity along the gas cooler.

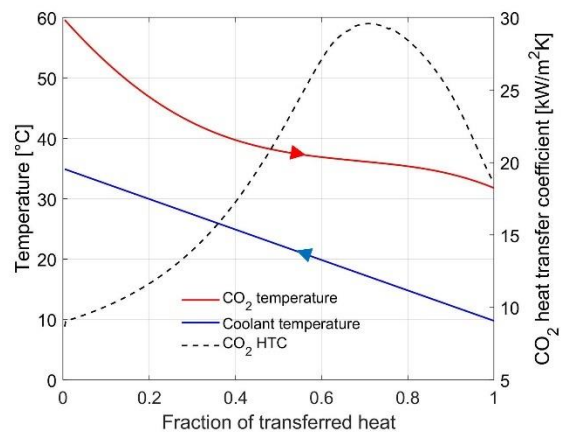


Figure 11: Temperature-heat diagram and CO₂ convective heat transfer coefficient along the gas cooler.

Table 3: Design parameters of the gas cooler.

Parameter	Value	Unit
CO ₂ temperatures (In – Out)	60 – 32	°C
CO ₂ operating pressure	83.3	bar
Coolant mass flow rate	2.48	kg/s
Coolant temperatures (In – Out)	10 – 35	°C
Dimensions	395 × 160 × 582	mm
Heat exchanged	261	kW

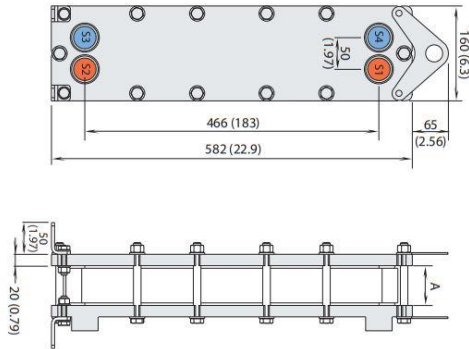


Figure 12: Technical drawing of the gas cooler

EVAPORATOR

In the evaporator, the hot gas leaving the compressor is cooled to 50 °C and the rejected heat is used to evaporate the liquid CO₂ directed to the compressor itself. The preliminary design of the evaporator was done assuming a countercurrent shell-and-tube configuration with the liquid CO₂ flowing in 20 tubes and the hot CO₂ in the shell-side. The buoyancy forces deriving by the evaporation of the liquid phase in the tubes were neglected in the preliminary design phase and a homogenous mixture between the two phases was assumed. In the shell-side, the maximum calculated value of Gr/Re_b^2 for the hot gas is $1.5 \cdot 10^{-2}$, suggesting that buoyancy may be relevant (Eq. 11). However, for the sake of simplicity, these effects were also not taken into account in the shell-side in the preliminary design phase. A representation of the temperature-heat diagram is depicted in Fig. 13. The evaporator is the most challenging component because of the high operating pressures in the hot side and its selection is still in progress.

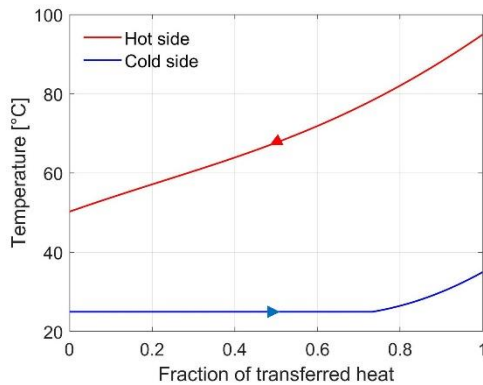


Figure 13: Temperature-heat diagram of the evaporator.

Table 4: Design parameters of the evaporator.

Parameter	Value	Unit
Hot side temperatures (In – Out)	94.8 – 50.2	°C
Hot side operating pressure	130	bar
Cold side temperatures (In – Out)	24.9 – 34.7	°C
Cold side operating pressure	64.3	bar
Heat exchanged	227	kW

SUPERSONIC TEST SECTION

The supersonic test section will be used to study the expansion process of CO₂ in the supercritical region, where the thermodynamic behavior of the fluid cannot be described by the ideal gas model. The test section consists of three components, depicted in a simplified sketch in Fig. 14: the contraction zone, the converging-diverging nozzle and the diffuser. The flow is initially expanded in the contraction zone up to a Mach number of 0.2 and completes a transition from a circular cross-section to a rectangular cross-section, which will ensure a two-dimensional flow field within the supersonic nozzle. The flow is further expanded in the converging part of the nozzle, reaching choking conditions in the throat. In the divergent section, the flow attains supersonic speeds and the thermodynamic properties fall within the two-phase region, triggering nucleation of small liquid droplets and subsequently their growth. The nozzle is designed to allow wall pressure and optical measurements to yield experimental data relevant to fundamental studies of CO₂ in the supercritical and two-phase region and to provide data required for validations. In order to recover the large kinetic head in the divergent part of the nozzle and to avoid a second throat that would significantly compromise the operability of the system, a shock-wave is generated that produces a near-instantaneous deceleration of the flow to subsonic speed, leading to an increase in pressure, temperature and entropy. A diffuser is placed downstream of the nozzle to fully recover the remaining kinetic energy.

A real-gas two-phase CFD simulation of the nozzle was run with Ansys CFX, coupling the solver with the lookup tables extracted from NIST REFPOP database [26]. Figures 15 and 16 present, respectively, the computed liquid mass fraction contours and the wall pressure along the nozzle.

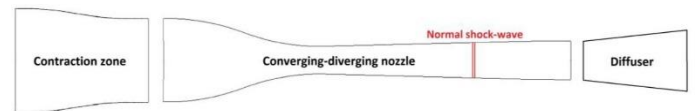


Figure 14: Simplified schematic of the supersonic test section.

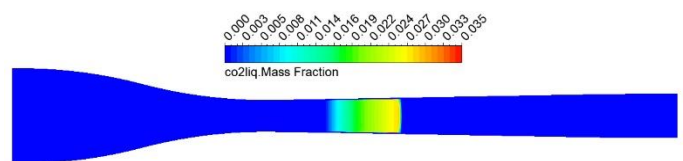


Figure 15: Liquid mass fraction contours in the nozzle.

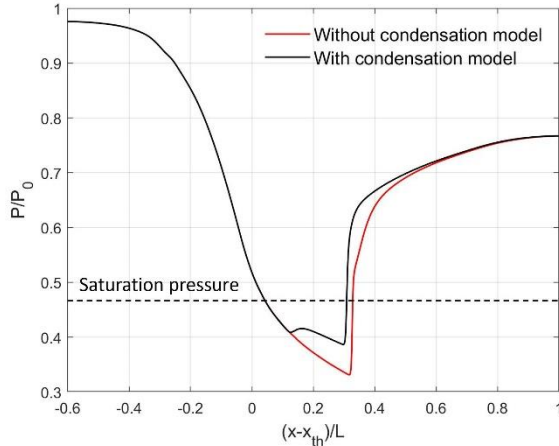


Figure 16: Wall pressure distribution along the nozzle.

CONCLUSIONS AND FUTURE WORK

This paper discusses the preliminary design of a sCO₂ closed-loop supersonic test facility and its components. The transcritical refrigeration cycle is preferred as an experimental layout because of its operational flexibility and the commercial availability of the components. The designed test loop allows experimental research to be performed in the supercritical region close to the critical point and in the two-phase region. Despite widespread use of sCO₂, such experimental data, which are required for study of fundamentals and for models validation, are still lacking.

In the study described, preliminary design of the heat exchangers was carried out. The flow field in the electric heater is greatly affected by the buoyancy effects, and a real-gas CFD simulation was therefore run to assess qualitatively the temperatures profiles along the heater walls. The choice of the turbulence model is of fundamental importance in order to capture the flow features and perform accurate calculation of the heat transfer within the boundary layer, particularly when the pseudo-boiling line is crossed. The unsteady scale resolving WMLES was adopted to obtain a qualitative solution. Assessment of the supersonic test section was carried out using a real-gas two-phase CFD simulation, which demonstrated that nucleation of the droplets is triggered in the divergent section of the nozzle. Future research will focus on design of the control and measurement systems that will be adopted, as well as assessment of more accurate numerical models to describe the CO₂ behavior in the supercritical region. The test setup is under commissioning and first experimental activities are foreseen in the second half of 2021.

ACKNOWLEDGEMENTS

The authors gratefully acknowledge the financial support of the Graduate School of Lappeenranta University of Technology.

NOMENCLATURE

c_p	Isobaric specific heat (J/kgK)
T	Temperature (K)
h	Specific enthalpy (J/kg)

P	Pressure (Pa)
u	Axial velocity (m/s)
k	Thermal conductivity (W/mK)
Re	Reynolds number (-)
Pr	Prandtl number (-)
Nu	Nusselt number (-)
h_{conv}	Convective heat transfer coefficient (W/m ² K)
\dot{Q}	Heat power (W)
\dot{m}	Mass flow rate (kg/s)
Gr	Grashof number (-)

Greek symbols

ρ	Density (kg/m ³)
μ	Dynamic viscosity (kg/ms)

Subscripts

pb	Pseudoboiling
cr	Critical
r	Reduced
T	Total
b	Bulk
w	Wall
DB	Dittus-Boelter
KP	Krasnoschekov-Protopopov

REFERENCES

- [1] Angelino, G. (1968). Carbon dioxide condensation cycles for power Production. ASME Journal of Engineering for Power, 90(3), pp. 287-295.
- [2] Feher, E.G. (1967). The supercritical thermodynamic power cycle. Proceedings of the IECEC, Miami Beach, FL, USA.
- [3] Dostal, V., Driscoll, M.J. and Hejzlar, P. (2006). High-performance supercritical carbon dioxide cycle for next-generation nuclear reactors. Nuclear Technology, 154(3), pp. 265-282.
- [4] Ahn, Y., Bae, S.J., Kim, M., Cho, S.K., Baik, S., Lee, J.I. and Cha, J.E. (2015). Review of supercritical CO₂ power cycle technology and current status of research and development. Nuclear Engineering and Technology, 47(6), pp. 647-661.
- [5] Le Moullec, Y. (2013). Conceptual study of a high efficiency coal-fired power plant with CO₂ capture using a supercritical CO₂ Brayton cycle. Energy, 49, pp. 32-46.
- [6] Turchi, C.S., Ma, Z., Neises, T.W. and Wagner, M.J. (2013). Thermodynamic study of advanced supercritical carbon dioxide power cycles for concentrating solar power systems. ASME Journal of Solar Energy Engineering, 135(4), 041007.
- [7] Uusitalo, A., Ameli, A. and Turunen-Saaresti, T. (2018). Thermodynamic and turbomachinery design analysis of supercritical Brayton cycles for exhaust gas heat recovery. Energy, 167, pp. 60-79.
- [8] Allam, R., Scott, M., Forrest, B., Fetvedt, J., Lu, X., Freed, D., Brown, G.W., Sasaki, T., Itoh, M. and Manning, J. (2017). Demonstration of the Allam Cycle: An update on the development status of a high efficiency supercritical carbon

dioxide power process employing full carbon capture. *Energy Procedia*, 114, pp. 5948-5966.

[9] Moore, J., Cich, S., Day, M., Allison, T., Wade, J. and Hofer, D. (2018). Commissioning of a 1 MWe supercritical CO₂ test loop. The 6th International supercritical CO₂ Power Cycles Symposium, Pittsburgh, PA, USA.

[10] Marchionni, M., Bianchi, G. and Tassou, S.A. (2020). Review of supercritical carbon dioxide (sCO₂) technologies for high-grade waste heat to power conversion. *SN Applied Sciences*, 2:611.

[11] Li, C. and Wang, H. (2016). Power cycles for waste heat recovery from medium to high temperature flue gas sources – from a view of thermodynamic optimization. *Applied Energy*, 180, pp. 707-721.

[12] Held, T.J. (2014). Initial test results of a megawatt-class supercritical CO₂ heat engine. The 4th International Symposium Supercritical CO₂ Power Cycles, Pittsburgh, PA, USA.

[13] Wright, S.A., Radel, R.F., Vernon, M.E., Rochau, G.E. and Pickard, P.S. (2010). Operation and analysis of a supercritical CO₂ Brayton cycle. Sandia National Laboratories, Albuquerque, NM, Sandia Report No. 2010-0171.

[14] Kimball, K. J., and Clementoni, E.M. (2012). Supercritical carbon dioxide Brayton power cycle development overview. Proceedings of the ASME Turbo Expo 2012, Copenhagen, Denmark.

[15] Utamura, M., Hasuike, H., Ogawa, K., Yamamoto, T., Fukushima, T., Watanabe, T. and Himeno, T. (2012). Demonstration of supercritical CO₂ closed regenerative Brayton cycle in a bench scale experiment. Proceedings of the ASME Turbo Expo 2012, Copenhagen, Denmark.

[16] Ahn, Y., Lee, J., Kum, S.G., Lee, J.I., Cha, J.E. and Lee, S.W. (2015). Design consideration of supercritical CO₂ power cycle integral experiment loop. *Energy*, 86, pp. 115-127.

[17] Cho, J., Shin, H., Ra, H.S., Lee, G., Roh, C., Lee, B. and Baik, Y.J. (2016). Development of the supercritical carbon dioxide power cycle experimental loop in KIER. Proceedings of the ASME Turbo Expo 2016, Seoul, South Korea.

[18] Anselmi, E., Bunce, I., Pachidis, V., Zachos, P. and Johnston, M. (2018). An overview of the Rolls-Royce sCO₂-test rig project at Cranfield University. The 6th International supercritical CO₂ Power Cycles Symposium, Pittsburgh, PA, USA.

[19] Bianchi, G., Saravi, S.S., Loeb, R., Tsamos, K., Marchionni, M., Leroux, A. and Tassou, S.A. (2019). Design of a high-temperature heat to power conversion facility for testing supercritical CO₂ equipment and packaged power units. *Energy Procedia*, 161, pp. 421-428.

[20] Xiao, G., Xing, K., Zhang, J., Le Moullec, Y., Zhou, P., Yang, T., Ni, M., and Cen, K. (2019). Heat transfer characteristics of sCO₂ and dynamic simulation model of sCO₂ loop. 3rd European supercritical CO₂ Conference, Paris, France.

[21] Flaig, W., Mertz, R. and Starflinger, J. (2018). Setup of the supercritical CO₂ test facility “SCARLETT” for Basic experimental investigations of a compact heat exchanger for an

innovative decay heat removal system. *ASME Journal of Nuclear Engineering and Radiation Science*, 4(3), 031004.

[22] Vojacek, A., Hacks, A.J., Melichar, T., Frybort, O. and Hájek, P. (2018). Challenges in supercritical CO₂ power cycle technology and first operational experience at CVR. 2nd European supercritical CO₂ Conference, Essen, Germany.

[23] Hacks, A., Freutel, T., Strätz, M., Vojacek, A., Hecker, F., Starflinger, J. And Brillert, D. (2019). Operational experiences and design of the sCO₂-HeRo loop. 3rd European supercritical CO₂ Conference, Paris, France.

[24] Simeoni, G., Bryk, T., Gorelli, F., Krisch, M., Ruocco, G., Santoro, M. and Scopigno, T. (2010). The Widom line as the crossover between liquid-like and gas-like behaviour in supercritical fluids. *Nature Physics*, 6, pp. 503-507.

[25] Banuti, D.T. (2015). Crossing the Widom-line – Supercritical pseudo-boiling. *Journal of Supercritical Fluids*, 98, pp. 12-16.

[26] Lemmon, E.W., Bell, I.H., Huber, M.L. and McLinden, M.O. (2018) NIST Standard Reference Database 23: Reference Fluid Thermodynamic and Transport Properties-REFPROP, Version 10.0. National Institute of Standards and Technology, Standard Reference Data Program, Gaithersburg.

[27] Span, R. and Wagner, W. (1996). A new equation of state for carbon dioxide covering the fluid region from the triple-point temperature to 1100 K at pressure up to 800 MPa. *Journal of Physical and Chemical Reference data*, 25, 1509-1596.

[28] Dittus, F.W. and Boelter L.M.K. (1930). Heat transfer in automobile radiators of the tubular type. *International Communications in Heat and Mass Transfer*, 1, pp. 3–22.

[29] Pioro, I.L and Duffey, R.B. (2007). *Heat Transfer & Hydraulic Resistance at Supercritical Pressures in Power Engineering Applications*. ASME Press, pp. 147-166.

[30] Bae, J. H., Yoo, J. Y. and Choi H. (2005). Direct numerical simulation of turbulent supercritical flows with heat transfer. *Physics of Fluids*, 17, 105104.

[31] Jackson, J.D., Hall, W.B., Fewster, J., Watson, A. and Watts, M.J., (1975). Heat transfer to supercritical pressure fluids. UKAEA, AERER 8158, Design Report 34.

[32] Kakac, S., Shah, R.K. and Aung, W. (1987). The Effect of Temperature-Dependent Fluid Properties on Convective Heat Transfer. *Handbook of single-phase convective heat transfer*, S. Kakac et al., eds., John Wiley & Sons, New York, pp. 18.1–18.56.

[33] Wang, J., Guan, Z., Gurgenci, H., Hooman, K., Veeraragavan, A. and Kang, X. (2018). Computational investigations of heat transfer to supercritical CO₂ in a large horizontal tube. *Energy Conversion and Management*, 157, pp. 536-548.

[34] Adebisi, G.A. and Hall, W.B. (1976). Experimental investigation of heat transfer to supercritical pressure carbon dioxide in a horizontal pipe. *International Journal of Heat and Mass Transfer*, 19, pp. 715-720.

GREENING A CEMENT PLANT USING sCO₂ POWER CYCLE

Ladislav Vesely*

Center for Advanced Turbomachinery and Energy
Research (CATER), University of Central Florida
Orlando, FL, 32816
Email: Ladislav.Vesely@ucf.edu

S. Gopinathan

Consultant, Bangalore,
India, 560094

Ganesan Subbaraman

Center for Advanced Turbomachinery and Energy
Research (CATER), University of Central Florida
Orlando, FL, 32816

&

PSG College of Technology, Peelamedu, Coimbatore,
India 641004

Prabu Thangavel

PSG college of technology, Peelamedu, Coimbatore,
India 641004

Otakar Frybort

Research Centre Řež, Husinec, Czech Republic

Jayanta Kapat

Center for Advanced Turbomachinery and Energy
Research (CATER), University of Central Florida
Orlando, FL, 32816

&

PSG College of Technology, Peelamedu, Coimbatore,
India 641004

ABSTRACT

This paper presents a case study for the greening of a cement plant located in India. Operating characteristics of the plant are described as well as sustainability actions previously undertaken to meet power requirements supplied by one of two subcritical coal boilers with renewables (photovoltaic and wind) and use of Municipal Solid Waste (MSW) to augment the cement kiln's heat requirements. The feasibility of deploying a sCO₂ power cycle was determined to recover waste heat from different extraction points. Current assessment indicates opportunities for a Demo plant to extract 700 kWe (Turbine power output) while minimally disturbing plant operations. The Demo is expected to provide data for a larger, 8MWe (net) sCO₂-derived power at higher turbine inlet temperatures and with potentially increased MSW use. Deployment of the larger sCO₂ system could lead to partially or fully replacing the second coal boiler, leading to further "greening" of the plant with a potentially attractive pay-back period. Related modeling and design considerations are described.

INTRODUCTION

Emissions of carbon dioxide, a green-house gas (GHG) pollutant from thermally intensive manufacturing processes (e.g., cement, steel, and glass) arise from use of fossil fuel for the required high-temperature heat (e.g., up to 1650 °C in cement

kiln operations) as well use of fossil fuel to generate secure and reliable electric power for the plant's operations from within the plant boundary. With respect to cement, reduction of the CO₂ emissions to achieve "green" production would therefore require multiple approaches to provide the required heat. One approach, for example, envisions replacing heat with combustion of green hydrogen instead of coal to reduce/eliminate the emissions, although such a principle remains to be tested [1]. Emissions reduction may be also achieved through use of renewables for the in-house power, but these would either require storage or supplementary fossil fuel use because of their intermittent availability.

Options exist for improving efficiency (and thus to further reduce emissions) in cement plants by recovering the relatively high-temperature enthalpy from the waste heat arising from kiln operations if such enthalpy is converted to power [2]. Exhaust gases from kiln operations can reach up to 600 °C. Supercritical Carbon dioxide (sCO₂) power conversion cycle may offer such an improved efficiency [3, 4]. Given the compactness of the sCO₂ turbomachinery, the equipment may also be retrofitted in existing plants [5]. Ref. [6] provides clear, worldwide examples and the extent to which use may be made of such waste heat. According to the same reference, these plants currently operate with traditional steam Rankine cycle power conversion technology. While subsequent literature mentions the potential

* corresponding author(s)

attractiveness of the sCO₂ power conversion for the cement industry [7], a detailed examination of its implementation is now possible in view of the maturing of this power conversion technology. In this paper, we offer, for what we believe to be the first time, a case study for retrofitting sCO₂ power conversion equipment in an existing cement plant. The plant, located in Tamil Nadu state in India, has already pioneered using renewable power to offset some coal use, and uses Municipal Solid Waste (MSW) to augment caloric needs of the kiln. Results of the study supports deploying a low-temperature, smaller scale demo to obtain scale-up data and techno-economics. Additional use of MSW may lead to design and operating conditions with lower CO₂ emissions, replacement of the existing (second) coal boiler and a desired pay-back period for the operator while lowering the landfill burden to neighboring communities, all leading to further “greening” cement production..

PLANT DESCRIPTION

The plant studied is part of the Associated Cement Company (ACC) business in the town of Madukkarai. The cement plant produces 1.18 million tonnes of cement per year. Cement making is an energy intensive process. Also, the cost of energy is a significant factor in the cost of cement, so improving the energy efficiency of a cement plant will dramatically improve its bottom line.

As shown in Figure 1, waste heat from the hot, dust-laden exhaust gases from the cement plant can be tapped from two sources — namely, clinker cooler and preheater. Unlike other cement plants, raw material of ACC Madukkarai plant is in slurry form and hence the complete exhaust gas from Preheater is used to dry the raw material. In this study, exhaust gas from Clinker cooler will be used for the proposed 0.7 MWe turbine power output demo project and Exhaust gas from Pre-heater (of dry-fed cement plant) will be considered for 8 MWe commercial scale-up.

As the ACC Madukkarai plant feeds the kiln in slurry form, the heat requirement is comparatively more to remove the water content comparing with the modern plants. Due to this additional process, the Madukkarai plant utilizes the waste heat for heating the slurry. Despite that as shown in Figure 1, the tertiary air duct and the cooler blowers can be managed for the hot air recovery of the plant and the temperature availability is varying from 500 °C to 201 °C at different tapping points. As this plant is equipped with Geocycle (GFR Co-processing), which uses the municipal waste as a heat source for combustion that reduces the coal requirement of the cement plant, the required additional heat can be tapped from the Geocycle. The proposed 8 MWe commercial scale-up plant can utilize the heat source from Geocycle in addition to the plant heat recovery considered here for the demonstration.

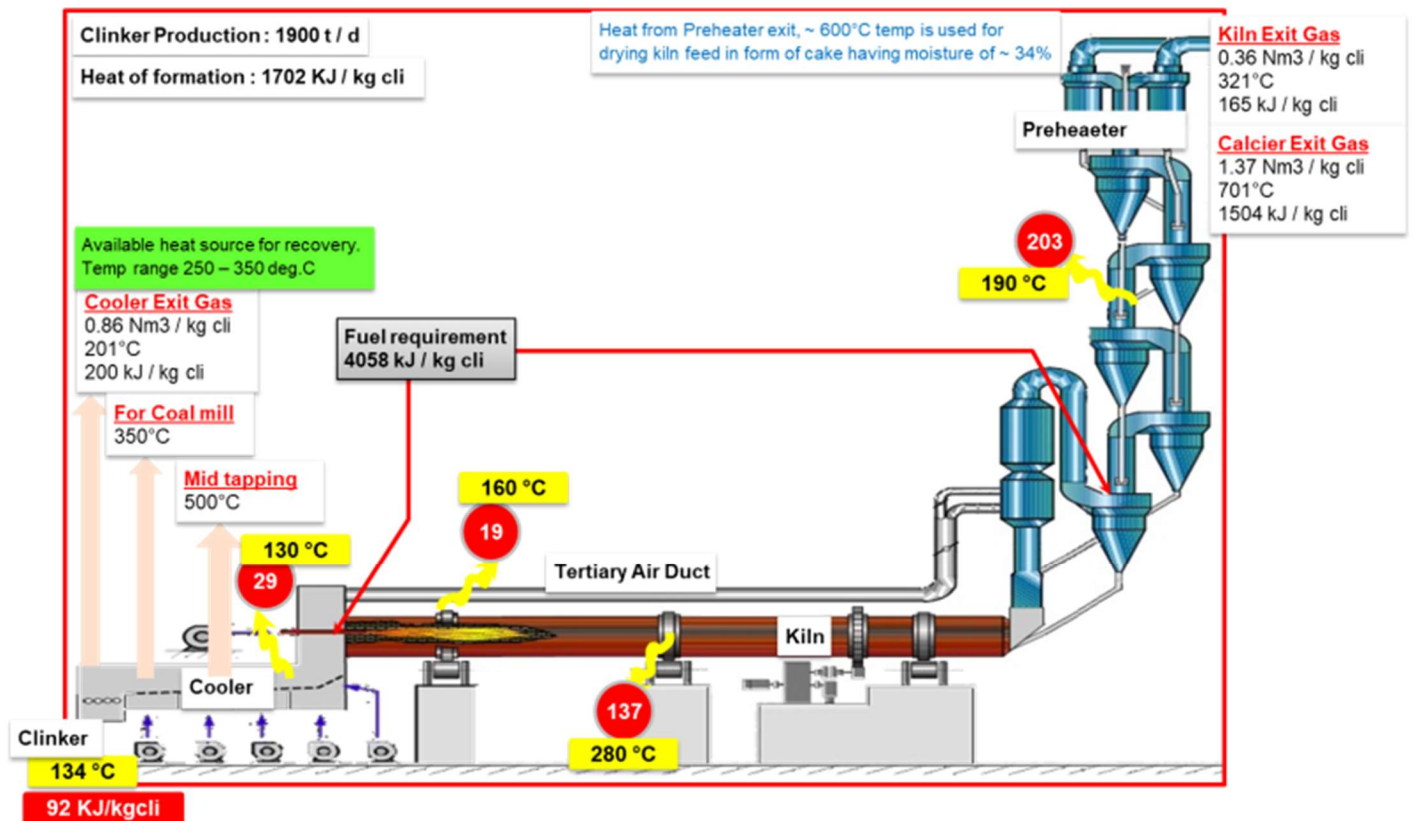


Figure 1.: Cement plant block flow diagram.

SCO₂ SYSTEM DESIGN

The sCO₂ power cycle is a gas-based power cycle with many advantages compared to steam Rankine or helium power cycle. The advantage of the sCO₂ power cycles is in its high efficiency for a given operating temperature [5,8], typically above 450 °C. Another advantage of the sCO₂ power cycles is their compact size compared to steam or helium Brayton cycles [8]. The compressor and the turbine are significantly smaller due to the high operating pressure [5,8]. However, the heat exchange size is significantly large compared to other systems. But a heat exchangers size can be optimized by operating parameters and type selection (cycle layout, design) [9].

Table 1.: Parameters for applications of sCO₂ power cycles [5].

Application	Power	Operation Temperature	Operation Pressure
	[MWe]	[°C]	[MPa]
Nuclear	10-300	350-700	20-35
Fossil fuel (syngas, natural gas, coal)	300-600	550-1500	15-35
Geothermal	10 - 50	100-300	15
Concentrating solar power	10 - 100	500 - 1000	35
Waste heat recovery	1 - 10	200 - 650	15- 35

The sCO₂ power cycle offers many different layouts for several potential applications. The potential applications of the sCO₂ power cycles includes, nuclear power plants [10,11], solar power plants [12,13], geothermal power plants or application to fossil fuel power plants [14, 15] and the waste heat recovery systems [2,16,17,18]. The typical parameters of the sCO₂ power cycle applications are shown in Table 1.

According to Table 1, the range of applications is quite wide [5]. The sCO₂ power cycle can be used for majority of heat sources, which are used in energy conversion systems.

For each application in Table 1, there exist several different cycle layouts. Each cycle layouts have several advantages and disadvantages according to heat source and operating parameters. The cycle layouts can be divided into groups with one or a multi-heat source.

SCO₂ WASTE HEAT RECOVERY SYSTEM

According to Table 1, the waste heat recovery systems are in range 1 to 10 MWe, with the operations temperature between 200 to 600 °C. The parameters are in the range of waste heat source which can be found in a cement plant [6].

In this paper the effort is focused on the ACC Madukkarai plant. As previously mentioned, Figure 1 shows the block flow diagram for the plant with several potential heat sources and with different temperature ranges. It can be seen that this plant has three potential heat sources with different temperature levels. Table 2 shows a list of the potential heat source for the cement plant.

Table 2.: Heat source for WHR.

Cooler exit gas	201	°C
Coal mill	250 - 350	
Preheater	600	

According to Figure 1 and Table 2, the system for waste heat recovery can be operated at different heating levels (*The potential heat sources range from 200 to 600 °C.*), which has an effect on the net power and cycle efficiency.

The sCO₂ waste heat recovery system layout can be designed for one or multi-heat source units, according to Table 2. The potential sCO₂ power systems layouts can be the following: [19,20]

- One heat source:
 - Simple Brayton sCO₂ cycle
 - Re-compression cycle
 - Pre-compression cycle
 - Split expansion cycle
- Multi-heat sources:
 - Dual Heater cycle
 - Dual Expansion cycle
 - Cascade
 - Kimzey cycle

Each cycle layout consists of a compressor (C) for isentropic compression, a turbine (T) for isentropic expansion, a cooler (CH), a heat source (H) and recuperative heat exchanger (RH, LHR and HTR), which is used for heat regeneration (improving the cycle efficiency). However, in this research, focus is on commercially available sCO₂ waste heat units [16,21,22], which is based on the simple Brayton sCO₂ cycle.

SCO₂ DEMO PLANT UNIT

The proposed demo plant unit is planned for the ACC Madukkarai plant with for the parameters shown in Table 2.

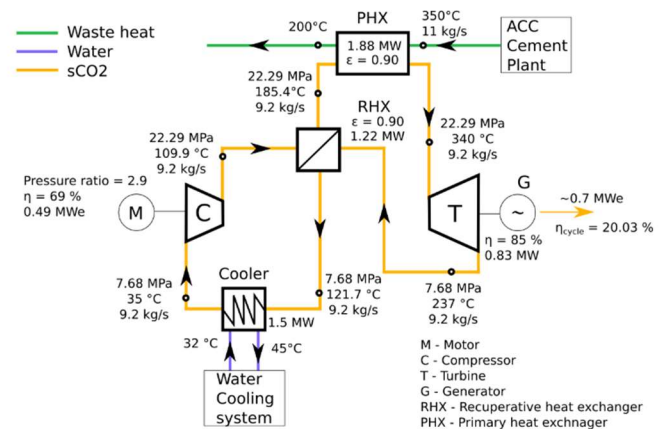


Figure 2.: sCO₂ block flow diagram of the proposed demo plant unit.

The design of the sCO₂ waste heat recovery system for the cement plant application is the simple Brayton cycle layout, which consists of a primary heat exchanger (PHX), Cooler (water or air, according to localization and cooling availability), recuperative heat exchanger (RHX), compressor (C) and turbine (T), as shown in Figure 2.

Accordingly, the system design utilizes input parameters from ACC Madukkarai (Table 2).

The heat source for the sCO₂ demo plant unit is from Clinker cooler (cooler exit gas with mid tapping) with outlet temperature 350 °C. The sCO₂ demo plant unit is designed as a compact system to provide data that can utilized to design the larger, commercial units with 8 MWe of net power output.

For this reason, the following parameters and design of the components were considered for the calculation.

The cooling system is designed as a water-cooling system with an inlet temperature of 32 °C. The turbine is not connected with the compressor on a common shaft. The compressor is driven by an electrical motor, as shown in Figure 2.

The proposed primary heat exchanger (PHX) has a vertical construction, which occupies very little floor space. Also, the vertical PHX requires only a single dust collection point and economical design. The reliable high temperature resisting guillotine dampers are installed in the inlet and bypass ducts so as to make it possible to isolate the PHX for maintenance without requiring production shutdown.

The recuperative heat exchanger (RHX) and cooler are designed as Printed Circuit Heat Exchangers (PCHE) with zigzag and semi-circular channels [23] is being considered.

The pressure ratio is 2.9 and the compressor outlet pressure is 22.29 MPa, according to commercial sCO₂ waste heat recovery units described in the literature [21]. The boundary parameters for all calculations are as shown in Table 3.

Table 3.: Boundary parameters

Compressor inlet temperature	35	°C
Turbine efficiency	85	%
Compressor efficiency	69	
Recuperator effectiveness	90	

The pressure drops are not considered in the calculation for all cases. When pressure losses are considered, the resulting efficiency and net power will show lower values. However, the difference between the values will not be large (because, the maximal pressure drops will be between 1 - 2 %) [24], according to pressure drops calculated from detail design of the heat exchangers.

The system in Figure 2 was designed for the turbine power output 700 kWe, which is 835 kW, if the generator efficiency is 96 %, clutch efficiency is 95 % and gearbox efficiency is 93 %. The required compressor power is 460 kW (490 kWe, for motor and clutch efficiency 95 %), which is generated with an electric motor, according to Figure 2. The mechanical losses are considered to be 1 %. The resulting parameters of the sCO₂ demo plant are shown in Table 4.

Table 4.: sCO₂ demo plant unit parameters

Flow rate	9.2	kg/s
Cycle efficiency	20.03	%
Compressor mechanical power	0.46	MW
Added heat	1.88	
Removed heat	1.5	
Regenerative heat	1.22	MWe
Turbine power output	0.7	

According to Table 4, the required heat input from the heat source is 1.88 MWth with the sCO₂ flow rate of 9.2 kg/s. The cooling power is 1.5 MWth, this power must be removed from the system and water outlet temperature can be maximal 45 °C.

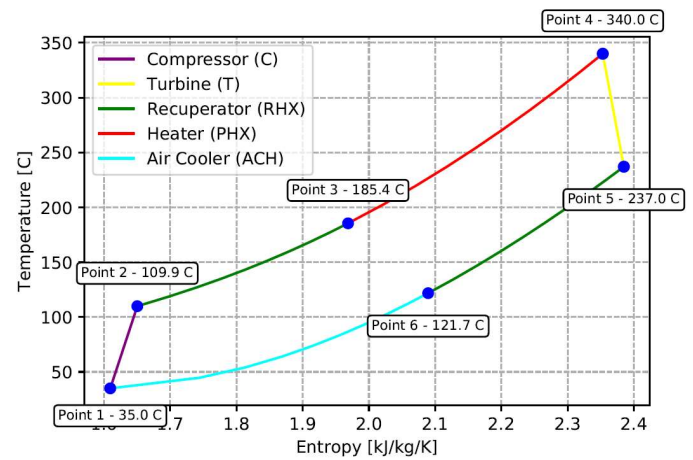


Figure 3.: T-S diagram of the sCO₂ demo plant unit

The T-S diagram for the sCO₂ demo plant unit is shown in Figure 3. According to results in Table 4 and T-S diagram in Figure 3, it is obvious that the sCO₂ plant units based on the operating parameters selected for the demo unit as such are not economically attractive for their commercial potential. However, the sCO₂ demo unit is a practical design, the results from which the design and optimization of the commercial scale sCO₂ waste heat power system with the net power up to 8 MWe may be implemented with the potential heat sources ranging from 250 to 600 °C, as noted in Table 2. These aspects are further described below.

COMPARISON OF DEMO AND COMMERCIAL UNITS

As was mentioned above, the sCO₂ demo plant unit was designed for the demonstration of the waste heat recovery system in the cement plant. In the case of the demo unit, to reduce the design complexity, the following points are considered:

1. **Electrical motor driven compressor:** To simplify turbo-machinery designs, a 0.7 MWe generator will be driven by sCO₂ turbine and sCO₂ compressor will be driven by an electrical motor. However, 8 MWe system will have sCO₂ turbine with a common shaft to drive both generator and compressor. This will have effect on the

turbine and compressor efficiency. However, for the calculation presented in this paper, the turbine and compressor efficiency with the mechanical losses are same as for 0.7 MWe demo plant unit. In reality, the commercial 8MWe system will have better component efficiencies, and hence better overall performance than what is projected here.

2. **Water cooled heat exchanger:** For the demo project, heat rejection from the system will be designed with water cooled heat exchanger, in order to simplify the design. The commercial (8 MWe) system is planned to be designed with an air-cooled heat exchanger.

Figure 4 shows the commercial version of sCO₂ waste heat recovery system for the cement plant with same parameters as sCO₂ demo unit, except flow rate and turbine inlet temperature (TIT), and 8 MWe net power. The results for this system are shown in Table 5 and T-S diagram is shown in Figure 5.

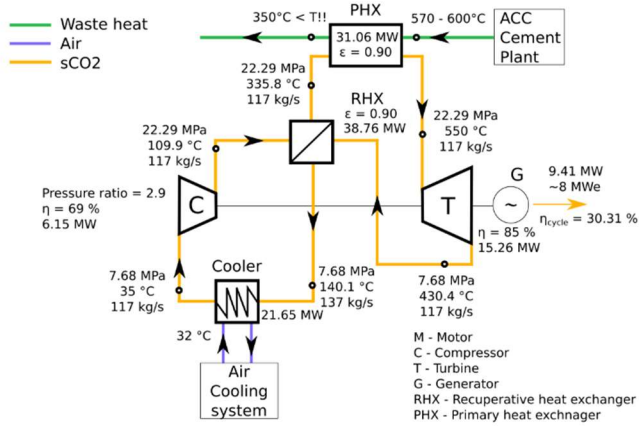


Figure 4.: sCO₂ block flow diagram of the 8 MWe waste heat recovery system with TIT 550 °C.

According to Figures 4 and 5 and Table 5, it is obvious that the simple sCO₂ Brayton cycle can be scaled up from the sCO₂ demo unit to commercial units in the same configuration with the two differences noted earlier.

Table 5.: 8 MWe waste heat recovery system with TIT 550 °C

Flow rate	117	kg/s
Cycle efficiency	30.31	%
Turbine mechanical power	15.29	MW
Compressor mechanical power	6.15	
Added heat	31.06	
Removed heat	21.65	
Reg heat	38.76	
Net power	8	MWe

RESULTS

The T-S and associated calculations were performed using inhouse sCO₂WHR code. The code was written in the Python

programming language. The Python is an open-source language for programming. The source of gas properties used was NIST Reference Fluid Thermodynamic and Transport Properties database, Version 9.1. [25] and CoolProp [26]. The CoolProp is the open-Source Thermo-physical Property Library.

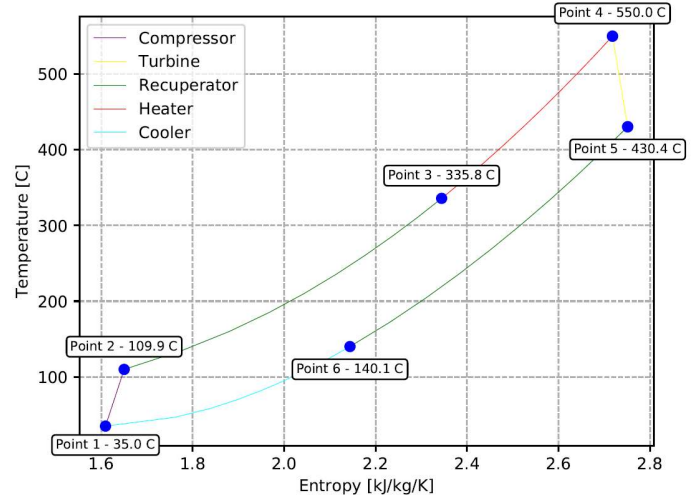


Figure 5.: T-S diagram of the 8 MWe waste heat recovery system with TIT 550 °C.

The parameters of the sCO₂ demo unit do not reach optimal values for the potential commercial application from a techno-economic point of view. The sCO₂ demo plant unit must be optimized and designed for different operating parameters, so that maximum possible net power can be produced from all available waste heat sources in the plant.

One of the ways to increase generated net power is to increase the turbine inlet temperature. With this increase, turbine output power increases. The turbine output power is defined according to Equation 1.

$$P_{tur} = m(h_{in} - h_{out_real}) \quad (1)$$

Here h_{in} is specific enthalpy for turbine inlet and h_{out_real} is specific enthalpy for turbine outlet under real operation with losses. The turbine efficiency is defined as:

$$\eta_t = \frac{h_{in} - h_{out_real}}{h_{in} - h_{out_ideal}} \quad (2)$$

where h_{out_ideal} is specific enthalpy for turbine outlet under ideal operation without any losses. The compressor efficiency is calculated according to an equation similar to Equation 2. Figure 5 shows the dependence of the net power and cycle efficiency on the TIT for the simple Brayton cycle layout. The results in Figure 5 are for the turbine inlet pressure 22.29 MPa and mass flow rate 9.2 kg/s. The black vertical line in Figure 5 correspond to the sCO₂ demo unit parameters.

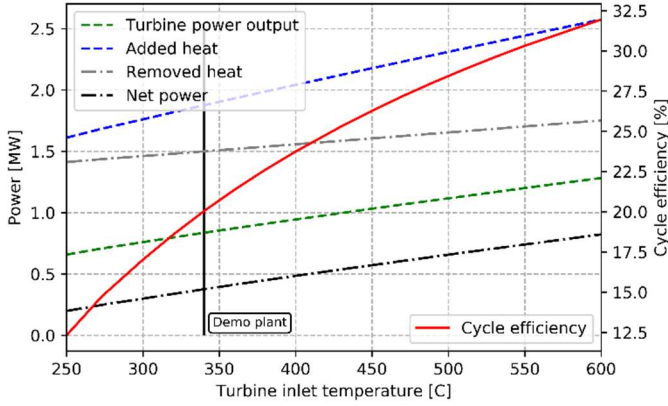


Figure 5.: Effect of the different TIT (mass flow rate = 9.2 kg/s).

The cycle efficiency is defined according to Equation 3, where P_{net} is net power generated from the system and Q_{in} is total the heat input. P_{tur} is turbine output power and P_c is compressor input power.

$$\eta_{th} = \frac{P_{net}}{Q_{in}} = \frac{P_{tur} - P_c}{Q_{in}} \quad (3)$$

The Q_{in} and Q_{out} (total heat input and rejected heat, respectively) are defined according to Equation 4, where \dot{m} is mass flow rate and h is specific enthalpy on inlet/outlet to the heat or cooler.

$$Q_{in} = \dot{m}(h_{out} - h_{in}), \quad Q_{out} = \dot{m}(h_{in} - h_{out}) \quad (4)$$

The tapping temperature ranges from 200 to 600 °C (Table 2) is possible in the cement plant and can be utilized for a power plant without affecting the cement manufacturing process. The sCO₂ demo unit is aimed to produce 700 kW_e for technology demonstration at affordably low capital and operating costs. Figure 5 explains the system characteristics according to the optimization model for the range of temperatures, where the turbine inlet temperature variation is considered from 250 °C to 600 °C. If the turbine inlet temperature is low, the system efficiency is considerably low due to the operational inefficiencies. The sCO₂ demo unit is planned to operate at 340 °C and the corresponding turbine power output is around 0.8 MW_{th}. The cycle efficiency is 20.03%.

On the other hand, if the turbine inlet temperature is for example 550 °C, the corresponding turbine power output is around 1.2 MW_{th} and can attain a cycle efficiency of around 30%. The compressor power is the same for all turbine inlet temperature in the considered range. The remarkable improvement is possible with the higher turbine inlet temperature. As the tapping provision at higher temperatures is not available in the ACC Madukarrai plant, the sCO₂ demo plant turbine inlet temperature is fixed as 340 °C.

The turbine inlet temperature at 340 °C was considered because the objective is to demonstrate the waste heat recovery

process on demo plant unit with the readily available heat source, which has temperature around 350 °C.

The sCO₂ demo plant operation will provide insight for the actual size plant which has the potential of 8 MWe and above. The scaling up to 8 MWe sCO₂ waste heat recovery system is shown in Figure 6.

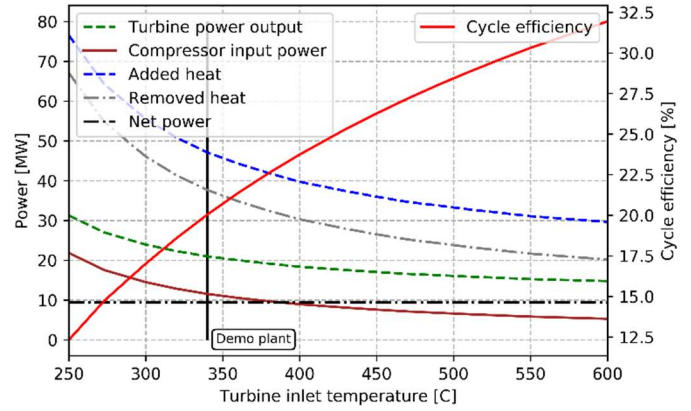


Figure 6.: Effect of the different TIT on the 9.44 MW_{th} (8 MWe) sCO₂ system.

The results in Figure 6 are for the turbine inlet pressure 22.29 MPa and the black vertical line in Figure 6 is shown the sCO₂ demo plant unit parameters. Figure 6 explains the system characteristic for the fixed net power output of 9.44 MW_{th}. As the temperature increases, the heat power required as input decreases which explains the performance improvement at the higher temperatures (red line). The thermal input is lower for the constant output with the rise in temperature from 250 °C to 550 °C. At the same time, the required input heat and compressor power decrease with the increase in the turbine inlet temperature. With the increased turbine inlet temperature, the required input heat is transferred with higher efficiency, and due to higher efficiency, the mass flow rate is reduced. This effect is shown in Figure 7.

According to Equations 1 to 4, it is clearly visible that with a decrease in the mass flow rate, the required input, cooling or compressor, and turbine power decrease. These dependencies are shown in Figure 7. However, the net power is dependent on the compressor and turbine power. The compressor power is decreased too and because the compressor is operated near the critical point of the CO₂, the required compressor power is lower. This is one of the biggest advantages of the sCO₂ power cycle.

CONCLUSIONS & RECOMMENDATIONS

Use of supercritical carbon dioxide as the working fluid in a closed, simple, recuperated Brayton cycle has been proposed here to convert a portion of the waste heat from an existing cement factory to electricity. This plant, located in Madukarrai, India has multiple sources of waste heat available at various temperatures. Based on practical considerations, this study has focused on what is available from clinker cooler at 350 °C for purposes of demonstration and subsequent scale up. The design

complexity for the demo plant was reduced by utilizing electrical motor driven compressor and water-cooled heat exchanger. From the perspective of the design complexity and low heat source temperature, the system shows suboptimal operation parameters as shown in the model calculations.

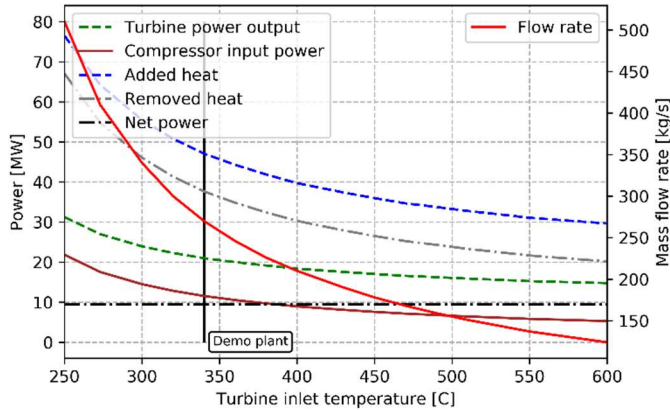


Figure 7.: Effect of the different TIT on the 9.44 MWth (8 MWe) sCO₂ system.

Optimization of cycle parameters, with consideration of integration of waste heat to power cycle, led to a sCO₂ cycle with a pressure ratio of 2.9 and a maximum pressure of 22.29 MPa at the compressor output. With *ad hoc* assumption of reasonable and realizable efficiencies of all relevant components, the cycle optimization could lead to a maximum overall waste-heat-to-electricity efficiency of 30.3% for a net power output of 8 MWe and a turbine inlet temperature of 550 C.

This paper considered one of multiple steps, and perhaps the easiest-to-implement step, in greening of an existing cement plant. Consideration of all other sources of waste heat as well as use of locally-sourced municipal solid waste can increase the exergy-content of the total waste heat at a higher temperature, and can lead to larger net electrical output at a higher overall cycle efficiency. Such an effort is necessary in continued greening of a cement plant. In addition, fossil-based heating source needs to be fully replaced for a fully green operation. If enough solid waste is not available, then use of green hydrogen, obtained through electrolysis of water using green electricity, with collocated storage is necessary. As noted in Ref. [1], however such a principle has not been tested. Meanwhile, considerations such as described in this paper are critical to ensure reduction of CO₂ emissions through improvements in performance using sCO₂ waste heat recovery, especially in existing plants.

This study focused on retrofitting of an existing cement plant in order to make in green. For a completely new design, an overall design optimization that considers both cement production and waste heat recovery in an integrated fashion is necessary, in order to have a very resource-efficient, cement factory.

NOMENCLATURE

η_{th}	Cycle efficiency (%)
h	Enthalpy (kJ/kg)
S	Entropy (kJ/kgK)
P	Power (MWth)
Q	Heat (MW)
m	mass flow rate (kg/s)

ABBREVIATIONS

MSW	Municipal Solid Waste
TIT	Turbine inlet temperature
C	Compressor
T	Turbine
CH	Cooler
H	Heat source
RH, LHR and HTR	Recuperative heat exchanger
PHX	Primary heat exchanger
G	Generator
M	Motor
PCHE	Printed Circuit Heat Exchangers
WHR	Waste Heat Recovery

ACKNOWLEDGEMENTS

The authors would like to thank Prof. Vaclav Dostal from Czech Technical University in Prague for their support and encouragement.

The first author likes to further acknowledge the support from UCF's Preeminent Postdoctoral Program (P3).

The authors would like to thank Mr. Uday Pawar, Mr. Rajkumar Chandran and Mr. Milan Trivedi from ACC Limited Madukkarai plant - India, for their support providing technical data on their existing plant.

The authors also would like to thank Mr. P. U. Gopi and Mr. Bhaskar. T R from Triveni Turbines, Bangalore - India unit for providing their design parameters of sCO₂ Turbine.

REFERENCES

- [1] Mineral Products Association, Cinar Ltd, VDZ gGmbH (2019). "Options for switching UK cement production sites to near zero CO₂ emission fuel: Technical and financial feasibility. Feasibility Study for the Department for Business Energy and Industrial Strategy"; TRN 1674/10/2018
- [2] A. Amiri and M. R. Vaseghi, "Waste Heat Recovery Power Generation Systems for Cement Production Process," in IEEE Transactions on Industry Applications, vol. 51, no. 1, pp. 13-19, Jan.-Feb. 2015, doi: 10.1109/TIA.2014.2347196.
- [3] Khadse A, Blanchette L, Kapat J, Vasu S, Hossain J, Donazzolo A., "Optimization of Supercritical CO₂ Brayton Cycle for Simple Cycle Gas Turbines Exhaust Heat Recovery Using Genetic Algorithm". Journal of Energy Resources Technology. 2018 Jul 1;140(7).
- [4] Wright S.A., Davidson C.S., Scammell W. O., "Thermo-Economic Analysis of Four S-CO₂ Waste Heat Recovery Power Systems", 2016: The 5th International Symposium-Supercritical CO₂ Power Cycle.

- [5] Brun K., Friedman P., Dennis R., *“Fundamentals and Applications of Supercritical Carbon Dioxide (S-CO₂) Based Power Cycles”*, 2016: Elsevier, ISBN: 978-0-08-100804-1.
- [6] International Finance Corporation: IFC World Bank. *“Waste Heat Recovery for the Cement Sector: Market and Supplier Analysis”*. (2014), Report number 46211.
- [7] Amiri, A, and Vaseghi, M.R., *“Waste Heat Recovery Power Generation Systems for Cement Production Process”* IEEE Transactions on Industry Applications. VOL. 51, NO. 1, 13, 2015 Jan-Feb.
- [8] Angelino G., *“Carbon Dioxide Condensation Cycles for Power Production”*, 1968: ASME Paper No. 68-GT-23.
- [9] Vesely L., Dostal V., Bartos O., Novotny V., *“Pinch Point Analysis of Heat Exchangers for Supercritical Carbon Dioxide with Gaseous Admixtures in CCS Systems”*, 2016: Energy Procedia, Volume 86, Pages 489-499, ISSN: 1876-6102.
- [10] V. Dostal, M. J. Driscoll, and P. Hejzlar, *“A supercritical carbon dioxide cycle for next generation nuclear reactors.”* Massachusetts Institute of Technology, Department of Nuclear Engineering ..., 2004.
- [11] Vesely L, Dostal V, Entler S., *“Study of the cooling systems with S-CO₂ for the DEMO fusion power reactor”*. Fusion Engineering and Design. 2017 Nov 1;124:244-7. <https://doi.org/10.1016/j.fusengdes.2017.05.029>
- [12] Zhiwen M, Turchi C.S., *“Advanced Supercritical Carbon Dioxide Power Cycle Configurations for Use in Concentrating Solar Power Systems”*, 2011: NREL/CP-5500-50787.
- [13] Iverson B.D., Conboy T.M., Pasch J.J., Kruiuzenga A.M., *“Supercritical CO₂ Brayton Cycles for Solar-thermal Energy”*, 2013: Elsevier Ltd. 1-s2.0-S0306261913005278-main.
- [14] Allam R.J., Fetvedt J.E., Forrest B.A., Freed D.A., *“The Oxy-Fuel, Supercritical CO₂ Allam Cycle: New Cycle Developments to Produce Even Lower-Cost Electricity From Fossil Fuels Without Atmospheric Emissions”*, 2014: ASME Turbo Expo 2014: Turbine Technical Conference and Exposition, Volume 3B: Oil and Gas Applications; ISBN: 978-0-7918-4566-0, doi:10.1115/GT2014-26952.
- [15] Maxson, Andrew, Miller, Jason, Buckmaster, David, Thome, Ted, Sakadjian, Bartev, Chamberland, Ray, Hong, Kiho, and Hogg, Dougal. High-Efficiency Thermal Integration of Closed Supercritical CO₂ Brayton Power Cycles with Oxy-Fired Heaters (Final Report). United States: N. p., 2018. Web.
- [16] Kaccludis A., Lyons S., Nadav D., Zdankiewicz E., *“Waste Heat to Power (WH2P) Applications Using a Supercritical CO₂-Based Power Cycle”*, 2012: Echogen Power Systems LLC: Presented at Power-Gen International 2012.
- [17] Marchionni, M., Bianchi, G. Tassou, S.A., *“Review of supercritical carbon dioxide (sCO₂) technologies for high-grade waste heat to power conversion”*, SN Appl. Sci. 2, 611 (2020). <https://doi.org/10.1007/s42452-020-2116-6>.
- [18] Khadse A, Blanchette L, Kapat J, Vasu S, Hossain J, Donazzolo A., *“Optimization of Supercritical CO₂ Brayton Cycle for Simple Cycle Gas Turbines Exhaust Heat Recovery Using Genetic Algorithm”*. Journal of Energy Resources Technology. 2018 Jul 1;140(7).
- [19] Kimzey G., *“Development of a Brayton Bottoming Cycle Using Supercritical Carbon Dioxide as the Working Fluid”*, Electric Power Research Institute Report, Palo Alto (CA), 2012.
- [20] Crespi, F., Gavagnin, G., Sánchez, D. and Martínez, G.S., 2017. *“Supercritical carbon dioxide cycles for power generation: A review”*. Applied Energy, 195, pp.152-183.
- [21] Held, T.J., 2014, *“September: Initial test results of a megawatt-class supercritical CO₂ heat engine”*, In The 4th International Symposium–Supercritical CO₂ Power Cycles (pp. 9-10).
- [22] Held, T.J., Miller, J., Buckmaster, D.J., 2016, March., *“A comparative study of heat rejection systems for sCO₂ power cycles”*, In The 5th International Symposium–Supercritical CO₂ Power Cycles (pp. 28-31).
- [23] Ngo T.L., Kato Y., Nikitin K., Ishizukam T., *“Heat Transfer and Pressure Drop Correlations of Microchannel Heat Exchangers with S-shaped and Zigzag Fins for Carbon Dioxide Cycles”*, 2007: Tokyo Institute of Technology, Japan.
- [24] Pratt & Whitney Rocketdyne Report, *“Turbine Technology Program Phase II: SCO₂ Turbomachinery Configuration and Control Trade Study,”* 2012, Sept. 14, Contract: DE-FE0004002 Subcontract Number: S163-PWR-PPM4002.
- [25] Lemmon E.W., Huber M.L., McLinden M.O., *NIST Standard Reference Database 23: Reference Fluid Thermodynamic and Transport Properties-REFPROP.*, 2013: Version 9.1.
- [26] Bell I.H., Wronski J., Quoilin S., Lemort V., *Pure and Pseudo-pure Fluid Thermophysical Property Evaluation and the Open-Source Thermophysical Property Library CoolProp.*, Industrial & Engineering Chemistry Research, volume = 53, 2014, doi10.1021/ie4033999.

SCO₂ POWER CYCLE DEVELOPMENT AND STEP DEMO PILOT PROJECT

Brian Lariviere *

GTI

Woodland Hills, CA, USA

Email: blariviere@gti.energy

John Marion

GTI

Des Plaines, IL, USA

Scott Macadam

GTI

Houston, TX, USA

Michael McDowell

GTI

Woodland Hills, CA, USA

Markus Lesemann

GTI

Des Plaines, IL, USA

Aaron McClung

Southwest Research Institute

San Antonio, TX, USA

Jason Mortzheim

General Electric Global Research

Niscayuna, NY, USA

ABSTRACT

Supercritical CO₂ (“sCO₂”) power cycles offer the potential for higher system efficiencies than other energy conversion technologies such as steam Rankine or organic Rankine cycles, especially when operating at elevated temperatures. These sCO₂ power cycles are being considered for a wide range of applications including fossil fuel-fired systems, waste heat recovery, concentrated solar power, and nuclear, and the potential for efficient thermal energy storage.

GTI is leading several sCO₂ power cycle technology development projects ranging from component level technology development to large scale integrated pilot testing. The efforts highlighted in this paper include: (1) The 10 MWe Supercritical Transformational Electric Power Pilot plant (“STEPDemo”, www.stepdemo.us) and (2) its relevance for sCO₂ development in general and of note, also in the context of waste heat recovery and thermal energy storage (TES) applications. In the STEPDemo project, a team led by GTI, Southwest Research Institute (SwRI), and General Electric Global Research (GE-GR), along with the University of Houston and the University of Wisconsin), Natural Resources Canada (NRCAN), and the Electric Power Research Institute (EPRI), is executing a project to design, construct, commission, and operate an integrated and reconfigurable 10 MWe sCO₂ Pilot Plant Test Facility located at SwRI’s San Antonio, Texas campus. The majority of the project funding is provided by the U.S. Department of Energy, and the remaining funding is by the project team members and a global consortium of industry partners: Engie, American Electric Power, Korea Electric Power Corporation (KEPCO), Natural

Resources Canada, and Southern Company. This project is a significant step toward commercialization of sCO₂ cycle based power generation and will inform the performance, operability, and scale-up for commercial implementation of sCO₂ technology across the potential application spectrum. The pilot plant is currently in the final construction phase, with installation of major equipment underway, and commissioning planned for early 2022. By the end of this six-year project, the operability of the sCO₂ power cycle will be demonstrated and documented starting with a simple recuperated cycle configuration initially operating at a 500°C turbine inlet temperature and progressing to a recompression closed Brayton cycle technology (RCBC) configuration operating at 715°C. The paper will also present a vision for the use of the STEPDemo facility as a testbed for other sCO₂ component testing, such as thermal energy storage. In TES applications, a thermal storage system could be installed adjacent to the STEPDemo power block to demonstrate the integrated operation of TES with a commercially relevant sCO₂ cycle. This is relevant to both concentrated solar power (CSP) applications as well as power-to-power storage systems that utilize sCO₂ cycles.

INTRODUCTION

The unique properties of supercritical CO₂ offer intrinsic benefits over steam as a working fluid in closed and

* corresponding author(s)

semi-closed cycles to absorb thermal energy, to be compressed, and to impart momentum to a turbine.

The temperature and pressure threshold conditions required for the supercritical state of CO₂ are nominally 31°C (88°F) and 7.4 MPa (1073 psia). These conditions are easily achieved, and above these conditions is a supercritical fluid with higher density and incompressibility as compared to steam or air. This results in much smaller turbomachinery (factor 10:1) for a given energy production level [1]. Given these attributes, sCO₂ power cycles can offer several benefits [1,2,3,4]:

- Higher cycle efficiencies due to the unique fluid and thermodynamic properties of sCO₂
- Reduced emissions resulting from lower fuel usage
- Compact turbomachinery, resulting in lower cost, reduced plant size and footprint, and more rapid response to load transients
- Reduced water usage, including water-free capability in dry-cooling applications
- Heat source flexibility

These benefits can be achieved in a wide range of power applications including gas and coal-fired power plants, bottoming cycles, industrial waste heat recovery, concentrated solar power, shipboard propulsion, biomass power plants, geothermal power, nuclear power, and energy storage systems. Some of these applications are shown in Figure 1, which maps the sCO₂ application space relative to incumbent steam and Organic Rankine Cycle (ORC) options as a function of power output, and heat source temperature [2].

Waste Heat Recovery (WHR) – Waste heat recovery has been identified as a near-term commercial application for sCO₂ power cycles with better costs and wider application than alternates. Incumbent technologies include steam Rankine cycles or Organic Rankine Cycles (ORCs) but may not scale well in the case of steam and in the case of ORC, are not capable of higher temperature applications of interest. Waste heat recovery is a significant energy resource which, if harvested with sCO₂ technology, would be economically attractive. One application of particular interest is heat recovery from smaller gas turbine exhaust gas, specifically from aero-derivative gas turbines used in compressor pipeline stations, offshore oil and gas platforms etc. Other industrial applications are being considered where high temperature process steps exist, such as in cement, steel and glass production. The design and operating conditions of the STEP facility closely match those anticipated for WHR cycles.

Thermal Energy Storage (TES) – In sCO₂ power cycle applications with TES, heat is stored in a thermal reservoir during charging periods and converted to power during discharge periods. In the latter step, the thermal reservoir serves as a heat source for the sCO₂ power cycle. One specific

application is concentrated solar power (CSP) plants where concentrated solar energy is stored in a TES system to improve the dispatchability of the plant. High temperature TES systems with >700°C capability can support high temperature sCO₂ cycles enabling cycle efficiencies over 50% [5]. These cycle conditions ranging from 500–700°C are being validated at an industrial scale in the STEP Demo project. A second application is in power-to-power storage systems in which a TES system is similarly heated during charging periods and used as the heat source for a sCO₂ cycle during discharge periods. However, in power-to-power storage, the TES is heated by an electrically driven heat pump or resistive heater. In this application, the unique thermodynamic properties of sCO₂ enable the use of low-cost hot and cold reservoirs. Examples include sand, graphite, or hot liquid tanks and ice/water slurry tanks [6, 7]. All these applications seek to exploit the synergies between sCO₂ cycles and TES systems.

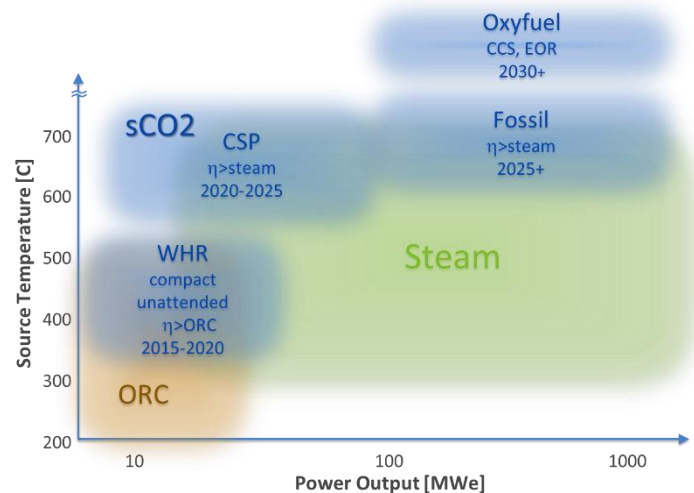


Figure 1: sCO₂ Application Map

STEP DEMO PILOT PROJECT OBJECTIVES

To facilitate the development and commercial deployment of the indirect sCO₂ cycle at elevated turbine inlet temperatures, pilot-scale testing is required to validate both component and system performance under realistic conditions at sufficient scale. The STEP Demo plant is of commercially relevant industrial scale and is a significant scale-up from previous cycle experiments (to 10 MWe) to a fully integrated and functional electric power plant. Several technical risks and challenges will be mitigated in this STEP Demo project:

- Turbomachinery (aerodynamics, seals, durability)
- Recuperators (design, size, fabrication, durability)
- Materials (corrosion, creep, fatigue)
- System integration and operability (startup, transients, load following).

The STEP Demo will advance the state of the art for high temperature sCO₂ power cycle performance from Proof of Concept (TRL 3) to System Prototype validated in an operational system (TRL 7).

The specific objectives of the STEP Demo pilot projects are:

- Demonstration of the operability of the Supercritical Carbon Dioxide (sCO₂) power cycle
- Verification of the performance of components including turbomachinery and recuperators
- Demonstration of the potential for producing a lower cost of electricity in relevant applications
- Demonstration of the potential for a thermodynamic cycle efficiency of greater than 50% (defined as the ratio of net power generation to the thermal input transferred to the working fluid in the primary heater)
- Demonstration of a 700 °C turbine inlet temperature or higher
- Validation of a recompression closed Brayton cycle (RCBC) configuration that can be used to evaluate system and components in steady state, transient, load following and limited endurance operation
- Reconfigurable facility to accommodate future testing:
 - System/cycle upgrades,
 - New cycle configurations such as cascade cycles and directly fired cycles,
 - Integrated Thermal energy storage
 - New or upgraded components (i.e. turbomachinery, recuperators and heat exchangers)

While advancing sCO₂ cycle technology for power generation, the STEP Demo pilot project will also provide the operating experience that is directly relevant for waste heat recovery applications.

- Scale: The STEP Demo scale of 10 MW_e matches the power levels of sCO₂ bottoming cycles for 25-30 MW_e gas turbines so that no further scale-up would be required for main system components in such a WHR application.
- Process conditions: simple cycle testing at sCO₂ turbine inlet conditions of 500 °C and 250 bar closely match the anticipated conditions of sCO₂ WHR cycles.
- Components: The STEP pilot will include an axial turbine, centrifugal compressors, compact (printed circuit) heat exchangers, and a primary heater with heat transfer characteristics and mechanical configuration resembling the primary heater in a WHR cycle. Also, the STEP heater is flexible enough to simulate transients expected in gas turbines.
- Controls and operating system: the project will develop, implement and optimize a control system and operating

procedures for the sCO₂ power cycles. Operating cases will include start-up, shut-down, load following, and other transient conditions.

- Process models: both steady state and transient process models will be anchored against the STEP test data and will be a useful design tool to simulate commercial WHR applications.

STEP DEMO PROJECT SCOPE

To manage risks, testing will occur in two phases as shown in Figures 2a and 2b. The initial system configuration will be the sCO₂ Simple Cycle operated at turbine inlet temperature of 500°C and 250 bar. The simple cycle configuration comprises a single compressor, turbine, recuperator, and cooler.

A natural-gas fired heater will supply the heat. In Simple Cycle testing, sCO₂ fluid will be delivered to the turbine at approximately 500°C and 250 bar. This test configuration offers the shortest time to steady-state and transient data, while demonstrating controls and operability of the system, as well as performance validation of key components. This configuration is relevant to waste heat recovery applications for example from small simple cycle gas turbines.

The second configuration is the Recompression Brayton Cycle (RCBC) which increases complexity but leads to higher efficiency. The RCBC adds a bypass loop adding another compressor, recuperator, and cooler to optimize the cycle performance. The RCBC configuration will deliver over 700°C to the turbine at 250 bar. The RCBC will allow testing to determine the full capability of the sCO₂ system.

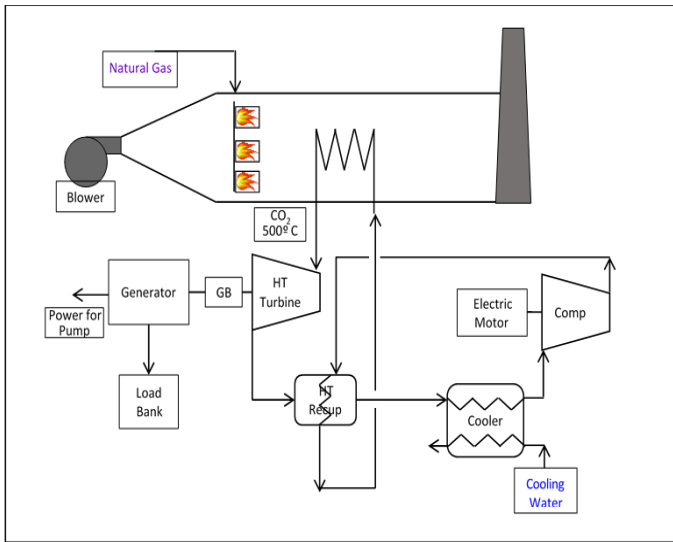


Figure 2a. Simple Cycle Configuration

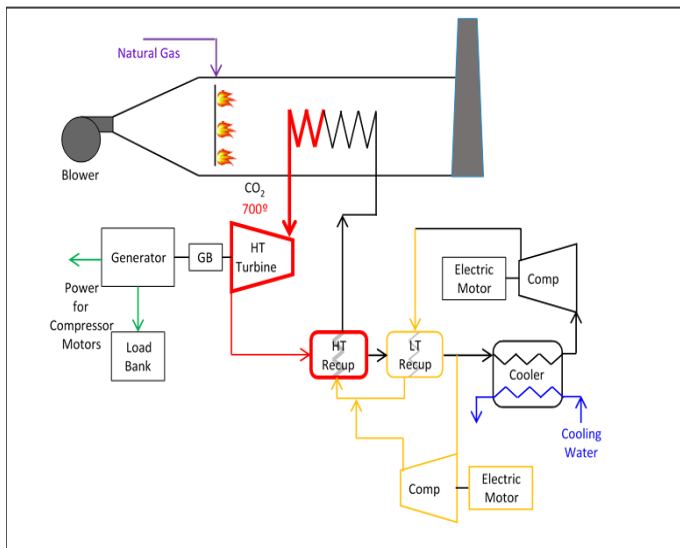


Figure 2b. Recompression Closed Brayton Cycle

Figure 2: Cycle Configurations for STEP Demo Project

PROGRAM TEAM

GTI, SwRI, and GE have formed a team to execute the STEP Demo project activities in line with program goals and objectives. GTI is responsible for the overall management of the project and is performing technology management, systems engineering, major component procurements, and will participate in testing in a test management role. SwRI is providing the host site for the test facility, and is responsible for the facility design engineering, and construction of test facility, and the supporting utility infrastructure. As host site, SwRI will manage the hardware installation and system assembly, perform facility commissioning, and execute test operations. GE Global Research (GE-GR) is providing the technical definition for the turbomachinery, the turbo-expander by GE-GR in collaboration with SwRI and the compression system by Baker Hughes, a former GE Company

(BHGE), as well as a first-of-a-kind sCO₂ turbine stop/control valve based on their product line of valves for high-pressure steam turbines and control hardware from GE Power.

The combined team have completed or are near to completing over two dozen sCO₂ technology related projects forming the building blocks for a successful STEP Demo [5,8,9,10,11,12,13]. Of note is the successful 1 MWe DOE SunShot program [8,12]. Previous descriptions and status updates of STEP Demo were also provided in [14, 15].

JOINT INDUSTRY PROGRAM

STEP Demo is meant to be an open project. Industry partners and other stakeholders in sCO₂ technology from around the world are invited to actively participate in the project. For that purpose, a Joint Industry Program (JIP) has been formed. This program has multiple industry partners who provide both funding and guidance for the project. It includes a Steering Committee with the U.S. DOE, project partners GTI, GE, and SwRI, and funding members including American Electric Power, Southern Company Services, Engie, Korean Electric Power Company, Natural Resources Canada, CSIRO, and the state of Texas TECQ office.



Figure 3: STEP Demo Team and Joint Industry Partners

SCHEDULE

The STEP project was launched in October 2016 and is a multi-year effort with three distinct phases (budget periods).

Phase 1 (ended January 2019)

Detailed Facility and Equipment Design

- System analysis, P&IDs, Component Specs
- Design major equipment
- Procure heat source, cooling tower and long-lead items
- Materials and seal tests
- Start site construction

Phase 2 (ends 2021)

Fabrication and Construction

- Complete site construction and civil works
- Fabrication and installation of major equipment
- Commissioning and simple-cycle test

Phase 3 (ending 2023)

Facility Operation and Testing

- Facility reconfiguration
- Test recompression cycle

PROJECT STATUS

The project involves the design, procurement, and construction of components, their integration, commissioning and testing to confirm performance and operability of a 10 MWe sCO₂ cycle based power plant. This effort is supported by several technology development tasks involving the turbine, the turbine stop/control valve, materials testing, and modeling.

System Design and Cycle Conditions - GTI has completed steady state and transient modeling of design and off-design cases, for both Simple Cycle and RCBC testing. Model results have been used to develop specifications for key components. The STEP cycle condition design and off-design cases are shown in Table 1.

The nine different steady state cases encompass the intended range of operating conditions for the STEP pilot. There are two simple cycle cases (max and min load) and seven RCBC cases, with varying parameters of turbine inlet temperature, main cooler outlet temperature, and power level. The RCBC baseline

is Case 151, shown in Figure 2. It is a 10 MWe net cycle with turbine inlet conditions of 715°C and 250 bar and an overall cycle efficiency of 43.4%. When this case is evaluated at a 450 MW commercial scale, the plant efficiency meets the program goal of 50%. Case 151 sets the design requirements for the major components, with the exception of the main cooler that was design-limited by Case 136, simple cycle max load. The cycle efficiencies of the remaining cases range from 22.6% to 37.4%.

Transient simulations have been run for both facility configurations, such as startup, normal shutdown, and emergency trips. The results from the transient model as well as an extensive hazardous operations (HAZOP) assessment were used to guide control methodologies, such as ensuring safe emergency shut-downs, defining how to start from cold or hot initial conditions, or ensuring stable operation as inventory is added and removed from the system. Note that sCO₂ inventory will be tested as a more efficient method of load control than throttling flow to the turbine (which also be tested). The transient model will be validated through testing of the STEP facility.

Table 1: Cases that encompass the intended range of operating conditions for the facility.

Model Names	Cycle Configuration	Description	Load %	Net Power Level (MWe)	Cooler Exit Temperature	Turbine Inlet Temperature	Cycle Efficiency
133	Simple	Simple cycle minimum load case	Min	2.5	35°C	500°C	22.6%
136	Simple	Simple cycle maximum load case	Max	6.4	35°C	500°C	28.3%
151	Recompression	Baseline case	100%	10.0	35°C	715°C	43.4%
152	Recompression	“Hot” Day Case	70%	6.6	50°C	675°C	37.4%
153	Recompression	“Cold” Day Case	100%	9.9	20°C	525°C	36.8%
154	Recompression	Partial load case using inventory control	40%	4.0	35°C	715°C	37.0%
155	Recompression	RCBC at 500°C turbine inlet temperature	70%	6.9	35°C	500°C	32.5%
157	Recompression	Partial load case using TSV throttling (transient condition)	40%	4.2	35°C	715°C	30.8%
157a	Recompression	Partial load case using TSV throttling	40%	3.9	35°C	675°C	29.6%

STEP DEMO TEST FACILITY

The STEP Pilot Plant is housed in a new General-Purpose Test Facility [GPTF] building and complex located on SwRI's campus in San Antonio, Texas (Figures 4, 5, and 6). This new test

facility is being developed to support the unique needs the current STEP project while providing flexibility for future test programs.

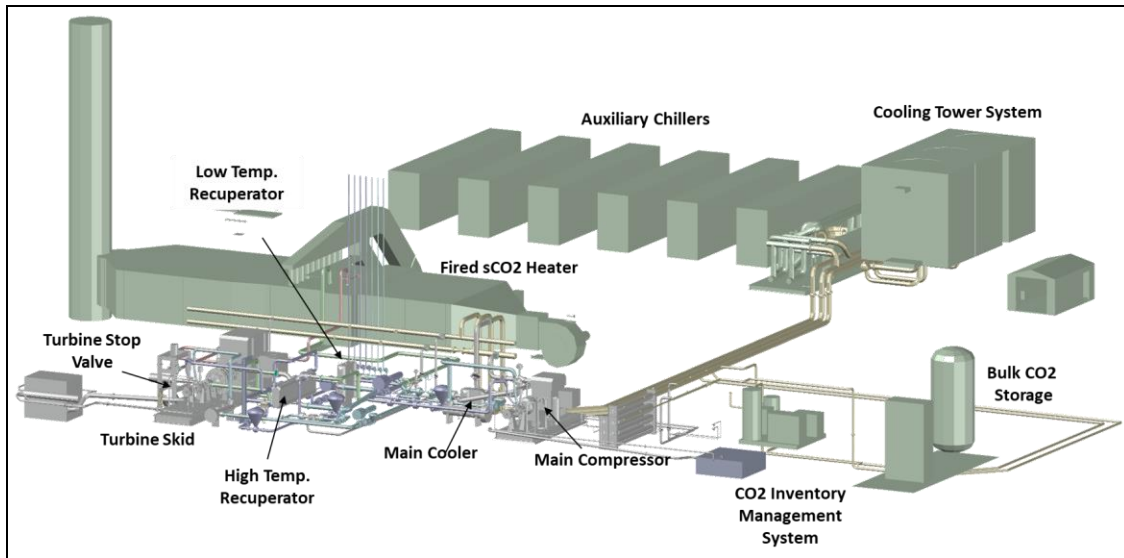


Figure 4: STEP facility layout



Figure 5: SwRI GPTF building in construction March 2020.



Figure 6: finalized facility, Summer 2020.

The test facility provides the infrastructure to support an 80 MW_{th} Natural Gas Heater, a 25 MW_{th} cooling tower system, 3,250 tons of auxiliary chilling capacity, electrical interconnects for grid connected operation, and load banks for 16 MWe gross turbine power when operating in island mode for first article acceptance or variable speed performance mapping. Process hardware will be installed in a 25,000 sq. ft high bay designed for flexibility and reconfiguration into alternate cycle or hardware configurations for future test campaigns. Equipment layout given in Figures 7 and 8. As of Fall 2020, the receipt, installation and acceptance of the sCO₂ process components in a Simple Recuperated Closed Brayton Cycle configuration is ongoing.

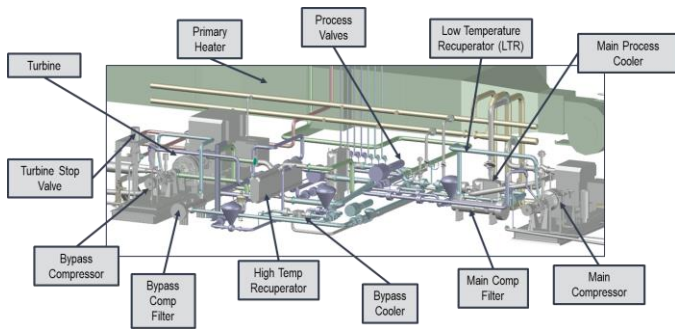


Figure 7: Equipment arrangement.

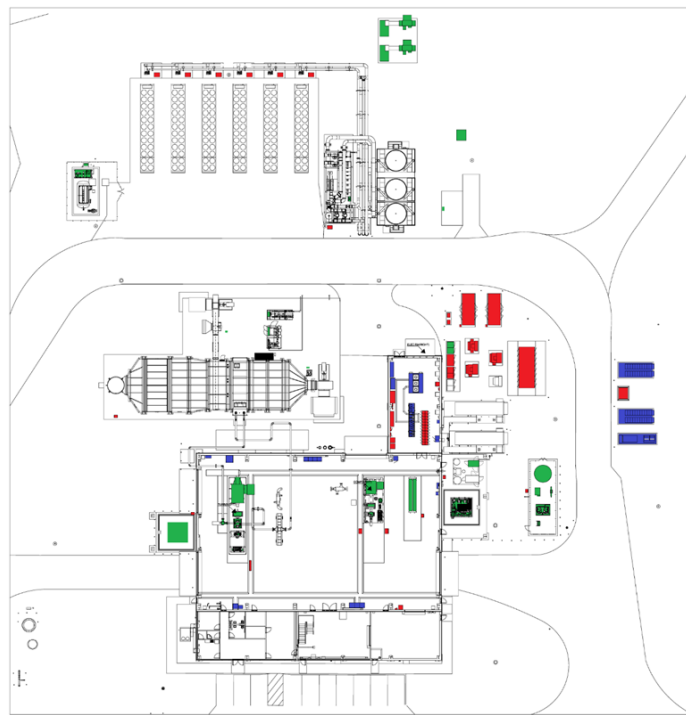


Figure 8: Plan view of STEP pilot facility arrangement.

MAJOR EQUIPMENT

Turbine Design – A schematic of the 16 MW_{th} (gross) sCO₂ turbine, jointly designed by SwRI and GE, is shown in Figure 9. This effort advances the existing U.S. DOE-funded SunShot project turbine in which SwRI and GE have fabricated and successfully tested to 715 °C and 27,000 rpm [8, 12]. The turbine design has passed design review with internal controlled title holders from SwRI and GE Power ensuring both organization’s years of industrial design experience has been applied. The STEP turbine will offer improvements over the SunShot turbine, including increased rotor life (100,000 hrs. vs 20,000 hrs.), shear ring retention rather than bolts, couplings on both shaft ends, and improved aerodynamic performance with an optimized volute flow area. The thermal management region will be enhanced based on lessons learned in the SunShot testing [16] and design enhancements developed under a related ARPA-e program [17].

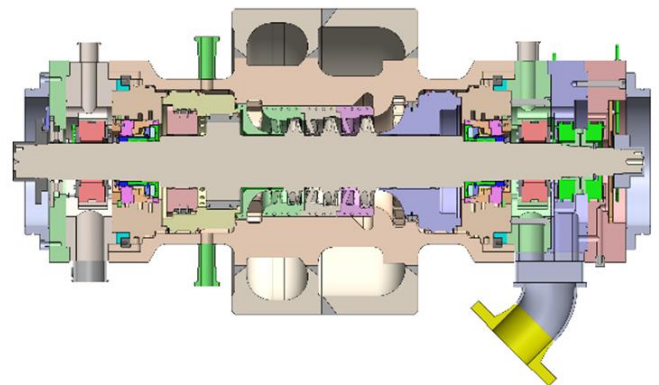


Figure 9: 10 MWe STEP sCO₂ Turbine.

A critical risk factor in compact turbomachinery at these temperatures is the short distance from the high temperature inlet at 715°C to the seal/bearing locations which are limited to 200°C. This drives the need for a thermal seal to control the high temperature gradient in both the casing and the rotor. The rotor with the increased loading due to the high rotational speed is of critical importance. In this regard, public data on LCF for the rotor material did not sufficiently cover the anticipated range of cycles expected for the sCO₂ power plant. The STEP team has developed its own set of LCF data for the rotor to ensure appropriate life anticipated for a commercial plant.

Aeromechanic design for high power density turbines of this compact nature is a significant challenge. Trade-offs between aerodynamic performance and operating margins for a multitude of blade natural frequencies are required. Using internal GE design rules in conjunction with an enhanced inlet and exit region plenum design led by SwRI, provided enough flexibility to meet acceptable aeromechanics safety margins while still increasing aerodynamic performance over the prior SunShot design.

Turbine Manufacturability – The compact design can increase the manufacturability challenges over conventional larger power equipment of similar power output. Figure 12 shows the

significant difference between the predecessor turbine (SunShot) and compressor (Apollo) rotors demonstrating the challenge for the turbine rotor. The turbine case with its small internal diameter relative to its length makes it challenging to find vendors that can reach within the case to manufacture tight tolerances.



Figure 10: Comparison of the turbine rotor (upper) based on SunShot (similar size to STEP) and the Apollo compressor rotor (lower).

The STEP project has struggled with the ability to manufacture the monolithic rotor design as the required machine tool capability significantly limits the vendor base. Unfortunately, the vendor used in the SunShot program was unable to meet cost and schedule targets; however, the STEP partner, Baker Hughes, having developed this capability to produce the compression system rotors, will produce the monolithic STEP turbine rotor.

Turbine Stop and Control Valve – GE is leading the design of the turbine control/stop valve that will be placed upstream of the turbine. The design is based on an existing commercial product line of steam valves, but with modifications to accommodate sCO₂ fluid and the high operating temperatures, including novel stem seal materials (Figure 11).



Figure 11: Turbine Stop Valve schematic and actual valve cast.

Four unique features for the sCO₂ valve that differ from that of standard industrial steam valves are:

1. The use of Haynes 282 high temperature nickel alloy material leveraging efforts under AUSC steam power development programs for industry leading high temperature, high-pressure materials and components [18, 19]
2. Density differences between steam and sCO₂ that required the use of high fidelity CFD to accurately predict internal flows and pressure balance.
3. The use of compact self-contained actuators that more appropriately match the compact nature of the sCO₂ turbomachinery. This design is leveraged from commercial designs used by Baker Hughes.
4. Advanced stem sealing.

The advanced stem sealing is critical for sCO₂. Typical small leakages allowed from current steam power stem seals have a minimal impact on the steam plant efficiency. However, for a sCO₂ cycle, the cost of the replacement CO₂ and the energy needed to increase that supply pressure to exceed the critical pressure of ~85bar, results in a significant performance penalty. Technology from Baker Hughes and GE Aviation was leveraged to provide advanced seals that are near hermetic in their sealing ability. These seals were tested for sealing performance, leakage and reliability in sCO₂ in a specially constructed test rig at GE Research (Figure 14, right view). An additional challenge was the operating temperature of ~715°C which necessitates a thermal management scheme in conjunction with the seal choice in the high temperature locations as many hermetic seals use materials with temperature limits below 715°C.

Compressor – The compressor is being provided by Baker Hughes and leverages an existing commercial product line as well as work undertaken in the DOE-funded APOLLO program [20]. The compression system (main and bypass compressors) have completed aerodynamic designs using a combination of Baker

Hughes internal design tools and two parallel CFD studies using real gas properties of CO₂. The STEP compressor aero design was frozen prior to completion of the full Apollo test data set due to test delays in the Apollo program; however, initial test data from the Apollo compressor program has been used to help validate these tools. The compressor rotors have used an industry leading monolithic design attractive for the reduced size impellers inherent in this compact sCO₂ power cycle. The Baker Hughes team developed a proprietary process with specialized equipment to make these small monolithic rotors.

The bypass compressor (two stage design) is shown in Figure 12. The compressors have completed factory testing at Baker Hughes' facility in Florence, Italy, and are being delivered to the STEP site.

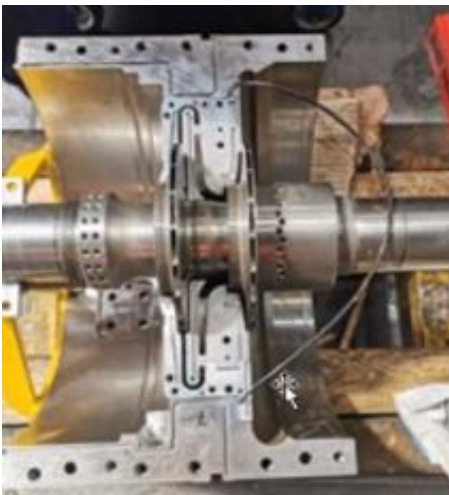


Figure 12: Bypass compressor impeller

Process Heater – The process heater is a natural gas fired unit with a high temperature tube bundle, headers and piping fabricated out of Inconel 740H to accommodate the >700°C, 250 bar sCO₂ conditions. Its arrangement is based upon a duct-fired Heat Recovery Steam Generator (HRSG) (Figure 13). The heater has been fabricated in ten modules. The high temperature IN740 fined tubing and 11.25" OD/ 7.5" ID diameter header are shown in Figures 14. The highest temperature duty section containing the IN 740H components is shown in Figure 15. Care has been given to the fabrication particularly welding and QA/QC inspection all in line with ASME PV guidance and certification.

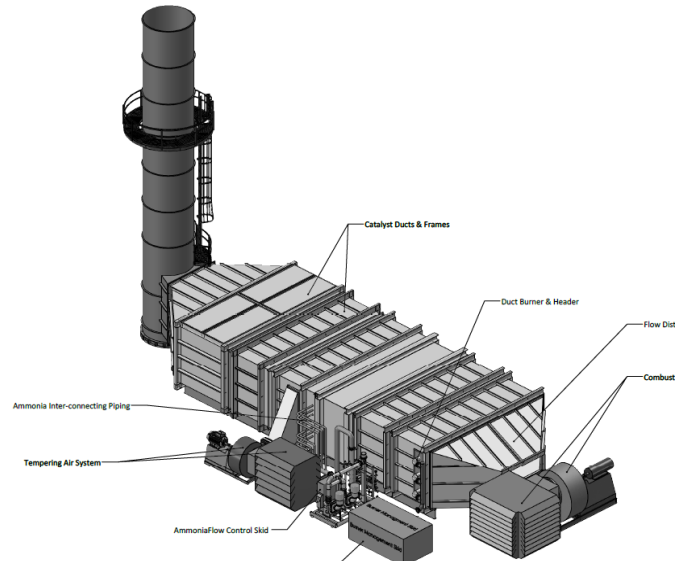


Figure 13: - Gas Fired Heater with 740H material for 715 °C sCO₂



Figure 14: IN740H tubing with 304 SS fins and welding tubing to 11.25" OD/ 7.5" ID diameter IN740 header.



Figure 15: High temperature sCO₂ coils for 715 °C sCO₂.

Recuperators – The heat exchangers include a High-Temperature Recuperator (HTR), Low-Temperature Recuperator (LTR), and coolers. All units are compact heat exchangers with high surface area/volume ratios. GTI engaged several vendors and evaluated their product offerings and the suitability for the STEP operating conditions. Candidate heat exchangers included printed circuit heat exchangers [PCHE], micro-tube, and compact stacked plate arrangements. Shell-and-tube arrangements also investigated as alternates. Following these evaluations all major heat exchangers will be PCHE-type. The suppliers are Heatric and VPE. The LTR and main process coolers are shown in Figures 16 & 17. The HTR has a 50 MW_{th} capacity and significant thermal mechanical design challenges have been encountered with the wide operating range and in general with the scale-up from current experience.

- New cycle configurations (i.e., cascade cycles, directly fired cycles, etc.)
- Integrated thermal energy storage
- New or upgraded components (turbomachinery, recuperators and heat exchangers)

At the conclusion of the STEP Demo project, the facility can be made available for projects that demonstrate the integration of sCO₂ power cycles with thermal energy storage (TES) systems at commercially relevant scales. In such projects, a TES system could be installed adjacent to the power block replacing the function of the gas-fired heater as the heat source. Also, depending on the specific TES configuration, the gas-fired heater could be used to heat the TES. The STEP Demo facility is unique in that it can enable the demonstration of high temperature TES technologies that can operate above 700°C and at power levels of up to 10 MWe.

SUMMARY

Supercritical CO₂ power cycles promise substantial cost, emissions, and operational benefits that apply to a wide range of power applications including coal, natural gas, waste heat, concentrated solar, biomass, geothermal, nuclear, shipboard propulsion, and energy storage systems.

The STEP 10 MWe pilot demo project will demonstrate in-direct fired sCO₂ cycles to known available materials limits (T>700 °C) in a fully integrated 10 MWe electric generating pilot plant. The project will enable the progression of technology readiness level from TRL of 3 level to a TRL of 7 and subsequent commercialization. The project is well under way and commissioning is expected in 2021.

Beyond the STEP Demo project, the 10 MWe facility will be available as a testbed for further sCO₂ cycle development and component testing. The scale and configuration make it highly relevant for waste heat recovery and thermal energy storage applications.

ACKNOWLEDGEMENTS

The authors would also like to acknowledge and thank the hard work of the team members of GTI, SwRI, GE and our other project participants, and gratefully acknowledge the U.S. Department of Energy, Office of Fossil Energy and the National Energy Technology Laboratory, under Award Number DE-FE0028979, support for this work . The Joint Industry Program member’s, (American Electric Power, Southern Company Services, Engie, Korean Electric Power Company, Natural Resources Canada, CSIRO and State of Texas TCEQ) support and guidance are acknowledged and critical to the project.

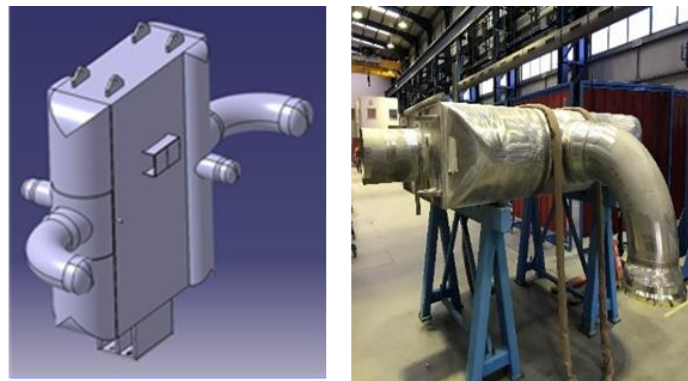


Figure 16: Compact Stacked Plate LTR sCO₂ Recuperator

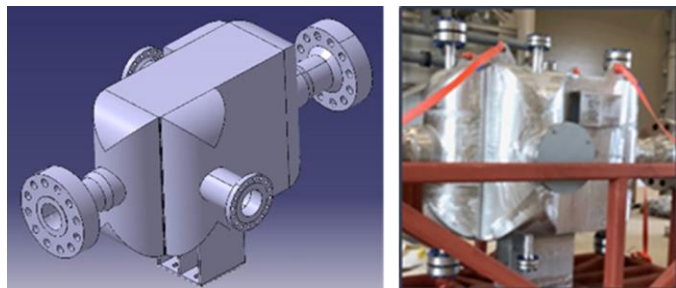


Figure 17: PCHE type main cooler.

TEST PLANS AND FUTURE USE

Commissioning is planned to start in 2021, assuming equipment fabrication, delivery and installation schedule is maintained. A program of parametric testing in simple cycle mode with a turbine inlet temperature up to 500 °C will be conducted shortly thereafter. Subsequently, the pilot will be reconfigured in Recompression Closed Brayton Cycle and tested in that mode up to 700 °C in 2022.

The STEP Demo facility has made provisions to be a reconfigurable facility and flexible platform to accommodate future testing such as:

- System/cycle upgrades

DISCLAIMER

This report was prepared as an account of work sponsored by an agency of the United States Government. Neither the United States Government nor any agency thereof, nor any of their employees, makes any warranty, express or Implied, or assumes any legal liability or responsibility for the accuracy, completeness, or usefulness of any information, apparatus, product, or process disclosed, or represents that its use would not infringe privately owned rights. Reference herein to any specific commercial product, process, or service by trade name, trademark, manufacturer, or otherwise does not necessarily constitute or imply its endorsement, recommendation, or favoring by the United States Government or any agency thereof. The views and opinions of authors expressed herein do not necessarily state or reflect those of the United States Government or any agency thereof.

REFERENCES

- [1] K. Brun, P. Friedman, R. Dennis, *Fundamentals and Applications of Supercritical Carbon Dioxide (sCO₂) Based Power Cycles*, Elsevier ltd, 2017
- [2] D. Hofer, “Phased Development of a High Temperature sCO₂ Power Cycle Pilot Test Facility”, 5th International Symposium Supercritical CO₂ Power Cycles, March 28-31, 2016, San Antonio, TX.
- [3] T. Held, “Transient Modeling of a Supercritical CO₂ Power Cycle and Comparison with Test Data”, GT2017-63279, Proceedings of ASME Turbo Expo 2017: Turbomachinery Technical Conference and Exposition, June 26-30, 2017, Charlotte, NC
- [4] S. Patel, “Pioneering Zero-Emission Natural Gas Power Cycle Achieves First-Fire”, Power Magazine, May 30, 2018
- [5] Concentrating Solar Power Gen3 Demonstration Roadmap, Mark Mehos et al, National Renewable Energy Laboratory, Technical Report NREL/TP-5500-67464, January 2017.
- [6] <https://arpa-e.energy.gov/technologies/programs/days>
- [7] “MAN ETES: A Cool Technology that’s Heating up Sector Coupling”, Raymond C. Decorvet and Mario Restelli, MAN Energy Solutions, Modern Power Systems, 16 July 2019
- [8] C. Kalra, D. Hofer, E. Sevincer, J. Moore and K. Brun, “Development of High Efficiency Hot Gas Turbo-Expander for Optimized CSP sCO₂ Power Block Operation”, in 4th International sCO₂ Power Cycles Symposium, Pittsburgh, PA, 2014.
- [9] R.A. Bidkar, G. Musgrove, M. Day, C.D. Kulhanek, T. Allison, A.M. Peter, D. Hofer and J. Moore, “Conceptual Designs of 50-450 MWe Supercritical CO₂ Turbomachinery Trains for Power Generation from Coal. Part 2 Compressors”, in The 5th International Symposium – Supercritical CO₂ Power Cycles, San Antonio, TX, 2016
- [10] R.A. Bidkar, E. Sevincer, J. Wang, A. Thatte, A. Mann, M. Peter, G. Musgrove, T. Allison, J. Moore, “Low Leakage Shaft-End Seals for Utility-Scale Supercritical CO₂ Turboexpanders”, Journal of Engineering for Gas Turbines and Power, ASME, 2017
- [11] <http://energy.gov/eere/sunshot/concentrating-solar-power>
- [12] J. Moore, et al, “Development of a 1 MWe Supercritical CO₂ Brayton Cycle Test Loop”, 4th International sCO₂ Power Cycles Symposium, Pittsburgh, PA, 2014
- [13] DE-EE-0005804 “Development of a High Efficiency Hot Gas Turbo-Expander and Low Cost Heat Exchangers for the Optimized CSP Supercritical CO₂ Operation” DoE SunShot Award
- [14] J. Marion, et al., “The STEP 10 MWe sCO₂ Pilot Plant Demonstration”, Proceedings of ASME Turbo Power Expo 2019, GT2019-91917
- [15] J. Marion, et al., “The STEP 10 MWe sCO₂ Pilot Plant Demonstration Status Update”, Proceedings of ASME Turbo Power Expo 2020, GT2020-14334
- [16] Moore, J.J., Cich, S., Day-Towler, M., Hofer, D., Mortzheim, J., “Testing of a 10 MWe Supercritical CO₂ Turbine” 47th Turbomachinery & 34th Pump Symposia, September 17-20, 2018.
- [17] DE-AR-0000467 “Electrochemical Energy Storage with a Multiphase Transcritical CO₂ Cycle” DoE Advanced Research Projects Award.
- [18] Purgert, R. et al, “Materials for Advanced Ultra supercritical Steam Turbines”, Final Technical Report, DOE Cooperative Agreement: DE-FE0000234, Dec. 2015.
- [19] J. Marion, F. Kluger, P. Sell, A. Skea, “Advanced Ultra-Supercritical Steam Power Plants”, Power GEN ASIA 2014, KLCC, Kuala Lumpur, Malaysia, September, 2014
- [20] DE-EE-0007109 “Compression System Design and Testing for sCO₂ CSP Operation” DoE Concentrating Solar Power Advanced Projects Offering Low LCoE Opportunities (APOLLO) Award.

EXERGOECONOMIC ANALYSIS OF A HYBRID sCO₂ BRAYTON POWER CYCLE

Abdurrahman Alenezi*

University of Central Florida
Orlando, USA

Email: aaalenezi@knights.ucf.edu

Ladislav Vesely

University of Central Florida
Orlando, USA

Jayanta Kapat

University of Central Florida
Orlando, USA

ABSTRACT

An exergetoeconomic analysis of a hybrid power generation cycle is performed on its standalone constituents. The hybrid is based on Allam cycle configuration. Allam cycle is a supercritical carbon dioxide oxy-combustion (OC) Brayton cycle. The proposed hybrid utilizes solar power as its primary heat source and natural gas OC as a complementing heat source. The purpose of the complementing heat source is to make up for the lost time when the sun is not available due to bad weather conditions or at nighttime. This is done to ensure the reliability, responsiveness, and availability of the cycle for power generation at all times. The hybrid is an attempt to provide power with minimal adverse effects on the environment. This study is divided into three major steps. The first and second are energy and exergy analysis. The third step is exergetoeconomic analysis to obtain the cost contribution of each component relative to the cycle's final product. Although both configurations brought similar power output and second law efficiency, the energy efficiency was higher for the OC configuration. The total product cost (\$/GJ) for the OC configuration was half of that for the concentrated solar power (CSP). The unit cost of electricity in (Cent/kWh) for the CSP standalone configuration is approximately 60% higher than that of the OC configuration. In the CSP configuration, the main heat exchanger and the recuperator are the most critical units to consider for savings. Therefore, reducing the exergy destruction in the CSP main heat exchanger and the recuperator units could be cost-effective for the entire cycle, even if this would increase the component investment costs. Therefore, for exergetoeconomic performance enhancement, using a recuperator with higher efficiency is recommended. On the other hand, the combustor and air separation unit (ASU) are the most critical units to consider for savings for the OC configuration. Therefore, a replacement for the ASU unit with a lower purchasing cost is recommended for overall exergetoeconomic performance enhancement. The parametric study results showed that increasing the turbine's

inlet temperature is conducive to improving both configurations' thermodynamic and exergetoeconomic performances. Similar trends were also obtained for the turbine inlet pressure for both configurations.

INTRODUCTION

Energy production and consumption are forecasted to increase for the foreseeable future due to population growth and higher living standards. Electricity production is projected to stay the primary type of energy demand globally up to 2050 [1].

Thermal power cycles converting thermal energy to electricity is the leading technology used to generate electricity [1]. Although various combustion technologies are utilized to convert fossil fuels to thermal energy to act as the heat source for thermal power cycles, this process's byproducts usually pollute the environment. Combustion of fossil fuels produces greenhouse gases (GHG), which is the main contributor to global warming. A good solution to this problem is to improve the existing power generation technologies efficiency, develop new clean technologies, or combine compatible technologies to produce more efficient hybrid cycles.

Compared to traditional power cycles, supercritical carbon dioxide (sCO₂) Brayton power cycles are promising because they have higher efficiency, smaller equipment size, and better economics. The cycle's higher efficiency is mainly due to its recuperative nature. Additionally, the critical point of CO₂ is near the surroundings temperature, which means that exergy losses due to temperature differences with the environment are minimal. Another good quality of this cycle is the high density of CO₂ near its critical point, which results in less work at the compressor. Furthermore, the sCO₂ power cycle can work with direct and indirect heat sources because it can accept a wide range of heat sources. This advantage allows it to work with high-temperature heat sources such as nuclear [2] and low-temperature heat sources such as waste heat [3].

* corresponding author(s)

Nevertheless, the sCO₂ cycle has some disadvantages as operating near CO₂ critical point brings its own challenges. Since CO₂ properties vary significantly near its critical point, a few degrees change in its temperature may substantially affect the cycle's operations and control. Therefore, keeping the cycle at its optimum operating conditions is difficult as small fluctuations in CO₂ properties can negatively affect its efficiency [4].

A good enhancement of Brayton power cycle is the use of OC technology. Oxy-combustion is a process in which fuel is combusted in an oxygen-rich environment instead of air. The combustion products, in this case, are mainly CO₂ and water (H₂O). Allam cycle is an OC cycle based on Brayton power cycle configuration. Allam cycle fuel feed is natural gas (NG), or synthetic gas produced from coal [5]. Allam cycle is considered semi-closed as it takes oxygen and fuel as its feed and rejects part of its produced CO₂ and water. Typically, an OC cycle uses an ASU to separate its air intake into Nitrogen (N₂), Oxygen (O₂), and Argon (Ar). The ASU outlet separation percentages are approximately 78.09%, 20.95% and 0.93% for N₂, O₂ and Ar, respectively [6]. Cryogenic air separation technology is the most common technology used for air separation.

In contrast to combustion utilizing air, OC avoids producing Nitrous Oxides (NO_x) by excluding N₂ from its combustor feed. OC is considered among the carbon capture technologies as it inhibits the release of CO₂ into the atmosphere by capturing it as part of its built-in technology [7]. The cycle also provides its export CO₂ in pure form and highly pressured, making it ideal for storage or export to other industries such as enhanced oil recovery. Since the withdrawn CO₂ is pure and pressurized, there is no need for additional physical or chemical processes prior to its export [8]. Hence, the pollution treatment cost is eliminated in this case. Another advantage of Allam cycle is that it can be heated directly and indirectly. A good example of direct heat addition is combustion, while an indirect heat addition can be, for example, solar power or waste heat.

There are several OC cycles; however, Allam cycle is considered one of the best. Barbra et al [9] performed a study on nineteen different OC power cycle configurations and concluded that Allam cycle configuration is the best for NG powered cycles. Allam cycle has higher efficiency compared to traditional Brayton power cycles. In a study by Allam et al, the authors claimed an overall cycle efficiency of 59% [10].

Another good strategy to avoid pollution from the power industry is to utilize renewable energy resources. The main categories of energy resources remain renewable, nuclear, and fossil fuels [11]. However, out of the three categories, renewable energy is the cleanest from the environmental perspective. Renewable energy resources comprise solar, wind, geothermal, hydropower, and biomass [12].

One of the most promising technologies in solar power is the CSP technology. In a typical CSP setup, solar radiation is focused using reflective surfaces against solar collectors [13]. A solar collector's job is to transform the collected solar radiation into thermal energy. Afterward, the converted thermal energy is used to heat the heat transfer fluid (HTF), such as molten salt. The heat accumulated within the HTF is then transferred to the

power generation cycle working fluid via a special heat exchanger. However, due to bad weather conditions and during nighttime, the sun is not always shining. Due to fluctuations in its thermal energy, most CSP systems have thermal storage vessels to store their HTF. The storage vessels' purpose is to provide a consistent quality stream to the heat exchanger and within the required operating conditions. One of the leading CSP technologies is the solar tower technology. Temperatures in a solar tower can reach an operating temperature between 300 °C and 1500 °C [14].

From a thermodynamic perspective, to achieve a higher thermal-to-electric conversion efficiency, higher operating temperatures are desirable [15]. Fossil fuel and nuclear power cycles have similar thermodynamics to the CSP cycles. However, nuclear and CSP cycles heat addition to the cycle is in the form of heat flux while fossil fuel heat is sensible heat [16].

Hybrid cycles are those combining more than one technology to produce an enhanced cycle with better outcomes. The combination of renewable and traditional fossil fuel cycles is an example of such hybrid cycles. In addition to better economics, hybrid cycles are generally more reliable than sole renewable energy cycles and usually have higher efficiency. For example, a study [17] evaluated hybridizing between conventional and standalone renewable power cycles. The study concluded that hybrid plants could save up to 50% compared to standalone ones.

This study carries out an exergoeconomic evaluation of a hybrid power cycle. The cycle is based on a simple recuperative Brayton cycle configuration with sCO₂ as its working fluid. The proposed cycle main processes are similar except for their heat source. The proposed cycle's primary heat source is CSP. However, CSP is complemented with natural gas OC to avoid solar energy discrepancy when the sun is not available. This combination is sought to provide better responsiveness to electrical grid demand fluctuations and add additional reliability to the cycle.

HYBRID CYCLE DESCRIPTION

As shown in Figure 1, the hybrid is simple recuperative based on Allam cycle configuration with two heat sources, solar and fossil fuel oxy-combustion. The solar power is provided by the CSP solar tower technology. The CSP heat source is the primary heat source; however, the OC heat source is utilized to complement the power generation requirements or act as a standalone in bad weather cases or at nighttime.

A conservation strategy was adopted in constructing the hybrid. Therefore, most of the hybrid equipment were made common for both configurations. The thinking behind this strategy of having the highest possible number of common equipment is to minimize cost both in terms of capital and operational costs. The common and unique units of the proposed hybrid cycle are shown in Table 1.

When the CSP heat source solely heats the hybrid as a standalone, the CSP main heat exchanger is exclusively providing 100% of the heat to the hybrid. The CSP main heat exchanger transfers heat between the HTF, molten salt, and the

power cycle working fluid, sCO₂. On the other hand, when the hybrid is solely heated by OC as a standalone, the NG combustor provides heat to the hybrid.

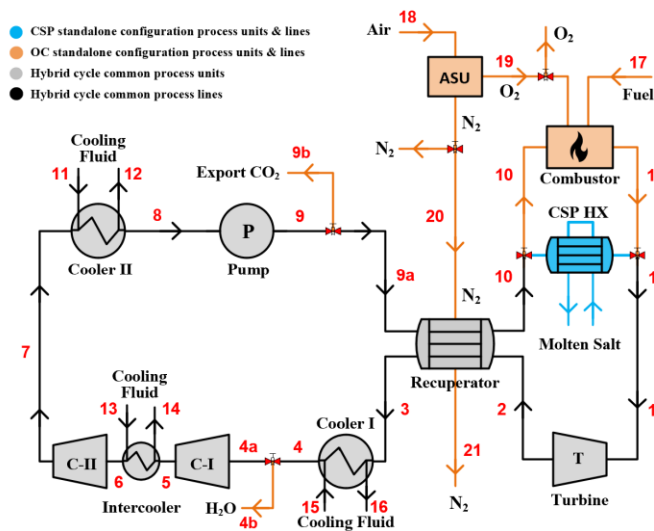


Figure 1: Schematic of the hybrid cycle

The CSP standalone configuration is a closed system. Furthermore, the OC standalone configuration is a semi-closed system where oxygen and NG are feed into the combustor, and water and export CO₂ are withdrawn out of the cycle. It is worth mentioning that the nitrogen stream coming from the ASU only contributes to heat transfer in the hybrid’s recuperator and has no mass interactions within the cycle.

Table 1: Hybrid cycle common and unique units

Hybrid Cycle Unit	Unique/Common
Turbine (Turb)	Common
Compressors (C)	Common
CO ₂ export pump (Pump)	Common
Coolers (C-I)	Common
Recuperator (Rec)	Common
CSP heat exchanger (CSP HX)	Unique to CSP configuration
Combustor (Comb)	Unique to OC configuration
ASU	Unique to OC configuration
Water separator (WS)	Unique to OC configuration

HYBRID CYCLE PROCESS

After gaining heat at the heat source, the high pressure and temperature working fluid at process point 1 is expanded in the turbine to produce work. The expanded working fluid at low pressure and high temperature at process point 2 then enters the recuperator's hot-stream side, where it cools down to process point 3. To prepare the working fluid to enter the compressor, it is further cooled down at cooler I. At this point, the process is at point 4. Then, CO₂ is compressed in compressors I and II and

cooled in-between at the compressor’s intercooler. The high pressure CO₂ at process point 7 is then cooled at cooler II to arrive at process point 8 before raising its pressure at the cycle’s pump. The high pressure CO₂ at process point 9 enters the recuperator's cold-side to raise its temperature before returning to the heat source again at process point 10.

It is worth mentioning that in the CSP standalone case, the working fluid is pure CO₂. However, in the OC standalone case, pure CO₂ is only present between process points 4a and 10, while between process points 1 and 4a, the working fluid is a mixture of water and CO₂. The water is withdrawn out of the cycle in the water separator between process points 4 and 4a. In both configurations, the working fluid is assumed either pure CO₂ or a mixture of pure CO₂ and water with no impurities throughout the whole cycle.

HYBRID CYCLE MODELING

This study is divided into three parts: (1) energy, (2) exergy, and (3) exergoeconomic analyses. For each of the three parts, the study is conducted for both configurations as a standalone case each. The mass flow rate into the turbine inlet at process point 1 is constant at 125 Kg/s for both standalone cases. The process schematics of the proposed hybrid cycle for both standalone configurations are shown in Figures 2 and 3, showing all process streams. The P-h diagrams of the two standalone configurations are in Figures 4 and 5 in Annex A.

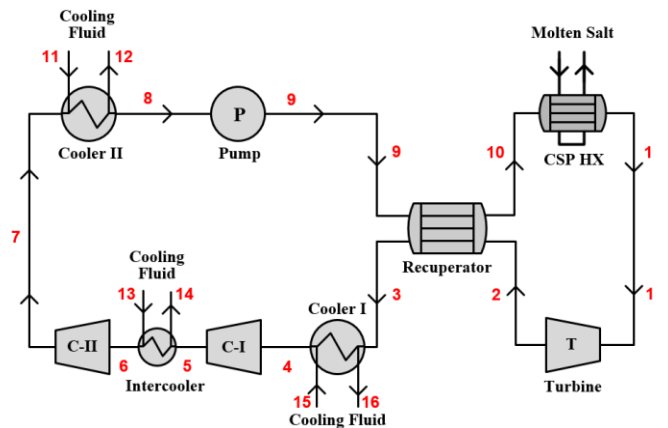


Figure 2: Schematic of the CSP standalone configuration

In addition to the aforementioned assumptions and constraints, the following are this study’s main assumptions:

- All processes are under steady-state conditions.
- System heat losses to the environment are negligible.
- Potential and kinetic energy changes are negligible.
- The combustion process is complete.
- Combustion process flue gases are only H₂O and CO₂.
- Environmental ambient conditions are 25 °C and 1 atm.
- Turbine, compressors, and pumps assigned mean value isentropic efficiencies.
- Pressure drop is negligible for all equipment except for heat exchangers.
- The pressure drop for heat exchangers is 2%.

Due to limited changes in their energy, the potential and kinetic energy terms are neglected as per the assumption made earlier. Therefore, at a given state, the specific exergy of a particular stream is calculated as the sum of its physical and chemical exergies as per the following equation [20]:

$$e = (h - h_o) - T_o(s - s_o) + \sum_{m=1}^n y_m(\mu_m^* - \mu_m^o) \quad (3)$$

Where h , T , s , μ , and y are the specific enthalpy, temperature, specific entropy, chemical potential, and mass fraction, respectively. The superscript (*) represents the initial concentration at ambient temperature and pressure, while the super and subscript (o) represents dead states. Finally, the subscript “ m ” represents an individual substance in a mixture stream.

The standalone CSP configuration is assumed to have a constant chemical composition, and hence chemical exergy is not present for this configuration calculations. On the other side, the OC standalone configuration has variable chemical compositions in the fuel- O_2 mixture combustion, and therefore, chemical exergy is present in its calculations. As discussed earlier, for the OC standalone configuration, the combustor flue gases are mainly CO_2 and steam up until the water content is cooled in cooler I and then separated at the water separator before reaching point 4a of the process. Therefore, the stream composition from process points 1 to point 3 is water and CO_2 , but between process points 4a and 10, the working fluid consists of pure CO_2 .

The exergy supplied to the CSP main heat exchanger is calculated for the CSP configuration as input heat. For the OC configuration, the combustor fuel exergy is calculated based on the equations provided in [20]. The fuel exergy for the CSP and OC configurations are calculated as follows, respectively:

$$\dot{E}_{Fuel,CSP} = \left(1 - \frac{T_o}{T_s}\right) \dot{Q}_{CSP} \quad (4)$$

$$\dot{E}_{Fuel,OC} = \dot{m}_{CH_4} \left[(h_{17} - h_{o,CH_4}) - T_o(s_{17} - s_{o,CH_4}) + \frac{824.348}{MW_{CH_4}} \right] \quad (5)$$

Where \dot{Q}_{CSP} is the heat supplied by molten salt to the CSP main heat exchanger, T_s and T_o are the heat source temperature supplied from the solar tower's storage tank and dead state temperatures, respectively. MW_{CH_4} is the molecular weight of natural gas.

The exergy destruction of all hybrid cycle units and the fuel and products' exergies are shown in Table 4 for the CSP standalone configuration and in Table 5 for the OC standalone configuration.

The second law of thermodynamics exergy efficiency for each component is calculated as:

$$\epsilon_k = \frac{\dot{E}_{Product,k}}{\dot{E}_{Fuel,k}} \quad (6)$$

Where $\dot{E}_{product,k}$ and $\dot{E}_{Fuel,k}$ are exergy of the product and fuel for the k^{th} component, respectively.

Table 4: Fuel exergy, product exergy, and exergy destruction for the CSP standalone configuration

Unit	Fuel Exergy (\dot{E}_{Fuel})	Product Exergy ($\dot{E}_{Product}$)	Exergy Destruction ($\dot{E}_D = \dot{E}_{Fuel} - \dot{E}_{Product}$)
CSP HX	$\dot{E}_{Fuel} + \dot{E}_{10}$	\dot{E}_1	$\dot{E}_{Fuel} - (\dot{E}_1 - \dot{E}_{10})$
Turb	$\dot{E}_2 - \dot{E}_1$	\dot{W}_{turb}	$(\dot{E}_2 - \dot{E}_1) - \dot{W}_{turb}$
Rec	$\dot{E}_2 - \dot{E}_3$	$\dot{E}_{10} - \dot{E}_9$	$(\dot{E}_2 - \dot{E}_3) - (\dot{E}_{10} - \dot{E}_9)$
Cl-I	$\dot{E}_{15} - \dot{E}_{16}$	$\dot{E}_4 - \dot{E}_3$	$(\dot{E}_{15} - \dot{E}_{16}) - (\dot{E}_4 - \dot{E}_3)$
C-I	$\dot{W}_{comp I}$	$\dot{E}_5 - \dot{E}_4$	$\dot{W}_{comp I} - (\dot{E}_5 - \dot{E}_4)$
IC	$\dot{E}_{13} - \dot{E}_{14}$	$\dot{E}_6 - \dot{E}_5$	$(\dot{E}_{13} - \dot{E}_{14}) - (\dot{E}_6 - \dot{E}_5)$
C-II	$\dot{W}_{comp II}$	$\dot{E}_7 - \dot{E}_6$	$\dot{W}_{comp II} - (\dot{E}_7 - \dot{E}_6)$
Cl-II	$\dot{E}_{11} - \dot{E}_{12}$	$\dot{E}_8 - \dot{E}_7$	$(\dot{E}_{11} - \dot{E}_{12}) - (\dot{E}_8 - \dot{E}_7)$
Pump	\dot{W}_{pump}	$\dot{E}_9 - \dot{E}_8$	$\dot{W}_{pump} - (\dot{E}_9 - \dot{E}_8)$

Table 5: Fuel exergy, product exergy, and exergy destruction for the OC standalone configuration

Unit	Fuel Exergy (\dot{E}_{Fuel})	Product Exergy ($\dot{E}_{Product}$)	Exergy Destruction ($\dot{E}_D = \dot{E}_{Fuel} - \dot{E}_{Product}$)
ASU	$\dot{E}_{18} + \dot{W}_{ASU}$	$\dot{E}_{19} + \dot{E}_{20}$	$(\dot{E}_{18} + \dot{W}_{ASU}) - (\dot{E}_{19} + \dot{E}_{20})$
Comb	$\dot{E}_{17} + \dot{E}_{19} + \dot{E}_{10}$	\dot{E}_1	$\dot{E}_{17} + \dot{E}_{19} + \dot{E}_{10} - \dot{E}_1$
Turb	$\dot{E}_2 - \dot{E}_1$	\dot{W}_{turb}	$(\dot{E}_2 - \dot{E}_1) - \dot{W}_{turb}$
Rec	$\dot{E}_2 - \dot{E}_3$	$\dot{E}_{10} - \dot{E}_{9a}$	$(\dot{E}_2 - \dot{E}_3) - (\dot{E}_{10} - \dot{E}_{9a})$
Cl-I	$\dot{E}_{15} - \dot{E}_{16}$	$\dot{E}_4 - \dot{E}_3$	$(\dot{E}_{15} - \dot{E}_{16}) - (\dot{E}_4 - \dot{E}_3)$
C-I	$\dot{W}_{comp I}$	$\dot{E}_5 - \dot{E}_{4a}$	$\dot{W}_{comp I} - (\dot{E}_5 - \dot{E}_{4a})$
IC	$\dot{E}_{13} - \dot{E}_{14}$	$\dot{E}_6 - \dot{E}_5$	$(\dot{E}_{13} - \dot{E}_{14}) - (\dot{E}_6 - \dot{E}_5)$
C-II	$\dot{W}_{comp II}$	$\dot{E}_7 - \dot{E}_6$	$\dot{W}_{comp II} - (\dot{E}_7 - \dot{E}_6)$
Cl-II	$\dot{E}_{11} - \dot{E}_{12}$	$\dot{E}_8 - \dot{E}_7$	$(\dot{E}_{11} - \dot{E}_{12}) - (\dot{E}_8 - \dot{E}_7)$
Pump	\dot{W}_{pump}	$\dot{E}_9 - \dot{E}_8$	$\dot{W}_{pump} - (\dot{E}_9 - \dot{E}_8)$

C. EXERGOECONOMIC ANALYSIS

The exergoeconomic analysis involves both exergy and economic inputs for each of the cycle unit. The exergoeconomic analysis can, in due course, be used as a tool to optimize the system's cost as the analysis goes through each unit and stream of the cycle. By the end of the exergoeconomic analysis, each of the cycle units and streams' contribution to the final product's cost is quantified. Note that the main final product of the hybrid cycle under this study is power production.

Assuming a cycle unit that receives heat and generates work, the following general cost rate balance equation is applied to its inlet and outlet streams [20]:

$$\dot{C}_{q,k} + \sum_i \dot{C}_{i,k} + \dot{Z}_k = \sum_e \dot{C}_{e,k} + \dot{C}_{w,k} \quad (7)$$

Where $\dot{C}_{q,k}$ is the cost rate associated with thermal energy, $\dot{C}_{i,k}$ and $\dot{C}_{e,k}$ are the cost rates associated with the inlet and outlet streams of a cycle unit, respectively and $\dot{C}_{w,k}$ is the cost rate associated with power. All previous cost rates are in units of (\$/hr). The above equation states that, for a unit or a system, the total cost of exergy of exiting streams is equal to the total spending to acquire them. In other words, the cost rate of a product is equal to the overall rate of spending utilized to generate that product. The cost per unit exergy (c) of a cycle unit in (\$/GJ) is calculated by dividing the stream's exergy cost rate \dot{C} by its exergy \dot{E} as per the following relationship:

$$c_k (\$/GJ) = \left(\frac{\dot{C}_k}{\dot{E}_k} \right) \quad (8)$$

Evaluating the cost of a power cycle involves accounting for capital, operating, and maintenance charges expended to produce the cycle's product. Capital costs account for expenses related to plant construction and purchase values of its equipment [21] while operating and maintenance costs represent expenses related to power, raw materials, fuel, manpower, ...etc. During the lifetime of a plant, the cost of a particular resource or commodity, such as fuel, usually varies from one point in time to another. Therefore, levelized costs are utilized in assessing the cycle under study [22].

The capital, operational, and maintenance costs are accounted for by the following equation [20, 23]:

$$\dot{Z}_k (\$/h) = (Z_k \cdot CRF) \left(\frac{\varphi}{\tau} \right) \quad (9)$$

Where φ is the plant maintenance factor, and τ is the annual operational availability of the plant in (hr/year). For the purpose of this study, the plant maintenance factor is assumed 1.06, and the annual availability of the plant for operations is assumed 8,000 hours per year [24]. The acronym CRF in the above equation is the capital recovery factor. The value of CRF accounts for three kinds of costs; the hourly capital investment cost, the operational cost, and maintenance cost. CRF is calculated by the following equation [20]:

$$CRF = \frac{i \cdot (1+i)^N}{(1+i)^N - 1} \quad (10)$$

The letter i in the above equation refers to the interest rate per year and is assumed a value of 5%, and the letter N is the plant lifetime in years and is assumed 20 years. To fit the original capital cost of equipment to the present time, the chemical engineering plant cost index [25] is utilized to convert the original cycle unit capital cost to reflect the year 2020 cost of that equipment. The following relationship is utilized for the fit:

$$Z_{k,Present} = Z_{k,original} \left(\frac{PCI_{Present}}{PCI_{original}} \right) \quad (11)$$

Where $PCI_{Present}$ is the cost value at the present time and awarded a value of 567.5 and $PCI_{original}$ is the equipment cost value equation at the original time. The capital cost of a cycle unit, Z_k for the proposed hybrid cycle equipment is shown in Table 6 [26, 27].

Table 6: Capital cost equations for the proposed hybrid units

Unit	Capital Cost of Unit (Z_k), (\$)	Ref.
ASU	$Z_{ASU,ref} \left(\frac{\dot{m}_{air,ASU}}{\dot{m}_{air,ASU,ref}} \right)^{0.6}$ $Z_{ASU,ref} = \$ 1.001 \times 10^8, \dot{m}_{air,ASU,ref} = 100 \left(\frac{kg}{s} \right)$	[28]
Comb	$\left(\frac{46.08\dot{m}_{10}}{0.995 - P_1/P_{10}} \right) (1 + \exp(0.0187T_1 - 26.4))$	[29]
CSP HX	$309.14(A_{CSP HX}^{0.85})$	[30]
Turb	$479.34 \left(\frac{\dot{m}_1}{0.92 - \eta_{turb}} \right) \ln(P_1/P_2) [1 + \exp(0.036T_1 - 54.4)]$	[31]
Rec	$2681(A_{recup}^{0.59})$	[32]
CI-I	$2143(A_{cooler I}^{0.514})$	[32]
C-I	$71.1 \left(\frac{\dot{m}_5}{0.92 - \eta_{comp I}} \right) [(PR)(\ln(PR))]$	[31]
IC	$2143(A_{intercooler}^{0.514})$	[32]
C-II	$71.1 \left(\frac{\dot{m}_6}{0.92 - \eta_{comp II}} \right) [(PR)(\ln(PR))]$	[31]
CI-II	$2143(A_{cooler II}^{0.514})$	[32]
Pump	$32 \times 0.435 \dot{m}_8^{0.55} \Delta P^{0.55} \left(\frac{\eta_{pump}}{\eta_{pump} - 1} \right)^{1.05}$	[33]

Table 7: Exergy cost balance for the CSP configuration

Unit	Exergy Cost Rate Balance	Auxiliary Equation
CSP HX	$\dot{C}_1 = \dot{C}_{10} + \dot{C}_{molten\ salt} + \dot{Z}_{CSP\ HX}$	$c_{molten\ salt} = 14.986 \left(\frac{\$/GJ} \right)$ [34]
Turb	$\dot{C}_2 + \dot{C}_{W,turb} = \dot{C}_1 + \dot{Z}_{turb}$	$c_1 = c_2$
Rec	$\dot{C}_{10} + \dot{C}_3 = \dot{C}_2 + \dot{C}_9 + \dot{Z}_{recup}$	$c_3 = c_2$
CI-I	$\dot{C}_4 + \dot{C}_{16} = \dot{C}_3 + \dot{C}_{15} + \dot{Z}_{cooler\ I}$	$c_3 = c_4$
C-I	$\dot{C}_5 = \dot{C}_4 + \dot{C}_{W,comp\ I} + \dot{Z}_{comp\ I}$	$c_{w,comp\ I} = c_{w,turb}$
IC	$\dot{C}_6 + \dot{C}_{14} = \dot{C}_5 + \dot{C}_{13} + \dot{Z}_{intercooler}$	$c_5 = c_6$
C-II	$\dot{C}_7 = \dot{C}_6 + \dot{C}_{W,comp\ II} + \dot{Z}_{comp\ II}$	$c_{w,comp\ II} = c_{w,turb}$
CI-II	$\dot{C}_8 + \dot{C}_{12} = \dot{C}_7 + \dot{C}_{11} + \dot{Z}_{cooler\ II}$	$c_7 = c_8$
Pump	$\dot{C}_9 = \dot{C}_8 + \dot{C}_{W,pump} + \dot{Z}_{pump}$	$c_{w,pump} = c_{w,turb}$

The total capital cost in (\$) is calculated by:

$$Z_{total} = \sum_{k=1}^n Z_k, n = \text{total number of equipment} \quad (12)$$

Applying equation (7) to all cycle units and their supplementary auxiliary equations leads to the formation of a system of linear equations representing the whole cycle, mathematically. To successfully solve the system's mathematical representation, the number of equations and unknowns must be equal. However, the number of unknowns is larger than the number of equations at this stage. Hence, auxiliary equations are utilized to bridge the gap between the number of equations and unknowns for the system in hand. Tables 7 and 8 show the system's cost balance equations and their subsequent auxiliary equations for both configurations. The product stream cost rate of the cycle is calculated utilizing the specific exergy costing (SPECOC) approach [35].

Table 8: Exergy cost balance for the OC configuration

Cycle Unit	Exergy Cost Rate Balance	Auxiliary Equation
ASU	$\dot{C}_{19} + \dot{C}_{20} = \dot{C}_{18} + \dot{C}_{WASU} + \dot{Z}_{ASU}$	$c_{W,ASU} = c_{w,turb}$ $\dot{C}_{19} = 0.2658 \dot{C}_{20}$
Comb	$\dot{C}_1 = \dot{C}_{10} + \dot{C}_{17} + \dot{C}_{19} + \dot{Z}_{comb}$	---
Turb	$\dot{C}_2 + \dot{C}_{Wturb} = \dot{C}_1 + \dot{Z}_{turb}$	$c_1 = c_2$
Rec	$\dot{C}_3 + \dot{C}_{10} + \dot{C}_{21} = \dot{C}_2 + \dot{C}_{9a} + \dot{C}_{20} + \dot{Z}_{recup}$	$c_3 = c_2$ $c_{20} = c_{21}$
Cl-I	$\dot{C}_4 + \dot{C}_{16} = \dot{C}_3 + \dot{C}_{15} + \dot{Z}_{cooler I}$	$c_3 = c_4$
C-I	$\dot{C}_5 = \dot{C}_{4a} + \dot{C}_{Wcomp I} + \dot{Z}_{comp I}$	$c_{w,comp I} = c_{w,turb}$
IC	$\dot{C}_6 + \dot{C}_{14} = \dot{C}_5 + \dot{C}_{13} + \dot{Z}_{intercooler}$	$c_5 = c_6$
C-II	$\dot{C}_7 = \dot{C}_6 + \dot{C}_{Wcomp II} + \dot{Z}_{comp II}$	$c_{w,comp II} = c_{w,turb}$
Cl-II	$\dot{C}_8 + \dot{C}_{12} = \dot{C}_7 + \dot{C}_{11} + \dot{Z}_{cooler II}$	$c_7 = c_8$
Pump	$\dot{C}_9 = \dot{C}_8 + \dot{C}_{Wpump} + \dot{Z}_{pump}$	$c_{w,pump} = c_{w,turb}$
SP-I	$\dot{C}_9 = \dot{C}_{9a} + \dot{C}_{9b}$	$\dot{C}_{9a} = \left(\frac{\dot{m}_{Rec,CO_2}}{\dot{m}_{CO_2}}\right) \dot{C}_9$
SP-II	$\dot{C}_4 = \dot{C}_{4a} + \dot{C}_{4b}$	$\dot{C}_{4a} = \left(\frac{\dot{m}_{Exp,CO_2}}{\dot{m}_{total}}\right) \dot{C}_4$

For the OC configuration, the unit cost of the natural gas (c_f) is \$3 per GJ of fuel. Assuming an escalation rate of $r_n = 6\%$ for the first quarter of operation [29], the levelized cost rate of stream 17 (fuel) supplied to the combustion chamber is calculated as:

$$\dot{C}_{17} = 3600 \times \dot{n}_f c_f \overline{LHV} N_h (1 + r_n)^5 CRF \times \frac{k_f (1 - k_f^{nt})}{1 - k_f} ; k_f = \frac{1+r_n}{1+i} \quad (13)$$

Where \dot{n}_f is the mole flowrate of fuel (kmol/h) and N_h is the annual operational availability of the plant in (h/year). The average fuel lower heating value (\overline{LHV}) in the above equation is 802,361 kJ/kmol.

D. HYBRID CYCLE PERFORMANCE PARAMETERS ANALYSIS

Sound performance measurement requires to assign specific criteria of performance. Hence, exergy efficiency (η_{ex}), energy

efficiency (η_{th}) and total product unit cost ($c_{p,total}$) are employed to perform the hybrid cycle performance in this study. The energy efficiency, according to the first law of thermodynamics, is the ratio of useful output energy to the input energy of the cycle and is determined as:

$$\eta_{th} = \frac{\dot{W}_{net}}{\dot{Q}_{in}} \quad (14)$$

The exergy efficiency, according to the second law of thermodynamics, is calculated as [20]:

$$\eta_{ex} = \frac{\dot{E}_{Product}}{\dot{E}_{Fuel}} = 1 - \frac{\dot{E}_{D,total}}{\dot{E}_{Fuel}} \quad (15)$$

Where $\dot{E}_{D,total}$ is the sum of all exergy destructed in all cycle units.

The total product unit is calculated by [24]:

$$c_{p,total} = \frac{\sum_{k=1}^{NK} \dot{Z}_{k,i} + \sum_{i=1}^{NF} \dot{C}_{Fuel,i}}{\sum_{i=1}^{NP} \dot{E}_{Product,i}} \quad (16)$$

Where \dot{C}_{Fuel} is the fuel exergy stream cost and $\dot{E}_{Product}$ is the product exergy stream. NK is the number of the cycle units, NF is the number of fuels to the cycle, and NP is the number of products of the cycle. The levelized cost of electricity (LCOE) in (\$/kWh) is calculated by dividing the total capital investment cost of the cycle units and the cost of fuel input by the net power produced from the hybrid cycle [36]:

$$LCOE = \frac{\sum_{k=1}^{NK} \dot{Z}_k + \dot{C}_{Fuel}}{\dot{W}_{net}} \quad (17)$$

The average cost per unit exergy of fuel in (\$/GJ) is calculated by [20]:

$$c_{F,k} = \dot{C}_{F,k} / \dot{E}_{F,k} \quad (18)$$

The cost rate of exergy destruction in (\$/h) is calculated by [20]:

$$\dot{C}_{D,k} = c_{F,k} \cdot \dot{E}_{D,k} \quad (19)$$

The cost rate of exergy loss in (\$/h) is calculated by [20]:

$$\dot{C}_{L,k} = c_{F,k} \cdot \dot{E}_{L,k} \quad (20)$$

The exergoeconomic factor is calculated by [20]:

$$f_k = \dot{Z}_k / (\dot{Z}_k + \dot{C}_{D,k} + \dot{C}_{L,k}) \quad (21)$$

The relative cost difference (r_k) is calculated by [20]:

$$r_k = \frac{1 - \epsilon_k}{\epsilon_k} + \frac{\dot{Z}_k}{c_{F,k} \dot{E}_{P,k}} \quad (22)$$

The energy, exergy, and exergoeconomic equations representing the hybrid cycle are modeled using the EES software.

RESULTS AND DISCUSSION

To analyze the impact of the main cycle thermodynamic parameters, a parametric study is performed, and its results are analyzed. The hybrid's model design input parameters for the base case of the CSP and OC standalone configurations are presented in Table 9. The inlet parameters apply for both cycle configurations.

Table 9: Model main input parameters

Parameter	Value
Dead state temperature (°C)	25
Dead state pressure (bar)	1
Turbine isentropic efficiency (%)	90
Turbine inlet temperature (°C)	700
Turbine inlet pressure (bar)	300
Turbine pressure ratio (--)	10
Turbine inlet mass flowrate (kg/s)	125
Minimum compressor inlet temperature (°C)	20
Compressor inlet pressure (bar)	28.8
Compressor pressure ratio (--)	2.78
Compressor isentropic efficiency (%)	85
Pump isentropic efficiency (%)	80
Fractional pressure drop (%)	2
Cooler pinch point temperature (°C)	5

A. EXERGY AND EXERGEOECONOMIC ANALYSIS

The main model output performance parameters are presented in Table 10 for CSP configurations and Table 11 for the OC configuration. A comparison between the two standalone configurations reveals that the produced net power output for both configurations is approximately the same at 30 MW. Although the second law of thermodynamics efficiency is within the same range, in terms of the first law of thermodynamics efficiency, the OC configuration is higher by 7%. The total unit product cost (\$/GJ) for the CSP standalone configuration is approximately twice that of the OC configuration. This means that fossil fuel combustion is less expensive than providing heat through solar energy. It is worth mentioning that the combustion chamber and the ASU supply the OC configuration heat, while heat supplied to the CSP configuration is provided by the CSP plant. The CSP plant is much more complicated and hence costs more. Finally, the unit cost of electricity in units of (Cent/kWh) is 9.8 for the CSP standalone configuration and 6.1 for the OC configuration.

The steady-state operations thermodynamic parameters of the base case for both configurations are displayed in Figure 6 and Figure 7 of Annex B. In addition to temperature, the mass, exergy, and cost flow rates of the cycle units are shown in both figures.

In exergoeconomic evaluation of thermal systems, certain quantities known as the thermo-economic variables play a vital role and give insight on the optimization potential. Such variables are useful for applications in existing power plants, as

they help identify improvements realized by increasing or decreasing the unit exergy cost. They also pinpoint the exergy destruction locations in the system under examination. These variables are the cost rate of exergy destruction ($\dot{C}_{D,k}$), relative cost difference (r_k) and exergoeconomic factor (f_k). The costs associated with exergy destruction and losses in a component are hidden costs and can be revealed only using exergoeconomic analysis.

Table 10: Model main output parameters for CSP configuration

Parameter	Value
Net power (MW)	29.52
First law efficiency (%)	40.55
Second law efficiency (%)	56.92
Total unit product cost (\$/GJ)	27.55
Unit cost of electricity (Cent/kWh)	9.8

Table 11: Model main output parameters for OC configuration

Parameter	Value
Net power (MW)	30.73
First law efficiency (%)	47.38
Second law efficiency (%)	54.72
Total unit product cost (\$/GJ)	12.98
Unit cost of electricity (Cent/kWh)	6.1

A cycle unit with a high value of $\dot{C}_{D,k} + \dot{Z}_k$ means that this unit is important and more attention towards it is recommended. The exergoeconomic factor is the contribution of non-exergy related cost to the total cost of the system units and is used to identify units with a significant cost. A low value of f_k for a unit suggests that cost savings for the entire system might be achieved by improving this unit's efficiency. This means reducing exergy destruction is essential, even if it means that this unit's capital and operating cost increases. While a higher value of f_k suggests a decrease in the unit's capital cost is beneficial even if at the expense of exergetic efficiency. The relative cost difference (r_k) for a unit represents the average cost per unit exergy between fuel and product, and it is useful to evaluate and optimize a system unit [29]

Table 12 and Table 13 show the results obtained from the exergoeconomic analysis of the proposed CSP and OC standalone configurations, respectively. The two tables summarize the base case values of exergy destruction, exergy efficiency, and exergoeconomic parameters of both configurations' major units. For the CSP case, it shows that the main CSP heat exchanger has the highest value of $\dot{C}_{D,k} + \dot{Z}_k$ along with the lowest value of f_k compared to other units, and then it is followed by the CSP recuperator. This is attributed to the high irreversibility arising from the high temperature difference existing in these units. Therefore, the two units are considered the most critical components from the thermo-economic perspective for the CSP configuration. The low value of f_k for the unit shows that the exergy destruction dominates the

cost associated with this unit while the remaining part is caused by the \dot{Z}_k value. So, it can be concluded that reducing the exergy destruction in the CSP main heat exchanger and the recuperator units could be cost-effective for the entire cycle, even if it increases the unit investment costs. Therefore, for exergoeconomic performance enhancement, using a recuperator with higher efficiency is recommended.

For the OC configuration, the highest value of $\dot{C}_{D,k} + \dot{Z}_k$ and the lowest value of f_k belongs to the combustor with exergetic efficiency of 76%. The ASU has the second highest $\dot{C}_{D,k} + \dot{Z}_k$ value. Therefore, replacing the ASU with a lower purchasing cost unit is recommended for an overall exergoeconomic performance enhancement for this configuration.

Table 12: Results of the exergoeconomic analysis for the base case of CSP configuration

Cycle Unit	ϵ_k (%)	$\dot{C}_{D,k}$ (\$/h)	\dot{Z}_k (\$/h)	$\dot{C}_{D,k} + \dot{Z}_k$ (\$/h)	r_k (%)	f_k (%)
CSP HX	90.46	669.9	0.3083	670.2	10.55	0.046
Turb	95.33	164.6	71.61	236.21	7.029	30.32
Rec	62.05	589.7	0.3977	590.1	8.078	0.067
Cl-I	96.11	75.93	0.941	76.87	1.61	1.224
C-I	87.56	24.47	5.818	30.29	18.12	19.21
IC	96.56	76.01	1.081	77.1	1.465	1.402
C-II	90.71	20.79	4.569	25.36	11.72	18.02
Cl-II	94.26	138.9	1.181	140.1	1.971	0.844
Pump	76.63	85.92	2.198	88.11	3.427	2.949

Table 13: Results of the exergoeconomic analysis for the base case of OC configuration

Cycle Unit	ϵ_k (%)	$\dot{C}_{D,k}$ (\$/h)	\dot{Z}_k (\$/h)	$\dot{C}_{D,k} + \dot{Z}_k$ (\$/h)	r_k (%)	f_k (%)
Comb	76.48	1076	3.947	1079.95	30.87	0.3655
Turb	97.38	119.9	69.99	189.9	8.791	36.86
Rec	95.21	222.7	0.5323	223.2	14.39	0.2384
Cl-I	96.4	43.2	0.9684	44.17	1.473	2.192
C-I	89.53	19.31	4.535	23.85	20.35	19.01
IC	96.57	45.9	1.066	46.9	1.475	2.271
C-II	91.82	17.25	4.025	21.28	14.58	18.91
Cl-II	94.19	85.47	1.164	86.63	2.032	1.344
Pump	77.3	50.8	2.17	52.9	3.373	4.097
ASU	93.93	69.98	572.5	642.5	60.1	89.25

B. PARAMETRIC ANALYSIS

The influence of specific thermodynamic parameters on the cycle performance is important. Therefore, energetic, exergetic, and economic parametric analysis is performed for such parameters. The parametric study is conducted under variable operating conditions while keeping all other parameters unchanged based on the mentioned assumptions and values provided in Table 6. The thermodynamic parameters considered for this study are the turbine's inlet pressure (P_1), the turbine's inlet temperature (T_1), the turbine's outlet pressure (P_2). On the

other hand, the performance parameters selected to assess the proposed system are the exergy efficiency and the levelized cost of electricity.

Figure 8a and Figure 8b of Annex C demonstrate the effect of the turbine inlet pressure on the proposed CSP and OC configurations' performance, respectively. Since the circulating mass flow rate of CO_2 is kept constant, the net power delivered for both configurations increases with η_{ex} . These results indicate that increasing T_1 is conducive to improving the thermodynamic and exergoeconomic performances of both configurations. It is worth mentioning that the increment of the net produced power is dominant compared with the increase in the capital installment cost, which in turn lowers the LCOE with the increase in the turbine inlet temperature. The total capital installment and maintenance cost of the two configurations (Z_{tot}) decreases with the rise in T_1 due to the decrements of the Z_k values of the turbine, compressors, and the recuperator units, which account for the main portion of Z_{tot} . Also, fuel cost ($\dot{C}_{molten\ salt}$) keeps constant when T_1 changes. In addition, the $c_{p,total}$ decreases with an increasing T_1 .

Similar trends were obtained when the turbine inlet pressure is increased from 24 MPa to 36 MPa for both configurations, as presented in Figure 9 of Annex C. It is known that the compressor's power consumption is dominant in comparison with that of the pump. Therefore, the net power output (W_{net}) is mainly related to the compressors' power consumption and the turbine's output power. Due to a constant turbine outlet pressure, both the turbine's output power and the compressors' power consumption increase with increased turbine inlet pressure. Note that the CSP main heat exchanger's outlet temperature is kept constant (700°C) as P_1 increases. W_{net} of both configurations increases with P_1 when the increment of the turbine's output work is larger than that of the compressors; otherwise, W_{net} decreases.

As shown in Figure 10 of Annex C, the increase in net power decreases LCOE for both configurations. In addition, for both configurations, the decrease in the turbine's outlet pressure reduces both turbine's produced power and compressor's power consumption. For the CSP configuration, the reduction in P_2 results in a decrease in the capital and operating cost, leading to a decrease in LCOE. Unfortunately, this is not the case for the OC configuration. As P_2 increases, LCOE first decreases and then increases. However, the same P_2 increase keeps the exergy efficiency constant at first before causing it to decrease. This indicates that there is an optimum turbine outlet pressure with which the total unit product cost is minimized for this particular configuration. The increase in the LCOE is attributed to the increase in the combustor, ASU, and recuperator capital installment cost, which is dominant in determining the total capital installment and maintenance cost of the OC configuration.

CONCLUSION

Although both configurations obtained similar power output and exergy efficiency, the thermal efficiency was higher for the OC configuration. The total product cost in (\$/GJ) for the OC

was half of that for the CSP. The unit cost of electricity in (Cent/kWh) for the CSP standalone configuration is approximately 60% higher than that of the OC configuration.

In the CSP configuration, the main heat exchanger and the recuperator are the most significant units to consider for savings. Therefore, reducing the exergy destruction in the CSP main heat exchanger and the recuperator units could be cost-effective for the entire cycle, even if this would increase the component investment costs. Therefore, for exergoeconomic performance enhancement, using a recuperator with higher efficiency is recommended. On the other hand, for the OC configuration, the combustor and ASU are the most critical units to consider for savings. Therefore, a replacement for the ASU unit with a lower purchasing cost is recommended for overall exergoeconomic performance enhancement.

The parametric study results showed that increasing the turbine's inlet temperature is conducive to improving both configurations' thermodynamic and exergoeconomic performances. Similar trends were also obtained for the turbine inlet pressure for both configurations.

Future work includes conducting an optimization study on the proposed hybrid cycle. Also, conducting another exergoeconomic analysis while the proposed hybrid is powered simultaneously by CSP and OC heat sources is considered for the next research topic.

NOMENCLATURE

c_f	Unit cost of the natural gas [\$/GJ]
$c_{F,k}$	Average cost per unit exergy of fuel for the k^{th} component [\$/GJ]
c_k	Cost per unit exergy for the k^{th} component [\$/GJ]
$\dot{C}_{D,k}$	Cost rate of exergy destruction for the k^{th} component [\$/h]
$\dot{C}_{e,k}$	Cost rate associated with the outlet streams of a unit for the k^{th} component [\$/h]
$\dot{C}_{i,k}$	Cost rate associated with the inlet streams of a unit for the k^{th} component [\$/h]
$\dot{C}_{L,k}$	Cost rate associated with exergy loss for k^{th} component [\$/hr]
$\dot{C}_{q,k}$	Cost rate associated with thermal energy for the k^{th} component [\$/h]
$\dot{C}_{w,k}$	Cost rate associated with power for the k^{th} component [\$/h]
$c_{p,total}$	Total unit cost of the product [\$/GJ]
\dot{E}_D	Exergy destruction [W]
E_e	Exergy of the exit [W]
E_i	Exergy of the inlet [W]
$\dot{E}_{Fuel,CSP}$	Exergy of the fuel for the CSP configuration [W]
$\dot{E}_{Fuel,i}$	Exergy of the fuel for the i^{th} component [W]
$\dot{E}_{Fuel,OC}$	Exergy of the fuel for the OC configuration [W]
$\dot{E}_{Product,i}$	Exergy of the product for the i^{th} component [W]
f_k	Exergoeconomic factor for the k^{th} component
h_i	Enthalpy at the inlet [J/Kg CO ₂]
h_{out}	Enthalpy at the Outlet [J/Kg CO ₂]

h_o	Enthalpy at the Outlet [J/Kg CO ₂]
k_f	Exergoeconomic factor for the k^{th} component
MW_{CH_4}	Molecular weight of methane
\dot{m}_e	Mass flowrate at the exit [Kg/s]
\dot{m}_I	Mass flowrate at the inlet [Kg/s]
\dot{n}_f	Mole flowrate of fuel [kmol/h]
N_h	The annual operational availability of the plant [h/year]
$PCI_{original}$	Equipment cost value at the original time
$PCI_{present}$	Equipment cost value at the present time
\dot{Q}_{CSP}	Heat transfer supplied by CSP main heat exchanger [W]
\dot{Q}_i	Heat transfer for the i^{th} component [W]
\dot{Q}_{in}	Heat input [W]
r_k	Relative cost difference
r_n	Escalation rate
T_s	Heat source temperature [K]
T_0	Dead state temperatures [K]
W	Work [W]
W_{net}	Network [W]
Z_k	Capital cost of a cycle unit for the k^{th} component [\$/h]
$Z_{present}$	Capital cost of a cycle unit at the present time [\$/h]
$Z_{original}$	Capital cost of a cycle unit at the original time [\$/h]
Z_{total}	Total capital cost [\$/h]
\dot{Z}_k (\$/h)	Capital, operational, and maintenance cost rate for the k^{th} component [\$/h]
ϵ_k	Efficiency according to the second law of thermodynamics for the k^{th} component
η_{ex}	Exergy efficiency
η_{th}	Energy efficiency according to the first law of thermodynamics
μ	Chemical potential
τ	The annual operational availability of the plant [h/year]
φ	The plant maintenance factor

REFERENCES

- Administration, U.E.I., *Annual energy outlook 2018 with projections to 2050*. 2018.
- Syblík, J., et al., *Analysis of supercritical CO₂ Brayton power cycles in nuclear and fusion energy*. Fusion Engineering and Design, 2019. 146: p. 1520-1523.
- Kacludis, A., et al., *Waste heat to power (WH2P) applications using a supercritical CO₂-based power cycle*, in *Power-Gen International*. 2012. p. 11-13.
- Brun, K., P. Friedman, and R. Dennis, *Fundamentals and applications of supercritical carbon dioxide (sCO₂) based power cycles*. 2017: Woodhead publishing.
- Allam, R., et al., *Demonstration of the Allam Cycle: an update on the development status of a high efficiency supercritical carbon dioxide power process employing full carbon capture*. Energy Procedia, 2017. 114: p. 5948-5966.
- Castle, W., *Air separation and liquefaction: recent developments and prospects for the beginning of the new*

- millennium. *International Journal of Refrigeration*, 2002. 25(1): p. 158-172.
7. Allam, R., et al., *High efficiency and low cost of electricity generation from fossil fuels while eliminating atmospheric emissions, including carbon dioxide*. *Energy Procedia*, 2013. 37: p. 1135-1149.
 8. Allam, R.J., M. Palmer, and G.W. Brown, *System and method for high efficiency power generation using a carbon dioxide circulating working fluid*. 2013, Google Patents.
 9. Barba, F.C., et al., *A technical evaluation, performance analysis and risk assessment of multiple novel oxy-turbine power cycles with complete CO₂ capture*. *Journal of cleaner production*, 2016. 133: p. 971-985.
 10. Allam, R., et al. *The oxy-fuel, supercritical CO₂ Allam Cycle: New cycle developments to produce even lower-cost electricity from fossil fuels without atmospheric emissions*. in *ASME Turbo Expo 2014: Turbine Technical Conference and Exposition*. 2014. American Society of Mechanical Engineers.
 11. Demirbas, A., *Recent advances in biomass conversion technologies*. *Energy Edu Sci Technol*, 2000. 6: p. 19-41.
 12. Panwar, N., S. Kaushik, and S. Kothari, *Role of renewable energy sources in environmental protection: a review*. *Renewable Sustainable Energy Reviews*, 2011. 15(3): p. 1513-1524.
 13. Ordorica-Garcia, G., A.V. Delgado, and A.F. Garcia, *Novel integration options of concentrating solar thermal technology with fossil-fuelled and CO₂ capture processes*. *Energy Procedia*, 2011. 4: p. 809-816.
 14. Barlev, D., R. Vidu, and P. Stroeve, *Innovation in concentrated solar power*. *Solar energy materials and solar cells*, 2011. 95(10): p. 2703-2725.
 15. Mehos, M., et al., *Concentrating solar power Gen3 demonstration roadmap*. 2017: National Renewable Energy Laboratory, Golden, Colorado, USA.
 16. Louis, A.T. and T. Neises. *Analysis and Optimization for Off-Design performance of the recompression s-CO₂ cycles for high temperature CSP applications*. in *The 5th International Symposium-Supercritical CO₂ Power Cycles*. 2016.
 17. Peterseim, J.H., et al., *Concentrating solar power hybrid plants—enabling cost effective synergies*. *Renewable energy*, 2014. 67: p. 178-185.
 18. Alenezi, A. and J.S. Kapat. *Thermodynamic Analysis of sCO₂ Allam Cycle for Concentrated Solar Power Complemented with Oxy-Combustion*. in *AIAA Propulsion and Energy 2019 Forum*. 2019.
 19. Sharqawy, M.H. and S.M. Zubair, *On exergy calculations of seawater with applications in desalination systems*. *International Journal of Thermal Sciences*, 2011. 50(2): p. 187-196.
 20. Bejan, A., G. Tsatsaronis, and M.J. Moran, *Thermal design and optimization*. 1995: John Wiley & Sons.
 21. El-Halwagi, M.M., *Sustainable design through process integration: fundamentals and applications to industrial pollution prevention, resource conservation, and profitability enhancement*. 2017: Butterworth-Heinemann.
 22. Sayyaadi, H. and A. Saffari, *Thermoeconomic optimization of multi effect distillation desalination systems*. *Applied Energy*, 2010. 87(4): p. 1122-1133.
 23. Alharbi, S., M.L. Elsayed, and L. Chow. *Thermo-Economic Analysis of an Integrated Supercritical CO₂ Brayton Cycle and Multiple Effect Desalination Systems*. in *ASME 2018 International Mechanical Engineering Congress and Exposition*. 2018. American Society of Mechanical Engineers.
 24. Vieira, L.S., J.L. Donatelli, and M.E. Cruz, *Exergoeconomic improvement of a complex cogeneration system integrated with a professional process simulator*. *Energy Conversion and Management*, 2009. 50(8): p. 1955-1967.
 25. Ozcan, H. and I. Dincer, *Exergoeconomic optimization of a new four-step magnesium–chlorine cycle*. *international journal of hydrogen energy*, 2017. 42(4): p. 2435-2445.
 26. Marchionni, M., G. Bianchi, and S.A. Tassou, *Techno-economic assessment of Joule-Brayton cycle architectures for heat to power conversion from high-grade heat sources using CO₂ in the supercritical state*. *Energy*, 2018. 148: p. 1140-1152.
 27. Alharbi, S., M.L. Elsayed, and L.C. Chow, *Exergoeconomic analysis and optimization of an integrated system of supercritical CO₂ Brayton cycle and multi-effect desalination*. *Energy*, 2020: p. 117225.
 28. Ebrahimi, A., et al., *Energetic, exergetic and economic assessment of oxygen production from two columns cryogenic air separation unit*. *Energy*, 2015. 90: p. 1298-1316.
 29. Bejan, A. and G. Tsatsaronis, *Thermal design and optimization*. 1996: John Wiley & Sons.
 30. Schultz, K., et al., *Large-scale production of hydrogen by nuclear energy for the hydrogen economy*. 2003, GENERAL ATOMICS (US).
 31. Ghaebi, H., et al., *Energy, exergy and thermoeconomic analysis of a combined cooling, heating and power (CCHP) system with gas turbine prime mover*. *International Journal of Energy Research*, 2011. 35(8): p. 697-709.
 32. Guo-Yan, Z., W. En, and T. Shan-Tung, *Techno-economic study on compact heat exchangers*. *International journal of energy research*, 2008. 32(12): p. 1119-1127.
 33. El-Sayed, Y., *Designing desalination systems for higher productivity*. *Desalination*, 2001. 134(1-3): p. 129-158.
 34. Ma, Y., et al., *Optimal integration of recompression supercritical CO₂ Brayton cycle with main compression intercooling in solar power tower system based on exergoeconomic approach*. *Applied energy*, 2019. 242: p. 1134-1154.
 35. Lazzaretto, A. and G. Tsatsaronis, *SPECO: a systematic and general methodology for calculating efficiencies and costs in thermal systems*. *Energy*, 2006. 31(8-9): p. 1257-1289.
 36. Nami, H., S. Mahmoudi, and A. Nematii, *Exergy, economic and environmental impact assessment and optimization of a novel cogeneration system including a gas turbine, a supercritical CO₂ and an organic Rankine cycle (GT-HRSG/SCO₂)*. *Applied Thermal Engineering*, 2017. 110: p. 1315-1330.

ANNEX A

P-H DIAGRAMS FOR THE CSP AND OC STANDALONE CONFIGURATIONS

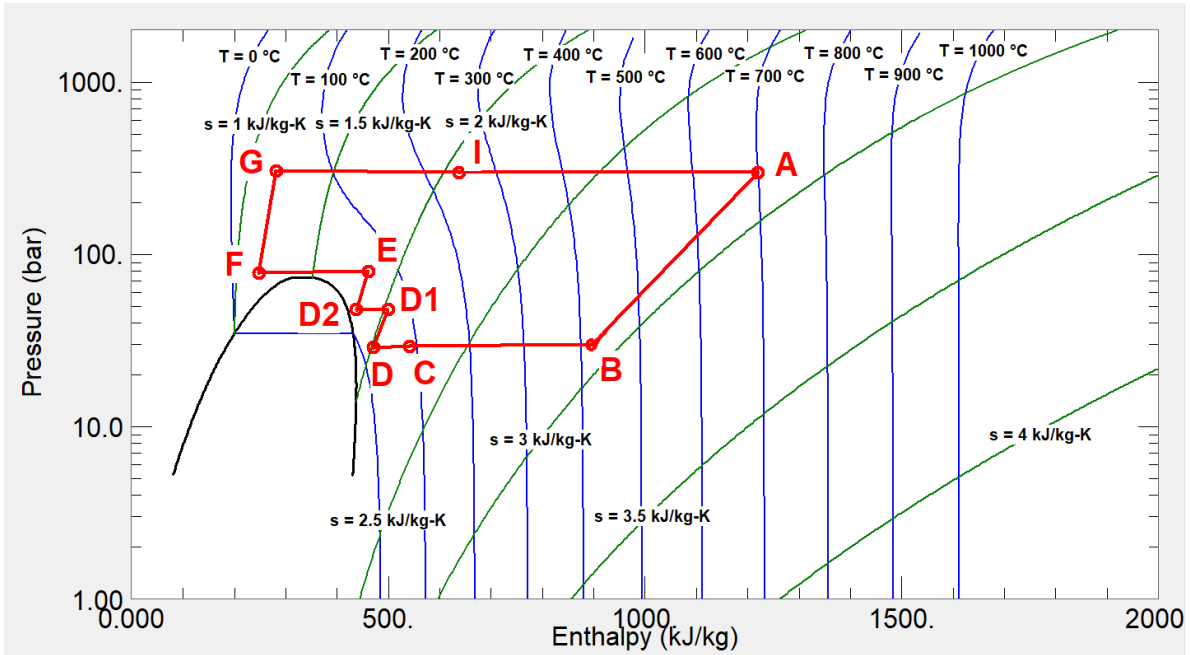


Figure 4: Pure CO₂ log P-h diagram of the CSP standalone configuration

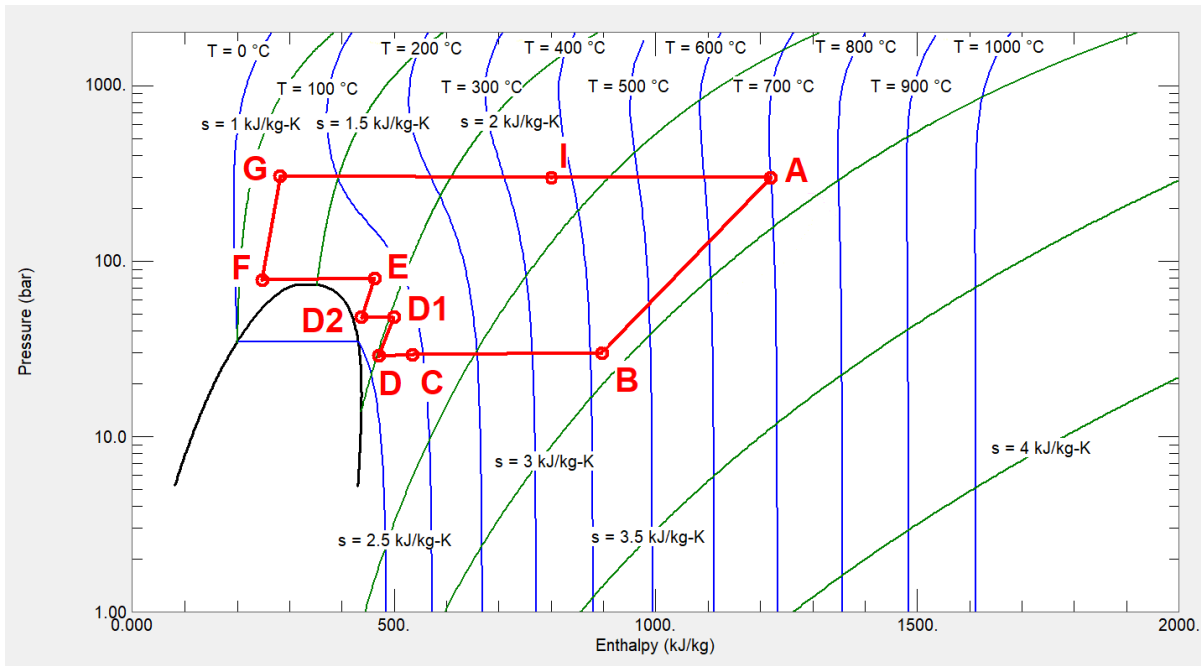


Figure 5: Pure CO₂ log P-h diagram of the OC standalone configuration

ANNEX B

STEADY STATE MASS, EXERGY, AND COST FLOWRATES FIGURES

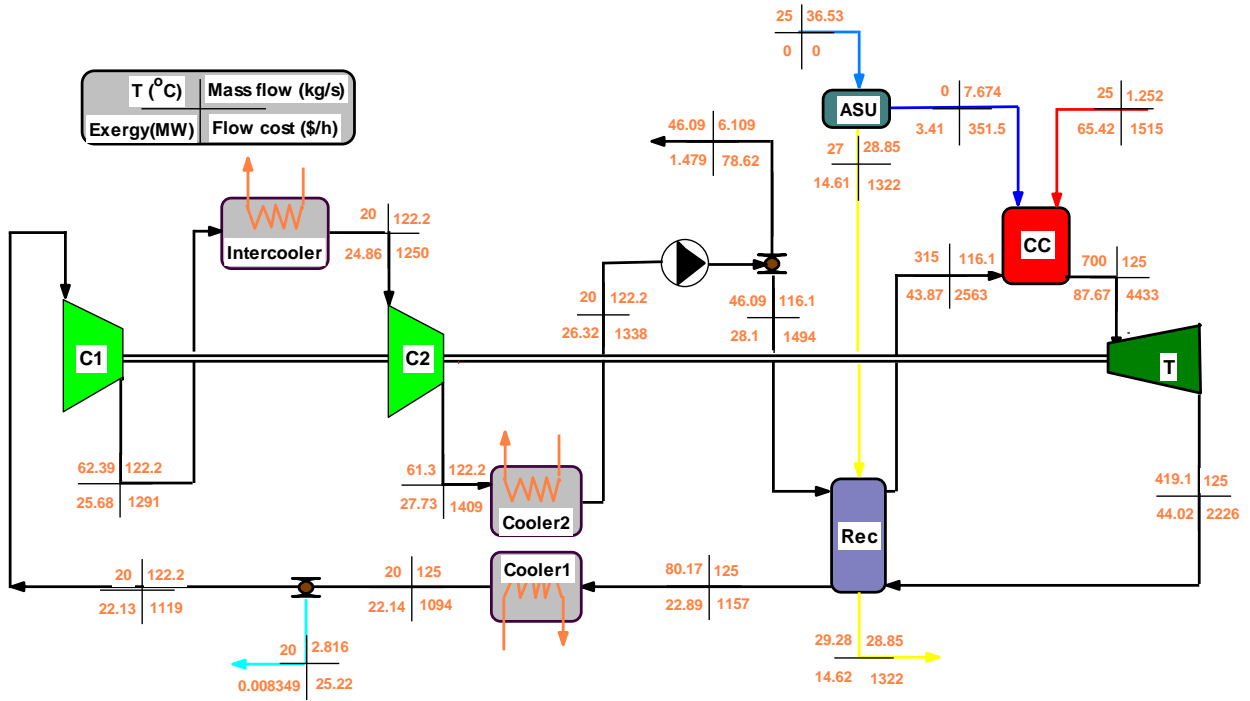


Figure 6: Mass, exergy, and cost flowrates of the hybrid cycle CSP standalone configuration

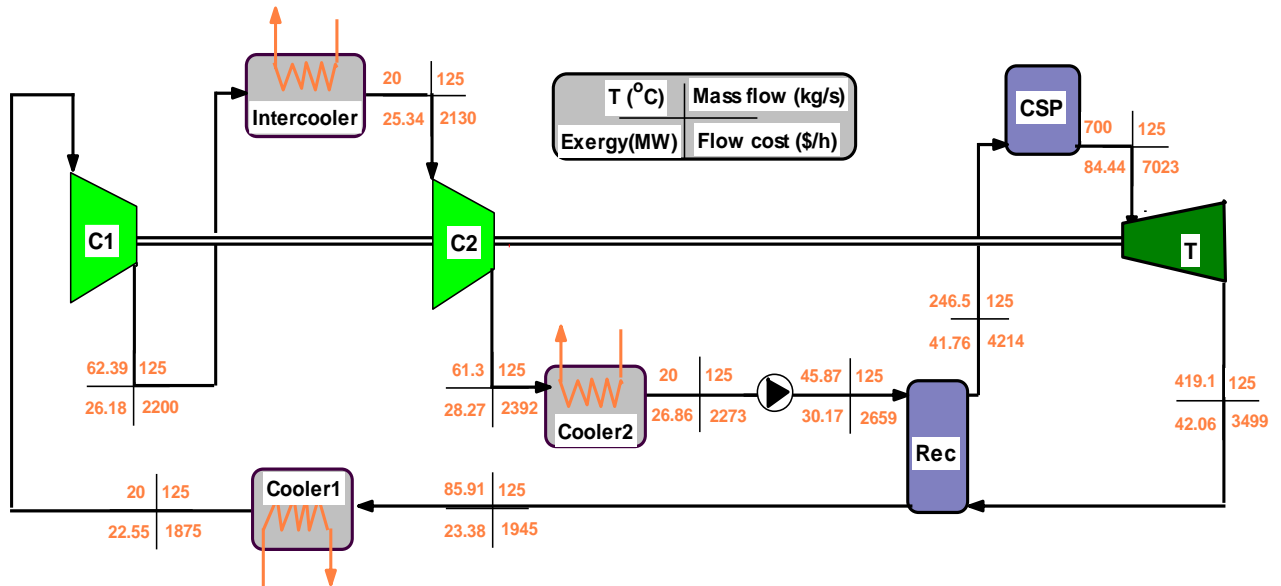


Figure 7: Mass, exergy, and cost flowrates of the hybrid cycle OC standalone configuration

ANNEX C:
PARAMETRIC STUDY FIGURES

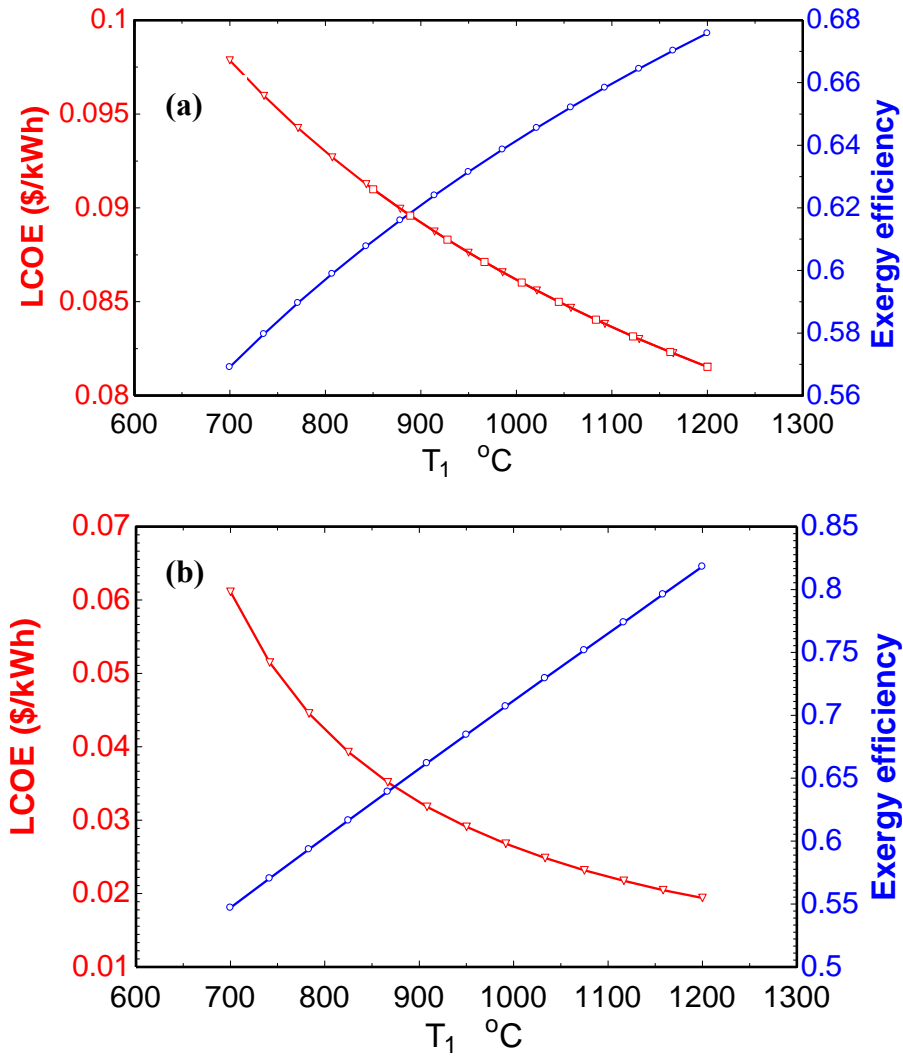


Figure 8: Variations of exergy efficiency and LCOE for (a) CSP and (b) OC configurations with turbine inlet temperature

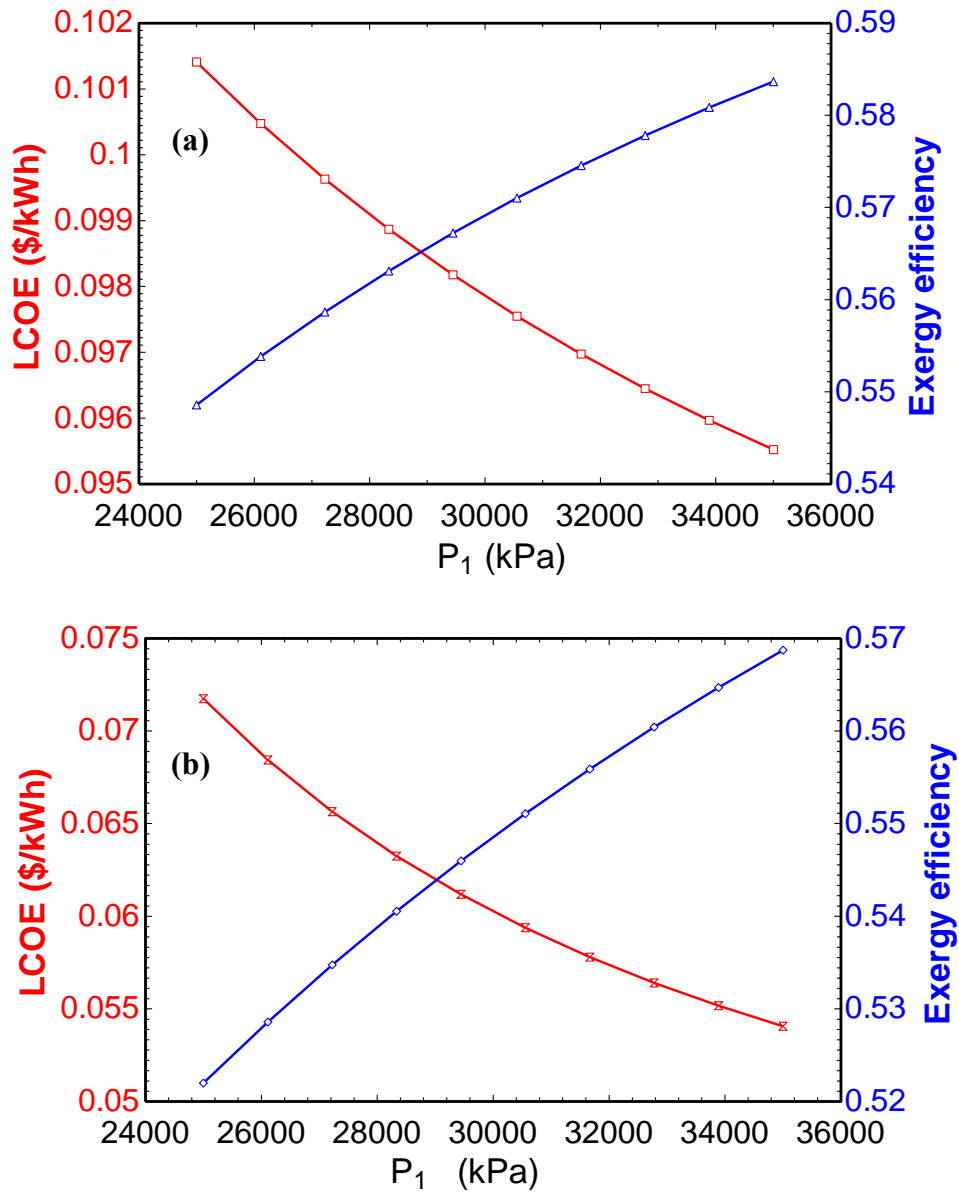


Figure 9: Variations of exergy efficiency and LCOE for (a) CSP and (b) OC configurations with turbine inlet pressure

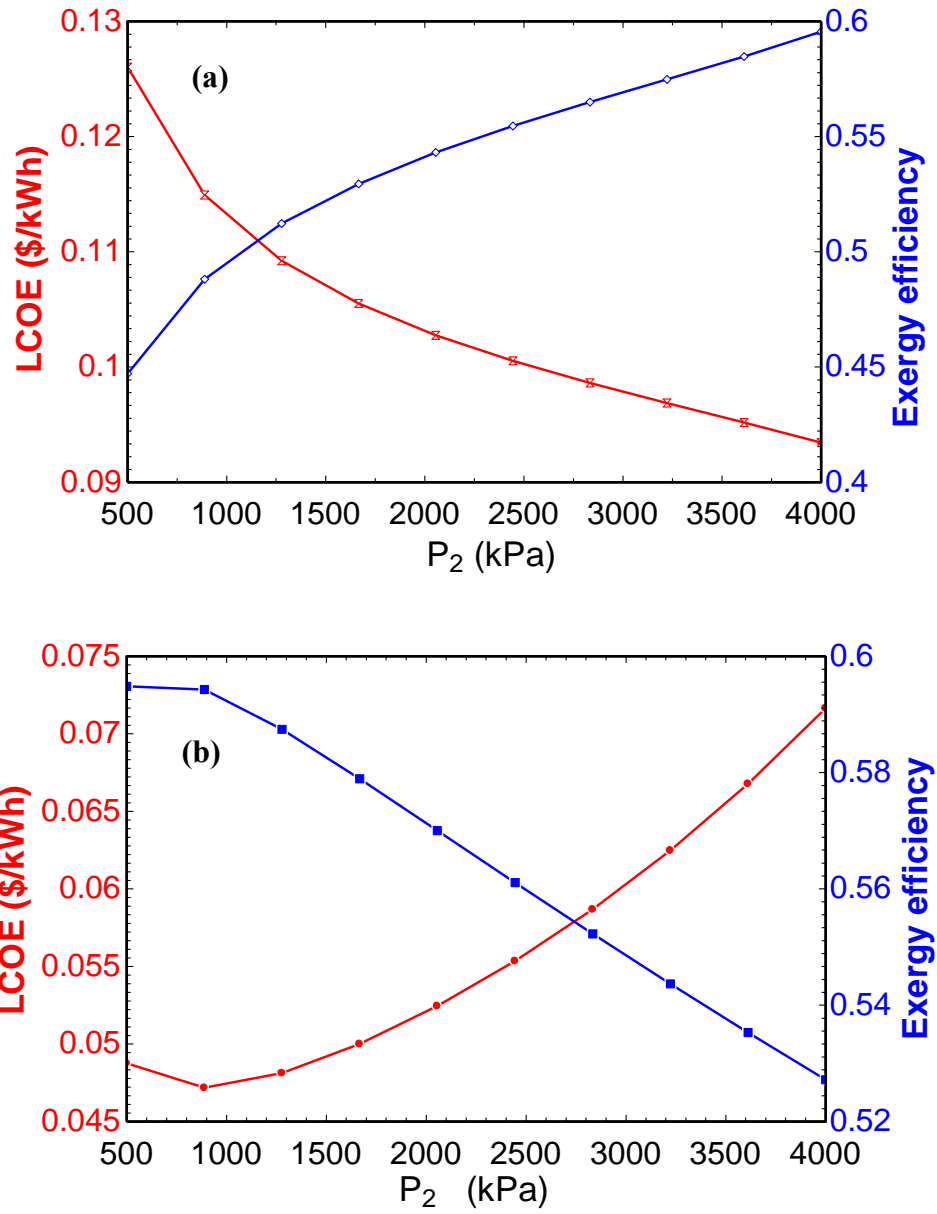


Figure 10: Variations of exergy efficiency and LCOE for (a) CSP and (b) OC configurations with turbine exit pressure

EFFECT OF THE AMBIENT TEMPERATURE ON THE PERFORMANCE OF SMALL SIZE sCO₂ BASED PULVERIZED COAL POWER PLANTS

Dario Alfani*

Politecnico di Milano
Milano, Italy
Email: dario.alfani@polimi.it

Marco Astolfi

Politecnico di Milano
Milano, Italy

Marco Binotti

Politecnico di Milano
Milano, Italy

Paolo Silva

Politecnico di Milano
Milano, Italy

ABSTRACT

The present work focuses on the analysis of a novel coal fired sCO₂ power plant concept developed in the frame of sCO₂-Flex H2020 EU funded project. Fossil fuel fired power plants are expected to improve their flexibility in the future energy scenario characterized by a large share of non-predictable and non-dispatchable renewable energy sources. This upcoming context requires a new generation of coal fired power plants with a smaller size, a high flexibility and minor requirements for the installation site like no need of water consumption. Carbon dioxide in supercritical cycles is recognized to be a possible solution for this technology shift and could replace in the future common steam Rankine cycles. This paper focuses on the impact of ambient temperature variation on a small size coal fired sCO₂ power plants equipped with a dry cooling heat rejection unit, with the aim of understanding the effect on plant operability and system performance. A dedicate tool is implemented for off-design behavior assessment and different control strategies are investigated. Results show that without a proper design of the heat rejection unit a small increase of ambient temperature may drastically limit the maximum attainable power output of the plant. This penalizing effect is more pronounced in hot locations, but this issue can be limited by adopting a sufficient over-sizing of the cycle heat rejection unit (HRU) or wet-and-dry solutions.

INTRODUCTION AND SCOPE OF WORK

In near future, the growing share of non-dispatchable renewable energy sources in the electricity mix [1] and the lack of economically viable large-scale electricity storage [2] will involve a drastic change of existing and new fossil fuel power plants operation. Coal power plants will gradually shift their role from base-load operation to cover peak demand and to provide energy services to the electrical grid. However, current coal power plants are not designed for part-load operation nor adequate to undergo rapid power output fluctuations, which are necessary characteristics to meet short noticed load variations

caused by unpredictable renewable energy sources. The founding idea of the H2020 sCO₂-Flex project [3] is to improve the flexibility of pulverized coal power plants by adopting smaller modular plants based on sCO₂ Brayton cycles instead of large plants based on conventional steam Rankine cycles. The advantage of adopting sCO₂ as working fluid is represented by a more compact cycle equipment and in particular the possibility to design low number of stage, small diameter turbomachinery that can allow faster start up and ramp-up/ramp-down transients. Another advantage is represented by the very low minimum load which is around 25%, a value remarkably higher than ultra-supercritical (USC) power plants (40-50%) and the high performance in part load as confirmed by numerical research on both fossil fuel based [4][5][6][7], concentrating solar power [8][9][10] and waste heat recovery power plants [11][12][13]. A final positive aspect related to the adoption of sCO₂ power plants is represented by the high working fluid temperature variation in the HRU (around 35°C) which allows to adopt air-cooled units with small cold end temperature difference without involving an excessive footprint or cooling air mass flow rate. This peculiarity allows a significant reduction of water consumption and an easy installation of such systems independently of the availability of a river or sea in proximity of the site location. However, differently from water-cooled HRU that can benefit from a relatively stable minimum temperature of the cooling medium, for dry-cooled units the ambient temperature variation on daily and seasonal base can affect the cycle minimum temperature with a consequent impact on sCO₂ power plant performance and operability. This aspect has been scarcely investigated by the scientific literature so far, generally just focusing on the techno-economic consequences related to HRU design assumptions and only considering the nominal operation of the plant [14][15][16][17].

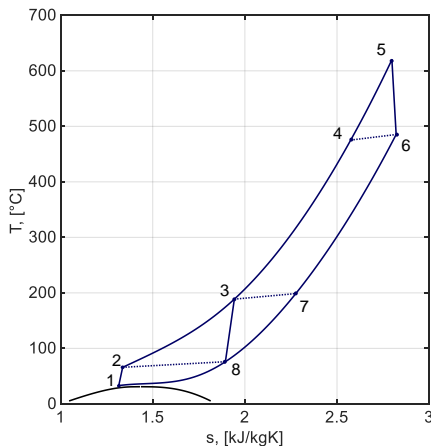
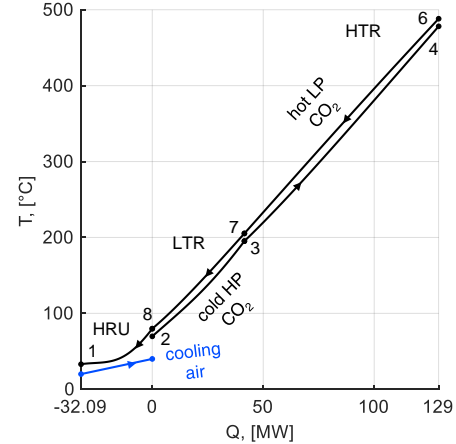
Pidaparti et al. highlighted the techno-economic potential of dry air cooling for the sCO₂ cycles limiting their analysis to the nominal design of the plant [18].

* corresponding author(s)

Table 3. sCO₂-Flex plant power balance and performance

System Power Balance	
Turbine electric power, MW _{el}	38.82
Main compressor electric power, MW _{el}	5.33
Secondary compressor electric power, MW _{el}	8.22
Heat rejection auxiliaries consumption, MW _{el}	0.273
Electrical and mechanical losses, MW _{el}	1.65
Q LHV coal, MW _{th}	62.53
Q HRU, MW _{th}	32.09
Q stack, MW _{th}	3.29
Cycle efficiency, %	42.36
Boiler efficiency, %	94.37
Overall efficiency, %	39.98

All the carbon dioxide streams thermodynamic properties of the optimized sCO₂ power cycle are reported in Table 4 while the T-s diagram and the cycle T-Q diagrams (recuperators and HRU) are reported in Figure 3 and Figure 4 respectively. Ad hoc numerical routines are implemented for the calculation of heat transfer area of each heat exchanger in the plant and validated against the data provided by sCO₂-Flex consortium partners. Table 5 reports the main results of the heat exchangers design showing how the two recuperators require a large overall heat exchange area and metal mass due to the small $\Delta T_{pp,LTR}$ and $\Delta T_{pp,HTR}$ selected. Finally, Table 6 reports the breakdown of plant capital cost computed adopting for each component a cost correlation from literature specially developed for sCO₂ power plants. More information about the validity range and the uncertainty of the cost correlations can be found in [25]. Results show a total investment cost of 52.23 million dollars for the 25 MW_{el} plant and a final specific cost which is around 2089 \$/kW_{el}. As coal-fired systems of such a small scale currently are not a commercial solution, it is not possible to provide a direct comparison of the specific plant cost. However, this figure seems to be competitive with other fuel combustion-based technologies as conventional biomass plants integrating a stoker boiler and a steam turbine present a plant specific costs in the order of 2000-4000 \$/kW_{el} [26].

**Figure 3.** T-s diagram of the optimal cycle.**Figure 4.** T-Q diagram of the optimal cycle.**Table 4.** Thermodynamic streams of the sCO₂ cycle.

Point	T (°C)	p (bar)	ρ (kg/m ³)	h (kJ/kg)	s (kJ/kgK)
1	33.00	79.78	609.40	306.29	1.34
2	69.73	250.00	738.30	336.50	1.36
3	195.19	249.95	332.83	575.77	1.96
4	478.13	249.85	170.18	941.94	2.58
5	620.00	246.10	138.70	1120.13	2.80
6	488.13	80.99	55.93	970.61	2.83
7	205.30	80.58	95.45	645.47	2.30
8	79.83	80.18	161.03	491.27	1.93

METHODOLOGY AND RESULTS

The impact of ambient temperature variation on the performance and the maximum attainable power output of the present pulverized coal sCO₂ power plant is investigated with a set of control strategies which mainly aim to guarantee the operability of the system while limiting the efficiency penalization. If no corrective actions are implemented, the increase of ambient temperature causes an increase of compressor inlet temperature with a progressive departure from the critical point region, resulting in a marked drop of density of the working fluid. The loss of real gas effects at compressor inlet leads to a higher main compressor specific consumption (for a given pressure ratio) and a rapid increase of the CO₂ volumetric flow rate (for a fixed coal mass flow rate at boiler burners). The first effect penalizes the cycle thermodynamic efficiency while the second one may significantly limit the operability of the system in part-load and off-design conditions.

Compressors off-design performances are evaluated through performance maps derived by the Baker Hughes General Electric manufacturer data. For each point characterized by a volumetric flow rate and an enthalpy rise, the shaft speed and the variable inlet guide vanes (VIGV) position have been optimized in order to maximize the component polytropic efficiency.

The normalized performance maps for the main and secondary compressor are reported in Figure 5.top and Figure 5.bottom respectively, showing the optimal polytropic efficiency of the component as function of its inlet volumetric flow rate ratio and enthalpy rise.

To ensure compressors operability and lifetime it is important to avoid the surge phenomenon. For this reason, if the required volumetric flow rate is lower than 1.1 times the compressor surge limit value, the anti-surge bypass valve is opened to guarantee stable compressor operation at the expenses of an increase in power consumption and thus penalizing system efficiency.

Considering the map of the main compressor (Figure 5.top), it is possible to notice that it is sufficient to increase the volumetric flow rate by 20% from the nominal point to reach the upper limit of the operative map and a similar limit stands also for the secondary compressor (Figure 5.bottom). Figure 6 depicts the ratio between the density of CO₂ and the density at compressor inlet point in nominal conditions varying compressor inlet temperature and pressure. It is possible to highlight that the operability of the main compressor (-20% in density) can be strongly limited by just an increase of inlet temperature equal to 1°C when cycle minimum pressure is kept unchanged (Figure 6.left) while an increase of around 30°C is required to the secondary compressor to reach the map limit at nominal pressure (Figure 6.right).

Table 5. sCO₂-Flex heat exchangers size and thermal duty.

Heat exchanger size				
	Duty, MW _{th}	ΔT_{mln} , °C	HX area, m ²	Metal mass, kg
HRU	32.09	15.05	2182.22	17217
LTR	41.51	12.56	4644.03	29120
HTR	87.52	14.69	11511.97	72185
HTRBP	11.05	227.39	504.12	30686
PHE	47.97	369.17	912.98	45330

Table 6. Breakdown of sCO₂-Flex plant capital cost.

Economic analysis		
HRU, M\$	2.09	3.99%
Main Compressor, M\$	2.38	4.56%
Secondary Compressor, M\$	2.83	5.42%
Turbine, M\$	2.20	4.21%
LTR, M\$	4.15	7.95%
HTR, M\$	6.50	12.45%
Boiler, M\$	21.49	41.14%
Compressors motors, M\$	1.38	2.65%
Gearbox, M\$	0.44	0.83%
Generator, M\$	0.80	1.54%
Contingency, M\$	3.10	5.93%
Engineering, M\$	4.87	9.32%
Total capital cost, M\$	52.23	
Plant specific cost, \$/kW _{el}	2089	

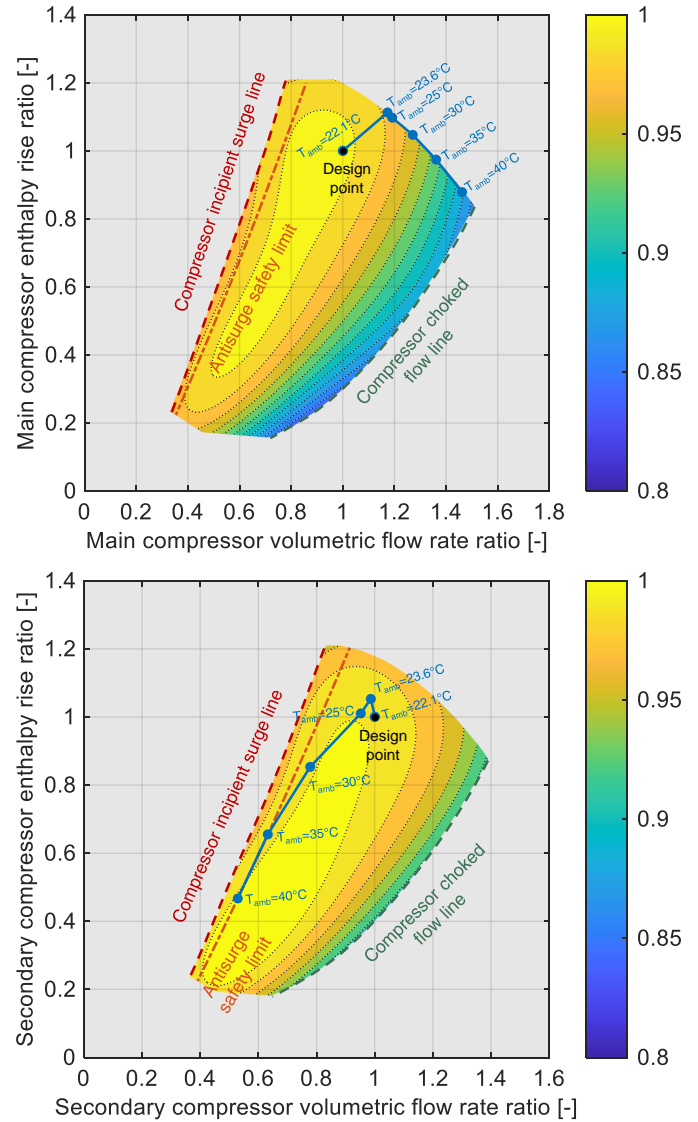


Figure 5. Normalized operational map of the main compressor (top) and secondary compressor (bottom).

An increase of compressor inlet pressure can mitigate this effect allowing to keep the volumetric inlet flow rate equal to the nominal one. However, for an inlet temperature increase of only 2°C the corresponding compressor inlet pressure should increase by 5.2 bar (which is 6% of nominal minimum pressure) causing a reduction of plant pressure ratio and a consequent loss of efficiency. Considering a system cooled by a dry air heat rejection unit, it is clear that a temperature departure from nominal point higher than the overmentioned limit can be easily obtained most of the year involving the need of facing this issue for closed Brayton supercritical sCO₂ cycles designed with compressor inlet condition close to the critical point. Therefore, in these plants it is important to implement some strategies in order to preserve the operability of the plant also for higher ambient temperature variations.

The same problem is faced also for conventional open-cycle gas turbines where the mitigation of performance decay at high ambient temperature is commonly pursued by adopting a water-cooled battery fin heat exchanger at compressor inlet or by ambient air humidification with demineralized water spraying. Differently, steam Rankine cycles performances are less affected by ambient temperature variations since these cycles are usually condensed by means of a water-cooled unit.

Figure 7 to Figure 10 depict the trend of different quantities as function of ambient temperature. Figure 7 depicts the plant gross power output, the HRU fan consumption and the plant net power output, Figure 8 depicts the coal mass flow rate, the cycle pressure ratio and the compressor inlet temperature, Figure 9 depicts the trend of cycle thermodynamic efficiency, boiler efficiency and overall plant efficiency, Figure 10 shows the variation of enthalpy variation in turbine, main compressor, secondary compressor plus the specific power output.

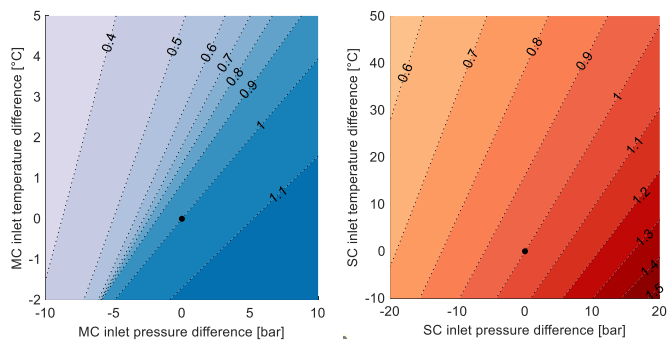


Figure 6. Ratio between the local density of CO₂ and the density at main compressor (left) and secondary compressor (right) inlet point in nominal conditions.

In each diagram three regions are present, corresponding to the following actions proposed to deal with ambient temperature increase considering the dry-cooled sCO₂-Flex power plant working at full load. All the simulations are carried out varying the cycle maximum pressure according to the sliding pressure turbine operative curve while keeping minimum pressure and maximum temperatures equal to the nominal values by inventory change.

1) A first action consists in keeping the main compressor inlet temperature equal to the nominal value by increasing the cooling air mass flow rate by adjusting the HRU fan rotational speed. This action would lead to a decrease of the HRU pinch point temperature difference as well as a reduction of the air temperature increase across the component. However, the maximum variation of the HRU fan rotational speed guaranteed by the electrical motors for V-shaped battery finned gas coolers is generally set at +25% of the nominal value. This strategy allows to feed the boiler with a nominal amount of coal (Figure 8) maintaining the gross power of the plant constant while the net power output slightly decreases because of the increased consumption of

HRU caused by the increase of both the cooling air mass flow rate and pressure drops (Figure 7). Since main compressor inlet conditions remains unchanged all the other cycle thermodynamic points are unvaried from those in Table 1. As result, the components specific power remains almost constant (Figure 10) and cycle thermodynamic efficiency and plant overall efficiency (Figure 9) just slightly decrease because of the larger HRU consumption.

2) For an ambient temperature of 22.1°C, the maximum HRU fan rotational speed is reached, and the compressor inlet temperature starts to rise but it is still possible to fuel the system with a nominal coal mass flow rate (Figure 8). The main compressor volumetric flow rate increases as the compressor enthalpy head (Figure 10) due to the larger temperature increase in the component and a nearly constant cycle pressure ratio (Figure 8). The main compressor operative point is rapidly pushed towards the performance map upper limit (Figure 5.top) while the secondary compressor operative point slightly changes since the higher temperature inlet in off design (+6.8°C) does not appreciably affect the fluid compressibility factor. The system efficiency decreases according to the larger main compressor specific consumption (Figure 9).

3) For an ambient temperature of 23.6°C corresponding to a compressor inlet of 33.9°C, the upper bound of the main compressor operative map is reached and the only possibility to operate the system for higher ambient temperatures is to reduce the amount of pulverized coal fed to the boiler burners. Reducing the amount of heat input in the cycle leads to a decrease of the CO₂ mass flow rate, allowing to maintain the compressor operative point at the limit of the operative map. On the contrary, the operative point of the secondary compressor is progressively pushed towards the surge safety limit involving the activation of the antisurge loop. Although, the plant efficiency is slightly penalized, the main issue consists in the significant limitation of the plant maximum power output that can be offered on the energy market, thus strongly limiting the plant revenues during hot ambient temperature hours. As reported in Figure 7 for a temperature of 35°C the maximum power output is below 40% of the nominal one.

Another possible solution is represented by the variation of the split ratio through a motorized valve: as the ambient temperature increases, it could be possible to send the additional CO₂ flow rate from the main to the secondary compressor preserving system operability at higher temperatures without limiting fuel mass flow rate. This solution has not been investigated in this work and it will be evaluated in future publications.

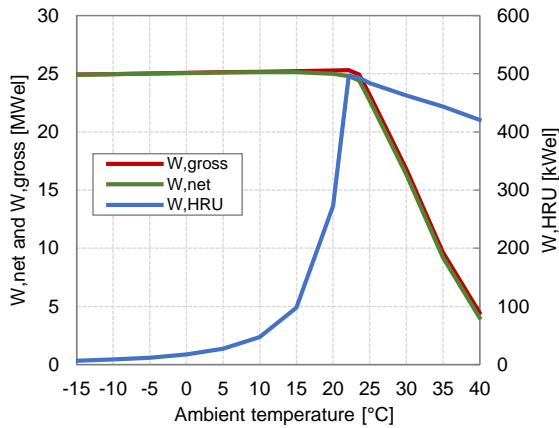


Figure 7. HRU fan consumption and plant net and gross power output as a function of the ambient temperature for the maximum attainable load.

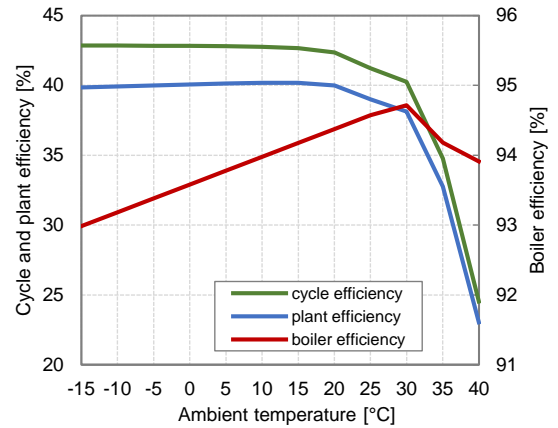


Figure 9. Cycle, plant, and boiler efficiencies as a function of the ambient temperature for the maximum attainable load.

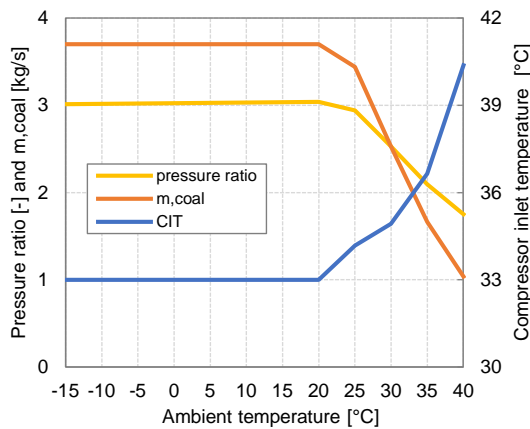


Figure 8. Compressor inlet temperature (CIT), coal mass flow rate and cycle pressure ratio as a function of the ambient temperature for the maximum attainable load.

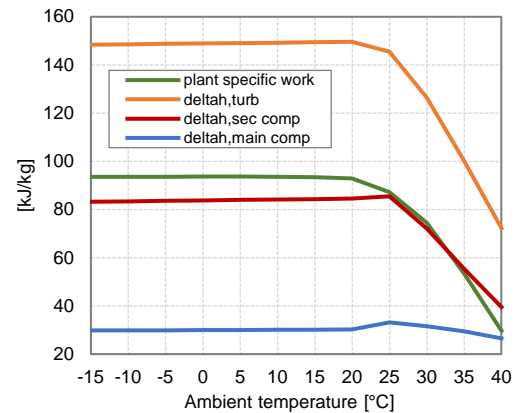


Figure 10. Plant specific work, turbine enthalpy drop and compressors enthalpy rise as a function of the ambient temperature for the maximum attainable load.

On the contrary, if ambient temperature decreases it would be possible to reduce the compressor inlet temperature below the nominal point. However, in agreement with BHGE [27][28], the sCO₂-Flex partner in charge of the turbomachinery design, this strategy is not recommended since reduction of the compressor inlet temperature may lead to cavitation issues at the impeller inlet as vapor bubbles may form during the working fluid acceleration in the distributor and the stator. On the other hand, if cycle minimum temperature is below the critical one it would be possible to enable condensation by a proper tuning of the cycle minimum pressure with positive effects on thermodynamic efficiency but issues on the main compressor/pump operation related to the change of fluid volumetric behaviour. For these reasons, when ambient temperature decreases the compressor inlet temperature is kept equal to the nominal value by reducing the HRU fan rotational speed. Plant efficiency and power output slightly decreases because of the reduction of boiler efficiency determined by the lower ambient temperature and the consequent lower combustion air temperature.

Finally, if the system is running at minimum load there is no limitation due to ambient temperature increase. Once HRU fan speed limit is reached strategy 2 can be adopted up to very high ambient temperatures because of the larger volumetric flow rate increase available starting from minimum load condition and nominal ambient temperature. The plant efficiency is progressively penalized by the increase of main compressor specific consumption, but the system operability is not limited (Figure 11).

EFFECT ON ANNUAL PLANT OPERATION

The effect due to power plant efficiency penalization and power output limitation can be evaluated on annual base for different site locations comparing the yearly energy production with a system working with a constant ambient temperature like for water cooled systems. Starting point is the knowledge of hourly data for dry bulb temperature and relative humidity plus information on the power plant load trend during the year. Weather data for different EU location can be obtained by EnergyPlus [29] while USA TMY3 data can be obtained from NREL System Advisor Model [30]. A reference coal fired power

plant weekly load trend is obtained by [31] where the role of fossil fuel power plants is discussed for future scenario with high share of RES. Coal fired power plants are expected to run at maximum load for 9 hours a day (from 6 am to 1 pm and from 7 pm to 9 pm) in correspondence of the peak of grid energy consumption and at minimum reduced load in the central weekday hours (because of the abundance of solar energy) and during the night and the weekend (because of the reduction of energy demand). The same power plan is adopted in this study considering a minimum load of 25% [4]. Results are provided for two location: Prague and Sevilla. Meteorological data are reported in Figure 12 while Table 7 reports monthly and yearly energy produced considering a constant ambient temperature or by considering the actual power plant penalization due to ambient temperature variation for both selected locations.

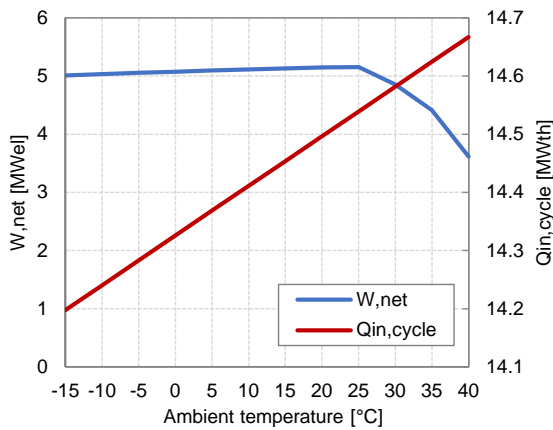


Figure 11. Plant net power output and cycle heat input at 25% of coal input as function of the ambient temperature.

Results clearly show that the larger difference between these two values is for Sevilla location (-6.3%) due to the higher average temperature while in Prague the penalization of energy output on annual base is extremely limited (-0.6%). This is mainly due to the power plan selected with sCO₂ cycle running at minimum load in central hour of the day where the penalization due to higher temperature is stronger. However, the same conclusions are also valid for different power plans and the penalization for a plant installed in Prague is always dramatically lower than the energy output penalization for Sevilla thanks to the lower average ambient temperature and the limited number of hours with dry bulb temperature above 20°C. From these results it seems not necessary to adopt corrective actions for locations with low annual average temperature since the penalization is very limited while for hot locations two possible solutions are proposed that can be followed separately or in combination:

- a) first one consists in designing the system with an oversized HRU in order to have the possibility exploit the larger heat transfer area and larger air mass flow rate with the aim to operate the thermodynamic cycle in nominal condition up to higher ambient temperatures;
- b) second one consists in adopting wet-and-dry solutions with the aim to reduce air temperature by the cooling

effect provided by heat and mass transfer process with a mass flow rate of softened water that is first sprayed on the fin battery and then distributed at the top of the adiabatic panel. Dry bulb ambient temperature, depending on the amount of water used, can be cooled down to almost the wet bulb temperature.

a) HRU oversizing

The quantification of the potential of adopting a larger HRU is evaluated by finding the maximum ambient temperature that allows to operate the thermodynamic cycle in nominal condition (Table 4) with maximum HRU fan rotational speed (+125%). The analysis is repeated for different multipliers of HRU heat transfer area and nominal air mass flow rate. System at nominal ambient condition can obviously work with all the HRU unit active and with a low fan speed with a reduction of HRU auxiliaries consumption or by bypassing some of them. Figure 13 reports the maximum ambient temperature attainable without varying the compressor inlet temperature against the HRU multiplier.

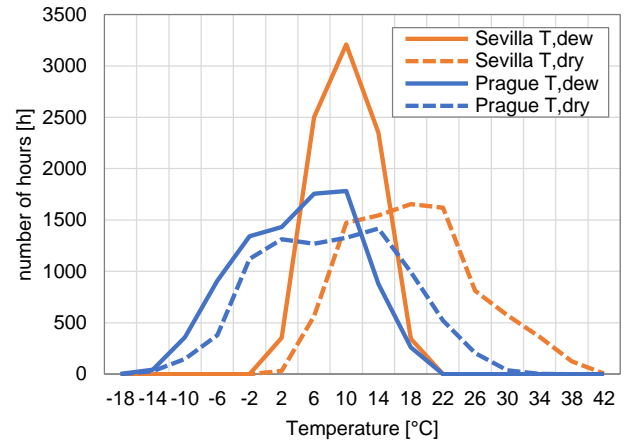


Figure 12. distribution of dry bulb and wet bulb temperature for Prague and Sevilla.

Table 7. Monthly and yearly energy yield for a constant ambient temperature or considering the actual penalization due to ambient temperature variation.

	20°C	Prague, T _{dry}		Sevilla, T _{dry}	
	GWh	GWh	ΔEel%	GWh	ΔEel%
Jan.	8.40	8.36	0.5%	8.40	0.0%
Feb.	7.43	7.39	0.5%	7.43	0.0%
Mar.	8.20	8.17	0.3%	8.19	0.1%
Apr.	7.88	7.86	0.2%	7.81	0.9%
May	8.40	8.32	0.9%	7.95	5.3%
Jun.	7.88	7.82	0.7%	6.96	11.7%
Jul.	8.20	8.13	0.9%	6.56	20.0%
Aug.	8.40	8.22	2.1%	6.74	19.7%
Sep.	7.68	7.68	0.0%	6.75	12.1%
Oct.	8.40	8.39	0.1%	7.97	5.1%
Nov.	8.07	8.05	0.3%	8.05	0.3%
Dec.	8.00	7.97	0.4%	8.00	0.0%
Year	96.92	96.36	-0.6%	90.80	-6.3%

Results show that with an oversize equal to 300% it is possible to run the system in nearly nominal condition up to 32°C ambient temperature thus partially solving the critical issues related to system operability and reduction of attainable power output. Above this ambient temperature strategy 2 and strategy 3 can be adopted. The associated capital cost increase is 4.17 M\$ involving a change of plant specific cost of about +8%. For Prague location where maximum ambient temperature is 32°C, an oversizing of HRU would allow to run the power plant close to nominal conditions with no limitation in power output. On the contrary, for Sevilla location where maximum ambient temperature is 41°C the HRU oversizing would allow to limit energy output penalization.

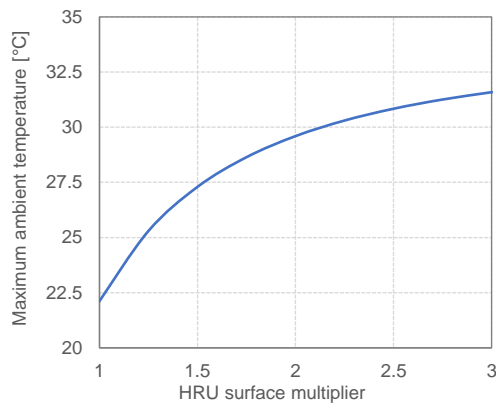


Figure 13. Maximum ambient temperature at which it is possible to maintain the nominal compressor inlet temperature as a function of the HRU size multiplier.

b) Wet-and-dry solution

Wet-and-dry heat rejection units adopt a system of water spray on the gas cooler heat transfer surface and/or use adiabatic panels which consists in a set of corrugated paper sheets mounted ahead the fin battery. Both solutions are already implemented in carbon dioxide gas coolers and condensers of refrigeration industry with an easy technological transfer to the power production sector. Figure 14 depicts the picture of a LU-VE EMERITUS unit with a schematic of the adiabatic panel-water spray system.

Wet-and-dry solution allows for a reduction of the aforementioned issues by enhancing the heat exchanger duty during hot hours for a fixed air mass flow rate thus limiting the compressor inlet temperature increase and reducing the HRU footprint. Main drawback of this concept is related to water consumption that shall be softened before the use in order to limit corrosion and salt deposition on heat transfer surface. The minimum annual consumption of water (thus neglecting the efficiency of spray and adiabatic panels) can be calculated from weather data and plant operation. Calculations are carried out considering the exact amount of water required to bring the actual ambient temperature equal to the nominal value (20°C) neglecting the effect of enhanced heat transfer coefficient given by liquid water droplets and fins and increased heat capacity due to air humidification, thus leading to conservative results.

Results reported in Table 8 show that for Sevilla location it is possible to always reduce the ambient temperature close to the target value with the exception of few hours during the year where maximum temperature attainable with complete saturation is 22.2°C. The total annual energy can be increase to a value slightly higher than the value of a system working with constant ambient temperature. The minimum amount of water is around 20000 ton/year with a higher consumption during summer months. This consumption seems very large but considering a cost of softened water of 1.17 \$/m³ [33] it represent a small variation of annual variable costs mainly related to coal consumption and in the order of 4.2 M\$ considering a specific cost of coal equal to 76\$/ton. Moreover, water consumption is around 0.13% of the water consumption associated to the adoption of a water cooled HRU demonstrating that wet-and-dry solution can be a powerful way to improve the energy production of a sCO₂ coal fired power plant in hot climate locations.

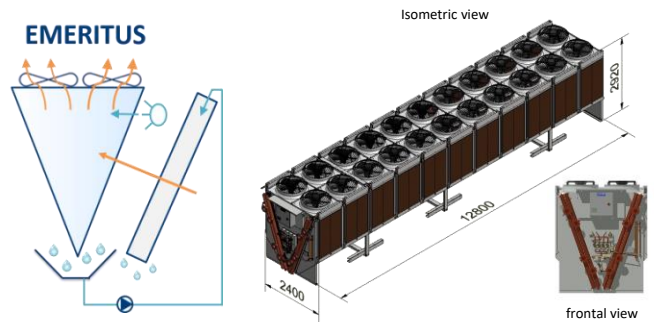


Figure 14. (left) Conceptual configuration of LU-VE EMERITUS technology, combining adiabatic panels and water spray system. Air is represented by orange streams while water by light blue streams. (right) Isometric and frontal views of a 22 fans Emeritus heat exchanger [32][33].

Table 8. Annual results for Sevilla location and wet-and-dry HRU.

	E _{el} , GWh	Spray hours	Water, ton
Jan.	8.40	0	0
Feb.	7.43	14	15
Mar.	8.20	88	194
Apr.	7.88	150	524
May	8.41	311	1637
Jun.	7.88	469	2944
Jul.	8.21	642	4987
Aug.	8.40	650	4996
Sep.	7.69	550	3167
Oct.	8.41	302	1512
Nov.	8.08	76	233
Dec.	8.00	7	4
Year	96.97	3259	20214

CONCLUSIONS

The present study allows to highlight the following aspects:

- Dry air cooled sCO₂ based coal fired power plants differently from steam Rankine power plants are strongly affected in their operation for ambient temperatures higher than the nominal one.
- Most critical component is the main compressor which volumetric flow rate increase is limited by the operative map leading to a decrease of maximum attainable power output for ambient temperatures just few degrees Celsius above the nominal value.
- The actual effect of this limitation on the plant operability during a representative year strongly depends on the location. Analysis is repeated for Prague and Sevilla demonstrating that in the first the annual penalization is nearly negligible while it is higher in the second.
- In case of strong penalization of annual energy output for hot climate locations two solutions are proposed: first one requires to oversize the HRU while the second to adopt wet-and-dry gas coolers. Both solutions are feasible from techno-economic point of view and can be implemented separately or in combination.

NOMENCLATURE

Symbols

A	Area (m ²)
h	Specific enthalpy (kJ/kgK)
E _{el}	Electric energy (GWh)
m _{in}	Mass Flow Rate (kg/s)
p	Pressure (bar)
Q	Thermal Power (W)
s	Specific entropy (kJ/kgK)
T	Temperature (°C)
W	Power (W)
η	Efficiency (%)
ρ	Density (kg/m ³)

Acronyms

APH	Air Preheater
BHGE	Baker Hughes General Electric
HRU	Heat Rejection Unit
LHV	Lower Heating Value
LTR	Low Temperature Recuperator
LT-PHE	Low Temperature Primary Heat Exchanger
HRU	Heat Rejection Unit
HTR	High Temperature Recuperator
HTRB	High Temperature Recuperator Bypass
HT-PHE	High Temperature Primary Heat Exchanger
HX	Heat Exchanger
sCO ₂	Supercritical CO ₂
USC	Ultra Super Critical

ACKNOWLEDGEMENTS

The sCO₂-flex project has received funding from the European Union's Horizon 2020 research and innovation programme under grant agreement N° 764690.

REFERENCES

- [1] IEA and IRENA, "Perspectives for the Energy Transition: Investment Needs for a Low-Carbon Energy System," *Int. Energy Agency*, 2017.
- [2] IRENA, "Battery Storage for Renewables: Market Status and Technology Outlook," *Irena*, 2015.
- [3] "sCO₂-Flex: Supporting the electricity system By making fossil fuel based electricity production more flexible. Available online at: <http://www.sco2-flex.eu>."
- [4] D. Alfani, M. Astolfi, M. Binotti, and P. Silva, "Part Load Strategy Definition and Annual Simulation for Small Size sCO₂ Based Pulverized Coal Power Plant," in *Proceedings of ASME Turbo Expo 2020 Turbomachinery Technical Conference and Exposition GT2020 June 22-26, 2020, London, England, 2020*, pp. 1–10.
- [5] D. Alfani, M. Astolfi, M. Binotti, E. Macchi, and P. Silva, "Part-Load Operation Of Coal Fired sCO₂ Power Plants," in *3rd European supercritical CO₂ Conference September 19-20, 2019, Paris, France, 2019*, pp. 1–9.
- [6] R. Scaccabarozzi, M. Gatti, and E. Martelli, "Thermodynamic Optimization and Part-load Analysis of the NET Power Cycle," *Energy Procedia*, vol. 114, no. November 2016, pp. 551–560, 2017.
- [7] M. Mecheri and Y. Le Moullec, "Supercritical CO₂ Brayton cycles for coal-fired power plants," *Energy*, vol. 103, pp. 758–771, 2016.
- [8] D. Alfani, M. Astolfi, M. Binotti, P. Silva, and E. Macchi, "Off-design Performance of CSP Plant Based on Supercritical CO₂ Cycles," in *SOLARPACES 2019: International Conference on Concentrating Solar Power and Chemical Energy Systems, 2019*, no. i.
- [9] T. Neises and C. Turchi, "A comparison of supercritical carbon dioxide power cycle configurations with an emphasis on CSP applications," *Energy Procedia*, vol. 49, pp. 1187–1196, 2014.
- [10] F. Crespi, D. Sánchez, G. S. Martínez, T. Sánchez-Lencero, and F. Jiménez-Espadafor, "Potential of supercritical carbon dioxide power cycles to reduce the levelised cost of electricity of contemporary concentrated solar power plants," *Appl. Sci.*, vol. 10, no. 15, 2020.
- [11] D. Alfani, M. Astolfi, M. Binotti, E. Macchi, and P. Silva, "Optimization of the Part-load Operation Strategy of sCO₂ Power Plants," in *5th International Seminar on ORC Power Systems, 2019*, no. i, pp. 1–10.
- [12] G. Manente and M. Costa, "On the conceptual design of novel supercritical CO₂ power cycles for waste heat recovery," *ECOS 2019 - Proc. 32nd Int. Conf. Effic. Cost, Optim. Simul. Environ. Impact Energy Syst.*, pp. 2219–2231, 2019.

- [13] M. Marchionni, G. Bianchi, and S. A. Tassou, "Techno-economic assessment of Joule-Brayton cycle architectures for heat to power conversion from high-grade heat sources using CO₂ in the supercritical state," *Energy*, vol. 148, pp. 1140–1152, 2018.
- [14] T. J. Held, J. Miller, and David J. Buckmaster, "A Comparative Study of Heat Rejection Systems for sCO₂ Power Cycles," in *The 5th International Symposium - Supercritical CO₂ Power Cycles*, 2016.
- [15] N. T. Weiland, C. W. White, and A. C. O'Connell, "Effects of cold temperature and main compressor intercooling on recuperator and recompression cycle performance," in *2nd European Supercritical CO₂ Conference*, 2018, pp. 1–11.
- [16] J. J. Sienicki, A. Moiseyev, and Q. Lv, "Dry Air Cooling and the sCO₂ Brayton Cycle," in *Volume 9: Oil and Gas Applications; Supercritical CO₂ Power Cycles; Wind Energy*, 2017, vol. 9, pp. 1–9.
- [17] S. R. Pidaparti, C. W. White, A. C. O. Connell, N. T. Weiland, and S. Co, "Cooling System Cost & Performance Models for Economic sCO₂ Plant Optimization with Respect to Cold sCO₂ Temperature Cooling Systems for sCO₂ Power Cycles," in *3rd European supercritical CO₂ Conference September 19-20, 2019, Paris, France*, 2019, pp. 19–20.
- [18] S. R. Pidaparti, A. Moiseyev, P. J. Hruska, J. J. Sienicki, and D. Ranjan, "Technical and Economic Feasibility of Dry Air Cooling for the Supercritical CO₂ Brayton Cycle Using Existing Technology," *5th Int. Symp. - Supercrit. CO₂ Power Cycles*, pp. 1–23, 2016.
- [19] H. Chen, W. Zhuge, Y. Zhang, and L. I. U. Hongdan, "Effect of compressor inlet condition on supercritical carbon dioxide compressor performance," *Proc. ASME Turbo Expo*, vol. 9, pp. 1–10, 2019.
- [20] M. Mecheri and S. Bedogni, "sCO₂-Flex D1.3 – Report on the selected cycle architecture," 2018.
- [21] D. Alfani *et al.*, "Part-Load Operation of Coal Fired sCO₂ Power Plants," in *Proceedings of the 3rd European supercritical CO₂ Conference*, 2019, pp. 1–9.
- [22] D. Alfani, M. Astolfi, M. Binotti, S. Campanari, F. Casella, and P. Silva, "Multi objective optimization of flexible supercritical CO₂ coal-fired power plant," *ASME Turbo Expo 2019 Turbomach. Tech. Conf. exhibition*, pp. 1–11, 2019.
- [23] D. Alfani, M. Astolfi, M. Binotti, and P. Silva, "sCO₂-Flex D5.2 - Proposed part load control strategies," 2019.
- [24] D. Alfani, M. Astolfi, M. Binotti, and P. Silva, "sCO₂-Flex D5.3 - First Annual Performance in Steady State and Operation Range," 2020.
- [25] N. T. Weiland, B. W. Lance, and S. R. Pidaparti, "sCO₂ power cycle component cost correlations from DOE data spanning multiple scales and applications," *Proc. ASME Turbo Expo*, vol. 9, pp. 1–17, 2019.
- [26] IRENA - International Renewable Energy Agency, "Biomass for Power Generation," *Renew. ENERGY Technol. COST Anal. Ser.*, vol. Volume 1:, 2012.
- [27] "Baker Hughes General Electric: an energy technology company. Available online at: <https://www.bakerhughes.com/>."
- [28] A. M. Bigi *et al.*, "sCO₂-Flex D3.13 – First turbomachinery models and report," 2020.
- [29] DOE, "EnergyPlus | EnergyPlus," *U.S. Dep. Energy's*, 2017.
- [30] NREL, "System Advisor Model (SAM)," *Natl. Renew. Energy Lab.*, 2011.
- [31] M. Astolfi, E. De Lena, and M. C. Romano, "Improved flexibility and economics of Calcium Looping power plants by thermochemical energy storage," *Int. J. Greenh. Gas Control*, 2019.
- [32] "LU-VE S.p.A. Available online at: <https://www.luvegroup.com/>."
- [33] M. Astolfi, L. N. La Diega, M. C. Romano, U. Merlo, S. Filippini, and E. Macchi, "Techno-economic optimization of a geothermal ORC with novel 'Emeritus' heat rejection units in hot climates," *Renew. Energy*, 2020.

ESTIMATED COST AND PERFORMANCE OF A NOVEL sCO₂ NATURAL CONVECTION CYCLE FOR LOW-GRADE WASTE HEAT RECOVERY

Kelsi M. Katcher

Southwest Research Institute
San Antonio, TX, USA
Email: kelsi.katcher@swri.org

Michael Marshall

Southwest Research Institute
San Antonio, TX, USA

Natalie R. Smith, Ph.D.

Southwest Research Institute
San Antonio, TX, USA

Cole Replogle

Southwest Research Institute
San Antonio, TX, USA

ABSTRACT

The current work focuses on development of a natural-convection-driven system for low-cost power generation from low-grade heat sources using supercritical carbon dioxide (sCO₂) as the working fluid. Cycle modelling sensitivity studies were conducted to predict available power generation and estimated installation cost for four applications of various thermal and physical scales; the considered applications ranged from a 2 MW-th data center to an 80 MW-th geothermal application. Sensitivity studies included variations in the sCO₂ temperatures and pressures, the flow loop pipe sizing, and the flow loop elevation change to quantify the impact of each design variable on the recoverable power, the thermal efficiency, and the estimated capital cost per power. Results of this study show that increasing the elevation change across the cycle and decreasing low-side CO₂ temperature (to near or below the critical temperature of 31.1°C) generated the most significant improvements in cycle performance and specific cost. It was also found that the cost per power is lowest for the largest thermal scales, namely geothermal-type applications. However, even though the small- and medium-scale applications have higher specific costs, the actual installation cost is still considered relatively low. Therefore, it is expected that these waste heat recovery cycles could still present competitive solutions for small electrical power requirements where very low-grade waste heat is available.

INTRODUCTION

Low-grade heat rejection (at <100-300°C) is commonplace among many industrial, commercial, and residential processes [1], accounting for as much as 80% of total waste heat available [2]. With the broad-reaching push to improve system efficiencies, waste heat recovery (WHR) technologies are

gaining more attention. The primary challenge with low-grade heat recovery systems is that the thermal conversion efficiency is inherently very low, resulting in a prohibitively high cost of electricity. Furthermore, most mechanical low-grade WHR installations rely on organic Rankine cycles or Kalina cycles, incorporating single or multiple pumps and expanders for power generation. Utilizing multiple turbomachines drives up system complexity and cost. In addition, process fluid leakage through shaft seals necessitates a makeup/reclamation system, which adds failure points to the system, further increases system cost, and decreases efficiency.

A proposed competitor to these technologies is the natural convection power cycle (or thermosiphon). By utilizing a vertical process loop with heat addition near the bottom and heat rejection near the top, mass flow can be motivated with temperature difference as the only driver (meaning no compressor or pump is required to drive the fluid). Figure 1 depicts the basic arrangement of the natural convection power cycle. The natural convection cycle relies on the differences in hydrostatic pressure between the hot fluid column and the cold fluid column (i.e. pressure equals the product of fluid density, gravity, and the height of the fluid column). If the density of the cold fluid is significantly greater than that of the hot fluid, there will be a net pressure gain across the loop. The achieved mass flow rate is then a function of the hydrostatic pressure gain and the round trip pressure losses, including the operating pressure drop across the power turbine, frictional losses, and minor losses through elbows, valves, heat exchangers, and etc.

The cycle investigated in this study uses supercritical CO₂ (sCO₂) as the working fluid. The fluid properties of sCO₂ are favorable for low-grade WHR because the near-ambient critical point (7.39 MPa and 31.1°C) allows for inherently large density swings near the target waste-heat source temperatures. Furthermore, the high fluid density and relatively low

viscosities in the supercritical phase allow for minimal frictional losses, increasing the mass flow potential.

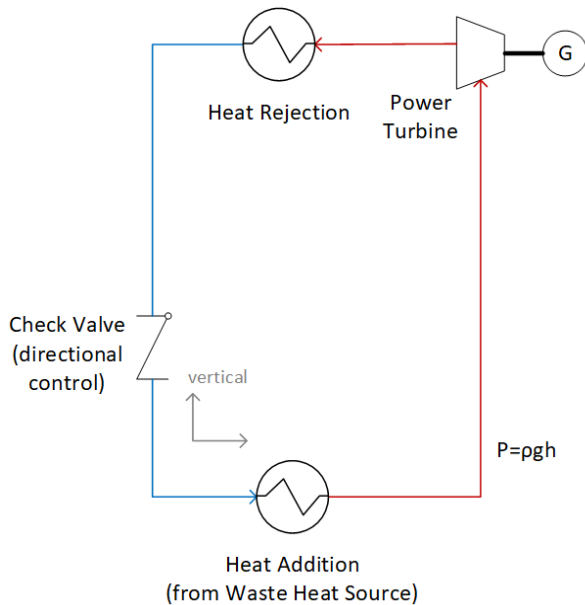


Figure 1: Schematic of natural convection power cycle.

BACKGROUND

Natural convection or thermosiphon loops are commonly used today as secondary fluid systems for heat transfer in applications such as refrigeration, air conditioning, solar collectors, and nuclear reactors. Previous research has shown that $s\text{CO}_2$ can provide increased heat transfer in more compact system when compared to traditional thermosiphons using refrigerants, water, or brine as the working fluid [3,4]. Natural convection work by Sharma (2014) documented Reynolds numbers of up to 10^5 for a CO_2 temperature difference of only 8°C between the source and sink temperatures, demonstrating the large mass flow potential of CO_2 with small changes in temperature [5]. Previous research on $s\text{CO}_2$ natural convection has focused heavily on the heat transfer characteristics of the fluid, showing the complex behavior of local buoyancy effects and localized fluid property gradients (effects that are commonly ignored in traditional cycles, but become significant in a natural convection cycle). Studies have documented large local variations in temperature and axial velocity across the cross section of the pipe [3,4] and large changes in mass flow and heat transfer properties as the fluid approached and crossed the pseudocritical temperature [4,5], the temperature at which the specific heat reaches a local maximum at constant pressure. The high volumetric expansion coefficient and the low viscosity of CO_2 result in strong local buoyancy effects which can cause high radial/azimuthal velocities in the pipe cross-section [4]. This can improve fluid mixing in the heat exchangers, but increased local velocities in the loop cross-section can deter bulk fluid motion around the loop. Therefore, the heat transfer and flow characteristics in the heat exchangers become critical

to loop stability [6]. Large deviations from standard heat transfer correlations have also been documented for $s\text{CO}_2$ natural convection. A study by Sharma and Murari (2015) documented that heat transfer coefficients in the fluid show a strong dependence on heat flux at the wall, and that heat transfer deterioration can occur at high heat fluxes [7]. Work by Lei et al. (2017) further explored this phenomenon, showing that a “vapor-like” fluid formed near the pipe wall at high heat fluxes, minimizing the heat transfer from the wall to the bulk fluid (similar to the film boiling phenomenon that occurs at subcritical pressures) [8]. Work by Yadav et al. (2012) proposed modified correlations for heat transfer and friction factor for $s\text{CO}_2$ natural convection, as the measured behaviors did not accurately follow the standard correlations [4].

Substantially less work has been documented on applying $s\text{CO}_2$ natural convection for power generation. A MW-scale $s\text{CO}_2$ thermosiphon was considered for geothermal power generation, utilizing a semi-open-loop cycle composed of separate injection and production wells where the working fluid flows through the rock strata [9-10]. Supercritical CO_2 thermosiphons for geothermal have gained increasing interest because the low viscosity allows for improved flow through the rock strata as compared to traditional thermosiphons operating with supercritical water. A second team presented a closed-loop $s\text{CO}_2$ cycle with the injection and production pipes running in a U-configuration in the same well [11]. Both concepts present utility-scale power generation capabilities.

In previous work by this team, it was found that a thermosiphon can be achieved at various source temperatures and various thermal scales [12]. When operating near the critical point, significant mass flow rates can be achieved with relatively small temperature deltas across the $s\text{CO}_2$ streams. A sensitivity study was conducted to understand the relative impact of the various cycle and loop parameters; changes in the hot CO_2 temperature, cold CO_2 temperature, CO_2 pressure, pipe diameter, and loop height were considered. It was found that the most significant power gains could be achieved by increasing the loop height and by decreasing the cold-side CO_2 temperature. Decreasing the cold-side temperature was found to have significantly more potential than increasing the hot-side temperature; for the loop size investigated, decreasing the cold-side CO_2 temperature from 34°C to 28°C improved the power output by the same amount as increasing the hot-side CO_2 temperature from 100°C to 140°C [12]. The highest values for available power were predicted when the cold-side CO_2 temperature was below the critical temperature (dropping the CO_2 into a pressurized liquid state). Furthermore, the achievable power increases with loop mass flow. Therefore, decreasing the pressure losses is critical for cycle performance. The previous study also quantified the pressure rise across the cycle that could be utilized across the power turbine. It was found that the pressure is expected to be relatively constant throughout the loop, so a low-head power turbine design is required for power conversion.

In general, the capital cost as well as operating and maintenance (O&M) costs must be minimized to make low-grade WHR economical and practical. To better understand the capabilities of the sCO₂ natural convection power cycle for low-grade WHR, a sensitivity study was performed to predict cycle performance and capital cost for four waste heat applications of various thermal and physical scales.

NATURAL CONVECTION CYCLE MODEL

A cycle model was developed to predict the fluid properties of the natural convection cycle. Inputs to the model include CO₂ hot-side and cold-side temperatures, pipe diameter, and linear pipe lengths (including piping and heat exchanger lengths). The pipe loop was assumed to be rectangular (four elbows) with a check valve just upstream of the heater and the power turbine just upstream of the cooler. The flow loop was discretized, and fluid properties were calculated at each node. The NIST REFPROP equations of state were used to calculate the fluid properties of the CO₂.

As a starting point, CO₂ pressure and temperature were defined at the power turbine outlet. From the turbine outlet, the pressure and temperature deltas were calculated between nodes around the cycle. Pressure deltas were calculated as the sum of the change in hydrostatic pressure (using fluid density and elevation change), the frictional losses through the piping and heat exchangers (using flow density, velocity, Reynolds number, friction factor, and piping dimensions), and the minor losses through pipe fittings and the check valve (using fluid density and velocity). In the current model, the vertical pipe runs were considered isothermal, and the heat exchangers were defined by the CO₂ outlet temperatures. In order to achieve the maximum pressure-gain across the cycle, the temperature differences (and density differences) must be maintained across the vertical legs of the loop; for this reason, it is assumed that the loop is insulated and the vertical legs would be near isothermal. The change in temperature due to change in pressure is expected to be relatively small for all above-ground cycles considered here; for the largest cycle the temperature is predicted to change by less than 1.5°C assuming constant enthalpy across the vertical leg. For the geothermal cycle, the change in CO₂ temperature with pressure will be more significant over the large elevation change. However, from the current literature, it is unclear how well-insulated the injection and recovery wells can be. Therefore, an isothermal assumption was used as a starting point for this cost analysis. Furthermore, in previous work by this team, it was found that the cycle performance is highly dependent on the heat exchanger performance and heat exchanger model. Because the heat exchanger geometries will be system-specific and a point of optimization, the heater and cooler in this model were defined by specifying the CO₂ outlet temperature at each.

An iterative, numerical solver was used to select the CO₂ mass flow rate that would satisfy the energy balance in the loop. Namely, this mass flow balances the pressure gain across the cycle with the total pressure loss, as well as matches the starting

fluid properties at the power turbine exit to those at the end of the cycle calculation (closing the loop). The pressure and enthalpy drop across the turbine were calculated using an isentropic efficiency value, specified by the turbine sizing calculations (summarized below). The solver was also setup to select the expander outlet pressure that would maximize power output; cycle performance is sensitive to the selected operating pressure [12]. A cycle trade study was used to calculate the head drop across the power turbine and the isentropic power for various temperature combinations and various pipe loop dimensions.

LAB- SCALE NATURAL CONVECTION VALIDATION

The developed cycle model was validated using a lab-scale natural convection test loop (see the constructed loop presented in Figure 2). The test loop was constructed using 1-inch stainless tubing and a height of approximately 4.5 meters. Heat addition and rejection were accomplished through a hot-water bath and an ice bath, respectively. The test loop utilized an orifice plate to simulate the pressure loss across a power turbine. The test loop was operated at varied conditions. The conditions for one steady-state operating point are summarized in Table 1. At this condition, the hot water bath temperature was 65.4°C, and the ice bath temperature was 12.9°C. Note that the cold-side CO₂ temperature dropped well below the critical temperature; therefore, a phase change was occurring in each heat exchanger. The measured mass flow rate was relatively constant, and no cycle instabilities were seen. Based on these results, all subsequent cycle designs considered a cold-side CO₂ temperature near or below the critical temperature.

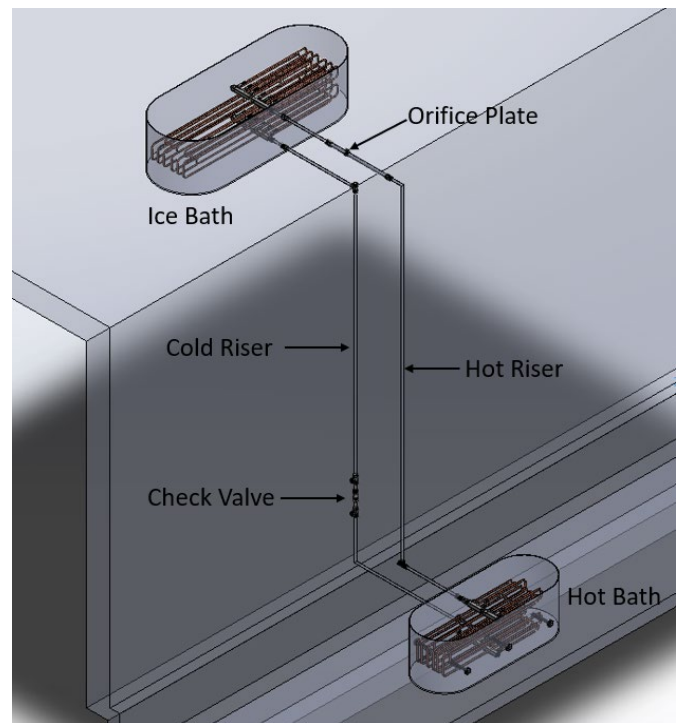


Figure 2: Lab-scale natural convection test loop

Table 1: Lab-scale natural convection test loop steady-state operating conditions

CO ₂ Conditions	Cooler Outlet	Heater Outlet
Temperature (°C)	16.0	48.1
Pressure (MPa)	8.768	8.784
Density (kg/m ³)	870.3	281.7
Mass Flow (kg/s)	0.143	

Note that the pressure change across the cycle is quite small. The maximum pressure difference is measured between the top of the hot-side vertical pipe (8.761 MPa) and the bottom of the cold-side vertical pipe (8.795 MPa). With this small change in pressure, a mass flow rate of 0.143 kg/s was achieved. This corresponded to a fluid velocity of 1.08 m/s at the expected turbine location.

METHODS

To evaluate the performance and capital cost of the natural convection cycle, a trade study was performed on four target waste-heat applications to quantify the impact of temperature, pipe size, and loop height. The four waste-heat applications selected were

- (1) 2 MW-th data center,
- (2) 4 MW-th data center,
- (3) 10 MW-th industrial, and
- (4) 80 MW-th geothermal.

The temperature range and loop sizes selected were intended to be representative of each specific application. Using the developed cycle model, the isentropic power was calculated for each loop configuration. Thermal efficiency was calculated as the isentropic power over the thermal input. A capital cost was also estimated for each configuration using defined cost functions for the various components. Cost functions are defined in the following sections. Note that the presented cost functions simplify the true capital cost of the various components, and are meant to represent general trends that can be used for understanding how the natural convection loop cost trends with scale. These cost trends are expected to be relatively accurate within the range of values presented, but should not be extrapolated outside what is presented in this study.

Turbine Cost Function

For each application, the inlet and outlet conditions for the power turbine were predicted using the cycle model. These conditions were run through a turbine sizing code based on radial turbine experience charts [13,14] to determine basic turbine sizing. See all values summarized in Table 2. For the first three waste-heat applications, a single stage turbine was sized due to the low available head rise. Multi-stage designs in these applications would operate at even lower speeds with smaller impeller diameters. For the geothermal turbine, sizing sweeps were conducted for rotational speeds of 5,000 to 30,000 RPM and one- to five-stage machines. The turbine design with the best isentropic efficiency was a single-stage machine operating at 20,000 RPM.

The turbine sizing analysis was used to estimate the capital cost of the power turbine for a natural convection cycle. The turbine design for the first three applications was assumed to utilize a sealed concept with immersed bearings and a magnetic coupling to minimize complexity and reduce cost at the smaller scale [15]. The geothermal power turbine design is expected to be similar to sCO₂ power turbines designed in previous work based on the head, rotational speed, and size [15]. The turbine cost model considered the cost of stock material, machining, and welding for the impeller and the housing; connection flanges; instrumentation connections; and the coupling. Based on the turbine sizing and the estimated fabrication costs, it was found that the turbine cost trended best with turbine power. The following turbine cost function was used for this study.

$$\text{Cost (USD)} = 227.10 * P + 23,288.47$$

where P is the isentropic turbine power in kilowatts.

Table 2: Radial turbine sizing for each waste-heat application

Application	1	2	3	4
Mass Flow (kg/s)	12.65	18.00	28.94	230.0
Inlet				
Temperature (°C)	66.6	76.3	200.0	210.0
Pressure (MPa)	8.70	8.55	8.37	20.00
Enthalpy (kJ/kg)	461.22	480.14	638.31	611.51
Entropy (kJ/kg-K)	1.83	1.89	2.28	2.08
Exit				
Temperature (°C)	65.9	75.8	198.7	133.7
Pressure (MPa)	8.619	8.50	8.24	8.50
Enthalpy (kJ/kg)	490.92	479.93	637.33	559.71
Entropy (kJ/kg-K)	1.83	1.89	2.28	2.08
Turbine Sizing				
Speed (RPM)	2,500	1,100	3,000	20,000
Impeller Diam. (mm)	138.0	316.7	206.9	210.0
Isentropic Efficiency	76.2%	95.0%	78.9%	95.6%

Heat Exchanger Cost Function

The heat exchanger cost function was developed using vendor quotes sourced for various sCO₂ applications. All quotes represent heat exchangers that are pressure- and temperature-rated for the target conditions. Quotes were for a mixture of water-cooled and air-cooled heat exchangers. See quotes summarized in Figure 3 as a function of thermal duty. Based on these data, a linear cost function was used

$$\text{Cost (USD)} = 70 * Q$$

where Q is the rated thermal duty of the heat exchanger in kilowatts.

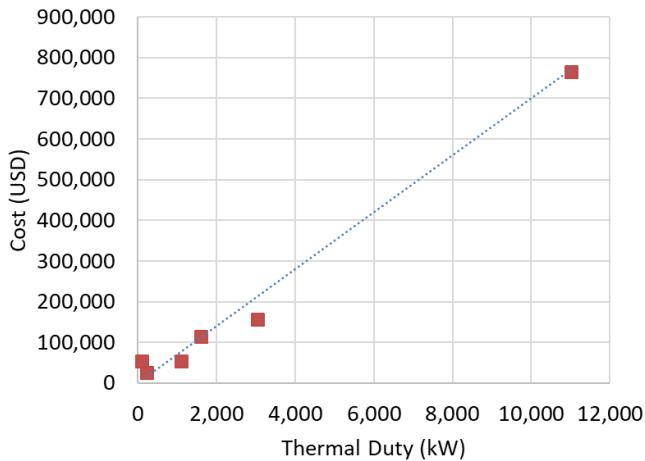


Figure 3: Summary of heat exchanger quotes used to define cost function.

Pipe Cost Functions

The linear pipe cost was segmented based on pipe size and rating. The minimum required pipe wall thickness was calculated using the methods detailed in the ASME B31.1 Power Piping Code. For the smaller scale applications where a very large elevation gain is not achievable (as in applications 1 through 3), the peak pressure in the cycle is very near the critical point. For this reason, a design pressure of 12 MPa was used to choose the minimum piping thickness. Stainless steel pipe was assumed for the increased corrosion resistance with sCO₂. For pipe sizes below 1.5-inch NPS, schedule 5 piping is sufficiently rated. For pipe sizes up to 3.5-inch NPS, schedule 10 piping is sufficient. For pipe sizes up to 12-inch NPS, schedule 40 piping is sufficient. The pipe sizing breaks and the estimated linear piping cost per length are presented in Figure 4.

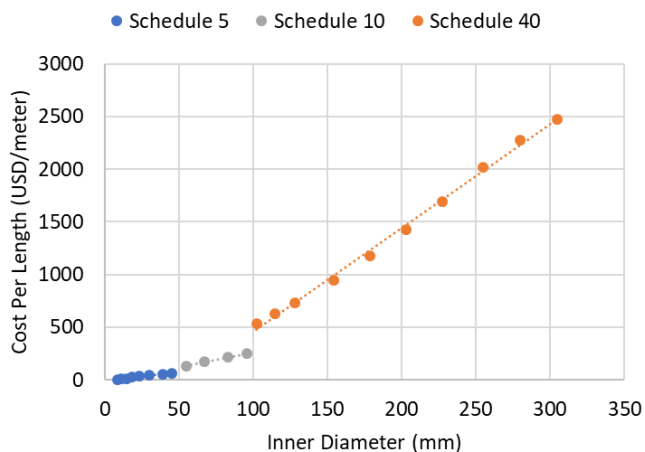


Figure 4: Linear cost function, pipe schedule selected using ASME B31.1 power piping code.

The associated linear cost functions (in U.S. dollars per meter) for each pipe schedule are

Schedule 5	Cost = 1.54 * ID - 4.18
Schedule 10	Cost = 2.81 * ID - 18.03
Schedule 40	Cost = 9.87 * ID - 531

where ID is the inner pipe diameter in millimeters.

The piping flange cost was accounted for separately. For pipe sizes below 1.5-inch NPS, a flat cost of 383.33 USD was used. For larger pipe sizes, the following cost function was utilized.

$$\text{Cost (USD)} = 0.049 * \text{ID}^2 - 0.65 * \text{ID} + 312.82$$

where ID is the inner pipe diameter in millimeters. This cost function assumes 900# ANSI raised-face flanges. This flange rating is sufficient at these pressures and temperatures, but at higher operating temperatures a higher flange rating will be required. For this study, it was assumed that six flanges will be required, one at each connection for the heat exchangers and the turbine.

The elbow costs were also accounted for separately. For pipe sizes below 1.5-inch NPS, the elbow cost was calculated as

$$\text{Cost (USD)} = 0.40 * \text{ID} + 11.19$$

where ID is the inner pipe diameter. For larger pipe sizes, the elbow cost was calculated as

$$\text{Cost (USD)} = 0.038 * \text{ID}^2 - 2.14 * \text{ID} + 23.00,$$

again, where ID is the inner pipe diameter.

The costs used here to estimate the cost functions for the linear pipe, the flanges, and the elbows were based on historical pricing and supplier quotes for stainless steel piping and fittings.

Power Generation/Conversion Cost Function

This cost function accounts for the cost of the generator and power conversion equipment to move from mechanical power to useable electrical power. Generator quotes were sourced for multiple sizes from three vendors. Vendor quotes were also collected to estimate the baseline cost for a rectifier, capacitors, inverter module, and a DC/DC module. Note that the power conversion setup must be customized for each specific application to suit the power output needs and the power generation scale. However, this cost was included as an estimate for the electrical power conversion. The following cost function was utilized in this study.

$$\text{Cost (USD)} = 0.106 * P + 3407.70$$

where P is the turbine power output in watts.

Geothermal Cost

It is expected that the cost functions presented here scale suitably for the first three applications (2 MW-th to 10 MW-th). However, it is expected that the cost of the geothermal application may be higher than what these cost functions will predict. The higher pressure turbine inlet pressure and higher rotational speeds present additional challenges with the turbine shaft and casing designs. Furthermore, drilling and casing a well is expected to be more costly than the sum of linear piping and a typical heat exchanger. For this reason, 20% additional cost was added to the value predicted using these simple linear cost functions.

RESULTS & DISCUSSION

Within this section, results of the trade study performed for each application are summarized. The input parameters, predicted isentropic turbine power, isentropic thermal efficiency, capital cost, and cost per power are presented for multiple configurations considered for each application.

(1) 2 MW-th Data Center

The 2 MW-th data center application considered heat rejection from data center servers with a thermal load of 2 MW. In a new installation, the cooling passages among the server racks could be built integral to the natural convection system, such that the CO₂ is providing direct cooling. Alternatively, the natural convection loop could be installed as a secondary system in which cooling air rejects heat from the servers and then an air-CO₂ heat exchanger cools the air before it is recycled through the servers. This installation would be well-suited for a data center retrofit.

Nine cycle configurations are presented here. The input conditions considered are presented in Table 3. In this study, the cold-side and hot-side CO₂ temperatures were held constant. All combinations of three pipe diameters and three loop heights were considered.

Table 3: Cycle input conditions for 2 MW-th data center

Config.	T-cold (°C)	T-hot (°C)	Pipe ID (mm)	Height (m)
1	30.0	66.6	154.1	15
2	30.0	66.6	202.8	15
3	30.0	66.6	254.3	15
4	30.0	66.6	154.1	20
5	30.0	66.6	202.8	20
6	30.0	66.6	254.3	20
7	30.0	66.6	154.1	25
8	30.0	66.6	202.8	25
9	30.0	66.6	254.3	25

Consistent with previous results, the highest available power and thermal efficiency are predicted for the natural convection loop with the highest elevation change (Figure 5). Among the cases with the same loop height, peak power and efficiency were achieved when the largest pipe size was used

(minimizing pressure losses and increasing mass flow). As expected, the capital cost of the natural convection loop increases with loop height and pipe size (Figure 6). However, the lowest cost per power is predicted for configuration 7, which has the largest loop height but the smallest pipe size. This result shows that the additional power output gained by increasing the loop height offsets the increased linear piping cost. However, the power output gained by increasing the pipe size does not offset the increase piping cost (including linear pipe, flanges, and elbows).

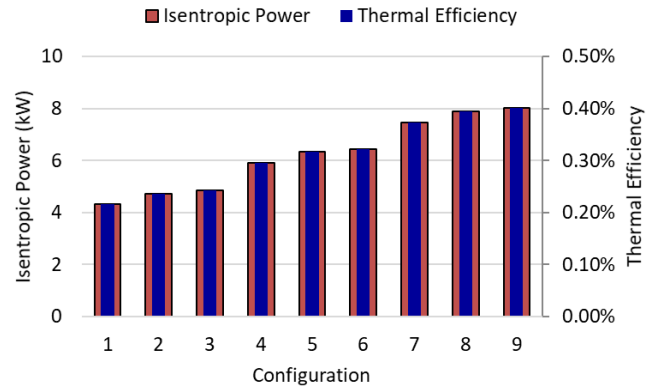


Figure 5: Cycle performance predictions for 2 MW-th data center

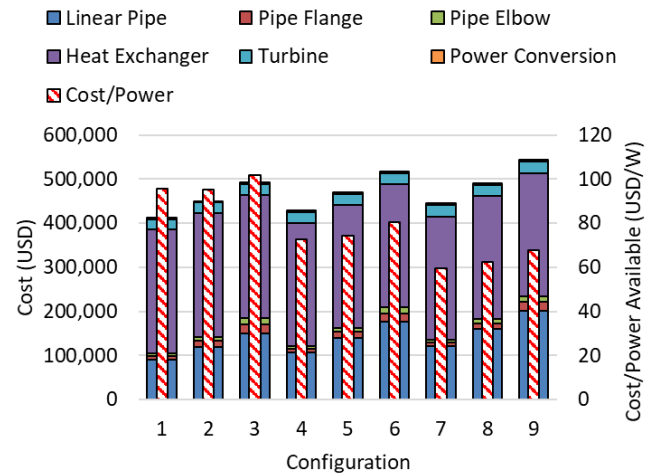


Figure 6: Capital cost predictions for 2 MW-th data center

Configuration 7 is considered the best case of those presented here. This configuration utilized a loop height of 25 meters and a pipe diameter of 154.1 mm (6-inch NPS). For CO₂ temperatures of 30.0°C and 66.6°C, an isentropic turbine power of 7.46 kW was predicted yielding a thermal efficiency of 0.37%. The predicted capital cost is \$444,494; the predicted cost per power is \$59.57/W. See the steady-state cycle operating point for configuration 7 presented in Table 4.

Table 4: Steady-state cycle operating conditions for 2 MW-th data center, configuration 7

CO ₂ Conditions	Cooler Inlet	Cooler Outlet	Heater Inlet	Heater Outlet
Temperature (°C)	65.4	30.0	30.0	66.6
Pressure (MPa)	7.5111	7.5108	7.6714	7.6708
Density (kg/m ³)	164.7	662.4	678.4	168.1
Enthalpy (kJ/kg)	474.0	291.4	288.4	474.2
Mass Flow (kg/s)	11.06			
Isen. Power (kW)	7.46			

(2) 4 MW-th Data Center

The 4 MW-th data center application is the same as the previous case, differing only by the thermal load. Eleven cycle configurations are presented. The input conditions are summarized in Table 5. For this trade study, the loop height was held constant. Three CO₂ temperature combinations were considered with various pipe sizes.

Consistent with previous results, the highest power and thermal efficiencies were predicted for the configurations utilizing the lowest CO₂ cold-side temperature and the largest pipe sizes (Figure 7). For the second temperature combination (30.0°C and 66.6°C), power gains did not increase significantly for pipe diameters greater than 254.3 mm. At this point, the frictional losses through the piping have been minimized, so further increasing pipe size presents no benefit.

As expected, the capital cost of the loop increases with pipe size (Figure 8). The lowest cost per power is predicted for the configurations utilizing the lowest cold-side CO₂ temperature. In this study, smaller pipe sizes were considered to determine the cost per power minimum for fixed temperature conditions. The lowest cost per power is predicted for configuration 6, which has a cold-side CO₂ temperature of 30.0°C, a hot-side temperature CO₂ of 66.6°C, and a pipe diameter of 254.3 mm. At smaller pipe sizes, the cost per power value is predicted to significantly increase because the produced power decreases as the frictional losses through the piping become larger.

Table 5: Cycle input conditions for 4 MW-th data center

Config.	T-cold (°C)	T-hot (°C)	Pipe ID (mm)	Height (m)
1	35.0	66.6	303.0	20
2	35.0	66.6	333.2	20
3	35.0	66.6	381.0	20
4	35.0	66.6	428.8	20
5	30.0	66.6	202.8	20
6	30.0	66.6	254.3	20
7	30.0	66.6	303.0	20
8	30.0	66.6	333.5	20
9	30.0	66.6	381.0	20
10	35.0	70.0	333.3	20
11	35.0	70.0	381.0	20

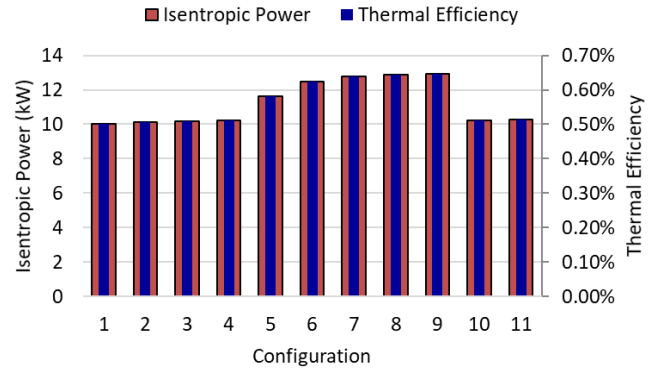


Figure 7: Cycle performance predictions for 4 MW-th data center

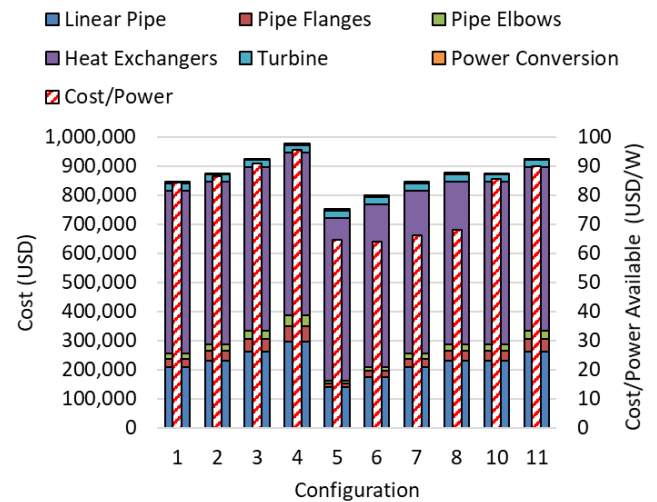


Figure 8: Capital cost predictions for 4 MW-th data center

Configuration 6 is considered the best case of those presented here (see Table 6). This configuration utilized a loop height of 20 meters and a pipe diameter of 254.3 mm (10-inch NPS). For CO₂ temperatures of 30.0°C and 66.6°C, an isentropic turbine power of 12.5 kW was predicted yielding a thermal efficiency of 0.62%. The predicted capital cost is \$799,712; the predicted cost per power is \$64.00/W.

Table 6: Steady-state cycle operating conditions for 4 MW-th data center, configuration 6

CO ₂ Conditions	Cooler Inlet	Cooler Outlet	Heater Inlet	Heater Outlet
Temperature (°C)	65.6	30.0	30.0	66.6
Pressure (MPa)	7.4880	7.4879	7.6166	7.6163
Density (kg/m ³)	164.6	659.6	673.5	166.3
Enthalpy (kJ/kg)	474.7	291.9	289.3	474.8
Mass Flow (kg/s)	22.12			
Isen. Power (kW)	12.50			

(3) 10 MW-th Industrial

This application considered heat rejection from an industrial process with a substantial heat load of 10 MW-th. An industrial facility is expected to have a large building that can support a tall natural convection loop; a loop height of 25 meters was considered. The hot-side heat exchanger would be specific to the heat rejection application, but the cold-side heat exchanger was assumed to be a finned-tube array exposed to ambient air. The cold-side CO₂ temperature was held at 32°C for this trade study, as the cooling potential would be limited by the ambient air conditions. Ten cycle configurations are presented. Hot-side CO₂ temperatures of 120°C and 200°C were considered with varied pipe sizes (Table 7).

Table 7: Cycle input conditions for 10 MW-th industrial application

Config.	T-cold (°C)	T-hot (°C)	Pipe ID (mm)	Height (m)
1	32.0	120.0	406.4	25
2	32.0	120.0	355.6	25
3	32.0	120.0	323.9	25
4	32.0	120.0	273.1	25
5	32.0	120.0	219.1	25
6	32.0	200.0	406.4	25
7	32.0	200.0	355.6	25
8	32.0	200.0	323.9	25
9	32.0	200.0	273.1	25
10	32.0	200.0	219.1	25

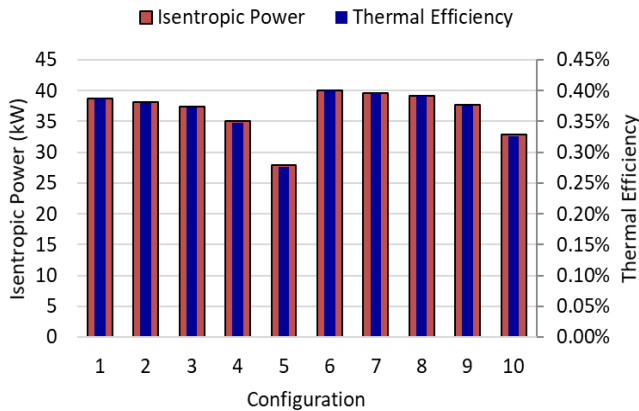


Figure 9: Cycle performance predictions for 10 MW-th industrial application

Consistent with previous results, the highest available power and thermal efficiency are predicted for the natural convection loop with the largest pipe size and the highest CO₂ hot-side temperature (Figure 9). As expected, the capital cost of the natural convection loop increases with pipe size (Figure 10). The lowest cost per power is predicted for configuration 8 (see Table 8), which utilizes a hot-side CO₂ temperature of 200°C

and a pipe diameter of 323.9 mm (12-inch NPS). This configuration yielded an isentropic turbine power of 39.2 kW and a thermal efficiency of 0.39%. The predicted capital cost is \$1.727M; the predicted cost per power is \$44.08/W.

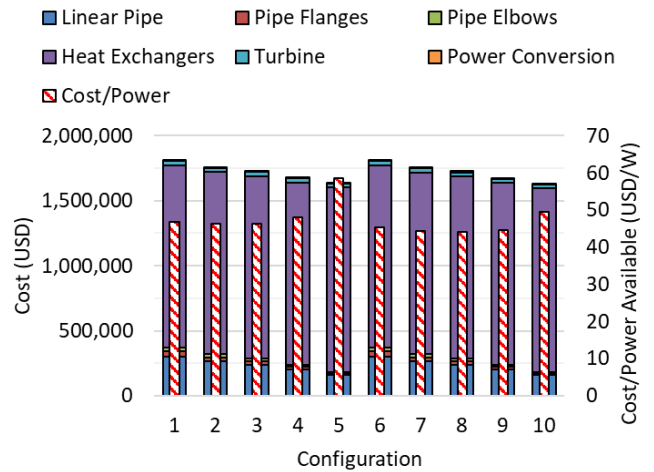


Figure 10: Capital cost predictions for 10 MW-th industrial application

Table 8: Steady-state cycle operating conditions for 10 MW-th industrial application, configuration 8

CO ₂ Conditions	Cooler Inlet	Cooler Outlet	Heater Inlet	Heater Outlet
Temperature (°C)	198.4	32.0	32.0	200.0
Pressure (MPa)	8.1869	8.1868	8.3505	8.3502
Density (kg/m ³)	99.0	669.9	682.1	100.6
Enthalpy (kJ/kg)	637.1	293.0	290.7	638.4
Mass Flow (kg/s)	28.93			
Isen. Power (kW)	39.17			

(4) 80 MW-th Geothermal

This application considered a geothermal application using a fully closed-loop well, meaning the downhole piping acts as the heat exchanger and the CO₂ does not directly contact the formation. An elevation change of 2,300 meters and a lateral length of 1,000 meters were assumed for this study. Cold-side and hot-side CO₂ temperatures of 25°C and 240°C were utilized for all configurations. Six configurations were considered with pipe size varying from 16-inch NPS to 34-inch NPS. See the cycle input parameters summarized in Table 9.

In this study, it was found that the peak power and thermal efficiency were achieved at the larger pipe sizes (Figure 11). However, these larger pipe sizes significantly increase the capital cost and the cost per power (Figure 12). The lowest cost per power was actually predicted for the smallest pipe size considered (configuration 1). Configuration 1 (see Table 10) yielded an isentropic turbine power of 13.35 MW and a thermal efficiency of 16.7%. The predicted capital cost is \$38.09M; the predicted cost per power is \$2.85/W.

Table 9: Cycle input conditions for 80 MW-th geothermal application

Config.	T-cold (°C)	T-hot (°C)	Pipe ID (mm)	Height (m)
1	25.0	240.0	381.0	2300
2	25.0	240.0	428.8	2300
3	25.0	240.0	478.0	2300
4	25.0	240.0	574.5	2300
5	25.0	240.0	777.8	2300
6	25.0	240.0	828.6	2300

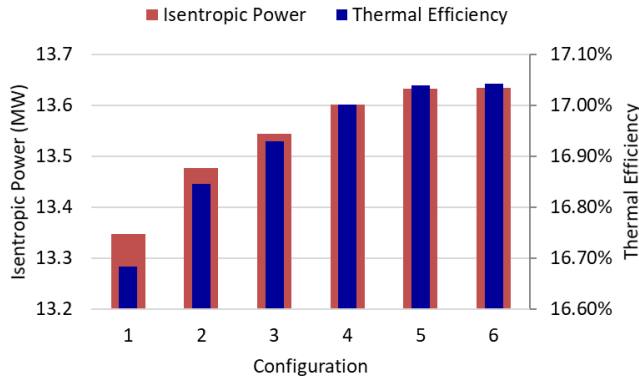


Figure 11: Cycle performance predictions for 80 MW-th geothermal application

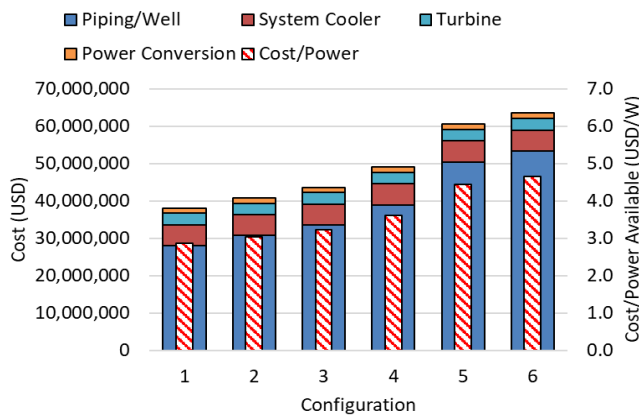


Figure 12: Capital cost predictions for 80 MW-th geothermal application

Table 10: Steady-state cycle operating conditions for 80 MW-th geothermal application, configuration 1

CO ₂ Conditions	Cooler Inlet	Cooler Outlet	Heater Inlet	Heater Outlet
Temperature (°C)	151.7	25.0	25.0	240.0
Pressure (MPa)	7.4000	7.3830	24.3830	24.3800
Density (kg/m ³)	102.9	757.9	939.8	275.9
Enthalpy (kJ/kg)	586.9	266.3	242.4	640.7
Mass Flow (kg/s)	190.23			
Isen. Power (kW)	13,346.21			

Scale Comparison

The capital cost is predicted to increase with the waste-heat thermal duty (Figure 13). The capital cost steps up two orders of magnitude from the 2 MW-th case to the 80 MW-th case. However, this study also shows that the specific capital cost per power significantly reduces with increased waste-heat load. This is due to the significant increase in power output with increased thermal scale. When comparing the first three cases (2 MW-th to 10 MW-th), the predicted power increases with thermal duty at about the same rate as the capital cost. There was a much more significant increase in power output between the 10 MW-th case and the 80 MW-th geothermal case (relative to the increase in capital cost); this is expected to be due to the increased thermal duty as well as the significantly larger elevation change in the loop. It is expected that the increased elevation change also significantly improved the thermal efficiency (to 16.7%), as the thermal efficiency predicted for the first three cases was relatively constant (between 0.37% and 0.62%).

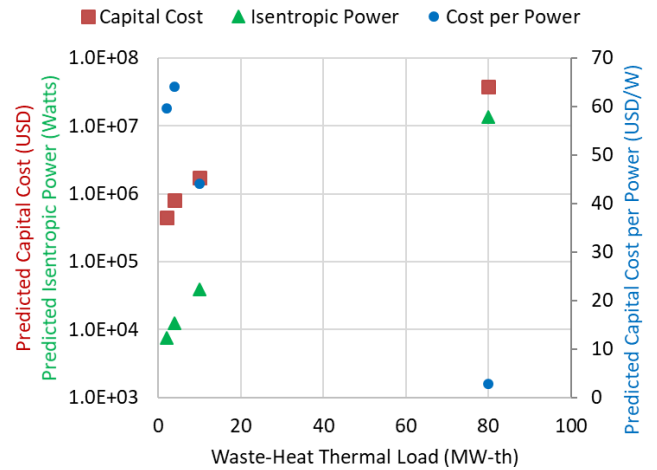


Figure 13: Capital cost and power output predictions for various thermal scales

CONCLUSIONS

In this study, it was found that a natural convection cycle can produce significant levels of power utilizing only waste heat and a single turbomachine. The performance was found to vary with thermal scale, CO₂ conditions, and loop sizing. These results were consistent with the results of previous studies. Here, it was also found that the capital cost is expected to follow the trends of cycle power, namely capital cost increases with pipe size, loop height, and CO₂ temperature delta. However, it was found that the specific capital cost per power did not necessarily follow these trends. In general, it was found that cost per power decreased with increasing loop height, meaning the additional power output gained by increasing the loop height offsets the increased linear piping cost. It was also found that the pipe size should be optimized for the target operating conditions. Increasing the pipe size above the

optimum increases cost without improving power; at this point the frictional losses in the piping have gone to zero, so further increasing diameter presents no power gains. However, using a pipe size below the optimum increases the frictional losses (limiting mass flow and power output), which decreases capital cost but increases the cost per power. In general, the capital cost per power can be minimized by increasing elevation change across the loop, reducing CO₂ cold-side temperature, and selecting an intermediate pipe size.

It was found that the cost per power also decreases with thermal duty. Increasing the amount of heat transfer to the natural convection cycle increases density change across the cycle, in turn increasing pressure gain, mass flow, and power output. The thermal efficiency was also predicted to improve at larger thermal scales. As the performance improves, the cost per power is driven down. This poses the geothermal application at a competitive cost point of 2.85 dollars per watt-electric for utility-scale power generation. This also meant that the smaller thermal scales have a relatively high cost per power, but it should be noted that the total capital cost is relatively low (well below \$1M for the smallest scales presented). Furthermore, the heat exchanger cost was predicted to make up the largest portion of the capital cost for the smaller-scale applications. Simplifying heat exchanger design for the target applications could further reduce the capital cost for a natural convection cycle installation.

The natural convection cycle calculations showed that significant power levels can be produced using CO₂ hot-side temperatures as low as 67°C; this could translate to waste-heat applications with source temperatures well below 100°C. These results show that the thermal efficiency and power increase proportionally with loop height and thermal load more significantly than with hot-side temperature, separating this cycle from the typical organic Rankine and Kalina cycles. If a substantial pressure gain can be achieved across the loop, high source temperatures are not required.

It is understood that the thermal efficiencies for the natural convection cycle at smaller scales are low. However, the system simplicity and the cycle's ability to operate in a self-sustaining and passive manner allow this technology to be competitive in very low-grade waste heat applications where the efficiencies of organic Rankine cycles and Kalina cycles cannot compete because the cost per power becomes too high. The simplicity and compactness of the natural convection power cycle make this an attractive option for building retrofit for residential, commercial, and industrial energy recovery.

NOMENCLATURE

ID	Inner pipe diameter
MW-th	megawatt thermal
NPS	nominal pipe size
P	isentropic turbine power
Q	rated thermal duty
sCO ₂	supercritical carbon dioxide
T	temperature

USD	United States dollars
WHR	waste heat recovery

ACKNOWLEDGEMENTS

This project was funded and supported by the Southwest Research Institute Internal Research & Development program.

REFERENCES

- [1] United States Department of Energy. (2015). Waste heat Recovery Technology Assessment.
- [2] BCS, Incorporated. (2008). Waste Heat Recovery: Technology and Opportunities in the U.S. Industry. U.S. Department of Energy, Industry Technologies Program.
- [3] Chandra, R.R. (2017). A study on Carbon-dioxide Based Thermosiphon Circulation Loop with End Heat Exchangers. *International Journal for Research in Applied Science & Engineering Technology (IJRASET)*, vol. 5, pp. 1721-1726.
- [4] Yadav, A.K., Gopal, M.R., and Bhattacharyya, S. (2012) CO₂ based natural circulation loops: New correlations for friction and heat transfer. *International Journal of Heat and Mass Transfer* 55, pp. 4621-4630.
- [5] Sharma, M. (2014) Investigation into steady state and stability behavior of natural circulation systems operating with supercritical fluids. Tokyo Metropolitan University, Japan, Tokyo.
- [6] Chen, L., Zhang, X.R., Cao, S., and Bai, H. (2012) Study of trans-critical CO₂ natural convection flow with unsteady heat input and its implications on system control. *International Journal of Heat and Mass Transfer*, vol 55, pp. 7119-7132.
- [7] Sharma, D. and Murari, P.K. (2015) Computational Study of Effect of Increasing Heat Flux on Convective Heat Transfer in Sub Channels of Carbon Dioxide Flow at Pressure Above Critical Value. *Applied Mechanics and Materials*, vol. 772, no. 1662-7482, pp. 8-13.
- [8] Lei, X., Zhang, Q., Zhang, J., and Li, H. (2017). Experimental and Numerical Integration of Convective Heat Transfer of Supercritical Carbon Dioxide at Low Mass Fluxes. *Applied Sciences*, vol. 7, issue. 12, no. 1260.
- [9] Atrens, A.D., Gurgenci, H., and Rudolph, V. (2009). CO₂ Thermosiphon for Competitive Geothermal Power Generation. *Energy & Fuels*, vol. 23, pp. 553-557.
- [10] Gurgenci, H., (2015). Options to Use Solar Heat to Enhance Geothermal Power Plant Performance. *Proceedings World Geothermal Congress, Melbourne, Australia.*
- [11] Higgins, B.S. and Oldenburg, C.M. (2016). Process Modeling of a Closed-Loop sCO₂ Geothermal Power Cycle. *The 5th International Supercritical CO₂ Power Cycles Symposium, San Antonio, TX, USA.*
- [12] Katcher, K. M., Allison, T., Marshall, M., and Smith, N. R. (2020). Low-Cost, Low-Grade Waste Heat Recovery Using sCO₂ Natural Convection. *Proceedings of the 7th*

International Supercritical CO₂ Power Cycles Symposium. San Antonio, Texas, USA.

- [13] Balje, O. E. (1981). *Turbomachines: A Guide to Design Selection and Theory*. John Wiley & Sons, New York.
- [14] Aungier, R. H. (2000). *Centrifugal Compressors: A Strategy for Aerodynamic Design and Analysis*. ASME Press.

- [15] Nielson, J.T., Smith, N.R., Katcher, K.M., Allison, T.A., Marshall, M. (2021) Novel Power Conversion to Utilize sCO₂ Natural Convection for Low-Grade Waste Heat Recovery. Proceedings of ASME Turbo Expo 2021.

OPERATIONAL ANALYSIS OF A SELF-PROPELLING HEAT REMOVAL SYSTEM USING SUPERCRITICAL CO₂ WITH ATHLET

Markus Hofer*
University of Stuttgart
Stuttgart, Germany
Email: hofer@ike.uni-
stuttgart.de

Michael Buck
University of Stuttgart
Stuttgart, Germany

Jörg Starflinger
University of Stuttgart
Stuttgart, Germany

ABSTRACT

This study proposes preliminary guidelines for the design and operation of a supercritical carbon-dioxide (sCO₂¹) heat removal system for nuclear power plants. Based on a thermodynamic optimization the design point is calculated incorporating an existing small-scale compressor map. The behavior of the cycle is tested under varying boundary conditions on the steam side of the compact heat exchanger. The simulations are carried out with the thermal-hydraulic system code ATHLET, which has been extended for the simulation of sCO₂ power cycles. The extensions include the thermodynamic properties, heat transfer and pressure drop correlations as well as performance map based turbomachinery models, which take the real gas behavior of sCO₂ into account. During the decay heat transient, compressor surge occurs in some of the simulated cases. In order to avoid compressor surge and to follow the decay heat curve, the compressor speed is reduced together with the steam temperature. This enables to operate one single system down to a thermal load of less than 50 % even under the design restriction caused by the application of the existing compressor performance map.

INTRODUCTION

In case of a station blackout (SBO) and loss of ultimate heat sink (LUHS) accident in a boiling water reactor (BWR) or pressurized water reactor (PWR), the plant accident management strongly depends on the depends on the recovery of electricity, e.g. by emergency diesel generators, or from external sources. If not available, core integrity may be violated, like in Fukushima Dachi. Such scenarios lead to the development of advanced

decay heat removal systems. Since space is a limitation in existing power plants, the supercritical carbon-dioxide (sCO₂) heat removal system “sCO₂-HeRo” was proposed [1–3]. This system can be incorporated in new nuclear power plants as well as retrofitted to existing nuclear power plants. The system consists of a compact heat exchanger (CHX), a gas cooler, serving as the ultimate heat sink (UHS), and the turbomachinery, one compressor and one turbine mounted on a common shaft together with a generator. Since the momentum from the turbine is sufficient to simultaneously drive the compressor and generate more electricity than used by the fans of the UHS, the system is self-propelling. The excess electricity can even be used to support other accident measures, e.g. recharging batteries. sCO₂ is selected as a working fluid because of its favorable fluid properties, enabling the design of a very compact system. Moreover, sCO₂ is not combustible, non-toxic and commercially available.

Figure 1 shows the scheme of the sCO₂-HeRo attached to a BWR. In the case of an accident the valves, which connect the compact heat exchanger (CHX) to the main steam line, open automatically. Driven by natural circulation, the steam condenses and heats the sCO₂ in the CHX. Due to the space limitations, the CHX consists of many channels with a small hydraulic diameter, so called mini-channels, in order to reach a large heat transfer area [1]. The pressurized and heated sCO₂ is expanded in the turbine, which drives the compressor and generates power for the fans of the gas cooler. After the turbine, the remaining heat of the sCO₂ is removed in the gas cooler to the ultimate heat sink. Finally, the sCO₂ is compressed and flows to the CHX. Similarly, the sCO₂-HeRo can be attached to the

¹ sCO₂ is defined as carbon dioxide at supercritical conditions with $p > 73.8$ bar and $T > 31$ °C

secondary loop of a PWR. In the primary loop natural circulation will develop due to the decay heat input and the heat removal via the steam generator. Consequently, the sCO₂-HeRo can be used for BWRs as well as PWRs.

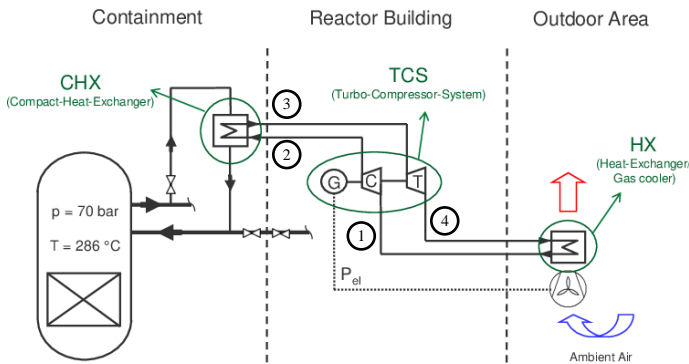


Figure 1: The sCO₂ heat removal system attached to a BWR [1] including the different states in the cycle: compressor inlet (1), compressor outlet (2), turbine inlet (3), turbine outlet (4)

For the simulation of nuclear power plants, different thermal hydraulic system codes are used, e.g. CATHARE, RELAP, TRACE and ATHLET [4]. Because sCO₂ is also considered as a working fluid in the power generation cycle of 4th generation reactor concepts, work is in progress to extend these system codes for the simulation of sCO₂ power cycles [1], [5], [6], [7], [8]. Venker investigated the feasibility of the sCO₂-HeRo approach for a BWR in detail and implemented first extensions in ATHLET for the simulation of the heat removal system. First simulations showed that the grace period can be extended to more than 72 h [1]. The grace period is the period of time for which the nuclear power plant remains in a safe condition without the need of human interaction [9]. In the frame of the sCO₂-HeRo-project further reports and studies were published, e.g. dealing with the start-up of the system or the design and control [2,10–12]. In the frame of the project, Hecker and Seewald [10] analysed the decay heat removal from a BWR with a nuclear power plant simulator. This analysis suggested that manual actions by operators and a higher heat removal capacity than proposed by Venker would be necessary to avoid automatic depressurisation at low level in the reactor vessel. Because a comparable level drop on the secondary side of a steam generator does not initiate automatic depressurization from the reactor protection system, more operational flexibility can be expected for a PWR. Hajek et al. describe the basic principles for the integration of the sCO₂-HeRo into the European PWR fleet including safety, reliability and thermodynamic design considerations [11,12]. Hofer et al. carried out preliminary design calculations and provided considerations for the operation of the Brayton cycle, e.g. it may be beneficial to locate the design point of the turbomachinery in part load and the system may be operated via a shaft speed control [13].

In general, the analysis of the sCO₂-HeRo approach can be conducted considering different time intervals and levels of

complexity. In terms of time, the accident can be divided into the first phase, where the decay heat exceeds the heat removal capacity of the system, and the second phase, where the heat removal capacity is higher. Regarding complexity, different parts of the system or the whole system can be analyzed. This paper focusses on the sCO₂ cycle including the steam side of the CHX and on the second phase regarding time. Compared to previous publications, the sCO₂ cycle is modelled and analyzed in more detail. In the theoretical section, this paper shortly presents design and operational considerations for the sCO₂-HeRo system and the extensions of the thermal-hydraulic system code ATHLET (Analysis of THERmal-hydraulics of LEaks and Transients). In the results section, the system design is provided using the scaled performance map of the compressor designed in the sCO₂-HeRo project [8,14]. Afterwards, the system is simulated in ATHLET considering and comparing different control strategies.

THEORY

Cycle design and operation

In case of an accident, the main purpose of the sCO₂-HeRo system is to remove the decay heat reliably over several days. Due to the exponential decrease of the decay heat and due to changing ambient conditions, the system must be able to operate over a wide range of conditions. From a thermodynamic point of view, the worst condition for the system occurs at the highest ambient temperature and the smallest decay heat input per system, which is considered. Consequently, it might be a valid approach to start the system design from this point. However, the lowest ambient temperatures must also be taken into account, because if no operational action is undertaken the compressor inlet temperature will decrease with the ambient temperature. This leads to an increasing compressor inlet density and potentially drives the compressor to surge. To avoid approaching the surge line, one option is to keep the compressor inlet temperature sufficiently high. This can be achieved by decreasing the fan speed in order to decrease the performance of the gas cooler. However, it must be checked if this measure is sufficient for the lowest ambient temperatures because heat transfer occurs also with the fans switched off. An additional measure is to design a modularized gas cooler which enables decoupling of certain sections or to increase the compressor mass flow rate via a bypass. Ambient temperature variations and extremely low ambient temperatures are not in the scope of this paper and will be analyzed in the future. This paper analyses the operation of the system at the highest ambient temperature, which is assumed to be 45 °C, with the naturally declining decay heat as boundary condition.

The next step to the system design is to define the maximum thermal power, which must be removed reliably by the system. Venker has shown that it is not necessary to design the system for the maximum decay heat occurring directly after the reactor scram [1]. Depending on the power plant type (BWR or PWR), the time delay allowed to start the system along with additional supporting systems, as well as the required system capacity differ. As a first step, the required system size can be determined

with a simple heat balance or obtained by means of reactor simulations where the system is represented by a heat sink. As long as the decay power exceeds the thermal power of the system, steam is blown off to keep the pressure below a certain threshold. Since, it is assumed that the water inventory cannot be replaced, the water level must be kept high enough to enable the operation of the sCO₂-HeRo as well as to ensure the cooling of the reactor core. Former analysis demonstrated that more than one system is needed to follow the declining decay heat curve [1]. In this paper, a system size of 10 MW is selected, which enables the use of this system for different reactor types and sizes, because just the number of systems has to be adapted. A simple heat balance suggested that 60 MW might be sufficient for a PWR with a thermal power of 3840 MW. Comparing the total power of the sCO₂-HeRo system to the decay heat curve suggests a power break even after 3000 s. Thus, the system operates at its maximum power from start-up to 3000 s and then the system has to adapt to the declining decay heat, shown in Figure 2. According to the User Manual of ATHLET ANS Standard ANS-5.1-1979 is used [15] and the same curve as in the analysis of Venker is applied, which is the decay heat occurring after 300 days of operation [1]. After the power break even, removing more power from the reactor than is produced by the decay heat will cause a cool down of the reactor. This results also in a lower temperature difference being available for the sCO₂-HeRo and eventually will stop the operation of the system because the power balance becomes negative as will be shown in the results section. Venker already demonstrated the need for a balance between heat generation and heat removal in order to obtain a stable operation of the sCO₂-cycle attached to a BWR [1]. Since the decay heat is decreasing continuously, it might be necessary to control the system in part load. The required part load capability of the system also depends on the number of systems installed and the control strategy. Future analysis will consider these aspects in more detail. However, the general procedure and the conclusion presented in this paper will still stay valid because this analysis is not dependent on the system size or the time of power break even.

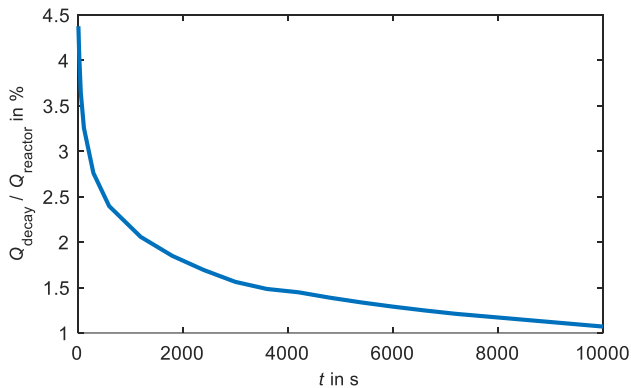


Figure 2: Decay power [1,10,15] divided by the thermal power of the reactor over time

After these general considerations the thermodynamic design of the system will be discussed in more detail. As mentioned before, the worst operation point of the system is the lowest power input per system at the highest ambient temperature. At this point, the turbomachinery efficiencies must be high enough to guarantee a self-propelling operation. This should be considered in future designs using an integrated design approach, which iteratively adapts the cycle and turbomachinery design. In this paper, the design will be carried out at the maximum power input per system with an existing compressor performance map. The heat exchangers should also be designed for this point because they are required to remove the design power. The thermodynamic cycle design can be conducted using a simple thermodynamic optimization [13] using the basic thermodynamic relations for and between the components also involving the isentropic efficiencies of the compressor and the turbine [16]. The optimization maximizes the specific power output of the system and not the efficiency because the system shall be self-propelling as long as possible and the system efficiency is of no interest. For given compressor inlet temperature ϑ_1 , turbine inlet temperature ϑ_3 , turbomachinery efficiencies η_c and η_t , pressure drops in the heat exchangers Δp_{UHS} and Δp_{CHX} and the relative power consumption of the fans k_{fan} , the compressor inlet and outlet pressure p_1 and p_2 are optimized to maximize the specific power output of the system

$$\Delta w = f(p_1, p_2, \vartheta_1, \vartheta_3, \eta_c, \eta_t, k_{fan}, \Delta p_{UHS}, \Delta p_{CHX}). \quad (1)$$

For the thermodynamic design point optimization, the piping pressure drop is neglected and the power of the fans is assumed to be a linear function of the heat removal capacity. The excess power of the cycle ΔP is calculated by multiplying Δw with the mass flow rate of the cycle.

Simulation of the Brayton cycle

The code extensions of ATHLET described in the following can be found in more detail in publications of Venker [1] and Hofer et al. [8,17]. In the supercritical region, the thermodynamic properties of CO₂ are calculated with fast splines, which were derived from the equation of state [18]. In ATHLET, the heat transfer coefficient of CO₂ is calculated with the Gnielinski correlation [19]. The pressure drop of supercritical CO₂ is derived from the Colebrook equation, which is recommended for normal pipes as well as for mini-channels [20]. Additionally, form loss coefficients can be applied, to e.g. model the inlet and outlet plenum of the CHX. For water the implemented correlations [21] are used except for the film condensation, where the ATHLET correlations were improved [17] and now the correlations given in [22,23] are used. For turbine and compressor, different models are available. In this paper, Stodola cone law [24] and an efficiency correlation for radial turbines [25] is used for the turbine. The compressor is simulated with a performance map approach [8,26]. The performance map generated from experimental data or CFD simulations is transposed to a dimensionless map, shown in Figure 3.

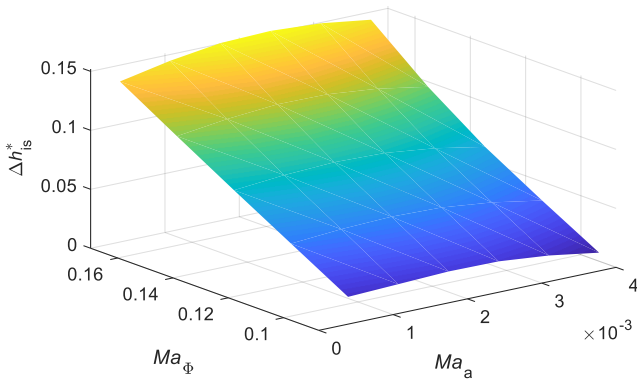


Figure 3: Dimensionless isentropic enthalpy difference Δh_{is}^* as a function of the axial and tangential Mach Numbers (Ma_a and Ma_θ)

The x- and y-axis are the axial and tangential Mach numbers, given by

$$Ma_a = \frac{\dot{m}}{\rho c D^2} \quad (2)$$

$$Ma_\theta = \frac{ND}{c}, \quad (3)$$

where N is the rotational speed, D the impeller diameter and c the speed of sound. All thermodynamic parameters are determined for the inlet condition. As main difference to other performance map approaches, the speed of sound is calculated via the equation of state and not using ideal gas assumptions. On the z-axis the dimensionless isentropic enthalpy difference Δh_{is}^* or the corrected pressure ratio π_c and the efficiency η can be presented. The equation for the dimensionless isentropic enthalpy difference is

$$\Delta h_{is}^* = \frac{\Delta h_{is}}{c^2}. \quad (4)$$

RESULTS AND DISCUSSION

Cycle design

As mentioned in the theory section, the cycle design is carried out for the maximum heat load, which is 10 MW per unit, at an ambient temperature of 45 °C. The boundary conditions for the design calculation are summarized in Table 1. With the pinch point temperature differences, the compressor and turbine inlet temperature can be calculated. Then the optimal design point can be found according to the procedure described in the theory section. However, for the simulation of the compressor an existing performance map of small-scale compressor [14] shall be scaled-up and used. This is carried out using equations 2, 3 and 4 and, but conservatively, without any additionally efficiency correction. Therefore, the efficiency of the large-scale compressor is equal to the efficiency of the given small-scale

compressor. The pressure ratio and the outlet state can be determined with the inlet state and the performance map using equation 4. Since, the condition at the compressor inlet is also given by the thermodynamic optimization, the compressor outlet condition is defined by the underlying performance map. Thus, the optimization of p_1 and p_2 reduces to an optimization of only p_1 with p_2 given by the compressor characteristic.

Table 1: Boundary conditions for the design process

Parameter	Unit	Value
\dot{Q}_{CHX}	MW	10
$\Delta T_{PP,CHX}$	K	10
$\Delta T_{PP,UHS}$	K	5
$\Delta T_{sub,H2O}$	K	8
Δp_{CHX}	bar	2
Δp_{UHS}	bar	0.25
$\vartheta_{in,H2O}$	°C	296
$h_{in,H2O}$	kJ/kg	2760
η_c	-	0.72
η_t	-	0.8
k_{fan}	kW _{el} / MW _{th}	8.5

The thermodynamic design parameters from the optimization process are summarized in Table 2. Compared to conventional sCO₂ cycles, the design point is located quite far above the critical point with a compressor inlet state of 50 °C and 12 MPa. The high compressor inlet pressure results from the high design point ambient temperature of the system.

Table 2: Optimal thermodynamic design point with the restriction of the existing compressor performance map

	ϑ in °C	p in MPa
Compressor Inlet (1)	50	12
Compressor Outlet (2)	69	18.8
Turbine Inlet (3)	286	18.7
Turbine Outlet (4)	246	12

In Figure 4, the power output for the optimized design conditions is shown varying the turbine inlet temperature and the pressure ratio. The actual design point is located at the maximum temperature and at a pressure ratio of 1.57. On the contrary, the theoretical optimal design point is also located at the maximum temperature and at a pressure ratio of 3.09. The power output of the system at these two points is 440 kW and 807 kW,

respectively. Due to the application of an existing small-scale compressor map, the thermodynamic design point deviates from the optimal design point in terms of pressure ratio. The efficiency of the system with 4.4 % is quite small. However, as mentioned before, the only task of the system is to remove the decay heat reliably and not to generate power, therefore, the efficiency is of no interest. The lower pressure ratio of the actual design might result in a worse performance in the transient calculation because e.g. reducing the shaft speed decreases the pressure ratio further. However, the main focus here is to present the procedure and to enable an off-design simulation of the system and not to give quantitative results for the best system design. Additionally, it might be sufficient to choose a compressor with a pressure ratio smaller than the optimum value, which might reduce the system cost keeping in mind that the pressure ratio of a single stage compressor is technically limited to approximately 2.0. The compressor speed and the impeller diameter of the large-scale compressor can be determined using equations 2 and 3. Since, the design point Mach numbers of the small-scale machine are the same for the large-scale machine and the compressor inlet condition is given by the thermodynamic optimization, it is possible to solve the two equations for the two unknowns. This results in a compressor impeller diameter of 0.22 m and a rotational speed of 12700 1/min.

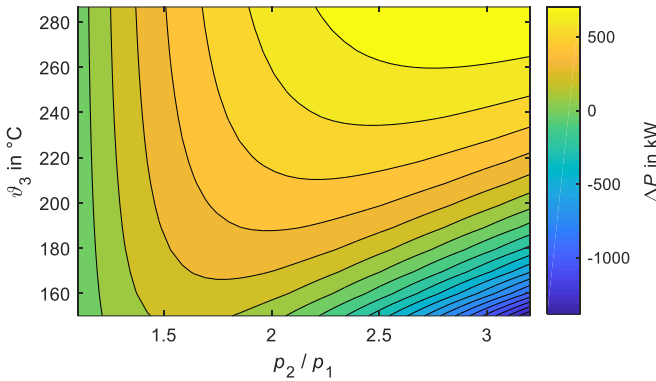


Figure 4: Maximized power output ΔP as a function of pressure ratio p_2/p_1 and turbine inlet temperature ϑ_3 for the given design boundary conditions

The geometry of the CHX plates follows [16,17]. The channel length and number are adapted to reach the desired temperatures and transferred power. The steam is assumed to enter the CHX saturated and to leave slightly subcooled. For the 2x1 mm rectangular channels, this results in 11070 channels with a length of 0.85 m. They can be arranged into 90 plates with 123 channels each, leading to a size of approximately 0.9 m x 0.4 m x 0.2 m. For the UHS an existing design [27] was scaled down leading to 190 pipes with a length of 15 m. For simplicity the design only covers the sCO₂-side. The pipe length between the components and the diameter is assumed to 22.5 m and 0.2 m, respectively [12]. The whole design is valid for a cycle attached to a PWR. In case of a BWR the steam temperature could be slightly lower due to the lower blow-off pressure. This can be

compensated by slightly modifying the whole design or by just adapting the CHX to reach a lower pinch point temperature difference.

Simulation of the Brayton cycle

In this section, the simulated system, the boundary conditions and the simulation results for the sCO₂-HeRo cycle are shown and operational conclusions are drawn. Assuming that in the first phase of the accident the heat removal system operates at its maximum capacity of 10 MW per unit, the transient analysis is started at 3000 s when the decay power is equal to the system capacity. As mentioned before, the ambient temperature is set to 45 °C. However, this is not modelled explicitly, because no design of the air-side of the UHS is available. Instead, it is assumed that the cooling power \dot{Q}_{UHS} can be controlled via the fan speed to reach the desired temperature difference between the compressor inlet temperature $\Delta T_{PP,UHS}$ and the ambient temperature. This assumption should be valid because the decay power is declining slowly after 3000 s. Since the nuclear power plant is not simulated, boundary conditions for the steam must be provided. The conditions at the start are given by the design with saturated steam at 296 °C at the inlet and slightly subcooled water at 288 °C at the outlet of the CHX. From a power balance, the steam mass flow rate can be determined, which is 7 kg/s at the design point of the system. The initial conditions are the same for all cases. During the transient, the enthalpy at the inlet of the CHX are always kept at the saturation point of steam for the given temperature. Therefore, the pressure at the inlet is also the saturation pressure. To provide an overview of the boundary conditions, they are summarized in Table 3 and the case specific boundary conditions will be explained in detail at the beginning of each case.

Table 3: Boundary conditions of analyzed cases

	Case 1	Case 2	Case 3a	Case 3b	Case 4
\dot{m}_{H_2O}	declining	constant	declining	declining	calculated
h_{in,H_2O}	at saturation point of steam ($x=1$) for all cases				
ϑ_{in,H_2O}	constant	declining	constant	constant	declining
$\Delta T_{sub,H_2O}$	not constant (result)		constant at design value		
$\Delta T_{PP,UHS}$	constant at design value except for 3b (increasing)				
N	constant at design value		controlled to match $\Delta T_{sub,H_2O}$		
\dot{Q}_{UHS}	controlled to match $\Delta T_{PP,UHS}$				
$\dot{Q}_{CHX} / \dot{Q}_{decay}$ (result)	>1	≈1	1		

The nodalization of the ATHLET model is shown in Figure 5. The H₂O side consists of an inlet, an outlet and the CHX channels. The enthalpy is specified at the inlet and the pressure at the outlet. Through a heat conduction object the H₂O side is

connected to the CO₂ side. The CO₂ side is a complete cycle with four pipes connecting the components, namely the compressor, the CHX, the turbine and the UHS. The compressor and the turbine component are described by lumped parameter models providing sink or source terms for the momentum and energy conservation equation [8]. The CHX is modelled with a representative channel pair including form loss coefficients for the inlet and outlet plenum [8,17]. As mentioned before, the heat transfer in the UHS is not modelled explicitly. Instead, the power input to the UHS is adapted, to match a certain compressor inlet temperature.

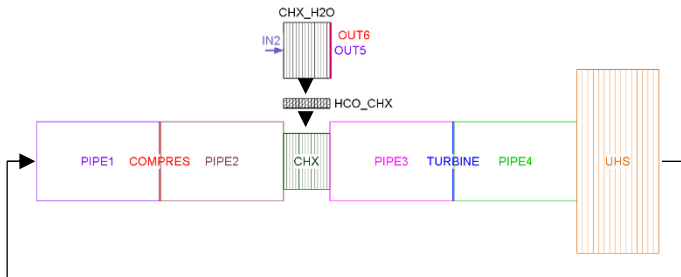


Figure 5: Nodalization of the ATHLET model

Case 1

In a first simulation, the system is operated at its design speed. The steam mass flow rate \dot{m}_{H_2O} is defined to follow the decay heat curve, which means if inlet and outlet conditions stayed constant at their design values given in Table 1, the transferred power would exactly equal the decay power. However, in off-design the transferred power is higher than the decay power, as shown in Figure 6, because the condensate is subcooled compared to the design point. Thermodynamically, this would lead to a decreasing steam temperature as well as steam pressure because of the negative thermal power balance. Therefore, the inlet conditions of the CHX would change in reality, which affects the performance of the system. This is analysed in case 2.

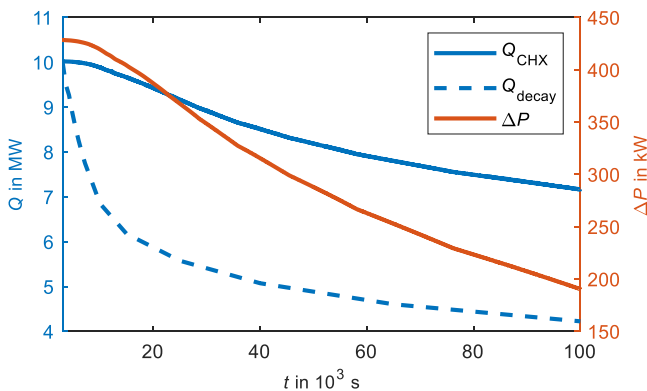


Figure 6: Decay power \dot{Q}_{decay} , removed power \dot{Q}_{CHX} and power output of the system ΔP over time for case 1

For completeness, Figure 6 also includes the power output of the system. However, this value has to be interpreted with care because the thermodynamic conditions in a real power plant will change as explained before. Another important point about this simulation is the operation of the compressor. It can be observed that the compressor operates at higher Ma_a and Ma_θ than in the design. This is caused by the decrease of the compressor inlet pressure at an almost constant mass flow rate. Since, the performance map ends at the design Ma_θ , the results of this simulation must be interpreted carefully because either the performance calculated by linear extrapolation might be unrealistic or the compressor might even not be able to work in this region anymore. At the time, when the simulation stops, Ma_θ is 9 % higher than its design value. Therefore, if the system shall be operated at constant speed all the time, it is necessary to extend the performance map and it might be required to design the compressor and the shaft for higher loads.

Case 2

In a second simulation, the shaft speed of the turbomachinery is kept constant again. The effect of the cool down of the steam side is examined. The steam mass flow rate is kept constant at its design point and the steam inlet temperature and pressure are decreased keeping the inlet saturated. The decrease is adapted to approximately follow the decay heat curve, which can be observed from Figure 7. This enables to analyse the influence of decreasing steam temperatures on the sCO₂ cycle. In the nuclear power plant, the steam temperature would decrease with some delay because of the large water inventory. In this case, the sCO₂ cycle stops operating at a steam temperature of 175 °C at 25000 s, because the power balance becomes negative, which is shown in Figure 7.

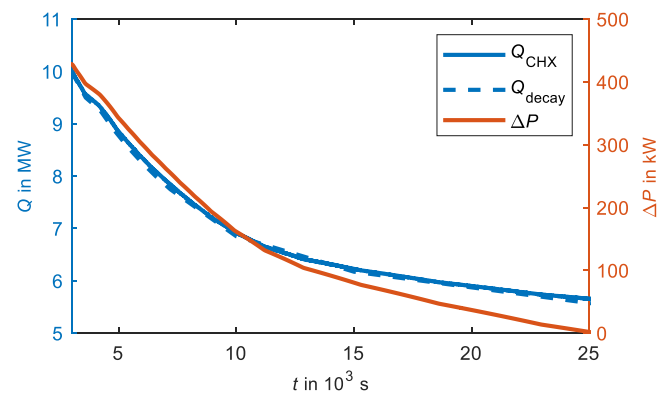


Figure 7: Decay power \dot{Q}_{decay} , removed power \dot{Q}_{CHX} and power output of the system ΔP over time for case 2

The negative influence of decreasing steam temperatures and, therefore, turbine inlet temperatures can be also observed from Figure 4. A failure of all sCO₂-HeRo systems can be avoided by either switching off single units at the right time, as suggested by Venker [1], or by controlling the transferred power of the systems or by a combination of both measures. The

disadvantage of just switching off single units at a certain time is that the right time for the shutdown needs to be determined. Another option would be to follow the decay heat curve by controlling the sCO₂ cycle. This will be analysed in the next case.

Like in the previous case, it has to be noted that the compressor operates at higher Ma_a and Ma_θ than in the design. This is due to the same reasons as in case 1. At the time, when the simulation stops, Ma_θ is 14 % higher than its design value. In this case, the effect is stronger because the compressor inlet pressure decreases further.

Case 3

In the third simulation, the boundary conditions of the first simulation are applied and, additionally, the shaft speed of the turbomachinery is controlled in order to keep the sub-cooling $\Delta T_{sub,H2O}$ at the water outlet constant. Thus, all thermodynamic conditions of the water-side remain constant, only the mass flow rate varies according to the decay heat. Therefore, the removed heat exactly equals the decay heat. At the beginning, this method works well, but after 20000 s the system stops because of compressor surge. The operation line of the compressor is shown in Figure 8 together with the numerical surge line. The current case is labelled “3a”. The numerical surge line is located where Δh_{is}^* reaches its maximum with changing Ma_a . To the right of the surge line is the stable operation range, to the left of it the unstable range. The other simulations also included in this figure are presented in the following sections. Additionally, the cycle mass flow rate over time is displayed in Figure 8 to indicate the stop of the system and support the following discussion.

When the compressor crosses the surge line in the simulation, the simulation becomes unstable and stops. In order to avoid compressor surge, the decrease of the axial Mach number Ma_a must be limited. According to equation 2, this can be achieved by reducing the density and the speed of sound at the compressor inlet (measure 1) or by limiting the mass flow rate decrease compared to the current simulation (measure 2). Measure 2 can be enforced by decreasing the steam temperature, as explained later together with case 4, or with a compressor recirculation line or a turbine bypass. In this paper, only the basic layout without additional bypasses is considered to keep the heat removal system as simple as possible. Furthermore, since no inventory control system has been considered, measure 1 can only be achieved by increasing the compressor inlet temperature ϑ_1 (measure 1.1) or by decreasing the inlet pressure p_1 (measure 1.2). An increase of ϑ_1 can be achieved by also increasing the temperature difference between the ambient air and the compressor inlet $\Delta T_{PP,UHS}$. This action corresponds to a decrease of the fan speed.

In simulation 3b, this measure is tested by applying all boundary conditions of simulation 3a except for $\Delta T_{PP,UHS}$, which is increased steadily during the simulation. From Figure 8, it can be observed that the compressor surge is postponed but still occurs after 45000 s. At this time, ϑ_1 is already increased by 13 K and the power output of the system almost decreased to zero.

Thus, the increase of ϑ_1 also leads to a lower power output of the system. Consequently, the system will stop due to either compressor surge or a negative power balance. The occurring compressor surge is mainly due to the decrease of the mass flow rate, which is similar to simulation 3a. Therefore, measure 1.1 is not sufficient without taking into account measure 2. Furthermore, measure 1.1 should be avoided due to the negative impact on the power output, as explained above.

Case 4

In order to define the boundary conditions for the next simulation, it is necessary to understand how the compressor inlet pressure (measure 1.2) and the mass flow rate of the cycle (measure 2) can be influenced. At a constant power input the cycle mass flow rate increases when the enthalpy difference of the sCO₂ over the CHX decreases. The current enthalpy difference is mainly linked to the steam temperature and decreases as the steam temperature decreases. A reduction of the steam temperature also reduces the temperatures at the hot side of the sCO₂ cycle and, therefore, increases the density. Due to constant mass inventory in the cycle, a part of the mass from the cold side moves to the hot side of the cycle and, therefore, pressure and density at the compressor inlet decrease. Thus, both measure 1.2 and measure 2 can be achieved by decreasing the steam temperature.

Therefore, simulation 4 investigates a steam temperature decrease. At the foreseen end of the simulation at 100000 s, the steam temperature is arbitrarily reduced to 200 °C and the temperature decrease is assumed to follow the decay heat curve. Like in the previous simulations, the enthalpy and pressure at the inlet are set to saturation conditions. It is assumed that the mass flow rate of the steam changes with the decreasing temperature. The current value of the mass flow rate is adapted to match the current decay power while keeping the temperature difference between steam inlet and water outlet constant at design conditions. Thus, the decay power equals the transferred power. The additional power for cool down of the water inventory is neglected because it only improves the behaviour of the system due to the higher power input. Furthermore, the additional power required for cool down depends on the water mass on the secondary side, which is not part of this analysis. Therefore, in the future the nuclear power plant model must be incorporated into the simulation. In Figure 8, the operation line of this simulation is shown. Similar to the previous simulation the operation condition moves towards the surge line. However, it stays in the stable region until the end of the simulation. The excess power of the system, shown in Figure 9 (top left), gradually reduces from 430 kW at full load to 40 kW at the end of the simulation. If the steam temperature is decreased further, or if the required power for other systems is too high, the power balance will become negative. Therefore, it can be concluded that the current design can be operated down to a part load of approximately 45 % in terms of thermal power. A better-optimized system might be able to reach even a lower load. To

follow the decay heat curve further, it would be necessary to switch off one system.

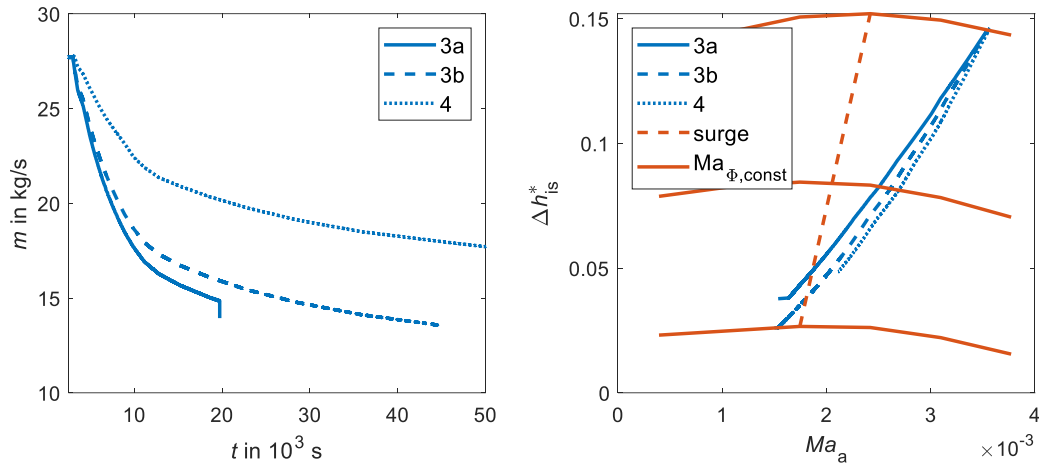


Figure 8: Compressor operation line on the dimensionless compressor map including the surge line (right) and mass flow rate of the sCO₂ cycle (left) for the simulations 3a, 3b and 4

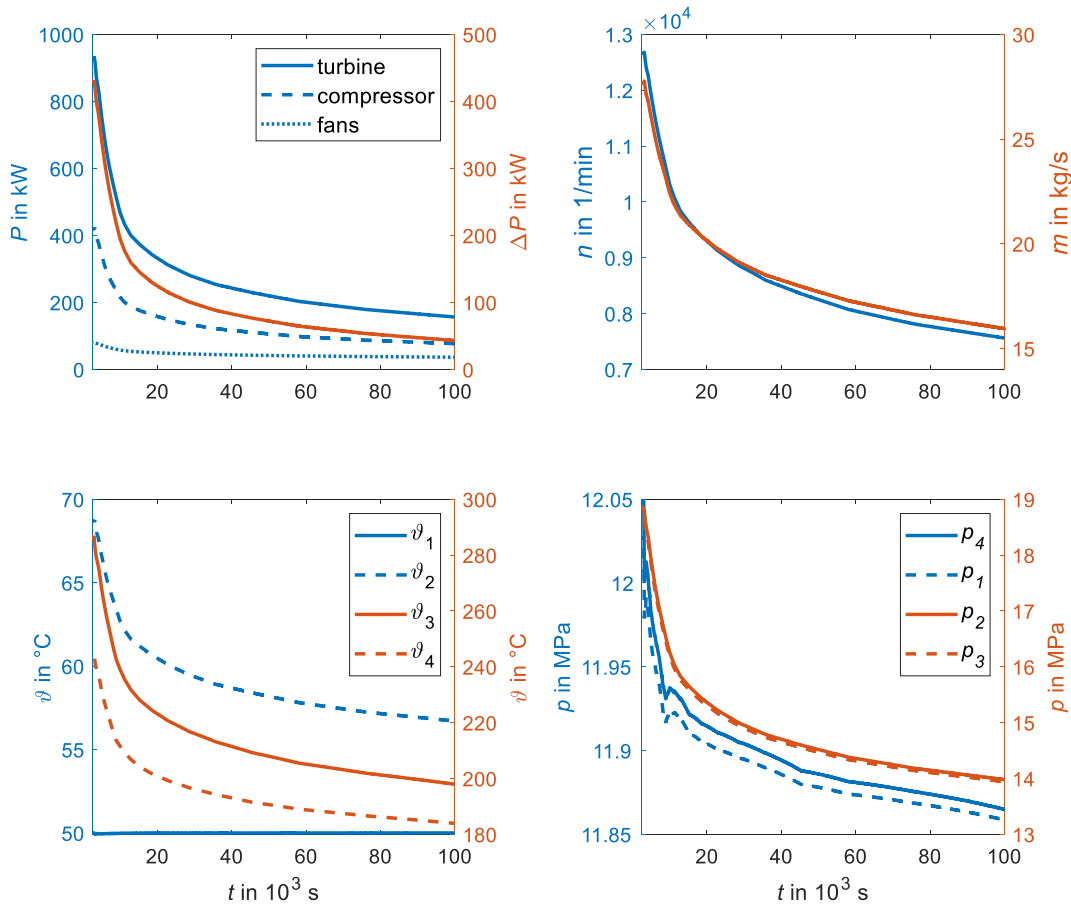


Figure 9: Power and excess power (top left), shaft speed and mass flow rate (top right), temperatures (bottom left) and pressures (bottom right) of simulation 4

In order to provide an overview of the successful simulation, the main results are summarized and displayed in Figure 9. At the end of the simulation, the speed of the turbomachinery is reduced to 60 % and the mass flow rate to 58 % (top right). The compressor inlet temperature ϑ_1 (bottom left) remains constant because it is controlled as proposed in the boundary conditions. The turbine inlet temperature ϑ_3 (bottom left) declines as a result of the declining steam temperature, which results in the intended decrease of the enthalpy difference over the CHX. The upper cycle pressures p_2 and p_3 (bottom right) are decreasing due to the decreasing pressure ratio of the compressor, which decreased from 1.57 at the design point to 1.18. The efficiencies of the turbomachinery stay close to their design values because the flow conditions inside the machines remained in a beneficial region. The non-smooth behaviour of the lower pressures p_1 and p_4 (bottom right) might be caused by the small change of the slope of the decay heat curve, which is input as table for this simulation. Furthermore, it must be noticed that p_1 and p_4 nearly stay constant, therefore small changes are clearly visible.

CONCLUSION

In this study, the sCO₂ heat removal system is designed and simulated under varying steam side boundary conditions. The simulations are carried out in the thermal-hydraulic system code ATHLET, which has been extended for the simulation of sCO₂ power cycles. The extensions include the thermodynamic properties, heat transfer and pressure drop correlations as well as performance map based turbomachinery models, which take the real gas behavior of sCO₂ into account.

The design of the sCO₂ cycle is conducted with a thermodynamic optimization maximizing the power output of the system. In order to extend the part load capability of the system, it might be beneficial to especially consider the part load operation of the turbomachinery together with the thermodynamic design in an integrated approach. Due to the application of an existing small-scale compressor map, the thermodynamic design point deviates from the optimal design point in terms of pressure ratio. However, this design with a relatively small pressure ratio of 1.57 was sufficient to ensure the operation of the system down to a part load of less than 50 % in terms of thermal power.

Two different failure modes of the system could be identified, namely a negative power balance and compressor surge. If the shaft speed of the cycle is not controlled, the cycle will remove more heat than is produced by the decay heat. This leads to a cool down of the steam side in the nuclear power plant and eventually stops the systems because the power balance becomes negative. To adapt to the declining decay heat curve, either single systems need to be switched off at the right time or the system must be controlled to remove less power from the nuclear power plant. The removed power can be adapted to the decay heat curve by controlling the shaft speed to keep the thermodynamic conditions at the steam side constant at design conditions. However, this drives the compressor to surge as the shaft speed is reduced. In order to avoid compressor surge, the steam side must be cooled down when the shaft speed is reduced.

In conclusion, instead of running the systems always at full speed also other operation strategies are possible. Considering all systems together, one operation strategy might be to follow the decay heat curve with all systems until the systems reach 50 % part-load. Then one system is switched off and the other systems are ramped up to a higher load again to compensate the loss of heat removal capacity. If the part load capability is 50 %, this procedure can be repeated until only one system is running, because when the second last system is shut down, the last system can be ramped up to 100 % again and compensates the loss of the second last system completely. If the operation point of the compressor moves too close to the surge line, the speed should not be reduced further. This causes a slow decline of the steam temperature since more power is removed than produced. Consequently, the operation point of the compressor moves away from the surge line and the speed can be reduced again. The advantage of this procedure is that, perhaps, this control strategy can be automatized and it is not necessary to determine the right time for the shutdown of single systems because in this strategy the shutdown condition of a single system is explicitly defined. Even if this strategy is not implemented in the beginning of the accident, it will be important in the long term when only one last system is still running.

The next step in the system analysis is to explicitly model the air-side of the UHS. Then it is possible to analyse the system behaviour and control under varying ambient temperatures. This enables to test strategies to avoid compressor surge at very low ambient temperatures. Afterwards, the condensation driven circulation loop on the steam side should be modelled and finally the whole nuclear power plant must be incorporated in the simulation to investigate the interaction of the sCO₂-HeRo system with the nuclear power plant and other safety systems. In the future, the analysis will be conducted for a BWR as well as for a PWR to confirm and extend the knowledge basis for this new safety system. In parallel, the data and the models will be improved and validated further, e.g. the performance map of a large-scale compressor will be used and the turbomachinery and heat transfer models will be compared to experimental data.

NOMENCLATURE

c	speed of sound (m/s)
D	impeller diameter (m)
h	enthalpy (J/kg)
k_{fan}	relative power consumption of the fans (kW_{el} / MW_{th})
\dot{m}	mass flow rate (kg/s)
Ma_a	axial Mach number
Ma_θ	tangential Mach number
N	rotational speed (1/min)
p	pressure (MPa)
\dot{Q}	transferred power (W)
t	time (s)
x	steam quality
<i>Greek letters</i>	
Δh_{is}^*	dimensionless isentropic enthalpy difference
Δp	pressure drop (MPa)

ΔT_{PP}	pinch point temperature difference (K)
Δw	specific power output (J/kg)
ϑ	temperature (°C)
η_c	isentropic efficiency of compressor
η_t	isentropic efficiency of turbine
ρ	density (kg/m ³)

Subscripts

1	compressor inlet
2	compressor outlet
3	turbine inlet
4	turbine outlet

Acronyms

ATHLET	Analysis of THERmal-hydraulics of LEaks and Transients
BWR	boiling water reactor
CHX	compact heat exchanger
H ₂ O	water/steam
HeRo	heat removal system
PWR	pressurized water reactor
sCO ₂	supercritical carbon dioxide
UHS	ultimate heat sink

ACKNOWLEDGEMENTS

The research presented in this paper has received funding from the Euratom research and training programme 2014-2018 under grant agreement No. 847606 “Innovative sCO₂-based Heat removal Technology for an Increased Level of Safety of Nuclear Power plants” (sCO₂-4-NPP).

The work of University of Stuttgart was also funded by the German Ministry for Economic Affairs and Energy (BMWi. Project No. 1501557) on basis of a decision by the German Bundestag.

REFERENCES

- [1] Venker, J. (2015) Development and Validation of Models for Simulation of Supercritical Carbon Dioxide Brayton Cycles and Application to Self-Propelling Heat Removal Systems in Boiling Water Reactors. Stuttgart. <https://doi.org/10.18419/opus-2364>
- [2] sCO₂-HeRo. <http://www.sco2-hero.eu/>
- [3] Benra, F.K., Brillert, D., Frybort, O., Hajer, P., Rohde, M., Schuster, S. et al. (2016) A supercritical CO₂ low temperature Brayton-cycle for residual heat removal. *The 5th International Symposium-Supercritical CO₂ Power Cycles*, 1–5. <https://doi.org/10.1007/s13398-014-0173-7.2>
- [4] Bestion, D. (2008) System code models and capabilities. *THICKET*, Grenoble. p. 81–106.
- [5] Mauger, G., Tauveron, N., Bentivoglio, F. and Ruby, A. (2019) On the dynamic modeling of Brayton cycle power conversion systems with the CATHARE-3 code. *Energy*, Elsevier Ltd. 168, 1002–16. <https://doi.org/10.1016/j.energy.2018.11.063>
- [6] Batet, L., Alvarez-Fernandez, J.M., Mas de les Valls, E., Martinez-Quiroga, V., Perez, M., Reventos, F. et al. (2014) Modelling of a supercritical CO₂ power cycle for nuclear fusion reactors using RELAP5–3D. *Fusion Engineering and Design*, North-Holland. 89, 354–9. <https://doi.org/10.1016/J.FUSENGDES.2014.03.018>
- [7] Hexemer, M.J., Hoang, H.T., Rahner, K.D., Siebert, B.W. and Wahl, G.D. (2009) Integrated Systems Test (IST) Brayton Loop Transient Model Description and Initial Results. *S-CO₂ Power Cycle Symposium*, Troy. p. 1–172.
- [8] Hofer, M., Buck, M. and Starflinger, J. (2019) ATHLET extensions for the simulation of supercritical carbon dioxide driven power cycles. *Kerntechnik*, 84, 390–6. <https://doi.org/10.3139/124.190075>
- [9] IAEA. (1991) Safety related terms for advanced nuclear plants. Vienna.
- [10] Hecker, F. and Seewald, M. (2018) Deliverable 4.2: BWR simulations of decay heat management. sCO₂-HeRo.
- [11] Hajek, P., Vojacek, A. and Hakl, V. (2018) Supercritical CO₂ Heat Removal System - Integration into the European PWR fleet. *2nd European SCO₂ Conference*, Essen. p. 0–7. <https://doi.org/10.17185/dupublico/460>
- [12] Vojacek, A., Hakl, V., Hajek, P., Havlin, J. and Zdenek, H. (2016) Deliverable 1.3: Documentation system integration into European PWR fleet. sCO₂-HeRo.
- [13] Hofer, M. and Starflinger, J. (2019) Preliminary analysis of the design and operation conditions of a sCO₂ heat removal system. *Annual Meeting on Nuclear Technology*, Berlin. p. 1–8.
- [14] Hacks, A.J., Vojacek, A., Dohmen, H.J. and Brillert, D. (2018) Experimental investigation of the sCO₂-HeRo compressor. *2nd European SCO₂ Conference 2018*, 0–10. <https://doi.org/10.17185/dupublico/46088>
- [15] Lerchl, G., Austregesilo, H., Schöffel, P., von der Cron, D. and Weyermann, F. (2016) ATHLET User 's Manual. Garching. <https://doi.org/10.1007/s00227-005-0161-8>
- [16] Straetz, M.R., Mertz, R. and Starflinger, J. (2018) Experimental investigation on the heat transfer between condensing steam and sCO₂ in a compact heat exchanger. *2nd European SCO₂ Conference 2018*,. <https://doi.org/10.17185/DUEPUBLICO/46078>
- [17] Hofer, M., Buck, M., Strätz, M. and Starflinger, J. (2019) Investigation of a correlation based model for sCO₂ compact heat exchangers. *3rd European Supercritical CO₂ Conference*, Paris. p. 1–9. <https://doi.org/10.17185/dupublico/48874>
- [18] Span, R. and Wagner, W. (1996) A new equation of state for carbon dioxide covering the fluid region from the triple-point temperature to 1100 K at pressures up to 800 MPa. *Journal of Physical and Chemical Reference Data*, 25, 1509–96. <https://doi.org/10.1063/1.555991>
- [19] Hewitt, G.F. (1998) Heat exchanger design handbook. Begell House, New York.
- [20] Dostal, V., Driscoll, M.J. and Hejzlar, P. (2004) A

- Supercritical Carbon Dioxide Cycle for Next Generation Nuclear Reactors. *Technical Report MIT-ANP-TR-100*, 1–317. <https://doi.org/MIT-ANP-TR-100>
- [21] Austregesilo, H., Bals, C., Hora, A., Lerchl, G., Romstedt, P., Schöffel, P. et al. (2016) ATHLET Models and Methods. Garching.
- [22] Böckh, P. von and Wetzel, T. (2017) Wärmeübertragung: Grundlagen und Praxis. 7th ed. Springer, Berlin. <https://doi.org/https://doi.org/10.1007/978-3-662-55480-7>
- [23] Numrich, R. and Müller, J. (2013) J1 Filmkondensation reiner Dämpfe. *VDI-Wärmeatlas*, Springer Berlin Heidelberg, Berlin, Heidelberg. p. 1011–28. https://doi.org/10.1007/978-3-642-19981-3_63
- [24] Grote, W. (2009) Ein Beitrag zur modellbasierten Regelung von Entnahmedampfturbinen. Bochum.
- [25] Dyreby, J.J., Klein, S.A., Nellis, G.F. and Reindl, D.T. (2012) Development of advanced off-design models for supercritical carbon dioxide power cycles. American Nuclear Society - ANS; La Grange Park (United States).
- [26] Pham, H.S., Alpy, N., Ferrasse, J.H., Boutin, O., Tothill, M., Quenaut, J. et al. (2016) An approach for establishing the performance maps of the sc-CO₂ compressor: Development and qualification by means of CFD simulations. *International Journal of Heat and Fluid Flow*, 61, 379–94. <https://doi.org/10.1016/j.ijheatfluidflow.2016.05.017>
- [27] GEA Luftkühler GmbH. (2013) Luftgekühlter Wärmetauscher für CO₂ (Angebot).

DuEPublico

Duisburg-Essen Publications online

UNIVERSITÄT
DUISBURG
ESSEN

Offen im Denken

ub | universitäts
bibliothek

This text is made available via DuEPublico, the institutional repository of the University of Duisburg-Essen. This version may eventually differ from another version distributed by a commercial publisher.

DOI: 10.17185/duepublico/73942

URN: urn:nbn:de:hbz:464-20210330-130134-5



This work may be used under a Creative Commons Attribution 4.0 License (CC BY 4.0).